

The Fast Stochastic Matching Pursuit for Neutrino and Dark Matter Experiments

Yuyi Wang^{1,2,3}, Aiqiang Zhang^{1,2,3}, Yiyang Wu^{1,2,3}, Benda Xu^{1,2,3*}, Jiajie Chen⁴, Zhe Wang^{1,2,3}, Shaomin Chen^{1,2,3}

¹ Department of Engineering Physics, Tsinghua University, Beijing,100084,China.

² Center for High Energy Physics, Tsinghua University, Beijing,100084,China.

³ Key Laboratory of Particle & Radiation Imaging (Tsinghua University), Ministry of Education, China.

⁴ Department of Computer Science and Technology, Tsinghua University, Beijing,100084,China.

*Corresponding author(s). E-mail(s): orv@tsinghua.edu.cn;

Abstract

Photomultiplier tubes (PMT) are widely deployed at neutrino and dark matter experiments for photon counting. When multiple photons hit a PMT consecutively, their photo-electron (PE) pulses pile up to hinder the precise measurements of the count and timings. We introduce Fast Stochastic Matching Pursuit (FSMP) to analyze the PMT signal waveforms into individual PEs with the strategy of reversible-jump Markov-chain Monte Carlo. We demonstrate that FSMP improves the energy and time resolution of PMT-based experiments, gains acceleration on GPUs and is extensible to microchannel-plate (MCP) PMTs with jumbo-charge outputs. In the condition of our laboratory characterization of 8-inch MCP-PMTs, FSMP improves the energy resolution by up to 12% from the long-serving method of waveform integration.

Keywords: waveform analysis, MCP-PMT, energy resolution, time resolution, GPU acceleration

1 Introduction

Large detectors with photomultiplier tubes (PMT) around are set up for the invisible, enigmatic, challenging-to-detect neutrinos and dark matters. The electronic systems read photon-induced pulses embedded in the time series of PMTs voltage outputs, or *waveforms*. Experiments deploying full waveform readout includes KamLAND [1], Borexino [2], JUNO [3], Jinping Neutrino Experiment (JNE) [4–6], as well as XMASS [7], PandaX-4T [8] and LUX-ZEPLIN [9].

To reconstruct the energy and time of the events from the waveforms, a common method is to integrate the waveform to get the *charge* [10] as a predictor of visible energy, and to locate the peaks of the waveforms measuring the 10%-rising-edge [11] as photoelectron (PE) times. More sophisticated approaches use fitting or deconvolution [10, 12] based on empirical single PE templates to obtain the charge and PE arrival times together.

When the time difference of two PEs is small, their waveforms *pile up* [13], preventing reliable counting of the PEs. Therefore, a posterior distribution of PEs in the Bayesian sense is necessary to properly represent the uncertainty of the inference from the waveforms. For a complete Bayesian solution, we face a hierarchical, discrete-continuous and trans-dimensional challenge. *Fast Stochastic Matching Pursuit* (FSMP) is a fast and flexible algorithm to utilize all information from the waveforms. It was introduced in our previous publication of Xu et al. [12] with a comprehensive comparison of all the waveform analysis methods. It was then utilized to analyze a variety of PMTs and most notably adopted to the new microchannel-plate (MCP) PMTs [11] showing outstanding performance. To facilitate its understanding and application, we present the principles and details of FSMP in this article.

Without loss of generality, we use JNE [6], a liquid-scintillator (LS) detector under construction, as our discussion context. Section 2 gives an introduction of our methodology to tackle the challenge of PE pile-up. Performance evaluation based on simulation in Section 3 demonstrates the GPU acceleration and substantial improvement in energy resolution. Application of FSMP to experimental data in Section 4 provides a firm analysis basis to unveil the physics process inside MCP-PMTs.

2 Methodology

In FSMP, we use Gibbs Markov chain Monte-Carlo (MCMC), mixed with reversible jump MCMC (RJMCMC) [14] and Metropolis-Hastings construction [15] to analyze the waveforms by sampling from the posterior distribution of PE sequences. We adopt the notations by Xu et al. [12] and review only the essential definitions with an emphasis on the new MCP-PMTs.

2.1 Physical process

After a scintillator photon is emitted in an event and comes into the PMT, it hits some PEs out. The number of PEs N follows Poisson distribution [16, 17], with expectation μ . The expectation of this Poisson process is a function of time, also known as

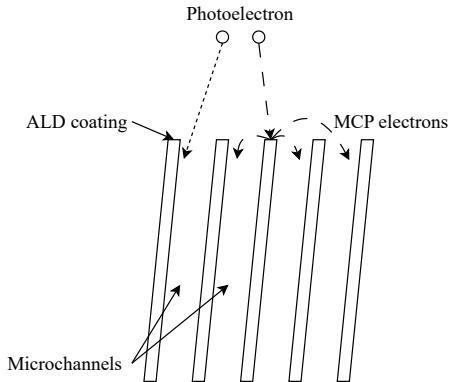
light curve: $\mu\phi(t - t_0)$, where $\phi(t)$ is a normalized function, and t_0 is a time offset. Lombardi [18] gives a method to calibrate light curve in LS.

A dynode PMT multiplies the electrons [19] on each of its many dynodes and collects them on the anode to produce a signal. Define the charge of a single PE as q , following normal distribution $\mathcal{N}(\mu_q, \sigma_q)$ [20]. Considering that N follows Poisson distribution $\pi(\mu)$, the charge distribution of waveforms is a compound Poisson-Gaussian distribution.

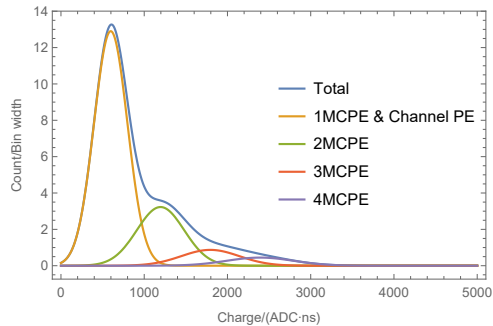
The dynodes may be replaced by MCP. The microchannels are atomic layer deposition (ALD) coated to improve the lifetime [21] and collection efficiency [22] but introduces *jumbo charges* [11]. In an MCP-PMT shown in Fig. 1a, there are two kinds of PE [23]. A PE may shoot directly into the microchannel and get multiplied, or hit on the ALD coating of the MCP upper surface. The latter produces multiple secondary electrons that we call *MCPes*. Here we define the case that PEs shot into the channel equal to the case that MCPes is 1. Define the MCPe count for one PE as $e \in E$, and generally $E = \mathbb{Z}_+$, while we choose $E = \{1, 2, 3, 4\}$ to make calculation simpler. In that way, the charge model of single PE inside the MCP-PMT is constructed by a mixture of normal distributions [24]. For one PE, define the probability of MCPe e as $G(e)$, and the charge model is like

$$\sum_{e \in E} G(e) f_{\mathcal{N}}(eq, \sqrt{e}\sigma_q) \quad (1)$$

$G(e), q, \sigma_q$ are the input parameters of FSMP. Fig. 1b shows a sketch of the charge distribution in this model.



(a) A sketch of MCP and MCPes.



(b) A sketch of the charge model of an MCP-PMT. It is not normalized, because the vertical axis represents the number of waveforms.

Fig. 1: Sketches of MCP, MCPe, and MCP-PMT charge model.

If there are no photons coming into a PMT, the electronics should read out *electronic noises* [25]. The average of noise is the *baseline* of a PMT [24, 26]. When electrons hit the anode, the voltage of the anode decreases, and the PMT produces a negative pulse [27]. To analyze the waveform, integrate it to calculate charge [25]. The dimension of waveform charge is voltage multiplied by time, proportional to the electric charge accumulated on the anode. This article uses the ADC as the unit of voltage, and nanosecond as the unit of time. The unit of the charge is ADC·ns.

When only one PE produced in the PMT and gets multiplied, the produced waveform is alike [27]. Define such single electron response (SER) of a PMT as $V_{\text{PE}}(t) = q\tilde{V}_{\text{PE}}(t)$, where q is the single PE charge, and \tilde{V} is the normalized SER. The single PE charge follows normal distribution: $q \sim \mathcal{N}(\mu_q, \sigma_q)$. With SER and the electronic noise ϵ , the final waveform w of a single PE is $w(t) = q\tilde{V}_{\text{PE}}(t) + \epsilon$.

2.2 Bayesian Inference

Let the light curve in Section 2.1 be $\mu\phi(t - t_0)$ while t_0 be the time of event. Define the PE sequence $\mathbf{z} = \{t_1, t_2, \dots, t_N\} \in T^N$ as the time of each PE, the number of PEs as N , and the waveform as \mathbf{w} . With Bayesian theory [28], we can write down

$$p(\mathbf{z}, t_0 | \mathbf{w}) = \frac{p(\mathbf{w} | \mathbf{z}, t_0)p(\mathbf{z}, t_0)}{p(\mathbf{w})} \quad (2)$$

For a specific waveform, $p(\mathbf{w})$ is a constant. $p(\mathbf{z}, t_0)$ is the prior, and $p(\mathbf{z}, t_0 | \mathbf{w})$ is the posterior. However, we do not know the true μ and the true prior $p(\mathbf{z}, t_0) = p(\mathbf{z} | \mu, t_0)p(t_0)$, where $p(\mathbf{z} | \mu, t_0)$ is defined in Section A.1 and $p(t_0)$ is the t_0 prior. Therefore, we guess a value μ_0 close to the true μ yielding

$$p(\mathbf{z}, t_0 | \mathbf{w}) = \frac{p(\mathbf{w} | \mathbf{z}, t_0)p(\mathbf{z} | \mu_0, t_0)p(t_0)}{p(\mathbf{w})} \quad (3)$$

Section 3.3 gives an example to construct a distribution of μ_0 to cover the truth, and Section 4 uses deconvolution result as μ_0 .

It is important to choose a well-formed prior, to make the posterior unbiased. We choose a prior close to the reality: the light curve with μ_0 , while μ_0 is obtained from the deconvolution in Section 2.5. As for the t_0 prior $p(t_0)$, different trigger system may follow different $p(t_0)$. Section 3 gives an example of a uniform prior, for both simulation and analysis.

The posterior $p(\mathbf{z}, t_0 | \mathbf{w})$ is still hard to calculate. Gibbs MCMC [29] is suitable to sample \mathbf{z} and t_0 from the conditional probabilities. To sample \mathbf{z} and t_0 , Metropolis-Hastings MCMC [15] is chosen for both. The number of PEs is also unknown, so we need RJMCMC [14], a variant dimensional Metropolis-Hastings MCMC. In the Gibbs MCMC, t_0 is sampled before \mathbf{z} . Therefore, $t_{0,i+1}$ is sampled from $p(t_{0,i+1} | \mathbf{z}_i)$, and \mathbf{z}_{i+1} is sampled from $p(\mathbf{z}_{i+1} | \mathbf{w}, t_{0,i+1})$.

2.3 Sampling

Sampling of t_0 is done by using Metropolis-Hastings with the acceptance:

$$\min \left\{ 1, \frac{p(\mathbf{z}_i | \mu_0, t'_{0,i+1})}{p(\mathbf{z}_i | \mu_0, t_{0,i})} \right\} \quad (4)$$

We accept a jump with the calculated acceptance, the possibility to accept the jump. The new sample will be recorded if the jump is accepted. Otherwise, record the previous sample. The prime in $t'_{0,i+1}$ means the proposed value is waiting for judgement of accept or reject.

Sampling \mathbf{z} is done by RJMCMC, also with acceptances for each kind of jumps. Denote the length of \mathbf{z}_i as N_i , and define the jumps: birth, death, and update in Fig. 2. All jumps are reversible: birth jump is the reverse of death jump, and update jump is the reverse of itself.

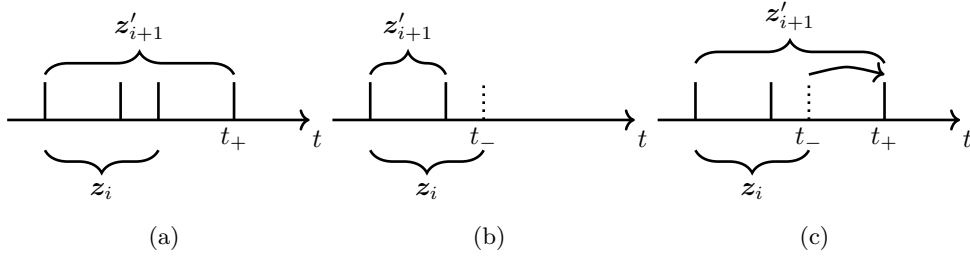


Fig. 2: Sketch of 3 jumps in RJMCMC. (a) Birth jump: the possibility of birth jump is $h(t_+)$. The possibility of the reverse jump is $\frac{1}{N'_{i+1}}$. (b) Death jump: the possibility of death jump is $\frac{1}{N_i}$. The possibility of the reverse jump is $h(t_-)$. (c) Update jump: the hit time t_- of one PE is updated to $t_+ = t_- + \Delta t$.

In the *birth jump* shown in Fig. 2a, a new PE t_+ is appended to the sequence \mathbf{z}_i . Therefore, $N'_{i+1} = N_i + 1$, and $\mathbf{z}'_{i+1} = \mathbf{z}_i \cup \{t_+\}$. The distribution of t_+ is the proposal $h(t)dt$ introduced in Section 2.5. The acceptance is

$$\min \left\{ 1, \frac{p(\mathbf{z}'_{i+1} | \mu_0, t_{0,i+1}) \frac{1}{N'_{i+1}}}{p(\mathbf{z}_i | \mu_0, t_{0,i+1}) h(t_+)} \right\} \quad (5)$$

In the *death jump* shown in Fig. 2b, a PE t_- is removed in equal probability from the sequence \mathbf{z}_i . Therefore, $N'_{i+1} = N_i - 1$, and $\mathbf{z}'_{i+1} = \mathbf{z}_i \setminus \{t_-\}$. The acceptance is

$$\min \left\{ 1, \frac{p(\mathbf{z}'_{i+1} | \mu_0, t_{0,i+1}) h(t_-)}{p(\mathbf{z}_i | \mu_0, t_{0,i+1}) \frac{1}{N_i}} \right\} \quad (6)$$

In the *update jump* shown in Fig. 2c, a PE is moved from t_- to $t_+ = t_- + \Delta t$, and Δt follows a symmetry distribution $\mathcal{N}(0, 1)$. Therefore, $N'_{i+1} = N_i$, and $\mathbf{z}'_{i+1} =$

$\mathbf{z}_i \setminus \{t_-\} \cup \{t_+\}$. The acceptance is

$$\min \left\{ 1, \frac{p(\mathbf{z}'_{i+1}|\mu_0, t_{0,i+1})}{p(\mathbf{z}_i|\mu_0, t_{0,i+1})} \right\} \quad (7)$$

In each step, at most one kind of jump is applied to a sequence. Initially, define a probability $Q < \frac{1}{2}$, and the probability of birth, death and update as $Q, Q, 1 - 2Q$. In practice, we choose $Q = \frac{1}{4}$. However, there is a corner case: an empty PE sequence could not be applied with death or update. Therefore, for an empty sequence, only birth jump is in consideration, and the acceptance should be multiplied by Q . Accordingly, the acceptance of death jump on a single PE sequence should be divided by Q .

2.4 Extended RJMCMC for MCP-PMTs

In the dynode PMT, the single PE charge follows normal distribution. While in MCP-PMTs, the single MCPe charge follows normal distribution, and there is at least one MCPe for one PE. Therefore, MCPe should be changed during birth and death jumps, and \mathbf{z} should be redefined as the sequence of both the time of PEs and the corresponding MCPes: $\mathbf{z} = \{(t_1, e_1), \dots, (t_N, e_N)\} \in (T, E)^N$.

The birth jump is extended to 2 possible choices: to add a new PE, or add an MCPe for an existing PE. For one PE k with MCPe e_k , the possibility to increase MCPe should be

$$p(e'_k = e_k + 1|e_k) = \frac{G(e_k + 1)}{G(e_k)} \quad (8)$$

If no MCPe has been added, then a new PE is added with possibility should be

$$p(e'_{k+1} = 1|e_k) = 1 - \frac{1}{N_i} \sum_{e_k \in \mathbf{z}_i} \frac{G(e_k + 1)}{G(e_k)} \quad (9)$$

So, the acceptance of adding a new PE is:

$$\min \left\{ 1, \frac{p(\mathbf{z}'_{i+1}|\mu_0, t_{0,i+1})}{p(\mathbf{z}_i|\mu_0, t_{0,i+1})} \frac{\frac{1}{N'_{i+1}}}{h(t_+) \left(1 - \frac{1}{N_i} \sum_{e_k \in \mathbf{z}_i} \frac{G(e_k+1)}{G(e_k)}\right)} \right\} \quad (10)$$

With Eq. (A14), if no PE is to be added, the acceptance of adding an MCPe is:

$$\min \left\{ 1, \frac{p(\mathbf{w}|\mathbf{z}'_{i+1}, t_{0,i+1})}{p(\mathbf{w}|\mathbf{z}_i, t_{0,i+1})} \right\} \quad (11)$$

The death jump is changed to decrease an MCPe of an existing PE. If the original MCPe is 1, the PE will be removed. If there's one PE removed, the acceptance is

$$\min \left\{ 1, \frac{p(\mathbf{z}'_{i+1}|\mu_0, t_{0,i+1})}{p(\mathbf{z}_i|\mu_0, t_{0,i+1})} \frac{h(t_d) \left(1 - \frac{1}{N'_{i+1}} \sum_{e_k \in \mathbf{z}'_{i+1}} \frac{G(e_k+1)}{G(e_k)}\right)}{\frac{1}{N_i}} \right\} \quad (12)$$

while if only one MCPe is removed, the acceptance is the same as Eq. (11).

2.5 The prerequisites

The initial states of the Markov chain should be close to the truth, to make the chain converge faster. For example, when the truth light curve and t_0 is known in Section 3, the initial value of t_0 is the truth. Deconvolution is one good candidate. Consider the charge of PE to be a function of time $q(t)$, and ignore the white noise, the waveform is expressed as a convolution

$$\mathbf{w}(t) = \int q(\tau)V_{\text{PE}}(t - \tau)d\tau = q \otimes \tilde{V}_{\text{PE}} \quad (13)$$

Therefore, representing deconvolution with \oslash , q is calculated by $q = \mathbf{w} \oslash \tilde{V}_{\text{PE}}$. Lucy [30] gives a deconvolution algorithm for the case that the elements of q are non-negative. Let r represent the step of iteration,

$$\begin{aligned} q^{r+1}(\tau) &= q^r(\tau) \sum_{t=\max\{\tau,0\}}^{\min\{l_w-1,\tau+l_V-1\}} \frac{\mathbf{w}(t)}{\mathbf{w}^r(t)} \tilde{V}_{\text{PE}}(t - \tau) \\ \mathbf{w}^r(t) &= \sum_{\tau=\max\{t,-l_V+1\}}^{\min\{l_w-1,t-l_V+1\}} q^r(\tau) \tilde{V}_{\text{PE}}(t - \tau) \end{aligned} \quad (14)$$

where $t \in [0, l_w - 1]$, $\tau \in [-l_V + 1, l_w - 1]$. l_w represents the length of \mathbf{w} , and l_V represents the length of \tilde{V}_{PE} . The initial q^0 could be any non-negative array that the summation is equal to the summation of \mathbf{w} . The two equations are two convolutions

$$\begin{aligned} q^{r+1}(\tau) &= q^r(\tau) \left(\frac{\mathbf{w}}{\mathbf{w}^r} \otimes \tilde{V}'_{\text{PE}} \right) (\tau + l_V - 1) \\ \mathbf{w}^r(t) &= (q^r \otimes \tilde{V}_{\text{PE}})(t) \end{aligned} \quad (15)$$

where \tilde{V}'_{PE} is the reverse array of \tilde{V}_{PE} .

In practice, we choose r up to 2000, and use the final $q^{2000}(\tau)$ as the initial PE sequence. If all elements of q are smaller than 0.2, the corresponding waveform will be treated as a zero PE waveform, and will not be analyzed by FSMP. The times τ where $q^{2000}(\tau) > 0$ is the initial \mathbf{z} . As for the initial value of t_0 , it depends on the light curve. When the light curve is unknown, the first PE time from the initial \mathbf{z} is used as t_0 , and only \mathbf{z} is sampled in FSMP; $q^{2000}(t)$ is also used as the temporary light curve $\phi(t - t_0)$, so the prior $p(\mathbf{z}|\mu_0, t_0)$ and proposal $h(t)$ in Section 2.3 are substituted correspondingly.

The solution space could be limited by the initial PE sequence provided by the deconvolution method. The limitation is optional, but decreases the execution time. Let the minimum and maximum PE time be t_{\min} and t_{\max} , the solution space *time window* \mathcal{T} is $[t_{\min} - 4 \text{ ns}, t_{\max} + 4 \text{ ns}]$. The definition range of \mathbf{w} should be also cut to $[t_{\min} - 4 \text{ ns}, t_{\max} + 4 \text{ ns} + l_V]$. 4 ns is an empirical value, to make the solution space

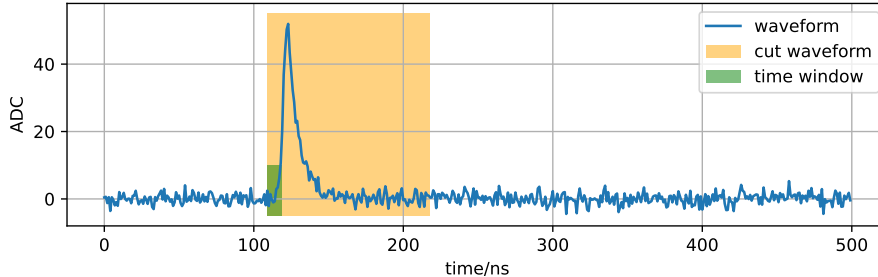


Fig. 3: The time window and solution space.

cover the truth. Fig. 3 shows the time window \mathcal{T} from the deconvolution result, and the cut waveform.

The probability of new PE time t_+ in birth jump, $h(t_+)$, is the proposal distribution of t_+ in RJMCMC. Although it could be any distribution covering the solution space, the chain will converge faster if it is proportional to the light curve $\phi(t - t_0)$. While ϕ is already normalized to the whole time space, it should be normalized again to the solution space:

$$h(t) = \frac{\phi(t - t_0)}{\int_{\mathcal{T}} \phi(t - t_0) dt} \quad (16)$$

2.6 Towards energy reconstruction

The total energy of scintillator photons in the event is called visible energy. There are nonlinearities from event energy to visible energy [31]. The following discussion concentrates from waveform analysis, to the estimation and resolution of visible energy.

In Section 2.2, $p(\mathbf{z}, t_0 | \mathbf{w})$ is calculated with a guessed μ_0 . To reconstruct the energy of the event, we still need an estimation of μ with likelihood $p(\mathbf{w} | \mu)$,

$$\hat{\mu}_{\text{MLE}} = \arg \max_{\mu} p(\mathbf{w} | \mu) \quad (17)$$

while

$$p(\mathbf{w} | \mu) = \sum_{\mathbf{z}, t_0} p(\mathbf{w} | \mathbf{z}, t_0) p(\mathbf{z}, t_0 | \mu) \quad (18)$$

Sample \mathbf{z} and t_0 by FSMP in Section 2.3, with Eqs. (A1) and (3),

$$\begin{aligned}
p(\mathbf{w}|\mu) &= \sum_{\mathbf{z}, t_0} p(\mathbf{w}|\mathbf{z}, t_0) p(\mathbf{z}, t_0|\mu_0) \frac{p(\mathbf{z}, t_0|\mu)}{p(\mathbf{z}, t_0|\mu_0)} \\
&= p(\mathbf{w}|\mu_0) \sum_{\mathbf{z}, t_0} p(\mathbf{z}, t_0|\mathbf{w}) \frac{p(\mathbf{z}, t_0|\mu)}{p(\mathbf{z}, t_0|\mu_0)} \\
&= C \mathbb{E}_{\mathbf{z}, t_0} \left[\frac{p(\mathbf{z}, t_0|\mu)}{p(\mathbf{z}, t_0|\mu_0)} \right] \\
&= \frac{C}{M} e^{-(\mu-\mu_0)} \sum_{\mathbf{z} \in \text{FSMP}} \left(\frac{\mu}{\mu_0} \right)^N
\end{aligned} \tag{19}$$

where C is a constant, M is the count of sampled \mathbf{z} , and N is the count of PE \mathbf{z} . $\mathbb{E}_{\mathbf{z}, t_0}$ is expectation by \mathbf{z}, t_0 , calculated by averaging over FSMP samples.

So the estimator $\hat{\mu}_{\text{MLE}}$ should be the root of the equation

$$\frac{d}{d\mu} \log p(\mathbf{w}|\mu) = 0 \Leftrightarrow \sum_{\mathbf{z} \in \text{FSMP}} (\mu^N - N\mu^{N-1}) = 0 \tag{20}$$

3 Performance

To test the performance of FSMP, we simulate a neutrino detector with slow liquid scintillator [32] with 8-inch MCP-PMTs [11] that are the candidates of the Jinping Neutrino Experiment [6]. The normalized light curve $\phi(t)$ in Fig. 4a and SER $\tilde{V}_{\text{PE}}(t)$ in Fig. 4b are,

$$\begin{aligned}
\phi(t) &= \frac{\tau_1 + \tau_2}{\tau_2} \left(1 - e^{-\frac{t}{\tau_1}} \right) e^{-\frac{t}{\tau_2}} \\
\tilde{V}_{\text{PE}}(t) &= \frac{1}{2\tau} e^{\frac{\sigma^2 - 2(t-4\sigma)\tau}{2\tau^2}} \left(1 + \text{Erf} \left(-\frac{\sigma^2 - (t-4\sigma)\tau}{\sqrt{2}\sigma\tau} \right) \right)
\end{aligned} \tag{21}$$

where $\tau_1 = 1.16$ ns, $\tau_2 = 26.76$ ns, $\sigma = 1.62$ ns, $\tau = 7.2$ ns and Erf is the error function.

Table 1 shows the basic parameters. We first prepare sets of waveforms with fixed PE counts N from 0 to 125, sample N from a Poisson with parameter μ and randomly choose a waveform from the corresponding set. The dataset for such a μ consists of 10000 waveforms by repeating the procedures. To sample t_0 , a uniform distribution between $t_{0\text{min}}$ and $t_{0\text{max}}$ is chosen:

$$p(t_0) = \frac{1}{t_{0\text{max}} - t_{0\text{min}}} \tag{22}$$

Two typical waveforms, one with $\mu = 1, N = 2$ (waveform A) and one with $\mu = 60, N = 96$ (waveform B), demonstrate the effectiveness of FSMP. To calculate convergence in Section 3.2, initial PE sequence is randomly chosen in the time window \mathcal{T} provided in Section 2.5. The initial PE count ranges from 0 to 31 and 86 to 106 for

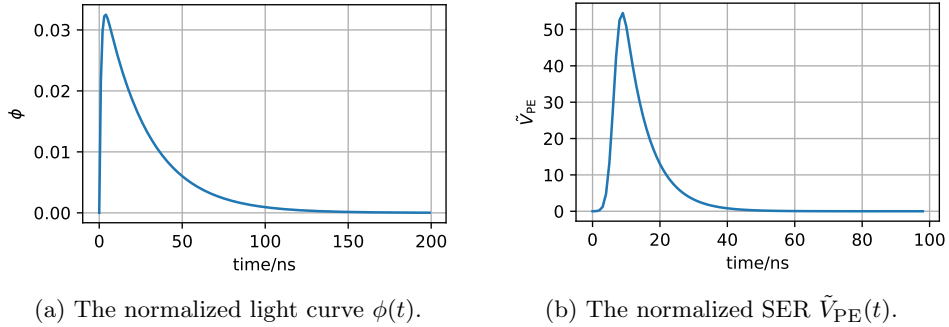


Fig. 4: Figures of light curve and SER in simulation.

Table 1: The basic parameters used in the simulation.

Parameter	Value
μ	0.1, 0.2, 0.5, 1, 2, ..., 10, 15, ..., 60
$t_{0\text{min}}$	100 ns
$t_{0\text{max}}$	200 ns
Baseline σ_ϵ	1.59(ADC)
Single MCPe charge q	597.88(ADC·ns)
Single MCPe charge σ_q	201.28(ADC·ns)
Waveform length	500 ns
Sampling rate	1/ns
Waveform samples per μ	10000
MCPe 1st peak $G(1)$	64.6 %
MCPe 2nd peak $G(2)$	23.2 %
MCPe 3rd peak $G(3)$	7.64 %
MCPe 4th peak $G(4)$	4.53 %

waveforms A and B. The initial and last sampled sequence is shown in Fig. 5. No matter what the initial sequence is, FSMP samples the correct parameters reproducing the input waveform.

3.1 Execution Speed and Precision

FSMP makes extensive use of linear algebraic procedures as shown in Section A.1. Fig. 6 shows our *batched* strategy [33] to accelerate FSMP, stacking the quantities of scalars, vectors and matrices from different waveforms into tensors with one extra batched dimension. The PE sequence, $\mathbf{z} = (t_1, t_2, \dots)$ is a vector with various lengths. We pad the short sequence with zeros to form the batched matrix, and introduce a new vector to store the number of PEs N of each waveform. Batching allows FSMP to be implemented in NumPy [34] and CuPy [35] efficiently for CPU and GPU executions.

Fig. 7a shows the comparison of performance on CPU and GPU. With small batch sizes, running all computation on CPU is faster than offloading to GPU, because data transfer between GPU and GPU takes time. When the batch size increases, GPU gains

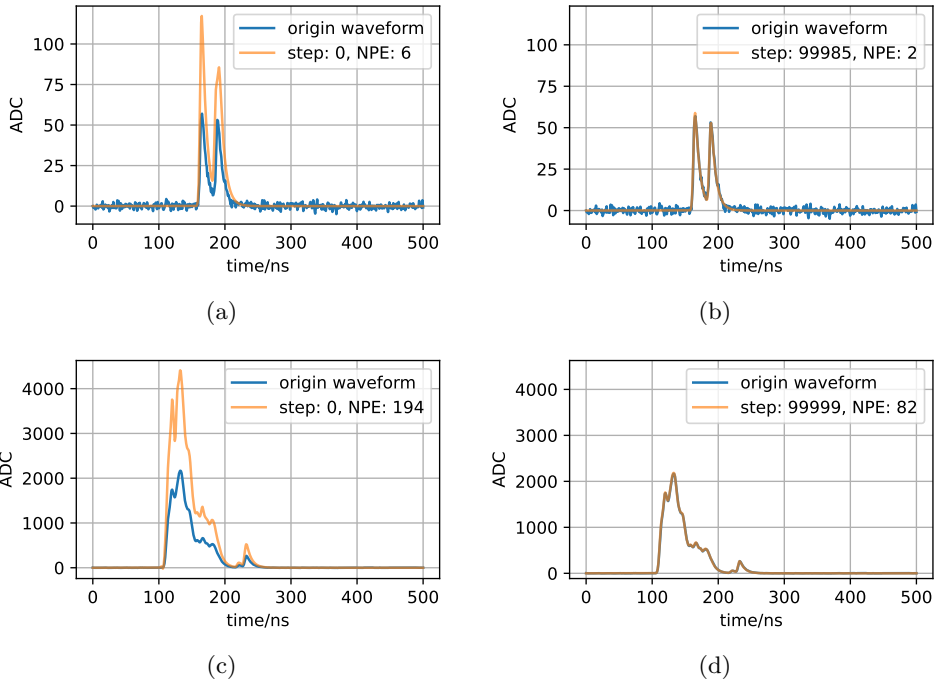


Fig. 5: Example of two Markov chains, upper figures for waveform A and lower for B, initial sample on the left and the last sample on the right. Orange lines are the predicted waveforms, getting closer to the original ones with the chain.

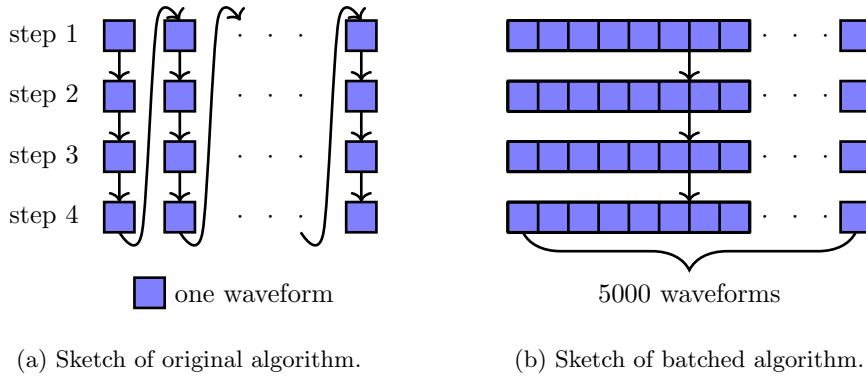


Fig. 6: A comparison of original algorithm and batched one. One square represents the data related to one waveform, and the arrows shows the execution directions.

performance on matrix computations up to 100 waveforms per second. The execution speed of CPU is mostly independent of batch size.

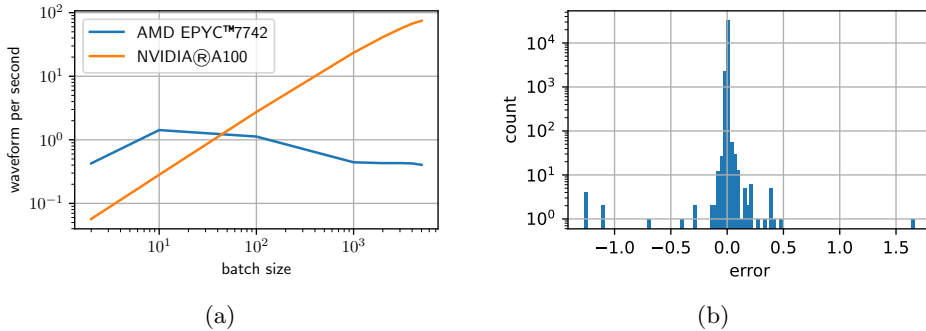


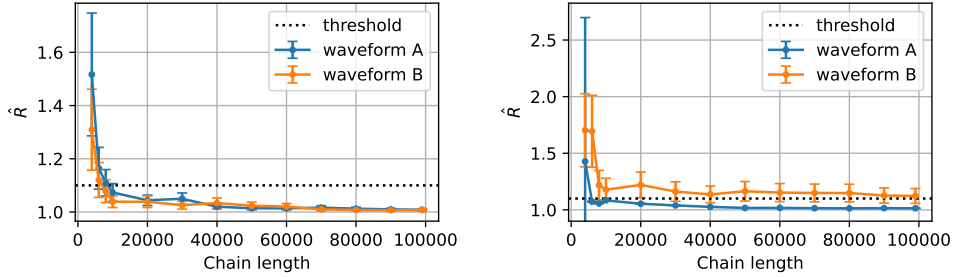
Fig. 7: FSMP comparison with (a) execution speed and (b) error of $\Delta\nu$, the waveform log-likelihood ratio of two PE sequences in Eq. (A11), on a single core of AMD EPYC™7742 CPU and NVIDIA®A100 GPU.

Matrix calculation may induce float-point rounding errors. We use `float64` on CPU because its native instruction set is 64-bit. To better utilize the computation units [36], we choose `float32` on GPU but with a risk of lower precision. For comparison, every accepted step in the RJMCMC chain is recorded. After the GPU version program, the waveform log-likelihood ratio of two PE sequences $\Delta\nu$ in Eq. (A11) is calculated by the CPU again. Fig. 7b shows the error of $\Delta\nu$ of each step for waveform B, with deconvolution provided initial PE sequence. The absolute value of error is mainly within 1.0.

3.2 Convergence

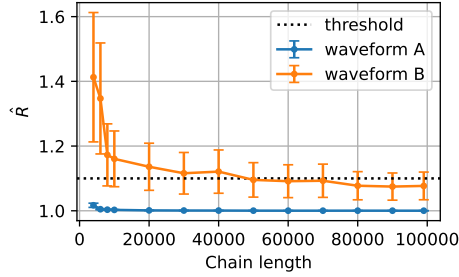
The Gelman-Rubin diagnostic checks whether a Metropolis-Hastings Markov chain is convergent [37]. It calculates a convergence indicator \hat{R} from multiple auxiliary chains with different initial conditions as a combination of within-group deviation and between-group deviation, which shows the consistency within each chain and among all chains. The chain is regarded as convergent when $\hat{R} < 1.1$. We chose the sampled time offset t_0 and the number of PEs N . Figs. 8a and 8b show the convergence of t_0 and N of the two waveforms in Fig. 5. The slower convergence of waveform B is expected for so large the solution space that the initial conditions of the chains are diverse.

PE sequence \mathbf{z} , although being the most important results from FSMP, is not suitable to directly compute \hat{R} which requires a fixed-dimensional input. Brooks and Galman [38] suggested several distance measures to quantify the similarity between trans-dimensional samples. Wasserstein distance [39] is such a distance measurement, and is chosen as a requirement of the convergence of PE sequence. Define MCPe sequence as all times of MCPes, and calculate the Wasserstein distance between MCPe sequence and an empty sequence as the scalar to use in calculating Gelman-Rubin



(a) t_0 convergence of two waveforms.

(b) N convergence of two waveforms.



(c) z convergence of two waveforms.

Fig. 8: The convergence of different representative scalars. The error bar represents the upper confidence limits of \hat{R} .

diagnostic. As Wasserstein distance could not handle empty sequences, a dummy PE at $t = 0$ is added to all PE sequences, with a very small weight 10^{-9} . Fig. 8c shows the convergence of MCPe sequence of the two waveforms discussed above. The basic trending is similar to the convergence of t_0 and N .

3.3 Bias and resolution

The estimator \hat{t}_0 should be the average value of the sampled t_0 chain. For comparison, we also sampled a chain of t_0 from true PE sequence, labeled “MCMC” in the figures. Another comparison is to use the first peak 10% rise time [11] as the biased estimator of t_0 . The resolution is defined by

$$\eta_t = \frac{\sqrt{\text{Var}[\hat{t}_0]}}{\text{E}[\hat{t}_0]} \quad (23)$$

Fig. 9a shows the bias of \hat{t}_0 , and Fig. 9b shows the resolution. The result shows that the bias is around 0.1 ns, and when $\mu < 20$, FSMP gives better time resolution than first PE time.

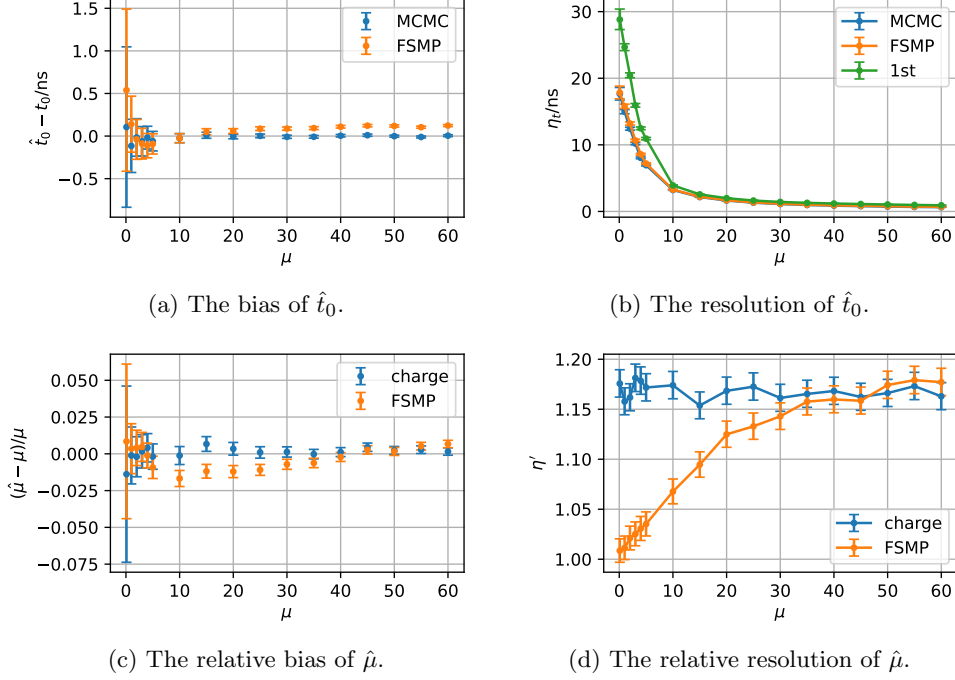


Fig. 9: The bias and resolution of \hat{t}_0 and $\hat{\mu}$ from FSMP, compared with other methods. 90% confidence interval.

The energy resolution of $\hat{\mu}$ is compared with the charge method. Define the charge of a waveform as Q , and estimation of μ as below, and $\hat{\mu}_{\text{charge}}$ is proved to be unbiased:

$$\hat{\mu}_{\text{charge}} = \frac{Q}{q_e}, q_e = \sum_{e=1}^4 G(e)eq \quad (24)$$

$$\text{E}[Q] = \text{E}[N]q_e = \mu q_e \Rightarrow \text{E}[\hat{\mu}_{\text{charge}}] = \mu \quad (25)$$

The relative bias of $\hat{\mu}$ is defined as the bias divided by the truth value $(\hat{\mu} - \mu)/\mu$. The resolution η [40] and relative resolution η' of $\hat{\mu}$ is defined as

$$\eta = \frac{\sqrt{\text{Var}[\hat{\mu}]}}{\text{E}[\hat{\mu}]}, \eta' = \frac{\eta}{\eta_{\text{theory}}} \quad (26)$$

where η_{theory} is the theoretical energy resolution. For both MLE in Section 2.6 and charge method, the theoretical resolution is the resolution of N , which is an unbiased MLE estimator of μ .

$$\eta_{\text{theory}} = \frac{\sqrt{\text{Var}[N]}}{\text{E}[N]} \quad (27)$$

Any waveform analysis result shouldn't give better μ estimation than using the PE truth. Therefore, η' should be always larger than 1.

FSMP in Section 2.2 requires μ_0 value in the prior $p(\mathbf{z}|\mu_0)$. Here it is sampled from a gamma distribution $\Gamma(\alpha = 2\mu, \beta = 2)$ for each waveform. The expectation of this sampling is the truth value μ , while the variance is $\frac{\mu}{2}$. It imitates the reality, when we don't exactly know the real μ .

Figs. 9c and 9d show the comparison result. When μ is relatively small, the resolution of FSMP method is better than charge method. Here is a qualitative explanation: when μ is small, number of PEs is also small. FSMP method should give more precise result in that case, because the possibility pile-up is rare. When μ is large, $\hat{\mu}$ from FSMP is still more biased than charge method. Charge method should be used in that case, because FSMP cannot give a better resolution. Choosing $\mu = 1$ as the standard, FSMP is $(12.5 \pm 1.4)\%$ better than charge method in estimation of μ . This conclusion could lead to the resolution of visible energy that, in the most optimistic case, FSMP improves the resolution of visible energy by 12%.

4 Analyze real data

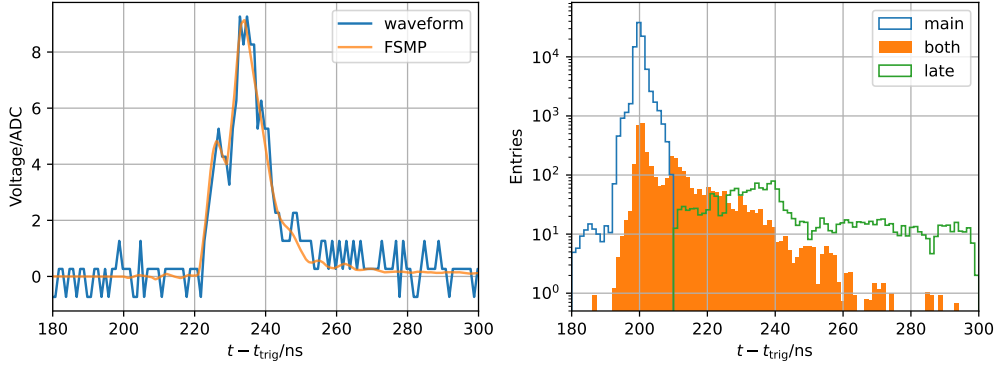
Zhang et al. [11] studied the performance of a new type 8-inch MCP-PMT. This section re-analyze the experimental data from their work to show the advantage of FSMP. The light curve and μ_0 is substituted following Section 2.5, and SER is obtained from Zhang's method. Only PE times are sampled with RJMCMC, and t_0 is not sampled because the light curve is not available, according to Section 2.5.

Fig. 10a shows a sample waveform. The FSMP sampled PE sequences are convoluted with single PE response, restored and averaged to the orange waveform. FSMP fits all peaks of the waveform well. Fig. 10b shows all PE samples of a PMT in a single run. The blue and green histogram represent the sampled PEs only before and only after 210 ns in each waveform samples. The orange filled histogram are the remaining samples. The orange one contains true-secondary electrons, while the green one is *late pulse*, which may contain the back-scattered and rediffused electrons. The figures demonstrate that FSMP gives all PE times from waveforms, and provides possibility to analyze the orange histogram and dig through the physical process with quantitative method.

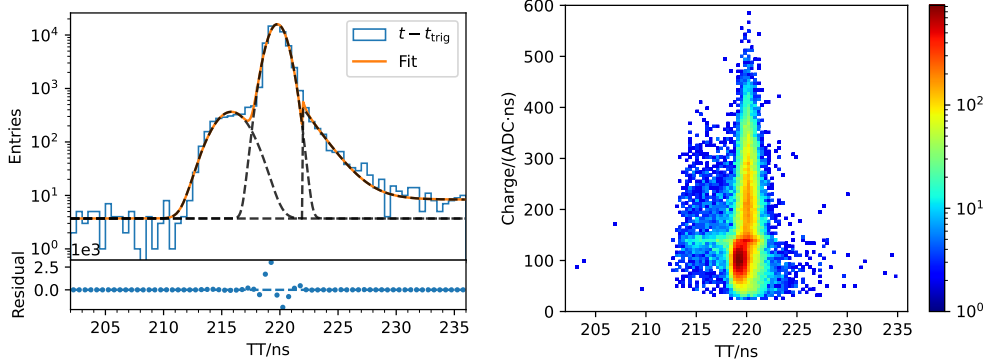
To compare the transition time spread (TTS) with Zhang's method, the transition time (TT) is defined as the interval between trigger time and the average first PE time of the samples of each waveform. Fig. 10d shows the histogram of charge and TT in logarithmic scale. The distribution of TT is fit in Fig. 10c. The fit TTS is (1.703 ± 0.007) ns, better than the result (1.719 ± 0.001) ns with Zhang's method.

5 Conclusion

We gave an introduction of FSMP method. It is a flexible and general Bayesian-based RJMCMC to sample PE sequence from posterior distribution. It is applied on both dynode PMT and ALD-coated MCP-PMT with jumbo charge outputs. FSMP makes full use of pulse shape and amplitude information to estimate the full PE sequence,



(a) Average restored waveform of all sampled PE sequences of one waveform. (b) The PE times sampled by FSMP, showing the main pulse and the late pulse.



(c) Fit of TT spread (TTS). (d) The 2D distribution of charge and TT.

Fig. 10: Analysis of MCP-PMT testing data.

which gives better precision. The GPU acceleration makes FSMP fast enough for large amount of waveform in experiments.

Applying FSMP to our simulated waveforms, it gives $(12.5 \pm 1.4)\%$ better resolution of $\hat{\mu}$ when $\mu = 1$. When $\mu < 20$, it performs better than charge method in estimating μ and better than 1st PE time in estimating t_0 . Therefore, for MeV neutrino experiments in liquid scintillator detectors, *e.g.*, Jinping Neutrino Experiment and JUNO, FSMP could improve resolution of visible energy by 12% in optimistic case.

6 Acknowledgements

We would like to acknowledge the valuable contributions of Shengqi Chen. He gave us much help on porting the algorithm to GPU, and much assistance on profiling. His professionalism on high performance computing is highly appreciated. We are also grateful to Zhuojing Zhang for her inspirational guidance to RJMCMC and Prof. Zhirui Hu

for the discussions on the convergence of Markov Chain Monte Carlo. Much appreciation to Tsinghua University TUNA Association, for the opportunity to communicate about our ideas on GPU programming.

Many thanks to Jun Weng for his patient guidance on MCP-PMT. He was one of the first FSMP users, and gave us a lot of helpful advice. Chuang Xu and Yiqi Liu deserve our appreciation on trying FSMP with experimental data. We are also thankful to Wentai Luo and Ye Liang for their expertise on the time properties of liquid scintillator. Thanks to other colleagues in Center for High Energy Physics for their assistance. Their help is necessary and indispensable.

This work was supported by the National key research and development program of China (Grant no. 2023YFA1606104, 2022YFA1604704), in part by the National Natural Science Foundation of China (No. 12127808) and the Key Laboratory of Particle and Radiation Imaging (Tsinghua University). Part of the GPU computing was supported by the Center of High Performance Computing, Tsinghua University.

Appendix A Calculation of possibilities

A.1 For FSMP

First we need to calculate $p(\mathbf{z}|\mu, t_0)$ for Eq. (3). This possibility depends on the light curve. It is calculated as

$$\begin{aligned} p(\mathbf{z}|\mu, t_0)d\mathbf{z} &= e^{-\mu} \prod_{k=1}^N \mu \phi(t_k - t_0) dt_k \\ &= e^{-\mu} \mu^N \prod_{k=1}^N \phi(t_k - t_0) dt_k \\ &= e^{-\mu} \mu^N \phi(\mathbf{z} - t_0) d\mathbf{z} \end{aligned} \tag{A1}$$

while $\phi(\mathbf{z} - t_0)d\mathbf{z}$ is an abbreviation of $\prod_{k=1}^N \phi(t_k - t_0) dt_k$.

Then we need to calculate $p(\mathbf{w}|\mathbf{z})$. Assume it is a multivariate normal distribution, and $\tilde{V}_{\text{PE}}(t)$ is the normalized single PE response (SER) of a PMT (see Section 2.1), and the variance of white noise is σ_ϵ^2 . Each value of the waveform $\mathbf{w}(t_w)$ follows Normal distribution $\mathcal{N}(\mathbf{U}(\mathbf{z}), \mathbf{\Sigma}(\mathbf{z}))$, where

$$\begin{aligned} U_w &:= \sum_{k=1}^N q_k \tilde{V}_{\text{PE}}(t_w - t_k) \\ \Sigma_{wv} &:= \sum_{k=1}^N \sigma_q^2 \tilde{V}_{\text{PE}}(t_w - t_k) \tilde{V}_{\text{PE}}(t_v - t_k) + \sigma_\epsilon^2 \delta_{wv} \\ &= \sum_{k=1}^N \Xi(t_w - t_k, t_v - t_k) + \sigma_\epsilon^2 \delta_{wv} \end{aligned} \tag{A2}$$

Tipping [41, 42] proved that in this model, we can write down

$$\log p(\mathbf{w}|\mathbf{z}) = -\frac{N_w}{2} \log(2\pi) - \frac{1}{2} \log |\boldsymbol{\Sigma}| - \frac{1}{2} (\mathbf{w} - \mathbf{U})^\top \boldsymbol{\Sigma}^{-1} (\mathbf{w} - \mathbf{U}) \quad (\text{A3})$$

where N_w is the length of the waveform, and Ξ is represented by direct product

$$\Xi = \mathbf{a}_0 \Lambda_0 \mathbf{a}_0^\top, \quad a_{0,wv} = \tilde{V}_{\text{PE}}(t_w - t_v), \quad \Lambda_{0,wv} = \sigma_q^2 \delta_{wv} \quad (\text{A4})$$

The update jump is a combination of death jump at t_- and birth jump at $t_+ = t_- + \Delta t$. We can combine the two jumps into one operation. For $\mathbf{z}'_{i+1}, t_-, t_+$ in Fig. 2c, define the waveform of PE t_- as $\mathbf{a}_{w-} = V_{\text{PE}}(t_w - t_-)$, aka \mathbf{a}_- . Simultaneously, define \mathbf{a}_+ as the single PE waveform of t_+ . Combine the two waveform into a matrix $\mathbf{a} = (\mathbf{a}_-, \mathbf{a}_+)$, we get

$$\begin{aligned} \Delta \boldsymbol{\Sigma} &= \Xi(\mathbf{z}') - \Xi(\mathbf{z}) = \mathbf{a} \Lambda \mathbf{a}^\top \\ \Lambda &:= \sigma_q^2 \begin{bmatrix} -1 & \\ & 1 \end{bmatrix}. \end{aligned} \quad (\text{A5})$$

For a birth jump, we can define $\mathbf{a}_- = 0$; for a death jump, define $\mathbf{a}_+ = 0$. Then we can unify the 3 kinds of jump into one formula.

RJMCMC only requires the ratio of $p(\mathbf{w}|\mathbf{z})$, thus we only need to calculate

$$\begin{aligned} \log \frac{p(\mathbf{w}|\mathbf{z}')}{p(\mathbf{w}|\mathbf{z})} &= -\frac{1}{2} (\Delta T + \Delta R) \\ \Delta T &:= \log \left(\frac{|\boldsymbol{\Sigma}(\mathbf{z}')|}{|\boldsymbol{\Sigma}(\mathbf{z})|} \right) \\ \Delta R &:= [\mathbf{w} - \mathbf{U}(\mathbf{z}')]^\top \boldsymbol{\Sigma}^{-1}(\mathbf{z}') [\mathbf{w} - \mathbf{U}(\mathbf{z}')] - [\mathbf{w} - \mathbf{U}(\mathbf{z})]^\top \boldsymbol{\Sigma}^{-1}(\mathbf{z}) [\mathbf{w} - \mathbf{U}(\mathbf{z})] \\ &= (\mathbf{y} - \Delta \mathbf{U})^\top \boldsymbol{\Sigma}^{-1}(\mathbf{z}') (\mathbf{y} - \Delta \mathbf{U}) - \mathbf{y}^\top \boldsymbol{\Sigma}^{-1}(\mathbf{z}) \mathbf{y}. \end{aligned} \quad (\text{A6})$$

where $\mathbf{y} := \mathbf{w} - \mathbf{U}(\mathbf{z})$. Like Eq. (A5),

$$\begin{aligned} \Delta \mathbf{U} &:= \mathbf{U}(\mathbf{z}') - \mathbf{U}(\mathbf{z}) \\ &= q(-\mathbf{a}_- + \mathbf{a}_+) \\ &= \mathbf{a} \boldsymbol{\lambda} \\ \boldsymbol{\lambda} &:= q \begin{bmatrix} -1 \\ 1 \end{bmatrix}. \end{aligned} \quad (\text{A7})$$

Therefore, the most important item is $\boldsymbol{\Sigma}^{-1}$. Let $\mathbf{c} := \boldsymbol{\Sigma}^{-1} \mathbf{a}$, $\mathbf{B} := (\Lambda^{-1} + \mathbf{a}^\top \mathbf{c})^{-1}$, we have Woodbury formula [43]

$$\begin{aligned} \boldsymbol{\Sigma}^{-1}(\mathbf{z}') &= (\boldsymbol{\Sigma} + \mathbf{a} \Lambda \mathbf{a}^\top)^{-1} \\ &= \boldsymbol{\Sigma}^{-1} - \boldsymbol{\Sigma}^{-1} \mathbf{a} (\Lambda^{-1} + \mathbf{a}^\top \boldsymbol{\Sigma}^{-1} \mathbf{a})^{-1} \mathbf{a}^\top \boldsymbol{\Sigma}^{-1} \\ &= \boldsymbol{\Sigma}^{-1} - \mathbf{c} \mathbf{B} \mathbf{c}^\top. \end{aligned} \quad (\text{A8})$$

Calculate ΔR with Eqs. (A6) to (A8):

$$\begin{aligned}\Delta R &= (\mathbf{y} - \mathbf{a}\boldsymbol{\lambda})^\top (\boldsymbol{\Sigma}^{-1} - \mathbf{c}\mathbf{B}\mathbf{c}^\top) (\mathbf{y} - \mathbf{a}\boldsymbol{\lambda}) - \mathbf{y}^\top \boldsymbol{\Sigma}^{-1} \mathbf{y} \\ &= -\Upsilon^\top \mathbf{B}\Upsilon + \boldsymbol{\lambda}^\top \boldsymbol{\Lambda}^{-1} \boldsymbol{\lambda}\end{aligned}\quad (\text{A9})$$

where $\Upsilon := \mathbf{c}^\top \mathbf{y} + \boldsymbol{\Lambda}^{-1} \boldsymbol{\lambda}$.

Calculate ΔT with Eqs. (A5) and (A8):

$$\begin{aligned}\Delta T &= \log \left(\frac{|\boldsymbol{\Sigma} + \mathbf{a}\boldsymbol{\Lambda}\mathbf{a}^\top|}{|\boldsymbol{\Sigma}|} \right) \\ &= \log (|1 + \mathbf{a}\boldsymbol{\Lambda}\mathbf{a}^\top \boldsymbol{\Sigma}^{-1}|) \\ &= \log (|\boldsymbol{\Lambda}\mathbf{B}^{-1}|) \\ &= -\log (|\mathbf{B}\boldsymbol{\Lambda}^{-1}|)\end{aligned}\quad (\text{A10})$$

With Eqs. (A6), (A9) and (A10), define $\Delta\nu$:

$$\Delta\nu = \log \frac{p(\mathbf{w}|\mathbf{z}')}{p(\mathbf{w}|\mathbf{z})} = \frac{1}{2} (\Upsilon^\top \mathbf{B}\Upsilon - \boldsymbol{\lambda}^\top \boldsymbol{\Lambda}^{-1} \boldsymbol{\lambda} + \log (|\mathbf{B}\boldsymbol{\Lambda}^{-1}|)) \quad (\text{A11})$$

From Eqs. (A1) and (A11), we have

$$\frac{p(\mathbf{z}'|\mu_0, t_0)}{p(\mathbf{z}|\mu_0, t_0)} = \frac{p(\mathbf{w}|\mathbf{z}')p(\mathbf{z}'|\mu_0, t_0)}{p(\mathbf{w}|\mathbf{z})p(\mathbf{z}|\mu_0, t_0)} = e^{\Delta\nu} \mu_0^{N'-N} \frac{\phi(\mathbf{z}' - t_0)}{\phi(\mathbf{z} - t_0)} \quad (\text{A12})$$

A.2 For extended FSMP

Obviously we have

$$\sum_{e \in E} G(e) = 1 \quad (\text{A13})$$

which means that G is a PDF of a discrete distribution. Then we can recalculate probability

$$p(\mathbf{z}|\mu) d\mathbf{z} = e^{-\mu} \mu^N \prod_{k=1}^N \phi(t_k - t_0) G(e_k) dt_k \quad (\text{A14})$$

Considering e_k , we should redefine

$$\begin{aligned}U_w &:= \sum_{k=1}^N e_k q_k \tilde{V}_{\text{PE}}(t_w - t_k) \\ \Sigma_{wv} &:= \sum_{k=1}^N e_k \Xi_{\text{PE}}(t_w - t_k, t_v - t_k) + \sigma_\epsilon^2 \delta_{wv} \\ \boldsymbol{\Lambda} &:= \sigma_q^2 \begin{bmatrix} -e_- & \\ & e_+ \end{bmatrix}\end{aligned}\quad (\text{A15})$$

For update jump, $e_- = e_+ = e_k$; for others, $e_- = e_+ = 1$. With the same derivation in Section A.1, we can calculate $\Delta\nu$, and finally $\frac{p(\mathbf{z}'_{i+1})}{p(\mathbf{z}_i)}$.

References

- [1] KamLAND Collaboration, Gando, A., Gando, Y., Hanakago, H., Ikeda, H., Inoue, K., Ishidoshiro, K., Ishikawa, H., Koga, M., Matsuda, R., Matsuda, S., Mitsui, T., Motoki, D., Nakamura, K., Obata, A., Oki, A., Oki, Y., Otani, M., Shimizu, I., Shirai, J., Suzuki, A., Takemoto, Y., Tamae, K., Ueshima, K., Watanabe, H., Xu, B.D., Yamada, S., Yamauchi, Y., Yoshida, H., Kozlov, A., Yoshida, S., Piepke, A., Banks, T.I., Fujikawa, B.K., Han, K., O'Donnell, T., Berger, B.E., Learned, J.G., Matsuno, S., Sakai, M., Efremenko, Y., Karwowski, H.J., Markoff, D.M., Tornow, W., Detwiler, J.A., Enomoto, S., Decowski, M.P.: Reactor on-off antineutrino measurement with KamLAND. *Physical Review D* **88**(3), 033001 (2013) <https://doi.org/10.1103/PhysRevD.88.033001> . Publisher: American Physical Society. Accessed 2023-10-28
- [2] Gatti, F., Lagomarsino, V., Musico, P., Pallavicini, M., Razeto, A., Testera, G., Vitale, S.: The Borexino read out electronics and trigger system. *Nuclear Instruments and Methods in Physics Research Section A: Accelerators, Spectrometers, Detectors and Associated Equipment* **461**(1), 474–477 (2001) [https://doi.org/10.1016/S0168-9002\(00\)01275-4](https://doi.org/10.1016/S0168-9002(00)01275-4) . Number: 1. Accessed 2020-10-09
- [3] Anfimov, N.: Large photocathode 20-inch PMT testing methods for the JUNO experiment. *Journal of Instrumentation* **12**(06), 06017 (2017) <https://doi.org/10.1088/1748-0221/12/06/C06017> . Accessed 2023-03-04
- [4] Beacom, J.F., Chen, S., Cheng, J., Doustimotlagh, S.N., Gao, Y., Gong, G., Gong, H., Guo, L., Han, R., He, H.-J., Huang, X., Li, J., Li, J., Li, M., Li, X., Liao, W., Lin, G.-L., Liu, Z., McDonough, W., Šrámek, O., Tang, J., Wan, L., Wang, Y., Wang, Z., Wang, Z., Wei, H., Xi, Y., Xu, Y., Xu, X.-J., Yang, Z., Yao, C., Yeh, M., Yue, Q., Zhang, L., Zhang, Y., Zhao, Z., Zheng, Y., Zhou, X., Zhu, X., Zuber, K.: Physics prospects of the Jinping neutrino experiment. *Chinese Physics C* **41**(2), 023002 (2017) <https://doi.org/10.1088/1674-1137/41/2/023002> . Publisher: IOP Publishing. Accessed 2022-05-09
- [5] Xu, B.: Jinping Neutrino Experiment: a Status Report. *Journal of Physics: Conference Series* **1468**(1), 012212 (2020) <https://doi.org/10.1088/1742-6596/1468/1/012212> . Publisher: IOP Publishing. Accessed 2022-11-20
- [6] Xu, B.: Design and Construction of hundred-ton liquid neutrino detector at CJPL II. *PoS ICHEP2022*, 926 (2022) <https://doi.org/10.22323/1.414.0926>
- [7] Abe, K., Hiraide, K., Ichimura, K., Kishimoto, Y., Kobayashi, K., Kobayashi, M., Moriyama, S., Nakahata, M., Ogawa, H., Sato, K., Sekiya, H., Suzuki, T., Takachio, O., Takeda, A., Tasaka, S., Yamashita, M., Yang, B.S., Kim, N.Y., Kim, Y.D., Itow, Y., Kanzawa, K., Masuda, K., Martens, K., Suzuki, Y., Xu, B.D., Miuchi, K., Oka, N., Takeuchi, Y., Kim, Y.H., Lee, K.B., Lee, M.K., Fukuda, Y., Miyasaka, M., Nishijima, K., Fushimi, K., Kanzaki, G., Nakamura, S.: A measurement of the scintillation decay time constant of nuclear recoils in liquid

xenon with the XMASS-I detector. *Journal of Instrumentation* **13**(12), 12032–12032 (2018) <https://doi.org/10.1088/1748-0221/13/12/P12032> . Publisher: IOP Publishing. Accessed 2022-07-26

- [8] Readout electronics and data acquisition system of PandaX-4T experiment - IOPscience. <https://iopscience.iop.org/article/10.1088/1748-0221/17/02/T02004> Accessed 2024-03-05
- [9] Collaboration, T.L., Akerib, D.S., Akerlof, C.W., Akimov, D.Y., Alsum, S.K., Araújo, H.M., Bai, X., Bailey, A.J., Balajthy, J., Balashov, S., Barry, M.J., Bauer, P., Beltrame, P., Bernard, E.P., Bernstein, A., Biesiadzinski, T.P., Boast, K.E., Bolozdynya, A.I., Boulton, E.M., Bramante, R., Buckley, J.H., Bugaev, V.V., Bunker, R., Burdin, S., Busenitz, J.K., Carels, C., Carlsmith, D.L., Carlson, B., Carmona-Benitez, M.C., Cascella, M., Chan, C., Cherwinka, J.J., Chiller, A.A., Chiller, C., Craddock, W.W., Currie, A., Cutter, J.E., Cunha, J.P., Dahl, C.E., Dasu, S., Davison, T.J.R., Viveiros, L., Dobi, A., Dobson, J.E.Y., Druszkiewicz, E., Edberg, T.K., Edwards, B.N., Edwards, W.R., Elnimr, M.M., Emmet, W.T., Faham, C.H., Fiorucci, S., Ford, P., Francis, V.B., Fu, C., Gaitskell, R.J., Gantos, N.J., Gehman, V.M., Gerhard, R.M., Ghag, C., Gilchriese, M.G.D., Gomber, B., Hall, C.R., Harris, A., Haselschwardt, S.J., Hertel, S.A., Hoff, M.D., Holbrook, B., Holtom, E., Huang, D.Q., Hurteau, T.W., Ignarra, C.M., Jacobsen, R.G., Ji, W., Ji, X., Johnson, M., Ju, Y., Kamdin, K., Kazkaz, K., Khaitan, D., Khazov, A., Khromov, A.V., Konovalov, A.M., Korolkova, E.V., Kraus, H., Krebs, H.J., Kudryavtsev, V.A., Kumpan, A.V., Kyre, S., Larsen, N.A., Lee, C., Lenardo, B.G., Lesko, K.T., Liao, F.-T., Lin, J., Lindote, A., Lippincott, W.H., Liu, J., Liu, X., Lopes, M.I., Lorenzon, W., Luitz, S., Majewski, P., Malling, D.C., Manalaysay, A.G., Manenti, L., Mannino, R.L., Markley, D.J., Martin, T.J., Marzoni, M.F., McKinsey, D.N., Mei, D.-M., Meng, Y., Miller, E.H., Mock, J., Monzani, M.E., Morad, J.A., Murphy, A.S.J., Nelson, H.N., Neves, F., Nikkel, J.A., O'Neill, F.G., O'Dell, J., O'Sullivan, K., Olevitch, M.A., Oliver-Mallory, K.C., Palladino, K.J., Pangilinan, M., Patton, S.J., Pease, E.K., Piepke, A., Powell, S., Preece, R.M., Pushkin, K., Ratcliff, B.N., Reichenbacher, J., Reichhart, L., Rhyne, C., Rodrigues, J.P., Rose, H.J., Rosero, R., Saba, J.S., Sarychev, M., Schnee, R.W., Schubnell, M.S.G., Scovell, P.R., Shaw, S., Shutt, T.A., Silva, C., Skarpaas, K., Skulski, W., Solovov, V.N., Sorensen, P., Sosnovtsev, V.V., Stancu, I., Stark, M.R., Stephenson, S., Stiegler, T.M., Sumner, T.J., Sundarnath, K., Szydagis, M., Taylor, D.J., Taylor, W., Tennyson, B.P., Terman, P.A., Thomas, K.J., Thomson, J.A., Tiedt, D.R., To, W.H., Tomás, A., Tripathi, M., Tull, C.E., Tvrznikova, L., Uvarov, S., Va'vra, J., Grinten, M.G.D., Verbus, J.R., Vuosalo, C.O., Waldron, W.L., Wang, L., Webb, R.C., Wei, W.-Z., While, M., White, D.T., Whitis, T.J., Wisniewski, W.J., Witherell, M.S., Wolfs, F.L.H., Woods, E., Woodward, D., Worm, S.D., Yeh, M., Yin, J., Young, S.K., Zhang, C.: LUX-ZEPLIN (LZ) Conceptual Design Report (2015)
- [10] Zhang, H.Q., Wang, Z.M., Zhang, Y.P., Huang, Y.B., Luo, F.J., Zhang, P., Zhang, C.C., Xu, M.H., Liu, J.C., Heng, Y.K., Yang, C.G., Jiang, X.S., Li, F., Ye, M.,

- Chen, H.S.: Comparison on PMT Waveform Reconstructions with JUNO Prototype. *JINST* **14**(08), 08002 (2019) <https://doi.org/10.1088/1748-0221/14/08/T08002>
- [11] Zhang, A., Xu, B., Weng, J., Chen, H., Shao, W., Xu, T., Ren, L., Qian, S., Wang, Z., Chen, S.: Performance evaluation of the 8-inch MCP-PMT for Jinping Neutrino Experiment. *Nuclear Instruments and Methods in Physics Research Section A: Accelerators, Spectrometers, Detectors and Associated Equipment* **1055**, 168506 (2023) <https://doi.org/10.1016/j.nima.2023.168506> . Accessed 2023-08-02
- [12] Xu, D.C., Xu, B.D., Bao, E.J., Wu, Y.Y., Zhang, A.Q., Wang, Y.Y., Zhang, G.L., Xu, Y., Guo, Z.Y., Pei, J.H., Mao, H.Y., Liu, J.S., Wang, Z., Chen, S.M.: Towards the ultimate PMT waveform analysis for neutrino and dark matter experiments. *Journal of Instrumentation* **17**(06), 06040 (2022) <https://doi.org/10.1088/1748-0221/17/06/P06040> . Publisher: IOP Publishing. Accessed 2022-09-18
- [13] Luo, X.L., Modamio, V., Nyberg, J., Valiente-Dobón, J.J., Nishada, Q., Angelis, G.d., Agramunt, J., Egea, F.J., Erduran, M.N., Ertürk, S., France, G.d., Gadea, A., González, V., Goasduff, A., Hüyük, T., Jaworski, G., Moszyński, M., Nitto, A.D., Palacz, M., Söderström, P.-A., Sanchis, E., Triossi, A., Wadsworth, R.: Pulse pile-up identification and reconstruction for liquid scintillator based neutron detectors. *Nuclear Instruments and Methods in Physics Research Section A: Accelerators, Spectrometers, Detectors and Associated Equipment* **897**, 59–65 (2018) <https://doi.org/10.1016/j.nima.2018.03.078>
- [14] Green, P.J.: Reversible jump markov chain monte carlo computation and bayesian model determination. *Biometrika* **82**(4), 711–732 (1995). Accessed 2023-11-25
- [15] Hastings, W.K.: Monte Carlo sampling methods using Markov chains and their applications. *Biometrika* **57**(1), 97–109 (1970) <https://doi.org/10.1093/biomet/57.1.97> . Accessed 2021-12-08
- [16] Bellamy, E.H., Bellettini, G., Budagov, J., Cervelli, F., Chirikov-Zorin, I., Incagli, M., Lucchesi, D., Pagliarone, C., Tokar, S., Zetti, F.: Absolute calibration and monitoring of a spectrometric channel using a photomultiplier. *Nuclear Instruments and Methods in Physics Research Section A: Accelerators, Spectrometers, Detectors and Associated Equipment* **339**(3), 468–476 (1994) [https://doi.org/10.1016/0168-9002\(94\)90183-X](https://doi.org/10.1016/0168-9002(94)90183-X) . Number: 3 00170. Accessed 2015-07-01
- [17] Stein, J., Kreuels, A., Kong, Y., Lentering, R., Ruhnau, K., Scherwinski, F., Wolf, A.: Experiment and modeling of scintillation photon-counting and current measurement for PMT gain stabilization. *Nuclear Instruments and Methods in Physics Research Section A: Accelerators, Spectrometers, Detectors and Associated Equipment* **782**, 20–27 (2015) <https://doi.org/10.1016/j.nima.2015.01.101>
- [18] Lombardi, P., Ortica, F., Ranucci, G., Romani, A.: Decay time and pulse shape

- discrimination of liquid scintillators based on novel solvents. *Nuclear Instruments and Methods in Physics Research Section A: Accelerators, Spectrometers, Detectors and Associated Equipment* **701**, 133–144 (2013) <https://doi.org/10.1016/j.nima.2012.10.061> . Accessed 2020-02-22
- [19] *Photomultiplier Tubes: Basics and Applications*, 4th edn. Hamamatsu Photonics (2017). 00126
- [20] Dossi, R., Ianni, A., Ranucci, G., Smirnov, O.J.: Methods for precise photoelectron counting with photomultipliers. *Nuclear Instruments and Methods in Physics Research Section A: Accelerators, Spectrometers, Detectors and Associated Equipment* **451**(3), 623–637 (2000) [https://doi.org/10.1016/S0168-9002\(00\)00337-5](https://doi.org/10.1016/S0168-9002(00)00337-5) . Accessed 2019-01-22
- [21] Lehmann, A., Böhm, M., Eyrich, W., Miehling, D., Pfaffinger, M., Stelter, S., Uhlig, F., Ali, A., Belias, A., Dzhygadlo, R., Gerhardt, A., Götzen, K., Kalicy, G., Krebs, M., Lehmann, D., Nerling, F., Patsyuk, M., Peters, K., Schepers, G., Schmitt, L., Schwarz, C., Schwiening, J., Traxler, M., Düren, M., Etzelmüller, E., Föhl, K., Hayrapetyan, A., Kreutzfeld, K., Merle, O., Rieke, J., Schmidt, M., Wasem, T., Achenbach, P., Cardinali, M., Hoek, M., Lauth, W., Schlimme, S., Sfienti, C., Thiel, M.: Lifetime of MCP-PMTs and other performance features. *Journal of Instrumentation* **13**(02), 02010–02010 (2018) <https://doi.org/10.1088/1748-0221/13/02/C02010> . Accessed 2023-05-22
- [22] Guo, L., Xin, L., Li, L., Gou, Y., Sai, X., Li, S., Liu, H., Xu, X., Liu, B., Gao, G., He, K., Zhang, M., Qu, Y., Xue, Y., Wang, X., Chen, P., Tian, J.: Effects of secondary electron emission yield properties on gain and timing performance of ALD-coated MCP. *Nuclear Instruments and Methods in Physics Research Section A: Accelerators, Spectrometers, Detectors and Associated Equipment* **1005**, 165369 (2021) <https://doi.org/10.1016/j.nima.2021.165369> . Accessed 2023-04-12
- [23] Weng, J., Zhang, A., Wu, Q., Ma, L., Xu, B., Qian, S., Wang, Z., Chen, S.: Single electron charge spectra of 8-inch MCP-PMTs coated by atomic layer deposition (2024)
- [24] Zhang, H.Q., Wang, Z.M., Luo, F.J., Yang, A.B., Wu, D.R., Li, Y.C., Qin, Z.H., Yang, C.G., Heng, Y.K., Wang, Y.F., Chen, H.S.: Gain and charge response of 20” MCP and dynode PMTs. *Journal of Instrumentation* **16**, 08009 (2021) <https://doi.org/10.1088/1748-0221/16/08/T08009> . ADS Bibcode: 2021JInst..16.8009Z. Accessed 2022-01-03
- [25] Huang, Y., Chang, J., Cheng, Y., Chen, Z., Hu, J., Ji, X., Li, F., Li, J., Li, Q., Qian, X., Jetter, S., Wang, W., Wang, Z., Xu, Y., Yu, Z.: The Flash ADC system and PMT waveform reconstruction for the Daya Bay experiment. *Nuclear Instruments and Methods in Physics Research Section A: Accelerators, Spectrometers, Detectors and Associated Equipment* **895**, 48–55 (2018) <https://doi.org/10.1016/j.nima.2018.03.061> . Accessed 2019-05-08

- [26] Grassi, M., Montuschi, M., Baldoncini, M., Mantovani, F., Ricci, B., Andronico, G., Antonelli, V., Bellato, M., E. Bernieri, A. Brigatti, Brugnera, R., Budano, A., Buscemi, M., Bussino, S., Caruso, R., Chiesa, D., Corti, D., Corso, F.D., Ding, X.F., Dusini, S., Fabbri, A., Fiorentini, G., Ford, R., Formozov, A., Galet, G., Garfagnini, A., M. Giammarchi, Giaz, A., Insolia, A., Isocrate, R., Lippi, I., Longhitano, F., Presti, D.L., Lombardi, P., F. Marini, Mari, S.M., Martellini, C., Meroni, E., Mezzetto, M., Miramonti, L., Monforte, S., Nastasi, M., F. Ortica, Paoloni, A., Parmeggiano, S., Pedretti, D., Pelliccia, N., Pompilio, R., Previtali, E., Ranucci, G., A.C. Re, Romani, A., Saggese, P., Salamanna, G., Sawy, F.H., Settanta, G., Sisti, M., Sirignano, C., Spinetti, M., L. Stanco, Strati, V., Verde, G., Votano, L.: Charge reconstruction in large-area photomultipliers. *Journal of Instrumentation* **13**(02), 02008 (2018) <https://doi.org/10.1088/1748-0221/13/02/P02008> . Accessed 2019-01-22
- [27] Jetter, S., Dwyer, D., Jiang, W.-Q., Liu, D.-W., Wang, Y.-F., Wang, Z.-M., Wen, L.-J.: PMT waveform modeling at the Daya Bay experiment. *Chinese Physics C* **36**(8), 733–741 (2012) <https://doi.org/10.1088/1674-1137/36/8/009> . Accessed 2019-05-08
- [28] Rosen, K.H.: *Discrete Mathematics and Its Applications*, 5th edn. McGraw-Hill Higher Education, USA (2002)
- [29] Geman, S., Geman, D.: Stochastic Relaxation, Gibbs Distributions, and the Bayesian Restoration of Images. *IEEE Transactions on Pattern Analysis and Machine Intelligence* **PAMI-6**(6), 721–741 (1984) <https://doi.org/10.1109/TPAMI.1984.4767596>
- [30] Lucy, L.B.: An iterative technique for the rectification of observed distributions. *The Astronomical Journal* **79**, 745 (1974) <https://doi.org/10.1086/111605> . Accessed 2019-04-18
- [31] Zhang, F., Yu, B., Hu, W., Yang, M., Cao, G., Cao, J., Zhou, L.: Measurement of the liquid scintillator nonlinear energy response to electron (2015). <http://hepnp.ihep.ac.cn/en/article/doi/10.1088/1674-1137/39/1/016003> Accessed 2019-03-01
- [32] Guo, Z., Yeh, M., Zhang, R., Cao, D.-W., Qi, M., Wang, Z., Chen, S.: Slow liquid scintillator candidates for MeV-scale neutrino experiments. *Astroparticle Physics* **109**, 33–40 (2019) <https://doi.org/10.1016/j.astropartphys.2019.02.001> . Accessed 2021-01-27
- [33] Dongarra, J., Hammarling, S., Higham, N.J., Relton, S.D., Valero-Lara, P., Zounon, M.: The design and performance of batched blas on modern high-performance computing systems. *Procedia Computer Science* **108**, 495–504 (2017) <https://doi.org/10.1016/j.procs.2017.05.138> . International Conference on Computational Science, ICCS 2017, 12-14 June 2017, Zurich, Switzerland
- [34] Harris, C.R., Millman, K.J., Walt, S.J., Gommers, R., Virtanen, P., Cournapeau,

- D., Wieser, E., Taylor, J., Berg, S., Smith, N.J., Kern, R., Picus, M., Hoyer, S., Kerkwijk, M.H., Brett, M., Haldane, A., R  o, J.F., Wiebe, M., Peterson, P., G  rard-Marchant, P., Sheppard, K., Reddy, T., Weckesser, W., Abbasi, H., Gohlke, C., Oliphant, T.E.: Array programming with NumPy. *Nature* **585**(7825), 357–362 (2020) <https://doi.org/10.1038/s41586-020-2649-2>
- [35] Okuta, R., Unno, Y., Nishino, D., Hido, S., Loomis, C.: Cupy: A numpy-compatible library for nvidia gpu calculations. In: Proceedings of Workshop on Machine Learning Systems (LearningSys) in The Thirty-first Annual Conference on Neural Information Processing Systems (NIPS) (2017). http://learningsys.org/nips17/assets/papers/paper_16.pdf
- [36] NVIDIA: Nvidia Tesla P100 GPU. Pascal Architecture White Paper **47** (2016)
- [37] Gelman, A., Rubin, D.: Inference from Iterative Simulation Using Multiple Sequences. *Statist. Sci* **7**(4) (1992)
- [38] Brooks, S., Gelman, A.: General Methods for Monitoring Convergence of Iterative Simulations. *Journal of Computational and Graphical Statistics* **7** (1998)
- [39] Villani, C.: The Wasserstein distances. In: Optimal Transport. Grundlehren der mathematischen Wissenschaften, pp. 93–111. Springer, Berlin, Heidelberg (2009)
- [40] Szydagis, M., Block, G.A., Farquhar, C., Flesher, A.J., Kozlova, E.S., Levy, C., Mangus, E.A., Mooney, M., Mueller, J., Rischbieter, G.R.C., Schwartz, A.K.: A Review of Basic Energy Reconstruction Techniques in Liquid Xenon and Argon Detectors for Dark Matter and Neutrino Physics Using NEST. *Instruments* **5**(1), 13 (2021) <https://doi.org/10.3390/instruments5010013> . Number: 1 Publisher: Multidisciplinary Digital Publishing Institute. Accessed 2022-07-03
- [41] Tipping, M.: The Relevance Vector Machine. In: Solla, S., Leen, T., M  ller, K. (eds.) *Advances in Neural Information Processing Systems*, vol. 12. MIT Press, USA (1999). https://proceedings.neurips.cc/paper_files/paper/1999/file/f3144cefe89a60d6a1afaf7859c5076b-Paper.pdf
- [42] Tipping, M.E.: Sparse Bayesian Learning and the Relevance Vector Machine. *Journal of Machine Learning Research* **1**, 211–244 (2001). Publisher: Journal of Machine Learning Research
- [43] Woodbury, M.A.: *Inverting Modified Matrices*. Princeton, NJ : Department of Statistics, Princeton University, USA (1950)

A mid-infrared dual-comb spectrometer in step-sweep mode for high-resolution molecular spectroscopy

Muriel Lepère^{*a}, Olivier Browet^a, Jean Clément^a, Bastien Vispoel^a, Pitt Allmendinger^b, Jakob Hayden^b, Florian Eigenmann^b, Andreas Hugi^b, and Markus Mangold^b,

^aResearch unit Lasers and Spectroscopies (LLS), Institute of Life, Earth and Environment (ILEE), University of Namur, 61, Rue de Bruxelles, Namur, Belgium;

^bIRsweep AG, Laubisrütistrasse 44, 8712 Stäfa, Switzerland

*muriel.lepere@unamur.be; phone +3281724496; <https://www.unamur.be/en/sci/physics/ur-en/lls/>

ABSTRACT

To meet the challenges of high-resolution molecular spectroscopy, increasingly sophisticated spectroscopic techniques were developed. For a long time FTIR and laser-based spectroscopies were used for these studies. The recent development of dual-comb spectroscopy at high-resolution makes this technique a powerful tool for gas phase studies. We report on the use and characterization of the IRis-F1, a tabletop mid-infrared dual-comb spectrometer, in the newly developed *step-sweep* mode. The resolution of the wavenumber axis is increased by step-wise tuning (interleaving) and accurate measurement of the laser center wavelength and repetition frequency. Doppler limited measurements of N₂O and CH₄ reveal a wavenumber accuracy of 10⁻⁴ cm⁻¹ on the covered range of > 50 cm⁻¹. Measured half-widths of absorption lines show no systematic broadening, indicating a negligible instrument response function. Finally, measurements of nitrogen pressure broadening coefficients in the ν₄ band of methane show that quantum cascade laser dual-comb spectroscopy in *step-sweep* mode is well adapted for measurements of precision spectroscopic data, in particular line shape parameters.

1. INTRODUCTION

High-resolution molecular spectroscopy has both fundamental and applied interests. It allows understanding intra- and inter-molecular interactions in gas phase, and is a powerful tool to study planetary atmospheres. On Earth, atmospheric pollution and global warming are challenges for all societies around the world [1, 2]. Different instruments installed on various platforms (space satellites, stratospheric balloons, ground-based stations) are continuously monitoring the atmosphere to characterize it and unravel the mechanisms occurring. The retrieval of atmospheric spectra relies on the computation of the radiative transfer that in turn requires many chemical and physical parameters, among them the spectroscopic parameters and their temperature evolution. The recent improvements of remote sensing mission instruments have pushed the need for high accuracy spectroscopic data [3, 4], as the quality of the retrieved information depends on the precision of the spectroscopic parameters [5] for which the line-shape parameters are the largest sources of uncertainties [6-8].

High-resolution infrared spectrometers, such as high-resolution dual-comb spectrometers, are able to provide precise spectroscopic parameters. This data is also very important for the development and improvement of theoretical models describing molecular interactions. For decades, theoretical models have been developed and used [9] to describe the molecular interactions and to compute line-shape parameters. The models rely on intermolecular potentials that must be validated by accurate measurements. Theoretical models and laboratory measurements complement, challenge and boost each other in this quest to understand chemical and physical phenomena that occur in the gas phase. In particular, the mid-infrared spectral region is very interesting since the fundamental vibrational bands of many molecules are located in this spectral domain. At room temperature, these bands are the most intense; this allows a great precision in the measurements of spectroscopic data.

To meet the challenges of molecular spectroscopy, increasingly sophisticated spectroscopic techniques have been developed. They compete in a variety of often conflicting parameters such as good spectral resolution and large coverage, accurate absolute frequency calibration, and high signal-to-noise ratio at short measurement times. For a long time, Fourier transform spectroscopy (Ref. [10] and therein) was the workhorse for mid-infrared studies providing a lot of accurate line

parameters. In addition to a large number of commercial FTIR spectrometers, the spectral resolution has been pushed with specialized instruments with an optical path difference of up to 22 m [11] (see Ref. [12] and therein). More recently, laser-based spectroscopies have made a big impact on high-resolution spectroscopy (Ref. [12] and references in it). While sources such as diode lasers or single mode quantum cascade lasers (QCL) limit the spectral range to a few wavenumbers at most, they provide great spectral resolution, high signal-to-noise ratio, and extremely short measurement times [13, 14]. These techniques have further been coupled with technologies such as cavity ring down [15, 16], allowing the measurement of gases in extremely low concentration, cold gases in molecular jets [17, 18], or specialized cells [19-23] that enable the study of line parameters over a large temperature range.

The advent of frequency combs has revolutionized the field of high-resolution molecular spectroscopy [24]. In the near-infrared spectral range, many different spectroscopic techniques have been developed which can roughly be divided in comb-assisted spectroscopy [25] and direct frequency comb spectroscopy [26-31]. Dual-frequency comb spectroscopy is a type of the latter, which got much attention because of its mechanical simplicity (no moving elements) and the resulting potential for fast measurements of full spectra [32-36]. The mid-infrared spectral range – of interest because it hosts the fundamental ro-vibrational transitions of many molecules – has proven technologically more challenging because direct frequency comb sources were not available for a long time. Comb-assisted techniques have pushed the spectral resolution of single-mode QCLs to their limit [37, 38], while direct frequency comb spectroscopy relied on non-linear conversion of near-infrared combs in optical parametric oscillators (OPOs) or by difference frequency generation (DFG) [39, 40].

Only more recently, chip-scale sources of mid-infrared frequency combs were demonstrated in micro-resonators [41], inter band cascade lasers (ICL) [42, 43] and quantum cascade lasers [44]. Chip-scale frequency comb sources bear some inherent advantages for molecular spectroscopy. Their small size in combination with their relatively low power consumption makes them particularly attractive for field-deployed sensors or mobile applications [43, 45, 46]. The large optical output power distributed on a rather low number of optical modes bears the potential for non-linear or saturated spectroscopy [47]. In dual-comb implementations, the large repetition frequency inherent to small-scale sources allows for rapid acquisition of the full spectrum covered by the combs [48-52]. Conversely, the large repetition frequency leads to a sparse sampling of the spectrum impeding the use for high-resolution spectroscopy. Interleaving – also known from other comb sources [53-55] – has been demonstrated in micro-resonators [56-58] and ICLs [42]. MHz-level resolution and frequency accuracy in the mid-infrared has been demonstrated with QCL frequency combs. Gianella and co-workers demonstrated so called *rapid-sweep* interleaving by applying synchronized current ramps to tune both combs simultaneously [59].

In a joint effort between IRsweep and the University of Namur, we have developed for the first time what we call a *step-sweep* approach to mid-infrared high-resolution dual-comb spectroscopy with QCLs, building on a method for spectral interleaving described by Villares, Hugi, Blaser and Faist [60]. The presented technique relies on step-by-step tuning of the lasers. In contrast to simultaneous tuning of the lasers, the demonstrated technique allows for direct measurement of the relative frequency axis from the heterodyne beat signal without relying on either high bandwidth locking loops or external frequency rulers, except for the clock of the acquisition card. Furthermore, *step-sweep* retains the microsecond time resolution of the dual-comb measurement making it applicable to studies of reacting gases or transient measurement of pulsed molecular beams [61]. For an absolute frequency calibration, two parameters (an overall offset and line spacing) need to be retrieved from the measurement of a known calibration substance. Despite the optical and electronic simplicity of the presented technique, we demonstrate, over the complete coverage of $> 50 \text{ cm}^{-1}$, a frequency accuracy of below 12 MHz (0.0004 cm^{-1}) in separately calibrated measurements and below 4 MHz (0.00012 cm^{-1}) when the calibration is simultaneous with the sample measurement. Furthermore, the line broadening due to the instrument response is found to be negligible for Doppler broadened absorption lines and the line width is determined with an inaccuracy of $< 1.5 \text{ MHz}$ (0.00005 cm^{-1}). With these characteristics, the here demonstrated *step-sweep* technique can be employed for challenging tasks in molecular spectroscopy such as measurement of line shape parameters, which is demonstrated by the study of the N_2 -collisional broadening coefficient of methane lines in the ν_4 fundamental band. We show that the agreement with literature is very good.

2. IRIS-F1, A MID-INFRARED DUAL-COMB SPECTROMETER

2.1 Principle

High-resolution spectra were recorded using a commercial quantum cascade laser dual-comb spectrometer (IRis-F1, IRsweep AG) that was customized with the *step-sweep* technology for wavelength tuning (compare section 2.2). Dual-comb spectroscopy is a type of Fourier transform spectroscopy, where the mechanical interferometer is replaced by the

beating of two multi-mode coherent light sources [26, 40], which we call the local oscillator and the sample comb. In brief: each frequency comb light source emits a spectrum consisting of multiple, spectrally narrow emission frequencies. In a given comb, all the emitted frequencies have a constant spacing. Each emission frequency of the local oscillator comb (green lines in top panel of figure 1) has a close-by emission frequency of the sample comb (blue lines in figure 1). Upon mixing on a detector, a beat signal at the difference frequency of the two lines is generated. Because of a slightly different spacing between the lines of the local oscillator and the sample comb, each pair of lines generates a beat signal at a distinct frequency. Note that, since only the sample comb passes through the sample, the attenuation observed on the radio frequency signal corresponds to half of the absorbance of the sample gas experienced by the sample comb (compare figure 1b).

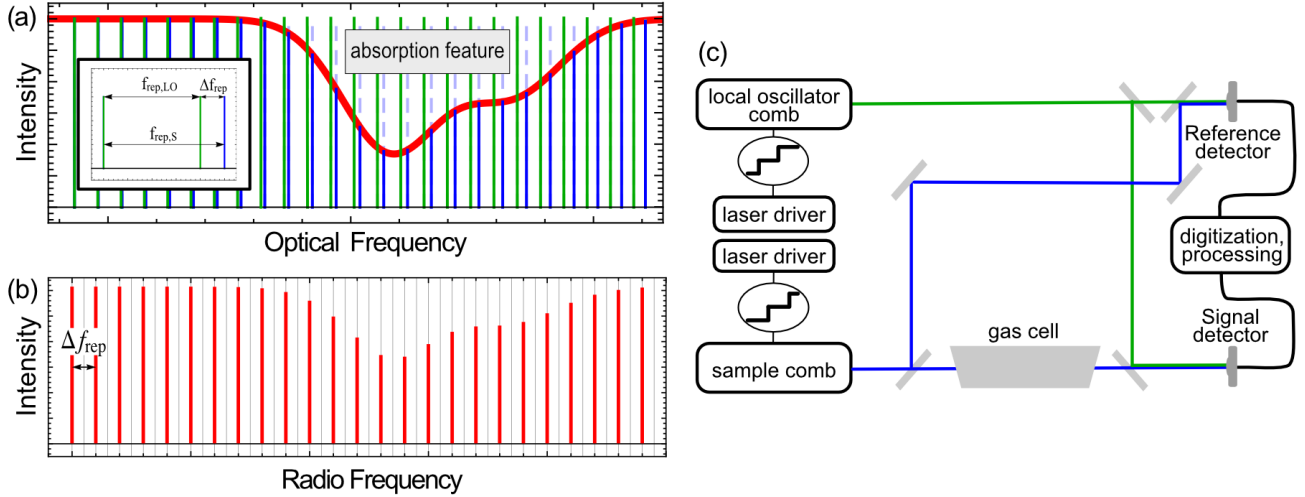


Figure 1. Left: Illustration of the optical spectrum of the sample (blue) and reference comb (green) (top panel) and the multiheterodyne spectrum measured on a detector in DCS (bottom panel). Right: Functional schematic of the IRis-F1 dual-comb spectrometer in phase sensitive configuration

A schematic of the spectrometer is shown in Figure 1. The spectrometer uses two closely matched QCL frequency comb sources emitting at a center frequency of 1308 cm^{-1} with a span of 50 cm^{-1} and a repetition rate of 9.891 GHz (0.3299 cm^{-1}) and 9.894 GHz , respectively. The spectrometer is operated in a phase sensitive configuration [59], *i.e.* only one of the beams (sample comb) passes through the sample and is overlapped with the beam from the second QCL frequency comb (local oscillator) before being detected on a thermoelectrically cooled HgCdTe detector of 1 GHz bandwidth. The detector signal displaying a multi-heterodyne beat note between the two frequency combs is digitized using a high speed digitizer (2 GS , 14 bit). The raw digitized signal is processed on dedicated hardware as described by Klocke *et al.* [48] to obtain the amplitude and phase of each line in the heterodyne beat note, corresponding to the intensity and phase of each line of the sample QCL frequency comb. Since the frequency combs are free running, *i.e.* they are not locked to one another, small frequency fluctuations result in amplitude and frequency noise on the recorded multiheterodyne beat note. This noise is strongly reduced using a reference beam-path and detector (compare Figure 1) and calculating the ratios of the complex sample and reference beat note amplitudes [48].

2.2 Step sweeping for high resolution

Although the narrow line width of the individual lines of the QCL frequency comb is well suited for high-resolution spectroscopy, the point spacing between adjacent lines is generally too large. While the high repetition rate f_{rep} of QCL frequency combs (0.3299 cm^{-1} in this work) and large Δf_{rep} of the IRis-F1 dual-comb spectrometer render it ideally suited for μs -time-resolved spectroscopy in condensed phase [48], narrow features of molecular gases are sampled insufficiently by the lines of the comb. To close the gaps between adjacent comb lines, the QCL frequency combs' emission frequencies can be tuned across a gap via temperature or current. Gianella *et al.* used a synchronized ramp of the sample and local oscillator comb's wavelengths to keep the difference frequencies between them, and hence the multiheterodyne beat note, within the detection bandwidth of the photo detectors [59]. Since the wavelength of both lasers were changed simultaneously, the wavelength and repetition rate tuning of the frequency combs cannot be retrieved from the

multiheterodyne beat note. Hence, the wavenumber axis must be retrieved from reference data, e.g. the interference fringes of an etalon, or by including frequency references, such as line-locked single-mode QCLs, in the experiment [62].

Here, we overcome this limitation by tuning only one QCL frequency comb at a time, using the second frequency comb as a fixed reference. The procedure is illustrated in figure 2. Initially, the optical spectrum of the local oscillator (LO) and signal (S) frequency comb are described by the amplitudes and phases of the comb lines of index j centered at frequencies

$$f_{j,LO} = f_{CEO,LO} + j \cdot f_{rep,LO}$$

$$f_{j,S} = f_{CEO,S} + j \cdot f_{rep,S}$$

Herein, f_{CEO} is the center frequency of the comb and f_{rep} the line spacing (repetition frequency) of the comb. For the combs used here, the index j covers roughly the range $-90 < j < 90$. The frequencies $f_{j,het}$ of the lines of the multiheterodyne spectrum measured on the detectors are described in the same way by a center frequency Δf_{CEO} and repetition frequency Δf_{rep} given by

$$f_{j,het} = \Delta f_{CEO} + j \cdot \Delta f_{rep}$$

$$\Delta f_{CEO} = f_{CEO,S} - f_{CEO,LO}$$

$$\Delta f_{rep} = f_{rep,S} - f_{rep,LO}$$

The amplitude R and phase ϕ of the lines in the multiheterodyne spectrum (used for calculating transmission and dispersion spectra) are measured relative to the multiheterodyne spectrum from a reference detector [48].

A step along the frequency axis is initiated by increasing the current of the signal comb by an increment, yielding a shift of $f_{CEO,S}$ and $f_{rep,S}$ and a corresponding change of Δf_{CEO} and Δf_{rep} (not shown in Figure 2) of the multiheterodyne spectrum. Since the local oscillator FC is unchanged, the shift of each line in the multiheterodyne spectrum corresponds directly to the shift of the optical frequency of the signal FC.

$$f_{CEO,S,k}(k = 1, 3, \dots) = f_{CEO,LO,k} + \Delta f_{CEO,k}$$

$$f_{rep,S,k}(k = 1, 3, \dots) = f_{rep,LO,k} + \Delta f_{rep,k}$$

$$f_{CEO,LO,k}(k = 1, 3, \dots) = f_{CEO,LO,k-1}$$

$$f_{rep,LO,k}(k = 1, 3, \dots) = f_{rep,LO,k-1}$$

where, k is the index of the current step. Odd and even values of k correspond to steps of the signal frequency comb and local oscillator frequency comb, respectively. After stabilization of the signal frequency comb and measurement of $\Delta f_{CEO,k}$ and $\Delta f_{rep,k}$, the local oscillator frequency comb is tuned in the same way. Thereby, $\Delta f_{CEO,k}$ and $\Delta f_{rep,k}$ of the multiheterodyne spectrum are shifted back close to their initial values. Again, since only the local oscillator frequency comb changes, the measured values $\Delta f_{CEO,k}$ and $\Delta f_{rep,k}$ in the beat note directly reflect the changes of the optical frequencies of local oscillator comb and the new $f_{CEO,LO,k}$ and $f_{rep,LO,k}$ are given by

$$f_{CEO,LO,k}(k = 2, 4, \dots) = f_{CEO,S,k} - \Delta f_{CEO,k}$$

$$f_{rep,LO,k}(k = 2, 4, \dots) = f_{rep,S,k} - \Delta f_{rep,k}$$

$$f_{CEO,S,k}(k = 2, 4, \dots) = f_{CEO,S,k-1}$$

$$f_{rep,S,k}(k = 2, 4, \dots) = f_{rep,S,k-1}$$

By repeating the current steps on the signal and local oscillator frequency comb, the gap between adjacent lines can be closed without moving the multiheterodyne beat note to frequencies outside the detection bandwidth. Since Δf_{CEO} and Δf_{rep} are measured in every step, only the initial values of $f_{CEO,S,k=0}$ and $f_{rep,S,k=0}$ are necessary to precisely locate each measurement on the frequency axis. Here, $f_{CEO,S,k=0}$ and $f_{rep,S,k=0}$ are determined in post-processing by fitting the recorded absorption line positions to reference data from published line lists.

In conclusion, the relative wavenumber scale can be obtained directly from each measurement via the heterodyne beat frequencies. However, we found that the repeatability of the wavenumber axis between scans was better than its measurement due to the accumulation of measurement errors over many steps. Therefore, the relative wavenumber scale

is obtained from a series of sweeps by co-averaging the step sizes and is then used for all subsequent measurements taken with the same laser conditions. After that, the absolute frequencies of one step of the sweep – given by the two parameters $f_{CEO,S,k=0}$ and $f_{rep,S,k=0}$ – have to be determined from at least two known absorption features of a sample. While best accuracy is achieved by measuring the calibration substance simultaneously with the sample of interest, we will show in section 3.2, that the long term stability of the frequency combs also allows determining the initial offset and repetition frequency in a separate measurement before or after the actual sample measurement.

To obtain transmission and dispersion spectra, a background spectrum is recorded by repeating the above procedure while the sample gas cell is evacuated (background spectrum) and filled with the sample (sample spectrum).

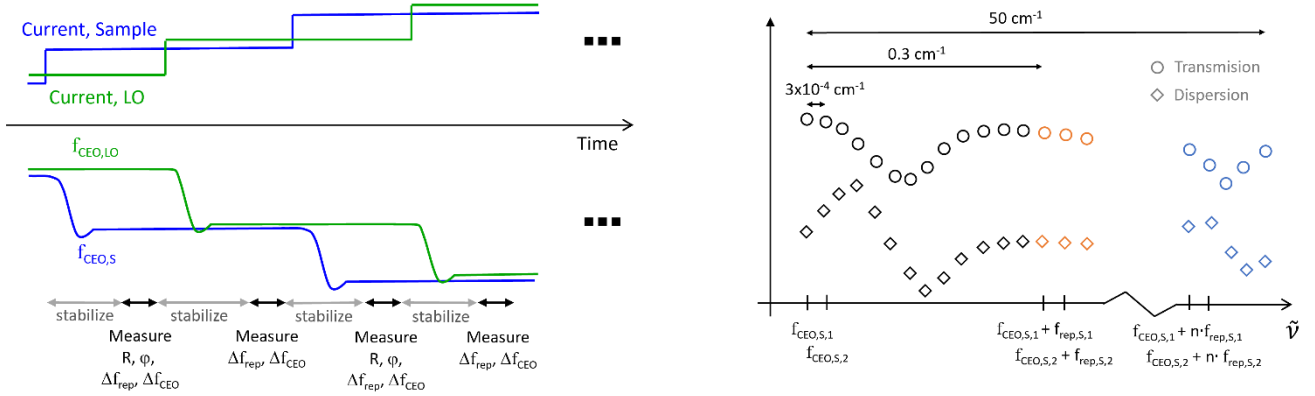


Figure 2. Illustration of the step sweep technique (see text). Left: Laser current and comb center frequency of the signal (S) and local oscillator (LO) comb during step sweeping. Right: Schematic transmission and dispersion spectra. Different colors indicate different comb lines that are tuned in a step-wise fashion to bridge the gap to the next comb line.

2.3 Experimental details

The step width can be varied between 6 MHz (0.0002 cm^{-1}) and approximately 200 MHz (0.0067 cm^{-1}), corresponding to 1700 to 50 steps to fill the gap between adjacent comb lines. The lower step width limit is given by the resolution of the digital to analog converter that is used to adjust the current setpoint on the laser driver. The upper limit is given by the bandwidth of the data acquisition card of 1 GHz, of which ~ 500 MHz is occupied by the width of the multiheterodyne beat-signal (~ 180 lines, $\Delta f_{rep} = 3.7$ MHz) and 0-50 MHz and 950 MHz – 1 GHz are typically avoided due to low frequency noise and the onset of the high-frequency roll-off, respectively.

The duration of a wavelength sweep depends on the number of steps ($\sim 1.1 \cdot f_{rep} / \text{step-width}$) and the target signal to noise ratio (SNR) on the vertical axis (transmission and dispersion). The SNR increases with the square root of the acquisition length in the range between $4 \mu\text{s}$ and ~ 125 ms. In this work, 4.2 ms were used (compare section 3.1). The stabilization time of 1 s after each current step is larger than the data processing time for the acquisition. The overall measurement time of 1200 s per step sweep measurement of 2×600 step is hence limited by the laser stabilization time. For acquisition lengths exceeding 4.2 ms, the data processing time becomes limiting.

3. CHARACTERISATION OF IRIS-F1 AT HIGH RESOLUTION

3.1 Spectral range, absorbance noise, and linear range

The spectral coverage in a dual-comb experiment is given by the overlap region of the two used frequency combs. The lasers used in this study overlap in a spectral range from 1283 to 1333 cm^{-1} . This range is well suited to study the Q-branch as well as the low rotational levels of the P- and R-branches of the ν_4 fundamental band of methane. In Figure 3 a), a measured transmission spectrum of pure methane at 0.185 mbar pressure is presented together with a calculated transmission spectrum based on line parameters from the HITRAN database [63]. Figure 3 b) shows the dispersion spectrum which is measured simultaneously in the dual-comb experiment.

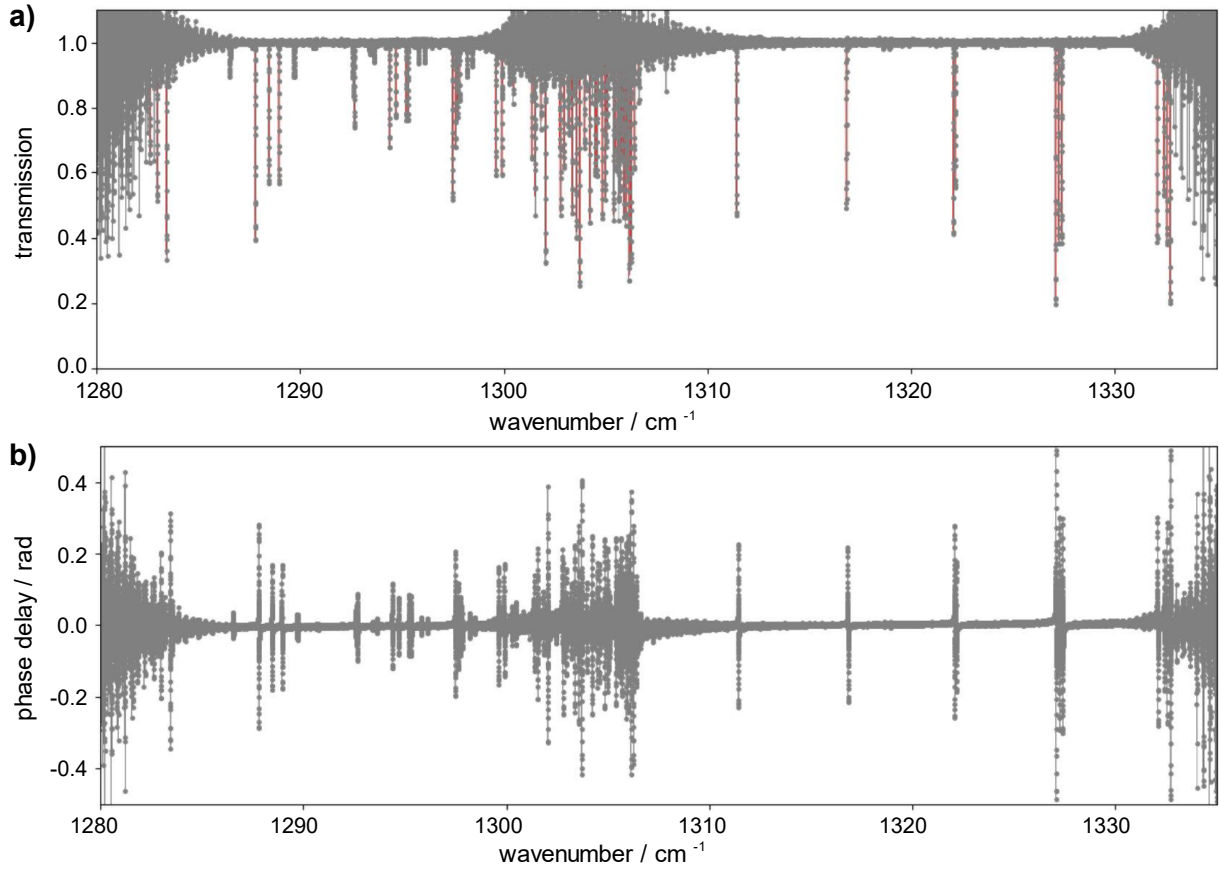


Figure 3: a) Transmission and b) corresponding dispersion spectrum of room temperature, Doppler broadened methane at 0.185 mbar pressure. The red line represents a calculated transmission spectrum based on Hitran line parameters.

Since the emission power varies from comb mode to comb mode (compare inset in Figure 4 b), the signal quality varies considerably within the covered spectral range. In Figure 4 a), we plot the absorbance $A = -\ln(T)$ of a transmission T measurement of an empty gas cell (grey dots). The red dots show a co-average of five subsequent measurements. We observe two low noise regions interrupted by a higher noise region covering roughly 1300-1308 cm^{-1} . The inset shows a zoom on the absorbance signal around 1292 cm^{-1} . A more comprehensive view of the same data is given in Figure 4 b), where for each comb mode the standard deviation of the 600 measurement steps is plotted vs. their center wavenumber. Again, the grey solid dots are values obtained with a single scan, while the red ones are computed after co-averaging five measurements. For a single scan, the standard deviation lies below 0.01 absorbance units on a range of 36 cm^{-1} , while in the complete range used for analysis in this paper from 1283 to 1333 cm^{-1} the standard deviation lies below 0.05 absorbance units. The signal quality can be improved by co-averaging approximately by the expected factor of $\sqrt{5}$ as shown by the red dots. Also, the high noise region in the center could be further suppressed by using spectral filters to shape the laser emission spectrum [64].

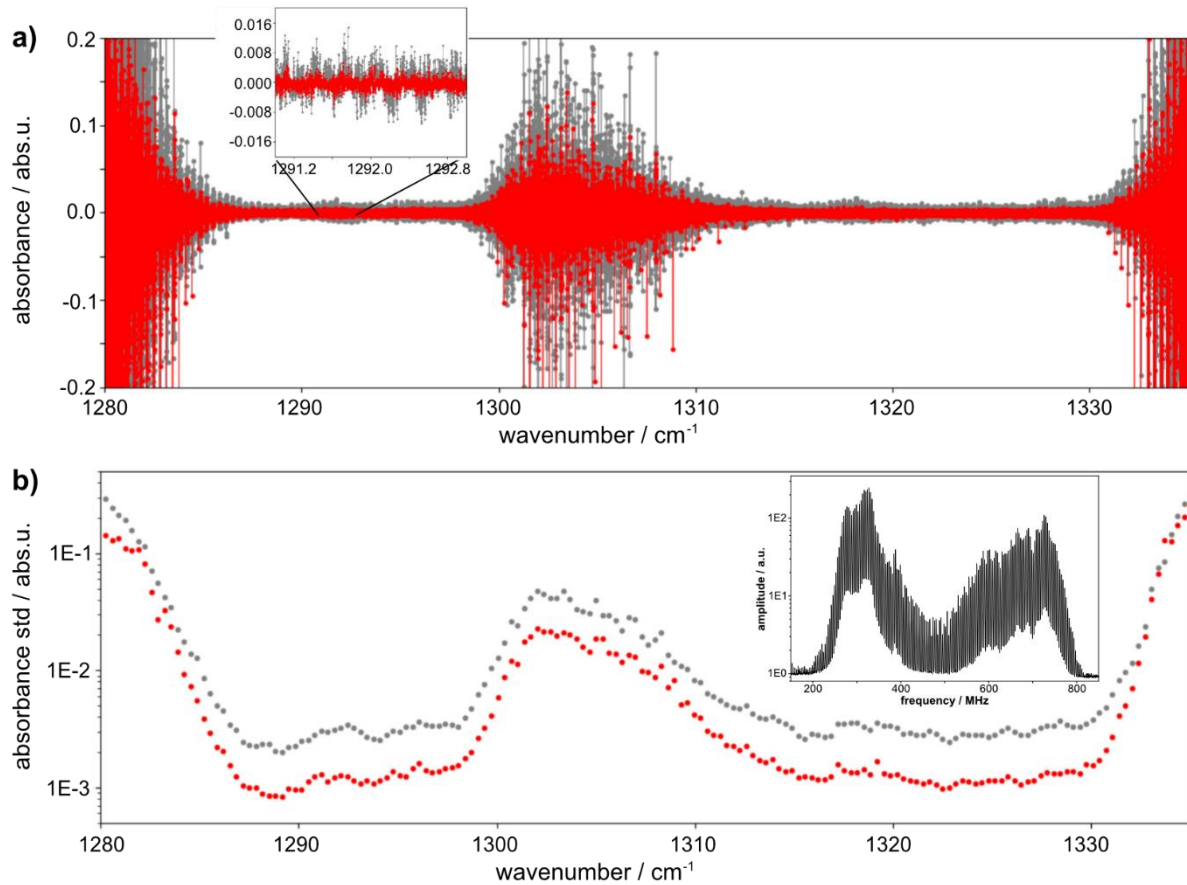


Figure 4: a) Absorbance measurement of an empty cell. Inset: zoom on the range 1291-1293 cm^{-1} . Grey dots result from a single scan, red dots are 5 scans co-averaged. b) Each grey (red) data point represents the standard deviation of the absorbance signal of a single comb mode calculated over all 600 steps for a single scan (5 scans co-averaged). Inset: Heterodyne emission spectrum of the dual-comb laser module.

To investigate the linear range of the dual-comb measurement and the performance at very high optical density (strong absorbance), the spectrum of CH_4 at a pressure of 5.06 mbar and at room temperature was recorded. In figure 5a), a section of the obtained absorption spectrum is plotted together with a reference spectrum calculated using line parameters from the HITRAN 2020 database [63].

The peak absorbance of lines from 1283 to 1333 cm^{-1} were extracted by means of peak finding without fitting of the absorption band. The found values were compared against the peak absorbance predicted by the HITRAN 2020 simulation. The result is shown in figure 5b) for absorption lines exceeding a peak absorbance of 0.006. Agreement with the HITRAN reference spectrum is observed for absorption lines of peak absorbance in the entire range from the measurement noise floor (compare figure 4 b) to 10 abs.u., limited by dark noise of the detection system. The ability to accurately measure very strong absorbance can be attributed to the phase coherent dual-comb measurement, which reduces the effect of incoherent dark noise of the detection system.

The linearity and large dynamic range of the transmission axis indicate that the spectrometer is well suited for measurements of line intensities. However, such measurements are beyond the scope of this article since a shorter gas cell of precisely defined length as well as a higher sample pressure would be needed.

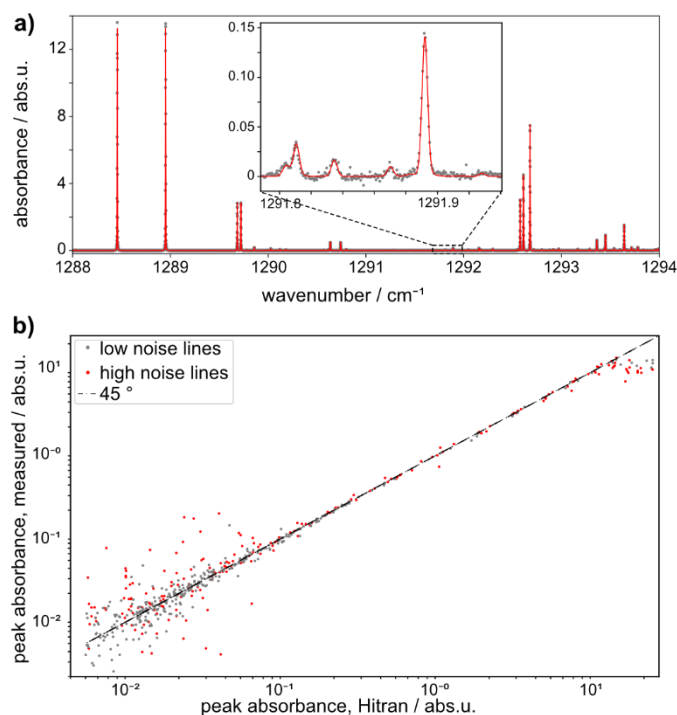


Figure 5. Linear range of absorption measurements. a) Measured (grey dots) and Hitran simulated spectrum (red line) of CH₄ at 5.06 mbar, featuring strong absorption lines. b) From the same measurement, measured peak absorbance of lines from 1283 to 1333 cm⁻¹ plotted against their predicted value. Data points are categorized into spectral regions with high and low measurement noise.

3.2 Wavenumber calibration of spectra

As described in section 2.2, the wavenumber axis calibration of the spectrometer consists of two steps: (i) creating a relative wavenumber axis from the measurement of the heterodyne beat frequencies of “empty” sweeps and (ii) determining the starting frequencies $f_{CEO,S,k=0}$ and $f_{rep,S,k=0}$ from the measurement of a well-known calibration spectrum. To assess the accuracy and repeatability of the relative wavenumber axis and the starting frequencies, we analyze measurements of the ν_1 band of N₂O and the ν_4 band of methane and compare them to tabulated values.

For the two considered molecules, the absorbance of each line in the spectrum has been fitted using a Gaussian profile (the partial pressure of active gas was respectively 0.045 mbar and 0.182 mbar for N₂O and CH₄, allowing us to neglect the contribution of collisions). In figure 6, we show a fit of a Gaussian profile to an absorption line of methane at 1288.457 cm⁻¹ in red. The standard deviation of the fit residual of 0.0019 absorbance units corresponds well to the standard deviation determined in the empty cell measurements shown in figure 4 b). We generally find that the residuals of Gaussian fits to low pressure methane transitions correspond to values expected from the measurement noise.

A fit of the corresponding dispersion signal with a Dawson function is shown in black in figure 6. Both, dispersion and absorbance signal, can well be used to determine the line position. We generally observe lower fit uncertainties in the dispersion signal in the high noise part of the spectrum. At the same time, the dispersion signal is more strongly influenced by other transitions close to the fitted transition. Therefore, it should only be used on well isolated transitions or multiple transitions have to be fitted simultaneously. To avoid these complications, for the rest of this study we only analyze results obtained by fitting the absorption signal.

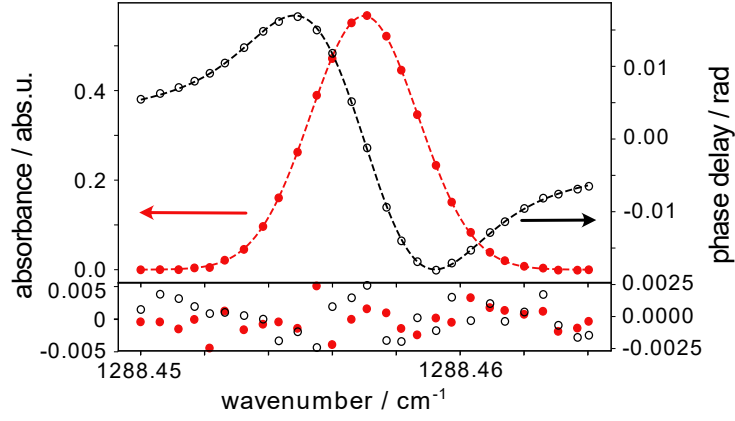


Figure 6. Top panel: absorbance (red dots) and dispersion (black circles) corresponding to the transmission and dispersion data shown in Figure 3, zoomed in around 1288.457 cm^{-1} . The red and black dashed lines indicate a fitted Gaussian and Dawson profile, respectively. Bottom panel: residuals of the fitted line shapes.

The quality of the relative frequency axis is assessed by comparing the observed line frequencies of the N_2O transitions to the HITRAN line positions [63]. Two recent experiments have confirmed the line positions given in Hitran to within < 2 MHz deviation [65, 66]. Comparing our data to these line lists leads to the same conclusion, therefore we restrict our comparison to the values given in Hitran. For this comparison, $f_{\text{CEO},S,k=0}$ and $f_{\text{rep},S,k=0}$ are calibrated directly on the data under consideration by minimizing the deviation between our observed line positions and the tabulated values. The deviation between our measurement and HITRAN is plotted in figure 7 a) as grey dots. The red line indicates a linear fit to the data. A non-vanishing slope of the linear fit indicates an error in $f_{\text{rep},S,k=0}$. Thus, $f_{\text{rep},S,k=0}$ is chosen such as to minimize the slope of the linear fit. The offset of the linear fit is minimized by the value of $f_{\text{CEO},S,k=0}$. Following this procedure, we find that all line positions agree with the HITRAN line positions to within 0.00012 cm^{-1} (± 4 MHz, red shaded area in figure 7 a), with a standard deviation of 0.00006 cm^{-1} (± 2 MHz). The one outlier at 1308.395 cm^{-1} is most likely caused by a weak nearby transition that distorts the fit. From this, we conclude that the relative wavenumber axis generated in the QCL dual-comb measurement is accurate to within 0.00012 cm^{-1} (± 4 MHz).

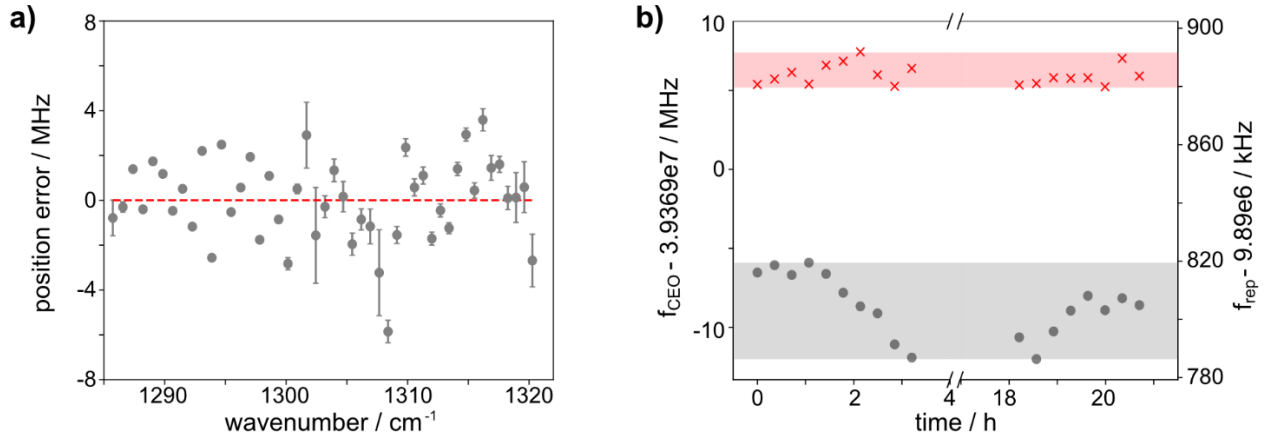


Figure 7. a) Deviation between fitted line positions and tabulated values in Hitran (grey dots) for a measurement of N_2O at 0.045 mbar. Error bars indicate the fit uncertainty. b) Evolution of the laser center frequency $f_{\text{CEO},S,k=0}$ (grey dots, left axis) and repetition frequency $f_{\text{rep},S,k=0}$ (red crosses, right axis) over 20 hours. The grey shaded area indicates a range of f_{CEO} of 6 MHz and the red shaded area indicates a range of f_{rep} of 12 kHz.

Applying the same procedure to measurements of the ν_4 band of methane, we have measured the position of 66 methane transitions (between 1283 and 1333 cm^{-1}) and compared them to HITRAN2020. IRis-F1 reproduces accurately the HITRAN data with a maximum deviation of $< 0.0004 \text{ cm}^{-1}$ (12 MHz), which is within the stated uncertainties provided by HITRAN. A relative wavenumber accuracy very similar to that shown for N_2O is found when comparing our data to data

from Germann *et al.* [67] measured using a Fourier transform spectrometer based on a GPS stabilized frequency comb [65]. This comparison is to be confirmed once the used line list has been published and peer reviewed. It has to be pointed out that, while many of the methane transitions are located in the region having a larger level of noise, the agreement with tabulated positions remains very good.

The repeatability of the absolute frequency calibration of subsequent measurements is assessed by determining $f_{CEO,S,k=0}$ and $f_{rep,S,k=0}$ in a series of measurements spread over a time range of more than 20 hours. This should simulate an experiment starting with a calibration measurement and subsequent measurements of samples of interest are taken later the same day or on the following day. In figure 7b), we show the time evolution of $f_{CEO,S,k=0}$ and $f_{rep,S,k=0}$ over 20 hours. The peak-to-peak deviation of $f_{CEO,S,k=0}$ amounts to 6 MHz. For $f_{rep,S,k=0}$, we observe peak-to-peak fluctuations of 12 kHz. Multiplied by the maximum of 180 comb modes, this amounts to a maximum frequency error of ~2 MHz. Summing the two contributions of the absolute frequency drift with the 4 MHz maximum error of the relative frequency axis, we estimate an overall maximum frequency error of < 12 MHz (< 0.0004 cm⁻¹) of the dual-comb spectrometer.

3.3 Instrumental distortion

A key advantage of laser-based spectrometers is their high spectral resolution. The jitter of the laser emission frequency on a time scale of a single measurement will lead to a broadening of observed spectral features and thereby limit the resolving power of the spectrometer.

For this characterization, we recorded spectra of pure methane at low pressure (< 1 mbar). In these conditions, the contribution of the collisions to observed profile is negligible and the experimental profile is a convolution between a Gaussian which represents the Doppler broadening and the apparatus function. Indeed, the collisional broadening is very weak and is negligible under these experimental conditions. The well-known Doppler half-width can be calculated as

$$\gamma_D = \sqrt{\frac{2 \ln(2) k_0 T}{m c^2}} v_0,$$

with k_0 the Boltzmann constant, $T = 296$ K the laboratory temperature, m the active molecule mass, c the speed of light and v_0 the center wavenumber of the transition.

We have tried to determine the width of the apparatus function and its line shape. We have tested a Gauss, Lorentz or Voigt profile, leading to Gauss or Voigt observed line shape (convolution between the Doppler line shape and the apparatus function). For each considered line, the low-pressure line shape was fitted with the three tested profiles. An example of the fit and residuals is given in Fig.8 for the P(3) F₁(2)←F₂(1) methane transition. The residuals do not show particular features, are very similar to each other and have the magnitude of the experimental noise. In Tab.1, the average values, over all studied lines, of the standard deviation of the residuals are presented. The three tested apparatus functions have very close and small values. The obtained half-widths of the apparatus functions are insignificant regarding the resolution of the spectrometer.

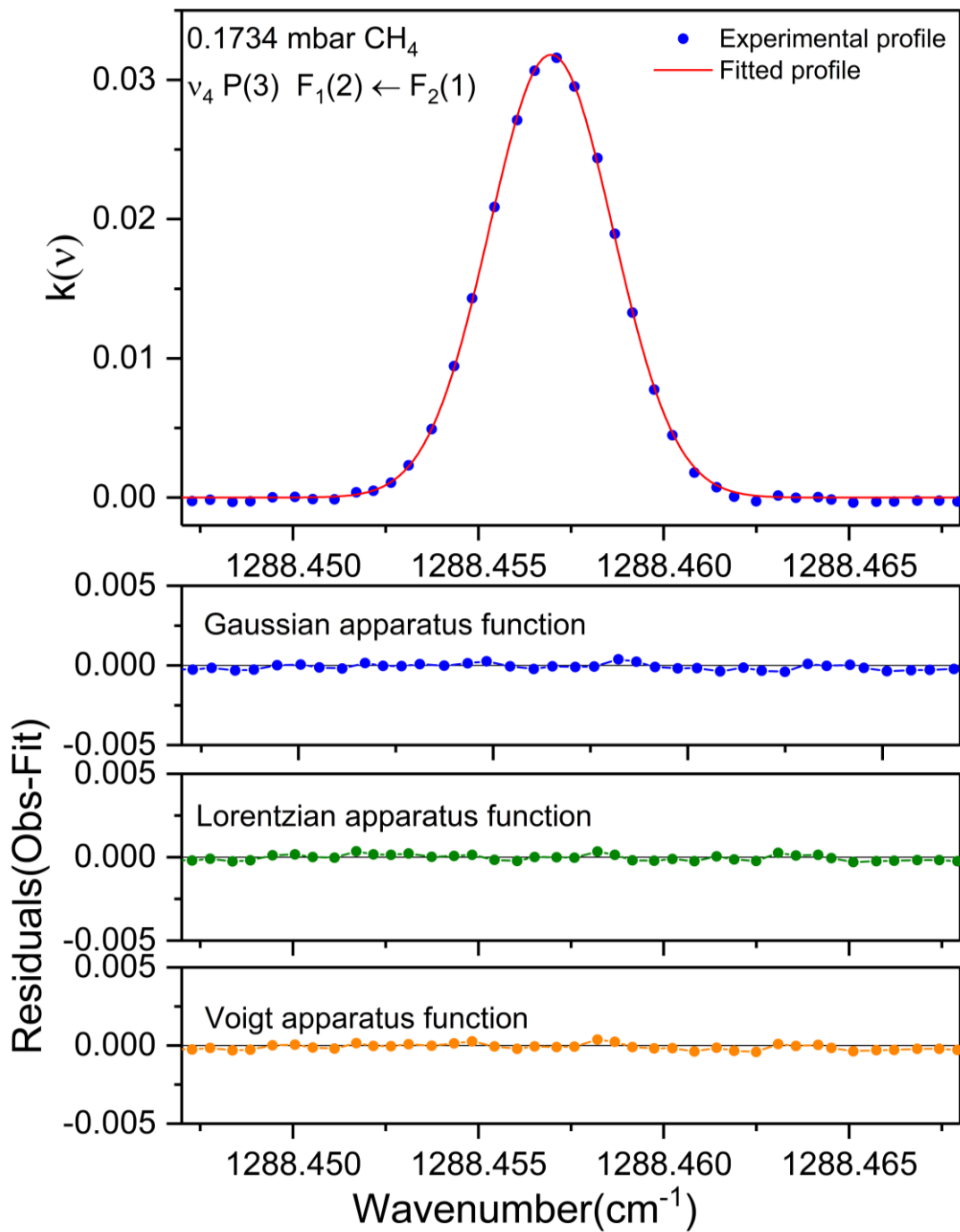


Figure 8: Example of low-pressure observed (●) profile and the Gaussian fitted profiles for the P(3) F₁(2) ← F₂(1) line in the ν_4 band of CH₄. The residuals (Obs-fit) for considered Gauss, Lorentz and Voigt apparatus functions are shown at the bottom.

	Gaussian apparatus function	Lorentzian apparatus function	Voigt apparatus function
Mean standard deviation of the residuals (cm^{-1})	0.00017	0.00017	0.00016

Table 1: Average values, over all studied lines, of the standard deviations of the residuals (Exp-fit) for the Gaussian, Lorentzian and Voigt apparatus functions.

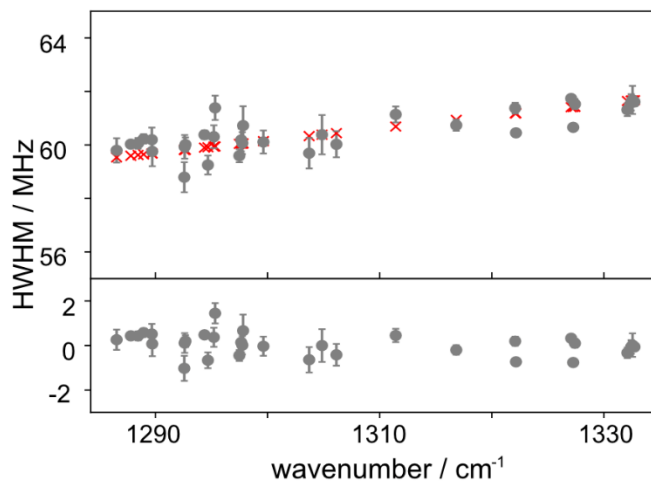


Figure 9: Upper panel: Half width at half maximum (HWHM) of Gaussian line fits (grey dots) and calculated Doppler width (red crosses) for a measurement of CH_4 at 0.182 mbar. Lower panel: deviation between calculated and observed HWHM.

Since none of the tested apparatus function gave significant improvement of the residuals, we compare the half-width at half-maximum of the fitted Gaussian profiles to the theoretical Doppler half-width at room temperature for methane lines within the IRis-F1 spectral range. Since the determination of the line width requires a higher SNR than determining the line center, we limit the analysis to the 31 transitions with $\text{SNR} > 50$. Figure 9 shows the difference between the fitted Gaussian (grey dots) and the theoretical Doppler half-widths (red crosses) as a function of their line positions. No systematic deviation of the observed absorption features was found. Rather, the observed line widths scatter around the theoretical Doppler values with a RMS deviation of 500 kHz (peak deviation $< 1.5 \text{ MHz} / 0.00005 \text{ cm}^{-1}$). We attribute the observed deviations to the remaining inaccuracy of the relative wavenumber axis and the limited SNR of the measurement. This result demonstrates that the line distortion due to the instrument response is negligible under the current experimental conditions (Doppler broadening and SNR) and that QCL frequency combs are well suited for applications that require high spectral resolution such as line-shape parameter measurements.

3.4 Example of results in high resolution molecular spectroscopy

We have recorded spectra of methane-nitrogen mixtures at 293K ($\pm 1 \text{ K}$) with an optical path length of 15.0 cm. The lines under study were located in the P-, Q and R-branches of the ν_4 band of methane. The partial pressure of CH_4 was kept constant and very low (0.606 mbar), in view to minimize the self-broadening contribution, while the nitrogen pressure was comprised between 26.2 and 105.5 mbar (Fig. 10).

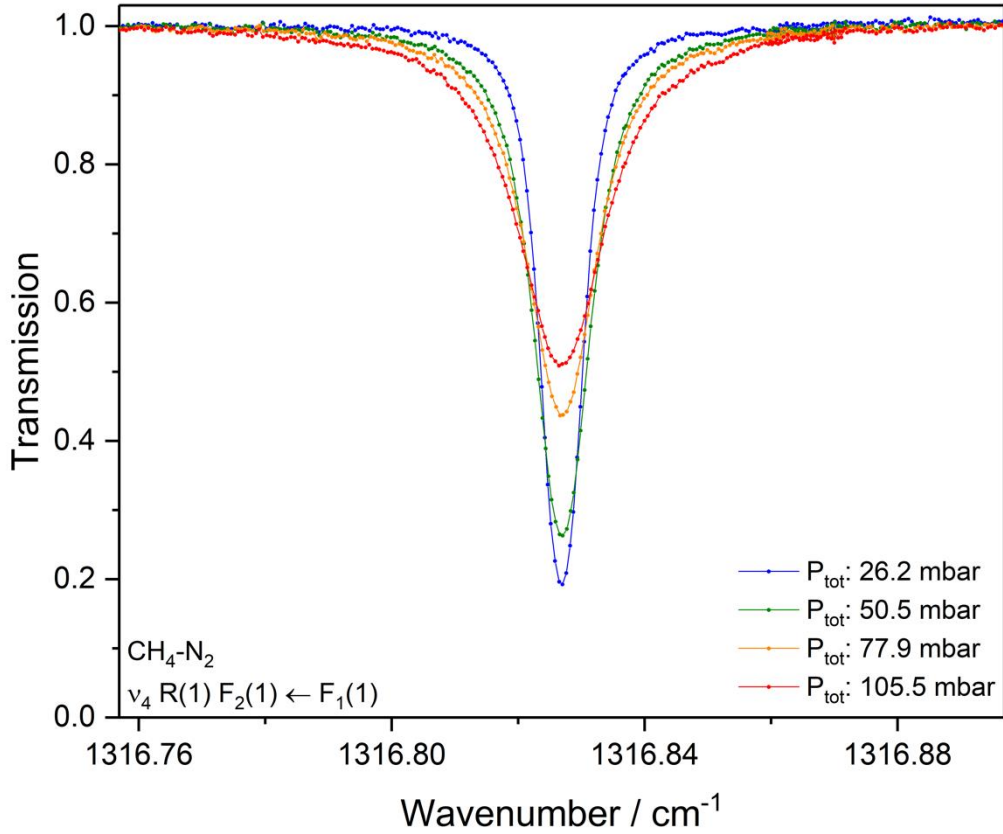


Figure 10: Example of high-resolution IRis-F1 spectra of methane diluted in nitrogen for the ν_4 band line $R(1) F_2(1) \leftarrow F_1(1)$. The wavenumber axis calibration was performed using the described procedure. The blue, green, orange and red spectra were recorded with 0.606 mbar of methane diluted in 26.2, 50.5, 77.9 and 105.5 mbar of nitrogen, respectively.

To determine the N_2 -collisional width of lines, a procedure of fit was used. In order to compare with published data, we have considered the well-known Voigt profile [68] that is given by:

$$k_V(x, y, A) = A \frac{y}{\pi} \int_{-\infty}^{+\infty} \frac{\exp(-t^2)}{y^2 + (x - t)^2} dt$$

with $A = \frac{S\sqrt{\ln 2}}{\gamma_D \sqrt{\pi}}$, $y = \sqrt{\ln 2} \frac{\gamma_C}{\gamma_D}$, $x = \sqrt{\ln 2} \frac{\nu - \nu_0 - \delta_C}{\gamma_D}$, where ν_0 is the line center position (in cm^{-1}), S the line intensity (in cm^{-2}), γ_C the collisional half-width (in cm^{-1}), δ_C the pressure-shift (in cm^{-1}) and γ_D the calculated Doppler half-width (in cm^{-1}). The Voigt profile was adjusted on the experimental profile for each considered pressure of N_2 using the Levenberg-Marquardt algorithm [69]. Figure 11 gives an example of Voigt profile adjusted on the experimental line shape of the ν_4 band $R(1) F_2(1) \leftarrow F_1(1)$ transition. The pressure of methane was 0.606 mbar for a total pressure of 26.2 mbar. Measurements were performed at 293 K with an optical path length of 15.0 cm. Agreement between observed and adjusted profiles is shown by the residuals, which have the typical “W” shape signature for the Voigt profile. This expected residual signature shows that the spectrometer can also be used to study beyond-Voigt line shape parameters.

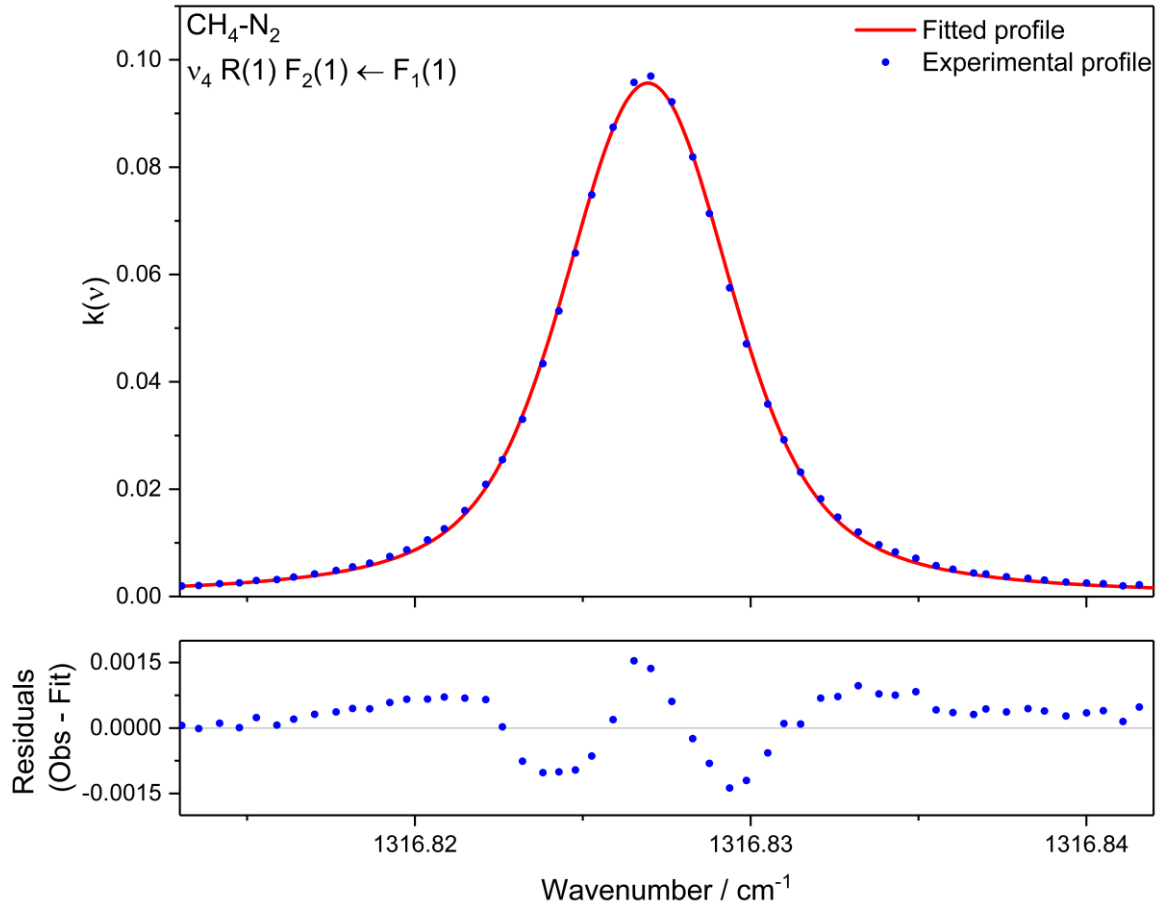


Figure 11 Example of observed (●) and Voigt fitted profiles for the R(1) F2(1) ← F1(1) line in the ν_4 band of CH4 for 0.606 mbar diluted in 26.2 mbar of N2 at 293K. The residuals (O-C) are shown at the bottom.

The Voigt fits allow the measurement of N₂-collisional half-width of lines (γ_c in cm⁻¹) at a given pressure of nitrogen. From these results, we can deduce the N₂-collisional broadening coefficient of lines (γ_0 in cm⁻¹.atm⁻¹) taking into account the weak self-broadening:

$$\gamma_c = \gamma_0 \times p_{N_2} + \gamma_0^{Self} \times p_{CH_4}$$

where p_{N_2} and p_{CH_4} are the N₂- and CH₄-pressures, while the self-broadening coefficients of lines (γ_0^{Self} in cm⁻¹.atm⁻¹) are taken from Ref [63]. For that, N₂-broadening coefficient is given by the slope of the best-fit straight line passing through the fitted half-widths at different pressures. An example is shown in Fig. 12.

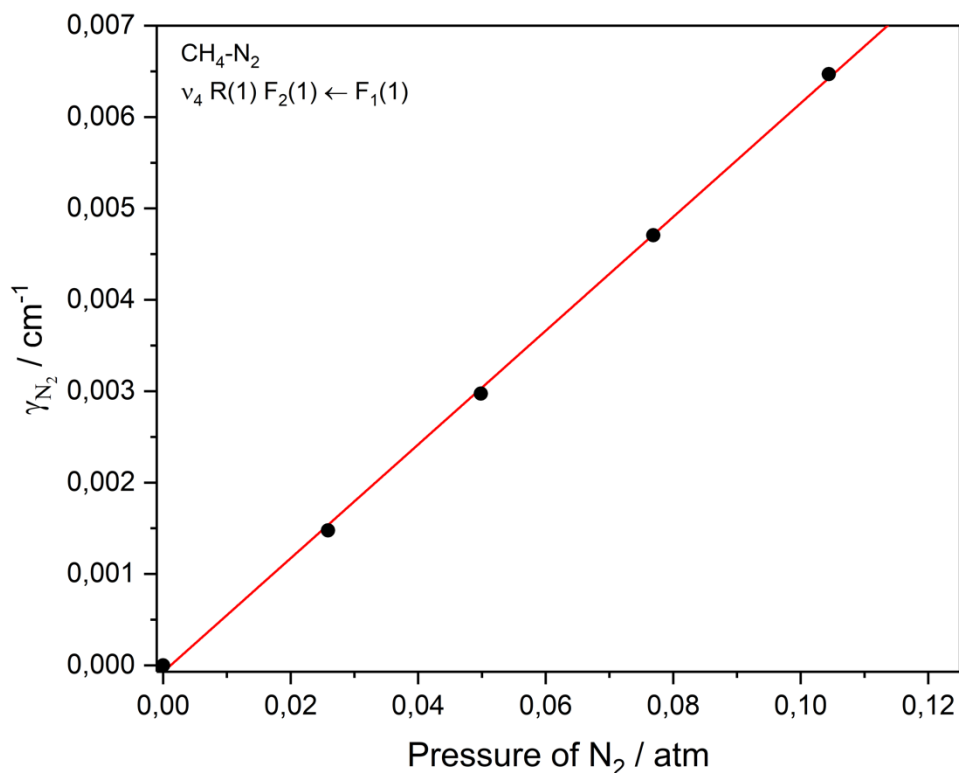


Figure 12 Plot of the nitrogen collisional half-widths γ_{N_2} versus the N_2 -pressure for the $R(1) F_2(1) \leftarrow F_1(1)$ line of the ν_4 band of methane. The half-widths are derived from the fits of the Voigt (\square) profile. The slope of the best-fit line, passing through zero, represents the N_2 -broadening coefficient γ_0 . The γ_{self} of CH_4 data are taken from [63].

40 transitions were analyzed using the described procedure. The uncertainties are determined as twice the standard deviation of the linear regression plus 2% of the coefficient itself in order to take into account the experimental errors such as the pressure, the optical path length measurements, or the considered line shape. The results are presented in Fig. 13 where we compare with previous studies in the ν_4 band of methane. The work of Devi *et al.* [70] were performed using a tunable diode-laser and a Fourier transform spectrometers with Voigt fits; Varanasi *et al.* [71] used a tunable diode-laser spectrometer and consider a Voigt profile; Smith *et al.* [72] used a Voigt profile on FTIR line-shape measurements. Finally, Lepère *et al.* [73] and Martin *et al.* [74] used a tunable diode-laser spectrometer to perform N_2 -broadening measurements considering the Voigt profile as well as line-shape models, which take into account fine physical effects. Figure 13 separates the A, E and F-species lines. In general, the lines under study are in good agreement with the literature, considering our experimental uncertainties (which are very conservative).

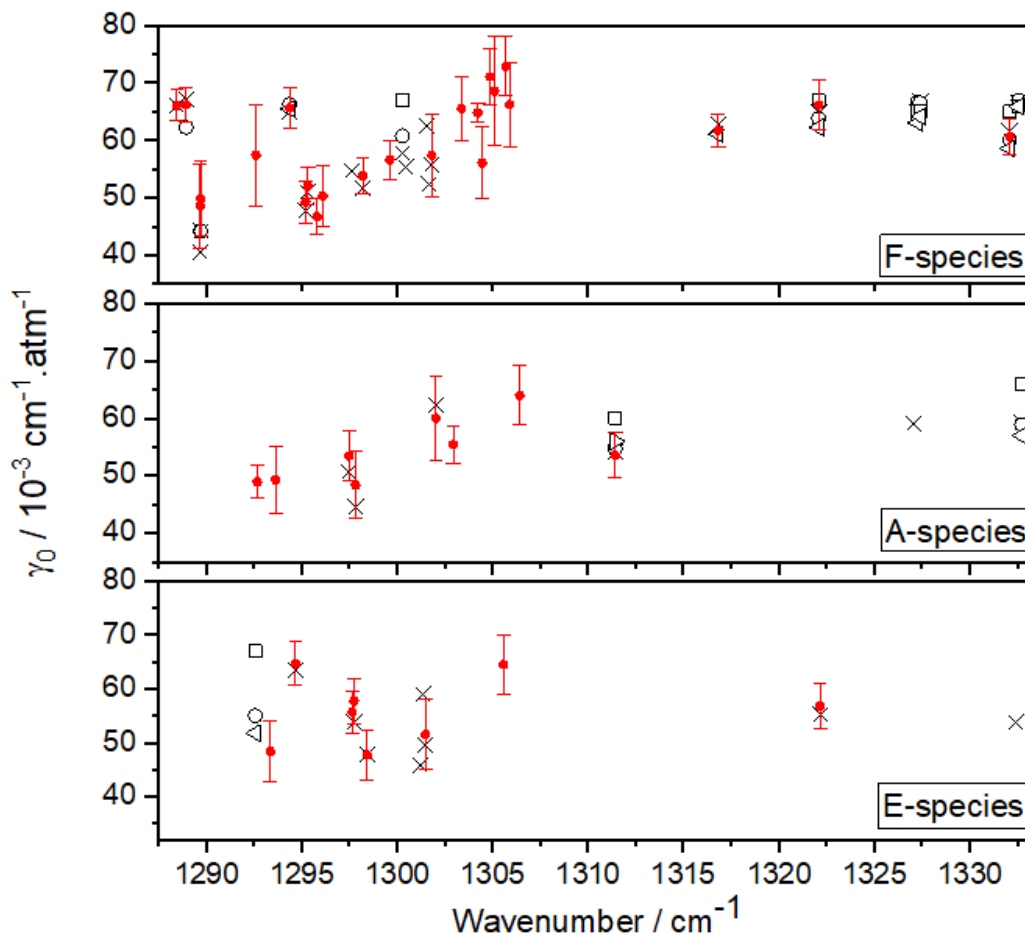


Figure 13 Comparison between our results (\bullet) and previous measurements for the same transitions in the ν_4 band: (\circ) Devi et al. [70] (TDLS and FTIR), (\square) Varanasi et al. [71] (TDLS), (\times) Smith et al. [72] (FTIR), (\triangleright) Lepère et al. [73] (TDLS), and (\triangleleft) Martin et al. [74] (TDLS). The results are separated for each symmetry species (A, E and F).

4. CONCLUSION AND PERSPECTIVES

The IRis-F1 is a tabletop dual-comb spectrometer building on quantum cascade laser frequency combs and emitting in the mid-infrared. We hereby report on the development of the *step-sweep* mode, which allows for high-resolution measurements with a very accurate knowledge of the wavenumber axis. Despite the optical and electronic simplicity of the presented technique, we demonstrate that we are able to record complete spectra covering over 50 cm^{-1} in 30 minutes with a frequency accuracy of below 12 MHz (0.0004 cm^{-1}) in separately calibrated measurements and below 4 MHz (0.00012 cm^{-1}) when the calibration is simultaneous with the sample measurement. Furthermore, measurements of Doppler broadened spectra have shown that the line distortion due to the instrument response is negligible. With these characteristics and the transmission noise floor of down to 10^{-3} , the *step-sweep* technique can be employed for challenging studies in molecular spectroscopy. This is illustrated by N_2 -collisional broadening measurements in the ν_4 band of methane lines. We envisage to use the spectrometer for a range of other studies such as the precise measurement of individual line intensities or line-mixing effect, including other spectral ranges between 900 cm^{-1} to 2300 cm^{-1} accessible with QCL frequency combs.

ACKNOWLEDGEMENTS

We acknowledge A. Foltynowicz for sharing her unpublished CH₄ line list to support our analysis. M. Lepère is acknowledging support from “Fonds de la Recherche Scientifique (F.R.S.-FNRS)”. B. Vispoel acknowledges the F.R.S.-FNRS for the post-doctoral support. IRsweep acknowledges funding for this project from the European Union’s Horizon 2020 research and innovation programme under the Marie Skłodowska-Curie grant agreement No 101032761.

REFERENCES

- [1] Field CB, V.R. Barros, D.J. Dokken, K.J. Mach, M.D. Mastrandrea, T.E. Bilir, M. Chatterjee, K.L. Ebi, Y.O. Estrada, R.C. Genova, B. Girma, E.S. Kissel, A.N. Levy, S. MacCracken, P.R. Mastrandrea, and L.L. White (eds. IPCC, 2014: Climate Change 2014: Impacts, Adaptation, and Vulnerability. Part A: Global and Sectoral Aspects. Contribution of Working Group II to the Fifth Assessment Report of the Intergovernmental Panel on Climate Change 2014.
- [2] Mora C, Spirandelli D, Franklin EC, Lynham J, Kantar MB, Miles W, et al. Broad threat to humanity from cumulative climate hazards intensified by greenhouse gas emissions. *Nature Climate Change*. 2018;8:1062-71, DOI: 10.1038/s41558-018-0315-6.
- [3] Crisp D, Atlas RM, Breon FM, Brown LR, Burrows JP, Ciais P, et al. The Orbiting Carbon Observatory (OCO) mission. *Advances in Space Research*. 2004;34:700-9, DOI: 10.1016/j.asr.2003.08.062.
- [4] Rothman LS, Gordon IE, Babikov Y, Barbe A, Chris Benner D, Bernath PF, et al. The HITRAN2012 molecular spectroscopic database. *Journal of Quantitative Spectroscopy and Radiative Transfer*. 2013;130:4-50, DOI: 10.1016/j.jqsrt.2013.07.002.
- [5] Flaud J-M, Oelhaf H. Infrared spectroscopy and the terrestrial atmosphere. *Comptes Rendus Physique*. 2004;5:259-71, DOI: 10.1016/j.crhy.2004.01.016.
- [6] Chu WP, Chiou EW, Larsen JC, Thomason LW, Rind D, Buglia JJ, et al. Algorithms and sensitivity analyses for Stratospheric Aerosol and Gas Experiment II water vapor retrieval. *Journal of Geophysical Research: Atmospheres*. 1993;98:4857-66, DOI: 10.1029/92jd01628.
- [7] Pumphrey HC, Bühler S. Instrumental and spectral parameters: their effect on and measurement by microwave limb sounding of the atmosphere. *Journal of Quantitative Spectroscopy and Radiative Transfer*. 2000;64:421-37, DOI: 10.1016/s0022-4073(99)00106-5.
- [8] Delamere JS, Clough SA, Payne VH, Mlawer EJ, Turner DD, Gamache RR. A far-infrared radiative closure study in the Arctic: Application to water vapor. *Journal of Geophysical Research*. 2010;115, DOI: 10.1029/2009jd012968.
- [9] Hartmann J-M, Tran H, Armante R, Boulet C, Campargue A, Forget F, et al. Recent advances in collisional effects on spectra of molecular gases and their practical consequences. *Journal of Quantitative Spectroscopy and Radiative Transfer*. 2018;213:178-227, DOI: 10.1016/j.jqsrt.2018.03.016.
- [10] Griffiths PR, De Haseth JA, Winefordner JD. *Fourier Transform Infrared Spectrometry*: Wiley; 2007.
- [11] Valentin A. Fourier spectroscopy with a very long optical path length. *Spectrochimica Acta Part A: Molecular and Biomolecular Spectroscopy*. 1995;51:1127-42, DOI: 10.1016/0584-8539(94)00146-3.
- [12] Merkt F, Quack M. *Handbook of High-resolution Spectroscopy: From MW to IR and UV spectroscopy*: Wiley; 2011.
- [13] Li J, Ding Y, Li Z, Peng Z. Quantum cascade laser measurements of CH₄ linestrength and temperature-dependent self-broadening and narrowing parameters at 7.16 μm . *Journal of Quantitative Spectroscopy and Radiative Transfer*. 2021;276:107901, DOI: 10.1016/j.jqsrt.2021.107901.
- [14] Li J, Yu B, Zhao W, Chen W. A Review of Signal Enhancement and Noise Reduction Techniques for Tunable Diode Laser Absorption Spectroscopy. *Applied Spectroscopy Reviews*. 2014;49:666-91, DOI: 10.1080/05704928.2014.903376.
- [15] Morville J, Romanini D, Kachanov AA, Chenevier M. Two schemes for trace detection using cavity ringdown spectroscopy. *Applied Physics B*. 2004;78:465-76, DOI: 10.1007/s00340-003-1363-8.
- [16] Macko P, Romanini D, Mikhailenko SN, Naumenko OV, Kassi S, Jenouvrier A, et al. High sensitivity CW-cavity ring down spectroscopy of water in the region of the 1.5 μm atmospheric window. *Journal of Molecular Spectroscopy*. 2004;227:90-108, DOI: 10.1016/j.jms.2004.05.020.
- [17] Bogomolov AS, Roucou A, Bejjani R, Herman M, Moazzen-Ahmadi N, Lauzin C. The rotationally resolved symmetric 2OH excitation in H₂O-CO₂ observed using pulsed supersonic expansion and CW-CRDS. *Chemical Physics Letters*. 2021;774:138606, DOI: 10.1016/j.cpllett.2021.138606.

- [18] Amrein A, Luckhaus D, Merkt F, Quack M. High-resolution FTIR spectroscopy of CHClF_2 in a supersonic free jet expansion. *Chemical Physics Letters*. 1988;152:275-80, DOI: 10.1016/0009-2614(88)80092-7.
- [19] Lerot C, Walrand J, Blanquet G, Bouanich J-P, Lepère M. H_2 -broadening coefficients in the ν_3 band of CH_3D at low temperatures. *Journal of Molecular Spectroscopy*. 2003;219:329-34, DOI: 10.1016/s0022-2852(03)00053-5.
- [20] Kassi S, Romanini D, Campargue A. Mode by Mode CW-CRDS at 80 K: Application to the 1.58 μm transparency window of CH_4 . *Chemical Physics Letters*. 2009;477:17-21, DOI: 10.1016/j.cplett.2009.06.097.
- [21] Klingbeil AE, Jeffries JB, Hanson RK. Temperature-dependent mid-IR absorption spectra of gaseous hydrocarbons. *Journal of Quantitative Spectroscopy and Radiative Transfer*. 2007;107:407-20, DOI: 10.1016/j.jqsrt.2007.03.004.
- [22] Bartlome R, Baer M, Sigrist MW. High-temperature multipass cell for infrared spectroscopy of heated gases and vapors. *Rev Sci Instrum*. 2007;78:013110, DOI: 10.1063/1.2432249.
- [23] Fissiaux L, Populaire J-C, Blanquet G, Lepère M. Infrared spectroscopy at high temperature : N_2 - and O_2 -broadening coefficients in the ν_4 band of CH_4 . *Journal of Molecular Spectroscopy*. 2015;317:26-31, DOI: 10.1016/j.jms.2015.06.001.
- [24] Hänsch TW. Nobel Lecture: Passion for precision. *Reviews of Modern Physics*. 2006;78:1297-309, DOI: 10.1103/RevModPhys.78.1297.
- [25] Pasquale Maddaloni MB, Paolo De Natale. *Laser-Based Measurements for Time and Frequency Domain Applications: A Handbook*. 1st Edition ed: CRC Press; 2013.
- [26] Picqué N, Hänsch TW. Frequency comb spectroscopy. *Nature Photonics*. 2019;13:146-57, DOI: 10.1038/s41566-018-0347-5.
- [27] Thorpe MJ, Moll KD, Jones RJ, Safdi B, Ye J. Broadband cavity ringdown spectroscopy for sensitive and rapid molecular detection. *Science*. 2006;311:1595-9, DOI: 10.1126/science.1123921.
- [28] Diddams SA, Hollberg L, Mbele V. Molecular fingerprinting with the resolved modes of a femtosecond laser frequency comb. *Nature*. 2007;445:627-30, DOI: 10.1038/nature05524.
- [29] Gohle C, Stein B, Schliesser A, Udem T, Hansch TW. Frequency comb Vernier spectroscopy for broadband, high-resolution, high-sensitivity absorption and dispersion spectra. *Phys Rev Lett*. 2007;99:263902, DOI: 10.1103/PhysRevLett.99.263902.
- [30] Mandon J, Guelachvili G, Picqué N. Fourier transform spectroscopy with a laser frequency comb. *Nature Photonics*. 2009;3:99-102, DOI: 10.1038/nphoton.2008.293.
- [31] Foltynowicz A, Ban T, Maslowski P, Adler F, Ye J. Quantum-noise-limited optical frequency comb spectroscopy. *Phys Rev Lett*. 2011;107:233002, DOI: 10.1103/PhysRevLett.107.233002.
- [32] Lee S-J, Widiyatmoko B, Kouroggi M, Ohtsu M. Ultrahigh Scanning Speed Optical Coherence Tomography Using Optical Frequency Comb Generators. *Japanese Journal of Applied Physics*. 2001;40:L878-L80, DOI: 10.1143/jjap.40.l878.
- [33] Coddington I, Swann WC, Newbury NR. Coherent multiheterodyne spectroscopy using stabilized optical frequency combs. *Phys Rev Lett*. 2008;100:013902, DOI: 10.1103/PhysRevLett.100.013902.
- [34] Charczun D, Nishiyama A, Kowzan G, Cygan A, Voumard T, Wildi T, et al. Dual-comb cavity-mode width and shift spectroscopy. *Measurement*. 2022;188:110519, DOI: 10.1016/j.measurement.2021.110519.
- [35] Hoghooghi N, Cole RK, Rieker GB. 11- μs time-resolved, continuous dual-comb spectroscopy with spectrally filtered mode-locked frequency combs. *Applied Physics B*. 2021;127, DOI: 10.1007/s00340-020-07552-y.
- [36] Luo PL. Long-wave mid-infrared time-resolved dual-comb spectroscopy of short-lived intermediates. *Opt Lett*. 2020;45:6791-4, DOI: 10.1364/OL.413754.
- [37] Lamperti M, AlSaif B, Gatti D, Fermann M, Laporta P, Farooq A, et al. Absolute spectroscopy near 7.8 μm with a comb-locked extended-cavity quantum-cascade-laser. *Sci Rep*. 2018;8:1292, DOI: 10.1038/s41598-018-19188-2.
- [38] Argence B, Chanteau B, Lopez O, Nicolodi D, Abgrall M, Chardonnet C, et al. Quantum cascade laser frequency stabilization at the sub-Hz level. *Nature Photonics*. 2015;9:456-60, DOI: 10.1038/nphoton.2015.93.
- [39] Muraviev AV, Konnov D, Vodopyanov KL. Broadband high-resolution molecular spectroscopy with interleaved mid-infrared frequency combs. *Sci Rep*. 2020;10:18700, DOI: 10.1038/s41598-020-75704-3.
- [40] Keilmann F, Gohle C, Holzwarth R. Time-domain mid-infrared frequency-comb spectrometer. *Opt Lett*. 2004;29:1542-4, DOI: 10.1364/ol.29.001542.
- [41] Kippenberg TJ, Holzwarth R, Diddams SA. Microresonator-based optical frequency combs. *Science*. 2011;332:555-9, DOI: 10.1126/science.1193968.
- [42] Sterczewski LA, Bagheri M, Frez C, Canedy CL, Vurgaftman I, Kim M, et al. Interband cascade laser frequency combs. *Journal of Physics: Photonics*. 2021;3:042003, DOI: 10.1088/2515-7647/ac1ef3.
- [43] Schwarz B, Hillbrand J, Beiser M, Andrews AM, Strasser G, Detz H, et al. Monolithic frequency comb platform based on interband cascade lasers and detectors. *Optica*. 2019;6:890-5, DOI: 10.1364/OPTICA.6.000890.

- [44] Hugi A, Villares G, Blaser S, Liu HC, Faist J. Mid-infrared frequency comb based on a quantum cascade laser. *Nature*. 2012;492:229-33, DOI: 10.1038/nature11620.
- [45] Dutt A, Joshi C, Ji X, Cardenas J, Okawachi Y, Luke K, et al. On-chip dual-comb source for spectroscopy. *Sci Adv*. 2018;4:e1701858, DOI: 10.1126/sciadv.1701858.
- [46] Stern B, Ji X, Okawachi Y, Gaeta AL, Lipson M. Battery-operated integrated frequency comb generator. *Nature*. 2018;562:401-5, DOI: 10.1038/s41586-018-0598-9.
- [47] Jouy P, Wolf JM, Bidaux Y, Allmendinger P, Mangold M, Beck M, et al. Dual comb operation of $\lambda \sim 8.2 \mu\text{m}$ quantum cascade laser frequency comb with 1 W optical power. *Applied Physics Letters*. 2017;111:141102, DOI: 10.1063/1.4985102.
- [48] Klocke JL, Mangold M, Allmendinger P, Hugi A, Geiser M, Jouy P, et al. Single-Shot Sub-microsecond Mid-infrared Spectroscopy on Protein Reactions with Quantum Cascade Laser Frequency Combs. *Anal Chem*. 2018;90:10494-500, DOI: 10.1021/acs.analchem.8b02531.
- [49] Pinkowski NH, Cassady SJ, Strand CL, Hanson RK. Quantum-cascade-laser-based dual-comb thermometry and speciation at high temperatures. *Measurement Science and Technology*. 2020;32:035501, DOI: 10.1088/1361-6501/abc029.
- [50] Yu M, Okawachi Y, Griffith AG, Lipson M, Gaeta AL. Microfluidic mid-infrared spectroscopy via microresonator-based dual-comb source. *Opt Lett*. 2019;44:4259-62, DOI: 10.1364/OL.44.004259.
- [51] Bao C, Yuan Z, Wu L, Suh MG, Wang H, Lin Q, et al. Architecture for microcomb-based GHz-mid-infrared dual-comb spectroscopy. *Nat Commun*. 2021;12:6573, DOI: 10.1038/s41467-021-26958-6.
- [52] Sterczewski L, Westberg J, Patrick C, Kim CS, Kim M, Canedy C, et al. Multiheterodyne spectroscopy using interband cascade lasers. *Optical Engineering*. 2017;57:011014.
- [53] Jacquet P, Mandon J, Bernhardt B, Holzwarth R, Guelachvili G, Hänsch TW, et al. Frequency Comb Fourier Transform Spectroscopy with kHz Optical Resolution. *Advances in Imaging*. Vancouver: Optical Society of America; 2009. p. FMB2.
- [54] Baumann E, Giorgetta FR, Swann WC, Zolot AM, Coddington I, Newbury NR. Spectroscopy of the methane ν_3 band with an accurate midinfrared coherent dual-comb spectrometer. *Physical Review A*. 2011;84, DOI: 10.1103/PhysRevA.84.062513.
- [55] Rutkowski L, Masłowski P, Johansson AC, Khodabakhsh A, Foltynowicz A. Optical frequency comb Fourier transform spectroscopy with sub-nominal resolution and precision beyond the Voigt profile. *Journal of Quantitative Spectroscopy and Radiative Transfer*. 2018;204:63-73, DOI: 10.1016/j.jqsrt.2017.09.001.
- [56] Yu M, Okawachi Y, Joshi C, Ji X, Lipson M, Gaeta AL. Gas-Phase Microresonator-Based Comb Spectroscopy without an External Pump Laser. *ACS Photonics*. 2018;5:2780-5, DOI: 10.1021/acsphotonics.8b00579.
- [57] Kuse N, Tetsumoto T, Navickaite G, Geiselmann M, Fermann ME. Continuous scanning of a dissipative Kerr-microresonator soliton comb for broadband, high-resolution spectroscopy. *Opt Lett*. 2020;45:927-30, DOI: 10.1364/OL.383036.
- [58] Lin T, Dutt A, Joshi C, Ji X, Phare CT, Okawachi Y, et al. Broadband Ultrahigh-Resolution chip-scale Scanning Soliton Dual-Comb Spectroscopy. 2020. p. arXiv:2001.00869.
- [59] Gianella M, Nataraj A, Tuzson B, Jouy P, Kapsalidis F, Beck M, et al. High-resolution and gapless dual comb spectroscopy with current-tuned quantum cascade lasers. *Opt Express*. 2020;28:6197-208, DOI: 10.1364/OE.379790.
- [60] Villares G, Hugi A, Blaser S, Faist J. Dual-comb spectroscopy based on quantum-cascade-laser frequency combs. *Nat Commun*. 2014;5:5192, DOI: 10.1038/ncomms6192.
- [61] U. Hollenstein. J. Agner PA, A. Hugi, P. Jouy, S. Albert, K. Keppler, M. Mangold, F. Merkt, M. Quack. High-resolution spectroscopic measurements of cold samples in supersonic beams using a QCL dual-comb spectrometer. submitted for publication in *Mol Phys Special Issue of the 27th Colloquium on High-Resolution Molecular Spectroscopy*.
- [62] Komagata K, Gianella M, Jouy P, Kapsalidis F, Shahmohammadi M, Beck M, et al. Absolute frequency referencing in the long wave infrared using a quantum cascade laser frequency comb. *Optics Express*. 2022, DOI: 10.1364/oe.447650.
- [63] Gordon IE, Rothman LS, Hargreaves RJ, Hashemi R, Karlovets EV, Skinner FM, et al. The HITRAN2020 molecular spectroscopic database. *Journal of Quantitative Spectroscopy and Radiative Transfer*. 2022;277:107949, DOI: 10.1016/j.jqsrt.2021.107949.
- [64] Pinkowski NH, Biswas P, Shao J, Strand CL, Hanson RK. Thermometry and speciation for high-temperature and -pressure methane pyrolysis using shock tubes and dual-comb spectroscopy. *Measurement Science and Technology*. 2021;32:125502, DOI: 10.1088/1361-6501/ac22ef.

- [65] Hjältén A, Germann M, Krzempek K, Hudzikowski A, Głuszek A, Tomaszewska D, et al. Optical frequency comb Fourier transform spectroscopy of $^{14}\text{N}_2^{16}\text{O}$ at 7.8 μm . *Journal of Quantitative Spectroscopy and Radiative Transfer*. 2021;271:107734, DOI: 10.1016/j.jqsrt.2021.107734.
- [66] AlSaif B, Lamperti M, Gatti D, Laporta P, Fermann M, Farooq A, et al. High accuracy line positions of the ν_1 fundamental band of $^{14}\text{N}_2^{16}\text{O}$. *Journal of Quantitative Spectroscopy and Radiative Transfer*. 2018;211:172-8, DOI: 10.1016/j.jqsrt.2018.03.005.
- [67] Germann M, Hjältén A, Boudon V, Richard C, Krzempek K, Hudzikowski A, et al. A methane line list with sub-MHz accuracy in the 1250 to 1380 cm^{-1} range from optical frequency comb Fourier transform spectroscopy. Submitted. 2022, DOI: 10.48550/ARXIV.2204.06356.
- [68] Armstrong BH. Spectrum line profiles: The Voigt function. *Journal of Quantitative Spectroscopy and Radiative Transfer*. 1967;7:61-88, DOI: 10.1016/0022-4073(67)90057-x.
- [69] Lepère M. Line profile study with tunable diode laser spectrometers. *Spectrochim Acta A Mol Biomol Spectrosc*. 2004;60:3249-58, DOI: 10.1016/j.saa.2003.12.052.
- [70] Malathy Devi V, Rinsland CP, Smith MA, Benner DC. Measurements of $^{12}\text{CH}_4$ ν_4 band halfwidths using a tunable diode laser system and a Fourier transform spectrometer. *Appl Opt*. 1985;24:2788-91, DOI: 10.1364/ao.24.002788.
- [71] Varanasi P, Chudamani S. Measurements of collision-broadened line widths in the 7.66- μm band of $^{12}\text{CH}_4$ at temperatures relevant to the atmosphere. *Journal of Geophysical Research*. 1989;94:13073, DOI: 10.1029/JD094iD10p13073.
- [72] Smith MAH, Rinsland CP, Devi VM, Benner DC. Temperature dependence of broadening and shifts of methane lines in the ν_4 band. *Spectrochimica Acta Part A: Molecular Spectroscopy*. 1992;48:1257-72, DOI: 10.1016/0584-8539(92)80263-v.
- [73] Lepère M, Valentin A, Henry A, Camy-Peyret C, Lengelé M, Populaire J-C, et al. Diode-laser spectroscopy: Temperature dependence of R(0) line in the ν_4 band of CH_4 perturbed by N_2 and O_2 . *Journal of Molecular Spectroscopy*. 2005;233:86-92, DOI: 10.1016/j.jms.2005.06.004.
- [74] Martin B, Lepère M. N_2 -broadening coefficients in the ν_4 band of $^{12}\text{CH}_4$ at room temperature. *Journal of Molecular Spectroscopy*. 2008;250:70-4, DOI: 10.1016/j.jms.2008.05.001.

Article

Performance of a modular ton-scale pixel-readout liquid argon time projection chamber

A. Abed Abud¹, B. Abi², R. Acciarri³, M. A. Acero⁴, M. R. Adames⁵, G. Adamov⁶, M. Adamowski³, D. Adams⁷, M. Adinolfi⁸, C. Adriano⁹, A. Aduszkiewicz¹⁰, J. Aguilar¹¹, B. Aimard¹², F. Akbar¹³, K. Allison¹⁴, S. Alonso Monsalve^{1,15}, M. Alrashed¹⁶, A. Alton¹⁷, R. Alvarez¹⁸, T. Alves¹⁹, H. Amar²⁰, P. Amedo^{21,20}, J. Anderson²², D. A. Andrade²³, C. Andreopoulos²⁴, M. Andreotti^{25,26}, M. P. Andrews³, F. Andrianala²⁷, S. Andringa²⁸, N. Anfimov²⁹, A. Ankowski³⁰, M. Antoniassi⁵, M. Antonova²⁰, A. Antoshkin²⁹, A. Aranda-Fernandez³¹, L. Arellano³², E. Arrieta Diaz³³, M. A. Arroyave³, J. Asaadi³⁴, A. Ashkenazi³⁵, D. Asner⁷, L. Asquith³⁶, E. Atkin¹⁹, D. Auguste³⁷, A. Aurisano³⁸, V. Aushev³⁹, D. Autiero⁴⁰, F. Azfar², A. Back⁴¹, H. Back⁴², J. J. Back⁴³, I. Bagaturia⁶, L. Bagby³, N. Balashov²⁹, S. Balasubramanian³, P. Baldi⁴⁴, W. Baldini²⁵, J. Baldonado⁴⁵, B. Baller³, B. Bambah⁴⁶, R. Banerjee⁴⁷, F. Barao^{28,48}, G. Barenboim²⁰, P. Barham Alzás¹, G. J. Barker⁴³, W. Barkhouse⁴⁹, G. Bari², J. Barranco Monarca⁵⁰, A. Barros⁵, N. Barros^{28,51}, D. Barrow², J. L. Barrow⁵², A. Basharina-Freshville⁵³, A. Bashyal²², V. Basque³, C. Batchelor⁵⁴, L. Bathe-Peters², J.B.R. Battat⁵⁵, F. Battisti², F. Bay⁵⁶, M. C. Q. Bazetto⁹, J. L. L. Bazo Alba⁵⁷, J. F. Beacom⁵⁸, E. Bechetoille⁴⁰, B. Behera⁵⁹, E. Belchior⁶⁰, G. Bell⁶¹, L. Bellantoni³, G. Bellettini^{62,63}, V. Bellini^{64,65}, O. Beltramello¹, N. Benekos¹, C. Benitez Montiel^{20,66}, D. Benjamin⁷, F. Bento Neves²⁸, J. Berger⁶⁷, S. Berkman⁶⁸, J. Bernal⁶⁶, P. Bernardini^{69,70}, A. Bersani⁷¹, S. Bertolucci^{72,73}, M. Betancourt³, A. Betancur Rodríguez⁷⁴, A. Bevan⁷⁵, Y. Bezawada⁷⁶, A. T. Bezerra⁷⁷, T. J. Bezerra³⁶, A. Bhat⁷⁸, V. Bhatnagar⁷⁹, J. Bhatt⁵³, M. Bhattacharjee⁸⁰, M. Bhattacharya³, S. Bhuller⁸, B. Bhuyan⁸⁰, S. Biagi⁸¹, J. Bian⁴⁴, K. Biery³, B. Bilki^{82,83}, M. Bishai⁷, A. Bitadze³², A. Blake⁸⁴, F. D. Blaszczyk³, G. C. Blazey⁸⁵, E. Blucher⁷⁸, J. Bogenschuetz³⁴, J. Boissevain⁸⁶, S. Bolognesi⁸⁷, T. Bolton¹⁶, L. Bomben^{88,89}, M. Bonesini^{88,90}, C. Bonilla-Diaz⁹¹, F. Bonini⁷, A. Booth⁷⁵, F. Boran⁴¹, S. Bordini¹, R. Borges Merlo⁹, A. Borkum³⁶, N. Bostan⁸³, J. Bracinik⁹², D. Braga³, B. Brahma⁹³, D. Brailsford⁸⁴, F. Bramati⁸⁸, A. Branca⁸⁸, A. Brandt³⁴, J. Bremer¹, C. Brew⁹⁴, S. J. Brice³, V. Brio⁶⁴, C. Brizzolari^{88,90}, C. Bromberg⁶⁸, J. Brooke⁸, A. Bross³, G. Brunetti^{88,90}, M. Brunetti⁴³, N. Buchanan⁶⁷, H. Budd¹³, J. Buergi⁹⁵, D. Burgardt⁹⁶, S. Butchart³⁶, G. Caceres V.⁷⁶, I. Cagnoli^{72,73}, T. Cai⁴⁷, R. Calabrese^{25,26}, J. Calcutt⁹⁷, M. Calin⁹⁸, L. Calivers⁹⁵, E. Calvo¹⁸, A. Caminata⁷¹, A. F. Camino⁹⁹, W. Campanelli²⁸, A. Campani^{71,100}, A. Campos Benitez¹⁰¹, N. Canci¹⁰², J. Capó²⁰, I. Caracas¹⁰³, D. Caratelli¹⁰⁴, D. Carber⁶⁷, J. M. Carceller¹, G. Carini⁷, B. Carlus⁴⁰, M. F. Carneiro⁷, P. Carniti⁸⁸, I. Caro Terrazas⁶⁷, H. Carranza³⁴, N. Carrara⁷⁶, L. Carroll¹⁶, T. Carroll¹⁰⁵, A. Carter¹⁰⁶, E. Casarejos⁴⁵, D. Casazza²⁵, J. F. Castaño Forero¹⁰⁷, F. A. Castaño¹⁰⁸, A. Castillo¹⁰⁹, C. Castromonte¹¹⁰, E. Catano-Mur¹¹¹, C. Cattadori⁸⁸, F. Cavalier³⁷, F. Cavanna³, S. Centro¹¹², G. Cerati³, C. Cerna¹¹³, A. Cervelli⁷², A. Cervera Villanueva²⁰, K. Chakraborty¹¹⁴, S. Chakraborty¹¹⁵, M. Chalifour¹, A. Chappell⁴³, N. Charitonidis¹, A. Chatterjee¹¹⁴, H. Chen⁷, M. Chen⁴⁴, W. C. Chen¹¹⁶, Y. Chen³⁰, Z. Chen-Wishart¹⁰⁶, D. Cherdack¹⁰, C. Chi¹¹⁷, R. Chirco²³, N. Chitirasreemadam^{62,63}, K. Cho¹¹⁸, S. Choate⁸⁵, D. Chokheli⁶, P. S. Chong¹¹⁹, B. Chowdhury²², D. Christian³, A. Chukanov²⁹, M. Chung¹²⁰, E. Church⁴², M. F. Cicala⁵³, M. Cicerchia¹¹², V. Cicero^{72,73}, R. Ciolini⁶², P. Clarke⁵⁴, G. Cline¹¹, T. E. Coan¹²¹, A. G. Cocco¹⁰², J. A. B. Coelho¹²², A. Cohen¹²², J. Collazo⁴⁵, J. Collot¹²³, E. Conley¹²⁴, J. M. Conrad⁵², M. Convery³⁰, S. Copello⁷¹, P. Cova^{125,126}, C. Cox¹⁰⁶, L. Cremaldi¹²⁷, L. Cremonesi⁷⁵, J. I. Crespo-Anadón¹⁸, M. Crisler³, E. Cristaldo^{88,66}, J. Crnkovic³, G. Crone⁵³, R. Cross⁴³, A. Cudd¹⁴, C. Cuesta¹⁸, Y. Cui¹²⁸, F. Curciarello¹²⁹, D. Cussans⁸, J. Dai¹²³, O. Dalager⁴⁴, R. Dallavalle¹²², W. Dallaway¹¹⁶, H. da Motta¹³⁰, Z. A. Dar¹¹¹, R. Darby³⁶, L. Da Silva Peres¹³¹, Q. David⁴⁰, G. S. Davies¹²⁷, S. Davini⁷¹, J. Dawson¹²², R. De Aguiar⁹, P. De Almeida⁹, P. Debbins⁸³, I. De Bonis¹², M. P. Decowski^{132,133}, A. de Gouvêa¹³⁴, P. C. De Holanda⁹, I. L. De Icaza Astiz³⁶, P. De Jong^{132,133}, P. Del Amo Sanchez¹², A. De la Torre¹⁸, G. De Lauretis⁴⁰,

Citation: Performance of a modular ton-scale pixel-readout liquid argon time projection chamber. *Instruments* 2024, 1, 0. <https://doi.org/>

Received:

Revised:

Accepted:

Published:

Copyright: © 2024 by the authors. Submitted to *Instruments* for possible open access publication under the terms and conditions of the Creative Commons Attribution (CC BY) license (<https://creativecommons.org/licenses/by/4.0/>).

A. Delbart⁸⁷, D. Delepine⁵⁰, M. Delgado^{88,90}, A. Dell'Acqua¹, G. Delle Monache¹²⁹, N. Delmonte^{125,126}, P. De Lurgio²², R. Demario⁶⁸, G. De Matteis⁶⁹, J. R. T. de Mello Neto¹³¹, D. M. DeMuth¹³⁵, S. Dennis¹³⁶, C. Densham⁹⁴, P. Denton⁷, G. W. Deptuch⁷, A. De Roeck¹, V. De Romeri²⁰, J. P. Detje¹³⁶, J. Devine¹, R. Dharmapalan¹³⁷, M. Dias¹³⁸, A. Diaz¹³⁹, J. S. Díaz⁴¹, F. Díaz⁵⁷, F. Di Capua^{102,140}, A. Di Domenico^{141,142}, S. Di Domizio^{71,100}, S. Di Falco⁶², L. Di Giulio¹, P. Ding³, L. Di Noto^{71,100}, E. Diociaiuti¹²⁹, C. Distefano⁸¹, R. Diurba⁹⁵, M. Diwan⁷, Z. Djurcic²², D. Doering³⁰, S. Dolan¹, F. Dolek¹⁰¹, M. J. Dolinski¹⁴³, D. Domenici¹²⁹, L. Domine³⁰, S. Donati^{62,63}, Y. Donon¹, S. Doran¹⁴⁴, D. Douglas³⁰, T.A. Doyle¹⁴⁵, A. Dragone³⁰, F. Drielsma³⁰, L. Duarte¹³⁸, D. Duchesneau¹², K. Duffy^{2,3}, K. Dugas⁴⁴, P. Dunne¹⁹, B. Dutta¹⁴⁶, H. Duyang¹⁴⁷, D. A. Dwyer¹¹, A. S. Dyshkant⁸⁵, S. Dytman⁹⁹, M. Eads⁸⁵, A. Earle³⁶, S. Edayath¹⁴⁴, D. Edmunds⁶⁸, J. Eisch³, P. Englezos¹⁴⁸, A. Ereditato⁷⁸, T. Erjavec⁷⁶, C. O. Escobar³, J. J. Evans³², E. Ewart⁴¹, A. C. Ezeribe¹⁴⁹, K. Fahey³, L. Fajt¹, A. Falcone^{88,90}, M. Fani⁸⁶, C. Farnese¹⁵⁰, S. Farrell¹⁵¹, Y. Farzan¹⁵², D. Fedoseev²⁹, J. Felix⁵⁰, Y. Feng¹⁴⁴, E. Fernandez-Martinez¹⁵³, G. Ferry³⁷, L. Fields¹⁵⁴, P. Filip¹⁵⁵, A. Filkins¹⁵⁶, F. Filthaut^{132,157}, R. Fine⁸⁶, G. Fiorillo^{102,140}, M. Fiorini^{25,26}, S. Fogarty⁶⁷, W. Foreman²³, J. Fowler¹²⁴, J. Franc¹⁵⁸, K. Francis⁸⁵, D. Franco⁷⁸, J. Franklin¹⁵⁹, J. Freeman³, J. Fried⁷, A. Friedland³⁰, S. Fuess³, I. K. Furic⁵⁹, K. Furman⁷⁵, A. P. Furmanski¹⁶⁰, R. Gaba⁷⁹, A. Gabrielli^{72,73}, A. M. Gago⁵⁷, F. Galizzi⁸⁸, H. Gallagher¹⁶¹, A. Gallas³⁷, N. Gallice⁷, V. Galymov⁴⁰, E. Gamberini¹, T. Gamble¹⁴⁹, F. Ganacim⁵, R. Gandhi¹⁶², S. Ganguly³, F. Gao¹⁰⁴, S. Gao⁷, D. Garcia-Gamez¹⁶³, M. Á. García-Peris²⁰, F. Gardim⁷⁷, S. Gardiner³, D. Gastler¹⁶⁴, A. Gauch⁹⁵, J. Gauvreau¹⁶⁵, P. Gauzzi^{141,142}, S. Gazzana¹²⁹, G. Ge¹¹⁷, N. Geffroy¹², B. Gelli⁹, S. Gent¹⁶⁶, L. Gerlach⁷, Z. Ghorbani-Moghaddam⁷¹, T. Giammaria^{25,26}, D. Gibin^{112,150}, I. Gil-Botella¹⁸, S. Gilligan⁹⁷, A. Gioiosa⁶², S. Giovannella¹²⁹, C. Girerd⁴⁰, A. K. Giri⁹³, C. Giugliano²⁵, V. Giusti⁶², D. Gnani¹¹, O. Gogota³⁹, S. Gollapinni⁸⁶, K. Gollwitzer³, R. A. Gomes¹⁶⁷, L. V. Gomez Bermeo¹⁰⁹, L. S. Gomez Fajardo¹⁰⁹, F. Gonnella⁹², D. Gonzalez-Diaz²¹, M. Gonzalez-Lopez¹⁵³, M. C. Goodman²², S. Goswami¹¹⁴, C. Gotti⁸⁸, J. Goudeau⁶⁰, E. Goudzovski⁹², C. Grace¹¹, E. Gramellini³², R. Gran¹⁶⁸, E. Granados⁵⁰, P. Granger¹²², C. Grant¹⁶⁴, D. R. Gratieri^{169,9}, G. Grauso¹⁰², P. Green², S. Greenberg^{170,11}, J. Greer⁸, W. C. Griffith³⁶, F. T. Groetschla¹, K. Grzelak¹⁷¹, L. Gu⁸⁴, W. Gu⁷, V. Guarino²², M. Guarise^{25,26}, R. Guenette³², E. Guerard³⁷, M. Guerzoni⁷², D. Guffanti^{88,90}, A. Guglielmi¹⁵⁰, B. Guo¹⁴⁷, Y. Guo¹⁴⁵, A. Gupta³⁰, V. Gupta^{132,133}, G. Gurung³⁴, D. Gutierrez¹⁷², P. Guzowski³², M. M. Guzzo⁹, S. Gwon¹⁷³, A. Habig¹⁶⁸, H. Hadavand³⁴, L. Haegel⁴⁰, R. Haenni⁹⁵, L. Hagaman¹⁷⁴, A. Hahn³, J. Haiston¹⁷⁵, J. Hakenmueller¹²⁴, T. Hamernik³, P. Hamilton¹⁹, J. Hancock⁹², F. Happacher¹²⁹, D. A. Harris^{47,3}, J. Hartnell³⁶, T. Hartnett⁹⁴, J. Harton⁶⁷, T. Hasegawa¹⁷⁶, C. Hasnip², R. Hatcher³, K. Hayrapetyan⁷⁵, J. Hays⁷⁵, E. Hazen¹⁶⁴, M. He¹⁰, A. Heavey³, K. M. Heeger¹⁷⁴, J. Heise¹⁷⁷, S. Henry¹³, M. A. Hernandez Morquecho²³, K. Herner³, V. Hewes³⁸, A. Higuera¹⁵¹, C. Hilgenberg¹⁶⁰, S. J. Hillier⁹², A. Himmel³, E. Hinkle⁷⁸, L.R. Hirsch⁵, J. Ho¹⁷⁸, J. Hoff³, A. Holin⁹⁴, T. Holvey², E. Hoppe⁴², S. Horiuchi¹⁰¹, G. A. Horton-Smith¹⁶, M. Hostert¹⁶⁰, T. Houdy³⁷, B. Howard³, R. Howell¹³, I. Hristova⁹⁴, M. S. Hronek³, J. Huang⁷⁶, R.G. Huang¹¹, Z. Hulcher³⁰, M. Ibrahim¹⁷⁹, G. Iles¹⁹, N. Ilic¹¹⁶, A. M. Iliescu¹²⁹, R. Illingworth³, G. Ingratta^{72,73}, A. Ioannisian¹⁸⁰, B. Irwin¹⁶⁰, L. Isenhower¹⁸¹, M. Ismerio Oliveira¹³¹, R. Itay³⁰, C.M. Jackson⁴², V. Jain¹⁸², E. James³, W. Jang³⁴, B. Jargowsky⁴⁴, D. Jena³, I. Jentz¹⁰⁵, X. Ji⁷, C. Jiang¹⁸³, J. Jiang¹⁴⁵, L. Jiang¹⁰¹, A. Jipa⁹⁸, F. R. Joaquim^{28,48}, W. Johnson¹⁷⁵, C. Jollet¹¹³, B. Jones³⁴, R. Jones¹⁴⁹, D. José Fernández²¹, N. Jovancevic¹⁸⁴, M. Judah⁹⁹, C. K. Jung¹⁴⁵, T. Junk³, Y. Jwa^{30,117}, M. Kabirnezhad¹⁹, A. C. Kaboth^{106,94}, I. Kadenko³⁹, I. Kakorin²⁹, A. Kalitkina²⁹, D. Kalra¹¹⁷, M. Kandemir¹⁸⁵, D. M. Kaplan²³, G. Karagiorgi¹¹⁷, G. Karaman⁸³, A. Karcher¹¹, Y. Karyotakis¹², S. Kasai¹⁸⁶, S. P. Kasetti⁶⁰, L. Kashur⁶⁷, I. Katsioulas⁹², A. Kauther⁸⁵, N. Kazaryan¹⁸⁰, L. Ke⁷, E. Kearns¹⁶⁴, P.T. Keener¹¹⁹, K.J. Kelly¹, E. Kemp⁹, O. Kemularia⁶, Y. Kermaidic³⁷, W. Ketchum³, S. H. Kettell⁷, M. Khabibullin¹⁸⁷, N. Khan¹⁹, A. Khotjantsev¹⁸⁷, A. Khvedelidze⁶, D. Kim¹⁴⁶, J. Kim¹³, B. King³, B. Kirby¹¹⁷, M. Kirby⁷, A. Kish³, J. Klein¹¹⁹, J. Kleykamp¹²⁷, A. Klustova¹⁹, T. Kobilarcik³, L. Koch¹⁰³, K. Koehler¹⁰⁵, L. W. Koerner¹⁰, D. H. Koh³⁰, L. Kolupaeva²⁹, D. Korablev²⁹,

M. Kordosky¹¹¹, T. Kosc¹²³, U. Kose¹, V. A. Kostelecký⁴¹, K. Kotheke⁸, I. Kotler¹⁴³, M. Kovalcuk¹⁵⁵, V. Kozhukalov²⁹, W. Krah¹³², R. Kralik³⁶, M. Kramer¹¹, L. Kreczko⁸, F. Krennrich¹⁴⁴, I. Kreslo⁹⁵, T. Kroupova¹¹⁹, S. Kubota³², M. Kubu¹, Y. Kudenko¹⁸⁷, V. A. Kudryavtsev¹⁴⁹, G. Kufatty¹⁸⁸, S. Kuhlmann²², S. Kulagin¹⁸⁷, J. Kumar¹³⁷, P. Kumar¹⁴⁹, S. Kumaran⁴⁴, P. Kunze¹², J. Kunzmann⁹⁵, R. Kuravi¹¹, N. Kurita³⁰, C. Kuruppu¹⁴⁷, V. Kus¹⁵⁸, T. Kutter⁶⁰, J. Kvasnicka¹⁵⁵, T. Labree⁸⁵, T. Lackey³, A. Lambert¹¹, B. J. Land¹¹⁹, C. E. Lane¹⁴³, N. Lane³², K. Lang¹⁸⁹, T. Langford¹⁷⁴, M. Langstaff³², F. Lanni¹, O. Lantwin¹², J. Larkin⁷, P. Lasorak¹⁹, D. Last¹¹⁹, A. Laudrain¹⁰³, A. Landrieu¹⁰⁵, G. Laurenti⁷², E. Lavaut³⁷, A. Lawrence¹¹, P. Laycock⁷, I. Lazanu⁹⁸, M. Lazzaroni^{125,190}, T. Le¹⁶¹, S. Leardini²¹, J. Learned¹³⁷, T. LeCompte³⁰, C. Lee³, V. Legin³⁹, G. Lehmann Miotto¹, R. Lehnert⁴¹, M. A. Leigui de Oliveira¹⁹¹, M. Leitner¹¹, D. Leon Silverio¹⁷⁵, L. M. Lepin^{188,32}, J.-Y. Li⁵⁴, S. W. Li⁷⁶, Y. Li⁷, H. Liao¹⁶, C. S. Lin¹¹, D. Lindebaum⁸, S. Linden⁷, R. A. Lineros⁹¹, J. Ling¹⁹², A. Lister¹⁰⁵, B. R. Littlejohn²³, H. Liu⁷, J. Liu⁴⁴, Y. Liu⁷⁸, S. Lockwitz³, M. Lokajicek¹⁵⁵, I. Lomidze⁶, K. Long¹⁹, T. V. Lopes⁷⁷, J. Lopez¹⁰⁸, I. López de Rego¹⁸, N. López-March²⁰, T. Lord⁴³, J. M. LoSecco¹⁵⁴, W. C. Louis⁸⁶, A. Lozano Sanchez¹⁴³, X.-G. Lu⁴³, K.B. Luk^{193,170}, B. Lunday¹¹⁹, X. Luo¹⁰⁴, E. Luppi^{25,26}, J. Maalmi³⁷, D. MacFarlane³⁰, A. A. Machado⁹, P. Machado³, C. T. Macias⁴¹, J. R. Macier³, M. MacMahon⁵³, A. Maddalena¹⁹⁴, A. Madera¹, P. Madigan^{170,11}, S. Magill²², C. Magueur³⁷, K. Mahn⁶⁸, A. Maio^{28,51}, A. Major¹²⁴, K. Majumdar²⁴, M. Man¹¹⁶, R. C. Mandujano⁴⁴, J. Maneira^{28,51}, S. Manly¹³, A. Mann¹⁶¹, K. Manolopoulos⁹⁴, M. Manrique Plata⁴¹, S. Manthey Corchado¹⁸, V. N. Manyam⁷, M. Marchan³, A. Marchionni³, W. Marciano⁷, D. Marfatia¹³⁷, C. Mariani¹⁰¹, J. Maricic¹³⁷, F. Marinho¹⁹⁵, A. D. Marino¹⁴, T. Markiewicz³⁰, F. Das Chagas Marques⁹, C. Marquet¹¹³, D. Marsden³², M. Marshak¹⁶⁰, C. M. Marshall¹³, J. Marshall⁴³, L. Martina⁶⁹, J. Martín-Albo²⁰, N. Martinez¹⁶, D.A. Martinez Caicedo¹⁷⁵, F. Martínez López⁷⁵, P. Martínez Miravé²⁰, S. Martynenko⁷, V. Mascagna⁸⁸, C. Massari⁸⁸, A. Mastbaum¹⁴⁸, F. Matichard¹¹, S. Matsuno¹³⁷, G. Matteucci^{102,140}, J. Matthews⁶⁰, C. Mauger¹¹⁹, N. Mauri^{72,73}, K. Mavrokoridis²⁴, I. Mawby⁸⁴, R. Mazza⁸⁸, A. Mazzacane³, T. McAskill⁵⁵, N. McConkey⁵³, K. S. McFarland¹³, C. McGrew¹⁴⁵, A. McNab³², L. Meazza⁸⁸, V. C. N. Meddage⁵⁹, A. Mefodiev¹⁸⁷, B. Mehta⁷⁹, P. Mehta¹⁹⁶, P. Melas¹⁹⁷, O. Mena²⁰, H. Mendez¹⁷², P. Mendez¹, D. P. Méndez⁷, A. Menegolli^{198,199}, G. Meng¹⁵⁰, A. C. E. A. Mercuri⁵, A. Mereaglia¹¹³, M. D. Messier⁴¹, S. Metallo¹⁶⁰, J. Metcalf^{161,52}, W. Metcalf⁶⁰, M. Mewes⁴¹, H. Meyer⁹⁶, T. Miao³, A. Miccoli⁶⁹, G. Michna¹⁶⁶, V. Mikola⁵³, R. Milincic¹³⁷, F. Miller¹⁰⁵, G. Miller³², W. Miller¹⁶⁰, O. Mineev¹⁸⁷, A. Minotti^{88,90}, L. Miralles¹, O. G. Miranda²⁰⁰, C. Mironov¹²², S. Miryala⁷, S. Miscetti¹²⁹, C. S. Mishra³, S. R. Mishra¹⁴⁷, A. Mislivec¹⁶⁰, M. Mitchell⁶⁰, D. Mladenov¹, I. Mocioiu²⁰¹, A. Mogan³, N. Moggi^{72,73}, R. Mohanta⁴⁶, T. A. Mohayai⁴¹, N. Mokhov³, J. Molina⁶⁶, L. Molina Bueno²⁰, E. Montagna^{72,73}, A. Montanari⁷², C. Montanari^{198,3,199}, D. Montanari³, D. Montanino^{69,70}, L. M. Montaña Zetina²⁰⁰, M. Mooney⁶⁷, A. F. Moor¹⁴⁹, Z. Moore¹⁵⁶, D. Moreno¹⁰⁷, O. Moreno-Palacios¹¹¹, L. Morescalchi⁶², D. Moretti⁸⁸, R. Moretti⁸⁸, C. Morris¹⁰, C. Mossey³, M. Mote⁶⁰, C. A. Moura¹⁹¹, G. Moustier⁸⁴, W. Mu³, L. Mualem¹³⁹, J. Mueller⁶⁷, M. Muether⁹⁶, F. Muheim⁵⁴, A. Muir⁶¹, M. Mulhearn⁷⁶, D. Munford¹⁰, L. J. Munteanu¹, H. Muramatsu¹⁶⁰, J. Muraz¹²³, M. Murphy¹⁰¹, T. Murphy¹⁵⁶, J. Muse¹⁶⁰, A. Mytilinaki⁹⁴, J. Nachtman⁸³, Y. Nagai¹⁷⁹, S. Nagu²⁰², R. Nandakumar⁹⁴, D. Naples⁹⁹, S. Narita²⁰³, A. Nath⁸⁰, A. Navrer-Agasson³², N. Nayak⁷, M. Nebot-Guinot⁵⁴, A. Nehm¹⁰³, J. K. Nelson¹¹¹, O. Neogi⁸³, J. Nesbit¹⁰⁵, M. Nessi^{3,1}, D. Newbold⁹⁴, M. Newcomer¹¹⁹, R. Nichol⁵³, F. Nicolas-Arnaldos¹⁶³, A. Nikolica¹¹⁹, J. Nikolov¹⁸⁴, E. Niner³, K. Nishimura¹³⁷, A. Norman³, A. Norrick³, P. Novella²⁰, J. A. Nowak⁸⁴, M. Oberling²², J. P. Ochoa-Ricoux⁴⁴, S. Oh¹²⁴, S.B. Oh³, A. Olivier¹⁵⁴, A. Olshevskiy²⁹, T. Olson¹⁰, Y. Onel⁸³, Y. Onishchuk³⁹, A. Oranday⁴¹, M. Osbiston⁴³, J. A. Osorio Vélez¹⁰⁸, L. Otiniano Ormachea^{204,110}, J. Ott⁴⁴, L. Pagani⁷⁶, G. Palacio⁷⁴, O. Palamara³, S. Palestini¹, J. M. Paley³, M. Pallavicini^{71,100}, C. Palomares¹⁸, S. Pan¹¹⁴, P. Panda⁴⁶, W. Panduro Vazquez¹⁰⁶, E. Pantic⁷⁶, V. Paolone⁹⁹, V. Papadimitriou³, R. Papaleo⁸¹, A. Papanestis⁹⁴, D. Papoulias¹⁹⁷, S. Paramesvaran⁸, A. Paris¹⁷², S. Parke³, E. Parozzi^{88,90}, S. Parsa⁹⁵, Z. Parsa⁷, S. Parveen¹⁹⁶, M. Parvu⁹⁸, D. Pasciuto⁶², S. Pascoli^{72,73}, L. Pasqualini^{72,73}, J. Pasternak¹⁹, C. Patrick^{54,53}, L. Patrizii⁷²,

R. B. Patterson¹³⁹, T. Patzak¹²², A. Paudel³, L. Paulucci¹⁹¹, Z. Pavlovic³, G. Pawloski¹⁶⁰, D. Payne²⁴, V. Pec¹⁵⁵, E. Pedreschi⁶², S. J. M. Peeters³⁶, W. Pellico³, A. Pena Perez³⁰, E. Pennacchio⁴⁰, A. Penzo⁸³, O. L. G. Peres⁹, Y. F. Perez Gonzalez¹⁵⁹, L. Pérez-Molina¹⁸, C. Pernas¹¹¹, J. Perry⁵⁴, D. Pershey¹⁸⁸, G. Pessina⁸⁸, G. Petrillo³⁰, C. Petta^{64,65}, R. Petti¹⁴⁷, M. Pfaff¹⁹, V. Pia^{72,73}, L. Pickering^{94,106}, F. Pietropaolo^{1,150}, V.L.Pimentel^{205,9}, G. Pinaroli⁷, J. Pinchault¹², K. Pitts¹⁰¹, K. Plows², R. Plunkett³, C. Pollack¹⁷², T. Pollman^{132,133}, D. Polo-Toledo⁴, F. Pompa²⁰, X. Pons¹, N. Poonthottathil^{115,144}, V. Popov³⁵, F. Poppi^{72,73}, J. Porter³⁶, M. Potekhin⁷, R. Potenza^{64,65}, J. Pozimski¹⁹, M. Pozzato^{72,73}, T. Prakash¹¹, C. Pratt⁷⁶, M. Prest⁸⁸, F. Psihas³, D. Pugnere⁴⁰, X. Qian⁷, J. L. Raaf³, V. Radeka⁷, J. Rademacker⁸, B. Radics⁴⁷, A. Rafique²², E. Raguzin⁷, M. Rai⁴³, S. Rajagopalan⁷, M. Rajaoalisoa³⁸, I. Rakhno³, L. Rakotondravohitra²⁷, L. Ralte⁹³, M. A. Ramirez Delgado¹¹⁹, B. Ramson³, A. Rappoldi^{198,199}, G. Raselli^{198,199}, P. Ratoff⁸⁴, R. Ray³, H. Razafinime³⁸, E. M. Rea¹⁶⁰, J. S. Real¹²³, B. Rebel^{105,3}, R. Rechenmacher³, M. Reggiani-Guzzo³², J. Reichenbacher¹⁷⁵, S. D. Reitzner³, H. Rejeb Sfar¹, E. Renner⁸⁶, A. Renshaw¹⁰, S. Rescia⁷, F. Resnati¹, D. Restrepo¹⁰⁸, C. Reynolds⁷⁵, M. Ribas⁵, S. Riboldi¹²⁵, C. Riccio¹⁴⁵, G. Riccobene⁸¹, J. S. Ricol¹²³, M. Rigan³⁶, E. V. Rincón⁷⁴, A. Ritchie-Yates¹⁰⁶, S. Ritter¹⁰³, D. Rivera⁸⁶, R. Rivera³, A. Robert¹²³, J. L. Rocabado Rocha²⁰, L. Rochester³⁰, M. Roda²⁴, P. Rodrigues², M. J. Rodriguez Alonso¹, J. Rodriguez Rondon¹⁷⁵, S. Rosauro-Alcaraz³⁷, P. Rosier³⁷, D. Ross⁶⁸, M. Rossella^{198,199}, M. Rossi¹, M. Ross-Lonergan⁸⁶, N. Roy⁴⁷, P. Roy⁹⁶, C. Rubbia²⁰⁶, A. Ruggeri⁷², G. Ruiz Ferreira³², B. Russell⁵², D. Ruterbories¹³, A. Rybnikov²⁹, A. Saa-Hernandez²¹, R. Saakyan⁵³, S. Sacerdoti¹²², S. K. Sahoo⁹³, N. Sahu⁹³, P. Sala^{125,1}, N. Samios⁷, O. Samoylov²⁹, M. C. Sanchez¹⁸⁸, A. Sánchez Bravo²⁰, P. Sanchez-Lucas¹⁶³, V. Sandberg⁸⁶, D. A. Sanders¹²⁷, S. Sanfilippo⁸¹, D. Sankey⁹⁴, D. Santoro¹²⁵, N. Saoulidou¹⁹⁷, P. Sapienza⁸¹, C. Sarasty³⁸, I. Sarcevic²⁰⁷, I. Sarra¹²⁹, G. Savage³, V. Savinov⁹⁹, G. Scanavini¹⁷⁴, A. Scaramelli¹⁹⁸, A. Scarff¹⁴⁹, T. Schefke⁶⁰, H. Schellman^{97,3}, S. Schifano^{25,26}, P. Schlabach³, D. Schmitz⁷⁸, A. W. Schneider⁵², K. Scholberg¹²⁴, A. Schukraft³, B. Schuld¹⁴, A. Segade⁴⁵, E. Segreto⁹, A. Selyunin²⁹, C. R. Senise¹³⁸, J. Sensenig¹¹⁹, M. H. Shaevitz¹¹⁷, P. Shanahan³, P. Sharma⁷⁹, R. Kumar²⁰⁸, K. Shaw³⁶, T. Shaw³, K. Shchablo⁴⁰, J. Shen¹¹⁹, C. Shepherd-Themistocleous⁹⁴, A. Sheshukov²⁹, W. Shi¹⁴⁵, S. Shin²⁰⁹, S. Shivakoti⁹⁶, I. Shoemaker¹⁰¹, D. Shooltz⁶⁸, R. Shrock¹⁴⁵, B. Siddi²⁵, M. Siden⁶⁷, J. Silber¹¹, L. Simard³⁷, J. Sinclair³⁰, G. Sinev¹⁷⁵, Jaydip Singh²⁰², J. Singh²⁰², L. Singh²¹⁰, P. Singh⁷⁵, V. Singh²¹⁰, S. Singh Chauhan⁷⁹, R. Sipos¹, C. Sironneau¹²², G. Sirri⁷², K. Siyeon¹⁷³, K. Skarpaas³⁰, J. Smedley¹³, E. Smith⁴¹, J. Smith¹⁴⁵, P. Smith⁴¹, J. Smolik^{158,155}, M. Smy⁴⁴, M. Snape⁴³, E.L. Snider³, P. Snopok²³, D. Snowden-Ifft¹⁶⁵, M. Soares Nunes³, H. Sobel⁴⁴, M. Soderberg¹⁵⁶, S. Sokolov²⁹, C. J. Solano Salinas^{211,110}, S. Söldner-Rembold³², S.R. Soleti¹¹, N. Solomey⁹⁶, V. Solovov²⁸, W. E. Sondheim⁸⁶, M. Sorel²⁰, A. Sotnikov²⁹, J. Soto-Oton²⁰, A. Sousa³⁸, K. Soustruznik²¹², F. Spinella⁶², J. Spitz²¹³, N. J. C. Spooner¹⁴⁹, K. Spurgeon¹⁵⁶, D. Stalder⁶⁶, M. Stancari³, L. Stanco^{150,112}, J. Steenis⁷⁶, R. Stein⁸, H. M. Steiner¹¹, A. F. Steklain Lisbôa⁵, A. Stepanova²⁹, J. Stewart⁷, B. Stillwell⁷⁸, J. Stock¹⁷⁵, F. Stocker¹, T. Stokes⁶⁰, M. Strait¹⁶⁰, T. Strauss³, L. Strigari¹⁴⁶, A. Stuart³¹, J. G. Suarez⁷⁴, J. Subash⁹², A. Surdo⁶⁹, L. Suter³, C. M. Suter^{64,65}, K. Sutton¹³⁹, Y. Suvorov^{102,140}, R. Svoboda⁷⁶, S. K. Swain²¹⁴, B. Szczerbinska²¹⁵, A. M. Szelc⁵⁴, A. Sztuc⁵³, A. Taffara⁶², N. Talukdar¹⁴⁷, J. Tamara¹⁰⁷, H. A. Tanaka³⁰, S. Tang⁷, N. Taniuchi¹³⁶, A. M. Tapia Casanova²¹⁶, B. Tapia Oregui¹⁸⁹, A. Tapper¹⁹, S. Tariq³, E. Tarpara⁷, E. Tatar²¹⁷, R. Tayloe⁴¹, D. Tedeschi¹⁴⁷, A. M. Teklu¹⁴⁵, J. Tena Vidal³⁵, P. Tennesen^{11,56}, M. Tenti⁷², K. Terao³⁰, F. Terranova^{88,90}, G. Testera⁷¹, T. Thakore³⁸, A. Thea⁹⁴, A. Thiebault³⁷, S. Thomas¹⁵⁶, A. Thompson¹⁴⁶, C. Thorn⁷, S. C. Timm³, E. Tiras^{185,83}, V. Tishchenko⁷, N. Todorović¹⁸⁴, L. Tomassetti^{25,26}, A. Tonazzo¹²², D. Torbunov⁷, M. Torti⁸⁸, M. Tortola²⁰, F. Tortorici^{64,65}, N. Tosi⁷², D. Totani¹⁰⁴, M. Touns³, C. Touramanis²⁴, D. Tran¹⁰, R. Travaglini⁷², J. Trevor¹³⁹, E. Triller⁶⁸, S. Trilov⁸, J. Truchon¹⁰⁵, D. Truncali^{141,142}, W. H. Trzaska²¹⁸, Y. Tsai⁴⁴, Y.-T. Tsai³⁰, Z. Tsamalaidze⁶, K. V. Tsang³⁰, N. Tsverava⁶, S. Z. Tu¹⁸³, S. Tufanli¹, C. Tunnell¹⁵¹, J. Turner¹⁵⁹, M. Tuzi²⁰, J. Tyler¹⁶, E. Tyley¹⁴⁹, M. Tzanov⁶⁰, M. A. Uchida¹³⁶, J. Ureña González²⁰, J. Urheim⁴¹, T. Usher³⁰, H. Utaegbulam¹³,

S. Uzunyan⁸⁵, M. R. Vagins^{219,44}, P. Vahle¹¹¹, S. Valder³⁶, G. A. Valdivieso⁷⁷, E. Valencia⁵⁰, R. Valentim¹³⁸, Z. Vallari¹³⁹, E. Vallazza⁸⁸, J. W. F. Valle²⁰, R. Van Berg¹¹⁹, R. G. Van de Water⁸⁶, D. V. Forero²¹⁶, A. Vannozzi¹²⁹, M. Van Nuland-Troost¹³², F. Varanini¹⁵⁰, D. Vargas Oliva¹¹⁶, S. Vasina²⁹, N. Vaughan⁹⁷, K. Vaziri³, A. Vázquez-Ramos¹⁶³, J. Vega²⁰⁴, S. Ventura¹⁵⁰, A. Verdugo¹⁸, S. Vergani⁵³, M. Verzocchi³, K. Vetter³, M. Vicenzi⁷, H. Vieira de Souza¹²², C. Vignoli¹⁹⁴, C. Vilela²⁸, E. Villa¹, S. Viola⁸¹, B. Viren⁷, A. Vizcaya-Hernandez⁶⁷, T. Vrba¹⁵⁸, Q. Vuong¹³, A. V. Waldron⁷⁵, M. Wallbank³⁸, J. Walsh⁶⁸, T. Walton³, H. Wang²²⁰, J. Wang¹⁷⁵, L. Wang¹¹, M.H.L.S. Wang³, X. Wang³, Y. Wang²²⁰, K. Warburton¹⁴⁴, D. Warner⁶⁷, L. Warsame¹⁹, M.O. Wascko², D. Waters⁵³, A. Watson⁹², K. Wawrowska^{94,36}, A. Weber^{103,3}, C. M. Weber¹⁶⁰, M. Weber⁹⁵, H. Wei⁶⁰, A. Weinstein¹⁴⁴, H. Wenzel³, S. Westerdale¹²⁸, M. Wetstein¹⁴⁴, K. Whalen⁹⁴, J. Whilhelmi¹⁷⁴, A. White³⁴, A. White¹⁷⁴, L. H. Whitehead¹³⁶, D. Whittington¹⁵⁶, M. J. Wilking¹⁶⁰, A. Wilkinson⁵³, C. Wilkinson¹¹, F. Wilson⁹⁴, R. J. Wilson⁶⁷, P. Winter²², W. Wisniewski³⁰, J. Wolcott¹⁶¹, J. Wolfs¹³, T. Wongjirad¹⁶¹, A. Wood¹⁰, K. Wood¹¹, E. Worcester⁷, M. Worcester⁷, M. Wospakrik³, K. Wresilo¹³⁶, C. Wret¹³, S. Wu¹⁶⁰, W. Wu³, W. Wu⁴⁴, M. Wurm¹⁰³, J. Wyenberg¹⁷⁸, Y. Xiao⁴⁴, I. Xiotidis¹⁹, B. Yaeggy³⁸, N. Yahlali²⁰, E. Yandel¹⁰⁴, K. Yang², T. Yang³, A. Yankelevich⁴⁴, N. Yershov¹⁸⁷, K. Yonehara³, T. Young⁴⁹, B. Yu⁷, H. Yu⁷, J. Yu³⁴, Y. Yu²³, W. Yuan⁵⁴, R. Zaki⁴⁷, J. Zalesak¹⁵⁵, L. Zambelli¹², B. Zamorano¹⁶³, A. Zani¹²⁵, O. Zapata¹⁰⁸, L. Zazueta¹⁵⁶, G. P. Zeller³, J. Zennaro³, K. Zeug¹⁰⁵, C. Zhang⁷, S. Zhang⁴¹, M. Zhao⁷, E. Zhivun⁷, E. D. Zimmerman¹⁴, S. Zucchelli^{72,73}, J. Zuklin¹⁵⁵, V. Zutshi⁸⁵, R. Zwaska³, and On behalf of the DUNE Collaboration

- 1 CERN, The European Organization for Nuclear Research, 1211 Meyrin, Switzerland
- 2 University of Oxford, Oxford, OX1 3RH, United Kingdom
- 3 Fermi National Accelerator Laboratory, Batavia, IL 60510, USA
- 4 Universidad del Atlántico, Barranquilla, Atlántico, Colombia
- 5 Universidade Tecnológica Federal do Paraná, Curitiba, Brazil
- 6 Georgian Technical University, Tbilisi, Georgia
- 7 Brookhaven National Laboratory, Upton, NY 11973, USA
- 8 University of Bristol, Bristol BS8 1TL, United Kingdom
- 9 Universidade Estadual de Campinas, Campinas - SP, 13083-970, Brazil
- 10 University of Houston, Houston, TX 77204, USA
- 11 Lawrence Berkeley National Laboratory, Berkeley, CA 94720, USA
- 12 Laboratoire d'Annecy de Physique des Particules, Université Savoie Mont Blanc, CNRS, LAPP-IN2P3, 74000 Annecy, France
- 13 University of Rochester, Rochester, NY 14627, USA
- 14 University of Colorado Boulder, Boulder, CO 80309, USA
- 15 ETH Zurich, Zurich, Switzerland
- 16 Kansas State University, Manhattan, KS 66506, USA
- 17 Augustana University, Sioux Falls, SD 57197, USA
- 18 CIEMAT, Centro de Investigaciones Energéticas, Medioambientales y Tecnológicas, E-28040 Madrid, Spain
- 19 Imperial College of Science Technology and Medicine, London SW7 2BZ, United Kingdom
- 20 Instituto de Física Corpuscular, CSIC and Universitat de València, 46980 Paterna, Valencia, Spain
- 21 Instituto Galego de Física de Altas Enerxías, University of Santiago de Compostela, Santiago de Compostela, 15782, Spain
- 22 Argonne National Laboratory, Argonne, IL 60439, USA
- 23 Illinois Institute of Technology, Chicago, IL 60616, USA
- 24 University of Liverpool, L69 7ZE, Liverpool, United Kingdom
- 25 Istituto Nazionale di Fisica Nucleare Sezione di Ferrara, I-44122 Ferrara, Italy
- 26 University of Ferrara, Ferrara, Italy
- 27 University of Antananarivo, Antananarivo 101, Madagascar
- 28 Laboratório de Instrumentação e Física Experimental de Partículas, 1649-003 Lisboa and 3004-516 Coimbra, Portugal
- 29 Joint Institute for Nuclear Research, Dzhelapov Laboratory of Nuclear Problems 6 Joliot-Curie, Dubna, Moscow Region, 141980 RU
- 30 SLAC National Accelerator Laboratory, Menlo Park, CA 94025, USA
- 31 Universidad de Colima, Colima, Mexico
- 32 University of Manchester, Manchester M13 9PL, United Kingdom
- 33 Universidad del Magdalena, Santa Marta - Colombia

34 University of Texas at Arlington, Arlington, TX 76019, USA
35 Tel Aviv University, Tel Aviv-Yafo, Israel
36 University of Sussex, Brighton, BN1 9RH, United Kingdom
37 Université Paris-Saclay, CNRS/IN2P3, IJCLab, 91405 Orsay, France
38 University of Cincinnati, Cincinnati, OH 45221, USA
39 Taras Shevchenko National University of Kyiv, 01601 Kyiv, Ukraine
40 Institut de Physique des 2 Infinis de Lyon, 69622 Villeurbanne, France
41 Indiana University, Bloomington, IN 47405, USA
42 Pacific Northwest National Laboratory, Richland, WA 99352, USA
43 University of Warwick, Coventry CV4 7AL, United Kingdom
44 University of California Irvine, Irvine, CA 92697, USA
45 University of Vigo, E- 36310 Vigo Spain
46 University of Hyderabad, Gachibowli, Hyderabad - 500 046, India
47 York University, Toronto M3J 1P3, Canada
48 Instituto Superior Técnico - IST, Universidade de Lisboa, 1049-001 Lisboa, Portugal
49 University of North Dakota, Grand Forks, ND 58202-8357, USA
50 Universidad de Guanajuato, Guanajuato, C.P. 37000, Mexico
51 Faculdade de Ciências da Universidade de Lisboa - FCUL, 1749-016 Lisboa, Portugal
52 Massachusetts Institute of Technology, Cambridge, MA 02139, USA
53 University College London, London, WC1E 6BT, United Kingdom
54 University of Edinburgh, Edinburgh EH8 9YL, United Kingdom
55 Wellesley College, Wellesley, MA 02481, USA
56 Antalya Bilim University, 07190 Döşemealtı/Antalya, Turkey
57 Pontificia Universidad Católica del Perú, Lima, Perú
58 Ohio State University, Columbus, OH 43210, USA
59 University of Florida, Gainesville, FL 32611-8440, USA
60 Louisiana State University, Baton Rouge, LA 70803, USA
61 Daresbury Laboratory, Cheshire WA4 4AD, United Kingdom
62 Istituto Nazionale di Fisica Nucleare Laboratori Nazionali di Pisa, Pisa PI, Italy
63 Università di Pisa, I-56127 Pisa, Italy
64 Istituto Nazionale di Fisica Nucleare Sezione di Catania, I-95123 Catania, Italy
65 Università di Catania, 2 - 95131 Catania, Italy
66 Universidad Nacional de Asunción, San Lorenzo, Paraguay
67 Colorado State University, Fort Collins, CO 80523, USA
68 Michigan State University, East Lansing, MI 48824, USA
69 Istituto Nazionale di Fisica Nucleare Sezione di Lecce, 73100 - Lecce, Italy
70 Università del Salento, 73100 Lecce, Italy
71 Istituto Nazionale di Fisica Nucleare Sezione di Genova, 16146 Genova GE, Italy
72 Istituto Nazionale di Fisica Nucleare Sezione di Bologna, 40127 Bologna BO, Italy
73 Università di Bologna, 40127 Bologna, Italy
74 Universidad EIA, Envigado, Antioquia, Colombia
75 Queen Mary University of London, London E1 4NS, United Kingdom
76 University of California Davis, Davis, CA 95616, USA
77 Universidade Federal de Alfenas, Poços de Caldas - MG, 37715-400, Brazil
78 University of Chicago, Chicago, IL 60637, USA
79 Panjab University, Chandigarh, 160014, India
80 Indian Institute of Technology Guwahati, Guwahati, 781 039, India
81 Istituto Nazionale di Fisica Nucleare Laboratori Nazionali del Sud, 95123 Catania, Italy
82 Beykent University, Istanbul, Turkey
83 University of Iowa, Iowa City, IA 52242, USA
84 Lancaster University, Lancaster LA1 4YB, United Kingdom
85 Northern Illinois University, DeKalb, IL 60115, USA
86 Los Alamos National Laboratory, Los Alamos, NM 87545, USA
87 IRFU, CEA, Université Paris-Saclay, F-91191 Gif-sur-Yvette, France
88 Istituto Nazionale di Fisica Nucleare Sezione di Milano Bicocca, 3 - I-20126 Milano, Italy
89 University of Insubria, Via Ravasi, 2, 21100 Varese VA, Italy
90 Università di Milano Bicocca, 20126 Milano, Italy
91 Universidad Católica del Norte, Antofagasta, Chile
92 University of Birmingham, Birmingham B15 2TT, United Kingdom
93 Indian Institute of Technology Hyderabad, Hyderabad, 502285, India
94 STFC Rutherford Appleton Laboratory, Didcot OX11 0QX, United Kingdom
95 University of Bern, CH-3012 Bern, Switzerland
96 Wichita State University, Wichita, KS 67260, USA

- 97 Oregon State University, Corvallis, OR 97331, USA
98 University of Bucharest, Bucharest, Romania
99 University of Pittsburgh, Pittsburgh, PA 15260, USA
100 Università degli Studi di Genova, Genova, Italy
101 Virginia Tech, Blacksburg, VA 24060, USA
102 Istituto Nazionale di Fisica Nucleare Sezione di Napoli, I-80126 Napoli, Italy
103 Johannes Gutenberg-Universität Mainz, 55122 Mainz, Germany
104 University of California Santa Barbara, Santa Barbara, CA 93106, USA
105 University of Wisconsin Madison, Madison, WI 53706, USA
106 Royal Holloway College London, London, TW20 0EX, United Kingdom
107 Universidad Antonio Nariño, Bogotá, Colombia
108 University of Antioquia, Medellín, Colombia
109 Universidad Sergio Arboleda, 11022 Bogotá, Colombia
110 Universidad Nacional de Ingeniería, Lima 25, Perú
111 William and Mary, Williamsburg, VA 23187, USA
112 Università degli Studi di Padova, I-35131 Padova, Italy
113 Laboratoire de Physique des Deux Infinis Bordeaux - IN2P3, F-33175 Gradignan, Bordeaux, France,
114 Physical Research Laboratory, Ahmedabad 380 009, India
115 Indian Institute of Technology Kanpur, Uttar Pradesh 208016, India
116 University of Toronto, Toronto, Ontario M5S 1A1, Canada
117 Columbia University, New York, NY 10027, USA
118 Korea Institute of Science and Technology Information, Daejeon, 34141, South Korea
119 University of Pennsylvania, Philadelphia, PA 19104, USA
120 Ulsan National Institute of Science and Technology, Ulsan 689-798, South Korea
121 Southern Methodist University, Dallas, TX 75275, USA
122 Université Paris Cité, CNRS, Astroparticule et Cosmologie, Paris, France
123 University Grenoble Alpes, CNRS, Grenoble INP, LPSC-IN2P3, 38000 Grenoble, France
124 Duke University, Durham, NC 27708, USA
125 Istituto Nazionale di Fisica Nucleare Sezione di Milano, 20133 Milano, Italy
126 University of Parma, 43121 Parma PR, Italy
127 University of Mississippi, University, MS 38677 USA
128 University of California Riverside, Riverside CA 92521, USA
129 Istituto Nazionale di Fisica Nucleare Laboratori Nazionali di Frascati, Frascati, Roma, Italy
130 Centro Brasileiro de Pesquisas Físicas, Rio de Janeiro, RJ 22290-180, Brazil
131 Universidade Federal do Rio de Janeiro, Rio de Janeiro - RJ, 21941-901, Brazil
132 Nikhef National Institute of Subatomic Physics, 1098 XG Amsterdam, Netherlands
133 University of Amsterdam, NL-1098 XG Amsterdam, The Netherlands
134 Northwestern University, Evanston, IL 60208, USA
135 Valley City State University, Valley City, ND 58072, USA
136 University of Cambridge, Cambridge CB3 0HE, United Kingdom
137 University of Hawaii, Honolulu, HI 96822, USA
138 Universidade Federal de São Paulo, 09913-030, São Paulo, Brazil
139 California Institute of Technology, Pasadena, CA 91125, USA
140 Università degli Studi di Napoli Federico II, 80138 Napoli NA, Italy
141 Sapienza University of Rome, 00185 Roma RM, Italy
142 Istituto Nazionale di Fisica Nucleare Sezione di Roma, 00185 Roma RM, Italy
143 Drexel University, Philadelphia, PA 19104, USA
144 Iowa State University, Ames, Iowa 50011, USA
145 Stony Brook University, SUNY, Stony Brook, NY 11794, USA
146 Texas A&M University, College Station, Texas 77840
147 University of South Carolina, Columbia, SC 29208, USA
148 Rutgers University, Piscataway, NJ, 08854, USA
149 University of Sheffield, Sheffield S3 7RH, United Kingdom
150 Istituto Nazionale di Fisica Nucleare Sezione di Padova, 35131 Padova, Italy
151 Rice University, Houston, TX 77005
152 Institute for Research in Fundamental Sciences, Tehran, Iran
153 Madrid Autonoma University and IFT UAM/CSIC, 28049 Madrid, Spain
154 University of Notre Dame, Notre Dame, IN 46556, USA
155 Institute of Physics, Czech Academy of Sciences, 182 00 Prague 8, Czech Republic
156 Syracuse University, Syracuse, NY 13244, USA
157 Radboud University, NL-6525 AJ Nijmegen, Netherlands
158 Czech Technical University, 115 19 Prague 1, Czech Republic
159 Durham University, Durham DH1 3LE, United Kingdom

- 160 University of Minnesota Twin Cities, Minneapolis, MN 55455, USA
161 Tufts University, Medford, MA 02155, USA
162 Harish-Chandra Research Institute, Jhansi, Allahabad 211 019, India
163 University of Granada CAFPE, 18002 Granada, Spain
164 Boston University, Boston, MA 02215, USA
165 Occidental College, Los Angeles, CA 90041
166 South Dakota State University, Brookings, SD 57007, USA
167 Universidade Federal de Goias, Goiania, GO 74690-900, Brazil
168 University of Minnesota Duluth, Duluth, MN 55812, USA
169 Fluminense Federal University, 9 Icaraí Niterói - RJ, 24220-900, Brazil
170 University of California Berkeley, Berkeley, CA 94720, USA
171 University of Warsaw, 02-093 Warsaw, Poland
172 University of Puerto Rico, Mayaguez 00681, Puerto Rico, USA
173 Chung-Ang University, Seoul 06974, South Korea
174 Yale University, New Haven, CT 06520, USA
175 South Dakota School of Mines and Technology, Rapid City, SD 57701, USA
176 High Energy Accelerator Research Organization (KEK), Ibaraki, 305-0801, Japan
177 Sanford Underground Research Facility, Lead, SD, 57754, USA
178 Dordt University, Sioux Center, IA 51250, USA
179 Eötvös Loránd University, 1053 Budapest, Hungary
180 Yerevan Institute for Theoretical Physics and Modeling, Yerevan 0036, Armenia
181 Abilene Christian University, Abilene, TX 79601, USA
182 University of Albany, SUNY, Albany, NY 12222, USA
183 Jackson State University, Jackson, MS 39217, USA
184 University of Novi Sad, 21102 Novi Sad, Serbia
185 Erciyes University, Kayseri, Turkey
186 National Institute of Technology, Kure College, Hiroshima, 737-8506, Japan
187 Institute for Nuclear Research of the Russian Academy of Sciences, Moscow 117312, Russia
188 Florida State University, Tallahassee, FL, 32306 USA
189 University of Texas at Austin, Austin, TX 78712, USA
190 Università degli Studi di Milano, I-20133 Milano, Italy
191 Universidade Federal do ABC, Santo André - SP, 09210-580, Brazil
192 Sun Yat-Sen University, Guangzhou, 510275, China
193 Hong Kong University of Science and Technology, Kowloon, Hong Kong, China
194 Laboratori Nazionali del Gran Sasso, L'Aquila AQ, Italy
195 Instituto Tecnológico de Aeronáutica, Sao Jose dos Campos, Brazil
196 Jawaharlal Nehru University, New Delhi 110067, India
197 University of Athens, Zografou GR 157 84, Greece
198 Istituto Nazionale di Fisica Nucleare Sezione di Pavia, I-27100 Pavia, Italy
199 Università degli Studi di Pavia, 27100 Pavia PV, Italy
200 Centro de Investigación y de Estudios Avanzados del Instituto Politécnico Nacional (Cinvestav), Mexico City, Mexico
201 Pennsylvania State University, University Park, PA 16802, USA
202 University of Lucknow, Uttar Pradesh 226007, India
203 Iwate University, Morioka, Iwate 020-8551, Japan
204 Comisión Nacional de Investigación y Desarrollo Aeroespacial, Lima, Peru
205 Centro de Tecnologia da Informacao Renato Archer, Amaraís - Campinas, SP - CEP 13069-901
206 Gran Sasso Science Institute, L'Aquila, Italy
207 University of Arizona, Tucson, AZ 85721, USA
208 Punjab Agricultural University, Ludhiana 141004, India
209 Jeonbuk National University, Jeonrabuk-do 54896, South Korea
210 Central University of South Bihar, Gaya, 824236, India
211 Universidad Nacional Mayor de San Marcos, Lima, Peru
212 Institute of Particle and Nuclear Physics of the Faculty of Mathematics and Physics of the Charles University, 180 00 Prague 8, Czech Republic
213 University of Michigan, Ann Arbor, MI 48109, USA
214 National Institute of Science Education and Research (NISER), Odisha 752050, India
215 Texas AM University - Corpus Christi, Corpus Christi, TX 78412, USA
216 University of Medellín, Medellín, 050026 Colombia
217 Idaho State University, Pocatello, ID 83209, USA
218 Jyväskylä University, FI-40014 Jyväskylä, Finland
219 Kavli Institute for the Physics and Mathematics of the Universe, Kashiwa, Chiba 277-8583, Japan
220 University of California Los Angeles, Los Angeles, CA 90095, USA

[†] In memory of our colleague, Dr. Davide Salvatore Porzio, who is no longer with us.

Abstract: The Module-0 Demonstrator is a single-phase 600 kg liquid argon time projection chamber operated as a prototype for the DUNE liquid argon near detector. Based on the ArgonCube design concept, Module-0 features a novel 80k-channel pixelated charge readout and advanced high-coverage photon detection system. In this paper, we present an analysis of an eight-day data set consisting of 25 million cosmic ray events collected in the spring of 2021. We use this sample to demonstrate the imaging performance of the charge and light readout systems as well as the signal correlations between the two. We also report argon purity and detector uniformity measurements, and provide comparisons to detector simulations.

1. Introduction

Charge readout in liquid argon time projection chambers (LArTPCs) has traditionally been accomplished via a set of projective wire planes, as successfully demonstrated e.g. in the ICARUS [1], ArgoNeuT [2], MicroBooNE [3] and ProtoDUNE-SP [4,5] experiments, and as planned for the first large detector module of the DUNE experiment currently in preparation at the Sanford Underground Research Facility (SURF) underground laboratory in South Dakota [6]. However, this approach leads to inherent ambiguities in the 3D reconstruction of charge information that present serious challenges for LArTPC-based near detectors, where a high rate of neutrino interactions and an associated high-intensity muon flux cannot be avoided. In particular, 3D reconstruction becomes limited by overlap of charge clusters in one or more projections, and the unique association of deposited charge to single interactions becomes intractable.

To overcome event pile-up, a novel approach has been proposed and is being developed for the LArTPC of the Near Detector (ND) complex of the DUNE experiment, close to the neutrino source at Fermilab. This technology implements three main innovations compared to traditional wire-based LArTPCs: a pixelated charge readout enabling true 3D reconstruction, a high-performance light readout system providing fast and efficient detection of scintillation light, and segmentation into optically isolated regions. By achieving a low signal occupancy in both readout systems, the segmentation enables efficient reconstruction and unambiguous matching of charge and light signals.

This paper describes the first tonne-scale prototype of this technology, referred to as Module-0, and its performance as evaluated with a large cosmic ray data set acquired over a period of several days at the University of Bern. Section 2 provides an overview of the detector, as well as of its charge and light readout systems. Section 3 discusses the performance of the charge readout system in detail, and Section 4 does the same for the light readout system. Section 5 then reviews several analyses performed with reconstructed tracks from the cosmic ray data set collected during the Module-0 that allow to assess the performance of the fully-integrated system. Important metrics for successful operation are addressed, such as electron lifetime, electric field uniformity, and the ability to match charge and light signals, among others. Section 6 offers some concluding thoughts.

2. The Module-0 Demonstrator

2.1. Detector Description

The Module-0 demonstrator is the first fully integrated, tonne-scale prototype of the DUNE Liquid Argon Near Detector (ND-LAr) design. That detector will consist of a 7×5 array of $1 \times 1 \times 3$ m³ detector modules [7] based on the ArgonCube detector concept [8], each housing two 50 cm-drift TPC volumes with 24.9% optical detector coverage of the interior area. Module-0 has dimensions of 0.7 m \times 0.7 m \times 1.4 m, and brings together the innovative features of LArPix [9,10] pixelated 3D charge readout, advanced ArCLight [11] and Light Collection Module (LCM) [12] optical detectors, and field shaping provided by a low-profile resistive shell [13]. This integrated prototype also tests the charge and light

system control interfaces, data acquisition, triggering, and timing. Module-0 is the first of four functionally-identical modules that together will comprise an upcoming 2×2 ND-LAr prototype, known as ProtoDUNE-ND. Following construction and initial tests with cosmic ray event samples, this larger detector will be deployed underground in the NuMI neutrino beam at Fermilab [14] to demonstrate the physics performance of the technology in a similar neutrino beam environment to the DUNE ND. The work presented here describes the analysis of a data set of cosmic ray events obtained with the Module-0 detector, installed in a liquid argon cryostat at the Laboratory for High-Energy Physics of the University of Bern. Over a period of eight days, the detector collected a sample of approximately 25 million self-triggered cosmic ray-induced events along with sets of diagnostic and calibration data. The data collection period included an array of characterization tests and data collection with changes to detector trigger conditions, thresholds, and with the TPC drift field as high as 1 kV/cm. For a brief second running period, the cryostat was emptied and refilled following a series of gas purges rather than complete evacuation, to assess the purity impact; this is discussed further in Section 5.1. A gallery of events of different types is shown in Fig. 1. These images illustrate the rich 3D raw data from the pixelated charge readout system, the imaging capabilities for complex event topologies, and the low noise levels.

A schematic showing an exploded view of Module-0 with annotations of the key components is provided in Fig. 2, and a photograph of the interior of the Module-0 detector as seen from the bottom prior to final assembly in Fig. 3. The module is divided into two identical TPC drift regions sharing a central high-voltage cathode that provides the drift electric field. Opposite the cathode at a distance of 30 cm are the anode planes, pixelated with charge-sensitive gold-plated pads where drifting ionization electrons are collected. The sides of the module are covered with photon detectors — alternating ArCLight and LCM tiles. The TPC drift region is surrounded by a resistive field shell made of carbon-loaded Kapton films. This low-profile field cage provides field shaping to ensure a uniform electric field throughout the TPC volumes.

2.2. The Charge Readout System

The charge readout is accomplished using a two-dimensional array of charge-sensitive pads on the two anode planes parallel to the cathode. While pixel-based charge readout has already been implemented in gaseous TPCs, LArTPCs have additional challenges due to restrictions on power dissipation. A proof of principle for pixelated charge readout in a single-phase LArTPC is described in Ref. [15], where a test device was exposed to cosmic ray muons. Readout electronics were also developed [9,16] and successfully applied in a pixel-readout LArTPC. Each of the anode planes on opposite sides of the central cathode is comprised of a 2×4 array of anode tiles. Each tile is a large-area printed circuit board (PCB) containing a 70×70 grid of 4,900 charge-sensitive pixel pads with a 4.43 mm pitch. On the back of each PCB is a 10×10 grid of custom low-power, low-noise cryogenic-compatible LArPix-v2 application-specific integrated circuits (ASICs) [10], as shown in Fig. 4. Each ASIC is a mixed-signal chip consisting of 64 analog front-end amplifiers, 64 analog-to-digital converters, and a shared digital core that manages configuration and data I/O. Each pixel channel functions as an independent self-triggering detector with nearly 100% uptime, and is only unresponsive to charge for 100 ns while the frontend resets. The LArPix ASIC leverages the sparsity of LArTPC signals. The chip is in a quiescent mode when not self-triggering on ionization activity higher than $\mathcal{O}(100)$ keV. Thus, it avoids digitization and readout of mostly-quiescent data. At liquid argon temperatures, the rate of accumulation of spurious charge (leakage current) is about 500 electrons/second. Each channel periodically resets to discard spurious charge that has collected at the input. In total, Module-0 comprises 78,400 instrumented LArTPC pixels.

Power and data I/O is provided to each tile by a single 34-pin twisted-pair ribbon cable. These cables are connected at the cryostat flange to a custom feedthrough PCB mounted on the cryostat lid. Data acquisition is controlled by the Pixel Array Controller and Network

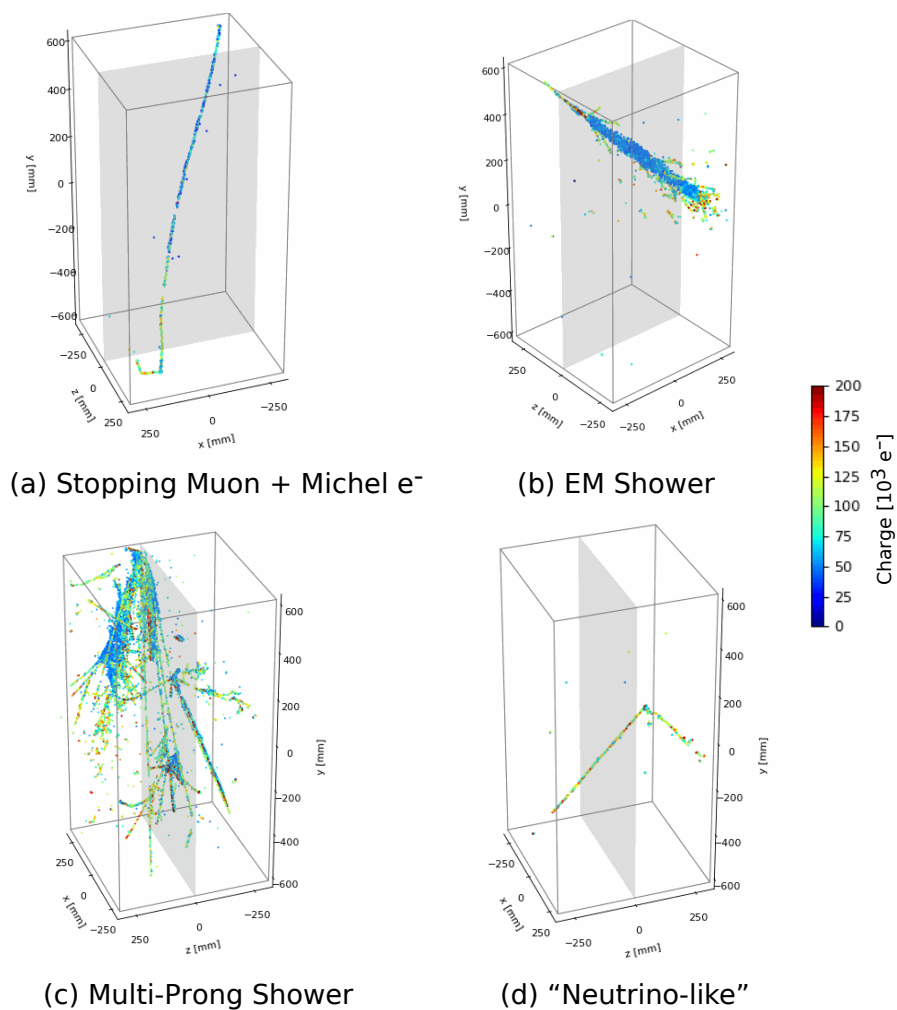


Figure 1. Gallery of four representative cosmic ray-induced events collected with Module-0, as recorded in the raw event data, with collected charge converted to units of thousands of electrons. In all cases, the central plane in grey denotes the cathode, and the color scale denotes the collected charge. (a) shows a stopping muon and the subsequent Michel electron decay, (b) denotes an electromagnetic (EM) shower, (c) is a multi-prong shower, and (d) is “neutrino-like” in that the vertex of this interaction appears to be inside the active volume.

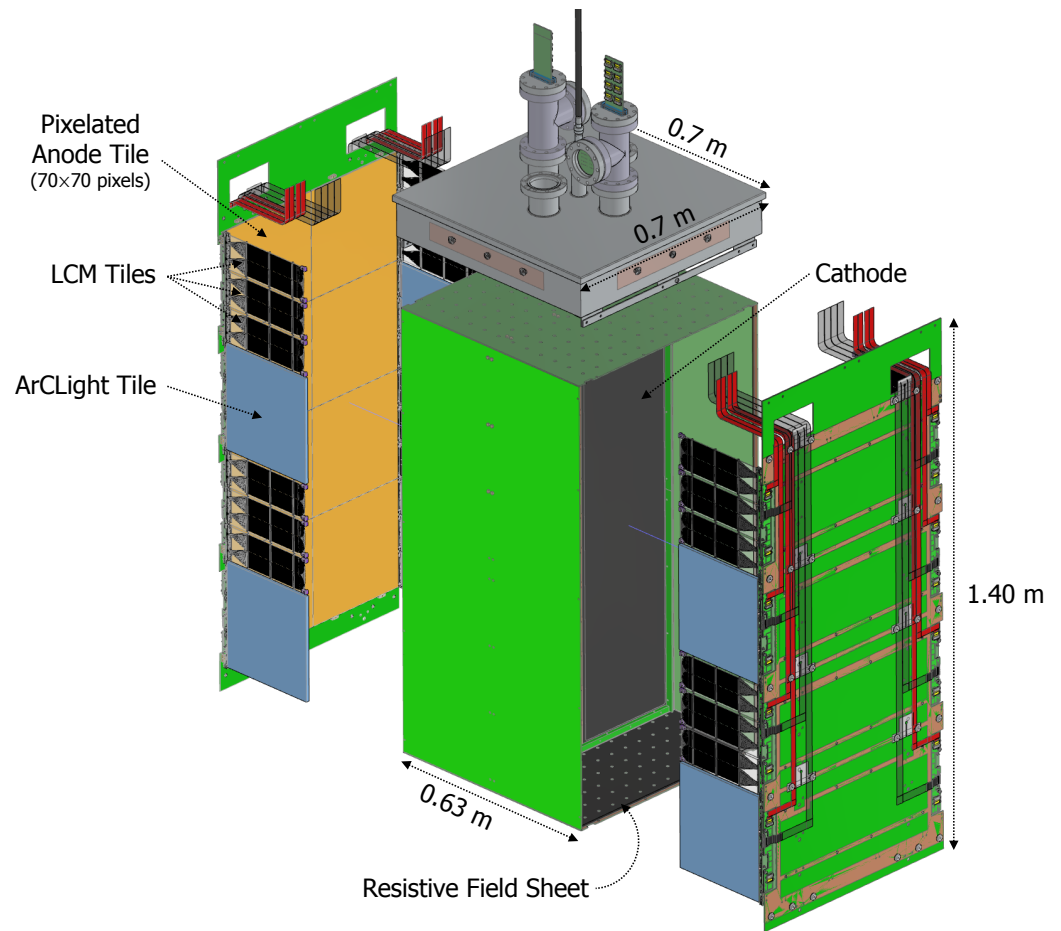


Figure 2. Schematic of the $0.7\text{ m} \times 0.7\text{ m} \times 1.4\text{ m}$ Module-0 detector with annotations of the key components.

(PACMAN) card (Fig. 5), which provides filtered power and noise-isolated data I/O to eight tiles. Two PACMAN controllers are mounted in metal enclosures attached to the outer surface of each feedthrough. During Module-0 operation, the PACMAN controller received a pulse-per-second timing signal for data synchronization between charge readout and light readout systems, and external trigger signals from the light readout system were embedded as markers into the charge readout data stream. Data are carried over a standard copper ethernet cable connected at each PACMAN to a network switch. Subsequently, data are transferred to and from the DAQ system via an optical fiber connection.

For the LArTPC ionization charge measurement, LArPix ASICs mainly operate in self-trigger mode, where a trigger is initiated on a per-channel basis when a channel-level charge threshold is exceeded. In this mode of operation LArPix incurs negligible dead time and produces only modest data volumes, due to the sparsity of ionization signals in 3D, even for high-energy events. Serial data packets stream out of the system continuously via the PACMAN boards and are processed offline for analysis. A programmable channel-level threshold is set using internal digital to analog converters (DACs), which are tuned so that the spurious (i.e. noise-related) trigger rate is less than 2 Hz for each channel. For Module-0, channel thresholds were operated in two regimes: low and high threshold (see Fig. 6). Low threshold ($\sim 5.8\text{ ke}^-/\text{pixel}$ or $\sim \frac{1}{4}\text{ MIP}/\text{pixel}$) operation optimized charge signal sensitivity at the expense of incurring additional triggers due to e.g. digital pickup, whereas high threshold ($\sim 10.7\text{ ke}^-/\text{pixel}$ or $\sim \frac{1}{2}\text{ MIP}/\text{pixel}$) operation benefited from improved trigger stability at the expense of charge sensitivity. Updated revisions of the LArPix ASIC include additional pickup mitigation that will allow channel thresholds to be lowered further. Also, a slight rising trend in event rate can be seen over some of the

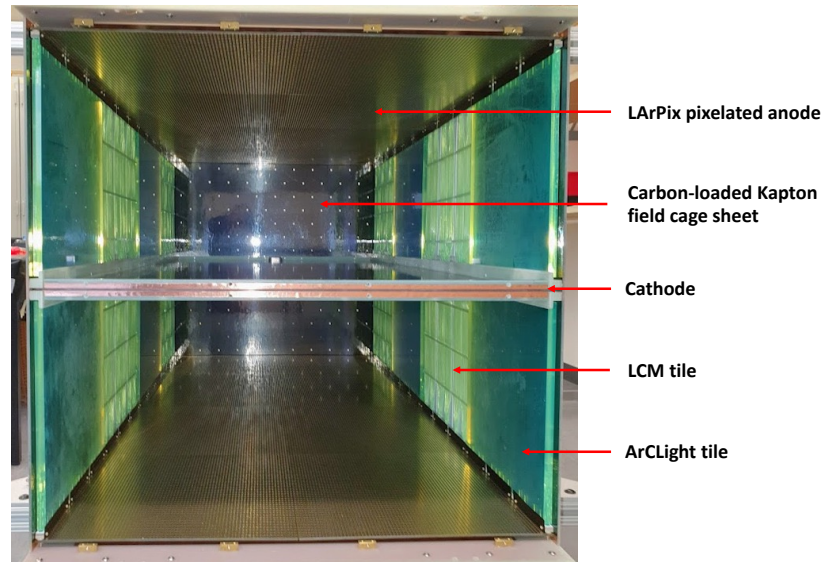


Figure 3. Photograph of the Module-0 detector interior as seen from the bottom, with annotations of the key components.

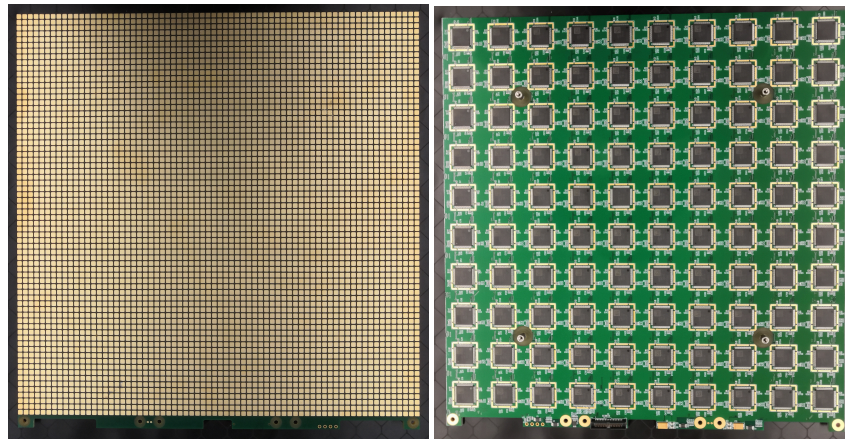


Figure 4. Front (left) and back (right) of a TPC anode tile. The front contains 4,900 charge-sensitive pixels with 4.43 mm pitch that face the cathode, and the back contains a 10×10 array of LARPix ASICs. The dimensions are 31 cm \times 32 cm, with the extra centimeter providing space for the light system attachment points.

different periods, most likely due to the emergence during data taking of pixels with a high data rate. It is believed that this small effect, which has no impact on the physics performance, can be mitigated by improving the procedure used to set the thresholds.

ASICs within an anode tile are routed out to the DAQ through a configurable “hydra” network, wherein each ASIC has the ability to pass data packets to and from any adjacent neighbor. The scheme allows for system robustness in the event that an ASIC along the signal path becomes nonfunctional, though none of the 1600 ASICs failed during Module-0 operation. A few-millisecond delay is incurred for data packets produced deeper in the network to reach the PACMAN controller relative to data packets produced closer to it. This is accounted for during hit digitization: each data packet carries a timestamp at creation when the hit signal is digitized, and when packets reach the PACMAN controller, a receipt timestamp is also assigned. Time ordering and filtering on packet trigger type is performed offline. In order to monitor the integrity of the data in near-real time, a dedicated nearline monitoring system was developed and operated during the Module-0 run. An automated analysis was performed on each run’s raw data once the run ended and provided metrics including system trigger rates, trigger timing and offsets, channel occupancy and trigger

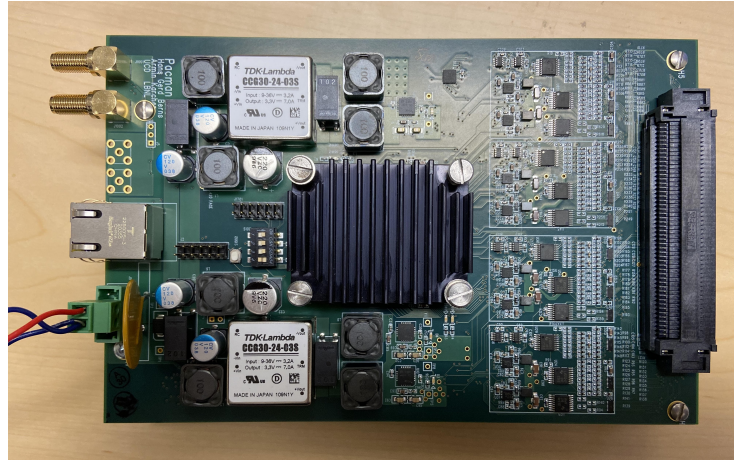


Figure 5. The Pixel Array Controller and Network card (PACMAN), which controls the data acquisition and power for the charge readout system.

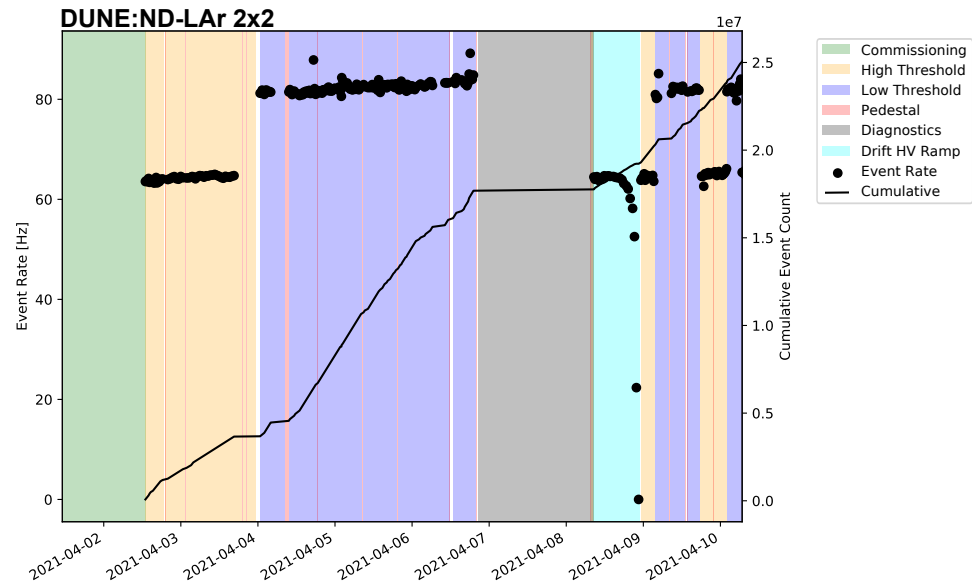


Figure 6. Run event rate and cumulative events as a function of time with respect to charge readout operating condition.

rates, and data corruption checks. Cosmic rays produced a self-trigger rate of ~ 0.25 Hz per pixel. This resulted in a total pixel hit rate of ~ 20 kHz for the entire Module-0 detector, yielding a modest data rate of 2.5 Mb/s.

2.3. The Light Readout System

The Light Readout System (LRS) provides fast timing information using the prompt ~ 128 nm scintillation light induced by charged particles in LAr. The detection of scintillation photons provides absolute reference for event timing (t_0) and, when operated in an intense neutrino beam, will allow for unambiguous association of charge signals from the specific neutrino interactions of interest (i.e. pile-up mitigation). The LRS uses a novel dielectric light detection technique capable of being placed inside the field-shaping structure to increase light yield and localization of light signals. The LRS consists of two functionally-similar silicon photomultiplier (SiPM)-based detectors for efficient collection of single UV photons with large surface coverage: the Light Collection Module (LCM) and the ArCLight module. The full LRS system includes these modules together with the ancillary readout, front-end electronics, DAQ (ADCs, synchronization, and trigger),

feedthrough flanges, SiPM power supply subsystem, and slow controls, as well as cabling and interconnection between different elements. LCM and ArCLight modules share the same basic operation principle. The vacuum ultraviolet (VUV) scintillation light produced by LAr is shifted from 128 nm to visible light by a wavelength shifter (WLS). Tetraphenyl butadiene (TPB) coated on the surface of the light collection systems provides an efficient WLS, and the emission spectrum of TPB is quite broad with a peak intensity of around 425 nm (violet light). Part of the light emitted at the surface of the light detection system eventually enters the bulk structure of the detector and is shifted to green light by a dopant (coumarin) in a bulk material, which also acts as a light trap (see Fig. 7).

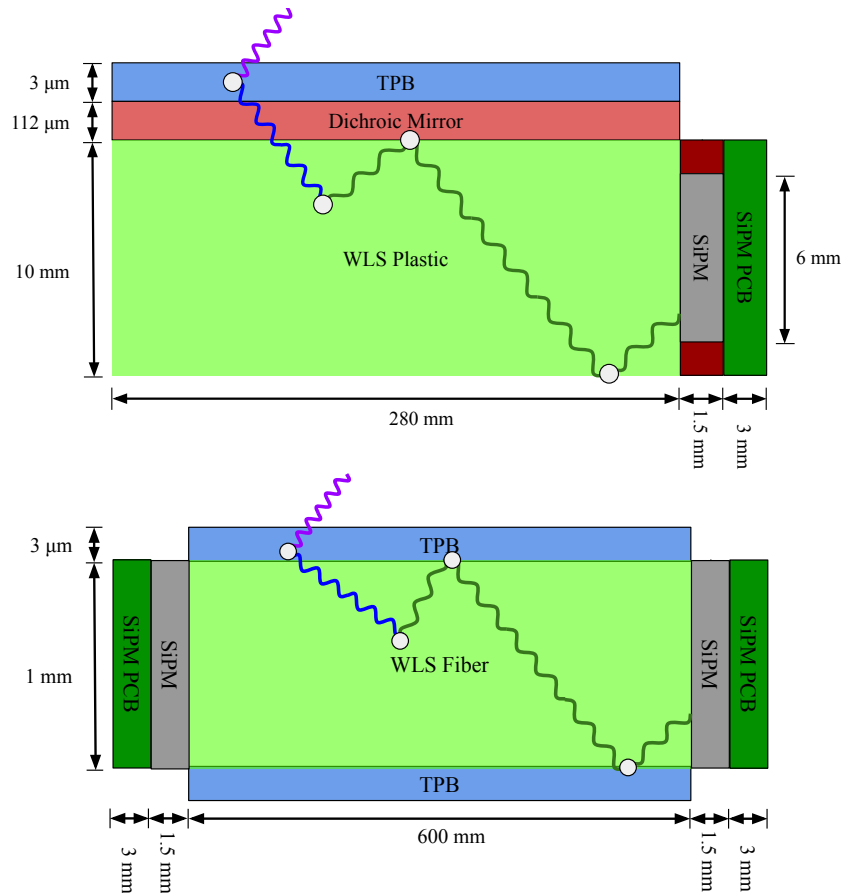


Figure 7. Detection principle of the two types of modules comprising the LRS: a segment of an ArCLight tile (top) and a single LCM optical fiber (bottom). The wave-like lines indicate example photon trajectories, where the white points indicate interactions. Drawings are not to scale.

The ArCLight module has been developed by Bern University [11] and uses the ARAPUCA [17] principle of light trapping. The general concept, illustrated in Fig. 7 (top), is that violet light enters a bulk WLS volume and is re-emitted as green light, and the volume has a coating reflective to green light on all sides except on the SiPM photosensor window. A dichroic filter transparent to the violet light and reflective for the green is used on the WLS (tetraphenyl butadiene, TPB) side. The overall module dimensions are 300 mm × 300 mm × 10 mm. A photograph of an ArCLight module is shown in Fig. 8 (left).

The LCM prototype is a frame cantilevered by a PVC plate that holds 25 WLS fibers bent into a bundle whose both ends are readout by a SiPM light sensor. Fibers are grouped and held by spacer bars with holes fixed on the PVC plate by means of polycarbonate screws to provide matching of thermal contraction. The PVC plate with the WLS fibers is coated with TPB, which re-emits the absorbed VUV light to the violet (~ 425 nm). This light

is then shifted inside multi-cladding $\varnothing=1.2$ mm Kuraray Y-11 fibers to green (~ 510 nm), and hence is trapped by total internal reflection guiding it to the SiPM readout at the fiber end, as depicted in Fig. 7 (bottom). For each group of LCMs, the center module uses bis-MSB as a WLS rather than TPB to evaluate this alternative option; the photon detection efficiency performance is discussed in Section 4 and the relative performance can be observed in Fig. 26. The LCM dimensions are 100 mm \times 300 mm \times 10 mm. Fig. 8 (right) shows three LCMs.

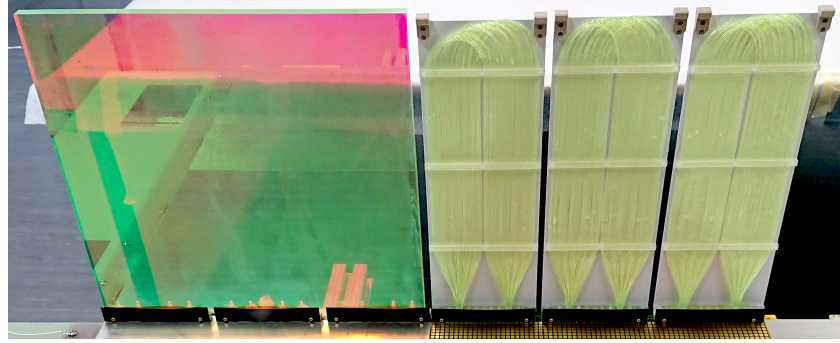


Figure 8. An ArCLight tile (left) and three LCM tiles (right), as assembled within the Module-0 structure.

In order to digitize analog signals from SiPMs, a 100 MHz, 10-bit, 64-channel (differential signals, full range ± 1.6 V) ADC prototype module in VME standard produced at the Joint Institute for Nuclear Research (JINR) was used (see Fig. 9 left). This ADC module streams UDP/TCP data packets via M-link MStream protocol using a 10 Gbps optical link. The ADC boards have the capability to be synchronized via a White Rabbit system [18]. This was not available for Module-0 run, for which timing synchronization between the charge light systems was provided by a dedicated system shown in Fig. 9 (right). To merge data between light and charge systems, a trigger signal generated by the LRS is written out to the charge readout data stream. This trigger signal is also fed to the analog input of both ADCs to allow for precise time matching between ADC boards for further LRS data analysis. Additionally, a pulse-per-second from a stable GPS source was used for both detection systems to provide accurate synchronization. For the LRS, the pulse-per-second signal was fed to the analog input of each ADC. During the Module-0 run, the LRS operated in a self-triggered mode with adjustable threshold settings. The thresholds for the LCMs are approximately 30 photoelectrons, as discussed in Section 4.

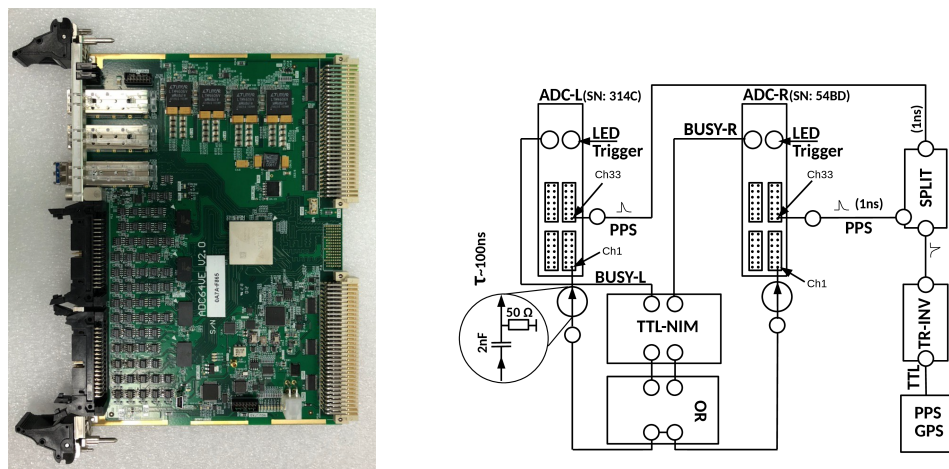


Figure 9. LRS data acquisition components: JINR ADC board (left), synchronization and trigger scheme (right).

3. Charge Readout Performance

3.1. System Overview

Module-0 operation represents the first demonstration of the LArPix-v2 pixelated charge readout system in a tonne-scale LArTPC. Continuous acquisition and imaging of self-triggered cosmic ray data were successfully exercised, demonstrating the excellent performance of this technology. This section presents an array of studies of the charge readout system performance, including: pixel channel signal baselines and time stability, charge response as a function of track position and angle relative to the pixel plane, response uniformity across the instrumented area, ADC saturation, and overall calorimetric measurement performance.

In parallel to this successful series of technological achievements, this first large-scale integrated test highlighted areas for continued improvement in future iterations of the module design. This includes improved anode tile grounding and optimization of the pixel pad geometry. In the former case, enhancements to the grounding scheme will enable improved system-wide per-channel charge threshold sensitivity and system trigger stability, specifically allowing readout of the pixels on the edge of neighboring tiles, and mitigating the effects of triggering induced by system synchronization signals observed in the Module-0 data. In the latter case, modifications to the pixel pad geometry will further minimize far-field current induction in the pixels, reducing the sensitivity of the readout system to drifting charge that is far from the anode plane. Additional improvements to the ASIC-related noise budget are planned for the next-generation LArPix design. Of the total 78,400 instrumented pixel channels in Module-0, 92.2% were enabled for LArTPC operation. The channels were disabled mainly due to limitations noted above — grounding near tile edges (4.2%), elevated noise levels due to signal pickup (3.1%), high noise or leakage current (0.5%) — and their locations are illustrated in Fig. 10. As noted above, no ASICs failed during Module-0 operations.

3.2. Noise and Stability

Periodic diagnostics (pedestal) runs were taken to monitor the stability of the charge readout system. These diagnostic runs entailed issuing a periodic trigger on a per-channel basis in a round-robin fashion among channels on a single ASIC. In this way, sub-threshold charge was digitized to monitor channel pedestal and the AC noise stability in time, with the ADC value returned by each digitization reflecting the sum of the quiescent pedestal voltage of the front-end amplifier and the integrated charge. The distributions of ADC values collected during pedestal runs were in agreement with the design expectations, with a median value of ~ 78 counts per channel, and pedestal voltage varied by approximately 30 mV between channels. To determine the integrated charge, a correction for this pedestal value must be applied. We computed the channel-by-channel pedestal ADC value by using the truncated mean around the peak of the ADC value distribution of each channel. The signal amplitude in mV was inferred based on the internal reference DAC values and the ASIC analog voltage, and a global gain value of $245 e^- / \text{mV}$ was then used to convert the signal amplitude to charge.

Additionally, the stability of the charge readout over time was verified using cosmic ray data samples, by measuring the most probable value (MPV) and the full width at half maximum (FWHM) of the dQ/dx distribution of minimum ionising particle (MIP) tracks for each data run, as shown in Fig. 11. To make these track-based measurements, 3D hits registered by the charge system are clustered together using the DBSCAN algorithm [19]. A principal component analysis of hits within each cluster then provides three-dimensional segments that we define as reconstructed tracks. The charge dQ corresponds to the sum of the hits associated to the reconstructed track and the 3D reconstructed track length dx . The dQ/dx distribution is then fitted with a Gaussian-convolved Moyal distribution [20], which is used to extract the MPV and the FWHM. Total system noise contributes $\sim 950 e^-$ equivalent noise charge (ENC) to each pixel hit, as assessed using periodic forced triggering of pixel channels in the absence of actual signals (Fig. 12). To put this metric in context, the

intrinsic energy loss fluctuations associated with the charge from a 4 GeV MIP would be $\sim 1800 e^-$ in ND-LAr's 3.7 mm pixel pitch. Therefore, the charge resolution is smaller than the intrinsic physical fluctuations for particle kinematics relevant to ND-LAr.

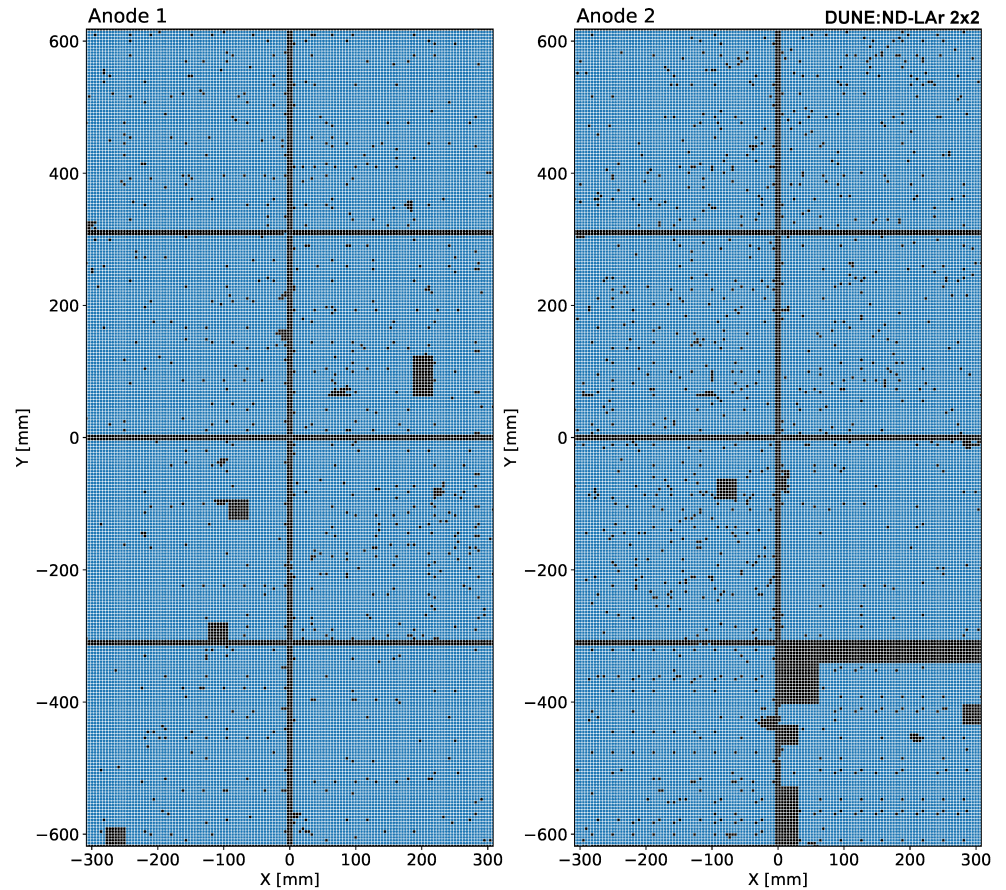


Figure 10. Self-trigger active pixel channels (in blue) and inactive channels (in black). In these coordinates, x is horizontal and y is vertical, both parallel to the anode plane, and z is the drift direction, perpendicular to the anode plane, completing a right-handed system. The origin is the center of the module.

Examining the corresponding charge in each pixel that has triggered (Fig. 13), we identify a sharp rising edge corresponding to the self-trigger threshold at approximately 5.8×10^3 electrons (low threshold) and 11×10^3 electrons (high threshold). Above the self-trigger threshold, a peak at roughly 24×10^3 electrons corresponds to the typical charge deposited by a MIP crossing the full pixel pitch of 4.43 mm. Of note are the markedly different charge distributions of the high- and low-threshold data. We find that for the low-threshold data, the average number of triggers per single channel for MIP energy deposition is substantially larger than for the high-threshold data, with mean values of 1.53 and 1.14 respectively. These numbers are well-reproduced by the Monte Carlo simulation (MC) described in Section 5, with values of 1.52 and 1.12 respectively for a similar set of reconstructed MIP tracks. Summing the charge of all digitizations on each specific channel for a given event increases the similarity between the low-threshold data with the high-threshold data (Fig. 14). This is indicative of a “pre-triggering” effect, in which a channel is triggered by the induced signal generated by the drifting charge in advance of the charge signal arrival at the anode plane, thus motivating the reduction of far-field effects discussed above.

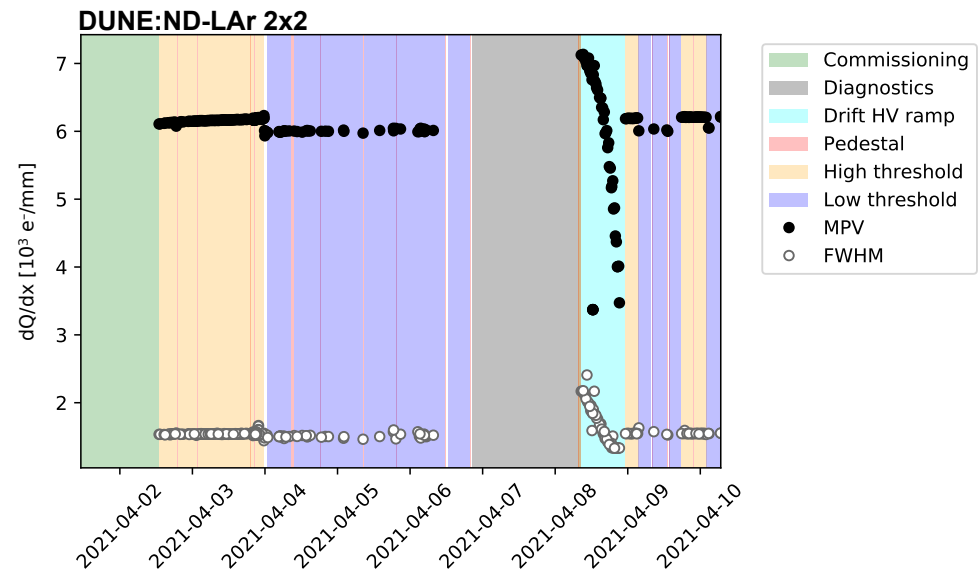


Figure 11. Most probable value (black circles) and full width at half maximum (white circles) of the dQ/dx distribution for each data run. The system shows a good charge readout stability during data taking periods, both for high threshold (yellow bands) and low threshold (purple bands) runs.

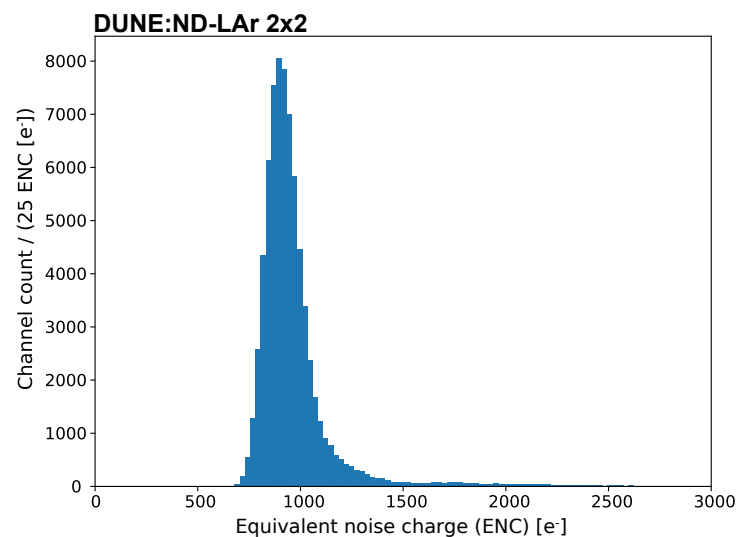


Figure 12. LArPix channel noise in units of electron charge signal, as observed using periodic forced triggers. The total system noise is $\sim 950 e^-$, compared to a signal amplitude of $\sim 1800 e^-$ for a 4 GeV MIP track in ND-LAr's 3.7 mm pixel pitch.

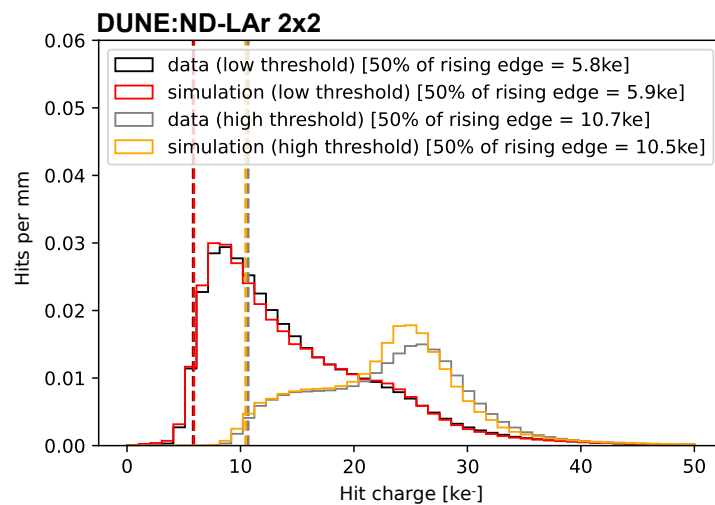


Figure 13. Self-trigger charge distribution for MIP tracks measured in thousands of electrons (ke^-); 50% of the rising edge are shown as indicators of the charge readout self-trigger thresholds. The low- and high-threshold curves are obtained from runs with the same 20 minute exposure. Each entry is normalized by hit charge over fitted track length. The MC simulation shown in comparison is described in Section 5.

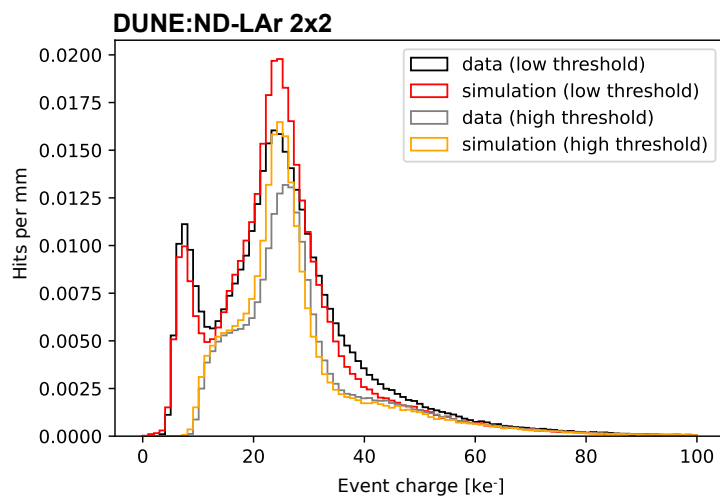


Figure 14. Total event charge per channel for MIP tracks measured in thousands of electrons (ke^-). The MC simulation shown in comparison is described in Section 5.

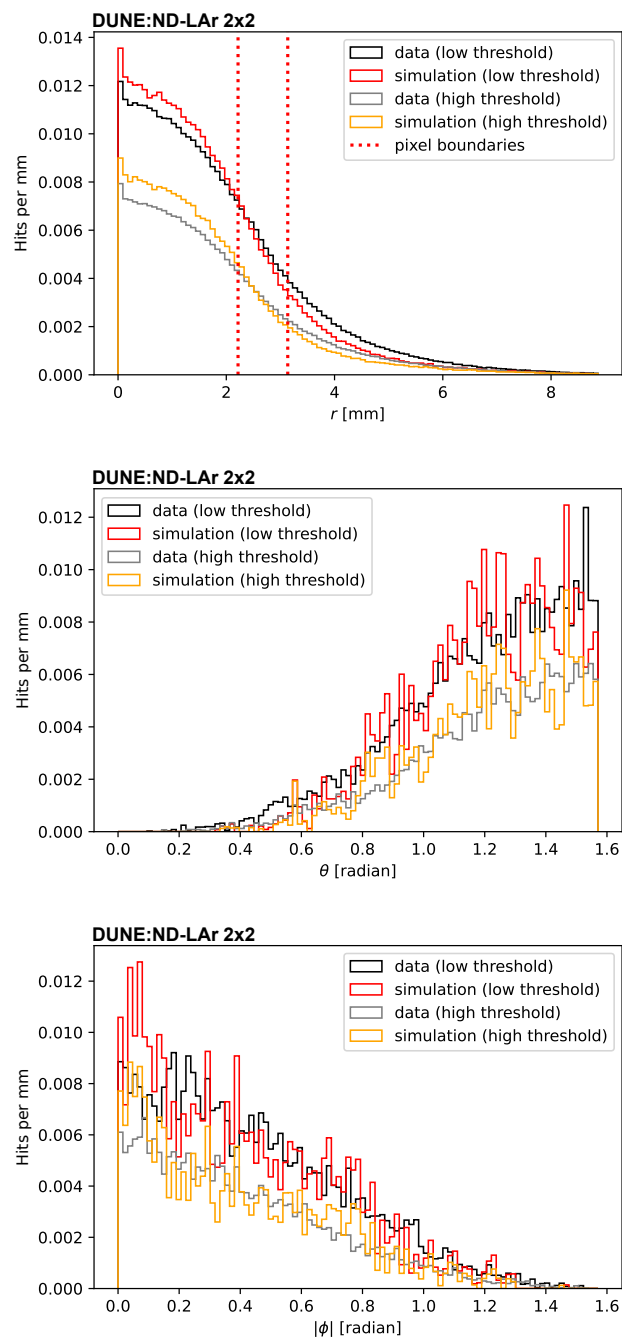


Figure 15. Comparisons of response variation in the radial distance from the pixel center to the point of closest approach of the track projected onto the anode plane (r , top), the track inclination relative to the anode plane (polar angle θ , middle), and the orientation angle of the track projected onto the anode plane (azimuthal angle ϕ , bottom). The MC shown in comparison is described in Section 5.

3.3. Pixel Charge Response

To study the individual pixel charge response, we examine the variation in response based on the track inclination relative to the anode plane (polar angle θ), the orientation angle of the track projected onto the anode plane (azimuthal angle ϕ), and the radial distance from the pixel center to the point of closest approach of the track projected onto the anode plane (r). Fig. 15 shows the distribution of these three quantities, normalized by the total track length. Generally, the θ and ϕ distributions are comparable between data and simulations. The r distribution shows significantly more triggers to peripheral tracks than simulated events. An overall normalization difference between high- and low-threshold data reflects the decreased sensitivity to tracks that clip the corners of the pixel.

A similar finding resulted from studying the distance between the MIP ionization axis and the center of the pixel. This ionization axis can be inferred by performing a Hough transform algorithm (HTA) on the x , y , and estimated z dimensions of the hit cloud. A projection of the HTA line onto the pixel plane provides the minimum array of pixels along the axis that could have recorded some charge. This line is then divided into 0.1 mm segments longitudinally. Each individual segment's center then falls into a specific pixel, which is used to determine the distance between the segment center and the pixel center in x and y . The segments are split into three categories: (1) all segments as mentioned above independent of the recorded charge on that particular pixel, (2) those that fell into a pixel which did give a response, and (3) those in pixels that did not trigger. Prior to this categorization, all segments contained by pixels known to be inactive are excluded. In Fig. 16, the ratios of the number of segments in the latter two categories to the first one are shown. The four corners are over-represented for pixels that did not give a response but had the main ionization line crossing their pad. This quantifies the sensitivity of individual pixels to tracks clipping the corners. This difference in sensitivity is characterized by only a 3% drop from pixel center to pixel edge where the minimum response is 85.5%.

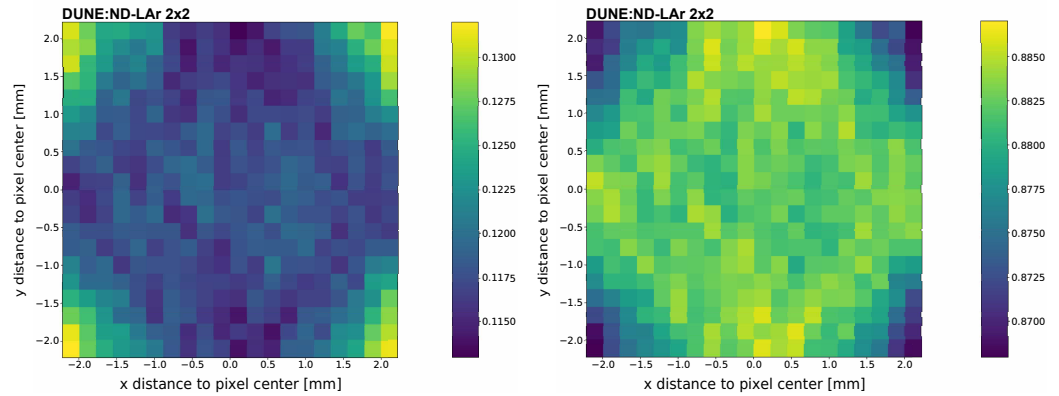


Figure 16. Relative rate of pixel response as a function of the distance between Hough line segments and segment containing pixel's center for pixels on gaps, i.e. no charge response (left), and on tracks, i.e. with charge response (right) to the total.

Figs. 17 and 18 show the charge distribution with respect to the track orientation for low- and high-threshold data, respectively. Overall, similar features appear in each panel: a prominent peak corresponding to the charge deposited by a MIP across a single pixel width. In the r distribution, a secondary distribution of low-charge hits is present, corresponding to tracks that clip the corners of the pixel. This feature is also present in the ϕ distribution as an increase in the spread of the charge as $\phi \rightarrow \pi/4$. The θ distribution shows a characteristic increase in the charge as $\theta \rightarrow 0$, which corresponds to tracks perpendicular to the anode plane, where each pixel can see a contribution from a relatively long track length. A flattening of the observed charge near $\theta = 0.8$ is a threshold effect and is not present in the low-threshold data. To test the responsiveness of individual pixels and identify potentially malfunctioning channels beyond those known to be inactive, a MIP response map of the entire pixel plane was constructed. This map is the ratio of recorded

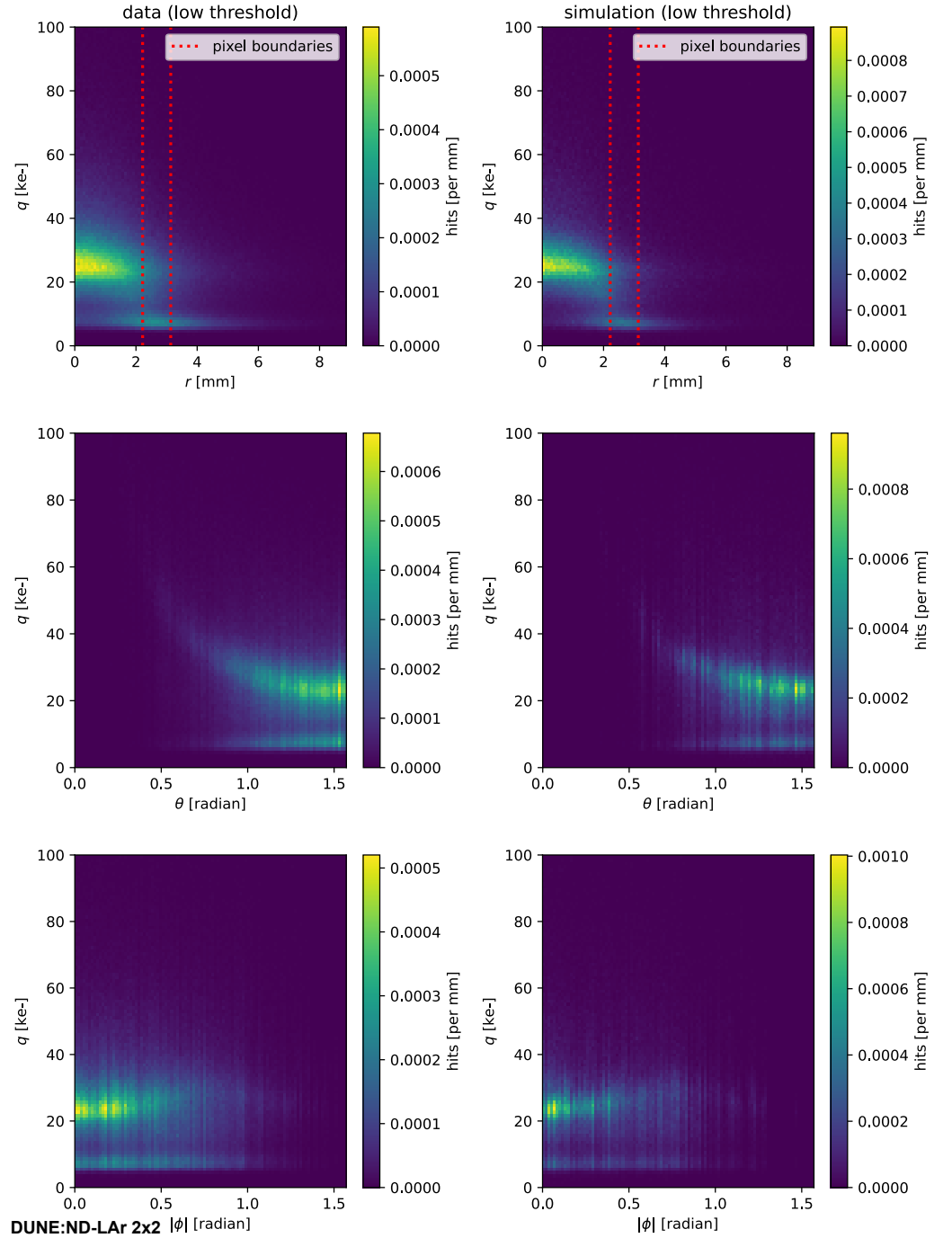


Figure 17. Self-trigger charge distribution for MIP tracks with different track orientations with respect to the pixel, normalized to number of triggered channels per reconstructed track length. Low-threshold data are used. The MC simulation shown in comparison in the second column is described in Section 5.

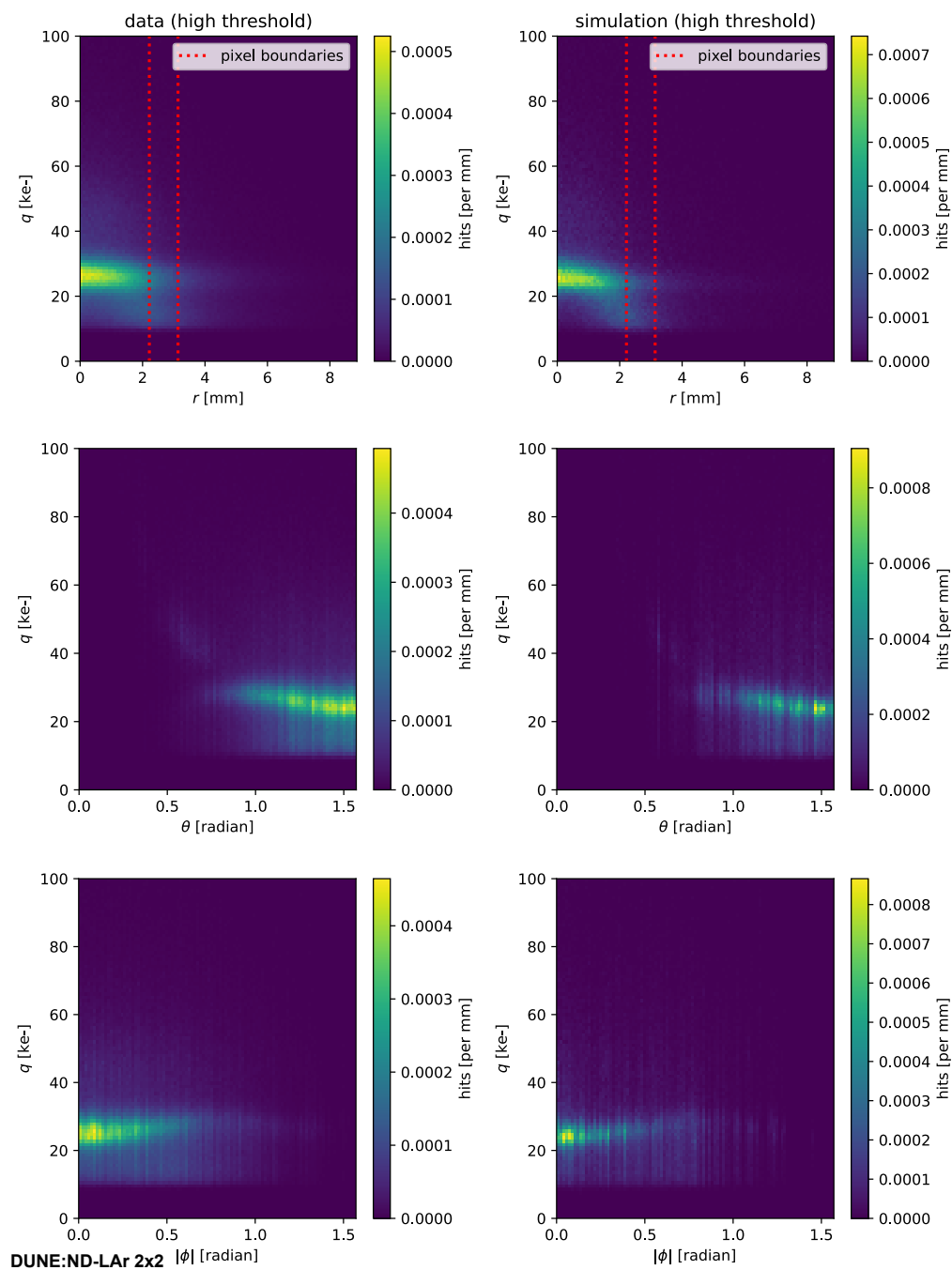


Figure 18. Same as Fig. 17 but for high threshold data.

over expected hits, and identifies regions on the pixel plane which are less responsive than others. Both components start off with the same principle of performing an HTA on the x , y , and inferred z dimensions of the hit cloud to obtain the MIP's central ionization axis in 3D. This axis is then projected onto the pixel plane to result in a 2D line. Next, all hits within 8 mm of the line are selected and the maximum track width is set equal to the most distant point within this radius. To then obtain the first map, all pixels that recorded hits within a radius equal to the maximum track width of the projected line receive an entry. To construct the second map, all existing pixels within that same radius receive an entry. If a pixel is unresponsive, it will not show up in the first but will appear in the second, leading to a low ratio in that specific area. Selection cuts place requirements on the straightness of tracks relative to the fit Hough lines as well as the consistency with a roughly constant energy deposition profile, to ensure that the events analyzed consist primarily of MIP-like tracks. Fig. 19 shows the resulting MIP response maps for both anode planes.

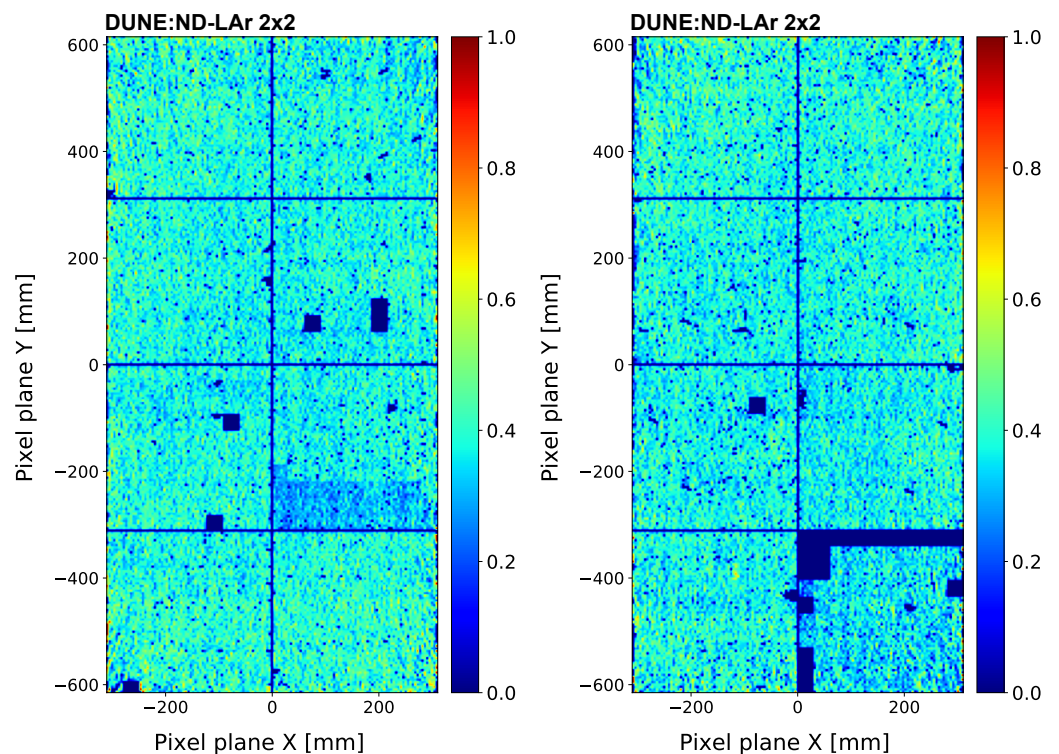


Figure 19. MIP response maps for anode plane 1 (left) and anode plane 2 (right), showing the fraction of triggered hits on each pixel relative to the expected number based on reconstructed track trajectories.

3.4. Saturation

An additional consideration is saturation in the LArPix-v2 ASIC's 8-bit successive-approximation ADC, which is expected to occur when the charge on a given channel exceeds 200 ke^- within a $2.6 \mu\text{s}$ time window. A scan for events including saturated packets was performed over eight hours of cosmic ray data acquired at high gain and low threshold. Packets within 1 s of a time synchronization pulse were found to include additional noise and saturation effects, and were excluded. After accounting for this, a small fraction (2.9×10^{-6}) of events with matching charge and light information contained a saturated ADC measurement. These events were manually inspected, and the saturation was clearly uncorrelated in space and time with the physical interactions, but rather they leaked into the event due to their proximity with a sync pulse. With low thresholds, $< 0.002\%$ of triggers resulted in ADC saturation, again driven by the pulse-per-second sync signal; channels 35-37 on all chips, which are located physically adjacent to the sync pulse

pin, saturated most often and together accounted for 15% of these saturated packets. The ADC count distribution for events with deposited energy between 2 and 10 GeV is shown in Fig. 20. These energies are of interest as they are representative of neutrino interactions at ND-LAr, and the distribution falls well within the dynamic range of the ADC.

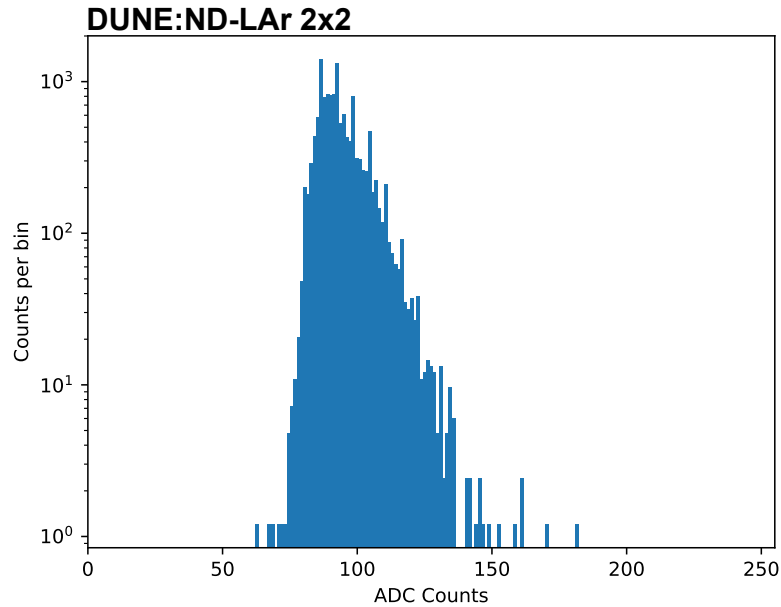


Figure 20. Per-pixel ADC value distribution for cosmic ray events between 2 and 10 GeV. All signals are well within the ADC dynamic range of 0–256 counts.

3.5. Calorimetric Response

Finally, the calorimetric response of Module-0 charge readout was also studied. Figs. 21 and 22 show the variation of the dQ/dx for segments of different lengths relative to the track orientation, defined by the azimuth angle ϕ and the θ angle between the track and a vector normal to the anode plane. The reconstructed tracks used for this analysis come from the low threshold runs (see Section 1). Events with more than 20 reconstructed tracks were excluded, since they often correspond to large showers or non-cosmic triggers. Tracks were required to be longer than 10 cm and to have at least 20 associated hits. They were then subdivided into segments of variable length from 10 to 400 mm and the distributions were fit with a Gaussian-convolved Moyal function. The MPV shows a slight dependence on $\cos\theta$, with tracks that impinge perpendicularly to the anode plane tending to have a larger amount of deposited charge per unit length. These data provide insight into subtle effects in the pixel charge response, such as those related to induction effects and electric field uniformity, and enable a data-driven calibration.

4. Light Readout Performance

4.1. Overview

The Module-0 detector also provided a large-scale, fully integrated test of the light readout system, enabling a detailed performance characterization of the ArCLight and LCM modules, readout, DAQ, triggering, and timing with a large set of events. Using cosmic ray data and dedicated diagnostic runs under a variety of detector configurations, a suite of tests was performed to assess the charge spectrum, inter- and intra-event timing accuracy, and photon detection efficiency. The subsequent matching of events between the charge and light system is considered in Section 5.3.

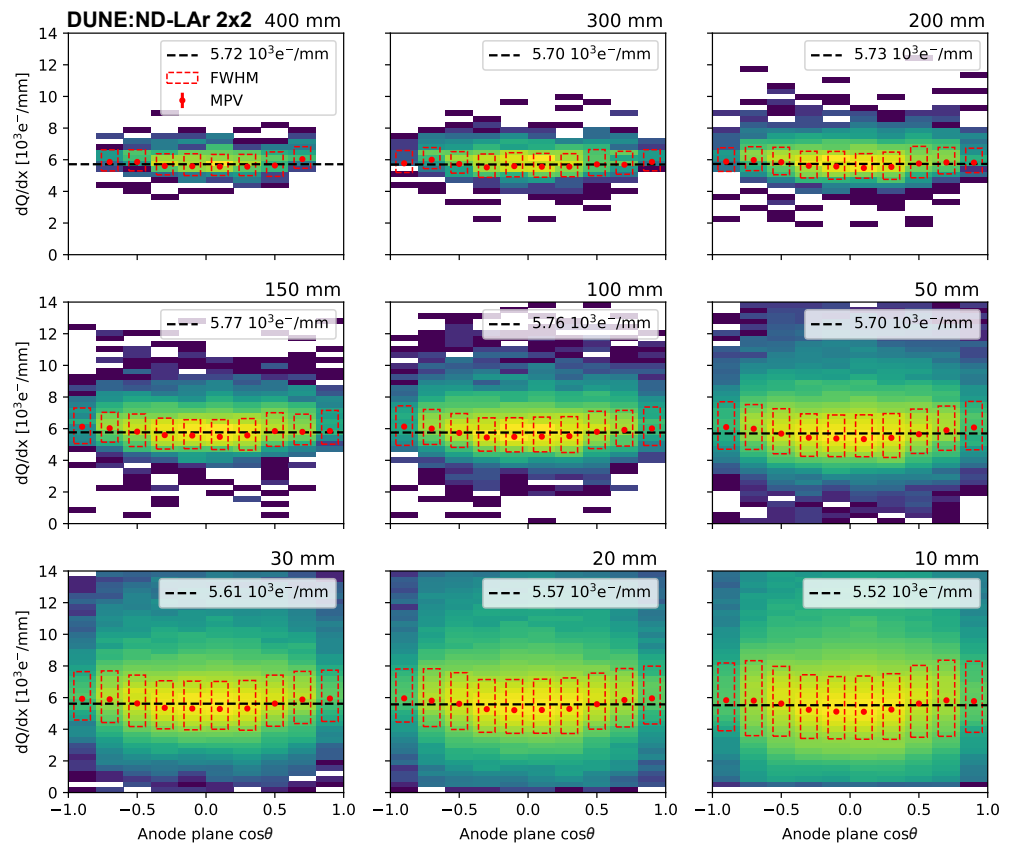


Figure 21. dQ/dx measured for segments of different lengths as a function of the orientation relative to the anode planes. A value of $\cos\theta = 0$ corresponds to segments parallel to the anode plane. The distributions in each bin have been fitted with a Gaussian-convolved Moyal function. The red points correspond to the most probable value of the fitted distribution and the dashed rectangles correspond to the full width at half maximum. The dashed black line represents the average MPV.

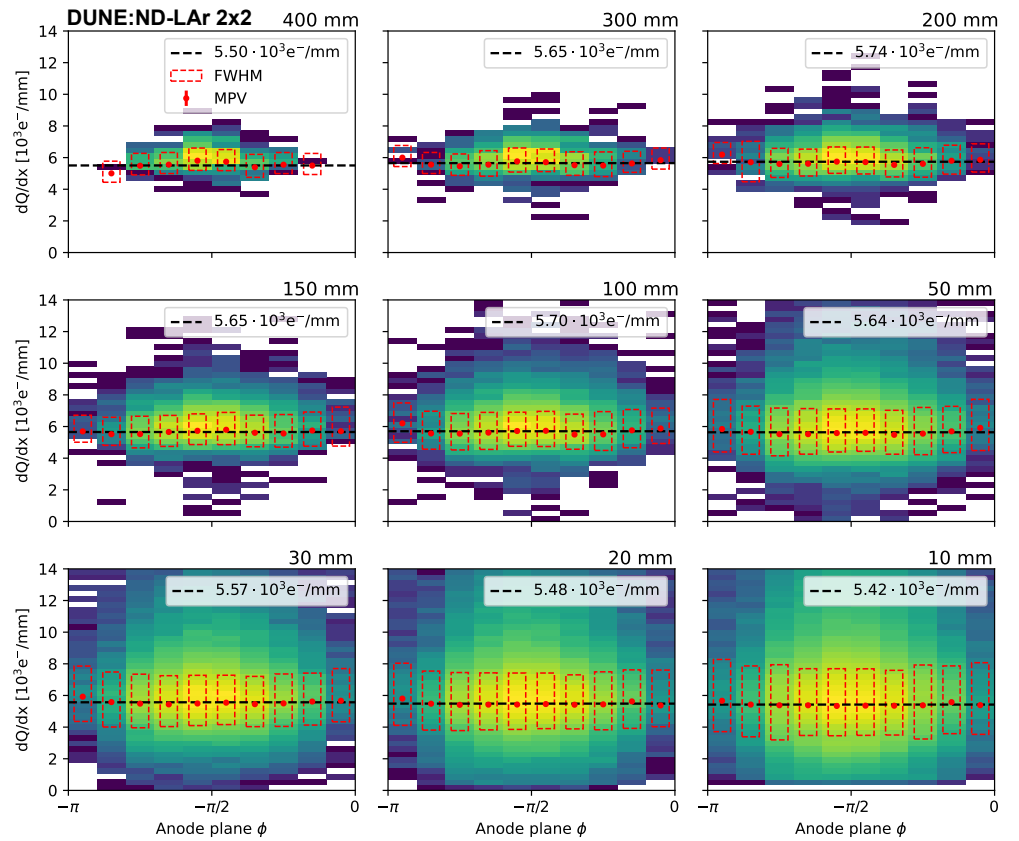


Figure 22. dQ/dx measured for segments of different lengths as a function of the azimuthal angle $\phi = \text{atan2}(y, x)$, where y and x are the components of the segment along the anode plane axes. The distributions in each bin are fitted with a Gaussian-convolved Moyal function. The red points correspond to the most probable value of the fitted distribution and the dashed rectangles correspond to the FWHM. The dashed black line represents the average MPV.

4.2. Calibration

Before collecting cosmic data, a SiPM gain calibration was performed using an LED source, where the bias voltage for each SiPM channel was adjusted to obtain a uniform gain distribution across the channels, as shown in Fig. 23. The amplification factors for the variable gain amplifiers used in the SiPM readout chain were also tuned, and set to maximum (31 dB) except for LCM channels (21 dB) during cosmic ray data taking, to adjust signals to the input dynamic range of the ADC. LCMs were used to provide an external trigger to the charge readout system, with an effective threshold of about 30 photoelectrons (p.e.). The trigger message, written into the continuous self-triggered data stream of the charge readout system, provides a precise timestamped flag for identifying coincidences between charge and light readout.

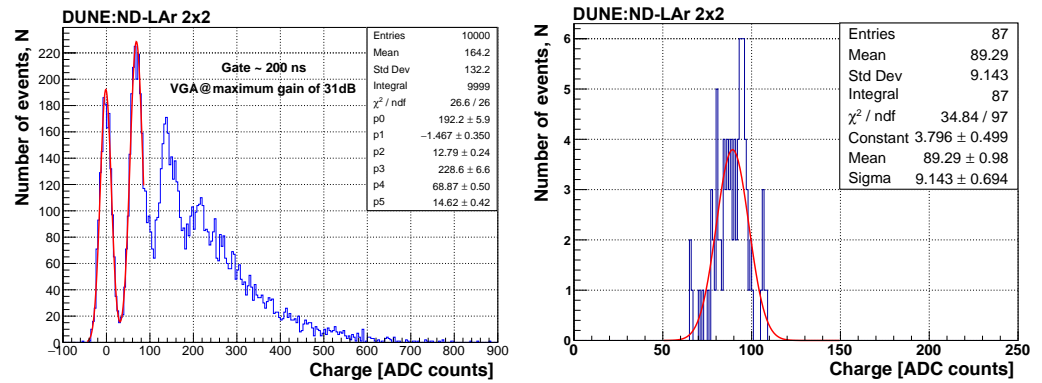


Figure 23. Typical charge spectrum obtained during SiPM gain calibration (left); SiPM gain distribution (right).

4.3. Time Resolution

Events induced by cosmic muons traversing the TPC volume were used to extract the time resolution of the light detectors. The time measurement proceeds as follows: each waveform is oversampled through a Fourier transform to increase the number of points on the rising edge, enabling a good linear fit of it. Then, a linear fit to the baseline is performed, and the crossing point of the rising edge of the signal with the baseline is calculated, providing a robust single-channel event time. This process is illustrated in Fig. 24 (left). The extracted time resolution for a pair of neighboring LCM channels is shown in Fig. 24 (right) as a function of the signal amplitude. This quantity is obtained by taking the standard deviation of the time difference recorded between the two channels over multiple events without any time-of-flight corrections. For large signals, this resolution approaches ~ 2 ns. An example application of the excellent timing resolution for the LCMs is the identification of Michel electrons from stopping muon decays, where the relative timing between the muon and electron signals is dominated by the mean lifetime of the muon, $\tau \sim 2.2 \mu\text{s}$. Two examples of signals from a stopping muon and a delayed Michel electron detected by the LCM are shown in Fig. 25. Since the muon decay time is variable but follows a well-understood exponential distribution, such events may be used, for example, to study event pile-up in neutrino interactions.

4.4. Efficiency

To assess the efficiency of the LRS, the scintillation light induced by tracks reconstructed from the TPC charge readout data is used. In particular, cosmic muon tracks crossing the entire detector vertically are considered. In a 3D simulation, the charge of a track is discretized to single points with a 1 mm resolution along the track, assuming an infinitely thin true trajectory. For each point in this voxelized event, the solid angle to the light detector in the detector module is then calculated. Next, assuming isotropic scintillation light emission, the solid angle can be used to compute the geometrical acceptance

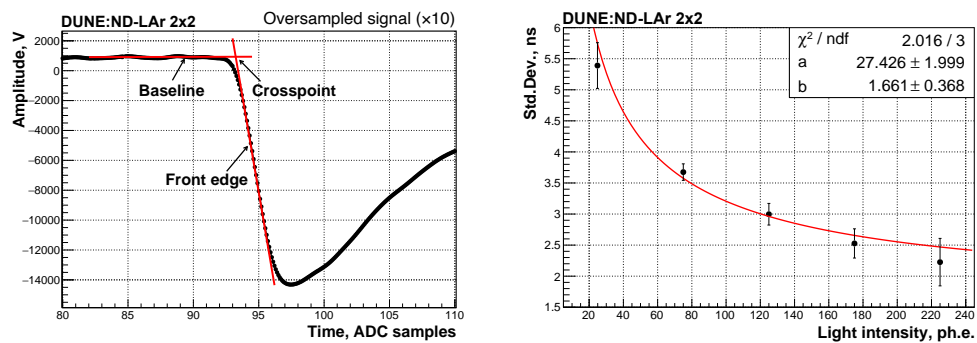


Figure 24. Oversampled signal using Fourier transformation. Red lines show the linear approximations of the rising edge and the baseline (left). The time resolution between two LCMs (LCM-011, LCM-017) as a function of the signal response (right).

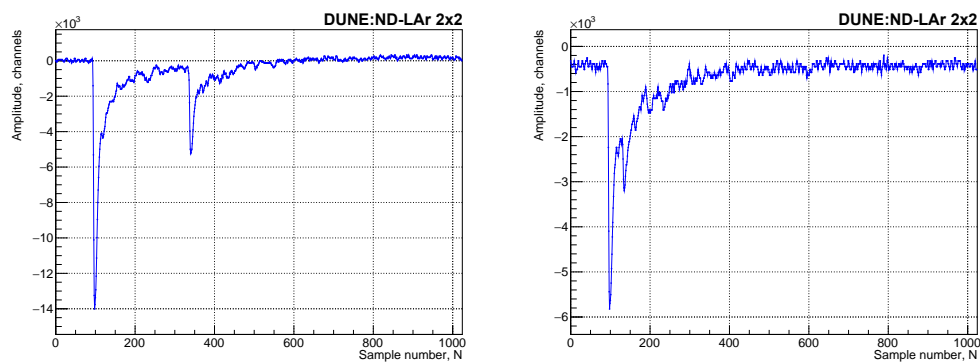


Figure 25. Two examples showing signals of the stopping muon and delayed Michel electron detected by the LCM. The waveforms were digitized at 10 ns intervals.

of the light for each detector tile. The number of photons hitting the detector surface is estimated by multiplying the geometrical acceptance by the number of emitted photons per unit track length and integrating over the full track length. Here, the number of emitted photons per unit track length has been calculated for the nominal electric field intensity of 0.5 kV cm^{-1} [21]. Rayleigh scattering, a small effect over the relevant distance scales, is neglected in this calculation.

The photon detection efficiency (PDE) of the light detection system can be estimated by comparing the measured number of p.e. and the estimated number of photons hitting the detector surface, as obtained from the simulation described above. Since the waveforms obtained with the light detectors have been integrated using a limited gate length, the actual scintillation light might be underestimated. This was corrected by multiplying the number of reconstructed photons by an integration gate acceptance factor, which is calculated based on the detector response and the scintillation timing characteristics. Fig. 26 shows the measured PDE for all ArCLight and LCM modules used in the Module-0 detector. The LCM shows an average PDE of 0.6%, which enables a light trigger for events depositing MeV-scale energies, with an accurate scintillation amplitude and energy reconstruction. The PDE of the ArCLight modules is about a factor of 10 lower than the corresponding value obtained with the LCMs, which allows for a larger dynamic range. The ArCLight technology additionally enables a high position sensitivity, which can be used to accurately triangulate the origin of the scintillation light emission point [11]. For the LCM it can be observed that tiles placed at the top (see Fig. 26 (right), LCM groups 4–6, 10–12, 16–18, and 22–24) of the TPC show a systematically lower PDE with respect to tiles placed in the middle of the TPC. This can be explained by an anisotropy of light collection of LCM with respect to the angle of incoming photons, driven by structural non-uniformity of fibers and spaces. The absence of non-uniform effects in the ArCLight tiles due to reflections on the TPC structure or Rayleigh scattering, meanwhile, further indicates that these effects are negligible within the experimental uncertainties. In Module-0, a Hamamatsu MPPC S13360-6025 [22] is used. By replacing the SiPM for future modules with the MPPC S13360-6050 with higher efficiency, the overall PDE would improve by a factor of 1.6 to yield a LCM efficiency of about 1%.

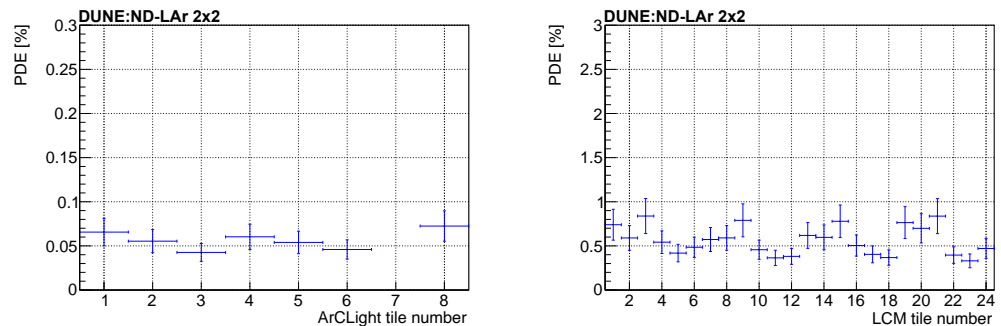


Figure 26. Absolute PDE for each ArCLight (left) and LCM (right) tile (arbitrary numbering). ArCLight tile 7 was disabled during Module-0 data taking. The LCM tiles are placed in sets of 3 to cover the same area as one ArCLight tile.

5. Measurements with Cosmic Ray Data Samples

The following sections discuss the analyses performed using reconstructed tracks from the large cosmic ray data set collected during the Module-0 run. As discussed in Section 1, the Module-0 detector incorporates several novel technologies for the first time in a LArTPC of this scale. These studies assess the performance of the fully-integrated system, including the LArPix charge readout with a very large channel count, the high-coverage hybrid LCM and ArCLight photon detection systems, and their matching; the capability to achieve the

necessary levels of LAr purity for physics measurements without prior evacuation of the cryostat; and the degree of drift field uniformity achievable with the low-profile resistive shell field cage. Detailed studies of each of these key detector parameters demonstrate excellent performance of the integrated system relative to the requirements in view of the operation for the DUNE ND-LAr.

In support of these studies, a sample of cosmic rays has been simulated using CORSIKA [23], a program for detailed simulation of extended air showers. The passage of the particles through matter has been simulated using a Geant4-based Monte Carlo [24]. The detector simulation has been performed with `larnd-sim` [25,26], a set of highly-parallelized GPU algorithms for the simulation of pixelated LArTPCs. A track-fitting algorithm is applied to provide an estimate of the particle track angle and location. First, a 3D point cloud is reconstructed using the unique channel index to determine the position transverse to the anode and the drift time. DBSCAN ($k = 5$, $\epsilon = 2.5$ cm) [19] is used to find the hit clusters. The cluster radius (ϵ) was tuned using the $k = 5$ th-neighbor distance of 3D points from a typical run. Each cluster is then passed through a RANSAC line fit [27] with an outlier radius of $\rho = 8$ mm and 100 random samples. This provides a set of highly-collinear points which constitute the reconstructed track.

5.1. Electron lifetime

The amount of charge collected by the readout system depends heavily on the electron lifetime, τ , in the argon of the TPC volume. The electron lifetime parameterizes (in units of time) how much charge is lost due to attachment to electronegative impurities in the argon, such as oxygen or water, during the drift of the deposited ionization charge toward the anode. The charge measured at the anode, Q , is given by

$$Q = e^{-t/\tau} \cdot R \cdot Q_0, \quad (1)$$

where Q_0 is the amount of the primary ionization charge deposited by a particle in the liquid argon, R is the recombination factor that describes the fraction of charge that survives prompt recombination of the ionization with argon ions prior to drift, and t is the drift time from the point of original charge deposition to detection in the anode plane. Measuring signals originating across the entire TPC via the charge readout system requires a sufficient electron lifetime in the detector. For the DUNE ND-LAr detector this requirement is > 0.5 ms at a drift electric field of 500 V/cm; this relatively low value compared to other large LArTPC detectors [4,28,29] is due to the relatively short maximum drift length of DUNE ND-LAr (~ 50 cm) and allows ND-LAr to meet the charge attenuation performance of the far detector, which specifies a 3 ms lifetime in a detector with a 3.5 m drift length at a 500 V/cm drift field [30]. A measurement of the electron lifetime with Module-0 has been carried out to confirm that the materials used in the detector, which will be similar to those of DUNE ND-LAr, are compatible with the argon purity requirement. Additionally, tracking this parameter as a function of time is necessary to provide a calibration of charge scale for other measurements carried out using the Module-0 charge data.

As seen in Eq. 1, charge measurements at the anode depend both on the electron lifetime and the recombination factor. However, by measuring Q as a function of the drift time for a collection of cosmic muon tracks that span the entire drift distance, the dependence on R , which is independent of drift time, can be ignored as an overall normalization factor. Additionally, a more fitting quantity to use in this study is dQ/dx , the measured charge per unit length along the cosmic muon track, given the dependence of the amount of charge seen by a single pixel channel on the orientation of each track. The electron lifetime for each Module-0 data run at a drift electric field of 500 V/cm is measured by applying an exponential fit to the mean dQ/dx of muon track segments as a function of drift time to the anode, assuming a uniform dQ/dx . A sample of anode-cathode-crossing tracks is used for this measurement; these tracks span the entire drift distance and the absolute drift time associated with each part of the track is known for this track sample. The electron lifetime values measured in Module-0 were consistently above 2 ms for the duration of the run,

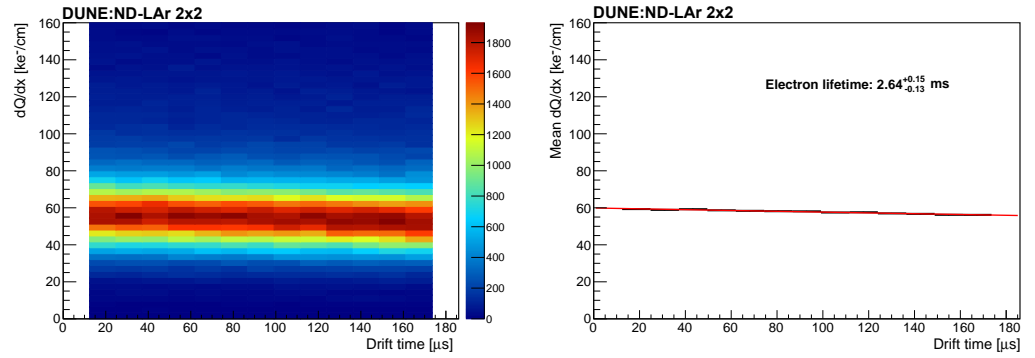


Figure 27. Measured dQ/dx versus drift time for ionization associated with anode-cathode-crossing muon tracks (left); mean dQ/dx versus drift time, along with exponential fit, for the same track sample (right).



Figure 28. Extracted electron lifetime as a function of time during Module-0 Run 1 (top) and Run 2 (bottom), with the average uniformly exceeding 2 ms in both cases.

thus satisfying the $\tau > 0.5$ ms requirement. This trend continued in the second run (Run 2) of Module-0, where cryogenic operations differed from those in Run 1. Run 1 achieved LAr purity through cryostat evacuation before cooldown and LAr filling, while Run 2 made use of a piston purge procedure (repeatedly purging the volume with clean gas), as this is the anticipated approach for the full-scale cryostat of ND-LAr. A recirculation system with filtration was operational during both runs. Results are shown in Fig. 28.

5.2. Electric field uniformity

The magnitude of electric field distortions due to space charge effects for Module-0 are expected to be much smaller than other, larger LArTPC detectors running near the surface, such as MicroBooNE [31] and ProtoDUNE-SP [32]. This is due to the relatively small maximum drift length of ~ 30 cm of Module-0, compared to ~ 2.5 m for MicroBooNE and ~ 3.6 m for ProtoDUNE-SP. Even for a maximum drift length of ~ 50 cm that is anticipated for DUNE ND-LAr, the impact from space charge effects is expected to be negligible; the fact that ND-LAr will operate 65 m underground will reduce this effect further due to the smaller flux of cosmic muons. However, it is possible that electric field inhomogeneities

arise in the Module-0 detector from other sources. In particular, it is important to determine whether or not the field cage design causes significant distortions of the electric field, which can alter the trajectories ionization electrons take while drifting to the anode plane. Such distortions could lead to incorrect reconstruction of the true position of original energy depositions in the detector due to primary particles ionizing the argon, consequently impacting their trajectory and energy reconstruction. Furthermore, associated modification to the electric field intensity throughout the detector can lead to significant impact on the amount of electron-ion recombination experienced by ionization electrons, leading to bias in reconstructed particle energy scale or degradation of reconstructed particle energy resolution. The use of the novel resistive field cage technology in Module-0, as is anticipated for DUNE ND-LAr, provides an important opportunity to study the impact on electric field homogeneity.

Following the methodology developed by the MicroBooNE experiment for analysis of space charge effects [31], electric field distortions are probed using end points of through-going cosmic muon tracks in Module-0 data. Tracks passing through an anode plane and another face of the detector that is not the other anode plane are selected for this study, providing a known absolute drift time associated with each part of the track via subtracting the time associated with the anode side of the track. The track end point associated with the non-anode side of the anode-crossing track is then probed by measuring the transverse (i.e., perpendicular to the drift direction) displacement from the edge of the TPC active volume, as measured from the y value (TPC top and bottom) or x value (TPC front and back sides, perpendicular to the drift direction) of the pixel channels at the edge of the detector. The average transverse displacement is recorded as a function of the two directions within the TPC face for all four non-anode faces of the Module-0 TPC. If there are no electric field distortions in the detector, there would be no inward migration of ionization electrons during drift, leading to zero transverse displacement of ionization charge with respect to the TPC face for this sample of through-going muon tracks (contamination from stopping muons is expected to be less than 1%). The result of the average transverse displacement measurement is shown for the TPC top and bottom in Fig. 29 and for the TPC front and back in Fig. 30. A few features not associated with electric field distortions in the detector should be pointed out. First, there are gaps in coverage near the anode planes (z values of roughly ± 30 cm) due to a requirement in the track selection that the non-anode side of the track is at least 5 cm away from both anode planes, and near the pixel plane edges (edges of the TPC face) due to a requirement that the non-anode side of the track is not located within 1 cm (2 cm) of these features. These selection criteria were introduced to minimize contamination of the sample from poorly-reconstructed muon tracks. Some residual contamination is seen near the edges of the pixel planes, where the measured average transverse spatial offset is artificially large due to edge channels of the pixel planes being turned off for data-taking, leading to the ends of tracks being clipped off near the edges of pixel planes. Second, the two horizontal bands in the bottom right corner of the right side of Fig. 30 are associated with a known grounding issue of an ArCLight unit in this part of the detector. The vertical gap in the right panel of Fig. 29 is due to inactive channels in this region of the anode plane (see Fig. 10).

After accounting for these two artifacts, non-negligible transverse spatial offsets are observed near the cathode (central horizontal lines in Fig. 29, central vertical lines in Fig. 30), roughly 1 cm on average but as large as 2.5 cm in some places in the TPC. After adding an additional ~ 1 cm to these measurements to account for the separation between the edge pixel channels and the field cage (or light detectors in the case of the front and back of the TPC), the average (maximum) transverse spatial offset experienced by drifting ionization charge originating near the cathode is roughly 2 cm (3.5 cm). Ascribing this transverse drift to an additional electric field component strictly in the direction transverse to the TPC faces, the average (maximum) transverse electric field magnitude leading to this amount of inward drift of ionization charge is roughly 30 V/cm (60 V/cm). The associated average (maximum) impact to the electric field magnitude in the detector is 0.2% (0.7%).

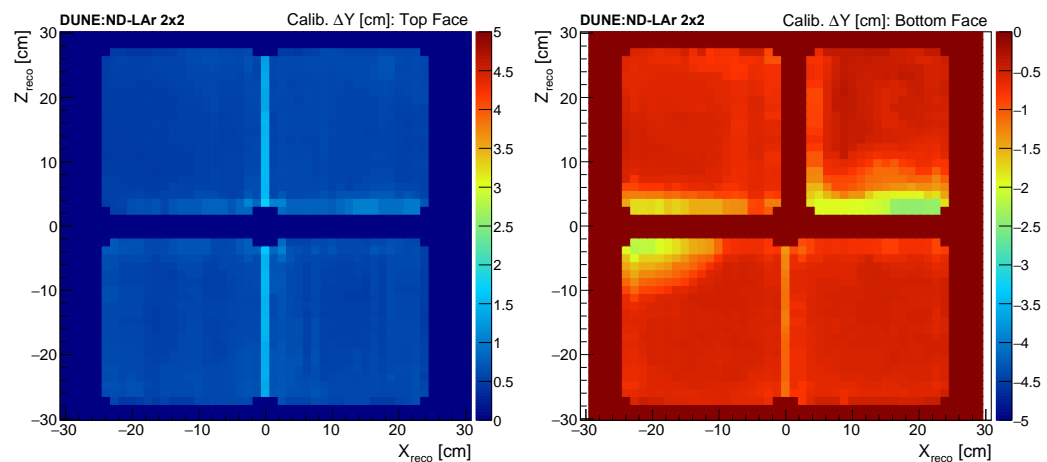


Figure 29. Average spatial offsets measured at the top (left) and bottom (right) of the Module-0 detector. These offsets in cm are measured with respect to the location of the pixel channels at the edge of the detector.

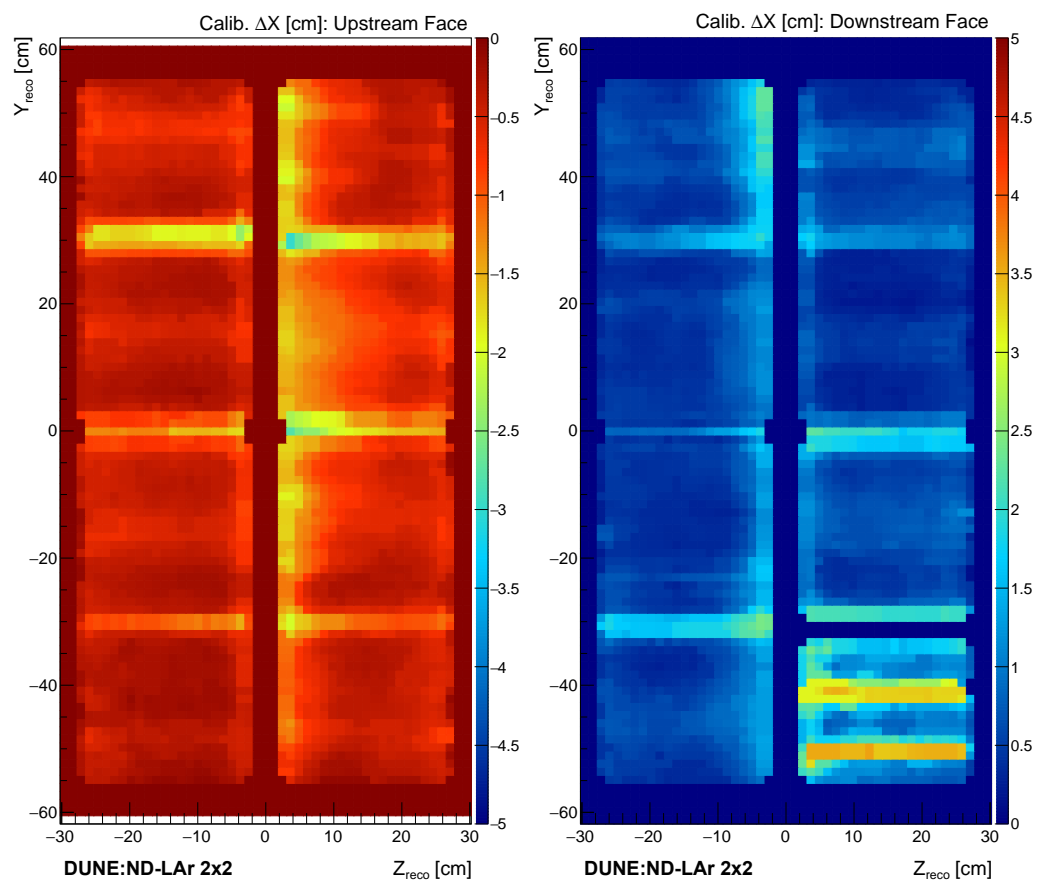


Figure 30. Average spatial offsets measured at the front (left) and back (right) of the Module-0 detector. These offsets in cm are measured with respect to the location of the pixel channels at the edge of the detector.

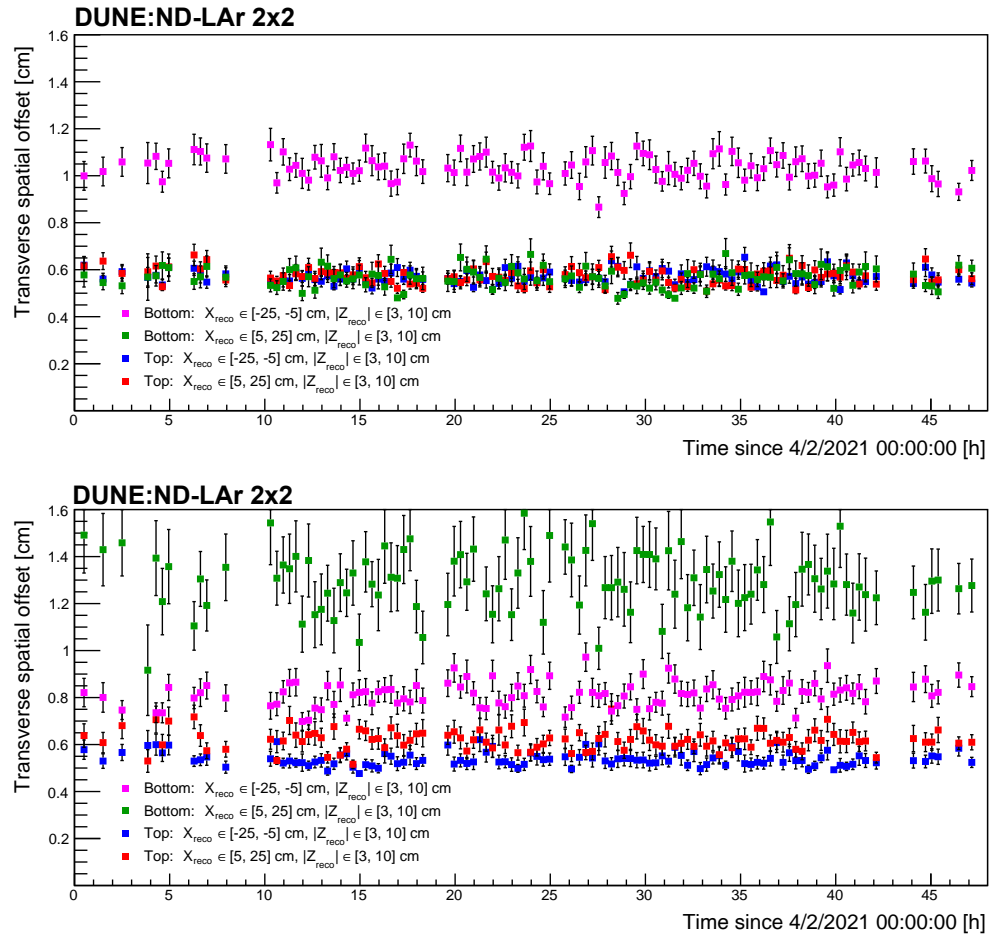


Figure 31. Time dependence of spatial offsets in the $-z$ (top) and $+z$ (bottom) drift volumes. These offsets are measured with respect to the location of the pixel channels at the edge of the detector.

This is below the conservative physics requirement of 1% maximum allowed deviation of the electric field magnitude within 95% of the detector volume, indicating that the design of the field cage is adequate for the physics goals of DUNE ND-LAr. It is worth pointing out that this physics requirement for electric field distortions corresponds to after detector calibrations have been carried out, while the measurements presented here have no calibration applied. It is thus expected that the calibrated electric field map would be even more homogeneous at DUNE ND-LAr. An additional study is carried out to determine if the small electric field distortions in the Module-0 detector vary substantially over time. A substantial time dependence of the electric field distortions may complicate efforts to obtain a calibrated electric field map in the DUNE ND-LAr detector using cosmic muons, neutrino-induced muons, or dedicated calibration hardware. Average transverse spatial offsets were measured at four different places on each side of the Module-0 cathode as a function of time, spanning two full days of data-taking. The results of the study are shown in Fig. 31. No substantial time dependence of transverse spatial offsets is observed (< 0.2 cm), indicating that calibration of the underlying electric field distortions is achievable by averaging measured spatial offsets over at least a few days of data-taking. A study of electric field stability over longer periods of time is planned in future prototyping of the DUNE ND-LAr detector concept.

5.3. Charge-light matching

Efficient matching between signals in the charge and light readout systems is essential, as this enables the use of light to disambiguate pile-up of separate neutrino interactions

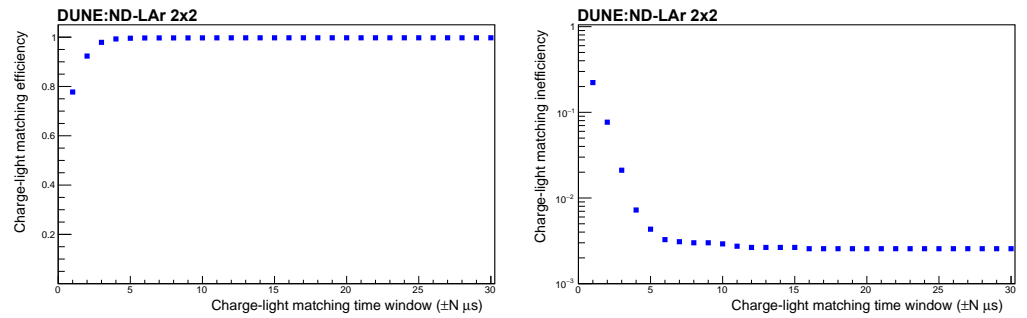


Figure 32. Charge-light matching efficiency in linear scale (left) and inefficiency in logarithmic scale (right) for light detector triggers matched to the arrival time of charge at the anode side of anode-cathode-crossing tracks.

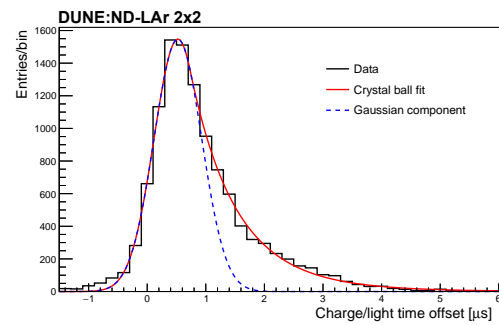


Figure 33. Time offset distribution for light detector triggers matched to the arrival time of charge at the anode side of anode-cathode-crossing tracks (charge minus light).

within a single beam spill. The unique association between charge and light signals is a nontrivial problem in a large-volume LArTPC, especially in an environment with a high rate of neutrino event pile-up, such as DUNE ND-LAr. This motivates the modular design, where the full active volume is composed of an array of optically-isolated TPC volumes, each with high coverage of optical detectors with fast timing and good spatial resolution. Charge-light matching in Module-0 has been accomplished via association of precision GPS-synchronized timestamps in the two systems. Here, two performance metrics are considered: the efficiency of matching for a selection of tracks as a function of the allowed coincidence time window and the resolution in terms of the offset between the two systems' timestamps. Fig. 32 shows the matching efficiency for varying definitions of the allowed time window for coincidence formation, for a selection of anode-cathode-crossing muon tracks. The overwhelming majority of these are single tracks, as the probability of having another event in the same $\sim 200 \mu\text{s}$ window is very small. For conservative matching parameters, an efficiency of $\geq 99.7\%$ is found. In this study, the timing resolution is limited by the spatial resolution of the tracking from the charge readout, not by the intrinsic light detector timing resolution, which is discussed in Section 4. Next, Fig. 33 illustrates the relative time offset between the two systems for the Module-0 prototype, again for a selection of anode-cathode-crossing tracks. The distribution exhibits a Gaussian core and a tail. The asymmetric tail of the distribution, captured by a Crystal Ball fit [33], is due to track truncation near the boundaries of the pixel planes. The Gaussian component of the Crystal Ball fit is also shown; the standard deviation of the Gaussian, $0.4 \mu\text{s}$, is identified as the charge readout timing resolution. The physics requirements for ND-LAr require that the resolution in the drift dimension be at least as precise as that across the anode plane, i.e. the pixel pitch divided by $\sqrt{12}$, or 1.3 mm. The resolution extracted in Module-0 corresponds to 0.6 mm at a drift electric field of 500 V/cm, thus meeting the requirement.

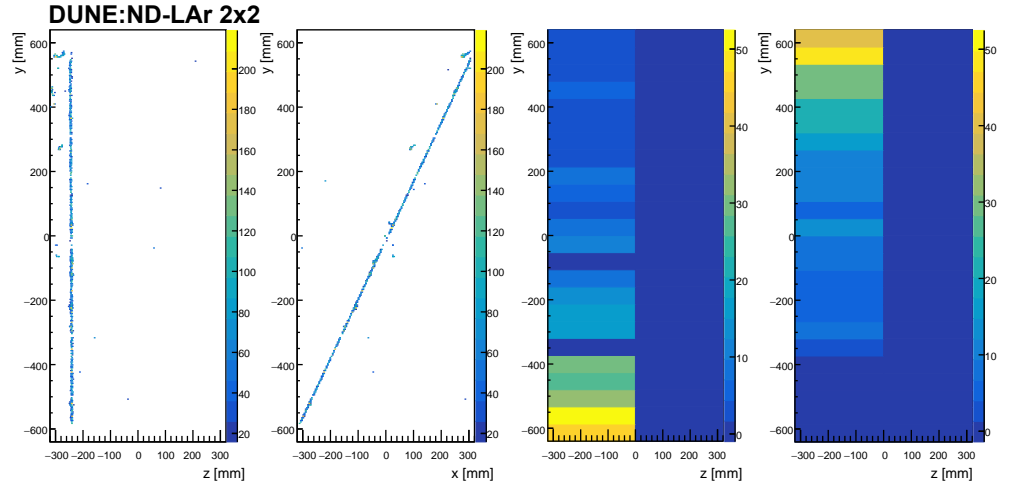


Figure 34. Charge-light matched event display of a cosmic muon track. The left two panels show the TPC charge readout, in a $z - y$ project (left) and $x - y$ projection (center left). The right two panels show the light detector responses for the arrays at $-x$ (center right) and $+x$ (right), with each bin along the vertical axis representing the strength of signal read by individual SiPMs.

5.4. Correlation of the charge and light yield

Matched charge and light events as shown in Figure 34 provide another data sample which may be used to study the correlation in the relative charge and light yields in the detector. These yields are related to electric-field dependent recombination effects.

To describe the recombination mechanism in LAr we formalize the ionization and excitation states generated by the deposited energy of a traversing particle as follows:

$$N_i + N_{ex} = QY + LY, \quad (2)$$

where the sum of available ionization (N_i) and excitation (N_{ex}) states determines the total number of electrons (QY) and photons (LY) generated in LAr. The number of ionization states N_i is given by

$$N_i = \frac{E_{dep}}{W_i}, \quad W_i = 23.6 \text{ eV}, \quad (3)$$

where W_i is the ionization work function [34] and E_{dep} is the deposited energy. In the absence of charge attenuation and impurities, the total charge Q arriving at the anode depends only on the initially-produced ionization charge $Q_0 = N_i e$ as

$$QY = N_i \cdot R_c, \quad (4)$$

$$LY = N_i \left(1 + \frac{N_{ex}}{N_i} - R_c \right), \quad (5)$$

where the charge recombination factor R_c is dependent on the electric field ϵ , and e is the electron charge. In the presence of impurities, the electron lifetime correction is applied first; see Eq. 1. Increasing ϵ leads to less recombination between argon ions and ionization electrons, and thus more free charge carriers are present in the TPC drift field, increasing the total detected charge at the anode plane. At the same time, a reduced charge recombination factor corresponds to less scintillation light produced within the TPC, leading to a decrease of the light yield at higher electric fields, as expressed by Eq. 4. Hence, the amount of charge yield and the amount of light yield observed in the detector are expected to be anti-correlated. To describe the recombination of electron-ion pairs, we focus on the most commonly used models, namely the Box [35] and the Birks' models [36], and compare the results of Module-0 measurements with those of the ICARUS [37] and ArgoNeuT [38]

experiments. The Box model assumes zero electron diffusion, zero ion mobility, and a distribution of ionization electrons that are uniformly produced within a 3D box along the path of the ionizing particle. The collected charge Q is given by

$$Q = Q_0 \cdot \frac{A_{\text{Box}}}{\xi} \cdot \ln(\xi), \quad (6)$$

where Q_0 denotes the primary ionization charge and ξ is

$$\xi = \frac{N_0 K_r}{4a^2 \mu \epsilon}, \quad (7)$$

where a is the linear size of the charge ‘box’, N_0 denotes the number of electrons in the box and K_r is the recombination rate constant. μ and ϵ define the electron mobility and the electric field, respectively. Note that in the limit of an infinite electric field intensity ϵ , the collected charge at the anode plane corresponds to the initially produced charge, Q_0 . Birks’ model describes the collected charge QY as

$$QY = N_i \cdot \frac{A_{\text{Birks}}}{1 + \frac{k_B}{\epsilon} \cdot \frac{dE}{dx}} = \frac{Q_0}{e} R_c, \quad (8)$$

where A_{Birks} and k_B are fitting constants. In this formulation of the Birks’ model, for infinite electric field intensities $\epsilon \rightarrow \infty$, the recombination factor does not go to 1 and is limited to $R_c \rightarrow A$. We can now express the light yield as

$$LY = N_i \left(1 + \frac{N_{ex}}{N_i} - \frac{A_{\text{Birks}}}{1 + \frac{k_B}{\epsilon} \cdot \frac{dE}{dx}} \right). \quad (9)$$

However, since the fraction of excited states $\frac{N_{ex}}{N_i}$ is not precisely known, the commonly used model for description of the light yield in scintillating materials uses the following formulation:

$$LY = L_0(1 - \alpha R_c) = L_0 R_L, \quad (10)$$

$$L_0 = \frac{E_{dep}}{W_L}, W_L = 19.5 \text{ eV}, \quad (11)$$

where L_0 denotes the number of scintillation photons at zero electric field intensity, α is a constant fitted to the data and W_L is the scintillation work function [39]. This formulation is used in this analysis to evaluate the parameters in the Birks’ model for the light yield.

To study the charge and light correlation in Module-0, data samples at different electric field intensities ranging from 0.05 kV cm^{-1} to 1.00 kV cm^{-1} were acquired and analysed. These events contain information about the collected charge and scintillation light. A selection of vertical through-going tracks, as expected from MIP muons, was used to extract the collected charge and light per unit length of the track. For the measurement of the collected charge per unit track length, the track was divided into 2 cm segments and the total charge collected each the segment was divided by the segment length. Then, the light yield per unit track length is extracted as:

$$\frac{dL}{dx} = \frac{L_{\text{detected}}}{\int \Omega dl \times \text{PDE} \times G}. \quad (12)$$

The factors in this expression include the geometrical acceptance $\int \Omega dl$, the readout gate acceptance G , and the overall PDE of each tile reported in Section 4. The geometrical acceptance was computed based on the charge data and the track segment position with respect to a light detection tile, integrated over the track length. The readout gate acceptance is an estimation of the fraction of photons which reach the SiPM within the readout

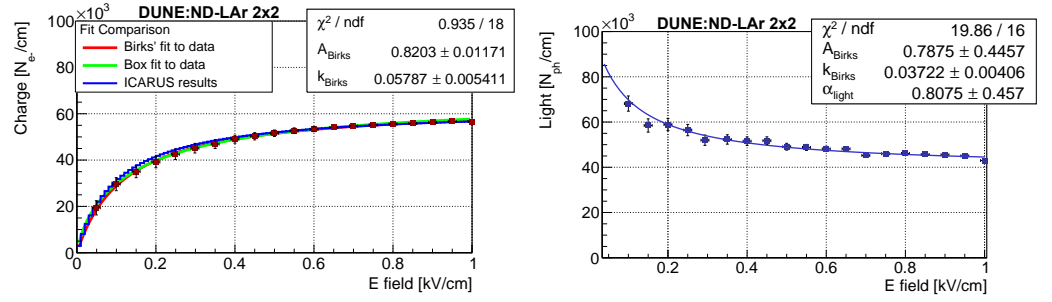


Figure 35. Charge yield as a function of the electric field intensity fitted with the Box and Birks' models, and compared to ICARUS results (left); Light yield as a function of the electric field intensity fitted separately with the Birks' model (right).

Fit parameters	A_{Birks} [kV g cm ⁻³ MeV ⁻¹]	k_{Birks} [kV g cm ⁻³ MeV ⁻¹]
Charge only fit	(0.820 ± 0.011)	(0.058 ± 0.005)
Light only fit	(0.79 ± 0.45)	(0.037 ± 0.004)
Combined fit	(0.794 ± 0.008)	(0.045 ± 0.003)

Table 1. The fitted parameters of the Birks' model using the Module-0 data.

integration gate of 500 ns. The gate acceptance was measured using the average waveform of the light signals in Module-0 data to be $\sim 64\%$ for both the LCM and ArCLight modules.

The dQ/dx and dL/dx distributions are well-described by a Landau-convolved Gaussian function, which is used to extract the most probable value (MPV). We note that the fits are performed on raw data, i.e. without additional calibration of the track dE/dx . Due to uncorrected charge losses, the extracted MPV values for charge measurements should be compared with an effective value of ~ 1.8 MeV/cm, while MPVs corresponding to light measurements correspond to an effective $dE/dx \sim 2.1$ MeV/cm. The dependence of the charge yield and the light yield MPV values with respect to the electric field density is illustrated in Fig. 35.

The charge yield and light yield data points were fitted separately to the Birks' model, with results shown in Fig. 35 and Tab. 1. We note that for the light yield fit (Fig. 35, right), per Eq. 10, the A_{Birks} and α_{light} parameters are totally correlated and cannot be extracted independently. The left panel of Fig. 35 also shows a comparison of the charge yield data (red points) to fits using a Birks' model (red curve) and Box model (green curve), alongside the results from the ICARUS experiment (blue curve), demonstrating good agreement between the results.

Next, a combined fit of the Birks' model to both charge and light yield data sets was performed. Fig. 36 shows the final result of the correlation study. The best fit results for the Birks' model parameters are $A_{\text{Birks}} = 0.794 \pm 0.008$ and $k_{\text{Birks}} = 0.045 \pm 0.003$, with a χ^2/ndf of 23.2/35, where the number of degrees of freedom calculated based on 19 fit points per dataset (charge and light) included in the fit and three fit parameters. Table 2 summarizes the Birks' model parameters obtained with the Module-0 detector and compares them with the parameters found in the ICARUS and the ArgoNeuT experiments. The results of the simultaneous fit of the Birks' model to the light and charge distributions show reasonable agreement with previous experiments.

5.5. Michel electrons

Michel electrons, i.e. electrons from stopped muon decay, constitute a readily available and versatile tool for the study and characterisation of the performance of a LArTPC. They are abundant for surface-level detectors exposed to a large cosmic ray muon flux, and with $\mu \rightarrow e\bar{\nu}_e\nu_\mu$ as the almost exclusive decay channel, the number of events is given by

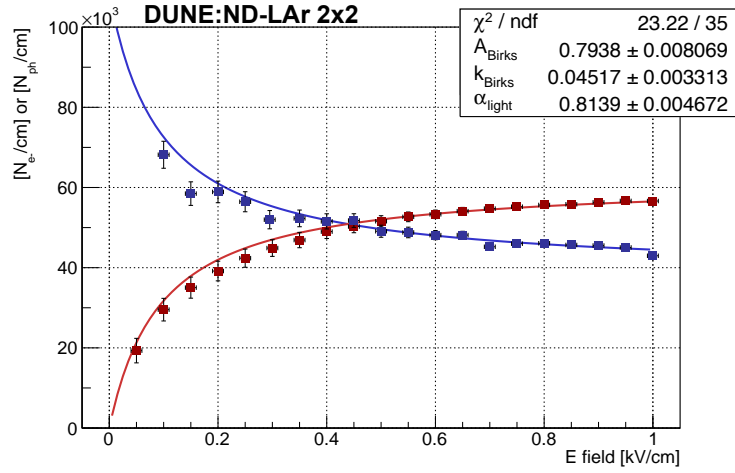


Figure 36. Light yield (blue) and charge yield (red) extracted from a simultaneous fit with the Birks' model.

Experiment	A_{Birks} [$\text{kV g cm}^{-3} \text{MeV}^{-1}$]	k_{Birks} [$\text{kV g cm}^{-3} \text{MeV}^{-1}$]	Reference
ICARUS	(0.800 ± 0.003)	(0.0486 ± 0.0006)	[37]
ArgoNeuT	(0.806 ± 0.010)	(0.052 ± 0.001)	[38]
Module-0	(0.794 ± 0.008)	(0.045 ± 0.003)	This work

Table 2. Comparison of the ICARUS and ArgoNeuT results with the current study.

the probability of the muon to come to rest in the detector. The electrons produced by the decay have a well-characterised energy spectrum with a cutoff at ~ 50 MeV and their topology is relatively easy to tag: a long muon track ending with a Bragg peak followed by a short ionization track from the electron at a different angle with respect to the muon direction. Fig. 1 includes one example of a stopping muon decaying with a Michel electron in Module-0. The effective muon lifetime of $\sim 2 \mu\text{s}$ is short relative to the TPC drift speed, leading to minimal displacement of the muon track endpoint and electron track start. However, it is large relative to the time resolution of the light readout system, allowing the two signals to be tagged separately: the first light pulse corresponding to the muon ionization, and the second to the electron, can be easily separated for a large majority of events due to the excellent timing resolution of ArCLight and LCM detectors. Fig. 37 shows the event display of a selected Michel electron candidate, with the two peaks showing the waveforms of the light detectors located in one of the two half-TPCs.

The Michel electron candidates' topology is mainly characterised by a long ionisation trail left over by the crossing muon. An automatic selection algorithm based on the event topology and the presence of the Bragg peak at the end of the muon track was developed and applied to the subset of cosmic data. Visual event validation was performed on selected events to validate the analysis. The final distribution of the reconstructed Michel electron energy based on the automated charge reconstruction is shown in Fig. 38. The end point is near the expected true end point of 53 MeV. The spectrum peaks at lower energies mainly as a consequence of partial containment, imperfect clustering, and charge below threshold, particularly from electrons Compton-scattered by Bremsstrahlung photons radiated from the primary electron [40–42].

5.6. Detector simulation validation with cosmic ray tracks

Finally, selected samples of cosmic ray tracks are compared in detail to a cosmic ray simulation based on the CORSIKA event generator and the detailed microphysical detector

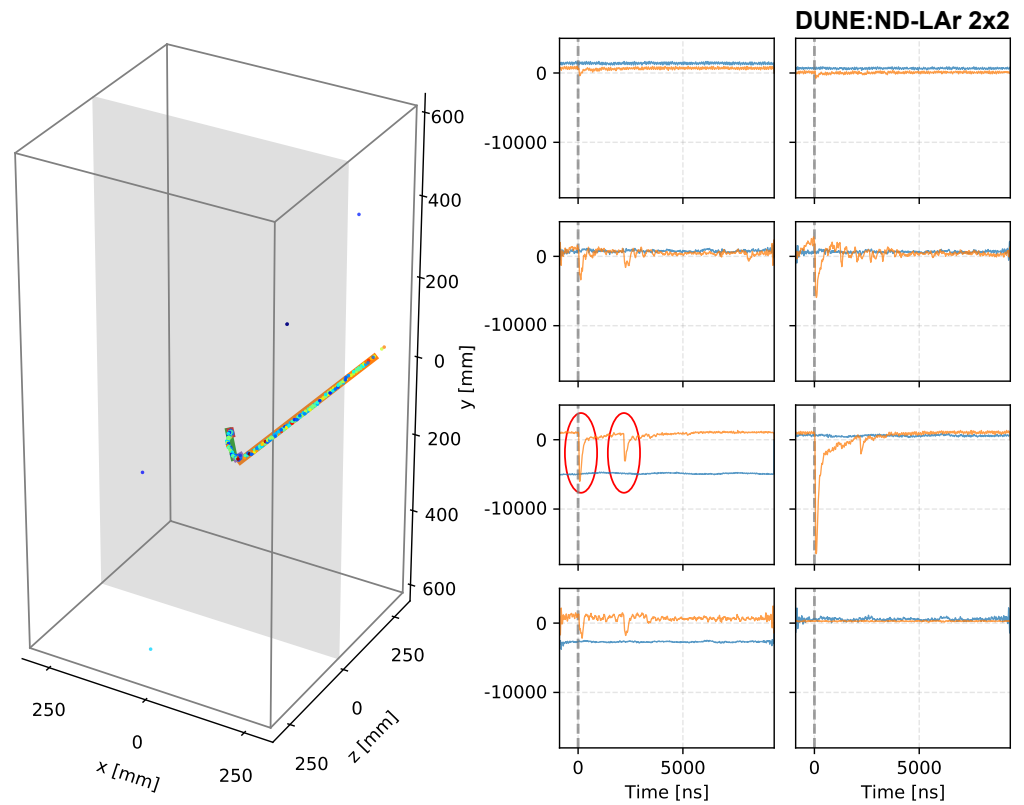


Figure 37. Event display of a Michel electron candidate shown in a 3D view (left) and with associated waveforms from photon detectors (right). In the right panel, orange and blue indicate the two optically isolated semi-TPCs. The red circles highlight an example the two pulses on the photon detectors correspond to the entering muon and the electron resulting from its decay.

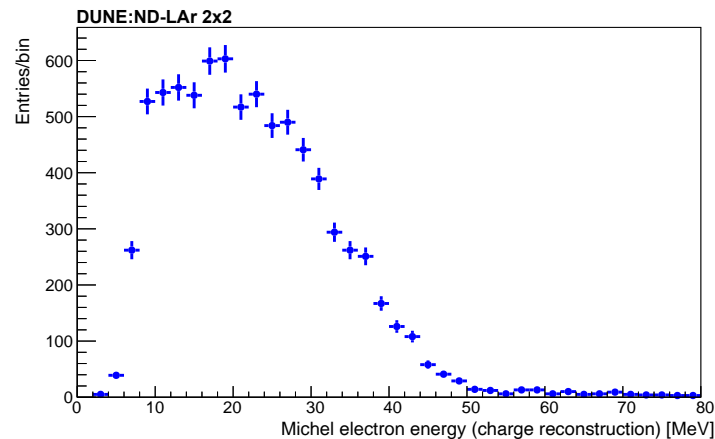


Figure 38. Charge-based energy spectrum of Michel electron candidates from a sample of reconstructed muon decays, using the full data set and automated event reconstruction.

simulation introduced in Section 5. Starting from the cosmic ray track reconstruction described there, the track's start and end points are found by projecting the 3D points onto the cluster's principal components. The DBSCAN+RANSAC fit is applied on outlying hits until all are placed within a cluster or no hits remain. This is sufficient for studies of low-level detector response, as it provides a local approximation of the track trajectory with minimal impact from δ -rays and hard scatters. Reconstructed tracks may show artificial gaps due to the presence of disabled channels. Also, cathode-piercing tracks will usually be reconstructed as separated tracks, due to the non-zero cathode thickness. Thus, tracks

with an angle smaller than 20° and closer than 10 cm are stitched together for the following studies. A comparison between the spatial coordinates of the stitched tracks in data and simulation is shown in Fig. 39.

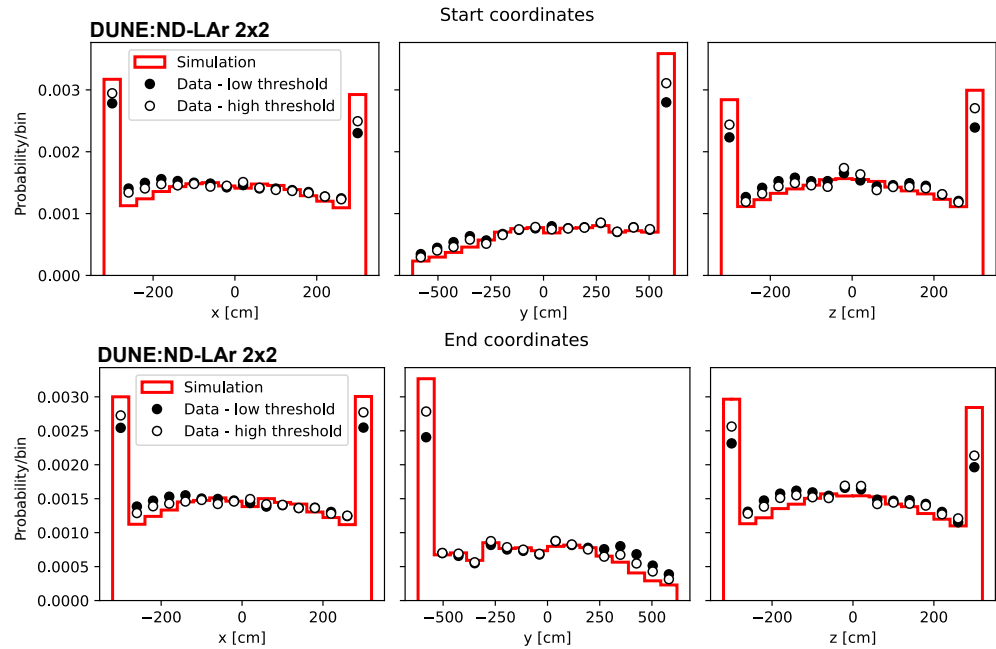


Figure 39. Start and end coordinates of stitched tracks in data (high and low threshold runs) and simulation.

Fig. 40 shows a comparison of the dQ/dx for low threshold and high threshold runs with a sample of simulated cosmic rays. The dQ/dx has been measured for segments of different lengths, following the procedure described in Section 5.6. The simulation assumes the Birks model for electron recombination and a gain of $4 \text{ mV}/10^3 \text{ e}^-$ [36]. In the data, the amount of charge that reaches the anode is corrected by the electron lifetime factor calculated in Section 5.1.

Next, the dQ/dx as a function of the reconstructed track residual range is considered. As noted in Section 5.5, for a muon that stops in the detector the amount of deposited charge per unit length will increase as it approaches the end point, forming a Bragg peak. Fig. 41 shows an example of a stopping muon and the subsequent Michel electron. The dQ/dx has been measured by subdividing the reconstructed track in 10 mm segments (our dx) and summing the charge contained in each segment (the dQ). The data show a Bragg peak near the end of the reconstructed track, where the residual range is close to zero. The theoretical prediction is obtained by taking the $\langle \frac{dE}{dx} \rangle$ values tabulated in Ref. [43] for muons in LAr, divided by the argon ionization energy (23.6 eV) and multiplied by the recombination factor $R_{\text{Birks}}^{\text{ICARUS}}$, calculated in Ref. [37].

The observed distributions indicate good overall agreement between data and simulations, in particular with the ability to correctly reproduce the position of the dQ/dx peak. Module-0 data provide input that can be used to further tune the detector simulation, including modeling of additional noise sources and details of the anode response. Meanwhile, the strong overall agreement in the vertex positioning and calorimetry indicates that the initial detector response model is able to capture the main features of the cosmic ray track samples.

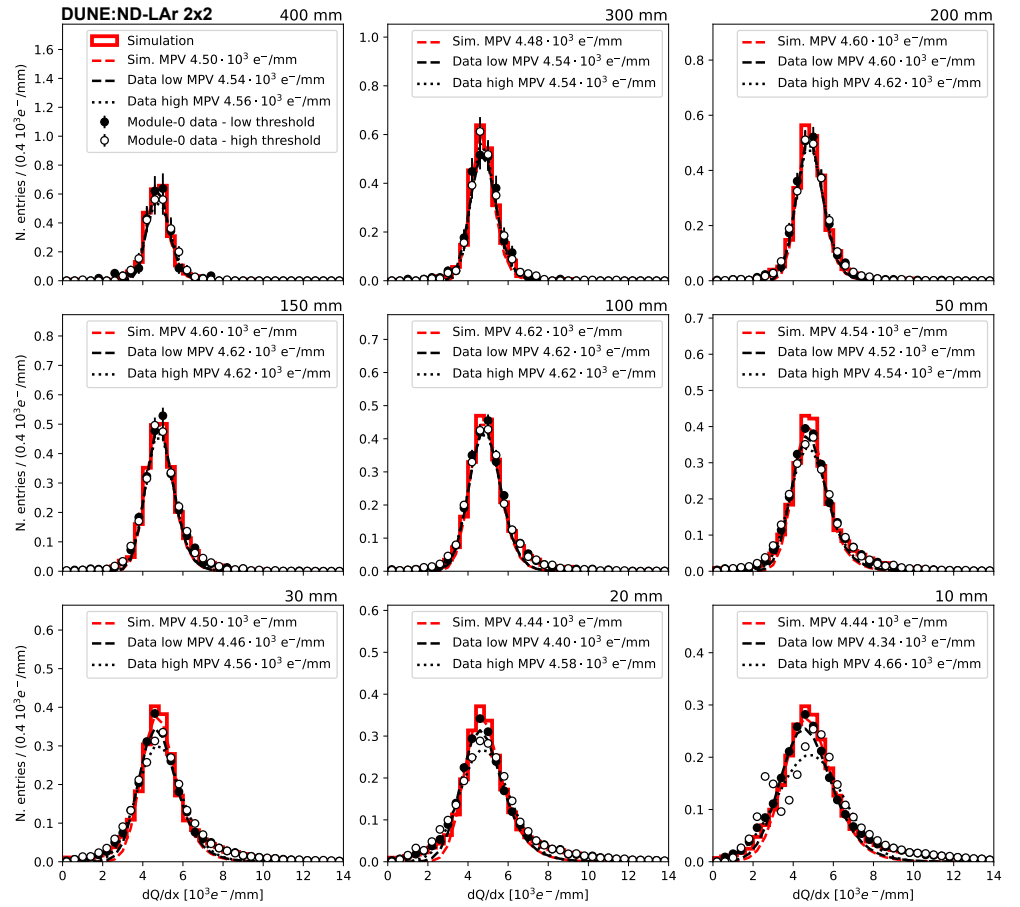


Figure 40. dQ/dx measured for segments of different lengths for low threshold runs (black dots), high threshold runs (white dots) and a sample of simulated cosmic rays (red line). The distributions have been fitted with a Gaussian-convolved Moyal function (dashed lines).

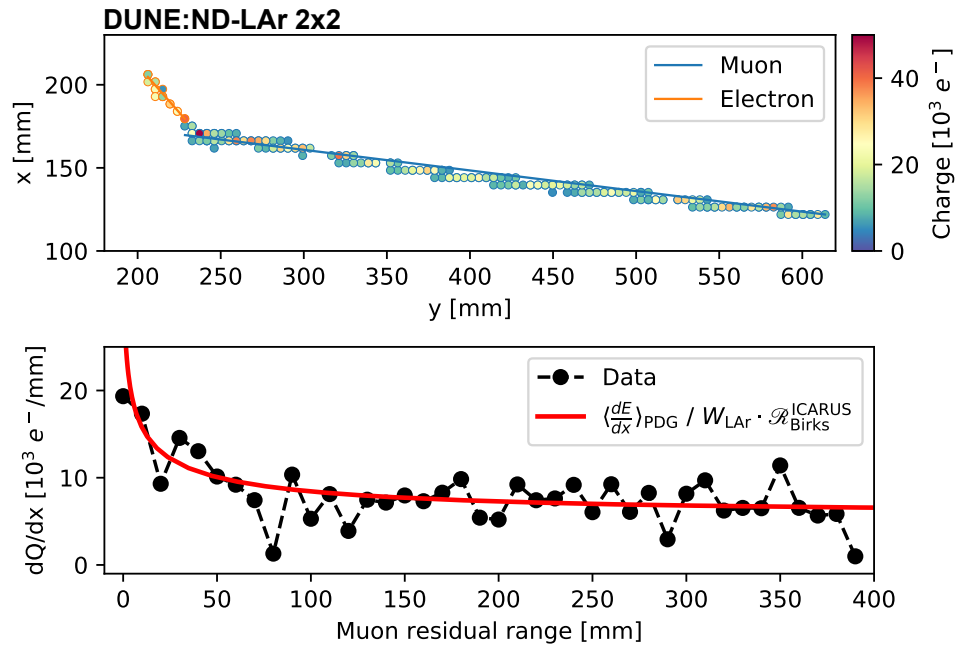


Figure 41. Top: event display of the anode plane for a selected stopping muon (blue) and subsequent Michel electron (orange). Bottom: dQ/dx for the reconstructed muon track as a function of the residual range dQ/dx and the theoretical curve for muons stopping in liquid argon (red line).

6. Conclusions

We have reported here the experimental results of exposing the Module-0 demonstrator, a tonne-scale LArTPC with pixel-based charge readout, to cosmic rays. This new type of neutrino detector is designed to meet the challenges of the near detector complex of the forthcoming DUNE experiment, which will be exposed to a very intense beam-related flux of particles. These challenges are expected to severely hamper the performance of a conventional, wire-readout, monolithic LArTPC, where reconstruction of complex 3D event topologies using a small number of 2D projections can lead to unsolvable ambiguities, particularly when multiple events overlap in the drift direction. The novel Module-0 design features a combination of new technological solutions: a pixelated anode to read out the ionization electron signal that provides native three-dimensional charge imaging, a modular structure with relatively short drift length, high-performance scintillation light detection systems, and an innovative approach to field shaping using a low-profile resistive shell. Module-0 is one of four units that will comprise the 2×2 demonstrator (ProtoDUNE-ND) being installed at Fermilab to be exposed to the NuMI neutrino beam.

A detailed assessment of this technology has been performed by operating Module-0, as well as the associated cryogenics, data acquisition, trigger, and timing infrastructure, at the University of Bern. A large sample of 25 million self-triggered cosmic ray-induced events was collected and analyzed, along with an array of dedicated diagnostic data runs. The response of the 78,400-pixel readout system was studied, as well as the performance of the two independent and complementary light detection systems. The data analysis demonstrated key physics requirements of this technology, such as the electron lifetime, the uniformity of the electric field, and the matching/correlation between the charge and light signals. The reconstruction of particle tracks and Michel electrons illustrates the physics capabilities, and the comparison with detailed, microphysical simulations has demonstrated a robust understanding of the workings of this new type of LArTPC detector. Overall, these results demonstrate the key design features of the technique and provide a confirmation of the outstanding imaging capabilities of this next-generation LArTPC design.

7. Acknowledgments

This document was prepared by the DUNE collaboration using the resources of the Fermi National Accelerator Laboratory (Fermilab), a U.S. Department of Energy, Office of Science, HEP User Facility. Fermilab is managed by Fermi Research Alliance, LLC (FRA), acting under Contract No. DE-AC02-07CH11359. This work was supported by CNPq, FAPERJ, FAPEG and FAPESP, Brazil; CFI, IPP and NSERC, Canada; CERN; MŠMT, Czech Republic; ERDF, H2020-EU and MSCA, European Union; CNRS/IN2P3 and CEA, France; INFN, Italy; FCT, Portugal; NRF, South Korea; CAM, Fundación “La Caixa”, Junta de Andalucía-FEDER, MICINN, and Xunta de Galicia, Spain; SERI and SNSF, Switzerland; TÜBİTAK, Turkey; The Royal Society and UKRI/STFC, United Kingdom; DOE and NSF, United States of America. This research used resources of the National Energy Research Scientific Computing Center (NERSC), a U.S. Department of Energy Office of Science User Facility operated under Contract No. DE-AC02-05CH11231.

1. Amerio, S.; et al. Design, construction and tests of the ICARUS T600 detector. *Nucl. Instrum. Meth. A* **2004**, *527*, 329–410. <https://doi.org/10.1016/j.nima.2004.02.044>.
2. Anderson, C.; et al. The ArgoNeuT Detector in the NuMI Low-Energy beam line at Fermilab. *JINST* **2012**, *7*, P10019, [[arXiv:physics.ins-det/1205.6747](https://arxiv.org/abs/physics.ins-det/1205.6747)]. <https://doi.org/10.1088/1748-0221/7/10/P10019>.
3. Acciarri, R.; et al. Design and Construction of the MicroBooNE Detector. *JINST* **2017**, *12*, P02017, [[arXiv:physics.ins-det/1612.05824](https://arxiv.org/abs/physics.ins-det/1612.05824)]. <https://doi.org/10.1088/1748-0221/12/02/P02017>.
4. Abi, B.; et al. First results on ProtoDUNE-SP liquid argon time projection chamber performance from a beam test at the CERN Neutrino Platform. *JINST* **2020**, *15*, P12004, [[arXiv:physics.ins-det/2007.06722](https://arxiv.org/abs/physics.ins-det/2007.06722)]. <https://doi.org/10.1088/1748-0221/15/12/P12004>.

5. Abud, A.A.; et al. Design, construction and operation of the ProtoDUNE-SP Liquid Argon TPC. *JINST* **2022**, *17*, P01005, [arXiv:physics.ins-det/2108.01902]. <https://doi.org/10.1088/1748-0221/17/01/P01005>.
6. Abi, B.; et al. Deep Underground Neutrino Experiment (DUNE), Far Detector Technical Design Report, Volume I Introduction to DUNE. *JINST* **2020**, *15*, T08008, [arXiv:physics.ins-det/2002.02967]. <https://doi.org/10.1088/1748-0221/15/08/T08008>.
7. DUNE Collaboration. Deep Underground Neutrino Experiment (DUNE) Near Detector Conceptual Design Report. *Instruments* **2021**, *5*. <https://doi.org/10.3390/instruments5040031>.
8. Asaadi, J.; et al. A New Concept for Kilotonne Scale Liquid Argon Time Projection Chambers. *Instruments* **2020**, *4*. <https://doi.org/10.3390/instruments4010006>.
9. Dwyer, D.; et al. LArPix: demonstration of low-power 3D pixelated charge readout for liquid argon time projection chambers. *Journal of Instrumentation* **2018**, *13*, P10007–P10007. <https://doi.org/10.1088/1748-0221/13/10/p10007>.
10. Russell, B.; et al. LArPix-v2: a commercially scalable large-format 3D charge-readout scheme for LArTPCs. *In preparation* **2022**.
11. Auger, M.; et al. ArCLight—A Compact Dielectric Large-Area Photon Detector. *Instruments* **2018**, *2*. <https://doi.org/10.3390/instruments2010003>.
12. Anfimov, N.; et al. Development of the Light Collection Module for the Liquid Argon Time Projection Chamber (LArTPC). *Journal of Instrumentation* **2020**, *15*, C07022–C07022. <https://doi.org/10.1088/1748-0221/15/07/c07022>.
13. Berner, R.; et al. First Operation of a Resistive Shell Liquid Argon Time Projection Chamber: A New Approach to Electric-Field Shaping. *Instruments* **2019**, *3*. <https://doi.org/10.3390/instruments3020028>.
14. Adamson, P.; et al. The NuMI Neutrino Beam. *Nucl. Instrum. Meth. A* **2016**, *806*, 279–306, [arXiv:physics.acc-ph/1507.06690]. <https://doi.org/10.1016/j.nima.2015.08.063>.
15. Asaadi, J.; et al. First Demonstration of a Pixelated Charge Readout for Single-Phase Liquid Argon Time Projection Chambers. *Instruments* **2020**, *4*, 9, [arXiv:physics.ins-det/1801.08884]. <https://doi.org/10.3390/instruments4010009>.
16. Asaadi, J.; et al. A pixelated charge readout for Liquid Argon Time Projection Chambers. *JINST* **2018**, *13*, C02008. <https://doi.org/10.1088/1748-0221/13/02/C02008>.
17. Machado, A.; Segreto, E. ARAPUCA a new device for liquid argon scintillation light detection. *Journal of Instrumentation* **2016**, *11*, C02004–C02004. <https://doi.org/10.1088/1748-0221/11/02/c02004>.
18. Serrano, J.; et al. The White Rabbit Project. In Proceedings of the Proc. 12th Int. Conf. on Accelerator and Large Experimental Physics Control Systems (ICALPECS'09). JACoW Publishing, Oct. 2009, pp. 93–95.
19. Ester, M.; Kriegel, H.P.; Sander, J.; Xu, X. A Density-Based Algorithm for Discovering Clusters in Large Spatial Databases with Noise. AAAI Press, 1996, KDD'96.
20. Moyal, J. XXX. Theory of ionization fluctuations. *The London, Edinburgh, and Dublin Philosophical Magazine and Journal of Science* **1955**, *46*, 263–280, [https://doi.org/10.1080/14786440308521076]. <https://doi.org/10.1080/14786440308521076>.
21. Baller, B. Liquid Argon Properties (Tables and Calculators) Version 4. <https://lar.bnl.gov/properties/>.
22. Hamamatsu. MPPC S13360 series datasheet. https://www.hamamatsu.com/resources/pdf/ssd/s13360_series_kapd1052e.pdf.
23. Heck, D.; Knapp, J.; Capdevielle, J.N.; Schatz, G.; Thouw, T. CORSIKA: A Monte Carlo code to simulate extensive air showers **1998**.
24. Agostinelli, S.; Allison, J.; Amako, K.; Apostolakis, J.; Araujo, H.; Arce, P.; Asai, M.; Axen, D.; Banerjee, S.; Barrand, G.; et al. Geant4—a simulation toolkit. *Nuclear Instruments and Methods in Physics Research Section A: Accelerators, Spectrometers, Detectors and Associated Equipment* **2003**, *506*, 250–303. [https://doi.org/https://doi.org/10.1016/S0168-9002\(03\)01368-8](https://doi.org/https://doi.org/10.1016/S0168-9002(03)01368-8).
25. Soleti, S.R.; Dwyer, D.; Vallari, Z. DUNE/larnd-sim, 2021. <https://doi.org/10.5281/zenodo.4582721>.
26. Abed Abud, A.; et al. Highly-parallelized simulation of a pixelated LArTPC on a GPU. *JINST* **2023**, *18*, P04034, [arXiv:physics.comp-ph/2212.09807]. <https://doi.org/10.1088/1748-0221/18/04/P04034>.
27. Fischler, M.A.; Bolles, R.C. Random Sample Consensus: A Paradigm for Model Fitting with Applications to Image Analysis and Automated Cartography. *Commun. ACM* **1981**, *24*, 381–395. <https://doi.org/10.1145/358669.358692>.

28. Adams, C.; Alrashed, M.; An, R.; Anthony, J.; Asaadi, J.; Ashkenazi, A.; Balasubramanian, S.; Baller, B.; Barnes, C.; Barr, G.; et al. Calibration of the charge and energy loss per unit length of the MicroBooNE liquid argon time projection chamber using muons and protons. *Journal of Instrumentation* **2020**, *15*, P03022–P03022. <https://doi.org/10.1088/1748-0221/15/03/p03022>.
29. Bettini, A.; Braggiotti, A.; Casagrande, F.; Casoli, P.; Cennini, P.; Centro, S.; Cheng, M.; Ciocio, A.; Cittolin, S.; Cline, D.; et al. A study of the factors affecting the electron lifetime in ultra-pure liquid argon. *Nuclear Instruments and Methods in Physics Research Section A: Accelerators, Spectrometers, Detectors and Associated Equipment* **1991**, *305*, 177–186. [https://doi.org/https://doi.org/10.1016/0168-9002\(91\)90532-U](https://doi.org/https://doi.org/10.1016/0168-9002(91)90532-U).
30. Abi, B.; et al. Deep Underground Neutrino Experiment (DUNE), Far Detector Technical Design Report, Volume IV: Far Detector Single-phase Technology. *JINST* **2020**, *15*, T08010, [[arXiv:physics.ins-det/2002.03010](https://arxiv.org/abs/physics.ins-det/2002.03010)]. <https://doi.org/10.1088/1748-0221/15/08/T08010>.
31. Abratenko, P.; et al. Measurement of space charge effects in the MicroBooNE LArTPC using cosmic muons. *Journal of Instrumentation* **2020**, *15*, P12037–P12037. <https://doi.org/10.1088/1748-0221/15/12/p12037>.
32. Abi, B.; et al. First results on ProtoDUNE-SP liquid argon time projection chamber performance from a beam test at the CERN Neutrino Platform. *Journal of Instrumentation* **2020**, *15*, P12004–P12004. <https://doi.org/10.1088/1748-0221/15/12/p12004>.
33. T. Skwarnicki, Ph.D Thesis, DESY F31-86-02(1986), Appendix E; M.J. Oreglia, Ph.D Thesis, SLAC-236(1980), Appendix D; J. E. Gaiser, Ph.D Thesis, SLAC-255(1982), Appendix F.
34. Shibamura, E.; Hitachi, A.; Doke, T.; Takahashi, T.; Kubota, S.; Miyajima, M. Drift velocities of electrons, saturation characteristics of ionization and W-values for conversion electrons in liquid argon, liquid argon-gas mixtures and liquid xenon. *Nucl. Instrum. Meth.* **1975**, *131*, 249–258. [https://doi.org/10.1016/0029-554X\(75\)90327-4](https://doi.org/10.1016/0029-554X(75)90327-4).
35. Thomas, J.; Imel, D.A. Recombination of electron-ion pairs in liquid argon and liquid xenon. *Phys. Rev. A* **1987**, *36*, 614–616. <https://doi.org/10.1103/PhysRevA.36.614>.
36. Birks, J.B. Scintillations from Organic Crystals: Specific Fluorescence and Relative Response to Different Radiations. *Proc. Phys. Soc. A* **1951**, *64*, 874–877. <https://doi.org/10.1088/0370-1298/64/10/303>.
37. Amoroso, S.; et al. Study of electron recombination in liquid argon with the ICARUS TPC. *Nucl. Instrum. Meth. A* **2004**, *523*, 275–286. <https://doi.org/10.1016/j.nima.2003.11.423>.
38. Acciarri, R.; et al. A study of electron recombination using highly ionizing particles in the ArgoNeuT Liquid Argon TPC. *Journal of Instrumentation* **2013**, *8*, P08005–P08005. <https://doi.org/10.1088/1748-0221/8/08/p08005>.
39. Doke, T.; Hitachi, A.; Kikuchi, J.; Masuda, K.; Okada, H.; Shibamura, E. Absolute Scintillation Yields in Liquid Argon and Xenon for Various Particles. *Japanese Journal of Applied Physics* **2002**, *41*, 1538. <https://doi.org/10.1143/JJAP.41.1538>.
40. Abed Abud, A.; et al. Identification and reconstruction of low-energy electrons in the ProtoDUNE-SP detector. *Phys. Rev. D* **2023**, *107*, 092012, [[arXiv:hep-ex/2211.01166](https://arxiv.org/abs/hep-ex/2211.01166)]. <https://doi.org/10.1103/PhysRevD.107.092012>.
41. Foreman, W.; et al. Calorimetry for low-energy electrons using charge and light in liquid argon. *Phys. Rev. D* **2020**, *101*, 012010, [[arXiv:physics.ins-det/1909.07920](https://arxiv.org/abs/physics.ins-det/1909.07920)]. <https://doi.org/10.1103/PhysRevD.101.012010>.
42. Acciarri, R.; et al. Michel Electron Reconstruction Using Cosmic-Ray Data from the MicroBooNE LArTPC. *JINST* **2017**, *12*, P09014, [[arXiv:physics.ins-det/1704.02927](https://arxiv.org/abs/physics.ins-det/1704.02927)]. <https://doi.org/10.1088/1748-0221/12/09/P09014>.
43. Groom, D.E.; Mokhov, N.V.; Striganov, S.I. Muon stopping power and range tables 10-MeV to 100-TeV. *Atom. Data Nucl. Data Tabl.* **2001**, *78*, 183–356. <https://doi.org/10.1006/adnd.2001.0861>.

Testbeam analysis of biasing structures for irradiated hybrid pixel detectors

C. M. Buttar^a Y. Gao^b R. González López^c D. Maneuski^a E. Pender^b Q. Qin^d A. G. Rennie^{e,1,2} M. Sullivan^c J. T. Taylor^c K. Wraight^a

^aUniversity of Glasgow

School of Physics and Astronomy, Kelvin Building, University Avenue, Glasgow, G12 8QQ

^bUniversity of Edinburgh

School of Physics and Astronomy, James Clerk Maxwell Building, Peter Guthrie Tait Road, Edinburgh, EH9 3FD

^cUniversity of Liverpool

Department of Physics, Oliver Lodge, Oxford Street, Liverpool, L69 7ZE

^dUniversity of Manchester

Department of Physics and Astronomy, Schuster Building, Oxford Road, Manchester, M13 9PL

^eUniversity of California, Irvine

Department of Physics and Astronomy, 4129 Frederick Reines Hall, Irvine, CA 92697-4575

E-mail: adam.rennie@cern.ch

ABSTRACT: Following the Phase-II upgrade during Long Shutdown (LS3), the LHC aims to reach a peak instantaneous luminosity of $7.5 \times 10^{34} \text{ cm}^{-2} \text{ s}^{-1}$, which corresponds to an average of around 200 inelastic proton-proton collisions per beam-crossing (every 25 ns). To cope with these conditions, the ATLAS Inner Detector will be replaced by a new all-silicon system — the Inner Tracker (ITk). The ITk will be operational for more than ten years, during which time ATLAS is expected to record approximately 4000 fb^{-1} of data. The ITk's pixel sub-system is based on hybrid pixel modules with new silicon sensors and readout chips. These studies focus on testbeam campaigns undertaken to study the spatial resolution and efficiencies of hybrid pixel detector modules based on the first large-structure prototype front-end readout chip — the RD53A — using planar silicon sensors. These devices have been irradiated to replicate the effect of the high radiation environment present during operation in the ATLAS detector. Results for devices using sensors with different punch-through bias structures and using different readout chips are summarised. Those with sensors incorporating a punch-through bias structure are found to exhibit systematically lower efficiency than those without, as a result of local areas of relative inefficiency around the punch-through dots. Despite this, all devices measured are found to satisfy the requirement of 97% efficiency at $V_{\text{bias}} = 400 \text{ V}$ after being irradiated to end-of-life fluence.

KEYWORDS: Hybrid detectors, Radiation-hard detectors, Particle tracking detectors (Solid-state detectors), Performance of High Energy Physics Detectors

¹Corresponding author.

²Previously at University of Glasgow, School of Physics and Astronomy, Kelvin Building, University Avenue, Glasgow, G12 8QQ.

Contents

1	Introduction	2
2	Devices under test	2
3	Testbeam facilities and detector setup	3
4	Reconstruction and analysis	6
4.1	Reconstruction: EU Telescope	6
4.2	Analysis: TBmon2	10
5	Results	12
5.1	October 2018 testbeam	12
5.2	December 2018 testbeam	15
5.3	Cross-testbeam comparisons	20
6	Conclusions	20

1 Introduction

For the High Luminosity era of the Large Hadron Collider (HL-LHC), the present ATLAS Inner Detector will be replaced by a new all-silicon Inner Tracker (ITk) [1, 2] in order to cope with increased occupancy and radiation. The ITk will consist of a pixel detector closest to the beamline and a strip detector for the outer section. This will provide coverage for charged particle reconstruction up to $|\eta| < 4$. The ATLAS upgrade physics programme drives the design and performance requirements of the pixel detector. The demand for high precision, radiation hard, rapid readout pixel modules has required the design of a new front-end readout chip and sensor architecture to meet the performance requirements necessary for the HL-LHC environment.

The pixel detector will consist of five barrel layers in the central region, and a number of ring-shaped layers in the forward region, leading to a total active area of around 13 m^2 . The innermost two layers of the ITk pixel detector [3] — the *inner system* — will experience the highest total ionising dose and so will feature 3D silicon sensors, which have heightened radiation hardness. The inner system is designed to be replaced after 2000 fb^{-1} . All remaining layers — the *outer system* — will be based on planar silicon sensors with thickness $150 \mu\text{m}$. Novel front-end ASICs, implemented in 65 nm technology, are connected to the silicon sensors using bump-bonding to form a bare modules. This is then glued and wire-bonded to a flexible printed circuit board (PCB). The off-detector readout electronics will be implemented in the framework of the general ATLAS trigger and DAQ system with a readout rate of up to 5 Gb/s per data link for the innermost layers.

The outer system is expected to experience a fluence up to $5 \times 10^{15} n_{\text{eq}} \text{ cm}^{-2}$ and a total ionising dose of 5 MGy .

Testbeam measurements are vital to study, understand, and verify the performance of the new readout chips and sensor technologies. This paper summarises several testbeam campaigns undertaken for several R&D sensors developed by the ATLAS UK ITk community. Different biasing structures, readout modes, and pixel module operation parameters such as the bias voltage and threshold are studied in detail using irradiated devices in order to mimic the effects of LHC operation on the detector modules.

2 Devices under test

The devices under test (DUTs) are hybrid pixel modules, each including a passive high resistivity silicon sensor (*n-in-p*) and a front-end readout chip combined by flip-chip bump-bonding, and a flexible PCB. In this paper, prototype modules with different silicon sensor designs, together with a prototype front-end readout chip, the RD53A [4], are characterised. The sensors were manufactured by Micron Semiconductor Ltd.

The DUTs presented here were all irradiated at the Karlsruher Institut für Technologie (KIT) to $3.4 \times 10^{15} n_{\text{eq}} \text{ cm}^{-2}$ using 25 MeV protons extracted from the Karlsruhe Kompakt Zyklotron [5].

Devices made from two different planar silicon *n-in-p* sensors are presented. Both sensors have the same pixel pitch ($50 \times 50 \mu\text{m}^2$) and thickness ($150 \mu\text{m}$), but are differentiated by *punch-through bias* (PTB) structure. Once in operation, the PTB structure is inactive. However, it serves a vital role in the production of the pixel modules in allowing for electrical testing of the sensor ahead of bump-bonding. Being able to measure the sensor *IV* curve before assembling a complete

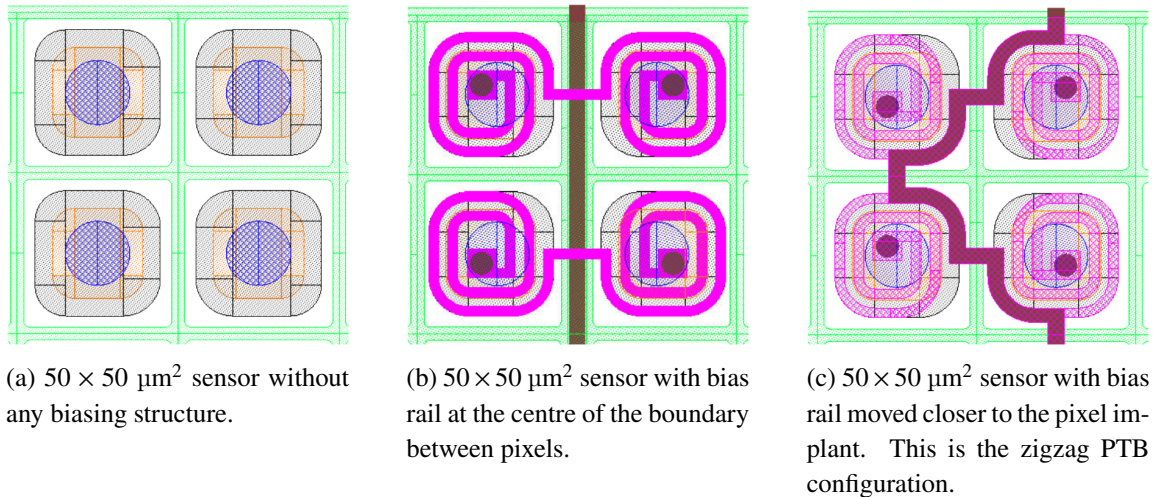


Figure 1: Possible biasing structures for a pixel detector sensor [6].

module can help keep the final module yields at higher levels than if this testing is restricted to fully assembled modules. Although beneficial in production, the PTB structure can also reduce charge collection efficiency of the sensor. In spite of this, the removal of these biasing structures is heavily disfavoured. In the measurements presented here, one device — referred to as DUT-A — has no PTB structure, whilst the other device — referred to as DUT-B — has a zigzag PTB structure variation, expected to reduce the loss of charge collection. These structures are shown in Figure 1.

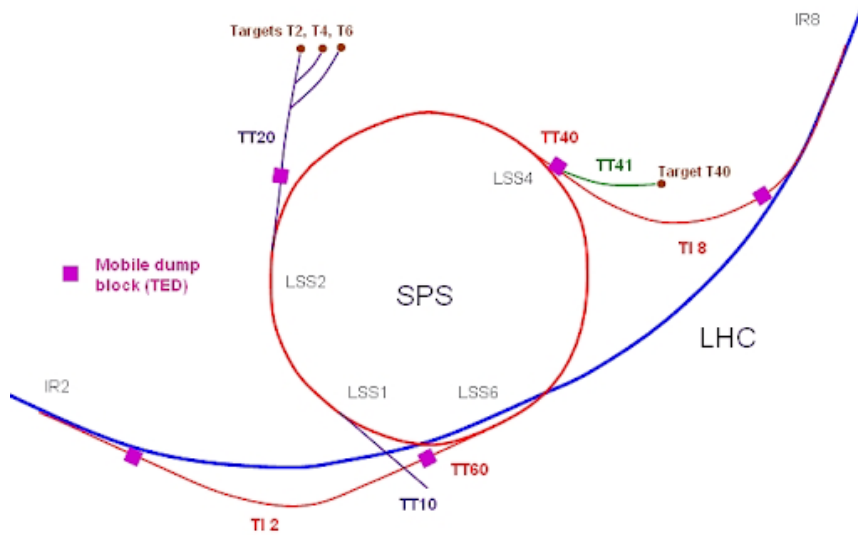
The final production front-end chip for the ITk pixel system — the ITkPix — will have 400×384 pixels over an area of $20.1 \times 21.6 \text{ mm}^2$. This will provide the resolution required throughout the ITk for precision track reconstruction. The ASIC will be a radiation hard CMOS chip with output data compression for the high radiation dose and data output requirements of the inner detector.

For the R&D phase, a first large-scale prototype chip, the RD53A [4], was produced in 65 nm CMOS technology by TSMC. RD53A is the basis for production designs for the ATLAS and CMS pixel detector upgrades for the HL-LHC era. The RD53A chip contains 400×192 pixels over an area of $20.1 \times 11.6 \text{ mm}^2$, half the area of the ITkPix. The RD53A chip has been designed to meet the radiation tolerance of 5 MGy, thinned to 150 μm . Three different analogue front-ends — *linear*, *differential* and *synchronous* — have been designed and implemented in the chip. Detailed evaluation programmes have been carried out in both ATLAS and CMS experiments for all three front-ends to select the most suitable design for their respective operation requirements.

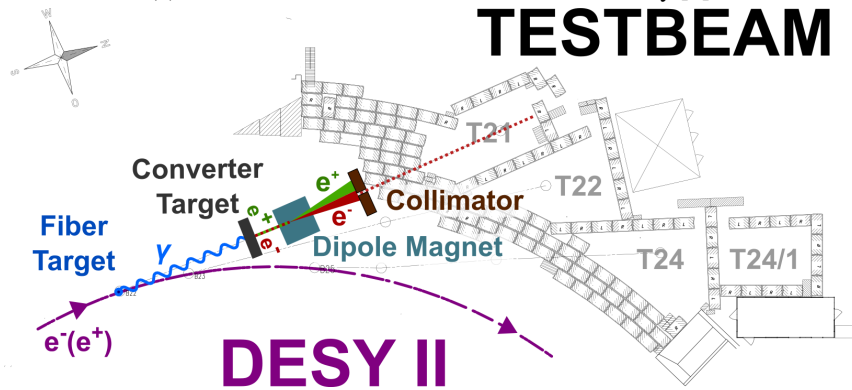
3 Testbeam facilities and detector setup

Testbeam facilities The testbeam campaigns considered in this paper were carried out at two facilities: the SPS testbeam facility at CERN and the DESY testbeam facility in Hamburg. The CERN SPS testbeam facility, shown in Figure 2a, is built around the SPS beamline [7] and supplies a beam of 120 GeV pions from converted protons. The DESY testbeam facility, shown in Figure 2b, is

built around DESY-II electron-positron synchrotron and supplies a beam of 1–6 GeV electrons from converted bremsstrahlung radiation. Both testbeam facilities house an EUDET-type [8] telescope providing identical apparatus at both sites, facilitating equivalent data reconstruction and analysis. Data was taken using the BDAQ readout system [9].



(a) Schematic of the CERN SPS testbeam facility [7].



(b) Schematic of the DESY testbeam facility [10].

Figure 2: Testbeam facilities used to make measurements of device efficiency.

The difference between the two sites comes from the beam supplied. The nature of the beam must be considered in the analysis due to the effect of multiple scattering, which occurs due to the Coulomb forces between the atoms in the detector material and the charged particles in the beam. This effect is larger at lower beam-momentum and contributes to the uncertainty on the track resolution.

Telescope setup An EUDET-type beam telescope, with a setup equivalent to that shown in Figure 3, is used to measure the track of a charged beam through the DUT.

The telescope contains six MIMOSA-26 [11] devices which are based on monolithic active pixel sensor technology with binary readout. These pixel modules have high spatial resolution

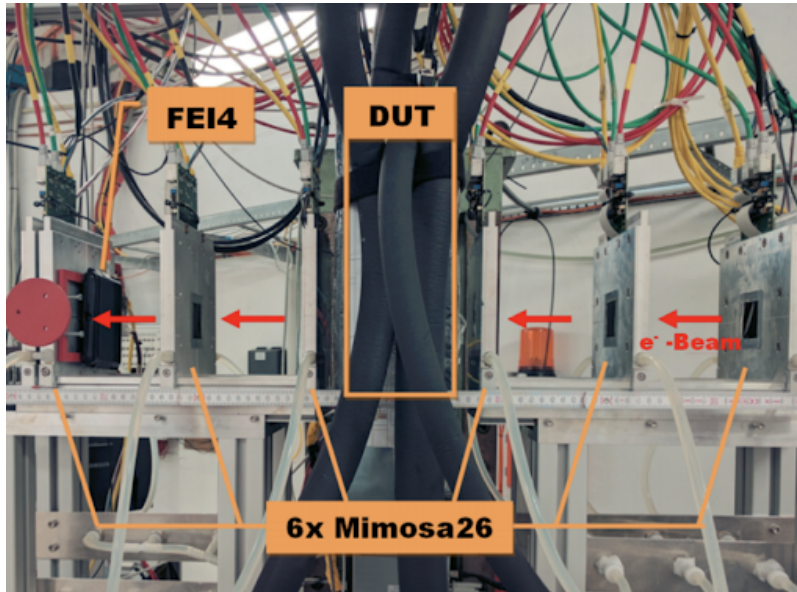


Figure 3: Telescope configuration at a DESY testbeam campaign. The DUT is placed between three upstream and three downstream MIMOSA-26 devices with high spatial resolution. Timing information is provided by an FE-I4 device fixed at the end of the telescope.

which translates into a high resolution on reconstructed tracks. Each device covers an area of $21.5 \times 13.7 \text{ mm}^2$ and has 576×1152 pixels with a pitch of $18.4 \times 18.4 \mu\text{m}^2$ and a thickness of $50 \mu\text{m}$, reducing the effect of multiple scattering. The MIMOSA-26 devices are operated in rolling shutter readout mode with an integration time of around $115.2 \mu\text{s}$. This corresponds to a readout rate of around 8 kHz , much slower than the 40 MHz DUT readout rate [12]. This means that for a given event read from a DUT, corresponding to a single trigger, there may be several tracks reconstructed in the telescope planes, corresponding to several triggers. Removing these out-of-time contributions from the analysis is essential to measuring the DUT efficiency. For this reason, an additional timing reference plane is placed at the end of the telescope. This timing plane is an FE-I4 pixel module [13], with the same readout rate as the DUT. Reconstructed tracks to be used for the analysis of the DUT are then required to have an associated hit in the timing plane.

Data acquisition The telescope uses dedicated trigger hardware called the trigger logic unit (TLU). The TLU receives a signal from two scintillators placed either side of the telescope and generates triggers which it distributes to the DUT, telescope planes, and timing reference. Each trigger is uniquely timestamped, within a resolution of 1.5 ns [14], enabling the synchronisation of hits across all planes. In addition, the DUT may respond to the TLU to indicate that it is busy, ensuring that no trigger signal is lost during the integration time. The EUDAQ software, used in conjunction with the the TLU, merges individual data streams into one and saves in histogram format for reconstruction.

Testbeam campaigns Data was taken in October 2018 and December 2018 at the CERN SPS and DESY facilities, respectively. Table 1 lists the testbeam campaigns and DUTs present for each.

Table 1: DUT and operating parameters for each testbeam campaign.

<i>Campaign</i>	<i>Beam</i>	<i>DUT (FE)</i>	<i>PTB</i>	<i>Bias voltage (V)</i>	<i>Threshold (e⁻)</i>
CERN Oct. 2018	120 GeV pions	DUT-A (lin)	none	600	1200, 1600
		DUT-A (diff)		600	1160, 1680, 2140
DESY Dec. 2018	1–6 GeV electrons	DUT-A (lin)	none	200, 400, 600	1027, 1200
		DUT-B (lin)	zigzag	100, 200, 300, 400, 500, 600	870, 1010, 1120

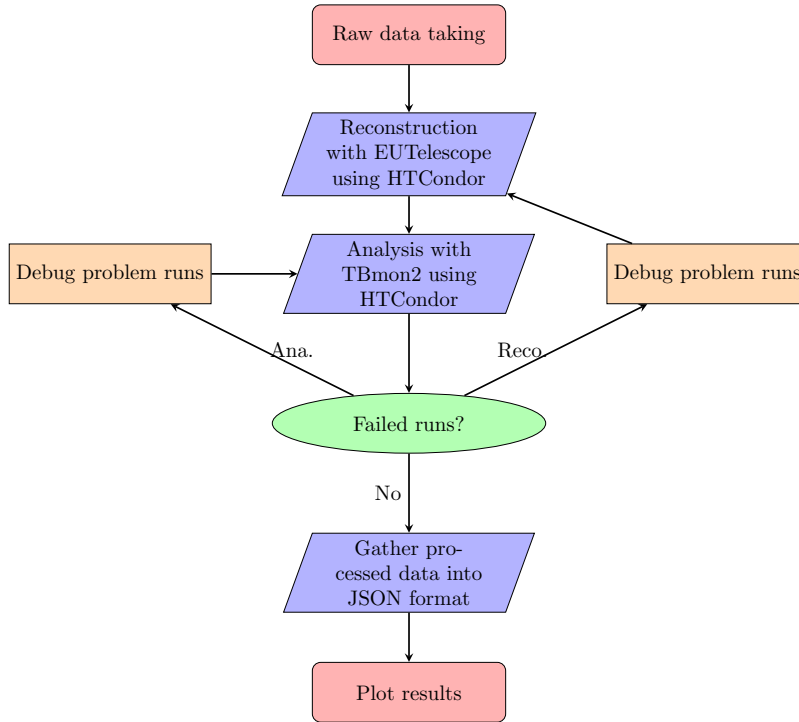


Figure 4: Flowchart showing the workflow for the results presented here, from the raw data-taking to final analysis of the reconstructed data.

4 Reconstruction and analysis

The workflow for the results presented here is summarised in Figure 4. The description of each stage in that workflow is given below.

4.1 Reconstruction: EUTelescope

Reconstruction of the testbeam data was carried out using EUTelescope [15], a modular framework widely used for particle trajectory reconstruction in data recorded with beam telescopes. The framework converts the raw data, as registered by the DAQ system, into a standardised data format — LCIO (Linear Collider Input/Output [16]) — with which clusters of hit pixels can be built and assigned to particle tracks.

EUTelescope uses the GEAR (GEometry API for Reconstruction [17]) framework for the geometric description of the framework. The testbeam setup (positions, alignment, detector geometry,

sensor layout, etc.) is described by an XML file which is read by the analysis framework to allow for transformations of hit positions from a local frame of reference to the telescope (global) reference frame.

Data conversion and noisy pixel detection The data recorded by the testbeam DAQ system needs to be converted from its original custom format into the standard LCIO format using EUDAQ [18]. LCIO data is event-based, containing an arbitrary amount of collections per triggered event. These collections can contain (hit) pixel indices, clustered pixels, and derived hits as the analysis moves along the reconstruction workflow.

Once the raw data has been converted into the LCIO format, one of EUTelescope processors, EUTelNoisyPixelFinder, can be applied. This uses the firing frequency (occupancy) of the pixels to determine whether a given pixel should be labelled as noisy. Pixels with firing frequency exceeding 0.1% in the case of DUTs and 0.5% in the case of the MIMOSA-26 planes are identified and removed from subsequent data analysis.

Clustering Neighbouring hit pixels belonging to the same LCIO collection are grouped and stored in a new cluster collection. Taking the masks created in the previous step, clusters containing at least one noisy pixel are tagged as noisy. Figure 5 shows typical distributions of total cluster charge in the form of time over threshold (ToT). The cluster charge is the sum of the charges of hit pixels forming the cluster. Also shown in the figure is the cluster size — the number of hit pixels forming a cluster.

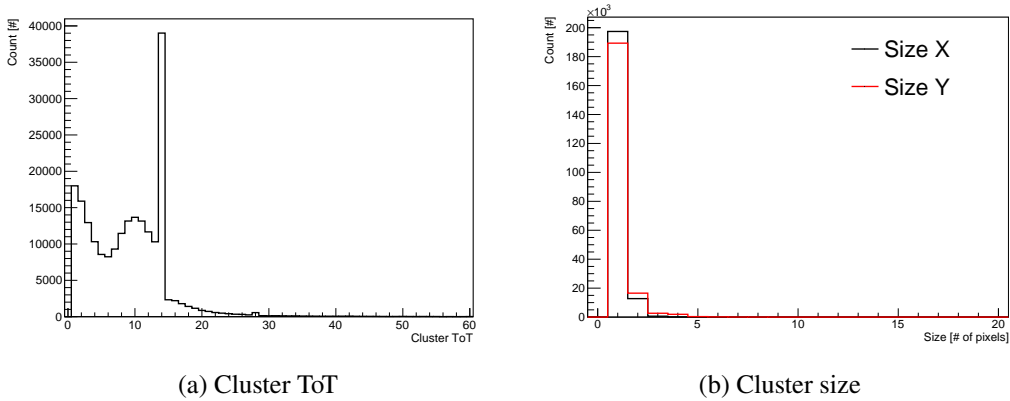


Figure 5: Example run taken during DESY December 2018 testbeam with device DUT-B, $V_{\text{bias}} = 600 \text{ V}$, and FE threshold of 1000 e^- ; (a) Cluster ToT in units of the beam crossing (25 ns). The exponential fall at low ToT originates from background noise. The gaussian-like peak around bin 10 represents the signal, and the spike at bin 15 from overflow stemming from noisy pixels, which are removed later in the reconstruction. (b) Cluster size in number of pixels.

Hitmaker and pre-alignment Using the cluster collections obtained in the previous step, hit positions in the local frame of reference are defined as the centre of the cluster coordinate, calculated

as the charge-weighted centre of the position of the hits forming the cluster:

$$\bar{x} = \frac{1}{Q} \sum_{i=0}^N x_i q_i, \quad (4.1)$$

where x_i is the position of the i^{th} pixel in the cluster, q_i the charge in that pixel and Q the sum of all charges collected by all pixels in the cluster. The position is calculated in the x and y axes independently and stored in a new LCIO collection.

The hit positions are translated from the local frame of reference for each plane to a global frame by rotating and shifting the local coordinates by the angles and global positions registered when performing data-taking (i.e. rotation and position of each plane and DUT in the testbeam). These values are provided by the GEAR file. Once the hits are provided in a global frame of reference, the positions of those hits registered in the first sensor are propagated to all sensors, calculating the difference between the propagated value and the registered hit in each sensor, referred to as residuals. These residuals are registered in one and two-dimensional histograms, taking the bins with highest counts as the pre-alignment factors, representing a rough estimate of the shift of the planes in x and y direction. These pre-alignment values are then written to a new GEAR file to be used in subsequent steps. Examples of correlations of the hit positions in x and y between hits in the DUT and a beam telescope plane are shown in Figure 6, where (c) shows the single dimension projection of (a) and (b) overlaid. The distance of the peak of each projection from the origin represents the displacement of the DUT from its optimum position relative to the telescope planes. This value is used to align planes.

Alignment In this step, updated global hits based on the corrected pre-aligned GEAR file are used to determine precise alignment of the telescope and DUT planes, using track finding and aligning algorithms based on General Broken Lines (GBL) track model [19]. In this model, the beam telescope, consisting of six planes, is divided into two groups – the upstream and downstream triplets. Within each triplet, a straight line (doublet) is calculated joining the first and last hits. Doublets that have slopes inconsistent with the beam direction are excluded to suppress false combinations. The threshold is given by user-defined cuts. The distance between the doublet and the hit in the middle sensor must also be within a user-defined range for the triplet to be considered valid. Both upstream and downstream triplets are then extrapolated to the centre of the beam telescope. The extrapolated position of these two triplets must be matched within a user-defined distance to be joined together as a track. Once the fitted line from each arm of telescope is matched the track is defined.

The alignment process is repeated 3 times per run, using a partial number of events to retrieve and estimate the values of the cuts to be used by GBL. As the alignment process is iterated, cut values are reduced, initially set high for a first estimate of the cut values, then optimised by performing a gaussian fit on the distribution of the distances and slopes previously explained.

Track fitting The final reconstruction step consists of a track fit using the six hits of the telescope planes associated to each track found in the previous step passing all required cuts. The tracks are output to a ROOT n -tuple so that they may be used for subsequent analysis. The resulting residuals for the hits in DUT in x and y , defined as the difference between the reconstructed cluster position

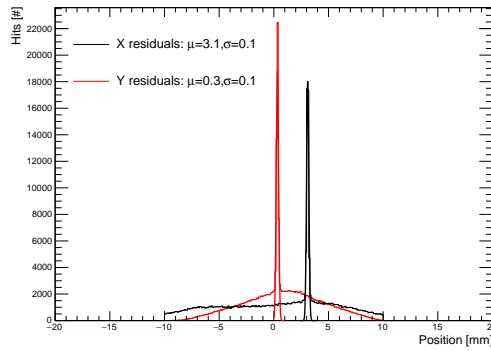
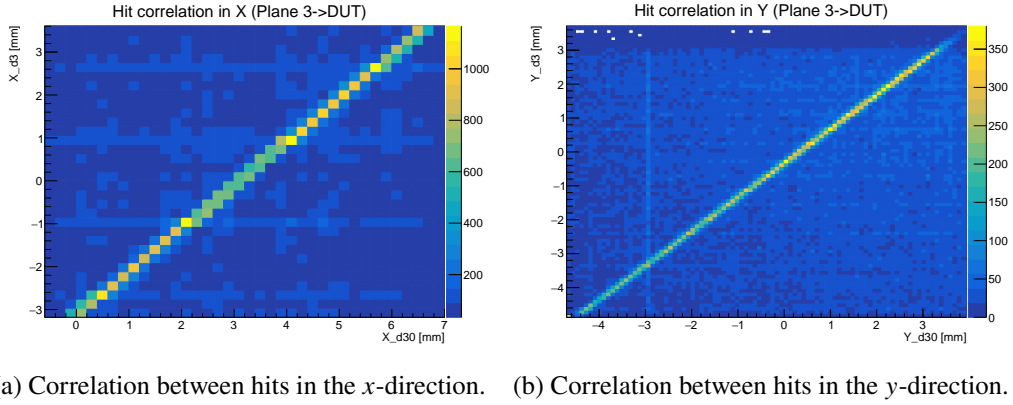


Figure 6: Correlations and residuals between DUT and adjacent telescope plane.

and the extrapolated values from the fitted track are shown in Figure 7. Both distributions are centred around zero, which shows good alignment with no systematic offset. The RMS of each distribution corresponds to the expected resolutions of the pixel pitches in each dimension. The χ^2 per degree of freedom distribution for the track fit peaks at low values and has a smooth tail, implying that the telescope is well aligned over the run.

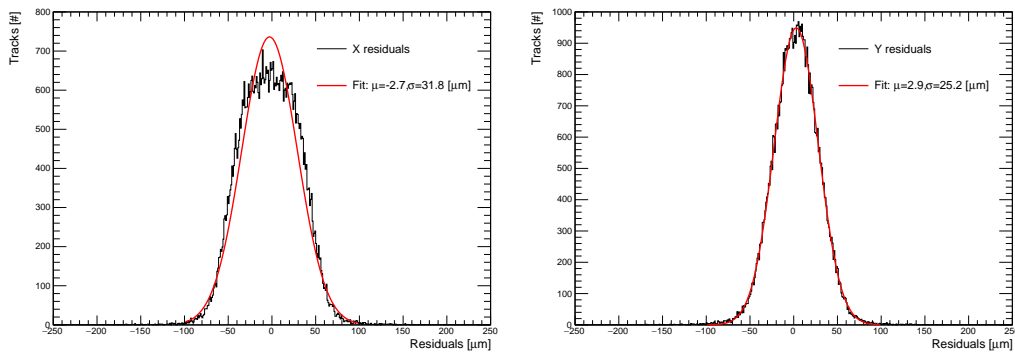


Figure 7: Residual distributions after the track fitting.

4.2 Analysis: TBmon2

The output files produced following reconstruction in EUTelescope are then analysed using TBmon2 [20], a testbeam analysis software package. The framework uses a core processor to read all relevant inputs, such as data paths and DUT geometry files, and then executes data pre-processing and different analyses. These analyses can be individually configured in dedicated configuration files with corresponding DUT specifications. Central configuration parameters, such as selection of fiducial regions and track quality criteria, are set by the user.

The pre-processing module first finds tracks that pass a set of basic quality criteria and are matched to at least one hit in the timing reference plane. When two DUTs are placed within the telescope planes, either one of the DUTs can serve as the timing reference plane to minimise potential timing difference between RD53A and FE-I4 devices. To mitigate multiple scattering effect when propagating tracks from the DUT plane to the reference plane, a radius matching requirement is applied on hits from both devices. The maximum distance between hits in each axis in the transverse plane is specified in the configuration file and is commonly set to half of the pitch of the DUT in that direction.

Once the pre-processing is complete, different analysis modules can be executed to study the performance of the DUT. In this paper, we focus on the pixel hit efficiency, defined as the ratio of the number of tracks with matching hits in the DUT to the total number of telescope tracks:

$$\epsilon = \frac{n_{\text{matched tracks}}}{n_{\text{total tracks}}}. \quad (4.2)$$

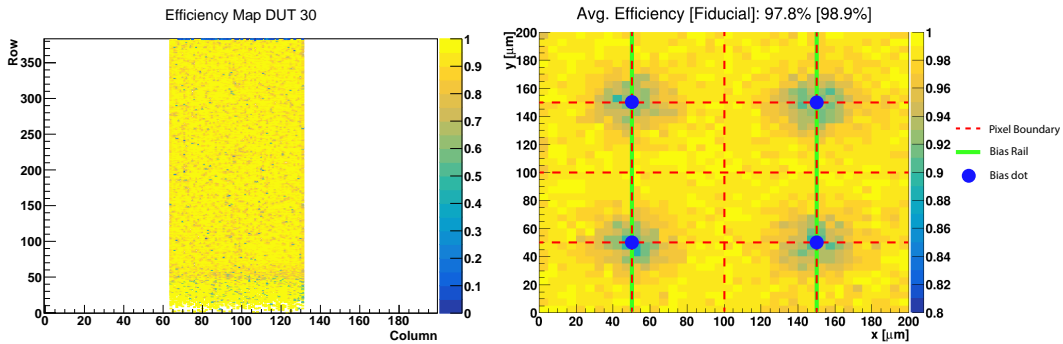
This quantity is one of the most important figure of merit to qualify sensor designs. During the ATLAS ITk Pixel Sensor Market Survey [3], devices achieving global efficiencies above 98.5% or 97% in the case of unirradiated or irradiated modules, respectively, were considered to have met the production requirements.

All tracks passing the quality selection criteria applied in the pre-processing are included in the total number of tracks. Hit-to-track matching criteria is specified by maximum matching distance in the $x - y$ plane between the extrapolated position in the DUT plane from the telescope tracks and the reconstructed pixel hit position in the DUT. The maximum threshold in each axis, x or y , is set to be twice the pitch size in the given axis of the DUT and specified in the configuration file.

In addition to the overall pixel efficiency, more detailed studies are also carried out to characterise the pixel hit efficiency dependence on position within the pixel matrix:

- Pixel hit maps: the efficiency is computed on a pixel-by-pixel basis by considering all hits and tracks which pass through that pixel. The outputs of this analysis are efficiency maps such as that shown in Figure 8a, where the efficiency is only computed for the front-end under study (columns 65-130).
- In-pixel efficiency: this analysis provides an in-depth look at the efficiency patterns that may arise due to different structures present in the device at a sub-pixel level, such as punch-through bias dots. The ability to make such a measurement is only possible as a result of the high resolution of the MIMOSA-26 sensors in the telescope in comparison to the DUTs. In order to analyse the efficiency in such a granular manner, a large number of hits per pixel are required. To achieve this, and avoid the need for extremely long data-taking runs, the

full pixel matrix is divided into blocks containing 4×4 pixels each, leading to a total block area of $200 \times 200 \mu\text{m}^2$, with each block across the whole pixel matrix then overlaid on top of one another to provide averaged information from across the whole sensor. The resulting efficiency maps are shown in Figure 8b, where it is possible to distinguish efficiency drops between pixels corresponding to the presence of a punch-through bias dot, which is at the same potential as the charge collection electrode and tends to collect the electrons around it rather than the pixels themselves. A fiducial area can be calculated by masking pixels in the region affected by the punch-through dots, providing a fiducial efficiency as well as the overall efficiency.



(a) Typical pixel efficiency map using one of three front-ends on the RD53A. (b) Typical in-pixel efficiency map for a device including punch-through bias.

Figure 8: Example run during the December 2018 testbeam campaign (Batch 1, DUT-B, $V_{\text{bias}} = 600 \text{ V}$, threshold = $1000 e^-$).

5 Results

Presented in the following sections are results of the final analysis for both testbeam campaigns, as well as a combined set of results comparing devices across campaigns. The criteria later adopted by the ATLAS planar sensor market survey required that devices irradiated to $2 \times 10^{15} n_{\text{eq}} \text{ cm}^{-2}$ achieve 97% efficiency at a bias voltage of $V_{\text{bias}} = 400 \text{ V}$ and that devices irradiated to $5 \times 10^{15} n_{\text{eq}} \text{ cm}^{-2}$ achieve 97% efficiency at a bias voltage of $V_{\text{bias}} = 600 \text{ V}$. Where possible, devices are evaluated in reference to the former criterion. This represents a conservative comparison in that the results presented here are for devices irradiated to $3.4 \times 10^{15} n_{\text{eq}} \text{ cm}^{-2}$ — almost double the fluence stipulated for that set of operating parameters. Efficiency values are also evaluated for various other sets of parameters. The statistical uncertainties on the results shown here are too small to be visible on the plots, so are omitted.

5.1 October 2018 testbeam

In this campaign, device DUT-A was characterised using both linear and differential front-ends. It contains no punch-through biasing structure.

Figure 9 shows the overall efficiency as a function of the threshold for the differential and linear FEs, at a $V_{\text{bias}} = 600 \text{ V}$. The highest efficiency of $\varepsilon = 99.47\%$ is observed with a threshold of $1158 e^-$ for the linear FE, and $\varepsilon = 99.05\%$ for the differential FE at a threshold of $1200 e^-$. Increasing the threshold beyond this point, the devices using both of the FEs exhibit a degradation in efficiency. This can be attributed to the loss of signal.

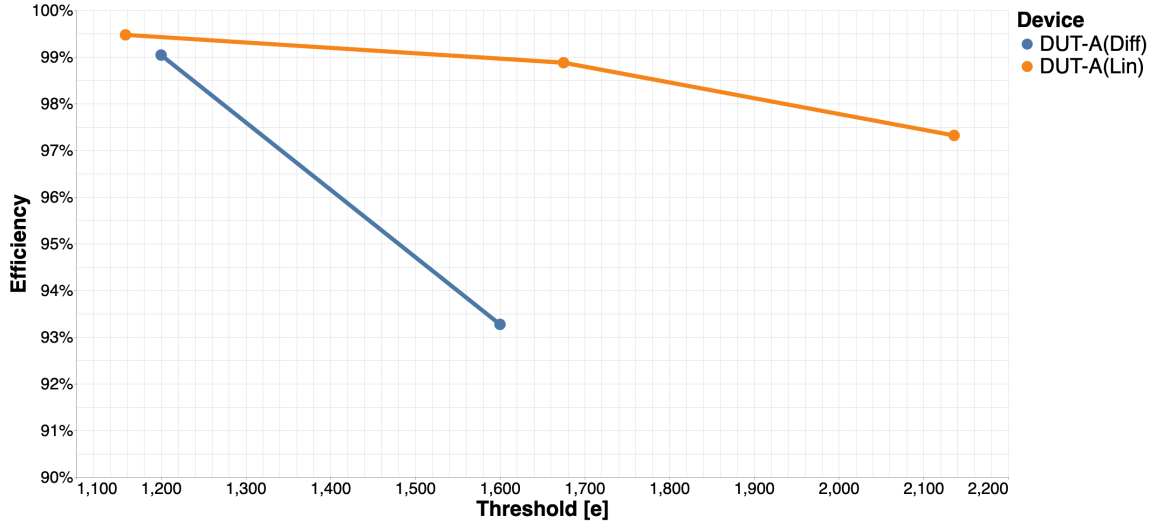


Figure 9: Evolution of the efficiency (as defined in Section 4.1), as a function of threshold, in the October 2018 testbeam for both front-ends at $V_{\text{bias}} = 600 \text{ V}$.

Figure 10 shows the in-pixel efficiency maps for the linear FEs at different thresholds. At the optimum threshold, the efficiency exhibits near-uniform distribution across the sensor. At higher threshold settings, efficiencies are reduced close to the pixel corner boundaries as a result of charge-sharing. Figure 11 shows the in-pixel efficiency maps for the differential FEs at different thresholds.

It can be seen that the device efficiency drops as the threshold is raised beyond the efficiency plateau such that signal is being cut away.

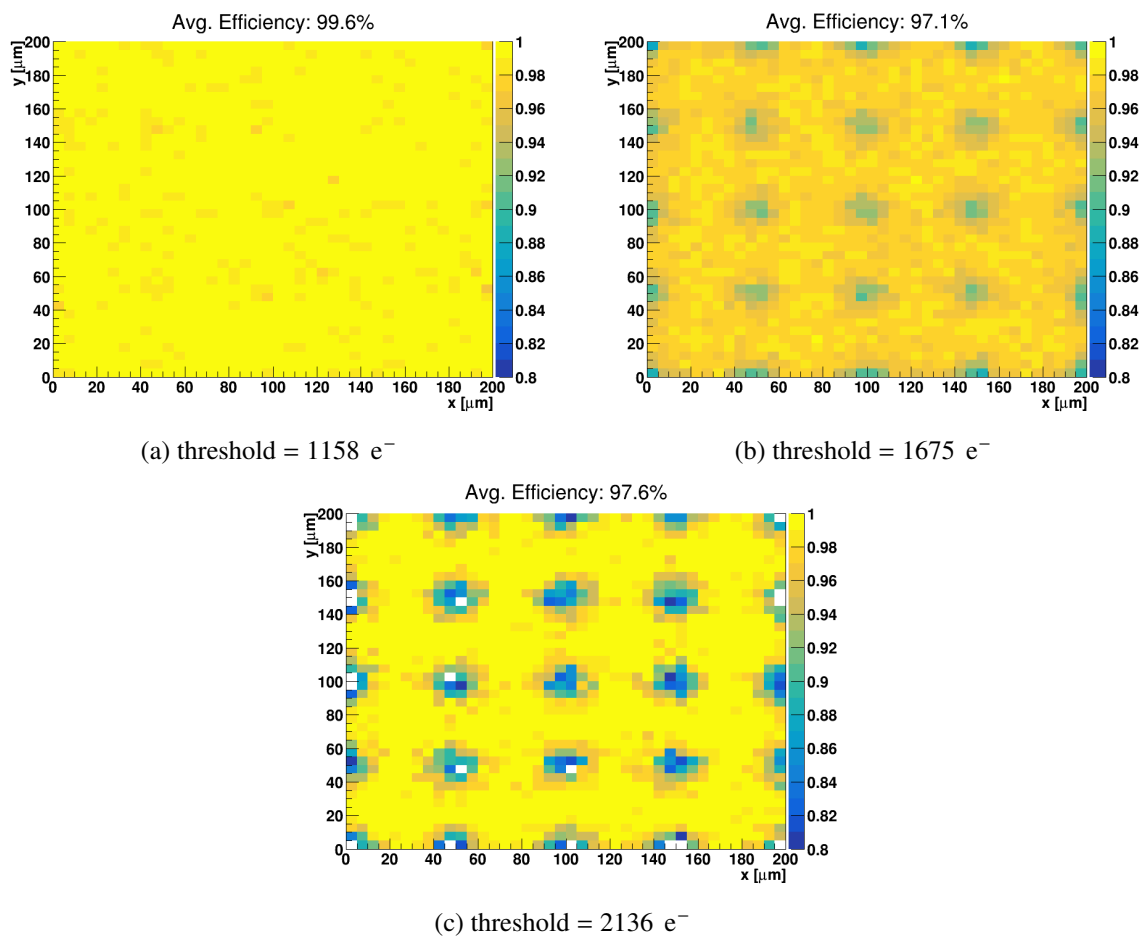


Figure 10: In-pixel efficiency maps, as defined in Section 4.2, for device DUT-A (linear FE) with $V_{\text{bias}} = 600 \text{ V}$.

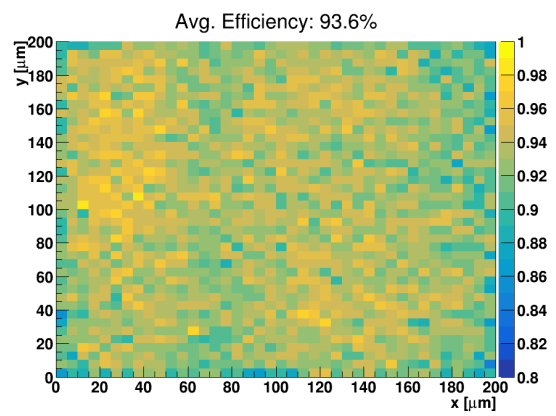
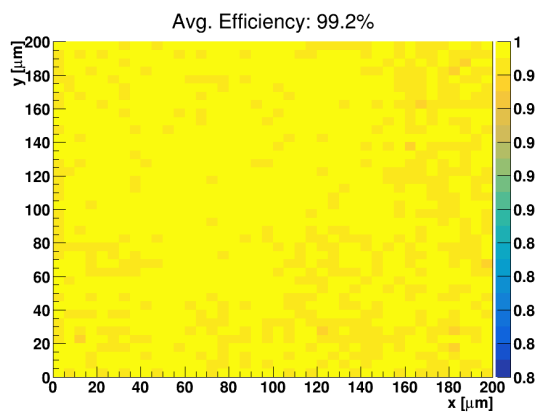


Figure 11: In-pixel efficiency maps for device DUT-A (differential FE) with $V_{\text{bias}} = 600 \text{ V}$.

5.2 December 2018 testbeam

In this campaign, both devices DUT-A and DUT-B were characterised using the linear front-end. DUT-A contains no PTB structure, whilst DUT-B uses the zigzag PTB structure.

Figure 12 shows the overall efficiency as a function of the V_{bias} for both DUTs. Both devices behave as expected, with efficiency increasing as V_{bias} increases before reaching a plateau. The efficiency reaches plateau at $V_{\text{bias}} = 300 \text{ V}$ and $V_{\text{bias}} = 400 \text{ V}$ for device DUT-B and DUT-A, respectively. Figure 13 shows the overall efficiency as a function of the threshold for both DUTs. The highest efficiency achieved for device DUT-B, $\varepsilon = 98.70\%$, is observed with threshold = 1013 e^- at $V_{\text{bias}} = 600 \text{ V}$. An efficiency of $\varepsilon = 99.55\%$ is reached for DUT-A at threshold = 1027 e^- at $V_{\text{bias}} = 600 \text{ V}$. At $V_{\text{bias}} = 400 \text{ V}$, both devices exceed the 97% efficiency criterion. Device DUT-B reaches the desired efficiency when using a threshold above 1000 e^- . For device DUT-A, the desired efficiency is reached for all threshold points with $V_{\text{bias}} \geq 400 \text{ V}$.

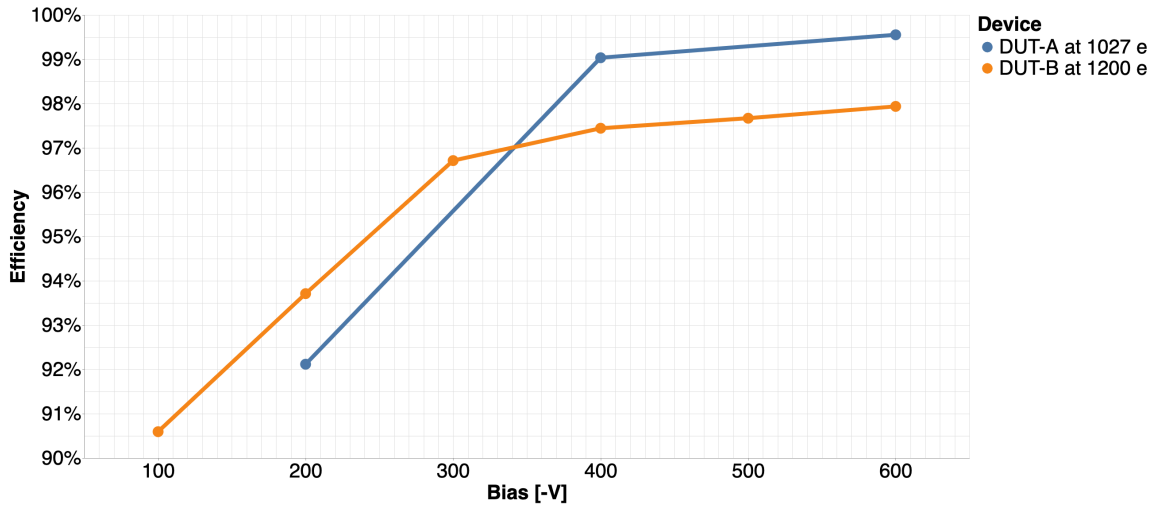


Figure 12: Evolution of the efficiency as a function of bias voltage during the December 2018 testbeam with threshold = 1200 e^- (DUT-B) and threshold = 1027 e^- (DUT-A). Both devices are using the linear front-end.

Figure 14 shows the in-pixel efficiency maps for device DUT-B at different V_{bias} points, with a threshold of 1200 e^- . Here, the efficiency of the device increases as V_{bias} is increased. Despite reaching near-perfect efficiency across the majority of the sensor, the regions around the punch-through dots retain their lower efficiency. Figure 15 shows the in-pixel efficiency maps for the same device at different threshold points and $V_{\text{bias}} = 600 \text{ V}$. Here, the efficiency of the device increases as the threshold is increased, until the efficiency reaches a plateau at the higher threshold values. Beyond this, an increase in the threshold begins to remove signal hits, to the detriment of the device efficiency. As with the V_{bias} scan, the regions around the punch-through dots have a persistently lower efficiency than the other areas on the sensor, which reach near-perfect efficiency. Figure 16 shows the in-pixel efficiency maps for device DUT-A at different V_{bias} points, with a threshold of 1027 e^- . Here, the efficiency of the device increases as the threshold is increased. Despite reaching near-perfect efficiency across the majority of the sensor at higher threshold values,

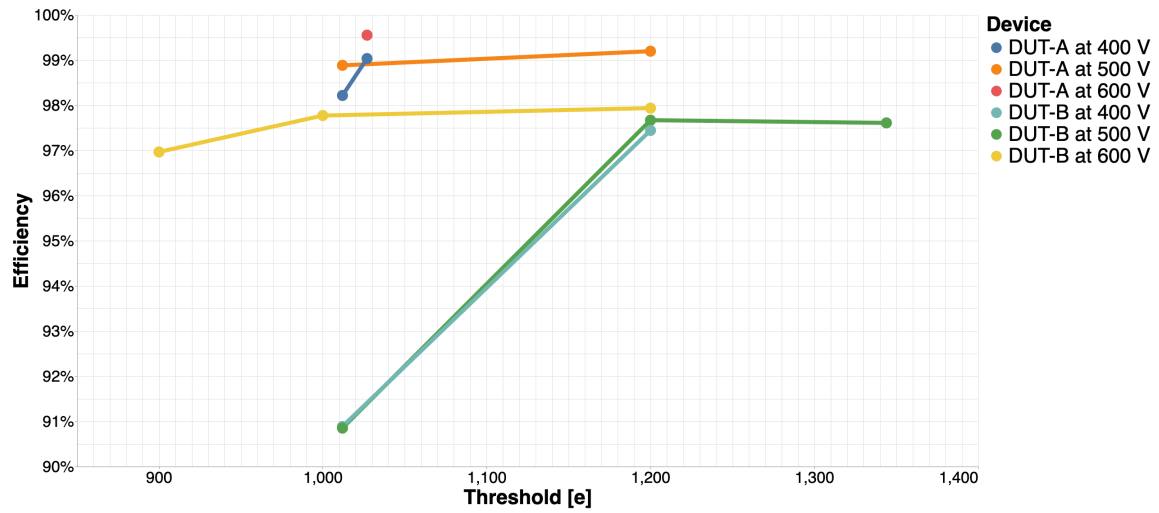


Figure 13: Evolution of the efficiency as a function of threshold during the December 2018 testbeam for both devices, using the linear front-end.

the regions around the pixel corners exhibit lower efficiency at lower threshold as a result of charge-sharing.

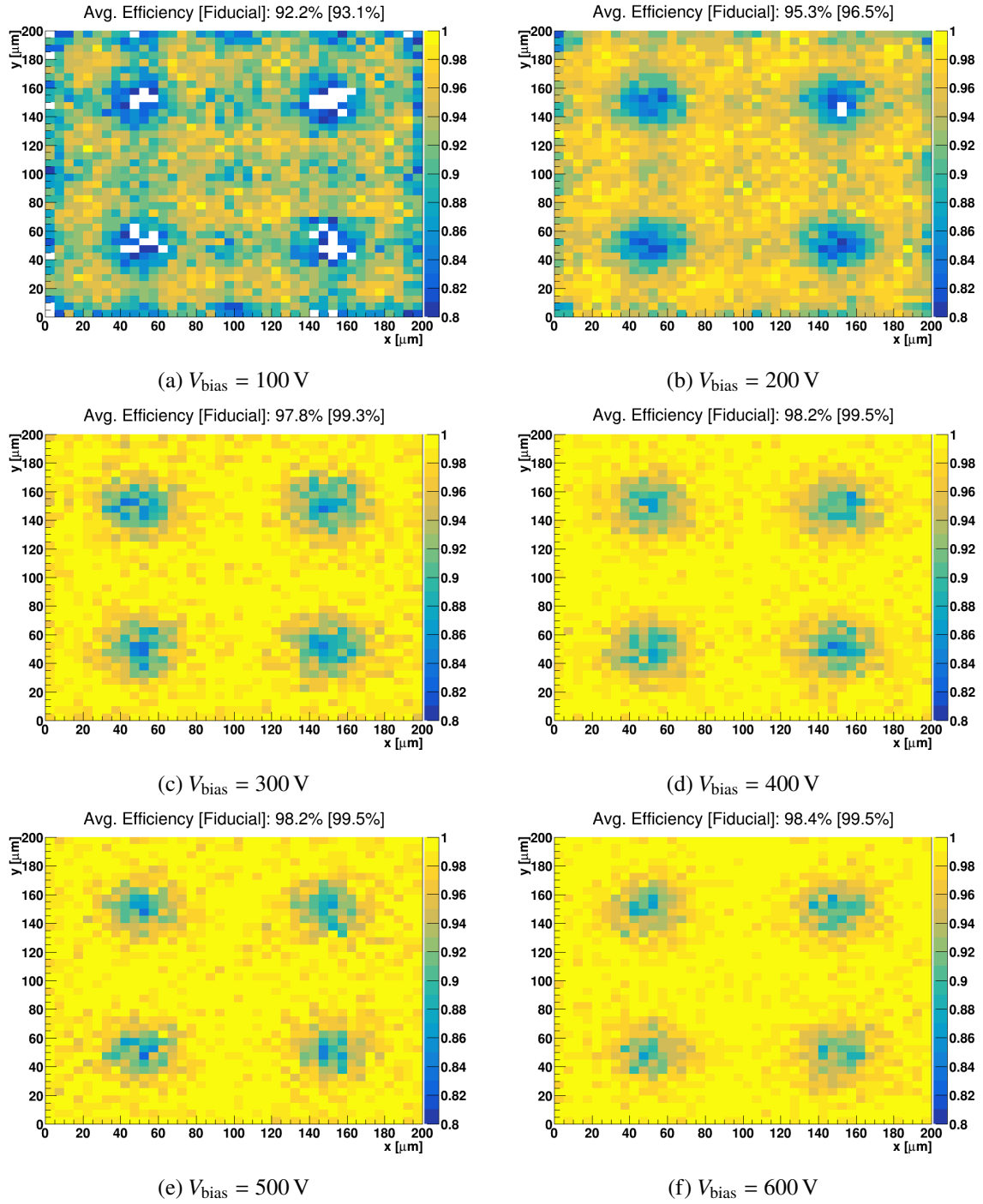


Figure 14: In-pixel efficiency maps, as defined in Section 4.2, for device DUT-B (linear FE) with a threshold of $1200 e^-$.

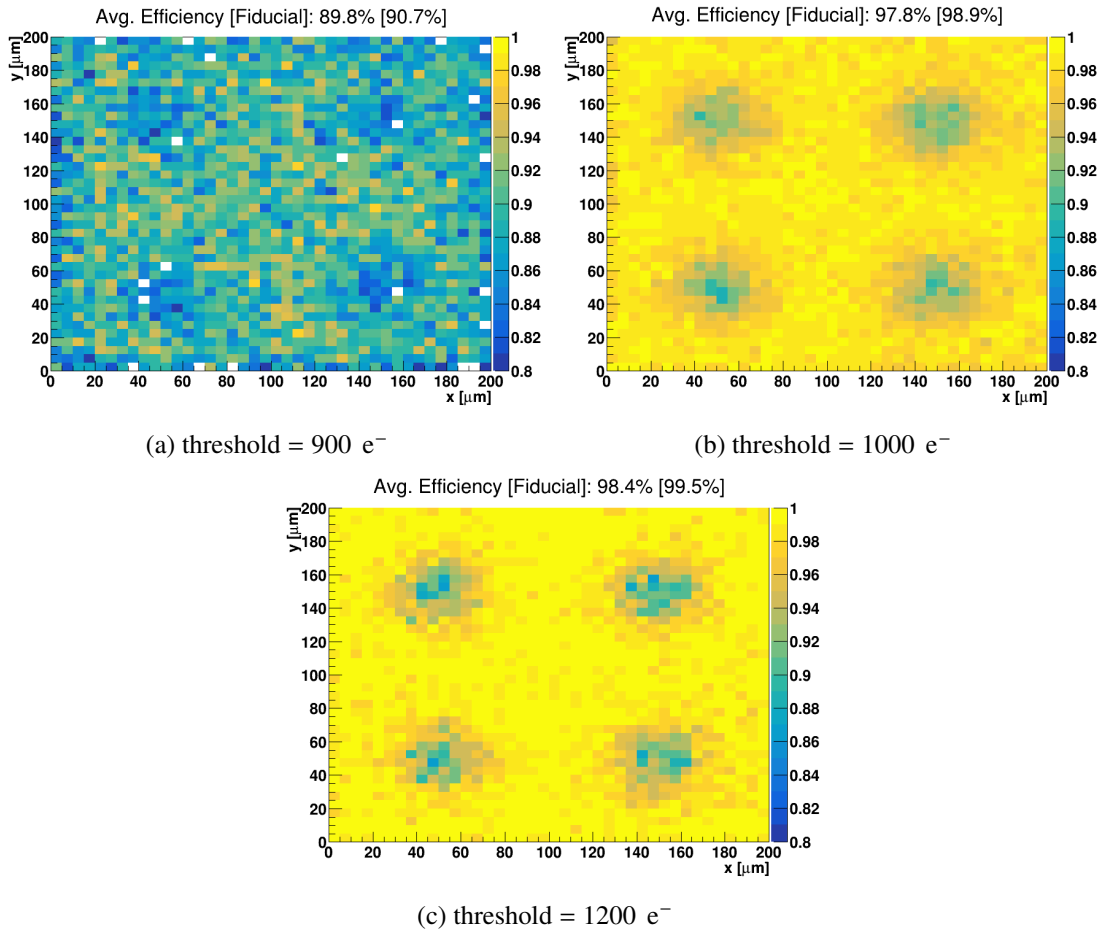


Figure 15: In-pixel efficiency maps, as defined in Section 4.2, for device DUT-B (linear FE) with $V_{\text{bias}} = 600 \text{ V}$

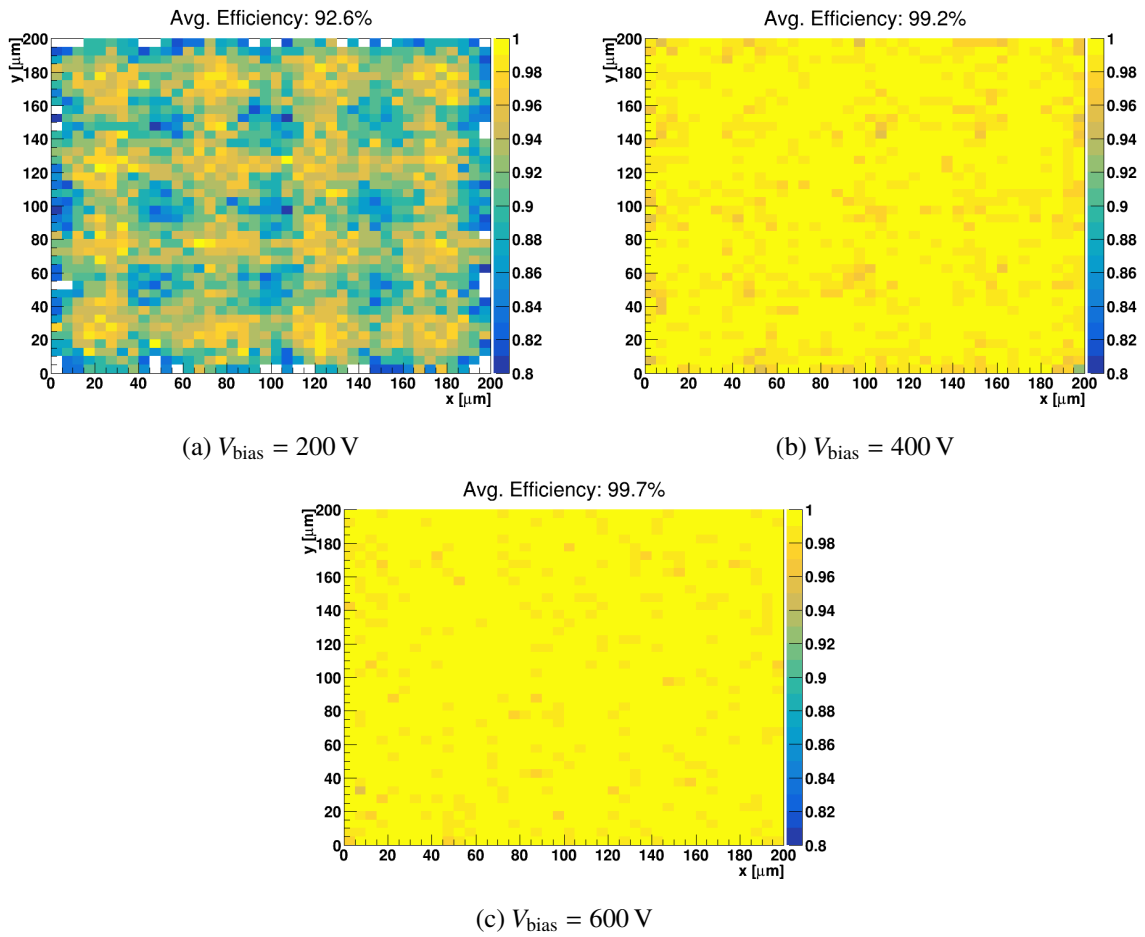


Figure 16: In-pixel efficiency maps, as defined in Section 4.2, for device DUT-A (linear FE) with threshold = 1027 e^- .

5.3 Cross-testbeam comparisons

Comparisons are performed between the October 2018 and December 2018 testbeams where the same devices were tested during both campaigns. Where overlapping operating parameters are present, bias and threshold scans are combined and summarised.

Figure 17 shows the overall efficiency as a function of the threshold for all devices under test at both October and December testbeam campaigns, selecting runs with $V_{\text{bias}} = 600 \text{ V}$. The efficiency generally increases when increasing the threshold to above 1000 e^- , at which point the effect of noise is reduced. Once the threshold reaches an optimal working point, efficiency will decrease as the threshold is increased further, as signal loss begins to occur. For all devices under test, the desired 97% efficiency is surpassed for optimal operation thresholds.

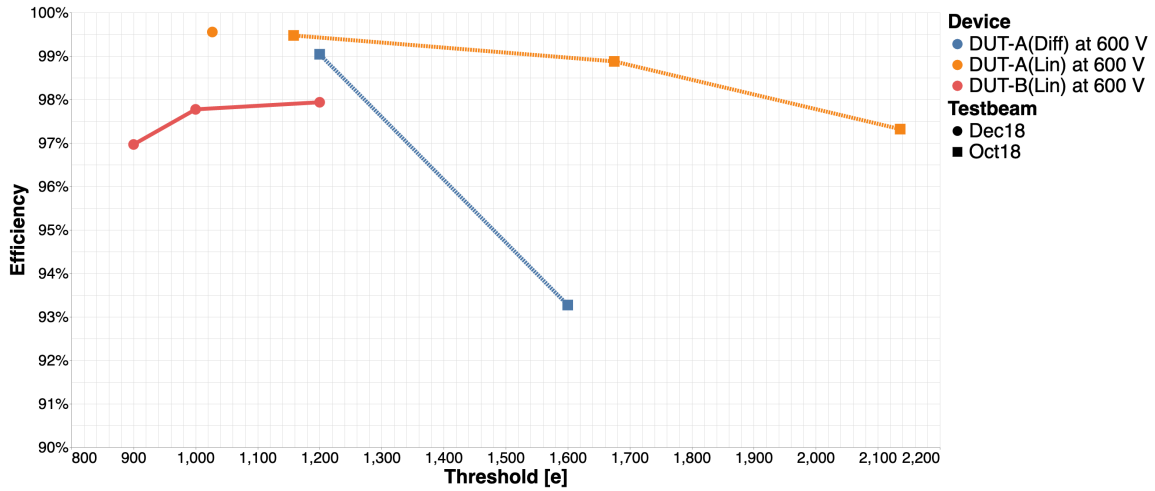


Figure 17: Overall pixel efficiency as a function of threshold for both October and December testbeam campaigns, selecting runs with $V_{\text{bias}} = 600 \text{ V}$.

Figure 18 shows the overall efficiency as a function of V_{bias} for both testbeam campaigns, selecting runs with FE threshold of $\text{th} = 1200 \text{ e}^-$. As discussed in Section 5.2, a turn-on curve is observed for device DUT-B (lin). The required efficiency is observed for all devices with $V_{\text{bias}} \geq 400 \text{ V}$.

6 Conclusions

Hybrid pixel detectors consisting of a planar silicon sensor bump-bonded to an RD53A readout chip have been characterised by the analysis of reconstructed testbeam data. Measurements were made using an EUDET-like beam telescope over two testbeam campaigns at the CERN SPS and DESY testbeam facilities in October 2018 and December 2018, respectively. Two devices were measured, with and without punch-through biasing structures, and using both linear and differential readout modes. Both devices used sensors with pixel pitch $50 \times 50 \mu\text{m}^2$, thickness of $150 \mu\text{m}$ and irradiated to $3.4 \times 10^{15} \text{ n}_{\text{eq}} \text{ cm}^{-2}$.

A range of V_{bias} and threshold scans were performed on the devices, with each device required to surpass 97% efficiency at $V_{\text{bias}} = 400 \text{ V}$.

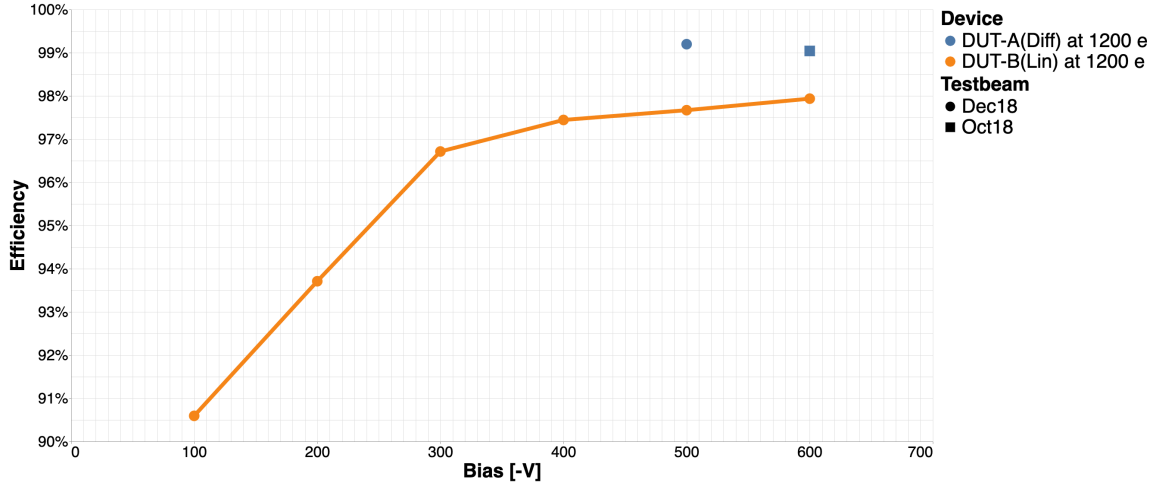


Figure 18: Overall efficiency as a function of V_{bias} comparing data from both testbeam campaigns, selecting the runs with FE threshold of $th = 1200 e^-$.

Across devices, the efficiency is observed to increase as the V_{bias} or threshold is increased until reaching an efficiency plateau. When the threshold is increased further, it is seen to reduce the device efficiency as signal hits begin to be cut away.

Devices which feature a punch-through bias structure are seen to reach an efficiency plateau at lower V_{bias} and threshold than those with no such structure. The efficiency at the plateau is also observed to be lower than the device with no biasing structure. In-pixel efficiency maps show regions of low efficiency around the punch-through dots on the device with the biasing structure.

At $V_{\text{bias}} = 600 \text{ V}$, the highest global efficiency was observed on device DUT-A, using the linear front-end with no punch-through biasing structure, at 99.6% efficiency, at a threshold of $threshold = 1158 e^-$. At the same V_{bias} , threshold, and operating mode, device DUT-B with a punch-through bias structure was observed to have a global efficiency of 98.4% and an efficiency of 99.5% in the fiducial area which masks out the regions contaminated by the biasing structure.

Although the biasing structure is seen to have a detrimental effect on the efficiency of the sensor, devices both with and without this feature comfortably surpass the 97% efficiency criteria. As such, the benefits provided by these biasing structures for production of modules is considered to outweigh the slight drop in efficiency which does not impact the ability of the device to pass QC criteria.

Device DUT-A was observed to achieve greater efficiency using the linear front-end than when using the differential front-end. At $V_{\text{bias}} = 600 \text{ V}$ and a threshold of around $1200 e^-$, the linear front-end produced a global efficiency of 99.6% whilst the differential front-end produced a global efficiency of 99.2%. In addition to this, the efficiency of the differential front-end was observed to fall off more quickly as the threshold was raised. At $V_{\text{bias}} = 600 \text{ V}$ and a threshold of around $1600 e^-$, the linear front-end produced a global efficiency of 97.1% whilst the differential front-end produced a global efficiency of 93.6%. In the absence of thresholds below around $1200 e^-$ to make comparisons with, and given that the differential front-end is expected to be capable of operating at lower threshold than the linear front-end, it is reasonable to suggest that the efficiency

of the differential front-end simply peaks at lower threshold than the linear front-end and would be expected to outperform the linear front-end at these lower thresholds.

Acknowledgments

The measurements leading to these results were made at the testbeam facility at DESY Hamburg (Germany), a member of the Helmholtz Association (HGF). We gratefully thank the operators of this facility.

The reconstruction and analysis presented here was performed within a framework based on one originally developed in collaboration with Tobias Fitschen. Our thanks to him for this.

References

- [1] A. Macchiolo, *The Phase-2 ATLAS ITk pixel upgrade*, *Nuclear Instruments and Methods in Physics Research Section A: Accelerators, Spectrometers, Detectors and Associated Equipment* **962** (2020) 162261.
- [2] J. S. Keller, *The ATLAS ITk strip detector system for the High Luminosity LHC upgrade*, *Nuclear Instruments and Methods in Physics Research Section A: Accelerators, Spectrometers, Detectors and Associated Equipment* **958** (2020) 162053.
- [3] S. Möbius, *Module development for the ATLAS ITk pixel detector*, *Journal of Instrumentation* **17** (2022) C03042.
- [4] RD53 COLLABORATION collaboration, *The RD53A Integrated Circuit*, tech. rep., CERN, Geneva, Oct, 2017.
- [5] Karlsruhe Institute of Technology, “KIT Proton Irradiation.” <https://www.etp.kit.edu/english/264.php>.
- [6] ATLAS Collaboration, *ATLAS Inner Tracker Pixel Detector: Technical Design Report*, .
- [7] J. Wenninger, “SPS operation.” <https://jwenning.web.cern.ch/SPS.html>.
- [8] H. Jansen et al., *Performance of the EUDET-type beam telescopes*, *EPJ Tech. Instrum.* **3** (2016) 7 [1603.09669].
- [9] M. Daas, Y. Dieter, J. Dingfelder, M. Frohne, G. Giakoustidis, T. Hemperek et al., *BDAQ53, a versatile pixel detector readout and test system for the ATLAS and CMS HL-LHC upgrades*, *Nuclear Instruments and Methods in Physics Research Section A: Accelerators, Spectrometers, Detectors and Associated Equipment* **986** (2021) 164721.
- [10] DESY, “Generation of the desy test beams.” https://particle-physics.desy.de/test_beams_at_desy/e252106/e252211.
- [11] A. Himmi et al., *Mimosa26 User Manual*, December, 2008.
- [12] RD53 COLLABORATION collaboration, *The RD53A Integrated Circuit*, tech. rep., CERN, Geneva, Oct, 2017.
- [13] M. Garcia-Sciveres et al., *The FE-I4 pixel readout integrated circuit*, *Nucl. Instrum. Meth. A* **636** (2011) S155.
- [14] P. Baesso, D. Cussans and J. Goldstein, *The AIDA-2020 TLU: a flexible trigger logic unit for test beam facilities*, *JINST* **14** (2019) P09019 [2005.00310].
- [15] T. Bisanz, H. Jansen, J.-H. Arling, A. Bulgheroni, J. Dreyling-Eschweiler, T. Eichhorn et al., *Eutelescope: A modular reconstruction framework for beam telescope data*, *Journal of Instrumentation* **15** (2020) P09020–P09020.
- [16] F. Gaede, T. Behnke, N. Graf and T. Johnson, *LCIO: A Persistency framework for linear collider simulation studies*, *eConf* **C0303241** (2003) TUKT001 [physics/0306114].
- [17] ilcSoft community, “GEometry API for Reconstruction.” https://ilcsoft.desy.de/portal/software_packages/gear/.
- [18] P. Ahlburg, S. Arfaoui, J.-H. Arling, H. Augustin, D. Barney, M. Benoit et al., *Eudaq—a data acquisition software framework for common beam telescopes*, *Journal of Instrumentation* **15** (2020) P01038–P01038.

- [19] C. Kleinwort, *General broken lines as advanced track fitting method*, *Nuclear Instruments and Methods in Physics Research Section A: Accelerators, Spectrometers, Detectors and Associated Equipment* **673** (2012) 107–110.
- [20] tbmon2 community, “TBmon2 - Testbeam Data Analysis Software.”
<https://gitlab.cern.ch/tbmon2/tbmon2>.

Front-end electronics development of large-area SiPM arrays for high-precision single-photon time measurement

W. Zhi^a, J.N. Tang^a, M.X. Wang^a, Y.Q. Tan^a, W.H. Wu^{a,1} and D.L. Xu^{a,b}

^a*School of Physics and Astronomy, Shanghai Jiao Tong University
800 Dongchuan Rd, Minhang District, Shanghai, China*

^b*Tsung-Dao Lee Institute, Shanghai Jiao Tong University
520 Shengrong Rd, Pudong New Area, Shanghai, China*

E-mail: wuweihao@sjtu.edu.cn

ABSTRACT: TRopIcal DEep-sea Neutrino Telescope (TRIDENT) plans to incorporate silicon photomultipliers (SiPMs) with superior time resolution in addition to photomultiplier tubes (PMTs) into its detection units, namely hybrid Optical Digital Modules (hDOMs), to improve its angular resolution. However, the time resolution significantly degrades for large-area SiPMs due to the increased parasitic capacitance, posing significant challenges for the readout electronics of SiPMs in hDOM. We designed the front-end readout electronics for large-area SiPM arrays dedicated to high-precision time measurements, which consists of a high-speed pre-amplifier based on transformers (MABA-007159) and radio frequency (RF) amplifiers (BGA2803), a series-parallel combination SiPM array with reduced capacitance, and an analog multi-channel summing circuit. We measured the single photon time resolution (SPTR) of a 4×4 SiPM (Hamamatsu S13360-3050PE) array (12×12 mm²) of approximately 300 ps FWHM with a power consumption of less than 100 mW. This front-end readout design enables the large-area SiPM array to achieve high-precision SPTR with low power consumption.

KEYWORDS: Neutrino detectors; Photon detectors for UV, visible and IR photons (solid-state); Front-end electronics for detector readout; Analogue electronic circuits

¹Corresponding author.

Contents

1	Introduction	1
2	SiPM array front-end readout scheme	2
3	Front-end readout electronics design	3
3.1	Pre-amplifier design	3
3.2	Series-parallel combination design	4
3.3	Multi-channel summing circuit design	5
4	SPTR measurements	6
5	Conclusions	9

1 Introduction

High-energy neutrinos from astrophysical sources, due to their small weak interaction cross section, can travel almost undisturbedly to Earth and directly point back to their sources. TRopIcal DEep-sea Neutrino Telescope (TRIDENT) is a next-generation neutrino telescope planned to be constructed in the South China Sea [1]. As a prospective development direction, neutrino telescopes require improved angular resolution to more precisely detect and locate astrophysical neutrino sources [2]. Improving angular resolution can be achieved with superior time resolution for neutrino telescopes since they reconstruct neutrinos' information by detecting the Cherenkov light produced by secondary charged particles generated after weak interactions. However, photomultiplier tubes (PMTs), commonly employed as photodetectors in neutrino telescopes, typically have a transit time (TT) on the order of tens of nanoseconds and the transit time spread (TTS) at the nanosecond level. To enhance time resolution, TRIDENT is currently exploring the feasibility of incorporating fast-response silicon photomultipliers (SiPMs), into its detection units, namely hybrid Optical Digital Modules (hDOMs) [3, 4]. SiPM, with a sub-nanosecond single photon time resolution (SPTR), is a solid-state semiconductor photodetector composed of thousands of micro cells capable of detecting single photons [5, 6]. With its compact size, ease of integration, and low operating voltage, SiPM is increasingly being employed in the field of single-photon detection, such as time-of-flight positron emission tomography (TOF-PET) and calorimeters [7, 8].

TRIDENT plans to construct about 1200 strings following a Penrose tiling distribution with a horizontal distance between two adjacent strings of 70 m or 110 m, and each string contains 20 hDOMs with a vertical distance between two hDOMs of 30 m [1]. hDOM can only receive a few photons with the photon number mostly at the single-photon level because Cherenkov light has a low light yield and attenuates significantly in seawater over long distances. To improve detection efficiency, the hDOM intends to comprise 24 SiPM arrays in addition to 31 PMTs, where PMTs

have a large photon collection area and SiPM arrays exhibit high-precision time resolution [3]. The SiPM array is aimed at achieving a detection area on the order of square centimeters and a SPTR at the order of hundreds of picoseconds to enhance the effective area and time resolution of hDOM and improve the angular resolution of the neutrino telescope.

The requirements of hDOM for SiPMs are unique, namely focusing on the single photon time resolution in large detection areas. SiPMs are usually coupled with scintillators to construct energy calorimeters for energy measurements in numerous particle physics experiments, which primarily rely on the charge resolution performance of SiPMs with relatively lower demands on the time resolution [8]. Compared to commonly used scintillators that generate plenty of photons, the number of Cherenkov photons is very small and the Cherenkov light yield is typically only one percent of scintillators. In addition, increasing the detection area cannot be achieved mainly by increasing the number of readout channels, because that would require hundreds or thousands of channels in one hDOM, posing significant challenges in terms of space, power consumption, data transmission bandwidth, and other factors. As a result, SiPM requires a large detection area on one readout channel and performs time measurements at the single-photon level.

However, the increased area will seriously affect the time resolution of SiPMs due to the increase in parasitic capacitance. For instance, a typical SPTR full width at half maximum (FWHM) result for a SiPM with a size of $1 \times 1 \text{ mm}^2$ is approximately 80 ps, whereas this value for a size of $3 \times 3 \text{ mm}^2$ can be around 180 ps [9]. Moreover, there are presently rare instances that have achieved the SPTR in the order of hundreds of picoseconds for large-area SiPMs at the square centimeter scale. As a result, currently, there are few examples where SiPMs are utilized for single photon time measurements, particularly in the context of large-area SiPM arrays. Furthermore, due to the large number of hDOMs in TRIDENT, it is essential to minimize the power consumption of hDOM, which poses a requirement for low power consumption in front-end readout electronics.

Focusing on high-precision time measurements based on large-area SiPM arrays, we analyze the existing challenges and propose an overall front-end readout scheme in section 2. In section 3, we propose the design of the front-end readout electronics for the SiPM array, including the pre-amplifier design scheme and the construction of large-area SiPM arrays. Additionally, we present the experimental setup and results of the SPTR measurements in section 4.

2 SiPM array front-end readout scheme

As mentioned in section 1, the primary challenge in the front-end readout of the SiPM array is maintaining its high-precision time measurement capability while constructing large-area SiPM array in one readout channel, which mainly involves the following aspects [4]. Initially, the pre-amplifier is required to have not only low noise and low power consumption but also a sufficiently high bandwidth to handle the high-speed leading edge signals from the SiPM, where the SiPM (Hamamatsu S13360-3050PE) exhibits a rapid rise time at around 1 ns [10]. The rise time and signal-to-noise ratio (SNR) of the waveform will directly influence the uncertainty of the time measurement results, as the timing scheme for SiPM arrays in hDOM involves a leading edge threshold trigger method [11]. Furthermore, to increase the detection area on one channel, it is necessary to combine multiple SiPMs with a size of such as $3 \times 3 \text{ mm}^2$ to a pre-amplifier, because it is improper to config one amplifier to each SiPM under the compact space and limited

power consumption constraints of hDOM. However, connecting SiPMs in parallel increases the total capacitance, leading to a reduction in signal amplitude, an increase in the rise time and fall time of the waveform, and ultimately a decrease in the SNR [12]. This is also the reason why directly choosing large-area SiPMs is not feasible, as SiPMs themselves are constructed with cells in parallel. Moreover, for the series connection scheme, the main issue is the variation in signal path lengths among each SiPM in the series, leading to time deviations that finally contribute to the total SPTR. For example, for the S13360-3050PE with an overall size of about 4 mm, this could lead to a time deviation of 20 ps between the signals of two SiPMs in series on the print circuit board (PCB). Therefore, constructing a large-area SiPM array involves a combination of series and parallel connection [13]. Additionally, the outputs of multiple series-parallel channels can be summed to further expand the detection area on one readout channel.

The front-end readout electronics design for the SiPM array includes three aspects that are detailed in section 3: high-bandwidth, low-noise and low-power pre-amplifier design; series-parallel combination array design; and multi-channel analog summing circuit design.

3 Front-end readout electronics design

3.1 Pre-amplifier design

The primary requirements for pre-amplifiers in the SiPM front-end readout of hDOM are high bandwidth, low noise, and low power consumption. For a rapid rise time of 1 ns corresponding to a bandwidth of 350 MHz, some commonly used front-end amplification schemes for photodiodes, such as transimpedance amplifiers (TIA), are not optimal for these requirements because their bandwidth is limited and the power consumption of a high-speed operational amplifier is high. However, compared to operational amplifiers, radio frequency (RF) amplifiers generally offer a high bandwidth, making them suitable for the readout of high-speed signals. Additionally, there are some techniques for reducing the effective capacitance of the detector, such as the bootstrap transimpedance amplifiers that apply bootstrapping to maintain zero AC voltage on the detector's capacitor and thereby reduce the input capacitance of TIA [14]. The amplifier-based bootstrap designs may introduce stability and power consumption issues, whereas some transformer-based bootstrap schemes can be more suitable for our requirements [15, 16].

Therefore, we design a high-speed pre-amplifier suitable for SiPMs readout in time measurements, as illustrated in figure 1. The pre-amplifier is designed based on a BGA2803 RF amplifier, which not only offers a bandwidth of approximately 2 GHz, a gain of 23.5 dB, and a noise figure of 3.6 dB but also features low power consumption with each channel consuming less than 20 mW [17, 18]. The balun transformer (MABA-007159) has a turn ratio of 1:1 and an impedance of 50 Ω matching the input impedance of the RF amplifier [19]. The balanced side of the balun transformer is used for inputting the signal from the SiPM, and the unbalanced side is used to output the converted voltage signal to the RF amplifier. The differential configuration at the balanced end of the balun transformer helps reduce the common-mode noise on the SiPM.

In order to directly demonstrate the effect of the transformer, we measure the waveforms under configurations with and without the transformer. In the configuration without the transformer, the SiPM (S13360-3050PE) is grounded through a 50 Ω resistor, and the voltage signal on this resistor

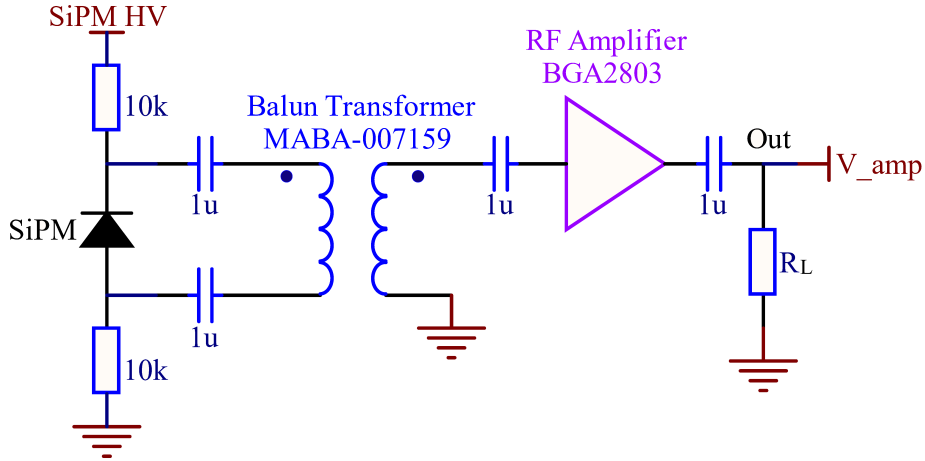


Figure 1. Schematic of the pre-amplifier circuit for SiPMs. These capacitors are used for AC coupling such as isolating the DC level of the RF amplifier.

is subsequently amplified by the RF amplifier. The root mean square (RMS) value of the amplified signal's baseline noise without the transformer is about 0.7 mV, while this value reduces to around 0.3 mV for the configuration equipped with the transformer and the signal amplitude remains about the same.

3.2 Series-parallel combination design

In order to increase the detection area and alleviate the pressure on the number of channels, power consumption, and space limitation in hDOM, several SiPMs are required to connect to one pre-amplifier. For the commonly used parallel connection scheme, the main disadvantage is that the increased capacitance will decrease the signal's amplitude and increase the rise and fall time. But the series connection can partially mitigate these effects because it possesses a function similar to high-pass filtering to reduce the signal's rise and fall time. Therefore, the series-parallel combination design scheme is illustrated in figure 2. In the series connection, it is necessary to design a voltage divider for each individual SiPM, and a commonly used method is using voltage divider resistors. The series-parallel combination SiPM array is subsequently connected with the pre-amplifier, replacing the single SiPM in figure 1.

There exist two primary factors influencing the timing performance in this design. Firstly, as mentioned in section 2, the series connection introduces differences in signal path lengths. In a series, the pulsed current signal from one SiPM must pass through others, resulting in fixed deviations in the path lengths from different SiPMs to the pre-amplifier. For S13360-3050PE, the deviation is about 4 mm for each SiPM, resulting in a fixed time deviation of about 20 ps, which directly contributes to the uncertainty in the overall time response of the SiPM array. Secondly, all SiPMs on this series-parallel array will receive the same bias voltage, but due to inherent variations in their breakdown voltages, there will be differences in overvoltage. This can lead to variations in gain, introducing deviations in signal amplitude and resulting in time walk effects in time measurements. Estimating its impact, consider a simple waveform in the linear form $U(t) = t \cdot V/T$, where V is the peak value and T is the time to rise from zero to the peak. The trigger time at which

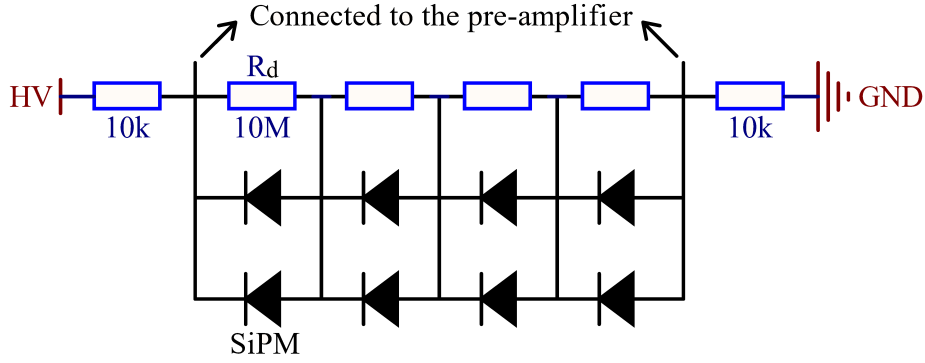


Figure 2. Schematic of series-parallel combination SiPM array. It shows the configuration of four SiPMs in series and two series in parallel, where R_d is the voltage divider resistor with a typical value of 10 M Ω .

the waveform reaches the threshold V_{th} is given by $t = T \cdot V_{th}/V$. If V has a small variation ΔV , the variation in trigger time is $\Delta t \approx T \cdot \frac{\Delta V}{V} \cdot \frac{V_{th}}{V}$. Assuming $T = 1ns$, $\frac{\Delta V}{V} = 1/10$ and $\frac{V_{th}}{V} = 1/2$, the calculated result yields $\Delta t \approx 50ps$. The standard deviation of breakdown voltages is about 0.4 V for 20,000 pieces of SiPMs (S13360-3050PE) manufactured by Hamamatsu, which means that the $\frac{\Delta V}{V}$ is less than 1/10 when the average overvoltage exceeds 4 V. Alleviating this effect can be achieved by selecting SiPMs with similar characteristics such as breakdown voltage and connecting them to the same series-parallel SiPM array, which can be conveniently done using the test data provided by the manufacturer. Additionally, increasing the bias voltage or reducing the threshold voltage can also mitigate this impact.

3.3 Multi-channel summing circuit design

The number of SiPMs that can be combined into a series-parallel array is limited by the capacitance introduced in parallel and the signal path differences introduced in the series. To further increase the number of SiPMs on one channel, multiple series-parallel channels can be integrated through an analog summing circuit, as shown in figure 3. Two series-parallel channels are summed to one readout channel, each combined by a pre-amplifier and a series-parallel combination SiPM array with four SiPMs in series and two series in parallel, resulting in a total of sixteen SiPMs.

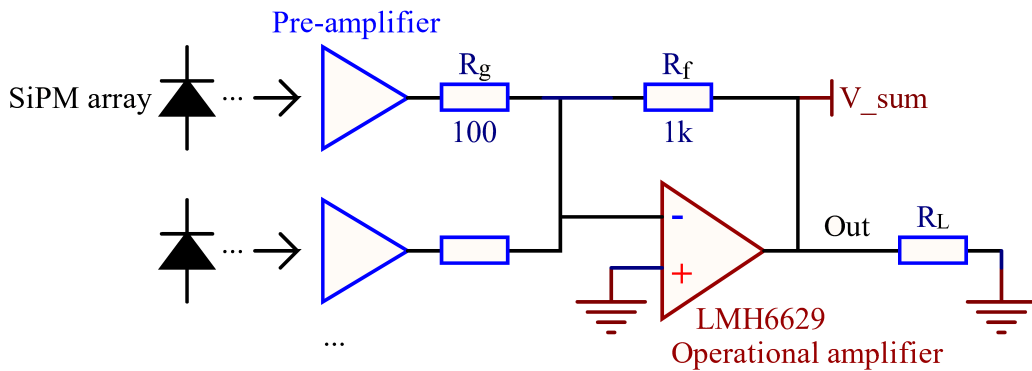


Figure 3. Schematic of multi-channel summing circuit design. It shows the summation of two series-parallel channels and additional channels can be appended in a similar way.

The number of input channels is primarily limited by the decrease in bandwidth and SNR of the summing circuit. The summing circuit is designed based on an LMH6629 operational amplifier, which features a gain bandwidth product (GBP) of 4 GHz and a minimum stable gain of 10 V/V [20]. In order to increase the phase margin and improve the loop stability, we set the gain of each input channel to $R_f/R_g = 10$ V/V, resulting in a noise gain of 21 V/V and a bandwidth of approximately 200 MHz. For an input channel number of N , the baseline noise after summation will be amplified by a factor of $\sqrt{N} * R_f/R_g$, leading to a decrease of SNR by a factor of $1/\sqrt{N}$. For instance, the SNR of the summing of four input series-parallel channels will be half that of one input channel. Additionally, the LMH6629 has a power consumption of less than 60 mW, so the overall power consumption of the front-end readout for 4*4 SiPMs is below 100 mW.

4 SPTR measurements

The test setup of SPTR measurement is illustrated on the left side of figure 4, primarily involving a narrow pulsed light source, SiPMs with their front-end readout electronics, and an oscilloscope. The light source emits two signals. One signal is the pulsed light that undergoes diffusion, attenuates to the single-photon level, and is ultimately received by SiPMs. The signal from SiPMs is processed by the front-end readout electronics described in section 3 and is subsequently output to the oscilloscope for further data analysis. The other signal is an electrical signal synchronized with the light signal, directly output to the oscilloscope as the reference of photons' arrival time.

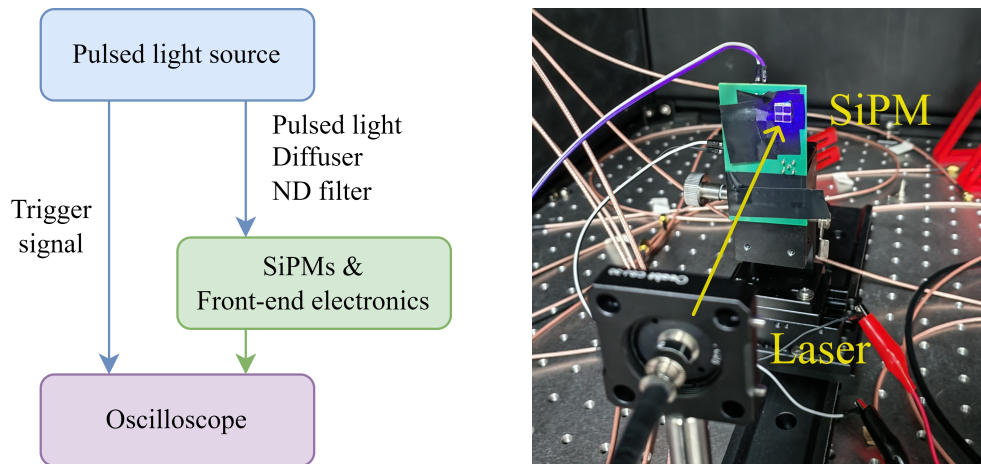


Figure 4. Left: The flowchart of SPTR measurement. Right: A picture of the setup for SPTR measurement experiment, where a 2×2 SiPM array with a configuration of two SiPMs in series and two series in parallel is utilized.

A photo of the experiment setup is shown on the right side of figure 4. The time duration of the pulsed light needs to be much smaller than the SPTR of SiPMs, thereby a 405 nm picosecond laser (Taiko PDL M1 LDH-IB-405-B) with a pulse width FWHM of less than 50 ps is used as the light source. Moreover, diffusers and neutral density (ND) filters are utilized to diffuse and attenuate the light pulses. The oscilloscope (TELEDYNE LECROY WavePro 254HD) provides a 20 GS/s sampling rate with 2.5 GHz bandwidth and 12-bit resolution.

The timing method used for data analysis involves fixed threshold triggering of the leading edge, which is consistent with the timing approach of hDOM, i.e., triggering using high-speed comparators. An example of waveforms for the pre-amplifier output from a SiPM is illustrated in figure 5, and it is easy to distinguish the baseline, single-photon, and double-photon events. The trigger time is searched within a pre-selected relatively narrow time window, such as from 10 ns to 20 ns in this figure, to minimize the ratio of dark noise events. Additionally, linear interpolation is employed here to obtain a more refined result using the upper and lower points around the threshold, reducing the impact of the limited sampling rate of the oscilloscope. As a result, the distribution of the relative trigger time and the signal amplitude is presented in the figure 6, where the threshold voltage is 1.5 mV and the photon number is represented by the signal amplitude. Applying a Gaussian fitting to the relative trigger time distribution within the single-photon region, a SPTR FWHM of approximately 200 ps can be obtained.

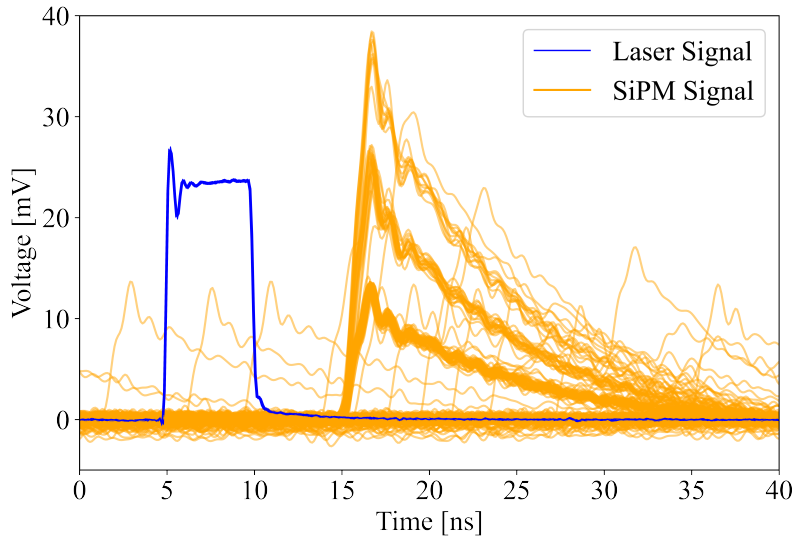


Figure 5. An example of 200 waveforms, where the SiPM is operated at 60 V bias voltage, and its signal is processed by the pre-amplifier. For ease of observation, the amplitude of the synchronized signal from the laser is scaled down to 1/40 and the timeline has been shifted.

The performance of the SiPM is closely related to the overvoltage, while a higher overvoltage leads to a higher gain but also results in a higher DCR. To investigate the impact of overvoltage on SPTR and determine the appropriate operating voltage, we test the SPTR of SiPMs at different operating voltages. The test result is shown in figure 7, where the breakdown voltage can be obtained by linear fitting using the signal amplitudes at different bias voltages. Since the SPTR measurement results vary at different threshold voltages, the best SPTR results are obtained by scanning the threshold voltages. It can be observed from this graph that the SPTR measurement results stabilize at around 200 ps when the overvoltage exceeds 5 V.

Using the experiment and analysis methods described before, we tested the SPTRs of the SiPMs under three configurations, as shown in table 1. According to the results in figure 7, each SiPM is operated at 60 V bias voltage to reduce the differences in the time performance among different SiPMs and alleviate the effects of time walk described in section 3. The 2×2 SiPM array

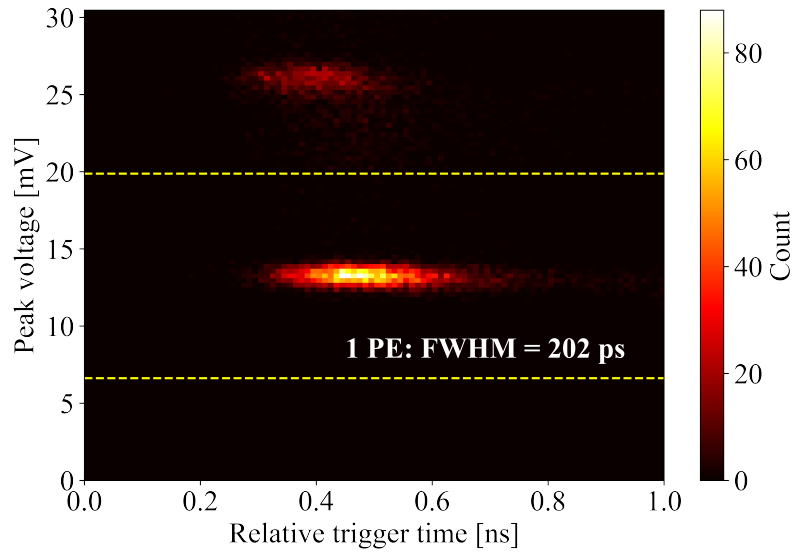


Figure 6. The distribution of the relative trigger time and the signal amplitude of a SiPM operating at 60 V bias voltage. The relative trigger time is the relative delay from when the laser signal is triggered, namely when the leading edge reaches the threshold, to when the SiPM signal is triggered.

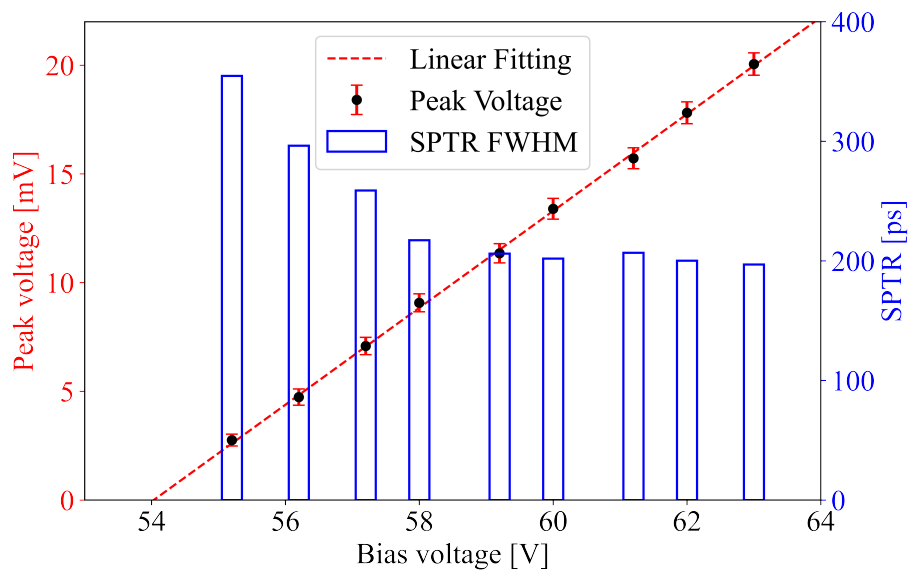


Figure 7. The signal amplitudes and SPTRs of a SiPM operating at different bias voltages. The breakdown voltage can be found to be about 54 V by linear fitting.

is constructed with a series-parallel combination SiPM array, with two SiPMs in series and two series in parallel, along with a pre-amplifier. The power consumption of the 2×2 SiPM array is similar to that of a single piece because they are both equipped with a pre-amplifier, which is the main source of power consumption. Moreover, the 4×4 SiPM array is a summing output of two series-parallel channels, with each series-parallel array configured as four SiPMs in series and two series in parallel. The operating voltages of the 2×2 SiPM array and 4×4 SiPM array are 120 V and 240 V, respectively. For the 4×4 SiPM array that has a detection area of $12 \times 12 \text{ mm}^2$, we obtain a SPTR of about 300 ps with an overall power consumption of less than 100 mW. Two photos of the 4×4 SiPM array are shown in figure 8.

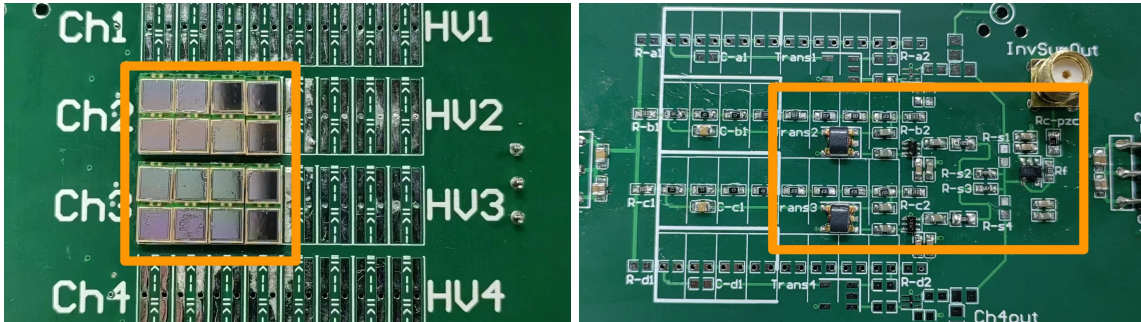


Figure 8. Photos of the 4×4 SiPM array. This board is used to test the performance of SiPM arrays in different configurations, so there are some extra pads.

Table 1. Results of SPTR measurements, with each SiPM operating at 60 V bias voltage. The capacitance of a SiPM (S13360-3050PE) is approximately 320 pF.

SiPM quantity	Detection area	Power consumption	SPTR FWHM
A single piece	$3 \times 3 \text{ mm}^2$	< 20 mW	$\approx 200 \text{ ps}$
A 2×2 SiPM array	$6 \times 6 \text{ mm}^2$	< 20 mW	$\approx 240 \text{ ps}$
A 4×4 SiPM array	$12 \times 12 \text{ mm}^2$	< 100 mW	$\approx 300 \text{ ps}$

5 Conclusions

TRIDENT is exploring the improvement of angular resolution by employing SiPMs with superior time resolution performance in its detection units (hDOM). In this article, we analyzed the challenges in the front-end readout of large-area SiPM arrays for hDOM and explained that the primary challenge is achieving a high-precision SPTR while increasing the area of the SiPM array. We designed a high-speed, low-noise, and low-power pre-amplifier based on a balun transformer and RF amplifier to deal with the rapid signal of SiPMs for high-precision SPTR measurements. In addition, we also designed a series-parallel combination SiPM array scheme and a multi-channel summing circuit to construct a large-area SiPM array on one readout channel. Finally, we conducted tests on the SPTR of SiPMs and obtained the single photon time resolution of a 4×4 SiPM array ($12 \times 12 \text{ mm}^2$) of approximately 300 ps FWHM with a power consumption of less than 100 mW.

Acknowledgments

We thank Jun Guo, Hualin Mei, Yong Yang, Wei Tian, Fuyudi Zhang, Jingtao Huang and Qichao Chang for their help to improve this paper. This work was sponsored by the Ministry of Science and Technology of China (No. 2022YFA1605500), Shanghai Pilot Program for Basic Research — Shanghai Jiao Tong University (No. 21TQ1400218), Yangyang Development Fund, Office of Science and Technology, Shanghai Municipal Government (No. 22JC1410100), Shanghai Jiao Tong University under the Double First Class startup fund and the Foresight grants (No. 21X010202013) and (No. 21X010200816).

References

- [1] Z.P. Ye, F. Hu and W. Tian et al., *A multi-cubic-kilometre neutrino telescope in the western pacific ocean*, *Nature Astronomy* **7** (2023) 1497.
- [2] K. Fang, K. Kotera, M. Miller, K. Murase and F. Oikonomou, *Identifying ultrahigh-energy cosmic-ray accelerators with future ultrahigh-energy neutrino detectors*, *Journal of Cosmology and Astroparticle Physics* **2016** (2016) .
- [3] F. Hu, Z. Li and D. Xu, *Exploring a pmt+sipm hybrid optical module for next generation neutrino telescopes*, in *Proceedings of 37th International Cosmic Ray Conference — PoS(ICRC2021)*, ICRC2021, Sissa Medialab, July, 2021, DOI.
- [4] W. Zhi, J. Zheng and W. Tian et al., *Preliminary Design of the Hybrid Digital Optical Module for TRIDENT*, *PoS ICRC2023* (2023) 1213.
- [5] H. Photonics, *A technical guide to silicon photomultipliers*, Tech. Rep. <https://hub.hamamatsu.com/us/en/technical-notes/mppc-sipms/a-technical-guide-to-silicon-photomultipliers-MPPC-overview.html>, Hamamatsu Photonics, Hamamatsu City, Japan (2018).
- [6] S. Gundacker, F. Acerbi, E. Auffray, A. Ferri, A. Gola, M. Nemallapudi et al., *State of the art timing in tof-pet detectors with luag, gagg and l(y)so scintillators of various sizes coupled to fbk-sipms*, *Journal of Instrumentation* **11** (2016) P08008.
- [7] H. Park, M. Yi and J.S. Lee, *Silicon photomultiplier signal readout and multiplexing techniques for positron emission tomography: a review*, *Biomedical Engineering Letters* **12** (2022) 263.
- [8] F. Simon, *Silicon photomultipliers in particle and nuclear physics*, *Nuclear Instruments and Methods in Physics Research Section A: Accelerators, Spectrometers, Detectors and Associated Equipment* **926** (2019) 85.
- [9] F. Acerbi, A. Ferri, A. Gola, M. Cazzanelli, L. Pavesi, N. Zorzi et al., *Characterization of single-photon time resolution: From single spad to silicon photomultiplier*, *IEEE Transactions on Nuclear Science* **61** (2014) 2678.
- [10] H.P. K.K., *MPPC S13360 series*.
- [11] F. Acerbi, A. Ferri, A. Gola, N. Zorzi and C. Piemonte, *Analysis of single-photon time resolution of fbk silicon photomultipliers*, *Nuclear Instruments and Methods in Physics Research Section A: Accelerators, Spectrometers, Detectors and Associated Equipment* **787** (2015) 34.
- [12] D. Marano, M. Belluso, G. Bonanno, S. Billotta, A. Grillo, S. Garozzo et al., *Silicon photomultipliers electrical model extensive analytical analysis*, *IEEE Transactions on Nuclear Science* **61** (2014) 23.

- [13] M. D’Incecco, C. Galbiati, G.K. Giovanetti, G. Korga, X. Li, A. Mandarano et al., *Development of a novel single-channel, 24 cm², sipm-based, cryogenic photodetector*, *IEEE Transactions on Nuclear Science* **65** (2018) 591.
- [14] M. Abraham, *Design of butterworth-type transimpedance and, bootstrap-transimpedance preamplifiers for fiber-optic receivers*, *IEEE Transactions on Circuits and Systems* **29** (1982) 375.
- [15] N. Zhang and M.J. Schmand, “Bootstrapping readout for large terminal capacitance analog-sipm based time-of-flight pet detector.”
<https://patents.google.com/patent/US20160327657A1/en>, 2016.
- [16] J.W. Cates, S. Gundacker, E. Auffray, P. Lecoq and C.S. Levin, *Improved single photon time resolution for analog sipms with front end readout that reduces influence of electronic noise*, *Physics in Medicine & Biology* **63** (2018) 185022.
- [17] M. Krake, V. Nadig, V. Schulz and S. Gundacker, *Power-efficient high-frequency readout concepts of sipms for tof-pet and hep*, *Nuclear Instruments and Methods in Physics Research Section A: Accelerators, Spectrometers, Detectors and Associated Equipment* **1039** (2022) 167032.
- [18] N.S. N.V., *BGA2803 MMIC wideband amplifier*.
- [19] M.T.S. Inc., *MABA-007159-000000*.
- [20] T. Instruments, *LMH6629 Ultra-Low Noise, High-Speed Operational Amplifier with Shutdown*.

Numerical simulation of charging up, accumulation of space charge and formation of discharges

Purba Bhattacharya^a, Promita Roy^b, Tanay Dey^c, Jaydeep Datta^d, Prasant K. Rout^e, Nayana Majumdar^f, Supratik Mukhopadhyay^g

^aDepartment of Physics, School of Basic and Applied Sciences, Adamas University, Kolkata, India

^bDepartment of Physics, , Virginia Polytechnic Institute & State University, VA, United States

^cSchool of Physical Sciences, National Institute for Science Education and Research, Jatni, Khurda, Odisha, India

^dCenter for Frontiers in Nuclear Science, Department of Physics and Astronomy, Stony Brook University, 100 Nicolls Road, Stony Brook, New York, 11794, USA

^eNational Central University, Taoyuan City, Taiwan

^fApplied Nuclear Physics Division, Saha Institute of Nuclear Physics, Kolkata, India

^gRetired from Applied Nuclear Physics Division, Saha Institute of Nuclear Physics, Kolkata, India

Abstract

Aging and stability of gaseous ionization detectors are intricately related to charging up, accumulation of space charge and formation of discharges. All these phenomena, in their turn, depend on the dynamics of charged particles within the device. Because of the large number of particles involved and their complex interactions, the dynamic processes of generation and loss of charged particles, and their transport within the detector volume are extremely expensive to simulate numerically. In this work, we propose and evaluate possible algorithms / approaches that show some promise in relation to the above-mentioned problems. Several important ionization detectors having parallel plate configurations, such as GEM, Micromegas, RPCs and THGEMs, are considered for this purpose. Information related to primary ionization is obtained from HEED, while all the transport properties are evaluated using MAGBOLTZ. The transport dynamics have been followed using two different approaches. In one, particle description using neBEM-Garfield++ combination has been used. For this purpose, the neBEM solver has been significantly improved such that perturbations due to the charged particles present within the device are considered while estimating electric field. In the other approach, the transport is simulated following hydrodynamic model using COMSOL during which the electric field is also provided by COMSOL where it is easy to set up space charge effects. A comparison between these possible approaches will be presented. Effect of different simulation parameters will also be demonstrated using simple examples.

Keywords: Gaseous detector, Aging, Stability, Space charge, Charging up, Discharge, Simulation,

1. Introduction

Charging up is a phenomena commonly observed in gaseous detectors having dielectric materials exposed to the active volume of gas mixture where primaries and secondaries are generated, and electron multiplication occurs. They can affect long-term stability of a detector and lead to response non-uniformity [1]. Space charge accumulation occurs in gaseous detectors due to the presence of charged

particles within the active gas volume before they are collected at suitable electrodes. Existence of space charge can distort the applied electric field configuration, make detector response non-uniform and unstable, and has the potential to lead to discharges [2], affecting detector performance significantly. Besides making a detector lose its stability in the immediate time scale, formation of discharges has the capability of accelerating detector aging and damaging it for good. Thus, it is important to understand these phenomena using both experimental and numerical tools. However, these topics, and the associated discharge formation process, are com-

Email address: purba.bhattacharya85@gmail.com
(Purba Bhattacharya)

plex and vast. As a result, it is difficult to build satisfactory numerical models for these phenomena because large number of charged particles, as well as different length and time scales, are involved.

In recent times, there have been a number of simulation attempts to improve the understanding of these processes. For example, charging up for GEMs and Thick GEMs (ThGEM) have been studied in [3] using the Garfield++ framework [4] (C++ version of Garfield) in conjunction with ANSYS [5] and COMSOL [6] as commercially available Finite Element Method (FEM) field solvers. Similarly, space charge problems have been investigated in [2, 7, 8, 9, 10, 11]. For these investigations, parallelization attempts have yielded significant advancements for particle models [7, 8, 11]. Similarly, interesting developments in fluid models (initially proposed in [12] and extended in [13]) have been carried out in [2, 9, 10].

In the present brief paper, an attempt will be made to only discuss recent developments of few numerical tools currently available to address these problems and their performance in some typical scenarios. In particular, extension of existing neBEM [14] field-solver to improve particle-based models will be discussed. Advancement of existing hydrodynamic models [2, 9] to include effects of additional physics phenomena like charging up will also be touched upon. A comparison between particle and hydrodynamic models will finally be carried out and likely future developments will be outlined.

The particle and fluid numerical models are discussed in section 2. The simulation implementation is detailed in section 3. The results obtained are described and analyzed in section 4, followed by the concluding remarks in section 5.

2. Numerical models

HEED [16] has been used for primary-ionization calculations and Magboltz [15] to estimate drift, diffusion as well as Townsend and attachment coefficients from within Garfield++. Using primary ionization data and the knowledge of different transport, multiplication and attachment coefficients, both particle and fluid models have been used to model transport of charged particles within Gas Electron Multiplier (GEM) [17] and Resistive Plate Chamber (RPC) [18] detectors. Recent developments in neBEM has allowed estimation of effects due to charging up and space charge accumulation

from the perspective of a particle model. COMSOL on the other hand, has been used to simulate the charged particle dynamics using a fluid description. While space-charge effects are automatically included in the fluid model, charging up effects have additionally been included within the computation.

2.1. neBEM improvements

It may be mentioned here that neBEM discretizes any given geometry into a large number of small elements. The initial device, set up using the Garfield++ interface, is represented as made up of a number of primitives (rectangles and right triangles) which, in their turn, are subdivided into small elements that are once again rectangle and right triangles. When a charged particle gets deposited on an element that has dielectric properties, the charge gets attached to that surface for a long time, rather than being transported out of the detector by conducting electrodes. These locations can be obtained from Garfield++ and they can be directly used if we want to consider each charge individually. In this case, the “end point” in the fig.1 will be the charge location. However, if we have a large number of charged particles, this approach can be computationally very expensive. A less demanding way can be to assign a surface charge density on the elements that collect the charges. The way the element collecting a charge can be found has been indicated in figure 1.

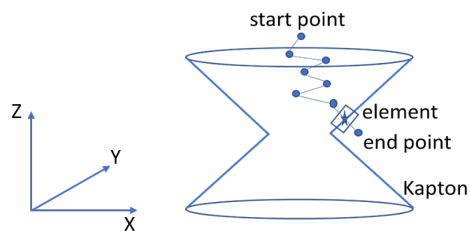


Figure 1: Identification of deposition location of a charged particle on the Kapton surface of a GEM hole.

Besides adding the capability of handling charging up effects, neBEM has also been improved to handle effect due to accumulation of charges within detector volume. Once again, direct computation of influence of each charge is computationally expensive and different models have been implemented in the code to simplify computation. By adopting a suitable model, it is possible to represent the charges as they really are (point charges), as uniformly charged lines, as uniformly charged areas

and as volumes having equivalent point charges concentrated at the centroid. It should be mentioned here that different versions of volume representation can lead to different Particle-In-Cell (PIC) algorithms.

2.2. COMSOL improvements

For solving transport of charged fluids, the device geometry is created using COMSOL, an example of which is shown in fig.2(a). The surface charge accumulation occurs on the Kapton surface exposed to the gas mixture, as shown in fig.2(b). The process is governed by the following equations

$$\frac{\partial \rho_s}{\partial t} = \hat{n} \cdot \vec{J}_i + \hat{n} \cdot \vec{J}_e \quad (1)$$

$$-\hat{n} \cdot (\vec{D}_1 - \vec{D}_2) = \rho_s \quad (2)$$

where t is the time, \hat{n} is the unit normal vector, ρ_s is the surface charge density, \vec{J}_e and \vec{J}_i are the electronic and ionic current densities and \vec{D}_1, \vec{D}_2 are displacement currents.

As mentioned earlier, the fluid model automatically incorporates space-charge effects through the electrostatics Poisson equation

$$\nabla \cdot (\epsilon_0 \epsilon_r \vec{E}) = \rho_v \quad (3)$$

where ϵ represents electrical permittivity, \vec{E} is the electric field and ρ_v is the space charge density. For a given instant, the space charge density needs to be estimated throughout the detector volume as a function of space. The equations governing the entire physics processes are well-described in [9] and not being repeated here. It may be noted here that for the presented results, “physics governed” “normal” mesh has been used in COMSOL.

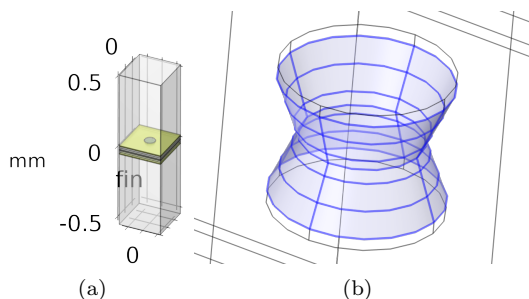


Figure 2: A schematic view of the (a) GEM detector and (b) GEM hole inner surface in COMSOL.

3. Implementation of numerical models

One single GEM-based detector and one RPC have been considered for the simulations presented in this paper. The single GEM has 70-50-70 μm bi-conical holes in copper clad Kapton foil of 50 μm . The holes are arranged in the usual hexagonal pattern 140 μm apart. The RPC, on the other hand, has a single gas gap of 2mm. It may be noted here that the gaseous mixture considered for all the results presented for GEM here is Ar-CO₂ mixed in 70:30 ratio at atmospheric pressure, and for RPC it is 97% Freon, 2.5% isobutane and 0.5% SF₆.

3.1. neBEM implementations

In order to observe the effect of radiation charging on an avalanche, we simulate the deposition of electrons and ions on Kapton surface of a GEM foil. The pattern of charge deposition due to one single event indicates that while electrons are found in both halves of the bi-conical GEM hole, ions are more localized (figures 3(a) and 3(b)). For this hole geometry, the ions are almost entirely found only in the GEM-half that faces the readout. Number of ions close to the middle of the GEM hole is larger in comparison to electrons. It is to be noted here that the pattern of charge deposition may change from event to event. There are several parameters that can affect charge deposition including geometry of the hole, electric field configuration, nature of the material etc. The case under consideration is one among many possibilities.

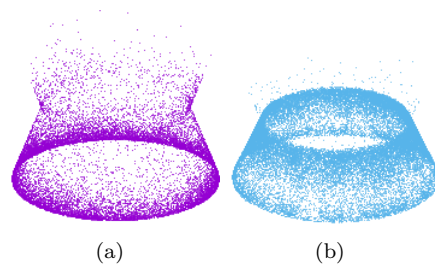


Figure 3: Deposition of charged particles on the inner surfaces of a single hole in a GEM foil (a) electrons and (b) ions.

The “end-point” locations have been used to compute charging up effects in one approach (termed as *algo 1*), while in the other approach, charge deposited on each element has been computed (termed as *algo 2*) to find out the effect.

Similarly, following the trajectory of each charged particle in Garfield++, it is possible to find out the

space charge configuration at any given instant. As indicated in section 2, the locations of the charged particles can be used to set up a point, line, area or volume representation, as appropriate for a given problem.

3.2. COMSOL implementations

For surface charge accumulation at a given position on a dielectric material, the difference between electron and ion currents was computed (eq. 1). For space charge density ρ_v in eq. 3, the difference between the number of electrons and ions per unit volume was considered. The effects of surface charge density and space charge density were incorporated within the solution process by invoking multiphysics options, where necessary. In order to simulate effects due to the accumulation of surface charge over a large number of events, charge density values obtained for one event were multiplied by 100.

4. Results and discussions

4.1. Charging up effects

4.1.1. Single event

Here, we have compared E_z and E_x for a) surface charge represented by *algo 1*, b) surface charge represented by *algo 2*, and c) without any surface charge. Since we are using only around 10^4 charged particles for this computation, the effect of charging up is not pronounced in the E_z component. In E_x , there is perceptible difference among the values, although the overall magnitude in this case is small in comparison to E_z . The maximum surface charge density, as estimated by *algo 2*, on an element in the present case is around $10^{-7} C/m^2$. This small charge density, which is due to only one single event, is unable to have a pronounced effect on important parameters such as gain. Please note that the coordinate system has been indicated in figure 1.

In order to cross-check the estimates of the particle approach, and also to evaluate the possibility of hydrodynamic modeling, we have simulated the dynamics of charge deposition on Kapton surface of a GEM hole for a similar event that was used in the particle model. It may be noted that, due to the very nature of modeling mathematics, the events can only be made similar, but not identical. The deposition of charge with time at various locations on the Kapton surface (one of the points is

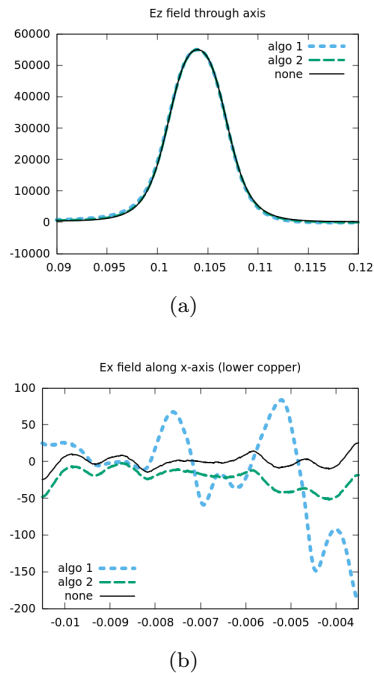


Figure 4: Electric field variations due to charging up in a GEM-based detector using *algo1*, *algo2* and no charging up *none*: (a) E_z field along hole axis and (b) E_x field variation along an X-line across GEM hole facing readout electrode.

indicated as a red dot in fig.5(a)) is presented in fig.5(b).

It can be seen that much negative charge deposition occurs close to the hole outlet facing the readout, as was also observed in the particle model. The maximum surface charge density is similar to that estimated by *algo 2* in the particle model ($\approx 50 \times 10^{-8} C/m^2$) and it has been confirmed by further calculations that there is hardly any effect on gain.

4.1.2. Charge accumulation over number of events

Charges get deposited on Kapton surface for a large number of events before they start getting attached, or lost to a conductor. In order to include the effects due to a large number of events, surface charge densities on Kapton surface equivalent to hundred times more than that estimated for a single event were specified. Long-term charging up effects could, thus, be simulated in an approximate manner. By this approach, keeping every other parameter unchanged, we could see that the gain has turned out to be as high as 1000 in contrast to 30 when no surface charge effects were considered.

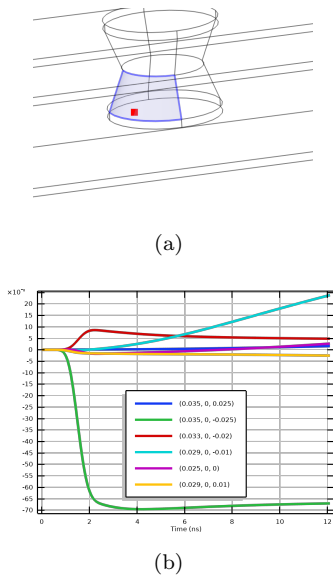


Figure 5: Use of COMSOL to estimate charging up effects in a GEM-based detector: (a) A typical location on the Kapton inner surface where surface charge accumulation is estimated, and (b) surface charge accumulation over time at various locations on the Kapton inner surface.

At this detector configuration, this large increase in gain seems to be indicative of the major effect that charging up has on detector response. However, further detailed studies are necessary before it is possible to conclude on this topic.

4.2. Space-charge effects

Modification of electric field in a GEM-based detector has been estimated by using point, line and area representation of a given charged particle distribution. Similar field modification has been estimated by using the COMSOL fluid model. The field modifications estimated using different numerical models have been plotted in fig. 6.

As can be observed, while there is significant quantitative mismatch, qualitatively the variation pattern is the same for all particle and fluid models. The agreement between various particle models and the fluid model is particularly encouraging because the mathematical representation is quite different in these cases.

4.3. Formation of discharges

Transition from avalanche to streamer formation in RPCs and GEMs has been studied using particle and fluid models. OpenMP [19] parallelization of neBEM and Garfield++ has been implemented

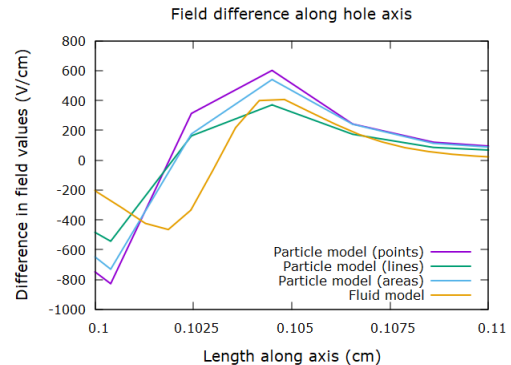


Figure 6: Estimation of space-charge effects in a GEM-based detector: Variation of E_z along hole axis using various particle models and the fluid model.

(details in [11]) to carry out the work in particle model. The strong effect of space charge in the estimation of transition from avalanche to streamer has been demonstrated in fig.7(a). In a particle model where the effect of space charge was ignored, the avalanche process seems to be unending, leading to the prediction of an unlikely streamer at an applied field of 50kV/cm. However, when space-charge effect is included, the avalanche process is found to be well-contained. It may be mentioned here that influence of negative ions on the electric field has also been found to be significant for these calculations [11]. Example of a streamer occurring in an RPC at 55kV/cm has been separately simulated using fluid model that automatically includes space charge effects, as shown in fig.7(b).

Similarly, occurrence of discharge within a GEM hole has been simulated using the fluid model, as shown in fig. 8(a). While the maximum applied field in this case was around 100kV/cm, the space charge effect increased the field to more than 250kV/cm, as shown in the figure. By repeating the computation over a large number of similar configurations, discharge probability for a single GEM has been estimated using the fluid model (details in [20]), as shown in fig. 8(b). Comparison with experimental results [21] shows that the discharge probability estimates agree with the experimental values in a qualitative manner.

5. Conclusion

In summary, it can be said that several capable models have been developed to simulate phenomena related to charging up, space charge and discharge

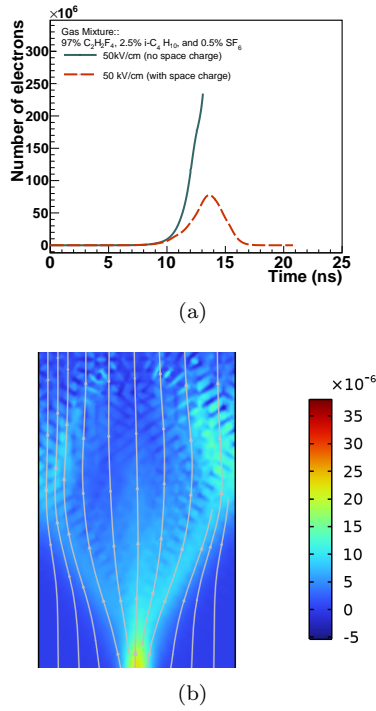


Figure 7: (a) Effect of space charge on avalanche formation in an RPC at 50kV/cm using particle model, (b) ion density distribution during streamer formation in an RPC at 55kV/cm using fluid model.

formation in a gaseous detector. These developments are already producing qualitatively acceptable results. As a result, it is possible to enrich our understanding of these phenomena using the numerical models. However, they need much further refinement before being generally applicable. For example, several possible representations are allowed for the particle model, but as yet there has been no attempt to optimize them for specific applications. Moreover, accumulation of effects over a large number of events has not been attempted, except at an *ad hoc* level.

Both particle and fluid approaches enjoy certain advantages and disadvantages over each other. While particle models are very realistic and it is easy to incorporate statistical fluctuations, they are computationally extremely expensive and may need drastic simplifications to be applicable under usual circumstances. Fluid models, on the other hand, are much less computationally demanding. However, they are usually less realistic and it may be difficult to include statistical fluctuations. Despite the inherent mathematical differences between the

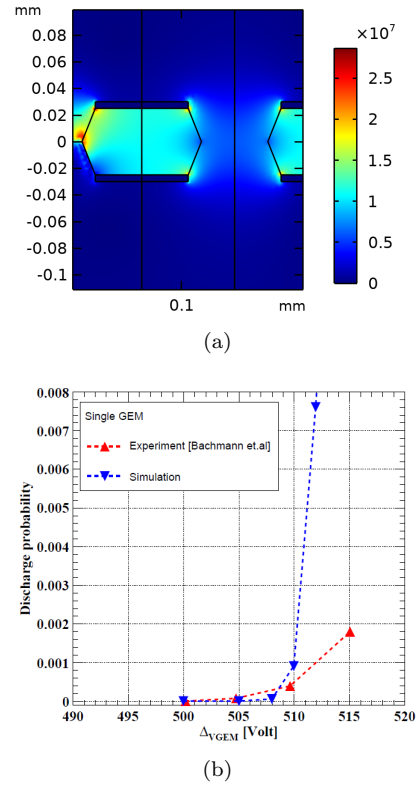


Figure 8: (a) Field distortion leading to streamer formation in a GEM hole, (b) estimation of streamer probability in a single GEM-based detector.

two approaches, predictions by both of them are found to be in general agreement, which is very encouraging.

6. Acknowledgment

We thank our respective Universities and Institutes for providing infrastructure necessary to carry out the research activities. Part of this research has been performed in the framework of RD51 collaboration. We wish to acknowledge the members of the RD51 collaboration for their help and suggestions, especially Dr. R. Veenhof and Dr. H. Schindler for their valuable comments. This research was supported in part by the SERB research grant SRG/2022/000531. Author Dr. P. Bhattacharya acknowledges the Science and Engineering Research Board and SRG scheme for the necessary support.

References

- [1] V. Kumar et al., Jour. Instr., 16 (2021) P01038.

- [2] P.K. Rout et al., Jour. Instr., 16 (2021) P02018.
- [3] Correira et al., Jour. Instr. 9 (2014) P07025
- [4] R. Veenhof, Nucl. Instr. A 419 (1998) 726.
- [5] www.ansys.com
- [6] www.comsol.com
- [7] A. Sheharyar and O. Bouhali, Jour. of Phys.: Conf Series 898 (2017) 072033.
- [8] S. Salvador, 3rd workshop on Gas-filled Detectors and Systems, 24 Jan 2019.
- [9] J. Datta et al., Jour. of Instr., 16 (2021) P07012.
- [10] Promita NIM A paper on space charge
- [11] T. Dey et al., Comp. Phys. Comm., 294 (2024) 108944.
- [12] P. Fonte, Jour. of Instr. 8 (2013) P11001.
- [13] F. Resnati, RD51 Open Lectures, 12 December 2017.
- [14] N. Majumdar, S. Mukhopadhyay, Jour. Instr. 2 (2007) P09006.
- [15] S.F. Biagi, Nucl. Instr. Meth. A 421 (1999) 234.
- [16] I.B. Smirnov, Nucl. Instr. Meth. A 554 (2005) 474.
- [17] F. Sauli, Nucl. Instr. Meth. A 386 (1997) 531.
- [18] Santonico et al., RPC, Nucl. Instr. Meth. A 187 (1981) 377
- [19] www.openmp.org
- [20] P.K. Rout et al., Jour. Instr., 16 (2021) P09001.
- [21] S. Bachmann et al., Nucl. Instr. Meth. A 479 (2002) 294.

Probabilistic assessment of the reactor vessel lifetime

V. V. Ryazanov

Institute for Nuclear Research, pr. Nauki, 47 Kiev, Ukraine, e-mail: vryazan19@gmail.com

Highlights

- A simple and rapid method for assessing neutron irradiation on a reactor vessel is proposed
- Queuing theory is used to estimate the lifetime of the reactor vessel walls
- The behavior of radiation defects is modeled by a random process of death and birth
- For assessments, information about neutron fluence and fast neutron energy is needed

Abstract

A simple and rapid method is proposed for assessing the reduction in the lifetime of steel walls of the reactor vessel under neutron irradiation. The method is based on modeling the number of radiation defects by the behavior of a general time-dependent random process of death and birth and queuing theory. Necessary data for assessments: the estimated operating time of the reactor (in years), the actual operating time of the reactor, the accumulated fluence depending on time, the temperature on the walls of the reactor vessel, the neutron absorption cross section of the steel of the reactor walls, the energy of fast neutrons striking the walls. The main problem: getting this accurate data.

Keywords: neutron irradiation, reactor vessel lifetime, process of death and birth

1. Introduction

The impact of neutron irradiation on the duration of the steady state of the walls of the reactor vessel (RV) is one of the main issues in nuclear energy. The safety and reliability of the operation of a nuclear power plant are associated with the reliability of predicting changes in the viscosity characteristics of the reactor vessel material. This problem is presented in detail in many studies [1-32]; it is associated with issues of safe operation of the reactor, extending the life of the reactor, and many other tasks. The procedure usually performed when considering problems of this kind is to measure the dependence of the change in the shift of the critical brittleness temperature (or radiation embrittlement coefficient) on the temperature of the witness samples.

Thus, a large amount of data was accumulated on the radiation embrittlement of low-alloy vessel steels, on the relationship between the critical temperature of embrittlement and the resulting fluence, and on other aspects of the problem under consideration, which was then used in predicting changes in the lifetime of RV materials. Probabilistic approaches to solving this problem have been considered; recent works have used Bayesian methods, approaches related to machine learning, etc.

This article proposes a simplified probabilistic approach to solving the problem of changing the lifetime of the walls of the RV under the influence of irradiation. This is an integral approach that does not take into account many details that do not have a decisive influence on the final result. As in experimental work, the influence of neutron fluence is considered important. Lattice atoms directly displaced by incident particles are defined as a primary knocked-out atom (PKA). PVAs have an energy spectrum even in the case of monochromatic irradiation; their energy varies from zero to a certain maximum value M_{\max} . Getting into a solid body, a fast particle is involved in a complex process of interaction with electrons and atomic nuclei in the crystal lattice. The statistical approach is based on determining the probability of the interaction process occurring. The emerging defects in the crystal lattice and crystalline crystals are considered as a statistical system, subject to the general laws of the theory of random processes, statistical physics and nonequilibrium thermodynamics. It is assumed that at

some random moment this system will change its structure under the influence of irradiation. It is assumed that these changes reduce the steel time of the RV.

In almost all studies investigating the phenomenon of radiation embrittlement under the influence of defects in the crystal structure, the shift in the embrittlement temperature under the influence of irradiation is chosen as an indicator characterizing the degree of embrittlement. In this article, such an indicator is chosen to reduce the time of stable functioning of the steel structure, the life time of steel RV. This indicator can be compared with the relative narrowing of RV steel, but with the opposite sign.

The article is structured as follows. The second section describes a mathematical model of the influence of radiation effects on the lifetime of the walls of the reactor vessel. The number of radiation defects is modeled by a model of a random process of death and birth. The queuing theory is used to describe the lifetime of a RV. In the third section, the dependences of the RV lifetime on the irradiation time are calculated. The fourth section discusses the results obtained.

2. Mathematical model of the influence of radiation effects on the lifetime of the walls of the reactor vessel

2.1. Radiation defects.

The reaction cross section is taken as a measure of the probability density of events during the interaction of particle beams with a solid body: $\sigma = m / \varphi$, where m is the number of interactions per unit time, φ is the flow of particles, Dimension of the interaction cross section $[\sigma]=10^{-24}\text{cm}^2$. Different types of irradiation differ in the number and energy spectrum of primary knocked out atoms (PKA), which is characterized by the differential cross section $K_p(E, M)dM$, used to calculate PKA with energy M when the energy of the incident particle is E . The rate of formation of PKA with energy M is determined as follows: $P = \varphi \int_{M_d}^{M_{\max}} dMK_p(E, M)$, where φ is the flux density of incident particles. Here, only those PKAs are taken into account that have received energy exceeding the threshold energy M_d required for displacement, M_{\max} is a certain maximum energy value.

Neutron irradiation leads to degradation of the original properties of the material. When a high-energy neutron collides with an atom in a crystal lattice, the atom is displaced or a cascade of displacements occurs in the lattice, depending on the amount of energy transferred by the neutron to the metal atom. The first atom hit by a neutron, striking other atoms, causes additional displacements in the lattice. The vacancy and its own interstitial atom formed as a result of the collision of a neutron with a lattice atom are called a Frenkel pair. As a result of the development of the cascade, volumes with a high concentration of vacancies are formed, surrounded at the periphery by zones with an increased density of interstitial atoms. In addition to displacements, large neutron fluxes, due to their energy, excite atoms and intensify their vibrations, which is accompanied by a local increase in temperature. An increase in temperature promotes radiation annealing, accompanied by the annihilation of vacancies and interstitial atoms. Further, in places where point defects accumulate, dislocation loops are formed, precipitates of elements such as copper, nickel, manganese and silicon, segregation of elements such as phosphorus and tin at interphase boundaries and grain boundaries. The basis of theoretical models of the evolution of radiation-induced defects is the kinetic equations for the concentration of point defects in a medium containing sinks. It is assumed that the concentration of radiation point defects exceeds the concentration of thermally equilibrium defects. Vacancies and interstitial atoms, migrating along the lattice, can: firstly, recombine; secondly, to form clusters of defects of the same name and, thirdly, to become sinks, which can be dislocation networks, dislocation loops, pores and other extended defects. Consequently, the rate of change in the concentration of interstitial atoms and vacancies is equal to the difference in the rates of their formation and death, which can be described by kinetic equations [32]:

$$\begin{aligned} dC_v/dt &= G - RC_iC_v - C_v \sum_j K_{jv}, \\ dC_i/dt &= G - RC_iC_v - C_i \sum_j K_{ij}, \end{aligned} \quad (1)$$

where C_v , C_i are the average concentrations of vacancies and interstitial atoms; $G = \sigma_f \phi$ – rate of introduction of freely migrating defects (σ_f – cross section for their formation, ϕ – irradiation intensity); $R = 4\pi r_{vi}(D_i + D_v)$ – recombination constant of point defects, where r_{vi} – radius of mutual recombination, $D_{i,v} = D_{0i,v} \exp(-E_{mi,v}/kT)$ – diffusion coefficients of interstitial atoms and vacancies, k – Boltzmann constant, T – absolute temperature, $E_{mi,v}$ – migration energy of interstitial atom and vacancy; $K_{j i,v} = S_{j i,v} D_{i,v}$ is the coefficient of absorption of point defects by sinks of type j , where $S_{j i,v}$ are quantities characterizing the power of sinks of type j for interstitial atoms and vacancies.

The embrittlement of steel walls of the RV is also influenced by impurities of phosphorus, copper and other elements, dilatation interactions between defects, the formation and evolution of partial and perfect dislocation loops, the formation of a dislocation network, the nucleation of pores and the evolution of the pore structure, radiation-induced segregation, and other reasons. Such influences can also be included in the consideration, but are not considered in this work.

2.2. Change in RV lifetime under irradiation

The behavior of a random process, for example, a branching random process [33], can be characterized using the generating function

$$F(s) = \sum_{k=0}^{\infty} p_k s^k, \quad |s| \leq 1, \quad (2)$$

where p_k is the probability that there are k particles in the system. Let us write the generating function in the form

$$F(s) = p_0 Q(s) = Q(s) / Q = p_0 / p_0(s), \quad p_0 = 1 / Q, \quad p_0(s) = 1 / Q(s), \quad Q(s) = 1 + p_1 s / p_0 + \dots + p_n s^n / p_0 + \dots \quad (3)$$

The value $p_0 = F(s=0)$ describes the probability of degeneracy of the system, that there are no particles in the system. As an example of the fulfillment of expressions (2)-(3), we can cite a large canonical ensemble [34-36].

In queuing theory (for example, [37]), the period of system occupancy, busy period, which can be compared with the lifetime of RV defects in the M/G/1 model (an exponential distribution for the flow of requests entering the system, an arbitrary distribution of the time required to service a request in the system). The average time value of busy period is equal to

$$\bar{T} = \rho / (1 - \rho), \quad p_0 = 1 - \rho, \quad \rho = 1 - p_0 = 1 - 1 / Q, \quad (4)$$

where $\rho = d\psi(\theta)/d\theta|_{\theta=0}$, the function ψ characterizes the entry of elements (defects) into the system. The reactor is operating and defects are accumulating in it. This is a busy period. Then annealing can occur, - an empty period, - there are no defects. Then the reactor starts working again - a busy period.

Let us assume that the same relationships are satisfied under the influence on the system, which we denote by parameter s . The average time value of the busy period under the influence of s on the system is equal to

$$\begin{aligned} \bar{T}(s) &= \rho(s) / (1 - \rho(s)), \quad p_0(s) = 1 - \rho(s), \quad \rho(s) = 1 - p_0(s) = 1 - 1 / Q(s), \\ \bar{T}(s) / \bar{T} &= (1 / p_0(s) - 1) / (1 / p_0 - 1) = (F(s) - p_0) / (1 - p_0) \quad 1, \quad F(s) \leq 1 \end{aligned} \quad (5)$$

The proposed description is simplified. It is strictly valid for the large canonical ensemble [34]. But below we consider the stationary case, for which relations (2)-(5) are satisfied with a certain approximation. A consideration of the general non-stationary case using queuing theory is given in [38-40]. In [39] it is shown that the argument s from (2)-(3), (5) is written as a function of s , the argument is replaced, $s \rightarrow D(\alpha=s) = f(s) \sim \exp(-U/k_B T_e)$. The function $Q(s)$ from (2)-(5) turns out to be a function of the form $Q[D(\alpha)]$, U is the additional potential energy received by the system, k_B is the Boltzmann constant, T_e is the absolute temperature. Below we consider the situation when $s = e^{-U/k_B T_e}$, and $Q(s)$ where U is the energy transferred to the RV by neutrons.

2.3. Model of “death-and-birth”

As in [41], we use the model of death and birth [33, 42]. We assume that the incoming flow G in equations (1) enters the system one particle at a time (particle birth). A hierarchical three-level model is

considered in [43]. This article assumes that the lower levels of the hierarchy are already implicitly included in the description. The concentrations of vacancies and interstitial atoms depend on time in (1) (we assume a constant input flow). Let us replace the time-dependent expressions for concentrations with average effective constant values. Taking into account concentrations after the moment when they take on stationary values leads to the same result. The generating function (2) for the process of death and birth is equal to

$$F(s, \tau, t) = \frac{1 + (1 - \xi - \eta)s}{1 - \eta s} = \sum_{n=0}^{\infty} P_n(t) z^n, \quad \rho_1(t) = \int_0^t (\mu(\tau) - \lambda(\tau)) d\tau, \quad (6)$$

$$\xi = 1 - e^{-\rho_1} / W, \quad \eta = 1 - 1 / W, \quad W(\tau, t) = e^{-\rho_1} [1 + K], \quad K = \int_{\tau}^t e^{\rho_1(t,x)} \mu(x) dx,$$

$$\bar{n}(t) = e^{-\rho_1(t)}, \quad \text{Var}(n(t)) = e^{-\rho_1(t)} (2W - 1 - e^{-\rho_1}),$$

$$P_0(t) = \xi(t) = 1 - e^{-\rho_1(t)} / W. \quad (7)$$

Here \bar{n} is the total average number of particles in the system, $\text{Var}(n(t))$ is the dispersion of the number of particles. Let us choose the parameter τ in (6)-(7) equal to 1 year in order to consider already established stationary states. It is shown in [44] that the stationary mode is established in a time of about $3 \cdot 10^7$ s, which is about 1 year. What probabilities $\lambda(t)$ and $\mu(t)$ appear in (6)-(7). In [33] says that any particle at moment t with probability $\mu(t)dt$ dies in the interval $(t, t+dt)$ and with probability $\lambda(t)dt$ is replaced by two new particles. For the flow G entering the system of defects from (1) $\lambda(t) \sim G/n(t)$, where $n(t)$ is the number of defects at time t . If we normalize the probability $\lambda(t)$ by dividing by $\int_{\tau}^{T_f} (G/n(t)) dt$, where T_f is the total operating time of the reactor, we obtain that

$$\lambda(t) = \frac{G}{n(t)} \left(\int_{\tau}^{T_f} \frac{G}{n(t)} dt \right)^{-1}. \quad (8)$$

In the stationary case $n(t)=\text{const}$. Then in (6) $\rho_1=0$, $\lambda=\mu$, and assuming the constant value of G , we obtain that

$$\lambda=\mu=1/(T_f-\tau). \quad (9)$$

The fluence is equal to $\Phi = dN / dS$, where dN is the number of particles penetrating into the sphere with cross section dS . Radiation intensity $\varphi=dF/dS$, where $F=dN/dt$ is the flux of ionized particles. Then $\Phi = \int_{\tau}^{T_f} \varphi dt$, since $\varphi=d(dN/dS)/dt$. In expression (8) with $n(t)=\text{const}$, $\sigma_f[\Phi(T_f) - \Phi(\tau)] = \int_{\tau}^{T_f} \sigma_f \varphi dt$.

3. Results

Work [45] presents the dependences of the shift in the critical embrittlement temperature when witness samples are irradiated with a fluence of $17.8 \cdot 10^{18}$ n cm^{-2} , which corresponds to a reactor operating time of 18 years. The total operating time of the reactor is assumed to be 40 years, the value of τ is assumed to be $\tau=1$. In the practice of analyzing radiation embrittlement of materials of VVER RVs in Ukraine, the fluence of neutrons with energies above 0.5 MeV is used as a dose characteristic of fast neutrons, that is, it is assumed that neutrons with energies less than 0.5 MeV do not lead to damage to the material.

We consider the stationary case when $K = \int_{\tau}^t \mu(x) dx = (t - \tau) / (T_f - \tau)$. From (5)-(8) for $\Delta T=T-T(s)$ we obtain

$$\frac{\Delta T}{T} \approx \frac{1}{1 + \frac{s}{1-s} \frac{1}{1+K}} = \frac{1}{1 + \frac{s}{1-s} \frac{T_f - \tau}{T_f + t - 2\tau}}, \quad s = e^{-U/k_B T_e}, \quad (10)$$

where U is the energy received by the walls of the reactor vessel during irradiation. The energy of the external field is added to the energy of the system as additional potential energy [46] in the grand canonical ensemble, for which relations (3), (10) are satisfied. The values vary: T_e - temperature in the reactor, σ_n - cross section for neutron absorption by the steel of the reactor walls, E_n - neutron energy;

$$U = \Phi(t) \sigma_n E_n. \quad (11)$$

For $T_f = 40$ years, $E_n = 1$ meV, $\sigma_n = 1 \cdot 10^{-26}$ cm², the dependence of the fluence growth on time t , we accept a linear dependence of the form $\Phi(t) = 0.98889 \cdot 10^{18} t$, in the interval $t = 0 - 18$ years [45]. The calculated curve of the relationship between the change in the average lifetime $\Delta T = T - T(s)$, to T , where T is the average lifetime of the RV without taking into account radiation effects, $T(s)$ - taking this into account, is shown in Fig. 1. For $t = 18$ years, $\Delta T/T = 0.631$.

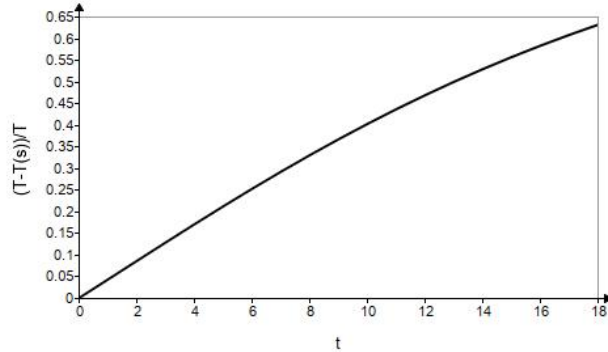


Fig.1. Dependence of the ratio of changes in the average lifetime $\Delta T = T - T(s)$, to T , where T is the average lifetime of the RV without taking into account radiation effects, $T(s)$ – taking into account, on the reactor operating time t (in years), $T_f = 40$ years, $E_n = 1$ MeV, $\sigma_n = 1 \cdot 10^{-26}$ cm², $T_e = 589$ K, fluence $\Phi(t) = 0.98889t \cdot 10^{18}$ n cm⁻², in the interval $t = 0 - 18$ years.

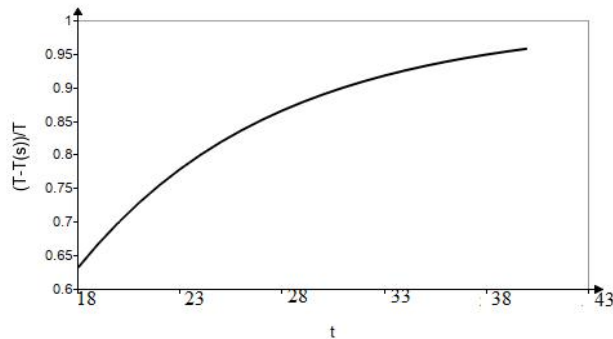


Fig.2. Dependence of the ratio of changes in the average lifetime $\Delta T = T - T(s)$, to T , where T is the average lifetime of the RV without taking into account radiation effects, $T(s)$ – taking this into account, on the reactor operating time t (in years), $T_f = 40$ years, $E_n = 1$ MeV, $\sigma_n = 1 \cdot 10^{-26}$ cm², $T_e = 589$ K, fluence $\Phi(t) = (17.8 + 1.78t) \cdot 10^{18}$ n cm⁻², in the interval $t = 18 - 40$ years. At $t = 40$ years, $\Delta T/T = 0.958$. A fluence of $6.3 \cdot 10^{19}$ n cm⁻² is achieved in $t = 43.19$ years. In this case, $\Delta T/T = 0.969$.

We will show the dependence on the parameters by replacing E_n (in Fig. 2 it was 1 MeV, in Fig. 3 it became 0.8 MeV) and σ_n (in Fig. 2 it was $1 \cdot 10^{-26}$ cm², in Fig. 3 it became $0.25 \cdot 10^{-26}$ cm²). A significant change is visible - a decrease in the effect. So $\Delta T/T$ for $t = 18$ years: it was in Fig. 2, $\Delta T/T = 0.631$, now it is in Fig. 3, $\Delta T/T = 0.196$; for $t = 40$ years: it was in Fig. 2, $\Delta T/T = 0.96$, now it is in Fig. 3, $\Delta T/T = 0.556$. Changes in temperature in the reactor core also have an effect.

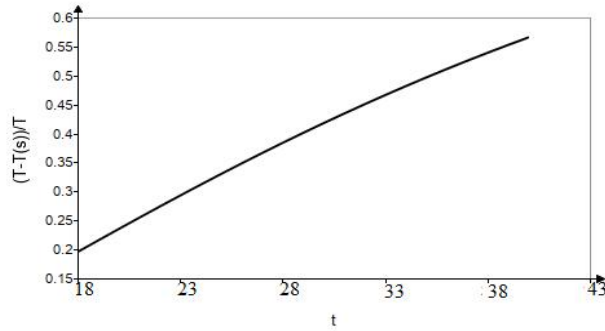


Fig. 3. Dependence of the ratio of changes in the average lifetime $\Delta T = T - T(s)$, to T , where T is the average lifetime of the RV without taking into account radiation effects, $T(s)$ – taking this into account, on the reactor operating time t (in years), $T_f = 40$ years, $E_n = 0.8$ MeV, $\sigma_n = 0.25 \cdot 10^{-26}$ cm², $T_e = 589$ K, fluence $\Phi(t) = (17.8 + 1.78t) \cdot 10^{18}$ n cm⁻², in the interval $t = 18 - 40$ years. At $t = 40$ years, $\Delta T/T = 0.566$. At $t = 18$ years, $\Delta T/T = 0.196$. A fluence of $6.3 \cdot 10^{19}$ n cm⁻² is achieved in $t = 43.19$ years. In this case, $\Delta T/T = 0.608$.

Other sources indicate other neutron fluence values. Thus, in [47], the estimated total maximum fluence of neutrons with $E_n > 0.5$ MeV at the Khmel'nitsky NPP Unit No. 1, RV for the first ten fuel campaigns is $1.1 \cdot 10^{19}$ cm⁻², with an average fluence accumulation rate of $1.1 \cdot 10^{18}$ cm⁻² per campaign. At $T_f = 40$ years and $\Phi(t=18) = 19.98 \cdot 10^{18}$ n cm⁻² it became $\Delta T/T = 0.489$ in 40 years, it was 0.566 (at $\Phi(t=18) = 17.8 \cdot 10^{18}$), $E_n = 0.8$ MeV and $\sigma_n = 0.25 \cdot 10^{-26}$ cm². At $T_f = 50$ years, $\Delta T/T = 0.587$, neutron absorption cross section by iron is $\sigma_n = 10^{-26}$ cm²; fast neutrons with $E_n > 0.5$ MeV are taken into account.

If this rate of accumulation of the neutron fluence of the RV continues in the future, then the maximum permissible fluence specified in the technical safety justification for reactor plant V-320 and equal to $5.7 \cdot 10^{19}$ n cm⁻² will be accumulated in approximately 50 years of operation, since the design service life of the VVER-1000 vessel is 40 years old.

Therefore, the task is to accurately determine such parameters as the energy of fast neutrons incident on the RV, neutron cross sections for the absorption of fast neutrons by the steels of the RV walls, fast neutron fluences, and temperature in the core. All these parameters significantly affect the change in the service life of the RV.

In [48], the relation obtained in [49] is given for the average energy of fast neutrons in a reactor of the form $\bar{E}_n (\text{MeV}) = 7.42R + 0.3$, where R is the ratio of the flux of neutrons with an energy greater than 3 MeV ($\Phi > 3$) to the flux of neutrons with an energy greater than 1 keV ($\Phi > 0.001$). In [48], measured the values of R at different points of the reactor OR, VVR [48] (left channel, level of the core center (LCC), in the same place, 20 cm below the LCC. There the same, 20 cm above the LCC. In the same place, 60 cm above LCC. Right channel of the LCC. Niche, on the central horizontal axis. In graphite reflector of the reactor, (the thickness of the graphite between the neutron detectors and the nearest fuel elements is 20-30 cm)). The average value of R is 0.153. Then $E_n = 1.4357$ MeV.

The $\Delta T/T$ value calculated with this value $E_n = 1.4357$ MeV and temperature on the reactor walls $T_e = 290$ C is shown in Fig. 4

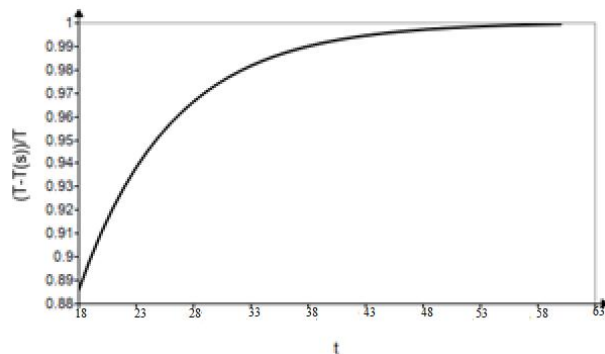


Fig.4. Dependence of the ratio of changes in the average lifetime $\Delta T=T-T(s)$, to T , where T is the average lifetime of the RV without taking into account radiation effects, $T(s)$ – taking this into account, on the reactor operating time t (in years), $T_f=60$ years, $E_n=1.4357$ MeV, $\sigma_n=1 \cdot 10^{-26}$ cm², $T_e=563$ K, fluence $\Phi(t)=(19.98+1.11t) \cdot 10^{18}$ n cm⁻², in the interval $t=18-60$ years. At $t=40$ years, $\Delta T/T=0.992$. At $t=18$ years, $\Delta T/T=0.885$. At $t=60$ years, $\Delta T/T=0.999$.

Since $\Delta T/T=1-T(s)/T$, then, for example, at $\Delta T/T=0.992$, $T(s)=(1-0.992)T=0.008T$, the average lifetime of the RV under the influence of irradiation is reduced for $t=40$ years. In Fig. 5 compared to Fig. 4 the value of σ_n changes: $E_n=1.4357$ MeV, $\sigma_n=0.25 \cdot 10^{-26}$ cm².

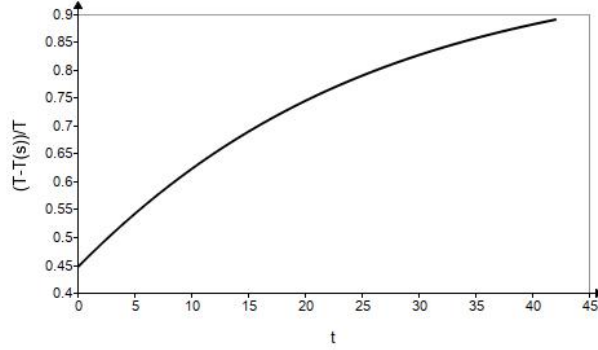


Fig. 5. Dependence of the ratio of changes in the average lifetime $\Delta T=T-T(s)$, to T , where T is the average lifetime of the RV without taking into account radiation effects, $T(s)$ – taking this into account, on the reactor operating time t (in years), $T_f=60$ years, $E_n=1.4$ MeV, $\sigma_n=0.25 \cdot 10^{-26}$ cm², $T_e=563$ K, fluence $\Phi(t)=(19.98+1.11t) \cdot 10^{18}$ n cm⁻², in the interval $t=18-60$ years. At $t=40$ years, $\Delta T/T=0.764$. At $t=18$ years, $\Delta T/T=0.446$. At $t=60$ years, $\Delta T/T=0.89$.

It is advisable to compare the resulting reduction in the lifetime of the RV with known results. For VVER-1000, the maximum fluence allowed is $6.3 \cdot 10^{19}$ n cm⁻². For the data in Fig. 5 this fluence will be achieved in 58.74 years. For $T_f=60$ years, $\Phi(t)=(19.98+1.11t) \cdot 10^{18}$ n cm⁻², $\sigma_n=0.25 \cdot 10^{-26}$ cm², $E_n=1.4357$ MeV, $t=18$ years, $T=563$ K, it became $\Delta T/T=0.446$, for $t=40$ years, $\Delta T/T=0.764$, for $t=50$ years, $\Delta T/T=0.839$; for maximum fluence $\Phi_{lim}=6.3 \cdot 10^{19}$ n cm⁻² and duration $t=58.74$ years, $T_f=60$ years, $\Delta T/T=0.876$, by $T_f=70$ years, $\Delta T/T=0.868$. If a fluence of $1.6 \cdot 10^{20}$ n cm⁻² is achieved, which is possible for VVER-440 [50], then for the data in Fig. 5 this fluence will be achieved in 145 years, with $\Delta T/T=0.997$.

Similar results for Fig.4. But for fig. 2, $\Delta T/T=0.958$ at $t=40$ years, $\Delta T/T=0.969$ at $t=43.19$ years. The set of maximum fluence $6.3 \cdot 10^{19}$ n cm⁻² at $T_f=40$ years, $E_n=1$ meV, $\sigma_n=1 \cdot 10^{-26}$ cm², $\Phi(t)=(17.8+0.178t) \cdot 10^{18}$ n cm⁻², occurs in $t=43.19$ years old. For this period $\Delta T/T=0.969$. For $t=18$ years, $\Delta T/T=0.63$, for $t=40$ years, $\Delta T/T=0.958$.

For Fig. 3, when $T_f=40$ years, $E_n=0.8$ MeV, $\sigma_n=0.25 \cdot 10^{-26}$ cm², $\Phi(t)=(17.8+1.78t) \cdot 10^{18}$ n cm⁻², time range $t=18-40$ years, $\Delta T/T=0.196$, for $t=18$ years, $\Delta T/T=0.566$, for $t=40$ years, $\Delta T/T=0.608$, for $t=43.19$ years. From the comparison of Fig. 2, 4 and fig. Figure 3 shows a strong dependence of E_n and σ_n on neutron energy.

For VVER-440 the maximum fluence allowed is $3 \cdot 10^{20}$ n cm⁻² for 50 years. When $\sigma_n=1 \cdot 10^{26}$ cm², $E_n=1$ MeV, the time of maximum fluence to reach is 252 years. In this case $\Delta T/T=1$; for 152 years, $\Delta T/T=0.97$. If the fluence is allowed to be $1.6 \cdot 10^{20}$ n cm⁻², then the time to reach it will be 145 years. For the parameters in Fig. 5 and for $t=145$ years ratio $\Delta T/T=0.994$.

A similar characteristic of the fragility and durability of the RV metal is the relative elongation δ , shear fracture percentage. This parameter, like $\Delta T/T$, varies from 0 to 1 (from 0 to 100%). The value of δ at which brittle fracture of a metal sample occurs can be compared with the value of $T(s)$ at which the end of the metal's lifetime occurs. Fragility is the property of materials to collapse under the influence of external forces without residual deformation. Under significant impacts, destruction occurs at small values of δ and at large values of $\Delta T/T$ (small values of $T(s)$). The parameter δ is usually measured depending on the temperature, and the parameter $\Delta T/T$ is discussed above depending on the irradiation

time t . But the values of these parameters correspond to each other, characterizing the end of the service life of the steel. For heavily irradiated metals, the values of the parameters δ are very small, amounting to fractions of a percent. And if, for example, $\delta=0.002$, then $T(s)=0.002T$, $\Delta T/T=0.998$. Therefore, you can give preference to Fig. 4 with higher $\Delta T/T$ values and small values of $T(s)$.

4. Discussion

A simple approach to estimating the remaining lifetime of a RV after irradiation with fast neutrons is proposed. It is possible to relate this approach to the commonly used practice of measuring the critical brittleness temperature (CBT) and its shear. The simplicity of the approach can be both a disadvantage and an advantage of the method. The disadvantage is the lack of consideration of many features of the ongoing processes. But this may also be an advantage of the method, which does not take into account unimportant details, but in an integral form considers the important characteristics of the processes responsible for the main indicator of the reactor vessel - its lifetime.

The value of $T(s)$ is not entirely clear; is it a real reduction in lifetime, or some conditional value? This value can be correlated with the change in the critical brittleness temperature. However, the latter value is also determined ambiguously. For example, an example of the spread of values was obtained within the framework of the IAEA project [51]. The corresponding results from all 8 laboratories are different.

To obtain more accurate results of the proposed approach, knowledge and strict consideration of the parameters of the problem are required. Thus, reactor steel is a complex alloy. For each component of this alloy, the neutron absorption cross sections for fast neutrons differ. Thus, for carbon, the neutron absorption cross section for fast neutrons is $\sigma_n=0.0001 \cdot 10^{-24} \text{ cm}^2$, and for iron - $\sigma_n=0.01 \cdot 10^{-24} \text{ cm}^2$. It is necessary to take into account all components of steel RV, and write $\sigma_n=\sum \sigma_{ni} x_i$, where σ_{ni} is the neutron absorption cross section of fast neutrons of the i -th component, x_i is the fraction of the i -th component. In a similar way, expressions for the neutron energy E_n should be written, taking into account the spectrum of fast neutrons and the contribution of this spectrum to the energy of neutrons incident on the walls of the RV. More precise and strict expressions for fluence are needed.

In the general case, in the original relation for the lifetime (4), one should consider not a single system, but a network of queuing theory systems. Each network system will describe a certain section of the RV wall. This approach was used in [41]. In a simple approximation, the factor $\exp[-U/k_B T]$ includes c in the form $\exp[-U/ck_B T]$, where c is the number of systems in the queuing network. It can be shown that $c \sim N_0$, where N_0 is the number of defects at the initial time. In this work, $N_0=1$ was assumed. However, the values of c and N_0 can take on other values, which can be used to correct the results obtained, taking, for example, the values of σ_n higher.

References

1. P. G. Tipping, *Understanding and Mitigating Ageing in Nuclear Power Plants* (Elsevier Science, 2010).
2. C. K. Gupta, *Materials in Nuclear Energy Applications: Volume I* (CRC Press, 2017).
3. G. R. Odette and G. E. Lucas, Embrittlement of Nuclear Reactor Pressure Vessels, *JOM* **53**, 18 (2001).
4. J. Pu, Radiation Embrittlement, *Physics* **241**, Stanford University, Winter 2013.
5. S. J. Zinkle and G. S. Was, Materials Challenges in Nuclear Energy, *Acta Mater.* **61**, 735 (2013).
6. T. Dayrit, Materials Challenges in Light-Water Reactors, *Physics* **241**, Stanford University, Winter 2019.
7. S. J. Zinkle, Microstructures and Mechanical Properties of Irradiated Materials, in *Materials Issues for Generation IV Systems*, edited by V. Ghetta *et al.* (Springer, 2008).
8. O. Kutsenko, I. Kadenko, X. Pitoiset, O. Kharytonov, N. Sakhno, I. Kravchenko, Effect of neutron irradiation hardening of the base metal on the results of WWER-1000 reactor pressure vessel residual

- lifetime assessment, *International-journal-of-pressure-vessels-and-piping*, Volume **171**, 2019, 173-183.
9. Integrity of reactor pressure vessels in nuclear power plants: assessment of irradiation embrittlement effects in reactor pressure vessel steels, *IAEA Nuclear energy series*, No. NP-T-3.11,— Vienna : International Atomic Energy Agency, 2009.
 10. E. Moslemi-Mehni, F. Khoshahval, R. Pour-Imani, M. A. Amirkhani-Dehkordi, Estimation of yield strength due to neutron irradiation in a pressure vessel of WWER-1000 reactor based on the correction of the secondary displacement model, *Nuclear Engineering and Technology*, **55**, 9, 2023, Pages 3229-3240.
 11. L. Zhou, J. Dai, Y. Li, X. Dai, C. Xie, L. Li, and L. Chen, Research Progress of Steels for Nuclear Reactor Pressure Vessels, *Materials* (Basel). 2022 Dec; **15**(24): 8761.
 12. Brumovský, M. Role of Irradiation Embrittlement in RPV Lifetime Assessment, *MRS Online Proceedings Library*, **1769**, 24 (2015). <https://doi.org/10.1557/opl.2015.128>.
 13. C. Xu, X. Liu, Y. Li, W. Jia, Q. Quan, W. Qian, J. Yin, and X. Jin, The development of prediction model on irradiation embitterment for low Cu RPV steels, *Heliyon*, 2023; **9** (6): e16581.
 14. I. Balachov, B. Fekete, D. D. Macdonald, and B. Spencer, Lifetime Estimation of a BWR Core Shroud in Terms of IGSCC, *Nuclear Engineering and Design*, **368**:110831, Nov. 2020. DOI: 10.1016/j.nucengdes.2020.110831.
 15. C. Xu, X. Liu, H. Wang, Y. Li, W. Jia, W. Qian, Q. Quan, H. Zhang, F. Xue, A study of predicting irradiation-induced transition temperature shift for RPV steels with XGBoost modeling, *Nuclear Engineering and Technology*, Volume **53**, Issue 8, 2021, Pages 2610-2615, ISSN 1738-5733, <https://doi.org/10.1016/j.net.2021.02.015>.
 16. S. Szávai, J. Dudra, Lifetime analysis of WWER Reactor Pressure Vessel Internals concerning material degradation, *20th International Conference on Structural Mechanics in Reactor Technology* (SMiRT 20) Espoo, Finland, August 9-14, 2009, SMiRT, 20-Division 2, Paper 1893.
 17. Al Mazouzi, A. Alamo, D. Lidbury, D. Moinereau, S. Van Dyck, PERFORM 60: Prediction of the effects of radiation for reactor pressure vessel and in-core materials using multi-scale modelling – 60 years foreseen plant lifetime, *Nuclear Engineering and Design*, **241**, 9, 2011, pp. 3403-3415.
 18. G-M. Fernandez, K. Higley, A. Tokuhiko, K. Welter, W-K. Wong, H. Yang, Status of research and development of learning-based approaches in nuclear science and engineering: A review, *Nuclear Engineering and Design*, **359**, 1, 2020, 110479.
 19. T. Flaspöhler and B. Petrovic, Radiation Damage Assessment in the Reactor Pressure Vessel of the Integral Inherently Safe Light Water Reactor (I2S-LWR), *EPJ Web of Conferences*, **106**, 03004 (2016) DOI: 10.1051/epjconf/201610603004
 20. Effect of irradiation on water reactors internals, Ageing Materials Evaluation and Studies (AMES) Report No. 11., Paris (1997). Hojna A., Ernestova M., Keilova E., Kocik J., Falcnik M., Kytka M., Pesek P., Rapp M., Material characteristics of materials from Greifswald active samples/active material database/core barrel, Report NRIRez, DITI 302/419 Rev.3, (2007) (3)
 21. CEA, TECNATOM and VTT, Effect of Irradiation on Water Reactors Internals, AMES report No. 11, EUR17694 EN, European Commission, Brussels–Luxemburg (1997), 4.
 22. S. Chen, D. Bernard, Recommendation for computing neutron irradiation damage from evaluated nuclear data, *J. Nucl. Mater.*, **562** (2022), Article 153610
 23. F. A. Garner, Radiation Damage in Austenitic Steels, (2012) In *Comprehensive Nuclear Materials*; Elsevier: Amsterdam, The Netherlands, **2012**; pp. 33–95.
 24. K. Nordlund, et al. Improving atomic displacement and replacement calculations with physically realistic damage models, *Nat. Commun.*, **9** (1) (2018), pp. 1-8.
 25. Nordlund, K. et al. *Primary Radiation Damage in Materials - Review of Current Understanding and Proposed New Standard Displacement Damage Model to Incorporate in Cascade Defect Production Efficiency and Mixing Effects*. NEA/NSC/DOC 9. 1–86 (Nuclear Energy Agency, OECD, Paris, 2015).

26. Wolfgang Hoffelner, *Irradiation Damage in Nuclear Power Plants, Handbook of Damage Mechanics*, pp 1427–1461, 2014.
27. Bakirov, Impact of operational loads and creep, fatigue corrosion interactions on nuclear power plant systems, structures and components (SSC), in *Understanding and mitigating ageing in nuclear power plants*, ed. by P. G. Tipping (Woodhead, Oxford, 2010), pp. 146–188
28. J. Chen, W. Hoffelner, Irradiation creep of oxide dispersion strengthened (ODS) steels for advanced nuclear applications. *J. Nucl. Mater.* **392**, 360–363 (2009)
29. Margolin B.Z., Shvetsova V.A., Gulenko A.G. Radiation embrittlement modeling in multiscale approach to brittle fracture of RPV steel. *Int. J. of Fracture*. Vol. **179** (2013), Issue 1-2, pp. 87-108.
30. Margolin B.Z., Yurchenko E.V., Morozov A.M., Pirogova N.E., Brumovsky M. Analysis of a link of embrittlement mechanisms and neutron flux effect as applied to reactor pressure vessel materials of WWER. // In: *J. Nucl. Mater.*, (2013), pp. 347-356.
31. Alekseenko N.N., Amaev A.D., Gorynin I.V., Nikolaev V.A.. Radiation Damage of Nuclear Power Plant Pressure Vessel Steels // *Am. Nucl. Soc.* – La Grange Park, Illin., USA, 1997.
32. Ivanov L.I., Platov Yu.M. *Radiatsionnaia fizika metallov i ee prilozheniia [Radiation physics of metals and its applications]*. Moscow: Interkontakt, Nauka, 2002, 300 p. [in Russian].
33. T. E. Harris, *The theory of branching processes*, Shpringer-Verlag, Berlin, 1963.
34. T. L. Hill, *Statistical Mechanics: Principles and Selected Applications*, McGraw-Hill, New York (1956).
35. V. V. Ryazanov, “Simulation of the generating function for the number of particles by a branching process with immigration [in Russian],” in: *Physics of the Liquid State*, Vol. 11, Vishcha Shkola, Kiev (1983), pp. 40–44; “Modeling of thermodynamic properties of a Gibbs statistical system [in Russian],” in: *Physics of the Liquid State*, Vol. 17, Vishcha Shkola, Kiev (1989), pp. 28–41; “A constructive description of pure substances and mixtures by relations of the type of the van der Waals equation [in Russian],” in: *Physics of the Liquid State*, Vol. 18, Vishcha Shkola, Kiev (1990), pp. 5–14; “Analytic modeling of Gibbs systems [in Russian],” in: *Physics of the Liquid State*, Vol. 19, Vishcha Shkola, Kiev (1991), pp. 24–35.
36. V. V. Ryazanov, Modeling of statistical systems. I. General characteristics of the method, *Ukrainian Journal of Physics*, v. **23**, No. 6, 1978, pp. 965-972.
37. L. Kleinrock, *Queueing Systems: V. I – Theory*. New York: Wiley, 1975, Interscience. pp. 417.
38. V. V. Ryazanov, Stochastic nonequilibrium thermodynamics and time, *Ukrainian Journal of Physics*, v. **38**, No. 4, 1993, pp. 615-631.
39. V. V. Ryazanov, Stochastic modeling in nonequilibrium thermodynamics and lifetimes of systems, in: *Physics of the Liquid State*, Vol. 20, Lybid, Kiev (1992), pp. 11–36.
40. V. V. Ryazanov, Kinetics of coagulation and stochastic processes of the storage theory, In: “*Aerosols: Science, Industry, Health and Environment*”, 1 band, pp. 142-145. Pergamon Press, Kyoto, 1990; V. V. Ryazanov, Stochastic Description of Aerosol Systems, *Journal of aerosol Science*, 1991, Suppl.1, S59-S64.
41. V. V. Ryazanov, Influence of the external field on the semi-coagulation time and on the aerosol lifetime, *Journal of aerosol Science*, 1989, v.**20**, N8, pp. 1055-1058.
42. D. G. Kendall, On the generalized 'birth-and-death' process, *Ann. Math. Stat.* v. **19**, 1-15, 1948.
43. V. V. Ryazanov, S. Shpyrko, Hierarchic stochastic model of radiation damages lifetimes of reactor materials, The 3rd International Conference Current Problems in Nuclear Physics and Atomic Energy, June 7 - 12, 2010, Kyiv, Ukraine, The Proceedings of the Conference, pp. 538-543
44. D. A. Kornilov, V. M. Kosenkov, P. P. Silantsev, Influence of the initial dislocation structure on the kinetics of point and macroscopic defects during irradiation, *Vestn. SamU. Natural science ser.*, 2016, issue 1, 69–84, [in Russian].
45. E. U. Grinik, L. I. Chirko, V. N. Revka, Assessment of the radiation resource of reactor vessels of the VVER-1000 type at nuclear power plants in Ukraine. *Zbirnik naukovih prac institute of nuclear sciences*, No. 1 (14) 2005, [in Russian].

46. M. A. Leontovich. *Introduction to thermodynamics. Statistical Physics*, M.: Nauka, 1983, 416 p., [in Russian].
47. I. N. Vishnevsky, V. N. Bukanov, E. G. Vasilyeva, V. I. Gavrilyuk, A. V. Gritsenko, V. L. Demekhin, O. V. Nedelin, Monitoring the radiation load of the VVER-1000 vessel for determining its service life, International Conference of the Ukrainian Nuclear Society: Modernization of the NPP with VVER reactor, 21 - 23/09/1999, Kyiv, 1999, p.42, [in Russian].
48. B. A. Levin, Approximate methods for determining the flux of neutrons with energies greater than 0.1 MeV in experimental reactor channels, Institute of Atomic Energy. I. V. Kurchatova, Moscow, 1971, [in Russian].
49. A. Д. Kantz, Average neutron energy of reactor spectra and its influence on displacement damage, *J. Appl. Phys.* V. **34**, n. 7, p. 1944 (1963)
50. A. M. Kryukov, V. I. Lebedinsky, Irradiation embrittlement of RPV steels irradiated by high neutron fluence, *Nuclear and radiation safety*, № 1 (95)-2020, p. 2-13.
51. I. V. Orynyak, M. N. Zarazovsky, A. V. Bogdan, Method for determining the critical brittleness temperature taking into account the scatter of experimental data on impact strength, Physico-chemical mechanics of materials. – 2015. – №1. – *Physicochemical of Materials, Materials Science*, Consultants Bureau Plenum Publishing Corporation, (Нью-Йорк, Лондон), pp 26-36.

An Experimentally Benchmarked Geant4 SiPM-Based Scintillator Detector Simulation Platform for Gamma Ray Detection

Lysander Miller^a, Airlie Chapman^a, Katie Auchettl^b, Jeremy M. C. Brown^c

^a*Department of Mechanical Engineering, The University of Melbourne, Parkville, VIC 3010, Australia*

^b*School of Physics, The University of Melbourne, Parkville, VIC 3010, Australia*

^c*Optical Sciences Centre, Department of Physics and Astronomy, Swinburne University of Technology, Hawthorn, VIC 3122, Australia*

Abstract

Radiation detection is vital for naturally occurring radioactive material detection, port and border monitoring, and homeland security operations. SiPM-based single-volume scintillator detectors offer a cost-effective and robust solution that enables timely radioactive site surveys, while retaining accuracy and sensitivity sufficient for isotope identification. Enhanced site surveying can be achieved by optimising scintillator detector design. In this work, a detailed GAGG:Ce, CLLBC:Ce, BGO, NaI:Tl, and CsI:Tl SiPM-based scintillator detector simulation platform was developed with the Monte Carlo radiation transport toolkit, Geant4, and experimentally benchmarked. This simulation platform successfully predicted the spectral features for selected gamma ray emitting isotopes with energies between 30 keV to 2 MeV. The full width half maximum (FWHM) and normalised cross-correlation coefficient (NCCC) between simulated and experimental energy spectra were also compared. The majority of simulated FWHM values reproduced the experimental results within 2% and the NCCC values demonstrated agreement between the simulated and experimental energy spectra. Discrepancies in these figures of merit can be attributed to detector signal processing electronics modelling, geometry approximations, and multiple Compton scattering within the detector and surrounding environment.

Keywords: GAGG, CLLBC, BGO, NaI, CsI, Geant4 optical physics

1. Introduction

Uncontrolled radiological and nuclear (R&N) material dispersion pose a significant threat to civil and military environments [1, 2, 3]. Radiation detection capabilities play an important role in large-area R&N surveying as they provide first responders with prompt situational awareness. Recent developments in new scintillator crystals, such as CLLBC:Ce [4, 5], and silicon photomultiplier (SiPM) technology allow for compact, lightweight, and rugged detectors that are suitable for large-area radiation detection. An important aspect of detector design is optimising the scintillator geometry and material for accurate radiation measurements given different R&N surveying modalities

(e.g., hand-held, ground vehicle mounted, and aerial drone mounted). This can be achieved by simulating the underlying gamma ray and optical scintillation transport processes as they have a significant effect on detector performance.

This work presents the development of a SiPM-based scintillator detector simulation platform in Geant4 version 11.1.2 [6, 7, 8]. Geant4 is the state-of-the-art Monte Carlo radiation transport toolkit that simulates the underlying physical process of interaction and production of particles through matter. The response of five different single-volume scintillator crystal materials to the gamma ray emissions from five radioactive isotopes was simulated. Scintillator crystals GAGG:Ce, CLLBC:Ce, BGO, NaI:Tl, and CsI:Tl were explored as they offer a range of desirable properties for R&N applications. For example, CLLBC:Ce has a high energy resolution, BGO provides a high sensitivity, GAGG:Ce offers a high sensitivity and good energy resolution, and NaI:Tl and CsI:Tl are cost effective. Radioactive sources ^{109}Cd (1 μCi), ^{57}Co (1 μCi), ^{137}Cs (0.1 μCi), ^{152}Eu (0.5 μCi), and ^{22}Na (1 μCi) were considered in this study as they are commonly found in R&N scenarios and provide a 30 keV to 2 MeV energy range where major spectral features such as photopeaks, Compton edges, Compton backscatter peaks, and Compton plateaus can be investigated. The simulation platform was experimentally benchmarked by comparison to the energy spectrum obtained for each scintillator crystal and isotope combination.

2. Method

2.1. Experimental Platform and Acquisition of Radiation Energy Spectra

An off-the-shelf SiPM-3000 from Bridgeport Instruments was chosen as the SiPM and MCA platform for this work [9]. Motivated by R&N surveying applications, the SiPM-3000 is desirable as it is operated using open-source interface software and is composed of a rugged detector housing, read-out electronics, and a Broadcom AFBR-S4N66C013 SiPM array, which has a maximum photodetection efficiency (PDE) over 55% [10]. The SiPM array consisted of a 4×4 array of SiPMs, each with a 6.14 mm side length and 0.32 mm gap between neighbouring SiPMs. Individual SiPMs were composed of a 0.2 mm thick glass plate attached to a 0.1 mm thick silicon plate. Scintillator crystals GAGG:Ce, CLLBC:Ce, BGO, NaI:Tl, and CsI:Tl were optically bonded to the SiPM array in the SiPM-3000 using 1 mm thick EJ-560 optical pads. Table (A.4) in the appendix summarises the dimensions, reflective materials, crystal housing, optical window, and manufacturer for each scintillator crystal.

The system was placed in a custom-made detector holder and positioned in the lab to minimise the chance of Compton scattering with the surrounding environment (see Fig. (1a)). The five radioactive check sources (^{109}Cd , ^{57}Co , ^{137}Cs , ^{152}Eu , and ^{22}Na) were placed on top of the scintillator crystal within the detector housing to further minimise scattering. After allowing an hour for the SiPM-3000 to thermalise, the detector was calibrated for each crystal type. The integration time, dead time, electronic gain, pulse trigger, and noise trigger were optimised to minimise the noise and low-level detection threshold. For this work, the low-level detection threshold was defined as the minimum energy where the count rate exceeded 5% relative counts to prevent detector noise defining the threshold. An integration time of 2 μs was set for GAGG:Ce, BGO, and NaI:Tl, whereas CLLBC:Ce and CsI:Tl used 3 μs due

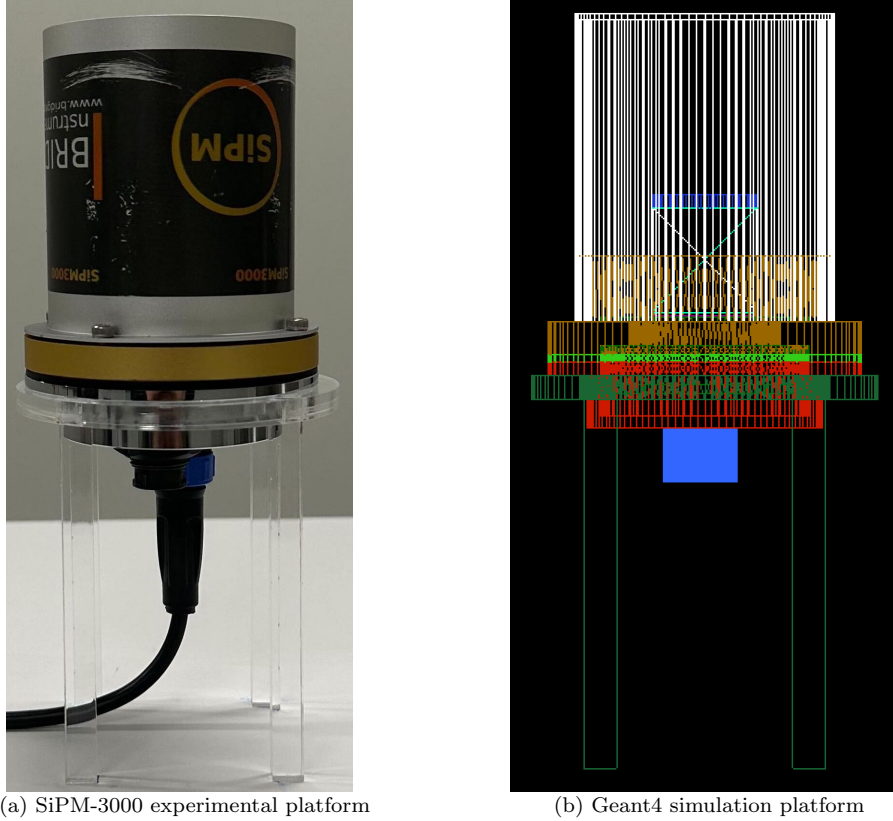


Figure 1: SiPM-based scintillator detector platforms.

to their longer optical decay times (see Table (A.4) in the appendix). The SiPM-3000 operating voltage was fixed at 33 V (default), yielding an overvoltage of 4.5 V. For each scintillator crystal and radioactive source combination, data acquisition occurred over 30 minutes to reduce statistical noise in the energy spectrum and ensure each photopeak could be resolved. Background measurements were also recorded over 30 minutes at standard temperature and pressure and subtracted from each energy spectrum during post-processing.

2.2. Geant4 Simulation Platform Geometry, Materials, and Optical Data Tables

The Geant4 simulation platform was designed to emulate the experimental platform described in Sec. (2.1). Scintillator crystal dimensions, material properties, and encapsulation implemented in the simulation platform are summarised in Table (A.4). The SiPM array and optical pad dimensions were consistent with the experimental platform described in Sec. (2.1). Table (A.5) displays the optical material properties for the SiPM, optical pad, and reflective materials implemented in the simulation platform. SiPM-3000 read-out electronics, detector housing, detector holder, radioactive check source, and lab environment were included in the Geant4 application. The description, dimensions, and materials for each geometry are summarised in Table (1). Other lab components, e.g., the remaining walls, were disregarded as their contribution of Compton scattering was assumed to be negligible as they were further away from the detector. Surrounding environmental air was modelled using the builtin Geant4 material G4_AIR [11]. A wire trace visualisation of the detector, detector holder, and each radioactive check source implemented in Geant4 is shown in Fig. (1b).

Geometry Name	Component Name	Dimensions	Materials
SiPM-3000	SiPM array PCB	Disc (radius, z): 25.4, 1 mm	FR4
	Internal PCBs (2x)	Disc (radius, z): 25.4, 2 mm	
	Gasket	Annulus (thickness, radius, z): 12.5, 38, 2 mm	Rubber H_8C_4 $\rho = 0.95 \text{ g/cm}^3$
	Pin connector	Annulus (thickness, radius, z): 1, 6.5, 12 mm	Plastic $H_6C_6O_2$ $\rho = 1.3 \text{ g/cm}^3$
	Plug connector	Annulus (thickness, radius, z): 3.5, 9, 13 mm	
	Fixture	Annulus (thickness, radius, z): 20, 38, 8 mm	G4_Al
	Lip	Annulus (thickness, radius, z): 1, 30.5, 16 mm	
	Join	Annulus (thickness, radius, z): 12.5, 38, 3 mm	
	Bulk	Annulus (thickness, radius, z): 3, 28.5, 13 mm	
	Detector cover	Annulus (thickness, radius, z): 1.25, 31.75, 75 mm	
Table	Legs (4x)	Box (x, y, z): 26, 26, 91 mm	MDF C:H:O 50%:6%:44% $\rho = 0.7 \text{ g/cm}^3$
	Body	Annulus (thickness, x, y, z): 18, 520, 520, 708 mm	
Detector holder	Base	Annulus (thickness, radius, z): 12, 42, 6 mm	Perspex H_8C_5O $\rho = 1.18 \text{ g/cm}^3$
	Legs (4x)	Box (x, y, z): 6, 8, 90 mm	
Radioactive check source	–	Disc (radius, z): 12.7, 3.2 mm	
Environment	Wall 1	Box (x, y, z): 1, 1.45, 3 m	G4_CONCRETE
	Wall 2	Box (x, y, z): 1, 3, 3 m	
	Floor	Box (x, y, z): world x, world y, 1 m	

Table 1: Name, dimensions, and materials of the SiPM-3000 and surrounding geometries implemented in the Geant4 application.

2.3. Geant4 Application Physics and Optical Surface Modelling

The Geant4 physics constructor QGSP_BIC_HP_EMZ was used to model the gamma ray, X-ray, and electron transport in the simulation platform [8, 11, 12]. The settings for radioactive decay, atomic de-excitation, PIXE, auger electrons, and fluorescence were enabled. Moreover, the particle production length cut was set to 100 μm and the low energy cut off was fixed at 100 eV. Optical photon generation and transportation through scintillation, absorption, refraction, and reflection were modelled using the Geant4 implementation of the Unified model [11, 13]. Optical surfaces in contact with the Teflon tape, ESR, and GORE diffuse reflector were defined as ‘dielectric-to-metal’, whereas the remaining surfaces were defined using the ‘dielectric-to-dielectric’ surface type. All optical surfaces were assumed to be highly polished and characterised by a ground finish featuring a 0.1-degree surface roughness [12, 14, 15].

2.4. Geant4 Application Validation Simulations and Figures of Merit

The simulation platform was used to model twenty million radioactive decays for each radioactive source and scintillator crystal combination, totaling 25 simulations. For these simulations, the isotope particle gun was positioned at the centre of each radioactive check source to approximate the isotope location. The optical photons produced by the scintillator crystals were scored by the SiPM array according to the integration time and wavelength-dependent PDE. The integration times were consistent with the experiments as described in Sec. (2.1), and the PDE data was interpolated for an overvoltage of 4.5 V using the 3.5 V and 8 V overvoltage from the AFBR-S4N66C013 SiPM array data sheet [10]. Energy calibration was implemented by least squares fitting photopeak centroids to the corresponding gamma ray energy and setting the minimum energy for the simulated data as the experimental low-level detection threshold. Quadratic functions were fit to the centroids of ^{109}Cd , ^{137}Cs , and ^{22}Na for GAGG:Ce, CLLBC:Ce, NaI:Tl, and CsI:Tl. A linear function was fit to the ^{137}Cs and ^{22}Na centroids for BGO as the ^{109}Cd centroid was filtered by the low-level detection threshold.

Two figures of merit were selected to benchmark the Geant4 application: full width half maximum (FWHM) and normalised cross-correlation coefficient (NCCC). The FWHM was used to quantify the performance of photopeaks in the simulation platform. It was calculated from the standard deviation of a Gaussian function with a quadratic background that was fit to each photopeak using linear least squares. The NCCC was used to quantify the overall performance of the simulated energy spectrum E_{sim} compared to the experimental energy spectrum E_{exp} :

$$\text{NCCC} = \frac{|\sum_{i=0}^n E_{\text{sim}}(i)E_{\text{exp}}(i)|}{|\sum_{i=0}^n E_{\text{sim}}^2(i)|^{1/2}|\sum_{i=0}^n E_{\text{exp}}^2(i)|^{1/2}}, \quad (1)$$

where values greater than 0.995, 0.999, and 0.9999 indicate ‘fair’, ‘good’, and ‘excellent’ fits respectively [16, 17]. For the NCCC calculations, the experimental energies were used as the $n + 1$ spectral channels in Eq. (1) and the corresponding simulation counts were determined via interpolation.

3. Results and Discussion

Figs. (2) to (6) present the simulated and experimental energy spectra for the five scintillation materials. Overall, the Geant4 application accurately predicted the spectral features observed in the experimental energy spectra. These features included the Compton continuum, Compton edge, photopeaks, annihilation peaks, double-sum peaks, and, in cases with sufficient low-level detection, X-ray peaks. The average difference between simulated and experimental photopeak FWHM was less than 2%, as shown in Table (2). Moreover, NCCC values demonstrated overall agreement between the experimental and simulated detector platforms (see Table (3)). This section discusses the performance of the simulation platform in more detail by comparing spectral features and figures of merit to the energy spectra generated from the experimental platform.

The experimental ^{22}Na spectra for GAGG:Ce and BGO revealed a double-sum peak at 1766 keV and 1769 keV (see Figs. (2c) and (4c)). This was caused by the 511 keV and 1275 keV gamma ray interacting with the SiPM in the same time window. As the double-sum peaks were not 1786 keV (511 keV + 1275 keV), the SiPM did not fully capture the optical response from the scintillator crystals. This was most likely caused by X-ray escape. Double-sum peaks were negligible in the ^{22}Na energy spectra for CLLBC:Ce, NaI:Tl, and CsI:Tl (Figs. (3c), (5c), and (6c)) due to their lower stopping power, making it less likely for both gamma rays to interact with them in the same time window. GAGG:Ce and BGO's high stopping power corresponded to less statistical noise in the ^{137}Cs spectra (Figs. (2d) and (4d)) compared to the other scintillators. Statistical noise was more prevalent for ^{137}Cs compared to other isotopes because ^{137}Cs had the lowest radioactivity. The peak immediately above the low-level detection threshold observed in the ^{22}Na and ^{137}Cs experimental spectra (e.g., GAGG:Ce in Figs. (2c) and (2d)) can be attributed to electronic noise. This peak was not observed in the simulated spectra because electronic noise was not accounted for in the simulation platform.

The average difference between simulated and experimental photopeak FWHM was <1% for CsI:Tl, 1% for GAGG:Ce and CLLBC:Ce, 2% for NaI:Tl, and 4% for BGO. For each scintillator, the energy resolution generally improved as the characteristic gamma ray energy increased. Although this was true for ^{152}Eu within the photopeaks for the same source, it was not true between photopeaks of other isotopes. For example, the 344 keV and 964 keV ^{152}Eu photopeaks for CsI:Tl had a FWHM of 9.55% and 7.17% respectively, however the FWHM for the 662 keV photopeak was 6.93%. This phenomena can be attributed to X-ray escape peak broadening and cascade summing from multiple ^{152}Eu radioactive decays. The poor energy resolution of BGO blurred the 122 keV and 136 keV ^{57}Co photopeaks together so that the 136 keV photopeak could not be resolved, as shown in Fig. (4b) and Table (2). Moreover, the poor energy resolution of BGO was attributed to the 16% difference between the simulated and experimental 245 keV ^{152}Eu photopeak FWHM. Overall, CLLBC:Ce had the best energy resolution (lowest photopeak FWHM) across the 30 keV to 2 MeV energy range. For the simulated 662 keV photopeak, CLLBC:Ce had an energy resolution of 3.52%, NaI:Tl with 6.70%, GAGG:Ce with 6.83%, CsI:Tl with 6.93%, and BGO with 13.4%.

The NCCC values for NaI:Tl were ~ 0.99 for the ^{57}Co and ^{22}Na energy spectra but 0.308, 0.798, and 0.758 for ^{109}Cd , ^{137}Cs , and ^{152}Eu . Across all isotopes, the NCCC value for CsI:Tl was > 0.98 . The differences in NCCC values between the NaI:Tl and CsI:Tl simulations were attributed to the differences in gamma ray interaction between sodium and caesium in the scintillators. As sodium is a low Z material, the gamma ray is more likely to Compton scatter out of the NaI:Tl and interact with the detector and surrounding environment. Smaller NCCC values were observed in the scintillators where more Compton scattering occurred, indicating a discrepancy in the likelihood of Compton scattering in the simulation platform compared to the experimental platform. This can be attributed to lower fidelity electronic modelling and geometry approximations made in the Geant4 application. Discrepancies in NCCC values for BGO can also be attributed to scintillator non-proportionality, which was not accounted for in the energy calibration process due to limited low energy photopeaks. For example, the ^{109}Cd energy spectrum had an NCCC value of 0.750, caused by the misaligned 88 keV photopeaks (see Fig. (4a)).

4. Conclusion

A detailed SiPM-based scintillator detector simulation platform was developed in Geant4. The response of GAGG:Ce, CLLBC:Ce, BGO, NaI:Tl, and CsI:Tl to characteristic gamma rays with energies between 30 keV to 2 MeV were simulated. These results were benchmarked against experiments. The simulation platform successfully predicted the spectral features measured in the experiments. Moreover, the average simulated photopeak FWHM was within 2% of the experiments and the NCCC values indicated overall agreement between simulated and experimental energy spectra. There were minor discrepancies in the simulated FWHM and NCCC values, which can be attributed to: (1) variations in the Compton continuum caused by geometry approximations, and (2) detector signal processing electronics modelling.

Acknowledgements

L. Miller would like to acknowledge the Optical Sciences Centre at Swinburne University of Technology for support of the project. This research was supported by The University of Melbourne's Research Computing Services, the Petascale Campus Initiative, and an Australian Government Research Training Program (RTP) Scholarship.

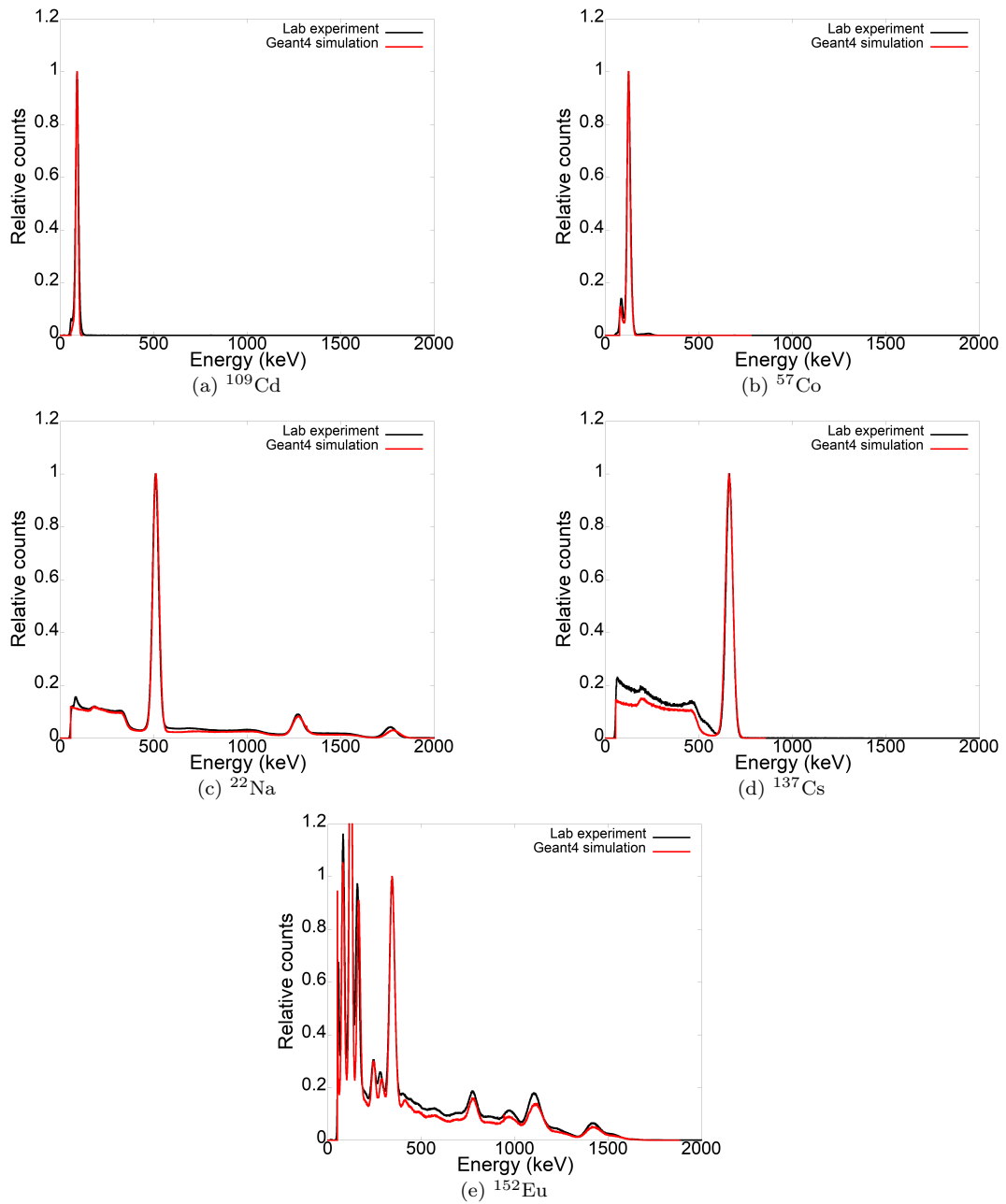


Figure 2: Experimental and simulated gamma ray energy spectra for the GAGG:Ce scintillator detector.

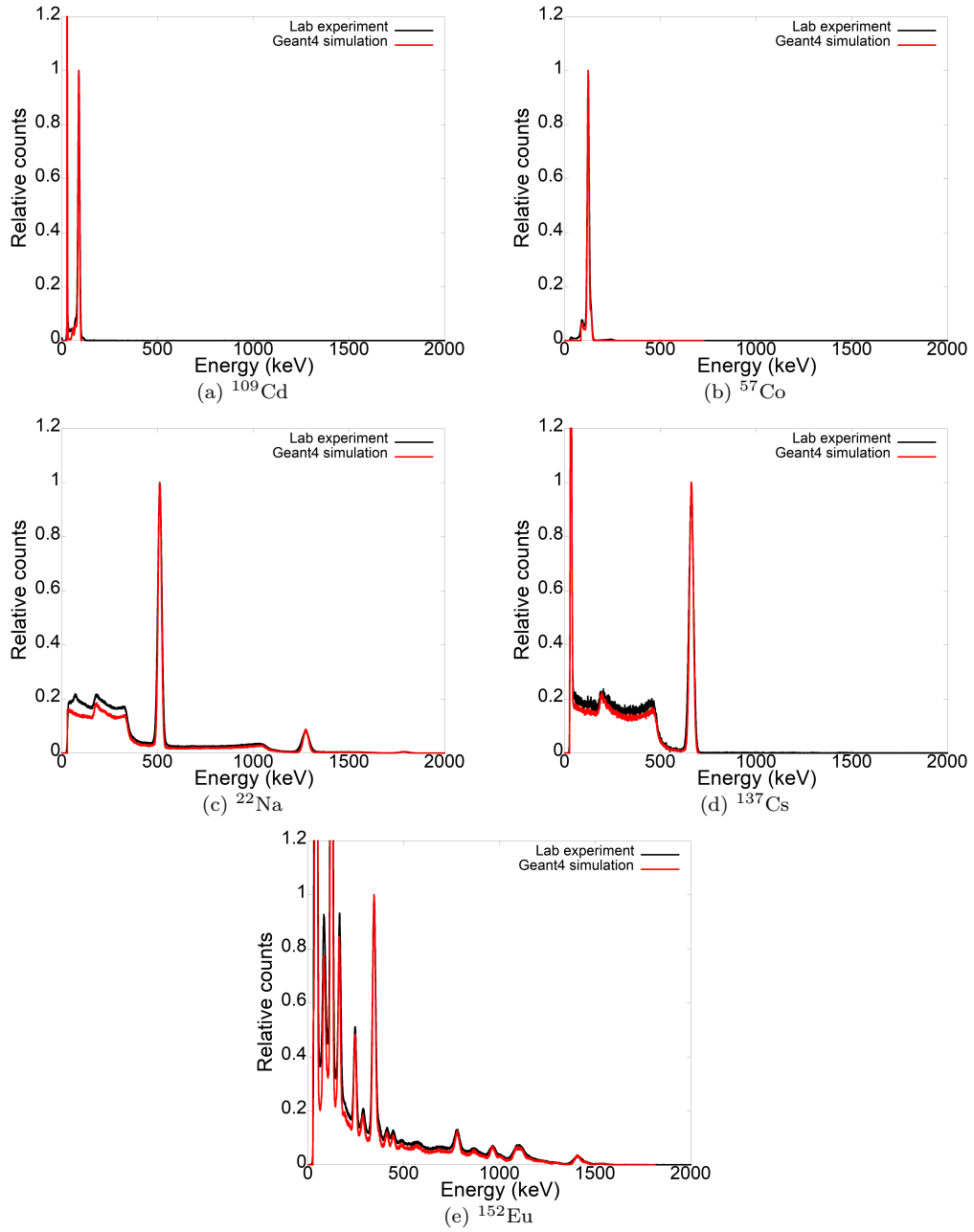


Figure 3: Experimental and simulated gamma ray energy spectra for the CLLBC:Ce scintillator detector.

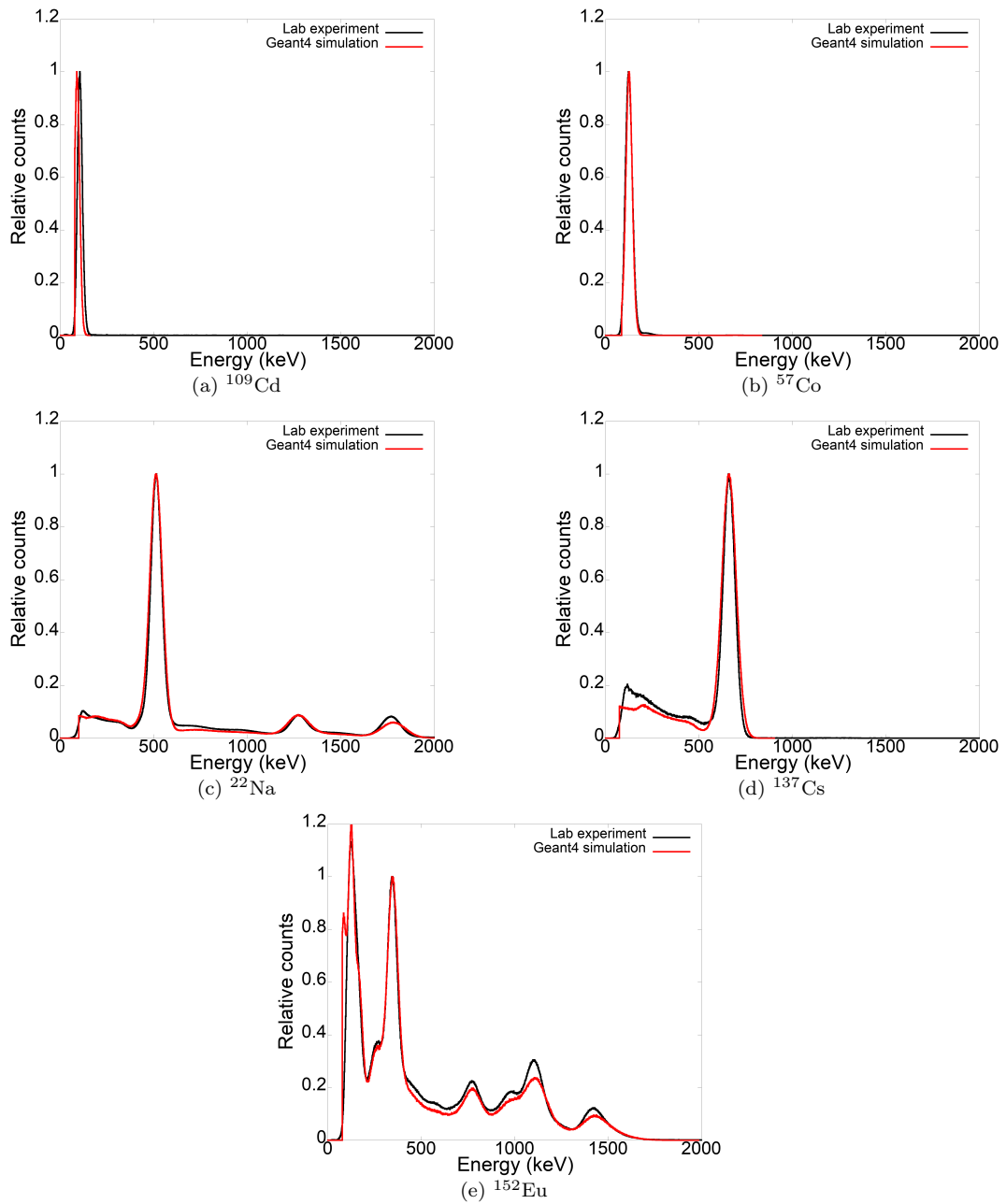


Figure 4: Experimental and simulated gamma ray energy spectra for the BGO scintillator detector.

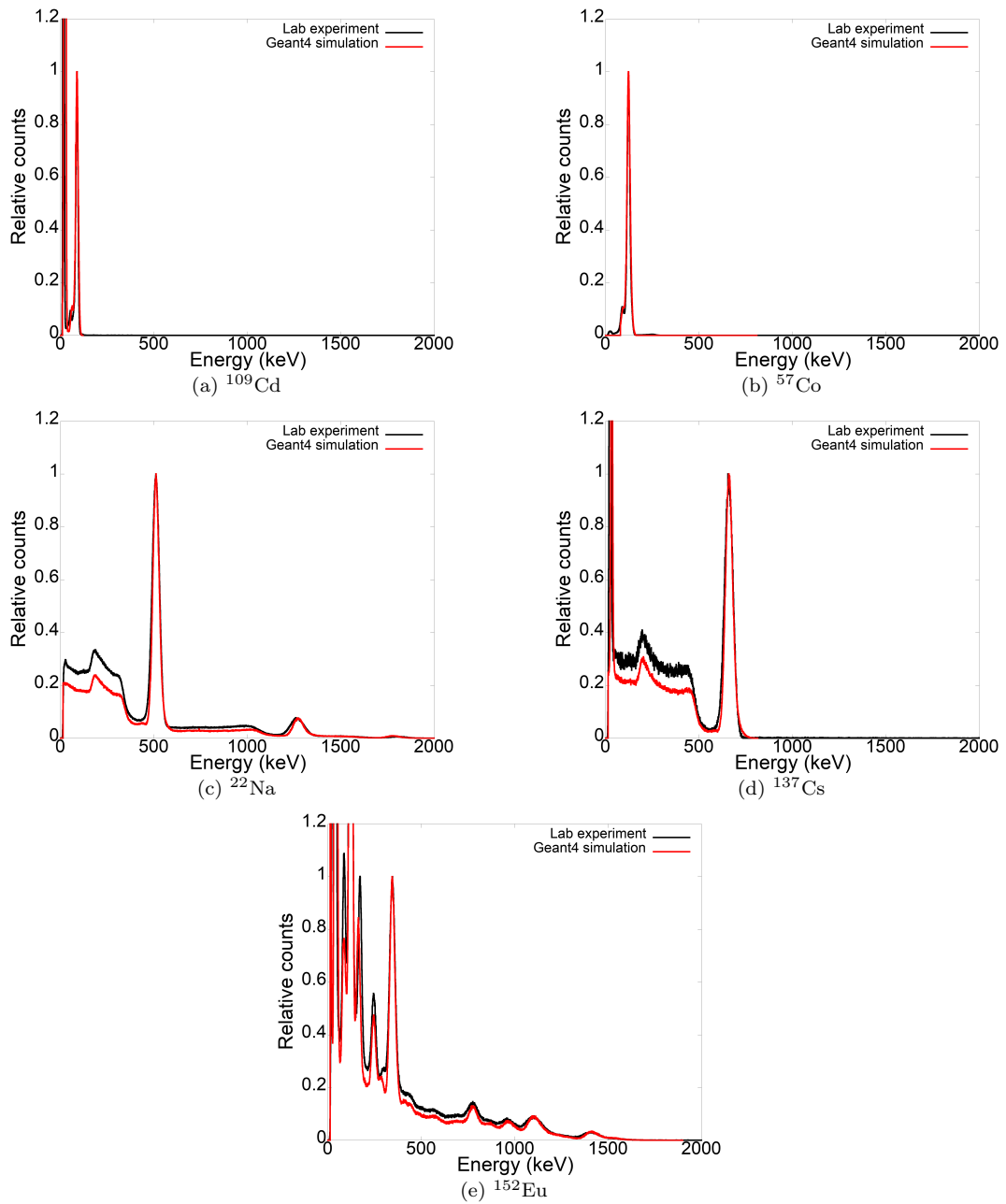


Figure 5: Experimental and simulated gamma ray energy spectra for the NaI:Tl scintillator detector.

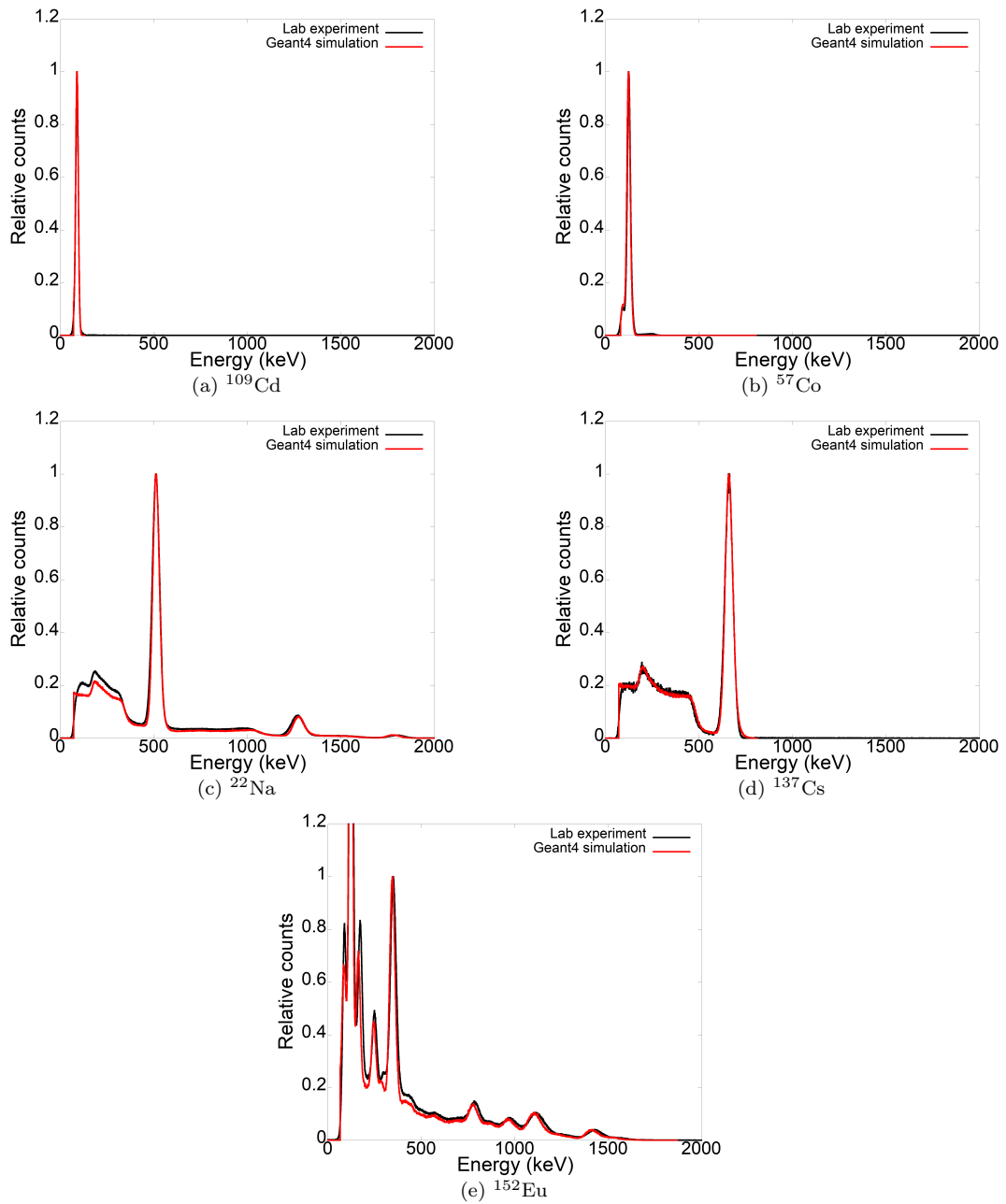


Figure 6: Experimental and simulated gamma ray energy spectra for the CsI:Tl scintillator detector.

Characteristic gamma ray (keV)	GAGG:Ce		CLLBC:Ce		BGO		NaI:Tl		CsI:Tl	
	Exp	Sim	Exp	Sim	Exp	Sim	Exp	Sim	Exp	Sim
^{109}Cd : 88.03	18.7	16.0	11.8	9.62	30.2	34.4	14.2	17.8	17.2	18.2
^{57}Co : 122.06	15.4	13.6	9.59	8.20	34.8	31.4	12.9	14.5	15.2	15.4
^{57}Co : 136.47	13.9	12.2	8.58	7.33	N/A	N/A	11.4	13.1	13.5	13.9
^{152}Eu : 244.70	10.4	10.4	6.64	5.95	38.4	54.9	11.0	10.8	11.0	11.1
^{152}Eu : 344.28	8.96	8.67	5.48	4.75	16.9	18.5	10.3	8.61	10.4	9.55
^{22}Na : 511.00	7.32	7.55	4.72	4.00	13.0	15.1	8.78	7.59	8.72	7.88
^{137}Cs : 661.66	6.43	6.83	4.19	3.52	11.2	13.4	8.09	6.70	7.72	6.93
^{152}Eu : 778.90	6.38	6.66	4.18	3.36	11.3	12.6	7.69	6.15	7.00	6.63
^{152}Eu : 964.06	7.34	9.18	3.50	2.49	12.4	16.0	7.86	6.91	6.73	7.17
^{22}Na : 1274.54	4.62	5.37	3.27	2.55	7.83	11.1	6.32	4.89	5.94	5.06
^{152}Eu : 1408.01	6.33	7.57	3.29	2.29	9.58	11.7	7.69	5.79	6.31	6.76

Table 2: Experimental and simulated full width half maximum (%) extracted from the energy spectra.

Radioactive source	GAGG:Ce	CLLBC:Ce	BGO	NaI:Tl	CsI:Tl
^{109}Cd	0.987	0.275	0.750	0.308	0.999
^{57}Co	0.996	0.993	0.998	0.996	0.989
^{137}Cs	0.987	0.978	0.987	0.798	0.997
^{152}Eu	0.965	0.962	0.972	0.758	0.982
^{22}Na	0.996	0.991	0.995	0.988	0.995

Table 3: NCCC between experimental and simulated energy spectra.

References

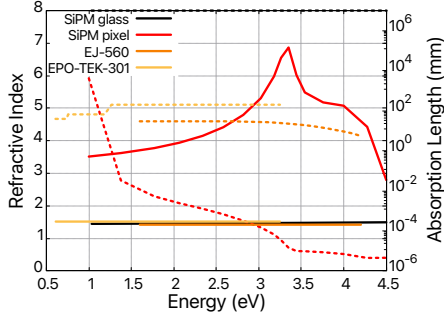
- [1] L. Marques, A. Vale, P. Vaz, State-of-the-art mobile radiation detection systems for different scenarios, *Sensors* 21 (2021) 1051. URL: <https://www.mdpi.com/1424-8220/21/4/1051>. doi:10.3390/s21041051.
- [2] D. Connor, P. G. Martin, T. B. Scott, Airborne radiation mapping: overview and application of current and future aerial systems, *International Journal of Remote Sensing* 37 (2016) 5953–5987. URL: <https://www.tandfonline.com/doi/full/10.1080/01431161.2016.1252474>. doi:10.1080/01431161.2016.1252474.
- [3] K. Vetter, R. Barnowski, A. Haefner, T. H. Joshi, R. Pavlovsky, B. J. Quiter, Gamma-ray imaging for nuclear security and safety: Towards 3-d gamma-ray vision, *Nuclear Instruments and Methods in Physics Research Section A: Accelerators, Spectrometers, Detectors and Associated Equipment* 878 (2018) 159–168. URL: <https://linkinghub.elsevier.com/retrieve/pii/S0168900217309269>. doi:10.1016/j.nima.2017.08.040.
- [4] R. Hawrami, L. S. Pandian, E. Ariesanti, J. Glodo, J. Finkelstein, J. Tower, K. Shah, Cs₂LiLa(Br,Cl)₆ crystals for nuclear security applications, *IEEE Transactions on Nuclear Science* 63 (2016) 509–512. URL: <http://ieeexplore.ieee.org/document/7454852/>. doi:10.1109/TNS.2016.2522188.
- [5] U. Shirwadkar, R. Hawrami, J. Glodo, E. V. Loef, K. Shah, Novel scintillation material Cs₂LiLaBr_{6-x}Cl_x:Ce for gamma-ray and neutron spectroscopy, *IEEE*, 2012, pp. 1963–1967. URL: <http://ieeexplore.ieee.org/document/6551453/>. doi:10.1109/NSSMIC.2012.6551453.
- [6] S. Agostinelli, et al., Geant4—a simulation toolkit, *Nuclear Instruments and Methods in Physics Research Section A: Accelerators, Spectrometers, Detectors and Associated Equipment* 506 (2003) 250–303. URL: <https://linkinghub.elsevier.com/retrieve/pii/S0168900203013688>. doi:10.1016/S0168-9002(03)01368-8.
- [7] J. Allison, et al., Geant4 developments and applications, *IEEE Transactions on Nuclear Science* 53 (2006) 270–278. URL: <http://ieeexplore.ieee.org/document/1610988/>. doi:10.1109/TNS.2006.869826.
- [8] J. Allison, et al., Recent developments in Geant4, *Nuclear Instruments and Methods in Physics Research Section A: Accelerators, Spectrometers, Detectors and Associated Equipment* 835 (2016) 186–225. URL: <https://linkinghub.elsevier.com/retrieve/pii/S0168900216306957>. doi:10.1016/j.nima.2016.06.125.
- [9] Bridgeport Instruments, SiPM-3000, 2020. URL: <https://www.bridgeportinstruments.com/products/sipm/sipm3k.html>.
- [10] Broadcom Inc., AFBR-S4N66C013 NUV-HD single silicon photo multiplier, 2023. URL: <https://docs.broadcom.com/doc/AFBR-S4N66C013-NUV-HD-Single-Silicon-Photo-Multiplier-DS>.
- [11] Geant4 Collaboration, Book for application developers (2022). URL: <https://geant4.web.cern.ch/>.
- [12] J. M. Brown, L. Chartier, D. Boardman, J. Barnes, A. Flynn, Modelling the response of CLLBC(Ce) and TLYC(Ce) SiPM-based radiation detectors in mixed radiation fields with Geant4, *Nuclear Instruments and Methods in Physics Research Section A: Accelerators, Spectrometers, Detectors and Associated Equipment* 1057 (2023) 168726. URL: <https://linkinghub.elsevier.com/retrieve/pii/S0168900223007179>. doi:10.1016/j.nima.2023.168726.

- [13] A. Levin, C. Moisan, A more physical approach to model the surface treatment of scintillation counters and its implementation into DETECT, volume 2, IEEE, 1996, pp. 702–706. URL: <http://ieeexplore.ieee.org/document/591410/>. doi:10.1109/NSSMIC.1996.591410.
- [14] J. Nilsson, V. Cuplov, M. Isaksson, Identifying key surface parameters for optical photon transport in GEANT4/GATE simulations, *Applied Radiation and Isotopes* 103 (2015) 15–24. URL: <https://linkinghub.elsevier.com/retrieve/pii/S096980431530018X>. doi:10.1016/j.apradiso.2015.04.017.
- [15] D. J. V. D. Laan, D. R. Schaart, M. C. Maas, F. J. Beekman, P. Bruyndonckx, C. W. V. Eijk, Optical simulation of monolithic scintillator detectors using GATE/GEANT4, *Physics in Medicine and Biology* 55 (2010) 1659–1675. doi:10.1088/0031-9155/55/6/009.
- [16] J. Brown, M. Dimmock, J. Gillam, D. Paganin, A low energy bound atomic electron compton scattering model for Geant4, *Nuclear Instruments and Methods in Physics Research Section B: Beam Interactions with Materials and Atoms* 338 (2014) 77–88. URL: <https://linkinghub.elsevier.com/retrieve/pii/S0168583X14006934>. doi:10.1016/j.nimb.2014.07.042.
- [17] J. Hernández-Andrés, J. Romero, R. L. Lee, Colorimetric and spectroradiometric characteristics of narrow-field-of-view clear skylight in Granada, Spain, *Journal of the Optical Society of America A* 18 (2001) 412. URL: <https://opg.optica.org/abstract.cfm?URI=josaa-18-2-412>. doi:10.1364/JOSAA.18.000412.
- [18] J. M. C. Brown, S. E. Brunner, D. R. Schaart, A high count-rate and depth-of-interaction resolving single-layered one-side readout pixelated scintillator crystal array for PET applications, *IEEE Transactions on Radiation and Plasma Medical Sciences* 4 (2020) 361–370. URL: <https://ieeexplore.ieee.org/document/8876605/>. doi:10.1109/TRPMS.2019.2948106.
- [19] H. R. Philipp, E. A. Taft, Optical constants of silicon in the region 1 to 10 eV, *Physical Review* 120 (1960) 37–38. URL: <https://link.aps.org/doi/10.1103/PhysRev.120.37>. doi:10.1103/PhysRev.120.37.
- [20] Eljen Technology, Silicone rubber optical interface EJ-560 datasheet (2021). URL: <https://eljentechnology.com/products/accessories/ej-560>.
- [21] Epoxy Technology, EPO-TEK-301 datasheet, 2021. URL: <https://www.epotek.com/docs/en/Datasheet/301.pdf>.
- [22] M. Janecek, Reflectivity spectra for commonly used reflectors, *IEEE Transactions on Nuclear Science* 59 (2012) 490–497. URL: <http://ieeexplore.ieee.org/document/6168236/>. doi:10.1109/TNS.2012.2183385.
- [23] J. M. Brown, Corrigendum to “in-silico optimisation of tileable philips digital SiPM based thin monolithic scintillator detectors for SPECT applications” [appl. radiat. isot. 168 109368 (2021)], *Applied Radiation and Isotopes* 194 (2023) 110721. URL: <https://linkinghub.elsevier.com/retrieve/pii/S096980432300074X>. doi:10.1016/j.apradiso.2023.110721.
- [24] J. M. Brown, In-silico optimisation of tileable philips digital SiPM based thin monolithic scintillator detectors for SPECT applications, *Applied Radiation and Isotopes* 168 (2021) 109368. URL: <https://linkinghub.elsevier.com/retrieve/pii/S0969804320305157>. doi:10.1016/j.apradiso.2020.109368.
- [25] 3M, Enhanced specular reflector datasheet, 2020. URL: <https://multimedia.3m.com/mws/media/12450890/3m-enhanced-specular-reflector-films-3m-esr-tech-data-sheet.pdf>.

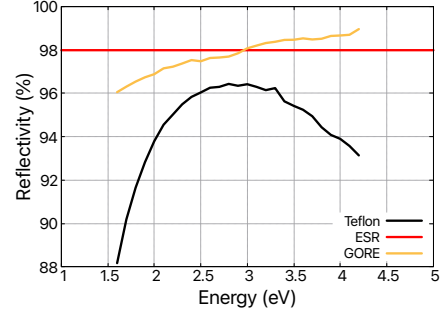
- [26] M. Kobayashi, Y. Tamagawa, S. Tomita, A. Yamamoto, I. Ogawa, Y. Usuki, Significantly different pulse shapes for γ - and α -rays in $\text{Gd}_3\text{Al}_2\text{Ga}_3\text{O}_{12}:\text{Ce}^{3+}$ scintillating crystals, *Nuclear Instruments and Methods in Physics Research Section A: Accelerators, Spectrometers, Detectors and Associated Equipment* 694 (2012) 91–94. URL: <https://linkinghub.elsevier.com/retrieve/pii/S0168900212008479>. doi:10.1016/j.nima.2012.07.055.
- [27] R. Mao, L. Zhang, R.-Y. Zhu, Optical and scintillation properties of inorganic scintillators in high energy physics, *IEEE Transactions on Nuclear Science* 55 (2008) 2425–2431. URL: <http://ieeexplore.ieee.org/document/4636955/>. doi:10.1109/TNS.2008.2000776.
- [28] EPIC Crystal, BGO datasheet, 2023. URL: <https://www.epic-crystal.com/data/upload/20230728/64c32f2b72b75.pdf>.
- [29] M. Moszynski, M. Kapusta, M. Mayhugh, D. Wolski, S. Flyckt, Absolute light output of scintillators, *IEEE Transactions on Nuclear Science* 44 (1997) 1052–1061. URL: <https://ieeexplore.ieee.org/document/603803/>. doi:10.1109/23.603803.
- [30] M. Grodzicka-Kobylka, T. Szczesniak, M. Moszyński, Comparison of SensL and Hamamatsu 4×4 channel SiPM arrays in gamma spectrometry with scintillators, *Nuclear Instruments and Methods in Physics Research Section A: Accelerators, Spectrometers, Detectors and Associated Equipment* 856 (2017) 53–64. URL: <https://linkinghub.elsevier.com/retrieve/pii/S0168900217303388>. doi:10.1016/j.nima.2017.03.015.

Appendix A. Geant4 Material Properties

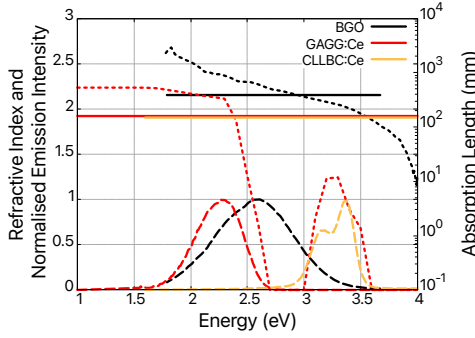
This appendix contains the density, elemental composition, and optical/ scintillation properties of all materials used in the Geant4 simulation platform. Scintillator material properties for GAGG:Ce, CLLBC:Ce, BGO, NaI:Tl, and CsI:Tl are summarised in Table (A.4) with reference to scintillator refractive index, emission spectrum, and absorption length data in Figs. (A.7c) and (A.7d). Material properties for EPO-TEK-301, Teflon tape, ESR, GORE diffuse reflector, glass, SiPM pixel, and EJ-560 optical pad can be seen in Table (A.5) with refractive index and optical reflectivity/ efficiency data presented in Figs. (A.7a) and (A.7b).



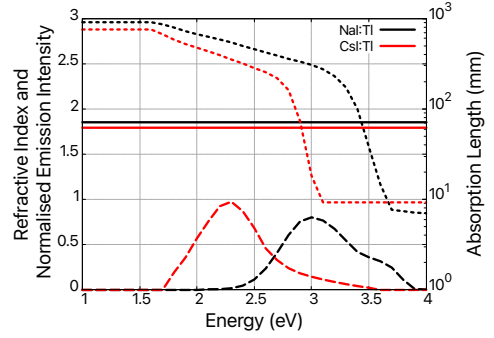
(a) Refractive index and absorption length for the glass [12, 18], SiPM pixel [12, 19], EJ-560 [12, 20], and EPO-TEK-301 [21].



(b) Reflectivity for the Teflon tape [22], ESR [23, 24, 25], and GORE diffuse reflector [12, 22].



(c) Refractive index, emission intensity, and absorption length for GAGG:Ce [23, 24, 26] and BGO [27, 28]. Refractive index and emission intensity for CLLBC:Ce [12, 5].



(d) Refractive index, emission intensity, and absorption length for NaI:Tl and CsI:Tl [23, 24, 27].

Figure A.7: Material refractive index and reflectivity (solid line), normalised emission intensity (dashed line), and absorption length (dotted line) data implemented in the Geant4 simulation platform.

Material	GAGG:Ce	CLLBC:Ce	BGO	NaI:Tl	CsI:Tl
Density (g/cm ³)	6.63 [26]	4.06 [5, 4]	7.13 [27]	3.67 [27]	4.51 [27]
Elemental composition	Gd ₃ Al ₂ Ga ₃ O ₁₂ (1% Ce)	Cs ₂ LiLaBr _{4.8} Cl _{1.2} (2% Ce)	Bi ₄ Ge ₃ O ₁₂	NaI (6.5% Tl)	CsI (0.08% Tl)
Refractive index	See Fig. (A.7c)	See Fig. (A.7c)	See Fig. (A.7c)	See Fig. (A.7d)	See Fig. (A.7d)
Optical yield (photons/MeV)	50,000 [23, 24]	45,000 [4]	8,500 [29]	41,000 [23, 24]	61,000 [29]
Emission spectrum	See Fig. (A.7c)	See Fig. (A.7c)	See Fig. (A.7c)	See Fig. (A.7d)	See Fig. (A.7d)
Absorption length	See Fig. (A.7c)	N/A [12] ^a	See Fig. (A.7c)	See Fig. (A.7d)	See Fig. (A.7d)
Optical decay time(s) (ns)	87 (90%), 255 (10%) [23, 24]	130 (82.5%), 784 (17.5%) [12]	317 (100%) [28]	220 (96%), 1500 (4%) [23, 24]	1000 (100%) [23, 24]
Resolution scale	3.08 [23, 24] (at 511 keV)	2.13 [4] (at 662 keV)	3.80 [28] (at 662 keV)	3.50 [23, 24] (at 511 keV)	4.87 [30] (at 662 keV)
Crystal dimensions	25.4 mm cube	24.98 mm diameter 25.33 mm height	25.4 mm cube	25.4 mm cube	25.4 mm cube
Reflective material	0.015 mm EPO-TEK 0.065 mm ESR	1 mm Teflon sides 1.5 mm GORE top	0.015 mm EPO-TEK 0.065 mm ESR	1 mm Teflon	1 mm Teflon
Crystal housing	–	2.5 mm neoprene 1 mm 2A12 Al	–	1 mm 2A12 Al	1 mm 2A12 Al
Optical window	–	1 mm EJ-560 0.25 mm glass	–	2 mm EPO-TEK 2 mm glass	2 mm EPO-TEK 2 mm glass
Manufacturer	Epic Crystal	RMD	Epic Crystal	Epic Crystal	Epic Crystal

Table A.4: Scintillator material properties for GAGG:Ce, CLLBC:Ce, BGO, NaI:Tl, and CsI:Tl.

^aUnavailable in the literature. However, Brown *et al.* illustrated that it was negligible for a small crystal volume [12].

Material	Density (g/cm ³)	Elemental composition	Refractive index	Optical reflectivity/ efficiency	Reference
EPO-TEK-301	1.2	HCO	See Fig. (A.7a)	See Fig. (A.7a)	[21]
Teflon tape	2.2	C ₂ F ₄	–	See Fig. (A.7b)	[12, 22]
ESR	1.29	H ₈ C ₁₀ O ₄	–	See Fig. (A.7b)	[23, 24, 25]
GORE diffuse reflector	0.65	C ₂ F ₄	–	See Fig. (A.7b)	[12, 22]
Glass	2.203	SiO ₂	See Fig. (A.7a)	See Fig. (A.7a)	[12, 18]
SiPM pixel	2.33	Si	See Fig. (A.7a)	See Fig. (A.7a)	[12, 19]
EJ-560 optical pad	1.03	H ₆ C ₂ OSi	See Fig. (A.7a)	See Fig. (A.7a)	[12, 20]

Table A.5: Scintillator detector optical material properties.

Microscopic parametrization of the near threshold oscillations of the nucleon time-like effective electromagnetic form factors

Francesco Rosini* and Simone Pacetti

Dipartimento di Fisica e Geologia, INFN Sezione di Perugia, 06123 Perugia, Italy

Olga Shekhovtsova

INFN Sezione di Perugia, 06123 Perugia, Italy and

National Science Centre, Kharkov Institute of Physics and Technology, Akademicheskaya, Ukraine

Egle Tomasi-Gustafsson

DPhN, IRFU, CEA, Université Paris-Saclay, 91191 Gif-sur-Yvette Cedex, France

We present an analysis of the recent near threshold BESIII data for the nucleon time-like effective form factors. The damped oscillation emerging from the subtraction of the dipole formula is treated in non-perturbative-QCD, making use of the light cone distribution amplitudes expansion. Non-perturbative effects are accounted for by considering Q^2 -dependent coefficients in such expansions, whose free parameters are determined by fitting to the proton and neutron data. Possible implications and future analysis have been discussed.

I. INTRODUCTION

The theoretical impossibility of describing the nucleon internal structure in terms of strongly interacting quarks and gluons, which are the fundamental fields of quantum chromodynamics, enhances the electromagnetic form factors (EMFFs) to the role of unique and privileged tools to unravel the dynamics underlying the electromagnetic interaction of nucleons. They provide the most effective description of the mechanisms that determine and rule the dynamic and static properties of nucleons. In specific reference frames, EMFFs represent the Fourier transforms of spatial charge and magnetic momentum densities.

Recently, the BESIII [1] experiment measured the time-like nucleon form factors (FFs) at center-of-mass energies between 2.0 GeV and 3.5 GeV [2–6]. These data present an oscillating behavior [7–12], which manifests itself as a periodic, exponentially damped component over the typical dipolar carrier, usually identified as the only contribution. The nature of such an oscillating component is still unknown. Possible explanations rely either on the final state interaction between the baryon and the antibaryon, or in a phenomenon intrinsic to the baryon structure. In the latter case, the invoked phenomenon would be encoded by the EMFFs of nucleons.

In order to investigate this eventuality we propose a parametrization for the EMFFs defined by considering the nucleons as triplets of collinear quarks lying at light-like distances in the light-front framework [13].

The matrix element of the “+” component of the hadronic current J^μ , which depends directly on the EMFFs, evaluated between the baryon and antibaryon particle states, can then be expanded using the Lorentz

invariance of the three quark Fock state’s matrix elements.

The resulting form depends on a set of functions of the four momentum squared fractions, called light cone distribution amplitudes (LCDAs), and a deep knowledge of their expression can provide further information about the form factors shape. Using the \mathcal{L}_{QCD} conformal symmetry [14], the LCDAs are expanded on a polynomial basis, the most common choice being represented by the orthonormal Appell polynomials, defined on the triangle $T(x_1, x_3) = \{(x_1, x_3) \in \mathbb{R} : x_1 > 0, x_3 > 0, x_1 + x_3 < 1\}$, where $x_i = k_i^+/P^+$ are the quark’s light front momentum fractions along is the (+) direction and so the following relation holds: $\sum_{i=1}^3 x_i = 1$. The only unknown quantities now are the expansion coefficients, which have to be determined considering the phenomenology of the problem. The nonperturbative coefficients admit an evolution equation in the conformal symmetry framework, and their values can be determined theoretically by QCD sum rules. On the other hand, we are considering a center of mass energy of the system between 2.0 GeV and 3.5 GeV, so we are not allowed to use perturbative methods. What we propose then is to perform a truncated Laurent expansion of the non-perturbative coefficients over the negative powers of the four momentum squared, subsequently performing a fit over the recent BESIII experimental data to determine these coefficients. The final goal of this description is to find whether the oscillations of the EMFFs can be described by the model functions.

II. THE MICROSCOPIC MODEL

One of the most effective ways to describe subnuclear processes is to work on a light front framework, expanding the involved particle states in a free particle state basis, commonly known as Fock states. For a baryon we

* francesco.rosini@studenti.unipg.it

have

$$|\text{baryon}\rangle = |0\rangle + |qqq\rangle + |qqqg\rangle + |qqqq\bar{q}\rangle + \dots, \quad (1)$$

where the three-quark state can be expanded in a Lorentz series of its matrix element between the vacuum and the particle states. The expansion has already been performed in Ref. [15], e.g., for the proton has the form

$$\begin{aligned} & \langle 0 | \varepsilon^{ijk} u_\alpha^i(a_1 z) u_\beta^j(a_2 z) d_\gamma^k(a_3 z) | P \rangle \\ &= \frac{1}{4} \left[S_1 M C_{\alpha\beta} (\gamma_5 N^+)_{\gamma} + V_1 (\not{p} C)_{\alpha\beta} (\gamma_5 N^+)_{\gamma} \right. \\ & \quad + P_1 M (\gamma_5 C)_{\alpha\beta} N_{\gamma}^+ + A_1 (\not{p} \gamma_5 C)_{\alpha\beta} N_{\gamma}^+ \\ & \quad \left. + T_1 (i\sigma_{\perp p} C)_{\alpha\beta} (\gamma^{\perp} \gamma_5 N^+)_{\gamma} + \dots \right], \quad (2) \end{aligned}$$

where the functions S_1 , V_1 , P_1 , A_1 and T_1 are called light cone distribution amplitudes, they are functions of the scalar product $P \cdot z$, z being a light like four-vector. The dots in Eq. (2) indicate that the expansion has been written explicitly only for twist-3 LCDAs, while the complete expansion includes 24 LCDAs.

Considering now the whole expansion, we can find some conditions for the LCDAs imposing that the nucleon state isospin is 1/2. For example, for twist-3 LCDAs, the following equation holds

$$\begin{aligned} 2T_1(x_1, x_2, x_3) &= [V_1 - A_1](x_1, x_3, x_2) \\ & \quad + [V_1 - A_1](x_2, x_3, x_1), \end{aligned}$$

which allows to restrict the study of twist-3 LCDAs to a single function, which is chosen to be

$$\varphi_N(\mathbf{x}) = V_1(\mathbf{x}) - A_1(\mathbf{x}),$$

where \mathbf{x} is 3-vector (x_1, x_2, x_3) . Taking advantage from the conformal symmetry of the Lagrangian density \mathcal{L}_{QCD} , the twist-3 LCDA φ_N can be expanded over the orthonormalized Appell polynomials set $\{P_n(\mathbf{x})\}_n$ as follows

$$\varphi_N(\mathbf{x}, Q^2) = 120x_1x_2x_3 \sum_n B_n(Q^2) P_n(\mathbf{x}).$$

The set of non-perturbative coefficients $\{B_n\}_n$ is unknown and contains all the information about the form factor for the leading twist.

Each coefficient B_n is linked to the φ_N LCDA's momenta. The first coefficient B_0 is fixed being linked to the normalization of φ_N , i.e.,

$$B_0 = \int_0^1 dx_1 \int_0^1 dx_2 \int_0^1 dx_3 \varphi_N(\mathbf{x}, Q^2) = 1.$$

As already stated, since we are considering the non perturbative aspect of the LCDAs, we can perform an expansion over the negative powers of the four-momentum squared,

$$B_n(Q^2) = \sum_{k=0}^{M_n} b_k^{(n)} Q^{-2k}, \quad (3)$$

where $Q^2 = -q^2$, $\{b_k^{(n)}\}_{k=0}^{M_n}$ is the set of coefficients and M_n is the maximum power of Q^{-2} in the expansion of the n^{th} parameter B_n .

III. LEADING ORDER CONTRIBUTING DIAGRAMS

Taking the leading order into account, the minimum number of contributing diagrams has been evaluated in Ref. [15], where fourteen diagrams have been considered. The Sachs form factors which we are interested in are related to the Pauli and Dirac ones by the relations

$$\begin{aligned} G_E(Q^2) &= F_1(Q^2) - \tau F_2(Q^2), \\ G_M(Q^2) &= F_1(Q^2) + F_2(Q^2), \end{aligned}$$

where $\tau = Q^2 / (4M_B^2)$. We performed our fit over the effective form factor data, which is linked to the Sachs form factors by the relation

$$|G_{\text{eff}}| = \sqrt{\frac{|G_E|^2 + 2\tau |G_M|^2}{1 + 2\tau}}.$$

Following the works of Brodsky and Lepage [16], the light front EMFF can be written as the convolution of three probabilities, namely the probability of describing the baryon and antibaryon as a system of three collinear quarks, $\varphi_N(\mathbf{x}, Q^2)$, and the probability of finding a certain strong interaction, known as *hard scattering kernel* K_H . At the leading order, each of the fourteen contributing diagrams corresponds to a hard scattering kernel $K_i(\mathbf{x}, \mathbf{y})$, here $\varphi_N(\mathbf{x}) = V_1(\mathbf{x}) - A_1(\mathbf{x})$, and $T(\mathbf{x}) = T_1(\mathbf{x})$ are the light cone distribution amplitudes involved in the calculation.

In order to evaluate the form factor G_M , we used the Chernyak-Zhitnitsky [15] asymptotic formula

$$\begin{aligned} q^4 G_M(q^2) &\rightarrow \frac{(4\pi\bar{\alpha}_s)^2}{54} |f_N|^2 \\ & \int [dx] \int [dy] \left(2 \sum_{i=1}^7 e_i K_i(\mathbf{x}, \mathbf{y}) + \sum_{i=8}^{14} e_i K_i(\mathbf{x}, \mathbf{y}) \right), \quad (4) \end{aligned}$$

where $[dx] = \delta(1 - \sum_{i=1}^3 x_i) dx_1 dx_2 dx_3$ and $\bar{\alpha}_s$ is the modified coupling constant. For the evaluation of the modified coupling constant $\bar{\alpha}_s^2$, we follow the procedure proposed by Chernyak and Zhitnitsky in Ref. [15]. The value of $\bar{\alpha}_s^2$ is given by the product of the coupling constants for the two subprocesses, namely the two gluon exchanges which appear in the tree-level diagrams shown in Table I. The average virtuality \bar{q}_1^2 of the lightest gluon is $\bar{x}_3 \bar{y}_3 q^2$, while the rest gluon has an averaged virtuality $\bar{q}_2^2 = (1 - x_1)(1 - y_1)q^2$. The typical values of a realistic nucleon wave function for the \bar{x}_i are $\bar{x}_1 \simeq 2/3$, $\bar{x}_2 \simeq \bar{x}_3 \simeq 1/6$. Therefore $\bar{\alpha}_s^2(q^2) = \alpha_s(\frac{1}{36}q^2) \alpha_s(\frac{1}{9}q^2)$.

TABLE I. Diagrams and leading twist baryon wave functions [15].

Index i	Diagram	$K_i(\mathbf{x}, \mathbf{y})$
1		$\frac{\varphi_N(\mathbf{x})\varphi_N(\mathbf{y}) + 4T(\mathbf{x})T(\mathbf{y})}{(1-x_1)^2x_3(1-y_1)^2y_3}$
2		0
3		$\frac{-4T(\mathbf{x})T(\mathbf{y})}{x_1x_3(1-x_2)y_1y_3(1-y_1)}$
4		$\frac{\varphi_N(\mathbf{x})\varphi_N(\mathbf{y})}{x_1x_3(1-x_3)y_1y_3(1-y_1)}$
5		$\frac{-\varphi_N(\mathbf{x})\varphi_N(\mathbf{y})}{x_2x_3(1-x_3)y_2y_3(1-y_1)}$
6		0
7		$\left(\frac{1}{x_1y_1} + \frac{1}{x_2y_2}\right) \frac{\varphi_N(\mathbf{x})\varphi_N(\mathbf{y})}{(1-x_3)^2(1-y_3)^2}$
8		0
9		$\frac{\varphi_N(\mathbf{x})\varphi_N(\mathbf{y}) + 4T(\mathbf{x})T(\mathbf{y})}{(1-x_1)^2x_2(1-y_1)^2y_2}$
10		$\frac{\varphi_N(\mathbf{x})\varphi_N(\mathbf{y}) + 4T(\mathbf{x})T(\mathbf{y})}{(1-x_1)^2x_2(1-y_1)^2y_2}$
11		0
12		$\frac{-\varphi_N(\mathbf{x})\varphi_N(\mathbf{y})}{x_1x_2(1-x_3)y_1y_2(1-y_1)}$
13		$\frac{4T(\mathbf{x})T(\mathbf{y})}{x_1x_2(1-x_1)y_1y_2(1-y_2)}$
14		$\frac{-\varphi_N(\mathbf{x})\varphi_N(\mathbf{y})}{x_1x_2(1-x_1)y_1y_2(1-y_3)}$

The integrals in Eq. (4) are (weakly) convergent, it is possible to solve them analytically. The results have already been obtained in Ref. [14], and are reported in Appendix C. Non-perturbative-QCD effects are accounted for by considering the Q^2 -dependence of the B_n defined in Eq. (3) as truncated expansions in powers of Q^{-2} . The first parameter B_0 is fixed to 1 and is related to the zero order of the LCDA φ_N , so it is considered a constant. As for the other parameters, we are for now limiting our discussion to the LCDA's second order momenta, so we are only interested in the first six parameters, namely those of the set $\{B_n\}_{n=0}^5$.

For the truncated expansion, we propose $M_0 = 0$, $M_1 = M_2 = 1$, $M_3 = M_4 = M_5 = 2$, so that

$$\begin{aligned}
 B_0 &= 1, \\
 B_n(Q^2) &= b_0^{(n)} + \frac{b_1^{(n)}}{Q^2}, \quad n = 1, 2, \\
 B_m(Q^2) &= b_0^{(m)} + \frac{b_1^{(m)}}{Q^2} + \frac{b_2^{(m)}}{(Q^2)^2}, \quad m = 3, 4, 5. \quad (5)
 \end{aligned}$$

We obtain a closed expression of the form factor G_M depending only on the non-perturbative parameters for the

proton and the neutron. Since the nucleons are related by the isospin symmetry, their parameters are the same we can performed a simultaneous fit to the recent BESIII data on proton and neutron cross sections to determine the sets of coefficients $\left\{ \{b_k^{(n)}\}_{k=0}^{M_n} \right\}_{n=0}^5$. The fit is performed using the ROOT Data Analysis Framework [17] program.

IV. RESULTS AND DISCUSSION

Figure 1 shows the results for the effective proton (upper panel) and neutron (lower panel) form factors in comparison with the experimental values measured by the BESIII experiment [2–4]. The fit functions depend on 13 free parameters, which are the coefficients of the expressions of Eq. (5). The normalized minimum χ^2 is

$$\frac{\chi^2}{n_{\text{DoF}}} = \frac{79.93}{43} \simeq 1.79.$$

It has been obtained by using 48 data points of the proton cross section and 18 of the neutron one. The error bands have been determined by considering both the errors of data, and the theoretical systematic error of the model, which has been estimated by using expressions for the $B_n(Q^2)$ parameters with the additional power $(Q^{-2})^{M_n+1}$.

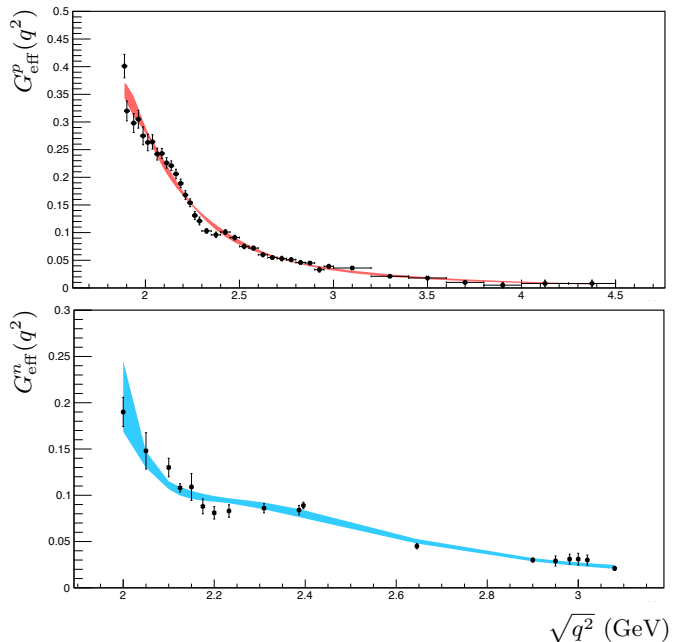


FIG. 1. The bands represent the fit results for the proton (upper panel) and neutron (lower panel) effective form factor. The data are from the BESIII experiment [2–4].

Figure 2 shows the twist-3 nucleon distribution amplitude

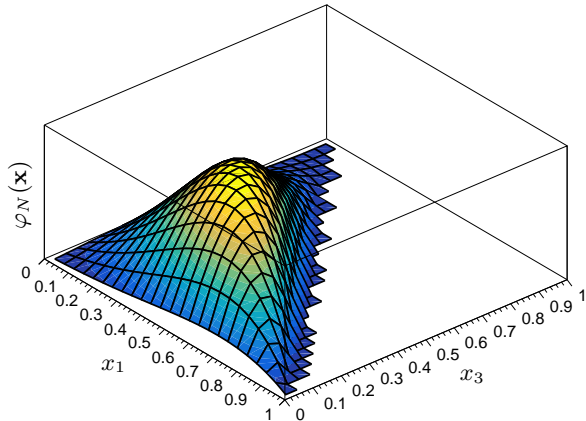


FIG. 2. The nucleon distribution function $\varphi_N(\mathbf{x})$ obtained at $\sqrt{-Q^2} = 2.5$ GeV as a function of x_1 and x_3 .

$\varphi_N(\mathbf{x})$ evaluated at $\sqrt{-Q^2} = 2.5$ GeV. The maximum value is reached at the light-cone momentum fractions

$$x_1 \simeq 0.49, \quad x_2 \simeq 0.24, \quad x_3 \simeq 0.27,$$

which agree with the assumption made in the Chernyak-Zhitnitsky formula [15] that the first quark has a momentum fraction about 50% larger than the other two, which equally divide the remaining momentum fraction.

Summarizing, a coherent model has been developed to reproduce the data on proton and neutron EMFFs, recently obtained by the BESIII collaboration. The model is based on a parameterization of the light-cone distribution amplitudes, and obeys conformal symmetry of the QCD Lagrangian.

The light-front quantization allows us to express the three-quark operator, occurring in the expression of the hard scattering kernel, as the Fourier transform of the light-cone distribution amplitudes, which, in turn, describe the behaviour of the three valence quarks constituting the baryon in a light-cone system. Always under the aegis of the QCD-Lagrangian conformal symmetry we expanded the leading-twist baryon distribution amplitudes over a set of Appell polynomials, which diagonalize the one gluon exchange kernel. The non-perturbative nature of the baryon distribution amplitudes is implemented by considering a Q^2 -dependence of the expansion parameters $\{B_n\}_n$. We have restricted our calculations to the first six Appell polynomials.

These distribution amplitudes have been used to calculate the near threshold behaviour of the nucleon effective form factors, extending the valence of an asymptotic formula to the low-momentum transfer region. Such a near-threshold extension has been obtained by considering a Q^2 -dependence of the expansion parameters $\{B_n(Q^2)\}_n$, as polynomials of zero, first and second degree of Q^{-2} .

Moreover, since the nucleon EMFFs are linked by the

isospin symmetry, the same set $\{B_n(Q^2)\}_n$ can be used and the free coefficients of their power series can be determined by means a simultaneous fit to the proton and neutron data. The error bands of the near-threshold effective nucleon form factors, have been obtained by considering the experimental uncertainties of the data, used to determine the free parameters of the model and the theoretical systematic uncertainties due to the particular parametrization used.

This study aims to identify the origin or at least the dominant cause of the oscillatory behaviour of the effective nucleon form factors. In particular, we would like to distinguish between two hypotheses about the oscillation phenomenon: the intrinsic dynamical origin and the final state interaction. In the first case, the oscillations appear at the form factor level, while in the second case, they are due to re-scattering reactions that happen when the nucleons are already formed. A necessary condition in favour of the intrinsic origin is that there exists a microscopic model of nucleons that can give oscillatory form factors.

Even though for the neutron effective form factor the model reproduces quite well the oscillatory behaviour, it seems to fail in the case of the proton. Indeed, the obtained behaviour of the effective proton form factor, the orange band shown in the upper panel of Fig. 1, is compatible with the so-called regular background of Refs. [7, 8, 11]. It can be interpreted as the contribution due to the short distance quark-level dynamics [18, 19], i. e., the $p\bar{p}$ final state is produced by the creation of quark-antiquark pairs within a small volume, with a linear dimension much smaller than the standard hadron size of about 1 fm.

Nevertheless, the model has the added value of proving that a unique parametrization in all the kinematical ranges where data are present is effective both for proton and neutron FFs. This is in contrast to previous works, where a common fit could only be achieved either in a restricted kinematical region, concluding in a change of the phase [3], or at the price of three different models applicable in different kinematical regions [5].

Appendix A: Contributing diagrams computation

Using the expressions [15]

$$\begin{aligned}\varphi_N(\mathbf{x}) &= 120x_1x_2x_3(ax_1^2 + bx_2^2 + cx_3^2 + dx_3 + e), \\ T(\mathbf{x}) &= 120x_1x_2x_3 \left[\frac{a+c}{2}(x_1^2 + x_2^2) + bp_3^2 + \right. \\ &\quad \left. \frac{d}{2}(1-x_3) + e \right],\end{aligned}\quad (\text{A1})$$

where the values of the coefficients a, b, c, d, e and f are given in Ref. [15], the analytic solutions of the integrals of Eq. (4), namely the ten non-vanishing expressions

$$\mathcal{K}_i = \int [dx] \int [dy] K_i(\mathbf{x}, \mathbf{y}), \quad (\text{A2})$$

where the functions $K_i(\mathbf{x}, \mathbf{y})$ are given in Table I, with $i \in \{1, 3, 4, 5, 7, 9, 10, 12, 13, 14\}$, are:

$$\begin{aligned}\mathcal{K}_1 &= \left(I_1^{(1)}\right)^2 + 4\left(I_1^{(2)}\right)^2, \\ I_1^{(1)} &= \frac{5}{12}(36a + 6b + 2c + 12d + 72e), \\ I_1^{(2)} &= \frac{5}{12}(21a + 20b + 3c + 32d + 72e); \quad (\text{A3})\end{aligned}$$

$$\begin{aligned}\mathcal{K}_3 &= -4I_3^{(1)}I_3^{(2)}, \\ I_3^{(1)} &= \frac{5}{3}(10a + 2b + 10c + 15d + 36e), \\ I_3^{(2)} &= \frac{5}{12}(15a + 6b + 15c + 28d + 72e); \quad (\text{A4})\end{aligned}$$

$$\begin{aligned}\mathcal{K}_4 &= I_4^{(1)}I_4^{(2)}, \\ I_4^{(1)} &= \frac{5}{2}(a + 3b + 2(c + 2d + 6e)), \\ I_4^{(2)} &= \frac{5}{6}(6a + 9b + 3c + 8d + 36e); \quad (\text{A5})\end{aligned}$$

$$\begin{aligned}\mathcal{K}_5 &= -I_5^{(1)}I_5^{(2)}, \\ I_5^{(1)} &= \frac{5}{2}(3a + b + 2(c + 2d + 6e)) \\ I_5^{(2)} &= \frac{10}{3}(9a + b + c + 3d + 18e); \quad (\text{A6})\end{aligned}$$

$$\begin{aligned}\mathcal{K}_7 &= \left(I_7^{(1)}\right)^2 + \left(I_7^{(2)}\right)^2, \\ I_7^{(1)} &= \frac{5}{6}(a + 3(b + 6c + 8d + 12e)), \\ I_7^{(2)} &= \frac{5}{6}(3a + b + 6(3c + 4d + 6e)); \quad (\text{A7})\end{aligned}$$

$$\begin{aligned}\mathcal{K}_9 &= \mathcal{K}_{10} = \left(I_9^{(1)}\right)^2 + 4\left(I_9^{(2)}\right)^2, \\ I_9^{(1)} &= \frac{5}{6}(18a + b + 3c + 8d + 36e), \\ I_9^{(2)} &= \frac{5}{12}(19a + 6b + 19c + 28d + 72e); \quad (\text{A8})\end{aligned}$$

$$\begin{aligned}\mathcal{K}_{12} &= -I_{12}^{(1)}I_{12}^{(2)}; \\ I_{12}^{(1)} &= \frac{10}{3}(a + b + 9c + 12d + 18e), \\ I_{12}^{(2)} &= \frac{5}{6}(6a + 3b + 9c + 16d + 36e); \quad (\text{A9})\end{aligned}$$

$$\begin{aligned}\mathcal{K}_{13} &= 4I_{13}^{(1)}I_{13}^{(2)} \\ I_{13}^{(1)} &= \frac{5}{12}(-3a + 90b - 3c + 100d + 360e), \\ I_{13}^{(2)} &= \frac{5}{12}(9a + 18b + 9c + 20d + 72e); \quad (\text{A10})\end{aligned}$$

$$\begin{aligned}\mathcal{K}_{14} &= -I_{14}^{(1)}I_{14}^{(2)}, \\ I_{14}^{(1)} &= \frac{5}{6}(6a + 3b + 9c + 16d + 36e), \\ I_{14}^{(2)} &= \frac{10}{3}(a + b + 9c + 12d + 18e). \quad (\text{A11})\end{aligned}$$

Appendix B: Distribution amplitudes computation

1. Quark distribution amplitudes complex conjugate computation

Omitting the color and current indices, there is a proportionality between the hadronic current matrix element and the quark distribution amplitudes, given by

$$\langle P' | J | P \rangle \propto \langle P' | \bar{u}_\mu \bar{u}_\nu \bar{d}_\rho | 0 \rangle \langle 0 | K_H^{\mu\nu\rho\alpha\beta\gamma} | 0 \rangle \langle 0 | u_\alpha u_\beta d_\gamma | P \rangle, \quad (\text{B1})$$

so that the transition amplitude is proportional to the vacuum expectation value of the hard scattering kernel. The Feynman diagram is depicted in Fig. 3.

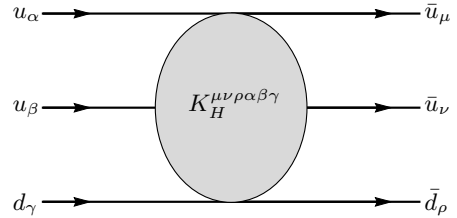


FIG. 3. Basic graph for the hard scattering kernel.

The hard scattering structure $K_H^{\mu\nu\rho\alpha\beta\gamma}$ is given by a product of the three Lorentz structures which give the coupling of the three fermion lines:

$$K_H^{\mu\nu\rho\alpha\beta\gamma} = \Gamma_1^{\alpha\mu} \Gamma_2^{\beta\nu} \Gamma_3^{\gamma\rho}. \quad (\text{B2})$$

First of all, we need to write the complex conjugate of the matrix element representing the distribution amplitude $\varphi_N(\mathbf{x})$. We calculate this directly as we can take the complex conjugate of the three parts composing the matrix element expansion:

$$\begin{aligned}\langle 0 | u_\alpha u_\beta d_\gamma | P \rangle^* &= \langle P | d_\gamma^\dagger u_\beta^\dagger u_\alpha^\dagger | 0 \rangle \\ &= \langle P | \bar{d}_i \bar{u}_j \bar{u}_k | 0 \rangle \gamma_{i\gamma}^0 \gamma_{j\beta}^0 \gamma_{k\alpha}^0. \quad (\text{B3})\end{aligned}$$

For the axial component we have

$$\begin{aligned}
\langle P | \bar{d}_i \bar{u}_j \bar{u}_k | 0 \rangle_A &= A_1^* (\not{P} \gamma_5 C)_{\alpha\beta}^* N(P)_\gamma \gamma_{\gamma i}^0 \gamma_{\beta j}^0 \gamma_{\alpha k}^0 \\
&= A_1^* \left((\not{P} \gamma_5 C)^\dagger \right)_{\beta\alpha} \bar{N}(P)_i \gamma_{\beta j}^0 \gamma_{\alpha k}^0 \\
&= A_1^* (C \gamma_5 \not{P})_{jk} \bar{N}(P)_i, \quad (\text{B4})
\end{aligned}$$

for the vector one

$$\begin{aligned}
\langle P | \bar{d}_i \bar{u}_j \bar{u}_k | 0 \rangle_V &= V_1^* (\not{P} C)_{\alpha\beta}^* (\gamma_5 N(P))_\gamma \gamma_{\gamma i}^0 \gamma_{\beta j}^0 \gamma_{\alpha k}^0 \\
&= -V_1^* \left((\not{P} C)^\dagger \right)_{\beta\alpha} (\bar{N}(P) \gamma_5)_i \gamma_{\beta j}^0 \gamma_{\alpha k}^0 \\
&= -V_1^* (C \not{P})_{jk} (\bar{N}(P) \gamma_5)_i, \quad (\text{B5})
\end{aligned}$$

and finally for the tensorial part

$$\begin{aligned}
\langle P | \bar{d}_i \bar{u}_j \bar{u}_k | 0 \rangle_T &= T_1^* (\not{\sigma}^{\mu\nu} P_\nu C)_{\alpha\beta}^* (\gamma_\mu \gamma_5 N(P))_\gamma \\
&\quad \gamma_{\gamma i}^0 \gamma_{\beta j}^0 \gamma_{\alpha k}^0 \\
&= -T_1^* \left((\not{\sigma}^{\mu\nu} P_\nu C)^\dagger \right)_{\beta\alpha} (\bar{N}(P) \gamma_5 \gamma_\mu)_i \\
&\quad \gamma_{\beta j}^0 \gamma_{\alpha k}^0 \\
&= -T_1^* (C P_\nu \not{\sigma}^{\mu\nu})_{jk} (\bar{N}(P) \gamma_5 \gamma_\mu)_i. \quad (\text{B6})
\end{aligned}$$

2. Distribution amplitudes convolutions

Here we compute the convolution of the distribution amplitudes used for the evaluation of the contributing diagrams. In each of the following calculations we use the anti-commutative properties of the gamma matrices, in particular the fact that the γ_5 matrix anti commutes with every component of the matrix four-vector γ^μ , while for the charge conjugation matrix C the following rule holds:

$$C \gamma^\mu C = -(\gamma^\mu)^T. \quad (\text{B7})$$

The axial, vector, tensor, and axial-vector components of the hadronic-current matrix element are, respectively,

$$\begin{aligned}
\langle P' | J | P \rangle_A &= \langle P' | \bar{u}_\mu \bar{u}_\nu \bar{d}_\rho | 0 \rangle_A \langle 0 | K_H^{\mu\nu\rho\alpha\beta\gamma} | 0 \rangle \langle 0 | u_\alpha u_\beta d_\gamma | P \rangle_A \\
&= A_1^* \left(C \gamma_5 \not{P}' \right)_{\mu\nu} (\bar{N} P')_\rho \Gamma_1^{\mu\alpha} \Gamma_2^{\nu\beta} \Gamma_3^{\rho\gamma} A_1 \\
&\quad (\not{P} \gamma_5 C)_{\alpha\beta} N(P)_\gamma \\
&= |A_1|^2 \bar{N}(P') \Gamma_3 N(P) \\
&\quad \left[-\Gamma_1^{\mu\alpha} (\not{P} \gamma_5 C)_{\alpha\beta} (\Gamma_2^T)^{\beta\nu} (C \gamma_5 \not{P}')_{\nu\mu} \right] \\
&= -|A_1|^2 \bar{N}(P') \Gamma_3 N(P) \\
&\quad \text{Tr} \left[\Gamma_1 \not{P} \gamma_5 C \Gamma_2^T C \gamma_5 \not{P}' \right] \\
&= (-1)^{1+2n_2} |A_1|^2 \bar{N}(P') \Gamma_3 N(P) \\
&\quad \text{Tr} \left[\Gamma_1 \not{P} \overleftrightarrow{\Gamma}_2 \not{P}' \right]; \quad (\text{B8})
\end{aligned}$$

$$\begin{aligned}
\langle P' | J | P \rangle_V &= \langle P' | \bar{u}_\mu \bar{u}_\nu \bar{d}_\rho | 0 \rangle_V \langle 0 | K_H^{\mu\nu\rho\alpha\beta\gamma} | 0 \rangle \langle 0 | u_\alpha u_\beta d_\gamma | P \rangle_V \\
&= -V_1^* \left(C \not{P}' \right)_{\mu\nu} (\bar{N}(P') \gamma_5)_\rho \Gamma_1^{\mu\alpha} \Gamma_2^{\nu\beta} \Gamma_3^{\rho\gamma} \\
&\quad V_1 (\not{P} C)_{\alpha\beta} (N(P) \gamma_5)_\gamma \\
&= (-1)^{1+n_3} |V_1|^2 \bar{N}(P') \Gamma_3 N(P) \\
&\quad \left[(\Gamma_1)_{\mu\alpha} (\not{P} C)_{\alpha\beta} (\Gamma_2^T)_{\beta\nu} (C \not{P}')_{\nu\mu} \right] \\
&= (-1)^{1+n_3} |V_1|^2 \bar{N}(P') \Gamma_3 N(P) \\
&\quad \text{Tr} \left[\Gamma_1 \not{P} C \Gamma_2^T C \not{P}' \right] \\
&= (-1)^{1+n_2+n_3} |V_1|^2 \bar{N}(P') \Gamma_3 N(P) \\
&\quad \text{Tr} \left[\Gamma_1 \not{P} \overleftrightarrow{\Gamma}_2 \not{P}' \right] \\
&= -|V_1|^2 \bar{N}(P') \Gamma_3 N(P) \text{Tr} \left[\Gamma_1 \not{P} \overleftrightarrow{\Gamma}_2 \not{P}' \right]; \quad (\text{B9})
\end{aligned}$$

$$\begin{aligned}
\langle P' | J | P \rangle_T &= \langle P' | \bar{u}_\mu \bar{u}_\nu \bar{d}_\rho | 0 \rangle_T \langle 0 | K_H^{\mu\nu\rho\alpha\beta\gamma} | 0 \rangle \langle 0 | u_\alpha u_\beta d_\gamma | P \rangle_T \\
&= T_1^* (C P'_\lambda \not{\sigma}^{\delta\lambda})_{\mu\nu} (\bar{N}(P') \gamma_5 \gamma_\delta)_\rho \Gamma_1^{\mu\alpha} \Gamma_2^{\nu\beta} \Gamma_3^{\rho\gamma} \\
&\quad T_1 (\not{\sigma}^{\eta\kappa} P_\kappa C)_{\alpha\beta} (\gamma_\eta \gamma_5 (N(P)))_\gamma \\
&= |T_1|^2 P'_\lambda P_\kappa \bar{N}(P') \gamma_\delta \Gamma_3 \gamma_\eta N(P) \\
&\quad \left[\Gamma_1^{\mu\alpha} (\not{\sigma}^{\eta\kappa} C)_{\alpha\beta} (\Gamma_2^T)_{\beta\nu} (C \not{\sigma}^{\delta\lambda})_{\nu\mu} \right] \\
&= |T_1|^2 P'_\lambda P_\kappa \bar{N}(P') \gamma_\delta \Gamma_3 \gamma_\eta N(P) \\
&\quad \text{Tr} \left[\Gamma_1 \not{\sigma}^{\eta\kappa} C \Gamma_2^T C \not{\sigma}^{\delta\lambda} \right] \\
&= |T_1|^2 P'_\lambda P_\kappa \bar{N}(P') \gamma_\delta \Gamma_3 \gamma_\eta N(P) \\
&\quad \text{Tr} \left[\Gamma_1 \not{\sigma}^{\eta\kappa} \overleftrightarrow{\Gamma}_2 \not{\sigma}^{\delta\lambda} \right]; \quad (\text{B10})
\end{aligned}$$

$$\begin{aligned}
&\langle P' | \bar{u}_\mu \bar{u}_\nu \bar{d}_\rho | 0 \rangle_A \langle 0 | K_H^{\mu\nu\rho\alpha\beta\gamma} | 0 \rangle \langle 0 | u_\alpha u_\beta d_\gamma | P \rangle_V \\
&+ \langle P' | \bar{u}_\mu \bar{u}_\nu \bar{d}_\rho | 0 \rangle_V \langle 0 | K_H^{\mu\nu\rho\alpha\beta\gamma} | 0 \rangle \langle 0 | u_\alpha u_\beta d_\gamma | P \rangle_A \\
&= \left[A_1^* \left(C \gamma_5 \not{P}' \right)_{\mu\nu} (\bar{N}(P'))_\rho V_1 (\not{P} C)_{\alpha\beta} (N(P) \gamma_5)_\gamma \right. \\
&\quad \left. - V_1^* \left(C \not{P}' \right)_{\mu\nu} (\bar{N}(P') \gamma_5)_\rho A_1 (\not{P} \gamma_5 C)_{\alpha\beta} N(P)_\gamma \right] \\
&\quad \Gamma_1^{\mu\alpha} \Gamma_2^{\nu\beta} \Gamma_3^{\rho\gamma} \\
&= -(V_1 A_1^* + V_1^* A_1) \bar{N}(P') \Gamma_3 \gamma_5 N(P) \text{Tr} \left[\Gamma_1 \not{P} \overleftrightarrow{\Gamma}_2 \not{P}' \right]. \quad (\text{B11})
\end{aligned}$$

Appendix C: Contributing diagrams in terms of the non-perturbative parameters

Here we write the integrals used for the calculation of the nucleon form factors $G_M^{p,n}$. The Chernyak-Zhitnitsky formula is

$$q^4 G_M^{p,n}(q^2) \rightarrow \frac{(4\pi\bar{\alpha}_s)^2}{54} |f_N|^2 I^{p,n}, \quad (\text{C1})$$

where the integrals $I^{p,n}$ up to the second degree polynomials are

$$\begin{aligned}
I^p &= 1400B_0B_1 + \frac{2000}{9}B_1^2 + 1800B_0B_2 + \frac{2800}{3}B_1B_2 \\
&\quad + 1200B_2^2 + 6600B_0B_3 + \frac{22000}{9}B_1B_3 + 4800B_2B_3 \\
&\quad + \frac{18800}{3}B_3^2 - \frac{1000}{3}B_0B_4 - \frac{2600}{27}B_1B_4 - \frac{2200}{9}B_2B_4 \\
&\quad - \frac{4600}{9}B_3B_5 + \frac{2600}{243}B_4^2 - 1400B_0B_5 - \frac{3500}{9}B_1B_5 \\
&\quad - \frac{1100}{3}B_2B_5 - \frac{5900}{3}B_3B_5 + \frac{4100}{81}B_4B_5 + \frac{7700}{27}B_5^2; \\
I^n &= 1800B_0^2 - 1400B_0B_1 + \frac{2000}{9}B_1^2 - 1800B_0B_2 \\
&\quad - \frac{2800}{3}B_1B_2 - 200B_2^2 - 1000B_0B_3 - \frac{22000}{9}B_1B_3 \\
&\quad - 2000B_2B_3 - \frac{17000}{9}B_3^2 + \frac{1000}{3}B_0B_4 - \frac{2600}{27}B_1B_4 \\
&\quad + \frac{2200}{9}B_2B_4 + \frac{4600}{9}B_3B_5 + \frac{2600}{243}B_4^2 + \frac{2000}{3}B_0B_5 \\
&\quad + \frac{3500}{9}B_1B_5 + \frac{500}{9}B_2B_5 + \frac{6500}{9}B_3B_5 - \frac{4100}{81}B_4B_5 \\
&\quad - \frac{7250}{81}B_5^2, \tag{C2}
\end{aligned}$$

where the coefficients $\{B_n\}_{n=0}^5$ are the ones appearing in the expansion of the LCDA $\varphi_N(\mathbf{x}, Q^2)$, and their operative form is given in Eq. (5).

-
- [1] Institute of high energy physics chinese academy of sciences, <https://web.archive.org/web/20160316234203/http://www.ihep.ac.cn/english/E-Bepc/>.
- [2] M. Ablikim, M. N. Achasov, P. Adlarson, and N. Amhed (BESIII Collaboration), Study of the process $e^+e^- \rightarrow p\bar{p}$ via initial state radiation at besiii, *Phys. Rev. D* **99**, 092002 (2019).
- [3] M. Ablikim, M. N. Achasov, P. Adlarson, S. Ahmed, and M. Albrecht, Oscillating features in the electromagnetic structure of the neutron, *Nature Physics* **17**, 1200 (2021).
- [4] M. Ablikim, M. N. Achasov, P. Adlarson, and N. Amhed (BESIII Collaboration), Measurement of proton electromagnetic form factors in $e^+e^- \rightarrow p\bar{p}$ in the energy region 2.00–3.08 gev, *Phys. Rev. Lett.* **124**, 042001 (2020).
- [5] Q.-H. Yang, D. Guo, L.-Y. Dai, J. Haidenbauer, X.-W. Kang, and U.-G. Meißner, New insights into the oscillations of the nucleon electromagnetic form factors, *Science Bulletin* **68**, 2729 (2023).
- [6] M. Ablikim, M. N. Achasov, P. Adlarson, S. Ahmed, and M. Albrecht, Measurement of proton electromagnetic form factors in the time-like region using initial state radiation at besiii, *Physics Letters B* **817**, 136328 (2021).
- [7] A. Bianconi and E. Tomasi-Gustafsson, Periodic interference structures in the timelike proton form factor, *Phys. Rev. Lett.* **114**, 232301 (2015), arXiv:1503.02140 [nucl-th].
- [8] A. Bianconi and E. Tomasi-Gustafsson, Phenomenological analysis of near threshold periodic modulations of the proton timelike form factor, *Phys. Rev. C* **93**, 035201 (2016), arXiv:1510.06338 [nucl-th].
- [9] A. Bianconi and E. Tomasi-Gustafsson, Fourth dimension of the nucleon structure: Spacetime analysis of the timelike electromagnetic proton form factors, *Phys. Rev. C* **95**, 015204 (2017), arXiv:1611.02149 [hep-ph].
- [10] A. Bianconi and E. Tomasi-Gustafsson, Soft rescattering in the timelike proton form factor within a spacetime scheme, *Phys. Rev. C* **98**, 055204 (2018), arXiv:1809.05709 [nucl-th].
- [11] E. Tomasi-Gustafsson, A. Bianconi, and S. Pacetti, New fit of timelike proton electromagnetic form factors from e^+e^- colliders, *Phys. Rev. C* **103**, 035203 (2021), arXiv:2012.14656 [hep-ph].
- [12] E. Tomasi-Gustafsson, A. Bianconi, and S. Pacetti, Dynamical Properties of Baryons, *Symmetry* **13**, 1480 (2021).
- [13] S. J. Brodsky, H.-C. Pauli, and S. S. Pinsky, Quantum chromodynamics and other field theories on the light cone, *Physics Reports* **301**, 299 (1998).
- [14] V. Braun, S. Derkachov, G. Korchemsky, and A. Manashov, Baryon distribution amplitudes in QCD, *Nuclear Physics B* **553**, 355 (1999).
- [15] V. Chernyak and I. Zhitnitsky, Nucleon wave function and nucleon form factors in qcd, *Nuclear Physics B* **246**, 52 (1984).
- [16] G. P. Lepage and S. J. Brodsky, Exclusive processes in perturbative quantum chromodynamics, *Phys. Rev. D* **22**, 2157 (1980).
- [17] R. Brun and F. Rademakers, Root — an object oriented data analysis framework, *Nuclear Instruments and Methods in Physics Research Section A: Accelerators, Spectrometers, Detectors and Associated Equipment* **389**, 81 (1997), new Computing Techniques in Physics Research

- V.
- [18] V. A. Matveev, R. M. Muradian, and A. N. Tavkhelidze, Automodellism in the large - angle elastic scattering and structure of hadrons, *Lett. Nuovo Cim.* **7**, 719 (1973).
- [19] S. J. Brodsky and G. R. Farrar, Scaling Laws at Large Transverse Momentum, *Phys. Rev. Lett.* **31**, 1153 (1973).

Rare B and K decays in a scotogenic model

Chuan-Hung Chen^{1,2,*} and Cheng-Wei Chiang^{3,2,†}

¹*Department of Physics, National Cheng-Kung University, Tainan 70101, Taiwan*

²*Physics Division, National Center for Theoretical Sciences, Taipei 10617, Taiwan*

³*Department of Physics and Center for Theoretical Physics,
National Taiwan University, Taipei 10617, Taiwan*

(Dated: March 6, 2024)

Abstract

A scotogenic model can radiatively generate the observed neutrino mass, provide a dark matter candidate, and lead to rare lepton flavor-violating processes. We aim to extend the model to establish a potential connection to the quark flavor-related processes within the framework of scotogenesis, enhancing the unexpectedly large branching ratio (BR) of $B^+ \rightarrow K^+ \nu \bar{\nu}$, observed by Belle II Collaboration. Meanwhile, the model can address tensions between some experimental measurements and standard model (SM) predictions in flavor physics, such as the muon $g - 2$ excess and the higher BR of $B_s \rightarrow \mu^- \mu^+$. We introduce in the model the following dark particles: a neutral singlet Dirac-type lepton (N); two inert Higgs doublets ($\eta_{1,2}$), with one of which carrying a lepton number; a charged singlet dark scalar (χ^+), and a singlet vector-like up-type dark quark (T). The first two entities are responsible for the radiative neutrino mass, and χ^+ couples to right-handed quarks and leptons and can resolve the tensions existing in muon $g - 2$ and $B_s \rightarrow \mu^- \mu^+$. Furthermore, the BR of $B^+ \rightarrow K^+ \nu \bar{\nu}$ can be enhanced up to a factor of 2 compared to the SM prediction through the mediations of the dark T and the charged scalars. In addition, we also study the impacts on the $K \rightarrow \pi \nu \bar{\nu}$ decays.

*E-mail: physchen@mail.ncku.edu.tw

†E-mail: chengwei@phys.ntu.edu.tw

I. INTRODUCTION

Under an enormous number of experimental tests and with great success in most of them, the standard model (SM) has been established as a very good effective theory at and below the electroweak scale. However, certain empirical observations, such as the existence of neutrino mass and dark matter (DM), still await definitive resolutions. In addition, a long-standing issue in the anomalous magnetic dipole moment of muon (muon $g - 2$), observed in BNL [1] and further confirmed by Fermilab experiments [2], strongly hints at possibly a new interaction in the lepton sector.

Recently, the Belle II Collaboration with 362 fb^{-1} of data has observed the first evidence of $B^+ \rightarrow K^+ \nu \bar{\nu}$ decay, and the resulting branching ratio (BR) is reported as [3]:

$$\mathcal{B}(B^+ \rightarrow K^+ \nu \bar{\nu}) = [2.3 \pm 0.5 (\text{stat}) \pm_{-0.4}^{+0.5} (\text{syst})] \times 10^{-5} = (2.3 \pm 0.7) \times 10^{-5}. \quad (1)$$

When combined with earlier results measured by BaBar [4, 5] and Belle [6, 7], the weighted average is given by $\mathcal{B}(B^+ \rightarrow K^+ \nu \bar{\nu}) = (1.3 \pm 0.4) \times 10^{-5}$. Compared to the SM prediction of $\mathcal{B}(B^+ \rightarrow K^+ \nu \bar{\nu})^{\text{SM}} = (4.92 \pm 0.30) \times 10^{-6}$ [8], the current data shows a 2.7σ deviation. This difference hints at the possibility of some peculiar interactions, predominantly manifesting in the $b \rightarrow s \nu \bar{\nu}$ or $b \rightarrow s + \text{invisible}$ transitions [9–23], rather than in $b \rightarrow s \ell^- \ell^+$ that is subject to strict constraints from $B \rightarrow X_s \ell^- \ell^+$ and $B_s \rightarrow \mu^- \mu^+$ decays.

A primary motivation of this study is to extend the existing scotogenic model [24] to enhance the $d_i \rightarrow d_j \nu \bar{\nu}$ decays and muon $g - 2$ while simultaneously explaining the observed neutrino data and dark matter relic density. To radiatively generate Majorana neutrino mass in a scotogenic model, lepton number-violating couplings are essential. Such violation of the lepton number could stem from the leptonic right-handed Majorana neutrino mass term, like in the type-I seesaw mechanism [25–28]. However, to prevent the mass scale of the introduced Majorana fermion from reaching an undetectable energy scale when the Yukawa couplings are of $O(m_\tau/v)$, either the Majorana fermion does not carry a lepton number [24] or a Dirac-type neutral fermion should be used instead [29]. In other words, the new heavy fermion mass term is unrelated to or retains the lepton number conservation. Therefore, within the framework of scotogenesis, the lepton number symmetry should be violated in some scalar coupling, for instance, a non-Hermitian quartic term, where the involved exotic scalar field carries a dark charge and is assigned a lepton number as proposed in the Ma model [24]. Since the lepton number symmetry will be restored when the scalar coupling,

which violates the lepton number, approaches zero, it can be considered as a technical naturalness if the scalar coupling is small [30].

If we focus on leptonic processes, one Higgs doublet, which carries a dark charge and lepton number, associated with 2 or 3 dark right-handed Majorana fermions in the Ma model can successfully account for the neutrino data observed from the neutrino oscillation experiments [24]. For simplicity, we will refer to a scalar carrying a dark charge as an inert scalar. As a result, this model has implications for rare leptonic decays, such as $\mu \rightarrow e\gamma$, $\mu \rightarrow 3e$, $\mu - e$ conversion in nucleus processes [31, 32], and DM candidate [24]. However, due to the absence of the lepton quantum number in quarks, the lepton number-carrying Higgs doublet in the Ma model has no interactions with the quarks. This remains true even with the introduction of a new heavy quark carrying a dark charge; otherwise, the lepton number violation will occur in the quark Yukawa couplings, leading to the breakdown of R_p -parity, defined as $R_p = (-1)^{3B+L+2S}$, where B , L , and S denote the baryon, lepton, and spin quantum numbers of a particle.

To incorporate the effects responsible for the loop-induced neutrino mass into the rare flavor-changing neutral-current (FCNC) B and K decay processes, a suitable extension of the Ma model is called for. We, therefore, aim to identify a minimal extension that not only addresses the issues of neutrino mass, DM relic density, and muon $g-2$ but also significantly enhances the BRs in the $d_i \rightarrow d_j \nu \bar{\nu}$ decays.

We find that the essential part to achieve our goal is the introduction of an inert Higgs doublet in the absence of the lepton number association. To preserve the lepton number conservation in the Yukawa sector, it is imperative to replace the Majorana-type neutral fermion used in the Ma model with a vector-like Dirac-type neutral lepton. Furthermore, to establish the connection between the SM quarks and the particles within the dark sector through the non-leptonic inert Higgs, it is necessary to introduce a new quark with an appropriate dark charge. For the sake of gauge anomaly-free conditions, the minimal choice of the new dark quark is an $SU(2)_L$ singlet vector-like up-type quark.

Since the non-leptonic inert Higgs is an $SU(2)_L$ doublet, the Yukawa couplings only involve the left-handed SM quarks. In other words, when $d_i \rightarrow d_j \nu \bar{\nu}$ are enhanced, the effects contributing to $B_s \rightarrow \mu^- \mu^+$ align with the SM contribution and could result in constructive interference and pushing its BR above the current experimental data. To address the constraint arising from $B_s \rightarrow \mu^- \mu^+$, a right-handed quark current used to cancel the effect from

the left-handed current in the $b \rightarrow s$ transition becomes helpful. What is more is that in fact, the SM predicts $\mathcal{B}(B_s \rightarrow \mu^- \mu^+) = 3.78_{-0.10}^{+0.15} \times 10^{-9}$ [8], slightly higher than the current experimental measurement $\mathcal{B}(B_s \rightarrow \mu^- \mu^+) = (3.01 \pm 0.35) \times 10^{-9}$ [33]. The introduction of right-handed quark currents helps alleviate this tension.

Because the right-handed quarks and leptons in the SM and the introduced dark quark are $SU(2)_L$ singlet, we can employ an $SU(2)_L$ singlet electrically charged dark scalar to couple these particles. As a result, the right-handed currents for the $b \rightarrow s$ transition can be generated from one-loop Feynman diagrams. Moreover, through mixing with the inert Higgs doublet, the left- and right-handed leptons can couple to the physical inert charged scalars. This results in the corrections to lepton $g - 2$ being linear in the lepton mass. Therefore, the muon $g - 2$ can be significantly enhanced in the model. Based on the above analysis, the additional dark particles introduced in the model to explain the neutrino measurements and the muon $g - 2$, to fit $\mathcal{B}(B_s \rightarrow \mu^- \mu^+)$, and to enhance the $d_i \rightarrow d_j \nu \bar{\nu}$ processes are: the non-leptonic inert Higgs doublet, the singlet vector-like up-type dark quark, and the singlet dark-charged scalar.

The paper is structured as follows. We set up the scotogenic model and derive the Yukawa and relevant gauge couplings in Sec. II. Utilizing the obtained Yukawa couplings and scalar mixings, we formulate the loop-induced neutrino mass matrix and lepton $g - 2$ in Sec. III. The constraints from $b \rightarrow s \gamma$ and $|\Delta F| = 2$ arising from box diagrams are analyzed. In addition, the effective Hamiltonian for $d_i \rightarrow d_j (\nu \bar{\nu}, \mu^- \mu^+)$, which arises from the Z -penguin diagrams, is derived in this section. Based on the new interactions, the BRs for $B \rightarrow K^{(*)} \nu \bar{\nu}$, $K \rightarrow \pi \nu \bar{\nu}$, $B \rightarrow X_s \ell^- \ell^+$, and $B_s \rightarrow \mu^- \mu^+$ are computed in Sec. IV. The detailed numerical analysis and discussions of the phenomenological results are shown in Sec. V. The findings of this study are summarized in Sec. VI.

II. THE MODEL AND COUPLINGS

As stated in the introduction, the Majorana neutrino mass can be radiatively generated in the scotogenic model if lepton number violation originates from the coupling of the leptonic inert Higgs doublet to the non-leptonic inert Higgs and the SM Higgs doublets in the scalar potential. Moreover, by introducing an $SU(2)_L$ singlet vector-like up-type quark, we can have interesting phenomenological contributions to the FCNC B and K decays. Therefore,

to investigate the impacts of new physics on the processes of $d_i \rightarrow d_j(\nu\bar{\nu}, \ell^-\ell^+)$ while avoiding the strict constraints from the $B \rightarrow X_s\ell^-\ell^+$ and $B_s \rightarrow \mu^+\mu^-$ decays, we extend the SM by adding two Higgs doublet $\eta_{1,2}$, one charged scalar χ^\pm , and singlet vector-like neutral leptons $N_{L,R}$ and up-type quarks $T_{L,R}$, one for each chirality.

It is found that with appropriate charge assignment to the new particles, a global $U(1)_X$ dark symmetry exists in the model. Since a Z' -gauge boson is not necessary for the study, we do not gauge the $U(1)_X$ symmetry. For clarity, we show the representations and assignments of $U(1)_X$ charge and lepton number as follows:

$$\begin{aligned} \eta_1 &\sim (2, 1, q_X, 0), \quad \eta_2 \sim (2, 1, -q_X, -2), \\ N_{L,R} &\sim (1, 0, q_X, 1), \quad T_{L,R} \sim (1, 4/3, q_X, 0), \quad \chi^+ \sim (1, 2, q_X, 0), \end{aligned} \quad (2)$$

where the numbers in the parentheses denote in sequence the $SU(2)_L$ representation, the $U(1)_Y$ charge, the $U(1)_X$ charge, and the lepton number. We note that both η_2 and N carry the lepton number. Moreover, to ensure the stability of a DM candidate in the model, we assume that the $U(1)_X$ is exact, and the $\eta_{1,2}$ are assumed to have no nonzero vacuum expectation values (VEVs). Hence, the masses of the dark-charged scalars do not originate from the electroweak symmetry breaking.

We will focus on the loop-induced quark flavor-changing processes in this work. Details of the scalar potential, the scalar mixings, and the scalar mass spectra are presented in Appendix A. The main free parameters associated with the scalar sector are the masses of the inert charged Higgs bosons.

A. Yukawa couplings

Based on the representations and charge assignments in Eq. (2), the Yukawa couplings for the new particles are given by:

$$\begin{aligned} -\mathcal{L}_Y &= \bar{L}\mathbf{y}_1\tilde{\eta}_1N_R + \bar{L}\mathbf{y}_2\tilde{\eta}_2N_L^C + \bar{\ell}_R\mathbf{y}_\ell N_L\chi^- + m_N\bar{N}_LN_R \\ &+ \bar{Q}_L\mathbf{y}_T^R\tilde{\eta}_1T_R + \bar{d}_R\mathbf{y}_T^L T_L\chi^- + m_T\bar{T}_LT_R + \text{H.c.}, \end{aligned} \quad (3)$$

where the flavor indices are suppressed, L and Q_L denote respectively the left-handed lepton and quark doublets in the SM, $\tilde{\eta}_j = i\tau_2\eta_j^*$, $N^C = C\bar{N}^T$ is the charge conjugation of N , and m_N (m_T) is the mass of N (T). After electroweak symmetry breaking, we introduce the unitary flavor-mixing matrices $V_{R,L}^\ell$ and $V_{R,L}^q$ to diagonalize the charged lepton and quark

mass matrices. Since the neutrinos are still massless at the tree level, we can absorb the lepton flavor-mixing matrices to the Yukawa couplings $\mathbf{y}_{1,2,\ell}$. If we rotate away the weak phase of \mathbf{y}_1 , both \mathbf{y}_2 and \mathbf{y}_ℓ in general contain complex parameters. Thus, \mathbf{y}_2 can lead to a complex Majorana neutrino mass matrix through radiative corrections. Using the physical charged and neutral scalar states defined in Eqs. (A5) and (A9), the lepton Yukawa couplings can be obtained as:

$$\begin{aligned}
-\mathcal{L}_Y^\ell = & \bar{\nu}_L \mathbf{y}_1 N_R (c_\phi(S_1 - iA_1) - s_\phi(S_2 + iA_2)) \\
& + \bar{\nu}_L \mathbf{y}_2 N_L^C (s_\phi(S_1 + iA_1) + c_\phi(S_2 - iA_2)) - \bar{\ell}_L \mathbf{y}_2 N_L^C \eta_2^- \\
& - \bar{\ell}_L \mathbf{y}_1 N_R (c_\theta H_1^- - s_\theta H_2^-) + \bar{\ell}_R \mathbf{y}_\ell N_L (s_\theta H_1^- + c_\theta H_2^-) + m_N \bar{N}_L N_R + \text{H.c.},
\end{aligned} \tag{4}$$

where θ denotes the mixing angle between η_1^\pm and χ^\pm . Besides the masses of neutral scalars, we will show later that the loop-induced Majorana neutrino mass matrix depends on $\mathbf{y}_{1,2}$ and the angle θ .

Before electroweak symmetry breaking, the weak phases of $\mathbf{y}_T^{R,T}$ can be rotated away by redefining the phases of the quark fields u_L and $d_{L,R}$. After the symmetry breaking, when the quark-flavor mixing matrices are introduced for diagonalizing the quark mass matrices, we can redefine $V_L^u \mathbf{y}_T^R$ as \mathbf{y}_T^R in the $\bar{u}_L \mathbf{y}_T^R T_R \eta_1^{0*}$ term. As a result, the term related to the left-handed down-type quark becomes $\bar{d}_L V^\dagger \mathbf{y}_T^R T_R \eta_1^-$, where $V = V_L^u V_L^{d\dagger}$ represents the Cabibbo-Kobayashi-Maskawa (CKM) matrix. In terms of physical quark and scalar states, the Yukawa couplings of the new quark in the model are expressed as:

$$\begin{aligned}
-\mathcal{L}_Y^q = & \bar{u}_L \mathbf{y}_T^R T_R [c_\phi(S_1 - iA_1) - s_\phi(S_2 + iA_2)] \\
& + \bar{d} (\mathbf{C}_{Ti}^{Rk} P_R + \mathbf{C}_T^{Lk} P_L) T H_k^- + m_T \bar{T}_L T_R + \text{H.c.}
\end{aligned} \tag{5}$$

Here, $\mathbf{C}_T^{R1(2)} = -c_\theta(s_\theta) \mathbf{Y}_T^R$, and $\mathbf{C}_T^{L1(2)} = s_\theta(c_\theta) \mathbf{Y}_T^L$, with

$$\mathbf{Y}_T^R = V^\dagger \mathbf{y}_T^R, \quad \mathbf{Y}_T^L = V_R^d \mathbf{y}_T^L. \tag{6}$$

From Eq. (5), it can be seen that the down-type quarks only couple to the charged Higgses. Although the Yukawa couplings $\mathbf{y}_T^{R,L}$ can be tightly restrained by the up-type quark processes mediated by the scalars S_i and pseudoscalars A_i , such as $D - \bar{D}$ mixing, the constraint is essentially close to that from the $K - \bar{K}$ mixing. Without loss of generality, we will focus on the charged Higgs-mediated phenomena.

If the up-type quarks in the weak eigenstates are initially aligned with their physical states (i.e., $V_L^u = \mathbb{1}$), we then have $V = V_L^{d\dagger}$, which is well-determined in experiments. Since there

is no information on the right-handed quark flavor mixings, V_R^d is essentially an unspecified unitary matrix. To reduce the number of free parameters, we adopt the assumption that $V_R^d = V_L^d$. Indeed, the assumption can be realized in the left-right symmetric model or model with a Hermitian quark mass matrix. The unique CP-violating phase in the quark sector then arises from the Kobayashi-Maskawa (KM) phase in the CKM matrix. We will apply the assumption in the numerical analysis.

B. Gauge couplings

In addition to the Yukawa couplings, the alternative interactions essential for the study of the FCNC B and K decays are the gauge couplings of the photon (A_μ) and Z -boson to T , χ^\pm , and η_1^+ . Being an $SU(2)_L$ singlet and charged under $U(1)_X$, T does not mix with the SM quarks or couple with the W boson.

To obtain the relevant gauge interactions, we write the covariant derivatives of T , χ^\pm and η_i as:

$$\begin{aligned} D_\mu T &= (\partial_\mu + iQ_T g' B_\mu) T , \\ D_\mu \chi^+ &= (\partial_\mu + i g' B_\mu) \chi^+ , \\ D_\mu \eta_1 &= \left(\partial_\mu + i \frac{g}{2} \vec{\tau} \cdot \vec{W}_\mu + i \frac{g'}{2} B_\mu \right) \eta_1 , \end{aligned} \tag{7}$$

where the hypercharges of $Y_T = 4/3 = 2Q_T$, $Y_{\chi^+} = 2$ and $Y_{\eta_1} = 1$ have been explicitly used. Because η_2 does not couple to quarks, we refrain from showing its gauge couplings. Using the weak mixing angle, defined by $\cos \theta_W = g/\sqrt{g^2 + g'^2}$ and $\sin \theta_W = g'/\sqrt{g^2 + g'^2}$, and the relation of $g \sin \theta_W = g' \cos \theta_W = e$, we parametrize the photon and Z -boson states as:

$$\begin{aligned} A_\mu &= c_W B_\mu + s_W W_\mu^3 , \\ Z_\mu &= -s_W B_\mu + c_W W_\mu^3 , \end{aligned} \tag{8}$$

with $c_W \equiv \cos \theta_W$ and $s_W \equiv \sin \theta_W$. The gauge couplings of A_μ and Z_μ to the heavy new quark can be found as:

$$\mathcal{L}_{TTV} = -e Q_T \bar{T} \gamma_\mu T A^\mu - \frac{g}{2c_W} (-2Q_T s_W^2) \bar{T} \gamma_\mu T Z^\mu . \tag{9}$$

Note that as T is a vector-like quark, it has a vectorial coupling to the Z gauge boson.

For the gauge couplings of the charged scalars H_i^\pm , they can be obtained as:

$$\begin{aligned} \mathcal{L}_{H^-H^+V} &= ieA^\mu \sum_{i=1}^2 (H_i^+ \partial_\mu H_i^- - H_i^- \partial_\mu H_i^+) \\ &\quad + i \frac{g}{2c_W} c_{ij}^Z Z^\mu ((\partial_\mu H_i^-) H_j^+ - H_i^- \partial_\mu H_j^+) , \end{aligned} \quad (10)$$

where $c_{11}^Z = c_\theta^2 - 2s_W^2$, $c_{12}^Z = c_{21}^Z = c_\theta s_\theta$, and $c_{22}^Z = s_\theta^2 - 2s_W^2$. Because η_1^\pm and χ^\pm mix together and belong to different $SU(2)_L$ representations, the Z couplings to these charged Higgs fields are not diagonal. We note that the gauge couplings of scalars S_i and pseudoscalars A_i to the Z gauge boson can be expressed as $\mathcal{L}_{\text{kin}} \supset g/(2c_W) (A_i \partial_\mu S_i - S_i \partial_\mu A_i) Z^\mu$. From the results shown in Appendix A, S_i and A_i are degenerate due to the $U(1)_X$ symmetry. Therefore, these bosons cannot be the DM candidates; otherwise, the scalar boson scattering off the nucleon, $S_i \mathcal{N} \rightarrow A_i \mathcal{N}$ or its inverse process, mediated by the Z gauge boson will lead to too large a cross section that has already been excluded by the DM direct detection. Thus, the neutral Dirac fermion N is the DM candidate in this model. Utilizing the Yukawa couplings in Eq. (4), the annihilation cross section of $N\bar{N} \rightarrow f_{\text{SM}} \bar{f}_{\text{SM}}$ can accommodate the observed DM relic density when $m_N \lesssim 600$ GeV, as detailed in Ref. [29].

III. LOOP-INDUCED PROCESSES

In the following, we examine various loop-mediated processes that receive additional contributions from the new particles in the model.

A. Radiative neutrino mass and muon $g-2$

According to the lepton Yukawa couplings shown in Eq. (4), the Majorana neutrino mass matrix elements mediated by the neutral scalars and N can be obtained as:

$$m_{ij}^\nu = \frac{\sin(2\phi)}{32\pi^2} \bar{y}_{ij} m_N \left[\frac{m_{S_1}^2}{m_{S_1}^2 - m_N^2} \ln \left(\frac{m_{S_1}^2}{m_N^2} \right) - \frac{m_{S_2}^2}{m_{S_2}^2 - m_N^2} \ln \left(\frac{m_{S_2}^2}{m_N^2} \right) \right] , \quad (11)$$

where we have included the pseudoscalar A_i contributions, used the mass relation $m_{A_i} = m_{S_i}$, and defined the symmetric Yukawa couplings \bar{y}_{ij} in flavor indices as $\bar{y}_{ij} = y_{1i}^* y_{2j}^* + y_{2i}^* y_{1j}^*$. For illustration purposes, we take $m_{S_1} = 600$ GeV, $m_{S_2} = 800$ GeV, $m_N = 300$ GeV, $\phi \sim \mathcal{O}(10^{-7})$, and $\mathbf{y}_{1,2} \sim \mathcal{O}(10^{-2})$ which is the order of τ lepton Yukawa coupling in the SM, and obtain $m_{ij}^\nu \sim \mathcal{O}(10^{-2})$ eV. To have more impacts on the lepton flavor-violating

processes, such $\mu \rightarrow e\gamma$, $\mu \rightarrow 3e$, and $\mu - e$ conversion, one can take $\mathbf{y}_{1,2}$ of $\mathcal{O}(1)$ while keeping $\phi \sim 10^{-11}$ or $\lambda_5 \sim \mathcal{O}(10^{-10})$. In the limit of $\lambda_5 = 0$, the lepton number symmetry is restored. Therefore, a small λ_5 can be regarded as technically natural [30].

When considering the scheme with $\mathbf{y}_1 \sim \mathcal{O}(1)$, one might anticipate significant effects on $d_i \rightarrow s(\nu\bar{\nu}, \ell^-\ell^+)$ from box diagrams, where the T -quark, N -lepton, and charged Higgses run inside the loops. However, unlike the Z -penguin diagrams that induce dimension-4 d_i - s - Z^* couplings, the effective operators arising from the box diagrams for $d_i \rightarrow s(\nu\bar{\nu}, \ell^-\ell^+)$ are of dimension-6. In other words, the effective Wilson coefficients resulting from \mathbf{y}_1 are suppressed by m_W^2/m_T^2 . Consequently, the lepton Yukawa couplings cannot have a significant effect on the quark flavor-changing processes.

Using the Yukawa couplings in Eq. (4), the radiative corrections to the muon magnetic dipole moment mediated by $H_{1,2}^+$ and N can be obtained as:

$$\Delta a_\mu = -\frac{m_\mu s_{2\theta}}{16\pi^2} m_N \operatorname{Re}(y_{\ell 2} y_{12}^*) \left(\frac{J_1(w_{H_1^+})}{m_{H_1^+}^2} - \frac{J_1(w_{H_2^+})}{m_{H_2^+}^2} \right), \quad (12)$$

where $w_{H_i^+} \equiv m_N^2/m_{H_i^+}^2$, and J_1 is a loop integral, defined as:

$$J_1(w) = \frac{1+w}{2(1-w)^2} + \frac{w \ln w}{(1-w)^3}. \quad (13)$$

Because η_1^+ and χ^+ couple to the left-handed and right-handed leptons, respectively, the resulting Δa_μ is proportional to m_μ . The mass insertion factor occurring in the N propagator further enhances Δa_μ . In addition, without introducing χ^+ , the contribution to Δa_μ from η_1^+ would always have a negative sign. Assuming $m_{H_1^+} = 600$ GeV, $m_{\chi_1^+} = 800$ GeV, $m_N = 300$ GeV, $s_\theta = 0.1$, and $\operatorname{Re}(y_{\ell 2} y_{12}^*) = 0.2$ as an illustration, we obtain $\Delta a_\mu \simeq 2.2 \times 10^{-9}$.

The above numerical estimate demonstrates that the model can readily accommodate the observed neutrino mass and the muon $g - 2$ anomaly. Since the purely lepton-related processes in the model are similar to the study in Ref. [29], a detailed analysis can be found therein. This study primarily focuses on exploring rare quark flavor-changing processes.

B. $b \rightarrow s\gamma$

Due to the precision measurement of $b \rightarrow s\gamma$ decays, the new physics effects contributing to $b \rightarrow s(\nu\bar{\nu}, \ell^-\ell^+)$ are severely constrained. In this subsection, we examine the influence of new couplings on the $b \rightarrow s\gamma$ decays.

The effective Hamiltonian for $b \rightarrow s\gamma^{(*)}$ from photon-penguin diagrams mediated by $H_{1,2}^\pm$ and T can be parametrized as:

$$\mathcal{H}_{b \rightarrow s\gamma}^{NP} = k^2 \bar{s} \gamma^\mu (A_L P_L + A_R P_R) b A_\mu + \bar{s} \sigma^{\mu\nu} (B_L P_L + B_R P_R) b F_{\mu\nu}, \quad (14)$$

where k_μ is the momentum of the emitted photon, and $F_{\mu\nu}$ is the field strength tensor of the electromagnetic field. For an on-shell photon, i.e., $k^2 = 0$, only the dipole operators contribute. By dimensional analysis, since A_L and A_R are associated with vector currents and the chiralities in the initial and final states of quarks are the same, A_L and A_R are proportional to $1/m_T^2$ if T -quark is the heaviest particle in the model. As a result, the processes $b \rightarrow s \ell^- \ell^+$ from the off-shell photon are indeed suppressed and negligible.

The situation for the dipole operators is more complicated. By dimensional analysis, $B_{L,R}$ can depend on m_b/m_T^2 and $1/m_T$, where m_b arises from the application of the equation of motion or chirality flip in the b -quark propagator. Since $m_s \ll m_b$, we take $m_s \approx 0$. In terms of the weak states of η_1^+ and χ^+ , one can easily understand that the contribution from each of η_1^+ and χ^+ results in the dependence of m_b/m_T^2 . Since η_1^+ and χ^+ only couple to the left-handed and the right-handed quarks, respectively, to flip the chirality of the b -quark in the tensor-type weak currents, the mass effect of b -quark must appear. Hence, the dimension-4 Hamiltonian mediated by η_1^+/χ^+ leads to $B_{R,L} \propto m_b/m_T^2$.

When considering the mixing effect of η_1^+ and χ^+ , the chirality flip in the tensor-type current is automatically satisfied. Moreover, instead of the m_b effect, a mass insertion factor appears in the propagator of T that runs in the photon-penguin loop. Consequently, the contributions from the $\eta_1^+-\chi^+$ mixing are expected to be $B_{L,R} \propto c_\theta s_\theta/m_T$, which are larger than those from the individual η_1^+ and χ^+ contributions. The dominant effects of $B_{L,R}$ can then be expressed as:

$$\begin{aligned} B_L &= \frac{(2 + Q_T)c_\theta s_\theta}{32\pi^2 m_T} Y_{T2}^L Y_{T3}^{R*} \left(J_1(z_{H_2^+}) - J(z_{H_1^+}) \right), \\ B_R &= \frac{(2 + Q_T)c_\theta s_\theta}{32\pi^2 m_T} Y_{T2}^R Y_{T3}^{L*} \left(J_1(z_{H_2^+}) - J(z_{H_1^+}) \right), \end{aligned} \quad (15)$$

with $z_{H_i^+} \equiv m_{H_i^+}^2/m_T^2$. To avoid the constraint on $\mathbf{Y}_T^{R,L}$ from $b \rightarrow s\gamma$, we can either consider s_θ to be sufficiently small or $m_{H_1^+} \sim m_{H_2^+}$ for a subtle cancellation in $J_1(z_{H_2^+}) - J(z_{H_1^+})$. For numerical illustration purposes, we rewrite Eq. (14) in terms of the standard magnetic

dipole operators as:

$$\begin{aligned} \mathcal{H}_{b \rightarrow s \gamma}^{\text{NP}} &= -\frac{G_F V_{ts}^* V_{tb}}{\sqrt{2}} (C_7^{\text{NP}} O_{7\gamma} + C_7^{\prime \text{NP}} O_{7\gamma}^{\prime}) , \\ O_{7\gamma}^{(\prime)} &= \frac{em_b}{4\pi^2} \bar{s} \sigma_{\mu\nu} P_{R(L)} b F^{\mu\nu} . \end{aligned} \quad (16)$$

The SM results are $C_{7\gamma}^{\text{SM}} \approx -0.3$ and $C_7^{\prime \text{SM}} \approx 0$. Using the typical values of the parameters: $m_T = 1.2$ TeV, $m_{H_1^+} = 0.6$ TeV, $m_{H_2^+} = 0.8$ TeV, $s_\theta = 0.1$, and $Y_{T_2}^L Y_{T_3}^{R*} \sim Y_{T_2}^L Y_{T_3}^{R*} \sim 0.1$, we obtain $|C_{7\gamma}^{(\prime)\text{NP}}/C_{7\gamma}^{\text{SM}}| \sim 0.19$. As no anomalous signals are found in the $b \rightarrow s\gamma$ processes, we can simply suppress $C_{7\gamma}^{(\prime)\text{NP}}$ without further limiting the Yukawa couplings $\mathbf{Y}_T^{R,L}$, which are the primary factors contributing to the $|\Delta F| = 1$ and $|\Delta F| = 2$ ($F = K, B_d$, and B_s) processes in the model.

C. $|\Delta F| = 2$ from box diagrams

Among loop-induced FCNCs involving the down-type quarks, the essential and most well-measured processes are K and B_q ($q = d, s$) meson oscillations, characterized by the mass differences between their mass eigenstate, denoted by $\Delta m_{K, B_q}$. To evaluate the impact of new physics effects in the model on the $|\Delta F| = 2$ processes, we derive the Δm_F , including the SM contributions, as follows.

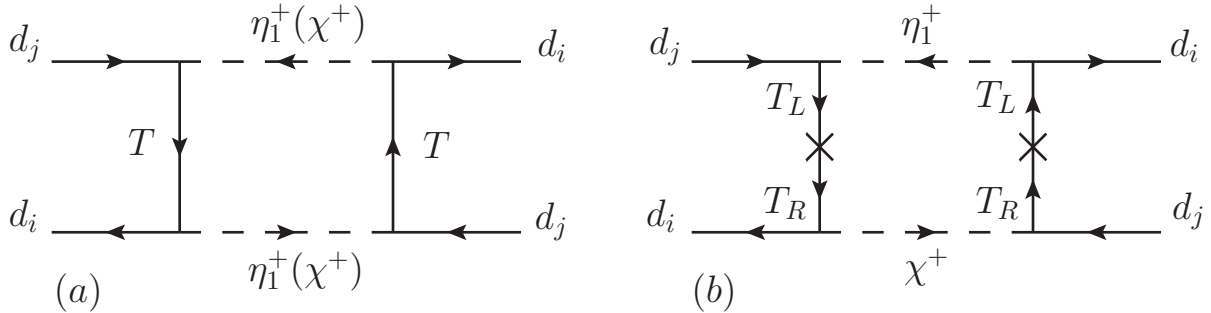


FIG. 1: Selected Feynman diagrams for $|\Delta F| = 2$ processes.

Since there is no FCNC coupling at the tree level, the $|\Delta F| = 2$ processes have to arise from the box diagrams, and the representative Feynman diagrams are sketched in Fig. 1, where the left-handed plot shows the mediation of $\eta_1^+ - \eta_1^+$ and $\chi^+ - \chi^+$, and the right-handed plot shows that of $\eta_1^+ - \chi^+$. Since the four fermions in the external legs of the box diagrams

lead to dimension-6 operators, the associated effective coefficients in the induced Hamiltonian have to be proportional to $1/m_T^2$. Although a m_T^2 factor appears at the propagators of T via the mass insertions, the dependence of $1/m_T^2$ is not changed in Fig. 1(b) because the denominator of the loop integrand has an eighth power of momentum in four-dimensional momentum integral. Therefore, the final result still shows the dependence of $1/m_T^2$. Using the Yukawa couplings shown in Eq. (5), the effective Hamiltonian for $|\Delta F| = 2$ can be obtained as:

$$\begin{aligned} \mathcal{H}^{\text{NP}}(|\Delta F| = 2) &= \frac{c_\theta^4}{4(4\pi)^2 m_T^2} (Y_{Ti}^R Y_{Tj}^{R*})^2 J_1(z_{H_1^+}) \bar{d}_i \gamma_\mu P_L d_j \bar{d}_i \gamma^\mu P_L d_j \\ &+ \frac{c_\theta^4}{4(4\pi)^2 m_T^2} (Y_{Ti}^L Y_{Tj}^{L*})^2 J_1(z_{H_2^+}) \bar{d}_i \gamma_\mu P_R d_j \bar{d}_i \gamma^\mu P_R d_j \\ &- \frac{c_\theta^4}{(4\pi)^2 m_T^2} (Y_{Ti}^L Y_{Tj}^{L*} Y_{Ti}^R Y_{Tj}^{R*}) J_2(z_{H_1^+}, z_{H_2^+}) \bar{d}_i P_L d_j \bar{d}_i P_R d_j, \end{aligned} \quad (17)$$

where all involved Feynman diagrams have been considered, the small contributions from the dependence of s_θ and m_b are neglected, and the flavor index pairs $(i, j) = (2, 1)$, $(3, 1)$, and $(3, 2)$ correspond to the K , B_d , and B_s mesons, respectively. The loop integral function J_1 is the same as that in Eq. (13), and J_2 is given by

$$J_2(w, x) = -\frac{1}{(1-w)(1-x)} - \frac{1}{w-x} \left[\frac{w \ln w}{(1-w)^2} - \frac{x \ln x}{(1-x)^2} \right]. \quad (18)$$

The mass differences between the heavy and light neutral K/B_q mesons are defined as:

$$\begin{aligned} \Delta m_K &= 2 \text{Re}(M_{12}^K) = 2 \text{Re}(\langle \bar{K} | \mathcal{H}(|\Delta S| = 2) | K \rangle), \\ \Delta m_{B_q} &= 2 |M_{12}^{B_q}| = 2 |\langle \bar{B}_q | \mathcal{H}(|\Delta S| = 2) | B_q \rangle|. \end{aligned} \quad (19)$$

To estimate the matrix elements of M_{12}^K and $M_{12}^{B_q}$ contributed from the new physics effects, we apply the results obtained in Ref. [34], where the QCD renormalization group effects from a high energy scale to a low μ scale are included. To apply the results from Ref. [34], the $|\Delta F| = 2$ Hamiltonian is parametrized by

$$\mathcal{H}(|\Delta F| = 2) = \frac{G_F^2}{16\pi^2} m_W^2 \sum_i C_i(\mu) Q_i, \quad (20)$$

where the operators Q_i are defined as [34]:

$$Q_1^{\text{VLL}} = (\bar{d}_i \gamma_\mu P_L d_j) (\bar{d}_i \gamma^\mu P_L d_j), \quad (21a)$$

$$Q_1^{\text{LR}} = (\bar{d}_i \gamma_\mu P_L d_j) (\bar{d}_i \gamma^\mu P_R d_j), \quad (21b)$$

$$Q_2^{\text{LR}} = (\bar{d}_i P_L d_j) (\bar{d}_i P_R d_j), \quad (21c)$$

$$Q_1^{\text{SLL}} = (\bar{d}_i P_L d_j) (\bar{d}_i P_L d_j), \quad (21d)$$

$$Q_2^{\text{SLL}} = (\bar{d}_i \sigma_{\mu\nu} P_L d_j) (\bar{d}_i \sigma^{\mu\nu} P_L d_j). \quad (21e)$$

Here we have suppressed the color indices. Since the matrix elements of the operators VRR and SRR are the same as those of VLL and SLL, we do not explicitly show these operators in Eq. (21). The master formula for the meson-antimeson matrix element is expressed as [34]:

$$M_{12}^{\text{F,NP}} = \frac{G_F^2 m_W^2 F_F^2 m_F}{16\pi^2 3} [P_1^{\text{VLL}} (C_1^{\text{VLL}} + C_1^{\text{RLL}}) + P_1^{\text{LR}} C_1^{\text{LR}} + P_2^{\text{LR}} C_2^{\text{LR}} + P_1^{\text{SLL}} (C_1^{\text{SLL}} + C_1^{\text{SRR}}) + P_2^{\text{SLL}} (C_2^{\text{SLL}} + C_2^{\text{SRR}})], \quad (22)$$

where P_i^α include the non-perturbative bag parameters and QCD running factors, C_i^α denote the effective coefficients at the high energy scale, and F_F is the decay constant of meson F . The values of P_i^α are shown in Table I [34]. We note that with the exception of P_1^{VLL} , the values of P_i^α in the K meson are one order of magnitude larger than those in the B_q meson due to the factor of $m_F^2/(m_{d_i} + m_{d_j})^2$. This factor in K is approximately 20 times larger than that in B_q .

TABLE I: Values of P_i^α used to estimate the matrix elements of the K , B_d , and B_s mesons.

	P_1^{VLL}	P_1^{LR}	P_2^{LR}	P_1^{SLL}	P_2^{SLL}
K	0.48	-36.1	59.2	-18.1	-32.2
B_d	0.84	-1.62	2.46	-1.47	-2.98
B_s	0.94	-1.83	2.78	-1.66	-3.37

From Eq. (17), the involved four-fermion operators are $Q_1^{\text{VLL,VRR}}$ and Q_2^{LR} . Using the master formula in Eq. (22), the resulting mixing matrix element for F transition to \bar{F} can

then be written as:

$$M_{12}^{\text{F, NP}} = \frac{F_F^2 m_F c_\theta^4}{48\pi^2 m_T^2} \left[\frac{P_1^{VLL}}{4} \left((Y_{T_i}^R T_{T_j}^{R*})^2 J_1(z_{H_1^+}) + (Y_{T_i}^L T_{T_j}^{L*})^2 J_1(z_{H_2^+}) \right) - P_2^{LR} (Y_{T_i}^R Y_{T_j}^{R*}) (Y_{T_i}^L Y_{T_j}^{L*}) J_2(z_{H_1^+}, z_{H_2^+}) \right]. \quad (23)$$

In order to combine the SM contributions, we write the SM results as [35]:

$$M_{12}^{\text{K, SM}} = \frac{G_F^2 m_W^2}{12\pi^2} F_K^2 m_K \hat{B}_K [\lambda_c^2 \xi_1 S_0(x_c) + \lambda_t^2 \xi_2 S_0(x_t) + 2\lambda_c \lambda_t \xi_3 S_0(x_c, x_t)] \quad (24)$$

$$M_{12}^{\text{Bq, SM}} = \frac{G_F^2 m_W^2}{12\pi^2} \lambda_t^2 F_{B_q}^2 m_{B_q} \hat{B}_{B_q} \xi_B S_0(x_t),$$

where $\lambda_k = V_{ki}^* V_{kj}$; $\xi_{1,2,3} = (1.87 \pm 0.76, 0.5765 \pm 0.0065, 0.496 \pm 0.047)$ [36] and $\xi_B = 0.5510 \pm 0.0022$ [37, 38] are the QCD correction factors, and \hat{B}_F is the renormalization scale-independent bag parameter. With $x_f \equiv m_f^2/m_W^2$, the S_0 functions are read as [35]:

$$S_0(x_c) = x_c,$$

$$S_0(x_t) = \frac{4x_t - 11x_t^2 + x_t^3}{4(1-x_t)^2} - \frac{3x_t^3 \ln x_t}{2(1-x_t)^3}, \quad (25)$$

$$S_0(x_c, x_t) = x_c \left(\ln \frac{x_t}{x_c} - \frac{3x_t}{4(1-x_t)} - \frac{3x_t^2 \ln x_t}{4(1-x_t)^2} \right).$$

Accordingly, the transition matrix element by combining the SM result and the charged-Higgs mediated effects is given by $M_{12}^F = M_{12}^{\text{F, SM}} + M_{12}^{\text{F, NP}}$. Using Eq. (19), we can obtain Δm_F .

D. Z-penguin induced $d_i \rightarrow d_j(\nu\bar{\nu}, \ell^-\ell^+)$

As alluded to earlier, the $d_i \rightarrow d_j \ell^-\ell^+$ processes mediated through the photon-penguin diagrams have negligible contributions due to the $1/m_T^2$ suppression. Box diagrams, mediated by T and N and governed by the Yukawa couplings \mathbf{y}_1 , can also induce $d_i \rightarrow d_j \ell^-\ell^+$. However, similar to the $|\Delta F| = 2$ case, the induced dimension-6 four-fermion operators of $d_i d_j \ell^-\ell^+$ are suppressed by $1/m_T^2$. Therefore, the primary contributions to $d_i \rightarrow d_j \ell' \bar{\ell}'$ ($\ell' = \nu_\ell, \ell^\pm$) in the model are predominantly from the Z-penguin diagrams. The dominant Feynman diagram is depicted in Fig. 2.

Analogous to Eq. (14), the loop-induced $d_i d_j Z^*$ vertices generally contain structures of vector and tensor currents. Through dimensional analysis and consideration of quark

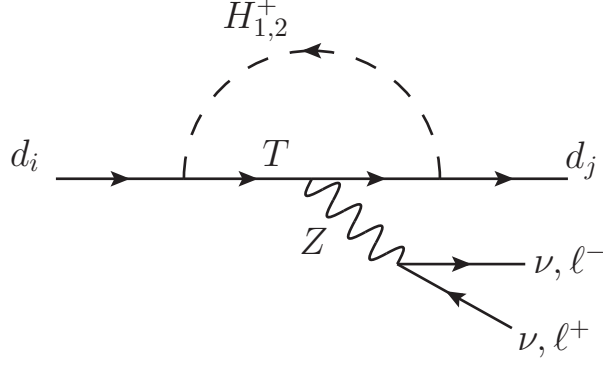


FIG. 2: Dominant Z -penguin Feynman diagrams for $d_i \rightarrow d_j(\nu\bar{\nu}, \ell^-\ell^+)$.

chirality, it can be found that the effective coefficients associated with the tensor currents are proportional to $c_\theta m_{d_i}/m_T^2$ and s_θ/m_T , where the former corresponds to the contributions from $\eta_1^+(\chi^+)$, and the latter is from the mixing of η_1^+ and χ^+ . As the tensor operator $\bar{d}_j\sigma_{\mu\nu}d_i Z^{\mu\nu}$ relates to the transition momentum $k_\mu = p_i - p_j$, roughly of the order of m_{d_i} , its contributions to $d_i \rightarrow d_j\ell\bar{\ell}$ are indeed suppressed by $c_\theta m_{d_i}\mathcal{O}(m_{d_i})/m_T^2$ and $s_\theta\mathcal{O}(m_{d_i})/m_T$. Hence, we can neglect the effects of the tensor operators.

Furthermore, when all Feynman diagrams, including self-energy diagrams, are considered to cancel the ultraviolet divergences, the dominant effects of Fig. 2 arise from the vector currents. Retaining the same chirality in the initial and final quarks requires a double mass insertion in the T -quark propagator; thus, the suppression factor of $1/m_T^2$ is replaced by the factor of m_T^2 in the induced effective coefficients. As a result, the effective Hamiltonian for $d_i \rightarrow d_j\ell\bar{\ell}$ can be derived as:

$$\mathcal{H}_{d_i \rightarrow d_j\ell\bar{\ell}}^{\text{NP}} = -\sqrt{2}G_F \bar{d}_j\gamma_\mu (C_{Zji}^L P_L + C_{Zji}^R P_R) d_i \bar{\ell}'\gamma^\mu (c_V^\ell - c_A^\ell\gamma_5) \ell', \quad (26)$$

where $c_V^\ell = I_\ell^3 - 2s_W^2 Q_\ell$ and $c_A^\ell = I_\ell^3$ with I_ℓ^3 being the third weak isospin of ℓ' , and the induced coefficients $C_{Zji}^{L,R}$ and loop integral function J_Z are given as:

$$\begin{aligned} C_{Zji}^L &= \frac{2Q_T s_W^2 c_\theta^2}{16\pi^2} Y_{Tj}^R Y_{Ti}^{R*} J_Z(z_{H_1^+}), \\ C_{Zji}^R &= \frac{2Q_T s_W^2 c_\theta^2}{16\pi^2} Y_{Tj}^L Y_{Ti}^{L*} J_Z(z_{H_2^+}), \\ J_Z(x) &= \frac{1}{1-x} + \frac{x \ln x}{(1-x)^2}. \end{aligned} \quad (27)$$

When $x \rightarrow 0$ and $x \rightarrow 1$, the asymptotic values of $J_Z(x)$ are 1 and 1/2, respectively.

Therefore, if we take the scheme of $s_\theta \ll 1$, the primary free parameters in the matrices $\mathbf{C}_Z^{L,R}$ are $\mathbf{Y}_T^{L,R}$.

IV. OBSERVABLES IN RARE B AND K DECAYS

Based on the Z -mediated interactions shown in Eq. (26), we discuss their contributions to the rare B and K decays in this section. The processes of interest include $B \rightarrow K^{(*)}\nu\bar{\nu}$, $K^+ \rightarrow \pi^+\nu\bar{\nu}$, $K_L \rightarrow \pi^0\nu\bar{\nu}$, $B_s \rightarrow \mu^-\mu^+$, and inclusive $B \rightarrow X_s\ell^-\ell^+$ decays. Since the influence on the angular observables of $B \rightarrow K^*\ell^-\ell^+$ is found to be insignificant for the parameters that enhance the BR of $B^+ \rightarrow K^+\nu\bar{\nu}$, we do not discuss them in this study.

A. $B \rightarrow (K, K^*)\nu\bar{\nu}$

Combining Eq. (26) with the interactions in the SM, the effective Hamiltonian for $b \rightarrow s\nu\bar{\nu}$ is written as:

$$\mathcal{H}_{b \rightarrow s\nu\bar{\nu}} = \frac{4G_F}{\sqrt{2}} \frac{\alpha}{2\pi s_W^2} \left[\left(V_{ts}^* V_{tb} X_t - \frac{\sqrt{2}G_F C_{Z23}^L}{C_{\text{SM}}^\nu} \right) \bar{s}\gamma^\mu P_L b \bar{\nu}\gamma_\mu P_L \nu - \frac{\sqrt{2}G_F C_{Z23}^R}{C_{\text{SM}}^\nu} \bar{s}\gamma^\mu P_R b \bar{\nu}\gamma_\mu P_L \nu \right], \quad (28)$$

where the neutrino flavors are suppressed, $\alpha = e^2/4\pi$, $X_t = 1.481 \pm 0.009$ [39], and $C_{\text{SM}}^\nu = 2G_F\alpha/(\sqrt{2}\pi s_W^2)$. The q^2 -dependent differential decay rate of $B \rightarrow K\nu\bar{\nu}$ is obtained as:

$$\frac{d\Gamma}{dq^2}(\bar{B} \rightarrow K\nu\bar{\nu}) = \frac{d\Gamma^{\text{SM}}}{dq^2}(B \rightarrow K\nu\bar{\nu}) \left| 1 - \frac{\sqrt{2}G_F(C_{Z23}^L + C_{Z23}^R)}{V_{ts}^* V_{tb} X_t C_{\text{SM}}^\nu} \right|^2. \quad (29)$$

Since the new interactions are lepton flavor-conserving and involve only the vector currents, we can factorize the new physics effects as a q^2 -independent scalar factor. Therefore, the ratio of BR in the model to the SM prediction can be simplified as:

$$R_K^\nu = \frac{\mathcal{B}(B^+ \rightarrow K^+\nu\bar{\nu})}{\mathcal{B}(B^+ \rightarrow K^+\nu\bar{\nu})^{\text{SM}}} = \left| 1 - \frac{\sqrt{2}G_F(C_{Z23}^L + C_{Z23}^R)}{V_{ts}^* V_{tb} X_t C_{\text{SM}}^\nu} \right|^2. \quad (30)$$

Using the form factors of $\bar{B} \rightarrow K^*$ defined in Appendix B, the partial differential decay

rate for $B \rightarrow K^* \nu \bar{\nu}$ is

$$\begin{aligned} \frac{d\Gamma}{dq^2}(B \rightarrow K^* \nu \bar{\nu}) = & \frac{G_F^2 \alpha^2}{256 \pi^5 s_W^4 m_B^3} q^2 \sqrt{\lambda_{K^*}} \left[\left| V_{ts}^* V_{tb} X_t + \frac{\sqrt{2} G_F}{C_{\text{SM}}^\nu} (C_{Z23}^L - C_{Z23}^R) \right|^2 H_{V,0}^2 \right. \\ & + \left(\left| V_{ts}^* V_{tb} X_t + \frac{\sqrt{2} G_F C_{Z23}^L}{C_{\text{SM}}^\nu} \right|^2 + \left| \frac{\sqrt{2} G_F C_{Z23}^R}{C_{\text{SM}}^\nu} \right|^2 \right) (H_{V,+}^2 + H_{V,-}^2) \\ & \left. - 4 \operatorname{Re} \left(\left(V_{ts}^* V_{tb} X_t + \frac{\sqrt{2} G_F C_{Z23}^L}{C_{\text{SM}}^\nu} \right) \frac{\sqrt{2} G_F C_{Z23}^R}{C_{\text{SM}}^\nu} \right) H_{V,+} H_{V,-} \right], \end{aligned} \quad (31)$$

where the q^2 -dependent λ_{K^*} and polarization factors $H_{V,0(\pm)}$ of K^* are defined as [10]:

$$\lambda_P(q^2) = m_B^4 + m_P^4 + q^4 - 2m_B^2 m_P^2 - 2m_P^2 q^2 - 2m_B^2 q^2, \quad (32a)$$

$$H_{V,0}(q^2) = \frac{8}{\sqrt{q^2}} m_B m_{K^*} A_{12}(q^2), \quad (32b)$$

$$H_{V,\pm}(q^2) = (m_B + m_{K^*}) A_1(q^2) \mp \frac{\sqrt{\lambda_{K^*}}}{m_B + m_{K^*}} V(q^2), \quad (32c)$$

with $A_{12}(q^2)$, $A_1(q^2)$, and $V(q^2)$ being the $\bar{B} \rightarrow K^*$ transition form factors. In our numerical estimates, we use the $\bar{B} \rightarrow K$ form factors obtained from the lattice QCD calculations [40], and the $\bar{B} \rightarrow K^*$ form factors obtained from the combination of light-cone sum rule and lattice QCD calculations [41]. To illustrate the influence of new physics, we define analogous to Eq. (30) the ratio:

$$R_{K^*}^\nu = \frac{\mathcal{B}(B_d \rightarrow K^{*0} \nu \bar{\nu})}{\mathcal{B}(B_d \rightarrow K^{*0} \nu \bar{\nu})^{\text{SM}}}. \quad (33)$$

B. $K^+ \rightarrow \pi^+ \nu \bar{\nu}$ and $K_L \rightarrow \pi \nu \bar{\nu}$

The effective Hamiltonian for $d \rightarrow s \nu \bar{\nu}$ in the model is written as:

$$\begin{aligned} \mathcal{H}_{d \rightarrow s \nu \bar{\nu}} = & C_{\text{SM}}^\nu \sum_{\ell=e,\mu,\tau} \left[\left(V_{cs}^* V_{cd} X_{\text{NNL}}^\ell + V_{ts}^* V_{td} X_t - \frac{\sqrt{2} G_F C_{Z21}^L}{C_{\text{SM}}^\nu} \right) \bar{s} \gamma^\mu P_L d \right. \\ & \left. - \frac{\sqrt{2} G_F C_{Z21}^R}{C_{\text{SM}}^\nu} \bar{s} \gamma^\mu P_R d \right] \bar{\nu}_\ell \gamma_\mu P_L \nu_\ell, \end{aligned} \quad (34)$$

where X_{NNL}^ℓ denotes the contributions from the charm quark with the QCD corrections calculated up to next-to-next-to-leading (NNL) order [42, 43], and the two-loop electroweak corrections also included [44]. Using the results formulated in Refs. [39, 45], the BRs of the

$K^+ \rightarrow \pi^+ \nu \bar{\nu}$ and $K_L \rightarrow \pi^0 \nu \bar{\nu}$ decays can be obtained respectively as:

$$\begin{aligned} \mathcal{B}(K^+ \rightarrow \pi^+ \nu \bar{\nu}) &= \kappa_+ (1 + \Delta_{\text{EM}}) \left[\left(\frac{\text{Im} X_{\text{eff}}}{\lambda^5} \right)^2 + \left(\frac{\text{Re}(V_{cs}^* V_{cd})}{\lambda} P_c(X) + \frac{\text{Re}(X_{\text{eff}})}{\lambda^5} \right)^2 \right], \\ \mathcal{B}(K_L \rightarrow \pi^0 \nu \bar{\nu}) &= \mathcal{B}(K_L \rightarrow \pi^0 \nu \bar{\nu})^{\text{SM}} \left| 1 - \frac{\sqrt{2} G_F \text{Im}(C_{Z21}^L + C_{Z21}^R)}{\text{Im}(V_{ts}^* V_{td}) X_t C_{\text{SM}}^\nu} \right|^2, \end{aligned} \quad (35)$$

where $\Delta_{\text{EM}} = -0.003$ is the electromagnetic radiative corrections, and $\kappa_+ = (5.173 \pm 0.025) \times 10^{-11} (\lambda/0.225)^8$. Here $P_c(X) = P_c^{\text{SD}}(X) + \delta P_{c,u} = 0.405 \pm 0.024$ denotes the charm-quark loop contributions, in which the short-distance part is given by [39]:

$$P_c^{\text{SD}}(X) = \frac{1}{\lambda^4} \left(\frac{2}{3} X_{\text{NNL}}^e + \frac{1}{3} X_{\text{NNL}}^\tau \right) = 0.365 \pm 0.012, \quad (36)$$

and the long-distance contribution is estimated as $\delta P_{c,u} = 0.04 \pm 0.02$ [46]. The factor X_{eff} that combines the SM and new physics effects is:

$$X_{\text{eff}} = V_{ts}^* V_{td} X_t - \frac{\sqrt{2} G_F}{C_{\text{SM}}^\nu} (C_{Z21}^L + C_{Z21}^R). \quad (37)$$

Similar to R_{K,K^*}^ν , we will explore the new physics effects contributing to rare K decays by using the ratio of the BR in the model to the SM prediction, defined as:

$$R_\pi^\nu = \frac{\mathcal{B}(K \rightarrow \pi \nu \bar{\nu})}{\mathcal{B}(K \rightarrow \pi \nu \bar{\nu})^{\text{SM}}}, \quad (38)$$

where $\pi = \pi^+(\pi^0)$ when $K = K^+(K_L)$.

It is worth mentioning that the new physics effects on $B^+ \rightarrow K^+ \nu \bar{\nu}$ and $K_L \rightarrow \pi^0 \nu \bar{\nu}$ can be factorized as a multiplicative factor as shown in Eqs. (30) and (35). Since we adopt $V_R^d = V_{\text{CKM}}$ in this study, the multiplicative factor in both equations indeed is approximately the same when the Yukawa couplings follow the hierarchy of $y_{T1}^{R(L)} \ll y_{T2}^{R(L)} \ll y_{T3}^{R(L)}$ due to the constraints from the $|\Delta F| = 2$ processes. If the small CP phase of V_{ts} is neglected, the new physics effect in Eqs. (30) and (35) can be expressed as:

$$\frac{(C_{Z23}^L + C_{Z23}^R)}{V_{ts}^* V_{tb}} \approx \frac{\text{Im}(C_{Z21}^L + C_{Z21}^R)}{\text{Im}(V_{ts}^* V_{td})} \approx \frac{2 Q_T s_W^2 c_\theta^2}{16 \pi^2} \left[\left(y_{T3}^R + \frac{y_{T2}^R}{V_{ts}} \right) y_{T3}^R + R \rightarrow L \right]. \quad (39)$$

That is, we obtain $R_K^\nu \simeq R_{\pi^0}^\nu$ in the model. We will explicitly demonstrate the relationship in the numerical analysis.

C. $B \rightarrow X_s \ell^- \ell^+$ and $B_s \rightarrow \mu^- \mu^+$

The effective Hamiltonian for the inclusive and exclusive $b \rightarrow s \ell^- \ell^+$ decays, including the loop matrix element effects that arise from the tree- and penguin-induced four-quark operators, is given as:

$$\mathcal{H}_{b \rightarrow s \ell^- \ell^+} = -\frac{4G_F}{\sqrt{2}} \frac{\alpha}{4\pi} V_{ts}^* V_{tb} \left[\sum_{k=9,10} (C_k^{\text{eff}} \mathcal{O}_k + C_k^{\prime\text{eff}} \mathcal{O}'_k) - \frac{2m_b}{q^2} C_7^{\text{eff}} \mathcal{O}_7 \right]. \quad (40)$$

The effective operators in the model are

$$\mathcal{O}_9^{(\prime)} = (\bar{s} \gamma_\mu P_{L(R)} b) (\bar{\ell} \gamma^\mu \ell), \quad (41a)$$

$$\mathcal{O}_{10}^{(\prime)} = (\bar{s} \gamma_\mu P_{L(R)} b) (\bar{\ell} \gamma^\mu \gamma_5 \ell), \quad (41b)$$

$$\mathcal{O}_7 = (\bar{s} i \sigma_{\mu\nu} q^\nu P_R b) (\bar{\ell} \gamma^\mu \ell), \quad (41c)$$

and the effective coefficients, combining the SM contributions and the effects from the new Z -penguin diagrams, are given as:

$$C_9^{\text{eff}} = C_9^{\text{eff,SM}} + \frac{\sqrt{2}G_F}{C_{\text{SM}}^\ell} c_V^\ell C_{Z23}^L, \quad (42a)$$

$$C_9^{\prime\text{eff}} = \frac{\sqrt{2}G_F}{C_{\text{SM}}^\ell} c_V^\ell C_{Z23}^R, \quad (42b)$$

$$C_{10}^{\text{eff}} = C_{10}^{\text{eff,SM}} - \frac{\sqrt{2}G_F}{C_{\text{SM}}^\ell} c_A^\ell C_{Z23}^L, \quad (42c)$$

$$C_{10}^{\prime\text{eff}} = -\frac{\sqrt{2}G_F}{C_{\text{SM}}^\ell} c_A^\ell C_{Z23}^R, \quad (42d)$$

with $C_{\text{SM}}^\ell = G_F \alpha V_{ts}^* V_{tb} / (\sqrt{2}\pi)$. The SM results, obtained by ignoring the q^2 -dependence at the energy scale of $\mu_b = 4.2$ GeV, are $C_9^{\text{eff,SM}} \approx 4.114$, $C_{10}^{\text{eff,SM}} \approx -4.193$, and $C_7^{\text{eff}} = C_7^{\text{eff,SM}} \approx -0.2957$ [47]. Their detailed NNLO results can be found in Refs. [48–50].

Since the new Z -mediated contributions to the angular observables of $B \rightarrow K^* \ell^- \ell^+$ are insignificant for the effects that enhance the $d_i \rightarrow s \nu \bar{\nu}$ processes, our attention focuses on the contributions to the $B \rightarrow X_s \ell^- \ell^+$ and $B_s \rightarrow \mu^- \mu^+$ processes, where both processes play a crucial role in constraining the parameters related to the $b \rightarrow s$ transition. Applying the interactions in Eq. (40), the differential decay rate for $b \rightarrow X_s \ell^- \ell^+$ as a function of

$s = q^2/m_b^2$ can be obtained as:

$$\frac{\Gamma(b \rightarrow X_s \ell^- \ell^+)}{ds} = \left(\frac{\alpha}{4\pi}\right)^2 \frac{G_F^2 m_b^5}{48\pi^3} |V_{ts}^* V_{tb}|^2 (1-s)^2 \left[\left(4 + \frac{8}{s}\right) |C_7^{\text{eff}}|^2 + (1+2s) (|C_9^{\text{eff}}|^2 + |C_9^{\prime\text{eff}}|^2 + |C_{10}^{\text{eff}}|^2 + |C_{10}^{\prime\text{eff}}|^2) + 12C_7^{\text{eff}} \text{Re}(C_9^{\text{eff}} + C_9^{\prime\text{eff}}) \right]. \quad (43)$$

Notably, $\mathcal{O}_9^{(\prime)}$ and \mathcal{O}_7 do not contribute to the chirality suppression process $B_s \rightarrow \mu^- \mu^+$. The BR for $B_s \rightarrow \mu^- \mu^+$ arising from $\mathcal{O}_{10}^{(\prime)}$ is given as [54–56]:

$$\mathcal{B}(B_s \rightarrow \mu^- \mu^+) = \tau_{\mu^- \mu^+} \frac{G_F^2}{\pi} \left| \frac{\alpha V_{ts}^* V_{tb}}{4\pi} \right|^2 F_{B_s}^2 m_{B_s} m_\mu^2 \sqrt{1 - \frac{4m_\mu^2}{m_{B_s}^2}} |C_{10}' - C_{10}|^2, \quad (44)$$

where $\tau_{\mu^- \mu^+}$ is the effective lifetime of B_s in the time-dependent $B_s \rightarrow \mu^- \mu^+$ decay and is related to the width difference between heavy and light B_s mesons. The simplified relation can be written as $\tau_{\mu^- \mu^+} = \tau_{B_s}/(1 - y_s)$ with $2y_s = \tau_{B_s} \Delta\Gamma_s = 0.128 \pm 0.007$ [51] and τ_{B_s} being the B_s lifetime. The Wilson coefficients $C_{10}^{(\prime)}$ are $C_{10}' = C_{10}^{\prime\text{eff}}$ and

$$C_{10} = \eta_{\text{eff}} \frac{0.315 x_t^{0.78}}{s_W^2} - \frac{\sqrt{2} G_F}{C_{\text{SM}}^\ell} c_A^\ell C_{Z23}^L, \quad (45)$$

where $\eta_{\text{eff}} = 0.9882 \pm 0.00024$ represents the QCD and electroweak corrections [52, 53].

V. NUMERICAL ANALYSIS AND DISCUSSIONS

There are only seven observables measured from the neutrino oscillation experiments. Therefore, the free parameters in the one-loop induced neutrino mass matrix given in Eq. (11), such as $m_{S_{1,2,N}}$, ϕ , and $y_{1i,2i}$, cannot be completely fixed. More related processes, such as $\ell_i \rightarrow \ell_j \gamma$, $\mu \rightarrow 3e$, $\mu - e$ conversion, and muon $g - 2$, should be included and analyzed together. Since the m_N , ϕ , and $y_{1i,2i}$ parameters are irrelevant to the semileptonic B and K decays, we don't repeat the numerical analysis of the neutrino physics and lepton flavor-violating processes in this work. The relevant study with detailed analysis can be found in Ref. [29]. Hence, we focus on the contributions from the parameters $\mathbf{y}_T^{R,L}$, $m_{H_{1,2}^+}$ and their mixing angle θ , and m_T .

A. Numerical inputs and parameter constraints

As discussed earlier, the weak phases of $\mathbf{y}_T^{R,L}$ can be rotated away; therefore, six free parameters are involved in the quark Yukawa couplings. To satisfy the perturbativity re-

quirement, we assume their upper limits to be $|\mathbf{y}_{T_i}^{R,L}| < \sqrt{4\pi}$. According to the fact that $\Delta m_K \ll \Delta m_{B_d} < \Delta m_{B_s}$ and $\Delta m_{B_d}^{\text{exp}}/\Delta m_{B_s}^{\text{exp}} \sim \Delta m_{B_d}^{\text{SM}}/\Delta m_{B_s}^{\text{SM}} \sim \lambda^2$ with $\lambda \approx 0.225$ being one of the Wolfenstein parameters, we further restrict the upper bounds on the parameters to be $|y_{T_3}^{R,L}| \lesssim 3.5$, $|y_{T_2}^{R,L}| \lesssim 1$, and $|y_{T_1}^{R,L}| \lesssim 0.5$ in the numerical calculations.

For the mass limit of the heavy quark T , we adopt the constraints based on the stop searches in R -parity conserving supersymmetry (SUSY). The data, obtained with an integrated luminosity of 139 fb^{-1} at $\sqrt{s} = 13 \text{ TeV}$ by ATLAS [57], show that mass below 1 TeV has been excluded when the neutralino mass is around 100 GeV. Since the lightest neutral inert scalar cannot be the DM in the model, i.e., $m_{S_{1,2}} > m_N$, the inert charged scalar should also be heavier than N . Thus, to reduce the number of free parameters in our numerical analysis, we fix the masses as follows: $m_T = 1.2 \text{ TeV}$, $m_{H_1^+}^2/m_T^2 = 0.3$, and $m_{H_2^+}^2/m_T^2 = 0.4$. For the scenario with a small mixing angle θ , we fix $s_\theta = 0.1$ in the numerical estimates.

With the above-specified values of m_T and $m_{H_{1,2}^+}$, more than six experimental observables are required to determine the allowed ranges of $\mathbf{y}_T^{R,L}$. Since we want to consider the processes of $B \rightarrow K^{(*)}\nu\bar{\nu}$ and $K_L \rightarrow \pi^0\nu\bar{\nu}$ as predictions in the model, they should be excluded from the inputs. Based on the discussions in Secs. III and IV, the experimental inputs can be $\Delta m_{K,B_q}$, $B_s \rightarrow \mu^-\mu^+$, $B \rightarrow X_s\ell^-\ell^+$, $K^+ \rightarrow \pi^+\nu\bar{\nu}$ as well as the CP asymmetry in the $B \rightarrow J/\Psi K$ decay, denoted as $S_{J/\Psi K^0}$. Thus, we can use these seven observables to put bounds on the six free parameters. Their SM predictions and current experimental values are shown in Table II.

TABLE II: The experimental measurements and the SM predictions.

Obs.	$\Delta m_K \cdot 10^{15} \text{ [GeV]}$	$\Delta m_{B_d} \cdot 10^{13} \text{ [GeV]}$	$\Delta m_{B_s} \cdot 10^{12} \text{ [GeV]}$	$S_{J/\Psi K^0}$
Exp [33]	3.482 ± 0.006	3.332 ± 0.013	11.688 ± 0.004	0.699 ± 0.017
SM	5.8 ± 2.4 [58]	$3.618_{-0.987}^{+1.052}$ [38]	$11.053_{-2.237}^{+3.618}$ [38]	0.831 ± 0.116 [38]
Obs.	$\mathcal{B}(B_s \rightarrow \mu^-\mu^+) \cdot 10^9$	$\mathcal{B}(b \rightarrow X_s\ell^-\ell^+) \cdot 10^6$	$\mathcal{B}(K^+ \rightarrow \pi^+\nu\bar{\nu}) \cdot 10^{11}$	$\mathcal{B}(K_L \rightarrow \pi^0\nu\bar{\nu}) \cdot 10^{11}$
Exp	3.01 ± 0.35 [33]	5.8 ± 1.3 [33]	$11.4_{-3.3}^{+4.0}$ [33]	$< 2 \times 10^{-9}$ [59]
SM	$3.78_{-0.10}^{+0.15}$ [8]	4.15 ± 0.7 [60]	8.60 ± 0.42 [8]	2.94 ± 0.15 [8]

To determine the ranges of the free parameters that are consistent with the chosen ex-

perimental data, we employ the minimum chi-square approach, where the weighted χ^2 is defined as follows:

$$\chi^2 = \sum_i \frac{(O_i^{\text{th}} - O_i^{\text{exp}})^2}{\sigma_i^2}. \quad (46)$$

Here O_i^{th} and O_i^{exp} represent the central values of the i -th observable predicted by the model and measured in experiments, respectively. The weight factor $\sigma_i^2 = (\sigma_i^{\text{SM}})^2 + (\sigma_i^{\text{exp}})^2$ [61] combines the uncertainties from both SM predictions and experimental data.

With the assumed values of masses and ranges of Yukawa couplings, the minimum value of the weighted χ^2 for the seven observable inputs is $\chi_{\text{min}}^2 = 0.23$, while the χ^2 value in the SM is $\chi_{\text{SM}}^2 = 4.93$. The best-fit parameter values are $\mathbf{y}_T^{L,\text{min}} \simeq (0.032, 0.150, 0.893)$ and $\mathbf{y}_T^{R,\text{min}} = (0.024, 0.111, 0.813)$. To clearly understand the parameter correlations, we show contours of the χ^2 function in the planes of $y_{T_3}^R - y_{T_2}^R$, $y_{T_3}^R - y_{T_1}^R$, $y_{T_3}^L - y_{T_2}^L$, and $y_{T_3}^L - y_{T_1}^L$ in Fig. 3(a)-(d), where the shaded areas represent probabilities of the χ^2 distribution within 68.27%, 95.45%, and 99.73% confidence level (CL), respectively. Note that when two parameters are selected as variables for the two-dimensional contours, the other parameters are held fixed at their best-fit values.

B. Numerical analysis of observables in rare B and K processes

Based on the results in Figs. 3(b) and (d), it is seen that the ranges of $y_{T_1}^{R,L}$ are localized in narrow regions at around $y_{T_1}^{R,\text{min}}$ and $y_{T_1}^{L,\text{min}}$. To efficiently illustrate numerical results for the studied processes in two-dimensional contour plots, we always fix $y_{T_1}^R = y_{T_1}^{R,\text{min}}$ and $y_{T_1}^L = y_{T_1}^{L,\text{min}}$. Since the areas within 2σ CL in the $y_{T_3}^R - y_{T_2}^R$ and $y_{T_3}^L - y_{T_2}^L$ planes with $y_{T_3}^{R,T} > 0$ have similar patterns and regions of parameters, we will demonstrate the observables in the rare B and K meson decays in the $y_{T_3}^R - y_{T_2}^R$ and $y_{T_3}^L - y_{T_2}^L$ planes. When we vary the parameters in the planes of $y_{T_3}^R - y_{T_2}^R$ and $y_{T_3}^L - y_{T_2}^L$ within the above-mentioned contour regions, the other parameters including $y_{T_1}^{R,L}$ are fixed at $\mathbf{y}_T^{R,\text{min}}$ and $\mathbf{y}_T^{L,\text{min}}$.

According to R_K^ν and $R_{K^*}^\nu$ defined in Eqs. (30) and (33), the contours for R_K^ν (dashed) and $R_{K^*}^\nu$ (dot-dashed) in the $y_{T_3}^R - y_{T_2}^R$ plane are shown in Fig. 4(a), with the values $R_K^\nu = (1, 5, 1.8, 2.0)$ and $R_{K^*}^\nu = (0.9, 1.0, 1.1, 1.2)$. The results indicate that R_K^ν can reach up to a factor of 2, while the influence of new physics effects in the model on $B \rightarrow K^* \nu \bar{\nu}$ is mild. Additionally, we show the BR of $B_s \rightarrow \mu^- \mu^+$ within the 1σ error of the experimental value in dotted curves. As stated in the introduction, a tension exists between the experimental

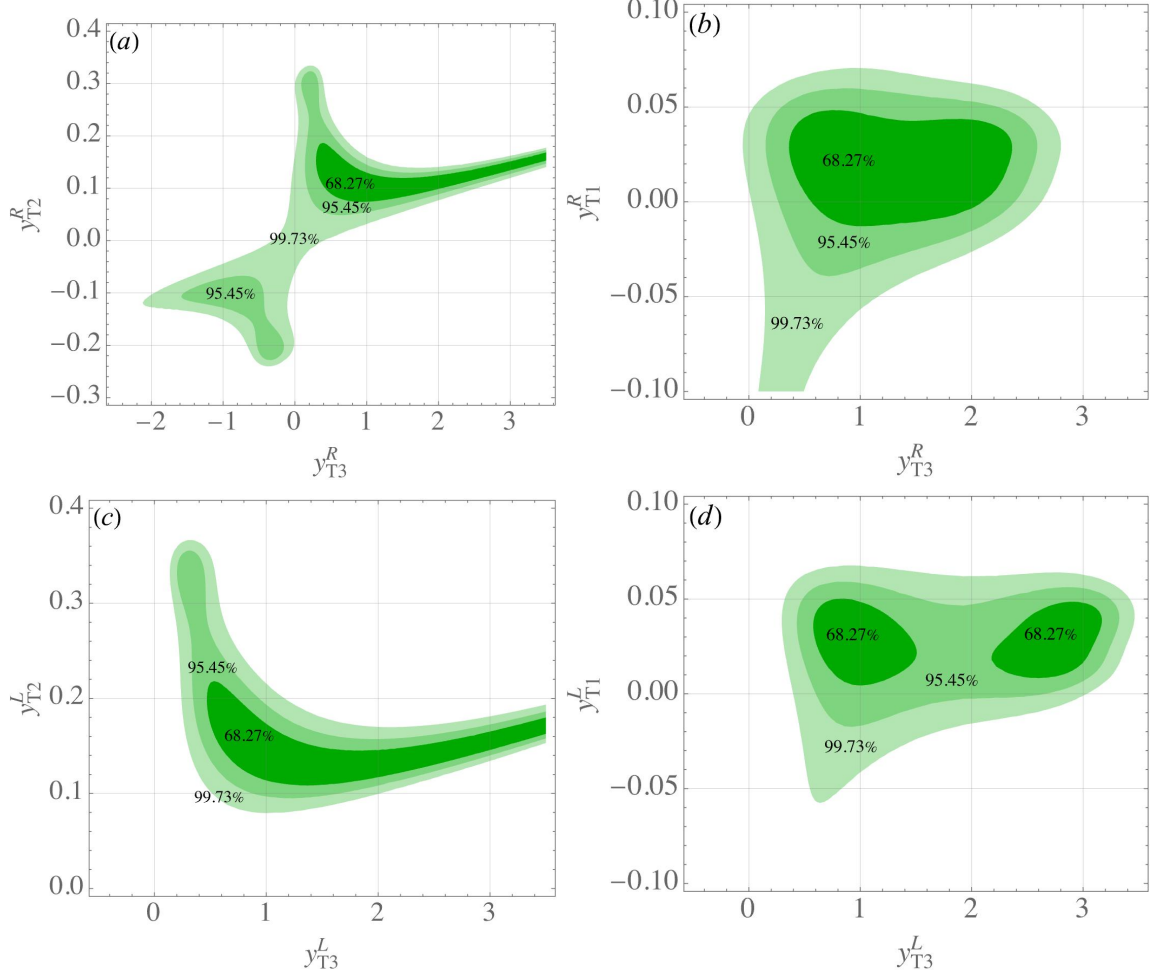


FIG. 3: Probabilities of χ^2 distribution within 68.27%, 95.45%, and 99.73% shown in the planes of (a) y_{T3}^R - y_{T2}^R , (b) y_{T3}^R - y_{T1}^R , (c) y_{T3}^L - y_{T2}^L , and (d) y_{T3}^L - y_{T1}^L .

data and SM prediction for $\mathcal{B}(B_s \rightarrow \mu^- \mu^+)$. Interestingly, the Z -penguin diagrams mediated by the inert charged scalars can resolve this tension and significantly enhance R_K^ν . For comparison, we show the χ^2 contours within the 3σ CL in the plot.

From the definition in Eq. (38), we show the contours for $R_{\pi^+}^\nu$ (dot-dashed) and $R_{\pi^0}^\nu$ (double-dot-dashed) in the plane of y_{T3}^R and y_{T2}^R in Fig. 4(b), with the values $R_{\pi^+}^\nu = (0.9, 1.3, 1.8)$ and $R_{\pi^0}^\nu = (1.2, 1.4, 1.8, 2.0)$, where the values of $R_{\pi^+}^\nu$ correspond the current experimental data with the 1σ error. The results indicate that $R_{\pi^0}^\nu = 2$ can be achieved within the 3σ CL in the model, and the BR for $K^+ \rightarrow \pi^+ \nu \bar{\nu}$ can be enhanced up to the $+1\sigma$ upper value of $\mathcal{B}(K^+ \rightarrow \pi^+ \nu \bar{\nu}) \simeq 15.4 \times 10^{-11}$ at $y_{T2}^R \sim 0.3$ and -0.2 .

In Figs. 4(c) and (d), we project the allowed parameter space onto the y_{T3}^R - y_{T3}^L plane

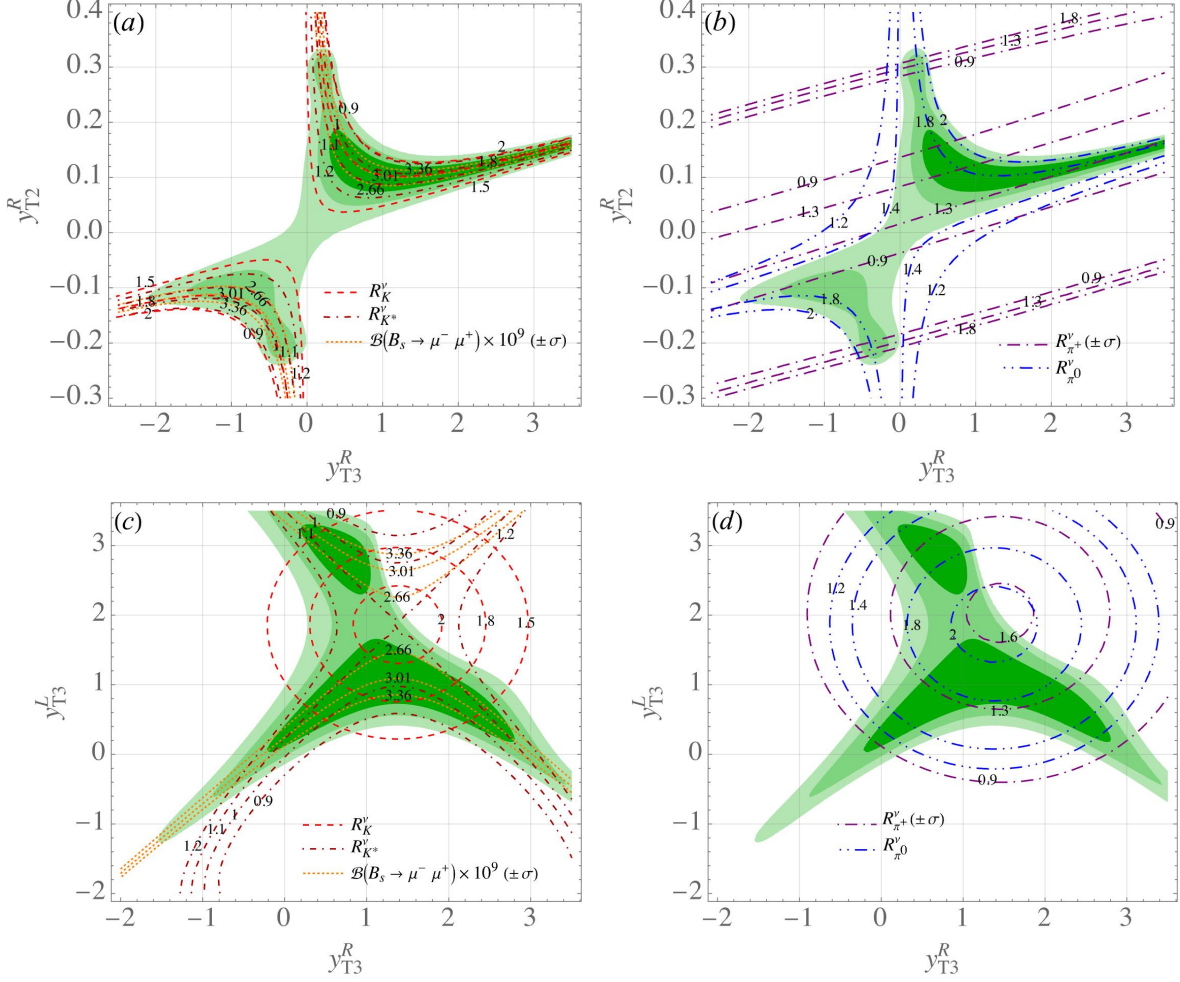


FIG. 4: Contours in the y_{T3}^R - y_{T2}^R plane for the observables of (a) R^ν , $R_{K^*}^\nu$, and $\mathcal{B}(B_s \rightarrow \mu^- \mu^+)$ and of (b) $R_{\pi^+}^\nu$ and $R_{\pi^0}^\nu$, where values of the parameters other than y_{T3}^R, y_{T2}^R are taken to be their best-fit values at χ_{\min}^2 . In the plots, $\pm\sigma$ denotes that the experimental data within one standard deviation are applied. Plots (c) and (d) resemble plots (a) and (b), but in the y_{T3}^L - y_{T3}^R plane.

the same physical quantities as those shown in Figs. 4(a) and (b), where $y_{T3}^{L,R}$ are the only Yukawa couplings that can be of $\mathcal{O}(1)$ in our setting. Note that the contour of the $+1\sigma$ upper value $R_{\pi^+}^\nu = 1.8$ is outside the range, and we use $R_{\pi^+}^\nu = 1.6$ instead. It is observed that the contours of these observables in the y_{T3}^R - y_{T3}^L plane exhibit distinct patterns. $R_{K^*}^\nu$ and $\mathcal{B}(B_s \rightarrow \mu^- \mu^+)$ behave like hyperbolic curves, while R_K^ν and R_π^ν exhibit circular patterns. In Fig. 4(b), the $R_{\pi^0}^\nu = 1.2$ and 1.4 contours do not overlap with the parameter region within the 3σ CL; however, the $R_{\pi^0}^\nu = 1.2$ and 1.4 contours do cross over the region when viewed in the y_{T3}^R - y_{T3}^L plane of Fig. 4(d).

According to the results in Fig. 4, we observe that when $y_{T3}^{R(L)} \sim y_{T3}^{R(L),\min}$, R_{K,π^+,π^0}^ν can be significantly enhanced and that $\mathcal{B}(B_s \rightarrow \mu^- \mu^+)$ can fit the experimental central value. Thus, it is interesting to explore the dependence of the considered processes on the $y_{T2}^{R,L}$ parameters, with the other parameter values fixed at $\mathbf{y}_T^{R,\min}$ and $\mathbf{y}_T^{L,\min}$. For illustration purposes, we show the contours as functions of y_{T2}^L and y_{T2}^R for R_{K,K^*}^ν and $\mathcal{B}(B_s \rightarrow \mu^- \mu^+)$ in Fig. 5(a) and for R_{π^+,π^0}^ν in Fig. 5(b). From the plots, it is evident that each observable in the selected values of contours can match the area within the 3σ CL. However, from Fig. 5(a), the curves of $R_{K^*}^\nu = 0.9$ and 1.2 do not overlap with the contours of $B_s \rightarrow \mu^- \mu^+$ in the $R_{K^*}^\nu$ -enhanced region within the 1σ error. The same behavior is also shown in Fig. 4(c). Hence, $R_{K^*}^\nu$ can be strictly bound by the measurement of $\mathcal{B}(B_s \rightarrow \mu^- \mu^+)$.

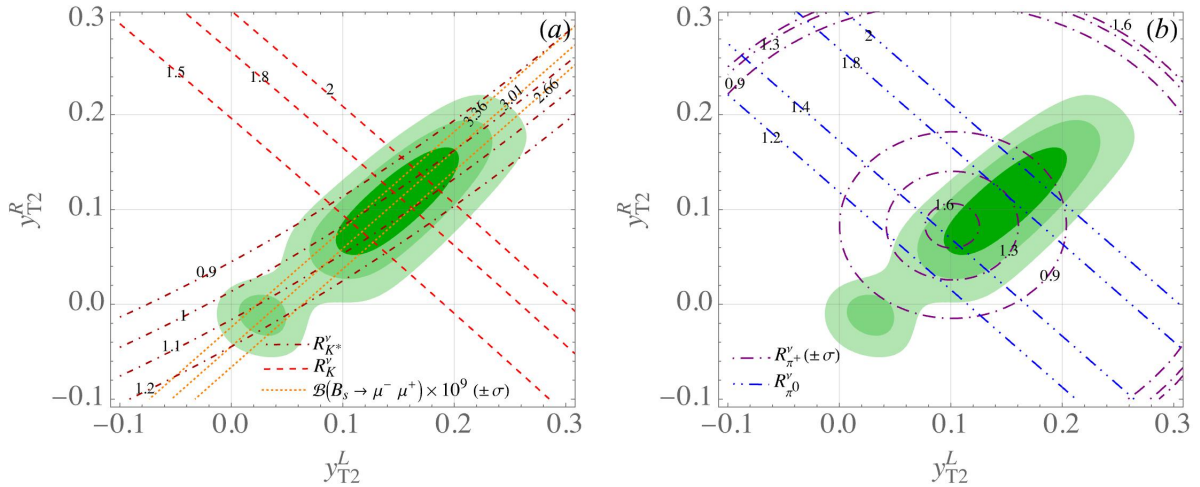


FIG. 5: Contours in the y_{T2}^L - y_{T2}^R plane for the observables of (a) R^ν , $R_{K^*}^\nu$, and $\mathcal{B}(B_s \rightarrow \mu^- \mu^+)$ and of (b) $R_{\pi^+}^\nu$ and $R_{\pi^0}^\nu$, where the parameter values, except for $y_{T2}^{L,R}$, are set to be $\mathbf{y}_T^{R(L),\min}$. In the plots, $\pm\sigma$ denotes that the experimental data within one standard deviation are applied.

To examine the correlations between observables, we need to vary all parameters simultaneously instead of merely varying two parameters as before. Based on the above analysis, except for $y_{T1}^{R(L)}$, which are fixed at the values of $y_{T1}^{R(L),\min}$, we set the ranges of the other parameters around $\mathbf{y}_T^{R(L),\min}$. We scan the parameters assuming a normal distribution with $\mathbf{y}_T^{R(L),\min}$ as the mean and setting the standard deviations as $\sigma(y_{T2}^{R(L)}) = y_{T2}^{R(L),\min}$ and $\sigma(y_{T3}^{R(L)}) = 0.1$. In addition to the 1σ experimental constraints shown in Table II, we further require that $\chi^2 - \chi_{\min}^2 \lesssim 3.84$.

Using 10^7 sampling points, Fig. 6 shows the scatter plot depicting the correlations between

R_K^ν and R_M^ν with $M = K^*, \pi^+, \pi^0$ at 95% CL. As alluded to before, the result of $R_K^\nu \simeq R_{\pi^0}^\nu$ given in Eq. (39) is numerically verified. Both ratios can be enhanced up to a factor of 2. As expected, due to the introduction of right-handed quark currents, which are used to fit the observed BR for $B_s \rightarrow \mu^- \mu^+$, the influence of new physics effects on $R_{K^*}^\nu$ in the model is mild. It is observed that both $R_{\pi^+}^\nu$ and R_K^ν increase simultaneously when $R_K^\nu \lesssim 1.4$. Subsequently, when $R_K^\nu > 1.4$, $R_{\pi^+}^\nu$ decreases as R_K^ν increases. This behavior of $R_{\pi^+}^\nu$ can be understood as follows. The imaginary part of X_{eff} , which also contributes to $K_L \rightarrow \pi^0 \nu \bar{\nu}$ and is defined in Eq. (37), increases linearly with R_K^ν . However, the real part of X_{eff} decreases after $R_K^\nu \simeq 1.4$. Since $K^+ \rightarrow \pi^+ \nu \bar{\nu}$ is dominated by the CP-conserving effect, this leads to a decrease in $\mathcal{B}(K^+ \rightarrow \pi^+ \nu \bar{\nu})$ for $R_K^\nu > 1.4$, although the BR of the CP-violating process $K_L \rightarrow \pi^0 \nu \bar{\nu}$ continues to increase. Since the resulting $\mathcal{B}(B_s \rightarrow \mu^- \mu^+)$ can be within 1σ errors of experimental data for any value of R_K^ν in the region of (1.2, 2.2), the scatter plot for the correlation between $\mathcal{B}(B_s \rightarrow \mu^- \mu^+)$ and R_K^ν is not shown. In all interesting regions of R_K^ν , the Z-penguin diagrams mediated by the charged Higgs bosons can alleviate the tension observed in $B_s \rightarrow \mu^- \mu^+$ between the experimental measurement and the SM prediction.

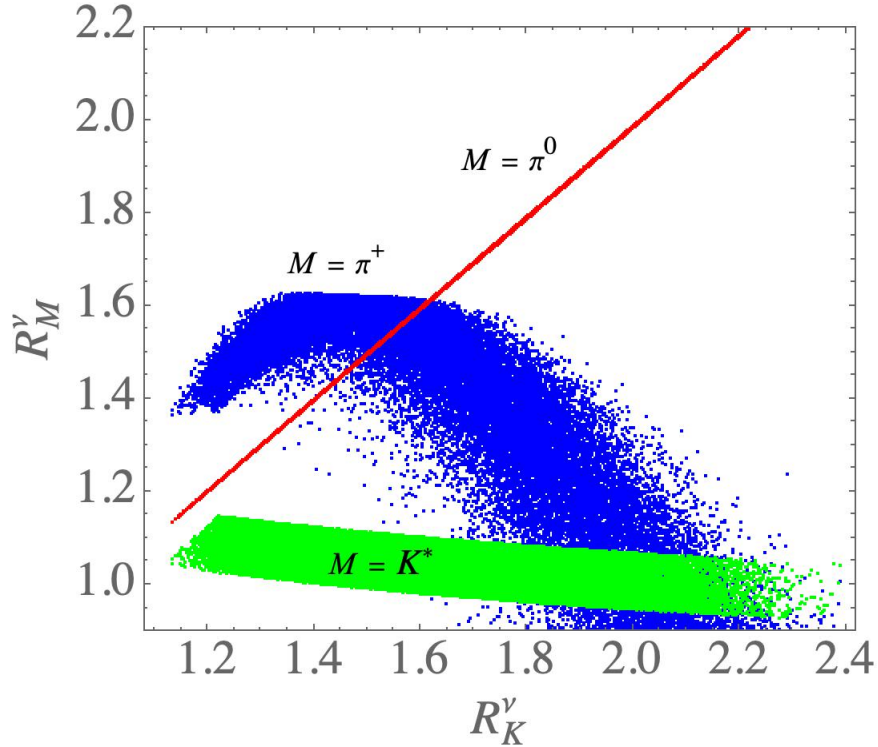


FIG. 6: Scatter plot illustrating the correlations between R_K^ν and R_M^ν with $M = K^*, \pi^+,$ and π^0 .

VI. SUMMARY

Scotogenesis, typically used for lepton-related phenomena such as neutrino mass and dark matter candidate, is rarely studied in the context of the quark flavor-related processes. Moreover, the minimal scotogenic model [24] cannot accommodate the muon $g - 2$ anomaly. To apply the mechanisms in a scotogenic model to the quark FCNC processes and preserve the characteristic features of scotogenesis, we propose in this work a scotogenic model whose dark particles include a neutral Dirac-type dark lepton, two inert Higgs doublets with one carrying a dark charge, a charged singlet dark scalar, and a singlet vector-like up-type dark quark. As demonstrated above, each of these particles plays a crucial role in this study.

With appropriate dark charge assignments, the model has a dark $U(1)$ symmetry with which the scalar and pseudoscalar in the same inert Higgs doublet are degenerate in mass. Consequently, the inert scalars cannot be dark matter candidates. Nevertheless, the singlet dark neutral lepton does not couple to the Z boson and the SM Higgs boson, and can self-scatter into the SM particles through the Yukawa couplings; thus, it can be dark matter in the model.

With the introduction of a dark up-type quark, the SM quarks can couple to this dark quark via the non-leptonic inert Higgs doublet. As a result, the loop-induced Z -penguin diagrams make significant contributions to the $B^+ \rightarrow K^+ \nu \bar{\nu}$ and $K \rightarrow \pi \nu \bar{\nu}$ processes. Furthermore, with the introduction of a singlet dark-charged scalar, not only can muon $g - 2$ be enhanced, but also the right-handed quark current for the $b \rightarrow s$ transition can be induced. As a result, the tension in $B_s \rightarrow \mu^- \mu^+$ between the experimental measurement and the SM prediction can be resolved.

Acknowledgments

C.-W. C would like to thank the High Energy Physics Theory Group at the University of Tokyo for their hospitality during his visit when part of this work was finished. This work was supported in part by the National Science and Technology Council, Taiwan, under Grant Nos. NSTC-110-2112-M-006-010-MY2 (C.-H. Chen) and NSTC-111-2112-M-002-018-MY3 (C.-W. Chiang).

Appendix A: Saclar potential and masses of scalars

The scalar potential for the SM Higgs H , $\eta_{1,2}$, and χ^\pm is written as:

$$\begin{aligned}
V &= V_{\text{SM}} + V(H, \eta_1, \eta_2, \chi^\pm) , \\
V_{\text{SM}} &= -\mu_H^2 H^\dagger H + \lambda_H (H^\dagger H)^2 , \\
V(H, \eta_1, \eta_2, \chi^\pm) &= \mu_1^2 \eta_1^\dagger \eta_1 + \mu_2^2 \eta_2^\dagger \eta_2 + \mu_3^2 \chi^- \chi^+ + (\mu_\chi \eta_1^T i \tau_2 H \chi^- + \text{H.c.}) + \lambda_1 (\eta_1^\dagger \eta_1)^2 \\
&\quad + \lambda_2 (\eta_2^\dagger \eta_2)^2 + \lambda_3 (\eta_1^\dagger \eta_1) (\eta_2^\dagger \eta_2) + \lambda_4 (\eta_1^\dagger \eta_2) (\eta_2^\dagger \eta_1) \\
&\quad + (\lambda_5 (H^\dagger \eta_1) (H^\dagger \eta_2) + \text{H.c.}) + \lambda_6 (H^\dagger \eta_1) (\eta_1^\dagger H) + \lambda_7 (H^\dagger \eta_2) (\eta_2^\dagger H) \\
&\quad + \lambda_8 (H^\dagger H) (\eta_1^\dagger \eta_1) + \lambda_9 (H^\dagger H) (\eta_2^\dagger \eta_2) + \lambda_{10} (\chi^- \chi^+)^2 \\
&\quad + (\chi^- \chi^+) (\lambda_{11} H^\dagger H + \lambda_{12} \eta_1^\dagger \eta_1 + \lambda_{13} \eta_2^\dagger \eta_2) .
\end{aligned} \tag{A1}$$

It can be seen that the non-self-Hermitian terms are the λ_5 and μ_χ terms, where the former violates the lepton number by two units and plays an important role in the radiative generation of the Majorana neutrino mass, and the latter leads to the mixing between η_1^\pm and χ^\pm . In addition to the leptonic Yukawa couplings shown in Eq. (3), the tiny neutrino mass can be achieved when $\lambda_5 \ll 1$. To spontaneously break the electroweak gauge symmetry, we take $\mu_H^2, \lambda_H > 0$ as in the SM. The masses of $\eta_{1,2}$ can be irrelevant to the electroweak symmetry breaking, and we thus require $\mu_{1,2}^2 (\lambda_{1,2}) > 0$. Using the charge assignment shown in Eq. (2), the scalar potential in Eq. (A1) has an unbroken global $U(1)_X$ symmetry. To preserve the global $U(1)_X$ symmetry, the VEVs of $\eta_{1,2}$ are kept zero. Therefore, the components of the three doublet scalars are parametrized as follows ($j = 1, 2$):

$$H = \begin{pmatrix} G^+ \\ \frac{1}{\sqrt{2}}(v + h + iG^0) \end{pmatrix}, \quad \eta_j = \begin{pmatrix} \eta_j^+ \\ \frac{1}{\sqrt{2}}(\eta_j^0 + ia_j) \end{pmatrix}, \tag{A2}$$

where $G^{\pm,0}$ are the Goldstone bosons, v is the VEV of H , and h is the SM Higgs boson.

From Eq. (A1), η_2^\pm does not mix with the other charged scalars. Its mass is given by:

$$m_{\eta_2^\pm}^2 = \mu_2^2 + \frac{\lambda_9 v^2}{2}. \tag{A3}$$

Because η_1^\pm mixes with χ^\pm via the μ_χ term, their mass-squared matrix is found to be:

$$\begin{aligned}
&(\eta_1^-, \chi^-) \begin{pmatrix} m_{11}^2 & m_{12}^2 \\ m_{12}^2 & m_{22}^2 \end{pmatrix} \begin{pmatrix} \eta_1^+ \\ \chi^+ \end{pmatrix}, \\
&\text{with } m_{11}^2 = \mu_1^2 + \frac{\lambda_8 v^2}{2}, \quad m_{12}^2 = \frac{\mu_\chi v}{\sqrt{2}}, \quad m_{22}^2 = \mu_3^2 + \frac{\lambda_{11} v^2}{2}.
\end{aligned} \tag{A4}$$

The mass matrix can be diagonalized by a 2×2 orthogonal rotation defined by

$$\begin{pmatrix} H_1^+ \\ H_2^+ \end{pmatrix} = \begin{pmatrix} c_\theta & s_\theta \\ -s_\theta & c_\theta \end{pmatrix} \begin{pmatrix} \eta_1^+ \\ \chi^+ \end{pmatrix}, \quad (\text{A5})$$

where $c_\theta \equiv \cos \theta$ and $s_\theta \equiv \sin \theta$. As a result, the mass eigenvalues and the mixing angle are obtained as:

$$\begin{aligned} m_{1(2)}^2 &= \frac{m_{11}^2 + m_{22}^2}{2} \pm \frac{1}{2} \sqrt{(m_{22}^2 - m_{11}^2)^2 + 4(m_{12}^2)^2}, \\ s_{2\theta} &= -\frac{2m_{12}^2}{m_2^2 - m_1^2}, \end{aligned} \quad (\text{A6})$$

where $s_{2\theta} \equiv \sin 2\theta$.

Since the terms $(H^\dagger \eta_j)^2$ are forbidden by the $U(1)_X$ symmetry, the scalar η_j^0 and pseudoscalar a_j are degenerate in mass. Although the λ_5 term would mix $\eta_1^0(a_1)$ and $\eta_2^0(a_2)$, it will not lift the degeneracy. To obtain the mass spectrum of the neutral scalar bosons, we write the mass matrices for (η_1^0, η_2^0) and (a_1, a_2) as follows:

$$m_S^2 = \begin{pmatrix} \bar{m}_{11}^2 & \bar{m}_{12}^2 \\ \bar{m}_{12}^2 & \bar{m}_{22}^2 \end{pmatrix}, \quad m_A^2 = \begin{pmatrix} \bar{m}_{11}^2 & -\bar{m}_{12}^2 \\ -\bar{m}_{12}^2 & \bar{m}_{22}^2 \end{pmatrix}, \quad (\text{A7})$$

where the matrix elements are:

$$\begin{aligned} \bar{m}_{11}^2 &= \mu_1^2 + \frac{v^2}{2}(\lambda_6 + \lambda_8), \\ \bar{m}_{22}^2 &= \mu_2^2 + \frac{v^2}{2}(\lambda_7 + \lambda_9), \\ \bar{m}_{12}^2 &= \frac{v^2}{2}\lambda_5. \end{aligned} \quad (\text{A8})$$

Analogous to the case of the charged scalar mass matrix, each of the two 2×2 mass-squared matrices can be diagonalized by the corresponding orthogonal matrix $O(\theta_\zeta)$ ($\zeta = S, A$) through $O(\theta_\zeta)m_\zeta^2 O^T(\theta_\zeta)$, where

$$O(\theta_\zeta) = \begin{pmatrix} \cos \theta_\zeta & \sin \theta_\zeta \\ -\sin \theta_\zeta & \cos \theta_\zeta \end{pmatrix}. \quad (\text{A9})$$

Since the matrix elements in m_A^2 are the same as those in m_S^2 except for the sign change in the off-diagonal elements, we therefore take $\theta_S = -\theta_A \equiv \phi$. The eigenvalues of m_S^2 are found to be:

$$m_{S_{1,2}}^2 = \frac{1}{2} \left[\bar{m}_{11}^2 + \bar{m}_{22}^2 \pm \sqrt{(\bar{m}_{22}^2 - \bar{m}_{11}^2)^2 - 4(\bar{m}_{12}^4)} \right]. \quad (\text{A10})$$

For the physical pseudoscalars $A_{1,2}$, we have $m_{A_{1(2)}}^2 = m_{S_{1(2)}}^2$. The mixing angle ϕ is defined by:

$$\sin 2\phi = -\frac{\lambda_5 v^2}{m_{S_2}^2 - m_{S_1}^2}. \quad (\text{A11})$$

Since the λ_5 term violates the lepton number and eventually leads to the Majorana mass, its value has to be sufficiently small, i.e., $\lambda_5 \ll 1$. As a result, the off-diagonal mass matrix element $|\bar{m}_{12}^2|$ is suppressed and the mixing angle $\phi \ll 1$.

Appendix B: Form factors for $\bar{B} \rightarrow (K, K^*)$

The q^2 -dependent form factors for $\bar{B} \rightarrow K$ are defined through the following relations:

$$\begin{aligned} \langle K(p_2) | V_\mu | \bar{B}(p_1) \rangle &= f_+(q^2) \left(P_\mu - \frac{P \cdot q}{q^2} \right) + \frac{P \cdot q}{q^2} f_0(q^2) q_\mu, \\ \langle K(p_2) | T_{\mu\nu} q^\nu | \bar{B}(p_1) \rangle &= \frac{f_T(q^2)}{m_B + m_K} (P \cdot q q_\mu - q^2 P_\mu), \end{aligned} \quad (\text{B1})$$

where $P = p_1 + p_2$, $q = p_1 - p_2$; $V_\mu = \bar{s}\gamma_\mu b$, and $T_{\mu\nu} = \bar{s}i\sigma_{\mu\nu}b$. For $\bar{B} \rightarrow K^*$, the form factors are parametrized as:

$$\begin{aligned} \langle K^*(p_2, \epsilon) | V_\mu | \bar{B}(p_1) \rangle &= i \frac{V(q^2)}{m_B + m_{K^*}} \varepsilon_{\mu\alpha\beta\rho} \epsilon^{*\alpha} P^\beta q^\rho, \\ \langle K^*(p_2, \epsilon) | A_\mu | \bar{B}(p_1) \rangle &= 2m_{K^*} A_0(q^2) \frac{\epsilon^* \cdot q}{q^2} q_\mu + (m_B + m_{K^*}) A_1(q^2) \left(\epsilon_\mu^* - \frac{\epsilon^* \cdot q}{q^2} q_\mu \right) \\ &\quad - A_2(q^2) \frac{\epsilon^* \cdot q}{m_B + m_{K^*}} \left(P_\mu - \frac{P \cdot q}{q^2} q_\mu \right), \end{aligned} \quad (\text{B2})$$

$$\langle K^*(p_2, \epsilon) | T_{\mu\nu} q^\nu | \bar{B}(p_1) \rangle = -i T_1(q^2) \varepsilon_{\mu\alpha\beta\rho} \epsilon^{*\alpha} P^\beta q^\rho,$$

$$\langle K^*(p_2, \epsilon) | T_{\mu\nu}^5 q^\nu | \bar{B}(p_1) \rangle = T_2(q^2) (\epsilon_\mu^* P \cdot q - \epsilon^* \cdot q P_\mu) + T_3(q^2) \epsilon^* \cdot q \left(q_\mu - \frac{q^2}{P \cdot q} P_\mu \right).$$

Here ϵ denotes the polarization vector of K^* , $A_\mu = \bar{s}\gamma_\mu\gamma_5 b$, and $T_{\mu\nu}^5 = \bar{s}i\sigma_{\mu\nu}\gamma_5 b$. It is useful to define additional form factors $A_{12}(q^2)$ and $T_{23}(q^2)$:

$$16m_B m_{K^*}^2 A_{12}(q^2) = (m_B + m_{K^*})(m_B^2 - m_{K^*}^2 - q^2) A_1(q^2) - \frac{\lambda_{K^*}(q^2)}{m_B + m_{K^*}} A_2(q^2), \quad (\text{B3})$$

$$8m_B m_{K^*}^2 T_{23}(q^2) = (m_B + m_{K^*})(m_B^2 + 3m_{K^*}^2 - q^2) T_2(q^2) - \frac{\lambda_{K^*}(q^2)}{m_B - m_{K^*}} T_3(q^2). \quad (\text{B4})$$

[1] G. W. Bennett *et al.* [Muon g-2], Phys. Rev. D **73**, 072003 (2006) [arXiv:hep-ex/0602035 [hep-ex]].

- [2] D. P. Aguillard *et al.* [Muon g-2], Phys. Rev. Lett. **131**, no.16, 161802 (2023) [arXiv:2308.06230 [hep-ex]].
- [3] I. Adachi *et al.* [Belle-II], [arXiv:2311.14647 [hep-ex]].
- [4] P. del Amo Sanchez *et al.* [BaBar], Phys. Rev. D **82**, 112002 (2010) [arXiv:1009.1529 [hep-ex]].
- [5] J. P. Lees *et al.* [BaBar], Phys. Rev. D **87**, no.11, 112005 (2013) [arXiv:1303.7465 [hep-ex]].
- [6] O. Lutz *et al.* [Belle], Phys. Rev. D **87**, no.11, 111103 (2013) [arXiv:1303.3719 [hep-ex]].
- [7] J. Grygier *et al.* [Belle], Phys. Rev. D **96**, no.9, 091101 (2017) [arXiv:1702.03224 [hep-ex]].
- [8] A. J. Buras, Eur. Phys. J. C **83**, no.1, 66 (2023) [arXiv:2209.03968 [hep-ph]].
- [9] A. J. Buras, J. Girrbach-Noe, C. Niehoff and D. M. Straub, JHEP **02**, 184 (2015) [arXiv:1409.4557 [hep-ph]].
- [10] T. E. Browder, N. G. Deshpande, R. Mandal and R. Sinha, Phys. Rev. D **104**, no.5, 053007 (2021) [arXiv:2107.01080 [hep-ph]].
- [11] P. Asadi, A. Bhattacharya, K. Fraser, S. Homiller and A. Parikh, [arXiv:2308.01340 [hep-ph]].
- [12] P. Athron, R. Martinez and C. Sierra, [arXiv:2308.13426 [hep-ph]].
- [13] R. Bause, H. Gisbert and G. Hiller, [arXiv:2309.00075 [hep-ph]].
- [14] L. Allwicher, D. Becirevic, G. Piazza, S. Rosauero-Alcaraz and O. Sumensari, [arXiv:2309.02246 [hep-ph]].
- [15] T. Felkl, A. Giri, R. Mohanta and M. A. Schmidt, [arXiv:2309.02940 [hep-ph]].
- [16] H. K. Dreiner, J. Y. Günther and Z. S. Wang, [arXiv:2309.03727 [hep-ph]].
- [17] Y. Amhis, M. Kenzie, M. Reboud and A. R. Wiederhold, [arXiv:2309.11353 [hep-ex]].
- [18] X. G. He, X. D. Ma and G. Valencia, [arXiv:2309.12741 [hep-ph]].
- [19] C. H. Chen and C. W. Chiang, [arXiv:2309.12904 [hep-ph]].
- [20] A. Datta, D. Marfatia and L. Mukherjee, Phys. Rev. D **109**, no.3, L031701 (2024) [arXiv:2310.15136 [hep-ph]].
- [21] W. Altmannshofer, A. Crivellin, H. Haigh, G. Inguglia and J. Martin Camalich, [arXiv:2311.14629 [hep-ph]].
- [22] F. Z. Chen, Q. Wen and F. Xu, [arXiv:2401.11552 [hep-ph]].
- [23] B. F. Hou, X. Q. Li, M. Shen, Y. D. Yang and X. B. Yuan, [arXiv:2402.19208 [hep-ph]].
- [24] E. Ma, Phys. Rev. D **73**, 077301 (2006) [hep-ph/0601225].
- [25] P. Minkowski, Phys. Lett. B **67**, 421-428 (1977).
- [26] T. Yanagida, Conf. Proc. C **7902131**, 95-99 (1979) KEK-79-18-95.

- [27] M. Gell-Mann, P. Ramond and R. Slansky, Conf. Proc. C **790927**, 315-321 (1979) [arXiv:1306.4669 [hep-th]].
- [28] R. N. Mohapatra and G. Senjanovic, Phys. Rev. Lett. **44**, 912 (1980).
- [29] C. H. Chen, C. W. Chiang, T. Nomura and C. W. Su, JHEP **09**, 166 (2022) [arXiv:2201.10759 [hep-ph]].
- [30] G. 't Hooft, "Naturalness, chiral symmetry, and spontaneous chiral symmetry breaking," NATO Sci. Ser. B **59**, 135-157 (1980).
- [31] T. Toma and A. Vicente, JHEP **01**, 160 (2014) [arXiv:1312.2840 [hep-ph]].
- [32] C. H. Chen and T. Nomura, JHEP **09**, 090 (2021) [arXiv:2001.07515 [hep-ph]].
- [33] R. L. Workman *et al.* [Particle Data Group], PTEP **2022**, 083C01 (2022).
- [34] A. J. Buras, S. Jager and J. Urban, Nucl. Phys. B **605**, 600-624 (2001) [arXiv:hep-ph/0102316 [hep-ph]].
- [35] G. Buchalla, A. J. Buras and M. E. Lautenbacher, Rev. Mod. Phys. **68**, 1125-1144 (1996) [arXiv:hep-ph/9512380 [hep-ph]].
- [36] J. Brod, M. Gorbahn and E. Stamou, Phys. Rev. Lett. **125**, no.17, 171803 (2020) [arXiv:1911.06822 [hep-ph]].
- [37] A. J. Buras, M. Jamin and P. H. Weisz, Nucl. Phys. B **347**, 491-536 (1990).
- [38] A. Lenz, U. Nierste, J. Charles, S. Descotes-Genon, A. Jantsch, C. Kaufhold, H. Lacker, S. Monteil, V. Niess and S. T'Jampens, Phys. Rev. D **83**, 036004 (2011) [arXiv:1008.1593 [hep-ph]].
- [39] A. J. Buras, D. Buttazzo, J. Girrbach-Noe and R. Knegjens, JHEP **11**, 033 (2015) [arXiv:1503.02693 [hep-ph]].
- [40] J. A. Bailey, A. Bazavov, C. Bernard, C. M. Bouchard, C. DeTar, D. Du, A. X. El-Khadra, J. Foley, E. D. Freeland and E. Gámiz, *et al.* Phys. Rev. D **93**, no.2, 025026 (2016) [arXiv:1509.06235 [hep-lat]].
- [41] A. Bharucha, D. M. Straub and R. Zwicky, JHEP **08**, 098 (2016) [arXiv:1503.05534 [hep-ph]].
- [42] A. J. Buras, M. Gorbahn, U. Haisch and U. Nierste, Phys. Rev. Lett. **95**, 261805 (2005) [arXiv:hep-ph/0508165 [hep-ph]].
- [43] A. J. Buras, M. Gorbahn, U. Haisch and U. Nierste, JHEP **11**, 002 (2006) [erratum: JHEP **11**, 167 (2012)] [arXiv:hep-ph/0603079 [hep-ph]].
- [44] J. Brod and M. Gorbahn, Phys. Rev. D **78**, 034006 (2008) [arXiv:0805.4119 [hep-ph]].

- [45] F. Mescia and C. Smith, Phys. Rev. D **76**, 034017 (2007) [arXiv:0705.2025 [hep-ph]].
- [46] G. Isidori, F. Mescia and C. Smith, Nucl. Phys. B **718**, 319 (2005) [hep-ph/0503107].
- [47] T. Blake, G. Lanfranchi and D. M. Straub, Prog. Part. Nucl. Phys. **92**, 50-91 (2017) [arXiv:1606.00916 [hep-ph]].
- [48] C. Bobeth, M. Misiak and J. Urban, Nucl. Phys. B **574**, 291-330 (2000) [arXiv:hep-ph/9910220 [hep-ph]].
- [49] C. Bobeth, P. Gambino, M. Gorbahn and U. Haisch, JHEP **04**, 071 (2004) [arXiv:hep-ph/0312090 [hep-ph]].
- [50] T. Huber, E. Lunghi, M. Misiak and D. Wyler, Nucl. Phys. B **740**, 105-137 (2006) [arXiv:hep-ph/0512066 [hep-ph]].
- [51] Y. S. Amhis *et al.* [HFLAV], Phys. Rev. D **107**, no.5, 052008 (2023) [arXiv:2206.07501 [hep-ex]].
- [52] C. Bobeth, M. Gorbahn, T. Hermann, M. Misiak, E. Stamou and M. Steinhauser, Phys. Rev. Lett. **112**, 101801 (2014) [arXiv:1311.0903 [hep-ph]].
- [53] A. J. Buras, F. De Fazio and J. Girrbach, JHEP **02**, 112 (2014) [arXiv:1311.6729 [hep-ph]].
- [54] K. De Bruyn, R. Fleischer, R. Knegjens, P. Koppenburg, M. Merk, A. Pellegrino and N. Tuning, Phys. Rev. Lett. **109**, 041801 (2012) [arXiv:1204.1737 [hep-ph]].
- [55] R. Fleischer, Nucl. Phys. B Proc. Suppl. **241-242**, 135-140 (2013) [arXiv:1208.2843 [hep-ph]].
- [56] A. J. Buras, R. Fleischer, J. Girrbach and R. Knegjens, JHEP **07**, 077 (2013) [arXiv:1303.3820 [hep-ph]].
- [57] G. Aad *et al.* [ATLAS], JHEP **04**, 165 (2021) [arXiv:2102.01444 [hep-ex]].
- [58] B. Wang, PoS **LATTICE2021**, 141 (2022) [arXiv:2301.01387 [hep-lat]].
- [59] Koji Shiomi, on behalf of KOTO Collaboration, talk presented at KEK IPNS and J-PARC Joint Seminar, 6th Sep 2023.
- [60] C. Bobeth, G. Hiller and G. Piranishvili, JHEP **12**, 040 (2007) [arXiv:0709.4174 [hep-ph]].
- [61] S. Descotes-Genon, J. Matias, M. Ramon and J. Virto, JHEP **01**, 048 (2013) [arXiv:1207.2753 [hep-ph]].

Macroscopic neutrinoless double beta decay: long range quantum coherence

Gordon Baym and Jen-Chieh Peng

*Illinois Center for Advanced Studies of the Universe
and Department of Physics, University of Illinois, 1110 W. Green Street, Urbana, IL 61801*

(Dated: March 6, 2024)

We introduce the concept of “macroscopic neutrinoless double beta decay” (MDBD) for Majorana neutrinos. In this process an antineutrino produced by a nucleus undergoing beta decay, $X \rightarrow Y + e^- + \bar{\nu}_e$, is absorbed as a neutrino by another identical X nucleus via the inverse beta decay reaction, $\nu_e + X \rightarrow e^- + Y$. The distinct signature of MDBD is that the total kinetic energy of the two electrons equals twice the endpoint energy of single beta decay. The amplitude for MDBD, a coherent sum over the contribution of different mass states of the intermediate neutrinos, reflects quantum coherence over macroscopic distances, and is a new macroscopic quantum effect. We evaluate the rate of MDBD for a macroscopic sample of “ X ” material, e.g., tritium, acting both as the source and the target. The accidental background for MDBD originating from two separate single beta decays, which contains two final state neutrinos, can be readily rejected by measuring the energy of the detected two electrons. We discuss the similarities and differences between the MDBD and conventional neutrinoless double beta decay.

PACS numbers:

I. INTRODUCTION

The neutrino, if a Majorana rather than a Dirac fermion, would be its own antiparticle. A key experimental signature distinguishing Majorana neutrinos from Dirac neutrinos is nuclear neutrinoless double beta decay ($0\nu\text{DBD}$),

$$(A, Z) \rightarrow (A, Z + 2) + e^- + e^-. \quad (1)$$

Despite the importance of determining whether neutrinos are Majorana or Dirac, and despite a major experimental effort, only upper limits for $0\nu\text{DBD}$ have so far been obtained [1–3]. Ongoing and future experiments with multi-ton detectors will further improve the sensitivity in these searches [4].

The existence of a Majorana neutrino implies lepton-number non-conservation, hence physics beyond the Standard Model. Majorana neutrinos have only two spin states: when massless the left-handed state is a neutrino and the right-handed an antineutrino. The “sea-saw” mechanism for Majorana neutrinos can then provide a natural explanation for the very light neutrino masses inferred from tritium beta decay (TBD) and neutrino oscillation experiments [5].

The standard picture of neutrinoless double beta decay is that the *antineutrino* emitted from a neutron in a nucleus is absorbed as a *neutrino* on a neutron in the same nucleus. But there is in general no requirement in neutrinoless double beta decay that the second neutron be in the same nucleus (or indeed that the second nucleus be the same nuclide as the first, or even that the two down quarks undergoing weak interactions be in different neutrons). In this paper, we introduce the concept of “macroscopic neutrinoless double beta decay” (MDBD), in which a Majorana neutrino emitted from one nucleus is absorbed in a second nucleus. For example, in the sin-

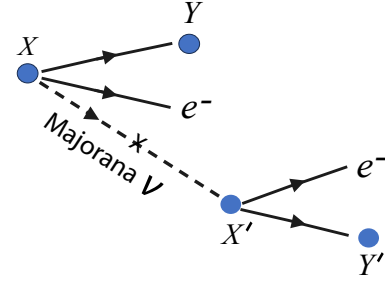


FIG. 1: Illustration of macroscopic neutrinoless double beta decay, with time running to the right. The first nucleus, X undergoes a beta decay emitting an electron and a Majorana antineutrino, which is absorbed as a neutrino by a second nucleus X' in an inverse beta decay. The sum of the energies of the two electron emitted is just the sum of the individual endpoint energies in the beta decays of X and X' .

gle beta decay (XBD) from parent nucleus $X = (A, Z)$ to daughter nucleus $Y = (A, Z + 1)$,

$$X \rightarrow Y + e^- + \bar{\nu}_e, \quad (2)$$

the antineutrino produced is, for Dirac type neutrinos, distinct from ν_e and cannot participate in the inverse beta decay (IXBD) reaction

$$\nu_e + X \rightarrow e^- + Y; \quad (3)$$

the nucleus X can only absorb an electron neutrino, ν_e , to reach the final state $e^- + Y$. If neutrinos are Majorana however, then the neutrino and antineutrino are not distinct particles, and the antineutrino in the XBD can then participate in the IXBD. The combination of these

two sequential reactions, (2) and (3), is the macroscopic neutrinoless double beta decay, illustrated in Fig. 1,

$$X + X' \rightarrow Y + Y' + e^- + e^-, \quad (4)$$

where we add a prime to indicate the freedom of the two nuclei being different nuclides. This process is the macroscopic analog of the conventional neutrinoless double beta decay, $0\nu\text{DBD}$. Both decays effectively turn two neutrons into two protons plus two electrons. Both decays violate lepton number conservation and require the neutrino to be Majorana.

Detection of neutrinoless double beta decay, whether in a single nucleus or via MDBD exchange of a non-zero mass Majorana neutrino between different nuclei would violate lepton number conservation and would establish that neutrinos are Majorana and not Dirac. In neutrinoless double beta decay the initial and final nuclei (or quarks more precisely) exchange a Majorana neutrino in various mass states. An important aspect of this exchange is the possibility of quantum interference between neutrino exchange in different mass states. This interference is implicitly included in calculation of microscopic $0\nu\text{DBD}$ [1]. Macroscopic beta decay, however, opens new quantum interference effects over the macroscopic distance scales of the separation between source and target nuclei.

The two processes have notable differences. All β -unstable nuclei are potential candidates for MDBD, while only a limited number of nuclei are candidates for $0\nu\text{DBD}$. The uncertainties in the rate of MDBD are considerably smaller than in $0\nu\text{DBD}$. In $0\nu\text{DBD}$ within a single nucleus, the uncertainty in the matrix elements [6, 7] owes both to the many processes within the standard model that can contribute to the decay, e.g., $n \rightarrow \Delta^{++} + 2e$, where the Δ^{++} lives virtually, as well as exchanges of virtual particles beyond the standard model in addition to Majorana neutrino exchange. Beyond-the-standard-model physics that could lead to $0\nu\text{DBD}$ include right-handed weak currents, exchange of heavy neutrinos or supersymmetric particles, etc.¹ By contrast, MDBD must come only from light massive Majorana neutrinos. Moreover, the matrix elements for sequential beta and inverse beta decay reactions in MDBD are precisely known.

Not only does the antineutrino source in neutrinoless MDBD not need to be the same nucleus as the target, the antineutrino emitted, as we detail later, does not need even to be an electron type. For example in $\pi^- \rightarrow \mu^- + \bar{\nu}_\mu$, the muon antineutrino, if Majorana, can be absorbed as an electron neutrino in an inverse beta decay.

In addition, while the $0\nu\text{DBD}$ rate is insensitive to the geometry of the source and is linearly proportional to

the source mass, the rate for MDBD rate, as we spell out below, depends sensitively on the geometry of the source and is proportional to the source mass to the 4/3 power.

We emphasize that we do not introduce MDBD as a replacement for traditional $0\nu\text{DBD}$ experiments. While we calculate yields for several model MDBD systems, realistic experiments with radioactive nuclei are not feasible at the moment. Nonetheless the new concept of MDBD should stimulate new ways of looking at neutrinoless weak interactions.

In the next Section, II, we first review the calculation of the rate of single beta decay, and the cross section for inverse beta decay. In Sec. III we derive the rate of MDBD as a coherent quantum process between the initial single beta decay and the inverse beta decay, and derive the dependence of the MDBD rate on the geometry of the source. Then in Sec. IV we discuss how the MDBD signal is readily differentiated from the experimental two electron backgrounds. We conclude in Sec. V.

II. BETA AND INVERSE BETA DECAY WITH MASSIVE NEUTRINOS

In this section we first review the role of chirality and helicity for massive neutrinos in beta and inverse beta decay. We then briefly review the rates for emission of an antineutrino of given helicity in beta decay and the absorption of a neutrino of given helicity in inverse beta decay.

A. Chirality and helicity

Eigenstates of γ_5 have definite chirality; we denote the γ_5 eigenvalue in these states as *positive* ($\gamma_5 = 1$) or *negative* ($\gamma_5 = -1$). While chirality and helicity (the eigenvalue h of the projection of the spin direction along the direction of motion, $\hat{\Sigma} \cdot \hat{p}$) coincide for massless neutrinos, where a positive chirality state always has positive helicity, $h=1$, and a negative chirality state always has negative helicity $h=-1$, they are not the same for finite mass neutrinos. We denote positive helicity as *right handed*, and negative helicity as *left handed*.

In beta decay, antineutrinos are emitted with positive chirality, $\gamma_5 = 1$, while neutrinos can be absorbed in the inverse reaction only if they have negative chirality. Neutrinos are preferentially absorbed with helicity opposite to that of the antineutrino in beta decay. Since chirality is conserved for massless neutrinos, a massless Majorana antineutrino emitted in beta decay has the wrong chirality ever to be absorbed as a neutrino; both MDBD and $0\nu\text{DBD}$ are forbidden.

Independent of the neutrino mass, however, neutrinos and antineutrinos, in the absence of external forces, e.g., gravitational [10] or magnetic [11], propagate in states of definite helicity. When neutrinos have finite mass, chirality is no longer a constant of the motion,

¹ Nonetheless, even if such processes were to underlie $0\nu\text{DBD}$, the observation of such double beta decays would establish that the neutrino is Majorana [8, 9].

since γ_5 does not commute with the mass term in the Hamiltonian. In detail, as reviewed in the Appendix, an antineutrino emitted with positive chirality has amplitude $\alpha^\pm = \sqrt{(1 \pm \beta_\nu)/2}$ to be right or left handed, where $\beta_\nu = v_\nu/c$, with v_ν the neutrino velocity. Similarly, a right or left handed neutrino has amplitude $\sqrt{(1 \mp \beta_\nu)/2} = \alpha^\mp$ to have the negative chirality needed to be absorbed in an inverse beta decay. Thus a Majorana neutrino effectively has a total amplitude for emission with positive chirality and absorption with negative chirality, summed over both intermediate helicities, $\alpha^+ \alpha^- + \alpha^- \alpha^+ = \sqrt{1 - \beta_\nu^2} = m_\nu/E_\nu$, where m_ν and E_ν are the neutrino mass and energy. States of definite helicity have amplitudes to be of either chirality, thus allowing neutrinoless double beta decay for finite mass Majorana neutrinos.

B. Single beta decay

We now discuss the amplitude, \mathcal{A}_{BD}^{ih} , and then the rate of beta decay, (2), with emission of a $\bar{\nu}_e$ in mass state i and helicity h , neglecting nuclear recoil (a better and better approximation the heavier the parent nucleus). The amplitude is

$$\mathcal{A}_{BD}^{ih} = \mathcal{M}_i \alpha_\nu^{ih}. \quad (5)$$

where $\mathcal{M}_i \propto G_F V_{ud} U_{ei}$, with G_F the Fermi weak coupling constant, $V_{ud} = 0.97425$ the Cabbibo-Kobayashi-Maskawa (CKM) up-down quark matrix element, and U_{ei} the Pontecorvo-Maki-Nakagawa-Sakata (PMNS) neutrino mixing matrix element. For right and left antineutrino helicities, $\alpha_\nu^{i,h=\pm 1} = \alpha^\pm$. For given neutrino energy, β_i depends on the neutrino mass, m_i ; since for $m_i \ll E_{\nu i}$, $\beta_i \simeq 1 - m_i^2/2E_{\nu i}^2$,

$$\alpha_\nu^{iR} \simeq 1, \quad \alpha_\nu^{iL} \simeq \frac{m_i}{2E_{\nu i}}. \quad (6)$$

The dependence on the neutrino mass state is through the factors U_{ei} and α_ν^{ih} , and the helicity dependence resides in α_ν^{ih} .

The full squared matrix element has the form

$$|\mathcal{M}_i|^2 = 2\pi W(E_e) |U_{ei}|^2, \quad (7)$$

where for tritium for example [12, 13],

$$W(E_e) = \frac{G_F^2}{2\pi} |V_{ud}|^2 F(Z, E_e) (m_{3\text{He}}/m_{3\text{H}}) |M_f|^2, \quad (8)$$

with $F(Z, E_e)$ the Fermi Coulomb factor for the electron- ^3He system, and $|M_f|^2$ the sum of the nuclear form factors for Fermi and Gamow-Teller transitions.² In further

calculation we symbolically write the matrix element as $\mathcal{M}_i = \sqrt{2\pi} W U_{ei}$.

The rate of beta decay with emission of a neutrino of given helicity is then

$$d\Gamma_{XBD}^h = \sum_i \frac{d^3 p_\nu}{(2\pi)^3} \frac{d^3 p_e}{(2\pi)^3} 2\pi |\mathcal{M}_i|^2 (\alpha_\nu^{ih})^2 \delta(\Delta M - E_e - E_{\nu i}), \quad (9)$$

where $\Delta M = m_X - m_Y$ is the total energy released in the beta decay.

Integrating over all electron states, and writing $d^3 p_\nu = 4\pi p_\nu E_\nu dE_\nu$, we have

$$\frac{d\Gamma_{XBD}^h}{dE_\nu} = \frac{\bar{\sigma}(E_e)}{2\pi^2} \sum_i |U_{ei}|^2 (1 + h\beta_i) E_\nu \sqrt{E_\nu^2 - m_i^2}, \quad (10)$$

where $E_e = \Delta M - E_\nu$ and

$$\bar{\sigma}(E_e) \equiv p_e E_e W(E_e). \quad (11)$$

The differential rate of beta decay, for $m_i \ll E_\nu$, summed over h and using $\sum_i |U_{ei}|^2 = 1$, is

$$\frac{d\Gamma_{XBD}}{dE_\nu} \simeq \frac{\bar{\sigma}(E_e)}{\pi^2} E_\nu^2. \quad (12)$$

For tritium, in the limit of a zero energy neutrino [12], $\bar{\sigma} \simeq 3.834 \times 10^{-45} \text{ cm}^2$. The inverse of the mean lifetime, τ , of the nucleus X against beta decay (17.8 yr for tritium) is then $\int dE_\nu (d\Gamma_{XBD}/dE_\nu)$.

C. Inverse beta decay

While the rate of beta decay is an incoherent sum over the mass states in the emitted antineutrino, the rate of inverse beta decay depends strongly on the nature of the neutrino impinging on the target nucleus. For example, neutrinos from the Big Bang arrive at Earth in definite mass eigenstates, a result of the spatial separation of the mass components of a neutrino wavepacket caused by the dependence of the neutrino velocity on the mass state. By contrast, neutrinos from nuclear weak interactions, in ^{51}Cr for example [14], are emitted in pure electron neutrino flavor states. These neutrinos can initiate inverse beta decay whether the neutrino is Dirac or Majorana. On the other hand, antineutrinos can participate in inverse beta decay (with electron emission) only if the neutrino is Majorana. These antineutrinos can be either in mass eigenstates, e.g., if they come from the Big Bang, or in flavor eigenstates, e.g., from tritium beta decay or a nuclear power plant. If the incident neutrino was emitted as a Majorana antineutrino, the amplitude for inverse beta decay is a coherent sum over the mass eigenstates in the neutrino.

² For tritium, $|M_f|^2 = 1 + 2.788(g_A/g_V)^2$, with $(g_A/g_V)^2 = 1.6116$, while for the neutron, $|M_f|^2 = 1 + 3(g_A/g_V)^2$.

Common to all these processes is the inverse beta decay amplitude for a neutrino in a given mass state. Specifically, the amplitude, \mathcal{A}_{IXBD}^{ih} , for inverse beta decay induced by a neutrino with velocity β_i , mass m_i and helicity h incident on a target nucleus, is

$$\mathcal{A}_{IXBD}^{ih} = \mathcal{M}_i \alpha_\nu^{ih}, \quad (13)$$

where $\alpha_\nu^{ih} = \sqrt{(1 - h\beta_i)/2}$, with \mathcal{M}_i the same as before.

The cross section for inverse beta decay for an incident neutrino in a given mass state i and helicity h is similarly (cf. Eq. (9)),

$$\begin{aligned} \frac{d\sigma_{IXBD}^{ih}}{d\Omega_e} &= \int \frac{p_e^2 dp_e}{(2\pi)^2} |\mathcal{M}_i|^2 (\alpha_\nu^{ih})^2 \delta(m_X + E_\nu - m_Y - E_e) \\ &= \frac{p_e E_e}{(2\pi)^2} |\mathcal{M}_i|^2 (\alpha_\nu^{ih})^2 = \frac{\bar{\sigma}(E_e)}{4\pi} |U_{ei}|^2 (1 - h\beta_i), \end{aligned} \quad (14)$$

and the total IXBD cross section σ_{IXBD}^{ih} equals $\bar{\sigma}|U_{ei}|^2(1 - h\beta_i)$. As in beta decay, the helicity dependence is in the factor α_ν^{ih} . The scale of both the lifetime of a nucleus under beta decay, and the IXBD cross section is set by $\bar{\sigma}(E_e)$.

If the initial neutrino is fully relativistic in mass state i ($\beta_\nu \rightarrow 1$), then only the left handed helicity component can lead to emission of an electron, and the cross section for an incident mass state i is $2\bar{\sigma}|U_{ei}|^2$. (Were the initial neutrino in an incoherent sum over mass states i , the cross section would become $2\bar{\sigma}$.) But for slowly moving relic neutrinos ($\beta_\nu \rightarrow 0$), $\alpha_\nu^{ih} \rightarrow 1/\sqrt{2}$ and the IXBD amplitude becomes independent of the neutrino helicity. More generally, if the initial neutrino state is a coherent sum of mass states, the rate of IXBD reflects interference between the states, a problem we focus on in calculating the rate of MDBD below.

III. MACROSCOPIC DOUBLE BETA DECAY

We turn now to calculating the rate of macroscopic double beta decay in terms of the known physics of the single beta decay, XBD, and inverse beta decay, IXBD. The rate of MDBD within a sample of atoms of nucleus X , with the sample acting both as the source of beta decays as well as the target for inverse beta decays, depends on both the microscopics of XBD and IXBD as well as the geometry of the ensemble of X atoms present. For spacing between the atoms large compared with the characteristic intermediate neutrino wavelength, the neutrinos can be taken to be on-shell, in contrast to neutrinoless double beta decay within a single nucleus. The MDBD process can take place for either helicity of the intermediate neutrino.

Since the Majorana neutrino in MDBD exists only as an intermediary between the initial electron and final

electron emission processes, the contributions of the different neutrino mass states are coherent, and give rise to quantum interference. To see this effect it is necessary to evaluate the MDBD rate in terms of the total amplitude for the process.

While neutrino oscillations become important in processes over astrophysical distances, e.g., in the sun and in neutron stars, they are insignificant in MDBD over laboratory distances, except for very small neutrino energies. The characteristic length (in meters) in neutrino oscillations for a neutrino of energy E_ν (in MeV) is $L(m)_{osc} \simeq E_\nu(\text{MeV})/\Delta m_{31}^2(\text{eV}^2)$, where $\Delta m_{31}^2 = m_3^2 - m_1^2 \simeq 2.5 \times 10^{-3} \text{eV}^2$ corresponds to the difference of the squares of the masses of the heaviest and lightest neutrinos. Thus $L_{osc} \sim E_\nu(\text{MeV}) \text{ km}$. Neutrinos of sub-keV energy could undergo neutrino oscillations in MDBD in large samples, but their effect would be hard to observe.

We assume the initial beta decay to take place at point \vec{r} and the inverse beta decay at \vec{r}' . The total amplitude for the process $X + X \rightarrow Y + Y + e^- + e^{-\prime}$ is

$$\begin{aligned} \mathcal{A}_{MDBD}(\vec{r} - \vec{r}') &= \sum_{ih} \int \frac{d^3 p_\nu}{(2\pi)^3} \frac{(\mathcal{A}_{XBD}^{ih} e^{i(\vec{p}_\nu + \vec{p}_e) \cdot \vec{r}}) (\mathcal{A}_{IXBD}^{ih} e^{i(\vec{p}'_e - \vec{p}_\nu) \cdot \vec{r}'})}{\Delta M - E_e - E_\nu + i\eta}, \end{aligned} \quad (15)$$

where $\eta \rightarrow 0^+$. Then using the amplitudes (5) and (13), doing the sum over helicities,

$$\sum_h \alpha_\nu^{ih} \alpha_\nu^{ih} = \sqrt{1 - \beta_i^2} = m_{\nu i}/E_\nu, \quad (16)$$

and the angular integration over the directions of the intermediate neutrino, we have

$$\begin{aligned} \mathcal{A}_{MDBD} &= e^{i(\vec{p}_e \cdot \vec{r} + \vec{p}'_e \cdot \vec{r}')} \frac{\sqrt{W(E_e)W(E'_e)}}{\pi |\vec{r} - \vec{r}'|} \sum_i U_{ei}^2 m_{\nu i} \\ &\times \int \frac{E_\nu dE_\nu \sin(p_\nu |\vec{r} - \vec{r}'|)}{\Delta M - E_e - E_\nu + i\eta}. \end{aligned} \quad (17)$$

For large $|\vec{r} - \vec{r}'|$ compared with characteristic $1/p_\nu$, only the on-shell contribution of the neutrino (from the imaginary part $-i\pi\delta(X)$ of the denominator term, $1/(X + i\eta)$) is significant. In this macroscopic limit the integral in the lower line of Eq. (17) becomes $-i\pi E_\nu \sin(p_\nu |\vec{r} - \vec{r}'|)$, where now $E_\nu = \Delta M - E_e$. We drop the overall phase factors, which do not enter the MDBD rate, and finally arrive at the MDBD amplitude,

$$\mathcal{A}_{MDBD} = \sqrt{W(E_e)W(E'_e)} \frac{\sin(p_\nu |\vec{r} - \vec{r}'|)}{|\vec{r} - \vec{r}'|} \sum_i U_{ei}^2 m_{\nu i}. \quad (18)$$

The total rate of MDBD with one emitter and one

absorber is then

$$\Gamma_{MDBD} = \int \frac{d^3 p_e}{(2\pi)^3} \frac{d^3 p'_e}{(2\pi)^3} |\mathcal{A}_{MDBD}|^2 2\pi \delta(2\Delta M - E_e - E'_e). \quad (19)$$

For $p_\nu |\vec{r} - \vec{r}'| \gg 1$ the \sin^2 factor, slightly cross-grained in \vec{r}' , becomes $1/2$, and thus

$$\Gamma_{MDBD} = \frac{\mathcal{K}}{4\pi |\vec{r} - \vec{r}'|^2}, \quad (20)$$

where the microscopic rate factor, after doing the E'_e integral, becomes

$$\mathcal{K} = \bar{m}^2 \int \frac{\bar{\sigma}(E_e) \bar{\sigma}(E'_e)}{\pi^2} dE_e. \quad (21)$$

Here $E'_e = 2\Delta M - E_e$, and

$$\bar{m} \equiv |\sum_i U_{ei}^2 m_{\nu i}| \quad (22)$$

is the average neutrino mass entering neutrinoless double beta decay.

We can understand the remaining structure of the MDBD rate by considering simply the single mass state contribution, denoted as Γ_{MDBD}^i . The beta decay of an X nucleus at point \vec{r} produces a flux, per unit neutrino energy, of neutrinos in helicity state h of energy E_ν at point \vec{r}' ,

$$\frac{dF^{ih}(\vec{r}')}{dE_{\nu i}} = \frac{1}{4\pi |\vec{r} - \vec{r}'|^2} \frac{d\Gamma_{XBD}^{ih}}{dE_{\nu i}}. \quad (23)$$

Thus the full rate for neutrinos emitted at point \vec{r} in mass state i to be absorbed at point \vec{r}' is

$$\Gamma_{MDBD}^i = \sum_h \int \frac{dF^{ih}(\vec{r}')}{dE_{\nu i}} dE_{\nu i} \sigma_{IXBD}^{ih} = \frac{\mathcal{K}_i}{4\pi |\vec{r} - \vec{r}'|^2}, \quad (24)$$

where

$$\begin{aligned} \mathcal{K}_i &= \int dE_{\nu i} \sum_h \frac{d\Gamma_{XBD}^{ih}}{dE_{\nu i}} \sigma_{IXBD}^{ih} \\ &= |U_{ei}|^4 m_{\nu i}^2 \int dE_{\nu i} \frac{\bar{\sigma}(E_e) \bar{\sigma}(E'_e)}{\pi^2}; \end{aligned} \quad (25)$$

this result is precisely the single neutrino mass state (i) contribution to \mathcal{K} , Eq. (21), with the identifications $E_e = \Delta M - E_{\nu i}$ and $E'_e = \Delta M + E_{\nu i} = 2\Delta M - E_e$.

The integral in \mathcal{K} depends very weakly on the neutrino masses since $m_\nu \ll m_e$, and we neglect them in the integral. Furthermore the $\bar{\sigma}$ do not vary greatly over the range of neutrino energies, and we write them as $\bar{\sigma}$ evaluated at the end point energy times a correction. Neglecting the energy dependence in the Fermi Coulomb term, F in $\bar{\sigma}$ we have

$$\mathcal{K} = \frac{1}{\pi^2} \bar{m}^2 \bar{\sigma}_{end}^2 K_{end} \mathcal{J}, \quad (26)$$

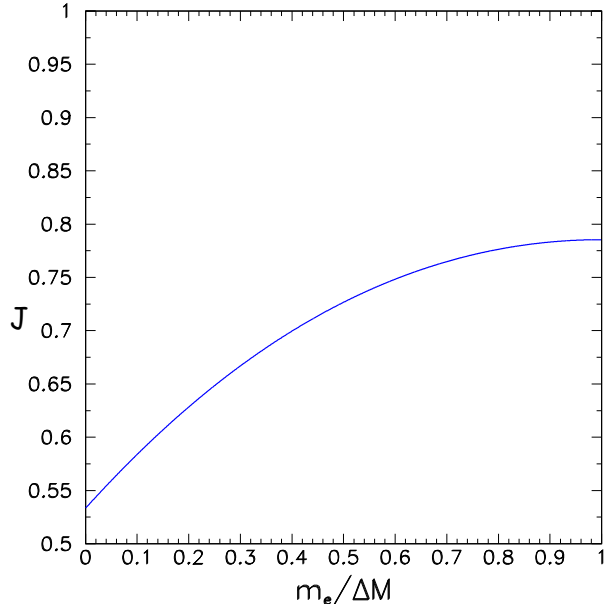


FIG. 2: The dimensionless integral \mathcal{J} entering the MDBD rate, as a function of $m_e/\Delta M$.

where $K_{end} = \Delta M - m_e$ is the endpoint kinetic energy of the XBD, $\bar{\sigma}_{end} \equiv \bar{\sigma}(E_e = \Delta M)$, and the dimensionless factor \mathcal{J} is given by

$$\mathcal{J}(m_e/\Delta M) = \int_0^{K_{end}} \frac{dE_\nu}{K_{end}} \frac{p_e E_e p'_e E'_e}{(K_{end}^2 - m_e^2) K_{end}^2}. \quad (27)$$

Figure 2 shows \mathcal{J} as a function of $m_e/\Delta M$. In the limit that the Q value in the XBD is small compared with the electron mass, or $\Delta M - m_e \ll m_e$, as in tritium, then $\mathcal{J} \rightarrow \pi/4$ (this factor arises from the averaging of the momenta of the electrons), and

$$\mathcal{K} \rightarrow \frac{\bar{m}^2 \bar{\sigma}_{end}^2}{4\pi} K_{end}. \quad (28)$$

In the opposite limit, $\Delta M \gg m_e$, the correction factor \mathcal{J} becomes $8/15$, and $\mathcal{K} \rightarrow (8\bar{m}^2 \bar{\sigma}_{end}^2 / 15\pi^2) K_{end}$.

A. Quantum interference and coherence

The rate of MDBD is proportional to the square of the weighted neutrino mass $|\sum_i U_{ei}^2 m_{\nu i}|^2$. This term includes both the direct ($i = j$) MDBD process, with a sum of the rates for single mass eigenstates, $\sum_i |U_{ei}|^4 m_{\nu i}^2$, as well as the interference between different mass eigenstates ($i \neq j$). By contrast, if the incident neutrino is an incoherent sum of mass states, then the rate is proportional to the $i = j$ term alone, i.e.,

$$\sum_i |U_{ei}|^4 m_{\nu i}^2 \equiv m_{incoh}^2, \quad (29)$$

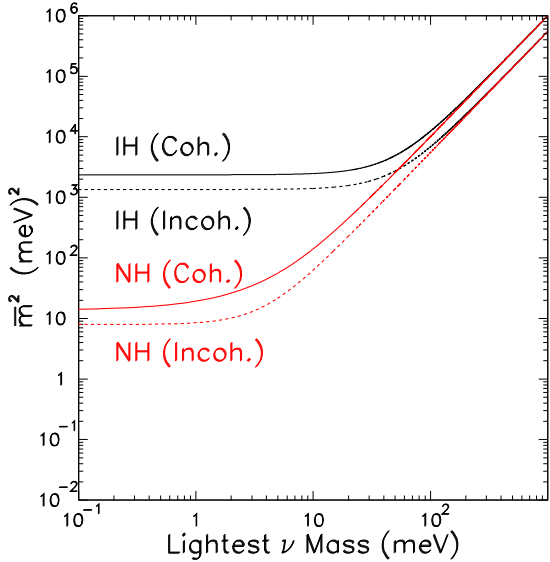


FIG. 3: The calculated \bar{m}^2 for the normal (NH) and inverted (IH) neutrino mass hierarchies with and without interference between the mass eigenstates. The curves labelled “coherent” assume zero Majorana phases (with respect to the CP phase), while the curves labelled “incoherent” neglect the off-diagonal interference between different mass eigenstates. In this case coherence increases \bar{m}^2 and the rate of MDBD.

a very different weighting of the neutrino masses.

The dependence of \bar{m} on possible phases of the U_{ei} is a consequence of quantum interference between different mass states i in macroscopic double beta decay. Explicitly, \bar{m} can be written in terms of the CP phase δ and Majorana phases λ_a and λ_b , as,

$$\bar{m} = \left| |U_{e1}|^2 e^{2i\lambda_a} m_1 + |U_{e2}|^2 e^{2i\lambda_b} m_2 + |U_{e3}|^2 e^{-2i\delta} m_3 \right|. \quad (30)$$

Figure 3 shows \bar{m}^2 as a function of lightest neutrino mass for the normal and inverted mass hierarchies, using the neutrino oscillation parameters tabulated in [17]. The curves labelled “incoherent” neglect the interference terms in \bar{m}^2 , and include only the diagonal sum over mass eigenstates, i.e., with \bar{m}^2 replaced by m_{incoh}^2 . In the curves labelled “coherent,” we assume that the Majorana CP phases equal $-\delta$, so that all the phases drop out of \bar{m} , and $\bar{m}^2 - m_{incoh}^2 = \sum_{i \neq j} |U_{ei}|^2 |U_{ej}|^2 m_{\nu i} m_{\nu j} > 0$. In this case, coherence increases the MDBD rate. For given neutrino mass splittings, the curves are in fact simply quadratic functions of the lightest neutrino mass.

On the other hand, if the Majorana CP phases differ from $-\delta$, coherence can, as illustrated in Fig. 4, decrease the rate, exactly as in 0ν DBD [1]. Figure 4 also shows, on the right hand scale, the MDBD rate for a spherical source of 100 g of tritium, calculated from Eq. (33) below.

Macroscopic double beta decay remains coherent as

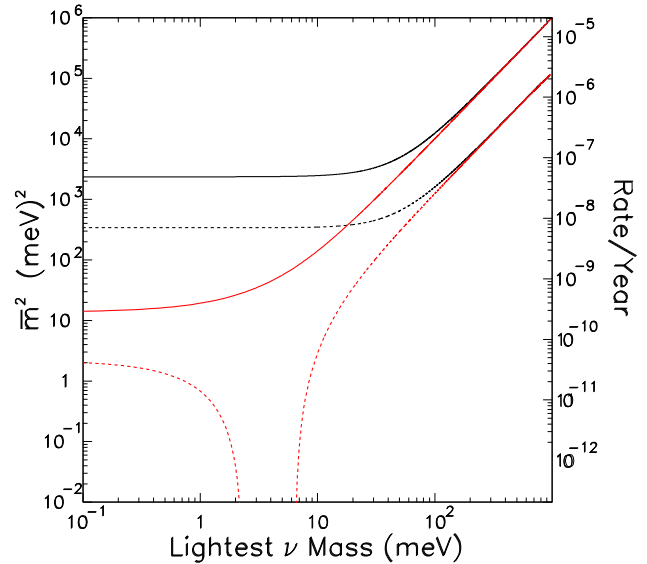


FIG. 4: Full range of \bar{m}^2 for the normal and inverted hierarchies. The solid curves show the same curves labelled “coherent” in Fig. 3, while the dashed curves show the maximal destructive interference from possible Majorana phases. The scale on the right shows the corresponding MDBD rate expected in a 100 g tritium target. The rate is proportional to the mass of the target to the 4/3 power.

long as the neutrino wavepacket travelling from source to target stays together. However, the different mass components of the wavepacket physically separate and destroy coherence at large distances owing to the mass dependence of their velocities, $\delta v/c \sim \frac{1}{2} \Delta m_\nu^2 / E_\nu^2$ [11]. If the initial neutrino wavepacket is of length ℓ , then decoherence takes place over distances $L_{dec} \sim \ell E_\nu^2 / \Delta m_\nu^2 \sim \ell E_\nu L_{osc}$, where L_{osc} , discussed above, is the length over which neutrino oscillations become significant. The estimate $\ell E_\nu \sim 1$ nm-MeV [15] implies that L_{dec} is $\sim 10^4 L_{osc}$, or $L_{dec} \sim 10^4 E_\nu (\text{MeV}) / \Delta m_\nu^2 (\text{eV}^2)$ m. A detailed discussion of decoherence over astrophysical distances must thus take flavor oscillations of the neutrino wave packets into account.

B. Dependence of the MDBD rate on geometry

We next consider the rate of MDBD in a macroscopic sample of N atoms of X with uniform density n . For an ensemble of beta emitters, Eq. (24) implies the total rate of MDBD,

$$\mathcal{R}_{MDBD} = \int d^3r d^3r' \frac{n^2 \mathcal{K}}{4\pi |\vec{r} - \vec{r}'|^2} = \frac{N^2 \mathcal{K}}{4\pi} \left\langle \frac{1}{(\vec{r} - \vec{r}')^2} \right\rangle. \quad (31)$$

For isotropic scaling at fixed density, the rate scales as the fourth power of the linear size of the system, or $N^{4/3}$. On the other hand, the rate of 0ν DBD scales with N .

The detailed evaluation of the integral depends on the geometry of the target. It is readily evaluated for a spherical target of radius R by writing,

$$\int \frac{d^3r d^3r'}{(\vec{r} - \vec{r}')^2} = \int \frac{d^3k}{4\pi k} \left| \int d^3r e^{i\vec{k}\cdot\vec{r}} \right|^2 = 4\pi^2 R^4, \quad (32)$$

where we use $\int d^3r e^{i\vec{k}\cdot\vec{r}} = (4\pi/k^3)(\sin kR - kR \cos kR)$.

The total double beta decay rate for a spherical source³ is then

$$\mathcal{R}_{MDBD} = \frac{9}{16\pi} \frac{N_T^2}{R^2} \mathcal{K}, \quad (33)$$

which shows explicitly the scaling with the size of the sample (at fixed density) as $N^{4/3}$.

C. Estimate of R_{MDBD}

We estimate R_{MDBD} from Eq. (33) with (28). For tritium,

$$\mathcal{R}_{MDBD} = \frac{9}{64\pi^2} \frac{N_T^2}{R^2} \bar{m}^2 \bar{\sigma}_T^2 K_{end}; \quad (34)$$

with a 100 g sphere of tritium ($N_T \simeq 2 \times 10^{25}$ nuclei), $\mathcal{R}_{MDBD} \simeq 2.32 \times 10^{-5} (\bar{m}/1 \text{ eV})^2/\text{year}$. It is instructive to compare this rate with the conventional neutrinoless double beta decay rates for various nuclei. No 0ν DBD events have been positively identified [4], and the most sensitive recent results include those on ^{76}Ge [18, 19], ^{136}Xe [20–22], ^{130}Te [23], ^{82}Se [24, 25], and ^{100}Mo [26]. Table I lists the expected 0ν DBD rates for these nuclei with an exposure of 100 g-yr, assuming $\bar{m} = 0.1 \text{ eV}$. As we see in the Table, the tritium MDBD rate is four to five orders of magnitude lower than those expected for 0ν DBD. This difference reflects the much smaller $Q=16.8 \text{ keV}$ value in tritium beta decay than in 0ν DBD, e.g., $Q = 2.04 \text{ MeV}$ for ^{76}Ge and $Q=2.46 \text{ MeV}$ for ^{136}Xe 0ν DBD.

To illustrate the importance of a large Q value, we compare MDBD for neutrons (where $n \rightarrow p + e^- + \bar{\nu}_e$ followed by $\nu_e + n \rightarrow p + e^-$) with tritium. In this double beta decay $Q = 2 \times 0.782 \text{ MeV} = 1.564 \text{ MeV}$. Furthermore $\bar{\sigma}_n$ is a factor ~ 20 larger than in tritium, which has comparable matrix elements. In a sample of 100 g of

neutrons occupying the spherical volume as would 100 g of tritium, the MDBD rate is a factor $\sim 10^5$ larger than in a comparable sample of tritium. In fact, the MDBD rate for such a neutron sample is comparable to that in an equivalent sample of nuclei in 0ν DBD. Clearly though, it would be impossible to do such an experiment in a cloud of laboratory neutrons.⁴

A somewhat more realistic candidate nucleus to consider in searching for MDBD is ^{11}C , which undergoes a β^+ decay with a half life of 22.3 min. with a Q value of 1.98 MeV. We estimate that a 100 g spherical sample of ^{11}C , which has a density 2.2 g/cm^3 , and contains 3/11 of the number of atoms in a 100 g sample of tritium, would have a MDBD rate of 5.14×10^{-5} per year for $\bar{m} = 0.1 \text{ eV}$, as shown in Table I. This rate is significantly larger than the MDBD rate for tritium, but still lower than the rate for the 0ν DBD sources listed in Table I. As mentioned, the MDBD rate contains no uncertainties arising from the nuclear matrix elements, distinctly different from in 0ν DBD.

IV. MDBD SIGNAL VS. BACKGROUND

A. Electron distribution in MDBD

The characteristic feature of MDBD is that the sum of the two electron energies is just twice the total energy released in a single beta decay. The distribution of the electron pairs has the structure, in the limit of small neutrino mass,

$$\begin{aligned} d^2 N(E_e, E'_e) &\propto p_e E_e F(E_e) dE_e p'_e E'_e F(E'_e) dE'_e \\ &\times \int dE_\nu \delta(\Delta M - E_\nu - E_e) \delta(\Delta M + E_\nu - E'_e) \\ &= p_e E_e F(E_e) F(E'_e) dE_e p'_e E'_e dE'_e \\ &\times \delta(2\Delta M - E_e - E'_e). \end{aligned} \quad (35)$$

The E_ν^2 from the neutrino phase space is canceled by neutrino helicity factor $1 - \beta^2 = (m_\nu/E_\nu)^2$. Then the single electron distribution in MDBD has the form,

$$\frac{dN_e}{dK_e} \propto p_e E_e F(E_e) F(E'_e) p'_e E'_e, \quad (36)$$

where here $E'_e = 2\Delta M - E_e$.

This distribution, shown in Fig. 5 in terms of the electron kinetic energy K_e for tritium MDBD, is clearly symmetric about the single beta decay endpoint, $K_e = K_{end}$.

³ We give the result for a spherical source only for illustration, ignoring the complication that electrons produced within a sufficiently large spherical sample rapidly lose energy traversing the source and cannot readily be detected. For such a reason, the PTOLEMY experiment [16] is aiming for two dimensional targets, using tritiated graphene. A realistic MDBD experimental design would similarly require a more planar geometry, at the cost of reducing the probability of a given antineutrino from the initial beta decay finding a target for inverse decay.

⁴ On the other hand, a neutron star contains beneath its crust a stable liquid of order 10^{57} neutrons in a $\sim 10 \text{ km}$ sphere, which implies a geometric enhancement over MDBD in 100 g of tritium by a factor $\sim 10^{53}$. The rate of MDBD is, however, significantly suppressed by Pauli exclusion in both URCA and modified URCA processes, as well as by BCS pairing. Unfortunately there is no way apparent to distinguish such MDBD processes in neutron stars, even in their cooling.

Nucleus	$T_{1/2}$ for $\bar{m} = 0.1$ eV	Yield per 100 g-yr
^3H (MDBD)	–	2.3×10^{-7}
n (MDBD)	–	3.4×10^{-2}
^{11}C (MDBD)	–	5.1×10^{-5}
^{76}Ge ($0\nu\text{DBD}$) [18, 19]	$3.7 \times 10^{25} < T_{1/2} < 2.0 \times 10^{26}$ yr	$2.7 \times 10^{-3} < Y < 1.5 \times 10^{-2}$
^{136}Xe ($0\nu\text{DBD}$) [20–22]	$0.1 \times 10^{26} < T_{1/2} < 1.8 \times 10^{26}$ yr	$1.7 \times 10^{-3} < Y < 3.0 \times 10^{-2}$
^{130}Te ($0\nu\text{DBD}$) [23]	$5.9 \times 10^{24} < T_{1/2} < 6.7 \times 10^{25}$ yr	$4.7 \times 10^{-3} < Y < 5.4 \times 10^{-2}$
^{82}Se ($0\nu\text{DBD}$) [24, 25]	$1.0 \times 10^{25} < T_{1/2} < 7.5 \times 10^{25}$ yr	$6.8 \times 10^{-3} < Y < 4.8 \times 10^{-2}$
^{100}Mo ($0\nu\text{DBD}$) [26]	$4.7 \times 10^{24} < T_{1/2} < 1.4 \times 10^{25}$ yr	$2.9 \times 10^{-2} < Y < 8.8 \times 10^{-2}$

TABLE I: Expected yields, Y , for MDBD and $0\nu\text{DBD}$ for a 100 g-yr exposure using various nuclei. We assume the Majorana neutrino effective mass $\bar{m} = 0.1$ eV. The uncertainties in the predicted $T_{1/2}$ and yield for $0\nu\text{DBD}$ reflect the range of uncertainties of the nuclear matrix elements adopted by Ref. [4] to relate the current experimental limits on $T_{1/2}$ to values of \bar{m} . For MDBD we assume 100 g spherical sources of tritium (and neutrons, for illustration) with density 1 g/cm³ and ^{11}C with density 2.2 g/cm³.

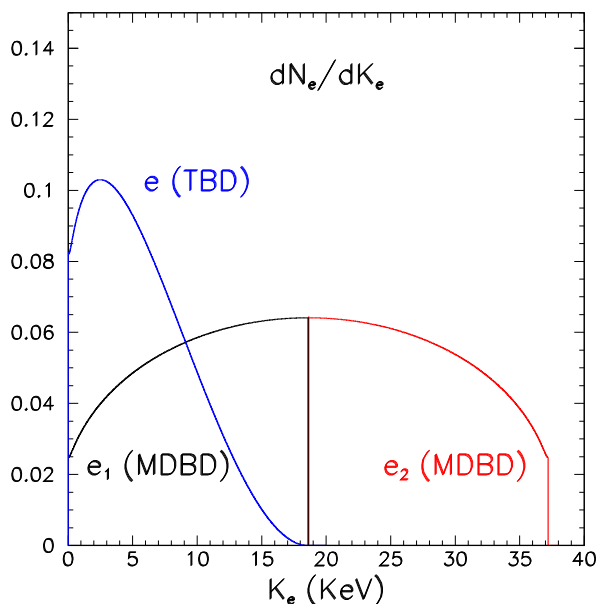


FIG. 5: The electron distributions in single tritium beta decay and in tritium MDBD, where e_1 is the lower energy and e_2 the higher energy electron. Here e_1 is the electron produced in the initial beta decay, and e_2 the electron emitted in the final inverse beta decay. The detailed structure of the single electron energy distributions at K_{end} , shown as a single vertical line, is in fact two curves separated essentially by $2m_\nu$, too fine to be seen in the figure.

The figure shows for comparison the electron distribution from single beta decay, which vanishes near K_{end} , as we see from Eq. (12), essentially as

$$\frac{dN_e}{dK_e} \propto \frac{d\Gamma}{dE_e} = \frac{\bar{\sigma}(E_e)}{2\pi^2} (\Delta M - m_e - K_e)^2; \quad (37)$$

the distribution is dominated by electrons emitted with a right handed neutrino. In this figure, we normalize the individual distributions to unity, and take the

Fermi Coulomb correction to be $2\pi\eta/(1 - e^{-2\pi\eta})$ with $\eta = Ze^2/v_e$. The non-zero neutrino mass leads to a falloff of the e_1 distribution at $K_{end} - m_\nu$ and a rise of the e_2 distribution at $K_{end} + m_\nu$, too fine a structure to see in the figure.

B. Background

Although the signal for a macroscopic neutrinoless double beta decay is that the sum of the energies of the two electrons in the event is precisely $2K_{end}$, it would seem, given the high rates of single beta decay, that the challenge of separating the signal from the background is insurmountable. The 2×10^{25} tritons in 100 g of tritium, with a half-life of 12.3 years, would produce $\sim 2.5 \times 10^{16}$ decays per second. However, only a tiny fraction of the decays give electrons with energy near the beta decay endpoint. An analogous challenge to separate the signal from the background is encountered in the proposed detection of relic neutrinos using the ITBD reaction [16, 27], where the signals are separated from the endpoint by twice the neutrino mass. Long et al. [12] show that an energy resolution better than $0.7 m_\nu$ is sufficient to reach a signal to background ratio better than 1.

The signal to noise ratios for MDBD should be much better than in relic neutrino detection, and do not require superb energy resolution. As shown in Fig. 5, one of the two electrons from MDBD has an energy greater the endpoint energy of TBD, and up to twice the endpoint energy. By requiring that the more energetic electron from the MDBD candidate event has an energy sufficiently higher than the endpoint energy, the background can be rejected at only a small cost to the MDBD detection efficiency.

The favorable background rejection capability of MDBD is further illustrated in Fig. 6a, where the axes are the individual electron kinetic energies. An MDBD event would appear as a point on the diagonal line

$K_1 + K_2 = \Delta M - 2m_e$ in this figure. The MDBD accidental background from two electrons emitted in two independent single beta decays would lie in the red box in the figure, and except at the single point where the red square touches the straight line, the background is separated from the two electron MDBD event. The background from the upper-right corner of the square in Fig. 6a can be readily rejected by requiring that the MDBD candidate events are well separated from this corner.

By contrast, the background in the $0\nu\text{DBD}$ reaction is from the $2\nu\text{DBD}$ reaction. The two electron kinetic energies from the $2\nu\text{DBD}$ background can reach the diagonal signal line in $0\nu\text{DBD}$ everywhere, as shown by the red triangle in Fig. 6b. These $2\nu\text{DBD}$ background events cannot be rejected without a significant loss of detection efficiency for the $0\nu\text{DBD}$ signals, unless superb energy resolution is achieved.

The time separation between the two electrons can also be used to reject accidental background in MDBD. The two electrons from an MDBD event occur in a narrow time window, the travel time from source to target, $\delta t \sim R/c$, which can be of order tens of picoseconds, while the electrons from single beta decays are uncorrelated in time. In contrast the $2\nu\text{DBD}$ background in $0\nu\text{DBD}$ cannot be rejected on the basis of time separation.

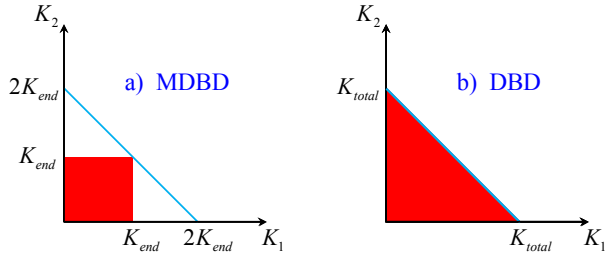


FIG. 6: The energy spectrum of two-electron events, with background in red, in a) MDBD and b) $0\nu\text{DBD}$. The axes are the kinetic energies of the individual electrons. The kinetic energies of the two electrons in both neutrinoless double beta decays lie along the (blue) diagonal line extending from the first electron having K_{total} (with $K_{total} = 2K_{end}$ in MDBD) and the second with 0, to the reverse. The energies of two electrons produced in single beta decays, the background in MDBD, lie in the red box in a), reaching the diagonal line only at a single point. In contrast, in $0\nu\text{DBD}$ experiments the background from double beta decay with neutrinos lies in the red triangle in b), coming up to the diagonal line everywhere.

V. CONCLUSION

While neutrinoless double beta decay of single nuclei is the most promising experimental tool for testing the fundamental question of the Dirac or Majorana nature of neutrinos, the new process of macroscopic neutrino-

less double beta decay we have introduced here is another manifestation of Majorana neutrinos with non-zero mass. The MDBD process shares features in common with single nucleus neutrinoless double beta decay; both depend on neutrinos being massive and Majorana, and both are affected by quantum interference between different neutrino mass states. The two processes have significant differences, however, including the absence of nuclear matrix element uncertainties for the MDBD rate and the different nature of the experimental backgrounds in these two processes. In addition MDBD exhibits the new phenomenon of quantum coherence over macroscopic distances, related, but not equivalent to neutrino oscillations.

Macroscopic double beta decay combines the processes of beta decay – as is being studied for tritium in the KATRIN [28] experiment for measuring the neutrino mass – and capture of neutrinos, as in the PTOLEMY experiment [16] to detect primordial neutrinos from the Big Bang. The MDBD process combining these two processes, could in principle be accessible in either of these two experiments. Our detailed analysis of various characteristics of MDBD, including expected rates, makes it clear that, given the quantities of tritium present, MDBD events are too rare to be detectable in the two experiments.

Nor is MDBD a viable alternative, at this point, to the well established neutrinoless double beta decay experiments to test the Majorana nature of neutrinos. We do not present MDBD as a currently feasible experiment. Nevertheless, the similarities and distinct differences between these two processes provide useful perspectives on the underlying mechanisms for these two processes, and indicate new directions in which the concept of MDBD can be explored.

An example, as mentioned earlier, is the analog of MDBD that can occur with emission of a Majorana antineutrino with a flavor α other than electron, e.g., in $\pi^- \rightarrow \mu^- + \bar{\nu}_\mu$. The amplitude for capture of the emitted antineutrino on a nucleus as an electron neutrino would be proportional to $\sum_i U_{\alpha i} U_{ei} m_{\nu i}$, which is non-zero even if no phases enter the $U_{\alpha i}$. Such conversion of a Majorana $\bar{\nu}_\mu$ into a ν_e cannot occur in neutrinoless double beta decay within a single nucleus, simply by energy conservation, but can occur macroscopically.

Acknowledgments

This research was supported in part by the NSF Grant No. PHY-1812377 and by the Japan Science and Technology Agency (JST) as part of the Adopting Sustainable Partnerships for Innovative Research Ecosystem (ASPIRE), Grant Number JPMJAP2318, and was carried out in part at the Aspen Center for Physics, which is supported by National Science Foundation grant PHY-2210452, and at the National Central University in Taiwan under the Yushan Fellow Program.

- [1] M. J. Dolinski, A. W. P. Poon, and W. Rodejohann, Neutrinoless double-beta decay: status and prospects, *Annu. Rev. Nucl. Part. Sci.* **69**, 219 (2019).
- [2] S. R. Elliott and P. Vogel, Double beta decay, *Annu. Rev. Nucl. Part. Sci.* **52**, 115 (2002).
- [3] M. Agostini, G. Benato, J. A. Detwiler, J. Menéndez, and F. Vissani, Toward the discovery of matter creation with neutrinoless $\beta\beta$ decay, *Rev. Mod. Phys.* **95**, 025002 (2023).
- [4] A. Barabash, Future beta decay experiments: recent achievements and future prospects, *Universe* **9**, 290 (2023).
- [5] A. Balantekin and B. Kayser, On the properties of neutrinos, *Annu. Rev. Nucl. Part. Sci.* **68**, 313 (2018).
- [6] W. C. Haxton and G. J. Stephenson, Double Beta Decay, *Prog. Part. Nucl. Phys.* **12**, 409 (1984).
- [7] J. Engel and J. Menéndez, Status and Future of Nuclear Matrix Elements for Neutrinoless Double-Beta Decay: A Review, *Rep. Prog. Phys.* **80**, 046301 (2017).
- [8] J. Schechter and J. F. Valle, Neutrinoless double- β decay in $SU(2)\times U(1)$ theories, *Phys. Rev. D* **25**, 2951 (1982).
- [9] M. Duerr, M. Lindner, and A. Merle, On the Quantitative Impact of the Schechter-Valle Theorem, *JHEP* **1106:091** (2011).
- [10] G. Baym and J. C. Peng, Evolution of Primordial Neutrino Helicities in Cosmic Gravitational Inhomogeneities, *Phys. Rev. D* **103**, 123019 (2021).
- [11] G. Baym and J. C. Peng, Evolution of Primordial Neutrino Helicities in Astrophysical Magnetic Fields and Implications for their Detection, *Phys. Rev. Lett.* **126**, 191803 (2021).
- [12] A. J. Long, C. Lunardini, and E. Sabancilar, Detecting non-relativistic cosmic neutrinos by capture on tritium: phenomenology and physics potential, *J. Cosm. and Astropart. Phys.* **JCAP 1408**, 038 (2014).
- [13] R. G. H. Robertson and D. A. Knapp, Direct Measurements of Neutrino Mass, *Annu. Rev. Nucl. Part. Sci.* **38**, 185 (1988).
- [14] J. C. Peng and G. Baym, Inverse tritium beta decay with relic neutrinos, solar neutrinos, and a ^{51}Cr source, *Phys. Rev. D* **106**, 063018 (2022).
- [15] B. J. P. Jones, E. Marzec, and J. Spitz, Width of a beta-decay-induced antineutrino wave packet, *Phys. Rev. D* **107**, 013008 (2023).
- [16] E. Baracchini et al., PTOLEMY: A Proposal for Thermal Relic Detection of Massive Neutrinos and Directional Detection of MeV Dark Matter; arXiv:1808.01892; M. G. Betti et al. (PTOLEMY Collaboration), Neutrino physics with the PTOLEMY project: active neutrino properties and the light sterile case, *JCAP* **07**, 047 (2019), arXiv:1902.05508 [astro-ph.CO].
- [17] X. Qian and J. C. Peng, Physics with Reactor Neutrinos, *Rep. Prog. Phys.* **82**, 036201 (2019).
- [18] I. J. Arnuquist et al. (Majorana Collaboration), Final Result of the Majorana Demonstrator's Search for Neutrinoless Double- β Decay in ^{76}Ge , *Phys. Rev. Letters* **130**, 062501 (2023).
- [19] M. Agostini et al. (GERDA Collaboration), Final Results of GERDA on the Search for Neutrinoless Double- β Decay, *Phys. Rev. Letters* **125**, 252502 (2020).
- [20] S. Abe et al. (KamLAND-Zen Collaboration), Search for the Majorana Nature of Neutrinos in the Inverted Mass Ordering Region with KamLAND-Zen., *Phys. Rev. Letters* **130**, 051801 (2023).
- [21] E. Aprile et al. (XENON Collaboration), Double-weak decays of ^{124}Xe and ^{136}Xe in the XENON1T and XENONnT experiments, *Phys. Rev. C* **106**, 024328 (2022).
- [22] G. Anton et al. (EXO-200 Collaboration), Search for Neutrinoless Double- β Decay with the Complete EXO-200 Dataset, *Phys. Rev. Letters* **123**, 161802 (2019).
- [23] D. Q. Adams et al. (CUORE Collaboration), Search for Majorana neutrinos exploiting millikelvin cryogenics with CUORE, *Nature* **604**, 53 (2022).
- [24] G. Anton et al. (CUPID Collaboration), Final result on the neutrinoless double beta decay of ^{82}Se with CUPID-0, *Phys. Rev. Letters* **129**, 111801 (2022).
- [25] R. Arnold et al. (NEMO Collaboration), Final results on ^{82}Se double beta decay to the ground state of ^{82}Kr from the NEMO-3 experiment, *Eur. Phys. J. C* **78**, 821 (2018).
- [26] C. Augier et al. (CUPID Collaboration), Final results on the $0\nu\beta\beta$ decay half-life limit of ^{100}Mo from the CUPID-Mo experiment, *Eur. Phys. J. C* **82**, 1033 (2022).
- [27] S. Weinberg, Universal Neutrino Degeneracy, *Phys. Rev.*, **1457** (1962).
- [28] M. Aker et al., New Constraint on the Local Relic Neutrino Background Overdensity with the First KATRIN Data Runs, *Phys. Rev. Lett.* **129**, 011806 (2022).

Appendix A: Helicity and chirality eigenstates eigenstates

Finite mass neutrinos can have positive in addition to negative helicity. Here we derive the decomposition of helicity eigenstates into chiral eigenstates.

The Dirac state of a left handed (negative helicity) neutrino of energy E and mass m , propagating in the $+z$ direction say, is

$$\begin{aligned} u_{\nu L} &= \sqrt{\frac{E+m}{2E}} \left(0, 1, 0, -\frac{p}{E+m}, 0 \right)^T \\ &\equiv (0, W_+, 0, -W_-)^T, \end{aligned} \quad (\text{A1})$$

where T denotes the transpose, and $W_{\pm} \equiv \sqrt{(E \pm m)/2E}$. From $W_+^2 + W_-^2 = 1$ and $W_+W_- = \beta_\nu/2$, we have $(W_+ \pm W_-)^2 = 1 \pm \beta_\nu$, and

$$W_{\pm} = \frac{1}{2} \left(\sqrt{1+\beta} \pm \sqrt{1-\beta} \right). \quad (\text{A2})$$

Similarly, the state of a right handed (positive helicity) neutrino is

$$u_{\nu R} = \sqrt{\frac{E+m}{2E}} \left(1, 0, \frac{p}{E+m}, 0 \right)^T \equiv (W_+, 0, W_-, 0)^T. \quad (\text{A3})$$

On the other hand, the γ_5 eigenstates for spin up or

down (denoted by arrows) along the z -direction are

$$u_{\pm\uparrow} = \frac{(1, 0, \pm 1, 0)^T}{\sqrt{2}}, \quad u_{\pm\downarrow} = \frac{(0, 1, 0, \pm 1)^T}{\sqrt{2}}. \quad (\text{A4})$$

The helicity eigenstates can thus be written as

$$u_{\nu R} = \sqrt{\frac{1 + \beta_\nu}{2}} u_{+\uparrow} + \sqrt{\frac{1 - \beta_\nu}{2}} u_{-\uparrow}, \quad (\text{A5})$$

and

$$u_{\nu L} = \sqrt{\frac{1 - \beta_\nu}{2}} u_{+\downarrow} + \sqrt{\frac{1 + \beta_\nu}{2}} u_{-\downarrow}. \quad (\text{A6})$$

The amplitude for a $\gamma_5 = \pm 1$ eigenstate to have right handed helicity is $\sqrt{(1 \pm \beta_\nu)/2}$ and to have left handed helicity is $\sqrt{(1 \mp \beta_\nu)/2}$. The expectation value of the neutrino helicity $\langle h \rangle$ in a $\gamma_5 = \pm 1$ state is simply $\pm \beta_\nu$.

Observation of Seven Astrophysical Tau Neutrino Candidates with IceCube

R. Abbasi,¹⁷ M. Ackermann,⁶³ J. Adams,¹⁸ S. K. Agarwalla,^{40,*} J. A. Aguilar,¹² M. Ahlers,²² J.M. Alameddine,²³ N. M. Amin,⁴⁴ K. Andeen,⁴² G. Anton,²⁶ C. Argüelles,¹⁴ Y. Ashida,⁵³ S. Athanasiadou,⁶³ S. N. Axani,⁴⁴ X. Bai,⁵⁰ A. Balagopal V.,⁴⁰ M. Baricevic,⁴⁰ S. W. Barwick,³⁰ V. Basu,⁴⁰ R. Bay,⁸ J. J. Beatty,^{20,21} J. Becker Tjus,^{11,†} J. Beise,⁶¹ C. Bellenghi,²⁷ C. Benning,¹ S. BenZvi,⁵² D. Berley,¹⁹ E. Bernardini,⁴⁸ D. Z. Besson,³⁶ E. Blaufuss,¹⁹ S. Blot,⁶³ F. Bontempo,³¹ J. Y. Book,¹⁴ C. Boscolo Meneguolo,⁴⁸ S. Böser,⁴¹ O. Botner,⁶¹ J. Böttcher,¹ E. Bourbeau,²² J. Braun,⁴⁰ B. Brinson,⁶ J. Brostean-Kaiser,⁶³ R. T. Burley,² R. S. Busse,⁴³ D. Butterfield,⁴⁰ M. A. Campana,⁴⁹ K. Carloni,¹⁴ E. G. Carnie-Bronca,² S. Chattopadhyay,^{40,*} N. Chau,¹² C. Chen,⁶ Z. Chen,⁵⁵ D. Chirkin,⁴⁰ S. Choi,⁵⁶ B. A. Clark,¹⁹ L. Classen,⁴³ A. Coleman,⁶¹ G. H. Collin,¹⁵ A. Connolly,^{20,21} J. M. Conrad,¹⁵ P. Coppin,¹³ P. Correa,¹³ D. F. Cowen,^{59,60} P. Dave,⁶ C. De Clercq,¹³ J. J. DeLaunay,⁵⁸ D. Delgado,¹⁴ S. Deng,¹ K. Deoskar,⁵⁴ A. Desai,⁴⁰ P. Desiati,⁴⁰ K. D. de Vries,¹³ G. de Wasseige,³⁷ T. DeYoung,²⁴ A. Diaz,¹⁵ J. C. Díaz-Vélez,⁴⁰ M. Dittmer,⁴³ A. Domi,²⁶ H. Dujmovic,⁴⁰ M. A. DuVernois,⁴⁰ T. Ehrhardt,⁴¹ P. Eller,²⁷ E. Ellinger,⁶² S. El Mentawi,¹ D. Elsässer,²³ R. Engel,^{31,32} H. Erpenbeck,⁴⁰ J. Evans,¹⁹ P. A. Evenson,⁴⁴ K. L. Fan,¹⁹ K. Fang,⁴⁰ K. Farrag,¹⁶ A. R. Fazely,⁷ N. Feigl,¹⁰ S. Fiedlschuster,²⁶ A. T. Fienberg,⁶⁰ C. Finley,⁵⁴ L. Fischer,⁶³ D. Fox,⁵⁹ A. Franckowiak,¹¹ A. Fritz,⁴¹ P. Fürst,¹ J. Gallagher,³⁹ E. Ganster,¹ A. Garcia,¹⁴ L. Gerhardt,⁹ A. Ghadimi,⁵⁸ C. Glaser,⁶¹ T. Glauch,²⁷ T. Glüsenkamp,^{26,61} N. Goehlike,³² J. G. Gonzalez,⁴⁴ S. Goswami,⁵⁸ D. Grant,²⁴ S. J. Gray,¹⁹ O. Gries,¹ S. Griffin,⁴⁰ S. Griswold,⁵² K. M. Groth,²² C. Günther,¹ P. Gutjahr,²³ C. Haack,²⁶ A. Hallgren,⁶¹ R. Halliday,²⁴ L. Halve,¹ F. Halzen,⁴⁰ H. Hamdaoui,⁵⁵ M. Ha Minh,²⁷ K. Hanson,⁴⁰ J. Hardin,¹⁵ A. A. Harnisch,²⁴ P. Hatch,³³ A. Haungs,³¹ K. Helbing,⁶² J. Hellrung,¹¹ F. Henningsen,²⁷ L. Heuermann,¹ N. Heyer,⁶¹ S. Hickford,⁶² A. Hidvegi,⁵⁴ C. Hill,¹⁶ G. C. Hill,² K. D. Hoffman,¹⁹ S. Hori,⁴⁰ K. Hoshina,^{40,‡} W. Hou,³¹ T. Huber,³¹ K. Hultqvist,⁵⁴ M. Hünnefeld,²³ R. Hussain,⁴⁰ K. Hyman,²³ S. In,⁵⁶ A. Ishihara,¹⁶ M. Jacquart,⁴⁰ O. Janik,¹ M. Jansson,⁵⁴ G. S. Japaridze,⁵ M. Jeong,⁵⁶ M. Jin,¹⁴ B. J. P. Jones,⁴ D. Kang,³¹ W. Kang,⁵⁶ X. Kang,⁴⁹ A. Kappes,⁴³ D. Kappesser,⁴¹ L. Kardum,²³ T. Karg,⁶³ M. Karl,²⁷ A. Karle,⁴⁰ U. Katz,²⁶ M. Kauer,⁴⁰ J. L. Kelley,⁴⁰ A. Khateeb Zathul,⁴⁰ A. Kheirandish,^{34,35} J. Kiryluk,⁵⁵ S. R. Klein,^{8,9} A. Kochocki,²⁴ R. Koirala,⁴⁴ H. Kolanoski,¹⁰ T. Kontrimas,²⁷ L. Köpke,⁴¹ C. Kopper,²⁶ D. J. Koskinen,²² P. Koundal,³¹ M. Kovacevich,⁴⁹ M. Kowalski,^{10,63} T. Kozynets,²² J. Krishnamoorthi,^{40,*} K. Kruiswijk,³⁷ E. Krupczak,²⁴ A. Kumar,⁶³ E. Kun,¹¹ N. Kurahashi,⁴⁹ N. Lad,⁶³ C. Lagunas Gualda,⁶³ M. Lamoureux,³⁷ M. J. Larson,¹⁹ S. Latseva,¹ F. Lauber,⁶² J. P. Lazar,^{14,40} J. W. Lee,⁵⁶ K. Leonard DeHolton,⁶⁰ A. Leszczyńska,⁴⁴ M. Lincetto,¹¹ Q. R. Liu,⁴⁰ M. Liubarska,²⁵ E. Lohfink,⁴¹ C. Love,⁴⁹ C. J. Lozano Mariscal,⁴³ F. Lucarelli,²⁸ W. Luszczak,^{20,21} Y. Lyu,^{8,9} J. Madsen,⁴⁰ K. B. M. Mahn,²⁴ Y. Makino,⁴⁰ E. Manao,²⁷ S. Mancina,^{40,48} W. Marie Sainte,⁴⁰ I. C. Maris,¹² S. Marka,⁴⁶ Z. Marka,⁴⁶ M. Marsee,⁵⁸ I. Martinez-Soler,¹⁴ R. Maruyama,⁴⁵ F. Mayhew,²⁴ T. McElroy,²⁵ F. McNally,³⁸ J. V. Mead,²² K. Meagher,⁴⁰ S. Mehbali,⁶³ A. Medina,²¹ M. Meier,¹⁶ Y. Merckx,¹³ L. Merten,¹¹ J. Micallef,²⁴ J. Mitchell,⁷ T. Montaruli,²⁸ R. W. Moore,²⁵ Y. Morii,¹⁶ R. Morse,⁴⁰ M. Moulai,⁴⁰ T. Mukherjee,³¹ R. Naab,⁶³ R. Nagai,¹⁶ M. Nakos,⁴⁰ U. Naumann,⁶² J. Necker,⁶³ A. Negi,⁴ M. Neumann,⁴³ H. Niederhausen,²⁴ M. U. Nisa,²⁴ A. Noell,¹ A. Novikov,⁴⁴ S. C. Nowicki,²⁴ A. Obertacke Pollmann,¹⁶ V. O'Dell,⁴⁰ M. Oehler,³¹ B. Oeyen,²⁹ A. Olivas,¹⁹ R. Orsoe,²⁷ J. Osborn,⁴⁰ E. O'Sullivan,⁶¹ H. Pandya,⁴⁴ D. V. Pankova,⁶⁰ N. Park,³³ G. K. Parker,⁴ E. N. Paudel,⁴⁴ L. Paul,^{42,50} C. Pérez de los Heros,⁶¹ J. Peterson,⁴⁰ S. Philippen,¹ A. Pizzuto,⁴⁰ M. Plum,⁵⁰ A. Pontén,⁶¹ Y. Popovych,⁴¹ M. Prado Rodriguez,⁴⁰ B. Pries,²⁴ R. Procter-Murphy,¹⁹ G. T. Przybylski,⁹ C. Raab,³⁷ J. Rack-Helleis,⁴¹ K. Rawlins,³ Z. Rechav,⁴⁰ A. Rehman,⁴⁴ P. Reichherzer,¹¹ G. Renzi,¹² E. Resconi,²⁷ S. Reusch,⁶³ W. Rhode,²³ B. Riedel,⁴⁰ A. Rifaie,¹ E. J. Roberts,² S. Robertson,^{8,9} S. Rodan,⁵⁶ G. Roellinghoff,⁵⁶ M. Rongen,²⁶ C. Rott,^{53,56} T. Ruhe,²³ L. Ruohan,²⁷ D. Ryckbosch,²⁹ I. Safa,^{14,40} J. Saffer,³² D. Salazar-Gallegos,²⁴ P. Sampathkumar,³¹ S. E. Sanchez Herrera,²⁴ A. Sandrock,⁶² M. Santander,⁵⁸ S. Sarkar,²⁵ S. Sarkar,⁴⁷ J. Savelberg,¹ P. Savina,⁴⁰ M. Schaufel,¹ H. Schieler,³¹ S. Schindler,²⁶ L. Schlickmann,¹ B. Schlüter,⁴³ F. Schlüter,¹² N. Schmeisser,⁶² T. Schmidt,¹⁹ J. Schneider,²⁶ F. G. Schröder,^{31,44} L. Schumacher,²⁶ G. Schwefer,¹ S. Sclafani,¹⁹ D. Seckel,⁴⁴ M. Seikh,³⁶ S. Seunarine,⁵¹ R. Shah,⁴⁹ A. Sharma,⁶¹ S. Shefali,³² N. Shimizu,¹⁶ M. Silva,⁴⁰ B. Skrzypek,¹⁴ B. Smithers,⁴ R. Snihur,⁴⁰ J. Soedingrekso,²³ A. Sjøgaard,²² D. Soldin,³² P. Soldin,¹ G. Sommani,¹¹ C. Spannfellner,²⁷ G. M. Spiczak,⁵¹ M. Stamatikos,²¹ T. Stanev,⁴⁴ T. Stezelberger,⁹ T. Stürwald,⁶² T. Stuttard,²² G. W. Sullivan,¹⁹ I. Taboada,⁶ S. Ter-Antonyan,⁷ M. Thiesmeyer,¹ W. G. Thompson,¹⁴ J. Thwaites,⁴⁰ S. Tilav,⁴⁴ K. Tollefson,²⁴ C. Tönnis,⁵⁶ S. Toscano,¹² D. Tosi,⁴⁰ A. Trettin,⁶³ C. F. Tung,⁶ R. Turcotte,³¹ J. P. Twagirayezu,²⁴ B. Ty,⁴⁰ M. A. Unland Elorrieta,⁴³ A. K. Upadhyay,^{40,*} K. Upshaw,⁷ N. Valtonen-Mattila,⁶¹ J. Vandenbroucke,⁴⁰ N. van Eijndhoven,¹³ D. Vannerom,¹⁵ J. van Santen,⁶³ J. Vara,⁴³ J. Veitch-Michaelis,⁴⁰ M. Venugopal,³¹ M. Vereecken,³⁷ S.

Verpoest,⁴⁴ D. Veske,⁴⁶ A. Vijai,¹⁹ C. Walck,⁵⁴ C. Weaver,²⁴ P. Weigel,¹⁵ A. Weindl,³¹ J. Weldert,⁶⁰ A. Y. Wen,¹⁴ C. Wendt,⁴⁰ J. Werthebach,²³ M. Weyrauch,³¹ N. Whitehorn,²⁴ C. H. Wiebusch,¹ N. Willey,²⁴ D. R. Williams,⁵⁸ L. Witthaus,²³ A. Wolf,¹ M. Wolf,²⁷ G. Wrede,²⁶ X. W. Xu,⁷ J. P. Yanez,²⁵ E. Yildizci,⁴⁰ S. Yoshida,¹⁶ R. Young,³⁶ F. Yu,¹⁴ S. Yu,²⁴ Z. Zhang,⁵⁵ P. Zhelnin,¹⁴ P. Zilberman,⁴⁰ and M. Zimmerman⁴⁰

(IceCube Collaboration)[§]

¹*III. Physikalisches Institut, RWTH Aachen University, D-52056 Aachen, Germany*

²*Department of Physics, University of Adelaide, Adelaide, 5005, Australia*

³*Dept. of Physics and Astronomy, University of Alaska Anchorage, 3211 Providence Dr., Anchorage, AK 99508, USA*

⁴*Dept. of Physics, University of Texas at Arlington, 502 Yates St., Science Hall Rm 108, Box 19059, Arlington, TX 76019, USA*

⁵*CTSPS, Clark-Atlanta University, Atlanta, GA 30314, USA*

⁶*School of Physics and Center for Relativistic Astrophysics, Georgia Institute of Technology, Atlanta, GA 30332, USA*

⁷*Dept. of Physics, Southern University, Baton Rouge, LA 70813, USA*

⁸*Dept. of Physics, University of California, Berkeley, CA 94720, USA*

⁹*Lawrence Berkeley National Laboratory, Berkeley, CA 94720, USA*

¹⁰*Institut für Physik, Humboldt-Universität zu Berlin, D-12489 Berlin, Germany*

¹¹*Fakultät für Physik & Astronomie, Ruhr-Universität Bochum, D-44780 Bochum, Germany*

¹²*Université Libre de Bruxelles, Science Faculty CP230, B-1050 Brussels, Belgium*

¹³*Vrije Universiteit Brussel (VUB), Dienst ELEM, B-1050 Brussels, Belgium*

¹⁴*Department of Physics and Laboratory for Particle Physics and Cosmology, Harvard University, Cambridge, MA 02138, USA*

¹⁵*Dept. of Physics, Massachusetts Institute of Technology, Cambridge, MA 02139, USA*

¹⁶*Dept. of Physics and The International Center for Hadron Astrophysics, Chiba University, Chiba 263-8522, Japan*

¹⁷*Department of Physics, Loyola University Chicago, Chicago, IL 60660, USA*

¹⁸*Dept. of Physics and Astronomy, University of Canterbury, Private Bag 4800, Christchurch, New Zealand*

¹⁹*Dept. of Physics, University of Maryland, College Park, MD 20742, USA*

²⁰*Dept. of Astronomy, Ohio State University, Columbus, OH 43210, USA*

²¹*Dept. of Physics and Center for Cosmology and Astro-Particle Physics, Ohio State University, Columbus, OH 43210, USA*

²²*Niels Bohr Institute, University of Copenhagen, DK-2100 Copenhagen, Denmark*

²³*Dept. of Physics, TU Dortmund University, D-44221 Dortmund, Germany*

²⁴*Dept. of Physics and Astronomy, Michigan State University, East Lansing, MI 48824, USA*

²⁵*Dept. of Physics, University of Alberta, Edmonton, Alberta, Canada T6G 2E1*

²⁶*Erlangen Centre for Astroparticle Physics, Friedrich-Alexander-Universität Erlangen-Nürnberg, D-91058 Erlangen, Germany*

²⁷*Physik-department, Technische Universität München, D-85748 Garching, Germany*

²⁸*Département de physique nucléaire et corpusculaire, Université de Genève, CH-1211 Genève, Switzerland*

²⁹*Dept. of Physics and Astronomy, University of Gent, B-9000 Gent, Belgium*

³⁰*Dept. of Physics and Astronomy, University of California, Irvine, CA 92697, USA*

³¹*Karlsruhe Institute of Technology, Institute for Astroparticle Physics, D-76021 Karlsruhe, Germany*

³²*Karlsruhe Institute of Technology, Institute of Experimental Particle Physics, D-76021 Karlsruhe, Germany*

³³*Dept. of Physics, Engineering Physics, and Astronomy, Queen's University, Kingston, ON K7L 3N6, Canada*

³⁴*Department of Physics & Astronomy, University of Nevada, Las Vegas, NV, 89154, USA*

³⁵*Nevada Center for Astrophysics, University of Nevada, Las Vegas, NV 89154, USA*

³⁶*Dept. of Physics and Astronomy, University of Kansas, Lawrence, KS 66045, USA*

³⁷*Centre for Cosmology, Particle Physics and Phenomenology - CP3, Université catholique de Louvain, Louvain-la-Neuve, Belgium*

³⁸*Department of Physics, Mercer University, Macon, GA 31207-0001, USA*

³⁹*Dept. of Astronomy, University of Wisconsin-Madison, Madison, WI 53706, USA*

⁴⁰*Dept. of Physics and Wisconsin IceCube Particle Astrophysics Center, University of Wisconsin-Madison, Madison, WI 53706, USA*

⁴¹*Institute of Physics, University of Mainz, Staudinger Weg 7, D-55099 Mainz, Germany*

⁴²*Department of Physics, Marquette University, Milwaukee, WI, 53201, USA*

⁴³*Institut für Kernphysik, Westfälische Wilhelms-Universität Münster, D-48149 Münster, Germany*

⁴⁴*Bartol Research Institute and Dept. of Physics and Astronomy, University of Delaware, Newark, DE 19716, USA*

⁴⁵*Dept. of Physics, Yale University, New Haven, CT 06520, USA*

⁴⁶*Columbia Astrophysics and Nevis Laboratories, Columbia University, New York, NY 10027, USA*

- ⁴⁷*Dept. of Physics, University of Oxford, Parks Road, Oxford OX1 3PU, United Kingdom*
⁴⁸*Dipartimento di Fisica e Astronomia Galileo Galilei, Università Degli Studi di Padova, 35122 Padova PD, Italy*
- ⁴⁹*Dept. of Physics, Drexel University, 3141 Chestnut Street, Philadelphia, PA 19104, USA*
- ⁵⁰*Physics Department, South Dakota School of Mines and Technology, Rapid City, SD 57701, USA*
- ⁵¹*Dept. of Physics, University of Wisconsin, River Falls, WI 54022, USA*
- ⁵²*Dept. of Physics and Astronomy, University of Rochester, Rochester, NY 14627, USA*
- ⁵³*Department of Physics and Astronomy, University of Utah, Salt Lake City, UT 84112, USA*
- ⁵⁴*Oskar Klein Centre and Dept. of Physics, Stockholm University, SE-10691 Stockholm, Sweden*
- ⁵⁵*Dept. of Physics and Astronomy, Stony Brook University, Stony Brook, NY 11794-3800, USA*
⁵⁶*Dept. of Physics, Sungkyunkwan University, Suwon 16419, Korea*
⁵⁷*Institute of Physics, Academia Sinica, Taipei, 11529, Taiwan*
- ⁵⁸*Dept. of Physics and Astronomy, University of Alabama, Tuscaloosa, AL 35487, USA*
- ⁵⁹*Dept. of Astronomy and Astrophysics, Pennsylvania State University, University Park, PA 16802, USA*
- ⁶⁰*Dept. of Physics, Pennsylvania State University, University Park, PA 16802, USA*
- ⁶¹*Dept. of Physics and Astronomy, Uppsala University, Box 516, S-75120 Uppsala, Sweden*
⁶²*Dept. of Physics, University of Wuppertal, D-42119 Wuppertal, Germany*
⁶³*Deutsches Elektronen-Synchrotron DESY, Platanenallee 6, 15738 Zeuthen, Germany*

We report on a measurement of astrophysical tau neutrinos with 9.7 years of IceCube data. Using convolutional neural networks trained on images derived from simulated events, seven candidate ν_τ events were found with visible energies ranging from roughly 20 TeV to 1 PeV and a median expected parent ν_τ energy of about 200 TeV. Considering backgrounds from astrophysical and atmospheric neutrinos, and muons from π^\pm/K^\pm decays in atmospheric air showers, we obtain a total estimated background of about 0.5 events, dominated by non- ν_τ astrophysical neutrinos. Thus, we rule out the absence of astrophysical ν_τ at the 5σ level. The measured astrophysical ν_τ flux is consistent with expectations based on previously published IceCube astrophysical neutrino flux measurements and neutrino oscillations.

In 2013 IceCube discovered a flux of neutrinos of astrophysical origin [1–3]. The astrophysical neutrino (ν_τ^{astro}) flux normalization and index γ carry information about neutrino sources and their environments [4–15]. Different ν_τ^{astro} production mechanisms lead to different $\nu_e:\nu_\mu:\nu_\tau$ ratios at the sources but, after standard neutrino oscillations over astrophysical distances, detectable numbers of all three neutrino flavors are expected at Earth [16–24]. Previous measurements at lower energies, using neutrinos produced at accelerators and in the atmosphere (ν_τ^{atm}), have detected ν_τ produced directly [25] and through neutrino oscillations [26–28]. At the much higher energies accessible to this analysis, ν_τ^{atm} are strongly suppressed relative to ν_τ^{astro} [29], while an unexpected level of presence of ν_τ^{astro} in the ν_τ^{atm} flux could be an indication of new physics [30–43].

Previous analyses [44–47] by IceCube to detect ν_τ^{astro} included searches for double-cascade signatures, such as the distinctive “double bang” [16] in the full detector or “double pulse” (DP) waveforms in one or two individual photosensors. The DP signature is produced by the distinct arrival times of light signals at one or more photosensors from the ν_τ interaction and τ decay vertices. IceCube previously observed two candidate ν_τ^{astro} , ruling out the null hypothesis of no ν_τ^{astro} at 2.8σ [46]. The analysis presented in this Letter reports on the low-background, high-significance detection of seven ν_τ^{astro} candidate events through the use of convolutional neural networks (CNNs).

IceCube [48] is a neutrino observatory with 5160 Dig-

ital Optical Modules (DOMs) on 86 strings [48, 49] in a cubic kilometer of ice at the South Pole. Charged particles produced in neutrino interactions emit Cherenkov light [50] while propagating through the ice; photomultiplier tubes in the DOMs convert this light into electrical pulses that are digitized *in situ*. Light is deposited in the detector in several distinct patterns: long tracks, single cascades, and double cascades. Tracks are produced by muons from, *e.g.*, ν_μ charged-current (CC) interactions, and can start or end inside, or pass through, the detector. Single cascades arise from electromagnetic and/or hadronic particle showers produced by deep inelastic neutrino-nucleon interactions in or near the detector, or by $\bar{\nu}_e$ via the Glashow Resonance [51, 52]. Double cascades are formed by high-energy ν_τ , CC interactions in or near the detector that produce a hadronic shower and a τ lepton at the interaction vertex, followed by a second electromagnetic or hadronic shower at the τ decay vertex ($\text{BR}[\tau \rightarrow (e, h)] \simeq 83\%$). With a decay length of ~ 50 m/PeV, the τ can travel a macroscopic distance in the ice. For ν_τ energies satisfying $E_{\nu_\tau} \gtrsim 1$ PeV and favorable geometric containment, the double-bang signature can be created, with two energetic and well-separated cascades. Such events are intrinsically rare. In contrast, for lower E_{ν_τ} between roughly 50 TeV – 1 PeV, the ν_τ flux is expected to be higher but in CC interactions the two cascades are closer together. Two cascades as close as about 10 m can produce distinctive patterns correlated across multiple DOMs and strings as the light from each cascade passes by, as well as DP waveforms in one

or more DOMs.

We analyzed 9.7 years of IceCube data from 2011–2020, triggering on approximately 10^{12} downward-going cosmic-ray muons, 10^6 ν^{atm} , and 10^4 ν^{astro} [53–56]. We required that the DOMs on the most illuminated string collected at least 2000 photoelectrons (p.e.) (see Fig. 1) and at least 10 p.e. in the two next-highest-charge, nearest-neighbor strings. Signal events will appear more like cascades than tracks in IceCube, so we also selected events whose morphology was better described by the cascade hypothesis. Aside from 0.6% (22 live-days) of the data sample used to confirm agreement between data and simulation (data that were subsequently excluded from our analysis and which contained no signal-like events), we performed a “blind” analysis that only used simulated data to devise all selection criteria and analysis methodologies. After application of these initial selection criteria, there was roughly 300 times more background than signal. The expected number of p.e. on the most illuminated string for $\nu_{\tau}^{\text{astro}}$ CC events after application of these criteria, and additional CNN criteria described below, is shown in Fig. 1.

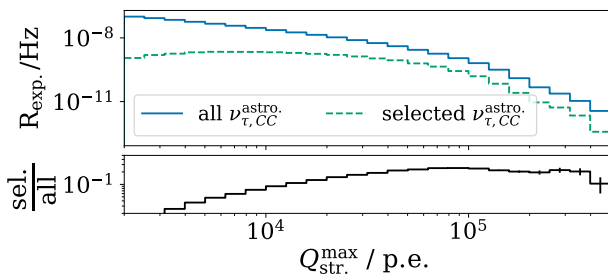


FIG. 1. Top: Simulated rate of $\nu_{\tau}^{\text{astro}}$ CC events binned by the number of p.e. detected by DOMs on the most illuminated string in the event, $Q_{\text{str.}}^{\text{max}}$, before any selection criteria (solid) and after the CNN-based criteria (dashed) described in the text. (Downward-going cosmic-ray muons trigger the detector at about 3 kHz, are effectively removed by our selection criteria, and are not shown on the plot; other backgrounds are similarly heavily reduced and also not shown.) Bottom: Ratio of rates (selected/all), showing that signal efficiency grows above about 2000 p.e. The IceCube “GlobalFit” ν^{astro} flux [53] is assumed. (Error bars statistical only.)

We then created 2-d images of DOM number (corresponding to depth) vs. time in 3.3 ns bins, with each pixel’s brightness proportional to the digitized waveform amplitude in that time bin. Images were created for the 180 DOMs on the most illuminated string and its two nearest and highest-illuminated neighbors, providing three images per event. The image for the highest-charge string on a candidate signal event is shown in Fig. 2 (left). The three images were then processed by CNNs, trained to distinguish images produced by simulated signal and background events and based on VGG16 [57], with a total of $\mathcal{O}(100\text{ M})$ trainable parameters for the

high-dimensional signal parameter space. Three separate CNNs were used to distinguish the ν_{τ} signal from remaining backgrounds produced by 1) single cascade neutrino interactions such as $\nu_{e,\mu,\tau}$ neutral current (NC) and ν_e CC, 2) downward-going muons (μ_{\downarrow}), and 3) both ν_{μ} interactions producing muon tracks and μ_{\downarrow} ; the associated CNN scores are denoted C_1 , C_2 and C_3 , respectively, with ranges [0,1]. Figure 2 (right) shows $S(C_1)$, the saliency [58] for C_1 , here defined as the magnitude of the gradient of the CNN score (scaled to [0,1]) of C_1 with respect to the signal amplitude at each pixel. For reference, the contour (solid line) shows where the detected light falls to zero, and is essentially an outline of the plot on the left. (Points outside the contour are variously acausally early, very late, or at distances that are many absorption lengths from the event vertices.) Large $S(C_1)$ values indicate where and when changes in light level most effectively change C_1 . Small $S(C_1)$ values appear in highly-illuminated regions and in regions with no light. Bright regions contribute to C_1 , but C_1 is not as sensitive there to changes in light level as at the leading and trailing edge envelopes of the light from the event, which are roughly coincident with the contour. The saliency thus shows that C_1 is sensitive to the overall shape of emitted light in the detector.

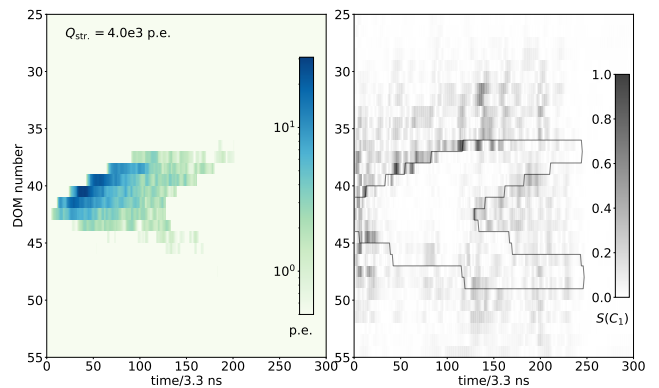


FIG. 2. Candidate $\nu_{\tau}^{\text{astro}}$ detected in Sep. 2015. The left plot shows the DOM number (proportional to depth) versus the time of the digitized PMT signal in 3.3 ns bins for the highest-charge string, with the scale giving the signal amplitude in p.e. in each time bin. The total p.e. detected on the string, $Q_{\text{str.}}$, is shown. The right plot shows $S(C_1)$, that string’s saliency map for C_1 , with darker regions indicating where the C_1 score is more sensitive to a changing light level (see text). (The Appendix shows three-string views and signed saliencies for all seven $\nu_{\tau}^{\text{astro}}$ candidates.)

The scores were calculated for each event, and a signal-to-noise ratio of ~ 14 was obtained by requiring events to have high scores ($C_1 \geq 0.99$, $C_2 \geq 0.98$ and $C_3 \geq 0.85$). The dominant backgrounds come from other ν^{astro} flavors and ν^{atm} . The expected energy spectra for signal and the dominant backgrounds, after application of initial and then final selection criteria (including the high

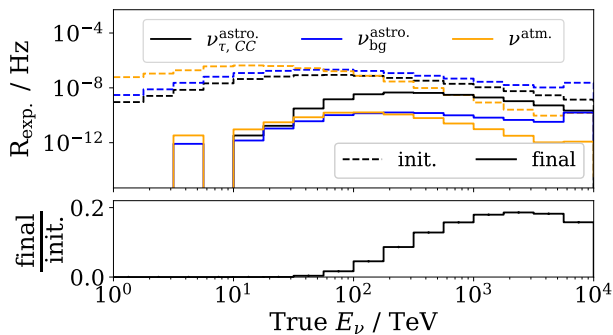


FIG. 3. Top: Expected rate vs. energy of $\nu_{\tau}^{\text{astro}}$ CC events, astrophysical and atmospheric neutrino backgrounds with initial selection criteria applied (dashed) and with final selection criteria then also applied (solid); for $\nu_{\tau}^{\text{astro}}$ the IceCube GlobalFit flux [53] was assumed. Bottom: Ratio of $\nu_{\tau}^{\text{astro}}$ CC rates after final and initial selection criteria. (Statistical error bars are too small to be visible. Although not shown in the plot, the backgrounds were simulated up to $E_{\nu} = 100$ PeV.)

	$\nu_{\tau,CC}^{\text{astro}}$ [59]	$\nu_{\text{other}}^{\text{astro}}$ [59]	$\nu_{\text{conv.}}^{\text{atm.}}$ [60–63]	$\nu_{\text{prompt}}^{\text{atm.}}$ [56, 64–66]	$\mu_{\text{conv.}}^{\text{atm.}}$ [67–70]	all background
initial	160 ± 0.2 (190 ± 0.3)	400 ± 0.7 (490 ± 0.8)	580 ± 7	72 ± 0.1	8400 ± 110	9450 ± 110 (9540 ± 110)
final	6.4 ± 0.02 (4.0 ± 0.02)	0.3 ± 0.02 (0.2 ± 0.01)	0.1 ± 0.008	0.1 ± 0.001	0.01 ± 0.008	0.5 ± 0.02 (0.4 ± 0.02)

TABLE I. Expected number of events after initial and final set of selection criteria (including all corrections described in the text) for signal ($\nu_{\tau,CC}^{\text{astro}}$) and backgrounds, assuming IceCube’s flux from Refs. [53] and (in parentheses) [56]. About 85% of the estimated contribution from $\nu_{\text{prompt}}^{\text{atm.}}$ is from ν_{τ} . Signal and astrophysical background levels vary with the flux. The simulation did not include the self-veto effect [71] that would reduce the conventional (conv.) and prompt $\nu^{\text{atm.}}$ backgrounds. References to associated simulation packages are given; see text for details. Errors are statistical only, arising from finite simulation samples.

The largest backgrounds are due to other astrophysical neutrino interactions, and conventional and prompt atmospheric neutrinos, followed by muons from π^{\pm}/K^{\pm} decays in cosmic-ray air showers. The backgrounds listed in Table I were estimated using simulation packages for astrophysical neutrinos [59], muons from cosmic-ray air showers [67, 68] (with cosmic-ray primary flux given by [69] and hadronic interaction model by [70]), conventional atmospheric neutrino flux from π^{\pm}/K^{\pm} decays [60] following our published $\nu^{\text{atm.}}$ flux measurements above $E_{\nu} \sim 50$ TeV [61–63], and prompt atmospheric neutrino flux [56, 64–66] postulated to arise from the decays of charm or heavier mesons produced in air-showers and modeled following Ref. [64]. Electromagnetic (EM) and hadronic showers below 1 PeV were simulated based on the parameterizations of the mean longitudinal and lateral profiles in Ref. [72] and included fluctuations in the energy of the hadronic component. Above 1 PeV the LPM effect [73–75] is used for EM showers. (Our treatment of possible prompt atmospheric muons is described in the Appendix.) The total νN deep inelastic scattering cross section is from [76].

CNN scores), are shown in Fig. 3.

A sub-dominant “edge event” background was observed from simulated cosmic-ray muons that deposited most of their Cherenkov light on a single string on the outer edge of the detector. We required $C_3 > 0.95$ for edge events, reducing this background by about an order of magnitude at an estimated 15% signal loss. Table I lists the expected number of events, after application of the initial and final sets of selection criteria, assuming the best-fit parameters from two IceCube flux measurements.

Additional potential background from muon deep inelastic scattering (μ DIS), given by $\mu + X \rightarrow \nu_{\mu} + X'$, where the light from the incoming μ followed by the light from the hadronic cascade could mimic the ν_{τ} signature, is estimated from the predicted atmospheric ν_{μ} CC background. At energies above roughly 100 TeV, we expect comparable numbers of atmospheric ν_{μ} and μ [71], but the μ energies will be diminished as they pass through the ice to the detector, decreasing their ability to mimic the ν_{τ} signature. We conservatively doubled the estimated background from atmospheric ν_{μ} CC interactions, from 0.005 to 0.01, to account for the potential background.

We also estimated the background expected from charmed hadrons produced in energetic ν_e CC and ν NC interactions. This background component had not initially been considered in designing the analysis. After unblinding, we became aware of recent results [77] that indicate that the strange sea in the nucleon is not as suppressed as had been previously believed, so that charm production would thereby be somewhat enhanced compared to our original estimate. Using a simulated neutrino dataset based on the HERAPDF1.5 [78] parton dis-

tribution functions (PDFs), and applying a modest correction to reflect more modern PDFs [77, 79–82], the estimated background from ν^{astro} increases by 23% relative to the simulations excluding these interactions. The theoretical uncertainty from the PDFs at the 100 TeV scale is roughly 3%, so the increase corresponds to only about $(15 \pm 0.5)\%$ (0.08 ± 0.002 events) of the total background estimation. We included this additional background directly to maintain our blindness protocol that disallowed retraining the CNNs to reject charm background. Uncertainties in the cross section for the interaction of charmed mesons and baryons with ordinary matter had a negligible impact. Backgrounds from on-shell W production [83] from high-energy ν_e/ν_μ interactions, top-quark decay and Glashow resonance interactions [84] can produce energetic ν_τ or τ , but are collectively estimated to contribute roughly an order of magnitude fewer background events than other sources and were not included in our background estimate.

For the range of astrophysical neutrino fluxes measured by IceCube (denoted $\phi_{\text{astro}}^{\text{IC}}$), and for a 1:1:1 neutrino flavor ratio at the detector, we predicted a final sample of 4–8 ν_τ CC signal events. Similarly, the predicted total background varied for each $\phi_{\text{astro}}^{\text{IC}}$. Using IceCube’s previous measurements of the spectral index γ_{astro} , this relatively small number of events constrains the ν^{astro} flux normalization ϕ_{astro} . Data satisfying $C_2 > 0.98$ were placed in 4×4 bins in their C_1 and C_3 scores.

We calculated confidence intervals following Ref. [85] and using the test statistic defined as $\text{TS}(\lambda_\tau) = \ln L(\hat{\lambda}_\tau) - \ln L(\lambda_\tau)$, where $\lambda_\tau = \phi(\nu_\tau^{\text{astro}})/\phi_{\text{nom.}}(\nu_\tau^{\text{astro}})$, the measured-to-nominal flux ratio. Here the nominal flux is one of the four IceCube measured values, and $\hat{\lambda}_\tau$ the value of λ_τ that maximizes the Poisson likelihood L across all 16 bins. Critical values were extracted at the desired confidence level using the TS distributions from a range of λ_τ values, each of which were simulated with 10^4 pseudo experiments. This procedure incorporated as nuisance parameters the systematic uncertainties in the estimated fluxes for each background component (prior width of 30% for ν^{atm} and ν^{astro} ; 50% for cosmic-ray muons), the detection efficiency of the DOMs (10%), and the optical scattering properties of the ice (5%). Since many of these parameters are degenerate in their effect on the analysis observables, and we expected fewer signal events than nuisance parameters, we estimated their impact by incorporating randomized versions of the parameters for each of the pseudo experiments used to calculate the critical value of our TS. This procedure increased the critical values relative to their values in the absence of the systematic uncertainties, widening the extracted confidence intervals.

Seven events remained after applying the final set of selection criteria to the data, consistent with expectation. Figure 4 shows the final expected signal and background, assuming IceCube’s GlobalFit flux, as a func-

tion of C_3 vs. C_1 . Five of the candidate ν_τ events are in the upper right bin and two are in the bin just below it. Three of the seven events were seen in previous IceCube analyses [1, 46, 47, 86], and one of these three had previously been identified [46, 47] as a candidate ν_τ^{astro} . For each candidate event we evaluated the “tauness” as $P_\tau(i) = n_s(i)/(n_s(i) + n_b(i))$, where n_s and n_b are the expected signal and background in bin i (see Fig. 4). P_τ ranges from 0.90 – 0.92 for two of the candidate ν_τ , and 0.94 – 0.95 for the other five, depending on the assumed $\phi_{\text{astro}}^{\text{IC}}$. For IceCube’s GlobalFit flux we predict a total background of 0.5 ± 0.02 events (see Table I); using the distribution of the seven observed events and expected backgrounds in the 16 bins in Fig. 4, we exclude the null hypothesis of no ν_τ^{astro} at a (single-sided) significance of 5.1σ . Under the other three flux assumptions [54–56], the significances are 5.2σ , 5.2σ and 5.5σ , respectively. The best-fit ν_τ flux normalizations are all within the 68% frequentist confidence intervals of the four IceCube fluxes.

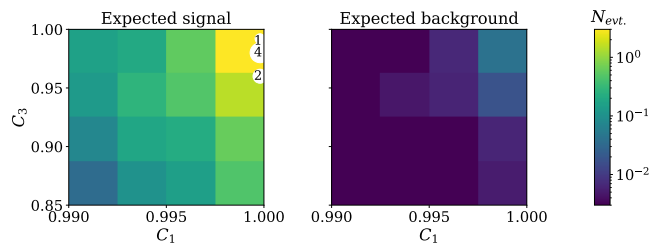


FIG. 4. Histogram of the C_3 vs. C_1 CNN scores with all selection criteria applied. The color in each bin gives the expected number of signal (left) and background (right) events in that bin, assuming IceCube’s GlobalFit flux [53]. The approximate (C_1, C_3) values of the seven observed candidate ν_τ^{astro} are shown by white circles, with the number inside each circle indicating the number of candidate events there.

We performed multiple checks on the candidate events to ensure they were consistent with expectation. For simplicity and to avoid introducing additional systematic uncertainties, the analysis did not employ a tailored ν_τ^{astro} reconstruction. However, as a post-unblinding check we used a reconstruction for single-cascade events [87] to estimate the energies and directions (Fig. 5) and vertex positions (see the Appendix). The median expected E_{ν_τ} was roughly 200 TeV (for the flux in Ref. [56]). The dominant up-down asymmetry is due to Earth absorption and consistent with expectation. Other polar angle effects such as higher vertical vs. horizontal DOM density and ν_τ regeneration [88] are also included. (Simulations predict that for $E_\tau \lesssim 0.5$ PeV, the selected events are biased toward higher average τ decay lengths $\langle L_\tau \rangle$; *e.g.*, for $E_\tau \sim 100$ TeV, $\langle L_\tau \rangle \sim 10$ m.) The events were more clustered in depth than expected but were consistent with a statistical fluctuation, as discussed in the Appendix. We observed no significant coincident activity in the IceTop

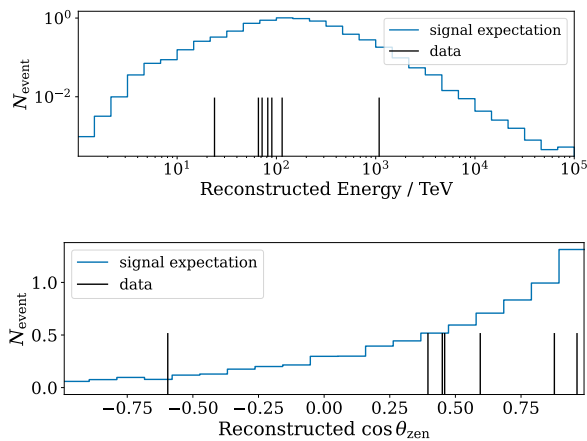


FIG. 5. Reconstructed visible energies (top) and $\cos \theta_{\text{zen}}$ (bottom) for simulated ν_{τ}^{CC} (solid histogram) and seven candidate events (vertical lines) for the flux in Ref. [53]. The upward-going event with $\cos \theta_{\text{zen}} \simeq -0.6$ had a reconstructed energy of ~ 90 TeV.

cosmic-ray air-shower surface array for any of the events.

We tested the robustness of the CNNs to hypothetical improperly modeled uncertainties by evaluating their susceptibility to correlated and uncorrelated variations of the raw data underlying the images. We found that the probability of background-to-signal migration was $< (2 \pm 0.2) \cdot 10^{-5}$ and of signal-to-background migration $< (3 \pm 0.8) \cdot 10^{-3}$. We also employed targeted tests to estimate the CNNs' robustness against less likely changes in the underlying raw data, including adversarial attacks [89] against candidate signal and simulated background events. We found that events only migrated in response to changes outside our uncertainty envelope. These tests are described in the Appendix. We conclude that the CNNs are robust against detector systematic effects that could present as either uncorrelated or correlated changes in light levels in one or more DOMs, or entire strings, in the detector.

Energetic astrophysical sources, in conjunction with neutrino oscillations over cosmic baselines, provide the only known way to produce large numbers of ν_{τ} energetic enough to create the observed event morphologies. The result presented in this Letter demonstrates that astrophysical ν_{τ} consistent with this hypothesis are present in the IceCube data and provides powerful confirmation of the earlier IceCube discovery of astrophysical neutrinos [2, 3, 90].

The IceCube Collaboration acknowledges the significant contributions to this manuscript from the Pennsylvania State University. We dedicate this paper to the memory of Lovisa Arnesson-Cronhamre, a young graduate student whose tragic and untimely passing stole from us all a promising neutrino physicist. USA – U.S. National Science Foundation-Office of Polar Programs, U.S. National Science Foundation-Physics Division, U.S. National Science Foundation-EPSCoR, U.S. National Science Foundation-Major Research Instrumentation Program, Deep Learning for Statistics, Astrophysics, Geoscience, Engineering, Meteorology and Atmospheric Science, Physical Sciences and Psychology (DL-SAGEMAPP) at the Institute for Computational and Data Sciences (ICDS) at the Pennsylvania State University, Wisconsin Alumni Research Foundation, Center for High Throughput Computing (CHTC) at the University of Wisconsin–Madison, Open Science Grid (OSG), Advanced Cyberinfrastructure Coordination Ecosystem: Services & Support (ACCESS), Frontera computing project at the Texas Advanced Computing Center, U.S. Department of Energy-National Energy Research Scientific Computing Center, Particle astrophysics research computing center at the University of Maryland, Institute for Cyber-Enabled Research at Michigan State University, and Astroparticle physics computational facility at Marquette University; Belgium – Funds for Scientific Research (FRS-FNRS and FWO), FWO Odysseus and Big Science programmes, and Belgian Federal Science Policy Office (Belspo); Germany – Bundesministerium für Bildung und Forschung (BMBF), Deutsche Forschungsgemeinschaft (DFG), Helmholtz Alliance for Astroparticle Physics (HAP), Initiative and Networking Fund of the Helmholtz Association, Deutsches Elektronen Synchrotron (DESY), and High Performance Computing cluster of the RWTH Aachen; Sweden – Swedish Research Council, Swedish Polar Research Secretariat, Swedish National Infrastructure for Computing (SNIC), and Knut and Alice Wallenberg Foundation; European Union – EGI Advanced Computing for research; Australia – Australian Research Council; Canada – Natural Sciences and Engineering Research Council of Canada, Calcul Québec, Compute Ontario, Canada Foundation for Innovation, WestGrid, and Compute Canada; Denmark – Villum Fonden, Carlsberg Foundation, and European Commission; New Zealand – Marsden Fund; Japan – Japan Society for Promotion of Science (JSPS) and Institute for Global Prominent Research (IGPR) of Chiba University; Korea – National Research Foundation of Korea (NRF); Switzerland – Swiss National Science Foundation (SNSF); United Kingdom – Department of Physics, University of Oxford.

-
- * also at Institute of Physics, Sachivalaya Marg, Sainik School Post, Bhubaneswar 751005, India
- † also at Department of Space, Earth and Environment, Chalmers University of Technology, 412 96 Gothenburg, Sweden
- ‡ also at Earthquake Research Institute, University of Tokyo, Bunkyo, Tokyo 113-0032, Japan
- § analysis@icecube.wisc.edu
- [1] M. G. Aartsen *et al.* (IceCube), *Phys. Rev. Lett.* **111**, 021103 (2013).
- [2] IceCube Collaboration, M. G. Aartsen, *et al.*, *Science* **342**, 1242856 (2013).
- [3] IceCube Collaboration, M. G. Aartsen, *et al.*, *Phys. Rev. Lett.* **113**, 101101 (2014).
- [4] E. Fermi, *Phys. Rev.* **75**, 1169 (1949).
- [5] A. R. Bell, *MNRAS* **182**, 147 (1978).
- [6] T. K. Gaisser, *Cosmic Rays and Particle Physics* (Cambridge University Press, 1990).
- [7] R. J. Protheroe and D. Kazanas, *Astrophys. J.* **265**, 620 (1983).
- [8] D. Kazanas and D. C. Ellison, *Astrophys. J.* **304**, 178 (1986).
- [9] M. Sikora *et al.*, *Astrophys. J. Lett.* **320**, L81 (1987).
- [10] F. W. Stecker, C. Done, M. H. Salamon, and P. Sommers, *Phys. Rev. Lett.* **66**, 2697 (1991).
- [11] F. W. Stecker, C. Done, M. H. Salamon, and P. Sommers, *Phys. Rev. Lett.* **69**, 2738(E) (1992).
- [12] K. Mannheim and P. L. Biermann, *Astron. Astrophys.* **253**, L21 (1992).
- [13] J. Matthews, A. Bell, and K. Blundell, *New Astron. Rev.* **89**, 101543 (2020).
- [14] W. Winter, *Phys. Rev.* **D88**, 083007 (2013).
- [15] K. Murase, M. Ahlers, and B. C. Lacki, *Phys. Rev.* **D88**, 121301(R) (2013).
- [16] J. G. Learned and S. Pakvasa, *Astropart. Phys.* **3**, 267 (1995).
- [17] H. Athar, C. S. Kim, and J. Lee, *Mod. Phys. Lett.* **A21**, 1049 (2006).
- [18] T. Kashti and E. Waxman, *Phys. Rev. Lett.* **95**, 181101 (2005).
- [19] S. R. Klein, R. E. Mikkelsen, and J. Becker Tjus, *Astrophys. J.* **779**, 106 (2013).
- [20] P. Lipari, M. Lusignoli, and D. Meloni, *Phys. Rev. D.* **75**, 123005 (2007).
- [21] M. Bustamante, J. F. Beacom, and W. Winter, *Phys. Rev. Lett.* **115**, 161302 (2015).
- [22] A. Esmaili and Y. Farzan, *Nucl. Phys.* **B821**, 197 (2009).
- [23] I. Esteban *et al.*, *JHEP* **01**, 106 (2019).
- [24] NuFIT 4.1, www.nu-fit.org (2019).
- [25] K. Kodama *et al.* (DONuT), *Phys. Rev. D* **78**, 052002 (2008).
- [26] N. Agafonova *et al.* (OPERA), *Phys. Rev. D* **100**, 051301 (2019).
- [27] Z. Li *et al.* (Super-Kamiokande), *Phys. Rev. D* **98**, 052006 (2018).
- [28] M. G. Aartsen *et al.* (IceCube), *Phys. Rev. D* **99**, 032007 (2019).
- [29] A. Bhattacharya, R. Enberg, Y. S. Jeong, C. S. Kim, M. H. Reno, I. Sarcevic, and A. Stasto, *JHEP* **11**, 16 (2016).
- [30] C. A. Argüelles, T. Katori, and J. Salvado, *Phys. Rev. Lett.* **115**, 161303 (2015).
- [31] G. Pagliaroli, A. Palladino, F. L. Villante, and F. Visani, *Phys. Rev. D* **92**, 113008 (2015).
- [32] I. M. Shoemaker and K. Murase, *Phys. Rev. D* **93**, 085004 (2016).
- [33] V. Brdar, J. Kopp, and X.-P. Wang, *JCAP* **01**, 026 (2017).
- [34] M. Bustamante, J. F. Beacom, and K. Murase, *Phys. Rev. D* **95**, 063013 (2017).
- [35] N. Klop and S. Ando, *Phys. Rev. D* **97**, 063006 (2018).
- [36] R. W. Rasmussen, L. Lechner, M. Ackermann, M. Kowalski, and W. Winter, *Phys. Rev. D* **96**, 083018 (2017).
- [37] M. Bustamante and S. K. Agarwalla, *Phys. Rev. Lett.* **122**, 061103 (2019).
- [38] P. B. Denton and I. Tamborra, *Phys. Rev. Lett.* **121**, 121802 (2018).
- [39] Y. Farzan and S. Palomares-Ruiz, *Phys. Rev. D* **99**, 051702 (2019).
- [40] R. Abbasi *et al.* (IceCube), *Nature Phys.* **18**, 1287 (2022).
- [41] A. Abdullahi and P. B. Denton, *Phys. Rev. D* **102**, 023018 (2020).
- [42] R. M. Abraham *et al.*, *Journal of Physics G: Nuclear and Particle Physics* **49**, 110501 (2022).
- [43] M. Ackermann *et al.*, [arXiv:2203.08096](https://arxiv.org/abs/2203.08096) (2022).
- [44] R. Abbasi *et al.* (IceCube Collaboration), *Phys. Rev. D* **86**, 022005 (2012).
- [45] M. G. Aartsen *et al.* (IceCube Collaboration), *Phys. Rev. D* **93**, 022001 (2016).
- [46] R. Abbasi *et al.* (IceCube), *Eur. Phys. J. C* **82**, 1031 (2022).
- [47] M. Meier and J. Soedingrekso (IceCube), *PoS ICRC2019*, 960 (2020).
- [48] M. G. Aartsen *et al.* (IceCube), *JINST* **12** (03), P03012 (2017).
- [49] R. Abbasi *et al.* (IceCube), *Astropart. Phys.* **35**, 615 (2012).
- [50] P. A. Cherenkov, *Dokl. Akad. Nauk SSSR* **2**, 451 (1934).
- [51] S. L. Glashow, *Phys. Rev.* **118**, 1 (1960).
- [52] M. G. Aartsen *et al.* (IceCube), *Nature* **591**, 220 (2021), [Erratum: *Nature* 592, E11 (2021)].
- [53] M. G. Aartsen *et al.* (IceCube), *Astrophys. J.* **809**, 98 (2015).
- [54] R. Abbasi *et al.* (IceCube), *Astrophys. J.* **928**, 50 (2022).
- [55] M. G. Aartsen *et al.* (IceCube), *Phys. Rev. D* **99**, 032004 (2019).
- [56] R. Abbasi *et al.* (IceCube), *Phys. Rev. D* **104**, 022002 (2021).
- [57] K. Simonyan and A. Zisserman, [arXiv:1409.1556](https://arxiv.org/abs/1409.1556) (2014).
- [58] K. Simonyan, A. Vedaldi, and A. Zisserman, (2014), [arXiv:1312.6034](https://arxiv.org/abs/1312.6034).
- [59] A. Gazizov and M. P. Kowalski, *Computer Physics Communications* **172** (2005).
- [60] M. Honda, T. Kajita, K. Kasahara, S. Midorikawa, and T. Sanuki, *Phys. Rev.* **D75**, 043006 (2007).
- [61] IceCube Collaboration, R. Abbasi, *et al.*, *Phys. Rev.* **D83**, 012001 (2011).
- [62] IceCube Collaboration, M. G. Aartsen, *et al.*, *Phys. Rev. Lett.* **110**, 151105 (2013).
- [63] IceCube Collaboration, M. G. Aartsen, *et al.*, *Phys. Rev.* **D91**, 122004 (2015).

- [64] A. Bhattacharya *et al.*, JHEP **06**, 110 (2015).
- [65] M. V. Garzelli, S. Moch, and G. Sigl, JHEP **10**, 115 (2015).
- [66] R. Gauld, J. Rojo, L. Rottoli, S. Sarkar, and J. Talbert, JHEP **02**, 130 (2016).
- [67] D. Heck, J. Knapp, J. N. Capdevielle, G. Schatz, and T. Thouw, FZKA-6019 (1998).
- [68] J. van Santen, Ph.D. thesis, University of Wisconsin-Madison (2014).
- [69] T. K. Gaisser, Spectrum of cosmic-ray nucleons, kaon production, and the atmospheric muon charge ratio, Astropart. Phys. **35**, 801 (2012).
- [70] E. J. Ahn, R. Engel, T. K. Gaisser, P. Lipari, and T. Stanev, Phys. Rev. **D80**, 094003 (2009).
- [71] S. Schonert, T. K. Gaisser, E. Resconi, and O. Schulz, Phys. Rev. D **79**, 043009 (2009).
- [72] L. Radel and C. Wiebusch, Calculation of the Cherenkov light yield from electromagnetic cascades in ice with Geant4, Astropart. Phys. **44**, 102 (2013).
- [73] L. D. Landau and I. Pomeranchuk, Electron cascade process at very high-energies, Dokl. Akad. Nauk Ser. Fiz. **92**, 735 (1953).
- [74] L. D. Landau and I. Pomeranchuk, Limits of applicability of the theory of bremsstrahlung electrons and pair production at high-energies, Dokl. Akad. Nauk Ser. Fiz. **92**, 535 (1953).
- [75] A. B. Migdal, Bremsstrahlung and pair production in condensed media at high-energies, Phys. Rev. **103**, 1811 (1956).
- [76] A. Cooper-Sarkar, P. Mertsch, and S. Sarkar, JHEP **08**, 042 (2011).
- [77] G. Aad *et al.* (ATLAS), Determination of the parton distribution functions of the proton using diverse ATLAS data from pp collisions at $\sqrt{s} = 7, 8$ and 13 TeV, Eur. Phys. J. C **82**, 438 (2022).
- [78] V. Radescu (H1, ZEUS), PoS ICHEP2010 , 168 (2010).
- [79] T.-J. Hou *et al.*, Phys. Rev. D **103**, 014013 (2021).
- [80] S. Bailey, T. Cridge, L. A. Harland-Lang, A. D. Martin, and R. S. Thorne, Eur. Phys. J. C **81**, 341 (2021).
- [81] F. Faura, S. Iranipour, E. R. Nocera, J. Rojo, and M. Ubiali, Eur. Phys. J. C **80**, 1168 (2020).
- [82] M. Aaboud *et al.* (ATLAS), Eur. Phys. J. C **77**, 367 (2017).
- [83] B. Zhou and J. F. Beacom, Phys. Rev. D **101**, 036010 (2020).
- [84] A. G. Soto, P. Zhelmin, I. Safa, and C. A. Argüelles, Phys. Rev. Lett. **128**, 171101 (2022).
- [85] G. J. Feldman and R. D. Cousins, Phys. Rev. D **57**, 3873 (1998).
- [86] L. Lu (IceCube), PoS ICRC2017 , 1002 (2018).
- [87] M. Huennefeld *et al.* (IceCube), PoS ICRC2021 , 1065 (2021).
- [88] F. Halzen and D. Saltzberg, Phys. Rev. Lett. **81**, 4305 (1998).
- [89] S.-M. Moosavi-Dezfooli, A. Fawzi, and P. Frossard, Deepfool: a simple and accurate method to fool deep neural networks, in *Proceedings of the IEEE conference on computer vision and pattern recognition* (2016) pp. 2574–2582.
- [90] IceCube Collaboration, M. G. Aartsen, *et al.*, Phys. Rev. Lett. **111**, 021103 (2013).
- [91] M. G. Aartsen *et al.* (IceCube), Measurement of South Pole ice transparency with the IceCube LED calibration system, Nucl. Instrum. Meth. A **711**, 73 (2013).
- [92] D. Chirkin (IceCube), in *33rd International Cosmic Ray Conference* (2013) p. 0580.
- [93] N. Kuiper, Nederl Akad Wetensch Proc Ser A. , 38 (1960).
- [94] J. Ranft, Phys. Rev. D **51**, 64 (1995).
- [95] A. Kolmogorov, G. Ist. Ital. Attuari. **4**, 83 (1933).
- [96] R. Abbasi *et al.* (IceCube), LeptonInjector and LeptonWeighter: A neutrino event generator and weighter for neutrino observatories, Comput. Phys. Commun. **266**, 108018 (2021).
- [97] M. G. Aartsen *et al.* (IceCube), Astropart. Phys. **78**, 1 (2016).
- [98] N. Y. Agafonova *et al.* (LVD), Phys. Rev. D **100**, 062002 (2019).
- [99] A. G. Bogdanov, R. P. Kokoulin, Y. F. Novoseltsev, R. V. Novoseltseva, V. B. Petkov, and A. A. Petrukhin, Astropart. Phys. **36**, 224 (2012).
- [100] D. Chirkin and M. Rongen, Light diffusion in birefringent polycrystals and the icecube ice anisotropy (2019), arXiv:1908.07608 [astro-ph.HE].

Appendix

The following appendix includes event displays and saliency maps not shown in the main text, and a more detailed discussion of backgrounds and data-driven studies of the CNN performance.

Event Displays

Images and saliency maps for all seven candidate $\nu_{\tau}^{\text{astro}}$ events are shown in Fig. A1.

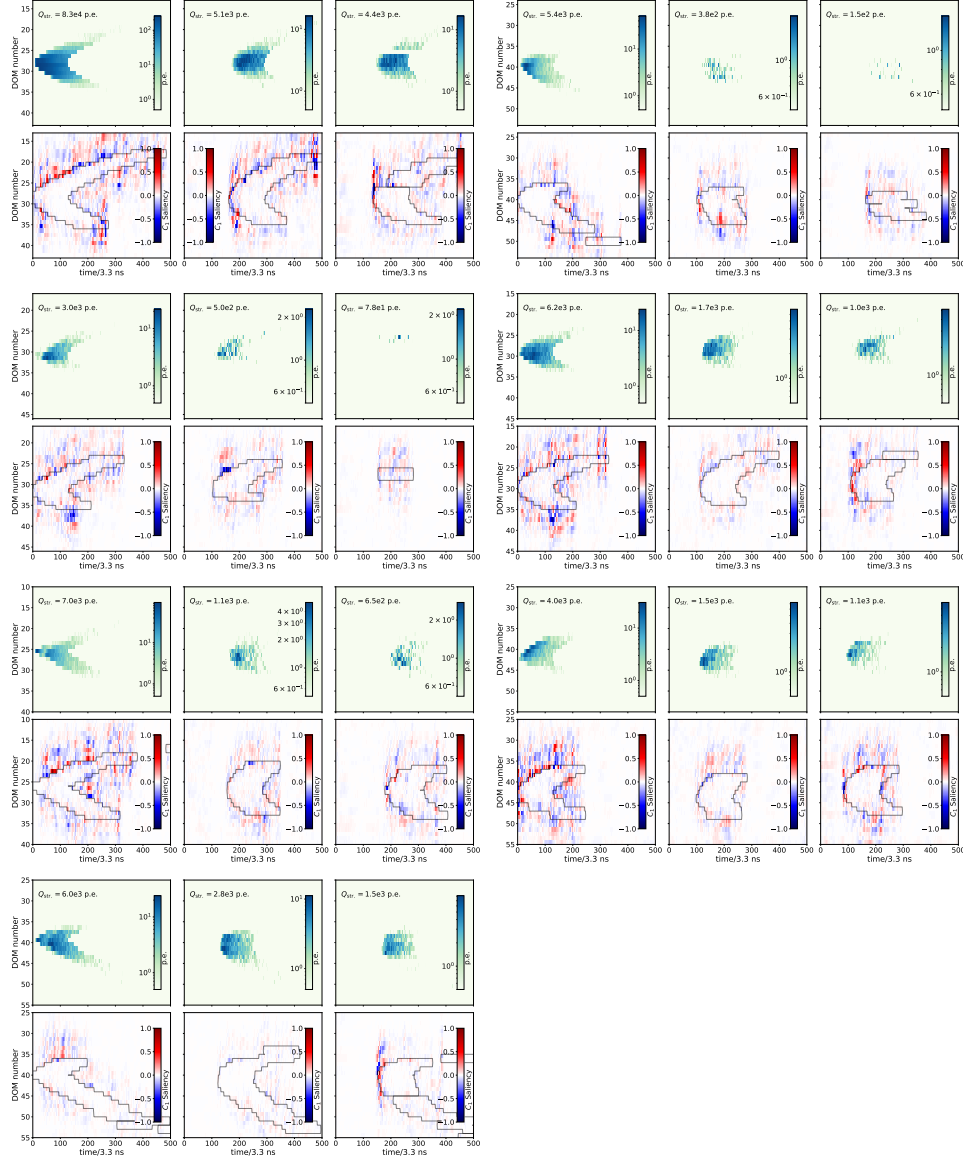


FIG. A1. The figures show the 2-d images and saliency maps for all candidate $\nu_{\tau}^{\text{astro}}$ events. The three columns in each figure correspond to the three strings in the selected event. The top row in each figure shows the measured light level as a function of DOM number (proportional to depth) and time (in 3.3 ns bins). These (60×500) -pixel images from simulated signal and background were used to train the CNNs. The bottom row in each figure shows the saliency, scaled from $[-1, 1]$, with red (blue) regions indicating where increased (decreased) light would increase C_1 (see text). The contour (solid line) superimposed on the saliency plots corresponds to the pixels where the light level went to zero, and is roughly an outline of the light-level plot above it. The events depicted were detected in Jan. 2012 (top left), Jul. 2013 (top right), Oct. 2013 (second row left), Dec. 2014 (second row right), Apr. 2015 (third row left), Sep. 2015 (third row right) and Nov. 2019 (bottom left). (In the top left figure, one of the DOMs in the third string is faulty and had been removed from the data stream, resulting in the blank horizontal region visible in the figure. As this is a very rare occurrence, the CNN was not trained with data that included it, but its absence did not have a noticeable impact on the CNN scores.)

Candidate Event Spatial Distribution

The seven ν_τ^{astro} candidate events were reconstructed *a posteriori* using the algorithm described in Ref. [87]. We also applied the same reconstruction to the $\nu_{\tau, \text{CC}}^{\text{astro}}$ signal simulation. Figure A2 shows a top view of the reconstructed vertices for the seven events and Fig. A3 shows a side view of the events, superimposed on the expected distribution from simulated signal. The numbers 1–7 next to each data point correspond to the images in Fig. A1 (moving left to right and top to bottom).

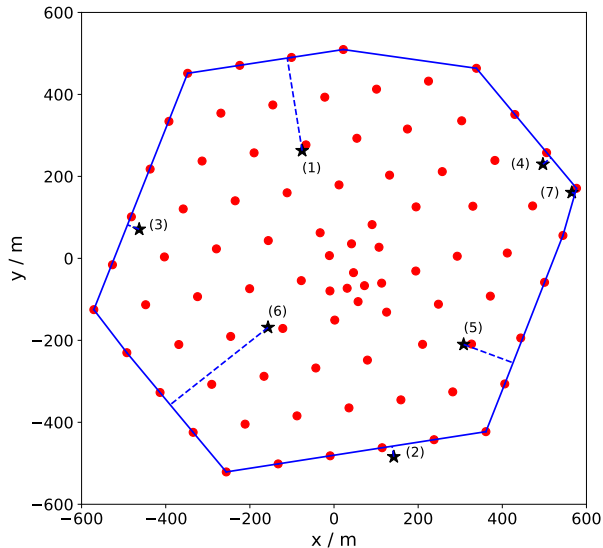


FIG. A2. Top view of the reconstructed vertex positions [87] of the seven ν_τ^{astro} candidate events, indicated by stars, with the positions of IceCube strings shown as circles. The dashed lines show the horizontal distance from the edge of the detector (delineated by the solid line) to the event vertex. (The numbers near each data point correspond to the events; see text.)

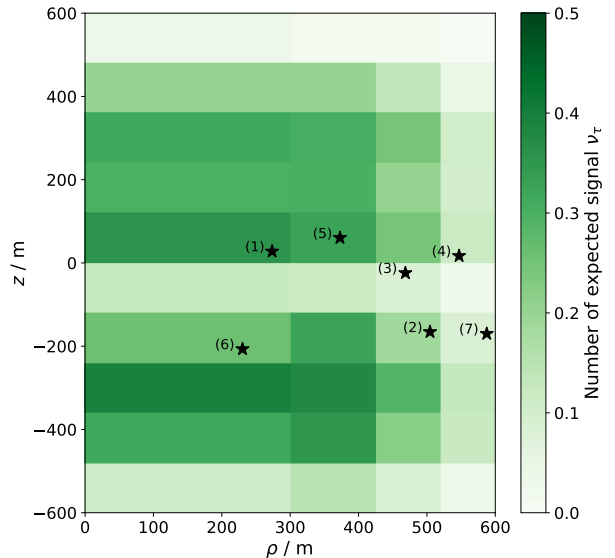


FIG. A3. Side view of the reconstructed vertex positions [87] of the seven ν_τ^{astro} candidate events, indicated by stars, as a function of vertical position z and horizontal position $\rho \equiv \sqrt{x^2 + y^2}$. (Strings at the detector's edge have ρ values from roughly 425–600 m.) The coordinates are measured with respect to the center of IceCube at a depth of 1950 m. The expected distribution of ν_τ^{astro} in 9.7 years for the astrophysical flux in Ref. [53] is overlaid. (The numbers near each data point correspond to the events; see text. The horizontal bin widths are scaled with ρ^2 .)

From the depth distribution, it becomes apparent that the events seem to cluster close to a prominent, 100 m thick, dust layer centered around $z = -80$ m [91, 92]. This region has high optical absorption, reducing detectable light. Photon scattering and absorption through all ice layers and their subsequent effects on the detection efficiency were included in our simulation. A Poisson goodness-of-fit test on the entire 2d histogram in Fig. A3 gives a moderate p -value of 0.38, based on a suite of pseudo-trials. On the other hand, the projected z -distribution indicates a clustering that is inconsistent with expectation at the 3σ level, according to a Kuiper test [93].

To investigate further, we explored the possibility that the discrepancy might be due to mismodeling of the dust layer or due to atmospheric muons from prompt decays of charm or unflavored vector mesons.

Impact of the Dust Layer

At the energies to which this analysis is sensitive, the selected events have τ leptons that travel 10–20 m. At roughly 100 m thickness, the dust layer is too thick for it to enable background events to mimic signal events. At our energies, the effect of the dust layer would be to obscure the light from one or both of the ν_τ cascades, making the event look instead like a single cascade, or simply too dim, respectively.

Nevertheless, we performed several tests to verify that the CNNs were not unduly sensitive to light signals in the dust layer. For candidate events near the dust layer, shifting the waveform times for all DOMs in the dust layer by

± 300 ns, or even removing those DOMs entirely from the event, did not change the CNN response. In another test, the times of individual pixels in the candidate events were shifted, and migration out of the signal region occurred only for shifts exceeding about 100 ns, well in excess of uncertainties expected from mismodeling of ice or DOM properties. (Each pixel holds the PMT charge in a 3.3 ns bin in the DOM's waveform. The timing uncertainty due to ice properties is estimated to be about 20 ns for distances of about 100 m.) We also altered simulated background events near the dust layer and found that the CNN scores were similarly robust (see next section for more details).

Impact of Prompt Cosmic-Ray Muons

The flux of muons from prompt decays of heavy mesons differs from the conventional flux as a function of both energy and arrival direction. To check whether the unanticipated z -distribution might be due to the (un-simulated) prompt muon component of cosmic-ray showers, a dedicated simulation was performed sampling muons from an E^{-2} power-law spectrum and using a parameterized prompt model based on DPMJet-2.55 [94]. The targeted simulation was performed at depth, efficiently sampling muons from the parameterized model. The simulated muon flux was then subjected to an analysis where we loosened the cut on the CNN C_3 score, designed to distinguish ν_τ^{astro} signal from muon tracks produced by ν_μ interactions and downward-going muons, from 0.85 (0.95 with charge asymmetry requirements for outer strings) to 0.75. If the candidate data events were contaminated by muons, loosening C_3 as described would result in more simulated muons entering the signal region. In this context, we performed a comparison of the spatial distribution across the detector of the generated muon events and that expected for data. Since all of the simulated events that survive this CNN selection reconstruct as not fully contained, either near the outer edge or top of the detector, for this comparison we excluded the three candidate ν_τ^{astro} events that were well-contained within the fiducial region of IceCube. (We note that one of the remaining four candidate ν_τ^{astro} events in this subsample reconstructs as having passed through hundreds of meters of active detector volume above its interaction vertex, and the absence of appreciable light in this region further supports its neutrino hypothesis, but in what follows we do not incorporate this information.)

Figure A4 shows a scatter plot of z vs. $\rho \equiv \sqrt{x^2 + y^2}$ (as measured from the center of IceCube at a depth of 1950 m) for data and unweighted simulated events classified as not fully contained. It is apparent that the additional data events allowed in by loosening the C_3 score mainly appear at the top of the detector. Comparing these data to the simulation of cosmic-ray muons, a Kolmogorov-Smirnov consistency test [95] in z gives a p -value of 0.1 for the hypothesis that all of the data events are muons. Moreover, reverting to the original definition of the C_3 selection criterion leaves only eight unweighted simulated cosmic-ray muons, along with the four candidate edge events. Performing again a Kolmogorov-Smirnov consistency test in z gives a p -value of 0.004, indicating that it is unlikely that all of the four candidate ν_τ^{astro} edge events are muons.

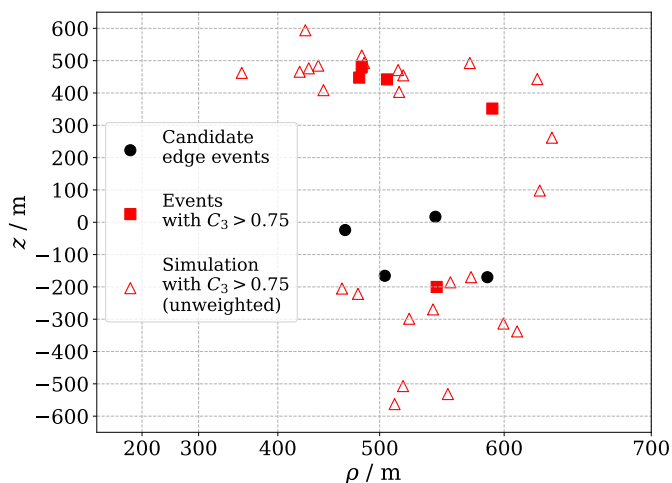


FIG. A4. Distribution of z vs. ρ for candidate ν_τ^{astro} events classified as edge events (solid black circles), other data events satisfying a looser C_3 criterion (solid red squares; see text for details), and unweighted simulated downward-going muons also satisfying a looser C_3 (open red triangles). All events were reconstructed using the algorithm described in Ref. [87]. (IceCube's use of event weighting in simulation is described in Ref. [96]. The horizontal axis is scaled with ρ^2 .)

Muons from cosmic-ray air showers enter primarily at the top of the detector. Muon rates were estimated from measurements of the cosmic-ray muon flux by IceCube and other instruments [53, 97–99]. These measurements are compatible with muons solely from π^\pm/K^\pm decays, although upper bounds on the prompt contribution exist. We therefore did not include muons from charm decays in the background simulations used here. For the sake of completeness, however, we calculated the effect of arbitrarily increasing the atmospheric muon background by an order of magnitude with respect to the originally expected value of 0.005 ± 0.004 (post-unblinding, using the sampling flux from Ref. [69]). We find that the significance remains above 5σ , even with such an increase.

Impact of Relaxing CNN scores C_1 and C_2

Finally, we investigated the effects of less strict requirements on CNN scores C_2 and C_1 . Loosening just the C_2 requirement only lets in events near the top of the detector, and therefore cannot provide an explanation for the observed z -clustering. Figure A5 shows a scatter plot of z vs. $\rho \equiv \sqrt{x^2 + y^2}$, demonstrating the effect of loosening just the C_1 score criterion to $C_1 > 0.90$ to determine if a larger population of events is concentrated near the dust layer, the top of the detector, or at the detector perimeter, as would be expected for an enhanced background. The additional events (red squares) instead broaden the spatial distribution, consistent with a statistical explanation for the originally observed clustering. From simulations, we expected that loosening C_1 would yield 9.4 signal and 2.9 background events, for a total of 12.3 events (assuming the IceCube GlobalFit [53] flux), consistent with the 12 events observed. The additional five events have an average “tauness” $\langle P_\tau \rangle = 0.49$. The 12 events also exclude the null hypothesis at approximately 5σ .

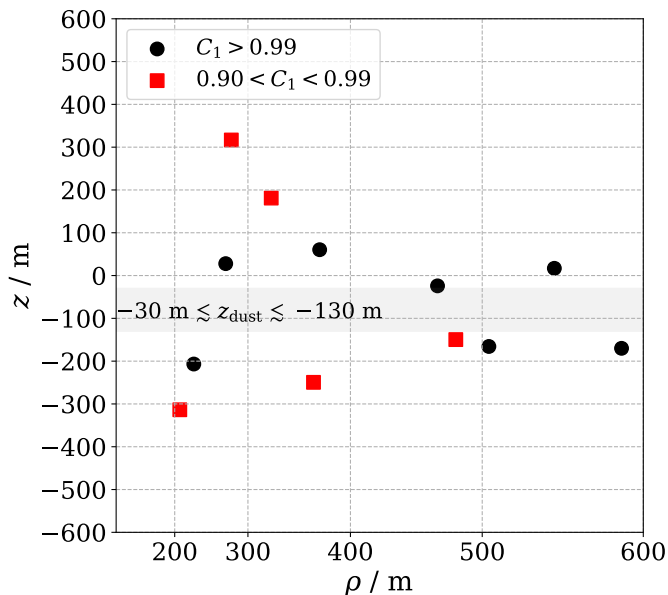


FIG. A5. Distribution of event z vs. $\rho \equiv \sqrt{x^2 + y^2}$, as measured from the center of IceCube at a depth of 1950 m, using the reconstruction in Ref. [87] to estimate the event vertex position. As discussed in the text, the original seven ν_τ^{astro} candidate events (black circles) appear to cluster near the prominent dust layer in the ice, shown as a horizontal gray band. However, the five additional events (red squares) broaden the spatial distribution. All events were reconstructed using the algorithm described in Ref. [87]. (The horizontal axis is scaled with ρ^2 .)

CNN Robustness

Pre-Unblinding Data vs. Simulation Agreement

Prior to unblinding we investigated the agreement in the CNN scores between data and simulation in the regions populated by background events. Figure A6 shows a cumulative plot of the number of data and expected signal and

background events vs. the CNN score C_1 ; CNN scores $C_{2,3}$ show similar levels of agreement.

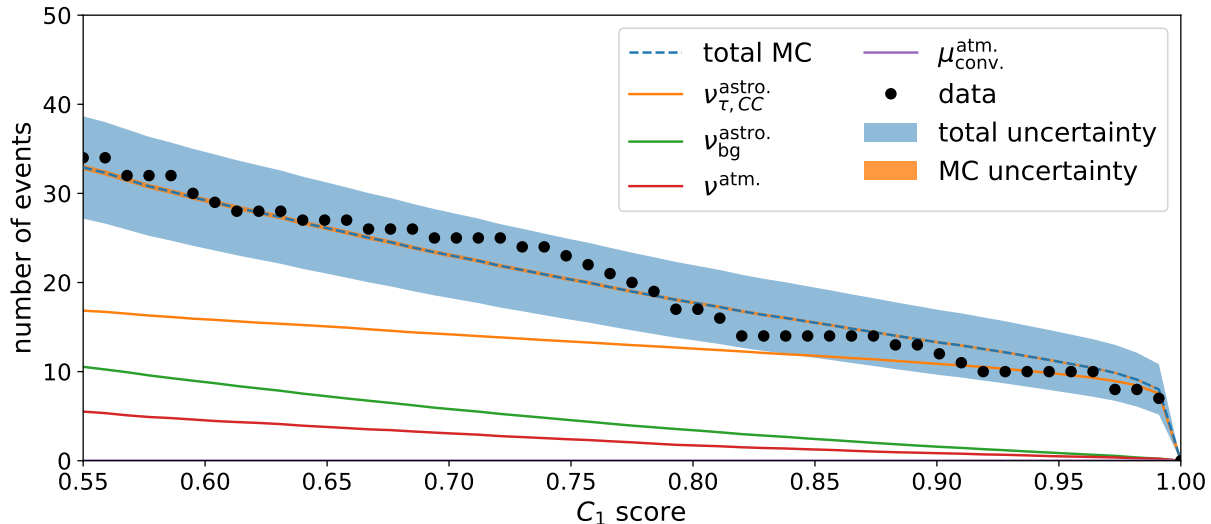


FIG. A6. Cumulative plot showing expected signal ($\nu_{\tau,CC}^{\text{astro.}}$); expected backgrounds from other astrophysical neutrinos ($\nu_{\text{bg}}^{\text{astro.}}$), atmospheric neutrinos ($\nu^{\text{atm.}}$), and conventional atmospheric muons ($\mu_{\text{conv.}}^{\text{atm.}}$); and observed data as a function of CNN score C_1 . The CNN scores $C_{2,3}$ were set to their final values. Similar plots for C_2 and C_3 also show comparable agreement between data and simulation. The IceCube GlobalFit ν^{astro} flux [53] is assumed.

Post-Unblinding Tests

Here we describe in more detail the various data-driven and simulation-based tests of CNN robustness that we performed. For the first suite of tests, we define the background region as $C_{1,2,3} < (0.9, 0.9, 0.75)$, comprising 8,175 of the original 8,188 events passing the preliminary selection criteria. We applied randomized scale factors to DOM waveforms that artificially increased or decreased the magnitude of the detected light level within expected systematic uncertainties, in five distinct patterns:

- each of 180 DOMs were randomly scaled independent of one another,
- dividing the detector into regions in depth, the group of DOMs in each region was randomly scaled by the same factor, as follows:
 - 20 groups of 9 DOMs each in regions in depth of about 50 m,
 - 15 groups of 12 DOMs each in regions in depth of about 68 m,
 - 12 groups of 15 DOMs each in regions in depth of about 85 m, and
- on each of the two less-illuminated strings, all 60 DOMs were randomly scaled by the same factor (a total of two distinct factors were used).

The first pattern addresses relative DOM detection efficiencies [48], the next three address ice optical properties as a function of depth, and the fifth addresses ice birefringence [100] as a function of azimuthal angle.

For each pattern, we performed 750 trials per event, for a total of $(5 \times 8175 \times 750)$ or about $3 \cdot 10^7$ trials. We found that the probability of background-to-signal migration did not exceed $(2 \pm 0.2) \cdot 10^{-5}$ in any of the tests, corresponding to 0.16 ± 0.02 events, and that migration occurred only when events were already close to the signal region. The final significance remains above 5σ whether we use simulated data sets (described earlier) or this data-driven approach to handle these detector systematics. The same tests performed on the seven signal events showed a signal-to-background migration probability of $(3 \pm 0.8) \cdot 10^{-3}$.

We also employed targeted tests to estimate the CNNs' robustness against less likely changes in the underlying raw data. In candidate events with prominent double pulse waveforms, we interpolated between the two peaks to merge

together the first and second pulses, and found that this did not cause any candidate events to migrate out of the signal region. As mentioned earlier, shifting pixel arrival times in individual DOM waveforms in candidate events by up to 100 ns did not appreciably change the CNN response.

We applied adversarial attacks [89] against the candidate events, using an optimization algorithm to find the pixel(s) whose physically reasonable alterations resulted in the largest changes to the CNN scores. Just one of the seven candidate events could be forced to migrate, and only when the average change over all pixels was at least 2.5%, a situation that is well outside our estimated uncertainties. Similarly attacking simulated background events, we found that in no particular region of the detector did the CNNs exhibit heightened susceptibility, and generally the changes required to induce migration were much larger than allowed by our uncertainties. We also attacked 634 simulated astrophysical ν_e , allowing the individual pixel uncertainties to be as high as 10%, finding in this harsh test that only one simulated ν_e was misclassified as a ν_τ . Finally, we attacked the candidate events after randomly varying their pixel values with 10% uncertainty. Using 10^4 trials per event, only one event was found to have a $(2.1 \pm 0.14)\%$ migration probability. These targeted tests, and other studies described earlier in this Supplemental Material, indicate that even under quite harsh conditions, the CNNs remained capable of rejecting the background events while retaining the candidate signal events.



MAX-PLANCK-MEDAILLE

Expedition to the Zeptouniverse

Flavour experiments promise insights into energy scales as high as 200 TeV and distances as small as 10^{-21} meter and offer the chance to identify New Physics.

Andrzej J. Buras

The Large Hadron Collider (LHC) at CERN will directly probe distance scales as short as 10^{-19} m, corresponding to energy scales at the level of a few TeV. Presently, higher resolution can only be achieved with the help of quantum fluctuations caused by new particles and new forces that act at very short distance scales and modify the predictions of the Standard Model of particle physics for very rare processes. In this context, weak decays of mesons and leptons play the prominent role besides the transitions between particles and antiparticles in which flavours of quarks and leptons are changed. In this manner, information about the Zeptouniverse corresponding to energy scales as high as 200 TeV or distances as small as 10^{-21} m can be obtained.

The year 1676 was very important for humanity, because Antoni van Leeuwenhoek discovered the empire of bacteria. He called these small creatures *animalcula* (small animals). His discovery was a milestone in our civilization for at least two reasons: He discovered creatures invisible to us which have been killing humans for thousands of years, often responsible for millions of deaths in one year. While Antoni van Leeuwenhoek did not know that bacteria could be dangerous for humans, his followers like Louis Pasteur, Robert Koch and other „microbe hunters“ realized the danger coming from these tiny creatures and also developed weapons against this empire [1].

Van Leeuwenhoek was the first human who looked at short distance scales invisible to us and discovered thereby

a new underground world. At that time, researchers looked mainly at large distances, discovering new planets and finding laws, such as the Kepler laws which Isaac Newton was able to derive from his mechanics.

While van Leeuwenhoek could reach a resolution of roughly 10^{-6} m, this could be improved by twelve orders of magnitude over the last 344 years. On the way down to shortest distance scales, scientists discovered the nanouniverse (10^{-9} m), the femtouniverse (10^{-15} m) relevant for nuclear particle physics and low-energy elementary particle physics and finally the attouniverse (10^{-18} m) which is the territory of contemporary high-energy elementary-particle physics.

Using this overture, I have opened my lecture at the 50th Cracow School of Theoretical Physics held in Zakopane, Poland, in June 2010. At that time, it was strongly believed that the LHC in addition to discovering the only then missing particle of the Standard Model, the Higgs boson, would discover a plethora of new particles, in particular supersymmetric particles or those related to the existence of large extra dimensions like Kaluza-Klein gluons. The Higgs boson was indeed discovered two years later at CERN. But even tremendous efforts of experimentalists and theorists to find New Physics beyond the Standard Model did not result in the discovery of any new particles at the LHC. Thereby, as of August 2020, shifting the masses of supersymmetric particles and Kaluza-Klein gluons significantly above the 1 TeV scale.¹⁾

Yet, we know that new particles and new forces beyond those present in the Standard Model must exist. The most convincing arguments are based on the following questions, none of which can be answered within the Standard Model:

- What is the dark matter that occupies 27 percent of our universe?
- Why is our universe dominated by matter? This is clearly required for our existence, but the size of the violation of CP symmetry required for the dominance of matter over antimatter soon after the Big Bang is much larger than the one found within the Standard Model.
- Why is the neutron heavier than the proton? This question is significant for our existence.
- What is the origin of neutrino masses and why are they by nine orders of magnitude smaller than the proton mass?
- Why is the mass of the heaviest quark, the top quark, by five orders of magnitude larger than the mass of the lightest quark, the up quark?

It is not the goal of this article to address these questions. Rather, being motivated by them and knowing that New Physics must exist at scales much shorter than explored by now, I would like to concentrate on the following questions:

- Can quantum fluctuations help us with getting some insight into the dynamics at very short distance scales. Could they answer some of these questions, if no direct clear signal of New Physics will be seen at the LHC, i.e., no new particles with masses below 6 TeV will be discovered?

1) Of course, one cannot exclude the existence of very light particles, like axions, that being very weakly coupled to standard matter could not be detected until now.

- Can we reach the Zeptouniverse, i.e., a resolution as high as 10^{-21} m or energies as large as 200 TeV, by means of quark flavour physics and lepton flavour violating processes in this decade well before this will be possible by means of any collider built in this century?

The photo opening this paper was chosen to illustrate that I am much more optimistic about the future of particle physics than Christoph Wetterich, the winner of Gentner-Kastler-Prize 2019 [2]. Christoph is an esteemed colleague of mine but, in my view, his vision of a desert between the LHC scales and the Planck scale cannot be correct and will be disproved in this decade precisely by flavour physics. In the landscape, photographed by my son Allan during one of his expeditions to the far north, first the Standard Model (our Base Camp) is placed and the energy gap which we are already crossing with the help of the renormalization group equations of the so-called Standard Model Effective Field Theory (SMEFT). However, in order to reach New Physics summits in the far distance, we have to cross the crevasses representing very difficult experiments and difficult theoretical calculations. To this end, we will need brilliant ideas which will guide us through these crevasses so that one day we will reach the summits that will help us to answer at least some of the questions listed above.

After a brief review of the particle content of the Standard Model and of the properties of strong and electroweak interactions described by it, I will present a number of strategies which, with the help of quantum fluctuations, should indeed allow us to get a view of the Zeptouniverse before the advent of future colliders. Subsequently, we will have a brief look at the most interesting anomalies, the departures of the experimental findings from Standard Model expectations. They can be considered as footprints of new particles and new interactions that appear to be beyond the reach of the LHC, although one should not give up the hope that some hints for them will be seen in the next LHC run.

It should be mentioned that this indirect search for new phenomena is by no means new. A classical analogy is the

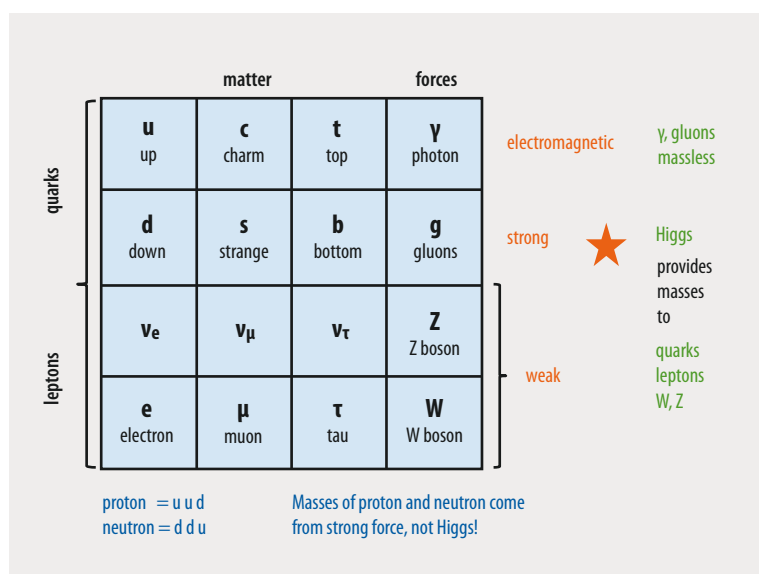


Fig. 1 The particle content of the Standard Model

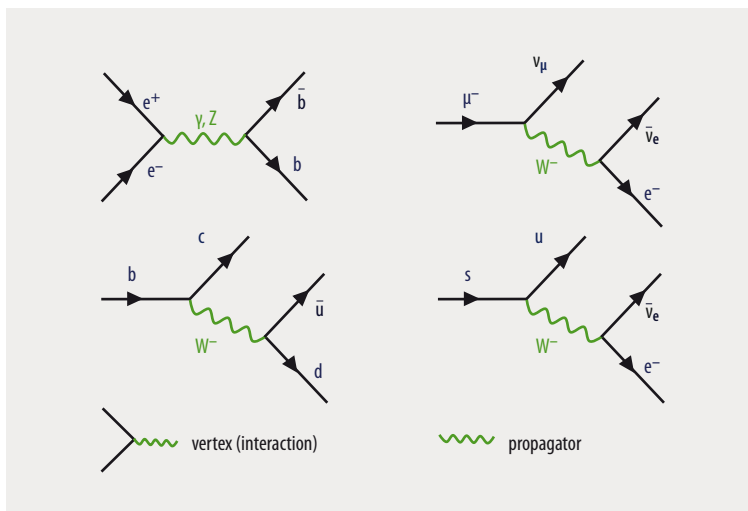


Fig. 2 The world of Feynman Diagrams: more complicated diagrams can be constructed and probabilities for a given process evaluated.

prediction of the existence of the planet Neptune in 1846 by Urbain Le Verrier based on an anomaly in the orbit of the Uranus. Neptune's existence was soon after confirmed by the German astronomer Johann Gottfried Galle. The gauge bosons W^\pm and Z^0 were seen indirectly in lower-energy experiments well before their discovery in 1983 at CERN. The presence of the W^\pm bosons was actually felt already in the 1930s in the context of the Fermi theory of β -decays even if only in the 1960s theorists realized what are the elementary particles mediating these decays. Z boson was seen first in 1973 through the discovery of neutral currents at CERN – ten years before this boson was discovered also at CERN.

Express Review of the Standard Model

In the Standard Model matter consists of four fermion families (**Fig. 1**): up quark (u, c, t), down quark (d, s, b), neutrino (ν_u, ν_c, ν_t) and electron (e, μ, τ). They correspond to the four rows in the table. Particles in a given family have the same quantum numbers, in particular similar electric charges: $2/3$, $-1/3$, 0 and -1 , respectively. Their antiparticles have opposite electric charges. The members of a given family can only be distinguished by their masses which increase in the table from left to right. The columns in this table correspond to three generations of these elementary particles and the different names of quarks and leptons are called flavours: six quark flavours and six lepton flavours.

The interactions between the matter fields are mediated by gauge bosons with spin 1. For strong interactions (Quantum Chromodynamics, QCD), these are the electrically neutral massless gluons (G^a). For the electroweak interactions (Quantum Flavourdynamics) these are the electrically neutral massless photon (γ), the electrically neutral heavy Z boson and finally the charged heavy W^\pm . The masses of all these particles, according to the Standard Model, are generated through their interactions with an electrically neutral scalar particle (Spin 0), the Higgs boson.

The strong and electroweak interactions have a number of properties encoded in the Lagrangian of the Standard

Model that can be found in any textbook on particle physics. The following four properties of these interactions (**Fig. 2**) will be relevant for us:

- By themselves, neutral gauge bosons (G^a, γ, Z) and the Higgs boson cannot transfer a fermion with one flavour into another fermion with a different flavour. There are simply no vertices in any Feynman diagram that involve any of these bosons and two fermions (quarks or leptons) with different flavours. For instance, a vertex with Z boson, b quark and a s quark does not exist. This is assured by the so-called Glashow-Iliopoulos-Maiani (GIM) mechanism. Needless to say, Standard Model gauge bosons cannot transfer a lepton into a quark or vice versa. This is already evident from charge conservation. The interactions mediated by these bosons also conserve parity (P), charge conjugation (C) and CP -parity. The charged gauge bosons W^\pm change flavour and violate maximally parity and charge conjugation implying that only left-handed quarks and left-handed leptons take part in the charged current weak interactions. These interactions are parametrized in the case of quarks by the unitary Cabibbo-Kobayashi-Maskawa (CKM) matrix which depends on three real parameters (the so-called mixing angles) and one complex phase responsible for CP -violation in the Standard Model. In the case of leptons, W^\pm interactions are parametrized by the unitary Pontecorvo-Maki-Nakagawa-Sakata (PMNS) matrix which can have two additional phases relative to the CKM matrix, the so-called Majorana phases, related to special properties of neutrinos, the only neutral fermions we know.

- The gauge interactions mediated by neutral G^a, Z and γ are universal in a given family. In particular the interactions of Z with e, μ and τ are the same.

- While electroweak interactions are weak and can be calculated within perturbation theory, the strong interactions are strong at scales below 1 GeV in order to bind quarks inside hadrons like mesons, the proton and the neutron. At these scales, only non-perturbative methods are useful. These are in particular the numerical Lattice QCD and analytical methods like Dual QCD and Chiral Perturbation Theory. For scales above 1 GeV, strong interactions are sufficiently weak due to the property of asymptotic freedom in QCD, so that their effect can be calculated within perturbation theory. Yet, in the presence of vastly different energy scales, like the hadronic scale $\mathcal{O}(1 \text{ GeV})$, the electroweak scale (246 GeV) and New Physics scales often well above 1 TeV, the appearance of large logarithms of the ratios of these scales multiplying the gauge couplings requires their summation to all order of perturbation theory. To this end, very efficient renormalization group methods, known also in the field of phase transitions, are used. They are discussed in much more detail in my recent book [3].

We have seen that, within the Standard Model, neutral gauge bosons are not able to change flavour by themselves. However, one can construct complicated Feynman diagrams (loop diagrams) involving these bosons together with W^\pm that do change flavour. One example of such a diagram is called penguin diagram (**Fig. 3**). But such loop diagrams can have a different shape like the so-called box diagrams, in which the neutral gauge boson is replaced by the pair W^\pm

and W^- that has zero charge. Processes of this type are called Flavour Changing Neutral Current (FCNC) processes and are very important for our discussion. Prominent examples are the decays $B_s^0 \rightarrow \mu^+ \mu^-$, $K^+ \rightarrow \pi^+ \nu \bar{\nu}$ and particle-antiparticle transitions like $(B_{s,d}^0 - \bar{B}_{s,d}^0)$ mixings.

According to the usual Feynman-diagram calculus, the probability for a given process to occur is proportional to the product of couplings present in the vertices of the diagrams governing this process. Involving several weak couplings and often small elements of the CKM matrix present in the vertices in one-loop diagrams, FCNC processes are strongly suppressed within the Standard Model. This suppression is partly lifted if the top-quark is present inside the loop and the contributions of such diagrams grow quadratically with the top-quark mass. This is only the case with the decays of K and B mesons but not for the D mesons and leptons, so that most interesting measurements of FCNCs to date come from weak decays of K and B mesons, $(B_{s,d}^0 - \bar{B}_{s,d}^0)$ mixings and $(K^0 - \bar{K}^0)$ mixing. But as these processes are very strongly suppressed in the Standard Model, they are more powerful in the search for New Physics than processes that are possible within the Standard Model through the exchange of a simple W^\pm (Fig. 2). In this way, the Standard Model contributions represent a significant background in the search for New Physics.

On the other hand, and beyond the Standard Model, the GIM mechanism is often absent and FCNC processes can be governed by simpler diagrams involving new heavy particles. For example, a very heavy neutral gauge boson Z' contributes to $(B_{s,d}^0 - \bar{B}_{s,d}^0)$ mixing (Fig. 4). Although its propagator $(1/M_{Z'}^2)$ strongly suppresses this contribution, the absence of several weak couplings relatively to one-loop diagrams partly lifts this suppression. Consequently, such contributions can be relevant and play often significant roles in finding new phenomena as we will explain now. Quantum fluctuations involving new particles can also generate flavour changing vertices in which Z bosons changes an s or d quark into the b quark (Fig. 4).

The Technology to Reach the Zeptouniverse

Main players in indirect searches for New Physics are presently the mesons, quark-antiquark bound states

$$B_d^0 = (\bar{b}d), B_s^0 = (\bar{b}s), B^+ = (\bar{b}u), K^+ = (\bar{s}u), K_L = (\bar{s}d), \pi^+ = (\bar{d}u),$$

but also leptons and mesons with charm quark will surely play important roles in the search for New Physics in this decade. In order to reach high resolution at short distance scales, one has to produce many of these mesons in high energy collisions. They subsequently decay into lighter particles. The goal of experimentalists is then to measure very accurately the probability with which a given meson decays into a particular final state such as $\mu^+ \mu^-$, $\pi^+ \nu \bar{\nu}$, $\pi^+ \pi^-$ among many possible final states. These probabilities, normalized to unity (100 percent), are called branching ratios.

The goal of theorists is to calculate these with high precision within the Standard Model and compare them with the experimentally measured branching ratios. Any difference

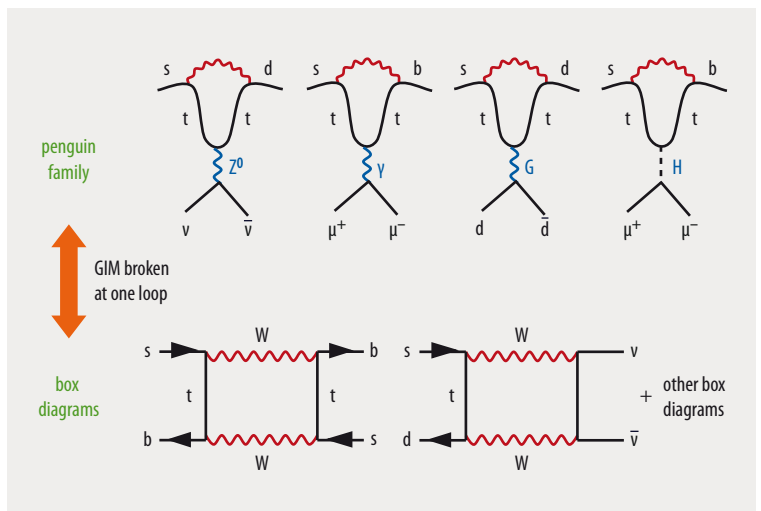


Fig. 3 Penguin diagrams and box diagrams

between the experimental branching ratio and the one predicted by the Standard Model is a hint at the existence of new particles that are often too massive to be produced at the LHC. But through quantum fluctuations represented by propagators in Feynman diagrams they can affect various branching ratios so that the latter can differ from the ones predicted in the Standard Model.

To identify new particles in this indirect manner, it is crucial to test many different branching ratios for the meson decays listed above. The Particle Data Group (PDG) collects the experimental values of these branching ratios and this collection amounts to thousands of different numbers. In the case of lepton decays, only upper limits on the branching ratios are known, because to date, no FCNC process in the lepton sector has been observed experimentally. Yet, they must exist at a certain level because of non-vanishing neutrino masses. However, these masses are tiny, and in the Standard Model, such processes are predicted to have very small branching ratios like $\mu \rightarrow e \gamma$ in the ballpark of 10^{-54} . Any observation of such decays would be a clear signal of New Physics.

As far as flavour expedition to the Zeptouniverse is concerned, only a fraction of the branching ratios collected by the PDG is of interest to us. These are the ones which are predicted to be very small in the Standard Model, because

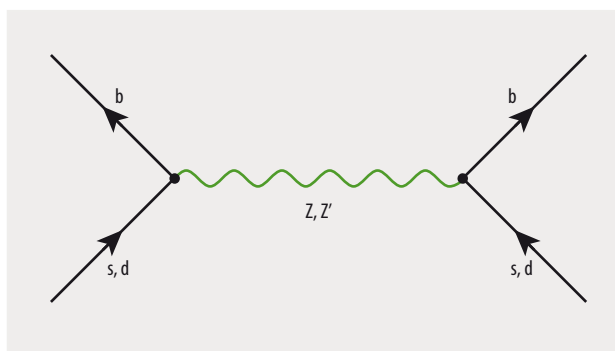


Fig. 4 This Feynman diagram shows a FCNC process mediated by a heavy neutral gauge boson Z' and/or Z .

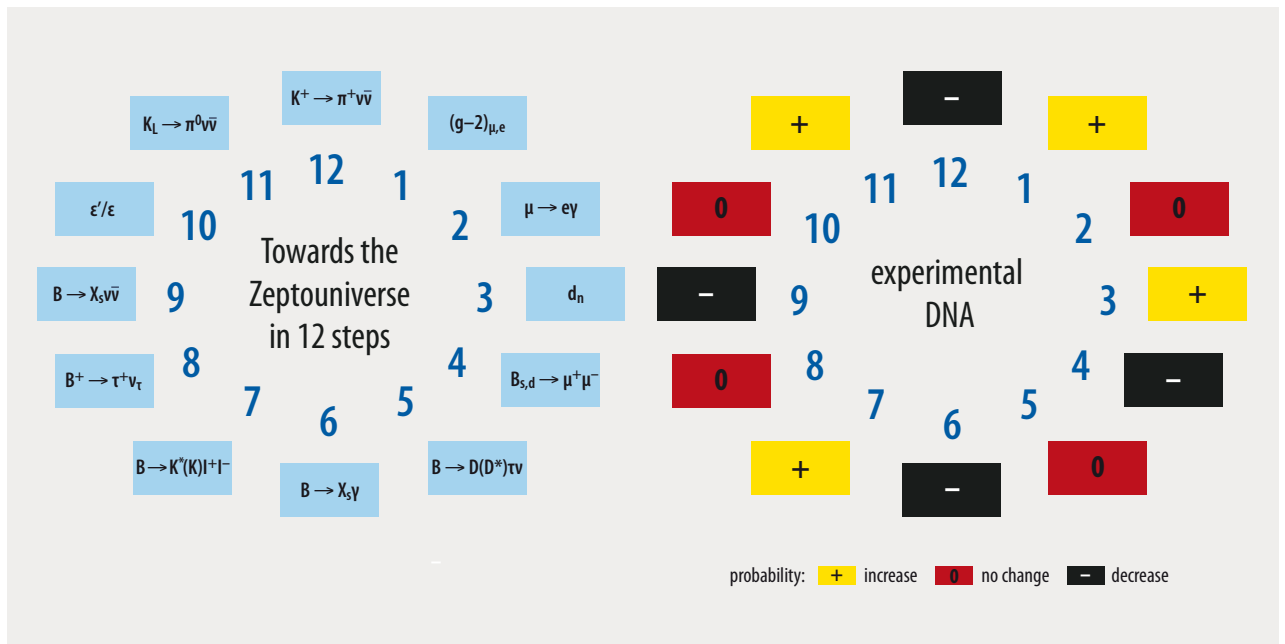


Fig. 5 General Structure of DNA: considered processes (left) and experimental DNA (right).

then the background from the Standard Model does not prevent seeing new phenomena. Very small does not mean 0.01 or 0.001 but often 10^{-6} , 10^{-9} and even 10^{-11} in the case of meson decays. For leptons, such branching ratios are even smaller as already stated above. For instance, the present experimental upper bound on the branching ratio of $\mu \rightarrow e\gamma$ amounts to 10^{-13} and it is amazing that experimentalists can measure such tiny values.

Let us assume that one day we will have hundreds of very precise measurements of various branching ratios for decays of mesons and leptons and very precise Standard Model predictions for them. This will allow us to construct a series of differences between experimental and theoretical

branching ratios calculated in the Standard Model. These differences will be generally positive, negative or consistent with zero. A positive difference means that there is a New Physics contribution enhancing the branching ratio, while a negative one signals New Physics which suppresses the branching ratio relative to the one predicted by the Standard Model. An example is given in Fig. 5 where a selected number of processes is shown compared to the coding for differences between Standard Model predictions and experimental data found in the possible future.

These twelve examples are representatives of the hundreds of branching ratios at our disposal one day, among them many that will correspond to yellow or black

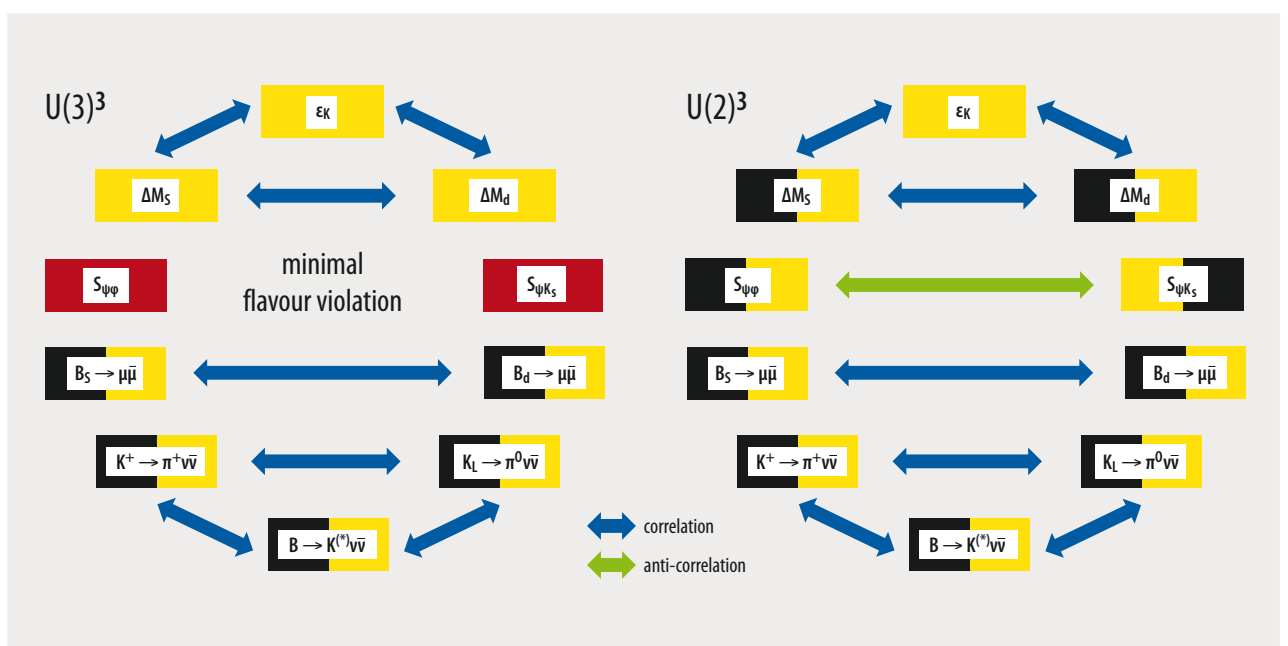


Fig. 6 DNA-chart of Minimal Flavour Violation models and DNA-chart of $U(2)^3$ models

colours thereby indicating the presence of New Physics. This is similar to having a DNA of a criminal, represented here by New Physics, and our goal is to identify him or her in the most efficient manner. Of course, there are many criminals behind these numbers, in general complicating this search.

Without any theoretical input, this goal cannot be realized. In addition to finding these new particles, we would obviously like to know their interactions which could again be mediated by gluons, photons and a Z boson. But generally new Feynman diagrams will include additional gauge bosons, new fermions and scalars that is brothers and sisters of Standard Model particles which could be both electrically neutral or charged. One restriction comes from the observation that for energy scales much larger than the scale of spontaneous breakdown of the Standard Model gauge symmetry $SU(3)_C \times SU(2)_L \times U(1)_Y$, this symmetry must be exact which reduces the number of possible theories. Yet, without additional dynamical assumptions, the New Physics contributions in full generality turn out to depend on 1350 real parameters and 1149 complex phases. This number becomes smaller if one considers a specific class of processes, but still it is not possible to determine all these parameters in low-energy experiments without some specific simplifying assumptions about the structure of New Physics. This fact is fortunately key to reduce the number of possibilities for physics beyond the Standard Model.

In my view the most efficient strategy in this context is to consider many concrete New Physics models or some simplified versions of them and calculate within each of them as many observables as possible. Most of my younger colleagues would then just put these results into a computer code to calculate χ^2 or a p number for each model. Others would present multi-dimensional plots in the space of the parameters of the model to identify the range of param-

eters that is ruled out by experiment, often leaving small oases where a given model can still survive. These are valid procedures, but in my view not sufficiently transparent as far as the nature of the New Physics we are searching for is concerned. In my view, it is better to first construct for each model its DNA consisting of +, 0 and – as explained above, and then compare it to the DNA of the criminal(s) determined by experiment as given in Fig. 5.

However, it is rare for a given observable in a given theory to be uniquely suppressed or enhanced relative to the Standard Model. Frequently, two observables are correlated or uncorrelated with each other. Thus, the enhancement of one observable implies uniquely an enhancement (correlation) or suppression (anticorrelation) of another observable. Among further possibilities, it can also happen that a change in the value of a given observable implies no change in another observable. After adjusting the parameters of a given theory in order to reproduce the enhancement of a given branching ratio, this theory predicts also enhanced or suppressed values for other observables and sometimes there is no effect of New Physics on some other branching ratios.

Applying then the information from a given theory requires sometimes further significant theoretical work. The strategy, developed in collaboration with Jennifer Girrbach-Noe [4], is to connect a given pair of branching ratios that are correlated or anticorrelated with each other by a line in a DNA-chart. The absence of a line means that two given observables are uncorrelated.

This strategy is illustrated with four simplified models discussed in detail in [3, 4]. In the left part of Fig. 6, we show the DNA-chart of the so-called Minimal Flavour Violation New Physics scenario which is based on the flavour symmetry $U(3)^3$. It is the minimal extension of the Standard Model. The right part of this figure shows the DNA of models with reduced flavour symmetry $U(2)^3$. Fig. 7 shows two theories with a heavy neutral Z' , which only interacts with

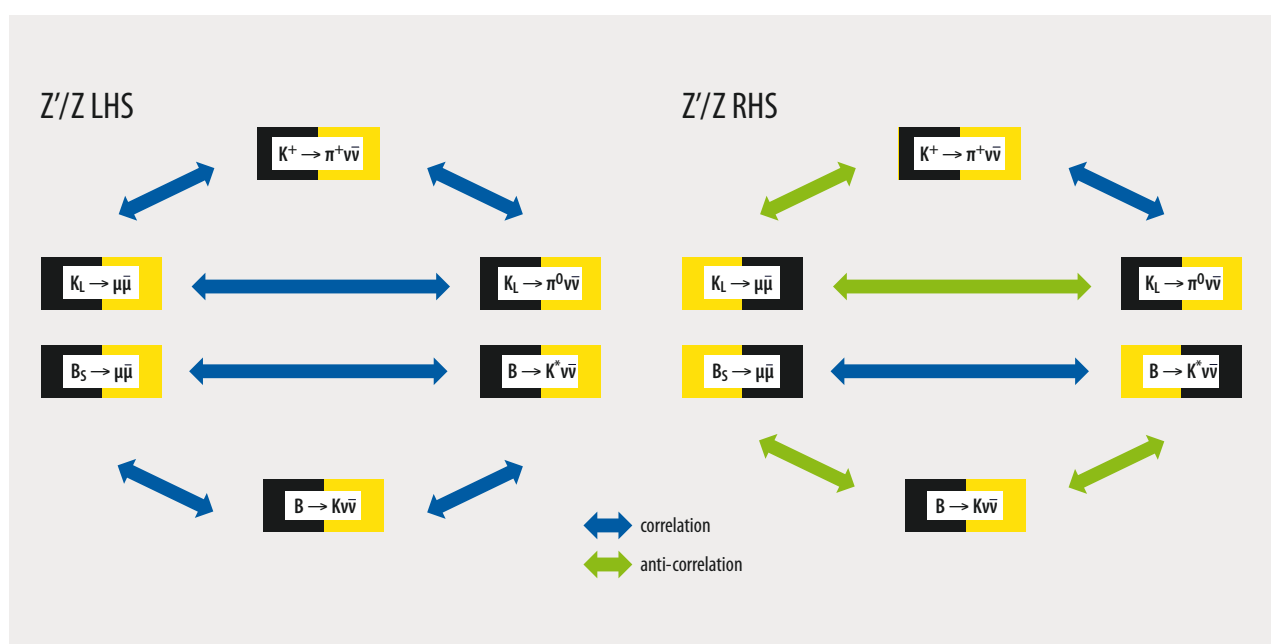


Fig. 7 DNA-charts of Z' models with LH and RH currents

left-handed and right-handed quarks, respectively. This two charts can also represent the Standard Model Z boson, which acquired flavour-changing interactions through New Physics. It should be noted that all four charts differ from each other. As soon as experiments favour one model, one can begin to investigate it in more detail within the chosen theory, calculating χ^2 and p -numbers. If neither is favoured by nature, new DNAs for other theories have to be constructed.

Anomalies

During the last ten years a number of deviations from Standard Model predictions have been measured by experimentalists. The most popular ones are presently the so-called B -physics anomalies observed in the BaBar, LHCb, CMS, ATLAS, and Belle experiments. The observed data imply that the lepton flavour universality breaks down, i.e., the branching ratios for rare decays of B mesons with muons and electrons in the final state differ from each other by 2 to 3 standard deviations. A similar phenomenon is observed when a B meson decays into muons compared with decays into τ leptons. The prime criminals behind such phenomena are leptoquarks, heavy bosons with spin 0 or 1 changing quarks into leptons or vice versa. In the case of the violation of the $\mu - e$ universality, a heavy gauge boson Z' could be responsible for this anomaly as well. Yet, we still have to wait for more precise data and in some cases for more precise calculations to be confident that these effects are indeed more than statistical fluctuations.

Another anomaly found already twenty years ago at the Brookhaven National Laboratory is the deviation of the anomalous magnetic moment of the muon, $(g-2)_\mu$, from its rather precise Standard Model value. A new experiment at FNAL and an independent experiment at J-PARC in Japan should clarify whether new physics is hidden in this finding. Again, leptoquarks could be responsible for this anomaly.

The study of the violation of CP symmetry in $K \rightarrow \pi\pi$ decays represented by the so-called ratio ϵ'/ϵ is also of considerable importance. Unfortunately, the calculation of this ratio is subject to large non-perturbative uncertainties. Presently, we do not know whether new phases beyond the CKM phase are necessary to explain the existing data from NA48 at CERN and KTeV at Fermilab, known to us already for twenty years. Such new phases, if required, could in principle explain the dominance of the matter over the antimatter in the universe. If that is the case the criminals among other possibilities could be a heavy Z' and heavy vector-like quarks in which left and right components transform identically under $SU(2)_L$. Leptoquarks turn out to be less useful in this case: Even the explanation of a moderate ϵ'/ϵ anomaly would imply very large branching ratios for rare Kaon decays, which are experimentally excluded. This result highlights the importance of correlations between various processes. Such correlations should be very powerful when the rare decays $K^+ \rightarrow \pi^+ \nu \bar{\nu}$ and $K_L \rightarrow \pi^0 \nu \bar{\nu}$ will be accurately measured by the NA62 experiment at CERN and by the KOTO experiment in Japan, respectively. In ad-

dition, the CLEVER experiment at CERN should contribute in the future to the study of $K_L \rightarrow \pi^0 \nu \bar{\nu}$.

Conclusions

Detailed studies of the ability of flavour physics to provide information about new physics beyond 100 TeV have been performed in [5, 6]. They show that the particle-antiparticle mixings are most efficient to reach these scales [5], but a detailed picture of the Zeptouniverse can only be obtained through the study of rare K and $B_{s,d}$ decays [6] and lepton flavour violating decays like $\mu \rightarrow e\gamma$ and $\mu^- \rightarrow e^- e^+ e^-$ [7]. Additionally, electric dipole moments of the neutron and of various atoms are very important in the search for new phenomena [8].

There is no question that flavour physics has a great future through experiments in Europe, Japan and USA. I am looking forward to the year 2030, when hopefully a concrete picture of the Zeptouniverse will be known.

References

- [1] Paul de Kruif, *Microbe Hunters*, Mariner Books, Boston (2002); the book was first published in 1926.
- [2] Ch. Wetterich, *Physik Journal*, August/September 2019, S. 67
- [3] A. J. Buras, *Gauge Theory of Weak Decays*, Cambridge University Press, Cambridge (2020)
- [4] A. J. Buras and J. Girrbach, *Rep. Prog. Phys.* **77**, 086201 (2014)
- [5] G. Isidori, Y. Nir and G. Perez, *Ann. Rev. Nucl. Part. Sci.* **60**, 355 (2010)
- [6] A. J. Buras, D. Buttazzo, J. Girrbach-Noe and R. Knegjens, *JHEP* **1411**, 121 (2014)
- [7] M. Lindner, M. Platscher and F. S. Queiroz, *Phys. Rep.* **731**, 1 (2018)
- [8] T. Chupp, P. Fierlinger, M. Ramsey-Muslof and J. Singh, *Rev. Mod. Phys.* **91**, 015001 (2019)

The Author



Andrzej J. Buras studied physics in Warsaw. He received his doctorate in 1972 at the Niels Bohr Institute (Copenhagen). Postdoctoral years at CERN (Geneva), Fermilab (Chicago) and SLAC (Stanford University) were followed by a position at the Max Planck Institute for Physics in

Munich. In 1988, he was appointed full professor at the Physics Department of the TU Munich. Since 2012, he is Emeritus of Excellence of the TUM and heads a group on Fundamental Physics at the Institute for Advanced Study of the university. Andrzej J. Buras was awarded the Smoluchowski-Warburg Medal of the German and Polish Physical Societies in 2007. From 2011 to 2016, he was funded by an ERC Advanced Grant. He is a full member of the Bavarian Academy of Sciences (2010), foreign member of the Polish Academy of Sciences (2013) and of the Polska Akademia Umiejętności in Cracow.

Prof. Dr. Andrzej J. Buras, TUM Institute for Advanced Study, Lichtenbergstraße 2a, 85748 Garching, Germany

No massive black holes in the Milky Way halo

Przemek Mróz^{1*}, Andrzej Udalski¹, Michał K. Szymański¹,
Igor Soszyński¹, Łukasz Wyrzykowski¹, Paweł Pietrukowicz¹,
Szymon Kozłowski¹, Radosław Poleski¹, Jan Skowron¹,
Dorota Skowron¹, Krzysztof Ulaczyk^{1,2}, Mariusz Gromadzki¹,
Krzysztof Rybicki^{1,3}, Patryk Iwanek¹, Marcin Wrona¹,
Milena Ratajczak¹

^{1*}Astronomical Observatory, University of Warsaw, Al. Ujazdowskie 4,
Warszawa, 00-478, Poland.

²Department of Physics, University of Warwick, Coventry CV4 7 AL, UK.

³Department of Particle Physics and Astrophysics, Weizmann Institute
of Science, Rehovot 76100, Israel.

*Corresponding author(s). E-mail(s): pmroz@astrouw.edu.pl;

The gravitational wave detectors have unveiled a population of massive black holes that do not resemble those observed in the Milky Way [1–3]. They may have formed due to the evolution of massive low-metallicity stars [4], dynamical interactions in dense stellar environments [5, 6], or density fluctuations in the very early Universe (primordial black holes) [7–9]. If the latter hypothesis is correct, primordial black holes should comprise from several to 100% of dark matter to explain the black hole merger rates observed by gravitational wave detectors [10–12]. If such black holes existed in the Milky Way dark matter halo, they would cause long-timescale gravitational microlensing events lasting years. Here, we present the results of the search for the long-timescale microlensing events among the light curves of 78.7 million stars located in the Large Magellanic Cloud (LMC) that were monitored for 20 years (2001-2020) by the Optical Gravitational Lensing Experiment (OGLE) survey [13]. We did not find any events with timescales longer than one year. The properties of all thirteen microlensing events with timescales shorter than one year detected by OGLE toward the LMC can be explained by astrophysical objects located either in the LMC itself or in the Milky Way disk, without the need to invoke dark matter

in the form of compact objects. We find that compact objects in the mass range from $1.8 \times 10^{-4} M_{\odot}$ to $6.3 M_{\odot}$ cannot compose more than 1% of dark matter, and compact objects in the mass range from $1.3 \times 10^{-5} M_{\odot}$ to $860 M_{\odot}$ cannot make up more than 10% of dark matter. This conclusively rules out primordial black hole mergers as a dominant source of gravitational waves.

Gravitational microlensing was proposed by [14] as a promising tool for searching for dark matter in the Milky Way halo. This idea prompted extensive searches by the first-generation microlensing surveys [15–18]. Here, we analyze the longest digital photometric data set to search for extremely long-timescale microlensing events. The data were collected for nearly 20 years during the third (OGLE-III; 2001–2009; [19]) and fourth (OGLE-IV; 2010–2020; [13]) phases of the OGLE project. Since OGLE-III and OGLE-IV had similar observing setups, it was possible to merge the observations to create a 20-year-long photometric time-series dataset. We developed a new method of reductions of photometric observations, which enabled us to obtain homogeneous light curves. The design of the survey, extraction of photometry, and methods used to search for microlensing events and calculate the event detection efficiency are described in detail in a companion paper [20].

About 33 million objects are detected in the overlapping OGLE-III/OGLE-IV region, and an additional 29 million objects are observed by OGLE-IV only. The number of stars that may be microlensed is even higher because of blending, which occurs when two or more stars cannot be resolved in ground-based seeing-limited images. We used the archival high-resolution images from the Hubble Space Telescope [21] to correct the star counts for blending. After removing the contribution from foreground Milky Way stars, we found that the survey monitored for microlensing about 78.7 million source stars in the LMC brighter than $I = 22$ mag [20].

We searched for microlensing events using a variation of the method described by [22]. The algorithm tries to identify a flat portion of the light curve, and then searches for consecutive data points that are magnified with respect to the flat part. Then, a standard point-source point-lens microlensing model [14] is fitted to the light curve, and the goodness-of-the-fit statistics are evaluated. The events are selected on the basis of a series of selection cuts. This procedure enabled us to find thirteen events that fulfill all detection criteria. Additionally, three events were identified by a manual inspection of the light curves, although they did not meet all selection criteria. The sample of thirteen events is used for a later statistical analysis [20].

We also carried out extensive light curve simulations to measure the event detection efficiency as a function of the event timescale [20]. To this end, we created synthetic light curves of microlensing events by injecting the microlensing signal into the light curves of constant stars observed by the project. Then, we measured the fraction of simulated events that passed all selection criteria. This procedure enabled us to take into account the noise in the data, as well as the effects of irregular sampling, gaps in the data, outliers, etc.

The contribution of primordial black holes (PBHs) and other compact objects to dark matter is often parameterized by $f = \Omega_{\text{PBH}}/\Omega_{\text{DM}}$, where Ω_{PBH} is the density of dark matter in the form of PBHs and Ω_{DM} is the density of dark matter. Note that we expect to detect some gravitational microlensing events even if $f = 0$: they come

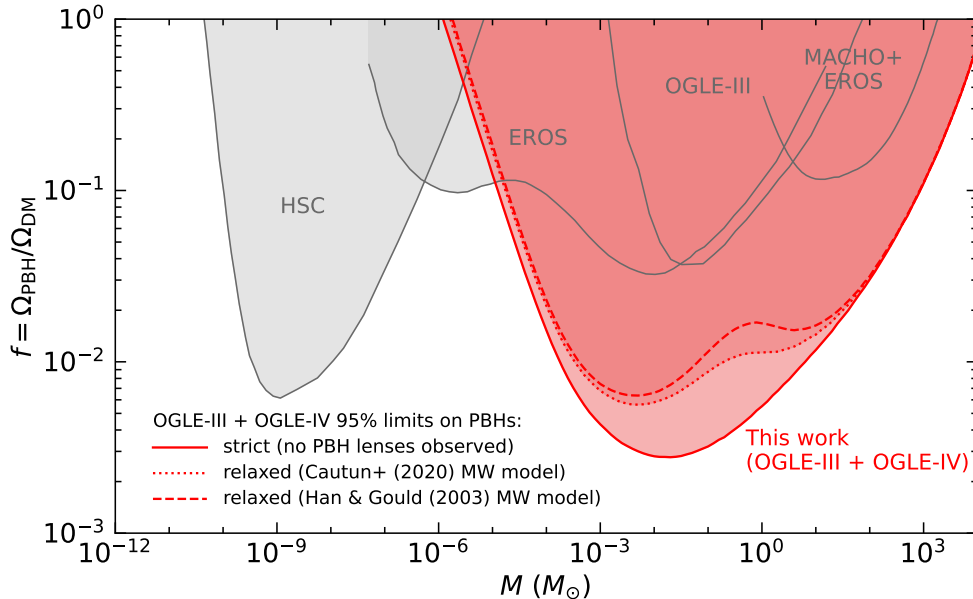


Fig. 1 95% upper limits on PBHs (and other compact objects) as constituents of dark matter. The solid red line marks the limits derived in this paper under the assumption that all gravitational microlensing events detected by OGLE in the direction of the LMC are due to objects in the LMC itself or the Milky Way disk. If this assumption is relaxed, the limits (dotted and dashed lines) depend on the choice of the Milky Way disk model ([23] or [24], respectively). The gray lines mark the limits determined by the following surveys: EROS [16], OGLE-III [17], Hyper Suprime-Cam (HSC) [25], and MACHO+EROS [18]. The new limits are publicly available online at https://www.astrouw.edu.pl/ogle/ogle4/LMC_OPTICAL_DEPTH/.

from lensing objects located in the Milky Way disk and the LMC itself. The latter phenomenon is also called self-lensing [e.g., 26].

We found that all thirteen microlensing events detected in our survey can be explained by brown dwarfs, stars, and stellar remnants located in the LMC and the foreground Milky Way disk (Methods). We adopted the LMC disk model from ref. [15] with some modifications, and considered two Milky Way disk models by [23] and [24] (Methods). We calculated the theoretical microlensing event rate and the event timescale distribution in each field analyzed by OGLE. Then, we estimated the expected number of events by multiplying the event rate by the duration of the observations, the number of source stars, and the average event detection efficiency. In total, we expected to find 12.7 or 20.4 events, depending on the Milky Way disk model, which can be compared to the total number of thirteen events in the final statistical sample. We also found that positions, timescales, and microlensing parallaxes of the detected events are consistent with the predictions of the adopted model (Methods).

To infer the constraints on the value of f , we calculated the expected number of events and their timescale distribution, assuming that the entire dark matter halo is composed of compact objects of the same mass M . We assumed the contracted

Milky Way halo model by [23] and the LMC halo model by [27] (Methods). Our experiment has the highest sensitivity to PBHs with masses of $0.01 M_{\odot}$; we should have detected more than 1100 events if the entire dark matter were composed of such objects. However, thanks to the long duration of observations, OGLE has a high sensitivity for even more massive objects. For $M = 1 M_{\odot}$, we should have detected 554 events; for $M = 10 M_{\odot}$ —258 events; for $M = 100 M_{\odot}$ —99 events; for $M = 1000 M_{\odot}$ —27 events. Additional information that can be used to further constrain the abundance of PBHs in the Milky Way and LMC haloes is included in the timescales of observed events (Methods).

Our 95% upper limits on PBHs (and other compact objects) as constituents of dark matter are presented in Figure 1. The solid red line marks the strict limits derived in this paper under the assumption that all gravitational microlensing events detected by OGLE in the direction of the LMC are due to known stellar populations in the LMC itself or the Milky Way disk. These limits are inversely proportional to the number of events expected if the entire dark matter was composed of compact objects of a given mass. As expected, the limits are strongest ($f = 2.8 \times 10^{-3}$) for $M \approx 0.01 M_{\odot}$, for which the model predicts the largest number of expected events. The compact objects of mass $M = 1 M_{\odot}$ may make up less than $f = 0.55\%$ of dark matter; $M = 10 M_{\odot}$ — $f = 1.2\%$; $M = 100 M_{\odot}$ — $f = 3.0\%$; $M = 1000 M_{\odot}$ — $f = 11\%$. The PBHs in the mass range $1.8 \times 10^{-4} M_{\odot} < M < 6.3 M_{\odot}$ cannot compose more than 1% of dark matter, and the PBHs in the mass range $1.3 \times 10^{-5} M_{\odot} < M < 8.6 \times 10^2 M_{\odot}$ cannot make up more than 10% of dark matter.

We also found that, thanks to the long duration of the survey and the large number of stars monitored, the derived limits weakly depend on the choice of the Milky Way halo model. In particular, we tested the dark matter halo model of [28] and found consistent results (as shown in Extended Data Figure 1). The latter model was based on recent measurements of the rotation curve in the outer regions of the Milky Way by the *Gaia* satellite.

The dotted and dashed lines in Figure 1 mark the relaxed limits, for the derivation of which we did not make any assumptions about the origin of events. These limits only slightly depend on the choice of the Milky Way disk model. Overall, the differences between different models are minimal for the least massive ($M \lesssim 10^{-4} M_{\odot}$) and the most massive ($M \gtrsim 10 M_{\odot}$) PBHs, because we do not expect that known stellar objects would produce microlensing events with timescales that could be attributed to those by extremely low- or high-mass PBHs. In the intermediate mass range ($10^{-4} M_{\odot} \lesssim M \lesssim 10 M_{\odot}$), microlensing events caused by PBHs may be mistaken with those caused by known stellar populations in the LMC or the Milky Way disk. Therefore, the relaxed limits are slightly weaker than the strict ones in this mass range.

Limits presented in Figure 1 are derived for a delta-function mass function of PBHs and, in principle, may become weaker if the underlying mass function is extended. Such extended mass functions of PBHs are frequently discussed in the context of binary black hole mergers discovered by gravitational wave detectors [10–12]. For example, the model presented by [10] predicts four peaks in the mass spectrum of PBHs at 10^{-6} , 1, 30, and $10^6 M_{\odot}$. These peaks would be associated with different phase transitions in the quark–gluon plasma filling the early universe (W^{\pm}/Z^0 decoupling,

the quark–hadron transitions, and e^+e^- annihilation), which are thought to enhance the formation of PBHs.

Several studies argue that such a multi-peak mass function of PBHs can naturally explain the observed merger rates of black hole binaries observed by gravitational wave detectors and a significant fraction (from several to 100%) of dark matter [e.g., 10–12]. This hypothesis has one important prediction: PBHs in the Milky Way dark matter halo should cause long-timescale gravitational microlensing events that last years. For example, if the entire dark matter was composed of PBHs with the mass spectrum described by the model of [10] (with the spectral index $\tilde{n}_s = 0.96$), we should have detected over 600 microlensing events. The non-detection gives us a 95% upper limit on the fraction of dark matter in the form of PBHs of $f = 1.2\%$ (assuming a Milky Way disk model by [24]). Similar limits of the order of 1% can be obtained for other multi-peak mass functions proposed in the literature. Our observations, therefore, conclusively rule out PBH mergers as a dominant source of gravitational waves.

Acknowledgements. We thank all the OGLE observers for their contribution to the collection of the photometric data over the decades. We thank T. Bulik for insightful comments on the manuscript. This research was funded in part by National Science Centre, Poland, grant OPUS 2021/41/B/ST9/00252 awarded to P.M.

Author contributions. P.M. led the analysis and interpretation of the data and wrote the manuscript. A.U. is the PI of the OGLE project, and was responsible for the data reduction. All authors collected the OGLE photometric observations, and reviewed, discussed, and commented on the presented results and on the manuscript.

Competing interests. The authors declare no competing interests.

Materials & Correspondence. Correspondence and requests for materials should be addressed to Przemek Mróz (pmroz@astrouw.edu.pl).

Methods

Model

Let us suppose that we have a sample of N_{obs} events and let $t_{\text{E},i}$ be the Einstein timescale of the i th event. We use that information to measure f (or derive upper limits on f) by maximizing the likelihood function defined as

$$\mathcal{L}(f, M) = e^{-N_{\text{exp}}(f, M)} \prod_{i=1}^{N_{\text{obs}}} \left[N_s \Delta t \frac{d\Gamma}{dt_{\text{E}}} (t_{\text{E},i}, f, M) \varepsilon(t_{\text{E},i}) \right], \quad (1)$$

where N_s is the number of microlensing sources observed in the experiment, Δt is the duration of observations, and $\varepsilon(t_{\text{E}})$ is the event detection efficiency in the experiment (as a function of the Einstein timescale). Here $d\Gamma/dt_{\text{E}}$ is the differential event rate, which contains contributions from lenses in the Milky Way disk, LMC, and Milky Way and LMC dark matter haloes:

$$\begin{aligned} \frac{d\Gamma}{dt_{\text{E}}} = & f \frac{d\Gamma_{\text{MW halo}}}{dt_{\text{E}}} (t_{\text{E}}, M) + f \frac{d\Gamma_{\text{LMC halo}}}{dt_{\text{E}}} (t_{\text{E}}, M) \\ & + \frac{d\Gamma_{\text{MW disk}}}{dt_{\text{E}}} (t_{\text{E}}) + \frac{d\Gamma_{\text{LMC}}}{dt_{\text{E}}} (t_{\text{E}}), \end{aligned} \quad (2)$$

and

$$N_{\text{exp}}(f, M) = N_s \Delta t \int \frac{d\Gamma}{dt_{\text{E}}} (t'_{\text{E}}, f, M) \varepsilon(t'_{\text{E}}) dt'_{\text{E}} \quad (3)$$

is the expected number of events. Eq. (1) can be derived by dividing the observed event timescale distribution into infinitesimally small bins that contain either one or zero events, and assuming that the number of events detected in each bin follows the Poisson distribution. The microlensing event rate and the event timescale distribution are calculated following the standard approach [e.g., 29]. We describe the components of the model in the following subsections.

Milky Way halo

Our model is based on the contracted halo model of [23], which was inferred by fitting physically motivated models to the *Gaia* DR2 Galactic rotation curve and other data [30]. The model includes the effect of the contraction of the dark matter halo in the presence of baryons, which was observed in large galaxy formation simulations [e.g., 31–33]. The model predicts the total mass of the dark matter Milky Way halo of $0.97 \times 10^{12} M_{\odot}$ within 200 kpc.

We use the best-fitting model of [23] to predict the rotation curve of the Milky Way $V_0(R)$ (which, by design, matches the *Gaia* data very well), where R is the Galactocentric radius. We assume that the distribution of velocities of halo particles (in the rest frame of the Galaxy) can be considered as Maxwellian [34] with the standard deviation of velocities in one direction equal to $V_0(R)/\sqrt{2}$. (There is some evidence that (at least some) black holes may attain a large recoil velocity after a binary black hole merger [e.g., 35]. If all PBHs had such additional velocity, the derived limits would be

modified, such that they would be moved toward more massive PBHs.) Assuming that the Milky Way halo is composed of objects of identical mass M , the mean Einstein timescale of events predicted by the model is equal to $t_E = 62 \text{ d} \sqrt{M/M_\odot}$, which is in good agreement with the predictions of models by [15] or [18].

LMC halo

The *Gaia* observations indicate that stars in the Orphan stream have velocity vectors that are significantly misaligned with the stream track [36]. Ref. [27] demonstrated that this effect can be explained by gravitational perturbations from the LMC, and inferred the total mass of the LMC of $1.49 \times 10^{11} M_\odot$ (in the model with the spherical Milky Way, which can move in response to the LMC; ref. [27] also considered models with an oblate or a prolate Milky Way halo, which result in the LMC mass that is 5–8% smaller). The total mass of the Milky Way in the [27] model (enclosed within a radius of 50 kpc) is $4.04 \times 10^{11} M_\odot$, which is in excellent agreement with that inferred from the [23] model of the Milky Way halo ($4.1 \times 10^{11} M_\odot$).

Following [27], we assume that the LMC halo can be modeled by a Hernquist profile with the total mass of $1.49 \times 10^{11} M_\odot$. The scale length is 17.1 kpc, and is taken so that the mass enclosed within 8.7 kpc matches the measured value of $1.7 \times 10^{10} M_\odot$ from [37].

Milky Way disk

For consistency with the Milky Way halo model presented above, we adopt the best-fitting thin and thick disk models from [23]. The stellar density is described by the double exponential profile with a scale height of 0.3 kpc (thin disk) or 0.9 kpc (thick disk) and a radial scale length of 2.63 kpc (thin disk) or 3.80 kpc (thick disk). The total masses of the thin and thick disks are $3.18 \times 10^{10} M_\odot$ and $0.92 \times 10^{10} M_\odot$, respectively. As an alternative, we also consider the thin and thick Milky Way disk models of [24]. The scale heights in the model are 0.156 kpc (thin disk) and 0.439 kpc (thick disk), the scale length is 2.75 kpc for both thin and thick disk. The total masses of the thin and thick disks are $0.98 \times 10^{10} M_\odot$ and $0.60 \times 10^{10} M_\odot$, respectively. We assume that stars in the Milky Way disk follow the circular velocity curve derived above with a dispersion of 30 km s^{-1} in each direction. We adopt the mass function of [38].

LMC

To take into account the effects of self-lensing by stars located within the LMC itself, we adopt the LMC disk model of [39] and [15] with some slight modifications. The disk is modeled as a double exponential profile with the scale length of 1.8 kpc and the scale height of 0.3 kpc [39], the total stellar mass of $2.7 \times 10^9 M_\odot$ [40], the inclination and position angle of 25° and 132° , respectively [41]. We adopt the LMC distance of 49.59 kpc [41]. We assume that the stellar mass function is identical to that of the Milky Way. We use an empirical model of the kinematics of stars in the LMC, which is based on *Gaia* EDR3 data (see below). Following [15], we do not consider a separate LMC bar component.

Limits on the PBH abundance

Limits under the hypothesis that all microlensing events detected by OGLE can be explained by known stellar populations

We start by deriving upper limits on the PBH abundance by assuming that all detected events can be explained by astrophysical objects located in the Milky Way disk or the LMC itself. In other words, we assume that we did not see any events due to dark matter in the form of compact objects. In this case, the likelihood function (Eq. (1)) simplifies to:

$$\mathcal{L}(f, M) = e^{-N_{\text{exp}}(f, M)}, \quad (4)$$

where $N_{\text{exp}}(f, M)$ is the expected number of microlensing events, defined in Eq. (3).

Extended Data Figure 2 shows the number of gravitational microlensing events expected to be detected by OGLE if the entire dark matter were composed of compact objects of a given mass. The blue and red lines in Figure 2 mark the expected number of events that originate from lenses in the Milky Way and LMC haloes, respectively. For PBHs more massive than $0.1 M_{\odot}$, Milky Way halo lenses contribute to $\approx 70\%$ of the expected events. For lower masses, LMC halo lenses start to dominate, because the LMC events generally have longer timescales than those by Milky Way halo objects and so are easier to detect. The thin solid lines in Figure 2 show the contribution from fields observed during both the OGLE-III and OGLE-IV phases (from 2001 to 2020), while dashed lines—fields observed during OGLE-IV only (from 2010 to 2020). The latter contribute less than 10% of the sensitivity of the experiment, because they are located on the outskirts of the LMC (and therefore contain fewer source stars) and were observed for a shorter period of time.

Given the likelihood function $\mathcal{L}(f, M)$ (Eqs. (1) and (4)) and our model (Section 3), we employ the Bayes' theorem to derive the posterior distribution for PBH abundance $P(f|M)$:

$$P(f|M) \propto \mathcal{L}(f, M)P_0(f), \quad (5)$$

where $P_0(f)$ is a flat (uniform) prior on $f \in [0, 10]$. We use the Markov chain Monte Carlo (MCMC) sampler of [42] to sample from the posterior and derive 95% upper limits on f as a function of the PBH mass M . To speed up the calculations, we first evaluate $\ln \mathcal{L}(f, M)$ on a grid of 101 logarithmically spaced masses ranging from $10^{-6} M_{\odot}$ to $10^4 M_{\odot}$ and 101 logarithmically spaced values of f from 10^{-4} to 10, and use the linear interpolation to calculate the likelihood between the grid points.

Can all microlensing events detected by OGLE be explained by non-dark-matter objects?

In this section, we would like to verify our assumption that all gravitational microlensing events detected by OGLE in the direction of the LMC can be explained by known astrophysical sources. We show that the presented simple models of the LMC (Section 3) and the Milky Way disk (Section 3) are capable of explaining the number and properties (positions, timescales, parallaxes) of virtually all gravitational microlensing events detected in our experiment. We emphasize that we did not attempt to construct a perfect Milky Way/LMC model nor we did not fit the components

of that model to match the data ideally, which would be beyond the scope of this work. Our main goal is to measure the contribution of compact objects to dark matter and study how the choice of an astrophysical model affects our limits on the PBH abundance.

First, we use our fiducial model of the Milky Way disk (Section 3) and the LMC (Section 3) to calculate the theoretical microlensing event rate and the event timescale distribution in each field analyzed by OGLE. Then, we estimate the expected number of events in each field by multiplying the event rate by the duration of the observations, the number of source stars, and the average event detection efficiency (Eq. (3)). The results are summarized in Extended Data Table 1, separately for fields observed during both the OGLE-III and OGLE-IV phases (2001–2020) and observed by OGLE-IV only (2010–2020).

We expect to detect 5.7 microlensing events due to self-lensing by stars in the LMC itself and 7.0 or 14.7 events due to stars in the Milky Way disk (assuming disk models by [24] or [23], respectively). The total mass of the Milky Way disk in the latter model is 2.6 times larger than in the former, which explains why the model predicts twice as many microlensing events. In total, we expect 12.7 or 20.4 events, depending on the Milky Way disk model, which can be compared to the total number of thirteen events in the final statistical sample of [20]. The Milky Way disk model of [24] is clearly favored, although the model of [23] is still allowed, because the Poisson probability of observing 13 or less events given the expected 20.4 events is 5.6%.

Extended Data Figure 3 shows the number of events expected to be detected in each OGLE field. Most events are expected to be found in the central regions of the LMC, where the self-lensing event rate is highest and the number of source stars is largest. Approximately 80% of the events are expected to be located within 3 deg from the LMC center (defined by [43]) in both the [24] and [23] models. There are two events in the [20] sample that are located more than 3 deg from the LMC center, OGLE-LMC-16 (3.2 deg) and OGLE-LMC-17 (4.9 deg), in excellent agreement with the predictions of the [24] model (2.5 events). The cumulative distribution of the angular distances of the detected events from the LMC center matches that expected from both models, with p -values of 0.29 and 0.16 for the [24] and [23] models, respectively.

The distribution of Einstein timescales of events that are expected to be detected by OGLE (taking into account the detection efficiencies in a given field) is presented in Extended Data Figure 4. 80% of the expected events should have timescales between 26 and 417 d in the [24] model (between 25 and 316 d in the [23] model). Events with lenses located in the LMC are expected to have generally longer timescales than those originating from the Milky Way disk lenses, because the relative lens-source proper motions are smaller.

The timescales of the detected events generally match those expected from the model (Extended Data Figure 4). However, three events in the sample have timescales shorter than 25 d (OGLE-LMC-08: $t_E = 13.5^{+6.0}_{-4.0}$ d, OGLE-LMC-13: $t_E = 7.0^{+2.0}_{-1.1}$ d, OGLE-LMC-17: $t_E = 13.8^{+1.9}_{-1.1}$ d), whereas the model predicts that about 10% of all events (that is, 1.3) should fall in this range. It is possible that this is due to a statistical fluctuation, the Poisson probability of observing three events given the expected 1.3 events is about 10%. The model may also underpredict the number of

low-mass lenses or the number of high-proper motion objects, both of which contribute to the population of short-timescale microlensing events.

Extended Data Figure 5 shows the distribution of the microlensing parallaxes of events expected to be detected in our experiment, assuming the Milky Way disk model by [24]. (The distribution of microlensing parallaxes is very similar in the [23] model, except that the second peak has a larger amplitude.) The distribution is clearly bimodal: the two peaks correspond to two distinct populations of lenses, those in the Milky Way disk, and those in the LMC. The Milky Way disk lenses are located nearby, and so their microlens parallaxes are relatively large; they peak at $\pi_E \approx 0.5$. The second population of lenses that reside in the LMC is characterized by small parallaxes (typically $\pi_E \approx 0.01$). The different values of the parallaxes are consistent with our expectations. For the same lens mass, the microlens parallax scales as $\pi_E \propto \sqrt{\pi_{\text{rel}}}$, where π_{rel} is the relative lens–source parallax. For events with Milky Way disk lenses, $\pi_{\text{rel}} \approx 1/D_1 \approx 1 \text{ mas}$. For the LMC lenses, $\pi_{\text{rel}} \approx \Delta D/D_s^2 \approx 1/2500 \text{ mas}$, where $\Delta D \approx 1 \text{ kpc}$ is the thickness of the LMC disk, so the LMC self-lensing events should have microlensing parallaxes that are about 50 times smaller than the Milky Way disk events, which is consistent with the simulations presented in Extended Data Figure 5.

The statistical sample of [20] contains four events with reliably measured microlensing parallaxes. This does not mean that the remaining events have parallaxes close to zero; rather, these events are too short or too faint to robustly measure the microlens parallax. However, whenever the parallax is clearly detected in the light curve and its value is larger than $\pi_E \approx 0.1$, the lensing object is very likely to be located in the Milky Way disk.

Full limits on PBHs

The Einstein timescales of detected events carry information that can be used to further constrain the abundance of PBHs in the Milky Way and LMC haloes. According to Extended Data Figure 2, if the entire dark matter was composed of black holes of $2200 M_\odot$, we ought to detect thirteen microlensing events. However, the typical Einstein timescales of these events should be on the order of 9 yr, in stark contrast to the observed values.

To take into account the information included in the timescales of the detected events, we evaluate the full likelihood function defined in Eq. (1). We follow the same procedure as above. We calculate $\ln \mathcal{L}(f, M)$ on a grid of 101 logarithmically spaced masses ranging from $10^{-6} M_\odot$ to $10^4 M_\odot$ and 101 logarithmically spaced values of f from 10^{-4} to 10.

Although most of the detected events have precisely measured timescales, the fractional error bar on t_E may be larger than 20% for some events. Thus, we replace the term $\varepsilon(t_{E,i}) d\Gamma/dt_E(t_{E,i}, f, M)$ in the definition of $\mathcal{L}(f, M)$ by the mean over N_i samples from the posterior distribution of $t_{E,i}$:

$$\frac{1}{N_i} \sum_{k=1}^{N_i} \left[\varepsilon(t_{E,ik}) \frac{d\Gamma}{dt_E}(t_{E,ik}, f, M) \right], \quad (6)$$

where the index i denotes the i th event and the index k runs from 1 through $N_i = 2 \times 10^5$.

Extended Data Figure 6 shows the contours of the log-likelihood function, separately for the [24] and [23] models. Regardless of the model chosen, it is clear there is no evidence that PBHs in the mass range $10^{-6} M_\odot < M_{\text{PBH}} < 10^4 M_\odot$ comprise a measurable fraction of the dark matter mass. For the [24] model, the likelihood is highest for $(\log M, \log f) = (-1.5, -2.55)$. However, the model with $\log f = -4$ is disfavored by only $\Delta\chi^2 \equiv 2(\ln \mathcal{L}_{\text{max}} - \ln \mathcal{L}) \approx 3.7$. Similarly, for the second model, the likelihood is highest for $(\log M, \log f) = (-1.8, -2.85)$, and the model with $\log f = -4$ is disfavored only by $\Delta\chi^2 \approx 1.5$.

We found that the highest-likelihood grid point has $\log f > -4$ mostly due to one event, OGLE-LMC-13, which has the shortest timescale in the sample of only $t_E = 7.0_{-1.1}^{+2.0}$ d. Indeed, such a short-timescale event seems to be very rare in our simulations (Extended Data Figure 4). If the event is removed from the sample, models with $\log f = -4$ are disfavored by less than $\Delta\chi^2 \approx 1.5$.

We calculate the posterior distribution for the PBH abundance $P(f|M)$ using the MCMC approach. Our 95% upper limits on the PBH abundance in dark matter are presented in Figure 1 by dashed ([24] model) and dotted ([23] model) lines, and they can be compared to those derived above (solid red line in Figure 1). Overall, the differences are very small for the least massive ($M_{\text{PBH}} \lesssim 10^{-4} M_\odot$) and the most massive ($M_{\text{PBH}} \gtrsim 10 M_\odot$) PBHs, because we do not expect that ordinary astrophysical lenses would produce microlensing events with timescales that could be attributed to those by extremely low- or high-mass PBHs.

In the intermediate mass range ($10^{-4} M_\odot \lesssim M_{\text{PBH}} \lesssim 10 M_\odot$), microlensing events caused by PBHs may be mistaken with those caused by known astrophysical objects in the LMC or the Milky Way disk. Therefore, the derived limits are slightly weaker. The difference between the 95% upper limits on PBHs calculated assuming the [24] Milky Way disk model and those calculated above is the largest for $\log M = -0.6$ and amounts to $\Delta \log f = 0.59$ dex (that is, the limits are about a factor of 3.9 weaker). The choice of the Milky Way model may also slightly affect the derived limits. The difference between the 95% upper limits on PBHs calculated assuming the [24] and the [23] models is greatest for $\log M = -0.1$ and equals to $\Delta \log f = 0.18$ dex at that mass.

Discussion

The limits on the PBH abundance that are presented in the previous section (and in Figure 1) are calculated based on a full statistical sample of thirteen microlensing events detected over 20 years of the OGLE observations of the LMC [20]. As discussed in a companion paper [20], the sample includes all microlensing events with source stars brighter than $I = 22$ mag. Likewise, the detection efficiencies $\varepsilon(t_E)$ and the number of source stars N_s used in the calculations include only sources brighter than $I = 22$ mag. However, the event detection efficiency rapidly drops with the brightness of source stars; the fainter the source, the lower the chances of detecting the microlensing event. Faint source stars are additionally more difficult to count because of the increased amount of blending from unrelated stars [20]. As a result, although the final sample

of events is larger, there is a risk of introducing unknown systematic errors in the analysis.

Events with brighter source stars should be less prone to such systematic effects. Therefore, we check how our results depend on the adopted limiting magnitude. We re-calculate the detection efficiency for all fields and the number of source stars for limiting magnitudes of $I = 21$ and $I = 21.5$ mag. Then, we follow the methods described above to infer the 95% upper limits on the PBH abundance. The results of the calculations are presented in Extended Data Figure 7. Red and blue lines in Extended Data Figure 7 mark the limits for the limiting magnitudes of 21 and 21.5 mag, respectively, whereas black lines indicate the original limits calculated for the limiting magnitude of 22 mag.

As expected, the differences between the inferred limits are relatively small. The limits for the limiting magnitudes of 21.5 and 22 mag differ by at most $\Delta \log f = -0.10$ dex, for the limiting magnitudes of 21 and 22 mag—by at most $\Delta \log f = -0.20$ dex. This demonstrates that possible systematic effects related to the inclusion of faint source stars are very small and do not influence our conclusions.

The recent studies of the Galactic rotation curve by [28] and [44] seem to indicate that the mass of the dark matter Milky Way halo may be smaller than in the adopted model. If we use the “B2” halo model of [28] (with the Einasto profile of index 0.43), then the optical depth toward the center of the LMC is approximately 4.2×10^{-7} , and our limits on PBHs as dark matter are very similar to those calculated with the fiducial model (Extended Data Figure 1).

LMC proper motion and rotation

We use the *Gaia* EDR3 data to measure the mean LMC proper motion and to devise a simple model of the LMC rotation. The proper motion and rotation of the LMC (and other nearby dwarf galaxies) were extensively studied by [45] based on *Gaia* DR2 data and here we closely follow their approach. We select stars brighter than $G = 19$ that are located within 8 deg of the dynamical center of the HI LMC disk ($\alpha_0 = 78.77^\circ$, $\delta_0 = -69.01^\circ$) [37, 45], have a reliable astrometric solution (with $\text{RUWE} \leq 1.4$), and have parallaxes consistent with that of the LMC ($\varpi \leq 1$ mas and $\varpi/\sigma_\varpi \leq 10$), in total about 4.8 million sources. We then calculate the positions x , y and proper motions μ_x , μ_y of all stars in an orthographic projection centered at (α_0, δ_0) using equations:

$$\begin{aligned} x &= \cos \delta \sin(\alpha - \alpha_0), \\ y &= \sin \delta \cos \delta_0 - \cos \delta \sin \delta_0 \cos(\alpha - \alpha_0), \\ \mu_x &= \mu_\alpha \cos(\alpha - \alpha_0) - \mu_\delta \sin \delta \sin(\alpha - \alpha_0), \\ \mu_y &= \mu_\alpha \sin \delta_0 \sin(\alpha - \alpha_0) \\ &\quad + \mu_\delta (\cos \delta \cos \delta_0 + \sin \delta \sin \delta_0 \cos(\alpha - \alpha_0)). \end{aligned} \tag{7}$$

The median proper motions of the selected stars are presented in Extended Data Figure 8.

The median proper motion of the LMC (which is determined using stars located within 5° of the dynamical center) is $\mu_x = 1.851 \pm 0.340$ mas yr $^{-1}$ and $\mu_y = 0.277 \pm$

0.382 mas yr⁻¹, in good agreement with the results of [45]. Here the uncertainties denote the dispersion of proper motions in a given direction. This corresponds to $\mu_l = -0.662 \pm 0.381$ mas yr⁻¹ and $\mu_b = 1.751 \pm 0.342$ mas yr⁻¹ in the Galactic coordinates.

The proper motion pattern seen in the middle and bottom panels of Extended Data Figure 8 reflects the rotation of the LMC and, in the first order, can be approximated by the central value and two gradients. Additional striping pattern of lower amplitude is indicative of small-scale systematics in *Gaia* EDR3 [46]. To minimize their influence, we calculate the median proper motion (and its dispersion) in 100×100 bins in the range $|x| \leq 0.15$ rad and $|y| \leq 0.15$ rad and fit the following linear model to the binned data:

$$\begin{aligned}\mu_x &= \mu_{x,0} + \frac{\partial\mu_x}{\partial x}x + \frac{\partial\mu_x}{\partial y}y, \\ \mu_y &= \mu_{y,0} + \frac{\partial\mu_y}{\partial x}x + \frac{\partial\mu_y}{\partial y}y.\end{aligned}\tag{8}$$

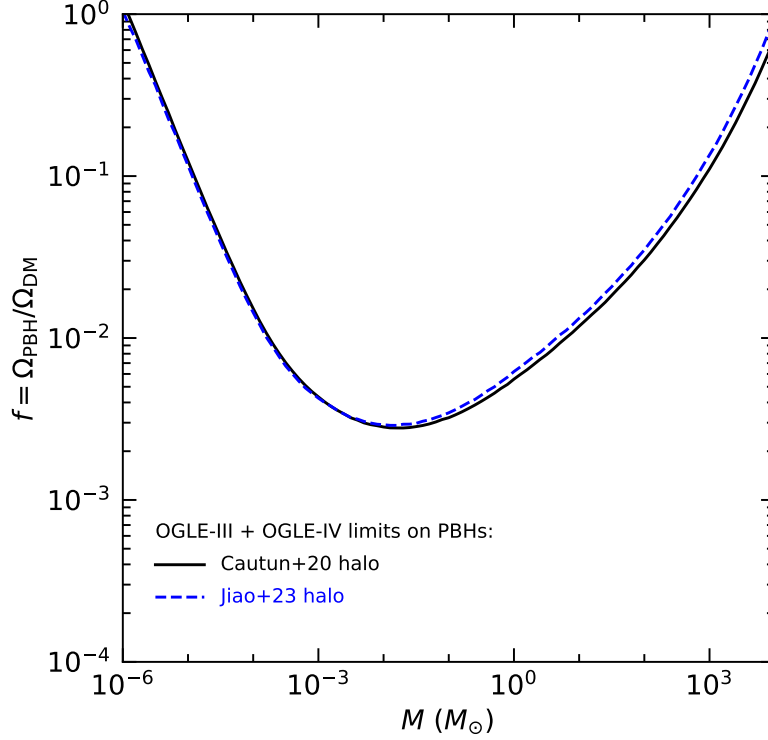
The six fit coefficients are determined using the least squares approach using bins with at least 10 stars. The model is fit in 7 annuli with a width of 1 deg. The best-fit parameters are presented in Extended Data Table 2.

Data availability

The data used to perform the analysis (event detection efficiencies, source star counts, posterior distributions of event parameters) are publicly available at https://www.astrouw.edu.pl/ogle/ogle4/LMC_OPTICAL_DEPTH/.

Code availability

The custom codes for the simulation of microlensing events toward the LMC and the calculation of limits on PBHs as dark matter are available upon request from the corresponding author.



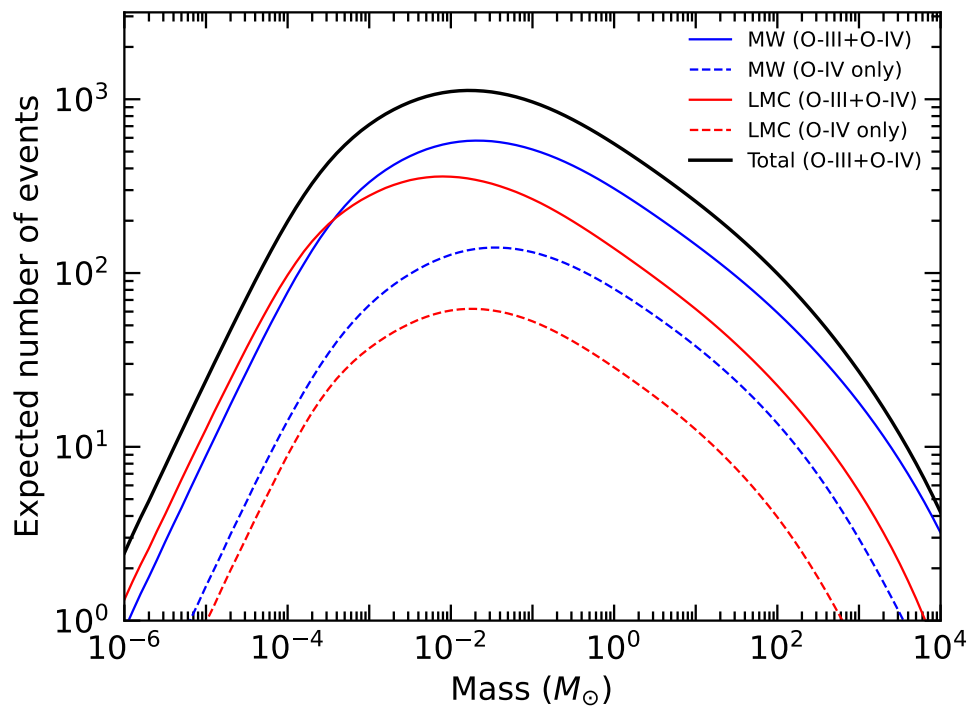
Extended Data Figure 1 95% upper limits on the PBH abundance for Cautun et al. (2020) [23] and Jiao et al. (2023) [28] dark matter halo models.

	OGLE-III & OGLE-IV	OGLE-IV Only	Total
Milky Way disk [24]	5.5	1.5	7.0
Milky Way disk [23]	11.5	3.2	14.7
LMC	5.3	0.4	5.7
Total (disk model [24])	10.8	1.9	12.7
Total (disk model [23])	16.8	3.6	20.4

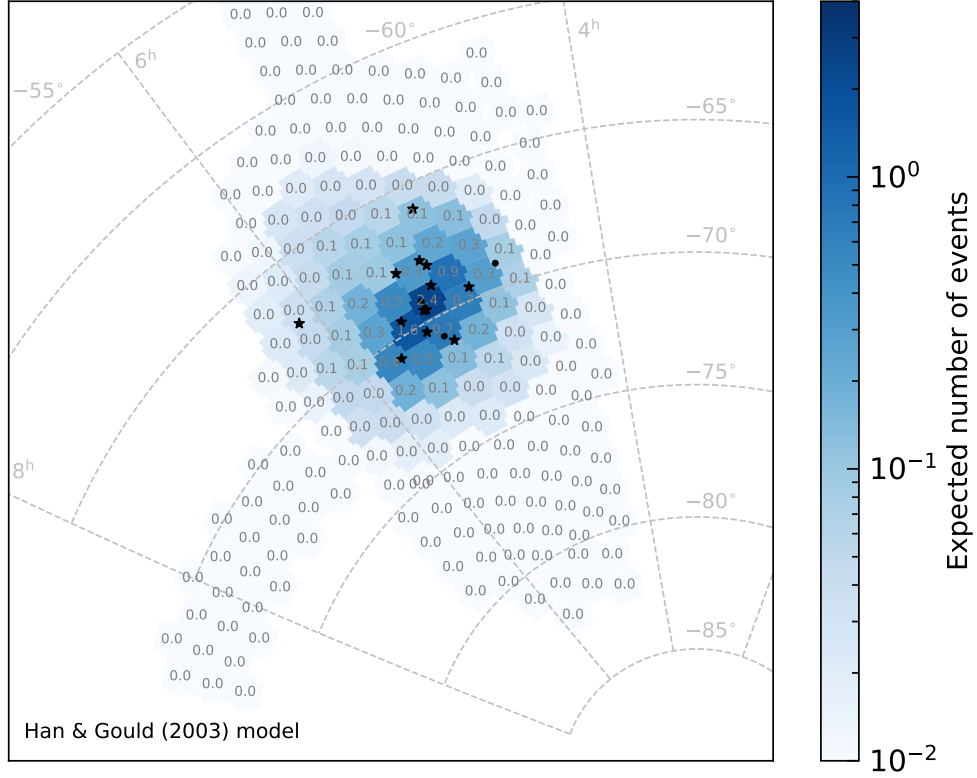
Extended Data Table 1 The expected number of microlensing events caused by astrophysical objects located in the Milky Way disk and the LMC.

ρ (deg)	$\partial\mu_x/\partial x$	$\partial\mu_x/\partial y$	$\mu_{x,0}$	$\partial\mu_y/\partial x$	$\partial\mu_y/\partial y$	$\mu_{y,0}$	$\text{rms}(\mu_x)$	$\text{rms}(\mu_y)$
$0 < \rho < 1$	-3.6832	-6.7018	1.8535	5.6324	-1.5691	0.2348	0.029	0.023
$1 < \rho < 2$	-2.3530	-5.6825	1.8565	5.7179	-0.7549	0.2135	0.041	0.027
$2 < \rho < 3$	-1.2292	-4.5601	1.8471	5.3498	-0.3510	0.2178	0.037	0.028
$3 < \rho < 4$	-1.0871	-3.5981	1.8355	4.5304	-0.5892	0.2357	0.035	0.036
$4 < \rho < 5$	-0.9070	-2.7004	1.8348	3.7424	-0.5745	0.2659	0.042	0.057
$5 < \rho < 6$	-0.7520	-2.1700	1.8430	3.2343	-0.4711	0.2770	0.049	0.058
$6 < \rho < 7$	-0.7497	-1.7328	1.8510	2.8296	-0.4742	0.2655	0.048	0.050

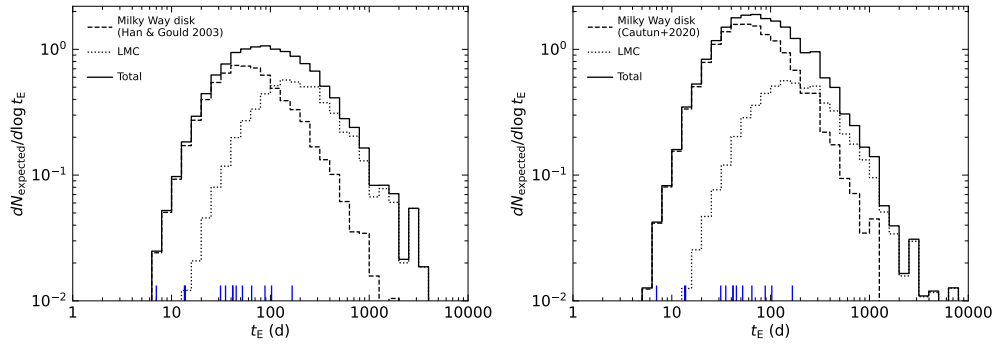
Extended Data Table 2 Parameters of the LMC proper motion model. Units of $\partial\mu_x/\partial x$, $\partial\mu_x/\partial y$, $\partial\mu_y/\partial x$, and $\partial\mu_y/\partial y$ are $\text{mas yr}^{-1} \text{ rad}^{-1}$, whereas $\mu_{x,0}$, $\mu_{y,0}$, $\text{rms}(\mu_x)$, and $\text{rms}(\mu_y)$ are given in mas yr^{-1} .



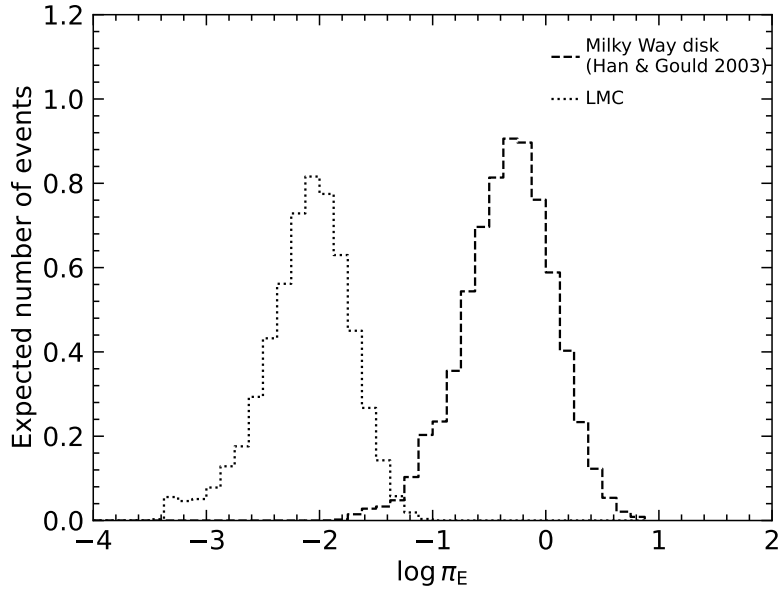
Extended Data Figure 2 Number of gravitational microlensing events expected to be detected by OGLE if entire dark matter were composed of compact objects of a given mass $N_{\text{exp}}(f = 1, M)$. Thin solid lines correspond to fields observed during OGLE-III and OGLE-IV phases (from 2001 to 2020), dashed lines – fields observed during OGLE-IV only (from 2010 to 2020). Blue lines mark the contribution from the Milky Way dark matter halo, red lines – the LMC dark matter halo.



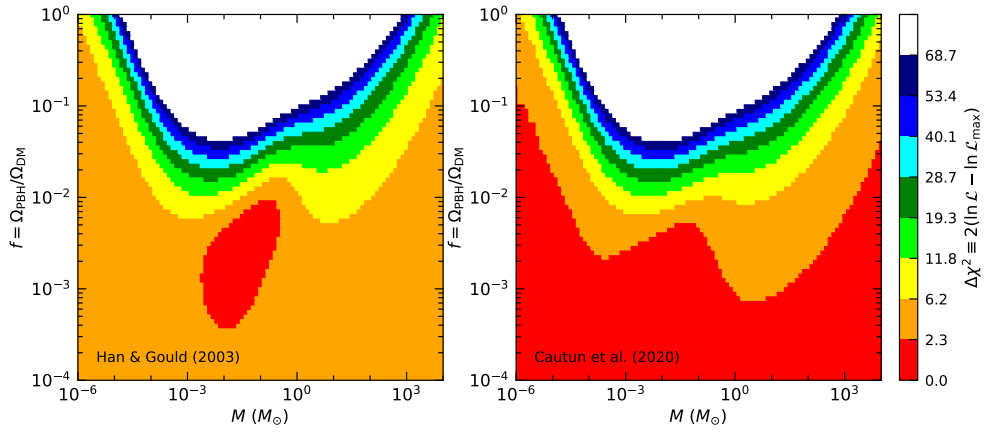
Extended Data Figure 3 Number of gravitational microlensing events from known stellar populations (Milky Way disk and LMC) expected to be detected by OGLE (assuming the [24] Milky Way disk model) in the analyzed fields. Black asterisks mark events that are a part of the statistical sample of [20], black dots mark other events.



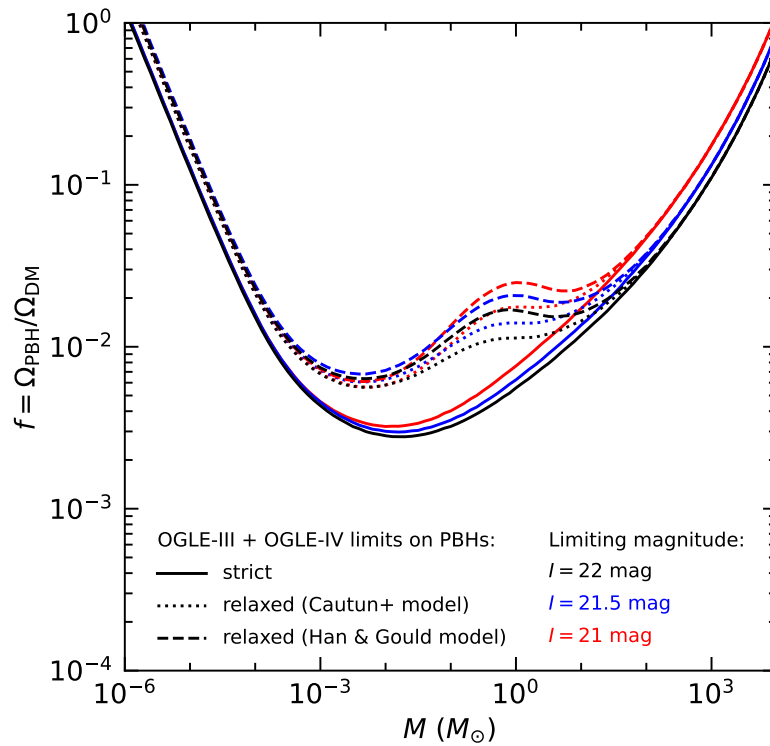
Extended Data Figure 4 Distribution of Einstein timescales of microlensing events that are expected to be detected in our experiment, for the [24] Milky Way disk model (left panel) and the [23] model (right). Vertical blue lines mark the detected events.



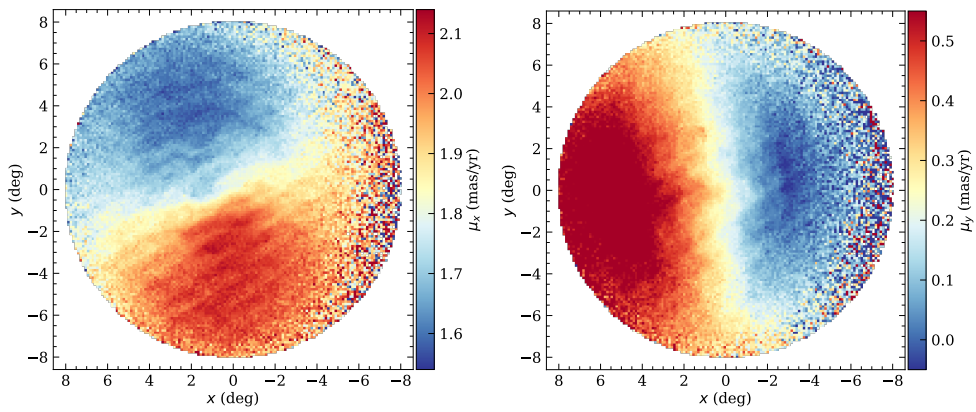
Extended Data Figure 5 Distribution of microlens parallaxes of events that are expected to be detected in our experiment (assuming the Milky Way disk model of [24]).



Extended Data Figure 6 The contours of the likelihood function (Eq. 1) for the [24] (left panel) and [23] Milky Way disk model (right panel). The color codes the difference $\Delta\chi^2 \equiv 2(\ln \mathcal{L}_{\max} - \ln \mathcal{L})$.



Extended Data Figure 7 95% upper limits on the PBH abundance as a function of the limiting magnitude.



Extended Data Figure 8 *Gaia* EDR3 proper motions of LMC stars.

References

- [1] Abbott, B. P. *et al.* Observation of Gravitational Waves from a Binary Black Hole Merger. *Phys. Rev. Lett.* **116**, 061102 (2016).
- [2] Abbott, B. P. *et al.* GWTC-1: A Gravitational-Wave Transient Catalog of Compact Binary Mergers Observed by LIGO and Virgo during the First and Second Observing Runs. *Phys. Rev. X* **9**, 031040 (2019).
- [3] Abbott, R. *et al.* Population Properties of Compact Objects from the Second LIGO-Virgo Gravitational-Wave Transient Catalog. *Astrophys. J. Lett.* **913**, L7 (2021).
- [4] Belczynski, K., Holz, D. E., Bulik, T. & O’Shaughnessy, R. The first gravitational-wave source from the isolated evolution of two stars in the 40-100 solar mass range. *Nature* **534**, 512–515 (2016).
- [5] Askar, A., Szkudlarek, M., Gondek-Rosińska, D., Giersz, M. & Bulik, T. MOCCA-SURVEY Database - I. Coalescing binary black holes originating from globular clusters. *Mon. Not. R. Astron. Soc.* **464**, L36–L40 (2017).
- [6] Rodriguez, C. L., Amaro-Seoane, P., Chatterjee, S. & Rasio, F. A. Post-Newtonian Dynamics in Dense Star Clusters: Highly Eccentric, Highly Spinning, and Repeated Binary Black Hole Mergers. *Phys. Rev. Lett.* **120**, 151101 (2018).
- [7] Bird, S. *et al.* Did LIGO Detect Dark Matter? *Phys. Rev. Lett.* **116**, 201301 (2016).
- [8] Sasaki, M., Suyama, T., Tanaka, T. & Yokoyama, S. Primordial Black Hole Scenario for the Gravitational-Wave Event GW150914. *Phys. Rev. Lett.* **117**, 061101 (2016).
- [9] Clesse, S. & García-Bellido, J. The clustering of massive Primordial Black Holes as Dark Matter: Measuring their mass distribution with advanced LIGO. *Phys. Dark Universe* **15**, 142–147 (2017).
- [10] Carr, B., Clesse, S., García-Bellido, J. & Kühnel, F. Cosmic conundra explained by thermal history and primordial black holes. *Phys. Dark Universe* **31**, 100755 (2021).
- [11] Jedamzik, K. Consistency of Primordial Black Hole Dark Matter with LIGO/Virgo Merger Rates. *Phys. Rev. Lett.* **126**, 051302 (2021).
- [12] Escrivà, A., Bagui, E. & Clesse, S. Simulations of PBH formation at the QCD epoch and comparison with the GWTC-3 catalog. *J. Cosmol. Astropart. P.* **2023**, 004 (2023).
- [13] Udalski, A., Szymański, M. K. & Szymański, G. OGLE-IV: Fourth Phase of the

- Optical Gravitational Lensing Experiment. *Acta Astronom.* **65**, 1–38 (2015).
- [14] Paczyński, B. Gravitational microlensing by the galactic halo. *Astrophys. J.* **304**, 1–5 (1986).
- [15] Alcock, C. *et al.* The MACHO Project: Microlensing Results from 5.7 Years of Large Magellanic Cloud Observations. *Astrophys. J.* **542**, 281–307 (2000).
- [16] Tisserand, P. *et al.* Limits on the Macho content of the Galactic Halo from the EROS-2 Survey of the Magellanic Clouds. *Astron. Astrophys.* **469**, 387–404 (2007).
- [17] Wyrzykowski, L. *et al.* The OGLE view of microlensing towards the Magellanic Clouds - IV. OGLE-III SMC data and final conclusions on MACHOs. *Mon. Not. R. Astron. Soc.* **416**, 2949–2961 (2011).
- [18] Blaineau, T. *et al.* New limits from microlensing on Galactic black holes in the mass range $10 M_{\odot} \leq M \leq 1000 M_{\odot}$. *Astron. Astrophys.* **664**, A106 (2022).
- [19] Udalski, A. The Optical Gravitational Lensing Experiment. Real Time Data Analysis Systems in the OGLE-III Survey. *Acta Astronom.* **53**, 291–305 (2003).
- [20] Mróz, P. *et al.* Microlensing optical depth and event rate toward the Large Magellanic Cloud based on 20 years of OGLE observations. *submitted* (2024).
- [21] Holtzman, J. A., Afonso, C. & Dolphin, A. The Local Group Stellar Populations Archive from the Hubble Space Telescope WFPC2. *Astrophys. J. Suppl. S.* **166**, 534–548 (2006).
- [22] Mróz, P. *et al.* No large population of unbound or wide-orbit Jupiter-mass planets. *Nature* **548**, 183–186 (2017).
- [23] Cautun, M. *et al.* The milky way total mass profile as inferred from Gaia DR2. *Mon. Not. R. Astron. Soc.* **494**, 4291–4313 (2020).
- [24] Han, C. & Gould, A. Stellar Contribution to the Galactic Bulge Microlensing Optical Depth. *Astrophys. J.* **592**, 172–175 (2003).
- [25] Niikura, H. *et al.* Microlensing constraints on primordial black holes with Subaru/HSC Andromeda observations. *Nature Astronomy* **3**, 524–534 (2019).
- [26] Sahu, K. C. Stars within the Large Magellanic Cloud as potential lenses for observed microlensing events. *Nature* **370**, 275–276 (1994).
- [27] Erkal, D. *et al.* The total mass of the Large Magellanic Cloud from its perturbation on the Orphan stream. *Mon. Not. R. Astron. Soc.* **487**, 2685–2700 (2019).

- [28] Jiao, Y. *et al.* Detection of the Keplerian decline in the Milky Way rotation curve. *Astron. Astrophys.* **678**, A208 (2023).
- [29] Clanton, C. & Gaudi, B. S. Synthesizing Exoplanet Demographics from Radial Velocity and Microlensing Surveys. I. Methodology. *Astrophys. J.* **791**, 90 (2014).
- [30] Eilers, A.-C., Hogg, D. W., Rix, H.-W. & Ness, M. K. The Circular Velocity Curve of the Milky Way from 5 to 25 kpc. *Astrophys. J.* **871**, 120 (2019).
- [31] Schaye, J. *et al.* The EAGLE project: simulating the evolution and assembly of galaxies and their environments. *Mon. Not. R. Astron. Soc.* **446**, 521–554 (2015).
- [32] Fattahi, A. *et al.* The APOSTLE project: Local Group kinematic mass constraints and simulation candidate selection. *Mon. Not. R. Astron. Soc.* **457**, 844–856 (2016).
- [33] Grand, R. J. J. *et al.* The Auriga Project: the properties and formation mechanisms of disc galaxies across cosmic time. *Mon. Not. R. Astron. Soc.* **467**, 179–207 (2017).
- [34] Griest, K. *et al.* Gravitational microlensing as a method of detecting disk dark matter and faint disk stars. *Astrophys. J. Lett.* **372**, L79–L82 (1991).
- [35] Varma, V. *et al.* Evidence of Large Recoil Velocity from a Black Hole Merger Signal. *Phys. Rev. Lett.* **128**, 191102 (2022).
- [36] Koposov, S. E. *et al.* Piercing the Milky Way: an all-sky view of the Orphan Stream. *Mon. Not. R. Astron. Soc.* **485**, 4726–4742 (2019).
- [37] van der Marel, R. P. & Kallivayalil, N. Third-epoch Magellanic Cloud Proper Motions. II. The Large Magellanic Cloud Rotation Field in Three Dimensions. *Astrophys. J.* **781**, 121 (2014).
- [38] Kroupa, P. On the variation of the initial mass function. *Mon. Not. R. Astron. Soc.* **322**, 231–246 (2001).
- [39] Gyuk, G., Dalal, N. & Griest, K. Self-lensing Models of the Large Magellanic Cloud. *Astrophys. J.* **535**, 90–103 (2000).
- [40] van der Marel, R. P., Alves, D. R., Hardy, E. & Suntzeff, N. B. New Understanding of Large Magellanic Cloud Structure, Dynamics, and Orbit from Carbon Star Kinematics. *Astron. J.* **124**, 2639–2663 (2002).
- [41] Pietrzyński, G. *et al.* A distance to the Large Magellanic Cloud that is precise to one per cent. *Nature* **567**, 200–203 (2019).
- [42] Foreman-Mackey, D., Hogg, D. W., Lang, D. & Goodman, J. emcee: The MCMC Hammer. *Publ. Astron. Soc. Pac.* **125**, 306 (2013).

- [43] Kim, S. *et al.* An H I Aperture Synthesis Mosaic of the Large Magellanic Cloud. *Astrophys. J.* **503**, 674–688 (1998).
- [44] Ou, X., Eilers, A.-C., Necib, L. & Frebel, A. The dark matter profile of the Milky Way inferred from its circular velocity curve. *Mon. Not. R. Astron. Soc.* **528**, 693–710 (2024).
- [45] Gaia Collaboration *et al.* Gaia Data Release 2. Kinematics of globular clusters and dwarf galaxies around the Milky Way. *Astron. Astrophys.* **616**, A12 (2018).
- [46] Lindegren, L. *et al.* Gaia Early Data Release 3. The astrometric solution. *Astron. Astrophys.* **649**, A2 (2021).

Study of forbidden β decays within the realistic shell model

G. De Gregorio,^{1,2} R. Mancino,^{3,4,5} L. Coraggio,^{1,2} and N. Itaco^{1,2}

¹*Dipartimento di Matematica e Fisica, Università degli Studi della Campania “Luigi Vanvitelli”,
viale Abramo Lincoln 5 - I-81100 Caserta, Italy*

²*Istituto Nazionale di Fisica Nucleare,
Complesso Universitario di Monte S. Angelo, Via Cintia - I-80126 Napoli, Italy*

³*Institute of Particle and Nuclear Physics, Faculty of Mathematics and Physics,
Charles University, V Holešovičkách 2, 180 00 Prague, Czech Republic*

⁴*Institut für Kernphysik (Theoriezentrum), Fachbereich Physik, Technische Universität Darmstadt,
Schlossgartenstrasse 2 - 64298 Darmstadt, Germany*

⁵*GSI Helmholtzzentrum für Schwerionenforschung, Planckstrasse 1, 64291 Darmstadt, Germany*

For the first time, half-lives and energy spectra of forbidden β decays are calculated within the realistic shell model. Namely, we approach this issue starting from a realistic nucleon-nucleon potential and deriving effective Hamiltonians and decay operators. Our goal is to explore the sensitivity of the shape of calculated energy spectra to the renormalization of forbidden β -decay operators, an operation that allows to take into account those configurations that are not explicitly included in the chosen model space. The region that has been considered for this investigation are nuclei outside the ^{78}Ni core, more precisely we have studied the second-forbidden β decays of ^{94}Nb and ^{99}Tc , and fourth-forbidden β decays of ^{113}Cd and ^{115}In , that are currently of a renewed experimental interest in terms of novel spectroscopic techniques. Our results evidence that the introduction of a renormalized β -decay operator leads to a marked improvement of the reproduction of experimental half-lives. As regards the spectra of both second-forbidden and fourth-forbidden decays, we have found that their calculated shapes are in good agreement with the observed ones, even if scarcely responsive to the renormalization of the decay operator. We carry out also a detailed inspection of the different components of the calculated spectra for a deeper insight about their role in reproducing the experimental shapes.

PACS numbers: 21.60.Cs, 21.30.Fe, 27.60.+j

I. INTRODUCTION

The understanding of the renormalization mechanisms of electroweak currents is nowadays a cornerstone of the nuclear structure research. The attention to this issue is motivated by the need of calculating reliable nuclear matrix elements $M^{0\nu}$ for the $0\nu\beta\beta$ decay, and relating the inverse half-life $[T_{1/2}^{0\nu}]^{-1}$ of such a rare process to the neutrino effective mass.

As a matter of fact, the accurate calculation of the wave functions of parent and grand-daughter nuclei does not ensure a trustable $M^{0\nu}$, since most nuclear models are based on the reduction of the dimension of the Hilbert space where the nuclear Hamiltonian is defined. Then, a sound knowledge of the renormalization of the electroweak currents, to account for the configurations that are not explicitly included in the components of the nuclear wave function, is crucial to enhance the predictivity of the calculated $M^{0\nu}$ s.

The ability of nuclear models to reproduce β -decay observables is, consequently, the better way to validate both wave functions and renormalization procedures, and such an issue is connected to the so-called “quenching puzzle” of the axial coupling constant, namely the need by most nuclear structure models to resort to a reduction of g_A to reproduce the observables directly linked to Gamow-Teller (GT) transitions [1–3]. However, this is an empirical procedure, and it cannot be generalized to any

β -decay operator that depends on the value of the axial coupling constant.

The realistic shell model (RSM) provides a consistent approach to derive effective Hamiltonians and decay operators, the only parameter that is involved being the nuclear force one starts from. In such a framework, single-particle (SP) energies and two-body matrix elements (TBMEs) of the effective shell-model Hamiltonian H_{eff} , as well as every matrix element of decay operators, are derived from a realistic free nucleon-nucleon (NN) potential V_{NN} by way of the many-body theory [4, 5]. The bare matrix elements of the NN potential, and of any transition operator, are renormalized with respect to the truncation of the full Hilbert space into the reduced shell-model (SM) model space, to take into account the neglected degrees of freedom without resorting to any empirical parameter [6]. In other words, this approach does not apply effective charges to calculate electromagnetic transition strengths, and empirical quenching of g_A to reproduce the β -decay matrix elements.

We have successfully employed RSM to study the $2\nu\beta\beta$ -decay of ^{48}Ca , ^{76}Ge , ^{82}Se , ^{100}Mo , ^{130}Te , and ^{136}Xe [7–10], and then extended it to predict the nuclear matrix elements of their $0\nu\beta\beta$ -decay [9, 11]. Now, in order to validate the RSM in predicting β -decay observables, in the present work we investigate the sensitivity to the renormalization of SM forbidden β -decay operators describing the energy spectra of the emitted electrons.

To this end, we have considered the second-forbidden

β -decays of ^{94}Nb and ^{99}Tc into ^{94}Mo and ^{99}Ru , as well as the fourth-forbidden β -decays of ^{113}Cd and ^{115}In into ^{113}In and ^{115}Sn , respectively, and compared their calculated $\log ft$ s and β -decay energy spectra as obtained with the bare and the renormalized decay operators, as well as with the available data.

The motivations of such a choice are twofold: first, these decays have been already the subject of a few works with a similar goal, where the effective operators was obtained tuning the quenching factor q of g_A , and the focus was spotted on the dependence of the shape of energy spectra on the value of q [12–16]. Second, novel experimental techniques have triggered new measurements of the energy spectra of β decays in the region of the $0\nu\beta\beta$ decay of ^{100}Mo . Among them, we mention the COBRA demonstrator [17], that has been developed for double- β decay experiments, and also adopted to study the spectra of β decays of ^{113}Cd [15, 18, 19]; the AC-CESS project that aims to perform precision measurements of forbidden β -decays using cryogenic calorimeters [20]. Another new experimental project is ASPECT-BET (An SDD-SPECTrometer for BETa decay studies), that has developed a new detection strategy based on silicon drift detectors (SDD), and it should be able to perform high-precision, high-accuracy measurements of the energy spectra of β decays at room temperature [21].

This paper is organized as follows. First, in Sec. II we sketch out briefly the derivation of the effective SM Hamiltonian and decay operators, as well as the basic theory of the β -decay and the structure of the second- and fourth-forbidden β -decay matrix elements.

The effective shell-model Hamiltonian and decay operators have been derived within a model space that is spanned by four $0f_{5/2}, 1p_{3/2}, 1p_{1/2}, 0g_{9/2}$ proton orbitals and five $0g_{7/2}, 1d_{5/2}, 1d_{3/2}, 2s_{1/2}, 0h_{11/2}$ neutron orbitals outside ^{78}Ni core starting from the high-precision CD-Bonn NN potential [22], whose repulsive high-momentum components are renormalized using the $V_{\text{low-}k}$ procedure [23]. This is the same framework we have employed in our previous study of the double- β decay of ^{100}Mo [9].

The results of the shell-model calculations are discussed and compared with the available experimental data in Sec. III. There, we check first our nuclear wave functions by comparing the calculated low-energy spectra and $E2$ transition strengths of parent and daughter nuclei, which are involved in the decays under consideration, with their experimental counterparts. Then, we report the results of our theoretical $\log ft$ s and energy spectra of the emitted electron and size up them to the available data. We complete our analysis with a detailed analysis of the different components of the spectra, and how the interplay among their contributions plays an important role in reproducing data.

In the last section (Sec. IV), we summarize the conclusions of this study, as well as the outlook of our current research project.

II. OUTLINE OF THE THEORY

A. The effective SM Hamiltonian

The procedure of the derivation of the effective SM Hamiltonian is the same as the one followed in Ref. [9]. First, we consider the high-precision CD-Bonn NN potential [22], then the non-perturbative repulsive high-momentum components are integrated out, by way of the $V_{\text{low-}k}$ unitary transformation [23, 24], that provides a smooth potential preserving all the two-nucleon observables calculated with the CD-Bonn one.

The $V_{\text{low-}k}$ matrix elements are chosen as the interaction vertices of a perturbative expansion of H_{eff} , and a detailed description of the many-body perturbation theory approach to the nuclear H_{eff} can be found in Refs. [6, 25, 26], so here we only sketch briefly the steps that have been followed to obtain H_{eff} .

The starting point is the full nuclear Hamiltonian H for A interacting nucleons, which, according to the SM ansatz, is divided into the one-body term H_0 , whose eigenvectors set up the SM basis, and the residual interaction H_1 , using the harmonic-oscillator (HO) auxiliary potential U :

$$\begin{aligned} H &= T + V_{\text{low-}k} = (T + U) + (V_{\text{low-}k} - U) = \\ &= H_0 + H_1 . \end{aligned} \quad (1)$$

The eigenvalue problem of H for a many-body system, in an infinite basis of eigenvectors of H_0 , cannot be solved, then an effective Hamiltonian is derived, which is defined in the truncated model space spanned by four proton – $0f_{5/2}, 1p_{3/2}, 1p_{1/2}, 0g_{9/2}$ – and five neutron orbitals – $0g_{7/2}, 1d_{5/2}, 1d_{3/2}, 2s_{1/2}, 0h_{11/2}$ – outside ^{78}Ni core.

The effective Hamiltonian is derived by way of the time-dependent perturbation theory, through the Kuo-Lee-Ratcliff folded-diagram expansion in terms of the \hat{Q} -box vertex function [4, 25, 26]:

$$H_1^{\text{eff}}(\omega) = \hat{Q}(\epsilon_0) - PH_1Q \frac{1}{\epsilon_0 - QHQ} \omega H_1^{\text{eff}}(\omega) , \quad (2)$$

where ω is the wave operator decoupling the model space P and its complement Q , and ϵ_0 is the eigenvalue of the unperturbed degenerate Hamiltonian H_0 .

The \hat{Q} box is defined as

$$\hat{Q}(\epsilon) = PH_1P + PH_1Q \frac{1}{\epsilon - QHQ} QH_1P , \quad (3)$$

and ϵ is an energy parameter called “starting energy”.

Since the exact calculation of the \hat{Q} box is not possible, then the term $1/(\epsilon - QHQ)$ is expanded as a power series

$$\frac{1}{\epsilon - QHQ} = \sum_{n=0}^{\infty} \frac{1}{\epsilon - QH_0Q} \left(\frac{QH_1Q}{\epsilon - QH_0Q} \right)^n , \quad (4)$$

namely we perform an expansion of the \hat{Q} box up to the third order in perturbation theory [6].

As a matter of fact, the calculation of the \hat{Q} box is the start to solve the non-linear matrix equation (2) and obtain H_{eff} by way of iterative techniques such as the Kuo-Krenciglowa and Lee-Suzuki ones [27, 28], or graphical non-iterative methods [29].

It should be pointed out that, since the nuclei that are involved in the decay processes under investigation are characterized by a large number of valence nucleons, we have included contributions from induced three-body forces in the calculation of the \hat{Q} box, that involve also three valence nucleons.

Since the SM code we have employed for our calculations [30] cannot diagonalize a three-body H_{eff} , we have performed a normal-ordering decomposition of the three-body induced-force contributions arising at second order in perturbation theory, and retained only the two-body term that is density-dependent from the number of valence nucleons. This procedure is presented in details in Refs. [6, 31], together with a discussion about the contribution of such terms to the eigenvalues of the SM Hamiltonian.

The SM parameters, namely the SP energies and the TBMEs of the residual interaction, are reported in the Supplemental Material [32].

B. β -decay theory

The theory of β -decay is here briefly outlined. More details can be found in Refs. [33, 34].

In the following we focus on the β^- -decay, moreover, we use natural units ($\hbar = c = m_e = 1$).

The total half-life of the β decay is expressed in terms of the k -th partial decay half-life $t_{1/2}^k$ as follows:

$$\frac{1}{T_{1/2}} = \sum_k \frac{1}{t_{1/2}^k}. \quad (5)$$

On the other hand, the partial half-life $t_{1/2}^k$ is related to the dimensionless integrated shape function \tilde{C} by way of the relation:

$$t_{1/2}^k = \frac{\kappa}{\tilde{C}}, \quad (6)$$

where $\kappa = 6144 \pm 2$ s [35].

For a given k -th final state, the integrated shape function \tilde{C} – whose integrand defines the β -decay energy spectrum – is written as

$$\tilde{C} = \int_1^{w_0} C(w_e) p_e w_e (w_0 - w_e)^2 F(Z, w_e) dw_e. \quad (7)$$

The quantities on the right-hand side of the above definition are listed as:

- a) Z is the atomic number of the daughter nucleus, w_e the adimensional energy of the emitted electron, w_0 the endpoint energy – namely the maximum electron energy for a given transition –, and p_e the electron momentum.
- b) The function $F(Z, w_e)$ is the Fermi function which is factorized in terms of two functions F_0 and L_0 :

$$F(Z, w_e) = F_0(Z, w_e) L_0(Z, w_e), \quad (8)$$

where F_0 defines the effects of the Coulomb interaction between the electron and the daughter nucleus, and L_0 accounts for the electromagnetic finite-size effect, whose explicit expressions can be found in Ref. [33].

- c) $C(w_e)$ is the so-called nuclear shape function, which depends on the nuclear matrix elements (NMEs). For allowed β transitions, it corresponds to the GT reduced transition probability, and in such a case does not depend on the electron energy.

For n -forbidden transitions, $C(w_e)$ depends on the electron energy, and is expressed as

$$C(w_e) = \sum_K \sum_{k_e, k_\nu} \lambda_{k_e} \left[M_K^2(k_e, k_\nu) + m_K^2(k_e, k_\nu) - \frac{2\gamma_{k_e}}{k_e w_e} M_K(k_e, k_\nu) m_K(k_e, k_\nu) \right], \quad (9)$$

where K is the tensor rank of the forbidden β -decay operators involved in the decay. K can range from 0 to 2 for $n = 1$, and from n to $n + 1$ for $n > 1$. The quantities k_e and k_ν are the positive integers emerging from the partial wave expansion of the leptonic wave functions. The latter, for a given value of K , must satisfy either $k_e + k_\nu = K + 1$ or $k_e + k_\nu = K + 2$.

The auxiliary quantities γ_{k_e} and λ_{k_e} are defined as

$$\gamma_{k_e} = \sqrt{k_e^2 - (\alpha Z)^2}, \quad \lambda_{k_e} = \frac{F_{k_e-1}(Z, w_e)}{F_0(Z, w_e)}, \quad (10)$$

where $F_{k_e-1}(Z, w_e)$ is the so-called generalized Fermi function (see Ref. [33] for its explicit expression). The quantities M_K and m_K are complicated combinations of some kinematic factors and coefficients $F_{KLS}^{(N)}(k_e, m, n, \rho)$, the latter being functions of the orbital, spin, and total rank of the transition operators L , S , and K , respectively, and the integers m , n and ρ depending on the nuclear charge distribution which accounts for the influence of the nuclear charge on the electron [33, 34]. The index N labels the order of the expansion in powers of qR (where R is the nuclear radius and q is the momentum transfer $q = |p_e + p_\nu|$) of the nuclear form factor F_{KLS} , which is defined by the following expression

$$F_{KLS}(q^2) = \sum_N \frac{(-1)^N (qR)^{2N} (2L+1)!!}{(2N)!! (2L+2N+1)!!} F_{KLS}^{(N)}. \quad (11)$$

If we adopt the impulse approximation ($qR \ll 1$) to derive the formalism of forbidden β -decay transitions, and also assume that bound nucleons interact weakly as free nucleons, then we may neglect the effect of any many-body current. Within such an approximation, it has been shown in Refs. [33, 34] that the form factor coefficients $V/A F_{KLS}^{(N)}(k_e, m, n, \rho)$ can be related to the NMEs

$V/A M_{KLS}^N(k_e, m, n, \rho)$ by a phase factor:

$$V/A F_{KLS}^{(N)}(k_e, m, n, \rho) = (-1)^{K-L} V/A M_{KLS}^N(k_e, m, n, \rho), \quad (12)$$

where the label V/A indicates the separation of the coefficients $F_{KLS}^{(N)}(k_e, m, n, \rho)$ according to the axial and vector components of the decay operator.

In a shell-model calculation, the NMEs can be expressed in terms of the single-particle matrix elements of the one-body decay operator (SPMEs) and the one-body transition densities (OBTDs), that can be obtained from the shell-model wave functions, through the expression

$$V/A M_{KLS}^{(N)}(k_e, m, n, \rho) = \frac{1}{\hat{J}_i} \sum_{\pi, \nu} V/A m_{KLS}^{(N)}(\pi, \nu)(k_e, m, n, \rho) \times \text{OBTD}(\Psi_f, \Psi_i, \pi, \nu, K), \quad (13)$$

where $\hat{J}_i = \sqrt{2J_i + 1}$, and J_i is the angular momentum of the initial state of the parent nucleus. The OBTDs are defined as

$$\text{OBTD}(\Psi_f, \Psi_i, \pi, \nu, K) = \frac{\langle \Psi_f || [a_\pi^\dagger \otimes \tilde{a}_\nu]^K || \Psi_i \rangle}{\hat{K}}, \quad (14)$$

where Ψ_i and Ψ_f are the wave function of the initial and

final state, respectively, a_π^\dagger is the particle creation operator, and $\tilde{a}_\nu = (-1)^{j_\nu + m_\nu} a_{\nu - m_\nu}$ is the tensor spherical form of the particle annihilation operator (a_ν). The indices π and ν label the proton (π) and neutron (ν) single-particle states, and the symbol \otimes denotes the angular-momentum coupling.

The SPMEs correspond to the following matrix elements:

$$V m_{KLS}^{(N)}(k_e, m, n, \rho) = \langle \phi_{\kappa\pi\mu} || \left(\frac{r}{R}\right)^{L+2N} \mathcal{I}(k_e, m, n, \rho, r) T_{KLS} || \phi_{\kappa\nu\mu} \rangle, \quad (15)$$

$$A m_{KLS}^{(N)}(k_e, m, n, \rho) = \langle \phi_{\kappa\pi\mu} || \left(\frac{r}{R}\right)^{L+2N} \mathcal{I}(k_e, m, n, \rho, r) \gamma_5 T_{KLS} || \phi_{\kappa\nu\mu} \rangle. \quad (16)$$

Now, it is worth to list and specify the quantities which appear in the Eqs. (15,16) for the matrix elements of the vector and axial components of the β -decay operator:

- The functions $\mathcal{I}(k_e, m, n, \rho, r)$ are the so-called Coulomb factors whose explicit expression can be found in Ref. [33].
- The operator T_{KLS} is the transition operator defined as

$$T_{KLS}^M = \begin{cases} Y_{LM} \delta_{KL} & S = 0, \\ (-1)^{L-K+1} \gamma_5 [Y_L \otimes \sigma]_{KM} & S = 1. \end{cases} \quad (17)$$

- The single-particle relativistic wave functions $\phi_{\kappa\mu}$ are the eigenfunctions of the operators J_z and $\mathcal{K} = \beta(\sigma \cdot L + \mathbb{I})$, and are labeled by their eigenvalues μ and κ :

$$\begin{aligned} J_z \phi_{\kappa\mu} &= \mu \phi_{\kappa\mu}, \\ \mathcal{K} \phi_{\kappa\mu} &= \beta(\sigma \cdot L + \mathbb{I}) \phi_{\kappa\mu} = \kappa \phi_{\kappa\mu}. \end{aligned}$$

It can be shown that the eigenvalue κ is related to the total and orbital angular momenta j and l through the relation

$$\kappa = \begin{cases} j + \frac{1}{2} & \text{for } l = j + \frac{1}{2} \\ -(j + \frac{1}{2}) & \text{for } l = j - \frac{1}{2}. \end{cases} \quad (18)$$

In the Condon-Shortley (CS) phase convention, the $\phi_{\kappa\mu}$ functions are defined as

$$\phi_{\kappa\mu} = \begin{pmatrix} -i f_\kappa(r) \chi_{-\kappa\mu} \\ g_\kappa(r) \chi_{\kappa\mu} \end{pmatrix}, \quad (19)$$

where $\chi_{\kappa\mu} = [Y_l(\hat{r}) \otimes \chi]^{j\mu}$, and the radial functions $f_\kappa(r)$ and $g_\kappa(r)$ are the solutions of the radial Dirac equations, and they are usually indicated as the *small* and *large*

components, respectively:

$$\frac{dg_\kappa(r)}{dr} + \frac{\kappa+1}{r}g_\kappa(r) - (E+M-V(r))f_\kappa(r) = 0, \quad (20)$$

$$\frac{df_\kappa(r)}{dr} - \frac{\kappa-1}{r}f_\kappa(r) + (E-M-V(r))g_\kappa(r) = 0. \quad (21)$$

The matrix elements of Eqs. (15,16) can be grouped

$$\begin{aligned} V m_{KK0}^{(N)}(\pi, \nu)(k_e, m, n, \rho) = & \sqrt{2}g_V \left[G_{KK0}(\kappa_\pi, \kappa_\nu) \int_0^\infty g_\pi(r, \kappa_\pi) \left(\frac{r}{R}\right)^{K+2N} \mathcal{I}(k_e, m, n, \rho, r) g_\nu(r, \kappa_\nu) r^2 dr \right. \\ & \left. + G_{KK0}(-\kappa_\pi, -\kappa_\nu) \int_0^\infty f_\pi(r, \kappa_\pi) \left(\frac{r}{R}\right)^{K+2N} \mathcal{I}(k_e, m, n, \rho, r) f_\nu(r, \kappa_\nu) r^2 dr \right], \end{aligned} \quad (22)$$

$$\begin{aligned} A m_{K L 1}^{(N)}(\pi, \nu)(k_e, m, n, \rho) = & \text{sign}(K-L+\frac{1}{2})\sqrt{2}g_A \left[G_{KK0}(\kappa_\pi, \kappa_\nu) \int_0^\infty g_\pi(r, \kappa_\pi) \left(\frac{r}{R}\right)^{L+2N} \mathcal{I}(k_e, m, n, \rho, r) g_\nu(r, \kappa_\nu) r^2 dr \right. \\ & \left. + G_{KK0}(-\kappa_\pi, -\kappa_\nu) \int_0^\infty f_\pi(r, \kappa_\pi) \left(\frac{r}{R}\right)^{L+2N} \mathcal{I}(k_e, m, n, \rho, r) f_\nu(r, \kappa_\nu) r^2 dr \right]. \end{aligned} \quad (23)$$

The second group contains the product of the small and large components of the initial and final wave func-

into two different types.

The first one contains the product of both small components of the initial and final wave functions, as well as the product of both large components of the same wave functions, which are the solutions of the coupled equations (20,21), and usually they are dubbed in literature as the *non-relativistic* matrix elements [33, 34, 36, 37]. Their explicit expression is:

tions that are the solutions of Eqs. (20,21), and in such a case they are dubbed as the *relativistic* matrix elements. Now, their expression is:

$$\begin{aligned} V m_{KL1}^{(N)}(\pi, \nu)(k_e, m, n, \rho) = & \text{sign}(K-L+\frac{1}{2})\sqrt{2}g_V \left[G_{KL1}(\kappa_\pi, -\kappa_\nu) \int_0^\infty g_\pi(r, \kappa_\pi) \left(\frac{r}{R}\right)^{L+2N} \mathcal{I}(k_e, m, n, \rho, r) f_\nu(r, \kappa_\nu) r^2 dr \right. \\ & \left. - G_{KK0}(-\kappa_\pi, \kappa_\nu) \int_0^\infty f_\pi(r, \kappa_\pi) \left(\frac{r}{R}\right)^{L+2N} \mathcal{I}(k_e, m, n, \rho, r) g_\nu(r, \kappa_\nu) r^2 dr \right], \end{aligned} \quad (24)$$

$$\begin{aligned} A m_{KK0}^{(N)}(\pi, \nu)(k_e, m, n, \rho) = & \sqrt{2}g_A \left[G_{KK0}(\kappa_\pi, -\kappa_\nu) \int_0^\infty g_\pi(r, \kappa_\pi) \left(\frac{r}{R}\right)^{K+2N} \mathcal{I}(k_e, m, n, \rho, r) f_\nu(r, \kappa_\nu) r^2 dr \right. \\ & \left. - G_{KK0}(-\kappa_\pi, \kappa_\nu) \int_0^\infty f_\pi(r, \kappa_\pi) \left(\frac{r}{R}\right)^{K+2N} \mathcal{I}(k_e, m, n, \rho, r) g_\nu(r, \kappa_\nu) r^2 dr \right]. \end{aligned} \quad (25)$$

It is worth to note that in the above equations we have introduced the quantity

$$\begin{aligned} G_{KLS}(\kappa_\pi, \kappa_\nu) = & (-1)^{j_\pi - j_\nu + l_\pi} \hat{S} \hat{K} \hat{j}_\pi \hat{j}_\nu \hat{l}_\pi \hat{l}_\nu \langle l_\pi l_\nu 00 | L0 \rangle \times \\ & \begin{Bmatrix} K & S & L \\ j_\pi & \frac{1}{2} & l_\pi \\ j_\nu & \frac{1}{2} & l_\nu \end{Bmatrix}, \end{aligned} \quad (26)$$

and we remind that L , S , and K are the orbital, spin, and total rank of the transition operators, respectively, and $l_\tau = k_\tau$ if $k_\tau > 0$ and $l_\tau = |k_\tau| - 1$ if $k_\tau < 0$.

Until now, the nucleon wave functions are expressed in a fully relativistic framework, being the solutions of the Dirac equation. However, within the nuclear shell model, the nucleon wave functions are expressed as solutions of the single-particle Schrödinger equation, introducing the auxiliary harmonic-oscillator potential.

Such an inconsistency impacts especially on the calculation of the *relativistic* matrix elements, and this problem may be tackled in two ways. The first approach is to resort to a non-relativistic reduction of the Dirac equation by considering the non-relativistic limit of the coupled Eqs. (20,21), namely the kinetic energy T and the auxiliary potential $V(r)$ satisfy the conditions $T = E - M_N \ll 2M_N$ and $V(r) \ll 2M_N$ [38]. Within this limit, the function g_κ becomes the solution of the Schrödinger equation, and f_κ is related to g_κ through the relation

$$f_\kappa(r) = \frac{1}{2M_N} \left(\frac{d}{dr} + \frac{\kappa+1}{r} \right) g_\kappa(r). \quad (27)$$

However, as it was observed in Ref. [33], whether or not such a limit of the Dirac equation is a good approximation to calculate the *relativistic* NMEs is a difficult question to answer, since to test this approach a fully rel-

ativistic calculation should be performed and compared with the approximated results.

Moreover, it should be noted that, if we consider the relation (27), the radial function $f_\kappa(r)$ is suppressed by a factor $1/(2M_N)$ with respect to the function $g_\kappa(r)$, but the *relativistic* form factor, even if it is small with respect to the *non-relativistic* ones, it has been found to be relevant to determine both the shape of the energy spectrum and the half-life of the β decay [34, 36, 39–41].

Its relevance, within such a reduction of the Dirac equation, is also stressed in Ref. [15], where a study of the dependence of the energy spectrum and half-life of the fourth-forbidden β decay of ^{113}Cd with respect to the quenching factor q of the axial coupling constant g_A has been carried out. As a matter of fact, the authors show that a fitting procedure of both q and of the *relativistic* form factor is needed to reproduce the experimental shape of the energy spectrum as well as the observed half-life.

An alternative approach to calculate the *relativistic* NMEs, is to resort to the conserved vector current theory (CVC) [33], which leads to derive a connection between the *relativistic* NMEs and the *non-relativistic* ones, that is developed as a relation between the corresponding form factors. An early application of this approach can be found in Ref. [36].

In particular, for the four decays under investigation, since we stop at the leading order in the expansion of $F_{KLS}(q^2)$ ($N = 0$ in Eq. (11)), the *relativistic* form factors entering in Eq. (9) are only the ${}^V F_{211}$, for the second-forbidden decay of ^{94}Nb , ^{99}Tc , and the ${}^V F_{431}$ for the fourth-forbidden decay of ^{113}Cd , ^{115}In . These form factors, using the CVC relation [33, 36], depends on ${}^V F_{220}$ and ${}^V F_{440}$, respectively, through the relations

$${}^V F_{211} = -\frac{1}{\sqrt{10}} R E_\gamma {}^V F_{220}, \quad {}^V F_{431} = -\frac{1}{\sqrt{36}} R E_\gamma {}^V F_{440}, \quad (28)$$

where

$$E_\gamma = [W_0 + \Delta E_C - (M_\nu - M_\pi)], \quad (29)$$

is the energy of the analogue electromagnetic transition [42], $M_{\nu(\pi)}$ is the neutron (proton) mass, and ΔE_C is the Coulomb displacement energy that can be evaluated in different ways. ΔE_C can be evaluated in different ways, here we have used the results of the fit procedure as outlined in Ref. [43], obtaining $\Delta E_C = 11.99, 12.38, 13.27,$ and 13.48 MeV for ^{94}Nb , ^{99}Tc , ^{113}Cd , and ^{115}In decays, respectively.

It is important to stress that these CVC relations have been employed in different studies, leading to a general improvement of the calculated spectra [34, 36, 39–41] and half-lives.

However, we point out that these relations are valid in the full nuclear Hilbert space of the single-particle configurations, and it is difficult to evaluate the impact of resorting to a truncated model space, but, on the other hand, it should be noted that our approach relies on the

derivation of effective Hamiltonians and operators by way of the many-body theory to account for the configurations outside the model space.

Nevertheless, the CVC relations for the relativistic form factors represent a viable route to get an estimation of the *relativistic* matrix elements entering the calculation, and/or, to understand the reliability of the non-relativistic reduction of the *relativistic* matrix elements.

C. Effective shell-model decay operators

In this section, we sketch briefly the procedure to derive effective SM decay operators Θ_{eff} by way of many-body perturbation theory.

As is well known, the diagonalization of the H_{eff} does not produce the true nuclear wave-functions, but their projections onto the chosen model space P . Then, any decay operator Θ should be renormalized by taking into account for the neglected degrees of freedom corresponding to the Q subspace.

The derivation of effective SM operators within a perturbative approach traces back to the pioneering period of employing NN potentials in SM calculations [44–49]. We have followed the method that has been introduced by Suzuki and Okamoto [5], which allows a derivation of decay operators Θ_{eff} which is consistent with the one of H_{eff} , as presented in Sec. II A. This is based on the perturbative expansion of a vertex function $\hat{\Theta}$ box – analogously with the derivation of H_{eff} in terms of the \hat{Q} box –, whose details may be found in Refs. [5, 6].

According to such a procedure, the starting point is the perturbative calculation of two energy-dependent vertex functions:

$$\hat{\Theta}(\epsilon) = P\Theta P + P\Theta Q \frac{1}{\epsilon - QHQ} QH_1 P,$$

$$\hat{\Theta}(\epsilon_1; \epsilon_2) = PH_1 Q \frac{1}{\epsilon_1 - QHQ} Q\Theta Q \frac{1}{\epsilon_2 - QHQ} QH_1 P,$$

and of their derivatives calculated in $\epsilon = \epsilon_0$, ϵ_0 being the eigenvalue of the degenerate unperturbed Hamiltonian H_0 :

$$\hat{\Theta}_m = \frac{1}{m!} \left. \frac{d^m \hat{\Theta}(\epsilon)}{d\epsilon^m} \right|_{\epsilon=\epsilon_0},$$

$$\hat{\Theta}_{mn} = \frac{1}{m!n!} \left. \frac{d^m}{d\epsilon_1^m} \frac{d^n}{d\epsilon_2^n} \hat{\Theta}(\epsilon_1; \epsilon_2) \right|_{\epsilon_1=\epsilon_0, \epsilon_2=\epsilon_0}$$

Then, a series of operators χ_n is calculated:

$$\begin{aligned}
\chi_0 &= (\hat{\Theta}_0 + h.c.) + \hat{\Theta}_{00} , \\
\chi_1 &= (\hat{\Theta}_1 \hat{Q} + h.c.) + (\hat{\Theta}_{01} \hat{Q} + h.c.) , \\
\chi_2 &= (\hat{\Theta}_1 \hat{Q}_1 \hat{Q} + h.c.) + (\hat{\Theta}_2 \hat{Q} \hat{Q} + h.c.) + \\
&\quad (\hat{\Theta}_{02} \hat{Q} \hat{Q} + h.c.) + \hat{Q} \hat{\Theta}_{11} \hat{Q} . \\
&\dots
\end{aligned} \tag{31}$$

At the end, Θ_{eff} is written in the following form:

$$\Theta_{\text{eff}} = H_{\text{eff}} \hat{Q}^{-1} (\chi_0 + \chi_1 + \chi_2 + \dots) , \tag{32}$$

the χ_n series being arrested in our calculations at $n = 2$, and the $\hat{\Theta}$ function expanded up to third order in perturbation theory.

In Refs. [8, 11, 50] we have tackled the issue of the convergence of the χ_n series and of the perturbative expansion of the $\hat{\Theta}$ box, showing the robustness of such a procedure.

It is worth to point out that, even if the decay operator has a one-body structure, the shell-model effective operator has many-body components which account for a number of valence of nucleons larger than one [11, 47]. As a matter of fact, the fourth-forbidden β decay of ^{115}In into ^{115}Sn involves 37 valence nucleons outside the doubly-magic ^{78}Ni , then for such a process Θ_{eff} should contain contributions up to a 37-body term.

The shell-model code KSHELL can employ transition operators with a one- and two-body components [30], then for the calculation of β -decay effective operators we include just the leading terms of these many-body contributions in the perturbative expansion of the $\hat{\Theta}$ box, namely the second-order two-body diagrams (a) and (b), that are reported in Fig. 1.

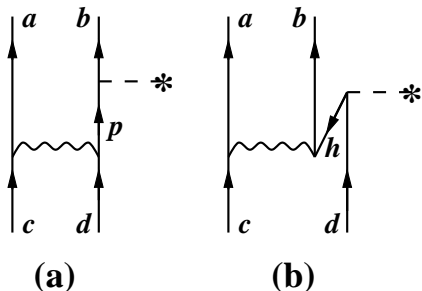


FIG. 1. Second-order two-body diagrams which are included in the perturbative expansion of Θ_{eff} . The dashed line indicates the bare second- and fourth-forbidden β -decay operators Θ , the wavy line the two-body potential $V_{\text{low-}k}$. For the sake of simplicity, for each topology only one of the diagrams which correspond to the permutation of the external lines has been drawn.

The two topologies of second-order connected two-valence-nucleon diagrams (a) and (b) accounts for the so-called “blocking effect”, which is necessary to consider the Pauli exclusion principle in systems with more than

one valence nucleon [49], if the transition operator has a one-body structure. It is worth to point out that these two-body contributions to the effective decay operators mirror the role of induced three-body forces in the calculation of the \hat{Q} box, which we have introduced in section II A.

In the present work, the decay operators Θ are the one-body electric-quadrupole $E2$ transition $q_{p,n} r^2 Y_m^2(\hat{r})$ – the charge $q_{p,n}$ being e for protons and 0 for neutrons –, as well as the one-body second- and fourth-forbidden β -decay operators, as introduced in Sec. II B.

III. RESULTS

In this section we present the results of our SM calculations. First, we compare theoretical and experimental low-energy spectroscopic properties of the parent and daughter nuclei under investigation, namely ^{94}Nb , ^{94}Mo , ^{99}Tc , ^{99}Ru , ^{113}Cd , ^{113}In , ^{115}In and ^{115}Sn . Successively, we focus to study β -decay properties between the ground states (g.s.) of these nuclei.

We point out that, rather than compare the experimental and calculated half-lives, we consider the quantity $\log ft$ to describe the strength of a β -transition. This is defined as the logarithm of

$$ft = \frac{\kappa}{\bar{C}} \int_1^{w_0} p_e w_e (w_0 - w_e)^2 F(Z, w_e) dw_e . \tag{33}$$

It is worth to stress again that all the calculations have been performed without any empirical renormalization of H_{eff} , as well as without resorting to quenching factors of the axial constant g_A .

A. Spectroscopy

In Table I we compare the low-energy spectra of the nuclei under investigation.

The calculated energy levels are in reasonable agreement with the corresponding experimental states with a few exceptions, while the comparison between theory and experiment for the observed $B(E2)$ (Table II) is less satisfactory for some transitions. In fact, except for the ^{99}Tc , almost all the other calculated $B(E2)$ s underestimate the experimental ones.

Here, it is worth to notice that a sound shell-model description of these nuclei is not an easy task for different reasons, especially in a parameter free calculation. In fact, we start from a ^{78}Ni core, and, therefore, the number of valence particle is sizeable, ranging from 16 to 37. Then, the inclusion of the contributions from three-body diagrams is only the leading order of many-body contributions, whose role grows when increasing the number of valence nucleons. Besides this, Cd, In and Sn isotopes are at the limit of the proton configuration space and, therefore, $Z = 50$ cross-shell excitations

TABLE I. Theoretical versus experimental low-energy levels of the nuclei under investigation.

	J^π	E^{th} (MeV)	E^{Exp} (MeV)
^{94}Nb	6^+	0.000	0.000
	3^+	0.014	0.041
	4^+	0.014	0.058
	7^+	0.017	0.079
^{94}Mo	0^+	0.000	0.000
	2^+	0.836	0.871
	4^+	1.450	1.574
^{99}Tc	9^+	0.000	0.000
	7^+	0.140	0.140
	1^-	0.794	0.143
	5^+	0.812	0.181
^{99}Ru	5^+	0.000	0.000
	3^+	0.343	0.096
	3^+	0.433	0.321
	7^+	0.588	0.341
^{113}Cd	1^+	0.000	0.000
	11^-	0.069	0.263
	2^+	0.019	0.299
	3^+	0.401	0.316
^{113}In	9^+	0.000	0.000
	1^-	1.375	0.392
	3^-	1.613	0.646
	5^+	1.270	1.024
^{115}In	9^+	0.000	0.000
	1^-	1.196	0.336
	2^-	1.445	0.597
	3^+	2.444	0.828
^{115}Sn	1^+	0.068	0.000
	3^+	0.000	0.497
	3^+	0.233	0.612
	7^+	0.396	0.713
	$\frac{11}{2}^-$		

may play a relevant role in the renormalization of the electric-quadrupole transition operator [52, 53]. Actually, the enlargement of the proton model space, in order to account explicitly for such excitations, is out of the present computational resources since the dimensions of the Hamiltonians to be diagonalized could reach $\approx 10^{13}$.

B. Forbidden β decays of ^{94}Nb , ^{99}Tc , ^{113}Cd , and ^{115}In

We focus now on the properties of the β decay between ground states, and it is important to start by discussing the relevance of the CVC relations (See Eq. 28) in determining the *relativistic* form factors.

As shown in Table III, in the case of ^{94}Nb , ^{99}Tc second-forbidden β decays, the *relativistic* form

TABLE II. Theoretical versus experimental [51] low-energy $B(E2)$ transition strengths, in W.u., of the nuclei under investigation.

Nucleus	$J_i \rightarrow J_f$	Theory	Experiment
^{94}Mo	$2^+ \rightarrow 0^+$	7.9	26 (4)
	$4^+ \rightarrow 2^+$	7.7	16.0 (4)
^{99}Tc	$\frac{7}{2}^+ \rightarrow \frac{9}{2}^+$	21	30 (19)
	$\frac{5}{2}^+ \rightarrow \frac{9}{2}^+$	10.3	15.1 (5)
^{99}Ru	$\frac{3}{2}^+ \rightarrow \frac{5}{2}^+$	7.4	50.1 (10)
^{113}Cd	$\frac{3}{2}^+ \rightarrow \frac{1}{2}^+$	2	20 (8)
	$\frac{5}{2}^+ \rightarrow \frac{1}{2}^+$	7.0	0.372 (25)
^{113}In	$\frac{5}{2}^+ \rightarrow \frac{9}{2}^+$	7.2	3.9 (4)
^{115}In	$\frac{1}{2}^+ \rightarrow \frac{3}{2}^+$	17	121 (23)
^{115}Sn	$\frac{3}{2}^+ \rightarrow \frac{1}{2}^+$	0.1	2.1 (6)
	$\frac{7}{2}^+ \rightarrow \frac{3}{2}^+$	0.010	0.130 (4)

factors ${}^V F_{211}$ obtained using the bare operator is zero since the SPMEs of the corresponding operator (Eq. 24) are identically zero in the model space. Even though the renormalization procedure gives SPMEs different from zero, the value of the ${}^V F_{211}$ form factors calculated using the effective operator has an opposite sign, and it is a factor two smaller than the form factor obtained by using the CVC relation (${}^V F_{211}^{CVC}$).

TABLE III. ^{99}Tc , ^{113}Cd , and ^{115}In β decay *relativistic* form factors determined with and without resorting to the CVC relations, and the *non-relativistic* form factors connected with the *relativistic* ones by CVC. The values are in adimensional units.

	Bare	Effective
^{94}Nb		
${}^V F_{211}$	0.000	0.009
${}^V F_{211}^{CVC}$	-0.031	-0.016
${}^V F_{220}$	0.304	0.164
^{99}Tc		
${}^V F_{211}$	0.000	0.008
${}^V F_{211}^{CVC}$	-0.030	-0.017
${}^V F_{220}$	0.286	0.161
^{113}Cd		
${}^V F_{431}$	0.0003	-0.008
${}^V F_{431}^{CVC}$	0.032	0.015
${}^V F_{440}$	-0.521	-0.237
^{115}In		
${}^V F_{431}$	-0.0004	-0.009
${}^V F_{431}^{CVC}$	0.031	0.017
${}^V F_{440}$	-0.473	-0.267

As regards the fourth-forbidden form factors of ^{113}Cd , it is interesting to note that, in this case, the bare value of the *relativistic* form factor ${}^V F_{431}$ has the same sign of ${}^V F_{431}^{CVC}$, but it is two order of magnitude smaller. The

effect of the renormalization is remarkable, but, as it happens for the *relativistic* form factor of the ^{94}Nb , ^{99}Tc decays, the final result again has an opposite sign and is a factor two smaller with respect to the one calculated with the form factor ${}^V F_{431}^{\text{CVC}}$.

The same considerations may be drawn for ^{115}In , except that, using the bare operator, the sign of ${}^V F_{431}$ form factor is not consistent with the one obtained with the ${}^V F_{431}^{\text{CVC}}$ one.

These results point out to a problem in determining the *relativistic* form factors within the non-relativistic reduction of the Dirac equation for the nuclei under investigations. On the above grounds, in the following calculation of the β decay properties we use the CVC relations for the *relativistic* form factors.

TABLE IV. Theoretical and experimental $\log ft$ values. Data are taken from Ref. [51].

	Bare	Effective	Exp.
^{94}Nb	11.30	11.58	11.95 (7)
^{99}Tc	11.580	11.876	12.325 (12)
^{113}Cd	21.902	22.493	23.127 (14)
^{115}In	21.22	21.64	22.53 (3)

We start the discussion of our results from the comparison between our calculated values of the $\log ft$ s and the experimental ones, as they are reported in Table IV. There, we have reported the $\log ft$ s obtained using both the bare second- and fourth-forbidden β -decay operators and the effective ones. It is worth stressing again that, as we have reported in Sec. II C, our SM effective operators consists of one- and two-body components.

As can be seen, the results that are obtained by employing the bare β -decay operators underestimate the experimental $\log ft$ s, a result that is consistent with the general consideration that nuclear models, which operate truncation of the Hilbert space of the single-nucleon configurations, require the introduction of a quenching factor q in order to reproduce the experimental half-lives for allowed β -decay transitions (see for example Refs. [1, 2]).

On the other hand, the calculations employing the SM effective operators provide results that substantially recover the gap with respect to the experimental $\log ft$ s, a result that is consistent with our previous studies of the allowed β -decay within the realistic shell model [7–10].

In order to discuss the role of the renormalization of the β -decay operator on the calculation of the shape of forbidden β -decay energy spectra, we evaluate the quenching factors that are needed to tune the axial coupling constant g_A in order to obtain the same results we have obtained for the $\log ft$ s by employing the SM effective operators. Using Eq. (7), we obtain that the quenching factors that reproduce the values in column “Effective” in Table IV are $q = 0.27, 0.50, 0.22,$ and 0.41 for ^{94}Nb , ^{99}Tc , ^{113}Cd , and ^{115}In decays, respectively.

In Fig. 2, the calculated and experimental normalized

spectra of the second-forbidden and fourth-forbidden decays, that are under our present investigation, are reported. The available data are drawn, with the corresponding errors, using red dots. It should be noted that the energy spectra are normalized in the energy region of the available data, and that those for ^{99}Tc decay have been extracted from Fig. (5) in Ref. [41]. Moreover, the experimental spectra of ^{99}Tc and ^{113}Cd are obtained after an unfolding procedure which takes into account the detector response function, as discussed in Ref. [54] and Refs. [41, 55], respectively. Conversely, in the energy spectrum of ^{115}In the detector response is not decoupled, leading to a more difficult direct comparison. However, according to the results presented in Refs. [20, 56], the detector response effects are expected to be small and, in any case, not significant for our purposes.

As regards ^{94}Nb decay, there are no experimental results, at present, and they are normalized in the full range of the kinetic-energy interval.

The calculated values are labelled and drawn as follows:

- (I) the calculated values, obtained using the bare operators, follow the dashed blue line;
- (II) the spectra calculated using the SM effective operators are drawn with a continuous black line;
- (III) finally, we report also the results coming out by using the bare operator, but quenching the axial coupling constant g_A with the q factors that reproduce the theoretical $\log ft$ s using the effective decay operators.

From the inspection of Fig. 2, we can clearly assert that the theoretical energy spectra, calculated employing the bare and the effective β -decay operators, are in a very good agreement with the corresponding experimental shapes [20, 41, 54, 57], for the forbidden β -decays of ^{99}Tc , ^{113}Cd , and ^{115}In . Moreover, all of them exhibit a small sensitivity to the renormalization of the β -decay operators, with small differences appearing only at low energy for all the decays ($\lesssim 100$ keV).

As regards the energy spectra obtained with the bare operator and quenching g_A , we see that they show a pronounced disagreement with the experimental shapes, for ^{99}Tc , ^{113}Cd , and ^{115}In , mostly in the low- and intermediate-energy intervals.

These results lead us to two main conclusions.

First, the calculated shapes of the normalized energy spectra are substantially insensitive to the renormalization of the forbidden β -decay operator by way of many-body perturbation theory, that is our approach to realistic shell model, and are in a good agreement with current data.

Second, it seems that the mere renormalization of the axial coupling constant g_A by a quenching factor q makes it difficult to provide simultaneously better $\log ft$ s and shapes of the energy spectra which reproduce the observed behavior.

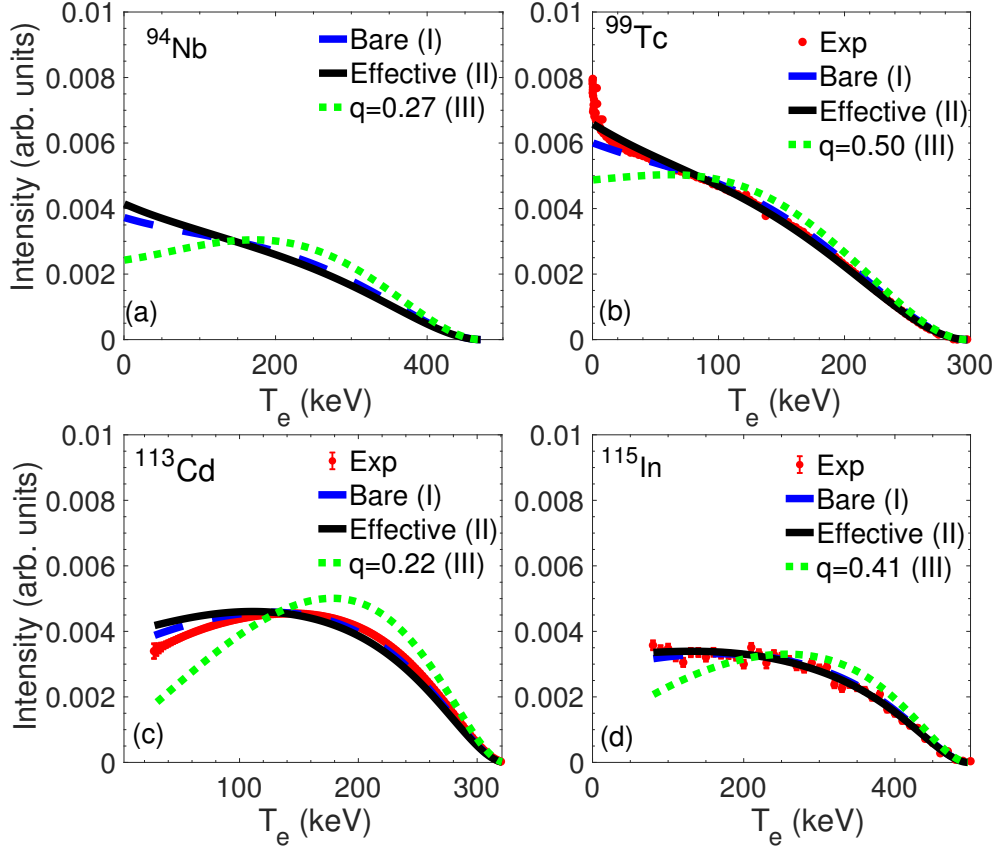


FIG. 2. Theoretical and experimental normalized β -spectra of ^{94}Nb (a), ^{99}Tc (b), ^{113}Cd (c) and ^{115}In (d) as a function of the electron kinetic energy T_e . The theoretical spectra are calculated with the bare operator (blue dashed line), the SM effective operator (continuous black line), and using the quenching factors for g_A extracted from Eq. (34) (green dashed line) (see text for details). The red dots corresponds to experimental values, where they are available [20, 41, 54, 57].

It is worth mentioning that in Refs. [13, 41, 58] the authors carried out a study of the sensitivity of their calculated spectra upon the renormalization of the axial coupling constant, and they found a noticeable dependence of their results on the choice of the quenching factor q .

Now, in order to reach a better insight of the results, we analyze the different components of the shape factor defined in Eq. (7). This factor can be divided in three components, the vector, axial and vector-axial terms, namely

$$C(w_e) = C_V(w_e) + C_A(w_e) + C_{VA}(w_e), \quad (34)$$

where C_V contains the coupling constant g_V^2 , C_A contains g_A^2 and C_{VA} contains $g_V \cdot g_A$.

The integrated shape functions \tilde{C}_k are reported in Table V, as well as the total value \tilde{C} (see Eq.(7)) for all the decays under investigation. As can be seen, at variance with what was observed in Ref. [14], for all the decays \tilde{C}_{VA} is positive and therefore it is summed in phase with the vector and axial components.

Actually, such a result is a consequence of the CVC theory, since if we do not use the CVC relations to determine the *relativistic* form factor, the mixed terms \tilde{C}_{VA} for the cases under investigation become negative, and

very close in absolute value to the sum of the correspondent vector and axial components. This is similar to the results reported in Ref. [14], and such a feature highlights the relevance of this form factor, as it was also discussed in other papers [34, 36, 39–41].

Even though it is small compared to the other form factors, the *relativistic* one is relevant to determine $C(w_e)$, and, therefore, shapes and half-lives, since, at variance with *non-relativistic* form factors, it enters the quantity $M_K(k_e, k_\nu)$ of Eq. (9) without any suppression coefficient (for the explicit expression of $M_K(k_e, k_\nu)$ see Table 4 in Ref. [33]).

The positive values of \tilde{C}_{VA} explain the stability of the shape with respect to the renormalization of the decay operators. In fact, without using the CVC relations, as a consequence of the delicate balance of the vector, axial and vector-axial terms, it is obtained a shape of the energy spectrum that is very sensitive to the renormalization procedure.

TABLE V. Integrated shape functions \tilde{C} of the studied transitions and their vector \tilde{C}_V , axial-vector \tilde{C}_A , and mixed components \tilde{C}_{VA} .

Parent	Op	\tilde{C}_V	\tilde{C}_A	\tilde{C}_{VA}	\tilde{C}
^{94}Nb	Bare	5.44×10^{-9}	1.23×10^{-8}	1.34×10^{-8}	3.11×10^{-8}
	Effective	1.40×10^{-9}	9.07×10^{-9}	5.72×10^{-9}	1.62×10^{-8}
^{99}Tc	Bare	3.10×10^{-9}	5.90×10^{-9}	7.15×10^{-9}	1.61×10^{-8}
	Effective	8.82×10^{-10}	4.14×10^{-9}	3.14×10^{-9}	8.17×10^{-9}
^{113}Cd	Bare	1.19×10^{-19}	3.72×10^{-19}	2.80×10^{-19}	7.70×10^{-19}
	Effective	2.14×10^{-20}	1.14×10^{-19}	6.20×10^{-20}	1.98×10^{-19}
^{115}In	Bare	6.14×10^{-19}	1.93×10^{-18}	1.15×10^{-18}	3.69×10^{-18}
	Effective	1.75×10^{-19}	8.68×10^{-19}	3.72×10^{-19}	1.42×10^{-18}

IV. CONCLUSIONS AND OUTLOOK

This work is the first attempt to describe the features of forbidden β -decays within the framework of the realistic shell model, without resorting to any phenomenological quenching factor for the axial and vector coupling constants.

Such a study represents not only a validation of our theoretical framework to assess the reliability to predict $0\nu\beta\beta$ nuclear matrix elements [11], but can give also useful information for the recent experimental studies of the electron energy spectra of forbidden β -decays.

First, we have verified the ability of our effective Hamiltonian and transition operators by comparing the calculated low-energy spectra and $E2$ transition strengths of parent and daughter nuclei, involved in the forbidden β -decays under consideration, with their experimental counterparts. The comparison of the spectroscopic data with the corresponding experimental ones is quite satisfactory, especially if we consider the large number of valence particles – ranging from 16 to 37 –, which characterizes the nuclear system we have investigated.

Then, we have calculated both the half-lives and the energy spectra of the emitted electrons of the second-forbidden β -decay of ^{94}Nb and ^{99}Tc , and the fourth-forbidden β -decay of ^{113}Cd and ^{115}In .

As regards the outcome of our calculation of the properties of the forbidden β -decay processes under investigation, the results may be outlined as follows:

- The exam of the theoretical $\log ft_s$ and the experimental ones shows that the results that are obtained with bare operators always underestimate the data, a feature that is resembling the problem of the quenching of g_A in the allowed β -decay transitions. The theory moves towards experiment by employing the theoretical effective operators, as expected.
- Starting from the wave functions that are obtained through the diagonalization of our H_{eff} , the shape of the calculated energy spectra is rather insensitive to the choice of the β -decay operator, bare or

effective, and in both cases the reproduction of the observed normalized energy spectra is more than satisfactory.

- The latter result seems to be unrelated to the considerations about the calculated $\log ft_s$, and the comparison with data. In fact, using the bare operator, but introducing a quenching factor of the axial constant to improve the reproduction of the experimental $\log ft_s$, it results in a distortion of the shape of the energy spectra, that affects the agreement with the observed ones.

Wrapping up the results we have obtained, we may say that the goal to obtain, on the same footing, a better reproduction of half-lives and the shape of the energy spectrum of the emitted electrons in forbidden β decays, by employing effective decay operators, is a delicate matter. As it has been mentioned in Sec. III B, such an issue was met also in other studies [13, 41, 58], where the authors showed that, without a renormalization of the β -decay operator that is framed in the many-body theory, the reproduction of the observed properties of forbidden β decays cannot rely only on the quenching of g_A , and other empirical parameters should be considered.

It is worth pointing out that such an issue does not emerge in the study of allowed β decays, since the calculated energy spectrum does not depend on the nuclear matrix element of the electroweak currents, and the most relevant observable to be tested is the half-life.

Our considerations lead to suggest that the study of forbidden β -decay processes could be a valuable tool to refine the theoretical knowledge of the renormalization of transition operators, and to rule out models that could be not reliable to predict the value of nuclear matrix elements for decays, such as in the case of the $0\nu\beta\beta$ decay.

On the above grounds, we plan to extend the present work by studying forbidden β decays in other mass regions, close to nuclei that are candidates for detecting the $0\nu\beta\beta$ decay. Another interesting subject could be to tackle the forbidden β -decay problem starting from the derivation of electroweak currents by way of the chiral perturbation theory, which represent the new frontier to

frame the nuclear many-body problem within its underlying fundamental theory – the QCD –, and it is currently employed to investigate GT transitions with different nuclear approaches [10, 59–64].

V. ACKNOWLEDGMENTS

We thank J. Kostensalo, T. Miyagi, M. Biassoni, C. Brofferio, S. Ghislandi, A. Nava and L. Pagnanini for useful comments and discussion. G. D. G. acknowledges the support from the EU-FESR, PON Ricerca e Innovazione 2014-2020 - DM 1062/2021. We acknowledge the CINECA award under the ISCRA initiative and under the INFN-CINECA agreement, for the availability of high performance computing resources and support. This work is partly supported by the Czech Science Foundation (Czech Republic) P203-23-06439S.

-
- [1] G. Martínez-Pinedo, A. Poves, E. Caurier, and A. P. Zuker, *Phys. Rev. C* **53**, R2602 (1996).
- [2] J. Barea, J. Kotila, and F. Iachello, *Phys. Rev. C* **91**, 034304 (2015).
- [3] J. Suhonen and J. Kostensalo, *Frontiers in Physics* **7**, 29 (2019).
- [4] T. T. S. Kuo and E. Osnes, *Lecture Notes in Physics*, vol. 364 (Springer-Verlag, Berlin, 1990).
- [5] K. Suzuki and R. Okamoto, *Prog. Theor. Phys.* **93**, 905 (1995).
- [6] L. Coraggio and N. Itaco, *Frontiers in Physics* **8**, 345 (2020).
- [7] L. Coraggio, L. De Angelis, T. Fukui, A. Gargano, and N. Itaco, *Phys. Rev. C* **95**, 064324 (2017).
- [8] L. Coraggio, L. De Angelis, T. Fukui, A. Gargano, N. Itaco, and F. Nowacki, *Phys. Rev. C* **100**, 014316 (2019).
- [9] L. Coraggio, N. Itaco, G. De Gregorio, A. Gargano, R. Mancino, and F. Nowacki, *Phys. Rev. C* **105**, 034312 (2022).
- [10] L. Coraggio, N. Itaco, G. De Gregorio, A. Gargano, Z. H. Cheng, Y. Z. Ma, F. R. Xu, and M. Viviani, *Phys. Rev. C* **109**, 014301 (2024).
- [11] L. Coraggio, A. Gargano, N. Itaco, R. Mancino, and F. Nowacki, *Phys. Rev. C* **101**, 044315 (2020).
- [12] M. T. Mustonen, M. Aunola, and J. Suhonen, *Phys. Rev. C* **73**, 054301 (2006).
- [13] M. Haaranen, P. C. Srivastava, and J. Suhonen, *Phys. Rev. C* **93**, 034308 (2016).
- [14] M. Haaranen, J. Kotila, and J. Suhonen, *Phys. Rev. C* **95**, 024327 (2017).
- [15] J. Kostensalo, J. Suhonen, J. Volkmer, S. Zatschler, and K. Zuber, *Phys. Lett. B* **822**, 136652 (2021).
- [16] J. Kostensalo, E. Lisi, A. Marrone, and J. Suhonen, *Phys. Rev. C* **107**, 055502 (2023).
- [17] K. Zuber, *Physics Letters B* **519**, 1 (2001).
- [18] C. Goessling, M. Junker, H. Kiel, D. Muenstermann, S. Oehl, and K. Zuber, *Phys. Rev. C* **72**, 064328 (2005).
- [19] L. Bodenstern-Dresler, Y. Chu, D. Gehre, C. Gößling, A. Heibold, C. Herrmann, R. Hodak, J. Kostensalo, K. Kröninger, J. Küttler, et al., *Physics Letters B* **800**, 135092 (2020).
- [20] L. Pagnanini, G. Benato, P. Carniti, E. Celi, D. Chiesa, J. Corbett, I. Dafinei, S. Di Domizio, P. Di Stefano, S. Ghislandi, et al., *The European Physical Journal Plus* **138**, 445 (2023).
- [21] M. Biassoni, C. Brofferio, S. Capelli, F. Cappuzzello, M. Carminati, M. Cavallaro, L. Coraggio, O. Cremonesi, G. De Gregorio, C. Fiorini, et al., *J. Phys. Conf. Ser.* **2453**, 012020 (2023).
- [22] R. Machleidt, *Phys. Rev. C* **63**, 024001 (2001).
- [23] S. Bogner, T. T. S. Kuo, L. Coraggio, A. Covello, and N. Itaco, *Phys. Rev. C* **65**, 051301(R) (2002).
- [24] L. Coraggio, A. Covello, A. Gargano, N. Itaco, and T. T. S. Kuo, *Prog. Part. Nucl. Phys.* **62**, 135 (2009).
- [25] M. Hjorth-Jensen, T. T. S. Kuo, and E. Osnes, *Phys. Rep.* **261**, 125 (1995).
- [26] L. Coraggio, A. Covello, A. Gargano, N. Itaco, and T. T. S. Kuo, *Ann. Phys. (NY)* **327**, 2125 (2012).
- [27] E. M. Krenciglowa and T. T. S. Kuo, *Nucl. Phys. A* **235**, 171 (1974).
- [28] K. Suzuki and S. Y. Lee, *Prog. Theor. Phys.* **64**, 2091 (1980).
- [29] K. Suzuki, R. Okamoto, H. Kumagai, and S. Fujii, *Phys. Rev. C* **83**, 024304 (2011).
- [30] N. Shimizu, T. Mizusaki, Y. Utsuno, and Y. Tsunoda, *Computer Physics Communications* **244**, 372 (2019).
- [31] L. Coraggio, G. De Gregorio, A. Gargano, N. Itaco, T. Fukui, Y. Z. Ma, and F. R. Xu, *Phys. Rev. C* **102**, 054326 (2020).
- [32] See Supplemental Material at [URL will be inserted by publisher] for the list of single-particle energies and two-body matrix elements of the shell-model Hamiltonian H_{eff} , derived for 20 and 15 valence protons and neutrons, respectively, namely for ^{113}Cd .
- [33] H. Behrens and W. Bühring, *Nucl. Phys. A* **162**, 111 (1971).
- [34] D. Fahlin Strömberg, Ph.D. thesis (2020), URL <https://tuprints.ulb.tu-darmstadt.de/13302>.
- [35] J. C. Hardy and I. S. Towner, *Phys. Rev. C* **79**, 055502 (2009).
- [36] R. Sadler and H. Behrens, *Zeitschrift für Physik A Hadrons and Nuclei* **346**, 25 (1993).
- [37] Q. Zhi, E. Caurier, J. J. Cuenca-García, K. Langanke, G. Martínez-Pinedo, and K. Sieja, *Phys. Rev. C* **87**, 025803 (2013).
- [38] M. E. Rose and R. K. Osborn, *Phys. Rev.* **93**, 1326 (1954).
- [39] O. S. Kirsebom, M. Hukkanen, A. Kankainen, W. H. Trzaska, D. F. Strömberg, G. Martínez-Pinedo, K. Andersen, E. Bodewits, B. A. Brown, L. Canete, et al., *Phys. Rev. C* **100**, 065805 (2019).

- [40] K. Kossert, M. Loidl, X. Mougeot, M. Paulsen, P. Ranitzsch, and M. Rodrigues, *Applied Radiation and Isotopes* **185**, 110237 (2022).
- [41] M. Paulsen, P. Ranitzsch, M. Loidl, M. Rodrigues, K. Kossert, X. Mougeot, A. Singh, S. Leblond, J. Beyer, L. Bockhorn, et al., arXiv (2023), 2309.14014.
- [42] H. A. Smith and P. C. Simms, *Phys. Rev. C* **1**, 1809 (1970).
- [43] M. Antony, A. Pape, and J. Britz, *Atomic Data and Nuclear Data Tables* **66**, 1 (1997).
- [44] H. A. Mavromatis, L. Zamick, and G. E. Brown, *Nucl. Phys. A* **80**, 545 (1966).
- [45] H. A. Mavromatis and L. Zamick, *Nucl. Phys. A* **104**, 17 (1967).
- [46] P. Federman and L. Zamick, *Phys. Rev.* **177**, 1534 (1969).
- [47] P. J. Ellis and E. Osnes, *Rev. Mod. Phys.* **49**, 777 (1977).
- [48] I. S. Towner and K. F. C. Khanna, *Nucl. Phys. A* **399**, 334 (1983).
- [49] I. S. Towner, *Phys. Rep.* **155**, 263 (1987).
- [50] L. Coraggio, L. De Angelis, T. Fukui, A. Gargano, and N. Itaco, *J. Phys. Conf. Ser.* **1056**, 012012 (2018).
- [51] Data extracted using the NNDC On-line Data Service from the ENSDF database., URL <https://www.nndc.bnl.gov/ensdf>.
- [52] L. Coraggio, A. Covello, A. Gargano, N. Itaco, and T. T. S. Kuo, *Phys. Rev. C* **91**, 041301 (2015).
- [53] L. Coraggio, A. Gargano, and N. Itaco, *Phys. Rev. C* **93**, 064328 (2016).
- [54] P. Belli, R. Bernabei, N. Bukilic, F. Cappella, R. Cerulli, C. J. Dai, F. A. Danevich, J. R. d. Laeter, A. Incicchitti, V. V. Kobychchev, et al., *Phys. Rev. C* **76**, 064603 (2007).
- [55] M. Paulsen, K. Kossert, and J. Beyer, *Nuclear Instruments and Methods in Physics Research Section A: Accelerators, Spectrometers, Detectors and Associated Equipment* **953**, 163128 (2020).
- [56] L. Pagnanini, G. Benato, P. Carniti, E. Celi, D. Chiesa, J. Corbett, I. Dafinei, S. D. Domizio, P. D. Stefano, S. Ghislandi, et al., arXiv (2024), 2401.16059.
- [57] P. Belli, R. Bernabei, F. A. Danevich, A. Incicchitti, and Tretyak, *Eur. Phys. J. A* **55**, 140 (2019).
- [58] J. Kostensalo and J. Suhonen, *Phys. Rev. C* **96**, 024317 (2017).
- [59] P. Gysbers, G. Hagen, J. D. Holt, G. R. Jansen, T. D. Morris, P. Navrátil, T. Papenbrock, S. Quaglioni, A. Schwenk, S. R. Stroberg, et al., *Nature Phys.* **15**, 428 (2019).
- [60] G. B. King, L. Andreoli, S. Pastore, M. Piarulli, R. Schiavilla, R. B. Wiringa, J. Carlson, and S. Gandolfi, *Phys. Rev. C* **102**, 025501 (2020).
- [61] A. Baroni, G. B. King, and S. Pastore, *Few-Body Syst.* **62**, 114 (2021).
- [62] A. Gnech, L. E. Marcucci, R. Schiavilla, and M. Viviani, *Phys. Rev. C* **104**, 035501 (2021).
- [63] A. Gnech and R. Schiavilla, *Phys. Rev. C* **106**, 044001 (2022).
- [64] G. B. King, A. Baroni, V. Cirigliano, S. Gandolfi, L. Hayen, E. Mereghetti, S. Pastore, and M. Piarulli, *Phys. Rev. C* **107**, 015503 (2023).

Thomas K. Gaisser, a Pioneer of Particle Astrophysics

Francis Halzen^a, Paolo Lipari^b

^a*Department of Physics and
Wisconsin IceCube Particle Astrophysics Center
UW-Madison, Madison, WI 53706 USA*

^b*INFN, Sezione Roma "Sapienza"
Piazzale Aldo Moro 2, 00185 Roma, Italy*

Abstract: We describe the pioneering contributions of Thomas K. Gaisser to the birth and development of particle astrophysics, a new field of research at the intersection of cosmic ray physics, astronomy, astrophysics, and particle physics that has emerged in the last few decades. We will especially focus on his studies of natural beams of neutrinos: those generated by the interactions of cosmic rays in the Earth's atmosphere and those emitted by astrophysical sources. Tom actively participated in the discovery of these cosmic neutrinos as well. His contributions also extend to gamma-ray astronomy, the study of the cosmic ray spectra and composition, and the modeling of cosmic ray interactions in the atmosphere and in astrophysical environments. Tom invariably focused his research on the theoretical and phenomenological problems of greatest interest at the time, producing frameworks that transparently interpreted often complex data. These studies have been very influential and have shaped the development of the field.

Starting in the late 1960s, the scientific life of Thomas K Gaisser spans more than five decades. This period saw the emergence and development of particle astrophysics, a new field of research at the intersection of cosmic ray physics, astronomy, astrophysics, and particle physics. If anyone could lay claim to the title of father of this new field of particle astrophysics, Tom could; he was also a true pioneer in gamma-ray and neutrino astronomy. His early career prepared him well, with research in particle and cosmic ray physics. He was a master of extracting science from the indirect information collected by air shower arrays, a skill he successfully applied in his later career to other particle astrophysics endeavors, most prominently the modeling of the atmospheric muon and neutrino fluxes. Tom's contributions to cosmic ray physics are reviewed in Ref. [1].

Early on, Tom studied the extensive air showers that are created when high-energy cosmic rays reach Earth. His contributions included the Gaisser-Hillas profile of longitudinal air showers developed in collaboration with Michael Hillas and the SIBYLL Monte Carlo for simulating air showers. He thus laid much of the groundwork for large experiments such as Auger and IceCube, and for how to use their data to probe fundamental questions in particle physics.

We herein emphasize Tom’s major contributions to neutrino physics. First and foremost, Tom’s research was vital for interpreting data from GeV-energy neutrino experiments using the atmospheric beam, such as IMB, Kamioka, and its next-generation successor, Super-Kamiokande. Tom provided calculations of atmospheric neutrino production that were important in establishing neutrino oscillations. With the discovery of nonvanishing neutrino masses that cannot be accommodated within the symmetries of the Standard Model, particle astrophysics made its first impactful contribution to particle physics in the era of accelerators and colliders. We will subsequently turn to Tom’s major role in launching neutrino astronomy by detailed modeling of the atmospheric backgrounds, by constructing surface detectors, and by providing leadership in the construction and operation of the IceCube experiment.

1. Hadronic Interactions

The importance of modeling hadronic interactions for high-energy astrophysics is easy to understand: the highest energy cosmic rays are protons and nuclei that can initiate hadronic interactions when they interact with ordinary matter and, in some astrophysical environments, with radiation fields. These interactions generate an ensemble of secondaries, and the problem is to describe with sufficient precision the multiplicity, composition, and energy spectra of these secondary particles. One motivation is to accurately describe the development of the extensive air showers generated by high-energy cosmic rays in the Earth’s atmosphere. This is necessary to allow for the reconstruction of the energy and mass number of the parent particles from the observations of air shower detectors on the ground. The description of hadronic interactions is also necessary to compute the inclusive spectra of gamma rays and neutrinos, generated when beams of cosmic ray particles interact with some target material. This is required to evaluate the fluxes of atmospheric neutrinos generated by cosmic rays interacting in the Earth’s atmosphere, and to calculate the fluxes of gamma rays and neutrinos produced in astrophysical sources, for instance, when freshly accelerated particles interact with matter inside or near a source that generates cosmic rays.

It is now universally accepted that, at a fundamental level, hadronic interactions are described by Quantum Chromo Dynamics (QCD), a gauge theory formulated in terms of quark and gluon fields. QCD theory is asymptotically free, and therefore it is possible to accurately compute “hard processes,” such as high p_{\perp} gluon-gluon scattering and heavy quark or Higgs boson production; however, we are not able to compute from first principles the cross sections and the properties of the multiparticle final states for the “soft processes” that account for most of the interactions. For cosmic ray physics, QCD remains “the dark side of the Standard Model.”

Tom Gaisser worked on the description of hadronic interactions and their relation to cosmic ray studies during his entire scientific life, making several important contributions. He also played a crucial role in making the community of cosmic ray physicists aware of the critical importance of the question.

Examples of these studies include the calculation of the atmospheric neutrino fluxes from a knowledge of the primary cosmic ray spectra at Earth, the study of the propagation of cosmic rays in the Galaxy via observations of secondaries such as positrons and antiprotons [2] generated by inelastic collisions in interstellar space, and the modeling of air showers, providing the tools to determine the properties of cosmic rays [3]. These problems span a very broad range of center of mass energies, and in many cases uncertainties in the modeling of the hadronic interactions represent the dominant source of systematic errors on the results.

Since we are not able to calculate the properties of hadronic interactions from first principles, they must be inferred from data obtained from experiments performed at accelerators, using as a guide a variety of phenomenological techniques. In many cases, this requires challenging extrapolations to higher energies from the kinematical range covered by the accelerator experiments. Tom was a master in this art.

The flow of information may also run in the opposite direction, that is, using cosmic ray observations to obtain information on the properties of hadronic interactions. In fact, today the cosmic ray spectra extend to energies that are above those accessible to the highest energy man-made accelerators. As an illustration, the collisions of a 10^{20} eV proton with a nucleon at rest corresponds to a c.m. energy of 433 TeV, more than thirty times the maximum energy (13.6 TeV) of the LHC. Tom explored this opportunity in several of his papers.

Examples of both approaches include two papers about the behavior of the proton-air cross section with energy. In the 1970s, experiments at the CERN ISR collider demonstrated that the pp cross section grows with energy. This result is obviously relevant for the interpretation of air shower experiments, and Tom promptly wrote papers [4, 5] that discussed the implications of the ISR results for the determination of the cosmic ray energy spectrum. In collaboration with Gaurang Yodh, Tom also discussed how the energy dependence of the p -air cross section could be inferred from cosmic ray observations [6]. Note that the program to evaluate the p -air and the pp cross sections at super-LHC-energy is currently pursued by air shower experiments, in particular at the highest energies by the Pierre Auger Observatory [7] and the Telescope Array[8].

Another example of the use of air shower observations to infer the properties of hadronic interactions is the estimate of the size of Feynman scaling violations. In 1969, Richard Feynman [9] proposed a scaling law for the longitudinal momentum distribution of the mesons created in high-energy inelastic interactions, referred to as “Feynman scaling.” It allows for the extrapolation of accelerator data to arbitrarily high energy, and it therefore has very important implications for cosmic ray studies. However, it was soon understood, including by Feynman himself [9], that this scaling is violated. A paper by Gaisser and Maurer [10] discussed how air shower observations indicated that the multiplicity of secondaries in hadronic collisions was indeed growing more rapidly than the logarithmic behavior predicted by Feynman scaling.

In 1980, Tom, together with Gaurang Yodh, wrote an influential review [11] summarizing the status of the problem of modeling hadronic interactions for

cosmic ray studies. It remains today an authoritative source discussing the systematic uncertainties in interpreting air shower experiments. Tom Gaisser pursued these studies for the following four decades. A major “product” of these studies has been the development of detailed Monte Carlo codes for the simulation of hadronic collisions and the development of air showers. The importance of these computer codes has been recognized for decades because a meaningful comparison of the results of different experiments requires the use of the same Monte Carlo codes for the simulation of air showers. This task became easier with the development in the 1990s of CORSIKA [12] a Monte Carlo code for air shower simulation intended for general use that also includes the possibility to use different hadronic interaction models.

Tom Gaisser and his collaborators played an important role in supporting and stimulating these developments, including by constructing and developing the SIBYLL model [13, 14, 15, 16]. This (open source) code was made public, included in CORSIKA air shower Monte Carlo program, and has been extensively used for the interpretation of air shower observations in a broad energy range that extends from 10^{12} to 10^{20} eV. The Monte Carlo codes developed for cosmic rays studies are complementary to those developed for accelerators studies in the sense that their emphasis is not on the small part of the cross section where hard parton-parton scattering occurs but focused on the “minimum bias” interactions, with special attention to the forward fragmentation region that is most important for shower development.

2. Atmospheric Neutrinos

The study of atmospheric neutrinos has been a topic of great importance in Tom Gaisser’s research, and it is in this field that he made some of his most important scientific contributions.

Atmospheric neutrinos are created in the weak decays of secondary particles produced by cosmic rays in the Earth’s atmosphere. The main channel of atmospheric neutrino production is the chain decay of charged pions: $\pi^+ \rightarrow \mu^+ \nu_\mu$ followed by $\mu^+ \rightarrow e^+ \nu_e \bar{\nu}_\mu$, and the charge conjugate mode. Subdominant contributions at the level of 10–20% are generated by the production and decay of kaons, in modes such as $K^+ \rightarrow \pi^0 + e^+ + \nu_e$ or $K_L \rightarrow \pi^\pm + e^\mp + \bar{\nu}_e(\nu_e)$.

The existence of atmospheric neutrinos had been anticipated during the extraordinary, one could say “heroic,” decade (1937–1947) of studies of cosmic ray radiation that saw the discovery of the muon and the charged pions and the observation of their decay modes. By the end of the 1940s, the study of cosmic ray interactions had established that they were a source of large fluxes of neutrinos, and the main channels of atmospheric neutrino production had been identified. The detection of this flux appeared to be very challenging, but this did not discourage physicists to investigate methods to detect it. Two experiments located in deep mines in India and South Africa [17, 18] obtained the first direct observations of the flux of atmospheric ν_μ and $\bar{\nu}_\mu$ by detecting the muons generated by the charged current interactions of atmospheric neutrinos in the rock surrounding the detector. The long range of the secondary muons

allows the use of a large volume of rock as target for the neutrino interactions, increasing significantly the event rate relative to events where the neutrinos interact inside the detection volume.

The development of Grand Unified Theories in the 1970s [19, 20, 21], along with their fascinating prediction of proton decay with a lifetime possibly observable by ambitious but realistic projects [22], stimulated the design and construction of very large mass underground detectors. These were also perfectly suited to study the interactions of atmospheric neutrinos in the GeV-energy range. This energy range, unfortunately in the vicinity of the proton mass, is in fact where, folding a rapidly falling neutrino spectrum with a cross section growing with energy, atmospheric neutrino interactions are most frequent and become a background in the search for proton decay. The calculation of atmospheric neutrino fluxes thus became a critical task. From the beginning, Tom Gaisser became a pioneer and a leader in these studies, constantly refining the modeling over several decades [23, 24, 25, 26, 27, 28, 29, 30, 31].

The task of predicting atmospheric neutrino fluxes acquired a greater importance when observations suggested the possibility that these fluxes may be modified by flavor oscillations. Confronting precise predictions that did not include oscillations with the data became essential to establish the existence of this new phenomenon.

The first method for estimating the atmospheric neutrino flux was to derive the flux directly from the measured muon flux. The μ and ν fluxes are related because they are generated in the decay of the same parent particles. However, this approach has its limits, as muons are unstable, with a lifetime of $2.2 \mu\text{s}$ corresponding to a decay length $\ell_\mu \simeq 6.2 E_{\text{GeV}} \text{ km}$. Because the atmosphere has a thickness on the order of 20 km, this implies that only muons with energies exceeding a few GeV reach the ground before decay, while lower-energy muons will decay before reaching the ground. It is relatively straightforward to extrapolate from the muon spectrum to the spectrum of $(\nu_\mu + \bar{\nu}_\mu)$ for energies $E \gtrsim 10 \text{ GeV}$, because each μ^\pm is accompanied by a $\nu_\mu(\bar{\nu}_\mu)$ created in the same π^\pm decay. On the other hand, the method has limited validity for the lower energies that are relevant for estimating the p -decay background. The “corresponding” muons decay in air. The extrapolation method is also not viable for estimating the ν_e and $\bar{\nu}_e$ fluxes.

The method followed by Tom Gaisser to estimate the atmospheric neutrino fluxes was to perform a “direct calculation,” starting from measurements of the primary cosmic ray flux and calculating the neutrino flux produced during shower development. Such a direct calculation of the atmospheric neutrino fluxes as a function of flavor, energy, and direction is based on the following elements: (a) a description of the primary cosmic ray fluxes, (b) a model for the hadronic interactions of relativistic protons and nuclei with the oxygen and nitrogen nuclei in the air, (c) the description of the weak decays of the unstable parent particles produced in these interactions, μ^\pm , π^\pm , K^\pm , \dots , and (d) a calculation scheme to put together the elements listed above. In addition, the calculation of the observable neutrino event rates requires a precise description of the neutrino cross section. Tom Gaisser developed all of the above elements of

the atmospheric neutrino calculations. The description of the initial cosmic ray spectra, their energy dependence, and mass composition is obviously a fundamental problem for cosmic ray astrophysics, and Tom had studied this problem extensively. Also, as previously discussed, the modeling of hadronic interactions is a topic of great importance not only for the physics of atmospheric neutrinos, but also in a wide range of problems in high-energy astrophysics, and was always central in Tom’s research.

Additionally, Tom and his collaborators were the first [24] to include muon polarization in the decay chains that generate the neutrinos. Polarization contributes non-negligible corrections that had been overlooked in the first calculations of the atmospheric neutrino fluxes.

Where observations of the neutrino flux are concerned, the description of the neutrino-nucleon cross sections, especially at the lower energies, is a non-trivial problem to which Tom contributed [32]. It is still a source of systematic uncertainties for long baseline neutrino experiments today.

Different computational methods were used to obtain the atmospheric neutrino fluxes. Tom preferred to use semi-analytic methods [28] that allow for a good understanding of the results and their systematic uncertainties, but the nature of the problem, eventually, required performing very detailed Monte Carlo calculations. The calculations of the atmospheric neutrino flux performed before 1999 made the simplifying assumption that the neutrino is collinear with the parent particle. In a Monte Carlo calculation, this can be implemented by rotating the 3-momenta of particles in the final state of an interaction (or decay) to align them to the momentum of the projectile (parent) particle. The use of this approximation allows saving a very large factor in computation time. A fully 3D Monte Carlo calculation is very inefficient, because only a small fraction of the neutrinos arrives close to the detector.

In the end, the availability of modern computers made a 3D calculation possible. The first study [33] was performed using the Fluka Monte Carlo code, showing that the 3D effects can be significant when the average angle between the neutrinos and the primary particle is large (as also discussed in Ref. [34]). Soon afterward, Tom and his collaborators [30] obtained detailed predictions, which also included a 3D treatment that is significant at low energy ($E \lesssim 1$ GeV).

The large mass detectors designed to search for proton decay, soon observed neutrino interactions inside the detector’s fiducial volume. In 1986, two water Cherenkov detectors, IMB [35] and Kamiokande [36], observed the first hints of an “anomaly” in the μ/e flavor ratio for contained events. The “anomaly” turned into a “hint for oscillations” when the Kamiokande collaboration released additional data [37, 38] with larger exposures, which strengthened the case for the flavor oscillations. The “hint” became “evidence” for oscillations when the new Super-Kamiokande experiment released its first 1.5 years of data with a 33-kton-yrs exposure at the Neutrino’98 conference in Toyama [39, 40]. The improved significance resulted not only from smaller statistical errors but also from the broader range in energy that the larger exposure made possible. This exposed the characteristic dependence of the neutrino pathlength and energy

expected for flavor oscillations. Additional support for the flavor oscillation hypothesis emerged from the study of the zenith angle dependence of upgoing muons from the decay of neutrinos of muon flavor, a result independently confirmed by MACRO [41].

The 2015 Nobel Prize in Physics was awarded to the spokesperson of the Super-Kamiokande experiment, Takaaki Kajita, and to Arthur McDonald, the spokesperson of the SNO solar neutrino detector, “for the discovery of neutrino oscillations, which shows that neutrinos have mass.” The discovery over the 1986–1998 period that flavor oscillations distort the spectra of atmospheric neutrinos is a fascinating and very instructive example of the “process of discovery.” While the experimentalists obtained measurements with decreasing statistical and systematic errors, the theoretical predictions were constantly refined, with Tom playing an essential role. The most accurate and better-controlled predictions used in the interpretation of the data of the experiments were obtained by Tom and his collaborators, the “Bartol model,” and by a Japanese group originally formed by Kajita together with Honda, Kasahara, and Midorikawa [42, 43]. An authoritative review of the subject was written by Tom, together with Morihiro Honda [44].

The calculation of the atmospheric neutrino flux at very high energy (from $E \gtrsim 10$ TeV up to several PeV) is important also because in this energy range the atmospheric flux is the foreground to the emerging signal of neutrinos emitted by astrophysical sources (that have a harder energy spectrum).

An important source of uncertainty in this calculation is the modeling of the spectrum and composition of the primary cosmic rays that generate the atmospheric neutrinos. In the relevant energy range, the primary CR spectrum and composition can only be measured by extensive air shower experiments, and this results in large uncertainties (and also some discrepancies between different measurements) because of the systematic errors associated with modeling of hadronic cascades. The situation is particularly difficult (and interesting) because it is in this range that the all-particle CR spectrum exhibits the softening feature known as the “knee,” where the composition is also rapidly changing, and because somewhere above the “knee” one also expects the transition from a CR flux generated by Galactic sources to a flux dominated by the extragalactic contribution.

Modeling the CR spectra and composition at very high energy was therefore a very important subject of study for Tom Gaisser, in part because of its relevance in the construction of precise predictions for the atmospheric neutrino fluxes and because of its fundamental significance for cosmic ray astrophysics.

The studies by Tom on this problem resulted in publication of several parametrizations of the CR spectra at very high energy (from 10^{14} to 10^{20} eV) obtained from an analysis of all existing measurements (combined, taking into account their systematic uncertainties), and using functional forms motivated by physical ideas about the properties of CR sources. A well-known result that emerged from these studies is the set of parametrizations of the CR spectra [45] (with Todor Stanev and Serap Tilav as coauthors) that has been used by a large number (several hundred) of subsequent publications.

3. High-Energy Neutrino Astronomy

The understanding that cosmic rays may be generated in discrete astrophysical sources emerged gradually, and with it the idea that sites where cosmic rays are produced should be sources of high-energy neutrinos, generated by the same mechanism that creates the atmospheric ν flux. These ideas made a powerful impact on astrophysics in the 1980s because of puzzling observations of Cygnus X-3 and the explosion of supernova SN1987A in the Large Magellanic Cloud.

Tom’s first papers on astrophysical neutrinos were inspired by the pioneering attempt to construct the DUMAND neutrino telescope off the coast of the Big Island of Hawaii. Using his skills as a particle physicist, he calculated the high-energy neutrino and antineutrino cross sections [46] a decade before the “early” papers evaluating the deep inelastic cross section for the interactions of neutrinos in water, which we still reference today. His next paper testifies to his roots in particle physics, with a calculation of the production of the Higgs boson in muon number violating processes [47]. He also suggested the construction of an air shower array near the DUMAND site [48], an idea that would be repeatedly and very successfully implemented with the development of neutrino astronomy in Antarctica.

The early origins of what is now referred to as particle astrophysics are partially rooted in two momentous events: the 1978 Topical Conference on Cosmic Rays and Particle Physics [49] and the “discovery” of gamma rays and muons from Cygnus X-3. One year after completing the transfer of the Bartol Institute from its location on the Swarthmore campus near Philadelphia to the University of Delaware, Tom organized a meeting uniting cosmic ray and particle physicists to discuss common interests. One need not be a historian to track early initiatives in the new discipline to this gathering of minds—among the particle physicists James Bjorken, Carlo Rubbia, David Cline, Gordon Kane, and César Lattes, and Saburo Miyake, Kiyoshi Niu, Michael Hillas, and George Cassidy among many others on the cosmic ray side.

In 1983, a paper by Samorski and Stamm [50] reported on “the first experimental evidence for a clearly identified gamma-ray point source” obtained with an air shower detector located in Kiel (Germany). The signal was observed for energies in the range of 1–20 PeV (10^{15} eV) and from a direction consistent with the position of the binary system Cygnus X-3, and it appeared to be time-modulated with the 4.8 hours orbital period of the system.

Several decades after this publication and a sequence of other detections, none totally compelling, observations by significantly more sensitive detectors and analyses based on more sophisticated and robust statistical methods, we can conclude that these experimental results were all incorrect, or perhaps associated to a time interval where the emission from Cygnus X-3 was much more powerful than what is observed today [51]. However, the fleeting reality of these exciting results had a profound impact on the field of high-energy astrophysics. On the experimental side, it stimulated the design and construction of better air shower detectors, such as the Chicago Air Shower Array (CASA), which together with Michigan Muon Array (MIA) operated in the 1990s, obtaining stringent limits

on the emission from Cygnus X-3 and other possible gamma ray sources. On the theoretical side, the observations of Cygnus X-3 stimulated more realistic modeling of the anticipated fluxes of gamma rays and neutrinos from potential cosmic ray sources.

In fact, for one decade, Cygnus X-3 became very much the focus of the new discipline, drawing more particle physicists into what was referred to at the time as non-accelerator particle physics. For astronomers, Cygnus X-3 is a high-mass X-ray binary and one of the stronger binary X-ray sources in the sky. It is believed to be a compact object, a neutron star or black hole, in a binary system that is pulling in a stream of gas from an ordinary star companion. For the particle physicist, it is a particle beam powered by a compact object aimed at a star that is the target for producing gamma rays and neutrinos. With others, Tom jumped on the fact that the observations of TeV gamma rays as well as muons, presumably produced by neutrinos, could not be accommodated by Standard Model physics [52]. Gamma rays can be separated in cosmic ray experiments by the fact that they initiate a purely electromagnetic shower except for the photoproduction of some pions in the development of the air shower; their decay is the source of a small muon component. One possibility was that the abundant production of muons required to accommodate the observations was associated with a “new physics” TeV threshold in the photoproduction cross section, a threshold that was anticipated by the particle community and inspired the construction of the LHC. Though the evidence faded with improved measurements and with a better understanding of statistical trials in the data analysis, the idea nevertheless took hold that one could do particle physics and search for physics beyond the Standard Model with experiments of modest cost at energies often exceeding those of earthbound accelerators. In this context, Tom started to write inspiring reviews on the prospects for neutrino astronomy, which he presented at the 2nd [53] and 6th Venice Neutrino Telescopes Workshop. These were early versions of the 1995 Physics Reports [54], which became the most widely cited review in the field. At this opportune time, Tom organized the Particle Astrophysics in Antarctica Meeting at the Bartol Institute, building on the historic role it played in Antarctic science with Martin Pomerantz [49]. The meeting transformed neutrino astronomy in Antarctica from an idea into a project.

Then supernova 1987A exploded. Supernova 1987A and its observation by neutrino detectors did create the realistic and much-explored opportunity to do particle physics with the data from an astronomical source. Tom did not pass up the opportunity [55], but he also drew attention to the fact that 1987A might become a source of GeV-energy gamma rays and neutrinos long after it faded [56]. Shockwaves may accelerate protons inside a young supernova shell, and subsequently energetic pions can be produced that decay into photons and neutrinos of much higher energy than the deleptonization and thermal neutrinos initially produced. Their observation will be possible when the next Galactic supernova explodes, relying on a wealth of 21st century instrumentation. At the time, the air shower array at the South Pole provided a unique opportunity because of its southern location [55].

What is missing in this narrative so far is Tom’s knack for occasionally producing or contributing to isolated papers that are real gems. The paper with Gary Steigman and Serap Tilav on searching for dark matter particles trapped in the sun [57] comes to mind, as well as the papers on muon-poor gamma ray astronomy applied to Jim Cronin’s effort to turn the CASA-MIA air shower array in Utah into a gamma ray telescope [58]. Also, the highly imaginative paper with Todor Stanev and David Seckel on the observation at Earth of solar atmospheric neutrinos deserves being singled out [59]. Even today these papers inspire active searches for high-energy neutrinos originating in the sun with GeV energy and above. These have resulted in the best limits on the cross section for dark matter interacting with ordinary matter via spin-dependent interactions [60]. The search for solar “atmospheric” neutrinos is closing in on their original predictions, while the corresponding photons have been recently observed by the NASA Fermi satellite [61].

Starting with the early deployments of AMANDA, neutrino astronomy became Tom’s focus, initially shared with his pioneering calculations of atmospheric neutrino fluxes [52, 23]. For AMANDA and IceCube observations, atmospheric neutrinos represent both signal and background depending on the science, and, maybe more important, they represent an opportunity to calibrate the detectors over a wide energy range [62, 63]. Tom led the development of the tools to evaluate the atmospheric neutrino flux, including uncertainties [64]. As a founding member of the IceCube Collaboration established in 2005, Tom was a leader whom everyone could count on. He was gracious and provided encouragement to many young scientists. He served the team in many ways, including as IceCube’s spokesperson between 2007 and 2011.

Tom was the soul of IceTop, the observatory’s surface air shower array built for calibrating IceCube but also devoted to cosmic-ray physics. Although a theorist, Tom took on the experimental task of building IceTop with gusto and participated in every season of IceCube’s construction. For several years he traveled to Antarctica, staying there for weeks at a time to participate in building the surface array. He delighted in the hard physical labor and the camaraderie of everyone, including mechanics, bulldozer drivers, and technicians engaged in the project. IceTop and IceCube mapped for the first time the cosmic-ray anisotropy in the Southern Hemisphere and performed precision measurements of the cosmic-ray energy spectrum from the “knee” to the “ankle” in the spectrum. As an IceCube member, Tom also became an ambassador of Antarctic science in large part through a blog documenting his team’s expeditions to the South Pole. In recognition of his work with IceCube, an area in Antarctica was named Gaisser Valley in 2005.

Given his pioneering role, from the first SPASE air shower array deployed at the South Pole to his leadership in IceCube from the time of construction to its present discoveries, it is appropriate to briefly summarize IceCube’s results. In its first decade of operation, IceCube collected on the order of one million neutrinos, mostly of atmospheric origin. Among these, it discovered neutrinos of TeV-PeV energy originating beyond our Galaxy, providing us with the only unobstructed view of the cosmic accelerators that power the highest

energy radiation reaching us from the extreme universe [65]. Increasingly precise measurements of their spectrum using multiple methodologies revealed two surprises. First, unlike the case for all wavebands of light, the contribution to the cosmic neutrino flux from our own Galaxy is only at the 10% level [66]. Second, the expected flux of gamma rays from the decay of the neutral pions accompanying the charged pions that decay into cosmic neutrinos exceeds the total extragalactic flux observed by gamma ray detectors. It implies that the targets in which the cosmic accelerators produce neutrinos are opaque to gamma rays. This has been confirmed by the identification of the first neutrino sources.

The self-veto of atmospheric muon neutrinos has been a critical tool for identifying cosmic neutrinos in the overwhelming atmospheric neutrino background. The latter are identified by accompanying muons from the neutrino decay, or muons produced in the same air shower as the neutrino. Even though the original idea was not his, it represents one more example demonstrating that Tom's research invariably focused on the theoretical and phenomenological aspects of the measurements that were of great interest at the time. Be it air showers, anti-proton production and propagation, lepton fluxes (and their dependence on the K/pi ratio, atmospheric parameters, etc.), or astrophysical neutrino and gamma-ray fluxes, he always produced estimates that were extremely helpful for interpreting data.

After 10 years of accumulated statistics, the active galaxy NGC 1068 has been associated with the hottest spot in the neutrino sky map. It is also the dominant source in a search at the positions of 110 preselected high-energy gamma-ray sources. At the location of NGC 1068, we observe an excess of 79_{-20}^{+22} neutrinos with TeV energies [67]. Additionally, IceCube has found evidence for the active galaxies PKS 1424+240, TXS 0506+056, and NGC 4151. TXS 0506+056 had already been identified as a neutrino source in a multimessenger campaign triggered by a neutrino of 290 TeV energy, IC170922 [68], and by the independent observation of a neutrino burst from this source in archival IceCube data in 2014 [69]. The observations point to active galaxies opaque to gamma rays, with the obscured dense cores near the supermassive black holes emerging as the sites where neutrinos originate, typically within 10-100 Schwarzschild radii. IceCube is thus closing in on the resolution of the century-old problem of where cosmic rays originate.

The background of atmospheric neutrinos provides IceCube with a high-statistic sample to study the oscillations of neutrinos. IceCube's measurements of the so-called atmospheric neutrino parameters have reached a precision similar to what has been achieved by accelerator experiments [70]. These measurements are performed at higher energies and will be further improved after the deployment of the IceCube Upgrade in the 1925-26 South Pole summer.

All of the important advances in particle astrophysics discussed above have followed in large part from the foundations laid by Tom Gaisser's work. And for that, Tom Gaisser's name will forever be associated with neutrino physics that takes advantage of the atmospheric neutrino beam and with the birth of high-energy neutrino astronomy.

References

- [1] D. Soldin, P. A. Evenson, H. Kolanoski, A. A. Watson, Cosmic-Ray Physics at the South Pole (11 2023). [arXiv:2311.14474](#).
- [2] T. K. Gaisser, B. G. Mauger, Calculation of Cosmic Ray anti-proton ratio, *Astrophys. J. Lett.* 252 (1982) L57–L59. [doi:10.1086/183719](#).
- [3] T. K. Gaisser, T. Stanev, P. Freier, C. J. Waddington, Nucleus-nucleus Collisions and Interpretation of Cosmic Ray Cascades Above 100-tev, *Phys. Rev. D* 25 (1982) 2341–2350. [doi:10.1103/PhysRevD.25.2341](#).
- [4] T. K. Gaisser, C. J. Noble, G. B. Yodh, Contribution of an Increasing Proton Proton Cross-Section to Steepening of the Cosmic Ray Energy Spectrum, *J. Phys. G* 1 (1975) L9, [Erratum: *J.Phys.G* 1, 789 (1975)]. [doi:10.1088/0305-4616/1/1/003](#).
- [5] T. K. Gaisser, F. Siohan, G. B. Yodh, An Estimation of the Primary Proton Spectrum Between 10^{12} -eV and 10^{14} -eV, *J. Phys. G* 3 (1977) L241–L244. [doi:10.1088/0305-4616/3/10/003](#).
- [6] T. K. Gaisser, G. B. Yodh, Energy dependence of $\sigma(\text{p-air})$ up to 20 tev, *Nucl. Phys. B* 76 (1974) 182–188. [doi:10.1016/0550-3213\(74\)90147-3](#).
- [7] P. Abreu, et al., Measurement of the proton-air cross-section at $\sqrt{s} = 57$ TeV with the Pierre Auger Observatory, *Phys. Rev. Lett.* 109 (2012) 062002. [arXiv:1208.1520](#), [doi:10.1103/PhysRevLett.109.062002](#).
- [8] R. U. Abbasi, et al., Measurement of the proton-air cross section with Telescope Array’s Middle Drum detector and surface array in hybrid mode, *Phys. Rev. D* 92 (3) (2015) 032007. [arXiv:1505.01860](#), [doi:10.1103/PhysRevD.92.032007](#).
- [9] R. P. Feynman, Very high-energy collisions of hadrons, *Phys. Rev. Lett.* 23 (1969) 1415–1417. [doi:10.1103/PhysRevLett.23.1415](#).
- [10] T. K. Gaisser, R. H. Maurer, Extensive air showers and Feynman scaling above 1000 GeV, *Phys. Lett. B* 42 (1972) 444–448. [doi:10.1016/0370-2693\(72\)90103-7](#).
- [11] T. K. Gaisser, G. B. Yodh, PARTICLE COLLISIONS ABOVE 10-TeV AS SEEN BY COSMIC RAYS, *Ann. Rev. Nucl. Part. Sci.* 30 (1980) 475–542. [doi:10.1146/annurev.ns.30.120180.002355](#).
- [12] D. Heck, J. Knapp, J. N. Capdevielle, G. Schatz, T. Thouw, CORSIKA: A Monte Carlo code to simulate extensive air showers, *Tech. Rep. FZKA 6019* (1998).
URL <http://inspirehep.net/record/469835/files/FZKA6019.pdf>

- [13] R. S. Fletcher, T. K. Gaisser, P. Lipari, T. Stanev, SIBYLL: An Event generator for simulation of high-energy cosmic ray cascades, *Phys. Rev. D* 50 (1994) 5710–5731. doi:10.1103/PhysRevD.50.5710.
- [14] E.-J. Ahn, R. Engel, T. K. Gaisser, P. Lipari, T. Stanev, Cosmic ray interaction event generator SIBYLL 2.1, *Phys. Rev. D* 80 (2009) 094003. arXiv:0906.4113, doi:10.1103/PhysRevD.80.094003.
- [15] A. Fedynitch, F. Riehn, R. Engel, T. K. Gaisser, T. Stanev, Hadronic interaction model sibyll 2.3c and inclusive lepton fluxes, *Phys. Rev. D* 100 (10) (2019) 103018. arXiv:1806.04140, doi:10.1103/PhysRevD.100.103018.
- [16] F. Riehn, R. Engel, A. Fedynitch, T. K. Gaisser, T. Stanev, Hadronic interaction model Sibyll 2.3d and extensive air showers, *Phys. Rev. D* 102 (6) (2020) 063002. arXiv:1912.03300, doi:10.1103/PhysRevD.102.063002.
- [17] C. V. Achar, et al., Detection of muons produced by cosmic ray neutrinos deep underground, *Phys. Lett.* 18 (1965) 196–199. doi:10.1016/0031-9163(65)90712-2.
- [18] F. Reines, M. F. Crouch, T. L. Jenkins, W. R. Kropp, H. S. Gurr, G. R. Smith, J. P. F. Sellschop, B. Meyer, Evidence for high-energy cosmic ray neutrino interactions, *Phys. Rev. Lett.* 15 (1965) 429–433. doi:10.1103/PhysRevLett.15.429.
- [19] J. C. Pati, A. Salam, Is Baryon Number Conserved?, *Phys. Rev. Lett.* 31 (1973) 661–664. doi:10.1103/PhysRevLett.31.661.
- [20] J. C. Pati, A. Salam, Unified Lepton-Hadron Symmetry and a Gauge Theory of the Basic Interactions, *Phys. Rev. D* 8 (1973) 1240–1251. doi:10.1103/PhysRevD.8.1240.
- [21] H. Georgi, S. L. Glashow, Unity of All Elementary Particle Forces, *Phys. Rev. Lett.* 32 (1974) 438–441. doi:10.1103/PhysRevLett.32.438.
- [22] H. Georgi, H. R. Quinn, S. Weinberg, Hierarchy of Interactions in Unified Gauge Theories, *Phys. Rev. Lett.* 33 (1974) 451–454. doi:10.1103/PhysRevLett.33.451.
- [23] T. K. Gaisser, T. Stanev, S. A. Bludman, H.-s. Lee, The Flux of Atmospheric Neutrinos, *Phys. Rev. Lett.* 51 (1983) 223–226. doi:10.1103/PhysRevLett.51.223.
- [24] S. M. Barr, T. K. Gaisser, P. Lipari, S. Tilav, Ratio of ν_e/ν_μ in Atmospheric Neutrinos, *Phys. Lett. B* 214 (1988) 147–150. doi:10.1016/0370-2693(88)90468-6.
- [25] G. Barr, T. K. Gaisser, T. Stanev, Flux of Atmospheric Neutrinos, *Phys. Rev. D* 39 (1989) 3532–3534. doi:10.1103/PhysRevD.39.3532.

- [26] V. Agrawal, T. K. Gaisser, P. Lipari, T. Stanev, Atmospheric neutrino flux above 1-GeV, *Phys. Rev. D* 53 (1996) 1314–1323. [arXiv:hep-ph/9509423](#), [doi:10.1103/PhysRevD.53.1314](#).
- [27] P. Lipari, T. Stanev, T. K. Gaisser, Geomagnetic effects on atmospheric neutrinos, *Phys. Rev. D* 58 (1998) 073003. [arXiv:astro-ph/9803093](#), [doi:10.1103/PhysRevD.58.073003](#).
- [28] T. K. Gaisser, Semianalytic approximations for production of atmospheric muons and neutrinos, *Astropart. Phys.* 16 (2002) 285–294. [arXiv:astro-ph/0104327](#), [doi:10.1016/S0927-6505\(01\)00143-8](#).
- [29] T. K. Gaisser, T. Stanev, Charge ratio of muons from atmospheric neutrinos, *Phys. Lett. B* 561 (2003) 125–129. [arXiv:astro-ph/0210512](#), [doi:10.1016/S0370-2693\(03\)00389-7](#).
- [30] G. Barr, T. Gaisser, P. Lipari, S. Robbins, T. Stanev, A Three - dimensional calculation of atmospheric neutrinos, *Phys.Rev. D*70 (2004) 023006. [arXiv:astro-ph/0403630](#), [doi:10.1103/PhysRevD.70.023006](#).
- [31] G. D. Barr, S. Robbins, T. K. Gaisser, T. Stanev, Uncertainties in Atmospheric Neutrino Fluxes, *Phys. Rev. D*74 (2006) 094009. [arXiv:astro-ph/0611266](#), [doi:10.1103/PhysRevD.74.094009](#).
- [32] T. K. Gaisser, J. S. O’Connell, Interactions of Atmospheric Neutrinos in Nuclei at Low-energy, *Phys. Rev. D* 34 (1986) 822–825. [doi:10.1103/PhysRevD.34.822](#).
- [33] G. Battistoni, A. Ferrari, P. Lipari, T. Montaruli, P. R. Sala, T. Rancati, A Three-dimensional calculation of atmospheric neutrino flux, *Astropart. Phys.* 12 (2000) 315–333. [arXiv:hep-ph/9907408](#), [doi:10.1016/S0927-6505\(99\)00110-3](#).
- [34] P. Lipari, The Geometry of atmospheric neutrino production, *Astropart. Phys.* 14 (2000) 153–170. [arXiv:hep-ph/0002282](#), [doi:10.1016/S0927-6505\(00\)00129-8](#).
- [35] T. J. Haines, et al., Calculation of Atmospheric Neutrino Induced Backgrounds in a Nucleon Decay Search, *Phys. Rev. Lett.* 57 (1986) 1986–1989. [doi:10.1103/PhysRevLett.57.1986](#).
- [36] M. Nakahata, et al., Atmospheric Neutrino Background and Pion Nuclear Effect for Kamioka Nucleon Decay Experiment, *J. Phys. Soc. Jap.* 55 (1986) 3786. [doi:10.1143/JPSJ.55.3786](#).
- [37] K. S. Hirata, et al., Observation of a small atmospheric muon-neutrino / electron-neutrino ratio in Kamiokande, *Phys. Lett. B* 280 (1992) 146–152. [doi:10.1016/0370-2693\(92\)90788-6](#).



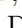
- [38] Y. Fukuda, et al., Atmospheric muon-neutrino / electron-neutrino ratio in the multiGeV energy range, *Phys. Lett. B* 335 (1994) 237–245. doi:10.1016/0370-2693(94)91420-6.
- [39] Y. Fukuda, et al., Evidence for oscillation of atmospheric neutrinos, *Phys. Rev. Lett.* 81 (1998) 1562–1567. arXiv:hep-ex/9807003, doi:10.1103/PhysRevLett.81.1562.
- [40] T. Kajita, Y. Totsuka, Observation of Atmospheric Neutrinos, *Rev. Mod. Phys.* 73 (2001) 85–118. doi:10.1103/RevModPhys.73.85.
- [41] M. Ambrosio, et al., Measurement of the atmospheric neutrino induced upgoing muon flux using MACRO, *Phys. Lett. B* 434 (1998) 451–457. arXiv:hep-ex/9807005, doi:10.1016/S0370-2693(98)00885-5.
- [42] M. Honda, T. Kajita, K. Kasahara, S. Midorikawa, Calculation of the flux of atmospheric neutrinos, *Phys. Rev. D* 52 (1995) 4985–5005. arXiv:hep-ph/9503439, doi:10.1103/PhysRevD.52.4985.
- [43] M. Honda, T. Kajita, K. Kasahara, S. Midorikawa, T. Sanuki, Calculation of atmospheric neutrino flux using the interaction model calibrated with atmospheric muon data, *Phys.Rev. D* 75 (2007) 043006. arXiv:astro-ph/0611418, doi:10.1103/PhysRevD.75.043006.
- [44] T. K. Gaisser, M. Honda, Flux of atmospheric neutrinos, *Ann. Rev. Nucl. Part. Sci.* 52 (2002) 153–199. arXiv:hep-ph/0203272, doi:10.1146/annurev.nucl.52.050102.090645.
- [45] T. K. Gaisser, T. Stanev, S. Tilav, Cosmic Ray Energy Spectrum from Measurements of Air Showers, *Front. Phys.(Beijing)* 8 (2013) 748–758. arXiv:1303.3565, doi:10.1007/s11467-013-0319-7.
- [46] T. K. Gaisser, A. Halprin, Detection of very high energy neutrinos, in: 15th International Cosmic Ray Conference, 1977.
- [47] T. K. Gaisser, A. Halprin, Higgs Meson Production in Muon Number Violating Processes, *Phys. Rev. D* 17 (1978) 159–162. doi:10.1103/PhysRevD.17.159.
- [48] J. W. Elbert, T. K. Gaisser, T. Stanev, Possible Studies with DUMAND and a Surface Air Shower Detector., in: 1980 DUMAND Symposium, 1980.
- [49] Proceedings, Topical Conference on Cosmic Rays and Particle Physics: Newark, Delaware, October 16-21, 1978, Vol. 49 of *Particles and Fields Subseries*.
- [50] M. Samorski, W. Stamm, Detection of 2×10^{15} -eV to 2×10^{16} -eV gamma Rays from Cygnus X-3, *Astrophys. J. Lett.* 268 (1983) L17–L21. doi:10.1086/184021.




- [51] A. A. Abdo, et al., Modulated High-Energy Gamma-Ray Emission from the Microquasar Cygnus X-3, *Science* 326 (5959) (2009) 1512–1516. doi:10.1126/science.1182174.
- [52] T. K. Gaisser, T. Stanev, Calculation of Neutrino Flux From Cygnus X-3, *Phys. Rev. Lett.* 54 (1985) 2265. doi:10.1103/PhysRevLett.54.2265.
- [53] M. Baldo Ceolin (Ed.), Neutrino telescopes. Proceedings, 2nd International Workshop, Venice, Italy, February 13-15, 1990, 1990.
- [54] T. K. Gaisser, F. Halzen, T. Stanev, Particle astrophysics with high-energy neutrinos, *Phys.Rept.* 258 (1995) 173–236. arXiv:hep-ph/9410384, doi:10.1016/0370-1573(95)00003-Y.
- [55] T. K. Gaisser, T. Stanev, F. Halzen, LIMITS ON THE ULTRAHIGH-ENERGY RADIATION BY YOUNG SUPERNOVAE (10 1987).
- [56] T. K. Gaisser, T. Stanev, Energetic ($> \text{GeV}$) Neutrinos as a Probe of Acceleration in the New Supernova, *Phys. Rev. Lett.* 58 (1987) 1695, [Erratum: *Phys.Rev.Lett.* 59, 844 (1987)]. doi:10.1103/PhysRevLett.58.1695.
- [57] T. K. Gaisser, G. Steigman, S. Tilav, Limits on Cold Dark Matter Candidates from Deep Underground Detectors, *Phys. Rev. D* 34 (1986) 2206. doi:10.1103/PhysRevD.34.2206.
- [58] T. K. Gaisser, T. Stanev, F. Halzen, W. F. Long, E. Zas, Gamma-ray astronomy above 50-TeV with muon poor showers, *Phys. Rev. D* 43 (1991) 314–318. doi:10.1103/PhysRevD.43.314.
- [59] D. Seckel, T. Stanev, T. K. Gaisser, Albedo gamma-ray from cosmic ray interactions on the solar surface, *AIP Conf. Proc.* 220 (1991) 227–231. doi:10.1063/1.40299.
- [60] C. A. Argüelles, A. Kheirandish, J. Lazar, Q. Liu, Search for Dark Matter Annihilation to Neutrinos from the Sun, *PoS ICRC2019* (2021) 527. arXiv:1909.03930, doi:10.22323/1.358.0527.
- [61] M. Ajello, et al., First Fermi-LAT Solar Flare Catalog, *Astrophys. J. Suppl.* 252 (2) (2021) 13, [Erratum: *Astrophys.J.Suppl.* 256, 24 (2021)]. arXiv:2101.10010, doi:10.3847/1538-4365/abd32e.
- [62] T. K. Gaisser, T. Stanev, Response of Deep Detectors to Extraterrestrial Neutrinos, *Phys. Rev. D* 31 (1985) 2770. doi:10.1103/PhysRevD.31.2770.
- [63] T. K. Gaisser, Fluxes of atmospheric neutrinos and related cosmic rays, *Nucl. Phys. B Proc. Suppl.* 77 (1999) 133–139. arXiv:hep-ph/9811315, doi:10.1016/S0920-5632(99)00408-9.
- [64] G. Barr, T. K. Gaisser, T. Stanev, Uncertainty Estimates for Atmospheric Neutrino Fluxes, in: 30th International Cosmic Ray Conference, Vol. 5, 2007, pp. 1495–1498.


- [65] M. G. Aartsen, et al., Evidence for High-Energy Extraterrestrial Neutrinos at the IceCube Detector, *Science* 342 (2013) 1242856. [arXiv:1311.5238](#), [doi:10.1126/science.1242856](#).
- [66] M. G. Aartsen, et al., Observation of High-Energy Astrophysical Neutrinos in Three Years of IceCube Data, *Phys. Rev. Lett.* 113 (2014) 101101. [arXiv:1405.5303](#), [doi:10.1103/PhysRevLett.113.101101](#).
- [67] R. Abbasi, et al., Evidence for neutrino emission from the nearby active galaxy NGC 1068, *Science* 378 (6619) (2022) 538–543. [arXiv:2211.09972](#), [doi:10.1126/science.abg3395](#).
- [68] M. G. Aartsen, et al., Multimessenger observations of a flaring blazar coincident with high-energy neutrino IceCube-170922A, *Science* 361 (6398) (2018) eaat1378. [arXiv:1807.08816](#), [doi:10.1126/science.aat1378](#).
- [69] M. G. Aartsen, et al., Neutrino emission from the direction of the blazar TXS 0506+056 prior to the IceCube-170922A alert, *Science* 361 (6398) (2018) 147–151. [arXiv:1807.08794](#), [doi:10.1126/science.aat2890](#).
- [70] S. Yu, J. Micallef, Recent neutrino oscillation result with the icecube experiment (2023). [arXiv:2307.15855](#).


Search for a $\mu^+\mu^-$ resonance in four-muon final states at Belle II



- I. Adachi , K. Adamczyk , L. Aggarwal , H. Ahmed , H. Aihara , N. Akopov , A. Aloisio , N. Anh Ky , D. M. Asner , H. Atmacan , V. Aushev , M. Aversano , R. Ayad , V. Babu , H. Bae , S. Bahinipati , P. Bambade , Sw. Banerjee , S. Bansal , M. Barrett , J. Baudot , A. Baur , A. Beaubien , F. Becherer , J. Becker , J. V. Bennett , F. U. Bernlochner , V. Bertacchi , M. Bertemes , E. Bertholet , M. Bessner , S. Bettarini , B. Bhuyan , F. Bianchi , T. Bilka , S. Bilokin , D. Biswas , A. Bobrov , D. Bodrov , A. Bolz , A. Bozek , M. Bračko , P. Branchini , T. E. Browder , A. Budano , S. Bussino , M. Campajola , L. Cao , G. Casarosa , C. Cecchi , J. Cerasoli , M.-C. Chang , P. Chang , R. Cheaib



, P. Cheema , B. G. Cheon , K. Chilikin , K. Chirapatpimol , H.-E. Cho , K. Cho , S.-J. Cho , S.-K. Choi , S. Choudhury , L. Corona , L. M. Cremaldi , S. Das , F. Dattola , E. De La Cruz-Burelo , S. A. De La Motte , G. De Nardo , M. De Nuccio , G. De Pietro , R. de Sangro , M. Destefanis , R. Dhamija , A. Di Canto , F. Di Capua , J. Dingfelder , Z. Doležal , T. V. Dong , M. Dorigo , K. Dort , S. Dreyer , S. Dubey , G. Dujany , P. Ecker , M. Eliachevitch , D. Epifanov , P. Feichtinger , T. Ferber , D. Ferlewicz , T. Fillinger , C. Finck , G. Finocchiaro , A. Fodor , F. Forti , A. Frey , B. G. Fulsom , A. Gabrielli , E. Ganiev , M. Garcia-Hernandez , R. Garg , G. Gaudino , V. Gaur , A. Gaz , A. Gellrich , G. Ghevondyan










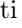


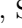
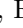



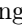
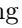
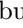
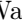



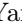

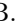


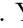






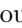
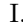
, D. Ghosh , H. Ghumaryan , G. Giakoustidis , R. Giordano , A. Giri , A. Glazov , B. Gobbo , R. Godang , O. Gogota , P. Goldenzweig , W. Gradl , T. Grammatico , E. Graziani , D. Greenwald , Z. Gruberová , T. Gu , K. Gudkova , S. Halder , Y. Han , T. Hara , H. Hayashii , S. Hazra , C. Hearty , M. T. Hedges , A. Heidelbach , I. Heredia de la Cruz , M. Hernández Villanueva , T. Higuchi , M. Hoek , M. Hohmann , P. Horak , C.-L. Hsu , T. Humair , T. Iijima , G. Inguglia , N. Ipsita , A. Ishikawa , R. Itoh , M. Iwasaki , P. Jackson , W. W. Jacobs , E.-J. Jang , Q. P. Ji , S. Jia , Y. Jin , K. K. Joo , H. Junkerkalefeld , D. Kalita , J. Kandra , K. H. Kang , G. Karyan , T. Kawasaki , F. Keil , C. Kiesling

, C.-H. Kim , D. Y. Kim , K.-H. Kim , Y.-K. Kim , H. Kindo , K. Kinoshita , P. Kodyš , T. Koga , S. Kohani , K. Kojima , A. Korobov , S. Korpar , E. Kovalenko , R. Kowalewski , T. M. G. Kraetzschmar , P. Križan , P. Krokovny , T. Kuhr , J. Kumar , M. Kumar , R. Kumar , K. Kumara , T. Kunigo , A. Kuzmin , Y.-J. Kwon , S. Lacaprara , Y.-T. Lai , T. Lam , L. Lanceri , J. S. Lange , M. Laurenza , K. Lautenbach , R. Lebourder , F. R. Le Diberder , M. J. Lee , D. Levit , P. M. Lewis , C. Li , L. K. Li , Y. Li , Y. B. Li , J. Libby , M. Liu , Q. Y. Liu , Z. Q. Liu , D. Liventsev , S. Longo , T. Lueck , C. Lyu , Y. Ma , M. Maggiora , S. P. Maharana , R. Maiti , S. Maity

, G. Mancinelli , R. Manfredi , E. Manoni , M. Mantovano , D. Marcantonio , S. Marcello , C. Marinas , L. Martel , C. Martellini , A. Martini , T. Martinov , L. Massaccesi , M. Masuda , K. Matsuoka , D. Matvienko , S. K. Maurya , J. A. McKenna , R. Mehta , F. Meier , M. Merola , F. Metzner , M. Milesi , C. Miller , M. Mirra , K. Miyabayashi , H. Miyake , R. Mizuk , G. B. Mohanty , N. Molina-Gonzalez , S. Mondal , S. Moneta , H.-G. Moser , M. Mrvar , R. Mussa , I. Nakamura , M. Nakao , Y. Nakazawa , A. Narimani Charan , M. Naruki , D. Narwal , Z. Natkaniec , A. Natochii , L. Nayak , M. Nayak , G. Nazaryan , C. Niebuhr , S. Nishida , S. Ogawa , Y. Onishchuk , H. Ono , Y. Onuki , P. Oskina , F. Otani , G. Pakhlova

, A. Panta , S. Pardi , K. Parham , H. Park , S.-H. Park , B. Paschen , A. Passeri , S. Patra , S. Paul , T. K. Pedlar , R. Peschke , R. Pestotnik , M. Piccolo , L. E. Piilonen , G. Pinna Angioni , P. L. M. Podesta-Lerma , T. Podobnik , S. Pokharel , C. Praz , S. Prell , E. Prencipe , M. T. Prim , H. Purwar , P. Rados , G. Raeuber , S. Raiz , N. Rauls , M. Reif , S. Reiter , M. Remnev , I. Ripp-Baudot , G. Rizzo , S. H. Robertson , M. Roehrken , J. M. Roney , A. Rostomyan , N. Rout , G. Russo , D. A. Sanders , S. Sandilya , L. Santelj , Y. Sato , V. Savinov , B. Scavino , C. Schmitt , C. Schwanda , M. Schwickardi , Y. Seino , A. Selce , K. Senyo , J. Serrano , M. E. Sevir , C. Sfienti , W. Shan

, C. P. Shen , X. D. Shi , T. Shillington , T. Shimasaki , J.-G. Shiu , D. Shtol , A. Sibidanov , F. Simon , J. B. Singh , J. Skorupa , R. J. Sobie , M. Sobotzik , A. Soffer , A. Sokolov , E. Solovieva , S. Spataro , B. Spruck , M. Starič , P. Stavroulakis , S. Stefkova , R. Stroili , M. Sumihama , K. Sumisawa , W. Sutcliffe , H. Svidras , M. Takizawa , U. Tamponi , S. Tanaka , K. Tanida , F. Tenchini , O. Tittel , R. Tiwary , D. Tonelli , E. Torassa , K. Trabelsi , I. Tsaklidis , M. Uchida , I. Ueda , K. Unger , Y. Unno , K. Uno , S. Uno

P. Urquijo , Y. Ushiroda , S. E. Vahsen , R. van Tonder , K. E. Varvell , M. Veronesi , A. Vinokurova ,
V. S. Vismaya , L. Vitale , V. Vobbiliseti , R. Volpe , B. Wach , M. Wakai , S. Wallner , E. Wang ,
M.-Z. Wang , X. L. Wang , Z. Wang , A. Warburton , S. Watanuki , C. Wessel , E. Won ,
X. P. Xu , B. D. Yabsley , S. Yamada , W. Yan , S. B. Yang , J. Yelton , J. H. Yin , K. Yoshihara ,
C. Z. Yuan , Y. Yusa , L. Zani , B. Zhang , V. Zhilich , Q. D. Zhou , X. Y. Zhou , and V. I. Zhukova 

(The Belle II Collaboration)

(Dated: March 5, 2024)

We report on a search for a resonance X decaying to a pair of muons in $e^+e^- \rightarrow \mu^+\mu^-X$ events in the 0.212–9.000 GeV/ c^2 mass range, using 178 fb $^{-1}$ of data collected by the Belle II experiment at the SuperKEKB collider at a center of mass energy of 10.58 GeV. The analysis probes two different models of X beyond the standard model: a Z' vector boson in the $L_\mu - L_\tau$ model and a muonphilic scalar. We observe no evidence for a signal and set exclusion limits at the 90% confidence level on the products of cross section and branching fraction for these processes, ranging from 0.046 fb to 0.97 fb for the $L_\mu - L_\tau$ model and from 0.055 fb to 1.3 fb for the muonphilic scalar model. For masses below 6 GeV/ c^2 , the corresponding constraints on the couplings of these processes to the standard model range from 0.0008 to 0.039 for the $L_\mu - L_\tau$ model and from 0.0018 to 0.040 for the muonphilic scalar model. These are the first constraints on the muonphilic scalar from a dedicated search.

PACS numbers:

I. INTRODUCTION

The standard model (SM) of particle physics is a highly predictive theoretical framework describing fundamental particles and their interactions. Despite its success, the SM is known to provide an incomplete description of nature. For example, it does not address the phenomenology related to dark matter, such as the observed relic density [1]. In addition, some experimental observations show inconsistencies with the SM. Prominent examples include the long-standing difference between the measured and the expected value of the muon anomalous magnetic-moment $(g-2)_\mu$ [2–4], possibly reduced by expectations based on lattice calculations [5], and the tensions in flavor observables reported by the BaBar, Belle, and LHCb experiments [6–8]. Some of these observations can be explained with the introduction of additional interactions, possibly lepton-universality-violating, mediated by non-SM neutral bosons [9–11]. Examples include the $L_\mu - L_\tau$ extension of the SM and a muonphilic scalar model.

The $L_\mu - L_\tau$ extension of the SM [12–14] gauges the difference between the muon and the τ -lepton numbers, giving rise to a new massive, neutral vector boson, the Z' . Among the SM particles, this particle couples only to μ , τ , ν_μ , and ν_τ , with a coupling constant g' . The Z' could also mediate interactions between SM and dark matter.

The muonphilic scalar S is primarily proposed as a solution for the $(g-2)_\mu$ anomaly [15–18]. This particle couples exclusively to muons through a Yukawa-like interaction, which is not gauge-invariant under the SM gauge symmetry and may arise from a high-dimension operator term at a mass scale beyond the SM. In contrast to the $L_\mu - L_\tau$ model, the muonphilic scalar model needs a high-energy completion.

Searches for a Z' decaying to muons have been re-

ported by the BaBar [19], Belle [20], and CMS [21] Collaborations. An invisibly decaying Z' has been searched for by the Belle II [22, 23] and NA64- e [24] experiments. The Belle II experiment also searched recently for a Z' decaying to $\tau^+\tau^-$ [25]. Constraints on the existence of a muonphilic scalar have been obtained by reinterpretations of Z' searches into muons [18]. However, important experimental details may be unaccounted for in these reinterpretation studies, including the significantly different kinematic properties of the signal and the corresponding variation of the efficiency.

Here we report a search for the process $e^+e^- \rightarrow \mu^+\mu^-X$, with $X \rightarrow \mu^+\mu^-$, where X indicates Z' or S . The signal signature is a narrow enhancement in the mass distribution of oppositely charged muons $M(\mu\mu)$ in $e^+e^- \rightarrow \mu^+\mu^-\mu^+\mu^-$ events. We use data collected by the Belle II experiment at a center-of-mass (c.m.) energy \sqrt{s} corresponding to the mass of the $\Upsilon(4S)$ resonance. The $L_\mu - L_\tau$ model is used as a benchmark to develop the analysis; we then apply the same selections to the muonphilic scalar model and evaluate the performance. In both models, the X particle is at leading order emitted as final-state radiation (FSR) from one of the muons, as shown in Fig. 1. For the range of couplings explored in this study, the lifetime of X is negligible compared to the experimental resolution. The analysis techniques are optimized using simulated events prior to examining data.

We select events with exactly four charged particles with zero net charge, where at least three are identified as muons, with an invariant mass $M(4\mu)$ close to \sqrt{s}/c^2 , and with negligible extra energy in the event. The dominant, non-peaking background is the SM $e^+e^- \rightarrow \mu^+\mu^-\mu^+\mu^-$ process, whose main production diagrams are shown in Fig. 2. The analysis uses kinematic variables combined with a multivariate technique to enhance the signal-to-background ratio. A kinematic fit improves the dimuon mass resolution. The signal yield is extracted through a

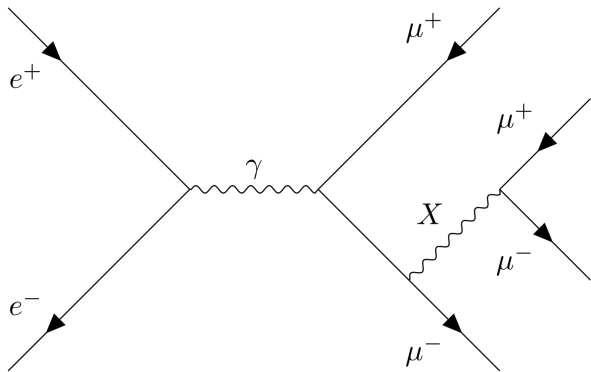


Figure 1: Leading-order Feynman diagram for the process $e^+e^- \rightarrow \mu^+\mu^-X, X \rightarrow \mu^+\mu^-$.

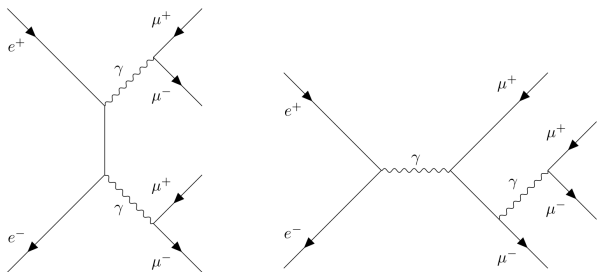


Figure 2: Leading-order Feynman diagrams for the two main contributions to the $e^+e^- \rightarrow \mu^+\mu^-\mu^+\mu^-$ SM background: double photon conversion (left) and annihilation (right).

series of fits to the $M(\mu\mu)$ distribution, which allows an estimate of the background directly from data.

The paper is organized as follows. In Sec. II we briefly describe the Belle II experiment. In Sec. III we report the datasets and the simulation used. In Sec. IV we present the event selections. In Sec. V we describe the signal modeling and the fit technique to extract the signal. In Sec. VI we discuss the systematic uncertainties. In Sec. VII we describe and discuss the results. Sec. VIII summarizes our conclusions.

II. THE BELLE II EXPERIMENT

The Belle II detector [26, 27] consists of several subdetectors arranged in a cylindrical structure around the e^+e^- interaction point. The longitudinal direction, the transverse plane, and the polar angle θ are defined with respect to the detector's cylindrical axis in the direction of the electron beam.

Subdetectors relevant for this analysis are briefly described here in order from innermost out; a full description of the detector is given in Refs. [26, 27]. The innermost subdetector is the vertex detector, which consists of two inner layers of silicon pixels and four outer layers of

silicon strips. The second pixel layer was only partially installed for the data sample we analyze, covering one sixth of the azimuthal angle. The main tracking subdetector is a large helium-based small-cell drift chamber. The relative charged-particle transverse momentum resolution, $\frac{\Delta p_T}{p_T}$, is typically $0.1\%p_T \oplus 0.3\%$, with p_T expressed in GeV/c . Outside of the drift chamber, time-of-propagation and aerogel ring-imaging Cherenkov detectors provide charged-particle identification in the barrel and forward endcap region, respectively. An electromagnetic calorimeter consists of a barrel and two endcaps made of CsI(Tl) crystals: it reconstructs photons and identifies electrons. A superconducting solenoid, situated outside of the calorimeter, provides a 1.5 T magnetic field. A K_L^0 and muon subdetector (KLM) is made of iron plates, which serve as a magnetic flux-return yoke, alternated with resistive-plate chambers and plastic scintillators in the barrel and with plastic scintillators only in the endcaps. In the following, quantities are defined in the laboratory frame unless specified otherwise.

III. DATA AND SIMULATION

We use a sample of e^+e^- collisions produced at c.m. energy $\sqrt{s} = 10.58 \text{ GeV}$ in 2020–2021 by the SuperKEKB asymmetric-energy collider [28] at KEK. The data, recorded by the Belle II detector, correspond to an integrated luminosity of 178 fb^{-1} [29].

Simulated signal $e^+e^- \rightarrow \mu^+\mu^-Z'$ with $Z' \rightarrow \mu^+\mu^-$ and $e^+e^- \rightarrow \mu^+\mu^-S$ with $S \rightarrow \mu^+\mu^-$ events are generated using `MadGraph5_aMC@NLO` [30] with initial-state radiation (ISR) included [31]. Two independent sets of Z' events are produced, with Z' masses, $m_{Z'}$, ranging from $0.212 \text{ GeV}/c^2$ to $10 \text{ GeV}/c^2$ in steps of $250 \text{ MeV}/c^2$, to estimate efficiencies, define selection requirements, and develop the fit strategy, and in steps of $5 \text{ MeV}/c^2$, exclusively dedicated to the training of the multivariate analysis. Samples of S events are generated in $40 \text{ MeV}/c^2$ steps for m_S masses between $0.212 \text{ GeV}/c^2$ and $1 \text{ GeV}/c^2$ and in $250 \text{ MeV}/c^2$ steps from $1 \text{ GeV}/c^2$ to $10 \text{ GeV}/c^2$.

Background processes are simulated using the following generators: $e^+e^- \rightarrow \mu^+\mu^-\mu^+\mu^-$, $e^+e^- \rightarrow e^+e^-\mu^+\mu^-$, $e^+e^- \rightarrow e^+e^-e^+e^-$, $e^+e^- \rightarrow \mu^+\mu^-\tau^+\tau^-$ and $e^+e^- \rightarrow e^+e^-\tau^+\tau^-$, with `AAFH` [32]; $e^+e^- \rightarrow \mu^+\mu^-(\gamma)$ with `KKMC` [33]; $e^+e^- \rightarrow \tau^+\tau^-(\gamma)$ with `KKMC` interfaced with `TAUOLA` [34]; $e^+e^- \rightarrow e^+e^-\pi^+\pi^-$ with `TREPS` [35]; $e^+e^- \rightarrow \pi^+\pi^-(\gamma)$ with `PHOKHARA` [36]; $e^+e^- \rightarrow e^+e^-(\gamma)$ with `BabaYaga@NLO` [37]; $e^+e^- \rightarrow u\bar{u}, d\bar{d}, s\bar{s}, c\bar{c}$ with `KKMC` interfaced with `PYTHIA8` [38] and `EVTGEN` [39] and $e^+e^- \rightarrow B^0\bar{B}^0$ and $e^+e^- \rightarrow B^+B^-$ with `EVTGEN` interfaced with `PYTHIA8`. Electromagnetic FSR is simulated with `PHOTOS` [40, 41] for processes generated with `EVTGEN`. The `AAFH` generator, used for the four-lepton processes, including the dominant $e^+e^- \rightarrow \mu^+\mu^-\mu^+\mu^-$ background, does not simulate ISR effects. This is a source of disagreement between data and simulation. Other sources of non-simulated backgrounds in-

clude $e^+e^- \rightarrow \mu^+\mu^-\pi^+\pi^-$ and more generally $e^+e^- \rightarrow \mu^+\mu^-h$ and $e^+e^- \rightarrow \pi^+\pi^-h$, where h is typically a low-mass hadronic system; $e^+e^- \rightarrow J/\psi \pi^+\pi^-$ with $J/\psi \rightarrow \mu^+\mu^-$; $e^+e^- \rightarrow \psi(2S)\gamma$ with $\psi(2S) \rightarrow J/\psi \pi^+\pi^-$ and $J/\psi \rightarrow \mu^+\mu^-$; and $e^+e^- \rightarrow \Upsilon(nS) \pi^+\pi^-$ with $\Upsilon(nS) \rightarrow \mu^+\mu^-$ and $n = 1, 2, 3$.

The detector geometry and interactions of final-state particles with detector material are simulated using `GEANT4` [42] and the Belle II software [43, 44].

IV. SELECTIONS

The selection requirements are divided into four categories: trigger, particle identification, candidate selections, and final background suppression.

A. Trigger selections

We filter events selected by the logical OR of a three-track trigger and a single-muon trigger. The efficiency of both triggers is measured using a reference calorimeter-only trigger, which requires a total energy deposit above 1 GeV in the polar angle region $22^\circ < \theta < 128^\circ$. We require a single electron of sufficient energy to activate the calorimeter trigger. The three-track trigger requires the presence of at least three tracks with $37^\circ < \theta < 120^\circ$. The efficiency of this trigger is measured in four-track events containing at least two pions and one electron and depends on the transverse momenta p_T of the two charged particles with lowest transverse momenta, reaching a plateau close to 100% for p_T above 0.5 GeV/ c . The single-muon trigger is based on the association of hits in the barrel KLM with geometrically matched tracks extrapolated from the inner tracker. The efficiency of this trigger is measured in a sample of two-track events with one electron and one muon, mostly from the $e^+e^- \rightarrow \tau^+\tau^-$ process, reaching a plateau of about 90% in the polar angle range $51^\circ < \theta < 117^\circ$. The efficiency for events with multiple muons is computed using the single-muon efficiency assuming no correlation. The overall trigger efficiency is 91% for $m_{Z'}$ close to the dimuon mass, increases smoothly to a plateau close to 99% in the mass range 2.5–8.5 GeV/ c^2 , and then drops to 89% at 10 GeV/ c^2 . It is slightly higher, 95%, for low masses in the S case, due to the harder spectrum of the muonphilic scalar (see Sec. IV E).

B. Particle identification

The identification of muons relies mostly on charged-particle penetration in the KLM for momenta larger than 0.7 GeV/ c and on information from the drift chamber and the calorimeter otherwise. The selection retains 93%–99% of the muons, and rejects 80%–97% of the pions, depending on their momenta. Electrons are identified

mostly by comparing measured momenta to the energies of the associated calorimeter deposits. Photons are reconstructed from calorimeter energy deposits greater than 100 MeV that are not associated with any track. Details of particle reconstruction and identification algorithms are given in Refs. [27, 45].

C. Candidate selections

We require that events have exactly four charged particles with zero net charge and invariant mass $M(4\mu)$ between 10 GeV/ c^2 and 11 GeV/ c^2 . To suppress backgrounds from misreconstructed and single-beam induced tracks, the transverse and longitudinal projections of the distance of closest approach to the interaction point of the tracks must be smaller than 0.5 cm and 2.0 cm, respectively. At least three of the tracks must be identified as muons. This requirement provides better performance than requiring four identified muons or a pair of same-sign muons. It rejects almost all backgrounds other than $e^+e^- \rightarrow \mu^+\mu^-\mu^+\mu^-$, while retaining good efficiency for signal.

In the low-mass region below 1 GeV/ c^2 , there are residual backgrounds from $e^+e^- \rightarrow \mu^+\mu^-\gamma$, in which the photon converts to an electron-positron pair, and $e^+e^- \rightarrow e^+e^-\mu^+\mu^-$ events. Some of these electrons that are misidentified as muons have low momenta, and thus do not reach the KLM. The remaining electrons leave signals in the KLM at the gap between the barrel and endcap or in the gaps between adjacent modules. In this mass region, we therefore require that no track be identified as an electron.

To suppress radiative backgrounds and, in general, backgrounds with neutral particles, we require that the total energy of all photons be less than 0.4 GeV. We add an additional requirement when $M(4\mu) < 10.4$ GeV/ c^2 , which exploits the correlation of the invariant mass with initial-state radiation, requiring that the total energy of all photons be less than that expected for a single radiated photon. In addition, we reject events in which the angle in the c.m. frame between the momentum of the four-muon system and that of the system composed of all the photons is larger than 160° .

At this level of the analysis, there is no a priori attempt to select a single $\mu^+\mu^-$ pair as a candidate X decay. Each event includes four possible $\mu^+\mu^-$ candidates, each with a different dimuon mass $M(\mu\mu)$, causing some combinatorial background. For each $\mu^+\mu^-$ candidate, the pair of the two remaining muons is labeled as the “recoil” pair. We consider independently all the $\mu^+\mu^-$ candidates, each with its recoil muons.

The resulting candidate $M(\mu\mu)$ distribution is shown in Fig. 3. The average data-to-simulation yield ratio is 0.76, due to the lack of ISR in the AAFH four-muon generator, in agreement with the values previously reported by BaBar [19] and Belle [20]. The excess of the simulation over data in the mass region below 2 GeV/ c^2 is also due

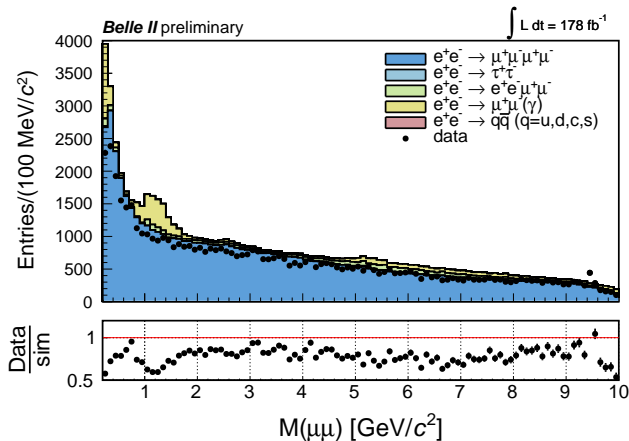


Figure 3: Dimuon invariant-mass distribution in data and simulation for candidates passing all selections but the final background suppression. Contributions from the various simulated processes are stacked. The subpanel shows the data-to-simulation ratio.

to an overestimate of the three-track-trigger efficiency for very low transverse-momentum tracks. Specifically, the enhancement in the range 1–2 GeV/ c^2 originates from the process $e^+e^- \rightarrow \mu^+\mu^-\gamma$ with a near-beam-energy photon, followed by conversion of the photon into electron-positron pairs in detector material. These events are almost entirely removed by the final background suppression. Other visible features include the unsimulated contributions from the ρ , J/ψ , and $\Upsilon(1S)$ resonances.

D. Final background suppression

The final selection relies on a few distinctive features that allow the discrimination of signal from background: signal events include a $\mu^+\mu^-$ resonance, which can be seen both in the candidate muon pair and in the mass of the system recoiling against the two recoil muons; the signal is emitted through FSR from a muon (Fig. 1), while the dominant four-muon background proceeds through double-photon-conversion process (Fig. 2, left); and the double-photon-conversion process has a distinctive momentum distribution. In the following, some of the relevant variables sensitive to these three classes of features are discussed: they are based both on the $\mu^+\mu^-$ candidate, where we search for signal, and on the recoil muons. For illustration, we show the case for a Z' signal with $m_{Z'} = 3 \text{ GeV}/c^2$ and for background, both with reconstructed candidate dimuon masses $2.75 < M(\mu\mu) < 3.25 \text{ GeV}/c^2$.

Magnitudes of the two candidate muon momenta, p_{μ^+} and p_{μ^-} , and their correlations are sensitive to the presence of a resonance (Fig. 4). Signal events cluster preferentially in the central part of the distribution, while background predominantly populates the extremes. A similar

effect occurs for the momenta of the two recoil muons, $p_{\mu^+}^{\text{rec}}$ and $p_{\mu^-}^{\text{rec}}$ (Fig. 5), which provide instrumentally uncorrelated access to the same information, though with a different resolution. The cosine of the helicity angle of the candidate-muon pair $\cos\phi_{\text{hel}}$, defined as the angle between the momentum direction of the c.m. frame and the μ^- in the candidate-muon-pair frame, has a uniform distribution for a scalar or an unpolarized massive vector decaying to two fermions, but not for the background processes (Fig. 6). The slight departure from uniformity in the signal case is due to momentum resolution, which smears the determination of the boost to the muon-pair frame.

The double-photon-conversion process (Fig. 2, left) accounts for 80% of the four-muon background cross section. It also includes the case of off-shell photon emission (and subsequent dimuon production) from one of the initial-state electrons, ISR double-photon conversion, which contributes mainly in the low mass region. The annihilation process (Fig. 2, right) is very similar to the signal process and constitutes an nearly irreducible background: it accounts for 20% of the cross section for $M(\mu\mu) < 1 \text{ GeV}/c^2$ and for 10% above. Transverse projections of the candidate-muon-pair momentum $p_{\mu\mu}$ on the direction of the recoil muon with minimum momentum, $p_T(p_{\mu\mu}, p_{\text{min}}^{\text{rec}})$, and on the direction of the recoil muon with maximum momentum, $p_T(p_{\mu\mu}, p_{\text{max}}^{\text{rec}})$, are sensitive to FSR emission (Fig. 7). This is because, in case of signal, these are the transverse momenta of X with respect to the direction of the muon from which it was emitted, and with respect to the direction of the other muon. We assign to the transverse projection $p_T(p_{\mu\mu}, p_{\text{min}}^{\text{rec}})$ the sign of the longitudinal projection, since this slightly increases the discriminating power. The transverse momentum of the candidate muon pair with respect to the z axis, $p_T(p_{\mu\mu}, z)$, which approximates the beam direction, is sensitive to the ISR double-photon conversion mechanism of emission because $p_T(p_{\mu\mu}, z)$ is the transverse momentum of the muon pair with respect to the initial-state-electron direction. This variable is shown in Fig. 8 in a two-dimensional distribution versus $p_T(p_{\mu\mu}, p_{\text{min}}^{\text{rec}})$ to illustrate the correlation between variables sensitive to ISR and FSR, respectively.

The double photon conversion process produces two muon pairs from two off-shell photons. The dominant background at a mass m_0 is produced when one pair has $M(\mu\mu)$ near m_0 and the other pair has a mass at the lowest possible value above $2m_\mu$. In these cases, the c.m. momentum p_0 of the two pairs can be analytically calculated. In $e^+e^- \rightarrow \mu^+\mu^-\mu^+\mu^-$ background events the dimuon c.m. momentum $p_{\mu\mu}$ peaks at p_0 , in contrast to the signal, at least for two of the dimuon candidates. This difference is visible in Fig. 9.

We select sixteen discriminating variables: the magnitude of the candidate-muon-pair momentum $p_{\mu\mu}$; the absolute value of the cosine of the helicity angle in the candidate-muon-pair rest frame; the magnitudes of the candidate-single-muon momenta; the candidate-single-

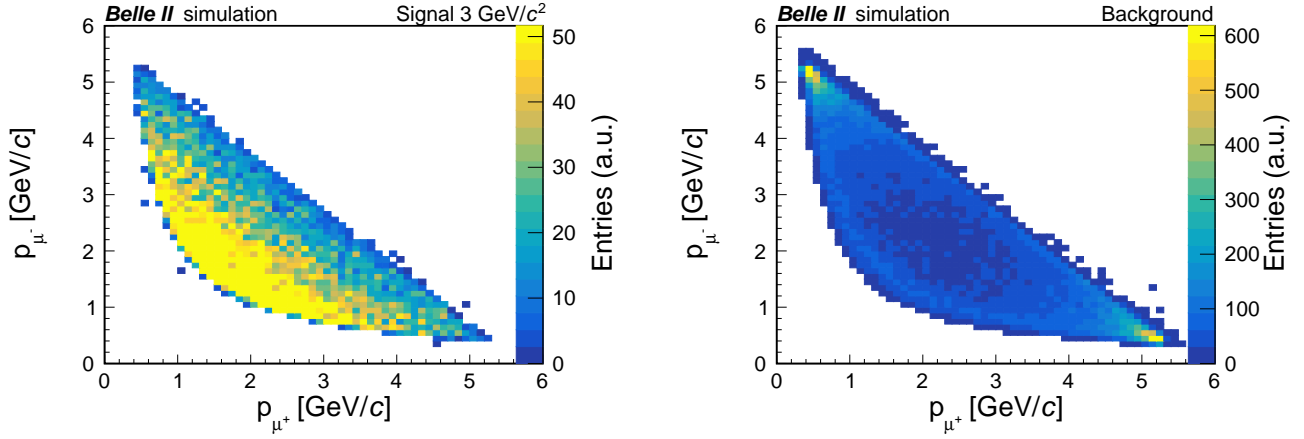


Figure 4: Candidate- μ^+ momentum versus candidate- μ^- momentum for simulated signal (left) with $m_{Z'}$ = $3 \text{ GeV}/c^2$ and simulated background (right), for dimuon masses $2.75 < M(\mu\mu) < 3.25 \text{ GeV}/c^2$.

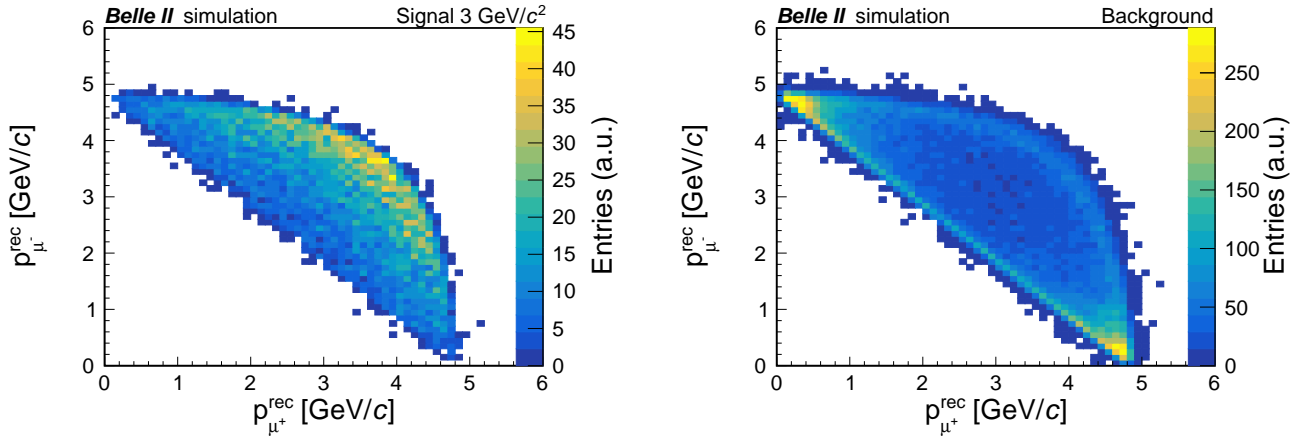


Figure 5: Recoil- μ^+ momentum versus recoil- μ^- momentum for simulated signal (left) with $m_{Z'}$ = $3 \text{ GeV}/c^2$ and simulated background (right), for dimuon masses $2.75 < M(\mu\mu) < 3.25 \text{ GeV}/c^2$.

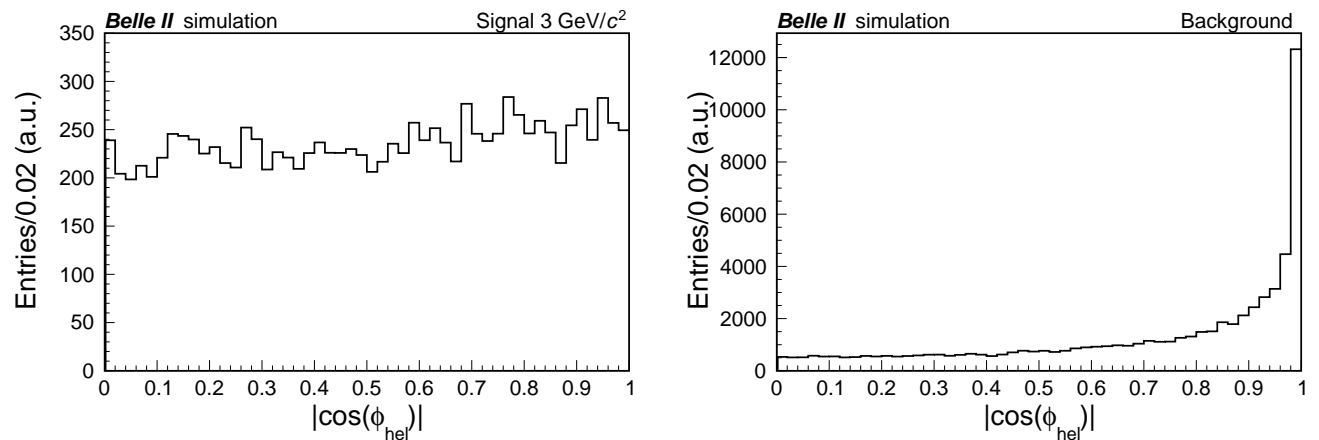


Figure 6: Absolute value of the cosine of the helicity angle for simulated signal (left) with $m_{Z'}$ = $3 \text{ GeV}/c^2$ and simulated background (right), for dimuon masses $2.75 < M(\mu\mu) < 3.25 \text{ GeV}/c^2$.

muon transverse momenta; the magnitudes of the recoil-

single-muon momenta; the recoil-single-muon transverse

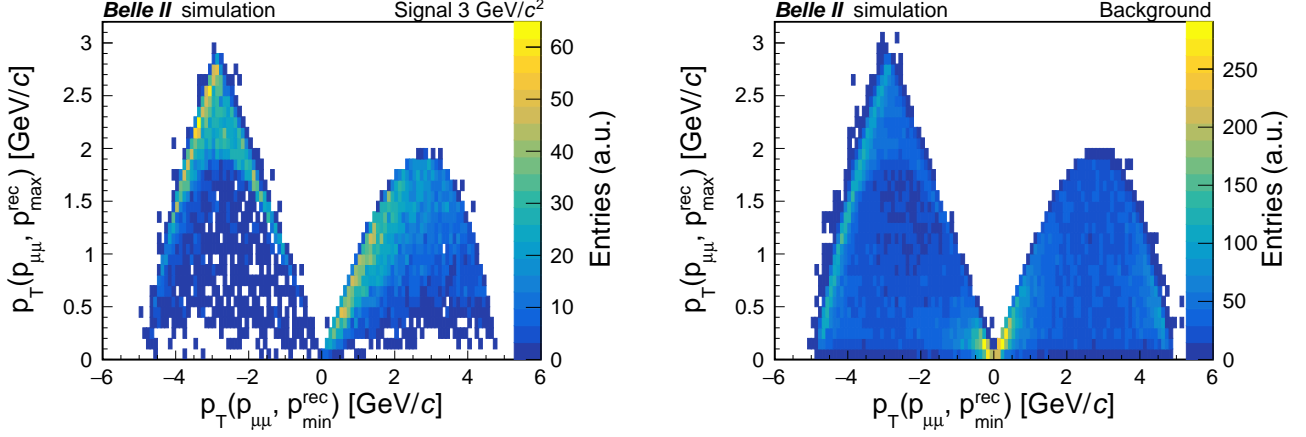


Figure 7: Candidate-muon-pair transverse momentum with respect to the maximum momentum recoil-muon direction versus the candidate-muon-pair transverse momentum with respect to the minimum momentum recoil-muon direction (with the sign of the longitudinal projection) for simulated signal (left) with $m_{Z'} = 3 \text{ GeV}/c^2$ and simulated background (right), for dimuon masses $2.75 < M(\mu\mu) < 3.25 \text{ GeV}/c^2$.

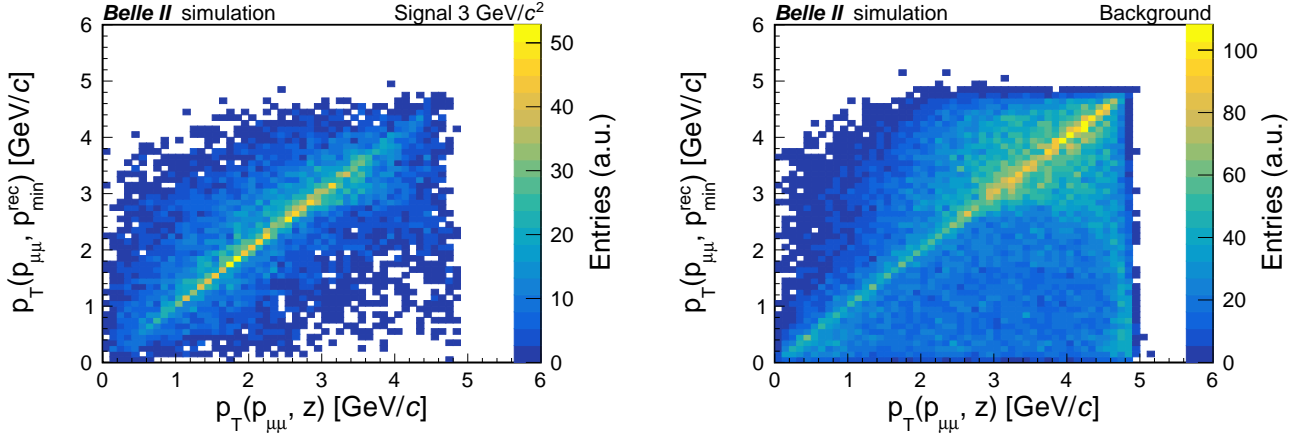


Figure 8: Candidate-muon-pair transverse momentum with respect to the minimum-momentum recoil-muon direction versus candidate-muon-pair transverse momentum with respect to the beam direction, for simulated signal (left) with $m_{Z'} = 3 \text{ GeV}/c^2$ and simulated background (right), for dimuon masses $2.75 < M(\mu\mu) < 3.25 \text{ GeV}/c^2$.

momenta; $p_T(p_{\mu\mu}, p_{\min}^{\text{rec}})$ and $p_T(p_{\mu\mu}, p_{\max}^{\text{rec}})$; the correlation of $p_T(p_{\mu\mu}, p_{\min}^{\text{rec}})$ with $p_T(p_{\mu\mu}, z)$; and the transverse projections of the recoil-muon-pair momentum on the directions of the momenta of the candidate muons with minimum and maximum momentum. All variables other than the helicity angle are defined in the c.m. frame.

The variables, with the exception of the helicity angle, are transformed to minimize their variation with $m_{Z'}$. For momentum-dimensional variables, we scale by p_0 , which is also the maximum c.m. momentum of the two muon pairs.

We use multilayer perceptron (MLP) artificial neural networks [46] with 16 input neurons, fed with the discriminant variables, and with one output neuron. The MLPs are developed using simulated Z' and simulated background events. To improve performance, we use five separate MLPs in different $M(\mu\mu)$ intervals, which

we refer to as MLP ranges: $0.21\text{--}1.00 \text{ GeV}/c^2$, $1.00\text{--}3.75 \text{ GeV}/c^2$, $3.75\text{--}6.25 \text{ GeV}/c^2$, $6.25\text{--}8.25 \text{ GeV}/c^2$, and $8.25\text{--}10.00 \text{ GeV}/c^2$. To ensure that MLPs are not biased to specific mass values, we use a training signal sample that has mass steps of $5 \text{ MeV}/c^2$, so as to approximate a continuous distribution. For nearly all masses, the most discriminating variable is $p_{\mu\mu}$, followed by the correlation of p_{μ^+} and p_{μ^-} .

The selection applied on the MLP output is studied separately in each MLP range, by maximizing the figure of merit described in Ref. [47], and then expressed as a function of $M(\mu\mu)$ by interpolation. The background rejection factor achieved by the MLP selection varies from 2.5 to 14, with the best value around $5 \text{ GeV}/c^2$. The resulting background is composed almost entirely of $e^+e^- \rightarrow \mu^+\mu^-\mu^+\mu^-$ events, with $e^+e^- \rightarrow \mu^+\mu^-(\gamma)$ and $e^+e^- \rightarrow e^+e^-\mu^+\mu^-$ processes contributing only be-

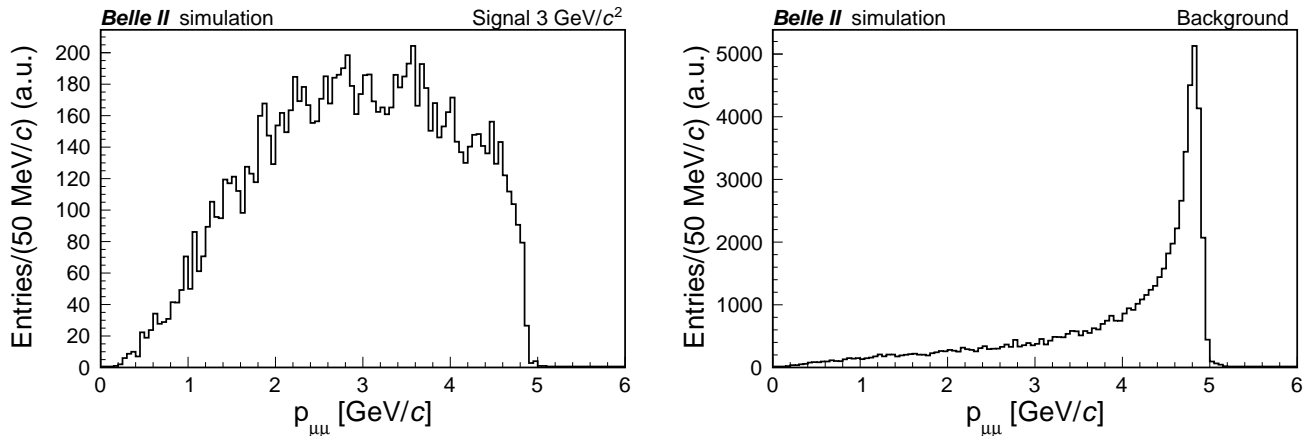


Figure 9: Candidate-muon-pair momentum $p_{\mu\mu}$ for signal (left) with $m_{Z'} = 3 \text{ GeV}/c^2$ and background (right), for dimuon masses $2.75 < M(\mu\mu) < 3.25 \text{ GeV}/c^2$.

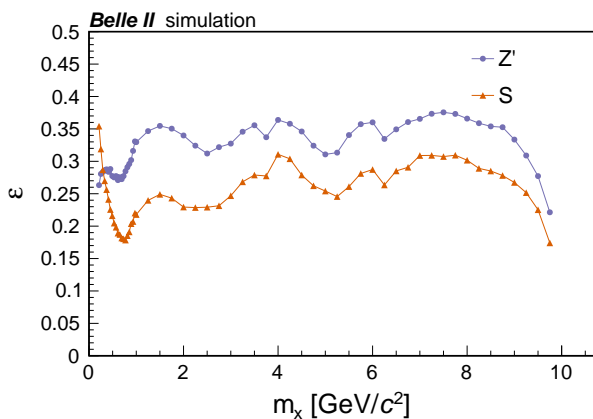


Figure 10: Signal efficiency as a function of $m_{Z'}$ (purple dots) and m_S (orange triangles) masses after all selections are applied.

low $1 \text{ GeV}/c^2$. The MLP selection is applied separately to each of the four candidates per event, reducing the average candidate multiplicity per background event to 1.7. The candidate multiplicity per signal event varies between 1.4 and 3, depending on the mass.

E. Efficiencies and dimuon spectrum

The efficiencies of the full selection for the $L_\mu - L_\tau$ and muonphilic scalar models are shown in Fig. 10. The efficiency for the scalar increases below $1 \text{ GeV}/c^2$ because the S , due to angular momentum conservation, is produced through a p-wave process, and has a harder momentum spectrum than the Z' , which is produced via an s-wave process. For masses above $1 \text{ GeV}/c^2$, the S efficiency is lower than the Z' because the analysis, particularly in the final background suppression part, is optimized for

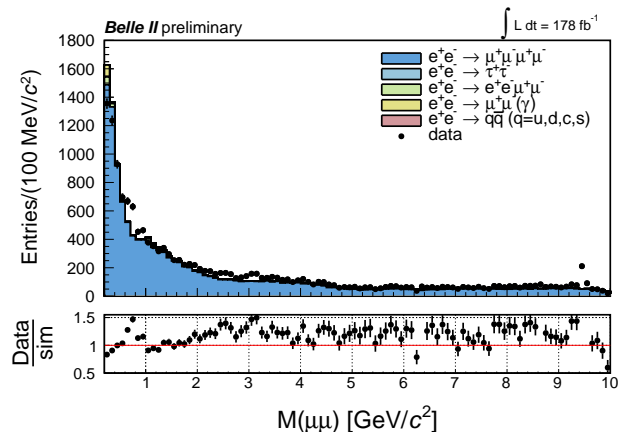


Figure 11: Dimuon invariant-mass distribution in data and simulation for candidates passing all the selections. Contributions from the various simulated process are stacked. The subpanel shows the data-to-simulation ratio.

the $L_\mu - L_\tau$ model.

The signal efficiencies shown here are corrected for ISR. Although the signal generator includes ISR, it does not include the large-angle hard-radiation component that can produce photons in the acceptance, and thereby veto events. This effect is studied using $e^+e^- \rightarrow \mu^+\mu^-\gamma$ events, generated with KKMC that simulates ISR in a complete way, and gives a relative reduction of 2.8% in efficiency.

To improve the m_X resolution, a kinematic fit is applied requiring that the sum of the four-momenta of the muons be equal to the four-momentum of the c.m. system, thus constraining the four-muon invariant mass to \sqrt{s}/c^2 . The resulting $M(\mu\mu)$ distribution is shown in Fig. 11. With the exception of the very low mass region, the data-to-simulation yield ratio is generally above one. This is because the MLPs perform worse on data, which naturally includes ISR, than on background simulation,

which does not. This is not the case for the signal, which is simulated with the ISR contribution. Also visible in Fig. 11 are modulations originating from the five MLP ranges. Neither of these effects produce narrow peaking structures at the scale of the signal resolution, 2–5 MeV/ c^2 (Sec. V). As in Fig. 3, contributions from the unsimulated ρ , J/ψ , and $\Upsilon(1S)$ resonances are visible.

V. SIGNAL MODELING AND FIT

To search for the signal, we use the reduced dimuon mass $M_R \equiv \sqrt{M^2(\mu\mu) - 4m_\mu^2}$, which has smoother behavior than the dimuon mass near the kinematic threshold. The reduced-mass resolution is 2–2.5 MeV/ c^2 for $m_{Z'}$ below 1 GeV/ c^2 , increases smoothly to 5 MeV/ c^2 for $m_{Z'}$ around 5 GeV/ c^2 , then decreases to 2.5 MeV/ c^2 at 9 GeV/ c^2 .

The signal yields are obtained from a scan over the M_R spectrum through a series of unbinned maximum likelihood fits. The signal M_R distributions are parameterized from the simulation as sums of two Crystal Ball functions [48] sharing the same mean. The background is described with a quadratic function with coefficients as free parameters in the fit for masses below 1 GeV/ c^2 , and with a straight line above. Higher-order polynomials are investigated, but their corresponding fitted coefficients are compatible with zero over the full mass spectrum. The broad ρ contribution is accommodated by the quadratic fit.

The scan step-size is set equal to the mass resolution, which is sufficient to detect the presence of a X resonance regardless of its mass. The fit interval is 60 times the mass resolution, following an optimization study. A total of 2315 fits are performed, covering dimuon masses from 0.212 GeV/ c^2 to 9 GeV/ c^2 . If a fitting interval extends over two different MLP ranges, we use the MLP corresponding to the central mass. We exclude the dimuon mass interval 3.07–3.12 GeV/ c^2 , which corresponds to the J/ψ mass. The $\Upsilon(1S)$ peak is beyond the mass range of the search. The fit yields are scaled by 7% based on a study of the J/ψ in an $e^+e^-\mu^+\mu^-$ control sample, which obtains a width 25% larger than in simulated signals of that mass. Propagating this 25% degradation in resolution to all masses gives an average yield bias of 7%. This is also included as a systematic uncertainty (Sec. VI).

Signal yields from the fits are then converted into cross sections, after correcting for signal efficiency and luminosity.

VI. SYSTEMATIC UNCERTAINTIES

Several sources of systematic uncertainties affecting the cross-section determination are taken into account: these include signal efficiency, luminosity, and fit procedure.

Uncertainties due to the trigger efficiency in signal events are evaluated by propagating the uncertainties on the measured trigger efficiencies. They are 0.3% for most of the mass spectrum, increasing to 1.7% at low masses and 0.5% at high masses.

Uncertainties due to the tracking efficiency are estimated in $e^+e^- \rightarrow \tau^+\tau^-$ events in which one τ decays to a single charged particle and the other τ to three charged particles. The relative uncertainty on the signal efficiency is 3.6%.

Uncertainties due to the muon identification requirement are studied using $e^+e^- \rightarrow \mu^+\mu^-\gamma$, $e^+e^- \rightarrow e^+e^-\mu^+\mu^-$ events, and final states with a J/ψ . The relative uncertainty on the signal efficiency varies between 0.7% and 3%, depending on the X mass.

Beam backgrounds in the calorimeter can accidentally veto events due to the requirements on photons (Sec. IV C). The effect is studied by changing the level of beam backgrounds in the simulation and by varying the photon energy requirement (see Sec. IV) according to the calorimeter resolution. The relative uncertainty on the signal efficiency due to this source is estimated to be below 1%.

To evaluate uncertainties due to the data-to-simulation discrepancies in MLP selection efficiencies, we apply a tight selection on $M(4\mu)$ around \sqrt{s}/c^2 requiring it to be in the range 10.54–10.62 GeV/ c^2 . With this selection, data and background simulation are more directly comparable, because ISR and FSR effects are much less important. We compare MLP efficiencies, defined as the ratio of the number of events before and after the MLP selection, in data and simulation and assume that the uncertainties estimated in those signal-like conditions are representative of signal. We also assume that these uncertainties hold in the full $M(4\mu)$ interval 10–11 GeV/ c^2 for the signal, which is generated with ISR. The differences found in each MLP range vary between 1.1% and 8.1%, which are taken as estimates of the systematic uncertainties. To exclude potential bias from the presence of a signal, we check that these differences do not change if we exclude, in each MLP range and for each of the 2315 mass points, intervals ten times larger than the signal mass resolution around the test masses.

Uncertainties due to the interpolation of the signal efficiency between simulated points are estimated to be 3%, which is assigned as a relative uncertainty on the signal efficiency.

Uncertainties due to the fit procedure, in addition to that arising from mass resolution, are evaluated using a bootstrap technique [49]. A number of simulated signal events corresponding to the yield excluded at 90% confidence level are overlaid on simulated background and fitted for each Z' mass. The distribution of the difference between the overlaid and the fitted yields, divided by the fit uncertainty, shows a negligible average bias with a width that deviates from one by 4%, which is assigned as a relative uncertainty on the signal-yield determination. Additional uncertainties related to the fit procedure are

Table I: Systematic uncertainties affecting the cross-section determination.

Source	uncertainty(%)
Trigger	0.3–1.7
Tracking	3.6
Particle identification	0.7–3
Beam background and calorimeter energy resolution	1
MLP selection	1.1–8.1
Efficiency interpolation	3
Fit bias	4
Mass resolution	7
Luminosity	1
Total	9.5–12.9

those due to the mass resolution, discussed in Sec. V. An uncertainty of 7%, equal to the average yield bias, is included.

Systematic uncertainties from data-to-simulation differences in momentum resolution and beam-energy shift are found to be negligible, due to the kinematic fitting procedure. Finally, the integrated luminosity has a systematic uncertainty of 1% [29].

The uncertainties are summed in quadrature to give a total that ranges from 9.5% to 12.9% depending on the X mass. The contributions to the systematic uncertainty are summarized in Table I. We account for systematic uncertainties through a Gaussian smearing of the signal efficiency.

VII. RESULTS

The significance of signal over background for each fit is evaluated as $\sqrt{2\log(\mathcal{L}/\mathcal{L}_0)}$, where \mathcal{L} and \mathcal{L}_0 are the likelihoods of the fits with and without signal. The largest local one-sided significance observed is 3.4σ at $M(\mu\mu) = 5.307 \text{ GeV}/c^2$, corresponding to a 1.6σ global significance after taking into account the look-elsewhere effect [50, 51]. The corresponding fit is shown in Fig. 12. Three additional mass points have local significances that exceed 3σ . They are at $M(\mu\mu)$ masses of $1.939 \text{ GeV}/c^2$, $4.518 \text{ GeV}/c^2$, and $4.947 \text{ GeV}/c^2$, with global significances of 0.6σ , 1.2σ , and 1.1σ , respectively.

Since we do not observe any significant excess above the background, we derive 90% confidence level (CL) upper limits (UL) on the process cross sections $\sigma(e^+e^- \rightarrow \mu^+\mu^-X) \times \mathcal{B}(X \rightarrow \mu^+\mu^-)$ separately for Z' and S (Fig. 13), using the frequentist procedure CL_S [52]. The expected limits in Fig. 13 are the median limits from background-only simulated samples that use yields from fits to data. We obtain upper limits ranging from 0.046 fb to 0.97 fb for the $L_\mu - L_\tau$ model, and from 0.055 fb to 1.3 fb for the muonphilic scalar model. These upper limits are dominated by sample size, with systematic uncertainties worsening them on average by less than 1%.

The cross-section results are translated into upper limits on the coupling constant g' of the $L_\mu - L_\tau$ model

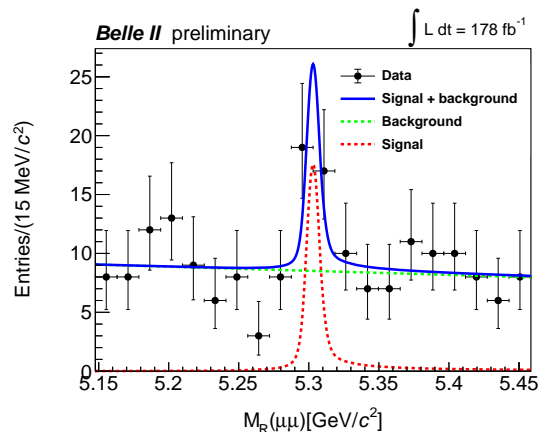


Figure 12: Fit for a Z' mass hypothesis of $5.307 \text{ GeV}/c^2$, for which we obtain the maximum local significance of 3.4σ .

and on the coupling constant g_S of the muonphilic scalar model (Fig. 14). For masses below $6 \text{ GeV}/c^2$, they range from 0.0008 to 0.039 for the $L_\mu - L_\tau$ model and from 0.0018 to 0.040 for the muonphilic-scalar model. These limits exclude the $L_\mu - L_\tau$ model and the muonphilic scalar model as explanations of the $(g-2)_\mu$ anomaly for $0.8 < m_{Z'} < 4.9 \text{ GeV}/c^2$ and $2.9 < m_S < 3.5 \text{ GeV}/c^2$, respectively. Our constraints on g' are similar to those set by BaBar [19] for $m_{Z'}$ above $1 \text{ GeV}/c^2$ and to those set by Belle [20] on the full $m_{Z'}$ spectrum, both based on much larger integrated luminosities than ours. For the muonphilic scalar model, we do not show the constraints in Ref. [18], since they may not take into account all the experimental details affecting the signal efficiency, particularly those related to the harder momentum spectrum compared to the Z' .

VIII. CONCLUSION

We search for the process $e^+e^- \rightarrow \mu^+\mu^-X$ with $X \rightarrow \mu^+\mu^-$, $X = Z', S$ in a data sample of electron-positron collisions at 10.58 GeV collected by Belle II at SuperKEKB in 2020 and 2021, corresponding to an integrated luminosity of 178 fb^{-1} . We find no significant excess above the background. We set upper limits on the cross sections for masses between $0.212 \text{ GeV}/c^2$ and $9 \text{ GeV}/c^2$, ranging from 0.046 fb to 0.97 fb for the $L_\mu - L_\tau$ model, and from 0.055 fb to 1.3 fb for the muonphilic scalar model. We derive exclusion limits on the couplings for the two different models. For masses below $6 \text{ GeV}/c^2$, they range from 0.0008 to 0.039 for the $L_\mu - L_\tau$ model and from 0.0018 to 0.040 for the muonphilic-scalar model. These limits exclude the $L_\mu - L_\tau$ model and the muonphilic scalar model as explanations of the $(g-2)_\mu$ anomaly for $0.8 < m_{Z'} < 4.9 \text{ GeV}/c^2$ and $2.9 < m_S < 3.5 \text{ GeV}/c^2$, respectively. These are the first results for the muonphilic scalar model based on a realistic evalu-

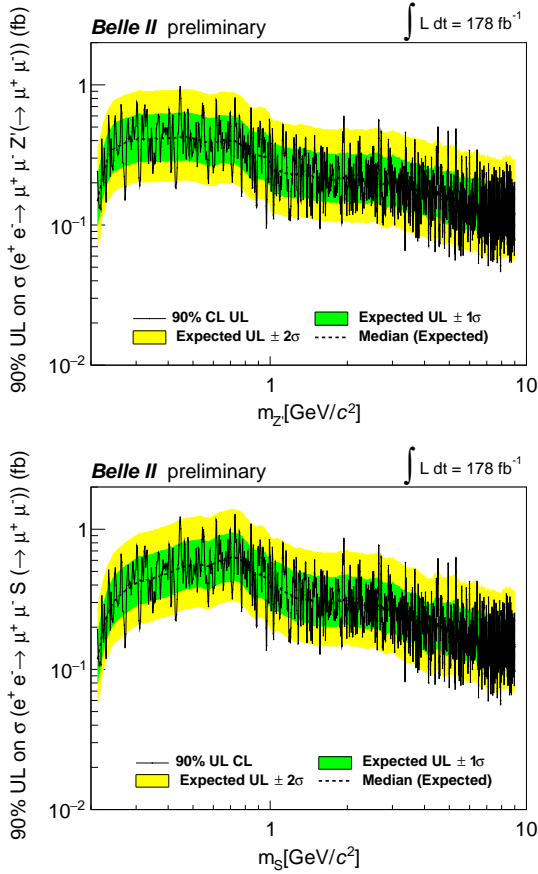


Figure 13: Observed 90% confidence level upper limits and corresponding expected limits on the cross sections for the processes $e^+e^- \rightarrow \mu^+\mu^-X$ with $X \rightarrow \mu^+\mu^-$, $X = Z', S$, as functions of the Z' mass (top) and S mass (bottom).

ation of the signal efficiency that takes into account all the experimental details.

This work, based on data collected using the Belle II detector, which was built and commissioned prior to March 2019, was supported by Higher Education and Science Committee of the Republic of Armenia Grant No. 23LCG-1C011; Australian Research Council and Research Grants No. DP200101792, No. DP210101900, No. DP210102831, No. DE220100462, No. LE210100098, and No. LE230100085; Austrian Federal Ministry of Education, Science and Research, Austrian Science Fund No. P 31361-N36 and No. J4625-N, and Horizon 2020 ERC Starting Grant No. 947006 “InterLeptons”; Natural Sciences and Engineering Research Council of Canada, Compute Canada and CANARIE; National Key R&D Program of China under Contract No. 2022YFA1601903, National Natural Science Foundation of China and Research Grants No. 11575017, No. 11761141009, No. 11705209, No. 11975076, No. 12135005, No. 12150004, No. 12161141008, and No. 12175041, and Shandong Provincial Natural Science Foundation Project ZR2022JQ02; the Czech Science

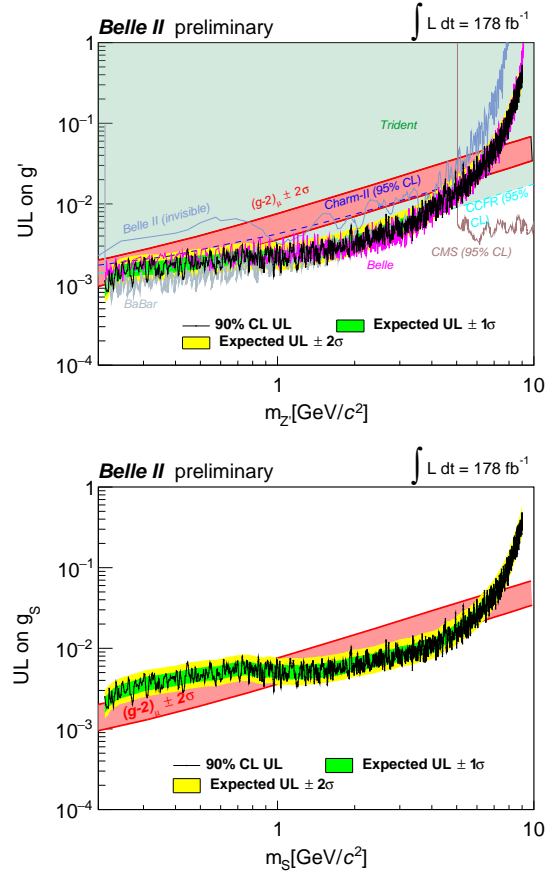


Figure 14: Observed 90% CL upper limits and corresponding expected limits on (top) the $L_\mu - L_\tau$ model coupling g' and on (bottom) the muonphilic scalar model coupling g_S . Also shown in the top panel are constraints from Belle II [22, 23] for invisible Z' decays, and from BaBar [19], Belle [20], and CMS [21] (95% CL) searches for Z' decays to muons, along with constraints (95% CL) derived from the trident production in neutrino experiments [53–55]. The red band in each panel shows the region that explains the muon anomalous magnetic moment $(g-2)_\mu \pm 2\sigma$.

Foundation Grant No. 22-18469S; European Research Council, Seventh Framework PIEF-GA-2013-622527, Horizon 2020 ERC-Advanced Grants No. 267104 and No. 884719, Horizon 2020 ERC-Consolidator Grant No. 819127, Horizon 2020 Marie Skłodowska-Curie Grant Agreement No. 700525 “NIOBE” and No. 101026516, and Horizon 2020 Marie Skłodowska-Curie RISE project JENNIFER2 Grant Agreement No. 822070 (European grants); L’Institut National de Physique Nucléaire et de Physique des Particules (IN2P3) du CNRS and L’Agence Nationale de la Recherche (ANR) under grant ANR-21-CE31-0009 (France); BMBF, DFG, HGF, MPG, and AvH Foundation (Germany); Department of Atomic Energy under Project Identification No. RTI 4002, Department of Science and Technology, and UPES SEED funding

programs No. UPES/R&D-SEED-INFRA/17052023/01 and No. UPES/R&D-SOE/20062022/06 (India); Israel Science Foundation Grant No. 2476/17, U.S.-Israel Binational Science Foundation Grant No. 2016113, and Israel Ministry of Science Grant No. 3-16543; Istituto Nazionale di Fisica Nucleare and the Research Grants BELLE2; Japan Society for the Promotion of Science, Grant-in-Aid for Scientific Research Grants No. 16H03968, No. 16H03993, No. 16H06492, No. 16K05323, No. 17H01133, No. 17H05405, No. 18K03621, No. 18H03710, No. 18H05226, No. 19H00682, No. 20H05850, No. 20H05858, No. 22H00144, No. 22K14056, No. 22K21347, No. 23H05433, No. 26220706, and No. 26400255, the National Institute of Informatics, and Science Information NETwork 5 (SINET5), and the Ministry of Education, Culture, Sports, Science, and Technology (MEXT) of Japan; National Research Foundation (NRF) of Korea Grants No. 2016R1D1A1B02012900, No. 2018R1A2B3003643, No. 2018R1A6A1A06024970, No. 2019R1I1A3A01058933, No. 2021R1A6A1A-03043957, No. 2021R1F1A1060423, No. 2021R1F1A-1064008, No. 2022R1A2C1003993, and No. RS-2022-00197659, Radiation Science Research Institute, Foreign Large-Size Research Facility Application Supporting project, the Global Science Experimental Data Hub Center of the Korea Institute of Science and Technology Information and KREONET/GLORIAD; Universiti Malaya RU grant, Akademi Sains Malaysia, and Ministry of Education Malaysia; Frontiers of Science Program Contracts No. FOINS-296, No. CB-221329, No. CB-236394, No. CB-254409, and No. CB-180023, and SEP-CINVESTAV Research Grant No. 237 (Mexico); the Polish Ministry of Science and Higher Education and the National Science Center; the Ministry of Science and Higher Education of the Russian Federation and

the HSE University Basic Research Program, Moscow; University of Tabuk Research Grants No. S-0256-1438 and No. S-0280-1439 (Saudi Arabia); Slovenian Research Agency and Research Grants No. J1-9124 and No. P1-0135; Agencia Estatal de Investigacion, Spain Grant No. RYC2020-029875-I and Generalitat Valenciana, Spain Grant No. CIDEGENT/2018/020; National Science and Technology Council, and Ministry of Education (Taiwan); Thailand Center of Excellence in Physics; TUBITAK ULAKBIM (Turkey); National Research Foundation of Ukraine, Project No. 2020.02/0257, and Ministry of Education and Science of Ukraine; the U.S. National Science Foundation and Research Grants No. PHY-1913789 and No. PHY-2111604, and the U.S. Department of Energy and Research Awards No. DE-AC06-76RLO1830, No. DE-SC0007983, No. DE-SC0009824, No. DE-SC0009973, No. DE-SC0010007, No. DE-SC0010073, No. DE-SC0010118, No. DE-SC0010504, No. DE-SC0011784, No. DE-SC0012704, No. DE-SC0019230, No. DE-SC0021274, No. DE-SC0021616, No. DE-SC0022350, No. DE-SC0023470; and the Vietnam Academy of Science and Technology (VAST) under Grants No. NVCC.05.12/22-23 and No. DL0000.02/24-25.

These acknowledgements are not to be interpreted as an endorsement of any statement made by any of our institutes, funding agencies, governments, or their representatives.

We thank the SuperKEKB team for delivering high-luminosity collisions; the KEK cryogenics group for the efficient operation of the detector solenoid magnet; the KEK computer group and the NII for on-site computing support and SINET6 network support; and the raw-data centers at BNL, DESY, GridKa, IN2P3, INFN, and the University of Victoria for off-site computing support.

-
- [1] G. Bertone, D. Hooper, and J. Silk, *Phys. Rep.* **405**, 279 (2005).
- [2] G. W. Bennett et al. (Muon $g - 2$ Collaboration), *Phys. Rev. D* **73**, 072003 (2006).
- [3] T. Aoyama et al., *Phys. Rep.* **887**, 1 (2020).
- [4] D. P. Aguillard et al. (Muon $g - 2$ Collaboration), *Phys. Rev. Lett.* **131**, 161802 (2023).
- [5] S. Borsanyi et al., *Nature* **593** (2021).
- [6] J. P. Lees et al. (BaBar Collaboration), *Phys. Rev. D* **88**, 072012 (2013).
- [7] R. Aaij et al. (LHCb Collaboration), *Phys. Rev. D* **97**, 072013 (2018).
- [8] G. Caria et al. (Belle Collaboration), *Phys. Rev. Lett.* **124**, 161803 (2020).
- [9] F. Sala and D. M. Straub, *Phys. Lett. B* **774**, 205 (2017).
- [10] C.-H. Chen and T. Nomura, *Phys. Lett. B* **777**, 420 (2018).
- [11] A. Greljo, P. Stangl, and A. Eller Thomsen, *Phys. Lett. B* **820**, 136554 (2021).
- [12] X. G. He, G. C. Joshi, H. Lew, and R. R. Volkas, *Phys. Rev. D* **43**, R22 (1991).
- [13] B. Shuve and I. Yavin, *Phys. Rev. D* **89**, 113004 (2014).
- [14] W. Altmannshofer, S. Gori, S. Profumo, and F. S. Queiroz, *J. High Energy Phys.* **12**, 106 (2016).
- [15] P. Harris, P. Schuster, and J. Zupan (2022), arXiv:2207.08990.
- [16] S. Gori, M. Williams, P. Ilten, N. Tran, G. Krnjaic, N. Toro, B. Batell, N. Blinov, C. Hearty, R. McGehee, et al. (2022), arXiv:2209.04671.
- [17] D. Forbes, C. Herwig, Y. Kahn, G. Krnjaic, C. M. Suarez, N. Tran, and A. Whitbeck, *Phys. Rev. D* **107**, 116026 (2023).
- [18] R. Capdevilla, D. Curtin, Y. Kahn, and G. Krnjaic, *J. High Energy Phys.* **04**, 129 (2022).
- [19] J. P. Lees et al. (BaBar Collaboration), *Phys. Rev. D* **94**, 011102 (2016).
- [20] T. Czank et al. (Belle Collaboration), *Phys. Rev. D* **106**, 012003 (2022).
- [21] A. Sirunyan et al. (CMS Collaboration), *Phys. Lett. B* **792**, 345 (2019).

- [22] I. Adachi et al. (Belle II Collaboration), Phys. Rev. Lett. **124**, 141801 (2020).
- [23] I. Adachi et al. (Belle II Collaboration), Phys. Rev. Lett. **130**, 231801 (2023).
- [24] Y. M. Andreev et al. (NA64 Collaboration), Phys. Rev. D **106**, 032015 (2022).
- [25] Adachi et al. (Belle II Collaboration), Phys. Rev. Lett. **131**, 121802 (2023).
- [26] T. Abe et al. (2010), arXiv:1011.0352.
- [27] E. Kou et al., Prog. Theor. Exp. Phys. **2019**, 123C01 (2019), Erratum: <https://doi.org/10.1093/ptep/ptaa008>.
- [28] K. Akai, K. Furukawa, and H. Koiso (SuperKEKB Accelerator Team), Nucl. Instrum. Methods Phys. Res. A **907**, 188 (2018).
- [29] F. Abudinén et al. (Belle II Collaboration), Chin. Phys. C **44**, 021001 (2020).
- [30] J. Alwall et al., J. High Energy Phys. **07**, 079 (2014).
- [31] Q. Li and Q.-S. Yan (2018), arXiv:1804.00125.
- [32] F. Berends, P. Daverveldt, and R. Kleiss, Nucl. Phys. B **253**, 441 (1985).
- [33] S. Jadach, B. F. L. Ward, and Z. Wąs, Comput. Phys. Commun. **130**, 260 (2000).
- [34] N. Davidson, G. Nanava, T. Przedzinski, E. Richter-Wąs, and Z. Wąs, Comput. Phys. Commun. **183**, 821 (2012).
- [35] S. Uehara (2013), arXiv:1310.0157.
- [36] H. Czyż, M. Gunia, and J. H. Kühn, J. High Energy Phys. **08**, 110 (2013).
- [37] G. Balossini, C. Bignamini, C. M. C. Calame, G. Montagna, O. Nicosini, and F. Piccinini, Phys. Lett. B **663**, 209 (2008).
- [38] T. Sjöstrand et al., Comput. Phys. Commun. **191**, 159 (2015).
- [39] D. J. Lange, Nucl. Instrum. Methods Phys. Res. A **462**, 152 (2001).
- [40] E. Barberio, B. van Eijk, and Z. Wąs, Comput. Phys. Commun. **66**, 115 (1991).
- [41] E. Barberio and Z. Wąs, Comput. Phys. Commun. **79**, 291 (1994).
- [42] S. Agostinelli et al. (GEANT4), Nucl. Instrum. Methods Phys. Res. A **506**, 250 (2003).
- [43] T. Kuhr, C. Pulvermacher, M. Ritter, T. Hauth, and N. Braun (Belle II Framework Software Group), Comput. Softw. Big Sci. **3**, 1 (2019).
- [44] *Belle II Analysis Software Framework (basf2)*, <https://doi.org/10.5281/zenodo.5574115>.
- [45] V. Bertacchi et al. (Belle II Tracking Group), Comput. Phys. Commun. **259**, 107610 (2021).
- [46] A. A. Hoecker et al. (2009), arXiv:physics/0703039.
- [47] G. Punzi, eConf **C030908**, MODT002 (2003), arXiv:physics/0308063.
- [48] T. Skwarnicki, Ph.D. thesis, Cracow, INP (1986).
- [49] B. Efron and R. J. Tibshirani, *An Introduction to the Bootstrap* (Chapman and Hall/CRC, New York, 1994).
- [50] G. Cowan, K. Cranmer, E. Gross, and O. Vitells, Eur. Phys. J. C **71**, 1554 (2011), Erratum: <https://doi.org/10.1140/epjc/s10052-013-2501-z>.
- [51] E. Gross and O. Vitells, Eur. Phys. J. C **70**, 525 (2010).
- [52] A. L. Read, J. Phys. G: Nucl. Part. Phys. **28**, 2693 (2002).
- [53] W. Altmannshofer, S. Gori, M. Pospelov, and I. Yavin, Phys. Rev. Lett. **113**, 091801 (2014).
- [54] G. Bellini et al. (Borexino Collaboration), Phys. Rev. Lett. **107**, 141302 (2011).
- [55] A. Kamada, K. Kaneta, K. Yanagi, and H.-B. Yu, J. High Energy Phys. **2018**, 117 (2018).



Fiducial and differential cross-section measurements of electroweak $W\gamma jj$ production in pp collisions at $\sqrt{s} = 13$ TeV with the ATLAS detector

The ATLAS Collaboration

The observation of the electroweak production of a W boson and a photon in association with two jets, using pp collision data at the Large Hadron Collider at a centre of mass energy of $\sqrt{s} = 13$ TeV, is reported. The data were recorded by the ATLAS experiment from 2015 to 2018 and correspond to an integrated luminosity of 140 fb^{-1} . This process is sensitive to the quartic gauge boson couplings via the vector boson scattering mechanism and provides a stringent test of the electroweak gauge symmetry breaking of the Standard Model. Events are selected if they contain one electron or muon, missing transverse momentum, at least one photon, and two jets. Multivariate techniques are used to distinguish the electroweak $W\gamma jj$ process from irreducible background processes. The observed significance of the electroweak $W\gamma jj$ process is well above six standard deviations, compared to an expected significance of 6.3 standard deviations. Fiducial and differential cross sections are measured in a fiducial phase space close to the detector acceptance, which are in reasonable agreement with leading order Standard Model predictions from MADGRAPH5+PYTHIA8 and SHERPA. The results are used to constrain new physics effects in the context of an effective field theory.

Contents

1	Introduction	2
2	ATLAS detector	4
3	Monte Carlo event simulation	5
4	Object reconstruction and event selection	6
5	Background estimation	9
6	Signal extraction	11
6.1	Signal extraction for observation	11
6.2	Signal extraction for the differential cross-section measurement	12
7	Correction for detector effects	15
8	Systematic uncertainties	16
9	Results	18
9.1	Observation and fiducial cross-section for EW $W\gamma jj$ process	18
9.2	Differential cross-section for EW $W\gamma jj$ process	19
10	EFT interpretation	22
11	Conclusion	24

1 Introduction

The scattering of two vector bosons, e.g. $WZ \rightarrow W\gamma$, is sensitive to both the triple and quartic electroweak-boson self-interactions [1, 2]. Consequently, vector boson scattering (VBS) provides an excellent opportunity to probe the nature of the electroweak (EW) gauge symmetry breaking of the Standard Model (SM).

In proton–proton (pp) collisions, the $W\gamma jj$ final state can be produced via many different mechanisms, as shown in Figure 1. Electroweak $W\gamma jj$ production concerns exclusively electroweak interactions of order α_{EW}^4 at tree level [3], where α_{EW} is the electroweak coupling constant. Although the contributions of interest are VBS interactions involving quartic gauge couplings (QGCs), these cannot be distinguished from other electroweak contributions in a gauge-invariant manner. Thus, the signal process studied in this paper is the combination of all processes of order α_{EW}^4 shown in Figures 1(a)-1(c). The dominant background for EW $W\gamma jj$ production concerns processes of order $\alpha_S^2\alpha_{\text{EW}}^2$ at tree level in Figure 1(d), where α_S is the strong coupling constant and the jets are produced via strong interaction vertices; these processes are collectively referred to as strong $W\gamma jj$ production in this paper. Triboson diagrams, such as the one shown in Figure 1(b), do contribute to EW $W\gamma jj$ production. However, due to their distinct topology they require separate signal selection and background estimation methods and are thus generally the subject of separate studies.

The large cross-section of EW $W\gamma jj$ production predicted by the SM allows differential cross-sections to be measured with higher precision than other VBS processes. The differential measurements further enhance our sensitivity to potential anomalous quartic couplings of $WW\gamma\gamma$ and $WW\gamma Z$. In addition to the VBS topology characterised by the two energetic jets in the forward and backward region, the leptonic decay channel of the EW $W\gamma jj$ production has a clean signature in the detector with exactly one lepton, missing transverse momentum, and at least one photon. This paper reports fiducial and differential cross-section measurements in the EW $W\gamma jj$ final state using 140 fb^{-1} of data recorded between 2015 and 2018 with the ATLAS detector.

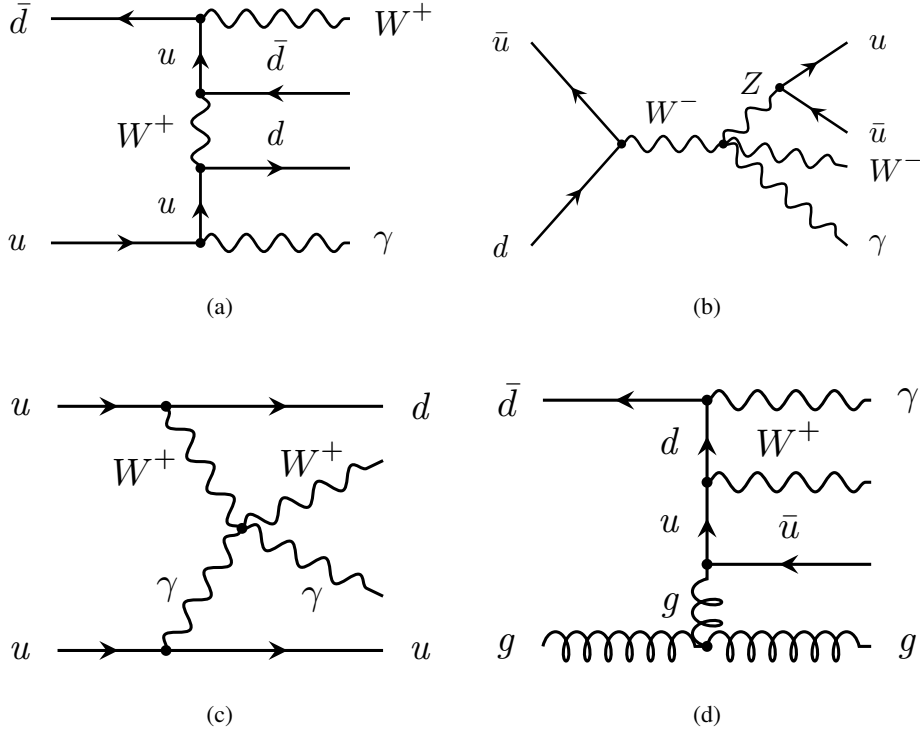


Figure 1: Representative Feynman diagrams for the $W\gamma jj$ final state: (a) EW $W\gamma jj$ production involving no gauge boson self-interactions, (b) bremsstrahlung EW $W\gamma jj$ non-VBS production involving quartic gauge boson interactions, (c) $W\gamma$ VBS involving quartic gauge boson interactions, and (d) Strong $W\gamma jj$ production.

The CMS Collaboration reported the observation of the EW $W\gamma jj$ process [4] and measured EW $W\gamma jj$ differential cross-sections [5]. This analysis exploits two innovations compared to the CMS publication. First, multivariate techniques involving a neural network are used to isolate the EW $W\gamma jj$ signal from the strong $W\gamma jj$ background in a VBS-enhanced phase space; the resulting observed yield is corrected for detector effects and a fiducial cross-section is reported in a fiducial phase space at particle level as close as possible to the reconstruction level. Secondly, observables sensitive to the charge conjugation (C) and parity (P) structure of $WW\gamma\gamma$ and $WW\gamma Z$ couplings are measured. These measurements can be used to explore new sources of CP violation (CPV) in the gauge-boson sector that may partly explain the predominance of matter over anti-matter in the universe. The differential cross-sections for EW $W\gamma jj$ production are measured as functions of two types of observables: *VBS observables* and *charge conjugation and parity observables*.

- The VBS observables are those that are used to characterise specifically the VBS nature of events;

they are additionally sensitive to anomalous QGCs (aQGC) via dimension-8 operators of an effective field theory (EFT) in the Eboli basis [2]. These observables include the invariant mass of the dijet system, m_{jj} , the transverse momentum of the two jets, p_{T}^{jj} , the lepton transverse momentum, p_{T}^l , and the invariant mass of the lepton and the photon, $m_{l\gamma}$.

- The charge conjugation and parity observables probe the CP structure of $WW\gamma\gamma$ and $WW\gamma Z$ couplings. Two observables are studied: the signed azimuthal angle difference between the two jets, $\Delta\phi_{jj} = \phi_f^j - \phi_b^j$, where the two highest transverse-momentum jets are ordered by rapidity y such that $y_f^j > y_b^j$, and the signed azimuthal angle difference between the lepton and the photon, $\Delta\phi_{l\gamma} = \phi_f - \phi_b$, where the lepton and the photon are ordered such that $y_f > y_b$. Measurements of $\Delta\phi_{jj}$ have previously been proposed to constrain the CP-odd component involving Higgs boson couplings in Vector Boson Fusion (VBF) processes [6] and the $t\bar{t}H$ process [7].

The paper is organised as follows. Section 2 briefly describes the ATLAS detector. Section 3 documents the simulated signal and background samples used in this analysis. The object reconstruction and event selection is presented in Section 4. The background estimate is detailed in Section 5. The methodologies used for the fiducial and differential cross-section measurements are discussed in Section 6. Corrections for detector effects are described in Section 7, followed by a description of the systematic uncertainties in Section 8. The fiducial and differential EW $W\gamma jj$ cross-sections are presented in Section 9. Section 10 presents constraints on the Wilson coefficients of dimension-8 EFT.

2 ATLAS detector

The ATLAS detector [8] at the LHC covers nearly the entire solid angle around the collision point.¹ It consists of an inner tracking detector surrounded by a thin superconducting solenoid, electromagnetic and hadronic calorimeters, and a muon spectrometer incorporating three large superconducting air-core toroidal magnets.

The inner-detector system (ID) is immersed in a 2 T axial magnetic field and provides charged-particle tracking in the range $|\eta| < 2.5$. The high-granularity silicon pixel detector covers the vertex region and typically provides four measurements per track, the first hit generally being in the insertable B-layer (IBL) installed before Run 2 [9, 10]. It is followed by the SemiConductor Tracker (SCT), which usually provides eight measurements per track. These silicon detectors are complemented by the transition radiation tracker (TRT), which enables radially extended track reconstruction up to $|\eta| = 2.0$. The TRT also provides electron identification information based on the fraction of hits (typically 30 in total) above a higher energy-deposit threshold corresponding to transition radiation.

The calorimeter system covers the pseudorapidity range $|\eta| < 4.9$. Within the region $|\eta| < 3.2$, electromagnetic calorimetry is provided by barrel and endcap high-granularity lead/liquid-argon (LAr) calorimeters, with an additional thin LAr presampler covering $|\eta| < 1.8$ to correct for energy loss in material upstream of the calorimeters. Hadronic calorimetry is provided by the steel/scintillator-tile calorimeter,

¹ ATLAS uses a right-handed coordinate system with its origin at the nominal interaction point (IP) in the centre of the detector and the z -axis along the beam pipe. The x -axis points from the IP to the centre of the LHC ring, and the y -axis points upwards. Polar coordinates (r, ϕ) are used in the transverse plane, ϕ being the azimuthal angle around the z -axis. The pseudorapidity is defined in terms of the polar angle θ as $\eta = -\ln \tan(\theta/2)$ and is equal to the rapidity $y = \frac{1}{2} \ln \left(\frac{E+p_z c}{E-p_z c} \right)$ in the relativistic limit. Angular distance is measured in units of $\Delta R \equiv \sqrt{(\Delta y)^2 + (\Delta\phi)^2}$.

segmented into three barrel structures within $|\eta| < 1.7$, and two copper/LAr hadronic endcap calorimeters. The solid angle coverage is completed with forward copper/LAr and tungsten/LAr calorimeter modules optimised for electromagnetic and hadronic energy measurements respectively.

The muon spectrometer (MS) comprises separate trigger and high-precision tracking chambers measuring the deflection of muons in a magnetic field generated by the superconducting air-core toroidal magnets. The field integral of the toroids ranges between 2.0 and 6.0 T m across most of the detector. Three layers of precision chambers, each consisting of layers of monitored drift tubes, cover the region $|\eta| < 2.7$, complemented by cathode-strip chambers in the forward region, where the background is highest. The muon trigger system covers the range $|\eta| < 2.4$ with resistive-plate chambers in the barrel, and thin-gap chambers in the endcap regions.

The luminosity is measured mainly by the LUCID-2 [11] detector that records Cherenkov light produced in the quartz windows of photomultipliers located close to the beam pipe.

Events are selected by the first-level trigger system implemented in custom hardware, followed by selections made by algorithms implemented in software in the high-level trigger [12]. The first-level trigger accepts events from the 40 MHz bunch crossings at a rate below 100 kHz, which the high-level trigger further reduces in order to record complete events to disk at about 1 kHz.

A software suite [13] is used in data simulation, in the reconstruction and analysis of real and simulated data, in detector operations, and in the trigger and data acquisition systems of the experiment.

3 Monte Carlo event simulation

Monte Carlo (MC) event generators are used in the analysis to simulate signal and background events produced in pp collisions. These simulated samples are used to design and optimise the analysis, evaluate systematic uncertainties, and characterise the effects of detector inefficiency and resolution.

Electroweak $W\gamma jj$ production is simulated with the SHERPA 2.2.12 [14] generator. Matrix elements at leading order (LO) in QCD with up to one additional emission are matched to a parton shower based on Catani–Seymour dipole factorisation [15, 16] using the MEPS@LO prescription [17–20]. Samples are simulated using the NNPDF3.0_{NNLO} parton distribution function (PDF) set [21], along with the dedicated set of tuned parton-shower parameters developed by the SHERPA authors. An alternative EW $W\gamma jj$ signal sample is produced using MADGRAPH5_AMC@NLO [22] at LO accuracy with the default dynamical scale choice and the NNPDF3.1_{LO} PDF set. PYTHIA 8.240 with the dipole recoil option turned on is used to add parton showering, hadronisation, and underlying-event activity. The A14 [23] set of tuned parton-shower parameters is used for PYTHIA 8.240, and EVTGEN [24] is used for the properties of bottom and charmed hadron decays. This alternative EW $W\gamma jj$ sample is used to evaluate a systematic uncertainty of the signal production due to the choice of event generator.

The dominant background process, strong $W\gamma jj$, is simulated using SHERPA 2.2.11 [14]. Matrix elements at next-to leading order (NLO) QCD accuracy for up to one additional parton and LO accuracy for up to three additional parton emissions are matched and merged with the SHERPA parton shower based on Catani–Seymour dipole factorisation [15, 16] using the MEPS@NLO prescription [17–20]. This sample uses NNPDF3.0_{NNLO} for the matrix element calculation with default parameters for parton showering, hadronisation, and underlying-event activity. An alternative strong $W\gamma jj$ sample is produced using MADGRAPH5_AMC@NLO at NLO accuracy for events with up to three partons in the final state with

the NNPDF3.0_{NLO} PDF set and is interfaced with PYTHIA 8.240 with A14 parameters to provide parton showering, hadronisation, and underlying-event activity. This alternative strong $W\gamma jj$ sample is used to evaluate a systematic uncertainty of the strong $W\gamma jj$ background estimate due to the choice of event generator.

Prompt background events are those that contain at least one prompt photon, exactly one prompt lepton, and two jets. SHERPA 2.2.12, with the same settings as EW and strong $W\gamma jj$, is also used to simulate EW and strong $Z\gamma jj$ production. The remaining prompt backgrounds can arise from $tW\gamma$, $tq\gamma$, and $t\bar{t}\gamma$ processes, which are simulated using MADGRAPH5_AMC@NLO [22] with NNPDF2.3_{NLO} for $tW\gamma$ and $t\bar{t}\gamma$ at LO, and $tq\gamma$ at NLO. To provide parton showering, hadronisation, and underlying-event activity these samples are interfaced PYTHIA 8.235, PYTHIA 8.212, and PYTHIA 8.240, respectively, with A14 parameters.

Contributions from background events arising from jets misidentified as leptons or photons, non-prompt leptons or photons from decays of hadrons, electrons reconstructed as photons, and photons arising from a separate pp interaction (“pile-up photons”) are estimated by using the data-driven methods that are outlined in Section 5. The term *fake leptons* is used to collectively refer to either non-prompt leptons or hadronic jets misreconstructed as leptons. MC simulated samples including W +jets, Z +jets, tW , $t\bar{t}$, diboson, and multijet events are used in the validation of data-driven methods and the evaluation of systematic uncertainties of the background estimations. In particular, simulated W +jets and Z +jets events, which are used in the validation of the non-prompt photon estimate, are produced at NLO accuracy using SHERPA 2.2.11 with NNPDF3.0_{NNLO} and default parameter tunes for parton showering, hadronisation, and underlying-event activity. Background events from electrons misreconstructed as photons can arise from tW , $t\bar{t}$, and Z +jets processes. The tW and $t\bar{t}$ processes are simulated using POWHEG at NLO accuracy with NNPDF3.0_{NNLO} and PYTHIA 8.230 with A14 parameters to provide parton showering, hadronisation, and underlying-event activity. Diboson and multijet events are used in the data-driven estimate of fake leptons. The diboson sample is simulated with SHERPA 2.2.2 at NLO with NNPDF3.0_{NLO} and default parameter tunes for parton showering, hadronisation, and underlying-event activity. The multijet sample is simulated using PYTHIA 8.235 at LO accuracy with NNPDF2.3_{LO} and A14 tunes for parton showering.

All simulated signal and background events are processed through the full ATLAS detector simulation using GEANT4 [25] and then reconstructed using the same algorithms as the recorded data events. Differences between reconstructed leptons, photons, jets and missing transverse momentum in simulations and data are corrected using event-by-event scale factors with p_T and η dependence. The effect of multiple interactions in the same and neighbouring bunch crossings (pile-up) is modelled by overlaying the simulated hard-scattering event with inelastic pp events simulated with PYTHIA 8.186 [26] using the NNPDF2.3_{LO} set of PDFs [27] and the A3 set of tuned parton-shower parameters [28].

4 Object reconstruction and event selection

This analysis is performed using pp collision data collected between 2015 and 2018 at a centre-of-mass energy of $\sqrt{s} = 13$ TeV, corresponding to an integrated luminosity of 140 fb^{-1} [29].

Events are required to satisfy the unrescaled single-lepton triggers that have transverse momentum thresholds of 20–26 GeV, depending on the lepton flavour and data-taking periods [30, 31]; this is complemented by triggers with higher p_T thresholds and no isolation requirements to increase the overall trigger efficiency. Events are also required to satisfy detector and data quality requirements during stable beam conditions [32]. Candidate pp interaction vertices are reconstructed using charged-particle tracks;

each candidate vertex must have at least two tracks with $p_T > 500$ MeV [33]. The vertex with the highest scalar sum of track p_T^2 is selected as the primary vertex. Events must contain at least one electron or muon, missing transverse momentum, at least one photon, and at least two jets.

Muons are reconstructed by matching tracks in the MS to a corresponding track in the ID. Each muon must satisfy the *tight* identification criteria and *tight* isolation working point [34]. Muons are constrained to originate from the primary vertex by requiring $|d_0/\sigma_{d_0}| < 3$ and $|z_0 \sin \theta| < 0.5$ mm, where d_0 is the distance of closest approach to the primary vertex in the transverse plane, with an uncertainty σ_{d_0} , and z_0 is the longitudinal difference between the point at which d_0 is defined and the primary vertex. Selected muons are required to have $p_T > 30$ GeV and $|\eta| < 2.5$.

Electrons are reconstructed from clusters of energy deposits in the ECAL and matched to a track reconstructed in the ID. Each electron must satisfy the *tight* identification and *tight* isolation working points [35]. Electrons are required to have $p_T > 30$ GeV and $|\eta| < 2.47$, excluding the calorimeter transition region $1.37 < |\eta| < 1.52$, $|d_0/\sigma_{d_0}| < 5$ and $|z_0 \sin \theta| < 0.5$ mm.

Photons are also reconstructed from clusters of energy deposits in the ECAL. Both converted and unconverted photons are used in the analysis. Converted photons are defined as photon clusters that are matched to one or two ID tracks consistent with a conversion vertex, while unconverted photons are defined as photon clusters that are matched to neither an ID electron track nor a conversion vertex. Each photon is required to satisfy *tight* identification and *tight* isolation working points [35]. Photons passing a *loose* identification requirement are retained in the analysis to define control regions for the data-driven background estimation method used to determine the background from jets misidentified as photons, which is described in Section 5. The *tight* isolation requirement is defined as $E_T^{\text{cone}40} < 0.022 \times p_T + 2.45$ GeV, where $E_T^{\text{cone}40}$ is computed as the sum of transverse energies of positive-energy topological clusters in the calorimeter within a distance of $\Delta R = 0.4$ around the photon candidate [35]. Photons are required to have $p_T > 22$ GeV and $|\eta| < 2.37$, excluding the calorimeter transition region $1.37 < |\eta| < 1.52$.

Jets are reconstructed using a particle-flow method [36] that combines charged-particle tracks in the ID with topo-clusters formed from energy deposits in the calorimeters. The anti- k_t algorithm [37] with radius parameter $R = 0.4$ is used to define the jet. Each jet is required to have $p_T > 25$ GeV and $|\eta| < 4.4$. Jets with $p_T < 60$ GeV and $|\eta| < 2.4$ are required to originate from the primary vertex by using the *tight* working point of the jet vertex tagger (JVT) [38]. Jets that originate from noise bursts in the calorimeters are removed [39]. Events must have at least two jets with $p_T > 50$ GeV. Jets with $|\eta| < 2.5$ that contain b -hadrons are identified by a multivariate algorithm (DL1r) [40] with 85% tagging efficiency working point. Events identified as containing a b -jet by the DL1r algorithm are excluded to suppress backgrounds from processes involving top quarks.

The magnitude of the missing transverse momentum, E_T^{miss} , and its direction are calculated from the negative vector sum of a track-based soft term and all reconstructed electrons, muons, photons, and jets [41]. The soft term is calculated from tracks from the primary vertex that are not matched to any hard physics objects. Events are required to satisfy $E_T^{\text{miss}} > 30$ GeV.

To resolve ambiguities in the object reconstruction, an overlap removal procedure is applied. Jet candidates are removed if $\Delta R(j, l) < 0.2$ ($l = e, \mu$). Then, leptons are removed if $\Delta R(l, j) < 0.4$, and photons are removed if $\Delta R(\gamma, l) < 0.4$ or $\Delta R(\gamma, j) < 0.4$. Finally, electron candidates are removed if shared ID tracks exist between a muon and an electron.

Events are required to satisfy $m_T^W > 30$ GeV, where $m_T^W = \sqrt{2p_T^l E_T^{\text{miss}} (1 - \cos \Delta\phi)}$ and $\Delta\phi$ is the azimuthal angle difference between the lepton and missing transverse momentum in the transverse plane, relative

to the beam axis. In addition, to reject events that have topologies consistent with leptonic Z decays, where one lepton is reconstructed as a photon, the invariant mass of the lepton and the photon must satisfy $|m_{l\gamma} - m_Z| > 10$ GeV. To further remove events containing two prompt leptons consistent with a Z boson or two W bosons, events are rejected if a second lepton satisfying the following requirements is present: $p_T > 7$ GeV, the lepton-specific pseudorapidity requirements, both track impact parameter requirements, and *loose* identification [34, 35]. Finally, the two leading jets must have a rapidity difference $|\Delta y_{jj}| > 2$ and invariant mass $m_{jj} > 500$ GeV, which ensures a topology consistent with EW $W\gamma jj$ production.

The preceding selection criteria comprise the baseline selection. Baseline selected events are further divided into different signal and control regions, which differ depending on the purpose. The selection for the fiducial cross-section measurement of EW $W\gamma jj$ production divides the baseline region into a signal region, SR^{fid} , and a control region, CR^{fid} , by counting jets in the rapidity interval between the two leading jets, $N_{\text{jets}}^{\text{gap}}$. SR^{fid} is defined by $N_{\text{jets}}^{\text{gap}} = 0$ and CR^{fid} is defined by $N_{\text{jets}}^{\text{gap}} > 0$. For the differential cross-section measurement, it is additionally required that events have $m_{jj} > 1$ TeV to enhance the EW $W\gamma jj$ signal purity; these events are then divided into three control regions (CR_A , CR_B , and CR_C) and one signal region (SR). The centrality of the lepton-photon system relative to the VBS tagged jets, j_1 and j_2 , is defined as $\xi_{l\gamma} = |(y_{l\gamma} - \frac{(y_{j_1} + y_{j_2})}{2}) / (y_{j_1} - y_{j_2})|$ and is used to form three control regions (CR_A , CR_B , and CR_C) and one signal region (SR), where $y_{l\gamma}$ is the rapidity of the lepton-photon system. The SR is defined by requiring that there must be little hadronic activity in the region between the two leading jets and that the reconstructed $l\gamma$ system is produced centrally ($N_{\text{jets}}^{\text{gap}} = 0, \xi_{l\gamma} < 0.35$). The remaining three regions are control regions with small EW $W\gamma jj$ contribution, and are used to constrain the dominant background from strong $W\gamma jj$ production: CR_A ($N_{\text{jets}}^{\text{gap}} > 0, \xi_{l\gamma} < 0.35$), CR_B ($N_{\text{jets}}^{\text{gap}} > 0, 0.35 < \xi_{l\gamma} < 1$), and CR_C ($N_{\text{jets}}^{\text{gap}} = 0, 0.35 < \xi_{l\gamma} < 1$). The signal and control regions for these two selections are summarised in Table 1.

Table 1: Summary table for signal and control regions for the fiducial and differential cross-section measurements.

Fiducial cross-section	SR^{fid}		CR^{fid}	
	$N_{\text{jets}}^{\text{gap}} = 0$		$N_{\text{jets}}^{\text{gap}} > 0$	
Differential cross-section	SR	CR_A	CR_B	CR_C
$m_{jj} > 1$ TeV	$N_{\text{jets}}^{\text{gap}} = 0$ $\xi_{l\gamma} < 0.35$	$N_{\text{jets}}^{\text{gap}} > 0$ $\xi_{l\gamma} < 0.35$	$N_{\text{jets}}^{\text{gap}} > 0$ $0.35 < \xi_{l\gamma} < 1$	$N_{\text{jets}}^{\text{gap}} = 0$ $0.35 < \xi_{l\gamma} < 1$

Table 2 shows the number of signal and background events in SR^{fid} and CR^{fid} , after computing the data-driven backgrounds, as described in Section 5. The strong $W\gamma jj$ process accounts for 63% of the event yield in CR^{fid} and 52% in the SR^{fid} . The remaining prompt backgrounds, including top quark processes and EW and strong $Z\gamma jj$ processes, contribute 11% in CR^{fid} and 8% in SR^{fid} , while the non-prompt background fraction is 22% in CR^{fid} and 23% in SR^{fid} .

Table 2: Expected number of events in the signal and control regions used for the fiducial cross-section measurement and observation of EW $W\gamma jj$ production. Statistical and systematic uncertainties estimated in Section 8 are included for each component. The number of observed events in each region are included for comparison. The “non-prompt” background category includes non-prompt photons and fake leptons.

	$\text{SR}^{\text{fid}} \left(N_{\text{jets}}^{\text{gap}} = 0 \right)$	$\text{CR}^{\text{fid}} \left(N_{\text{jets}}^{\text{gap}} > 0 \right)$
EW $W\gamma jj$	520 ± 141	120 ± 49
Strong $W\gamma jj$	1550 ± 830	1970 ± 950
Non-prompt	692 ± 57	698 ± 58
Top quark processes	109 ± 18	183 ± 37
EW + strong $Z\gamma jj$	128 ± 34	163 ± 77
Total	3000 ± 830	3140 ± 960
Data	3341	3143

5 Background estimation

The main source of background arises from strong $W\gamma jj$ production. This background is estimated by using MC simulation and constrained using data in the control regions defined in Table 1; a detailed description of this procedure is provided in Section 6. Additional prompt backgrounds arise from $Z\gamma jj$ production and the production of one or more top quarks in association with photons. These prompt backgrounds are estimated by using MC simulations described in Section 3.

The largest non-prompt background arises primarily from W +jet production, where a jet is misidentified as a photon. This non-prompt photon background is estimated by using a data-driven template fit to the p_{T} -corrected photon isolation energy ($E_{\text{T}}^{\text{iso},\gamma} = E_{\text{T}}^{\text{cone40}} - 0.022 \times p_{\text{T}}$) distributions of prompt and non-prompt photons. The prompt photon template is determined from prompt photons in $W\gamma jj$ MC simulation. A control region enriched with non-prompt photons is defined by requiring photons to satisfy the *loose* identification criteria but fail to satisfy the selection criteria for at least one of four variables in the *tight* identification that define the photon shower shape. This selection is referred to as *LoosePrime4* [35]. The shape of the non-prompt photon template is extracted by parameterising the $E_{\text{T}}^{\text{iso},\gamma}$ distribution in this control region. Contributions from processes with prompt photons in the non-prompt photon control region are minimal but are accounted for with a systematic uncertainty of the background estimate. The fractions of prompt and non-prompt photons are extracted for each bin of each distribution using an unbinned, maximum-likelihood fit of the prompt and non-prompt templates to data. The extracted yields are verified using an “ABCD sideband method” [42] with the two dimensional plane defined by photon identification and isolation requirements. The dominant uncertainty in the non-prompt photon background is due to the choice of photon identification criteria used to define the non-prompt template regions. This non-prompt photon definition is varied by requiring photons to fail to satisfy at least one of two, three, or five shower shape selection variables used to define the tight identification [35], and the systematic uncertainty due to this identification choice varies from 4% to 16%. Other sources of systematic uncertainty arise from statistical uncertainties of the samples in the template and fit regions; prompt photon leakage into the non-prompt template regions, estimated from signal MC simulation; and the effect of photon isolation energy modelling uncertainties on the prompt photon templates.

A “fake factor” method is used to estimate the background from fake leptons: leptons arising from misreconstructed jets or in-flight decays of hadrons. The method defines *tight* leptons as those satisfying

all selection criteria described in Section 4 and *non-tight* leptons as those failing to satisfy either the *tight* identification or *tight* isolation criteria. *Non-tight* leptons must still satisfy *loose* identification in addition to the identification and isolation requirements associated with the single lepton triggers. The fake factor is defined as the ratio of events with one *tight* lepton to those events with one *non-tight* lepton. It is calculated differentially in lepton p_T and η in a non-prompt control region defined by exactly one lepton and at least one jet. Contributions from processes with prompt leptons are subtracted from the data prior to calculating the fake factor. The non-prompt lepton background is then determined in each bin of each measured distribution by applying the fake factor to prompt, background-subtracted data events that satisfy all the selection criteria except the *tight* lepton criteria. Sources of uncertainty arise from data and MC sample size in the control regions, relative fractions between heavy flavour decays and photon conversions, control region definitions for fake factor calculation, theoretical uncertainties of the prompt background, and the binning in p_T^l and η .

An electron can be misreconstructed as a converted photon ($e \rightarrow \gamma$) if the track reconstruction algorithm either fails to associate a B-layer hit to the track or associates a spurious conversion track to the electron. This background arises predominantly from Z +jets and $t\bar{t}$ processes, and the fake rate is determined using data by selecting candidate ee and $e\gamma$ events in a range of ± 20 GeV around the Z boson mass. The object selections for the electron and photon candidates satisfies the same criteria specified in Section 4. Compared with the analysis region selections described in Section 4, events must satisfy the following criteria: $E_T^{\text{miss}} < 20$ GeV, $m_T^W < 20$ GeV, and there are no jet requirements. The ee and $e\gamma$ event yields are obtained by fitting a double-sided Crystal Ball function [43] to m_{ee} or $m_{e\gamma}$ to model the Z boson decay along with an exponential function to account for backgrounds. The ratio of $N_{e\gamma}/N_{ee}$ is parameterised as functions of electron p_T and η and applied to data events with $eejj$ and $e\mu jj$ final states, where one electron replaces the photon in the event selection, to estimate the $e \rightarrow \gamma$ background in electron and muon channels, respectively. Sources of systematic uncertainties for the $e \rightarrow \gamma$ fake rate arise from variations in the invariant mass fit range, varying the binning in p_T and η , and replacing the exponential background parameterisation with a fourth-order Bernstein polynomial [44].

No explicit requirement is imposed on the longitudinal position of the photon relative to the primary vertex, Δz_γ , as it is not well-measured for unconverted photons. As a result, a combinatorial background arises whereby a photon originating from one pp interaction is selected alongside a Wjj event from another pp interaction from the same bunch crossing. This pile-up photon background is estimated by using a data-driven method [45] that exploits the difference in Δz_γ between hard scatter and pile-up photons. Because the pile-up photon fraction, f_{PU} , is independent of the photon conversion status, events are selected if they contain a converted photon with two tracks and a conversion vertex with radius < 125 mm such that the conversion occurs within the pixel detector, allowing for an accurate measurement of Δz_γ . The sidebands of the Δz_γ distribution in background-subtracted data and $W\gamma jj$ simulation are used to estimate the fraction of events in each analysis region that have photons originating from a pile-up interaction. A control region dominated by pile-up photon background is defined by $|\Delta z_\gamma| > 50$ mm. Due to the limited number of events in this data control region, the statistical uncertainty of f_{PU} is almost 90% while the systematic uncertainty is negligible compared with the statistical uncertainty. The pile-up background contains a component where a pile-up jet can be misidentified as a photon. The fraction of prompt photons is estimated by using inclusive prompt photon events obtained from data recorded using single photon triggers, and f_{PU} is then multiplied by this fraction. The estimated f_{PU} is $(1.7 \pm 1.6)\%$ in SR^{fid} and $(0.45 \pm 0.39)\%$ in CR^{fid} ; it is neglected for the differential cross-section measurement due to the limited number of events in the control region of pile-up photons arising from the additional requirement of $m_{jj} > 1$ TeV. The procedure to extract the EW $W\gamma jj$ fiducial cross-section is repeated without the pile-up photon background, and the uncertainty on the fiducial cross-section is unchanged.

6 Signal extraction

6.1 Signal extraction for observation

A neural network (NN) is used to classify signal and background processes. The NN is trained on the EW $W\gamma jj$ process as the signal model and the sum of strong $W\gamma jj$, $Z\gamma jj$, and top quark processes as the background model, which are weighted according to their cross-sections. All events used in the training satisfy the signal region SR^{fid} selection described in Section 4. Two NN classifiers are created after training on two statistically independent but otherwise identical samples. A binary cross-entropy loss function is used during the training and the loss for each event is weighted by its weight. The NN consists of a batch normalisation layer followed by three densely connected hidden layers of 512 nodes each. Each hidden node uses a LeakyRelu activation function [46], whereas the hidden layer is densely connected with the neighbouring hidden layer that uses a sigmoid activation function. The model is trained with the Adam learning rate optimiser [47] with an initial learning rate of 3×10^{-5} . The NN is trained to discriminate signal from background using 13 kinematic observables. These 13 observables, ranked according to importance, consist of the lepton-photon centrality, $\xi_{l\gamma}$; pseudorapidity difference between the two jets, $\Delta\eta_{jj}$; angular distance between the lepton-photon system and the dijet system, $\Delta R(l\gamma, jj)$; p_{T}^{γ} ; p_{T}^l ; photon centrality, ξ_{γ} ; angular distance between leading jet and photon, $\Delta R(j_{\text{lead}}, \gamma)$; angular distance between lepton and photon, $\Delta R(l, \gamma)$; transverse momentum of the lepton-photon system, $p_{\text{T}}^{l\gamma}$; azimuthal angle difference between the lepton-photon and the dijet system, $\Delta\phi(l\gamma, jj)$; m_{T}^W ; leading jet transverse momentum, $p_{\text{T}}^{j_{\text{lead}}}$; and $\eta_{j_{\text{lead}}}$. The optimal hyperparameters are determined using a grid search by repeating the training with different combinations of the number of hidden layers, number of nodes, and learning rate; the model architecture with the lowest loss on test data is chosen. The NN trained on one statistically independent sample is applied to the other for evaluation. No significant differences between the two NNs are found, and thus the average value of the two NN output scores is used for data and data-driven background events.

A profile likelihood fit to the NN score in the SR^{fid} and CR^{fid} region is performed simultaneously to maximise the likelihood of observing n^{data} events given the number of predicted events. The expected number of events depends on two floating normalisation factors: μ_{strong} for strong $W\gamma jj$ and μ_{EW} as the EW $W\gamma jj$ signal strength. The likelihood function \mathcal{L} can be written in a simplified form as the product of Poisson distributions multiplied by the product of Gaussian constraints,

$$\mathcal{L} = \prod_r \prod_i P(n_{r,i}^{\text{data}} | \mu_{\text{EW}} S_{r,i}(\boldsymbol{\theta}) + B_{r,i}(\mu_{\text{strong}}, \boldsymbol{\theta})) \times \prod_j G(\theta_j), \quad (1)$$

where r is either SR^{fid} or CR^{fid} , i represents the bin number of the NN score in region r , $\boldsymbol{\theta}$ refers to nuisance parameters constrained by the Gaussian term $G(\theta_j)$ for each systematic uncertainty source j , $S_{r,i}(\boldsymbol{\theta})$ is the number of predicted events from EW $W\gamma jj$ simulation, $B_{r,i}(\boldsymbol{\theta})$ is the number of background events, which depends on μ_{strong} and μ_{EW} .

The shape of the NN score for EW $W\gamma jj$ and strong $W\gamma jj$ is taken from the corresponding MC while the normalisation for each process is floated, namely, μ_{EW} and μ_{strong} , respectively. The other backgrounds are allowed to vary within their respective uncertainties. The EW $W\gamma jj$ measurement depends on a set of nuisance parameters that represent the impact of uncertainties on the fit; these uncertainties are discussed in Section 8. The observed significance is evaluated by performing a background-only simultaneous fit

to data in SR^{fid} and CR^{fid} to estimate the probability of rejecting the background-only hypothesis. The signal region was blinded when analysis decisions and optimisations were made to avoid biasing the measurement.

Figure 2 shows the top three ranked observables of the NN in the signal region with nuisance parameters injected from the fit to the NN score and Figure 3 shows the output NN score in SR^{fid} and CR^{fid} after performing the profile likelihood fit in the corresponding observables. Good agreement with the observed data is seen in both the regions except for the slight shape difference in $\xi_{l\gamma}$ between MC and data. Instead of injecting the nuisance parameter from the fit to the NN score, the maximum-likelihood fit was performed to $\xi_{l\gamma}$ directly to obtain the nuisance parameters, resulting in excellent agreement between MC and data after the fit. Therefore the maximum-likelihood fit has sufficient flexibility to give reliable results despite mismodelling between MC and data before the fit.

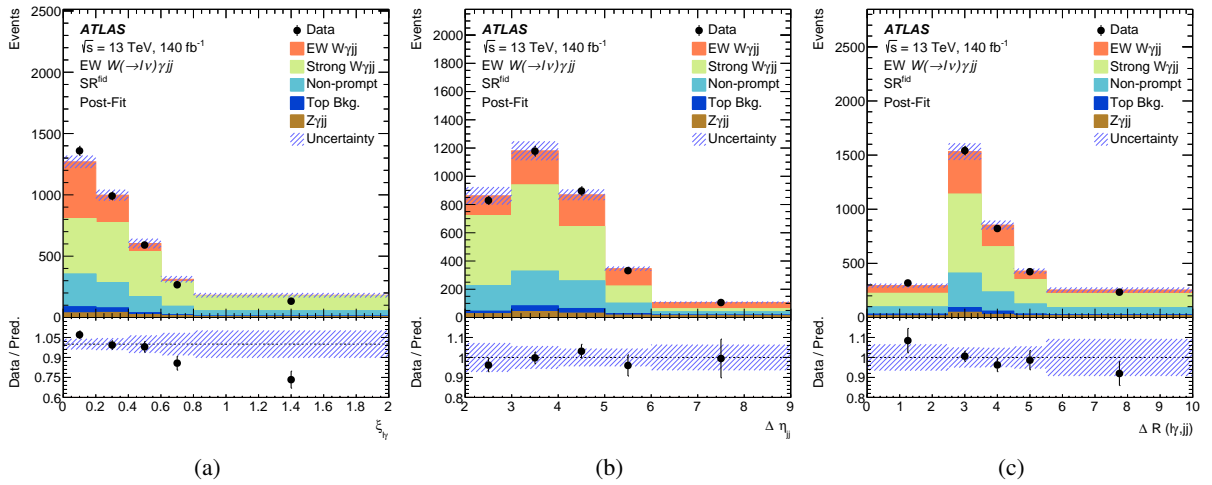


Figure 2: Distribution of the predicted and observed yields for the three highest ranked variables in the NN after performing the profile likelihood fit: namely (a) $\xi_{l\gamma}$, (b) $\Delta\eta_{jj}$, and (c) $\Delta R(l\gamma, jj)$. The observed data is represented by solid circles and the associated vertical error bar represents the statistical uncertainty of the data. The predicted yields comprise simulated EW $W\gamma jj$ signal, backgrounds from non-prompt photons and leptons that are estimated by using data-driven methods, and backgrounds that are estimated with simulation. The hashed band represents the quadrature sum of the statistical and systematic uncertainties.

6.2 Signal extraction for the differential cross-section measurement

The EW $W\gamma jj$ event yields are also extracted differentially as functions of m_{jj} , p_T^{jj} , $\Delta\phi_{jj}$, p_T^l , $m_{l\gamma}$, and $\Delta\phi_{l\gamma}$ using the methodology documented in Ref. [48]. This method exploits signal and control regions in a binned log-likelihood fit [49, 50], which are used to constrain both the shape and normalisation of the strong $W\gamma jj$ background. The data are split into four regions (SR , CR_A , CR_B , and CR_C) by imposing the selection criteria for $\xi_{l\gamma}$ and $N_{\text{jets}}^{\text{gap}}$ defined in Table 1 in Section 4.

The binned log likelihood is defined as:

$$\ln \mathcal{L} = - \sum_{r,i} v_{ri}^s + \sum_{r,i} N_{ri}^{\text{data}} \ln v_{ri}^s,$$

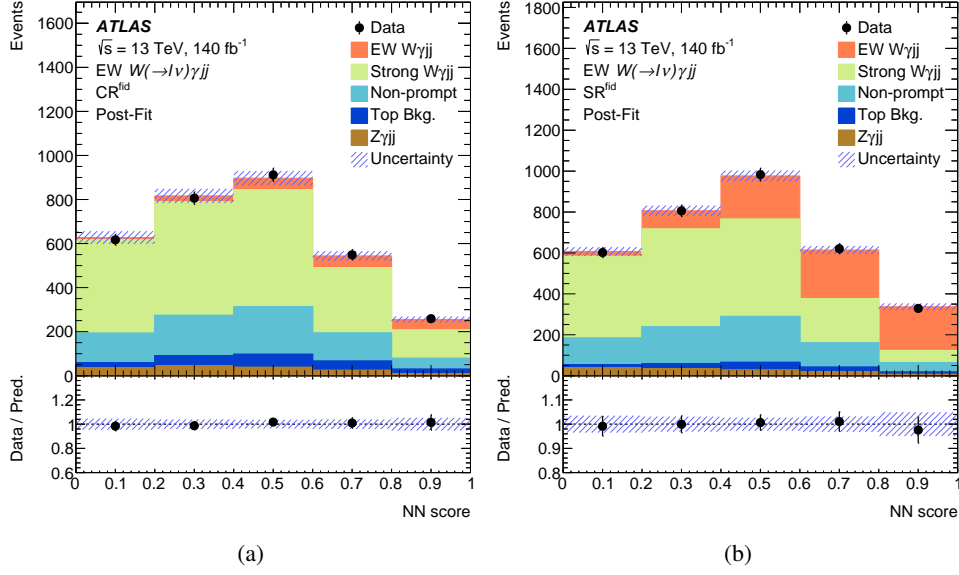


Figure 3: Distribution of the predicted and observed yields as a function of the NN score in the CR^{fid} (a) and SR^{fid} (b) regions after performing the profile likelihood fit. Data is represented by solid circles, and the associated vertical error bar represents the statistical uncertainty on the data. The predicted yields comprise simulated EW $W\gamma jj$ signal, backgrounds from non-prompt photons and leptons that are estimated by using data-driven methods, and backgrounds that are estimated with simulation. The hashed band represents the quadrature sum of the statistical and systematic uncertainties.

where r corresponds to one of the four regions SR , CR_A , CR_B , and CR_C , i corresponds to the bin of the kinematic observable, N_{ri}^{data} corresponds to the data yield in bin i of region r , and v_{ri}^s corresponds to the prediction that relies on the s sources of experimental systematic uncertainty.

The fitted number of events in region r and bin i is expressed as

$$v_{ri} = \mu_{\text{EW},i} v_{ri}^{\text{EW,MC}} + v_{ri}^{\text{strong}} + v_{ri}^{\text{other,bkg}}, \quad (2)$$

where $\mu_{\text{EW},i}$ is the signal strength of EW $W\gamma jj$ in bin i , and $v_{ri}^{\text{EW,MC}}$ and $v_{ri}^{\text{other,bkg}}$ correspond to the EW $W\gamma jj$ prediction and contributions from reducible background processes, respectively. The strong $W\gamma jj$ prediction is constrained using the signal-suppressed control regions based on the following four relations:

$$\begin{aligned} v_{\text{CR}_A,i}^{\text{strong}} &= b_{L,i} v_{\text{CR}_A,i}^{\text{strong,MC}}, & v_{\text{CR}_B,i}^{\text{strong}} &= b_{H,i} v_{\text{CR}_B,i}^{\text{strong,MC}}, \\ v_{\text{SR},i}^{\text{strong}} &= b_{L,i} c v_{\text{SR},i}^{\text{strong,MC}}, & v_{\text{CR}_C,i}^{\text{strong}} &= b_{H,i} c v_{\text{CR}_C,i}^{\text{strong,MC}}. \end{aligned} \quad (3)$$

The parameters $b_{L,i}$ and $b_{H,i}$ are sets of bin-dependent free parameters that correspond to the $\xi_{l\gamma} < 0.35$ and $\xi_{l\gamma} > 0.35$ regions, respectively. The low- $\xi_{l\gamma}$ parameter, $b_{L,i}$, is primarily constrained by CR_A , while $b_{H,i}$ is primarily constrained by CR_B . These two sets of parameters introduce additional degrees of freedom to the predicted strong $W\gamma jj$ event yield to allow the fitted number of strong $W\gamma jj$ events to be more consistent with the observed data. A floating parameter c is used to provide a residual correction that can account for any mismodelling across $N_{\text{jets}}^{\text{gap}}$. This configuration is found to be more robust against

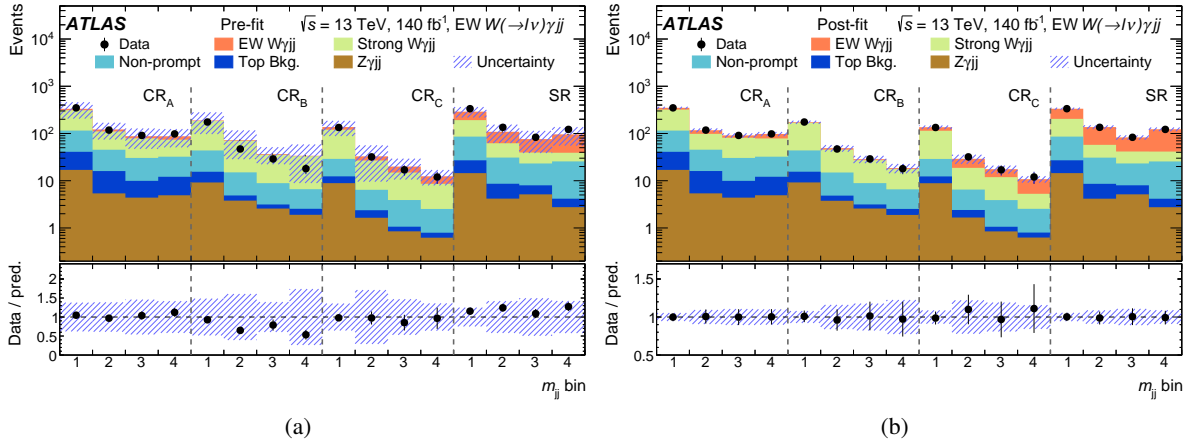


Figure 4: Distribution of the observed and predicted yields as a function of m_{jj} in the SR, CR_A, CR_B, and CR_C regions, both (a) pre-fit and (b) post-fit. Data is represented by solid circles, and the associated vertical error bar represents the statistical uncertainty of the data. The predicted yields comprise simulated EW $W\gamma jj$ signal, backgrounds from non-prompt photons and leptons that are estimated by using data-driven methods, and backgrounds that are estimated with simulation. The hashed band represents the quadrature sum of the statistical and systematic uncertainties, which are constrained in the fit. The bin edges are (1, 1.4, 1.7, 2.1, 5.3) TeV.

fit instability than the two-parameter linear fit in Ref. [48], due to the limited number of observed data events.

For each bin i , the binned maximum-likelihood fit consists of the following free parameters: the signal strength $\mu_{EW,i}$, the free parameter c , and the $b_{L,i}$ and $b_{H,i}$ corrections to the strong $W\gamma jj$ process. This constitutes an overall number of $3 \times N_{\text{bins}} + 1$ parameters that are constrained by the $4 \times N_{\text{bins}}$ measurements in data, where N_{bins} corresponds to the number of bins in the measurement of the differential observable.

The alternative predictions for EW $W\gamma jj$ and strong $W\gamma jj$ introduced in Section 3 are used to assess the systematic uncertainties discussed in Section 8. The statistical uncertainty arising from the limited size of the data and simulated MC samples is evaluated using the bootstrap method [51], each with 10 000 toy experiments. The signal extraction is repeated for each toy experiment, where the event yields in each bin of the signal and control regions are sampled according to a Poisson distribution. The mean and RMS of the extracted event yields among these toy experiments are used to define the extracted EW $W\gamma jj$ yield and associated statistical uncertainty. Each source of systematic uncertainty is varied and applied to the templates coherently in each region and propagated through the fit. The theory uncertainties due to QCD scales, PDFs, and α_S are evaluated following the procedures discussed in Section 8.

Figure 4 shows the pre- and post-fit agreement between data and predicted yields as functions of m_{jj} in SR, CR_A, CR_B, and CR_C. The floating parameter c ranges from 1.06 to 1.22 depending on the observable while the overall scaling factor for strong $W\gamma jj$ ($b_{L,i} c$) ranges between 1.07 and 1.39. Good post-fit agreement between the predicted yields and data is observed in all four regions. The pre-fit systematic uncertainties presented on the figures are estimated as documented in Section 8. The three control regions allow for a constraint of the systematic uncertainties, in particular the strong $W\gamma jj$ modelling uncertainties.

The differential EW $W\gamma jj$ signal extraction method is validated with two procedures. In the first cross-check, a different choice of control regions for the strong $W\gamma jj$ process is assigned in Equation 3, where $b_{L,i}$ and $b_{H,i}$ instead link the strong background yields at same $N_{\text{jets}}^{\text{gap}}$ values, and are thus constrained at

high $\xi_{l\gamma}$, and the free parameter c provides residual corrections considering the mismodelling across $\xi_{l\gamma}$. In the second method, the data-driven corrections to the strong $W\gamma jj$ contributions are derived only in either CR_A or CR_C . The extracted EW $W\gamma jj$ event yields obtained using each of these two methods are consistent with the nominal results.

7 Correction for detector effects

The fiducial and differential cross-sections at particle level are obtained by correcting the reconstruction-level EW $W\gamma jj$ event yield for the detector effects of inefficiency and resolution.

The particle-level regions are defined using all final-state stable particles with a mean lifetime of $c\tau > 10$ mm. To reduce model-dependence associated with extrapolations across phase space, the particle-level selection is defined to mimic the detector-level event selection described in Section 4. Particle-level dressed leptons are formed by combining the four momenta of each prompt electron or muon with the prompt photons that lie within $\Delta R = 0.1$ of the prompt lepton excluding electrons or muons from tau decays. Events must contain exactly one dressed lepton with $p_T > 30$ GeV. Leptons are required to fall within the same detector acceptance as the reconstruction level, with muons satisfying $|\eta| < 2.5$ and electrons satisfying $|\eta| < 2.47$ excluding the region $1.37 < |\eta| < 1.52$. Events must contain at least one prompt photon with $p_T > 22$ GeV and $|\eta| < 2.37$, excluding the region $1.37 < |\eta| < 1.52$. At particle level, the photon isolation energy, E_T^{iso} , defined as the sum of the transverse energy of stable particles within a cone of $\Delta R = 0.4$ around the prompt photon, excluding the photon itself and neutrinos, must satisfy $E_T^{\text{iso}} < 0.2E_T^\gamma$. The photon isolation requirement is optimised using SHERPA EW $W\gamma jj$ simulation to minimise model dependence. Jets are reconstructed with the anti- k_t algorithm using all final-state particles as input except the dressed lepton and prompt neutrinos. Events are required to contain zero jets that fall within $\Delta R = 0.4$ around a b -hadron, and must contain at least two jets with $p_T > 50$ GeV and $|\eta| < 4.4$. The particle-level missing transverse momentum, defined as the vector sum of the transverse momenta of all non-interacting, final-state stable particles, must satisfy $E_T^{\text{miss}} > 30$ GeV. These leptons, jets, and photons are then selected in a VBS topology by using the same requirements as the reconstruction-level selection, which are listed in Table 3. The particle-level phase space definition is slightly different for the fiducial and differential cross-section measurements to ensure the definitions are as close as possible to the signal extraction method at reconstruction level.

The integrated fiducial cross-section, $\sigma_{EW W\gamma jj}^{\text{fid}}$, is defined as :

$$\sigma_{EW W\gamma jj}^{\text{fid}} = \frac{N_{EW W\gamma jj}}{L \cdot C_{EW W\gamma jj}}, \quad (4)$$

where $N_{EW W\gamma jj}$ is the number of extracted EW $W\gamma jj$ events after performing the fit described in Section 6.1, L is the integrated luminosity, and $C_{EW W\gamma jj}$ is the correction factor estimated by using the EW $W\gamma jj$ MC. The statistical uncertainty due to the limited size of data and simulation samples are propagated through Equation 4, along with each source of systematic uncertainty affecting $N_{EW W\gamma jj}$ and $C_{EW W\gamma jj}$, which are treated as fully correlated.

For the differential cross-section measurement each distribution is unfolded using an iterative Bayesian method with two iterations [52, 53]. The binnings of the observables are optimised to ensure the relative statistical precision of the extracted EW $W\gamma jj$ event yield is similar across bins using an Asimov dataset [54] formed by the $W\gamma$ and non- $W\gamma$ simulation samples. The binning for each observable is optimised using

Table 3: Particle-level definition for the fiducial and differential EW $W\gamma jj$ measurement.

Object	Selection requirements
Dressed muons	$p_T > 30$ GeV and $ \eta < 2.5$
Dressed electrons	$p_T > 30$ GeV and $ \eta < 2.47$ (excluding $1.37 < \eta < 1.52$)
Isolated photons	$E_T^\gamma > 22$ GeV and $ \eta < 2.37$ (excluding $1.37 < \eta < 1.52$) and $E_T^{\text{iso}} < 0.2E_T^\gamma$
Jets	At least two jets with $p_T > 50$ GeV and $ y < 4.4$, b -jet veto
Missing transverse momentum	$E_T^{\text{miss}} > 30$ GeV and $m_T^W > 30$ GeV
VBS topology	$N_\ell = 1, N_\gamma \geq 1, m_{\ell\gamma} - m_Z > 10$ GeV $\Delta R_{\min}(\ell, j) > 0.4, \Delta R_{\min}(\gamma, j) > 0.4, \Delta R_{\min}(\ell, \gamma) > 0.4$ $\Delta R_{\min}(j_1, j_2) > 0.4, \Delta\phi_{\min}(E_T^{\text{miss}}, j) > 0.4$ $N_{\text{jets}} \geq 2, p_T^{j_1}, p_T^{j_2} > 50$ GeV $m_{jj} > 500$ GeV, $ \Delta y_{jj} > 2$
Fiducial measurement	VBS topology
Differential measurement	VBS topology $\oplus (m_{jj} > 1000$ GeV, $N_{\text{jets}}^{\text{gap}} = 0$, and $\xi_{W\gamma} < 0.35$)

the EW $W\gamma jj$ and strong $W\gamma jj$ simulation samples, such that a similar statistical precision is obtained for each bin of the extracted yield. An additional requirement that the bin width is not smaller than twice the resolution of the observable is enforced. The number of iterations are determined by minimising the quadrature sum of the bias and the statistical uncertainty due to unfolding, where the bias is estimated by comparing the unfolded distribution after a certain number of iterations to the true distribution in the EW $W\gamma jj$ simulation. The value and statistical uncertainty on the fiducial EW $W\gamma jj$ cross-section are derived from the mean and root mean square (RMS) of the 10 000 toy experiments described in Section 6.2, propagated through the unfolding. These modified distributions and response matrices are then used to repeat the unfolding procedure for each toy experiment. The statistical uncertainty in each bin corresponds to the standard deviation of the unfolded results from the ensemble of 10 000 toy experiments. Systematic uncertainties that affect both the signal extraction and the unfolding are treated as correlated and propagated through the unfolding to the final results.

8 Systematic uncertainties

Experimental sources of systematic uncertainty arise from the reconstruction and energy calibration of objects including leptons, photons, jets, heavy-flavour tagging of jets, and missing transverse momentum. These uncertainties affect both the normalisation and shape of the simulated background processes, the shape of the simulated EW $W\gamma jj$ process in the signal extraction, and the normalisation and shape of simulations used to unfold the inclusive and differential cross-sections of the EW $W\gamma jj$ process.

The lepton trigger efficiencies and lepton and photon reconstruction, identification, and isolation efficiencies in simulations are corrected using scale factors derived from data, as described in Section 4. Systematic uncertainties due to this procedure are evaluated by varying the scale factors based on their associated uncertainties [34, 35]. Uncertainties arising from differences between simulation and data in the

reconstructed lepton (photon) momentum are evaluated by scaling and smearing the lepton (photon) transverse momentum.

Jets are calibrated using a combination of MC-based and data-driven corrections [55]. Uncertainties in the measurements due to uncertainties in the jet energy scale and resolution corrections are evaluated by scaling and smearing the jet four-momentum in the simulation by the uncertainties associated with each of these corrections. Uncertainties arising from the imperfect modelling of the JVT in the simulation are estimated by varying the JVT requirement. Furthermore, uncertainties arising from differences between simulation and data in b -jet tagging efficiencies are estimated by varying the associated scale factors [40].

Uncertainties from the E_T^{miss} measurement are estimated by propagating the uncertainties in the transverse momenta of hard physics objects and by applying uncertainties associated with momentum scale and resolution to the track-based term [41].

Additional sources of experimental uncertainty arise due to the modelling of pile-up and the luminosity determination. The uncertainty in the combined 2015–2018 integrated luminosity is 0.83% [29], obtained using the LUCID-2 detector [11] for the primary luminosity measurements, complemented by measurements using the inner detector and calorimeters.

For the EW $W\gamma jj$ fiducial cross-section measurement, each source of experimental systematic uncertainty is introduced as a nuisance parameter using a Gaussian constraint in the likelihood, as described in Section 6.1. For the differential signal extraction, 10 000 pseudo-experiments are constructed for simulated MC samples, where each pseudo-experiment samples each simulated MC event with a unit-mean Poisson distribution. For data, in each experiment the number of data events in each bin is determined by sampling a Poisson distribution of mean equal to the nominal bin content. Each pseudo-experiment maintains statistical correlations between the nominal and varied samples by keeping the same values from the unit-mean Poisson distributions for each event, for both the nominal and systematic variations. The EW $W\gamma jj$ yield is extracted for each pseudo-experiment, and the effect of the systematic uncertainty on the yield is calculated as the mean of the distribution of differences between the varied and nominal for each pseudo-experiment. The statistical significance of each experimental systematic uncertainty is evaluated by computing the RMS of the distribution of differences between the varied and nominal pseudo-experiments. A smoothing procedure is applied to reduce bin-to-bin statistical fluctuations such that the difference between uncertainties with or without smoothing is statistically insignificant. All experimental systematic uncertainties are treated as correlated between processes and regions. For both the inclusive and differential cross-sections, the dominant experimental systematic uncertainties arise from the calibration of jets and modelling of pile-up conditions, resulting in approximately 4% uncertainty in the inclusive cross-section and 5%–9% uncertainty in the differential measurements.

Theoretical uncertainties are accounted for from all simulated signal and background processes that affect the EW $W\gamma jj$ signal extraction. Each source of theoretical uncertainty is estimated by repeating the signal extraction and unfolding procedure with an uncertainty variation applied and propagating this through the unfolded measurements. Theoretical uncertainties arise due to higher-order QCD corrections, the PDFs used in the simulations, the accuracy of the strong coupling constant α_S , and the choice of event generators. The effects of higher-order QCD corrections are estimated by varying each of the renormalisation (μ_R) and factorisation (μ_F) scales by a factor of two with $0.5 \leq \mu_F/\mu_R \leq 2.0$. Uncertainties due to the PDFs are evaluated by varying each Hessian eigenvector of the nominal NNPDF3.0_{NNLO} set and comparing results obtained from nominal PDFs to alternative PDFs such as NNPDF3.1_{NNLO} [56], CT18_{NNLO} [57], MSHT2020_{NNLO} [58], and PDF4LHC15_{NNLO} [59]. If the difference between the nominal PDF and alternative PDF is not covered by the quadrature sum of the eigenvector changes in NNPDF3.0_{NNLO}, an

additional uncertainty is assigned. The uncertainty due to α_S is evaluated with the nominal PDF by varying the nominal $\alpha_S = 0.118$ by ± 0.001 . For the EW $W\gamma jj$ signal extraction, the systematic uncertainty arising from the choice of event generator for the strong $W\gamma jj$ and EW $W\gamma jj$ processes is estimated using the symmetrised envelope formed by the difference between the extracted event yield between the nominal generator, SHERPA, and the alternative generator, MADGRAPH5+PYTHIA8. For the differential cross-section measurement, the choice of event generator is extracted using the same method as with the experimental systematic uncertainties.

Treatment of the theory uncertainties is briefly discussed here. For the fiducial cross-section measurement, the QCD scale uncertainties are treated as uncorrelated between signal and control regions, because it is a conservative approach in this case. The PDF and α_S uncertainties are treated as correlated between regions but kept uncorrelated between different processes. Unlike the decorrelation of theory uncertainties across regions for the fiducial cross-section measurement of EW $W\gamma jj$, this treatment of theory uncertainties is not necessary for the differential cross-section measurement for two reasons: first, the differential cross-section is measured in each bin of the observable using the fit described above, hence the theory uncertainties are decorrelated between bins of observables; and second, correlations of QCD scale variations across $N_{\text{jets}}^{\text{gap}}$ are taken into account by the floating parameter c in Equation 3 in Section 6.2 such that only the uncertainties in c are required.

Systematic uncertainties related to the unfolding procedure in the differential cross-section measurements are evaluated as follows. First, the EW $W\gamma jj$ process simulated with the alternative generator, MADGRAPH, is used to extract the EW $W\gamma jj$ signal and unfold the data. The difference from the nominal result is applied as a systematic uncertainty on the unfolded EW $W\gamma jj$ distributions. Second, 10 000 truth toy experiments are generated for the particle-level distribution according to a Gaussian distribution with mean equal to the value of the corresponding bin and RMS equal to the statistical uncertainty of the bin. The nominal response matrix is then applied to the particle-level distribution from each toy experiment to create a reconstruction-level pseudo-dataset, which is then unfolded with the nominal response matrix to produce an unfolded pseudo-dataset. The difference in the observable distribution between the truth toy experiment and the unfolded pseudo-dataset constitutes a systematic uncertainty on the unfolded result.

Table 4 shows the impact of the statistical and systematic uncertainties on the fiducial and differential cross-section measurement. The precision of the fiducial cross-section is limited by the statistical precision of the sample followed by the modelling uncertainties, and the largest experimental uncertainties arise from uncertainties in the jet energy scale and jet energy resolution of reconstructed jets. Figure 5 shows the fractional systematic uncertainties as functions of m_{jj} and p_T^l . The uncertainties in the differential measurement are mostly dominated by the systematic variations arising from strong $W\gamma jj$ and EW $W\gamma jj$ modelling and the impact of the jet energy scale and resolution uncertainties, for distributions including jets.

9 Results

9.1 Observation and fiducial cross-section for EW $W\gamma jj$ process

The measured signal strength, μ_{EW} , is 1.5 ± 0.5 and the observed significance is well above six standard deviations, compared with an expected significance of 6.3σ , using SHERPA for EW $W\gamma jj$ signal. The measured EW $W\gamma jj$ fiducial cross-section in the phase space defined in Section 7 is determined to be $\sigma_{\text{EW}} = 13.2 \pm 2.5$ fb. The difference in fractional uncertainty between μ_{EW} and σ_{EW} is due to a large

Table 4: Impact of uncertainties on the measured fiducial cross-section. Squared values of impacts are obtained by fixing a set of nuisance parameters of the uncertainty sources corresponding to the category to the best-fit values, then calculating the difference between the squares of the resulting uncertainty from the total uncertainty of the nominal fit.

Uncertainty Source	Fractional Uncertainty [%]
Statistics	11
Jets	8
Lepton, photon, pile-up	8
EW $W\gamma jj$ modelling	7
Strong $W\gamma jj$ modelling	6
Non-prompt background	2
Luminosity	2
Other Background modelling	2
E_T^{miss}	1

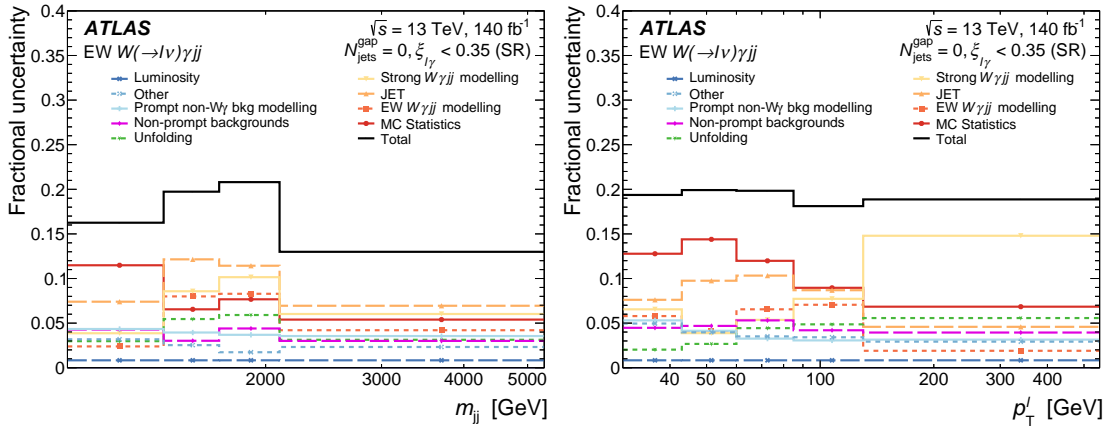


Figure 5: Fractional uncertainty in the EW $W\gamma jj$ measurement as functions of m_{jj} and p_T^l . Uncertainties are grouped in categories that are added in quadrature to give total uncertainties. Systematic uncertainties due to reconstruction of leptons, photons, pile-up, and heavy-flavour jets are grouped in the category “Other”.

normalisation component of the signal modelling uncertainty from the choice of event generator. These predictions from SHERPA and MADGRAPH5+PYTHIA8 are compared with the measured fiducial cross-section in Figure 6. The MADGRAPH5+PYTHIA8 prediction is in agreement with the data within uncertainties while SHERPA underestimates the data within two standard deviations. The theoretical uncertainties in the predicted cross-sections include systematic uncertainties from the QCD scales, PDFs, and α_S variations. The difference between the predicted cross-section between MADGRAPH5+PYTHIA8 and SHERPA arises due to the third parton included in the matrix element of SHERPA [60].

9.2 Differential cross-section for EW $W\gamma jj$ process

Figure 7 shows the differential cross-sections for EW $W\gamma jj$ production as functions of m_{jj} , p_T^{jj} , $\Delta\phi_{jj}$, p_T^l , $m_{l\gamma}$, and $\Delta\phi_{l\gamma}$. The predictions from both MADGRAPH5+PYTHIA8 and SHERPA are in agreement with the data within uncertainties, where MADGRAPH5+PYTHIA8 predictions slightly overshoot the measurement at

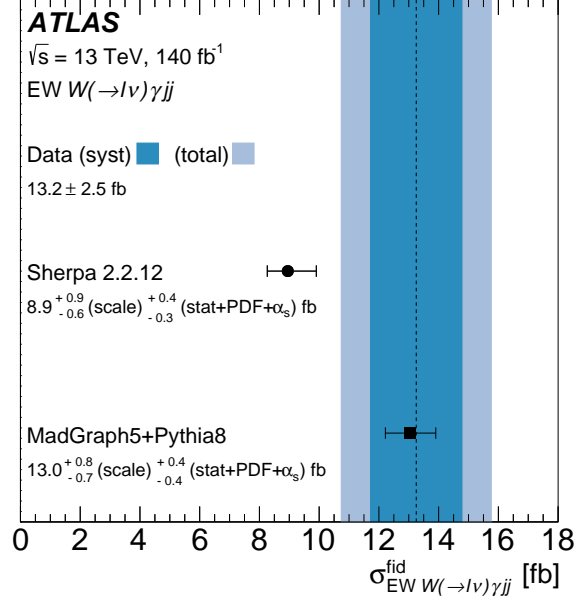


Figure 6: The measured EW $W\gamma jj$ fiducial cross-section compared with the predictions of SHERPA and MADGRAPH5+PYTHIA8. The central value of the measured fiducial cross-section is represented by a dashed vertical line. The light shaded band represents the total uncertainty on the measured fiducial cross-section, while the darker shaded band represents the systematic uncertainty. Each MC prediction is represented with a solid circle, and the associated horizontal error bars correspond to the quadrature sum of statistical uncertainties and theoretical uncertainties. The impacts of various sources of systematic and theoretical modelling uncertainties in the fiducial cross-section are shown in Table 4.

high m_{jj} and p_T^{jj} while the SHERPA predictions tend to underestimate the measured cross-section across the six observables, particularly at low p_T^{jj} , $-2.5 < \Delta\phi_{jj} < 0$, and $\Delta\phi_{l\gamma} < 0$.

The presence of anomalous quartic gauge coupling can modify the distributions of these observables at the tails of m_{jj} , p_T^{jj} , p_T^l or $m_{l\gamma}$. This is investigated further in Section 10. Enhancement of CPV of Higgs and gauge boson couplings in the diboson sector may distort the shape of $\Delta\phi_{jj}$ and $\Delta\phi_{l\gamma}$, thus the measurements of these two observables can be used to constrain the presence of CP-odd contributions to the EW $W\gamma jj$ process.

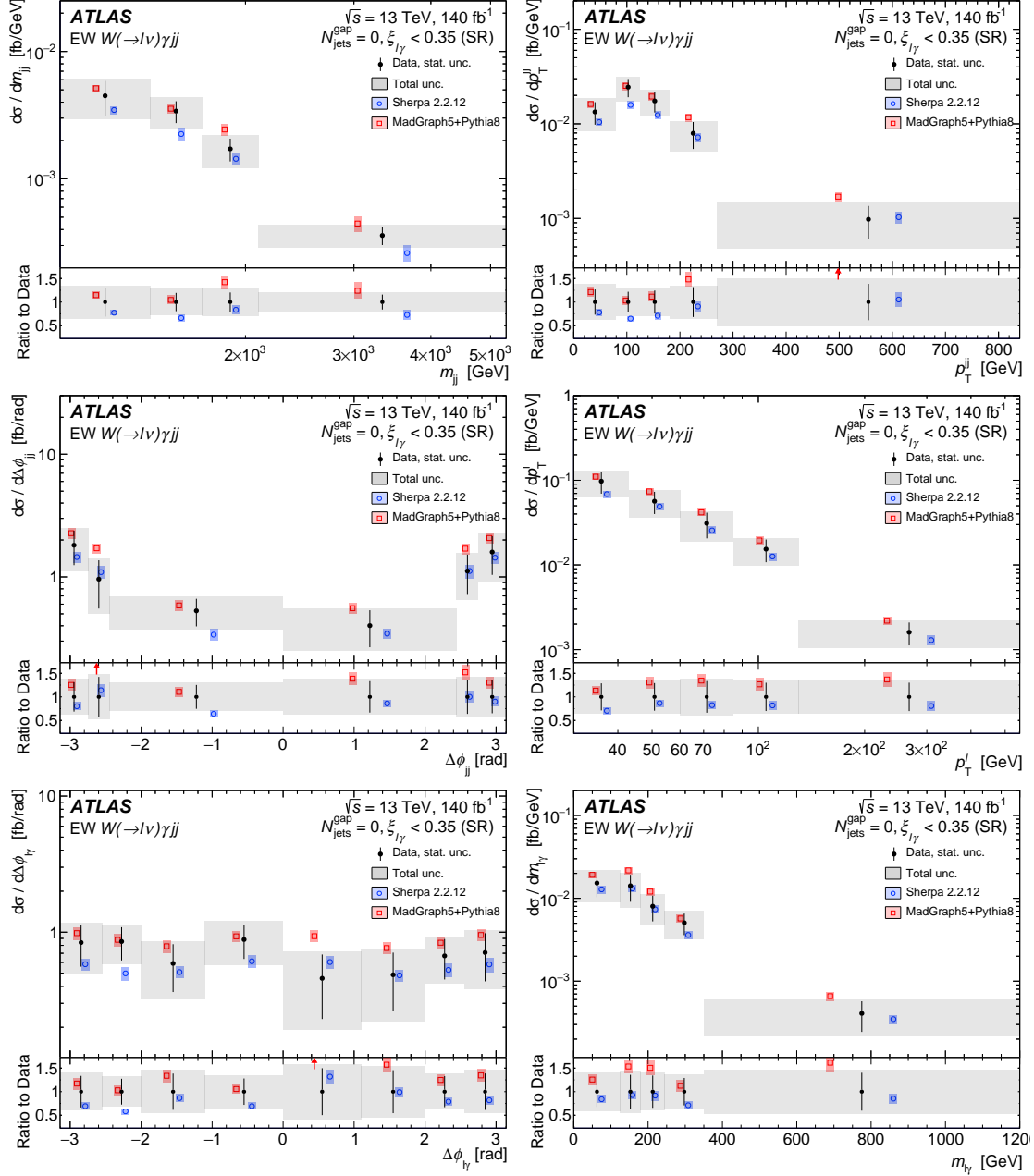


Figure 7: EW $W\gamma jj$ measured differential cross-section (solid circles) as functions of m_{jj} , p_T^{jj} , $\Delta\phi_{jj}$, p_T^l , $m_{l\gamma}$ and $\Delta\phi_{l\gamma}$ in comparison to SHERPA (open circles) and MADGRAPH5+PYTHIA8 (open squares) predictions. The vertical error bars on the predictions are determined by varying QCD scales, PDFs, α_S (for SHERPA), and MC statistical uncertainties. The vertical (shaded) error bars on the data correspond to the data statistical (total) uncertainties.

10 EFT interpretation

The differential cross-section measurements presented in Section 9 are used to constrain dimension-8 (D-8) operators [2]. These operators are implemented in the Eboli model including twenty independent, charge-conjugation and parity conserving D-8 operators that can change the QGC. The measured distributions for the six observables are sensitive to sixteen D-8 operators and the most stringent limits from interpretations of these distributions are reported.

The effective Lagrangian, \mathcal{L}_{eff} , including aQGC interactions represented by the higher dimension operators and the corresponding Wilson coefficients, is given by:

$$\mathcal{L}_{\text{eff}} = \mathcal{L}_{\text{SM}} + \sum_j \frac{f_j^{(8)}}{\Lambda^4} \mathcal{O}_j^{(8)}, \quad (5)$$

where \mathcal{L}_{SM} is the SM Lagrangian, $\mathcal{O}_i^{(8)}$ correspond to D-8 operators with dimensionless couplings $f_j^{(8)}$ (Wilson coefficients), and Λ is the energy scale of new physics. The D-8 operators are the lowest-order operators that can change QGCs without affecting the triple gauge couplings². These D-8 operators can be classified into two groups: mixed-scalar operators ($\mathcal{O}_{M0,1,2,3,4,5,7}$), consisting of two covariant derivatives of the Higgs field and two field strength tensors, and tensor-type operators, consisting of four field strength tensors ($\mathcal{O}_{T0,1,2,3,4,5,6,7}$).

Theoretical predictions for the EW $W\gamma jj$ process are constructed based on the effective Lagrangian in Equation 5. The amplitude for the EW $W\gamma jj$ process, \mathcal{M} , consists of the SM contribution, \mathcal{M}_{SM} , and the pure D-8 part including the aQGC interactions, $\mathcal{M}_{\text{D-8}}$.

The differential cross-section can be decomposed into the following three terms:

$$|\mathcal{M}|^2 = |\mathcal{M}_{\text{SM}}|^2 + 2\text{Re}(\mathcal{M}_{\text{SM}}^* \mathcal{M}_{\text{D-8}}) + |\mathcal{M}_{\text{D-8}}|^2, \quad (6)$$

where the pure SM term is $|\mathcal{M}_{\text{SM}}|^2$, $|\mathcal{M}_{\text{D-8}}|^2$ is the pure D-8 term that scales quadratically with $f_j^{(8)}$, and the interference term between the SM and D-8 amplitudes is $2\text{Re}(\mathcal{M}_{\text{SM}}^* \mathcal{M}_{\text{D-8}})$, which scales linearly with $f_j^{(8)}$. It was found that the pure D-8 term affects the differential cross-section measurements significantly more than the interference term. The pure SM part in Equation 6 is taken to be the prediction from MADGRAPH5+PYTHIA8, described in Section 3. The D-8 and interference terms are generated at LO using MADGRAPH5+PYTHIA8, with the same PDF and parameter tunes for modelling as the SM terms.

Limits on the D-8 operator coefficients are determined using test statistics based on the profile likelihood ratio. The profile likelihood ratio is constructed in terms of the measured cross-section as functions of each of the six observables and the corresponding theoretical prediction parameterised in terms of Wilson coefficients. The profile-likelihood test statistics, which are assumed to follow a χ^2 distribution with one degree of freedom according to Wilks' theorem [61], allows the evaluation of each Wilson coefficient at 95% confidence level (CL). The expected 95% coverage is further validated using 1000 pseudo experiments.

The most stringent expected limit on each coefficient is obtained from either the p_T^{jj} or p_T^l distribution. Observed and expected limits on the Wilson coefficients at 95% CL are presented in Table 5 and Table 6 with or without unitarity preservation by introducing the clipping technique described in Ref. [62].

² Triple gauge couplings are represented by dimension-6 operators that affect both strong and EW production of VBS processes. These are strongly constrained by vector boson fusion processes.

The limits on the D-8 Wilson coefficients using the clipping technique are estimated as functions of a cut-off scale, and for values of $M_{W\gamma}$ greater than the cut-off scale the anomalous interaction contribution is set to zero. Figure 8 shows a scan of the cut-off scale for the $T3$ operator when fitting the p_T^{jj} distribution. p_T^{jj} is found to be the most sensitive observable to the tensor-type operators while p_T^l is found to be the most sensitive observable to the mixed scalar operators. The constraints on the f_{T3} and f_{T4} operators represent the first such limits at the LHC.

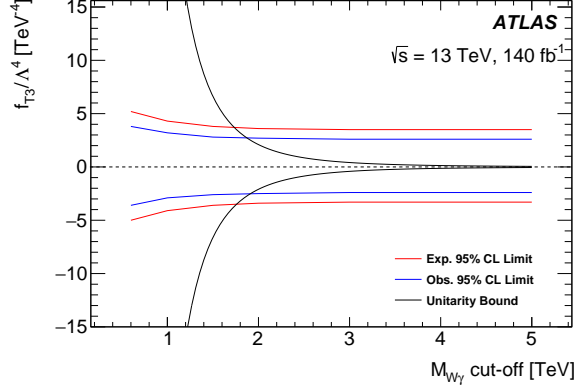


Figure 8: Expected and observed 95% CL limits of the tensor-type operator coupling f_{T3} from the fit to p_T^{jj} at different values of $m_{W\gamma}$. Bounds from partial wave unitarity constraints are also shown.

Table 5: Expected and observed limits on dimension-8 operators modifying the $WW\gamma\gamma$ coupling when fitting either the p_T^{jj} or p_T^l distribution.

Coefficients [TeV ⁻⁴]	Observable	Expected [TeV ⁻⁴]	Observed [TeV ⁻⁴]
f_{T0}/Λ^4	p_T^{jj}	[-2.4, 2.4]	[-1.8, 1.8]
f_{T1}/Λ^4	p_T^{jj}	[-1.5, 1.6]	[-1.1, 1.2]
f_{T2}/Λ^4	p_T^{jj}	[-4.4, 4.7]	[-3.1, 3.5]
f_{T3}/Λ^4	p_T^{jj}	[-3.3, 3.5]	[-2.4, 2.6]
f_{T4}/Λ^4	p_T^{jj}	[-3.0, 3.0]	[-2.2, 2.2]
f_{T5}/Λ^4	p_T^{jj}	[-1.7, 1.7]	[-1.2, 1.3]
f_{T6}/Λ^4	p_T^{jj}	[-1.5, 1.5]	[-1.0, 1.1]
f_{T7}/Λ^4	p_T^{jj}	[-3.8, 3.9]	[-2.7, 2.8]
f_{M0}/Λ^4	p_T^l	[-28, 28]	[-24, 24]
f_{M1}/Λ^4	p_T^l	[-43, 44]	[-37, 38]
f_{M2}/Λ^4	p_T^l	[-10, 10]	[-8.6, 8.5]
f_{M3}/Λ^4	p_T^l	[-16, 16]	[-13, 14]
f_{M4}/Λ^4	p_T^l	[-18, 18]	[-15, 15]
f_{M5}/Λ^4	p_T^l	[-17, 14]	[-14, 12]
f_{M7}/Λ^4	p_T^l	[-78, 77]	[-66, 65]

Table 6: Expected and observed 95% CL limits for specified $M_{W\gamma}$ cut-off values, where the expected limit intersects with the unitarity bounds derived from partial wave unitarity constraints. The fit to either the p_T^{jj} or p_T^l distribution is used to extract the limits.

Coefficients [TeV ⁻⁴]	Observable	$M_{W\gamma}$ cut-off [TeV]	Expected [TeV ⁻⁴]	Observed [TeV ⁻⁴]
f_{T0}/Λ^4	p_T^{jj}	1.4	[-2.5, 2.6]	[-1.9, 1.9]
f_{T1}/Λ^4	p_T^{jj}	1.9	[-1.6, 1.6]	[-1.1, 1.2]
f_{T2}/Λ^4	p_T^{jj}	1.6	[-4.9, 5.3]	[-3.6, 4.0]
f_{T3}/Λ^4	p_T^{jj}	1.9	[-3.4, 3.6]	[-2.5, 2.7]
f_{T4}/Λ^4	p_T^{jj}	2.2	[-3.1, 3.1]	[-2.2, 2.3]
f_{T5}/Λ^4	p_T^{jj}	1.8	[-1.8, 1.8]	[-1.3, 1.3]
f_{T6}/Λ^4	p_T^{jj}	2.1	[-1.5, 1.5]	[-1.1, 1.1]
f_{T7}/Λ^4	p_T^{jj}	2.1	[-4.0, 4.1]	[-2.9, 3.0]
f_{M0}/Λ^4	p_T^l	1.1	[-45, 44]	[-32, 31]
f_{M1}/Λ^4	p_T^l	1.4	[-60, 62]	[-43, 44]
f_{M2}/Λ^4	p_T^l	1.4	[-15, 15]	[-11, 11]
f_{M3}/Λ^4	p_T^l	1.8	[-22, 22]	[-16, 16]
f_{M4}/Λ^4	p_T^l	1.5	[-28, 27]	[-20, 20]
f_{M5}/Λ^4	p_T^l	1.9	[-21, 23]	[-14, 17]
f_{M7}/Λ^4	p_T^l	1.5	[-100, 99]	[-73, 71]

11 Conclusion

An observation of the electroweak production of $W\gamma jj$ and measurements of its fiducial and differential cross-section are reported, using pp collision data collected with the ATLAS detector at a centre-of-mass energy of $\sqrt{s} = 13$ TeV that correspond to an integrated luminosity of 140 fb^{-1} . This process provides a unique probe of the quartic gauge coupling via the vector boson scattering production mechanism. Measurements of the EW $W\gamma jj$ production are therefore sensitive to the $WW\gamma Z$ and $WW\gamma\gamma$ couplings and provide an ideal opportunity to probe the electroweak gauge symmetry breaking of the Standard Model.

Advanced machine learning techniques are used to establish the observation of the EW $W\gamma jj$ process with a significance of well above six standard deviations. The measured fiducial cross-section for the EW $W\gamma jj$ process is determined to be $13.2 \pm 2.5 \text{ fb}$, consistent with LO predictions from MADGRAPH5+PYTHIA8 and SHERPA. Differential cross-sections are measured as functions of six kinematic observables in a stricter fiducial phase space. These observables are either sensitive to the quartic gauge couplings or the CPV structure of $WW\gamma Z$ and $WW\gamma\gamma$ couplings. The data are corrected for detector effects of inefficiency and resolution using an iterative Bayesian unfolding method and are compared with theoretical predictions from MADGRAPH5+PYTHIA8 and SHERPA 2.2.12. These unfolded distributions are described by LO predictions within uncertainties, in which MADGRAPH5+PYTHIA8 tends to overshoot the measurement at high m_{jj} and p_T^{jj} while SHERPA 2.2.12 shows reasonable agreement but tends to underestimate the data across the six observables. The shape of these distributions are described reasonably well by both predictions. These differential measurements are used to search for anomalous quartic boson interactions using dimension-8 operators in the context of an effective field theory. The transverse momentum of the dijet system is found to be the most sensitive observable to the tensor-type operators while the lepton transverse momentum is found to be the most sensitive observable to the mixed scalar operators. The first LHC constraints on f_{T3}

and f_{T4} are presented.

Acknowledgements

We thank CERN for the very successful operation of the LHC and its injectors, as well as the support staff at CERN and at our institutions worldwide without whom ATLAS could not be operated efficiently.

The crucial computing support from all WLCG partners is acknowledged gratefully, in particular from CERN, the ATLAS Tier-1 facilities at TRIUMF/SFU (Canada), NDGF (Denmark, Norway, Sweden), CC-IN2P3 (France), KIT/GridKA (Germany), INFN-CNAF (Italy), NL-T1 (Netherlands), PIC (Spain), RAL (UK) and BNL (USA), the Tier-2 facilities worldwide and large non-WLCG resource providers. Major contributors of computing resources are listed in Ref. [63].

We gratefully acknowledge the support of ANPCyT, Argentina; YerPhI, Armenia; ARC, Australia; BMWFW and FWF, Austria; ANAS, Azerbaijan; CNPq and FAPESP, Brazil; NSERC, NRC and CFI, Canada; CERN; ANID, Chile; CAS, MOST and NSFC, China; Minciencias, Colombia; MEYS CR, Czech Republic; DNRF and DNSRC, Denmark; IN2P3-CNRS and CEA-DRF/IRFU, France; SRNSFG, Georgia; BMBF, HGF and MPG, Germany; GSRI, Greece; RGC and Hong Kong SAR, China; ISF and Benozziyo Center, Israel; INFN, Italy; MEXT and JSPS, Japan; CNRST, Morocco; NWO, Netherlands; RCN, Norway; MEiN, Poland; FCT, Portugal; MNE/IFA, Romania; MESTD, Serbia; MSSR, Slovakia; ARRS and MIZŠ, Slovenia; DSI/NRF, South Africa; MICINN, Spain; SRC and Wallenberg Foundation, Sweden; SERI, SNSF and Cantons of Bern and Geneva, Switzerland; MOST, Taipei; TENMAK, Türkiye; STFC, United Kingdom; DOE and NSF, United States of America.

Individual groups and members have received support from BCKDF, CANARIE, CRC and DRAC, Canada; PRIMUS 21/SCI/017 and UNCE SCI/013, Czech Republic; COST, ERC, ERDF, Horizon 2020, ICSC-NextGenerationEU and Marie Skłodowska-Curie Actions, European Union; Investissements d’Avenir Labex, Investissements d’Avenir Idex and ANR, France; DFG and AvH Foundation, Germany; Herakleitos, Thales and Aristeia programmes co-financed by EU-ESF and the Greek NSRF, Greece; BSF-NSF and MINERVA, Israel; Norwegian Financial Mechanism 2014-2021, Norway; NCN and NAWA, Poland; La Caixa Banking Foundation, CERCA Programme Generalitat de Catalunya and PROMETEO and GenT Programmes Generalitat Valenciana, Spain; Göran Gustafssons Stiftelse, Sweden; The Royal Society and Leverhulme Trust, United Kingdom.

In addition, individual members wish to acknowledge support from CERN: European Organization for Nuclear Research (CERN PJAS); Chile: Agencia Nacional de Investigación y Desarrollo (FONDECYT 1190886, FONDECYT 1210400, FONDECYT 1230987); China: National Natural Science Foundation of China (NSFC - 12175119, NSFC 12275265); European Union: European Research Council (ERC - 948254, ERC 101089007), Horizon 2020 Framework Programme (MUCCA - CHIST-ERA-19-XAI-00), Italian Center for High Performance Computing, Big Data and Quantum Computing (ICSC, NextGenerationEU); France: Agence Nationale de la Recherche (ANR-20-CE31-0013, ANR-21-CE31-0022), Investissements d’Avenir Labex (ANR-11-LABX-0012); Germany: Baden-Württemberg Stiftung (BW Stiftung-Postdoc Eliteprogramme), Deutsche Forschungsgemeinschaft (DFG - 469666862, DFG - CR 312/5-2); Italy: Istituto Nazionale di Fisica Nucleare (ICSC, NextGenerationEU); Japan: Japan Society for the Promotion of Science (JSPS KAKENHI 22H01227, JSPS KAKENHI 22KK0227, JSPS KAKENHI JP21H05085, JSPS KAKENHI JP22H04944); Netherlands: Netherlands Organisation for Scientific Research (NWO Veni 2020 - VI.Veni.202.179); Norway: Research Council of Norway (RCN-314472); Poland: Polish National

Agency for Academic Exchange (PPN/PPO/2020/1/00002/U/00001), Polish National Science Centre (NCN 2021/42/E/ST2/00350, NCN OPUS nr 2022/47/B/ST2/03059, NCN UMO-2019/34/E/ST2/00393, UMO-2020/37/B/ST2/01043, UMO-2022/47/O/ST2/00148); Slovenia: Slovenian Research Agency (ARIS grant J1-3010); Spain: BBVA Foundation (LEO22-1-603), Generalitat Valenciana (Artemisa, FEDER, IDIFEDER/2018/048), Ministry of Science and Innovation (RYC2019-028510-I, RYC2020-030254-I), PROMETEO and GenT Programmes Generalitat Valenciana (CIDEAGENT/2019/023, CIDEAGENT/2019/027); Sweden: Swedish Research Council (VR 2022-03845), Knut and Alice Wallenberg Foundation (KAW 2022.0358); Switzerland: Swiss National Science Foundation (SNSF - PCEFP2_194658); United Kingdom: Leverhulme Trust (Leverhulme Trust RPG-2020-004); United States of America: Neubauer Family Foundation.

References

- [1] O. J. P. Éboli, M. C. Gonzalez-Garcia and S. M. Lietti, *Bosonic quartic couplings at CERN LHC*, *Phys. Rev. D* **69** (2004) 095005, arXiv: [hep-ph/0310141](#).
- [2] O. J. P. Éboli and M. C. Gonzalez-Garcia, *Classifying the bosonic quartic couplings*, *Phys. Rev. D* **93** (2016) 093013, arXiv: [1604.03555 \[hep-ph\]](#).
- [3] E. Accomando, A. Ballestrero, A. Belhouari and E. Maina, *Isolating vector boson scattering at the CERN LHC: Gauge cancellations and the equivalent vector boson approximation versus complete calculations*, *Phys. Rev. D* **74** (2006) 073010, arXiv: [hep-ph/0608019](#).
- [4] CMS Collaboration, *Observation of electroweak production of $W\gamma$ with two jets in proton–proton collisions at $\sqrt{s} = 13$ TeV*, *Phys. Lett. B* **811** (2020) 135988, arXiv: [2008.10521 \[hep-ex\]](#).
- [5] CMS Collaboration, *Measurement of the electroweak production of $W\gamma$ in association with two jets in proton–proton collisions at $\sqrt{s} = 13$ TeV*, *Phys. Rev. D* **108** (2023) 032017, arXiv: [2212.12592 \[hep-ex\]](#).
- [6] T. Plehn, D. Rainwater and D. Zeppenfeld, *Determining the Structure of Higgs Couplings at the LHC*, *Phys. Rev. Lett.* **88** (2002), arXiv: [hep-ph/0105325](#).
- [7] G. Klamke and D. Zeppenfeld, *Higgs plus two jet production via gluon fusion as a signal at the CERN LHC*, *JHEP* **0704** (2007), arXiv: [hep-ph/0703202](#).
- [8] ATLAS Collaboration, *The ATLAS Experiment at the CERN Large Hadron Collider*, *JINST* **3** (2008) S08003.
- [9] ATLAS Collaboration, *ATLAS Insertable B-Layer: Technical Design Report*, ATLAS-TDR-19; CERN-LHCC-2010-013, 2010, URL: <https://cds.cern.ch/record/1291633>, Addendum: ATLAS-TDR-19-ADD-1; CERN-LHCC-2012-009, 2012, URL: <https://cds.cern.ch/record/1451888>.
- [10] B. Abbott et al., *Production and integration of the ATLAS Insertable B-Layer*, *JINST* **13** (2018) T05008, arXiv: [1803.00844 \[physics.ins-det\]](#).
- [11] G. Avoni, *The new LUCID-2 detector for luminosity measurement and monitoring in ATLAS*, *JINST* **13** (2018) P07017.
- [12] ATLAS Collaboration, *Performance of the ATLAS trigger system in 2015*, *Eur. Phys. J. C* **77** (2017) 317, arXiv: [1611.09661 \[hep-ex\]](#).
- [13] ATLAS Collaboration, *The ATLAS Collaboration Software and Firmware*, ATL-SOFT-PUB-2021-001, 2021, URL: <https://cds.cern.ch/record/2767187>.
- [14] E. Bothmann et al., *Event generation with Sherpa 2.2*, *SciPost Phys.* **7** (2019) 034, arXiv: [1905.09127 \[hep-ph\]](#).
- [15] T. Gleisberg and S. Höche, *Comix, a new matrix element generator*, *JHEP* **12** (2008) 039, arXiv: [0808.3674 \[hep-ph\]](#).
- [16] S. Schumann and F. Krauss, *A parton shower algorithm based on Catani–Seymour dipole factorisation*, *JHEP* **03** (2008) 038, arXiv: [0709.1027 \[hep-ph\]](#).

- [17] S. Höche, F. Krauss, M. Schönherr and F. Siegert, *A critical appraisal of NLO+PS matching methods*, *JHEP* **09** (2012) 049, arXiv: [1111.1220 \[hep-ph\]](#).
- [18] S. Höche, F. Krauss, M. Schönherr and F. Siegert, *QCD matrix elements + parton showers. The NLO case*, *JHEP* **04** (2013) 027, arXiv: [1207.5030 \[hep-ph\]](#).
- [19] S. Catani, F. Krauss, B. R. Webber and R. Kuhn, *QCD Matrix Elements + Parton Showers*, *JHEP* **11** (2001) 063, arXiv: [hep-ph/0109231](#).
- [20] S. Höche, F. Krauss, S. Schumann and F. Siegert, *QCD matrix elements and truncated showers*, *JHEP* **05** (2009) 053, arXiv: [0903.1219 \[hep-ph\]](#).
- [21] NNPDF Collaboration, R. D. Ball et al., *Parton distributions for the LHC run II*, *JHEP* **04** (2015) 040, arXiv: [1410.8849 \[hep-ph\]](#).
- [22] J. Alwall et al., *The automated computation of tree-level and next-to-leading order differential cross sections, and their matching to parton shower simulations*, *JHEP* **07** (2014) 079, arXiv: [1405.0301 \[hep-ph\]](#).
- [23] ATLAS Collaboration, *ATLAS Pythia 8 tunes to 7 TeV data*, ATL-PHYS-PUB-2014-021, 2014, URL: <https://cds.cern.ch/record/1966419>.
- [24] D. J. Lange, *The EvtGen particle decay simulation package*, *Nucl. Instrum. Meth. A* **462** (2001) 152.
- [25] S. Agostinelli et al., *GEANT4 – a simulation toolkit*, *Nucl. Instrum. Meth. A* **506** (2003) 250.
- [26] T. Sjöstrand, S. Mrenna and P. Skands, *A brief introduction to PYTHIA 8.1*, *Comput. Phys. Commun.* **178** (2008) 852, arXiv: [0710.3820 \[hep-ph\]](#).
- [27] NNPDF Collaboration, R. D. Ball et al., *Parton distributions with LHC data*, *Nucl. Phys. B* **867** (2013) 244, arXiv: [1207.1303 \[hep-ph\]](#).
- [28] ATLAS Collaboration, *The Pythia 8 A3 tune description of ATLAS minimum bias and inelastic measurements incorporating the Donnachie–Landshoff diffractive model*, ATL-PHYS-PUB-2016-017, 2016, URL: <https://cds.cern.ch/record/2206965>.
- [29] ATLAS Collaboration, *Luminosity determination in pp collisions at $\sqrt{s} = 13$ TeV using the ATLAS detector at the LHC*, *Eur. Phys. J. C* **83** (2023), arXiv: [2212.09379 \[hep-ex\]](#).
- [30] ATLAS Collaboration, *Performance of the ATLAS muon triggers in Run 2*, *JINST* **15** (2020) P09015, arXiv: [2004.13447 \[physics.ins-det\]](#).
- [31] ATLAS Collaboration, *Performance of electron and photon triggers in ATLAS during LHC Run 2*, *Eur. Phys. J. C* **80** (2020) 47, arXiv: [1909.00761 \[hep-ex\]](#).
- [32] ATLAS Collaboration, *ATLAS data quality operations and performance for 2015–2018 data-taking*, *JINST* **15** (2020) P04003, arXiv: [1911.04632 \[physics.ins-det\]](#).
- [33] ATLAS Collaboration, *Vertex Reconstruction Performance of the ATLAS Detector at $\sqrt{s} = 13$ TeV*, ATL-PHYS-PUB-2015-026, 2015, URL: <https://cds.cern.ch/record/2037717>.
- [34] ATLAS Collaboration, *Muon reconstruction and identification efficiency in ATLAS using the full Run 2 pp collision data set at $\sqrt{s} = 13$ TeV*, *Eur. Phys. J. C* **81** (2021) 578, arXiv: [2012.00578 \[hep-ex\]](#).

- [35] ATLAS Collaboration, *Electron and photon performance measurements with the ATLAS detector using the 2015–2017 LHC proton–proton collision data*, *JINST* **14** (2019) P12006, arXiv: [1908.00005 \[hep-ex\]](#).
- [36] ATLAS Collaboration, *Jet reconstruction and performance using particle flow with the ATLAS Detector*, *Eur. Phys. J. C* **77** (2017) 466, arXiv: [1703.10485 \[hep-ex\]](#).
- [37] M. Cacciari, G. P. Salam and G. Soyez, *The anti- k_t jet clustering algorithm*, *JHEP* **04** (2008) 063, arXiv: [0802.1189 \[hep-ph\]](#).
- [38] ATLAS Collaboration, *Performance of pile-up mitigation techniques for jets in pp collisions at $\sqrt{s} = 8$ TeV using the ATLAS detector*, *Eur. Phys. J. C* **76** (2016) 581, arXiv: [1510.03823 \[hep-ex\]](#).
- [39] ATLAS Collaboration, *Selection of jets produced in 13 TeV proton–proton collisions with the ATLAS detector*, ATLAS-CONF-2015-029, 2015, URL: <https://cds.cern.ch/record/2037702>.
- [40] ATLAS Collaboration, *Optimisation and performance studies of the ATLAS b-tagging algorithms for the 2017-18 LHC run*, ATL-PHYS-PUB-2017-013, 2017, URL: <https://cds.cern.ch/record/2273281>.
- [41] ATLAS Collaboration, *Performance of missing transverse momentum reconstruction with the ATLAS detector using proton–proton collisions at $\sqrt{s} = 13$ TeV*, *Eur. Phys. J. C* **78** (2018) 903, arXiv: [1802.08168 \[hep-ex\]](#).
- [42] ATLAS Collaboration, *Measurement of the inclusive isolated prompt photon cross section in pp collisions at $\sqrt{s} = 7$ TeV with the ATLAS detector*, *Phys. Rev. D* **83** (2011) 052005, arXiv: [1012.4389 \[hep-ex\]](#).
- [43] Gaiser, J., *Charmonium spectroscopy from radiative decays of J/Ψ and Ψ'* , SLAC-R-255 (1982).
- [44] S., Bernstein, *Proof of theorem of Weierstrass based on the calculus of probabilities*, *Comm. Kharkov Math. Soc.* **13** (1912) 1.
- [45] ATLAS Collaboration, *Measurement of the $Z(\rightarrow \ell^+\ell^-)\gamma$ production cross-section in pp collisions at $\sqrt{s} = 13$ TeV with the ATLAS detector*, *JHEP* **03** (2020) 054, arXiv: [1911.04813 \[hep-ex\]](#).
- [46] A. L. Maas, ‘Rectifier Nonlinearities Improve Neural Network Acoustic Models’, *Proceedings of the 30th International Conference on Machine Learning*, vol. 28, 3, 2013.
- [47] D. P. Kingma and J. Ba, *Adam: A Method for Stochastic Optimization*, (2014), arXiv: [1412.6980 \[hep-ex\]](#).
- [48] ATLAS Collaboration, *Differential cross-section measurements for the electroweak production of dijets in association with a Z boson in proton–proton collisions at ATLAS*, *Eur. Phys. J. C* **81** (2021) 163, arXiv: [2006.15458 \[hep-ex\]](#).
- [49] R. Barlow, *Extended maximum likelihood*, *Nucl. Instrum. Meth. A* **297** (1990) 496.
- [50] M. Tanabashi and others (Particle Data Group), *Review of Particle Physics*, *Phys. Rev. D* **98** (2018) 030001.
- [51] ATLAS Collaboration, *Evaluating statistical uncertainties and correlations using the bootstrap method*, ATL-PHYS-PUB-2021-011, 2021, URL: <https://cds.cern.ch/record/2759945>.

- [52] G. D’Agostini, *A multidimensional unfolding method based on Bayes’ theorem*, [Nucl. Instrum. Meth. A **362** \(1995\) 487](#), ISSN: 0168-9002.
- [53] T. Adye, ‘Unfolding algorithms and tests using RooUnfold’, *Proceedings, 2011 Workshop on Statistical Issues Related to Discovery Claims in Search Experiments and Unfolding (PHYSTAT 2011)* (CERN, Geneva, Switzerland, 17th–20th Jan. 2011) 313, arXiv: [1105.1160 \[physics.data-an\]](#).
- [54] G. Cowan, K. Cranmer, E. Gross and O. Vitells, *Asymptotic formulae for likelihood-based tests of new physics*, [Eur. Phys. J. C **71** \(2011\) 1554](#), arXiv: [1007.1727 \[physics.data-an\]](#), Erratum: [Eur. Phys. J. C **73** \(2013\) 2501](#).
- [55] ATLAS Collaboration, *Jet energy scale and resolution measured in proton–proton collisions at $\sqrt{s} = 13$ TeV with the ATLAS detector*, [Eur. Phys. J. C **81** \(2021\) 689](#), arXiv: [2007.02645 \[hep-ex\]](#).
- [56] NNPDF Collaboration, *Parton distributions from high-precision collider data*, [Eur. Phys. J. C **77** \(2017\)](#), arXiv: [1706.00428 \[hep-ex\]](#).
- [57] T.-J. Hou et al., *Progress in the CTEQ-TEA NNLO global QCD analysis*, (2019), arXiv: [1908.11394 \[hep-ph\]](#).
- [58] S. Bailey, T. Cridge, L. A. Harland-Lang, A. D. Martin and R. Thorne, *Parton distributions from LHC, HERA, Tevatron and fixed target data: MSHT20 PDFs*, [Eur. Phys. J. C **81** \(2021\)](#), arXiv: [2012.04684](#).
- [59] J. Butterworth et al., *PDF4LHC recommendations for LHC Run II*, [J. Phys. G **43** \(2016\) 023001](#), arXiv: [1510.03865 \[hep-ph\]](#).
- [60] A. Ballestrero et al., *Precise predictions for same-sign W-boson scattering at the LHC*, [Eur. Phys. J. C **78** \(2018\)](#), arXiv: [1803.07943](#).
- [61] S. S. Wilks, *The Large-Sample Distribution of the Likelihood Ratio for Testing Composite Hypotheses*, [Ann. Math. Statist. **9** \(1938\) 60](#).
- [62] E. d. S. Almeida, O. J. P. Éboli and M. C. Gonzalez-Garcia, *Unitarity constraints on anomalous quartic couplings*, [Phys. Rev. D **101** \(2020\) 113003](#), arXiv: [2004.05174 \[hep-ph\]](#).
- [63] ATLAS Collaboration, *ATLAS Computing Acknowledgements*, ATL-SOFT-PUB-2023-001, 2023, URL: <https://cds.cern.ch/record/2869272>.

The ATLAS Collaboration

G. Aad ¹⁰³, E. Aakvaag ¹⁶, B. Abbott ¹²¹, K. Abeling ⁵⁵, N.J. Abicht ⁴⁹, S.H. Abidi ²⁹, M. Aboeela ⁴⁴, A. Aboulhorma ^{35e}, H. Abramowicz ¹⁵², H. Abreu ¹⁵¹, Y. Abulaiti ¹¹⁸, B.S. Acharya ^{69a,69b,1}, A. Ackermann ^{63a}, C. Adam Bourdarios ⁴, L. Adamczyk ^{86a}, S.V. Addepalli ²⁶, M.J. Addison ¹⁰², J. Adelman ¹¹⁶, A. Adiguzel ^{21c}, T. Aducci ¹³⁵, A.A. Affolder ¹³⁷, Y. Afik ³⁹, M.N. Agaras ¹³, J. Agarwala ^{73a,73b}, A. Aggarwal ¹⁰¹, C. Agheorghiesei ^{27c}, A. Ahmad ³⁶, F. Ahmadov ^{38,y}, W.S. Ahmed ¹⁰⁵, S. Ahuja ⁹⁶, X. Ai ^{62e}, G. Aielli ^{76a,76b}, A. Aikot ¹⁶⁴, M. Ait Tamlihat ^{35e}, B. Aitbenchikh ^{35a}, I. Aizenberg ¹⁷⁰, M. Akbiyik ¹⁰¹, T.P.A. Åkesson ⁹⁹, A.V. Akimov ³⁷, D. Akiyama ¹⁶⁹, N.N. Akolkar ²⁴, S. Aktas ^{21a}, K. Al Houry ⁴¹, G.L. Alberghi ^{23b}, J. Albert ¹⁶⁶, P. Albicocco ⁵³, G.L. Albouy ⁶⁰, S. Alderweireldt ⁵², Z.L. Alegria ¹²², M. Aleksa ³⁶, I.N. Aleksandrov ³⁸, C. Alexa ^{27b}, T. Alexopoulos ¹⁰, F. Alfonsi ^{23b}, M. Algren ⁵⁶, M. Alhroob ¹⁴², B. Ali ¹³³, H.M.J. Ali ⁹², S. Ali ¹⁴⁹, S.W. Alibocus ⁹³, M. Aliev ^{33c}, G. Alimonti ^{71a}, W. Alkakhri ⁵⁵, C. Allaire ⁶⁶, B.M.M. Allbrooke ¹⁴⁷, J.F. Allen ⁵², C.A. Allendes Flores ^{138f}, P.P. Allport ²⁰, A. Aloisio ^{72a,72b}, F. Alonso ⁹¹, C. Alpigiani ¹³⁹, M. Alvarez Estevez ¹⁰⁰, A. Alvarez Fernandez ¹⁰¹, M. Alves Cardoso ⁵⁶, M.G. Alviggi ^{72a,72b}, M. Aly ¹⁰², Y. Amaral Coutinho ^{83b}, A. Ambler ¹⁰⁵, C. Amelung ³⁶, M. Amerl ¹⁰², C.G. Ames ¹¹⁰, D. Amidei ¹⁰⁷, K.J. Amirie ¹⁵⁶, S.P. Amor Dos Santos ^{131a}, K.R. Amos ¹⁶⁴, S. An ⁸⁴, V. Ananiev ¹²⁶, C. Anastopoulos ¹⁴⁰, T. Andeen ¹¹, J.K. Anders ³⁶, S.Y. Andreev ^{47a,47b}, A. Andreazza ^{71a,71b}, S. Angelidakis ⁹, A. Angerami ^{41,aa}, A.V. Anisenkov ³⁷, A. Annovi ^{74a}, C. Antel ⁵⁶, M.T. Anthony ¹⁴⁰, E. Antipov ¹⁴⁶, M. Antonelli ⁵³, F. Anulli ^{75a}, M. Aoki ⁸⁴, T. Aoki ¹⁵⁴, J.A. Aparisi Pozo ¹⁶⁴, M.A. Aparo ¹⁴⁷, L. Aperio Bella ⁴⁸, C. Appelt ¹⁸, A. Apyan ²⁶, S.J. Arbiol Val ⁸⁷, C. Arcangeletti ⁵³, A.T.H. Arce ⁵¹, E. Arena ⁹³, J-F. Arguin ¹⁰⁹, S. Argyropoulos ⁵⁴, J.-H. Arling ⁴⁸, O. Arnaez ⁴, H. Arnold ¹¹⁵, G. Artoni ^{75a,75b}, H. Asada ¹¹², K. Asai ¹¹⁹, S. Asai ¹⁵⁴, N.A. Asbah ³⁶, K. Assamagan ²⁹, R. Astalos ^{28a}, K.S.V. Astrand ⁹⁹, S. Atashi ¹⁶⁰, R.J. Atkin ^{33a}, M. Atkinson ¹⁶³, H. Atmani ^{35f}, P.A. Atlasiddha ¹²⁹, K. Augsten ¹³³, S. Auricchio ^{72a,72b}, A.D. Auriol ²⁰, V.A. Austrup ¹⁰², G. Avolio ³⁶, K. Axiotis ⁵⁶, G. Azuelos ^{109,ae}, D. Babal ^{28b}, H. Bachacou ¹³⁶, K. Bachas ^{153,p}, A. Bachiu ³⁴, F. Backman ^{47a,47b}, A. Badea ³⁹, T.M. Baer ¹⁰⁷, P. Bagnaia ^{75a,75b}, M. Bahmani ¹⁸, D. Bahner ⁵⁴, K. Bai ¹²⁴, J.T. Baines ¹³⁵, L. Baines ⁹⁵, O.K. Baker ¹⁷³, E. Bakos ¹⁵, D. Bakshi Gupta ⁸, V. Balakrishnan ¹²¹, R. Balasubramanian ¹¹⁵, E.M. Baldin ³⁷, P. Balek ^{86a}, E. Ballabene ^{23b,23a}, F. Balli ¹³⁶, L.M. Baltos ^{63a}, W.K. Balunas ³², J. Balz ¹⁰¹, E. Banas ⁸⁷, M. Bandieramonte ¹³⁰, A. Bandyopadhyay ²⁴, S. Bansal ²⁴, L. Barak ¹⁵², M. Barakat ⁴⁸, E.L. Barberio ¹⁰⁶, D. Barberis ^{57b,57a}, M. Barbero ¹⁰³, M.Z. Barel ¹¹⁵, K.N. Barends ^{33a}, T. Barillari ¹¹¹, M-S. Barisits ³⁶, T. Barklow ¹⁴⁴, P. Baron ¹²³, D.A. Baron Moreno ¹⁰², A. Baroncelli ^{62a}, G. Barone ²⁹, A.J. Barr ¹²⁷, J.D. Barr ⁹⁷, F. Barreiro ¹⁰⁰, J. Barreiro Guimarães da Costa ^{14a}, U. Barron ¹⁵², M.G. Barros Teixeira ^{131a}, S. Barsov ³⁷, F. Bartels ^{63a}, R. Bartoldus ¹⁴⁴, A.E. Barton ⁹², P. Bartos ^{28a}, A. Basan ¹⁰¹, M. Baselga ⁴⁹, A. Bassalat ^{66,b}, M.J. Basso ^{157a}, R. Bate ¹⁶⁵, R.L. Bates ⁵⁹, S. Batlamous ¹⁰⁰, B. Batool ¹⁴², M. Battaglia ¹³⁷, D. Battulga ¹⁸, M. Baucé ^{75a,75b}, M. Bauer ³⁶, P. Bauer ²⁴, L.T. Bazzano Hurrell ³⁰, J.B. Beacham ⁵¹, T. Beau ¹²⁸, J.Y. Beaucamp ⁹¹, P.H. Beauchemin ¹⁵⁹, P. Bechtel ²⁴, H.P. Beck ^{19,o}, K. Becker ¹⁶⁸, A.J. Beddall ⁸², V.A. Bednyakov ³⁸, C.P. Bee ¹⁴⁶, L.J. Beemster ¹⁵, T.A. Beermann ³⁶, M. Begalli ^{83d}, M. Beger ²⁹, A. Behera ¹⁴⁶, J.K. Behr ⁴⁸, J.F. Beirer ³⁶, F. Beisiegel ²⁴, M. Belfkir ^{117b}, G. Bella ¹⁵², L. Bellagamba ^{23b}, A. Bellerive ³⁴, P. Bellos ²⁰, K. Beloborodov ³⁷, D. Bencheekroun ^{35a}, F. Bendebba ^{35a}, Y. Benhammou ¹⁵²,

K.C. Benkendorfer [ID61](#), L. Beresford [ID48](#), M. Beretta [ID53](#), E. Bergeaas Kuutmann [ID162](#), N. Berger [ID4](#),
 B. Bergmann [ID133](#), J. Beringer [ID17a](#), G. Bernardi [ID5](#), C. Bernius [ID144](#), F.U. Bernlochner [ID24](#),
 F. Bernon [ID36,103](#), A. Berrocal Guardia [ID13](#), T. Berry [ID96](#), P. Berta [ID134](#), A. Berthold [ID50](#), S. Bethke [ID111](#),
 A. Betti [ID75a,75b](#), A.J. Bevan [ID95](#), N.K. Bhalla [ID54](#), M. Bhamjee [ID33c](#), S. Bhatta [ID146](#),
 D.S. Bhattacharya [ID167](#), P. Bhattarai [ID144](#), K.D. Bhide [ID54](#), V.S. Bhopatkar [ID122](#), R.M. Bianchi [ID130](#),
 G. Bianco [ID23b,23a](#), O. Biebel [ID110](#), R. Bielski [ID124](#), M. Biglietti [ID77a](#), C.S. Billingsley [ID44](#), M. Bindi [ID55](#),
 A. Bingul [ID21b](#), C. Bini [ID75a,75b](#), A. Biondini [ID93](#), C.J. Birch-sykes [ID102](#), G.A. Bird [ID32](#), M. Birman [ID170](#),
 M. Biros [ID134](#), S. Biryukov [ID147](#), T. Bisanz [ID49](#), E. Bisceglie [ID43b,43a](#), J.P. Biswal [ID135](#), D. Biswas [ID142](#),
 I. Bloch [ID48](#), A. Blue [ID59](#), U. Blumenschein [ID95](#), J. Blumenthal [ID101](#), V.S. Bobrovnikov [ID37](#),
 M. Boehler [ID54](#), B. Boehm [ID167](#), D. Bogavac [ID36](#), A.G. Bogdanchikov [ID37](#), C. Bohm [ID47a](#),
 V. Boisvert [ID96](#), P. Bokan [ID36](#), T. Bold [ID86a](#), M. Bomben [ID5](#), M. Bona [ID95](#), M. Boonekamp [ID136](#),
 C.D. Booth [ID96](#), A.G. Borbély [ID59](#), I.S. Bordulev [ID37](#), H.M. Borecka-Bielska [ID109](#), G. Borissov [ID92](#),
 D. Bortoletto [ID127](#), D. Boscherini [ID23b](#), M. Bosman [ID13](#), J.D. Bossio Sola [ID36](#), K. Bouaouda [ID35a](#),
 N. Bouchhar [ID164](#), J. Boudreau [ID130](#), E.V. Bouhova-Thacker [ID92](#), D. Boumediene [ID40](#),
 R. Bouquet [ID57b,57a](#), A. Boveia [ID120](#), J. Boyd [ID36](#), D. Boye [ID29](#), I.R. Boyko [ID38](#), J. Bracinik [ID20](#),
 N. Brahimí [ID4](#), G. Brandt [ID172](#), O. Brandt [ID32](#), F. Braren [ID48](#), B. Brau [ID104](#), J.E. Brau [ID124](#),
 R. Brenner [ID170](#), L. Brenner [ID115](#), R. Brenner [ID162](#), S. Bressler [ID170](#), D. Britton [ID59](#), D. Britzger [ID111](#),
 I. Brock [ID24](#), G. Brooijmans [ID41](#), E. Brost [ID29](#), L.M. Brown [ID166](#), L.E. Bruce [ID61](#), T.L. Bruckler [ID127](#),
 P.A. Bruckman de Renstrom [ID87](#), B. Brüers [ID48](#), A. Bruni [ID23b](#), G. Bruni [ID23b](#), M. Bruschi [ID23b](#),
 N. Bruscinò [ID75a,75b](#), T. Buanes [ID16](#), Q. Buat [ID139](#), D. Buchin [ID111](#), A.G. Buckley [ID59](#), O. Bulekov [ID37](#),
 B.A. Bullard [ID144](#), S. Burdin [ID93](#), C.D. Burgard [ID49](#), A.M. Burger [ID36](#), B. Burghgrave [ID8](#),
 O. Burlayenko [ID54](#), J.T.P. Burr [ID32](#), C.D. Burton [ID11](#), J.C. Burzynski [ID143](#), E.L. Busch [ID41](#),
 V. Büscher [ID101](#), P.J. Bussey [ID59](#), J.M. Butler [ID25](#), C.M. Buttar [ID59](#), J.M. Butterworth [ID97](#),
 W. Buttinger [ID135](#), C.J. Buxo Vazquez [ID108](#), A.R. Buzykaev [ID37](#), S. Cabrera Urbán [ID164](#),
 L. Cadamuro [ID66](#), D. Caforio [ID58](#), H. Cai [ID130](#), Y. Cai [ID14a,14e](#), Y. Cai [ID14c](#), V.M.M. Cairo [ID36](#),
 O. Cakir [ID3a](#), N. Calace [ID36](#), P. Calafiura [ID17a](#), G. Calderini [ID128](#), P. Calfayan [ID68](#), G. Callea [ID59](#),
 L.P. Caloba [ID83b](#), D. Calvet [ID40](#), S. Calvet [ID40](#), M. Calvetti [ID74a,74b](#), R. Camacho Toro [ID128](#),
 S. Camarda [ID36](#), D. Camarero Munoz [ID26](#), P. Camarri [ID76a,76b](#), M.T. Camerlingo [ID72a,72b](#),
 D. Cameron [ID36](#), C. Camincher [ID166](#), M. Campanelli [ID97](#), A. Camplani [ID42](#), V. Canale [ID72a,72b](#),
 A.C. Canbay [ID3a](#), E. Canonero [ID96](#), J. Cantero [ID164](#), Y. Cao [ID163](#), F. Capocasa [ID26](#), M. Capua [ID43b,43a](#),
 A. Carbone [ID71a,71b](#), R. Cardarelli [ID76a](#), J.C.J. Cardenas [ID8](#), F. Cardillo [ID164](#), G. Carducci [ID43b,43a](#),
 T. Carli [ID36](#), G. Carlino [ID72a](#), J.I. Carlotto [ID13](#), B.T. Carlson [ID130,q](#), E.M. Carlson [ID166,157a](#),
 J. Carmignani [ID93](#), L. Carminati [ID71a,71b](#), A. Carnelli [ID136](#), M. Carnesale [ID75a,75b](#), S. Caron [ID114](#),
 E. Carquin [ID138f](#), S. Carrá [ID71a](#), G. Carratta [ID23b,23a](#), A.M. Carroll [ID124](#), T.M. Carter [ID52](#),
 M.P. Casado [ID13,i](#), M. Caspar [ID48](#), F.L. Castillo [ID4](#), L. Castillo Garcia [ID13](#), V. Castillo Gimenez [ID164](#),
 N.F. Castro [ID131a,131e](#), A. Catinaccio [ID36](#), J.R. Catmore [ID126](#), T. Cavaliere [ID4](#), V. Cavaliere [ID29](#),
 N. Cavalli [ID23b,23a](#), Y.C. Cekmecelioglu [ID48](#), E. Celebi [ID21a](#), S. Cella [ID36](#), F. Celli [ID127](#),
 M.S. Centonze [ID70a,70b](#), V. Cepaitis [ID56](#), K. Cerny [ID123](#), A.S. Cerqueira [ID83a](#), A. Cerri [ID147](#),
 L. Cerrito [ID76a,76b](#), F. Cerutti [ID17a](#), B. Cervato [ID142](#), A. Cervelli [ID23b](#), G. Cesarini [ID53](#), S.A. Cetin [ID82](#),
 D. Chakraborty [ID116](#), J. Chan [ID171](#), W.Y. Chan [ID154](#), J.D. Chapman [ID32](#), E. Chapon [ID136](#),
 B. Chargeishvili [ID150b](#), D.G. Charlton [ID20](#), M. Chatterjee [ID19](#), C. Chauhan [ID134](#), Y. Che [ID14c](#),
 S. Chekanov [ID6](#), S.V. Chekulaev [ID157a](#), G.A. Chelkov [ID38,a](#), A. Chen [ID107](#), B. Chen [ID152](#), B. Chen [ID166](#),
 H. Chen [ID14c](#), H. Chen [ID29](#), J. Chen [ID62c](#), J. Chen [ID143](#), M. Chen [ID127](#), S. Chen [ID154](#), S.J. Chen [ID14c](#),
 X. Chen [ID62c,136](#), X. Chen [ID14b,ad](#), Y. Chen [ID62a](#), C.L. Cheng [ID171](#), H.C. Cheng [ID64a](#), S. Cheong [ID144](#),
 A. Cheplakov [ID38](#), E. Cheremushkina [ID48](#), E. Cherepanova [ID115](#), R. Cherkaoui El Moursli [ID35e](#),
 E. Cheu [ID7](#), K. Cheung [ID65](#), L. Chevalier [ID136](#), V. Chiarella [ID53](#), G. Chiarelli [ID74a](#), N. Chiedde [ID103](#),
 G. Chiodini [ID70a](#), A.S. Chisholm [ID20](#), A. Chitan [ID27b](#), M. Chitishvili [ID164](#), M.V. Chizhov [ID38](#),

K. Choi ¹¹, Y. Chou ¹³⁹, E.Y.S. Chow ¹¹⁴, K.L. Chu ¹⁷⁰, M.C. Chu ^{64a}, X. Chu ^{14a,14e},
 J. Chudoba ¹³², J.J. Chwastowski ⁸⁷, D. Cieri ¹¹¹, K.M. Ciesla ^{86a}, V. Cindro ⁹⁴, A. Ciocio ^{17a},
 F. Cirotto ^{72a,72b}, Z.H. Citron ¹⁷⁰, M. Citterio ^{71a}, D.A. Ciubotaru ^{27b}, A. Clark ⁵⁶, P.J. Clark ⁵²,
 C. Clarry ¹⁵⁶, J.M. Clavijo Columbie ⁴⁸, S.E. Clawson ⁴⁸, C. Clement ^{47a,47b}, J. Clercx ⁴⁸,
 Y. Coadou ¹⁰³, M. Cobal ^{69a,69c}, A. Coccaro ^{57b}, R.F. Coelho Barrue ^{131a},
 R. Coelho Lopes De Sa ¹⁰⁴, S. Coelli ^{71a}, B. Cole ⁴¹, J. Collot ⁶⁰, P. Conde Muiño ^{131a,131g},
 M.P. Connell ^{33c}, S.H. Connell ^{33c}, E.I. Conroy ¹²⁷, F. Conventi ^{72a,af}, H.G. Cooke ²⁰,
 A.M. Cooper-Sarkar ¹²⁷, F.A. Corchia ^{23b,23a}, A. Cordeiro Oudot Choi ¹²⁸, L.D. Corpe ⁴⁰,
 M. Corradi ^{75a,75b}, F. Corriveau ^{105,w}, A. Cortes-Gonzalez ¹⁸, M.J. Costa ¹⁶⁴, F. Costanza ⁴,
 D. Costanzo ¹⁴⁰, B.M. Cote ¹²⁰, G. Cowan ⁹⁶, K. Cranmer ¹⁷¹, D. Cremonini ^{23b,23a},
 S. Crépe-Renaudin ⁶⁰, F. Crescioli ¹²⁸, M. Cristinziani ¹⁴², M. Cristoforetti ^{78a,78b}, V. Croft ¹¹⁵,
 J.E. Crosby ¹²², G. Crosetti ^{43b,43a}, A. Cueto ¹⁰⁰, H. Cui ^{14a,14e}, Z. Cui ⁷, W.R. Cunningham ⁵⁹,
 F. Curcio ¹⁶⁴, J.R. Curran ⁵², P. Czodrowski ³⁶, M.M. Czurylo ³⁶,
 M.J. Da Cunha Sargedas De Sousa ^{57b,57a}, J.V. Da Fonseca Pinto ^{83b}, C. Da Via ¹⁰²,
 W. Dabrowski ^{86a}, T. Dado ⁴⁹, S. Dahbi ¹⁴⁹, T. Dai ¹⁰⁷, D. Dal Santo ¹⁹, C. Dallapiccola ¹⁰⁴,
 M. Dam ⁴², G. D'amen ²⁹, V. D'Amico ¹¹⁰, J. Damp ¹⁰¹, J.R. Dandoy ³⁴, M. Danninger ¹⁴³,
 V. Dao ³⁶, G. Darbo ^{57b}, S.J. Das ^{29,ag}, F. Dattola ⁴⁸, S. D'Auria ^{71a,71b}, A. D'Avanzo ^{72a,72b},
 C. David ^{33a}, T. Davidek ¹³⁴, B. Davis-Purcell ³⁴, I. Dawson ⁹⁵, H.A. Day-hall ¹³³, K. De ⁸,
 R. De Asmundis ^{72a}, N. De Biase ⁴⁸, S. De Castro ^{23b,23a}, N. De Groot ¹¹⁴, P. de Jong ¹¹⁵,
 H. De la Torre ¹¹⁶, A. De Maria ^{14c}, A. De Salvo ^{75a}, U. De Sanctis ^{76a,76b}, F. De Santis ^{70a,70b},
 A. De Santo ¹⁴⁷, J.B. De Vivie De Regie ⁶⁰, D.V. Dedovich ³⁸, J. Degens ⁹³, A.M. Deiana ⁴⁴,
 F. Del Corso ^{23b,23a}, J. Del Peso ¹⁰⁰, F. Del Rio ^{63a}, L. Delagrangé ¹²⁸, F. Deliot ¹³⁶,
 C.M. Delitzsch ⁴⁹, M. Della Pietra ^{72a,72b}, D. Della Volpe ⁵⁶, A. Dell'Acqua ³⁶,
 L. Dell'Asta ^{71a,71b}, M. Delmastro ⁴, P.A. Delsart ⁶⁰, S. Demers ¹⁷³, M. Demichev ³⁸,
 S.P. Denisov ³⁷, L. D'Eramo ⁴⁰, D. Derendarz ⁸⁷, F. Derue ¹²⁸, P. Dervan ⁹³, K. Desch ²⁴,
 C. Deutsch ²⁴, F.A. Di Bello ^{57b,57a}, A. Di Ciaccio ^{76a,76b}, L. Di Ciaccio ⁴,
 A. Di Domenico ^{75a,75b}, C. Di Donato ^{72a,72b}, A. Di Girolamo ³⁶, G. Di Gregorio ³⁶,
 A. Di Luca ^{78a,78b}, B. Di Micco ^{77a,77b}, R. Di Nardo ^{77a,77b}, M. Diamantopoulou ³⁴, F.A. Dias ¹¹⁵,
 T. Dias Do Vale ¹⁴³, M.A. Diaz ^{138a,138b}, F.G. Diaz Capriles ²⁴, M. Didenko ¹⁶⁴, E.B. Diehl ¹⁰⁷,
 S. Díez Cornell ⁴⁸, C. Díez Pardos ¹⁴², C. Dimitriadi ^{162,24}, A. Dimitrievska ²⁰, J. Dingfelder ²⁴,
 I-M. Dinu ^{27b}, S.J. Dittmeier ^{63b}, F. Dittus ³⁶, M. Divisek ¹³⁴, F. Djama ¹⁰³, T. Djobava ^{150b},
 C. Doglioni ^{102,99}, A. Dohnalova ^{28a}, J. Dolejsi ¹³⁴, Z. Dolezal ¹³⁴, K.M. Dona ³⁹,
 M. Donadelli ^{83c}, B. Dong ¹⁰⁸, J. Donini ⁴⁰, A. D'Onofrio ^{72a,72b}, M. D'Onofrio ⁹³,
 J. Dopke ¹³⁵, A. Doria ^{72a}, N. Dos Santos Fernandes ^{131a}, P. Dougan ¹⁰², M.T. Dova ⁹¹,
 A.T. Doyle ⁵⁹, M.A. Dragnet ¹²⁷, E. Dreyer ¹⁷⁰, I. Drivas-koulouris ¹⁰, M. Drnevich ¹¹⁸,
 M. Drozdova ⁵⁶, D. Du ^{62a}, T.A. du Pree ¹¹⁵, F. Dubinin ³⁷, M. Dubovsky ^{28a}, E. Duchovni ¹⁷⁰,
 G. Duckeck ¹¹⁰, O.A. Ducu ^{27b}, D. Duda ⁵², A. Dudarev ³⁶, E.R. Duden ²⁶, M. D'uffizi ¹⁰²,
 L. Duflost ⁶⁶, M. Dührssen ³⁶, I. Duminica ^{27g}, A.E. Dumitriu ^{27b}, M. Dunford ^{63a}, S. Dungs ⁴⁹,
 K. Dunne ^{47a,47b}, A. Duperrin ¹⁰³, H. Duran Yildiz ^{3a}, M. Düren ⁵⁸, A. Durglishvili ^{150b},
 B.L. Dwyer ¹¹⁶, G.I. Dyckes ^{17a}, M. Dyndal ^{86a}, B.S. Dziedzic ⁸⁷, Z.O. Earnshaw ¹⁴⁷,
 G.H. Eberwein ¹²⁷, B. Eckerova ^{28a}, S. Eggebrecht ⁵⁵, E. Egidio Purcino De Souza ¹²⁸,
 L.F. Ehrke ⁵⁶, G. Eigen ¹⁶, K. Einsweiler ^{17a}, T. Ekelof ¹⁶², P.A. Ekman ⁹⁹, S. El Farkh ^{35b},
 Y. El Ghazali ^{35b}, H. El Jarrari ³⁶, A. El Moussaouy ¹⁰⁹, V. Ellajosyula ¹⁶², M. Ellert ¹⁶²,
 F. Ellinghaus ¹⁷², N. Ellis ³⁶, J. Elmsheuser ²⁹, M. Elsayy ^{117a}, M. Elsing ³⁶,
 D. Emelianov ¹³⁵, Y. Enari ¹⁵⁴, I. Ene ^{17a}, S. Epari ¹³, P.A. Erland ⁸⁷, M. Errenst ¹⁷²,
 M. Escalier ⁶⁶, C. Escobar ¹⁶⁴, E. Etzion ¹⁵², G. Evans ^{131a}, H. Evans ⁶⁸, L.S. Evans ⁹⁶,
 A. Ezhilov ³⁷, S. Ezzarqtouni ^{35a}, F. Fabbri ^{23b,23a}, L. Fabbri ^{23b,23a}, G. Facini ⁹⁷,

V. Fadeyev ¹³⁷, R.M. Fakhrutdinov ³⁷, D. Fakoudis ¹⁰¹, S. Falciano ^{75a},
L.F. Falda Ulhoa Coelho ³⁶, P.J. Falke ²⁴, F. Fallavollita ¹¹¹, J. Faltova ¹³⁴, C. Fan ¹⁶³,
Y. Fan ^{14a}, Y. Fang ^{14a,14e}, M. Fanti ^{71a,71b}, M. Faraj ^{69a,69b}, Z. Farazpay ⁹⁸, A. Farbin ⁸,
A. Farilla ^{77a}, T. Farooque ¹⁰⁸, S.M. Farrington ⁵², F. Fassi ^{35e}, D. Fassouliotis ⁹,
M. Faucci Giannelli ^{76a,76b}, W.J. Fawcett ³², L. Fayard ⁶⁶, P. Federic ¹³⁴, P. Federicova ¹³²,
O.L. Fedin ^{37,a}, M. Feickert ¹⁷¹, L. Feligioni ¹⁰³, D.E. Fellers ¹²⁴, C. Feng ^{62b}, M. Feng ^{14b},
Z. Feng ¹¹⁵, M.J. Fenton ¹⁶⁰, L. Ferencz ⁴⁸, R.A.M. Ferguson ⁹², S.I. Fernandez Luengo ^{138f},
P. Fernandez Martinez ¹³, M.J.V. Fernoux ¹⁰³, J. Ferrando ⁹², A. Ferrari ¹⁶², P. Ferrari ^{115,114},
R. Ferrari ^{73a}, D. Ferrere ⁵⁶, C. Ferretti ¹⁰⁷, F. Fiedler ¹⁰¹, P. Fiedler ¹³³, A. Filipčič ⁹⁴,
E.K. Filmer ¹, F. Filthaut ¹¹⁴, M.C.N. Fiolhais ^{131a,131c,c}, L. Fiorini ¹⁶⁴, W.C. Fisher ¹⁰⁸,
T. Fitschen ¹⁰², P.M. Fitzhugh ¹³⁶, I. Fleck ¹⁴², P. Fleischmann ¹⁰⁷, T. Flick ¹⁷², M. Flores ^{33d,ab},
L.R. Flores Castillo ^{64a}, L. Flores Sanz De Acedo ³⁶, F.M. Follega ^{78a,78b}, N. Fomin ¹⁶,
J.H. Foo ¹⁵⁶, A. Formica ¹³⁶, A.C. Forti ¹⁰², E. Fortin ³⁶, A.W. Fortman ^{17a}, M.G. Foti ^{17a},
L. Fountas ^{9j}, D. Fournier ⁶⁶, H. Fox ⁹², P. Francavilla ^{74a,74b}, S. Francescato ⁶¹,
S. Franchellucci ⁵⁶, M. Franchini ^{23b,23a}, S. Franchino ^{63a}, D. Francis ³⁶, L. Franco ¹¹⁴,
V. Franco Lima ³⁶, L. Franconi ⁴⁸, M. Franklin ⁶¹, G. Frattari ²⁶, W.S. Freund ^{83b}, Y.Y. Frid ¹⁵²,
J. Friend ⁵⁹, N. Fritzsche ⁵⁰, A. Froch ⁵⁴, D. Froidevaux ³⁶, J.A. Frost ¹²⁷, Y. Fu ^{62a},
S. Fuenzalida Garrido ^{138f}, M. Fujimoto ¹⁰³, K.Y. Fung ^{64a}, E. Furtado De Simas Filho ^{83e},
M. Furukawa ¹⁵⁴, J. Fuster ¹⁶⁴, A. Gabrielli ^{23b,23a}, A. Gabrielli ¹⁵⁶, P. Gadow ³⁶,
G. Gagliardi ^{57b,57a}, L.G. Gagnon ^{17a}, S. Gaid ¹⁶¹, S. Galantzan ¹⁵², E.J. Gallas ¹²⁷,
B.J. Gallop ¹³⁵, K.K. Gan ¹²⁰, S. Ganguly ¹⁵⁴, Y. Gao ⁵², F.M. Garay Walls ^{138a,138b}, B. Garcia ²⁹,
C. García ¹⁶⁴, A. Garcia Alonso ¹¹⁵, A.G. Garcia Caffaro ¹⁷³, J.E. García Navarro ¹⁶⁴,
M. Garcia-Sciveres ^{17a}, G.L. Gardner ¹²⁹, R.W. Gardner ³⁹, N. Garelli ¹⁵⁹, D. Garg ⁸⁰,
R.B. Garg ^{144,m}, J.M. Gargan ⁵², C.A. Garner ¹⁵⁶, C.M. Garvey ^{33a}, P. Gaspar ^{83b}, V.K. Gassmann ¹⁵⁹,
G. Gaudio ^{73a}, V. Gautam ¹³, P. Gauzzi ^{75a,75b}, I.L. Gavrilenko ³⁷, A. Gavrilyuk ³⁷, C. Gay ¹⁶⁵,
G. Gaycken ⁴⁸, E.N. Gazis ¹⁰, A.A. Geanta ^{27b}, C.M. Gee ¹³⁷, A. Gekow ¹²⁰, C. Gemme ^{57b},
M.H. Genest ⁶⁰, A.D. Gentry ¹¹³, S. George ⁹⁶, W.F. George ²⁰, T. Geralis ⁴⁶,
P. Gessinger-Befurt ³⁶, M.E. Geyik ¹⁷², M. Ghani ¹⁶⁸, K. Ghorbanian ⁹⁵, A. Ghosal ¹⁴²,
A. Ghosh ¹⁶⁰, A. Ghosh ⁷, B. Giacobbe ^{23b}, S. Giagu ^{75a,75b}, T. Giani ¹¹⁵, P. Giannetti ^{74a},
A. Giannini ^{62a}, S.M. Gibson ⁹⁶, M. Gignac ¹³⁷, D.T. Gil ^{86b}, A.K. Gilbert ^{86a}, B.J. Gilbert ⁴¹,
D. Gillberg ³⁴, G. Gilles ¹¹⁵, L. Ginabat ¹²⁸, D.M. Gingrich ^{2,ae}, M.P. Giordani ^{69a,69c},
P.F. Giraud ¹³⁶, G. Giugliarelli ^{69a,69c}, D. Giugni ^{71a}, F. Giuli ³⁶, I. Gkialas ^{9j}, L.K. Gladilin ³⁷,
C. Glasman ¹⁰⁰, G.R. Gledhill ¹²⁴, G. Glemža ⁴⁸, M. Glisic ¹²⁴, I. Gnesi ^{43b,f}, Y. Go ²⁹,
M. Goblirsch-Kolb ³⁶, B. Gocke ⁴⁹, D. Godin ¹⁰⁹, B. Gokturk ^{21a}, S. Goldfarb ¹⁰⁶, T. Golling ⁵⁶,
M.G.D. Gololo ^{33g}, D. Golubkov ³⁷, J.P. Gombas ¹⁰⁸, A. Gomes ^{131a,131b}, G. Gomes Da Silva ¹⁴²,
A.J. Gomez Delegido ¹⁶⁴, R. Gonçalo ^{131a,131c}, L. Gonella ²⁰, A. Gongadze ^{150c}, F. Gonnella ²⁰,
J.L. Gonski ¹⁴⁴, R.Y. González Andana ⁵², S. González de la Hoz ¹⁶⁴, R. Gonzalez Lopez ⁹³,
C. Gonzalez Renteria ^{17a}, M.V. Gonzalez Rodrigues ⁴⁸, R. Gonzalez Suarez ¹⁶²,
S. Gonzalez-Sevilla ⁵⁶, L. Goossens ³⁶, B. Gorini ³⁶, E. Gorini ^{70a,70b}, A. Gorišek ⁹⁴,
T.C. Gosart ¹²⁹, A.T. Goshaw ⁵¹, M.I. Gostkin ³⁸, S. Goswami ¹²², C.A. Gottardo ³⁶,
S.A. Gotz ¹¹⁰, M. Gouighri ^{35b}, V. Goumarre ⁴⁸, A.G. Goussiou ¹³⁹, N. Govender ^{33c},
I. Grabowska-Bold ^{86a}, K. Graham ³⁴, E. Gramstad ¹²⁶, S. Grancagnolo ^{70a,70b}, C.M. Grant ^{1,136},
P.M. Gravila ^{27f}, F.G. Gravili ^{70a,70b}, H.M. Gray ^{17a}, M. Greco ^{70a,70b}, C. Grefe ²⁴,
I.M. Gregor ⁴⁸, K.T. Greif ¹⁶⁰, P. Grenier ¹⁴⁴, S.G. Grewe ¹¹¹, A.A. Grillo ¹³⁷, K. Grimm ³¹,
S. Grinstein ^{13,s}, J.-F. Grivaz ⁶⁶, E. Gross ¹⁷⁰, J. Grosse-Knetter ⁵⁵, J.C. Grundy ¹²⁷,
L. Guan ¹⁰⁷, C. Gubbels ¹⁶⁵, J.G.R. Guerrero Rojas ¹⁶⁴, G. Guerrieri ^{69a,69c}, F. Guescini ¹¹¹,
R. Gugel ¹⁰¹, J.A.M. Guhit ¹⁰⁷, A. Guida ¹⁸, E. Guilloton ¹⁶⁸, S. Guindon ³⁶, F. Guo ^{14a,14e},

J. Guo ^{62c}, L. Guo ⁴⁸, Y. Guo ¹⁰⁷, R. Gupta ⁴⁸, R. Gupta ¹³⁰, S. Gurbuz ²⁴, S.S. Gurdasani ⁵⁴,
 G. Gustavino ³⁶, M. Guth ⁵⁶, P. Gutierrez ¹²¹, L.F. Gutierrez Zagazeta ¹²⁹, M. Gutsche ⁵⁰,
 C. Gutschow ⁹⁷, C. Gwenlan ¹²⁷, C.B. Gwilliam ⁹³, E.S. Haaland ¹²⁶, A. Haas ¹¹⁸,
 M. Habedank ⁴⁸, C. Haber ^{17a}, H.K. Hadavand ⁸, A. Hadeef ⁵⁰, S. Hadzic ¹¹¹, A.I. Hagan ⁹²,
 J.J. Hahn ¹⁴², E.H. Haines ⁹⁷, M. Haleem ¹⁶⁷, J. Haley ¹²², J.J. Hall ¹⁴⁰, G.D. Hallewell ¹⁰³,
 L. Halser ¹⁹, K. Hamano ¹⁶⁶, M. Hamer ²⁴, G.N. Hamity ⁵², E.J. Hampshire ⁹⁶, J. Han ^{62b},
 K. Han ^{62a}, L. Han ^{14c}, L. Han ^{62a}, S. Han ^{17a}, Y.F. Han ¹⁵⁶, K. Hanagaki ⁸⁴, M. Hance ¹³⁷,
 D.A. Hangal ⁴¹, H. Hanif ¹⁴³, M.D. Hank ¹²⁹, J.B. Hansen ⁴², P.H. Hansen ⁴², K. Hara ¹⁵⁸,
 D. Harada ⁵⁶, T. Harenberg ¹⁷², S. Harkusha ³⁷, M.L. Harris ¹⁰⁴, Y.T. Harris ¹²⁷, J. Harrison ¹³,
 N.M. Harrison ¹²⁰, P.F. Harrison ¹⁶⁸, N.M. Hartman ¹¹¹, N.M. Hartmann ¹¹⁰, R.Z. Hasan ^{96,135},
 Y. Hasegawa ¹⁴¹, S. Hassan ¹⁶, R. Hauser ¹⁰⁸, C.M. Hawkes ²⁰, R.J. Hawkings ³⁶,
 Y. Hayashi ¹⁵⁴, S. Hayashida ¹¹², D. Hayden ¹⁰⁸, C. Hayes ¹⁰⁷, R.L. Hayes ¹¹⁵, C.P. Hays ¹²⁷,
 J.M. Hays ⁹⁵, H.S. Hayward ⁹³, F. He ^{62a}, M. He ^{14a,14e}, Y. He ¹⁵⁵, Y. He ⁴⁸, Y. He ⁹⁷,
 N.B. Heatley ⁹⁵, V. Hedberg ⁹⁹, A.L. Heggelund ¹²⁶, N.D. Hehir ^{95,*}, C. Heidegger ⁵⁴,
 K.K. Heidegger ⁵⁴, W.D. Heidorn ⁸¹, J. Heilman ³⁴, S. Heim ⁴⁸, T. Heim ^{17a}, J.G. Heinlein ¹²⁹,
 J.J. Heinrich ¹²⁴, L. Heinrich ^{111,ac}, J. Hejbal ¹³², A. Held ¹⁷¹, S. Hellesund ¹⁶, C.M. Helling ¹⁶⁵,
 S. Hellman ^{47a,47b}, R.C.W. Henderson ⁹², L. Henkelmann ³², A.M. Henriques Correia ³⁶, H. Herde ⁹⁹,
 Y. Hernández Jiménez ¹⁴⁶, L.M. Herrmann ²⁴, T. Herrmann ⁵⁰, G. Herten ⁵⁴, R. Hertenberger ¹¹⁰,
 L. Hervas ³⁶, M.E. Hesping ¹⁰¹, N.P. Hessey ^{157a}, M. Hidaoui ^{35b}, E. Hill ¹⁵⁶, S.J. Hillier ²⁰,
 J.R. Hinds ¹⁰⁸, F. Hinterkeuser ²⁴, M. Hirose ¹²⁵, S. Hirose ¹⁵⁸, D. Hirschbuehl ¹⁷²,
 T.G. Hitchings ¹⁰², B. Hiti ⁹⁴, J. Hobbs ¹⁴⁶, R. Hobincu ^{27e}, N. Hod ¹⁷⁰, M.C. Hodgkinson ¹⁴⁰,
 B.H. Hodgkinson ¹²⁷, A. Hoecker ³⁶, D.D. Hofer ¹⁰⁷, J. Hofer ⁴⁸, T. Holm ²⁴, M. Holzbock ¹¹¹,
 L.B.A.H. Hommels ³², B.P. Honan ¹⁰², J. Hong ^{62c}, T.M. Hong ¹³⁰, B.H. Hooberman ¹⁶³,
 W.H. Hopkins ⁶, Y. Horii ¹¹², S. Hou ¹⁴⁹, A.S. Howard ⁹⁴, J. Howarth ⁵⁹, J. Hoya ⁶,
 M. Hrabovsky ¹²³, A. Hrynevich ⁴⁸, T. Hryn'ova ⁴, P.J. Hsu ⁶⁵, S.-C. Hsu ¹³⁹, T. Hsu ⁶⁶,
 M. Hu ^{17a}, Q. Hu ^{62a}, S. Huang ^{64b}, X. Huang ^{14a,14e}, Y. Huang ¹⁴⁰, Y. Huang ¹⁰¹,
 Y. Huang ^{14a}, Z. Huang ¹⁰², Z. Hubacek ¹³³, M. Huebner ²⁴, F. Hugging ²⁴, T.B. Huffman ¹²⁷,
 C.A. Hugli ⁴⁸, M. Huhtinen ³⁶, S.K. Huijberts ¹⁶, R. Hulsken ¹⁰⁵, N. Huseynov ¹², J. Huston ¹⁰⁸,
 J. Huth ⁶¹, R. Hyneman ¹⁴⁴, G. Iacobucci ⁵⁶, G. Iakovidis ²⁹, I. Ibragimov ¹⁴²,
 L. Iconomidou-Fayard ⁶⁶, J.P. Iddon ³⁶, P. Iengo ^{72a,72b}, R. Iguchi ¹⁵⁴, T. Iizawa ¹²⁷,
 Y. Ikegami ⁸⁴, N. Ilic ¹⁵⁶, H. Imam ^{35a}, M. Ince Lezki ⁵⁶, T. Ingebretsen Carlson ^{47a,47b},
 G. Introzzi ^{73a,73b}, M. Iodice ^{77a}, V. Ippolito ^{75a,75b}, R.K. Irwin ⁹³, M. Ishino ¹⁵⁴, W. Islam ¹⁷¹,
 C. Issever ^{18,48}, S. Istin ^{21a,ai}, H. Ito ¹⁶⁹, R. Iuppa ^{78a,78b}, A. Ivina ¹⁷⁰, J.M. Izen ⁴⁵,
 V. Izzo ^{72a}, P. Jacka ^{132,133}, P. Jackson ¹, B.P. Jaeger ¹⁴³, C.S. Jagfeld ¹¹⁰, G. Jain ^{157a},
 P. Jain ⁵⁴, K. Jakobs ⁵⁴, T. Jakoubek ¹⁷⁰, J. Jamieson ⁵⁹, K.W. Janas ^{86a}, M. Javurkova ¹⁰⁴,
 L. Jeanty ¹²⁴, J. Jejelava ^{150a,z}, P. Jenni ^{54,g}, C.E. Jessiman ³⁴, C. Jia ^{62b}, J. Jia ¹⁴⁶, X. Jia ⁶¹,
 X. Jia ^{14a,14e}, Z. Jia ^{14c}, C. Jiang ⁵², S. Jiggins ⁴⁸, J. Jimenez Pena ¹³, S. Jin ^{14c}, A. Jinaru ^{27b},
 O. Jinnouchi ¹⁵⁵, P. Johansson ¹⁴⁰, K.A. Johns ⁷, J.W. Johnson ¹³⁷, D.M. Jones ¹⁴⁷, E. Jones ⁴⁸,
 P. Jones ³², R.W.L. Jones ⁹², T.J. Jones ⁹³, H.L. Joos ^{55,36}, R. Joshi ¹²⁰, J. Jovicevic ¹⁵,
 X. Ju ^{17a}, J.J. Junggeburth ¹⁰⁴, T. Junkermann ^{63a}, A. Juste Rozas ^{13,s}, M.K. Juzek ⁸⁷,
 S. Kabana ^{138e}, A. Kaczmarzka ⁸⁷, M. Kado ¹¹¹, H. Kagan ¹²⁰, M. Kagan ¹⁴⁴, A. Kahn ⁴¹,
 A. Kahn ¹²⁹, C. Kahra ¹⁰¹, T. Kaji ¹⁵⁴, E. Kajomovitz ¹⁵¹, N. Kakati ¹⁷⁰, I. Kalaitzidou ⁵⁴,
 C.W. Kalderon ²⁹, N.J. Kang ¹³⁷, D. Kar ^{33g}, K. Karava ¹²⁷, M.J. Kareem ^{157b}, E. Karentzos ⁵⁴,
 I. Karkanas ¹⁵³, O. Karkout ¹¹⁵, S.N. Karpov ³⁸, Z.M. Karpova ³⁸, V. Kartvelishvili ⁹²,
 A.N. Karyukhin ³⁷, E. Kasimi ¹⁵³, J. Katzy ⁴⁸, S. Kaur ³⁴, K. Kawade ¹⁴¹, M.P. Kawale ¹²¹,
 C. Kawamoto ⁸⁸, T. Kawamoto ^{62a}, E.F. Kay ³⁶, F.I. Kaya ¹⁵⁹, S. Kazakos ¹⁰⁸, V.F. Kazanin ³⁷,
 Y. Ke ¹⁴⁶, J.M. Keaveney ^{33a}, R. Keeler ¹⁶⁶, G.V. Kehris ⁶¹, J.S. Keller ³⁴, A.S. Kelly ⁹⁷,

J.J. Kempster ¹⁴⁷, P.D. Kennedy ¹⁰¹, O. Kepka ¹³², B.P. Kerridge ¹³⁵, S. Kersten ¹⁷²,
B.P. Kerševan ⁹⁴, L. Keszezhova ^{28a}, S. Ketabchi Haghighat ¹⁵⁶, R.A. Khan ¹³⁰, A. Khanov ¹²²,
A.G. Kharlamov ³⁷, T. Kharlamova ³⁷, E.E. Khoda ¹³⁹, M. Kholodenko ³⁷, T.J. Khoo ¹⁸,
G. Khoriauli ¹⁶⁷, J. Khubua ^{150b}, Y.A.R. Khwaira ⁶⁶, B. Kibirige^{33g}, A. Kilgallon ¹²⁴,
D.W. Kim ^{47a,47b}, Y.K. Kim ³⁹, N. Kimura ⁹⁷, M.K. Kingston ⁵⁵, A. Kirchhoff ⁵⁵, C. Kirfel ²⁴,
F. Kirfel ²⁴, J. Kirk ¹³⁵, A.E. Kiryunin ¹¹¹, C. Kitsaki ¹⁰, O. Kivernyk ²⁴, M. Klassen ¹⁵⁹,
C. Klein ³⁴, L. Klein ¹⁶⁷, M.H. Klein ⁴⁴, S.B. Klein ⁵⁶, U. Klein ⁹³, P. Klimek ³⁶,
A. Klimentov ²⁹, T. Klioutchnikova ³⁶, P. Kluit ¹¹⁵, S. Kluth ¹¹¹, E. Kneringer ⁷⁹,
T.M. Knight ¹⁵⁶, A. Knue ⁴⁹, R. Kobayashi ⁸⁸, D. Kobylanski ¹⁷⁰, S.F. Koch ¹²⁷,
M. Kocian ¹⁴⁴, P. Kodyš ¹³⁴, D.M. Koeck ¹²⁴, P.T. Koenig ²⁴, T. Koffas ³⁴, O. Kolay ⁵⁰,
I. Koletsou ⁴, T. Komarek ¹²³, K. Köneke ⁵⁴, A.X.Y. Kong ¹, T. Kono ¹¹⁹, N. Konstantinidis ⁹⁷,
P. Kontaxakis ⁵⁶, B. Konya ⁹⁹, R. Kopeliansky ⁴¹, S. Koperny ^{86a}, K. Korcyl ⁸⁷, K. Kordas ^{153,e},
A. Korn ⁹⁷, S. Korn ⁵⁵, I. Korolkov ¹³, N. Korotkova ³⁷, B. Kortman ¹¹⁵, O. Kortner ¹¹¹,
S. Kortner ¹¹¹, W.H. Kostecka ¹¹⁶, V.V. Kostyukhin ¹⁴², A. Kotsokechagia ¹³⁶, A. Kotwal ⁵¹,
A. Koulouris ³⁶, A. Kourkoumeli-Charalampidi ^{73a,73b}, C. Kourkoumelis ⁹, E. Kourlitis ^{111,ac},
O. Kovanda ¹²⁴, R. Kowalewski ¹⁶⁶, W. Kozanecki ¹³⁶, A.S. Kozhin ³⁷, V.A. Kramarenko ³⁷,
G. Kramberger ⁹⁴, P. Kramer ¹⁰¹, M.W. Krasny ¹²⁸, A. Krasznahorkay ³⁶, J.W. Kraus ¹⁷²,
J.A. Kremer ⁴⁸, T. Kresse ⁵⁰, J. Kretschmar ⁹³, K. Kreul ¹⁸, P. Krieger ¹⁵⁶,
S. Krishnamurthy ¹⁰⁴, M. Krivos ¹³⁴, K. Krizka ²⁰, K. Kroeninger ⁴⁹, H. Kroha ¹¹¹, J. Kroll ¹³²,
J. Kroll ¹²⁹, K.S. Krowpman ¹⁰⁸, U. Kruchonak ³⁸, H. Krüger ²⁴, N. Krumnack⁸¹, M.C. Kruse ⁵¹,
O. Kuchinskaia ³⁷, S. Kuday ^{3a}, S. Kuehn ³⁶, R. Kuesters ⁵⁴, T. Kuhl ⁴⁸, V. Kukhtin ³⁸,
Y. Kulchitsky ^{37,a}, S. Kuleshov ^{138d,138b}, M. Kumar ^{33g}, N. Kumari ⁴⁸, P. Kumari ^{157b},
A. Kupco ¹³², T. Kupfer⁴⁹, A. Kupich ³⁷, O. Kuprash ⁵⁴, H. Kurashige ⁸⁵, L.L. Kurchaninov ^{157a},
O. Kurdysh ⁶⁶, Y.A. Kurochkin ³⁷, A. Kurova ³⁷, M. Kuze ¹⁵⁵, A.K. Kvam ¹⁰⁴, J. Kvita ¹²³,
T. Kwan ¹⁰⁵, N.G. Kyriacou ¹⁰⁷, L.A.O. Laatu ¹⁰³, C. Lacasta ¹⁶⁴, F. Lacava ^{75a,75b},
H. Lacker ¹⁸, D. Lacour ¹²⁸, N.N. Lad ⁹⁷, E. Ladygin ³⁸, A. Lafarge ⁴⁰, B. Laforge ¹²⁸,
T. Lagouri ¹⁷³, F.Z. Lahbabi ^{35a}, S. Lai ⁵⁵, I.K. Lakomiec ^{86a}, J.E. Lambert ¹⁶⁶, S. Lammers ⁶⁸,
W. Lampl ⁷, C. Lampoudis ^{153,e}, G. Lamprinoudis¹⁰¹, A.N. Lancaster ¹¹⁶, E. Lançon ²⁹,
U. Landgraf ⁵⁴, M.P.J. Landon ⁹⁵, V.S. Lang ⁵⁴, O.K.B. Langrekken ¹²⁶, A.J. Lankford ¹⁶⁰,
F. Lanni ³⁶, K. Lantzsch ²⁴, A. Lanza ^{73a}, A. Lapertosa ^{57b,57a}, J.F. Laporte ¹³⁶, T. Lari ^{71a},
F. Lasagni Manghi ^{23b}, M. Lassnig ³⁶, V. Latonova ¹³², A. Laudrain ¹⁰¹, A. Laurier ¹⁵¹,
S.D. Lawlor ¹⁴⁰, Z. Lawrence ¹⁰², R. Lazaridou¹⁶⁸, M. Lazzaroni ^{71a,71b}, B. Le¹⁰²,
E.M. Le Boulicaut ⁵¹, L.T. Le Pottier ^{17a}, B. Leban ^{23b,23a}, A. Lebedev ⁸¹, M. LeBlanc ¹⁰²,
F. Ledroit-Guillon ⁶⁰, S.C. Lee ¹⁴⁹, S. Lee ^{47a,47b}, T.F. Lee ⁹³, L.L. Leeuw ^{33c}, H.P. Lefebvre ⁹⁶,
M. Lefebvre ¹⁶⁶, C. Leggett ^{17a}, G. Lehmann Miotto ³⁶, M. Leigh ⁵⁶, W.A. Leight ¹⁰⁴,
W. Leinonen ¹¹⁴, A. Leisos ^{153,r}, M.A.L. Leite ^{83c}, C.E. Leitgeb ¹⁸, R. Leitner ¹³⁴,
K.J.C. Leney ⁴⁴, T. Lenz ²⁴, S. Leone ^{74a}, C. Leonidopoulos ⁵², A. Leopold ¹⁴⁵, C. Leroy ¹⁰⁹,
R. Les ¹⁰⁸, C.G. Lester ³², M. Levchenko ³⁷, J. Levêque ⁴, L.J. Levinson ¹⁷⁰, G. Levrimi^{23b,23a},
M.P. Lewicki ⁸⁷, C. Lewis ¹³⁹, D.J. Lewis ⁴, A. Li ⁵, B. Li ^{62b}, C. Li^{62a}, C-Q. Li ¹¹¹, H. Li ^{62a},
H. Li ^{62b}, H. Li ^{14c}, H. Li ^{14b}, H. Li ^{62b}, J. Li ^{62c}, K. Li ¹³⁹, L. Li ^{62c}, M. Li ^{14a,14e},
Q.Y. Li ^{62a}, S. Li ^{14a,14e}, S. Li ^{62d,62c,d}, T. Li ⁵, X. Li ¹⁰⁵, Z. Li ¹²⁷, Z. Li ¹⁰⁵, Z. Li ^{14a,14e},
S. Liang^{14a,14e}, Z. Liang ^{14a}, M. Liberatore ¹³⁶, B. Liberti ^{76a}, K. Lie ^{64c}, J. Lieber Marin ^{83e},
H. Lien ⁶⁸, K. Lin ¹⁰⁸, R.E. Lindley ⁷, J.H. Lindon ², E. Lipeles ¹²⁹, A. Lipniacka ¹⁶,
A. Lister ¹⁶⁵, J.D. Little ⁴, B. Liu ^{14a}, B.X. Liu ¹⁴³, D. Liu ^{62d,62c}, E.H.L. Liu ²⁰, J.B. Liu ^{62a},
J.K.K. Liu ³², K. Liu ^{62d}, K. Liu ^{62d,62c}, M. Liu ^{62a}, M.Y. Liu ^{62a}, P. Liu ^{14a}, Q. Liu ^{62d,139,62c},
X. Liu ^{62a}, X. Liu ^{62b}, Y. Liu ^{14d,14e}, Y.L. Liu ^{62b}, Y.W. Liu ^{62a}, J. Llorente Merino ¹⁴³,
S.L. Lloyd ⁹⁵, E.M. Lobodzinska ⁴⁸, P. Loch ⁷, T. Lohse ¹⁸, K. Lohwasser ¹⁴⁰, E. Loiacono ⁴⁸,











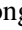




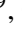


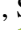








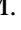





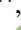





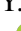


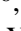
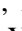


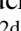
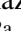

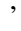




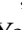

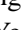
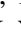










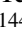

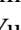
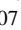
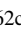

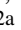

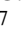



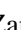






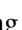




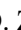



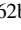

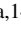

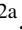
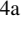

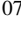



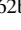
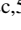

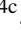


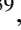


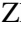
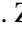

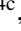
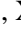

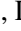
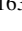
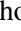
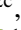
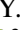


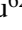
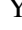
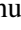


















M. Lokajicek [id](#)^{132,*}, J.D. Lomas [id](#)²⁰, J.D. Long [id](#)¹⁶³, I. Longarini [id](#)¹⁶⁰, L. Longo [id](#)^{70a,70b},
R. Longo [id](#)¹⁶³, I. Lopez Paz [id](#)⁶⁷, A. Lopez Solis [id](#)⁴⁸, N. Lorenzo Martinez [id](#)⁴, A.M. Lory [id](#)¹¹⁰,
G. Löschcke Centeno [id](#)¹⁴⁷, O. Loseva [id](#)³⁷, X. Lou [id](#)^{47a,47b}, X. Lou [id](#)^{14a,14e}, A. Lounis [id](#)⁶⁶,
P.A. Love [id](#)⁹², G. Lu [id](#)^{14a,14e}, M. Lu [id](#)⁶⁶, S. Lu [id](#)¹²⁹, Y.J. Lu [id](#)⁶⁵, H.J. Lubatti [id](#)¹³⁹, C. Luci [id](#)^{75a,75b},
F.L. Lucio Alves [id](#)^{14c}, F. Luehring [id](#)⁶⁸, I. Luise [id](#)¹⁴⁶, O. Lukianchuk [id](#)⁶⁶, O. Lundberg [id](#)¹⁴⁵,
B. Lund-Jensen [id](#)¹⁴⁵, N.A. Luongo [id](#)⁶, M.S. Lutz [id](#)³⁶, A.B. Lux [id](#)²⁵, D. Lynn [id](#)²⁹, R. Lysak [id](#)¹³²,
E. Lytken [id](#)⁹⁹, V. Lyubushkin [id](#)³⁸, T. Lyubushkina [id](#)³⁸, M.M. Lyukova [id](#)¹⁴⁶, M.Firdaus M. Soberi [id](#)⁵²,
H. Ma [id](#)²⁹, K. Ma [id](#)^{62a}, L.L. Ma [id](#)^{62b}, W. Ma [id](#)^{62a}, Y. Ma [id](#)¹²², D.M. Mac Donell [id](#)¹⁶⁶,
G. Maccarrone [id](#)⁵³, J.C. MacDonald [id](#)¹⁰¹, P.C. Machado De Abreu Farias [id](#)^{83e}, R. Madar [id](#)⁴⁰,
T. Madula [id](#)⁹⁷, J. Maeda [id](#)⁸⁵, T. Maeno [id](#)²⁹, H. Maguire [id](#)¹⁴⁰, V. Maiboroda [id](#)¹³⁶,
A. Maio [id](#)^{131a,131b,131d}, K. Maj [id](#)^{86a}, O. Majersky [id](#)⁴⁸, S. Majewski [id](#)¹²⁴, N. Makovec [id](#)⁶⁶,
V. Maksimovic [id](#)¹⁵, B. Malaescu [id](#)¹²⁸, Pa. Malecki [id](#)⁸⁷, V.P. Maleev [id](#)³⁷, F. Malek [id](#)^{60,n}, M. Mali [id](#)⁹⁴,
D. Malito [id](#)⁹⁶, U. Mallik [id](#)⁸⁰, S. Maltezos [id](#)¹⁰, S. Malyukov [id](#)³⁸, J. Mamuzic [id](#)¹³, G. Mancini [id](#)⁵³,
M.N. Mancini [id](#)²⁶, G. Manco [id](#)^{73a,73b}, J.P. Mandalia [id](#)⁹⁵, I. Mandić [id](#)⁹⁴,
L. Manhaes de Andrade Filho [id](#)^{83a}, I.M. Maniatis [id](#)¹⁷⁰, J. Manjarres Ramos [id](#)⁹⁰, D.C. Mankad [id](#)¹⁷⁰,
A. Mann [id](#)¹¹⁰, S. Manzoni [id](#)³⁶, L. Mao [id](#)^{62c}, X. Mapekula [id](#)^{33c}, A. Marantis [id](#)^{153,r}, G. Marchiori [id](#)⁵,
M. Marcisovsky [id](#)¹³², C. Marcon [id](#)^{71a}, M. Marinescu [id](#)²⁰, S. Marium [id](#)⁴⁸, M. Marjanovic [id](#)¹²¹,
A. Markhoos [id](#)⁵⁴, M. Markovitch [id](#)⁶⁶, E.J. Marshall [id](#)⁹², Z. Marshall [id](#)^{17a}, S. Marti-Garcia [id](#)¹⁶⁴,
T.A. Martin [id](#)¹⁶⁸, V.J. Martin [id](#)⁵², B. Martin dit Latour [id](#)¹⁶, L. Martinelli [id](#)^{75a,75b}, M. Martinez [id](#)^{13,s},
P. Martinez Agullo [id](#)¹⁶⁴, V.I. Martinez Outschoorn [id](#)¹⁰⁴, P. Martinez Suarez [id](#)¹³, S. Martin-Haugh [id](#)¹³⁵,
G. Martinovicova [id](#)¹³⁴, V.S. Martoiu [id](#)^{27b}, A.C. Martyniuk [id](#)⁹⁷, A. Marzin [id](#)³⁶, D. Mascione [id](#)^{78a,78b},
L. Masetti [id](#)¹⁰¹, T. Mashimo [id](#)¹⁵⁴, J. Masik [id](#)¹⁰², A.L. Maslennikov [id](#)³⁷, P. Massarotti [id](#)^{72a,72b},
P. Mastrandrea [id](#)^{74a,74b}, A. Mastroberardino [id](#)^{43b,43a}, T. Masubuchi [id](#)¹⁵⁴, T. Mathisen [id](#)¹⁶²,
J. Matousek [id](#)¹³⁴, N. Matsuzawa [id](#)¹⁵⁴, J. Maurer [id](#)^{27b}, A.J. Maury [id](#)⁶⁶, B. Maček [id](#)⁹⁴, D.A. Maximov [id](#)³⁷,
A.E. May [id](#)¹⁰², R. Mazini [id](#)¹⁴⁹, I. Maznas [id](#)¹¹⁶, M. Mazza [id](#)¹⁰⁸, S.M. Mazza [id](#)¹³⁷, E. Mazzeo [id](#)^{71a,71b},
C. Mc Ginn [id](#)²⁹, J.P. Mc Gowan [id](#)¹⁶⁶, S.P. Mc Kee [id](#)¹⁰⁷, C.C. McCracken [id](#)¹⁶⁵, E.F. McDonald [id](#)¹⁰⁶,
A.E. McDougall [id](#)¹¹⁵, J.A. Mcfayden [id](#)¹⁴⁷, R.P. McGovern [id](#)¹²⁹, G. Mchedlidze [id](#)^{150b},
R.P. Mckenzie [id](#)^{33g}, T.C. Mclachlan [id](#)⁴⁸, D.J. Mclaughlin [id](#)⁹⁷, S.J. McMahon [id](#)¹³⁵,
C.M. Mcpartland [id](#)⁹³, R.A. McPherson [id](#)^{166,w}, S. Mehlhase [id](#)¹¹⁰, A. Mehta [id](#)⁹³, D. Melini [id](#)¹⁶⁴,
B.R. Mellado Garcia [id](#)^{33g}, A.H. Melo [id](#)⁵⁵, F. Meloni [id](#)⁴⁸, A.M. Mendes Jacques Da Costa [id](#)¹⁰²,
H.Y. Meng [id](#)¹⁵⁶, L. Meng [id](#)⁹², S. Menke [id](#)¹¹¹, M. Mentink [id](#)³⁶, E. Meoni [id](#)^{43b,43a}, G. Mercado [id](#)¹¹⁶,
C. Merlassino [id](#)^{69a,69c}, L. Merola [id](#)^{72a,72b}, C. Meroni [id](#)^{71a,71b}, J. Metcalfe [id](#)⁶, A.S. Mete [id](#)⁶,
C. Meyer [id](#)⁶⁸, J-P. Meyer [id](#)¹³⁶, R.P. Middleton [id](#)¹³⁵, L. Mijović [id](#)⁵², G. Mikenberg [id](#)¹⁷⁰,
M. Mikestikova [id](#)¹³², M. Mikuž [id](#)⁹⁴, H. Mildner [id](#)¹⁰¹, A. Milic [id](#)³⁶, D.W. Miller [id](#)³⁹, E.H. Miller [id](#)¹⁴⁴,
L.S. Miller [id](#)³⁴, A. Milov [id](#)¹⁷⁰, D.A. Milstead [id](#)^{47a,47b}, T. Min [id](#)^{14c}, A.A. Minaenko [id](#)³⁷,
I.A. Minashvili [id](#)^{150b}, L. Mince [id](#)⁵⁹, A.I. Mincer [id](#)¹¹⁸, B. Mindur [id](#)^{86a}, M. Mineev [id](#)³⁸, Y. Mino [id](#)⁸⁸,
L.M. Mir [id](#)¹³, M. Miralles Lopez [id](#)⁵⁹, M. Mironova [id](#)^{17a}, A. Mishima [id](#)¹⁵⁴, M.C. Missio [id](#)¹¹⁴,
A. Mitra [id](#)¹⁶⁸, V.A. Mitsou [id](#)¹⁶⁴, Y. Mitsumori [id](#)¹¹², O. Miu [id](#)¹⁵⁶, P.S. Miyagawa [id](#)⁹⁵,
T. Mkrtychyan [id](#)^{63a}, M. Mlinarevic [id](#)⁹⁷, T. Mlinarevic [id](#)⁹⁷, M. Mlynarikova [id](#)³⁶, S. Mobius [id](#)¹⁹,
P. Mogg [id](#)¹¹⁰, M.H. Mohamed Farook [id](#)¹¹³, A.F. Mohammed [id](#)^{14a,14e}, S. Mohapatra [id](#)⁴¹,
G. Mokgatitswane [id](#)^{33g}, L. Moleri [id](#)¹⁷⁰, B. Mondal [id](#)¹⁴², S. Mondal [id](#)¹³³, K. Mönig [id](#)⁴⁸,
E. Monnier [id](#)¹⁰³, L. Monsonis Romero [id](#)¹⁶⁴, J. Montejo Berlingen [id](#)¹³, M. Montella [id](#)¹²⁰,
F. Montekali [id](#)^{77a,77b}, F. Monticelli [id](#)⁹¹, S. Monzani [id](#)^{69a,69c}, N. Morange [id](#)⁶⁶,
A.L. Moreira De Carvalho [id](#)⁴⁸, M. Moreno Llácer [id](#)¹⁶⁴, C. Moreno Martinez [id](#)⁵⁶, P. Morettini [id](#)^{57b},
S. Morgenstern [id](#)³⁶, M. Morii [id](#)⁶¹, M. Morinaga [id](#)¹⁵⁴, F. Morodei [id](#)^{75a,75b}, L. Morvaj [id](#)³⁶,
P. Moschovakos [id](#)³⁶, B. Moser [id](#)³⁶, M. Mosidze [id](#)^{150b}, T. Moskalets [id](#)⁵⁴, P. Moskvitina [id](#)¹¹⁴,
J. Moss [id](#)^{31,k}, P. Moszkowicz [id](#)^{86a}, A. Moussa [id](#)^{35d}, E.J.W. Moyse [id](#)¹⁰⁴, O. Mtintsilana [id](#)^{33g},

S. Muanza ¹⁰³, J. Mueller ¹³⁰, D. Muenstermann ⁹², R. Müller ¹⁹, G.A. Mullier ¹⁶²,
 A.J. Mullin ³², J.J. Mullin ¹²⁹, D.P. Mungo ¹⁵⁶, D. Munoz Perez ¹⁶⁴, F.J. Munoz Sanchez ¹⁰²,
 M. Murin ¹⁰², W.J. Murray ^{168,135}, M. Muškinja ⁹⁴, C. Mwewa ²⁹, A.G. Myagkov ^{37,a},
 A.J. Myers ⁸, G. Myers ¹⁰⁷, M. Myska ¹³³, B.P. Nachman ^{17a}, O. Nackenhorst ⁴⁹, K. Nagai ¹²⁷,
 K. Nagano ⁸⁴, J.L. Nagle ^{29,ag}, E. Nagy ¹⁰³, A.M. Nairz ³⁶, Y. Nakahama ⁸⁴, K. Nakamura ⁸⁴,
 K. Nakkalil ⁵, H. Nanjo ¹²⁵, R. Narayan ⁴⁴, E.A. Narayanan ¹¹³, I. Naryshkin ³⁷, M. Naseri ³⁴,
 S. Nasri ^{117b}, C. Nass ²⁴, G. Navarro ^{22a}, J. Navarro-Gonzalez ¹⁶⁴, R. Nayak ¹⁵², A. Nayaz ¹⁸,
 P.Y. Nechaeva ³⁷, S. Nechaeva ^{23b,23a}, F. Nechansky ⁴⁸, L. Nedic ¹²⁷, T.J. Neep ²⁰,
 A. Negri ^{73a,73b}, M. Negrini ^{23b}, C. Nellist ¹¹⁵, C. Nelson ¹⁰⁵, K. Nelson ¹⁰⁷, S. Nemecek ¹³²,
 M. Nessi ^{36,h}, M.S. Neubauer ¹⁶³, F. Neuhaus ¹⁰¹, J. Neundorf ⁴⁸, R. Newhouse ¹⁶⁵,
 P.R. Newman ²⁰, C.W. Ng ¹³⁰, Y.W.Y. Ng ⁴⁸, B. Ngair ^{117a}, H.D.N. Nguyen ¹⁰⁹,
 R.B. Nickerson ¹²⁷, R. Nicolaidou ¹³⁶, J. Nielsen ¹³⁷, M. Niemeyer ⁵⁵, J. Niermann ⁵⁵,
 N. Nikipforou ³⁶, V. Nikolaenko ^{37,a}, I. Nikolic-Audit ¹²⁸, K. Nikolopoulos ²⁰, P. Nilsson ²⁹,
 I. Ninca ⁴⁸, H.R. Nindhito ⁵⁶, G. Ninio ¹⁵², A. Nisati ^{75a}, N. Nishu ², R. Nisius ¹¹¹,
 J-E. Nitschke ⁵⁰, E.K. Nkadimeng ^{33g}, T. Nobe ¹⁵⁴, D.L. Noel ³², T. Nommensen ¹⁴⁸,
 M.B. Norfolk ¹⁴⁰, R.R.B. Norisam ⁹⁷, B.J. Norman ³⁴, M. Noury ^{35a}, J. Novak ⁹⁴, T. Novak ⁴⁸,
 L. Novotny ¹³³, R. Novotny ¹¹³, L. Nozka ¹²³, K. Ntekas ¹⁶⁰, N.M.J. Nunes De Moura Junior ^{83b},
 J. Ocariz ¹²⁸, A. Ochi ⁸⁵, I. Ochoa ^{131a}, S. Oerdek ^{48,t}, J.T. Offermann ³⁹, A. Ogrodnik ¹³⁴,
 A. Oh ¹⁰², C.C. Ohm ¹⁴⁵, H. Oide ⁸⁴, R. Oishi ¹⁵⁴, M.L. Ojeda ⁴⁸, Y. Okumura ¹⁵⁴,
 L.F. Oleiro Seabra ^{131a}, S.A. Olivares Pino ^{138d}, G. Oliveira Correa ¹³, D. Oliveira Damazio ²⁹,
 D. Oliveira Goncalves ^{83a}, J.L. Oliver ¹⁶⁰, Ö.O. Öncel ⁵⁴, A.P. O'Neill ¹⁹, A. Onofre ^{131a,131e},
 P.U.E. Onyisi ¹¹, M.J. Oreglia ³⁹, G.E. Orellana ⁹¹, D. Orestano ^{77a,77b}, N. Orlando ¹³,
 R.S. Orr ¹⁵⁶, V. O'Shea ⁵⁹, L.M. Osojnak ¹²⁹, R. Ospanov ^{62a}, G. Otero y Garzon ³⁰,
 H. Otono ⁸⁹, P.S. Ott ^{63a}, G.J. Ottino ^{17a}, M. Ouchrif ^{35d}, F. Ould-Saada ¹²⁶,
 T. Ovsiannikova ¹³⁹, M. Owen ⁵⁹, R.E. Owen ¹³⁵, K.Y. Oyulmaz ^{21a}, V.E. Ozcan ^{21a},
 F. Ozturk ⁸⁷, N. Ozturk ⁸, S. Ozturk ⁸², H.A. Pacey ¹²⁷, A. Pacheco Pages ¹³,
 C. Padilla Aranda ¹³, G. Padovano ^{75a,75b}, S. Pagan Griso ^{17a}, G. Palacino ⁶⁸, A. Palazzo ^{70a,70b},
 J. Pampel ²⁴, J. Pan ¹⁷³, T. Pan ^{64a}, D.K. Panchal ¹¹, C.E. Pandini ¹¹⁵, J.G. Panduro Vazquez ⁹⁶,
 H.D. Pandya ¹, H. Pang ^{14b}, P. Pani ⁴⁸, G. Panizzo ^{69a,69c}, L. Panwar ¹²⁸, L. Paolozzi ⁵⁶,
 S. Parajuli ¹⁶³, A. Paramonov ⁵, C. Paraskevopoulos ⁵³, D. Paredes Hernandez ^{64b},
 A. Pareti ^{73a,73b}, K.R. Park ⁴¹, T.H. Park ¹⁵⁶, M.A. Parker ³², F. Parodi ^{57b,57a}, E.W. Parrish ¹¹⁶,
 V.A. Parrish ⁵², J.A. Parsons ⁴¹, U. Parzefall ⁵⁴, B. Pascual Dias ¹⁰⁹, L. Pascual Dominguez ¹⁵²,
 E. Pasqualucci ^{75a}, S. Passaggio ^{57b}, F. Pastore ⁹⁶, P. Patel ⁸⁷, U.M. Patel ⁵¹, J.R. Pater ¹⁰²,
 T. Pauly ³⁶, C.I. Pazos ¹⁵⁹, J. Pearkes ¹⁴⁴, M. Pedersen ¹²⁶, R. Pedro ^{131a}, S.V. Peleganchuk ³⁷,
 O. Penc ³⁶, E.A. Pender ⁵², G.D. Penn ¹⁷³, K.E. Penski ¹¹⁰, M. Penzin ³⁷, B.S. Peralva ^{83d},
 A.P. Pereira Peixoto ¹³⁹, L. Pereira Sanchez ¹⁴⁴, D.V. Perepelitsa ^{29,ag}, E. Perez Codina ^{157a},
 M. Perganti ¹⁰, H. Pernegger ³⁶, O. Perrin ⁴⁰, K. Peters ⁴⁸, R.F.Y. Peters ¹⁰², B.A. Petersen ³⁶,
 T.C. Petersen ⁴², E. Petit ¹⁰³, V. Petousis ¹³³, C. Petridou ^{153,e}, T. Petru ¹³⁴, A. Petrukhin ¹⁴²,
 M. Pettee ^{17a}, N.E. Pettersson ³⁶, A. Petukhov ³⁷, K. Petukhova ¹³⁴, R. Pezoa ^{138f},
 L. Pezzotti ³⁶, G. Pezzullo ¹⁷³, T.M. Pham ¹⁷¹, T. Pham ¹⁰⁶, P.W. Phillips ¹³⁵, G. Piacquadio ¹⁴⁶,
 E. Pianori ^{17a}, F. Piazza ¹²⁴, R. Piegai ³⁰, D. Pietreanu ^{27b}, A.D. Pilkington ¹⁰²,
 M. Pinamonti ^{69a,69c}, J.L. Pinfeld ², B.C. Pinheiro Pereira ^{131a}, A.E. Pinto Pinoargote ^{101,136},
 L. Pintucci ^{69a,69c}, K.M. Piper ¹⁴⁷, A. Pirttikoski ⁵⁶, D.A. Pizzi ³⁴, L. Pizzimento ^{64b},
 A. Pizzini ¹¹⁵, M.-A. Pleier ²⁹, V. Plesanovs ⁵⁴, V. Pleskot ¹³⁴, E. Plotnikova ³⁸, G. Poddar ⁹⁵,
 R. Poettgen ⁹⁹, L. Poggioli ¹²⁸, I. Pokharel ⁵⁵, S. Polacek ¹³⁴, G. Polesello ^{73a}, A. Poley ^{143,157a},
 A. Polini ^{23b}, C.S. Pollard ¹⁶⁸, Z.B. Pollock ¹²⁰, E. Pompa Pacchi ^{75a,75b}, D. Ponomarenko ¹¹⁴,
 L. Pontecorvo ³⁶, S. Popa ^{27a}, G.A. Popeneciu ^{27d}, A. Poreba ³⁶, D.M. Portillo Quintero ^{157a},

S. Pospisil ¹³³, M.A. Postill ¹⁴⁰, P. Postolache ^{27c}, K. Potamianos ¹⁶⁸, P.A. Potepa ^{86a},
 I.N. Potrap ³⁸, C.J. Potter ³², H. Potti ¹, J. Poveda ¹⁶⁴, M.E. Pozo Astigarraga ³⁶,
 A. Prades Ibanez ¹⁶⁴, J. Pretel ⁵⁴, D. Price ¹⁰², M. Primavera ^{70a}, M.A. Principe Martin ¹⁰⁰,
 R. Privara ¹²³, T. Procter ⁵⁹, M.L. Proffitt ¹³⁹, N. Proklova ¹²⁹, K. Prokofiev ^{64c}, G. Proto ¹¹¹,
 J. Proudfoot ⁶, M. Przybycien ^{86a}, W.W. Przygoda ^{86b}, A. Psallidas ⁴⁶, J.E. Puddefoot ¹⁴⁰,
 D. Pudzha ³⁷, D. Pyatiizbyantseva ³⁷, J. Qian ¹⁰⁷, D. Qichen ¹⁰², Y. Qin ¹³, T. Qiu ⁵²,
 A. Quadt ⁵⁵, M. Queitsch-Maitland ¹⁰², G. Quetant ⁵⁶, R.P. Quinn ¹⁶⁵, G. Rabanal Bolanos ⁶¹,
 D. Rafanoharana ⁵⁴, F. Ragusa ^{71a,71b}, J.L. Rainbolt ³⁹, J.A. Raine ⁵⁶, S. Rajagopalan ²⁹,
 E. Ramakoti ³⁷, I.A. Ramirez-Berend ³⁴, K. Ran ^{48,14e}, N.P. Rapheeha ^{33g}, H. Rasheed ^{27b},
 V. Raskina ¹²⁸, D.F. Rassloff ^{63a}, A. Rastogi ^{17a}, S. Rave ¹⁰¹, B. Ravina ⁵⁵, I. Ravinovich ¹⁷⁰,
 M. Raymond ³⁶, A.L. Read ¹²⁶, N.P. Readioff ¹⁴⁰, D.M. Rebutzi ^{73a,73b}, G. Redlinger ²⁹,
 A.S. Reed ¹¹¹, K. Reeves ²⁶, J.A. Reidelsturz ¹⁷², D. Reikher ¹⁵², A. Rej ⁴⁹, C. Rembser ³⁶,
 M. Renda ^{27b}, M.B. Rendel ¹¹¹, F. Renner ⁴⁸, A.G. Rennie ¹⁶⁰, A.L. Rescia ⁴⁸, S. Resconi ^{71a},
 M. Ressegotti ^{57b,57a}, S. Rettie ³⁶, J.G. Reyes Rivera ¹⁰⁸, E. Reynolds ^{17a}, O.L. Rezanova ³⁷,
 P. Reznicek ¹³⁴, H. Riani ^{35d}, N. Ribaric ⁹², E. Ricci ^{78a,78b}, R. Richter ¹¹¹, S. Richter ^{47a,47b},
 E. Richter-Was ^{86b}, M. Ridel ¹²⁸, S. Ridouani ^{35d}, P. Rieck ¹¹⁸, P. Riedler ³⁶, E.M. Riefel ^{47a,47b},
 J.O. Rieger ¹¹⁵, M. Rijssenbeek ¹⁴⁶, M. Rimoldi ³⁶, L. Rinaldi ^{23b,23a}, T.T. Rinn ²⁹,
 M.P. Rinnagel ¹¹⁰, G. Ripellino ¹⁶², I. Riu ¹³, J.C. Rivera Vergara ¹⁶⁶, F. Rizatdinova ¹²²,
 E. Rizvi ⁹⁵, B.R. Roberts ^{17a}, S.H. Robertson ^{105,w}, D. Robinson ³², C.M. Robles Gajardo ^{138f},
 M. Robles Manzano ¹⁰¹, A. Robson ⁵⁹, A. Rocchi ^{76a,76b}, C. Roda ^{74a,74b}, S. Rodriguez Bosca ³⁶,
 Y. Rodriguez Garcia ^{22a}, A. Rodriguez Rodriguez ⁵⁴, A.M. Rodríguez Vera ¹¹⁶, S. Roe ³⁶,
 J.T. Roemer ¹⁶⁰, A.R. Roepe-Gier ¹³⁷, J. Roggel ¹⁷², O. Røhne ¹²⁶, R.A. Rojas ¹⁰⁴,
 C.P.A. Roland ¹²⁸, J. Roloff ²⁹, A. Romaniouk ³⁷, E. Romano ^{73a,73b}, M. Romano ^{23b},
 A.C. Romero Hernandez ¹⁶³, N. Rompotis ⁹³, L. Roos ¹²⁸, S. Rosati ^{75a}, B.J. Rosser ³⁹,
 E. Rossi ¹²⁷, E. Rossi ^{72a,72b}, L.P. Rossi ⁶¹, L. Rossini ⁵⁴, R. Rosten ¹²⁰, M. Rotaru ^{27b},
 B. Rottler ⁵⁴, C. Rougier ⁹⁰, D. Rousseau ⁶⁶, D. Rouso ⁴⁸, A. Roy ¹⁶³, S. Roy-Garand ¹⁵⁶,
 A. Rozanov ¹⁰³, Z.M.A. Rozario ⁵⁹, Y. Rozen ¹⁵¹, A. Rubio Jimenez ¹⁶⁴, A.J. Ruby ⁹³,
 V.H. Ruelas Rivera ¹⁸, T.A. Ruggeri ¹, A. Ruggiero ¹²⁷, A. Ruiz-Martinez ¹⁶⁴, A. Rummler ³⁶,
 Z. Rurikova ⁵⁴, N.A. Rusakovich ³⁸, H.L. Russell ¹⁶⁶, G. Russo ^{75a,75b}, J.P. Rutherford ⁷,
 S. Rutherford Colmenares ³², K. Rybacki ⁹², M. Rybar ¹³⁴, E.B. Rye ¹²⁶, A. Ryzhov ⁴⁴,
 J.A. Sabater Iglesias ⁵⁶, P. Sabatini ¹⁶⁴, H.F.W. Sadrozinski ¹³⁷, F. Safai Tehrani ^{75a},
 B. Safarzadeh Samani ¹³⁵, S. Saha ¹, M. Sahinsoy ¹¹¹, A. Saibel ¹⁶⁴, M. Saimpert ¹³⁶,
 M. Saito ¹⁵⁴, T. Saito ¹⁵⁴, A. Sala ^{71a,71b}, D. Salamani ³⁶, A. Salnikov ¹⁴⁴, J. Salt ¹⁶⁴,
 A. Salvador Salas ¹⁵², D. Salvatore ^{43b,43a}, F. Salvatore ¹⁴⁷, A. Salzburger ³⁶, D. Sammel ⁵⁴,
 E. Sampson ⁹², D. Sampsonidis ^{153,e}, D. Sampsonidou ¹²⁴, J. Sánchez ¹⁶⁴,
 V. Sanchez Sebastian ¹⁶⁴, H. Sandaker ¹²⁶, C.O. Sander ⁴⁸, J.A. Sandesara ¹⁰⁴, M. Sandhoff ¹⁷²,
 C. Sandoval ^{22b}, D.P.C. Sankey ¹³⁵, T. Sano ⁸⁸, A. Sansoni ⁵³, L. Santi ^{75a,75b}, C. Santoni ⁴⁰,
 H. Santos ^{131a,131b}, A. Santra ¹⁷⁰, E. Sanzani ^{23b,23a}, K.A. Saoucha ¹⁶¹, J.G. Saraiva ^{131a,131d},
 J. Sardain ⁷, O. Sasaki ⁸⁴, K. Sato ¹⁵⁸, C. Sauer ^{63b}, F. Sauerburger ⁵⁴, E. Sauvan ⁴,
 P. Savard ^{156,ae}, R. Sawada ¹⁵⁴, C. Sawyer ¹³⁵, L. Sawyer ⁹⁸, I. Sayago Galvan ¹⁶⁴, C. Sbarra ^{23b},
 A. Sbrizzi ^{23b,23a}, T. Scanlon ⁹⁷, J. Schaarschmidt ¹³⁹, U. Schäfer ¹⁰¹, A.C. Schaffer ^{66,44},
 D. Schaile ¹¹⁰, R.D. Schamberger ¹⁴⁶, C. Scharf ¹⁸, M.M. Schefer ¹⁹, V.A. Schegelsky ³⁷,
 D. Scheirich ¹³⁴, F. Schenck ¹⁸, M. Schernau ¹⁶⁰, C. Scheulen ⁵⁵, C. Schiavi ^{57b,57a},
 M. Schioppa ^{43b,43a}, B. Schlag ^{144,m}, K.E. Schleicher ⁵⁴, S. Schlenker ³⁶, J. Schmeing ¹⁷²,
 M.A. Schmidt ¹⁷², K. Schmieden ¹⁰¹, C. Schmitt ¹⁰¹, N. Schmitt ¹⁰¹, S. Schmitt ⁴⁸,
 L. Schoeffel ¹³⁶, A. Schoening ^{63b}, P.G. Scholer ³⁴, E. Schopf ¹²⁷, M. Schott ¹⁰¹,
 J. Schovancova ³⁶, S. Schramm ⁵⁶, T. Schroer ⁵⁶, H-C. Schultz-Coulon ^{63a}, M. Schumacher ⁵⁴,

B.A. Schumm ¹³⁷, Ph. Schune ¹³⁶, A.J. Schuy ¹³⁹, H.R. Schwartz ¹³⁷, A. Schwartzman ¹⁴⁴,
 T.A. Schwarz ¹⁰⁷, Ph. Schwemling ¹³⁶, R. Schwienhorst ¹⁰⁸, A. Sciandra ²⁹, G. Sciolla ²⁶,
 F. Scuri ^{74a}, C.D. Sebastiani ⁹³, K. Sedlaczek ¹¹⁶, P. Seema ¹⁸, S.C. Seidel ¹¹³, A. Seiden ¹³⁷,
 B.D. Seidlitz ⁴¹, C. Seitz ⁴⁸, J.M. Seixas ^{83b}, G. Sekhniaidze ^{72a}, L. Selem ⁶⁰,
 N. Semprini-Cesari ^{23b,23a}, D. Sengupta ⁵⁶, V. Senthilkumar ¹⁶⁴, L. Serin ⁶⁶, L. Serkin ^{69a,69b},
 M. Sessa ^{76a,76b}, H. Severini ¹²¹, F. Sforza ^{57b,57a}, A. Sfyrla ⁵⁶, Q. Sha ^{14a}, E. Shabalina ⁵⁵,
 A.H. Shah ³², R. Shaheen ¹⁴⁵, J.D. Shahinian ¹²⁹, D. Shaked Renous ¹⁷⁰, L.Y. Shan ^{14a},
 M. Shapiro ^{17a}, A. Sharma ³⁶, A.S. Sharma ¹⁶⁵, P. Sharma ⁸⁰, P.B. Shatalov ³⁷, K. Shaw ¹⁴⁷,
 S.M. Shaw ¹⁰², A. Shcherbakova ³⁷, Q. Shen ^{62c,5}, D.J. Sheppard ¹⁴³, P. Sherwood ⁹⁷, L. Shi ⁹⁷,
 X. Shi ^{14a}, C.O. Shimmin ¹⁷³, J.D. Shinner ⁹⁶, I.P.J. Shipsey ¹²⁷, S. Shirabe ⁸⁹,
 M. Shiyakova ^{38,u}, J. Shlomi ¹⁷⁰, M.J. Shochet ³⁹, J. Shojaii ¹⁰⁶, D.R. Shope ¹²⁶,
 B. Shrestha ¹²¹, S. Shrestha ^{120,ah}, E.M. Shrif ^{33g}, M.J. Shroff ¹⁶⁶, P. Sicho ¹³², A.M. Sickles ¹⁶³,
 E. Sideras Haddad ^{33g}, A.C. Sidley ¹¹⁵, A. Sidoti ^{23b}, F. Siegert ⁵⁰, Dj. Sijacki ¹⁵, F. Sili ⁹¹,
 J.M. Silva ⁵², M.V. Silva Oliveira ²⁹, S.B. Silverstein ^{47a}, S. Simion ⁶⁶, R. Simoniello ³⁶,
 E.L. Simpson ¹⁰², H. Simpson ¹⁴⁷, L.R. Simpson ¹⁰⁷, N.D. Simpson ⁹⁹, S. Simsek ⁸²,
 S. Sindhu ⁵⁵, P. Sinervo ¹⁵⁶, S. Singh ¹⁵⁶, S. Sinha ⁴⁸, S. Sinha ¹⁰², M. Sioli ^{23b,23a}, I. Siral ³⁶,
 E. Sitnikova ⁴⁸, J. Sjölin ^{47a,47b}, A. Skaf ⁵⁵, E. Skorda ²⁰, P. Skubic ¹²¹, M. Slawinska ⁸⁷,
 V. Smakhtin ¹⁷⁰, B.H. Smart ¹³⁵, S.Yu. Smirnov ³⁷, Y. Smirnov ³⁷, L.N. Smirnova ^{37,a},
 O. Smirnova ⁹⁹, A.C. Smith ⁴¹, D.R. Smith ¹⁶⁰, E.A. Smith ³⁹, H.A. Smith ¹²⁷, J.L. Smith ¹⁰²,
 R. Smith ¹⁴⁴, M. Smizanska ⁹², K. Smolek ¹³³, A.A. Snesarev ³⁷, S.R. Snider ¹⁵⁶, H.L. Snoek ¹¹⁵,
 S. Snyder ²⁹, R. Sobie ^{166,w}, A. Soffer ¹⁵², C.A. Solans Sanchez ³⁶, E.Yu. Soldatov ³⁷,
 U. Soldevila ¹⁶⁴, A.A. Solodkov ³⁷, S. Solomon ²⁶, A. Soloshenko ³⁸, K. Solovieva ⁵⁴,
 O.V. Solovyanov ⁴⁰, P. Sommer ³⁶, A. Sonay ¹³, W.Y. Song ^{157b}, A. Sopczak ¹³³, A.L. Soppio ⁹⁷,
 F. Sopkova ^{28b}, J.D. Sorenson ¹¹³, I.R. Sotarriva Alvarez ¹⁵⁵, V. Sothilingam ^{63a},
 O.J. Soto Sandoval ^{138c,138b}, S. Sottocornola ⁶⁸, R. Soualah ¹⁶¹, Z. Soumami ^{35e}, D. South ⁴⁸,
 N. Soybelman ¹⁷⁰, S. Spagnolo ^{70a,70b}, M. Spalla ¹¹¹, D. Sperlich ⁵⁴, G. Spigo ³⁶, S. Spinali ⁹²,
 D.P. Spiteri ⁵⁹, M. Spousta ¹³⁴, E.J. Staats ³⁴, R. Stamen ^{63a}, A. Stampekis ²⁰, M. Standke ²⁴,
 E. Stanecka ⁸⁷, W. Stanek-Maslouska ⁴⁸, M.V. Stange ⁵⁰, B. Stanislaus ^{17a}, M.M. Stanitzki ⁴⁸,
 B. Stapf ⁴⁸, E.A. Starchenko ³⁷, G.H. Stark ¹³⁷, J. Stark ⁹⁰, P. Staroba ¹³², P. Starovoitov ^{63a},
 S. Stärz ¹⁰⁵, R. Staszewski ⁸⁷, G. Stavropoulos ⁴⁶, J. Steentoft ¹⁶², P. Steinberg ²⁹,
 B. Stelzer ^{143,157a}, H.J. Stelzer ¹³⁰, O. Stelzer-Chilton ^{157a}, H. Stenzel ⁵⁸, T.J. Stevenson ¹⁴⁷,
 G.A. Stewart ³⁶, J.R. Stewart ¹²², M.C. Stockton ³⁶, G. Stoicea ^{27b}, M. Stolarski ^{131a},
 S. Stonjek ¹¹¹, A. Straessner ⁵⁰, J. Strandberg ¹⁴⁵, S. Strandberg ^{47a,47b}, M. Stratmann ¹⁷²,
 M. Strauss ¹²¹, T. Strebler ¹⁰³, P. Strizenc ^{28b}, R. Ströhmer ¹⁶⁷, D.M. Strom ¹²⁴,
 R. Stroynowski ⁴⁴, A. Strubig ^{47a,47b}, S.A. Stucci ²⁹, B. Stugu ¹⁶, J. Stupak ¹²¹, N.A. Styles ⁴⁸,
 D. Su ¹⁴⁴, S. Su ^{62a}, W. Su ^{62d}, X. Su ^{62a}, D. Suchy ^{28a}, K. Sugizaki ¹⁵⁴, V.V. Sulin ³⁷,
 M.J. Sullivan ⁹³, D.M.S. Sultan ¹²⁷, L. Sultanaliyeva ³⁷, S. Sultansoy ^{3b}, T. Sumida ⁸⁸,
 S. Sun ¹⁰⁷, S. Sun ¹⁷¹, O. Sunneborn Gudnadottir ¹⁶², N. Sur ¹⁰³, M.R. Sutton ¹⁴⁷,
 H. Suzuki ¹⁵⁸, M. Svatos ¹³², M. Swiatlowski ^{157a}, T. Swirski ¹⁶⁷, I. Sykora ^{28a}, M. Sykora ¹³⁴,
 T. Sykora ¹³⁴, D. Ta ¹⁰¹, K. Tackmann ^{48,t}, A. Taffard ¹⁶⁰, R. Tafirout ^{157a}, J.S. Tafoya Vargas ⁶⁶,
 Y. Takubo ⁸⁴, M. Talby ¹⁰³, A.A. Talyshev ³⁷, K.C. Tam ^{64b}, N.M. Tamir ¹⁵², A. Tanaka ¹⁵⁴,
 J. Tanaka ¹⁵⁴, R. Tanaka ⁶⁶, M. Tanasini ¹⁴⁶, Z. Tao ¹⁶⁵, S. Tapia Araya ^{138f}, S. Tapprogge ¹⁰¹,
 A. Tarek Abouelfadl Mohamed ¹⁰⁸, S. Tarem ¹⁵¹, K. Tariq ^{14a}, G. Tarna ^{27b}, G.F. Tartarelli ^{71a},
 M.J. Tartarin ⁹⁰, P. Tas ¹³⁴, M. Tasevsky ¹³², E. Tassi ^{43b,43a}, A.C. Tate ¹⁶³, G. Tateno ¹⁵⁴,
 Y. Tayalati ^{35e,v}, G.N. Taylor ¹⁰⁶, W. Taylor ^{157b}, A.S. Tee ¹⁷¹, R. Teixeira De Lima ¹⁴⁴,
 P. Teixeira-Dias ⁹⁶, J.J. Teoh ¹⁵⁶, K. Terashi ¹⁵⁴, J. Terron ¹⁰⁰, S. Terzo ¹³, M. Testa ⁵³,
 R.J. Teuscher ^{156,w}, A. Thaler ⁷⁹, O. Theiner ⁵⁶, N. Themistokleous ⁵², T. Theveneaux-Pelzer ¹⁰³,

O. Thielmann ¹⁷², D.W. Thomas ⁹⁶, J.P. Thomas ²⁰, E.A. Thompson ^{17a}, P.D. Thompson ²⁰, E. Thomson ¹²⁹, R.E. Thornberry ⁴⁴, Y. Tian ⁵⁵, V. Tikhomirov ^{37,a}, Yu.A. Tikhonov ³⁷, S. Timoshenko ³⁷, D. Timoshyn ¹³⁴, E.X.L. Ting ¹, P. Tipton ¹⁷³, S.H. Tlou ^{33g}, K. Todome ¹⁵⁵, S. Todorova-Nova ¹³⁴, S. Todt ⁵⁰, L. Toffolin ^{69a,69c}, M. Togawa ⁸⁴, J. Tojo ⁸⁹, S. Tokár ^{28a}, K. Tokushuku ⁸⁴, O. Toldaiev ⁶⁸, R. Tombs ³², M. Tomoto ^{84,112}, L. Tompkins ^{144,m}, K.W. Topolnicki ^{86b}, E. Torrence ¹²⁴, H. Torres ⁹⁰, E. Torró Pastor ¹⁶⁴, M. Toscani ³⁰, C. Toscirci ³⁹, M. Tost ¹¹, D.R. Tovey ¹⁴⁰, A. Traeet ¹⁶, I.S. Trandafir ^{27b}, T. Trefzger ¹⁶⁷, A. Tricoli ²⁹, I.M. Trigger ^{157a}, S. Trincaz-Duvoid ¹²⁸, D.A. Trischuk ²⁶, B. Trocmé ⁶⁰, L. Truong ^{33c}, M. Trzebinski ⁸⁷, A. Trzupek ⁸⁷, F. Tsai ¹⁴⁶, M. Tsai ¹⁰⁷, A. Tsiamis ^{153,e}, P.V. Tsiarehka ³⁷, S. Tsigaridas ^{157a}, A. Tsirigotis ^{153,r}, V. Tsiskaridze ¹⁵⁶, E.G. Tskhadadze ^{150a}, M. Tsopoulou ¹⁵³, Y. Tsujikawa ⁸⁸, I.I. Tsukerman ³⁷, V. Tsulaia ^{17a}, S. Tsuno ⁸⁴, K. Tsurii ¹¹⁹, D. Tsybychev ¹⁴⁶, Y. Tu ^{64b}, A. Tudorache ^{27b}, V. Tudorache ^{27b}, A.N. Tuna ⁶¹, S. Turchikhin ^{57b,57a}, I. Turk Cakir ^{3a}, R. Turra ^{71a}, T. Turtuvshin ^{38,x}, P.M. Tuts ⁴¹, S. Tzamarias ^{153,e}, E. Tzovara ¹⁰¹, F. Ukegawa ¹⁵⁸, P.A. Ulloa Poblete ^{138c,138b}, E.N. Umaka ²⁹, G. Unal ³⁶, A. Undrus ²⁹, G. Unel ¹⁶⁰, J. Urban ^{28b}, P. Urquijo ¹⁰⁶, P. Urrejola ^{138a}, G. Usai ⁸, R. Ushioda ¹⁵⁵, M. Usman ¹⁰⁹, Z. Uysal ⁸², V. Vacek ¹³³, B. Vachon ¹⁰⁵, T. Vafeiadis ³⁶, A. Vaitkus ⁹⁷, C. Valderanis ¹¹⁰, E. Valdes Santurio ^{47a,47b}, M. Valente ^{157a}, S. Valentinetti ^{23b,23a}, A. Valero ¹⁶⁴, E. Valiente Moreno ¹⁶⁴, A. Vallier ⁹⁰, J.A. Valls Ferrer ¹⁶⁴, D.R. Van Arneman ¹¹⁵, T.R. Van Daalen ¹³⁹, A. Van Der Graaf ⁴⁹, P. Van Gemmeren ⁶, M. Van Rijnbach ¹²⁶, S. Van Stroud ⁹⁷, I. Van Vulpen ¹¹⁵, P. Vana ¹³⁴, M. Vanadia ^{76a,76b}, W. Vandelli ³⁶, E.R. Vandewall ¹²², D. Vannicola ¹⁵², L. Vannoli ⁵³, R. Vari ^{75a}, E.W. Varnes ⁷, C. Varni ^{17b}, T. Varol ¹⁴⁹, D. Varouchas ⁶⁶, L. Varriale ¹⁶⁴, K.E. Varvell ¹⁴⁸, M.E. Vasile ^{27b}, L. Vaslin ⁸⁴, G.A. Vasquez ¹⁶⁶, A. Vasyukov ³⁸, R. Vavricka ¹⁰¹, F. Vazeille ⁴⁰, T. Vazquez Schroeder ³⁶, J. Veatch ³¹, V. Vecchio ¹⁰², M.J. Veen ¹⁰⁴, I. Veliscek ²⁹, L.M. Veloce ¹⁵⁶, F. Veloso ^{131a,131c}, S. Veneziano ^{75a}, A. Ventura ^{70a,70b}, S. Ventura Gonzalez ¹³⁶, A. Verbytskyi ¹¹¹, M. Verducci ^{74a,74b}, C. Vergis ⁹⁵, M. Verissimo De Araujo ^{83b}, W. Verkerke ¹¹⁵, J.C. Vermeulen ¹¹⁵, C. Vernieri ¹⁴⁴, M. Vessella ¹⁰⁴, M.C. Vetterli ^{143,ae}, A. Vgenopoulos ^{153,e}, N. Viaux Maira ^{138f}, T. Vickey ¹⁴⁰, O.E. Vickey Boeriu ¹⁴⁰, G.H.A. Viehhauser ¹²⁷, L. Vigani ^{63b}, M. Villa ^{23b,23a}, M. Villaplana Perez ¹⁶⁴, E.M. Villhauer ⁵², E. Vilucchi ⁵³, M.G. Vincter ³⁴, A. Visibile ¹¹⁵, C. Vittori ³⁶, I. Vivarelli ^{23b,23a}, E. Voevodina ¹¹¹, F. Vogel ¹¹⁰, J.C. Voigt ⁵⁰, P. Vokac ¹³³, Yu. Volkotrub ^{86b}, J. Von Ahnen ⁴⁸, E. Von Toerne ²⁴, B. Vormwald ³⁶, V. Vorobel ¹³⁴, K. Vorobev ³⁷, M. Vos ¹⁶⁴, K. Voss ¹⁴², M. Vozak ¹¹⁵, L. Vozdecky ¹²¹, N. Vranjes ¹⁵, M. Vranjes Milosavljevic ¹⁵, M. Vreeswijk ¹¹⁵, N.K. Vu ^{62d,62c}, R. Vuillermet ³⁶, O. Vujinovic ¹⁰¹, I. Vukotic ³⁹, S. Wada ¹⁵⁸, C. Wagner ¹⁰⁴, J.M. Wagner ^{17a}, W. Wagner ¹⁷², S. Wahdan ¹⁷², H. Wahlberg ⁹¹, M. Wakida ¹¹², J. Walder ¹³⁵, R. Walker ¹¹⁰, W. Walkowiak ¹⁴², A. Wall ¹²⁹, E.J. Wallin ⁹⁹, T. Wamorkar ⁶, A.Z. Wang ¹³⁷, C. Wang ¹⁰¹, C. Wang ¹¹, H. Wang ^{17a}, J. Wang ^{64c}, R.-J. Wang ¹⁰¹, R. Wang ⁶¹, R. Wang ⁶, S.M. Wang ¹⁴⁹, S. Wang ^{62b}, T. Wang ^{62a}, W.T. Wang ⁸⁰, W. Wang ^{14a}, X. Wang ^{14c}, X. Wang ¹⁶³, X. Wang ^{62c}, Y. Wang ^{62d}, Y. Wang ^{14c}, Z. Wang ¹⁰⁷, Z. Wang ^{62d,51,62c}, Z. Wang ¹⁰⁷, A. Warburton ¹⁰⁵, R.J. Ward ²⁰, N. Warrack ⁵⁹, S. Waterhouse ⁹⁶, A.T. Watson ²⁰, H. Watson ⁵⁹, M.F. Watson ²⁰, E. Watton ^{59,135}, G. Watts ¹³⁹, B.M. Waugh ⁹⁷, J.M. Webb ⁵⁴, C. Weber ²⁹, H.A. Weber ¹⁸, M.S. Weber ¹⁹, S.M. Weber ^{63a}, C. Wei ^{62a}, Y. Wei ⁵⁴, A.R. Weidberg ¹²⁷, E.J. Weik ¹¹⁸, J. Weingarten ⁴⁹, M. Weirich ¹⁰¹, C. Weiser ⁵⁴, C.J. Wells ⁴⁸, T. Wenaus ²⁹, B. Wendland ⁴⁹, T. Wengler ³⁶, N.S. Wenke ¹¹¹, N. Wermes ²⁴, M. Wessels ^{63a}, A.M. Wharton ⁹², A.S. White ⁶¹, A. White ⁸, M.J. White ¹, D. Whiteson ¹⁶⁰, L. Wickremasinghe ¹²⁵, W. Wiedenmann ¹⁷¹, M. Wielers ¹³⁵, C. Wiglesworth ⁴², D.J. Wilbern ¹²¹, H.G. Wilkens ³⁶, J.J.H. Wilkinson ³², D.M. Williams ⁴¹, H.H. Williams ¹²⁹, S. Williams ³², S. Willocq ¹⁰⁴,

B.J. Wilson ¹⁰², P.J. Windischhofer ³⁹, F.I. Winkel ³⁰, F. Winklmeier ¹²⁴, B.T. Winter ⁵⁴, J.K. Winter ¹⁰², M. Wittgen¹⁴⁴, M. Wobisch ⁹⁸, T. Wojtkowski⁶⁰, Z. Wolffs ¹¹⁵, J. Wollrath¹⁶⁰, M.W. Wolter ⁸⁷, H. Wolters ^{131a,131c}, M.C. Wong¹³⁷, E.L. Woodward ⁴¹, S.D. Worm ⁴⁸, B.K. Wosiek ⁸⁷, K.W. Woźniak ⁸⁷, S. Wozniowski ⁵⁵, K. Wraight ⁵⁹, C. Wu ²⁰, M. Wu ^{14d}, M. Wu ¹¹⁴, S.L. Wu ¹⁷¹, X. Wu ⁵⁶, Y. Wu ^{62a}, Z. Wu ⁴, J. Wuerzinger ^{111,ac}, T.R. Wyatt ¹⁰², B.M. Wynne ⁵², S. Xella ⁴², L. Xia ^{14c}, M. Xia ^{14b}, J. Xiang ^{64c}, M. Xie ^{62a}, X. Xie ^{62a}, S. Xin ^{14a,14e}, A. Xiong ¹²⁴, J. Xiong ^{17a}, D. Xu ^{14a}, H. Xu ^{62a}, L. Xu ^{62a}, R. Xu ¹²⁹, T. Xu ¹⁰⁷, Y. Xu ^{14b}, Z. Xu ⁵², Z. Xu^{14c}, B. Yabsley ¹⁴⁸, S. Yacoob ^{33a}, Y. Yamaguchi ¹⁵⁵, E. Yamashita ¹⁵⁴, H. Yamauchi ¹⁵⁸, T. Yamazaki ^{17a}, Y. Yamazaki ⁸⁵, J. Yan^{62c}, S. Yan ⁵⁹, Z. Yan ¹⁰⁴, H.J. Yang ^{62c,62d}, H.T. Yang ^{62a}, S. Yang ^{62a}, T. Yang ^{64c}, X. Yang ³⁶, X. Yang ^{14a}, Y. Yang ⁴⁴, Y. Yang^{62a}, Y. Yang ¹⁰⁵, Z. Yang ^{62a}, W-M. Yao ^{17a}, H. Ye ^{14c}, H. Ye ⁵⁵, J. Ye ^{14a}, S. Ye ²⁹, X. Ye ^{62a}, Y. Yeh ⁹⁷, I. Yeletsikh ³⁸, B.K. Yeo ^{17b}, M.R. Yexley ⁹⁷, T.P. Yildirim ¹²⁷, P. Yin ⁴¹, K. Yorita ¹⁶⁹, S. Younas ^{27b}, C.J.S. Young ³⁶, C. Young ¹⁴⁴, C. Yu ^{14a,14e}, Y. Yu ^{62a}, M. Yuan ¹⁰⁷, R. Yuan ^{62d,62c}, L. Yue ⁹⁷, M. Zaazoua ^{62a}, B. Zabinski ⁸⁷, E. Zaid⁵², Z.K. Zak ⁸⁷, T. Zakareishvili ¹⁶⁴, N. Zakharchuk ³⁴, S. Zambito ⁵⁶, J.A. Zamora Saa ^{138d,138b}, J. Zang ¹⁵⁴, D. Zanzi ⁵⁴, O. Zaplatilek ¹³³, C. Zeitnitz ¹⁷², H. Zeng ^{14a}, J.C. Zeng ¹⁶³, D.T. Zenger Jr ²⁶, O. Zenin ³⁷, T. Ženiš ^{28a}, S. Zenz ⁹⁵, S. Zerradi ^{35a}, D. Zerwas ⁶⁶, M. Zhai ^{14a,14e}, D.F. Zhang ¹⁴⁰, J. Zhang ^{62b}, J. Zhang ⁶, K. Zhang ^{14a,14e}, L. Zhang ^{62a}, L. Zhang ^{14c}, P. Zhang ^{14a,14e}, R. Zhang ¹⁷¹, S. Zhang ¹⁰⁷, S. Zhang ⁴⁴, T. Zhang ¹⁵⁴, X. Zhang ^{62c}, X. Zhang ^{62b}, Y. Zhang ^{62c,5}, Y. Zhang ⁹⁷, Y. Zhang ^{14c}, Z. Zhang ^{17a}, Z. Zhang ⁶⁶, H. Zhao ¹³⁹, T. Zhao ^{62b}, Y. Zhao ¹³⁷, Z. Zhao ^{62a}, Z. Zhao ^{62a}, A. Zhemchugov ³⁸, J. Zheng ^{14c}, K. Zheng ¹⁶³, X. Zheng ^{62a}, Z. Zheng ¹⁴⁴, D. Zhong ¹⁶³, B. Zhou ¹⁰⁷, H. Zhou ⁷, N. Zhou ^{62c}, Y. Zhou ^{14c}, Y. Zhou⁷, C.G. Zhu ^{62b}, J. Zhu ¹⁰⁷, X. Zhu^{62d}, Y. Zhu ^{62c}, Y. Zhu ^{62a}, X. Zhuang ^{14a}, K. Zhukov ³⁷, N.I. Zimine ³⁸, J. Zinsser ^{63b}, M. Ziolkowski ¹⁴², L. Živković ¹⁵, A. Zoccoli ^{23b,23a}, K. Zoch ⁶¹, T.G. Zorbas ¹⁴⁰, O. Zormpa ⁴⁶, W. Zou ⁴¹, L. Zwalinski ³⁶.

¹Department of Physics, University of Adelaide, Adelaide; Australia.

²Department of Physics, University of Alberta, Edmonton AB; Canada.

³(^a)Department of Physics, Ankara University, Ankara; (^b)Division of Physics, TOBB University of Economics and Technology, Ankara; Türkiye.

⁴LAPP, Université Savoie Mont Blanc, CNRS/IN2P3, Annecy; France.

⁵APC, Université Paris Cité, CNRS/IN2P3, Paris; France.

⁶High Energy Physics Division, Argonne National Laboratory, Argonne IL; United States of America.

⁷Department of Physics, University of Arizona, Tucson AZ; United States of America.

⁸Department of Physics, University of Texas at Arlington, Arlington TX; United States of America.

⁹Physics Department, National and Kapodistrian University of Athens, Athens; Greece.

¹⁰Physics Department, National Technical University of Athens, Zografou; Greece.

¹¹Department of Physics, University of Texas at Austin, Austin TX; United States of America.

¹²Institute of Physics, Azerbaijan Academy of Sciences, Baku; Azerbaijan.

¹³Institut de Física d'Altes Energies (IFAE), Barcelona Institute of Science and Technology, Barcelona; Spain.

¹⁴(^a)Institute of High Energy Physics, Chinese Academy of Sciences, Beijing; (^b)Physics Department, Tsinghua University, Beijing; (^c)Department of Physics, Nanjing University, Nanjing; (^d)School of Science, Shenzhen Campus of Sun Yat-sen University; (^e)University of Chinese Academy of Science (UCAS), Beijing; China.

¹⁵Institute of Physics, University of Belgrade, Belgrade; Serbia.

¹⁶Department for Physics and Technology, University of Bergen, Bergen; Norway.

- ¹⁷(*a*) Physics Division, Lawrence Berkeley National Laboratory, Berkeley CA; (*b*) University of California, Berkeley CA; United States of America.
- ¹⁸Institut für Physik, Humboldt Universität zu Berlin, Berlin; Germany.
- ¹⁹Albert Einstein Center for Fundamental Physics and Laboratory for High Energy Physics, University of Bern, Bern; Switzerland.
- ²⁰School of Physics and Astronomy, University of Birmingham, Birmingham; United Kingdom.
- ²¹(*a*) Department of Physics, Bogazici University, Istanbul; (*b*) Department of Physics Engineering, Gaziantep University, Gaziantep; (*c*) Department of Physics, Istanbul University, Istanbul; Türkiye.
- ²²(*a*) Facultad de Ciencias y Centro de Investigaciones, Universidad Antonio Nariño, Bogotá; (*b*) Departamento de Física, Universidad Nacional de Colombia, Bogotá; Colombia.
- ²³(*a*) Dipartimento di Fisica e Astronomia A. Righi, Università di Bologna, Bologna; (*b*) INFN Sezione di Bologna; Italy.
- ²⁴Physikalisches Institut, Universität Bonn, Bonn; Germany.
- ²⁵Department of Physics, Boston University, Boston MA; United States of America.
- ²⁶Department of Physics, Brandeis University, Waltham MA; United States of America.
- ²⁷(*a*) Transilvania University of Brasov, Brasov; (*b*) Horia Hulubei National Institute of Physics and Nuclear Engineering, Bucharest; (*c*) Department of Physics, Alexandru Ioan Cuza University of Iasi, Iasi; (*d*) National Institute for Research and Development of Isotopic and Molecular Technologies, Physics Department, Cluj-Napoca; (*e*) National University of Science and Technology Politehnica, Bucharest; (*f*) West University in Timisoara, Timisoara; (*g*) Faculty of Physics, University of Bucharest, Bucharest; Romania.
- ²⁸(*a*) Faculty of Mathematics, Physics and Informatics, Comenius University, Bratislava; (*b*) Department of Subnuclear Physics, Institute of Experimental Physics of the Slovak Academy of Sciences, Kosice; Slovak Republic.
- ²⁹Physics Department, Brookhaven National Laboratory, Upton NY; United States of America.
- ³⁰Universidad de Buenos Aires, Facultad de Ciencias Exactas y Naturales, Departamento de Física, y CONICET, Instituto de Física de Buenos Aires (IFIBA), Buenos Aires; Argentina.
- ³¹California State University, CA; United States of America.
- ³²Cavendish Laboratory, University of Cambridge, Cambridge; United Kingdom.
- ³³(*a*) Department of Physics, University of Cape Town, Cape Town; (*b*) iThemba Labs, Western Cape; (*c*) Department of Mechanical Engineering Science, University of Johannesburg, Johannesburg; (*d*) National Institute of Physics, University of the Philippines Diliman (Philippines); (*e*) University of South Africa, Department of Physics, Pretoria; (*f*) University of Zululand, KwaDlangezwa; (*g*) School of Physics, University of the Witwatersrand, Johannesburg; South Africa.
- ³⁴Department of Physics, Carleton University, Ottawa ON; Canada.
- ³⁵(*a*) Faculté des Sciences Ain Chock, Réseau Universitaire de Physique des Hautes Energies - Université Hassan II, Casablanca; (*b*) Faculté des Sciences, Université Ibn-Tofail, Kénitra; (*c*) Faculté des Sciences Semlalia, Université Cadi Ayyad, LPHEA-Marrakech; (*d*) LPMR, Faculté des Sciences, Université Mohamed Premier, Oujda; (*e*) Faculté des sciences, Université Mohammed V, Rabat; (*f*) Institute of Applied Physics, Mohammed VI Polytechnic University, Ben Guerir; Morocco.
- ³⁶CERN, Geneva; Switzerland.
- ³⁷Affiliated with an institute covered by a cooperation agreement with CERN.
- ³⁸Affiliated with an international laboratory covered by a cooperation agreement with CERN.
- ³⁹Enrico Fermi Institute, University of Chicago, Chicago IL; United States of America.
- ⁴⁰LPC, Université Clermont Auvergne, CNRS/IN2P3, Clermont-Ferrand; France.
- ⁴¹Nevis Laboratory, Columbia University, Irvington NY; United States of America.
- ⁴²Niels Bohr Institute, University of Copenhagen, Copenhagen; Denmark.
- ⁴³(*a*) Dipartimento di Fisica, Università della Calabria, Rende; (*b*) INFN Gruppo Collegato di Cosenza,

Laboratori Nazionali di Frascati; Italy.

⁴⁴Physics Department, Southern Methodist University, Dallas TX; United States of America.

⁴⁵Physics Department, University of Texas at Dallas, Richardson TX; United States of America.

⁴⁶National Centre for Scientific Research "Demokritos", Agia Paraskevi; Greece.

⁴⁷(^a) Department of Physics, Stockholm University; (^b) Oskar Klein Centre, Stockholm; Sweden.

⁴⁸Deutsches Elektronen-Synchrotron DESY, Hamburg and Zeuthen; Germany.

⁴⁹Fakultät Physik, Technische Universität Dortmund, Dortmund; Germany.

⁵⁰Institut für Kern- und Teilchenphysik, Technische Universität Dresden, Dresden; Germany.

⁵¹Department of Physics, Duke University, Durham NC; United States of America.

⁵²SUPA - School of Physics and Astronomy, University of Edinburgh, Edinburgh; United Kingdom.

⁵³INFN e Laboratori Nazionali di Frascati, Frascati; Italy.

⁵⁴Physikalisches Institut, Albert-Ludwigs-Universität Freiburg, Freiburg; Germany.

⁵⁵II. Physikalisches Institut, Georg-August-Universität Göttingen, Göttingen; Germany.

⁵⁶Département de Physique Nucléaire et Corpusculaire, Université de Genève, Genève; Switzerland.

⁵⁷(^a) Dipartimento di Fisica, Università di Genova, Genova; (^b) INFN Sezione di Genova; Italy.

⁵⁸II. Physikalisches Institut, Justus-Liebig-Universität Giessen, Giessen; Germany.

⁵⁹SUPA - School of Physics and Astronomy, University of Glasgow, Glasgow; United Kingdom.

⁶⁰LPSC, Université Grenoble Alpes, CNRS/IN2P3, Grenoble INP, Grenoble; France.

⁶¹Laboratory for Particle Physics and Cosmology, Harvard University, Cambridge MA; United States of America.

⁶²(^a) Department of Modern Physics and State Key Laboratory of Particle Detection and Electronics, University of Science and Technology of China, Hefei; (^b) Institute of Frontier and Interdisciplinary Science and Key Laboratory of Particle Physics and Particle Irradiation (MOE), Shandong University, Qingdao; (^c) School of Physics and Astronomy, Shanghai Jiao Tong University, Key Laboratory for Particle Astrophysics and Cosmology (MOE), SKLPPC, Shanghai; (^d) Tsung-Dao Lee Institute, Shanghai; (^e) School of Physics and Microelectronics, Zhengzhou University; China.

⁶³(^a) Kirchhoff-Institut für Physik, Ruprecht-Karls-Universität Heidelberg, Heidelberg; (^b) Physikalisches Institut, Ruprecht-Karls-Universität Heidelberg, Heidelberg; Germany.

⁶⁴(^a) Department of Physics, Chinese University of Hong Kong, Shatin, N.T., Hong Kong; (^b) Department of Physics, University of Hong Kong, Hong Kong; (^c) Department of Physics and Institute for Advanced Study, Hong Kong University of Science and Technology, Clear Water Bay, Kowloon, Hong Kong; China.

⁶⁵Department of Physics, National Tsing Hua University, Hsinchu; Taiwan.

⁶⁶IJCLab, Université Paris-Saclay, CNRS/IN2P3, 91405, Orsay; France.

⁶⁷Centro Nacional de Microelectrónica (IMB-CNM-CSIC), Barcelona; Spain.

⁶⁸Department of Physics, Indiana University, Bloomington IN; United States of America.

⁶⁹(^a) INFN Gruppo Collegato di Udine, Sezione di Trieste, Udine; (^b) ICTP, Trieste; (^c) Dipartimento Politecnico di Ingegneria e Architettura, Università di Udine, Udine; Italy.

⁷⁰(^a) INFN Sezione di Lecce; (^b) Dipartimento di Matematica e Fisica, Università del Salento, Lecce; Italy.

⁷¹(^a) INFN Sezione di Milano; (^b) Dipartimento di Fisica, Università di Milano, Milano; Italy.

⁷²(^a) INFN Sezione di Napoli; (^b) Dipartimento di Fisica, Università di Napoli, Napoli; Italy.

⁷³(^a) INFN Sezione di Pavia; (^b) Dipartimento di Fisica, Università di Pavia, Pavia; Italy.

⁷⁴(^a) INFN Sezione di Pisa; (^b) Dipartimento di Fisica E. Fermi, Università di Pisa, Pisa; Italy.

⁷⁵(^a) INFN Sezione di Roma; (^b) Dipartimento di Fisica, Sapienza Università di Roma, Roma; Italy.

⁷⁶(^a) INFN Sezione di Roma Tor Vergata; (^b) Dipartimento di Fisica, Università di Roma Tor Vergata, Roma; Italy.

⁷⁷(^a) INFN Sezione di Roma Tre; (^b) Dipartimento di Matematica e Fisica, Università Roma Tre, Roma; Italy.

- ⁷⁸(*a*) INFN-TIFPA; (*b*) Università degli Studi di Trento, Trento; Italy.
- ⁷⁹Universität Innsbruck, Department of Astro and Particle Physics, Innsbruck; Austria.
- ⁸⁰University of Iowa, Iowa City IA; United States of America.
- ⁸¹Department of Physics and Astronomy, Iowa State University, Ames IA; United States of America.
- ⁸²Istinye University, Sariyer, Istanbul; Türkiye.
- ⁸³(*a*) Departamento de Engenharia Elétrica, Universidade Federal de Juiz de Fora (UFJF), Juiz de Fora; (*b*) Universidade Federal do Rio De Janeiro COPPE/EE/IF, Rio de Janeiro; (*c*) Instituto de Física, Universidade de São Paulo, São Paulo; (*d*) Rio de Janeiro State University, Rio de Janeiro; (*e*) Federal University of Bahia, Bahia; Brazil.
- ⁸⁴KEK, High Energy Accelerator Research Organization, Tsukuba; Japan.
- ⁸⁵Graduate School of Science, Kobe University, Kobe; Japan.
- ⁸⁶(*a*) AGH University of Krakow, Faculty of Physics and Applied Computer Science, Krakow; (*b*) Marian Smoluchowski Institute of Physics, Jagiellonian University, Krakow; Poland.
- ⁸⁷Institute of Nuclear Physics Polish Academy of Sciences, Krakow; Poland.
- ⁸⁸Faculty of Science, Kyoto University, Kyoto; Japan.
- ⁸⁹Research Center for Advanced Particle Physics and Department of Physics, Kyushu University, Fukuoka ; Japan.
- ⁹⁰L2IT, Université de Toulouse, CNRS/IN2P3, UPS, Toulouse; France.
- ⁹¹Instituto de Física La Plata, Universidad Nacional de La Plata and CONICET, La Plata; Argentina.
- ⁹²Physics Department, Lancaster University, Lancaster; United Kingdom.
- ⁹³Oliver Lodge Laboratory, University of Liverpool, Liverpool; United Kingdom.
- ⁹⁴Department of Experimental Particle Physics, Jožef Stefan Institute and Department of Physics, University of Ljubljana, Ljubljana; Slovenia.
- ⁹⁵School of Physics and Astronomy, Queen Mary University of London, London; United Kingdom.
- ⁹⁶Department of Physics, Royal Holloway University of London, Egham; United Kingdom.
- ⁹⁷Department of Physics and Astronomy, University College London, London; United Kingdom.
- ⁹⁸Louisiana Tech University, Ruston LA; United States of America.
- ⁹⁹Fysiska institutionen, Lunds universitet, Lund; Sweden.
- ¹⁰⁰Departamento de Física Teórica C-15 and CIAFF, Universidad Autónoma de Madrid, Madrid; Spain.
- ¹⁰¹Institut für Physik, Universität Mainz, Mainz; Germany.
- ¹⁰²School of Physics and Astronomy, University of Manchester, Manchester; United Kingdom.
- ¹⁰³CPPM, Aix-Marseille Université, CNRS/IN2P3, Marseille; France.
- ¹⁰⁴Department of Physics, University of Massachusetts, Amherst MA; United States of America.
- ¹⁰⁵Department of Physics, McGill University, Montreal QC; Canada.
- ¹⁰⁶School of Physics, University of Melbourne, Victoria; Australia.
- ¹⁰⁷Department of Physics, University of Michigan, Ann Arbor MI; United States of America.
- ¹⁰⁸Department of Physics and Astronomy, Michigan State University, East Lansing MI; United States of America.
- ¹⁰⁹Group of Particle Physics, University of Montreal, Montreal QC; Canada.
- ¹¹⁰Fakultät für Physik, Ludwig-Maximilians-Universität München, München; Germany.
- ¹¹¹Max-Planck-Institut für Physik (Werner-Heisenberg-Institut), München; Germany.
- ¹¹²Graduate School of Science and Kobayashi-Maskawa Institute, Nagoya University, Nagoya; Japan.
- ¹¹³Department of Physics and Astronomy, University of New Mexico, Albuquerque NM; United States of America.
- ¹¹⁴Institute for Mathematics, Astrophysics and Particle Physics, Radboud University/Nikhef, Nijmegen; Netherlands.
- ¹¹⁵Nikhef National Institute for Subatomic Physics and University of Amsterdam, Amsterdam;

Netherlands.

¹¹⁶Department of Physics, Northern Illinois University, DeKalb IL; United States of America.

¹¹⁷(^a)New York University Abu Dhabi, Abu Dhabi;(^b)United Arab Emirates University, Al Ain; United Arab Emirates.

¹¹⁸Department of Physics, New York University, New York NY; United States of America.

¹¹⁹Ochanomizu University, Otsuka, Bunkyo-ku, Tokyo; Japan.

¹²⁰Ohio State University, Columbus OH; United States of America.

¹²¹Homer L. Dodge Department of Physics and Astronomy, University of Oklahoma, Norman OK; United States of America.

¹²²Department of Physics, Oklahoma State University, Stillwater OK; United States of America.

¹²³Palacký University, Joint Laboratory of Optics, Olomouc; Czech Republic.

¹²⁴Institute for Fundamental Science, University of Oregon, Eugene, OR; United States of America.

¹²⁵Graduate School of Science, Osaka University, Osaka; Japan.

¹²⁶Department of Physics, University of Oslo, Oslo; Norway.

¹²⁷Department of Physics, Oxford University, Oxford; United Kingdom.

¹²⁸LPNHE, Sorbonne Université, Université Paris Cité, CNRS/IN2P3, Paris; France.

¹²⁹Department of Physics, University of Pennsylvania, Philadelphia PA; United States of America.

¹³⁰Department of Physics and Astronomy, University of Pittsburgh, Pittsburgh PA; United States of America.

¹³¹(^a)Laboratório de Instrumentação e Física Experimental de Partículas - LIP, Lisboa;(^b)Departamento de Física, Faculdade de Ciências, Universidade de Lisboa, Lisboa;(^c)Departamento de Física, Universidade de Coimbra, Coimbra;(^d)Centro de Física Nuclear da Universidade de Lisboa, Lisboa;(^e)Departamento de Física, Universidade do Minho, Braga;(^f)Departamento de Física Teórica y del Cosmos, Universidad de Granada, Granada (Spain);(^g)Departamento de Física, Instituto Superior Técnico, Universidade de Lisboa, Lisboa; Portugal.

¹³²Institute of Physics of the Czech Academy of Sciences, Prague; Czech Republic.

¹³³Czech Technical University in Prague, Prague; Czech Republic.

¹³⁴Charles University, Faculty of Mathematics and Physics, Prague; Czech Republic.

¹³⁵Particle Physics Department, Rutherford Appleton Laboratory, Didcot; United Kingdom.

¹³⁶IRFU, CEA, Université Paris-Saclay, Gif-sur-Yvette; France.

¹³⁷Santa Cruz Institute for Particle Physics, University of California Santa Cruz, Santa Cruz CA; United States of America.

¹³⁸(^a)Departamento de Física, Pontificia Universidad Católica de Chile, Santiago;(^b)Millennium Institute for Subatomic physics at high energy frontier (SAPHIR), Santiago;(^c)Instituto de Investigación Multidisciplinario en Ciencia y Tecnología, y Departamento de Física, Universidad de La Serena;(^d)Universidad Andres Bello, Department of Physics, Santiago;(^e)Instituto de Alta Investigación, Universidad de Tarapacá, Arica;(^f)Departamento de Física, Universidad Técnica Federico Santa María, Valparaíso; Chile.

¹³⁹Department of Physics, University of Washington, Seattle WA; United States of America.

¹⁴⁰Department of Physics and Astronomy, University of Sheffield, Sheffield; United Kingdom.

¹⁴¹Department of Physics, Shinshu University, Nagano; Japan.

¹⁴²Department Physik, Universität Siegen, Siegen; Germany.

¹⁴³Department of Physics, Simon Fraser University, Burnaby BC; Canada.

¹⁴⁴SLAC National Accelerator Laboratory, Stanford CA; United States of America.

¹⁴⁵Department of Physics, Royal Institute of Technology, Stockholm; Sweden.

¹⁴⁶Departments of Physics and Astronomy, Stony Brook University, Stony Brook NY; United States of America.

- ¹⁴⁷Department of Physics and Astronomy, University of Sussex, Brighton; United Kingdom.
- ¹⁴⁸School of Physics, University of Sydney, Sydney; Australia.
- ¹⁴⁹Institute of Physics, Academia Sinica, Taipei; Taiwan.
- ¹⁵⁰^(a)E. Andronikashvili Institute of Physics, Iv. Javakhishvili Tbilisi State University, Tbilisi; ^(b)High Energy Physics Institute, Tbilisi State University, Tbilisi; ^(c)University of Georgia, Tbilisi; Georgia.
- ¹⁵¹Department of Physics, Technion, Israel Institute of Technology, Haifa; Israel.
- ¹⁵²Raymond and Beverly Sackler School of Physics and Astronomy, Tel Aviv University, Tel Aviv; Israel.
- ¹⁵³Department of Physics, Aristotle University of Thessaloniki, Thessaloniki; Greece.
- ¹⁵⁴International Center for Elementary Particle Physics and Department of Physics, University of Tokyo, Tokyo; Japan.
- ¹⁵⁵Department of Physics, Tokyo Institute of Technology, Tokyo; Japan.
- ¹⁵⁶Department of Physics, University of Toronto, Toronto ON; Canada.
- ¹⁵⁷^(a)TRIUMF, Vancouver BC; ^(b)Department of Physics and Astronomy, York University, Toronto ON; Canada.
- ¹⁵⁸Division of Physics and Tomonaga Center for the History of the Universe, Faculty of Pure and Applied Sciences, University of Tsukuba, Tsukuba; Japan.
- ¹⁵⁹Department of Physics and Astronomy, Tufts University, Medford MA; United States of America.
- ¹⁶⁰Department of Physics and Astronomy, University of California Irvine, Irvine CA; United States of America.
- ¹⁶¹University of Sharjah, Sharjah; United Arab Emirates.
- ¹⁶²Department of Physics and Astronomy, University of Uppsala, Uppsala; Sweden.
- ¹⁶³Department of Physics, University of Illinois, Urbana IL; United States of America.
- ¹⁶⁴Instituto de Física Corpuscular (IFIC), Centro Mixto Universidad de Valencia - CSIC, Valencia; Spain.
- ¹⁶⁵Department of Physics, University of British Columbia, Vancouver BC; Canada.
- ¹⁶⁶Department of Physics and Astronomy, University of Victoria, Victoria BC; Canada.
- ¹⁶⁷Fakultät für Physik und Astronomie, Julius-Maximilians-Universität Würzburg, Würzburg; Germany.
- ¹⁶⁸Department of Physics, University of Warwick, Coventry; United Kingdom.
- ¹⁶⁹Waseda University, Tokyo; Japan.
- ¹⁷⁰Department of Particle Physics and Astrophysics, Weizmann Institute of Science, Rehovot; Israel.
- ¹⁷¹Department of Physics, University of Wisconsin, Madison WI; United States of America.
- ¹⁷²Fakultät für Mathematik und Naturwissenschaften, Fachgruppe Physik, Bergische Universität Wuppertal, Wuppertal; Germany.
- ¹⁷³Department of Physics, Yale University, New Haven CT; United States of America.
- ^a Also Affiliated with an institute covered by a cooperation agreement with CERN.
- ^b Also at An-Najah National University, Nablus; Palestine.
- ^c Also at Borough of Manhattan Community College, City University of New York, New York NY; United States of America.
- ^d Also at Center for High Energy Physics, Peking University; China.
- ^e Also at Center for Interdisciplinary Research and Innovation (CIRI-AUTH), Thessaloniki; Greece.
- ^f Also at Centro Studi e Ricerche Enrico Fermi; Italy.
- ^g Also at CERN, Geneva; Switzerland.
- ^h Also at Département de Physique Nucléaire et Corpusculaire, Université de Genève, Genève; Switzerland.
- ⁱ Also at Departament de Física de la Universitat Autònoma de Barcelona, Barcelona; Spain.
- ^j Also at Department of Financial and Management Engineering, University of the Aegean, Chios; Greece.
- ^k Also at Department of Physics, California State University, Sacramento; United States of America.
- ^l Also at Department of Physics, King's College London, London; United Kingdom.

- m* Also at Department of Physics, Stanford University, Stanford CA; United States of America.
- n* Also at Department of Physics, Stellenbosch University; South Africa.
- o* Also at Department of Physics, University of Fribourg, Fribourg; Switzerland.
- p* Also at Department of Physics, University of Thessaly; Greece.
- q* Also at Department of Physics, Westmont College, Santa Barbara; United States of America.
- r* Also at Hellenic Open University, Patras; Greece.
- s* Also at Institutio Catalana de Recerca i Estudis Avancats, ICREA, Barcelona; Spain.
- t* Also at Institut für Experimentalphysik, Universität Hamburg, Hamburg; Germany.
- u* Also at Institute for Nuclear Research and Nuclear Energy (INRNE) of the Bulgarian Academy of Sciences, Sofia; Bulgaria.
- v* Also at Institute of Applied Physics, Mohammed VI Polytechnic University, Ben Guerir; Morocco.
- w* Also at Institute of Particle Physics (IPP); Canada.
- x* Also at Institute of Physics and Technology, Mongolian Academy of Sciences, Ulaanbaatar; Mongolia.
- y* Also at Institute of Physics, Azerbaijan Academy of Sciences, Baku; Azerbaijan.
- z* Also at Institute of Theoretical Physics, Ilia State University, Tbilisi; Georgia.
- aa* Also at Lawrence Livermore National Laboratory, Livermore; United States of America.
- ab* Also at National Institute of Physics, University of the Philippines Diliman (Philippines); Philippines.
- ac* Also at Technical University of Munich, Munich; Germany.
- ad* Also at The Collaborative Innovation Center of Quantum Matter (CICQM), Beijing; China.
- ae* Also at TRIUMF, Vancouver BC; Canada.
- af* Also at Università di Napoli Parthenope, Napoli; Italy.
- ag* Also at University of Colorado Boulder, Department of Physics, Colorado; United States of America.
- ah* Also at Washington College, Chestertown, MD; United States of America.
- ai* Also at Yeditepe University, Physics Department, Istanbul; Türkiye.
- * Deceased



Differential cross-sections for events with missing transverse momentum and jets measured with the ATLAS detector in 13 TeV proton–proton collisions

The ATLAS Collaboration

Measurements of inclusive, differential cross-sections for the production of events with missing transverse momentum in association with jets in proton–proton collisions at $\sqrt{s} = 13$ TeV are presented. The measurements are made with the ATLAS detector using an integrated luminosity of 140 fb^{-1} and include measurements of dijet distributions in a region in which vector-boson fusion processes are enhanced. They are unfolded to correct for detector resolution and efficiency within the fiducial acceptance, and are designed to allow robust comparisons with a wide range of theoretical predictions. A measurement of differential cross sections for the $Z \rightarrow \nu\nu$ process is made. The measurements are generally well-described by Standard Model predictions except for the dijet invariant mass distribution. Auxiliary measurements of the hadronic system recoiling against isolated leptons, and photons, are also made in the same phase space. Ratios between the measured distributions are then derived, to take advantage of cancellations in modelling effects and some of the major systematic uncertainties. These measurements are sensitive to new phenomena, and provide a mechanism to easily set constraints on phenomenological models. To illustrate the robustness of the approach, these ratios are compared with two common Dark Matter models, where the constraints derived from the measurement are comparable to those set by dedicated detector-level searches.

Contents

1	Introduction	3
2	ATLAS detector	4
3	Measured observables and fiducial phase spaces	4
3.1	Particle-level objects	5
3.2	Phase-space regions	5
3.3	Measured observables	6
4	Theoretical predictions and simulation	7
4.1	Fully simulated Standard Model samples	7
4.2	Standard Model predictions	8
4.3	Standard Model theory uncertainties	9
5	Event selection and reconstruction	10
5.1	Trigger selection	10
5.2	Reconstruction and offline selection	11
6	Background estimation	14
6.1	Non-collision background	14
6.2	Multijet background in the p_T^{miss} +jets selection	14
6.3	Background from misidentified photons and leptons in the auxiliary measurements	16
6.4	Contributions from other SM processes	18
7	Detector correction and systematic uncertainties	19
7.1	Unfolding procedure	19
7.2	Detector calibration, resolution and identification uncertainties	23
8	Results and discussion	26
8.1	p_T^{miss} measurements	26
8.2	$Z \rightarrow \nu\bar{\nu}$ measurement	27
8.3	Quantitative comparison to SM predictions	33
9	Implications for physics beyond the Standard Model	33
10	Conclusion	36

1 Introduction

A high priority goal of experiments at the Large Hadron Collider (LHC) is to establish to what extent the Standard Model (SM) remains valid at the accessible energies above the electroweak symmetry-breaking scale. If the measured data agree with the SM, it is important to both quantify that agreement and to interpret it in terms of limits on physics beyond the SM (BSM). If the data are inconsistent with SM predictions, this could constitute evidence for BSM physics.

One key reason to suspect BSM physics exists is the astrophysical and cosmological evidence for the existence of Dark Matter (DM) [1–3]. Many BSM theories postulate a DM particle that may be produced at the LHC, giving rise to missing transverse momentum (p_T^{miss}) in proton–proton (pp) collision events, over and above that expected from SM processes producing neutrinos. Searches have exploited this signature to set limits on DM models [4, 5]. In addition, the cross-section for the principal SM process producing large p_T^{miss} , in which a Z boson decaying to neutrinos recoils against jets, has recently been measured by the CMS Collaboration [6]. The ATLAS Collaboration has also recently produced a measurement of the Z -boson invisible width which exploits this signature [7].

The main purpose of this analysis is to make precise, detector-corrected measurements of p_T^{miss} produced in association with jets, inclusively and with as little model dependence as possible. This is the first such measurement made using the full 140 fb^{-1} of integrated luminosity collected by the ATLAS detector in Run 2 of the LHC. The results are presented alongside auxiliary measurements, made in the same phase space, of the transverse momentum of the hadronic system, p_T^{recoil} , recoiling against isolated leptons, and photons. This allows modelling effects and major uncertainties to cancel when a ratio of cross-sections is taken. This complements and extends the approach of taking ratios presented in a previous study [8]. The results are compared quantitatively to state-of-the-art SM predictions.

The measurements also serve another purpose. Contributions from DM production would typically *not* cancel out in the cross-section ratios, making them sensitive to DM and other BSM signatures. A secondary objective of the paper is therefore to demonstrate that the measurements can be used for searches and setting constraints, with only a minor penalty in sensitivity, and without the need to repeat complex and time-consuming detector simulation. This means they can be readily reinterpreted to gain information about models, and model parameter points, beyond those considered here.

Cross-sections differential in p_T^{miss} and p_T^{recoil} , and in several jet observables, are defined in fiducial phase spaces designed to probe different aspects of the SM. The dominant SM contribution to the p_T^{miss} -plus-jets final state comes from Z bosons produced in association with jets and decaying into neutrinos, $Z(\rightarrow \nu\nu) + \text{jets}$; other contributions come from leptonic W boson decays where the lepton does not enter the fiducial phase space. Diboson and triboson production can also provide small contributions. All relevant kinematic selections are included in the fiducial phase space definition, and detector effects, including instrumental sources of p_T^{miss} , are corrected for using an unfolding procedure. Motivated by ease of comparison to SM predictions, and to validate the consistency of the approach, a measurement of $Z \rightarrow \nu\nu$ production is also made, where the contributions from other SM processes are treated as backgrounds and subtracted before unfolding.

For the BSM interpretation, two example models are chosen to illustrate the constraints that can be extracted from the measurements. First, a common simplified DM model [9], which was searched for previously in this final state by ATLAS [4] using the same data sample as the current analysis, and by CMS [5]. Second, a more complicated model that introduces an additional Higgs doublet and a pseudoscalar that couples to DM [10, 11] and has also been searched for previously [12, 13] is considered.

The paper is structured as follows. After a brief description of the experimental apparatus in Section 2, the cross-sections and observables to be measured are defined in Section 3. The theoretical predictions, Monte Carlo event generation, and detector simulation are discussed in Section 4. The details of the event selection and object reconstruction are given in Section 5, and the treatment of backgrounds is described in Section 6. The correction for detection effects, and the associated systematic uncertainties, are described in Section 7. Results are reported in Section 8, and interpreted in terms of SM and BSM calculations in Section 9. Finally, the conclusions are summarised.

2 ATLAS detector

The ATLAS experiment [14] at the LHC is a multipurpose particle detector with a forward–backward symmetric cylindrical geometry and a near 4π coverage in solid angle.¹ It consists of an inner tracking detector surrounded by a thin superconducting solenoid providing a 2 T axial magnetic field, electromagnetic and hadronic calorimeters, and a muon spectrometer. The inner tracking detector covers the pseudorapidity range $|\eta| < 2.5$. It consists of silicon pixel, silicon microstrip, and transition radiation tracking detectors. Lead/liquid-argon (LAr) sampling calorimeters provide electromagnetic (EM) energy measurements with high granularity within the region $|\eta| < 3.2$. A steel/scintillator-tile hadronic calorimeter covers the central pseudorapidity range ($|\eta| < 1.7$). The endcap and forward regions are instrumented with LAr calorimeters for EM and hadronic energy measurements up to $|\eta| = 4.9$. The muon spectrometer surrounds the calorimeters and is based on three large superconducting air-core toroidal magnets with eight coils each. The field integral of the toroids ranges between 2.0 and 6.0 T m across most of the detector. The muon spectrometer includes a system of precision tracking chambers up to $|\eta| = 2.7$ and fast detectors for triggering up to $|\eta| = 2.4$. The luminosity is measured mainly by the LUCID-2 [15] detector, which is located close to the beam pipe. A two-level trigger system is used to select events [16]. The first-level trigger is implemented in hardware and uses a subset of the detector information to accept events at a rate below 100 kHz. This is followed by a software-based trigger that reduces the accepted event rate to 1 kHz on average depending on the data-taking conditions. A software suite [17] is used in data simulation, in the reconstruction and analysis of real and simulated data, in detector operations, and in the trigger and data acquisition systems of the experiment.

3 Measured observables and fiducial phase spaces

The differential cross-sections to be measured are defined within a fiducial phase space, specified in terms of requirements applied to final state particles. These requirements are chosen to closely reflect the acceptance of the detector, thus reducing the need for theory-based extrapolations.

¹ ATLAS uses a right-handed coordinate system with its origin at the nominal interaction point (IP) in the centre of the detector and the z -axis along the beam pipe. The x -axis points from the IP to the centre of the LHC ring, and the y -axis points upwards. Polar coordinates (r, ϕ) are used in the transverse plane, ϕ being the azimuthal angle around the z -axis. The pseudorapidity is defined in terms of the polar angle θ as $\eta = -\ln \tan(\theta/2)$. Angular distance is measured in units of $\Delta R \equiv \sqrt{(\Delta\eta)^2 + (\Delta\phi)^2}$.

3.1 Particle-level objects

At particle-level, the following objects are defined. Charged leptons (electrons or muons) are required to be prompt, in that they do not originate from the decay of a hadron. Leptons from the decay of prompt τ -leptons are allowed. The four-momenta of prompt photons within a cone of $\Delta R = 0.1$ is added to the four-momentum of the lepton to produce a ‘dressed’ lepton.

Photons are required to be prompt and isolated. The photon isolation is chosen such that it mimics the isolation requirement at the detector level, requiring that the transverse energy in a cone around the photon be less than $(2.45 \text{ GeV} + 0.044 \times p_T)$ where p_T is the transverse momentum of the photon in GeV.

For the inclusive p_T^{miss} measurement, the particle-level p_T^{miss} is defined as the magnitude of a vector, which is the negative two-momentum (x, y components) sum of all visible final-state particles with $|\eta| < 5$, excluding muons with $|\eta| > 2.5$ or $p_T < 7 \text{ GeV}$. For the auxiliary measurements, p_T^{recoil} is defined in a similar way, but the identified charged dressed leptons, and isolated photons, are excluded from the sum. Thus, for the inclusive p_T^{miss} measurements, $p_T^{\text{recoil}} \equiv p_T^{\text{miss}}$. For the measurement of $Z \rightarrow \nu\nu$, the particle-level p_T^{miss} is defined as the summed p_T of the neutrinos from the decayed boson.

Jets are defined using the anti- k_t jet algorithm [18, 19] with a radius parameter of 0.4. All stable final-state particles are used as input to the jet algorithm, except that for the inclusive p_T^{miss} measurement neutrinos and other invisible particles as well as muons are excluded, while for the $Z \rightarrow \nu\nu$ measurement invisible particles as well as the boson decay products are excluded. Any jets that contain a hadron consistent with coming from the decay of a prompt τ -lepton are classified as hadronically decaying τ -leptons.

Jets are removed if the jet momentum direction is closer than $\Delta R < 0.2$ to any lepton. Next, all leptons that are within $\Delta R = 0.4$ of a jet are discarded. If no leptons remain, jets are removed if the jet momentum direction is closer than $\Delta R < 0.2$ to any photon. These conditions mirror closely the overlap removal of reconstructed objects described in Section 5.2.

3.2 Phase-space regions

Measurements are made in six regions defined in terms of the number and flavour of leptons or the presence of a photon: p_T^{miss} +jets, e +jets, $2e$ +jets, μ +jets, 2μ +jets and γ +jets. The first of these is the primary measurement, while the others are auxiliary measurements with similar topologies to the primary, which constrain the uncertainties through correlations across the regions. The similarity in topologies is ensured by using the same event selection, and by the fact that for the signal regions, $p_T^{\text{recoil}} \equiv p_T^{\text{miss}}$. Table 3.2 summarises the selections that define these regions. The differences between the pseudorapidity requirements between electrons and muons arise from their different experimental acceptance, and the desire to minimise extrapolation during the unfolding procedure.

For each of these regions, two sub-regions are defined by further selection on the jet content of the hadronic recoil system, the ≥ 1 jet and vector boson fusion (VBF) regions. These are designed to enhance the sensitivity to particular classes of BSM physics involving DM, such as those that are studied in Section 9. Table 3.2 summarises the selections that define these sub-regions.

Table 1: Requirements defining the six principal phase-space regions of the measurement. For the inclusive p_T^{miss} measurement, $p_T^{\text{miss}} \equiv p_T^{\text{recoil}}$. In the $Z \rightarrow \nu\nu$ measurement, it corresponds to the p_T of the Z boson. Transverse mass, m_T , is defined as $\sqrt{2p_T p_T^{\text{recoil}}(1 - \cos(\phi))}$ where p_T is the lepton transverse momentum and ϕ is the angle between the lepton and p_T^{recoil} .

Attribute	$p_T^{\text{miss}}+\text{jets}$	$e+\text{jets}$	$2e+\text{jets}$	$\mu+\text{jets}$	$2\mu+\text{jets}$	$\gamma+\text{jets}$
Lepton or photon rapidity	–	$ y \leq 1.37$ or $1.52 \leq y \leq 2.47$		$ y \leq 2.5$		$ y \leq 1.37$ or $1.52 \leq y \leq 2.47$
Leading lepton or photon p_T [GeV]	–	> 30	> 80	> 7	> 80	> 160
Sub-leading lepton p_T [GeV]	–	–	> 7	–	> 7	–
Dilepton mass, $m_{\ell\ell}$ [GeV]	–	–	$m_{\ell\ell} \in (66, 116)$	–	$m_{\ell\ell} \in (66, 116)$	–
(Additional) muons	None with $p_T > 7$ GeV, $ \eta < 2.5$					
(Additional) electrons	None with $p_T > 7$ GeV, $ \eta < 1.37$ or $1.52 < \eta < 2.47$					
m_T [GeV]	–	$m_T \in (30, 100)$	–	–	–	–
p_T^{miss} [GeV]	> 200	> 60	–	–	–	–
p_T^{recoil} [GeV]	> 200	> 200	> 200	> 200	> 200	> 200

Table 2: A summary of the fiducial selections applied to the hadronic recoil system to define the subregions of the measurement. The veto on ‘in-gap jets’ is applied to jets with a rapidity lying between the rapidities of the leading and the sub-leading jets.

Attribute	≥ 1 jet	VBF
$\Delta\phi$ (jet, p_T^{miss})	> 0.4	for four leading p_T jets
Hadronic τ -lepton	None with $p_T > 20$ GeV, $ \eta < 1.37$ or $1.52 < \eta < 2.47$	
Leading jet p_T [GeV]	> 120	> 80
Sub-leading jet p_T [GeV]	–	> 50
Leading jet $ y $	< 2.4	< 4.4
Sub-leading jet $ y $	–	< 4.4
Dijet invariant mass m_{jj} [GeV]	–	> 200
$ \Delta y_{jj} $	–	> 1
In-gap jets	–	None with $p_T > 30$ GeV

3.3 Measured observables

Differential cross-sections as a function of several observables are measured in the regions defined in Section 3.2. The p_T^{recoil} distribution, defined in Section 3.1 is measured for all selections in all regions. It is sensitive both to the SM processes involving neutrinos (predominantly $Z \rightarrow \nu\nu$) and to potential contributions from BSM invisible particles. In addition, in the VBF phase-space region the m_{jj} and $\Delta\phi_{jj}$ distributions are also measured, where m_{jj} is the invariant mass of the two leading jets and $\Delta\phi_{jj} = \phi_1 - \phi_2$ is the signed difference in azimuthal angle between the jets ordered in their rapidities such that $y_1 > y_2$.

This observable probes the CP structure of the VBF interaction [20]. The m_{jj} distribution is sensitive to the presence of potential new particles decaying into jets. All these distributions are available from HEPData [21] and implemented in Rivet [22].

4 Theoretical predictions and simulation

Monte Carlo (MC) event generators capable of simulating the complete final state of collision events are used as input to a detailed GEANT4 [23, 24] simulation of the ATLAS detector [25]. The output from this is passed through the same reconstruction and analysis chain as the data, to evaluate efficiencies and the migration matrix used to unfold for detector effects, and to make measurements at particle level. Given the inclusive nature of the measurement, several important processes contribute, requiring a wide range of sophisticated configurations for the event generators. The generated samples are also reweighted as appropriate to improve their modelling of the data (with a negligible effect on the unfolded results).

Event generator predictions are also used for comparison with the final particle-level results. Since the data are corrected for detector effects, new predictions can be used directly for the comparisons, without the full detector simulation. For this reason, the predictions used for the final comparison are in some cases improved versions that embody the most accurate and precise predictions available at the time of publication. The samples employed for each use case are described in turn below.

4.1 Fully simulated Standard Model samples

Events containing a single W or Z/γ^* boson in association with jets (V +jets), as well as prompt single-photon production, were simulated with the SHERPA 2.2.1 [26] event generator. In this set-up, the OPENLOOPS [27, 28] and COMIX [29] libraries provided matrix elements with next-to-leading-order (NLO) virtual quantum chromodynamics (QCD) corrections for up to two jets, and matrix elements accurate to leading-order (LO) for up to four jets. The default SHERPA parton shower [30] based on Catani–Seymour dipoles and the cluster hadronisation model [31] was used. This used the parameters developed by the SHERPA authors for this version based on the NNPDF3.0_{NNLO} parton distribution function (PDF) set [32]. The NLO matrix elements of a given jet multiplicity were matched to the parton shower using a colour-exact variant of the MC@NLO algorithm [33]. Different jet multiplicities were then merged into an inclusive sample using an improved CKKW matching procedure [34, 35] that was extended to NLO accuracy using the MEPS@NLO prescription [33–36]. The merging scale was set to $Q_{\text{cut}} = 20$ GeV. For single-photon production a dynamic merging scale [37] of 20 GeV was used, and photons were required to be isolated according to a smooth-cone isolation criterion [38]. In all cases, matrix elements were matched with the SHERPA parton shower [30] using the MEPS@NLO prescription.

Electroweak (EW) production of two forward jets in association with a W or Z/γ^* boson and up to one additional parton emission at LO accuracy was simulated using SHERPA 2.2.11 [39]. The Catani–Seymour dipole-based parton shower was used, matched with the matrix element using the MEPS@LO prescription, and a cluster hadronisation model was employed. Diagrams arising from semileptonic diboson production, with one boson decaying hadronically, were removed in a gauge-invariant manner by requiring a colour-singlet exchange in the t -channel, also known as the ‘VBF approximation’.

Samples of leptonically decaying dibosons were simulated with SHERPA 2.2.2 [26], with a similar set-up to the V +jets samples [40]. The QCD corrections to matrix elements at NLO accuracy were provided

by the OPENLOOPS library [27, 28]. The parameters and PDFs were the same as for the V +jets samples. Triboson production was simulated with the same set-up as the fully leptonically decaying diboson samples. Semileptonically decaying diboson samples were simulated with almost the identical set-up to the fully leptonic ones, except that the SHERPA 2.2.1 [26] generator was used.

The production of on-shell $t\bar{t}$ events was modelled using the POWHEG BOX [41–44] v2 generator at NLO with the NNPDF3.0_{NLO} [32] PDF set and the h_{damp} parameter² set to $1.5 m_t$ [45]. The events were interfaced to PYTHIA 8.230 [46] using the A14 set of tuned parameters (tune) [47] and the NNPDF2.3_{LO} PDF set [48]. The NLO $t\bar{t}$ inclusive production cross-section was corrected to the theory prediction at next-to-next-to-leading order (NNLO) in QCD including the resummation of next-to-next-to-leading logarithmic (NNLL) soft-gluon terms calculated using TOP++2.0 [49–55].

Single-top tW associated production was modelled using the POWHEG BOX [42–44, 56] v2 generator at NLO in QCD in the five flavour scheme with the NNPDF3.0_{NLO} [32] PDF set. The diagram removal scheme [57] was used to treat the overlap with top-quark pair production [45]. Single-top t -channel and s -channel production were modelled using the POWHEG BOX [42–44, 58, 59] v2 generator at NLO in QCD in the four- and five-flavour schemes with the corresponding NNPDF3.0_{NLO} [32] PDF sets respectively. The matrix element generators were interfaced to PYTHIA 8.230 [46] using the A14 tune [47] and the NNPDF2.3_{LO} PDF set. The inclusive cross-sections were corrected to the theory prediction calculated at NLO in QCD with HATHOR v2.1 [60, 61].

Additional pile-up collisions were overlaid, based on soft QCD processes simulated with PYTHIA 8.186 using the NNPDF2.3_{LO} PDF set and the A3 tune [62] over the original hard-scattering events. Additional weighting factors are applied to the fully simulated samples to improve the modelling, including a factor to reproduce the distribution of the average number of interactions per bunch crossing observed in the data.

4.2 Standard Model predictions

For the particle-level predictions, no data-driven scale factors are applied, and pile-up events are not added. The settings described above are also valid for the SM predictions used for comparison with the final result, with the following exceptions.

A particle-level prediction for top-quark pair production was produced with SHERPA 2.2.11, using NLO-accurate matrix elements for up to one additional parton, and LO-accurate matrix elements for up to four additional partons calculated with the Comix [29] and OPENLOOPS 2 [27, 28, 63, 64] libraries. They were matched with the SHERPA parton shower [30] using the MEPS@NLO prescription [33–36].

The diboson and single EW boson MC samples were also replaced with calculations produced with SHERPA 2.2.11 and OPENLOOPS 2 [27, 28, 63, 64]. In the case of V +jets production, the matrix-element-level description of additional emissions was extended up to five jets at LO. The PDF4LHC PDF set [65] was used, supplemented with quantum electrodynamics (QED) effects from LUXQED [66]. To improve the description of W +jets and Z +jets processes, these MC predictions were then reweighted to account for higher-order EW corrections. The reweighting procedure was based on parton-level predictions for W/Z +jets production from Ref. [67], and included NLO EW corrections [68–71] supplemented by Sudakov logarithms at two loops [72–75].

² The h_{damp} parameter controls the transverse momentum p_T of the first additional emission beyond the leading-order Feynman diagram in the parton shower and therefore regulates the high- p_T emission against which the $t\bar{t}$ system recoils.

In the ≥ 1 jet region, an alternative prediction was obtained by extending the reweighting procedure to include NNLO QCD corrections [76–79] from Ref. [67]. These corrections were provided separately for W +jets, $Z(\rightarrow \ell\ell)$ +jets (where $\ell = e$ or μ) and $Z(\rightarrow \nu\nu)$ +jets processes, as a function of the vector-boson p_T , to improve the description of the measured Z boson p_T distribution [80]. The reweighting procedure took into account the difference between the intrinsic perturbative accuracy of the generated MC samples and the provided parton-level calculations. In addition, the reweighting was extended in the VBF region to include NLO EW corrections [81] for Vjj production, which were provided separately for each decay channel as a function of dijet invariant mass and azimuthal difference between the tagging jets.

In the VBF region, an additional prediction for V +jets was obtained using the high energy jets (HEJ) framework [82, 83]. HEJ calculates the tower of leading logarithmic QCD corrections in the ratio of the partonic centre-of-mass energy and transverse momentum squared, s/p_T^2 , to all orders in the strong coupling α_s , for all relevant SM processes. These corrections are relevant in regions of phase space where jets span a large range of rapidity or where pairs of jets have a large invariant mass. The framework includes the matching of these corrections to both tree-level high-multiplicity matrix elements point-by-point in phase space, and to NLO corrections for distributions. The framework was implemented in a partonic event generator [84].

4.3 Standard Model theory uncertainties

The uncertainties in the SM predictions are estimated following the prescription developed in Ref. [67]. Uncertainties on pure QCD higher-order corrections in the SM processes are estimated by varying the renormalisation and factorisation scales by factors of 0.5 and 2. The difference between the nominal prediction and the envelope of the seven possible versions (the cases where both the renormalisation and factorisation scales vary upwards or downward at the same time are excluded) is assigned as an uncertainty, denoted by $\delta^{(1)}K_{(N)NLO}$. To account for possible differences in the shape of the p_T^V and m_{jj} spectra between low and high scales in the V +jets channels, additional uncertainties $\delta^{(2)}K_{(N)NLO}$ and $\delta^{(4)}K_{(N)NLO}$ are constructed from conservative shape distortions of the nominal scale-uncertainty band as a function of p_T^V and m_{jj} , respectively. The distortion is given by $(x^2 - x_0^2)/(x^2 + x_0^2)$ where x_0 is the midpoint of the observable of interest in logarithmic space, namely 650 GeV and 1300 GeV for p_T^V and m_{jj} , respectively. As discussed in Ref. [67], this shape uncertainty increases the scale uncertainties by a factor of up to $\sqrt{2}$.

All pure-QCD systematic uncertainties are taken as correlated between observable bins as well as weak bosons and their decay channels, but uncorrelated between different processes, including EW V +jets production. Following the approach in [67], the residual level of decorrelation between the decay modes is estimated from the difference between the differential higher-order K -factors for W +jets production and $Z(\rightarrow \ell\ell)$ +jets and $Z(\rightarrow \nu\nu)$ +jets production relative to their average and assigned as an additional uncertainty, denoted by $\delta^{(3)}K_{(N)NLO}$. A similar uncertainty is estimated for EW Vjj production using the higher-order K -factors calculated in Ref. [81]. The uncertainty band for the HEJ predictions in the VBF region is estimated from the envelope of the seven variations of the renormalisation and factorisation scales by factors of 0.5 and 2.

Pure EW uncertainties in V +jets and Vjj production arise predominantly from unknown high- p_T EW effects due to truncation of the perturbative series. This uncertainty is estimated through naive Sudakov exponentiation, denoted $\delta^{(1)}\kappa_{nNLOEW}$, which is taken to be correlated between the weak boson decay channels. In the case of V +jets production, an additional conservative uncertainty $\delta^{(2)}\kappa_{nNLOEW}$ is assigned, given by 5% of the absolute full NLO EW correction, which is taken to be uncorrelated between the

weak boson decay channels. Moreover, an uncertainty in the Sudakov approximation at two-loop level in V +jets production is estimated by assigning an additional uncertainty $\delta^{(3)}\kappa_{\text{nNLOEW}}$, given by the difference between the next-to-leading logarithmic Sudakov approximation and the naive exponentiation of the full NLO EW correction, which is also taken to be uncorrelated between the weak boson decay channels. All pure EW systematic uncertainties are taken to be correlated across bins in a given observable.

An uncertainty in unknown non-factorising mixed QCD and EW effects is estimated from the difference between the additive and multiplicative combination of QCD and EW higher-order corrections, denoted δK_{mix} . This systematic uncertainty is taken to be correlated between bins in a given observable and between weak boson decay channels.

PDF uncertainties are estimated by using the sum in quadrature of the set of independent PDF4LHC+LUXQED Hessian eigenvectors. The α_s uncertainty is estimated from ± 0.001 shifts around the nominal value of 0.118 in the PDF sets.

To evaluate systematic uncertainties, prompt single-photon production was also simulated using the PYTHIA 8.186 [85] generator. Events were simulated using tree-level matrix elements for γ +jet final states and LO QCD dijet events, with the inclusion of initial- and final-state parton showers.

The PYTHIA simulation includes LO γ +jet events from both the direct processes (the ‘hard’ $qg \rightarrow q\gamma$ and $q\bar{q} \rightarrow g\gamma$ component) and the photon bremsstrahlung in LO QCD dijet events. The bremsstrahlung component was modelled by final-state QED radiation arising from calculations of all $2 \rightarrow 2$ QCD processes. The NNPDF2.3LO PDF set was used in the matrix element calculation, the parton shower, and the simulation of the multi-parton interactions. The samples include a simulation of the underlying event with parameters set according to the A14 tune [47]. The Lund string model [86, 87] was used for the description of the fragmentation into hadrons.

Finally, the uncertainty in the interference between top-quark pair production and tW production is estimated by taking the difference relative to the prediction where the nominal tW sample is replaced with a version employing an alternative diagram subtraction scheme [57].

5 Event selection and reconstruction

The data used in this analysis were collected with the ATLAS detector in pp collisions at $\sqrt{s} = 13$ TeV during the Run 2 data-taking from 2015 to 2018. After applying necessary selections to ensure good detector operation conditions, a total integrated luminosity of 140 fb^{-1} is available. The uncertainty in the combined Run 2 integrated luminosity is 0.83% [88], obtained using the LUCID-2 detector [15] for the primary luminosity measurements. The average number of inelastic pp collisions per bunch crossing is 33.7 in the data sample considered. Most of these pp collisions have an interaction vertex that is consistent with the beam-spot envelope.

5.1 Trigger selection

Events for the primary $p_{\text{T}}^{\text{miss}}$ measurement were selected by the two-stage trigger system [16] using the transverse momentum imbalance within the calorimeter system [89] and requiring hadronic jets in the final state. Due to increasing number of simultaneous pp interactions in different years of the Run 2 data-taking the minimum $p_{\text{T}}^{\text{miss}}$ threshold of the triggers used increased from 70 GeV to 120 GeV over the data-taking

period to suppress the impact of the energy contributed by pile-up collisions on the rate of accepted events. The algorithm used to calculate this p_T^{miss} also varied for the same reason. All p_T^{miss} triggers used in the analysis were fully efficient in events for which the offline $p_T^{\text{miss}} > 200$ GeV.

Since muons deposit very little energy in the calorimeters, the calorimeter-based p_T^{miss} triggers also selected events with high- p_T muons in the final-state. These events are used for the single-muon and double-muon auxiliary measurements. For events with $p_T^{\text{recoil}} > 200$ GeV, this trigger selection was 100% efficient for the subset of those events with a muon with $p_T \geq 30$ GeV.

A combination of low- and high- p_T single-electron triggers was used to select events for the single-electron and double-electron auxiliary measurements. Two single-electron triggers, with a minimum p_T threshold of 24 (26) GeV in 2015–2016 (2017–2018) and Tight electron identification criteria [90], selected events in the low- p_T region. In the high- p_T region, where the rate of single electron triggers is low compared to that which can be accommodated by the trigger system bandwidth, several triggers with less restrictive electron identification were employed to increase the trigger efficiency. Events satisfying the low- or high- p_T threshold trigger were retained, with an efficiency of around 97% for electrons with $p_T \geq 80$ GeV. The details of the electron trigger combination procedure are summarised in Ref. [90]. The simulation reproduces the single-electron trigger efficiency measured in data to within 5% for electrons with $p_T < 60$ GeV, and to better than 1% in the high- p_T region. The residual mismodelling is corrected for by reweighting simulated events using data-driven scale factors. Both statistical and systematic uncertainties in the derived trigger scale factors are propagated to the measured observables.

Events selected for the single photon auxiliary measurement are required to have a photon candidate with a minimum p_T of 120 (140) GeV at the trigger-level satisfying the Loose photon identification criteria [90] in 2015 (2016–2018). In the p_T range above 200 (300) GeV a trigger with only a p_T selection was used in addition (logical ‘OR’) to improve the efficiency of the trigger selection during 2015 (2016–2018) data-taking. The photon triggers were fully efficient in the single photon auxiliary measurement region phase space.

5.2 Reconstruction and offline selection

Events selected by the trigger system undergo a number of offline reconstruction and calibration steps before they can be used for the analysis.

Candidate interaction vertices are reconstructed by associating at least two reconstructed tracks with $p_T > 500$ MeV to a common origin along the pp collision axis [91]. Events with at least one such vertex are selected. In the case of multiple candidate vertices in an event, the primary vertex is defined to be one with the highest sum of squared transverse momenta of associated tracks.

Reconstructed tracks in the ID and clusters of energy deposits in the EM calorimeter are used as inputs to the reconstruction of electrons and photons. The electron and photon reconstruction [92] uses three-dimensional clusters of energy depositions (topo-clusters) built from topologically connected EM and hadronic calorimeter cells [93] to restore energy from bremsstrahlung photons or from electrons from photon conversions. The transition region between the barrel and endcaps of the EM calorimeter, $1.37 < |\eta| < 1.52$, is excluded. The electron candidates are reconstructed from topo-clusters matched to ID tracks. These tracks are refitted to account for energy losses due to bremsstrahlung. Topo-clusters not matched to any track or matched to conversion vertices are reconstructed as unconverted or converted photon candidates, respectively. The conversion vertices are formed from one or two tracks that are

consistent with a massless particle decaying within the ID volume. Electron candidates in the e +jets ($2e$ +jets) region are required to satisfy the **Tight** (**Medium**) identification working point (WP) [94]. The efficiency to select **Tight** (**Medium**) electron candidates reaches a plateau of 88% (93%) for $p_T > 80$ GeV electrons. To reject electrons from heavy-flavour decays the **HighPtCaloOnly** isolation selection [92], with 92%–98% efficiency depending on the electron p_T , is applied.

Photon candidates with shower shape variables corresponding to the **Tight** identification working point and satisfying **Tight** isolation criteria are accepted for the single-photon auxiliary measurement [92]. This combination of identification and isolation requirements provides a good rejection of photons from non-prompt backgrounds while maintaining high efficiency for prompt photon selection. The electron or photon candidate energy is calibrated using energy depositions in the calorimeters and track measurements in the ID [92]. The precision of the energy calibration of electrons (photons) is better than 0.2% (0.5%), verified in situ using $Z \rightarrow \ell\ell$ and $Z \rightarrow \ell\ell\gamma$ events.

The muon reconstruction uses track segments in the ID and MS, as well as calorimeter information. Muon candidates are formed by matching the MS and ID tracks and performing a combined fit that makes use of corresponding MS and ID hits, and accounts for the energy depositions in the calorimeter cells along the muon candidate trajectory. Identification requirements for muons are formed using selections on track quality and the compatibility between the ID and MS tracks. Muon candidates in single-muon and two-muon auxiliary measurements are required to satisfy the **Medium** [95] identification WP. The efficiency for identifying **Medium** muons exceeds 98% for the selection criteria applied in this analysis. To reject muons produced in semileptonic decays of hadrons, the **FixedCutLoose** [96] requirement is imposed on the activity around muon candidates in the muon auxiliary measurement. The **FixedCutLoose** efficiency for selecting a prompt muon ranges from 93% in the low- p_T region to 100% for muons with $p_T > 50$ GeV. The muon momentum scale is calibrated using $J/\psi \rightarrow \mu\mu$ and $Z \rightarrow \mu\mu$ events. The precision of the muon momentum measurements changes from 0.05% for muons within $|\eta| = 1$ to 0.15% for muons in the $|\eta| \sim 2.5$ forward region.

Events with no **Loose** electrons or muons [92, 95] (regardless of their isolation conditions) are selected for the primary p_T^{miss} measurement. These criteria ensure a very high purity of the signal event sample, since the **Loose** identification WPs select at least 92% of prompt fiducial electrons or photons and more than 99% of prompt fiducial muons. These requirements also reject events with electrons or muons coming from τ -lepton decays. Hadronically decaying τ -leptons are reconstructed using jets identified by the anti- k_t jet algorithm, with the radius parameter $R = 0.4$, as a seed, which is then associated to tracks consistent with τ -lepton production at the interaction vertex [97]. They are then identified as τ -leptons by a recurrent neural network (RNN) algorithm [98]. The **Loose** identification WP provides between 87% and 79% identification efficiency for τ -leptons while providing a multijet background rejection factor of 21 to 90 respectively depending on the number of associated tracks. Events with at least one hadronically decaying τ -lepton satisfying the **Loose** selection are removed.

Jets are reconstructed using the anti- k_t jet algorithm with the radius parameter $R = 0.4$ using an algorithmic combination of the calorimeter energy depositions and the charged-particle tracks. First, calorimeter cells are grouped into topo-clusters using a nearest-neighbour algorithm [93] that exploits the significance of the cell energy compared to the noise expected in the pile-up environment for each year of running. The direction of each topo-cluster receives an origin correction to account for the primary vertex position that is different in every event. The jet measurements are further improved using the particle flow (PFlow) algorithm [99], which replaces the charged particle calorimeter energy deposits by the momenta of the tracks measured in the ID that are associated with the topo-clusters. The PFlow jets have better energy and angular resolution, as well as reduced sensitivity to pile-up, compared to jets reconstructed from calorimeter

information only. To suppress signals arising from calorimeter noise and other non-collision backgrounds, reconstructed jets are required to satisfy a Loose identification selection [100]. This selection has a better than 99.5% efficiency for keeping jets from pp collisions. Due to the large instantaneous luminosity, the jets reconstructed in one bunch crossing could originate from different pp collisions. To suppress jets arising from vertices other than the primary collision vertex a jet-vertex tagging algorithm (JVT) [101, 102], based on a combination of track-based variables, is used. Jets with $p_T < 60$ GeV in the central $|\eta| < 2.5$ region are accepted only if the Tight JVT selection is satisfied. In addition, a Tight requirement from the forward jet vertex-tagging algorithm (fJVT) is used to reject pile-up jets in the forward region $|\eta| \geq 2.5$.

The jet four-momentum measurement is calibrated using information from both simulation and data [103]. First, the jet energy is corrected for pile-up contamination. An MC-based absolute jet energy correction is used to restore the energy and direction of the jet to that at the particle-level. Next, the global sequential calibration is employed to remove the dependence of the jet response on the energy distribution inside the jet, and the fluctuations of the shower development in the calorimeter. Finally a residual in situ correction, determined from Z +jets, γ +jet and multijet events, is applied to recover the remaining differences between data and simulation. Over the rapidity range considered, the jet energy is measured with 1%–3.5% accuracy depending on transverse momentum.

The missing transverse momentum vector p_T^{miss} (p_T^{recoil} in the events with prompt leptons or photons) is calculated as the magnitude of the vector sum of the transverse momenta of all particles produced in the event [104]. Detector signals associated with identified physics objects constitute a hard term, while the signals that are not part of these objects form a soft term. The p_T^{miss} reconstruction uses energy deposits from the calorimeter, muons reconstructed in the muon spectrometer, and tracks from the inner detector.

The p_T^{miss} is then given by $p_T^{\text{miss}} = \sqrt{(p_x^{\text{miss}})^2 + (p_y^{\text{miss}})^2}$, where $p_{x(y)}^{\text{miss}}$ are calculated as follows:

$$p_{x(y)}^{\text{miss}} = p_{x(y)}^{\text{miss},e} + p_{x(y)}^{\text{miss},\gamma} + p_{x(y)}^{\text{miss},\tau} + p_{x(y)}^{\text{miss},\mu} + p_{x(y)}^{\text{miss},\text{jets}} + p_{x(y)}^{\text{miss},\text{soft}} \quad (1)$$

where each term is calculated as the negative sum of the calibrated reconstructed objects, projected onto the x and y directions. The soft term, $p_{x(y)}^{\text{miss},\text{soft}}$, is calculated from tracks associated with the primary vertex but not to any of the high- p_T objects.

For the calculation of p_T^{recoil} in the auxiliary measurements, the same expression is used, but the identified prompt leptons or photons are excluded.

Events involving τ -leptons can enter the signal region if the τ -lepton is not reconstructed. Conversely, in the auxiliary measurement regions, it is possible for events where a jet is misreconstructed as a τ -lepton to affect the $p_{x(y)}^{\text{miss}}$ calculation. In principle, if this effect is not accounted for it could lead to biases when correlating the regions. However, τ -lepton reconstruction is found to be well modelled across all the measured regions.

Since physics objects are reconstructed independently of each other, there is a possibility that the same detector signals are used to build multiple jets, photons or leptons. To avoid double-counting of particle level physics objects, the following procedure is employed. First, leptonically decaying τ -leptons closer than $\Delta R = 0.2$ to an electron or muon are discarded. Second, electrons that share the same ID track with a muon are rejected. Third, jets are removed if the jet momentum direction is closer than $\Delta R < 0.2$ to any electron candidate. In turn, all electrons that are within $\Delta R = 0.4$ of a jet are discarded. Similarly, jets are discarded if they are within $\Delta R = 0.2$ of a muon and have less than three associated tracks, while muons within $\Delta R = 0.4$ of a jet are rejected. Finally, jets that are within $\Delta R = 0.2$ of a hadronically decaying

τ -lepton are removed. If a lepton is removed by this procedure, the event is still considered for other measurement regions with fewer or no leptons.

6 Background estimation

Two categories of background contribute to all the measurements made: non-collision backgrounds, produced by beam–gas or cosmic rays events or calorimeter noise, and reducible backgrounds, which arise when a miscalibration or a misidentification of physics objects leads to an artificially large missing transverse momentum or a spurious particle candidate. In addition, in the $Z \rightarrow \nu\nu$ measurement, contributions from other SM processes that satisfy the true event selection and therefore cannot be distinguished from $Z \rightarrow \nu\nu$ events within the fiducial region are treated as an irreducible background. In this section the background estimation methods are briefly described.

6.1 Non-collision background

Muons produced away from the proton–proton collision but in-time with it can create significant energy depositions in the calorimeter that can be reconstructed as hadronic jets, and thus lead to events with a single jet and a large p_T^{miss} signature. Such muons can be created by the cosmic-ray showers, or by interactions upstream of the ATLAS detector between the beam and the LHC collimators, or residual gas in the beam pipe. The azimuthal angle distribution of the fake jets they produce has a characteristic shape, with pronounced peaks at $\phi = 0$ and $\phi = \pi$. Moreover, these muons enter the calorimeter earlier than jets from the interaction point, and so have very different timing properties. The non-collision background contribution is strongly reduced by the identification requirements applied to the leading jet in event. The residual contribution from this background source is evaluated using a data-driven approach that exploits the differences in time between the signal jets produced in the collision vertex and the non-collision background jets, and is subtracted. This amounts to a few thousand events over the course of the data-taking period. The difference between the subtracted and non-subtracted sample is taken as the uncertainty and propagated through to the final results.

6.2 Multijet background in the p_T^{miss} +jets selection

Jet production processes containing no prompt p_T^{miss} can contribute to the event yield in the primary measurements when jets are mis-reconstructed or mis-calibrated, giving rise to fake p_T^{miss} . In addition, decays of heavy flavour hadrons among the jet constituents may produce neutrinos that can generate the p_T^{miss} . In such cases the p_T^{miss} vector will typically be aligned with the direction of the jet, and the $\Delta\phi(\text{jet}, p_T^{\text{miss}}) > 0.4$ requirement removes most of this type of background. However, the p_T^{miss} +jets selection will contain a residual multijet background, since in such cases the p_T^{miss} can receive contributions from several jets and the resulting p_T^{miss} direction may not align with any one of them. The probability to reconstruct a large p_T^{miss} in any given multijet event is rather low, but the jet production cross-section is large. This implies that a simulation-based approach would require a very large simulated event sample, with an extremely accurate modelling of hadron production and calorimeter performance, especially in the tails of the distributions. These considerations mandate a data-driven method.

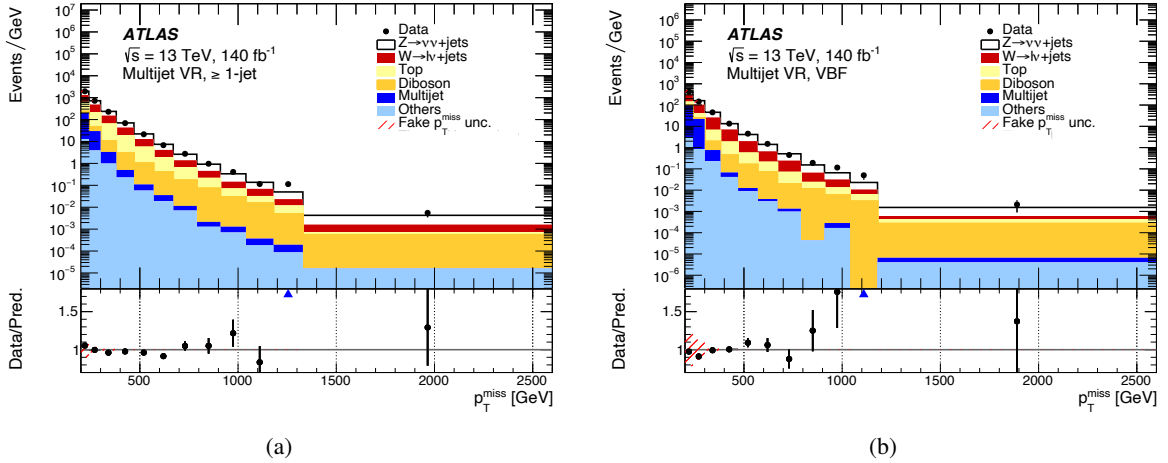


Figure 1: The event yield in the multijet background validation region as a function of p_T^{miss} for the (a) ≥ 1 jet selection and (b) VBF selection. Points denote the data, and different SM backgrounds are shown as histograms. The hatched band shows the full uncertainty assigned to the multijet estimate, which, since it represents a very small contribution to the final event sample and is subject to statistical variations due to the nature of the evaluation, is conservatively taken to be 100% of the estimated yield. The vertical lines represent the statistical uncertainty. The bottom panels show the ratios of the data to the predictions; the blue triangle indicate values which are out of the display range.

Reference [105] contains a detailed description of the jet smearing method used to estimate the multijet background contribution in the primary measurements. A high-statistics sample of low- p_T^{miss} events with well-measured hadron jets is collected using a set of inclusive jet triggers with different p_T^{jet} thresholds. A set of ‘pseudodata’ events is created by fluctuating the jet energies in these events using a function, constrained using data, that models the detector response to jets. Each fluctuation is considered as a separate event; the altered four-momenta of the jets are stored and the p_T^{miss} vector is recalculated. This approach produces pseudodata events with fake p_T^{miss} populating a range up to about 2 TeV.

The distribution of the multijet background in each differential cross-section measured is taken from the pseudodata distributions after applying the ≥ 1 jet or VBF event selection as appropriate, while the normalisations are obtained from the fit to data in a dedicated multijet background-enriched control region, defined using the $p_T^{\text{miss}} + \text{jets}$ event selection as given in Table 3.2, but with the requirement on the azimuthal angle between the jet direction and p_T^{miss} vectors inverted i.e., $\Delta\phi(\text{jet}, p_T^{\text{miss}}) \leq 0.3$.

Events with $0.3 < \Delta\phi(\text{jet}, p_T^{\text{miss}}) < 0.4$ satisfying the $p_T^{\text{miss}} + \text{jets}$ requirements but with the p_T^{miss} selection relaxed to 130 GeV (as low as possible considering trigger thresholds) are used to verify the multijet background estimation procedure. In this region, where the multijet background contributes approximately four times more events than the other SM processes, very good agreement is observed between the data and predictions. A similar region without the relaxed p_T^{miss} requirement, which is closer to the kinematic regime probed by this analysis, is also tested. Figure 1 shows the distribution of events in this validation region as a function of p_T^{miss} . Although the multijet background is not the dominant contributor to the yield in this validation region, it represents a significant fraction of the first few bins, where its inclusion leads to a good agreement between prediction and data. The multijet component in these validation regions is approximately an order of magnitude more important than in the signal region. There is a very good agreement between the prediction and data.

The multijet background contribution in the $p_T^{\text{miss}}+\text{jets}$ event selection in the ≥ 1 jet region is smaller than 1% for $p_T^{\text{recoil}} \leq 300$ GeV and falls steeply as p_T^{miss} increases. In the VBF region the multijet background contribution is around 1%–2% in the $m_{jj} < 2$ TeV region, and is negligible in the high- m_{jj} range.

6.3 Background from misidentified photons and leptons in the auxiliary measurements

The main source of background in the electron and photon auxiliary measurements comes from jets that are misidentified as leptons or photons. This can occur due to fluctuations in jet formation, or in the development of hadronic showers in the calorimeter, leading to an apparently large amount of EM energy. In conjunction with inefficiencies in the inner tracker, this can lead to energy depositions that are reconstructed as a photon or an electron. Jets containing heavy flavour hadrons that decay into final states including a muon are the main source of the non-prompt muon background. The yields of such ‘fake’ photons and leptons are heavily suppressed by the reconstruction algorithms, while the remaining contributions are removed using a set of data-driven techniques described below.

6.3.1 Jet-photon misidentification contribution to the $\gamma+\text{jets}$ selection

Multijet production is the dominant source of background in the $\gamma+\text{jets}$ auxiliary measurement. The **Tight** photon identification WP [92] together with the **Tight** requirement on the photon isolation energy strongly suppress the jet-photon misidentification. A data-driven two-dimensional side-band method [106, 107] is used to determine the shape and the normalisation of the residual photon misidentification background.

For this, four samples (A, B, C and D) are selected by splitting the **Tight** (A, B) and non-**Tight** (C, D) photon samples into **isolated** (A, C) and non-**isolated** (B, D) samples. Background-enriched samples of non-**Tight** photons are collected by requiring the photon to satisfy the **LoosePrime4** and to simultaneously fail to satisfy the **Tight** identification criteria. The **LoosePrime4** WP has a relaxed selection on the photon shower-shape properties that is unconnected to the photon isolation conditions, meaning the background in the four sub-regions can be treated as being uncorrelated. The yield N_A of background events in the $\gamma+\text{jets}$ region is determined by interpolating the measured event yields in the other three control regions, $N_A = N_B \times \frac{N_C}{N_D}$. The effect of leakage of signal photons into the control regions is determined from the simulation.

In most parts of the phase space the contribution of the jet-photon background is around 2%–3%. It increases to 4% in the $p_T^{\text{miss}} \leq 300$ GeV region, while in the $m_{jj} \leq 400$ GeV range up to 5% of events are from the photon misidentification.

6.3.2 Misidentified electrons in the $e+\text{jets}$ selection

Multijet events may satisfy the electron identification and isolation requirements because of the presence of semileptonic heavy-flavour decays, photon conversions, or hadrons inside jets being misidentified as electrons. This background is evaluated using a data-driven matrix method [108] that exploits the fact that prompt electrons (P) are better isolated in comparison to background electrons (B).

The number of electrons that satisfy the **Tight** selection, N_T , and which satisfy the **Loose** but fail to satisfy the **Tight** selection, $N_{!T}$, can be expressed in terms of the efficiency ϵ_P (ϵ_B) with which prompt (background) electrons that satisfy the **Loose** selection also satisfy the **Tight** selection as:

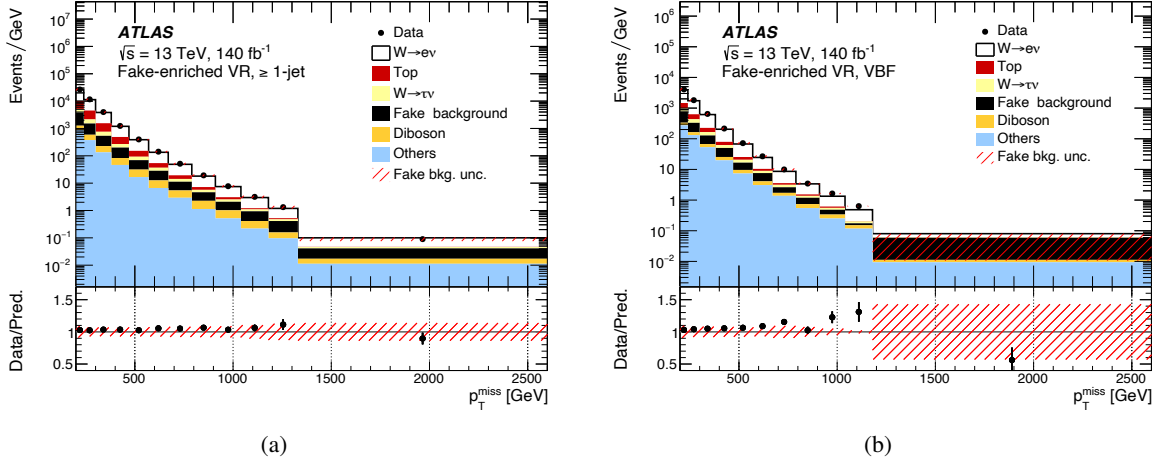


Figure 2: The event yield in the e +jets background validation region as a function of p_T^{miss} for the (a) ≥ 1 jet selection and (b) VBF selection. Points denote data, and estimated backgrounds are shown as histograms. The hatched band shows the full uncertainty in the fake-lepton yields (described in Sec. 7.2) and vertical the lines represent the statistical uncertainty. The bottom panels show the ratios of the data to the predictions.

$$\begin{pmatrix} N_T \\ N_{!T} \end{pmatrix} = \begin{pmatrix} \epsilon_P & \epsilon_B \\ 1 - \epsilon_P & 1 - \epsilon_B \end{pmatrix} \begin{pmatrix} N_P \\ N_B \end{pmatrix}, \quad (2)$$

where N_P (N_B) is the number of prompt (background) electrons. Solving this matrix equation, the number of background electrons in data that satisfy the **Tight** requirements can be obtained using event yields measured in data as:

$$\epsilon_B N_B = N_T^{\text{Bkg}} = \frac{\epsilon_B}{\epsilon_P - \epsilon_B} ((\epsilon_P - 1) N_T + \epsilon_P N_{!T}). \quad (3)$$

The ϵ_P efficiency is estimated from simulation binned in electron p_T and η . It changes from 85% to 95% as the electron p_T increases from 100 GeV to 600 GeV, where it reaches a plateau.

The ϵ_B efficiency is determined from data in a dedicated control region with the nominal e +jets requirements on the m_T and p_T^{miss} inverted to enhance the background electron contribution, and the p_T^{recoil} requirement removed. The events with genuine prompt electrons in this region are subtracted by using the simulation. The resulting ϵ_B efficiency is measured in bins of electron p_T and η . It decreases rapidly from 15% for electrons with p_T around 50 GeV to about 1% in the $p_T \geq 500$ GeV region. Combining the measured ϵ_P and ϵ_B efficiencies, the multijet background in the e +jets auxiliary measurement is found to be less than 5% in the $p_T^{\text{recoil}} < 500$ GeV region, while it increases up to almost 20% in the $p_T^{\text{recoil}} > 1500$ GeV range.

This estimate of the background contribution from misidentified electrons is validated using the e +jets event selection but without a requirement on m_T or p_T^{miss} . Figure 2 shows the distributions of events passing this modified selection as a function of p_T^{miss} . The fake electron background contributes a significantly larger proportion of the total yield in these validation regions compared with the auxiliary measurement regions. Very good agreement between data and prediction is seen after accounting for the fake background.

6.3.3 Non-prompt lepton background in the μ +jets, 2μ +jets and $2e$ +jets auxiliary measurements

Heavy-flavour hadron decays with a muon in the final state are the dominant source of muon misidentification in multijet events. The relatively low branching ratio for muon-channel hadronic decays, together with a high efficiency for identifying prompt muons, leads to a very high purity in the single-muon and dimuon event samples, allowing the use of the ‘fake-factor’ method. A similar argument (high purity of the dielectron sample) implies that the same method can also be used in the $2e$ +jets auxiliary measurement.

The fake-factor method is a simplification of Eq. (2). It relies on the quality of the simulation in describing the detector response to a prompt lepton. Accordingly, the number of non-prompt leptons satisfying the **Tight** lepton identification, N_T^{Bkg} , can be estimated as:

$$N_T^{\text{Bkg}} = \frac{\epsilon_B}{1 - \epsilon_B} (N_{!T} - N_{!T}^{\text{P}}), \quad (4)$$

where $N_{!T}$ is the yield of **Loose** leptons that fail to satisfy the **Tight** identification WP observed in data and $N_{!T}^{\text{P}}$ is the number of prompt leptons satisfying **Loose** but failing the **Tight** lepton identification determined in the simulation.

The fraction of fake leptons satisfying the selection ϵ_B is measured in data using a dedicated sample of events containing a pair of leptons with different flavour but the same sign charge. A small fraction of events in this sample can be attributed to true prompt lepton production in the two-boson or $t\bar{t}$ processes, while the rest are fakes. The prompt lepton contribution is accounted for using the simulation. As a function of lepton p_T , ϵ_B for muons is flat at 5% up to around 30 GeV, after which it increases up to 55% at 1 TeV. The same ϵ_B is used in both single-muon and dimuon auxiliary measurements. The fake muon background in the μ +jets (2μ +jets) event selection is around 5% (<1%).

Similarly, ϵ_B for the electron definition in the $2e$ +jets region is measured as a function of electron p_T . It is found to be 14% for 7 GeV electrons and steadily increases up to 31% for 110 GeV electrons. Fake electrons are predominantly at low p_T , and due to the analysis selection these are generally accompanied by a high p_T electron, where the fake rate is low. Therefore the estimate of non-prompt electron background for $2e$ +jets events is found to be relatively small, and does not exceed 1%.

6.4 Contributions from other SM processes

SM processes with single or double electroweak bosons in the final-state, as well as single top-quark and $t\bar{t}$ production, can contribute to the measured observables, for example when one or two final-state leptons are produced outside of the analysis p_T or η acceptance or are not reconstructed because of detector inefficiencies or a poor lepton isolation due to underlying event or pile-up activity around the final-state lepton.

In the inclusive p_T^{miss} and p_T^{recoil} measurements, events from these sources that satisfy the fiducial phase-space selection are treated as signal, and instrumental effects are corrected for later. In the $Z \rightarrow \nu\nu$ measurement, they are treated as irreducible backgrounds, and are accounted for with a semi-data-driven approach: the shapes of the distributions are taken from the SM predictions, while the normalisations are extracted from fits to data using a set of control regions defined by adding a lepton requirement to the other p_T^{miss} selection criteria. A summary of the SM contributions and their relative importance in various signal regions of the analysis is given in Table 6.4. The level of contribution varies strongly with measurement region. The photon auxiliary region contains >99% γ +jets events, and the two-lepton

auxiliary measurements are expected to consist of around 95% Z boson production events. Due to this very high purity, both the shape and normalisation of the top-quark and multi-boson contributions in these regions are taken directly from the corresponding simulation.

Table 3: The relative contributions of SM processes to the p_T^{miss} +jets and auxiliary measurements event selections. The contributions are calculated using the MC simulation.

Production process	Final-state event selection					
	p_T^{miss} +jets	$2e$ +jets	2μ +jets	e +jets	μ +jets	γ +jets
$Z \rightarrow \nu\nu$ + jets	55%	–	–	–	–	–
$Z \rightarrow ee$ + jets	–	94%	–	–	–	–
$Z \rightarrow \mu\mu$ + jets	–	–	95%	–	2%	–
$W \rightarrow e\nu$ + jets	6%	–	–	68%	–	–
$W \rightarrow \mu\nu$ + jets	9%	–	–	–	67%	–
$W \rightarrow \tau\nu$ + jets	20%	–	–	5%	7%	–
γ + jets	–	–	–	–	–	>99%
Top	7%	3%	2%	25%	21%	–
Multi-boson	3%	3%	3%	2%	3%	<1%

The normalisations of the $W \rightarrow \tau\nu$ and top-quark background distributions are determined in a combined fit to the W and top-background control regions. The fit is performed separately in the electron and muon channels for each ≥ 1 jet and VBF event selection. The scale-factors for the top-quark background are found to be around 0.70–0.78, while the $W \rightarrow \tau\nu$ distributions are rescaled by factors of 1.10–1.12. The background normalisation factors in different phase-space regions and τ -lepton decay channels agree with each other within statistical and systematic errors in the background estimation procedure.

The normalisations of the $W \rightarrow e\nu, W \rightarrow \mu\nu, W \rightarrow \tau\nu$ and top-quark contributions to the p_T^{miss} +jets event selection are extracted in a simultaneous fits to data in control regions for the ≥ 1 jet and VBF event selections separately. As a result, the W production contributions in the p_T^{miss} +jets event selection are rescaled by factors ranging from 1.04 to 1.13, depending of the phase-space region and the W boson leptonic decay channel. The top-quark background distributions scale-factors are 0.97–0.98 in both the ≥ 1 jet and VBF regions.

For the inclusive measurement, rescaled contributions are used to construct the simulated sample for unfolding. For the $Z \rightarrow \nu\nu$ measurement, they are subtracted from the data before unfolding.

7 Detector correction and systematic uncertainties

The data are corrected for detector effects so that they are presented in terms of particle-level objects, as defined in Section 3.1.

7.1 Unfolding procedure

An efficiency correction and an iterative Bayesian unfolding technique are used to correct the data and obtain particle-level differential cross-sections. The technique accounts for biases from the *a priori*

unknown shape of the true distribution by iterating the unfolding after reweighting the input distributions to the corrected data from the previous iteration. The optimal number of iterations is determined by balancing the fact that fewer iterations results in a stronger bias from the input prior (which is treated as a systematic uncertainty), whilst increasing the number of iterations increases the statistical uncertainty. Two iterations proves to be an optimal number for all measured distributions.

The inputs to the unfolding procedure are:

- **Migration matrix.** Events in a specific bin at particle level can migrate to a different bin in the reconstructed distribution, due to finite detector resolution. The migration matrix maps the true distribution onto the reconstructed distribution using events satisfying both the particle- and detector-level selections.
- **Reconstruction matching efficiency.** Due to the efficiency and acceptance of the detector, only a fraction of particle-level events are reconstructed within the target phase space. The reconstruction efficiency accounts for this and is defined as the ratio of simulated events that satisfy both the particle- and detector-level selections to all events satisfying the particle-level selection, as a function of the particle-level value of the observable being considered.
- **Fiducial fraction.** Due to the finite resolution of the detector, events that do not satisfy the particle-level selection can still satisfy the detector-level selection and be included in the detector-level distribution. The fiducial fraction accounts for this and is defined as the ratio of simulated events satisfying both the particle- and detector-level selections to those that satisfy only the detector-level selection, as a function of the detector-level value of the observable being considered.
- **Purity.** This quantity encapsulates the size of migrations between bins for events as a function of detector-level values of the observable being considered. It is defined as the fraction of the entries in a detector-level bin that are in the same bin at particle level.
- **Stability.** This quantity encapsulates the size of migrations between bins for events as a function of particle-level values of the observable being considered. It is defined as the fraction of the entries in a particle-level bin that are in the same bin at reconstruction level.

The binning of each distribution is defined so that each bin is expected to contain at least expected 20 reconstructed events, with a purity of at least 60%.

Figure 3 shows, as an example, the migration matrices for p_T^{miss} in the p_T^{miss} +jets and p_T^{recoil} in the γ +jets region both for the ≥ 1 jet phases space, while Figure 4 shows the matching efficiency, fiducial fraction, purity and stability for p_T^{recoil} for all auxiliary measurements in the ≥ 1 jet phase space.

The efficiency is lowest for the e +jets region, due to the requirements applied to the real p_T^{miss} and transverse mass. The highest efficiency is seen in the p_T^{miss} +jets region, which has no leptons to reconstruct. The fiducial fraction is lowest in the p_T^{miss} +jets region, due to contributions from W +jets events with a particle-level lepton that is within the fiducial acceptance. These fail to satisfy the particle-level lepton veto, but satisfy the reconstruction-level lepton veto due to inefficiencies in reconstructing the lepton. The migration matrices and purity plots are similar between all regions as the migration between p_T^{miss} bins depends primarily on the hadronic recoil. The same qualitative features are present in the p_T of the leading jet in the VBF phase space (not shown).

Several sources of systematic uncertainty in the particle-level measurements are considered:

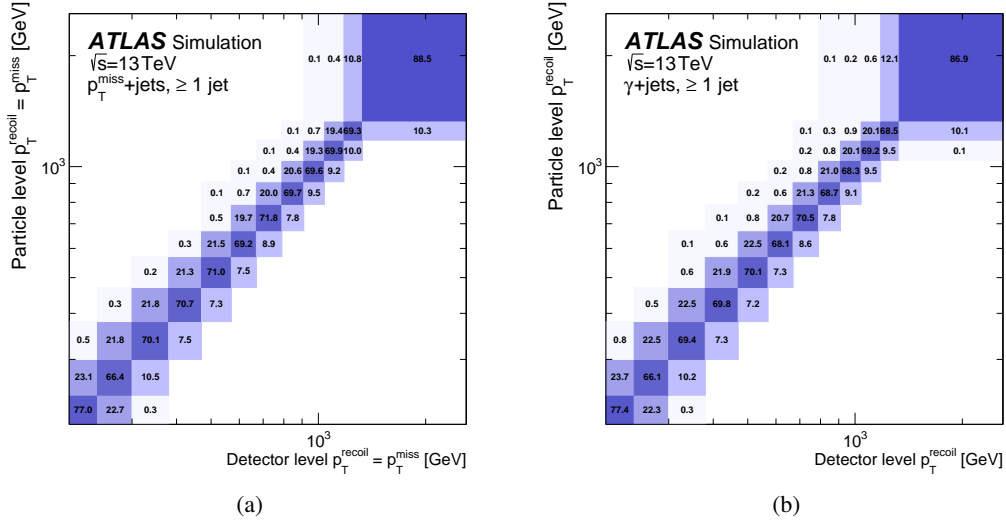
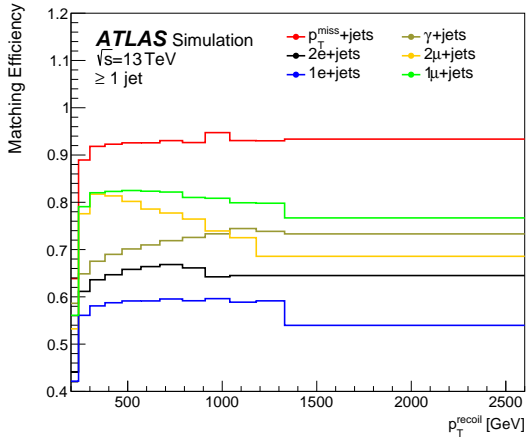


Figure 3: Migration matrices for (a) the p_T^{miss} in the $p_T^{\text{miss}}+\text{jets}$ region and (b) p_T^{recoil} in $\gamma+\text{jets}$ region, the ≥ 1 jet phase space, constructed for all processes that enter the fiducial phase space.

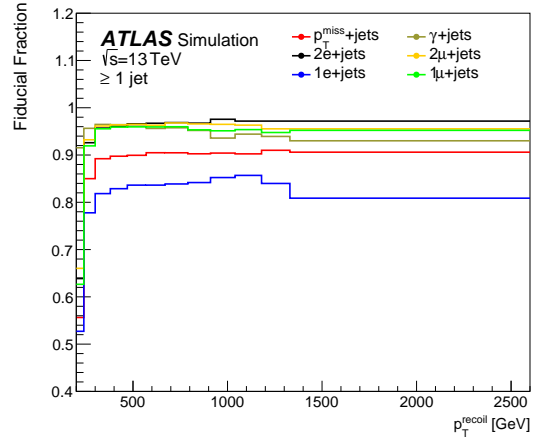
Hidden variables: While the iterative unfolding handles biases from the assumed prior for the distribution being unfolded, the unfolded result may still be influenced by the (mis)modelling of other ‘hidden’ event variables, especially if they form part of the selection. This is studied by reweighting simulated events at particle level so that the reweighted reconstructed distribution of the hidden variable matches the data. The variables considered are the leading-jet and leading-lepton kinematics, the number of jets, and the invariant mass of the dilepton system. Differences in the unfolded results with and without this additional weighting are taken as uncertainties, although they are below the percent level.

Migrations into the fiducial phase space: The events that satisfy the selection criteria defining the fiducial phase space (Table 3.2) at reconstruction-level are not identical to those that satisfy at particle-level. If this difference, or the underlying distributions for each variable that is used in the selection, is not well modelled then the migrations in and out of the phase space will not be properly corrected for in the unfolding. For all observables in all regions, comparisons of data and simulation are made, and in each case the requirement in question is relaxed in order to study the behaviour of the observable below the selection value. Simulated events are reweighted such that the reconstructed distribution matches the data. The changes to the measurement caused by this reweighting are negligible.

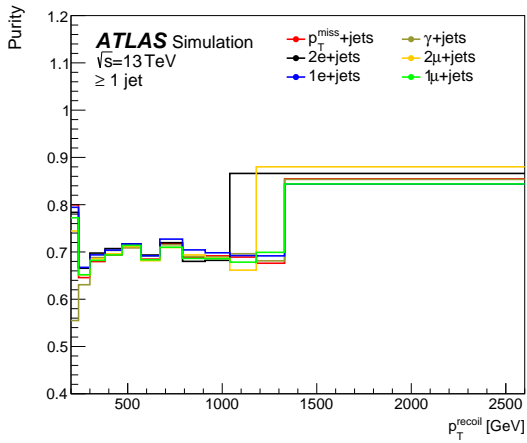
Signal injection tests: Although the unfolding procedure and fiducial definition are designed to minimise dependence on the simulated distributions, a residual bias may be present due to the absence of BSM effects from the samples used for unfolding, while such physics may be present in the data. To test whether this is the case, various BSM processes are injected into the simulated samples, which are then treated as pseudodata and unfolded with nominal SM simulation. Three samples of Higgs boson events decaying invisibly were used, with three different Higgs boson masses (75 GeV, 125 GeV and 750 GeV), thus emulating some very extreme Higgs-to-invisible BSM scenarios. The test is repeated for p_T^{miss} in the ≥ 1 jet phase space using a model with s -channel production of a DM particle (χ) via a spin-1 axial-vector



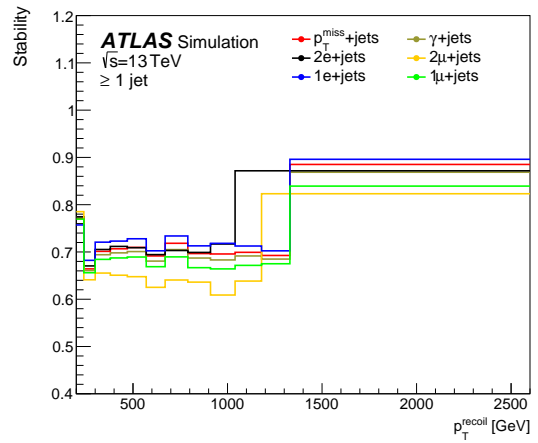
(a)



(b)



(c)



(d)

Figure 4: (a) Matching efficiency, (b) fiducial fraction, (c) purity and (d) stability for p_T^{recoil} , in the $p_T^{\text{miss}}+\text{jets}$, $\gamma+\text{jets}$, $e+\text{jets}$, $\mu+\text{jets}$, $2e+\text{jets}$, $2\mu+\text{jets}$ regions of the ≥ 1 jet phase space, constructed for all processes that enter the fiducial phase space. The purity and stability are high at high values of p_T^{recoil} because of the large bin widths dictated by the requirement that there be at least 20 events in each bin.

mediator A , for $m_\chi = 1$ GeV with $m_A = 50$ GeV and 700 GeV, and $m_\chi = 355$ GeV and $m_A = 700$ GeV, as well as spin-0 pseudoscalar mediator with $m_\chi = 1$ GeV and $m_A = 50$ GeV. The maximum bias even for any of these scenarios is 10%, seen at large p_T^{miss} , and all the models introducing bias are so extreme that if they were present in reality, the discrepancy would already be clearly seen in the detector-level data, before unfolding. No additional source of systematic uncertainty is therefore added from this source.

Sample composition variations For the measurement of the p_T^{miss} cross-sections, the simulated samples used in the unfolding include all contributing SM processes; the mixture of these processes is constrained by applying the normalisation factors discussed in Section 6.4. Uncertainties are derived by varying the composition within the uncertainties in these normalisation factors. The derived uncertainties are then propagated through the unfolding to the final measurement. SM processes involving top quarks are among those whose contribution is varied. Events originating from these processes are enriched in the presence of b -quarks. This uncertainty therefore also ensures that the resulting measurement can be used safely when comparing to predictions with increased b -quark activity.

For the measurement of $Z \rightarrow \nu\nu$ cross-sections, the contributions from non- $Z \rightarrow \nu\nu$ SM processes are subtracted before unfolding, with the amount subtracted being constrained using both the high- p_T^{miss} measurement region and the control regions. The simulated sample used in the unfolding then includes only $Z \rightarrow \nu\nu$ processes. The subtraction uncertainties are propagated through the unfolding to the final measurement.

7.2 Detector calibration, resolution and identification uncertainties

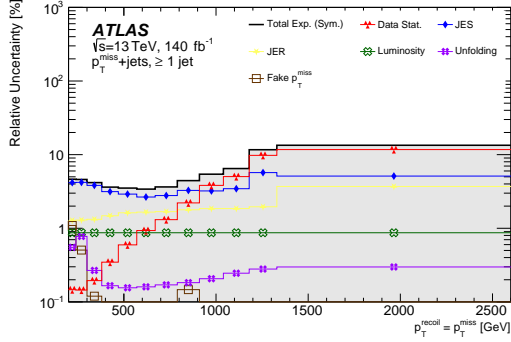
The unfolding procedure relies on knowledge of the detector response, which has uncertainties associated with it. The impact of these uncertainties is determined by varying the response function in question and re-running the analysis, including the final unfolding step. The sources of uncertainty considered are given below.

- Uncertainties related to jet energy scale (JES) and jet energy resolution (JER) are derived using dijet samples following the procedures documented in Ref. [103]. A subclass of JES uncertainties deals with whether the jet is likely to have been initiated by a quark or a gluon. The proportion the quark-initiated jets in the measurement regions is estimated from simulation as a function of transverse momentum and pseudorapidity.
- Uncertainties related to the electron efficiency measurement and calibration are obtained from tag-and-probe measurements of J/ψ and $Z \rightarrow e^+e^-$ events, as described in Ref. [92].
- Muon uncertainties are related to muon calibration and efficiencies are obtained from J/ψ and $Z \rightarrow \mu^+\mu^-$ events, as described in Ref. [95].
- τ -lepton calibration uncertainties are accounted for as documented in Ref. [109].
- Measurements of $Z \rightarrow \ell\ell\gamma$ events are used to study the performance of photon reconstruction, as documented in Ref. [92].
- The uncertainty in those (soft) components of p_T^{miss} not accounted for already is represented by three systematic uncertainties, detailed in Ref. [110].

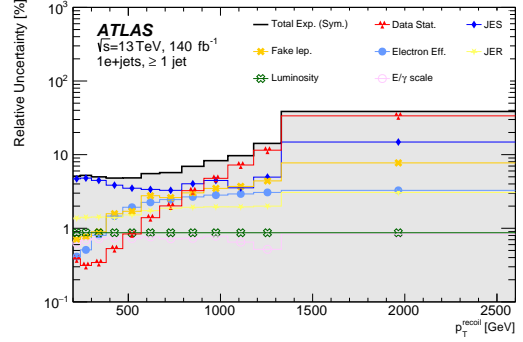
Figure 5 shows the breakdown of the statistical and systematic uncertainties for the p_T^{miss} observable in the ≥ 1 jet phase space. At high p_T^{miss} , the statistical uncertainty dominates, and over most of the distribution, the JES is the most significant systematic uncertainty, with the JER next in the region with no leptons or photons. Uncertainties associated with lepton and photon identification contribute in the other regions. The uncertainty due to the unfolding, and the (forward) jet vertex tagging uncertainty, are below 2%, and much smaller in most cases.

Figure 6 shows the breakdown of statistical and systematic uncertainties for the R^{miss} ratio of cross-sections, as a function of p_T^{miss} , in the ≥ 1 jet region. At low p_T^{miss} , the cancellation of JES uncertainties leads to a reduction in the combined estimate of the experimental uncertainty.

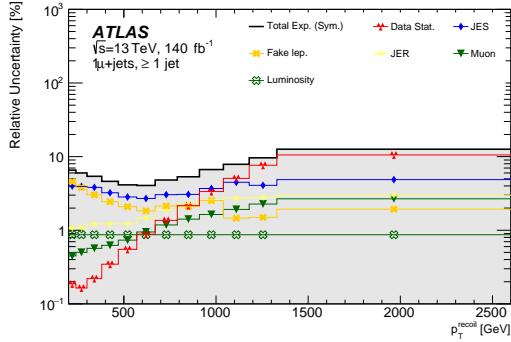
Finally, uncertainties associated with the estimation of fake backgrounds are accounted for. For the fake-lepton backgrounds, the dominant source comes from theory uncertainties, such as QCD scale variations, affecting the generator predictions in the regions used to measure the efficiencies. This uncertainty can be up to 100% of the predicted background yield. Smaller sources include statistical uncertainties relating to the limited number of events in data in those regions, and uncertainties in the method (evaluated for example by modifying the definition of the regions). Uncertainties from these sources are typically around 10% of the predicted yield. After unfolding, the fake leptons uncertainties collectively have an effect of the order of 1%–4% depending on the bin. For the fake-photon background, three sources of uncertainty are considered: the choice of WP used when selecting photons, the correlation between the A, B, C and D regions used for the estimation and the choice of generator for the prompt photon prediction. Together, these three sources result in an uncertainty of around 30% in the predicted fake photon yields. This amounts to approximately 1% in the measured cross-section after unfolding. The uncertainties in the multijet and non-collision backgrounds in the signal region represent very small contributions to the final event sample and are subject to statistical variations due to the nature of the evaluation. Therefore, they are conservatively taken to be 100% of the estimated yield, corresponding to a less than 1% uncertainty in the final measurement in the most affected bin.



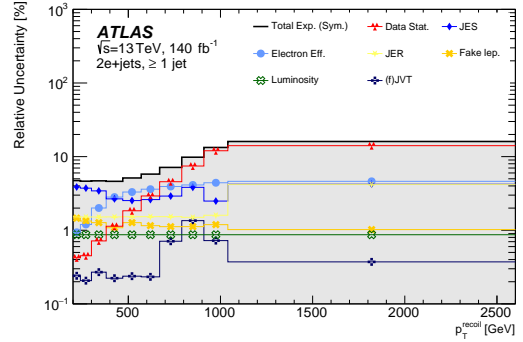
(a)



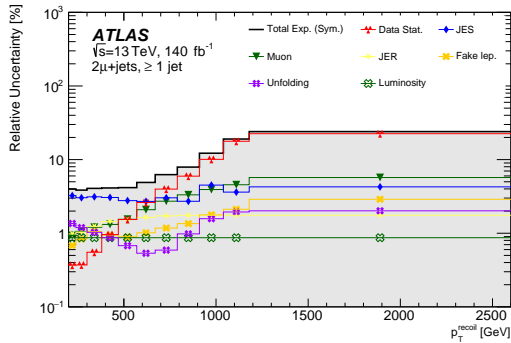
(b)



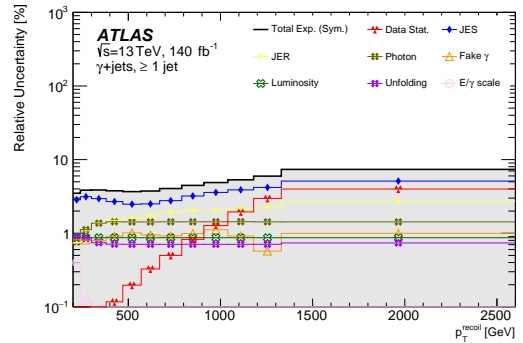
(c)



(d)



(e)



(f)

Figure 5: Uncertainty breakdown for p_T^{recoil} measurements in the ≥ 1 jet phase space for the (a) $p_T^{\text{miss}} + \text{jets}$, (b) $e + \text{jets}$, (c) $\mu + \text{jets}$, (d) $2e + \text{jets}$, (e) $2\mu + \text{jets}$, and (f) $\gamma + \text{jets}$ regions, showing the statistical uncertainty and the most significant systematic uncertainties in each case. For illustrative purposes this figure shows the symmetrised uncertainties, calculated as the average of the asymmetric error in each bin. Total Exp. (Sym.) is the combination of statistical and systematic uncertainties and indicates the symmetrised total experimental uncertainty.

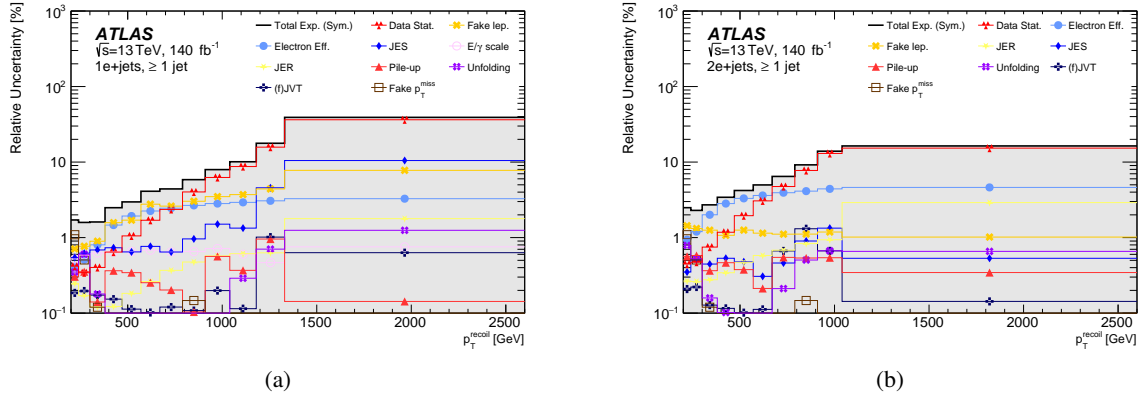


Figure 6: Uncertainty breakdown of the R^{miss} ratio as a function of p_T^{recoil} . As examples, the breakdowns for the ≥ 1 jet phase space are shown for the (a) e +jets and (b) $2e$ +jets region. For illustrative purposes this figure shows the symmetrised uncertainties, calculated as the average of the asymmetric error in each bin. Total Exp. (Sym.) is the combination of statistical and systematic uncertainties and indicates the symmetrised total experimental uncertainty. Compared to the individual measurements in Figure 5(b) and 5(d), a cancellation of the JES and JER uncertainties is observed.

8 Results and discussion

8.1 p_T^{miss} measurements

The measured differential cross-section as a function of the magnitude of the missing transverse momentum, p_T^{miss} , is shown in Figure 7 for the single jet and VBF phase spaces, in the region with no signal leptons or photons. In both cases, the cross-section falls by more than five orders of magnitude as p_T^{miss} increases from 200 to 2500 GeV. The cross-section in the VBF phase space is lower than the single jet phase space due to the jet requirements.

Similar behaviour is seen for the transverse momentum of the hadronic system, p_T^{recoil} , after the charged lepton requirements are imposed, as shown in Figure 8 for the single jet phase space. When a single muon is required, the cross-section is similar in magnitude to the zero-lepton/photon cross-section, while requiring two muons reduces it by about an order of magnitude. The cross-sections after electron requirements are somewhat smaller due to the more restrictive fiducial requirements imposed on electrons.

The SM predictions described in Section 4 are also shown in Figure 7 and Figure 8. Apart from a difference between the normalisations, they describe the data well in all regions; a quantitative study is presented in Section 8.3. Also shown are the subcomponents of the MEPS@NLO prediction. With no leptons or photons present, the dominant contribution is $Z \rightarrow \nu\nu$, with a top-quark contribution of a few per cent at low p_T^{miss} that falls to the per-mille level at higher values. The contribution from W +jets is around 25% at low p_T^{miss} , but falls rapidly with p_T^{miss} to form about 10% of the cross-section at higher values. The contribution from electroweak production mechanisms is around 1% at low p_T^{miss} , but rises rapidly with p_T^{miss} to form about 10% of the cross-section at higher values.

For the one-electron and one-muon phase spaces, the top-quark contribution is around 15% at low p_T^{recoil} , falling to a few percent at high values. It is never more than a few percent of the two-charged-lepton

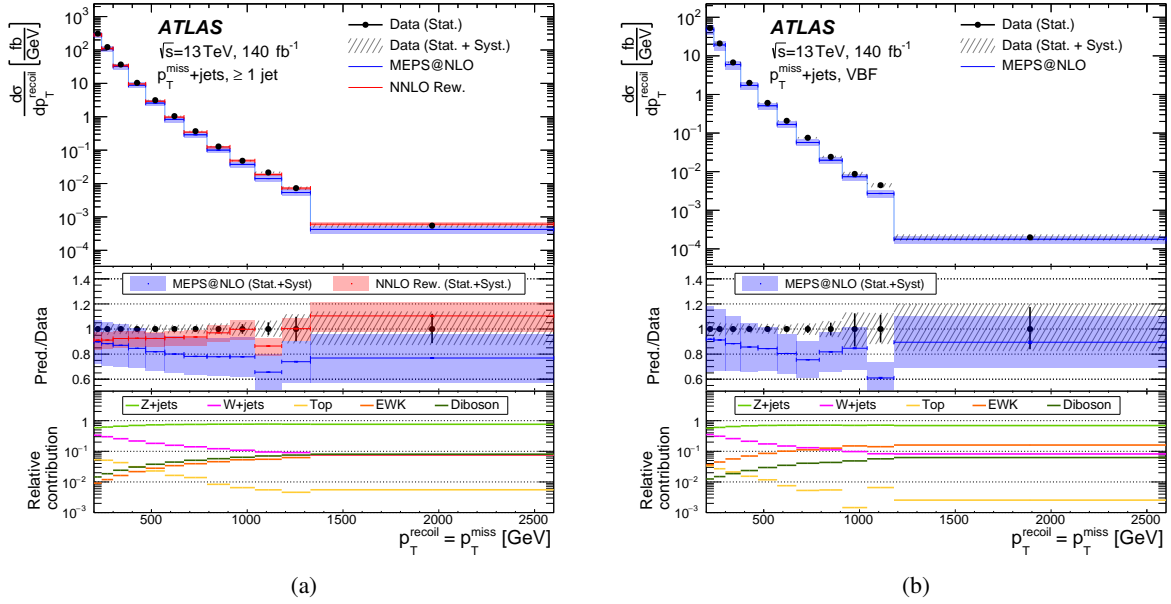


Figure 7: The measured p_T^{miss} differential cross-sections in the $p_T^{\text{miss}} + \text{jets}$ region in (a) $\geq 1 \text{ jet}$ and (b) VBF phase spaces, compared with the SM predictions. The middle panels show the ratios of the predictions to the data, along with their uncertainties, while the lower panels show the relative contributions from different SM processes relative to the total MEPS@NLO prediction.

cross-sections. For all the charged-lepton cross-sections, the electroweak contribution is around 1% at low p_T^{recoil} , rising with p_T^{recoil} to be just below 10% of the cross-section.

The measured differential cross-section as a function of the m_{jj} and $\Delta\phi_{jj}$ is shown for the VBF selection in Figure 9, along with the SM predictions for different sub-processes, for the $p_T^{\text{miss}} + \text{jets}$ and the $2\mu + \text{jets}$ regions. The cross-section falls rapidly with dijet mass, and the electroweak contribution rises from around 1% to 50% as m_{jj} rises from 600 GeV to 6 TeV. The overall $\Delta\phi_{jj}$ distribution peaks mildly at $\pm\pi/4$, as do all the predicted sub-process contributions except the top-quark one, which peaks at $\pm\pi/2$.

The description of the data by the SM predictions is generally good, except for the m_{jj} distribution, where the SM lies below the data at low values, but falls less steeply, to lie above the data around 2 TeV. This is discussed further in Section 8.3. A resummed calculation using HEJ is also shown, which describes the m_{jj} distribution somewhat better.

Figure 10 shows some examples of the R^{miss} ratios of the results presented so far. The ratios tend to be flat or slowly falling across the measured spectra. The R^{miss} ratios benefit from a cancellation of discrepancies in modelling and some systematic uncertainties, and thus the agreement between data and theory is improved compared to that for the cross-sections, most notably for the m_{jj} observable.

8.2 $Z \rightarrow \nu\bar{\nu}$ measurement

The Z+jets process dominates the zero-lepton phase space. As discussed in Section 7, non-Z+jets SM processes can be subtracted from the data before detector corrections to extract a measurement of Z+jets. This method gives consistent results with the inclusive measurements when the particle-level predictions

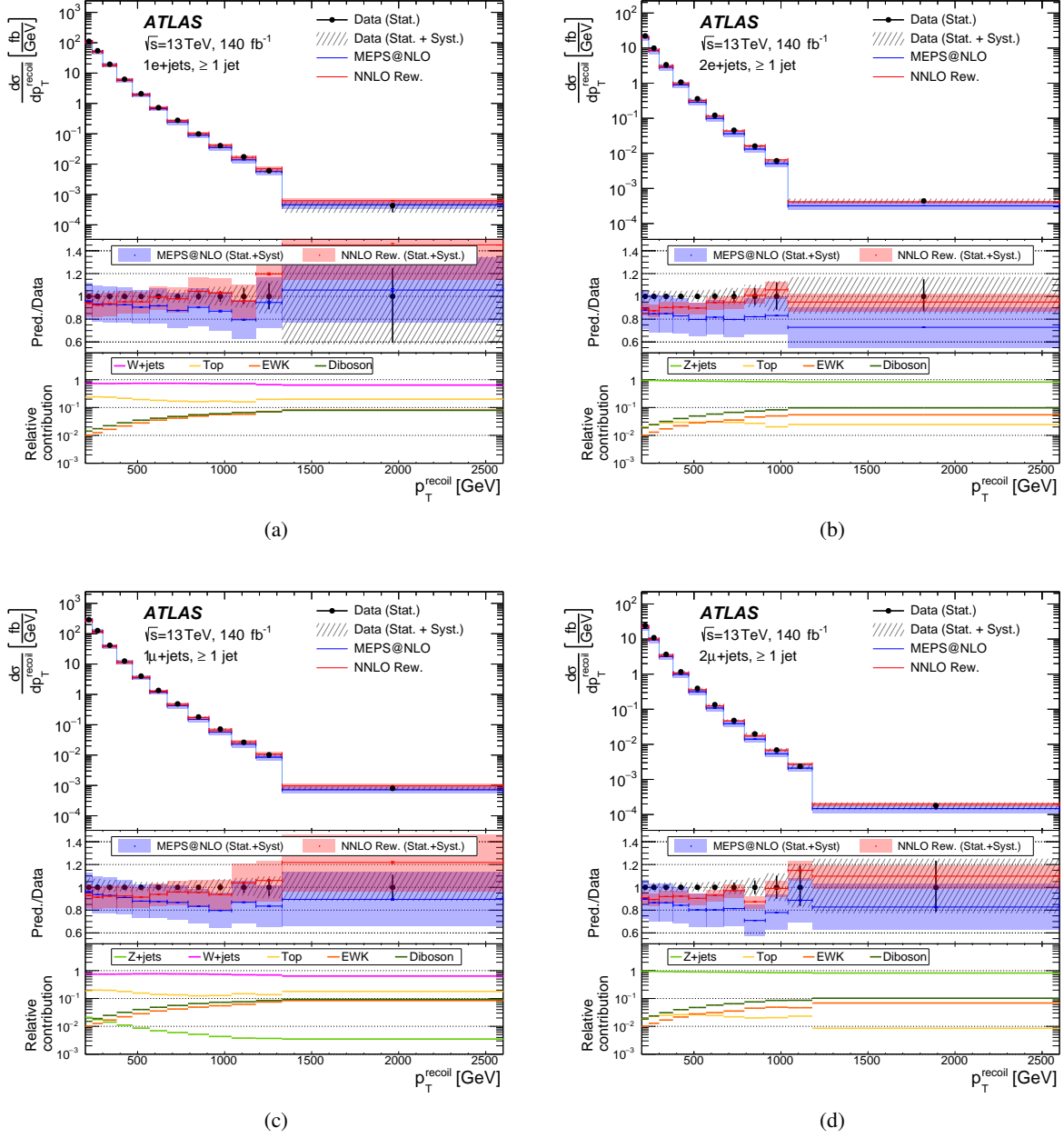


Figure 8: The measured p_T^{recoil} differential cross-sections in the inclusive jet phase space compared with the SM predictions: (a) e +jets (b) $2e$ +jets (c) μ +jets and (d) 2μ +jets. The middle panels show the ratios of the predictions to the data, along with their uncertainties, while the lower panels show the relative contributions from different SM processes relative to the total MEPS@NLO prediction.

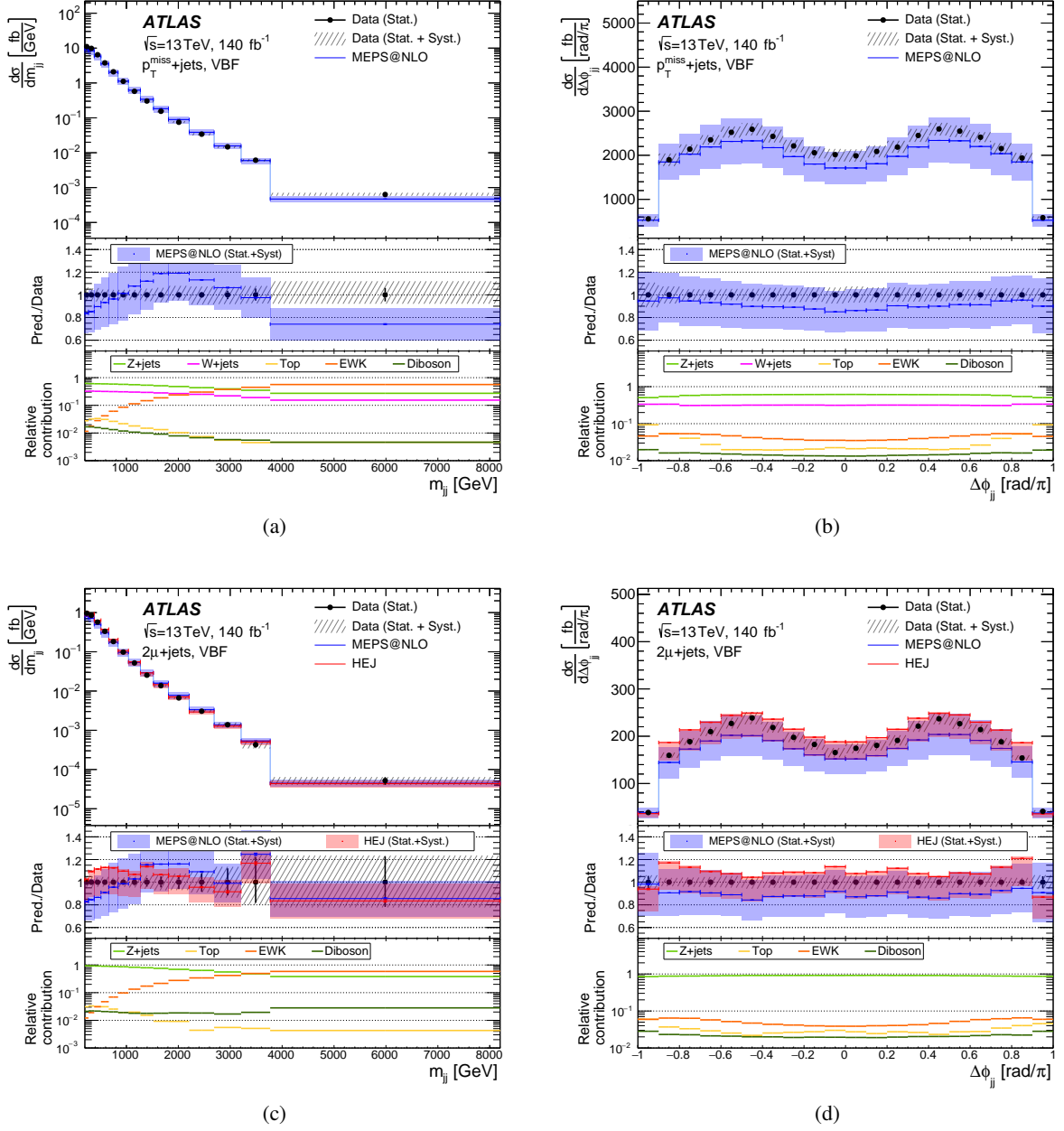


Figure 9: The measured m_{jj} and $\Delta\phi_{jj}$ distributions in the VBF phase space compared with the SM predictions, for (a) and (b) the $p_T^{\text{miss}}+\text{jets}$ and (c) and (d) the $2\mu+\text{jets}$ regions, for illustration. The middle panels show the ratios of the predictions to the data, along with their uncertainties, while the lower panels show the relative contributions from different SM processes relative to the total MEPS@NLO prediction.

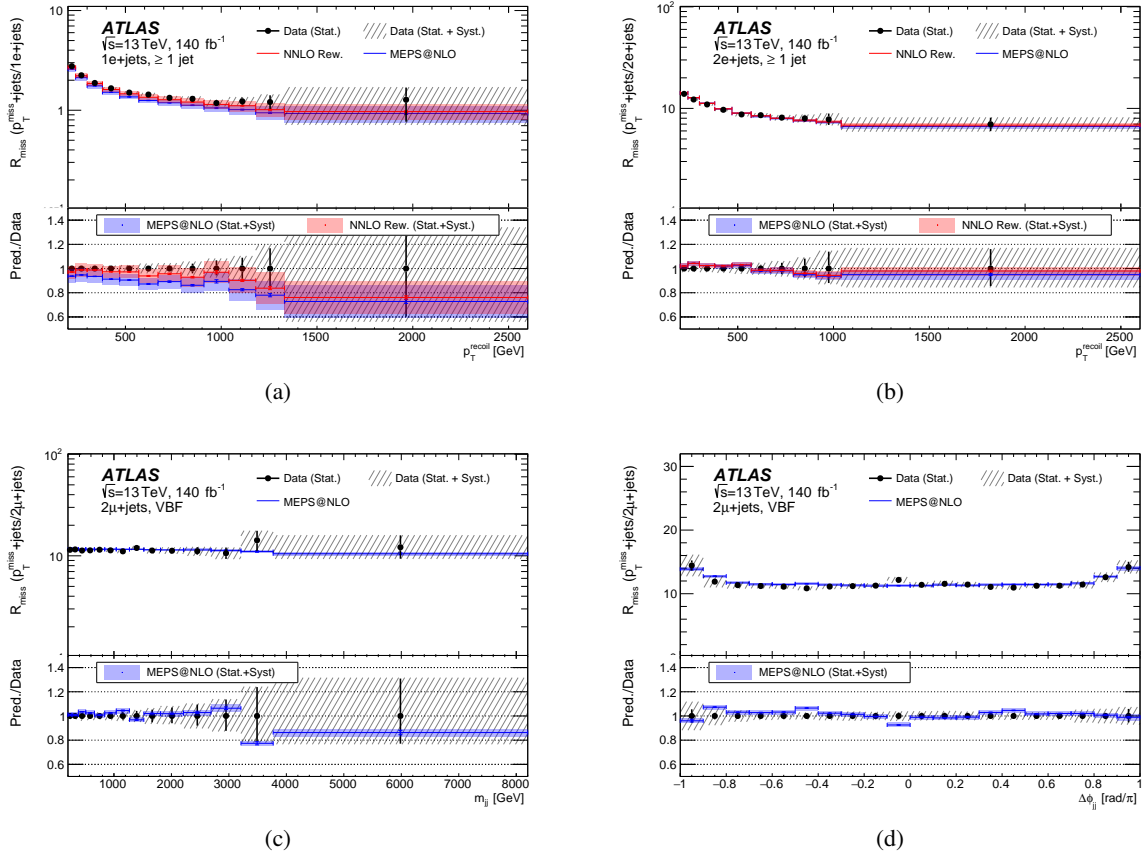


Figure 10: Comparison with SM predictions of the R^{miss} ratios of the measured differential cross-sections for (a) and (b) p_T^{recoil} in the inclusive jet phase space for (a) e +jets and (b) $2e$ +jets and for (c) m_{jj} and (d) $\Delta\phi_{jj}$ in the 2μ +jets region of the VBF phase space. The bottom panels show the ratios of the predictions to the data, along with their uncertainties.

for the subtracted processes are added back in after unfolding. The differential cross-section for Z +jets is shown in Figure 11 as a function of p_T^Z in the ≥ 1 jet and VBF phase spaces, and as a function of m_{jj} and $\Delta\phi_{jj}$ in the VBF phase space. The level of description by the SM is similar to that for the inclusive measurement.

The production of an isolated photon in association with jets, γ +jets, in a similar kinematic region, shares several theoretical and experiment uncertainties with the Z +jets process. The measurements of this final state are shown in Figure 12.

The γ +jets cross-section is generally a factor of about five above the Z +jets cross-section, with similar features and a similar level of agreement with the SM prediction regarding the shape of the distributions. The prediction is 10%–20% above the data, although generally lies within the uncertainties in the calculation for the cross-section measurements. The discrepancy remains in the R^{miss} measurements, since this normalisation issue only applies in the denominator and therefore does not cancel out. Similar shifts were observed in independent studies [111], and were found to be induced by photon isolation criteria.

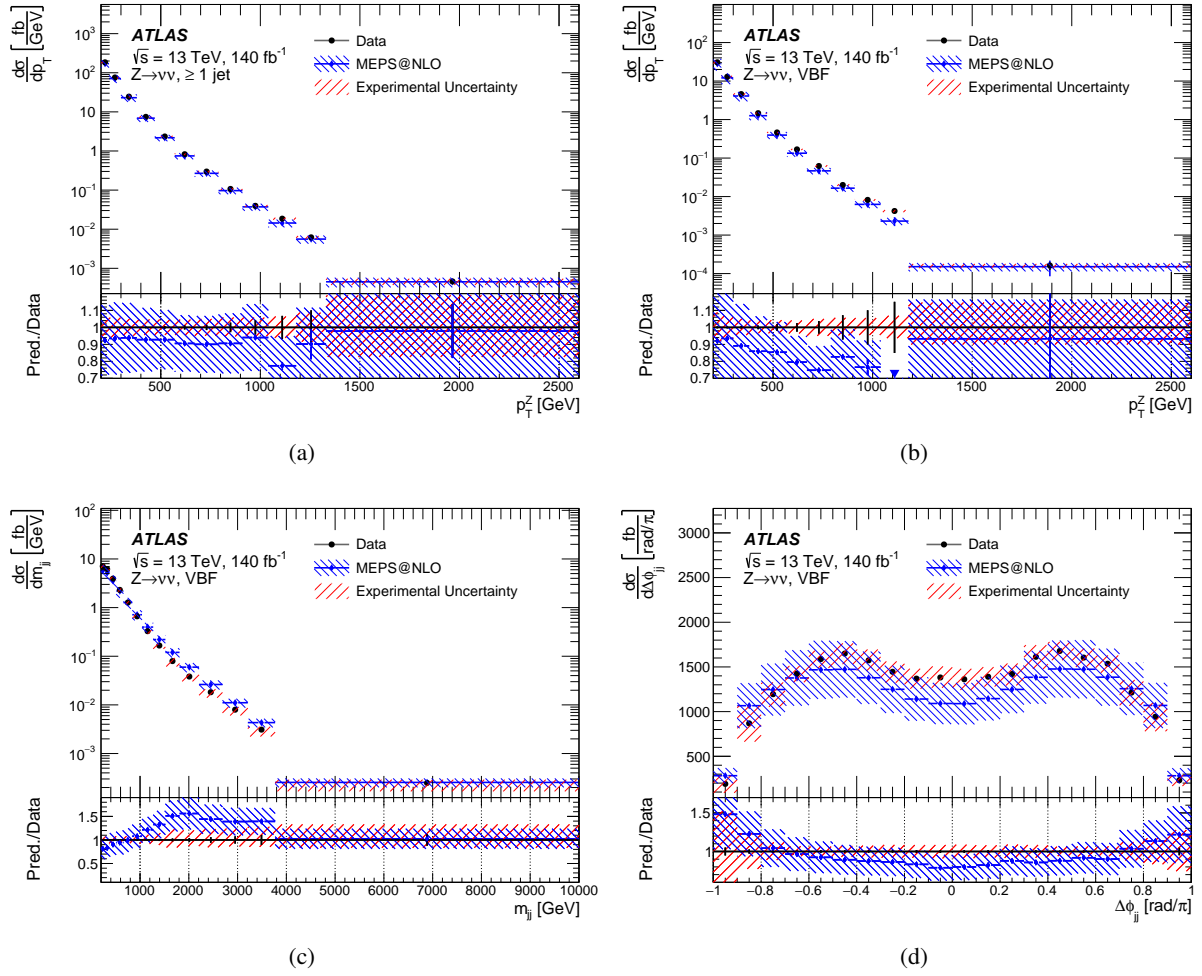


Figure 11: The measured $Z \rightarrow \nu\nu$ cross-section, differential in p_T^Z in the (a) single jet and (b) VBF phase spaces, and differential in (c) m_{jj} and (d) $\Delta\phi_{jj}$ in the VBF phase spaces, compared with the SM predictions. The lower panels show the ratios of the predictions to the data, along with the data statistical uncertainties (black bars) and systematic uncertainties (red shading).

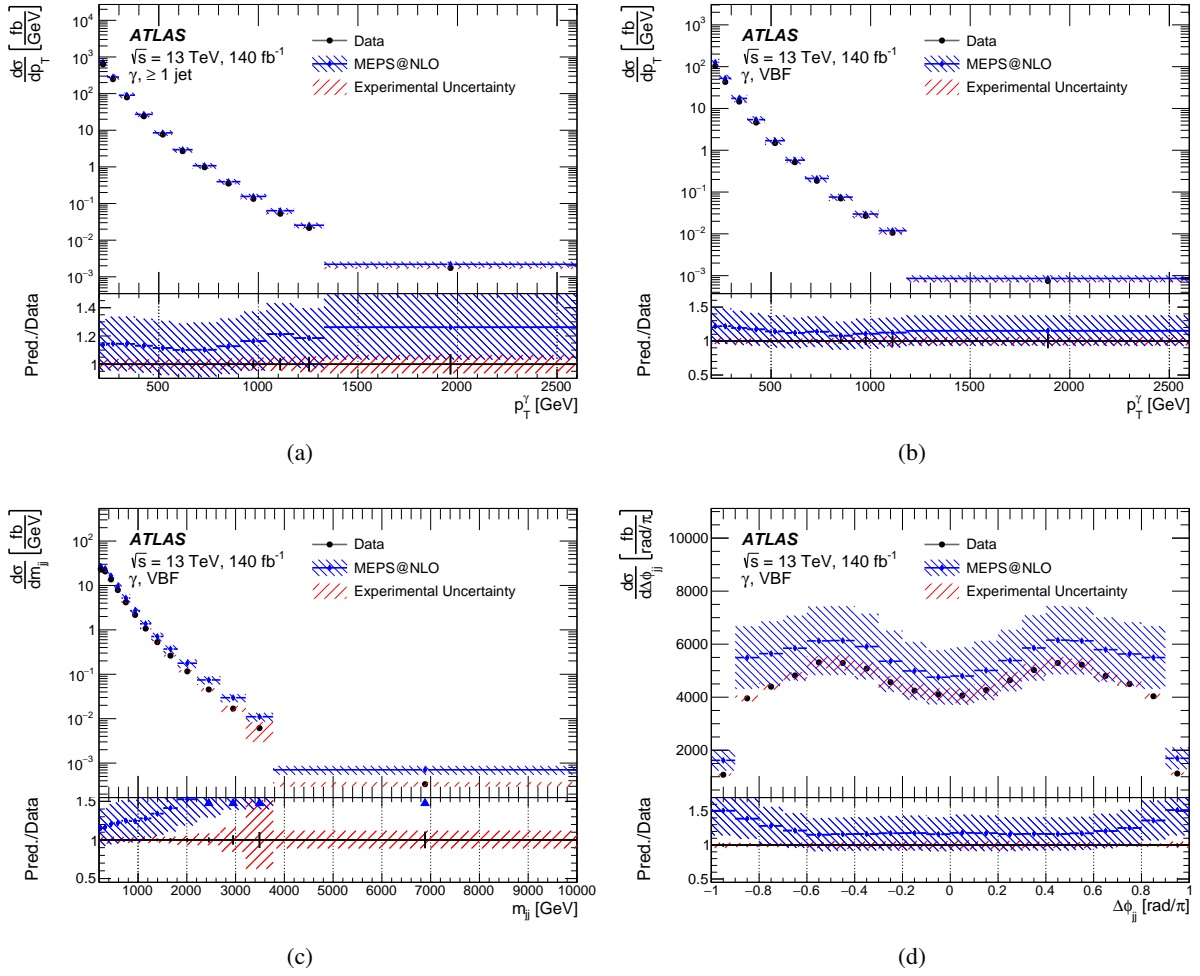


Figure 12: The measured γ +jets cross-section, differential in p_T^γ in the (a) single jet and (b) VBF phase spaces, and differential in (c) m_{jj} and (d) $\Delta\phi_{jj}$ in the VBF phase spaces, compared with the SM predictions. The lower panels show the ratios of the predictions to the data, along with the data statistical uncertainties (black bars) and systematic uncertainties (red shading).

8.3 Quantitative comparison to SM predictions

To quantify the level of agreement or disagreement between the measurement and the SM predictions, fits are performed by minimising the negative logarithm of the likelihood. Experimental and theoretical uncertainties are either added to a covariance matrix (if their impact is below one percent everywhere in the fitted distributions) or otherwise assigned to a nuisance parameter (NP) that is allowed to float according to the estimated uncertainty. The likelihood is evaluated for the resulting level of agreement, under the condition that the SM is the correct underlying model and taking into account the residuals, the covariance matrix and pulls on the nuisance parameters. Fits to the differential cross-sections are performed using the inclusive measurements, in all phase spaces, using the MEPS@NLO prediction. Since the γ +jets measurements show a strong normalisation offset not present in the other regions, only the p_T^{miss} +jets, e +jets, $2e$ +jets, μ +jets and 2μ +jets regions (or their respective R^{miss} ratios) are used in the fits. Since the phase spaces are not orthogonal, statistical correlations exist between some measurements. These are evaluated using the Bootstrap method [112], and are accounted for in the correlation matrix in the fitting procedure.

The level of agreement between the fitted results and the SM for p_T^{recoil} is reasonable, with a $\chi^2/\text{d.o.f.} \approx 101/57$. For the differential cross-section as a function of $\Delta\phi_{jj}$, the post-fit distributions also show reasonable agreement between the measurement and the SM. For m_{jj} however, the agreement is not good, due to the poor modelling of this distribution seen in Figure 9. Because of this, the combined fit using all distributions for all observables, regions and phase spaces simultaneously also shows poor agreement, with a $\chi^2/\text{d.o.f.} \approx 390/70$.

Fits are also performed to ratios of the measurements, R^{miss} , defined as the fiducial cross-section differential in each kinematic variable for p_T^{miss} +jets events, divided by the same cross-section for events in each of the e +jets, μ +jets, $2e$ +jets and 2μ +jets regions. In this case, some of the uncertainties largely or completely cancel out, and thus do not have an associated nuisance parameter. In addition, the modelling discrepancy in m_{jj} is seen in all regions and so cancels out to a large extent in R^{miss} . The ratio plots are therefore expected to give improved fit results compared to the cross-section fits. Indeed a $\chi^2/\text{d.o.f.} \approx 62/56$ is obtained for the combined R^{miss} fit to all distributions in all regions, with the individual fit to R^{miss} as a function of m_{jj} having $\chi^2/\text{d.o.f.} \approx 323/220$, indicating that indeed the discrepancy between data and SM cancels out between the different regions.

For re-interpretation, the R^{miss} measurements are always used. Specifically, the fits use the R^{miss} distributions as a function of p_T^{miss} : either using just the inclusive jet phase space ($\chi^2/\text{d.o.f.} \approx 48/45$) or both the inclusive jet and VBF phase spaces ($\chi^2/\text{d.o.f.} \approx 110/84$). Both of these options display good agreement between the SM predictions and the measurements, and therefore can be safely used for re-interpretation and establishing constraints on new physics models.

9 Implications for physics beyond the Standard Model

Part of the motivation of these particle-level measurements is that they can easily be confronted with new SM predictions, and predictions from extensions to the SM. Since the measurements of p_T^{miss} and R^{miss} are consistent with the SM, they can thus be used to set limits on BSM physics, particularly models that contain a DM candidate, the presence of which could affect the p_T^{miss} distribution. This procedure was already demonstrated in the previous measurement [8] using a subset of the current data, and is extended and updated here.

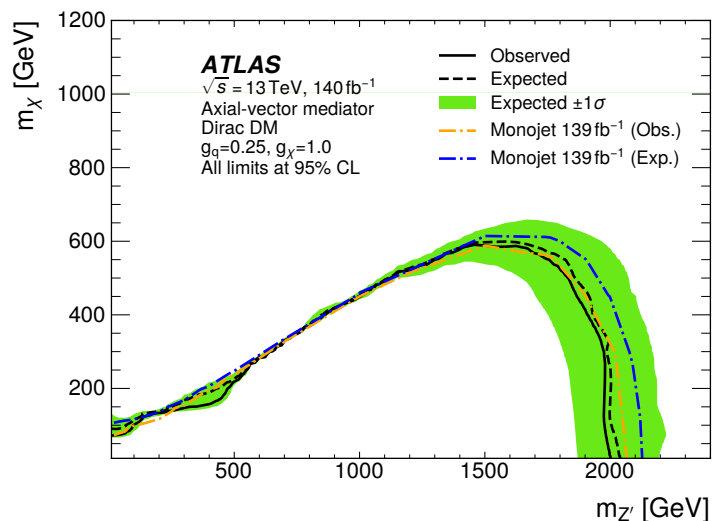
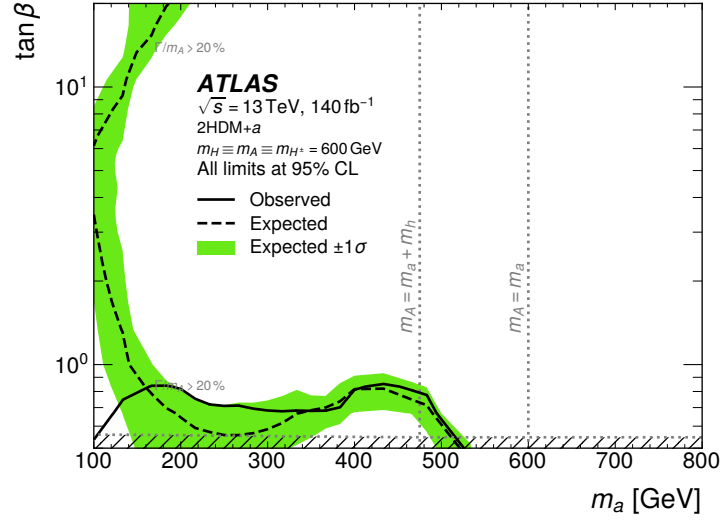


Figure 13: Exclusion limits at 95% in the plane of Dark Matter mass and mediator mass for a simplified DM model with an axial-vector coupling to the SM. The limits from this analysis, evaluated using the particle-level R^{miss} measurements, are compared with the limits from the ATLAS monojet search [4].

A common benchmark simplified model involves extending the SM with an additional U(1) gauge symmetry, in which a DM candidate, χ , is a Dirac fermion that has charges only under this gauge group [9]. If SM quarks are also charged under this gauge group, DM particles can be produced at the LHC via the gauge boson, Z' , associated with the new U(1) symmetry, which is massive assuming the U(1) symmetry is spontaneously broken. This model was searched for previously by ATLAS [4] using the same data sample as the current analysis, and by CMS [5].

The case where χ has axial-vector couplings $g_\chi = 1.0$ to the Z' , and the coupling between the quarks and the Z' , $g_q = 0.25$, is studied in this analysis in the $(m_\chi, m_{Z'})$ plane, to compare the sensitivity of the current measurement to that of the search results. The fitting procedure described in the previous section is used to evaluate the likelihoods associated with a fit to R^{miss} when excluding or including a BSM contribution from this model. During fitting, the predicted R^{miss} is recalculated to include the signal. The limits obtained from the likelihood ratio, shown in Figure 13, are very similar to those previously published in the ATLAS search analysis [4], with mediator masses up to about 2.1 TeV excluded in the region $m_{Z'} > 2m_\chi$. The residual differences are attributed to the slightly different kinematic selections used, and the requirement for a minimum number of events in the high p_T^{miss} bin for unfolding. This demonstrates that particle-level measurements can be used for searches and setting constraints with only a minor penalty in sensitivity, and with the advantage that it can be done in future without the need to repeat complex and time-consuming detector simulation.

A more complicated model for DM involves the introduction of an additional Higgs doublet, along with a pseudoscalar, a , which couples to DM [10, 11]. Through mixing with the pseudoscalar component of the Higgs doublet, the pseudoscalar a acts as a mediator between the SM and the dark sector. The model, referred to as 2HDM+ a , has a rich phenomenology with a wide variety of possible final states produced [113–118], many of which involve p_T^{miss} produced in association with jets or other SM objects. In this analysis, a signal scan is conducted in the $(m_a, \tan\beta)$ plane where $m_A = 600$ GeV, as shown in Figure 14. The scan makes use of the full set of R^{miss} measurements, in both the ≥ 1 jet and VBF phase spaces, taking into account statistical and systematic correlations.



(a)

Figure 14: Exclusion limits at 95% in the $(m_a, \tan\beta)$ plane for the 2HDM+a model. A region of $\tan\beta$ below 0.7 is excluded for m_a values between approximately 150 GeV and 500 GeV. The regions shaded with diagonal lines indicate the region where the width of any of the Higgs bosons exceeds 20% of its mass; in this region the narrow-width approximation is violated and predictions become less precise. Moreover, the two vertical dashed lines represent scenarios where the mass of the neutral pseudoscalar A is either equal to the mass of the pseudoscalar a or a sum of the masses of a and Higgs boson h .

The scan reveals two major regions of sensitivity:

- For $\tan\beta < 0.7$, masses of the pseudoscalar a up to 520 GeV are excluded because of loop-induced production of a and its subsequent decay into DM particles, $pp \rightarrow a(\rightarrow \chi\bar{\chi})+\text{jets}$. The sensitivity is larger at $m_a > 350 \text{ GeV} \approx 2m_{\text{top}}$ because here the a can be produced resonantly from top quarks. For $\tan\beta \gg 10$, there is a second island of sensitivity because of b -quark induced production of a and its subsequent decay into DM particles.
- At small m_a , the expected exclusion limits are generally stronger because of processes almost independent of $\tan\beta$, e.g., $pp \rightarrow H \rightarrow aZ$ and $pp \rightarrow H^\pm \rightarrow aW^\pm$. However, the sensitivity to these processes is not large enough to close the sensitivity gap between small and large values of $\tan\beta$.

Qualitatively the sensitivity is similar to the existing exclusion from p_T^{miss} -based searches in different final states [13]. Differences in the exclusion limits originate from differences in the SM calculations used, and from the use of the VBF phase space in addition to the ≥ 1 jet region.

Overall these studies show that the inclusive, particle-level measurement provides good sensitivity to BSM physics, and is amenable to reinterpretation in terms of different models.

10 Conclusion

Inclusive measurements of p_T^{miss} are made using 140 fb^{-1} of pp collision data at $\sqrt{s} = 13 \text{ TeV}$ collected with the ATLAS detector during Run 2 of the LHC. The measurements are made in fiducial regions closely reflecting the detector acceptance, and are corrected for detector effects within these regions, yielding differential cross-sections defined in terms of final-state particles. Differential cross-sections are measured as a function of p_T^{miss} in a ≥ 1 jet and a VBF phase space. The latter is defined by the presence of two jets, and the cross-section is also measured as a function of the azimuthal angular distance between the jets, $\Delta\phi_{jj}$, and the dijet invariant mass, m_{jj} . The cross-section for $Z \rightarrow \nu\nu$ production is determined, differential in the p_T^{miss} and, in the VBF phase space, in $\Delta\phi_{jj}$ and m_{jj} .

Measurements of lepton-plus-jet, dilepton-plus jet and photon-plus-jet final states are also made in the same kinematic regions. Many uncertainties, both theoretical and experimental, are correlated between these measurements and the p_T^{miss} measurements, and therefore cancel out in the ratio of cross-sections, R^{miss} .

Quantitative comparisons with state-of-the-art SM predictions show a reasonable description of all measured cross-sections as a function of most observables, except m_{jj} . The discrepancy in the shape of the distribution of this observable is present in the lepton-plus-jet, dilepton-plus jet and photon-plus-jet measurements as well as the p_T^{miss} region. It therefore cancels in R^{miss} , which is well described by the predictions. The resummed calculation in the HEJ prediction, available for the leptonic measurements, provides a better description of m_{jj} .

The measurements are designed to be readily reinterpreted, and the effectiveness of this is illustrated by comparisons with two DM models. Specifically, the measured R^{miss} distribution is used to reproduce limits on a simplified DM model, obtaining results consistent with a previously published search using the same data set. Limits are also set on a model involving an additional Higgs doublet and a pseudoscalar coupling to a DM particle, where again they are similar to those obtained in searches, with extended sensitivity in some regions due to the use of the VBF phase space in addition to the ≥ 1 jet region. The derived constraints are found to be only marginally weaker than for dedicated searches, while eliminating the need for complicated detector simulations. The published results can consequently be directly used for future interpretations. Information about uncertainties and correlations is provided on HEPData, along with a Rivet analysis, to facilitate the use of this LHC Run 2 measurement in future studies with other new physics models and improved SM predictions, as they become available.

Acknowledgements

We thank CERN for the very successful operation of the LHC and its injectors, as well as the support staff at CERN and at our institutions worldwide without whom ATLAS could not be operated efficiently.

The crucial computing support from all WLCG partners is acknowledged gratefully, in particular from CERN, the ATLAS Tier-1 facilities at TRIUMF/SFU (Canada), NDGF (Denmark, Norway, Sweden), CC-IN2P3 (France), KIT/GridKA (Germany), INFN-CNAF (Italy), NL-T1 (Netherlands), PIC (Spain), RAL (UK) and BNL (USA), the Tier-2 facilities worldwide and large non-WLCG resource providers. Major contributors of computing resources are listed in Ref. [119].

We gratefully acknowledge the support of ANPCyT, Argentina; YerPhI, Armenia; ARC, Australia; BMWFW and FWF, Austria; ANAS, Azerbaijan; CNPq and FAPESP, Brazil; NSERC, NRC and CFI, Canada; CERN;

ANID, Chile; CAS, MOST and NSFC, China; Minciencias, Colombia; MEYS CR, Czech Republic; DNR and DNSRC, Denmark; IN2P3-CNRS and CEA-DRF/IRFU, France; SRNSFG, Georgia; BMBF, HGF and MPG, Germany; GSRI, Greece; RGC and Hong Kong SAR, China; ISF and Benozio Center, Israel; INFN, Italy; MEXT and JSPS, Japan; CNRST, Morocco; NWO, Netherlands; RCN, Norway; MEiN, Poland; FCT, Portugal; MNE/IFA, Romania; MESTD, Serbia; MSSR, Slovakia; ARRS and MIZŠ, Slovenia; DSI/NRF, South Africa; MICINN, Spain; SRC and Wallenberg Foundation, Sweden; SERI, SNSF and Cantons of Bern and Geneva, Switzerland; MOST, Taipei; TENMAK, Türkiye; STFC, United Kingdom; DOE and NSF, United States of America.

Individual groups and members have received support from BCKDF, CANARIE, CRC and DRAC, Canada; PRIMUS 21/SCI/017 and UNCE SCI/013, Czech Republic; COST, ERC, ERDF, Horizon 2020, ICSC-NextGenerationEU and Marie Skłodowska-Curie Actions, European Union; Investissements d’Avenir Labex, Investissements d’Avenir Idex and ANR, France; DFG and AvH Foundation, Germany; Herakleitos, Thales and Aristeia programmes co-financed by EU-ESF and the Greek NSRF, Greece; BSF-NSF and MINERVA, Israel; Norwegian Financial Mechanism 2014-2021, Norway; NCN and NAWA, Poland; La Caixa Banking Foundation, CERCA Programme Generalitat de Catalunya and PROMETEO and GenT Programmes Generalitat Valenciana, Spain; Göran Gustafssons Stiftelse, Sweden; The Royal Society and Leverhulme Trust, United Kingdom.

In addition, individual members wish to acknowledge support from CERN: European Organization for Nuclear Research (CERN PJA5); Chile: Agencia Nacional de Investigación y Desarrollo (FONDECYT 1190886, FONDECYT 1210400, FONDECYT 1230987); China: National Natural Science Foundation of China (NSFC - 12175119, NSFC 12275265); European Union: European Research Council (ERC - 948254, ERC 101089007), Horizon 2020 Framework Programme (MUCCA - CHIST-ERA-19-XAI-00), Italian Center for High Performance Computing, Big Data and Quantum Computing (ICSC, NextGenerationEU); France: Agence Nationale de la Recherche (ANR-20-CE31-0013, ANR-21-CE31-0022), Investissements d’Avenir Labex (ANR-11-LABX-0012); Germany: Baden-Württemberg Stiftung (BW Stiftung-Postdoc Eliteprogramme), Deutsche Forschungsgemeinschaft (DFG - 469666862, DFG - CR 312/5-2); Italy: Istituto Nazionale di Fisica Nucleare (ICSC, NextGenerationEU); Japan: Japan Society for the Promotion of Science (JSPS KAKENHI 22H01227, JSPS KAKENHI 22KK0227, JSPS KAKENHI JP21H05085, JSPS KAKENHI JP22H04944); Netherlands: Netherlands Organisation for Scientific Research (NWO Veni 2020 - VI.Veni.202.179); Norway: Research Council of Norway (RCN-314472); Poland: Polish National Agency for Academic Exchange (PPN/PPO/2020/1/00002/U/00001), Polish National Science Centre (NCN 2021/42/E/ST2/00350, NCN OPUS nr 2022/47/B/ST2/03059, NCN UMO-2019/34/E/ST2/00393, UMO-2020/37/B/ST2/01043, UMO-2022/47/O/ST2/00148); Slovenia: Slovenian Research Agency (ARIS grant J1-3010); Spain: BBVA Foundation (LEO22-1-603), Generalitat Valenciana (Artemisa, FEDER, IDIFEDER/2018/048), La Caixa Banking Foundation (LCF/BQ/PI20/11760025), Ministry of Science and Innovation (RYC2019-028510-I, RYC2020-030254-I), PROMETEO and GenT Programmes Generalitat Valenciana (CIDEAGENT/2019/023, CIDEAGENT/2019/027); Sweden: Swedish Research Council (VR 2022-03845), Knut and Alice Wallenberg Foundation (KAW 2022.0358); Switzerland: Swiss National Science Foundation (SNSF - PCEFP2_194658); United Kingdom: Leverhulme Trust (Leverhulme Trust RPG-2020-004); United States of America: Neubauer Family Foundation.

References

- [1] G. Bertone, D. Hooper and J. Silk, *Particle dark matter: Evidence, candidates and constraints*, *Phys. Rept.* **405** (2005) 279, arXiv: [hep-ph/0404175](https://arxiv.org/abs/hep-ph/0404175).

- [2] V. Trimble, *Existence and Nature of Dark Matter in the Universe*, *Ann. Rev. Astron. Astrophys.* **25** (1987) 425.
- [3] J. L. Feng, *Dark Matter Candidates from Particle Physics and Methods of Detection*, *Ann. Rev. Astron. Astrophys.* **48** (2010) 495, arXiv: [1003.0904 \[astro-ph.CO\]](#).
- [4] ATLAS Collaboration, *Search for new phenomena in events with an energetic jet and missing transverse momentum in pp collisions at $\sqrt{s}=13$ TeV with the ATLAS detector*, *Phys. Rev. D* **103** (2021) 112006, arXiv: [2102.10874 \[hep-ex\]](#).
- [5] CMS Collaboration, *Search for new particles in events with energetic jets and large missing transverse momentum in proton-proton collisions at $\sqrt{s} = 13$ TeV*, *JHEP* **11** (2021) 153, arXiv: [2107.13021 \[hep-ex\]](#).
- [6] CMS Collaboration, *Measurement of the Z boson differential production cross section using its invisible decay mode ($Z \rightarrow \nu\bar{\nu}$) in proton-proton collisions at $\sqrt{s} = 13$ TeV*, *JHEP* **05** (2021) 205, arXiv: [2012.09254 \[hep-ex\]](#).
- [7] ATLAS Collaboration, *Measurement of the Z boson invisible width at $\sqrt{s} = 13$ TeV with the ATLAS detector*, (2023), arXiv: [2312.02789 \[hep-ex\]](#).
- [8] ATLAS Collaboration, *Measurement of detector-corrected observables sensitive to the anomalous production of events with jets and large missing transverse momentum in pp collisions at $\sqrt{s} = 13$ TeV using the ATLAS detector*, *Eur. Phys. J. C* **77** (2017) 765, arXiv: [1707.03263 \[hep-ex\]](#).
- [9] J. Abdallah et al., *Simplified Models for Dark Matter Searches at the LHC*, *Phys. Dark Univ.* **9-10** (2015) 8, arXiv: [1506.03116 \[hep-ph\]](#).
- [10] M. Bauer, U. Haisch and F. Kahlhoefer, *Simplified dark matter models with two Higgs doublets: I. Pseudoscalar mediators*, *JHEP* **05** (2017) 138, arXiv: [1701.07427 \[hep-ph\]](#).
- [11] T. Abe et al., *LHC Dark Matter Working Group: Next-generation spin-0 dark matter models*, *Phys. Dark Univ.* **27** (2020) 100351, arXiv: [1810.09420 \[hep-ex\]](#).
- [12] CMS Collaboration, *Search for dark matter produced in association with a leptonically decaying Z boson in proton-proton collisions at $\sqrt{s} = 13$ TeV*, *Eur. Phys. J. C* **81** (2021) 13, arXiv: [2008.04735 \[hep-ex\]](#), Erratum: *Eur. Phys. J. C* **81** (2021) 333.
- [13] ATLAS Collaboration, *Combination and summary of ATLAS dark matter searches interpreted in a 2HDM with a pseudo-scalar mediator using 139 fb^{-1} of $\sqrt{s} = 13$ TeV pp collision data*, (2023), arXiv: [2306.00641 \[hep-ex\]](#).
- [14] ATLAS Collaboration, *The ATLAS Experiment at the CERN Large Hadron Collider*, *JINST* **3** (2008) S08003.
- [15] G. Avoni et al., *The new LUCID-2 detector for luminosity measurement and monitoring in ATLAS*, *JINST* **13** (2018) P07017.
- [16] ATLAS Collaboration, *Performance of the ATLAS trigger system in 2015*, *Eur. Phys. J. C* **77** (2017) 317, arXiv: [1611.09661 \[hep-ex\]](#).
- [17] ATLAS Collaboration, *The ATLAS Collaboration Software and Firmware*, ATL-SOFT-PUB-2021-001, 2021, URL: <https://cds.cern.ch/record/2767187>.

- [18] M. Cacciari, G. P. Salam and G. Soyez, *The anti- k_t jet clustering algorithm*, **JHEP** **04** (2008) 063, arXiv: [0802.1189 \[hep-ph\]](#).
- [19] M. Cacciari, G. P. Salam and G. Soyez, *FastJet User Manual*, **Eur. Phys. J. C** **72** (2012) 1896, arXiv: [1111.6097 \[hep-ph\]](#).
- [20] F. U. Bernlochner et al., *Angles on CP-violation in Higgs boson interactions*, **Phys. Lett. B** **790** (2019) 372, arXiv: [1808.06577 \[hep-ph\]](#).
- [21] E. Maguire, L. Heinrich and G. Watt, *HEPData: a repository for high energy physics data*, **J. Phys. Conf. Ser.** **898** (2017) 102006, ed. by R. Mount and C. Tull, arXiv: [1704.05473 \[hep-ex\]](#).
- [22] C. Bierlich et al., *Robust Independent Validation of Experiment and Theory: Rivet version 3*, **SciPost Phys.** **8** (2020) 026, arXiv: [1912.05451 \[hep-ph\]](#).
- [23] S. Agostinelli et al., *GEANT4 – a simulation toolkit*, **Nucl. Instrum. Meth. A** **506** (2003) 250.
- [24] J. Allison et al., *Geant4 developments and applications*, **IEEE Trans. Nucl. Sci.** **53** (2006) 270.
- [25] ATLAS Collaboration, *The ATLAS Simulation Infrastructure*, **Eur. Phys. J. C** **70** (2010) 823, arXiv: [1005.4568 \[physics.ins-det\]](#).
- [26] T. Gleisberg et al., *Event generation with SHERPA 1.1*, **JHEP** **02** (2009) 007, arXiv: [0811.4622 \[hep-ph\]](#).
- [27] F. Cascioli, P. Maierhöfer and S. Pozzorini, *Scattering Amplitudes with Open Loops*, **Phys. Rev. Lett.** **108** (2012) 111601, arXiv: [1111.5206 \[hep-ph\]](#).
- [28] A. Denner, S. Dittmaier and L. Hofer, *COLLIER: A fortran-based complex one-loop library in extended regularizations*, **Comput. Phys. Commun.** **212** (2017) 220, arXiv: [1604.06792 \[hep-ph\]](#).
- [29] T. Gleisberg and S. Höche, *Comix, a new matrix element generator*, **JHEP** **12** (2008) 039, arXiv: [0808.3674 \[hep-ph\]](#).
- [30] S. Schumann and F. Krauss, *A parton shower algorithm based on Catani–Seymour dipole factorisation*, **JHEP** **03** (2008) 038, arXiv: [0709.1027 \[hep-ph\]](#).
- [31] J.-C. Winter, F. Krauss and G. Soff, *A modified cluster-hadronisation model*, **Eur. Phys. J. C** **36** (2004) 381, arXiv: [hep-ph/0311085](#).
- [32] NNPDF Collaboration, R. D. Ball et al., *Parton distributions for the LHC run II*, **JHEP** **04** (2015) 040, arXiv: [1410.8849 \[hep-ph\]](#).
- [33] S. Höche, F. Krauss, M. Schönherr and F. Siegert, *A critical appraisal of NLO+PS matching methods*, **JHEP** **09** (2012) 049, arXiv: [1111.1220 \[hep-ph\]](#).
- [34] S. Catani, F. Krauss, B. R. Webber and R. Kuhn, *QCD Matrix Elements + Parton Showers*, **JHEP** **11** (2001) 063, arXiv: [hep-ph/0109231](#).
- [35] S. Höche, F. Krauss, S. Schumann and F. Siegert, *QCD matrix elements and truncated showers*, **JHEP** **05** (2009) 053, arXiv: [0903.1219 \[hep-ph\]](#).
- [36] S. Höche, F. Krauss, M. Schönherr and F. Siegert, *QCD matrix elements + parton showers. The NLO case*, **JHEP** **04** (2013) 027, arXiv: [1207.5030 \[hep-ph\]](#).

- [37] F. Siegert, *A practical guide to event generation for prompt photon production with Sherpa*, *J. Phys. G* **44** (2017) 044007, arXiv: [1611.07226 \[hep-ph\]](#).
- [38] S. Frixione, *Isolated photons in perturbative QCD*, *Phys. Lett. B* **429** (1998) 369, arXiv: [hep-ph/9801442](#).
- [39] E. Bothmann et al., *Event generation with Sherpa 2.2*, *SciPost Phys.* **7** (2019) 034, arXiv: [1905.09127 \[hep-ph\]](#).
- [40] ATLAS Collaboration, *Multi-Boson Simulation for 13 TeV ATLAS Analyses*, ATL-PHYS-PUB-2017-005, 2017, URL: <https://cds.cern.ch/record/2261933>.
- [41] S. Frixione, G. Ridolfi and P. Nason, *A positive-weight next-to-leading-order Monte Carlo for heavy flavour hadroproduction*, *JHEP* **09** (2007) 126, arXiv: [0707.3088 \[hep-ph\]](#).
- [42] P. Nason, *A new method for combining NLO QCD with shower Monte Carlo algorithms*, *JHEP* **11** (2004) 040, arXiv: [hep-ph/0409146](#).
- [43] S. Frixione, P. Nason and C. Oleari, *Matching NLO QCD computations with parton shower simulations: the POWHEG method*, *JHEP* **11** (2007) 070, arXiv: [0709.2092 \[hep-ph\]](#).
- [44] S. Alioli, P. Nason, C. Oleari and E. Re, *A general framework for implementing NLO calculations in shower Monte Carlo programs: the POWHEG BOX*, *JHEP* **06** (2010) 043, arXiv: [1002.2581 \[hep-ph\]](#).
- [45] ATLAS Collaboration, *Studies on top-quark Monte Carlo modelling for Top2016*, ATL-PHYS-PUB-2016-020, 2016, URL: <https://cds.cern.ch/record/2216168>.
- [46] T. Sjöstrand et al., *An introduction to PYTHIA 8.2*, *Comput. Phys. Commun.* **191** (2015) 159, arXiv: [1410.3012 \[hep-ph\]](#).
- [47] ATLAS Collaboration, *ATLAS Pythia 8 tunes to 7 TeV data*, ATL-PHYS-PUB-2014-021, 2014, URL: <https://cds.cern.ch/record/1966419>.
- [48] NNPDF Collaboration, R. D. Ball et al., *Parton distributions with LHC data*, *Nucl. Phys. B* **867** (2013) 244, arXiv: [1207.1303 \[hep-ph\]](#).
- [49] M. Beneke, P. Falgari, S. Klein and C. Schwinn, *Hadronic top-quark pair production with NNLL threshold resummation*, *Nucl. Phys. B* **855** (2012) 695, arXiv: [1109.1536 \[hep-ph\]](#).
- [50] M. Cacciari, M. Czakon, M. Mangano, A. Mitov and P. Nason, *Top-pair production at hadron colliders with next-to-next-to-leading logarithmic soft-gluon resummation*, *Phys. Lett. B* **710** (2012) 612, arXiv: [1111.5869 \[hep-ph\]](#).
- [51] P. Bärnreuther, M. Czakon and A. Mitov, *Percent-Level-Precision Physics at the Tevatron: Next-to-Next-to-Leading Order QCD Corrections to $q\bar{q} \rightarrow t\bar{t} + X$* , *Phys. Rev. Lett.* **109** (2012) 132001, arXiv: [1204.5201 \[hep-ph\]](#).
- [52] M. Czakon and A. Mitov, *NNLO corrections to top-pair production at hadron colliders: the all-fermionic scattering channels*, *JHEP* **12** (2012) 054, arXiv: [1207.0236 \[hep-ph\]](#).
- [53] M. Czakon and A. Mitov, *NNLO corrections to top pair production at hadron colliders: the quark-gluon reaction*, *JHEP* **01** (2013) 080, arXiv: [1210.6832 \[hep-ph\]](#).

- [54] M. Czakon, P. Fiedler and A. Mitov,
Total Top-Quark Pair-Production Cross Section at Hadron Colliders Through $O(\alpha_S^4)$,
Phys. Rev. Lett. **110** (2013) 252004, arXiv: [1303.6254 \[hep-ph\]](#).
- [55] M. Czakon and A. Mitov,
Top++: A program for the calculation of the top-pair cross-section at hadron colliders,
Comput. Phys. Commun. **185** (2014) 2930, arXiv: [1112.5675 \[hep-ph\]](#).
- [56] E. Re,
Single-top Wt -channel production matched with parton showers using the POWHEG method,
Eur. Phys. J. C **71** (2011) 1547, arXiv: [1009.2450 \[hep-ph\]](#).
- [57] S. Frixione, E. Laenen, P. Motylinski, C. White and B. R. Webber,
Single-top hadroproduction in association with a W boson, *JHEP* **07** (2008) 029,
arXiv: [0805.3067 \[hep-ph\]](#).
- [58] R. Frederix, E. Re and P. Torrielli,
Single-top t -channel hadroproduction in the four-flavour scheme with POWHEG and aMC@NLO,
JHEP **09** (2012) 130, arXiv: [1207.5391 \[hep-ph\]](#).
- [59] S. Alioli, P. Nason, C. Oleari and E. Re,
NLO single-top production matched with shower in POWHEG: s - and t -channel contributions,
JHEP **09** (2009) 111, arXiv: [0907.4076 \[hep-ph\]](#), Erratum: *JHEP* **02** (2010) 011.
- [60] M. Aliev et al., *HATHOR – HAdronic Top and Heavy quarks crOss section calculator*,
Comput. Phys. Commun. **182** (2011) 1034, arXiv: [1007.1327 \[hep-ph\]](#).
- [61] P. Kant et al., *HatHor for single top-quark production: Updated predictions and uncertainty estimates for single top-quark production in hadronic collisions*,
Comput. Phys. Commun. **191** (2015) 74, arXiv: [1406.4403 \[hep-ph\]](#).
- [62] ATLAS Collaboration, *The Pythia 8 A3 tune description of ATLAS minimum bias and inelastic measurements incorporating the Donnachie–Landshoff diffractive model*,
ATL-PHYS-PUB-2016-017, 2016, URL: <https://cds.cern.ch/record/2206965>.
- [63] F. Buccioni et al., *OpenLoops 2*, *Eur. Phys. J. C* **79** (2019) 866, arXiv: [1907.13071 \[hep-ph\]](#).
- [64] F. Buccioni, S. Pozzorini and M. Zoller, *On-the-fly reduction of open loops*,
Eur. Phys. J. C **78** (2018) 70, arXiv: [1710.11452 \[hep-ph\]](#).
- [65] J. Butterworth et al., *PDF4LHC recommendations for LHC Run II*, *J. Phys. G* **43** (2016) 023001,
arXiv: [1510.03865 \[hep-ph\]](#).
- [66] V. Bertone, S. Carrazza, N. P. Hartland, and J. Rojo,
Illuminating the photon content of the proton within a global PDF analysis,
SciPost Phys. **5** (2018) 008, arXiv: [1712.07053 \[hep-ph\]](#).
- [67] J. M. Lindert et al., *Precise predictions for $V+$ jets dark matter backgrounds*,
Eur. Phys. J. C **77** (2017) 829, arXiv: [1705.04664 \[hep-ph\]](#).
- [68] A. Denner, S. Dittmaier, T. Kasprzik and A. Mück,
Electroweak corrections to dilepton + jet production at hadron colliders, *JHEP* **06** (2011) 069,
arXiv: [1103.0914 \[hep-ph\]](#).
- [69] A. Denner, S. Dittmaier, T. Kasprzik and A. Mück,
Electroweak corrections to monojet production at the Tevatron and the LHC,
Eur. Phys. J. C **73** (2013) 2297, arXiv: [1211.5078 \[hep-ph\]](#).

- [70] S. Kallweit, J. M. Lindert, P. Maierhöfer, S. Pozzorini and M. Schönherr, *NLO QCD+EW predictions for $V + jets$ including off-shell vector-boson decays and multijet merging*, [JHEP **04** \(2016\) 021](#), arXiv: [1511.08692 \[hep-ph\]](#).
- [71] A. Denner, S. Dittmaier, T. Kasprzik and A. Mück, *Electroweak corrections to $W + jet$ hadroproduction including leptonic W -boson decays*, [JHEP **08** \(2009\) 075](#), arXiv: [0906.1656 \[hep-ph\]](#).
- [72] J. H. Kühn, A. Kulesza, S. Pozzorini and M. Schulze, *Logarithmic electroweak corrections to hadronic $Z+1 jet$ production at large transverse momentum*, [Phys. Lett. B **609** \(2005\) 277](#), arXiv: [hep-ph/0408308](#).
- [73] J. H. Kühn, A. Kulesza, S. Pozzorini and M. Schulze, *Electroweak corrections to large transverse momentum production of W bosons at the LHC*, [Phys. Lett. B **651** \(2007\) 160](#), arXiv: [hep-ph/0703283](#).
- [74] J. H. Kühn, A. Kulesza, S. Pozzorini and M. Schulze, *One-loop weak corrections to hadronic production of Z bosons at large transverse momenta*, [Nucl. Phys. B **727** \(2005\) 368](#), arXiv: [hep-ph/0507178](#).
- [75] J. H. Kühn, A. Kulesza, S. Pozzorini and M. Schulze, *Electroweak corrections to hadronic production of W bosons at large transverse momenta*, [Nucl. Phys. B **797** \(2008\) 27](#), arXiv: [0708.0476 \[hep-ph\]](#).
- [76] A. Gehrmann-De Ridder, T. Gehrmann, E. W. N. Glover, A. Huss and T. A. Morgan, *Precise QCD predictions for the production of a Z boson in association with a hadronic jet*, [Phys. Rev. Lett. **117** \(2016\) 022001](#), arXiv: [1507.02850 \[hep-ph\]](#).
- [77] A. Gehrmann-De Ridder, T. Gehrmann, E. W. N. Glover, A. Huss and T. A. Morgan, *The NNLO QCD corrections to Z boson production at large transverse momentum*, [JHEP **07** \(2016\) 133](#), arXiv: [1605.04295 \[hep-ph\]](#).
- [78] R. Boughezal, X. Liu and F. Petriello, *Phenomenology of the Z boson plus jet process at NNLO*, [Phys. Rev. D **94** \(2016\) 074015](#), arXiv: [1602.08140 \[hep-ph\]](#).
- [79] R. Boughezal, X. Liu and F. Petriello, *W -boson plus jet differential distributions at NNLO in QCD*, [Phys. Rev. D **94** \(2016\) 113009](#), arXiv: [1602.06965 \[hep-ph\]](#).
- [80] ATLAS Collaboration, *Measurements of the production cross section of a Z boson in association with jets in pp collisions at $\sqrt{s} = 13$ TeV with the ATLAS detector*, [Eur. Phys. J. C **77** \(2017\) 361](#), arXiv: [1702.05725 \[hep-ex\]](#).
- [81] J. M. Lindert, S. Pozzorini and M. Schönherr, *Precise predictions for $V + 2 jet$ backgrounds in searches for invisible Higgs decays*, [JHEP **01** \(2023\) 070](#), arXiv: [2204.07652 \[hep-ph\]](#), We are very grateful to Jonas Lindert for insights and providing dedicated calculations for this analysis.
- [82] J. R. Andersen and J. M. Smillie, *Constructing All-Order Corrections to Multi-Jet Rates*, [JHEP **01** \(2010\) 039](#), arXiv: [0908.2786 \[hep-ph\]](#).
- [83] J. R. Andersen and J. M. Smillie, *High Energy Description of Processes with Multiple Hard Jets*, [Nucl. Phys. B Proc. Suppl. **205-206** \(2010\) 205](#), ed. by J. Blümlein, S.-O. Moch and T. Riemann, arXiv: [1007.4449 \[hep-ph\]](#).

- [84] J. R. Andersen et al.,
HEJ 2.2: W boson pairs and Higgs boson plus jet production at high energies, (2023),
arXiv: [2303.15778 \[hep-ph\]](#), We are very grateful to Jeppe Andersen, Conor Elrick,
Andreas Maier and Jennifer Smillie for providing dedicated predictions for this analysis.
- [85] T. Sjöstrand, S. Mrenna and P. Skands, *A brief introduction to PYTHIA 8.1*,
Comput. Phys. Commun. **178** (2008) 852, arXiv: [0710.3820 \[hep-ph\]](#).
- [86] B. Andersson, G. Gustafson, G. Ingelman and T. Sjöstrand,
Parton fragmentation and string dynamics, *Phys. Rept.* **97** (1983) 31.
- [87] T. Sjöstrand, *Jet fragmentation of multiparton configurations in a string framework*,
Nucl. Phys. B **248** (1984) 469.
- [88] ATLAS Collaboration,
Luminosity determination in pp collisions at $\sqrt{s} = 13$ TeV using the ATLAS detector at the LHC,
Eur. Phys. J. C **83** (2023) 982, arXiv: [2212.09379 \[hep-ex\]](#).
- [89] ATLAS Collaboration, *Performance of the missing transverse momentum triggers for the ATLAS
detector during Run-2 data taking*, *JHEP* **08** (2020) 080, arXiv: [2005.09554 \[hep-ex\]](#).
- [90] ATLAS Collaboration, *Performance of electron and photon triggers in ATLAS during LHC Run 2*,
Eur. Phys. J. C **80** (2020) 47, arXiv: [1909.00761 \[hep-ex\]](#).
- [91] ATLAS Collaboration, *Vertex Reconstruction Performance of the ATLAS Detector at $\sqrt{s} = 13$ TeV*,
ATL-PHYS-PUB-2015-026, 2015, URL: <https://cds.cern.ch/record/2037717>.
- [92] ATLAS Collaboration, *Electron and photon performance measurements with the ATLAS detector
using the 2015–2017 LHC proton–proton collision data*, *JINST* **14** (2019) P12006,
arXiv: [1908.00005 \[hep-ex\]](#).
- [93] ATLAS Collaboration,
Topological cell clustering in the ATLAS calorimeters and its performance in LHC Run 1,
Eur. Phys. J. C **77** (2017) 490, arXiv: [1603.02934 \[hep-ex\]](#).
- [94] ATLAS Collaboration, *Electron and photon energy calibration with the ATLAS detector using
2015–2016 LHC proton–proton collision data*, *JINST* **14** (2019) P03017,
arXiv: [1812.03848 \[hep-ex\]](#).
- [95] ATLAS Collaboration, *Muon reconstruction and identification efficiency in ATLAS using the full
Run 2 pp collision data set at $\sqrt{s} = 13$ TeV*, *Eur. Phys. J. C* **81** (2021) 578,
arXiv: [2012.00578 \[hep-ex\]](#).
- [96] ATLAS Collaboration, *Muon reconstruction performance of the ATLAS detector in proton–proton
collision data at $\sqrt{s} = 13$ TeV*, *Eur. Phys. J. C* **76** (2016) 292, arXiv: [1603.05598 \[hep-ex\]](#).
- [97] ATLAS Collaboration, *Reconstruction, Energy Calibration, and Identification of Hadronically
Decaying Tau Leptons in the ATLAS Experiment for Run-2 of the LHC*,
ATL-PHYS-PUB-2015-045, 2015, URL: <https://cds.cern.ch/record/2064383>.
- [98] ATLAS Collaboration,
Identification of hadronic tau lepton decays using neural networks in the ATLAS experiment,
ATL-PHYS-PUB-2019-033, 2019, URL: <https://cds.cern.ch/record/2688062>.
- [99] ATLAS Collaboration,
Jet reconstruction and performance using particle flow with the ATLAS Detector,
Eur. Phys. J. C **77** (2017) 466, arXiv: [1703.10485 \[hep-ex\]](#).

- [100] ATLAS Collaboration, *Selection of jets produced in 13 TeV proton–proton collisions with the ATLAS detector*, ATLAS-CONF-2015-029, 2015, URL: <https://cds.cern.ch/record/2037702>.
- [101] ATLAS Collaboration, *Performance of pile-up mitigation techniques for jets in pp collisions at $\sqrt{s} = 8$ TeV using the ATLAS detector*, *Eur. Phys. J. C* **76** (2016) 581, arXiv: [1510.03823](https://arxiv.org/abs/1510.03823) [[hep-ex](#)].
- [102] ATLAS Collaboration, *Forward Jet Vertex Tagging: A new technique for the identification and rejection of forward pileup jets*, ATL-PHYS-PUB-2015-034, 2015, URL: <https://cds.cern.ch/record/2042098>.
- [103] ATLAS Collaboration, *Jet energy scale and resolution measured in proton–proton collisions at $\sqrt{s} = 13$ TeV with the ATLAS detector*, *Eur. Phys. J. C* **81** (2021) 689, arXiv: [2007.02645](https://arxiv.org/abs/2007.02645) [[hep-ex](#)].
- [104] ATLAS Collaboration, *Performance of algorithms that reconstruct missing transverse momentum in $\sqrt{s} = 8$ TeV proton–proton collisions in the ATLAS detector*, *Eur. Phys. J. C* **77** (2017) 241, arXiv: [1609.09324](https://arxiv.org/abs/1609.09324) [[hep-ex](#)].
- [105] ATLAS Collaboration, *Search for squarks and gluinos with the ATLAS detector in final states with jets and missing transverse momentum using 4.7 fb^{-1} of $\sqrt{s} = 7$ TeV proton–proton collision data*, *Phys. Rev. D* **87** (2013) 012008, arXiv: [1208.0949](https://arxiv.org/abs/1208.0949) [[hep-ex](#)].
- [106] ATLAS Collaboration, *Measurement of the inclusive isolated prompt photon cross section in pp collisions at $\sqrt{s} = 8$ TeV with the ATLAS detector*, *JHEP* **08** (2016) 005, arXiv: [1605.03495](https://arxiv.org/abs/1605.03495) [[hep-ex](#)].
- [107] ATLAS Collaboration, *Measurement of the cross section for isolated-photon plus jet production in pp collisions at $\sqrt{s} = 13$ TeV using the ATLAS detector*, *Phys. Lett. B* **780** (2018) 578, arXiv: [1801.00112](https://arxiv.org/abs/1801.00112) [[hep-ex](#)].
- [108] ATLAS Collaboration, *Tools for estimating fake/non-prompt lepton backgrounds with the ATLAS detector at the LHC*, *JINST* **18** (2023) T11004, arXiv: [2211.16178](https://arxiv.org/abs/2211.16178) [[hep-ex](#)].
- [109] ATLAS Collaboration, *Measurement of the tau lepton reconstruction and identification performance in the ATLAS experiment using pp collisions at $\sqrt{s} = 13$ TeV*, ATLAS-CONF-2017-029, 2017, URL: <https://cds.cern.ch/record/2261772>.
- [110] ATLAS Collaboration, *Performance of missing transverse momentum reconstruction with the ATLAS detector using proton–proton collisions at $\sqrt{s} = 13$ TeV*, *Eur. Phys. J. C* **78** (2018) 903, arXiv: [1802.08168](https://arxiv.org/abs/1802.08168) [[hep-ex](#)].
- [111] X. Chen, T. Gehrmann, N. Glover, M. Höfer and A. Huss, *Isolated photon and photon+jet production at NNLO QCD accuracy*, *JHEP* **04** (2020) 166, arXiv: [1904.01044](https://arxiv.org/abs/1904.01044) [[hep-ph](#)].
- [112] ATLAS Collaboration, *Evaluating statistical uncertainties and correlations using the bootstrap method*, ATL-PHYS-PUB-2021-011, 2021, URL: <https://cds.cern.ch/record/2759945>.
- [113] P. Pani and G. Polesello, *Dark matter production in association with a single top-quark at the LHC in a two-Higgs-doublet model with a pseudoscalar mediator*, *Phys. Dark Univ.* **21** (2018) 8, arXiv: [1712.03874](https://arxiv.org/abs/1712.03874) [[hep-ph](#)].

- [114] X. Cid Vidal et al., *Beyond the Standard Model physics at the HL-LHC and HE-LHC*, [CERN Yellow Rep. Monogr. 7 \(2019\) 585](#), ed. by A. Dainese et al., arXiv: [1812.07831 \[hep-ph\]](#).
- [115] ATLAS Collaboration, *ATLAS sensitivity to Two-Higgs-Doublet models with an additional pseudoscalar exploiting four top quark signatures with $3ab^{-1}$ of $\sqrt{s} = 14$ TeV proton–proton collisions*, ATL-PHYS-PUB-2018-027, 2018, URL: <https://cds.cern.ch/record/2645845>.
- [116] U. Haisch and G. Polesello, *Searching for heavy Higgs bosons in the $t\bar{t}Z$ and tbW final states*, [JHEP 09 \(2018\) 151](#), arXiv: [1807.07734 \[hep-ph\]](#).
- [117] J. M. Butterworth, M. Habedank, P. Pani and A. Vaitkus, *A study of collider signatures for two Higgs doublet models with a Pseudoscalar mediator to Dark Matter*, [SciPost Phys. Core 4 \(2021\) 003](#), arXiv: [2009.02220 \[hep-ph\]](#).
- [118] T. Robens, *The THDMa Revisited*, [Symmetry 13 \(2021\) 2341](#), arXiv: [2106.02962 \[hep-ph\]](#).
- [119] ATLAS Collaboration, *ATLAS Computing Acknowledgements*, ATL-SOFT-PUB-2023-001, 2023, URL: <https://cds.cern.ch/record/2869272>.

The ATLAS Collaboration

G. Aad ¹⁰³, E. Aakvaag ¹⁶, B. Abbott ¹²¹, K. Abeling ⁵⁵, N.J. Abicht ⁴⁹, S.H. Abidi ²⁹, M. Aboeela ⁴⁴, A. Aboulhorma ^{35e}, H. Abramowicz ¹⁵², H. Abreu ¹⁵¹, Y. Abulaiti ¹¹⁸, B.S. Acharya ^{69a,69b,1}, A. Ackermann ^{63a}, C. Adam Bourdarios ⁴, L. Adamczyk ^{86a}, S.V. Addepalli ²⁶, M.J. Addison ¹⁰², J. Adelman ¹¹⁶, A. Adiguzel ^{21c}, T. Adye ¹³⁵, A.A. Affolder ¹³⁷, Y. Afik ³⁹, M.N. Agaras ¹³, J. Agarwala ^{73a,73b}, A. Aggarwal ¹⁰¹, C. Agheorghiesei ^{27c}, A. Ahmad ³⁶, F. Ahmadov ^{38,y}, W.S. Ahmed ¹⁰⁵, S. Ahuja ⁹⁶, X. Ai ^{62e}, G. Aielli ^{76a,76b}, A. Aikot ¹⁶⁴, M. Ait Tamlihat ^{35e}, B. Aitbenchikh ^{35a}, I. Aizenberg ¹⁷⁰, M. Akbiyik ¹⁰¹, T.P.A. Åkesson ⁹⁹, A.V. Akimov ³⁷, D. Akiyama ¹⁶⁹, N.N. Akolkar ²⁴, S. Aktas ^{21a}, K. Al Houry ⁴¹, G.L. Alberghi ^{23b}, J. Albert ¹⁶⁶, P. Albicocco ⁵³, G.L. Albouy ⁶⁰, S. Alderweireldt ⁵², Z.L. Alegria ¹²², M. Aleksa ³⁶, I.N. Aleksandrov ³⁸, C. Alexa ^{27b}, T. Alexopoulos ¹⁰, F. Alfonsi ^{23b}, M. Algren ⁵⁶, M. Alhroob ¹⁴², B. Ali ¹³³, H.M.J. Ali ⁹², S. Ali ¹⁴⁹, S.W. Alibocus ⁹³, M. Aliev ^{33c}, G. Alimonti ^{71a}, W. Alkakhri ⁵⁵, C. Allaire ⁶⁶, B.M.M. Allbrooke ¹⁴⁷, J.F. Allen ⁵², C.A. Allendes Flores ^{138f}, P.P. Allport ²⁰, A. Aloisio ^{72a,72b}, F. Alonso ⁹¹, C. Alpigiani ¹³⁹, M. Alvarez Estevez ¹⁰⁰, A. Alvarez Fernandez ¹⁰¹, M. Alves Cardoso ⁵⁶, M.G. Alviggi ^{72a,72b}, M. Aly ¹⁰², Y. Amaral Coutinho ^{83b}, A. Ambler ¹⁰⁵, C. Amelung ³⁶, M. Amerl ¹⁰², C.G. Ames ¹¹⁰, D. Amidei ¹⁰⁷, K.J. Amirie ¹⁵⁶, S.P. Amor Dos Santos ^{131a}, K.R. Amos ¹⁶⁴, S. An ⁸⁴, V. Ananiev ¹²⁶, C. Anastopoulos ¹⁴⁰, T. Andeen ¹¹, J.K. Anders ³⁶, S.Y. Andrean ^{47a,47b}, A. Andreazza ^{71a,71b}, S. Angelidakis ⁹, A. Angerami ^{41,aa}, A.V. Anisenkov ³⁷, A. Annovi ^{74a}, C. Antel ⁵⁶, M.T. Anthony ¹⁴⁰, E. Antipov ¹⁴⁶, M. Antonelli ⁵³, F. Anulli ^{75a}, M. Aoki ⁸⁴, T. Aoki ¹⁵⁴, J.A. Aparisi Pozo ¹⁶⁴, M.A. Aparo ¹⁴⁷, L. Aperio Bella ⁴⁸, C. Appelt ¹⁸, A. Apyan ²⁶, S.J. Arbiol Val ⁸⁷, C. Arcangeletti ⁵³, A.T.H. Arce ⁵¹, E. Arena ⁹³, J-F. Arguin ¹⁰⁹, S. Argyropoulos ⁵⁴, J.-H. Arling ⁴⁸, O. Arnaez ⁴, H. Arnold ¹¹⁵, G. Artoni ^{75a,75b}, H. Asada ¹¹², K. Asai ¹¹⁹, S. Asai ¹⁵⁴, N.A. Asbah ³⁶, K. Assamagan ²⁹, R. Astalos ^{28a}, K.S.V. Astrand ⁹⁹, S. Atashi ¹⁶⁰, R.J. Atkin ^{33a}, M. Atkinson ¹⁶³, H. Atmani ^{35f}, P.A. Atlasiddha ¹²⁹, K. Augsten ¹³³, S. Auricchio ^{72a,72b}, A.D. Auriol ²⁰, V.A. Austrup ¹⁰², G. Avolio ³⁶, K. Axiotis ⁵⁶, G. Azuelos ^{109,ae}, D. Babal ^{28b}, H. Bachacou ¹³⁶, K. Bachas ^{153,p}, A. Bachiu ³⁴, F. Backman ^{47a,47b}, A. Badea ³⁹, T.M. Baer ¹⁰⁷, P. Bagnaia ^{75a,75b}, M. Bahmani ¹⁸, D. Bahner ⁵⁴, K. Bai ¹²⁴, A.J. Bailey ¹⁶⁴, J.T. Baines ¹³⁵, L. Baines ⁹⁵, O.K. Baker ¹⁷³, E. Bakos ¹⁵, D. Bakshi Gupta ⁸, V. Balakrishnan ¹²¹, R. Balasubramanian ¹¹⁵, E.M. Baldin ³⁷, P. Balek ^{86a}, E. Ballabene ^{23b,23a}, F. Balli ¹³⁶, L.M. Baltes ^{63a}, W.K. Balunas ³², J. Balz ¹⁰¹, E. Banas ⁸⁷, M. Bandieramonte ¹³⁰, A. Bandyopadhyay ²⁴, S. Bansal ²⁴, L. Barak ¹⁵², M. Barakat ⁴⁸, E.L. Barberio ¹⁰⁶, D. Barberis ^{57b,57a}, M. Barbero ¹⁰³, M.Z. Barel ¹¹⁵, K.N. Barends ^{33a}, T. Barillari ¹¹¹, M-S. Barisits ³⁶, T. Barklow ¹⁴⁴, P. Baron ¹²³, D.A. Baron Moreno ¹⁰², A. Baroncelli ^{62a}, G. Barone ²⁹, A.J. Barr ¹²⁷, J.D. Barr ⁹⁷, F. Barreiro ¹⁰⁰, J. Barreiro Guimarães da Costa ^{14a}, U. Barron ¹⁵², M.G. Barros Teixeira ^{131a}, S. Barsov ³⁷, F. Bartels ^{63a}, R. Bartoldus ¹⁴⁴, A.E. Barton ⁹², P. Bartos ^{28a}, A. Basan ¹⁰¹, M. Baselga ⁴⁹, A. Bassalat ^{66,b}, M.J. Basso ^{157a}, R.L. Bates ⁵⁹, S. Batlamous ^{35e}, B. Batool ¹⁴², M. Battaglia ¹³⁷, D. Battulga ¹⁸, M. Bauce ^{75a,75b}, M. Bauer ³⁶, P. Bauer ²⁴, L.T. Bazzano Hurrell ³⁰, J.B. Beacham ⁵¹, T. Beau ¹²⁸, J.Y. Beaucamp ⁹¹, P.H. Beauchemin ¹⁵⁹, P. Bechtle ²⁴, H.P. Beck ^{19,o}, K. Becker ¹⁶⁸, A.J. Beddall ⁸², V.A. Bednyakov ³⁸, C.P. Bee ¹⁴⁶, L.J. Beemster ¹⁵, T.A. Beermann ³⁶, M. Begalli ^{83d}, M. Begel ²⁹, A. Behera ¹⁴⁶, J.K. Behr ⁴⁸, J.F. Beirer ³⁶, F. Beisiegel ²⁴, M. Belfkir ^{117b}, G. Bella ¹⁵², L. Bellagamba ^{23b}, A. Bellerive ³⁴, P. Bellos ²⁰, K. Beloborodov ³⁷, D. Benckekroun ^{35a}, F. Bendebba ^{35a}, Y. Benhammou ¹⁵²,

K.C. Benkendorfer ⁶¹, L. Beresford ⁴⁸, M. Beretta ⁵³, E. Bergeaas Kuutmann ¹⁶², N. Berger ⁴,
 B. Bergmann ¹³³, J. Beringer ^{17a}, G. Bernardi ⁵, C. Bernius ¹⁴⁴, F.U. Bernlochner ²⁴,
 F. Bernon ^{36,103}, A. Berrocal Guardia ¹³, T. Berry ⁹⁶, P. Berta ¹³⁴, A. Berthold ⁵⁰, S. Bethke ¹¹¹,
 A. Betti ^{75a,75b}, A.J. Bevan ⁹⁵, N.K. Bhalla ⁵⁴, M. Bhamjee ^{33c}, S. Bhatta ¹⁴⁶,
 D.S. Bhattacharya ¹⁶⁷, P. Bhattarai ¹⁴⁴, K.D. Bhide ⁵⁴, V.S. Bhopatkar ¹²², R.M. Bianchi ¹³⁰,
 G. Bianco ^{23b,23a}, O. Biebel ¹¹⁰, R. Bielski ¹²⁴, M. Biglietti ^{77a}, C.S. Billingsley ⁴⁴, M. Bindi ⁵⁵,
 A. Bingul ^{21b}, C. Bini ^{75a,75b}, A. Biondini ⁹³, C.J. Birch-sykes ¹⁰², G.A. Bird ³², M. Birman ¹⁷⁰,
 M. Biros ¹³⁴, S. Biryukov ¹⁴⁷, T. Bisanz ⁴⁹, E. Bisceglie ^{43b,43a}, J.P. Biswal ¹³⁵, D. Biswas ¹⁴²,
 K. Bjørke ¹²⁶, I. Bloch ⁴⁸, A. Blue ⁵⁹, U. Blumenschein ⁹⁵, J. Blumenthal ¹⁰¹,
 V.S. Bobrovnikov ³⁷, M. Boehler ⁵⁴, B. Boehm ¹⁶⁷, D. Bogovac ³⁶, A.G. Bogdanchikov ³⁷,
 C. Bohm ^{47a}, V. Boisvert ⁹⁶, P. Bokan ³⁶, T. Bold ^{86a}, M. Bomben ⁵, M. Bona ⁹⁵,
 M. Boonekamp ¹³⁶, C.D. Booth ⁹⁶, A.G. Borbély ⁵⁹, I.S. Bordulev ³⁷, H.M. Borecka-Bielska ¹⁰⁹,
 G. Borissov ⁹², D. Bortoletto ¹²⁷, D. Boscherini ^{23b}, M. Bosman ¹³, J.D. Bossio Sola ³⁶,
 K. Bouaouda ^{35a}, N. Bouchhar ¹⁶⁴, J. Boudreau ¹³⁰, E.V. Bouhova-Thacker ⁹², D. Boumediene ⁴⁰,
 R. Bouquet ^{57b,57a}, A. Boveia ¹²⁰, J. Boyd ³⁶, D. Boye ²⁹, I.R. Boyko ³⁸, J. Bracinik ²⁰,
 N. Brahimy ⁴, G. Brandt ¹⁷², O. Brandt ³², F. Braren ⁴⁸, B. Brau ¹⁰⁴, J.E. Brau ¹²⁴,
 R. Brenner ¹⁷⁰, L. Brenner ¹¹⁵, R. Brenner ¹⁶², S. Bressler ¹⁷⁰, D. Britton ⁵⁹, D. Britzger ¹¹¹,
 I. Brock ²⁴, G. Brooijmans ⁴¹, E. Brost ²⁹, L.M. Brown ¹⁶⁶, L.E. Bruce ⁶¹, T.L. Bruckler ¹²⁷,
 P.A. Bruckman de Renstrom ⁸⁷, B. Brüers ⁴⁸, A. Bruni ^{23b}, G. Bruni ^{23b}, M. Bruschi ^{23b},
 N. Brusino ^{75a,75b}, T. Buanes ¹⁶, Q. Buat ¹³⁹, D. Buchin ¹¹¹, A.G. Buckley ⁵⁹, O. Bulekov ³⁷,
 B.A. Bullard ¹⁴⁴, S. Burdin ⁹³, C.D. Burgard ⁴⁹, A.M. Burger ³⁶, B. Burghgrave ⁸,
 O. Burlayenko ⁵⁴, J.T.P. Burr ³², C.D. Burton ¹¹, J.C. Burzynski ¹⁴³, E.L. Busch ⁴¹,
 V. Büscher ¹⁰¹, P.J. Bussey ⁵⁹, J.M. Butler ²⁵, C.M. Buttar ⁵⁹, J.M. Butterworth ⁹⁷,
 W. Buttinger ¹³⁵, C.J. Buxo Vazquez ¹⁰⁸, A.R. Buzykaev ³⁷, S. Cabrera Urbán ¹⁶⁴,
 L. Cadamuro ⁶⁶, D. Caforio ⁵⁸, H. Cai ¹³⁰, Y. Cai ^{14a,14e}, Y. Cai ^{14c}, V.M.M. Cairo ³⁶,
 O. Cakir ^{3a}, N. Calace ³⁶, P. Calafiura ^{17a}, G. Calderini ¹²⁸, P. Calfayan ⁶⁸, G. Callea ⁵⁹,
 L.P. Caloba ^{83b}, D. Calvet ⁴⁰, S. Calvet ⁴⁰, M. Calvetti ^{74a,74b}, R. Camacho Toro ¹²⁸,
 S. Camarda ³⁶, D. Camarero Munoz ²⁶, P. Camarri ^{76a,76b}, M.T. Camerlingo ^{72a,72b},
 D. Cameron ³⁶, C. Camincher ¹⁶⁶, M. Campanelli ⁹⁷, A. Camplani ⁴², V. Canale ^{72a,72b},
 A.C. Canbay ^{3a}, E. Canonero ⁹⁶, J. Cantero ¹⁶⁴, Y. Cao ¹⁶³, F. Capocasa ²⁶, M. Capua ^{43b,43a},
 A. Carbone ^{71a,71b}, R. Cardarelli ^{76a}, J.C.J. Cardenas ⁸, F. Cardillo ¹⁶⁴, G. Carducci ^{43b,43a},
 T. Carli ³⁶, G. Carlino ^{72a}, J.I. Carlotto ¹³, B.T. Carlson ^{130,q}, E.M. Carlson ^{166,157a},
 L. Carminati ^{71a,71b}, A. Carnelli ¹³⁶, M. Carnesale ^{75a,75b}, S. Caron ¹¹⁴, E. Carquin ^{138f},
 S. Carrá ^{71a}, G. Carratta ^{23b,23a}, A.M. Carroll ¹²⁴, T.M. Carter ⁵², M.P. Casado ^{13,i},
 M. Caspar ⁴⁸, F.L. Castillo ⁴, L. Castillo Garcia ¹³, V. Castillo Gimenez ¹⁶⁴, N.F. Castro ^{131a,131e},
 A. Catinaccio ³⁶, J.R. Catmore ¹²⁶, T. Cavaliere ⁴, V. Cavaliere ²⁹, N. Cavalli ^{23b,23a},
 Y.C. Cekmecelioglu ⁴⁸, E. Celebi ^{21a}, S. Cella ³⁶, F. Celli ¹²⁷, M.S. Centonze ^{70a,70b},
 V. Cepaitis ⁵⁶, K. Cerny ¹²³, A.S. Cerqueira ^{83a}, A. Cerri ¹⁴⁷, L. Cerrito ^{76a,76b}, F. Cerutti ^{17a},
 B. Cervato ¹⁴², A. Cervelli ^{23b}, G. Cesarini ⁵³, S.A. Cetin ⁸², D. Chakraborty ¹¹⁶, J. Chan ¹⁷¹,
 W.Y. Chan ¹⁵⁴, J.D. Chapman ³², E. Chapon ¹³⁶, B. Chargeishvili ^{150b}, D.G. Charlton ²⁰,
 M. Chatterjee ¹⁹, C. Chauhan ¹³⁴, Y. Che ^{14c}, S. Chekanov ⁶, S.V. Chekulaev ^{157a},
 G.A. Chelkov ^{38,a}, A. Chen ¹⁰⁷, B. Chen ¹⁵², B. Chen ¹⁶⁶, H. Chen ^{14c}, H. Chen ²⁹,
 J. Chen ^{62c}, J. Chen ¹⁴³, M. Chen ¹²⁷, S. Chen ¹⁵⁴, S.J. Chen ^{14c}, X. Chen ^{62c,136},
 X. Chen ^{14b,ad}, Y. Chen ^{62a}, C.L. Cheng ¹⁷¹, H.C. Cheng ^{64a}, S. Cheong ¹⁴⁴, A. Cheplakov ³⁸,
 E. Cheremushkina ⁴⁸, E. Cherepanova ¹¹⁵, R. Cherkaoui El Moursli ^{35e}, E. Cheu ⁷, K. Cheung ⁶⁵,
 L. Chevalier ¹³⁶, V. Chiarella ⁵³, G. Chiarelli ^{74a}, N. Chiedde ¹⁰³, G. Chiodini ^{70a},
 A.S. Chisholm ²⁰, A. Chitan ^{27b}, M. Chitishvili ¹⁶⁴, M.V. Chizhov ³⁸, K. Choi ¹¹, Y. Chou ¹³⁹,

E.Y.S. Chow [id114](#), K.L. Chu [id170](#), M.C. Chu [id64a](#), X. Chu [id14a,14e](#), J. Chudoba [id132](#),
 J.J. Chwastowski [id87](#), D. Cieri [id111](#), K.M. Ciesla [id86a](#), V. Cindro [id94](#), A. Ciocio [id17a](#), F. Ciroto [id72a,72b](#),
 Z.H. Citron [id170](#), M. Citterio [id71a](#), D.A. Ciubotaru [id27b](#), A. Clark [id56](#), P.J. Clark [id52](#), C. Clarry [id156](#),
 J.M. Clavijo Columbie [id48](#), S.E. Clawson [id48](#), C. Clement [id47a,47b](#), J. Clercx [id48](#), Y. Coadou [id103](#),
 M. Cobal [id69a,69c](#), A. Coccaro [id57b](#), R.F. Coelho Barrue [id131a](#), R. Coelho Lopes De Sa [id104](#),
 S. Coelli [id71a](#), B. Cole [id41](#), J. Collot [id60](#), P. Conde Muiño [id131a,131g](#), M.P. Connell [id33c](#),
 S.H. Connell [id33c](#), E.I. Conroy [id127](#), F. Conventi [id72a,af](#), H.G. Cooke [id20](#), A.M. Cooper-Sarkar [id127](#),
 A. Cordeiro Oudot Choi [id128](#), L.D. Corpe [id40](#), M. Corradi [id75a,75b](#), F. Corriveau [id105,w](#),
 A. Cortes-Gonzalez [id18](#), M.J. Costa [id164](#), F. Costanza [id4](#), D. Costanzo [id140](#), B.M. Cote [id120](#),
 G. Cowan [id96](#), K. Cranmer [id171](#), D. Cremonini [id23b,23a](#), S. Crépe-Renaudin [id60](#), F. Crescioli [id128](#),
 M. Cristinziani [id142](#), M. Cristoforetti [id78a,78b](#), V. Croft [id115](#), J.E. Crosby [id122](#), G. Crosetti [id43b,43a](#),
 A. Cueto [id100](#), H. Cui [id14a,14e](#), Z. Cui [id7](#), W.R. Cunningham [id59](#), F. Curcio [id164](#), J.R. Curran [id52](#),
 P. Czodrowski [id36](#), M.M. Czurylo [id36](#), M.J. Da Cunha Sargedas De Sousa [id57b,57a](#),
 J.V. Da Fonseca Pinto [id83b](#), C. Da Via [id102](#), W. Dabrowski [id86a](#), T. Dado [id49](#), S. Dahbi [id149](#),
 T. Dai [id107](#), D. Dal Santo [id19](#), C. Dallapiccola [id104](#), M. Dam [id42](#), G. D'amen [id29](#), V. D'Amico [id110](#),
 J. Damp [id101](#), J.R. Dandoy [id34](#), M. Danninger [id143](#), V. Dao [id36](#), G. Darbo [id57b](#), S.J. Das [id29,ag](#),
 F. Dattola [id48](#), S. D'Auria [id71a,71b](#), A. D'avanzo [id72a,72b](#), C. David [id33a](#), T. Davidek [id134](#),
 B. Davis-Purcell [id34](#), I. Dawson [id95](#), H.A. Day-hall [id133](#), K. De [id8](#), R. De Asmundis [id72a](#),
 N. De Biase [id48](#), S. De Castro [id23b,23a](#), N. De Groot [id114](#), P. de Jong [id115](#), H. De la Torre [id116](#),
 A. De Maria [id14c](#), A. De Salvo [id75a](#), U. De Sanctis [id76a,76b](#), F. De Santis [id70a,70b](#), A. De Santo [id147](#),
 J.B. De Vivie De Regie [id60](#), D.V. Dedovich [id38](#), J. Degens [id93](#), A.M. Deiana [id44](#), F. Del Corso [id23b,23a](#),
 J. Del Peso [id100](#), F. Del Rio [id63a](#), L. Delagrangé [id128](#), F. Deliot [id136](#), C.M. Delitzsch [id49](#),
 M. Della Pietra [id72a,72b](#), D. Della Volpe [id56](#), A. Dell'Acqua [id36](#), L. Dell'Asta [id71a,71b](#), M. Delmastro [id4](#),
 P.A. Delsart [id60](#), S. Demers [id173](#), M. Demichev [id38](#), S.P. Denisov [id37](#), L. D'Eramo [id40](#),
 D. Derendarz [id87](#), F. Derue [id128](#), P. Dervan [id93](#), K. Desch [id24](#), C. Deutsch [id24](#), F.A. Di Bello [id57b,57a](#),
 A. Di Ciaccio [id76a,76b](#), L. Di Ciaccio [id4](#), A. Di Domenico [id75a,75b](#), C. Di Donato [id72a,72b](#),
 A. Di Girolamo [id36](#), G. Di Gregorio [id36](#), A. Di Luca [id78a,78b](#), B. Di Micco [id77a,77b](#), R. Di Nardo [id77a,77b](#),
 M. Diamantopoulou [id34](#), F.A. Dias [id115](#), T. Dias Do Vale [id143](#), M.A. Diaz [id138a,138b](#),
 F.G. Diaz Capriles [id24](#), M. Didenko [id164](#), E.B. Diehl [id107](#), S. Díez Cornell [id48](#), C. Diez Pardos [id142](#),
 C. Dimitriadi [id162,24](#), A. Dimitrievska [id17a](#), J. Dingfelder [id24](#), I-M. Dinu [id27b](#), S.J. Dittmeier [id63b](#),
 F. Dittus [id36](#), M. Divisek [id134](#), F. Djama [id103](#), T. Djobava [id150b](#), C. Doglioni [id102,99](#), A. Dohnalova [id28a](#),
 J. Dolejsi [id134](#), Z. Dolezal [id134](#), K.M. Dona [id39](#), M. Donadelli [id83c](#), B. Dong [id108](#), J. Donini [id40](#),
 A. D'Onofrio [id72a,72b](#), M. D'Onofrio [id93](#), J. Dopke [id135](#), A. Doria [id72a](#), N. Dos Santos Fernandes [id131a](#),
 P. Dougan [id102](#), M.T. Dova [id91](#), A.T. Doyle [id59](#), M.A. Draguet [id127](#), E. Dreyer [id170](#),
 I. Drivas-koulouris [id10](#), M. Drnevich [id118](#), M. Drozdova [id56](#), D. Du [id62a](#), T.A. du Pree [id115](#),
 F. Dubinin [id37](#), M. Dubovsky [id28a](#), E. Duchovni [id170](#), G. Duckeck [id110](#), O.A. Ducu [id27b](#), D. Duda [id52](#),
 A. Dudarev [id36](#), E.R. Duden [id26](#), M. D'uffizi [id102](#), L. Duflost [id66](#), M. Dührssen [id36](#), I. Duminica [id27g](#),
 A.E. Dumitriu [id27b](#), M. Dunford [id63a](#), S. Dungs [id49](#), K. Dunne [id47a,47b](#), A. Duperrin [id103](#),
 H. Duran Yildiz [id3a](#), M. Düren [id58](#), A. Durglishvili [id150b](#), B.L. Dwyer [id116](#), G.I. Dyckes [id17a](#),
 M. Dyndal [id86a](#), B.S. Dziedzic [id87](#), Z.O. Earnshaw [id147](#), G.H. Eberwein [id127](#), B. Eckerova [id28a](#),
 S. Eggebrecht [id55](#), E. Egidio Purcino De Souza [id128](#), L.F. Ehrke [id56](#), G. Eigen [id16](#), K. Einsweiler [id17a](#),
 T. Ekelof [id162](#), P.A. Ekman [id99](#), S. El Farkh [id35b](#), Y. El Ghazali [id35b](#), H. El Jarrari [id36](#),
 A. El Moussaouy [id109](#), V. Ellajosyula [id162](#), M. Ellert [id162](#), F. Ellinghaus [id172](#), N. Ellis [id36](#),
 J. Elmsheuser [id29](#), M. Elsayy [id117a](#), M. Elsing [id36](#), D. Emeljanov [id135](#), Y. Enari [id154](#), I. Ene [id17a](#),
 S. Epari [id13](#), P.A. Erland [id87](#), M. Errenst [id172](#), M. Escalier [id66](#), C. Escobar [id164](#), E. Etzion [id152](#),
 G. Evans [id131a](#), H. Evans [id68](#), L.S. Evans [id96](#), A. Ezhilov [id37](#), S. Ezzarqtouni [id35a](#), F. Fabbri [id23b,23a](#),
 L. Fabbri [id23b,23a](#), G. Facini [id97](#), V. Fadeyev [id137](#), R.M. Fakhruddinov [id37](#), D. Fakoudis [id101](#),

S. Falciano ^{75a}, L.F. Falda Ulhoa Coelho ³⁶, P.J. Falke ²⁴, F. Fallavollita ¹¹¹, J. Faltova ¹³⁴,
 C. Fan ¹⁶³, Y. Fan ^{14a}, Y. Fang ^{14a,14e}, M. Fanti ^{71a,71b}, M. Faraj ^{69a,69b}, Z. Farazpay ⁹⁸,
 A. Farbin ⁸, A. Farilla ^{77a}, T. Farooque ¹⁰⁸, S.M. Farrington ⁵², F. Fassi ^{35e}, D. Fassouliotis ⁹,
 M. Faucci Giannelli ^{76a,76b}, W.J. Fawcett ³², L. Fayard ⁶⁶, P. Federic ¹³⁴, P. Federicova ¹³²,
 O.L. Fedin ^{37,a}, M. Feickert ¹⁷¹, L. Feligioni ¹⁰³, D.E. Fellers ¹²⁴, C. Feng ^{62b}, M. Feng ^{14b},
 Z. Feng ¹¹⁵, M.J. Fenton ¹⁶⁰, L. Ferencz ⁴⁸, R.A.M. Ferguson ⁹², S.I. Fernandez Luengo ^{138f},
 P. Fernandez Martinez ¹³, M.J.V. Fernoux ¹⁰³, J. Ferrando ⁹², A. Ferrari ¹⁶², P. Ferrari ^{115,114},
 R. Ferrari ^{73a}, D. Ferrere ⁵⁶, C. Ferretti ¹⁰⁷, F. Fiedler ¹⁰¹, P. Fiedler ¹³³, A. Filipčič ⁹⁴,
 E.K. Filmer ¹, F. Filthaut ¹¹⁴, M.C.N. Fiolhais ^{131a,131c,c}, L. Fiorini ¹⁶⁴, W.C. Fisher ¹⁰⁸,
 T. Fitschen ¹⁰², P.M. Fitzhugh ¹³⁶, I. Fleck ¹⁴², P. Fleischmann ¹⁰⁷, T. Flick ¹⁷², M. Flores ^{33d,ab},
 L.R. Flores Castillo ^{64a}, L. Flores Sanz De Acedo ³⁶, F.M. Follega ^{78a,78b}, N. Fomin ¹⁶,
 J.H. Foo ¹⁵⁶, A. Formica ¹³⁶, A.C. Forti ¹⁰², E. Fortin ³⁶, A.W. Fortman ^{17a}, M.G. Foti ^{17a},
 L. Fountas ^{9j}, D. Fournier ⁶⁶, H. Fox ⁹², P. Francavilla ^{74a,74b}, S. Francescato ⁶¹,
 S. Franchellucci ⁵⁶, M. Franchini ^{23b,23a}, S. Franchino ^{63a}, D. Francis ³⁶, L. Franco ¹¹⁴,
 V. Franco Lima ³⁶, L. Franconi ⁴⁸, M. Franklin ⁶¹, G. Frattari ²⁶, W.S. Freund ^{83b}, Y.Y. Frid ¹⁵²,
 J. Friend ⁵⁹, N. Fritzsche ⁵⁰, A. Froch ⁵⁴, D. Froidevaux ³⁶, J.A. Frost ¹²⁷, Y. Fu ^{62a},
 S. Fuenzalida Garrido ^{138f}, M. Fujimoto ¹⁰³, K.Y. Fung ^{64a}, E. Furtado De Simas Filho ^{83e},
 M. Furukawa ¹⁵⁴, J. Fuster ¹⁶⁴, A. Gabrielli ^{23b,23a}, A. Gabrielli ¹⁵⁶, P. Gadow ³⁶,
 G. Gagliardi ^{57b,57a}, L.G. Gagnon ^{17a}, S. Galantzan ¹⁵², E.J. Gallas ¹²⁷, B.J. Gallop ¹³⁵,
 K.K. Gan ¹²⁰, S. Ganguly ¹⁵⁴, Y. Gao ⁵², F.M. Garay Walls ^{138a,138b}, B. Garcia ²⁹, C. García ¹⁶⁴,
 A. Garcia Alonso ¹¹⁵, A.G. Garcia Caffaro ¹⁷³, J.E. García Navarro ¹⁶⁴, M. Garcia-Sciveres ^{17a},
 G.L. Gardner ¹²⁹, R.W. Gardner ³⁹, N. Garelli ¹⁵⁹, D. Garg ⁸⁰, R.B. Garg ^{144,m}, J.M. Gargan ⁵²,
 C.A. Garner ¹⁵⁶, C.M. Garvey ^{33a}, P. Gaspar ^{83b}, V.K. Gassmann ¹⁵⁹, G. Gaudio ^{73a}, V. Gautam ¹³,
 P. Gauzzi ^{75a,75b}, I.L. Gavrilenko ³⁷, A. Gavrilyuk ³⁷, C. Gay ¹⁶⁵, G. Gaycken ⁴⁸, E.N. Gazis ¹⁰,
 A.A. Geanta ^{27b}, C.M. Gee ¹³⁷, A. Gekow ¹²⁰, C. Gemme ^{57b}, M.H. Genest ⁶⁰, A.D. Gentry ¹¹³,
 S. George ⁹⁶, W.F. George ²⁰, T. Geralis ⁴⁶, P. Gessinger-Befurt ³⁶, M.E. Geyik ¹⁷²,
 M. Ghani ¹⁶⁸, K. Ghorbanian ⁹⁵, A. Ghosal ¹⁴², A. Ghosh ¹⁶⁰, A. Ghosh ⁷, B. Giacobbe ^{23b},
 S. Giagu ^{75a,75b}, T. Giani ¹¹⁵, P. Giannetti ^{74a}, A. Giannini ^{62a}, S.M. Gibson ⁹⁶, M. Gignac ¹³⁷,
 D.T. Gil ^{86b}, A.K. Gilbert ^{86a}, B.J. Gilbert ⁴¹, D. Gillberg ³⁴, G. Gilles ¹¹⁵, L. Ginabat ¹²⁸,
 D.M. Gingrich ^{2,ae}, M.P. Giordani ^{69a,69c}, P.F. Giraud ¹³⁶, G. Giugliarelli ^{69a,69c}, D. Giugni ^{71a},
 F. Giuli ³⁶, I. Gkialas ^{9j}, L.K. Gladilin ³⁷, C. Glasman ¹⁰⁰, G.R. Gledhill ¹²⁴, G. Glemža ⁴⁸,
 M. Glisic ¹²⁴, I. Gnesi ^{43b,f}, Y. Go ²⁹, M. Goblirsch-Kolb ³⁶, B. Gocke ⁴⁹, D. Godin ¹⁰⁹,
 B. Gokturk ^{21a}, S. Goldfarb ¹⁰⁶, T. Golling ⁵⁶, M.G.D. Gololo ^{33g}, D. Golubkov ³⁷,
 J.P. Gombas ¹⁰⁸, A. Gomes ^{131a,131b}, G. Gomes Da Silva ¹⁴², A.J. Gomez Delegido ¹⁶⁴,
 R. Gonçalves ^{131a,131c}, L. Gonella ²⁰, A. Gongadze ^{150c}, F. Gonnella ²⁰, J.L. Gonski ¹⁴⁴,
 R.Y. González Andana ⁵², S. González de la Hoz ¹⁶⁴, R. Gonzalez Lopez ⁹³,
 C. Gonzalez Renteria ^{17a}, M.V. Gonzalez Rodrigues ⁴⁸, R. Gonzalez Suarez ¹⁶²,
 S. Gonzalez-Sevilla ⁵⁶, L. Goossens ³⁶, B. Gorini ³⁶, E. Gorini ^{70a,70b}, A. Gorišek ⁹⁴,
 T.C. Gosart ¹²⁹, A.T. Goshaw ⁵¹, M.I. Gostkin ³⁸, S. Goswami ¹²², C.A. Gottardo ³⁶,
 S.A. Gotz ¹¹⁰, M. Gouighri ^{35b}, V. Goumarre ⁴⁸, A.G. Goussiou ¹³⁹, N. Govender ^{33c},
 I. Grabowska-Bold ^{86a}, K. Graham ³⁴, E. Gramstad ¹²⁶, S. Grancagnolo ^{70a,70b}, C.M. Grant ^{1,136},
 P.M. Gravila ^{27f}, F.G. Gravili ^{70a,70b}, H.M. Gray ^{17a}, M. Greco ^{70a,70b}, C. Grefe ²⁴,
 I.M. Gregor ⁴⁸, K.T. Greif ¹⁶⁰, P. Grenier ¹⁴⁴, S.G. Grewe ¹¹¹, A.A. Grillo ¹³⁷, K. Grimm ³¹,
 S. Grinstein ^{13,s}, J.-F. Grivaz ⁶⁶, E. Gross ¹⁷⁰, J. Grosse-Knetter ⁵⁵, J.C. Grundy ¹²⁷,
 L. Guan ¹⁰⁷, C. Gubbels ¹⁶⁵, J.G.R. Guerrero Rojas ¹⁶⁴, G. Guerrieri ^{69a,69c}, F. Guescini ¹¹¹,
 R. Gugel ¹⁰¹, J.A.M. Guhit ¹⁰⁷, A. Guida ¹⁸, E. Guilloton ¹⁶⁸, S. Guindon ³⁶, F. Guo ^{14a,14e},
 J. Guo ^{62c}, L. Guo ⁴⁸, Y. Guo ¹⁰⁷, R. Gupta ⁴⁸, R. Gupta ¹³⁰, S. Gurbuz ²⁴, S.S. Gurdasani ⁵⁴,

G. Gustavino ³⁶, M. Guth ⁵⁶, P. Gutierrez ¹²¹, L.F. Gutierrez Zagazeta ¹²⁹, M. Gutsche ⁵⁰, C. Gutschow ⁹⁷, C. Gwenlan ¹²⁷, C.B. Gwilliam ⁹³, E.S. Haaland ¹²⁶, A. Haas ¹¹⁸, M. Habedank ⁴⁸, C. Haber ^{17a}, H.K. Hadavand ⁸, A. Hadeef ⁵⁰, S. Hadzic ¹¹¹, A.I. Hagan ⁹², J.J. Hahn ¹⁴², E.H. Haines ⁹⁷, M. Haleem ¹⁶⁷, J. Haley ¹²², J.J. Hall ¹⁴⁰, G.D. Hallelwell ¹⁰³, L. Halser ¹⁹, K. Hamano ¹⁶⁶, M. Hamer ²⁴, G.N. Hamity ⁵², E.J. Hampshire ⁹⁶, J. Han ^{62b}, K. Han ^{62a}, L. Han ^{14c}, L. Han ^{62a}, S. Han ^{17a}, Y.F. Han ¹⁵⁶, K. Hanagaki ⁸⁴, M. Hance ¹³⁷, D.A. Hangal ⁴¹, H. Hanif ¹⁴³, M.D. Hank ¹²⁹, J.B. Hansen ⁴², P.H. Hansen ⁴², K. Hara ¹⁵⁸, D. Harada ⁵⁶, T. Harenberg ¹⁷², S. Harkusha ³⁷, M.L. Harris ¹⁰⁴, Y.T. Harris ¹²⁷, J. Harrison ¹³, N.M. Harrison ¹²⁰, P.F. Harrison ¹⁶⁸, N.M. Hartman ¹¹¹, N.M. Hartmann ¹¹⁰, Y. Hasegawa ¹⁴¹, S. Hassan ¹⁶, R. Hauser ¹⁰⁸, C.M. Hawkes ²⁰, R.J. Hawkins ³⁶, Y. Hayashi ¹⁵⁴, S. Hayashida ¹¹², D. Hayden ¹⁰⁸, C. Hayes ¹⁰⁷, R.L. Hayes ¹¹⁵, C.P. Hays ¹²⁷, J.M. Hays ⁹⁵, H.S. Hayward ⁹³, F. He ^{62a}, M. He ^{14a,14e}, Y. He ¹⁵⁵, Y. He ⁴⁸, Y. He ⁹⁷, N.B. Heatley ⁹⁵, V. Hedberg ⁹⁹, A.L. Heggelund ¹²⁶, N.D. Hehir ^{95,*}, C. Heidegger ⁵⁴, K.K. Heidegger ⁵⁴, W.D. Heidorn ⁸¹, J. Heilman ³⁴, S. Heim ⁴⁸, T. Heim ^{17a}, J.G. Heinlein ¹²⁹, J.J. Heinrich ¹²⁴, L. Heinrich ^{111,ac}, J. Hejbal ¹³², A. Held ¹⁷¹, S. Hellesund ¹⁶, C.M. Helling ¹⁶⁵, S. Hellman ^{47a,47b}, R.C.W. Henderson ⁹², L. Henkelmann ³², A.M. Henriques Correia ³⁶, H. Herde ⁹⁹, Y. Hernández Jiménez ¹⁴⁶, L.M. Herrmann ²⁴, T. Herrmann ⁵⁰, G. Herten ⁵⁴, R. Hertenberger ¹¹⁰, L. Hervas ³⁶, M.E. Hesping ¹⁰¹, N.P. Hessey ^{157a}, E. Hill ¹⁵⁶, S.J. Hillier ²⁰, J.R. Hinds ¹⁰⁸, F. Hinterkeuser ²⁴, M. Hirose ¹²⁵, S. Hirose ¹⁵⁸, D. Hirschbuehl ¹⁷², T.G. Hitchings ¹⁰², B. Hiti ⁹⁴, J. Hobbs ¹⁴⁶, R. Hobincu ^{27e}, N. Hod ¹⁷⁰, M.C. Hodgkinson ¹⁴⁰, B.H. Hodgkinson ¹²⁷, A. Hoecker ³⁶, D.D. Hofer ¹⁰⁷, J. Hofer ⁴⁸, T. Holm ²⁴, M. Holzbock ¹¹¹, L.B.A.H. Hommels ³², B.P. Honan ¹⁰², J. Hong ^{62c}, T.M. Hong ¹³⁰, B.H. Hooberman ¹⁶³, W.H. Hopkins ⁶, Y. Horii ¹¹², S. Hou ¹⁴⁹, A.S. Howard ⁹⁴, J. Howarth ⁵⁹, J. Hoya ⁶, M. Hrabovsky ¹²³, A. Hrynevich ⁴⁸, T. Hryn'ova ⁴, P.J. Hsu ⁶⁵, S.-C. Hsu ¹³⁹, M. Hu ^{17a}, Q. Hu ^{62a}, S. Huang ^{64b}, X. Huang ^{14a,14e}, Y. Huang ¹⁴⁰, Y. Huang ^{14a}, Z. Huang ¹⁰², Z. Hubacek ¹³³, M. Huebner ²⁴, F. Huegging ²⁴, T.B. Huffman ¹²⁷, C.A. Hugli ⁴⁸, M. Huhtinen ³⁶, S.K. Huiberts ¹⁶, R. Hulsken ¹⁰⁵, N. Huseynov ¹², J. Huston ¹⁰⁸, J. Huth ⁶¹, R. Hyneman ¹⁴⁴, G. Iacobucci ⁵⁶, G. Iakovidis ²⁹, I. Ibragimov ¹⁴², L. Iconomidou-Fayard ⁶⁶, J.P. Iddon ³⁶, P. Iengo ^{72a,72b}, R. Iguchi ¹⁵⁴, T. Iizawa ¹²⁷, Y. Ikegami ⁸⁴, N. Ilic ¹⁵⁶, H. Imam ^{35a}, M. Ince Lezki ⁵⁶, T. Ingebretsen Carlson ^{47a,47b}, G. Introzzi ^{73a,73b}, M. Iodice ^{77a}, V. Ippolito ^{75a,75b}, R.K. Irwin ⁹³, M. Ishino ¹⁵⁴, W. Islam ¹⁷¹, C. Issever ^{18,48}, S. Istin ^{21a,ai}, H. Ito ¹⁶⁹, R. Iuppa ^{78a,78b}, A. Ivina ¹⁷⁰, J.M. Izen ⁴⁵, V. Izzo ^{72a}, P. Jacka ^{132,133}, P. Jackson ¹, B.P. Jaeger ¹⁴³, C.S. Jagfeld ¹¹⁰, G. Jain ^{157a}, P. Jain ⁵⁴, K. Jakobs ⁵⁴, T. Jakoubek ¹⁷⁰, J. Jamieson ⁵⁹, K.W. Janas ^{86a}, M. Javurkova ¹⁰⁴, L. Jeanty ¹²⁴, J. Jejelava ^{150a,z}, P. Jenni ^{54,g}, C.E. Jessiman ³⁴, C. Jia ^{62b}, J. Jia ¹⁴⁶, X. Jia ⁶¹, X. Jia ^{14a,14e}, Z. Jia ^{14c}, C. Jiang ⁵², S. Jiggins ⁴⁸, J. Jimenez Pena ¹³, S. Jin ^{14c}, A. Jinaru ^{27b}, O. Jinnouchi ¹⁵⁵, P. Johansson ¹⁴⁰, K.A. Johns ⁷, J.W. Johnson ¹³⁷, D.M. Jones ¹⁴⁷, E. Jones ⁴⁸, P. Jones ³², R.W.L. Jones ⁹², T.J. Jones ⁹³, H.L. Joos ^{55,36}, R. Joshi ¹²⁰, J. Jovicevic ¹⁵, X. Ju ^{17a}, J.J. Junggeburth ¹⁰⁴, T. Junkermann ^{63a}, A. Juste Rozas ^{13,s}, M.K. Juzek ⁸⁷, S. Kabana ^{138e}, A. Kaczmarska ⁸⁷, M. Kado ¹¹¹, H. Kagan ¹²⁰, M. Kagan ¹⁴⁴, A. Kahn ⁴¹, A. Kahn ¹²⁹, C. Kahra ¹⁰¹, T. Kaji ¹⁵⁴, E. Kajomovitz ¹⁵¹, N. Kakati ¹⁷⁰, I. Kalaitzidou ⁵⁴, C.W. Kalderon ²⁹, N.J. Kang ¹³⁷, D. Kar ^{33g}, K. Karava ¹²⁷, M.J. Kareem ^{157b}, E. Karentzos ⁵⁴, I. Karkanias ¹⁵³, O. Karkout ¹¹⁵, S.N. Karpov ³⁸, Z.M. Karpova ³⁸, V. Kartvelishvili ⁹², A.N. Karyukhin ³⁷, E. Kasimi ¹⁵³, J. Katzy ⁴⁸, S. Kaur ³⁴, K. Kawade ¹⁴¹, M.P. Kawale ¹²¹, C. Kawamoto ⁸⁸, T. Kawamoto ^{62a}, E.F. Kay ³⁶, F.I. Kaya ¹⁵⁹, S. Kazakos ¹⁰⁸, V.F. Kazanin ³⁷, Y. Ke ¹⁴⁶, J.M. Keaveney ^{33a}, R. Keeler ¹⁶⁶, G.V. Kehris ⁶¹, J.S. Keller ³⁴, A.S. Kelly ⁹⁷, J.J. Kempster ¹⁴⁷, P.D. Kennedy ¹⁰¹, O. Kepka ¹³², B.P. Kerridge ¹³⁵, S. Kersten ¹⁷², B.P. Kerševan ⁹⁴, L. Keszeghova ^{28a},

S. Ketabchi Haghighat ¹⁵⁶, R.A. Khan ¹³⁰, A. Khanov ¹²², A.G. Kharlamov ³⁷, T. Kharlamova ³⁷, E.E. Khoda ¹³⁹, M. Kholodenko ³⁷, T.J. Khoo ¹⁸, G. Khorauli ¹⁶⁷, J. Khubua ^{150b}, Y.A.R. Khwaira ⁶⁶, B. Kibirige ^{33g}, A. Kilgallon ¹²⁴, D.W. Kim ^{47a,47b}, Y.K. Kim ³⁹, N. Kimura ⁹⁷, M.K. Kingston ⁵⁵, A. Kirchhoff ⁵⁵, C. Kirfel ²⁴, F. Kirfel ²⁴, J. Kirk ¹³⁵, A.E. Kiryunin ¹¹¹, C. Kitsaki ¹⁰, O. Kivernyk ²⁴, M. Klassen ^{63a}, C. Klein ³⁴, L. Klein ¹⁶⁷, M.H. Klein ⁴⁴, S.B. Klein ⁵⁶, U. Klein ⁹³, P. Klimek ³⁶, A. Klimentov ²⁹, T. Klioutchnikova ³⁶, P. Kluit ¹¹⁵, S. Kluth ¹¹¹, E. Kneringer ⁷⁹, T.M. Knight ¹⁵⁶, A. Knue ⁴⁹, R. Kobayashi ⁸⁸, D. Kobylanskii ¹⁷⁰, S.F. Koch ¹²⁷, M. Kocian ¹⁴⁴, P. Kodyš ¹³⁴, D.M. Koeck ¹²⁴, P.T. Koenig ²⁴, T. Koffas ³⁴, O. Kolay ⁵⁰, I. Koletsou ⁴, T. Komarek ¹²³, K. Köneke ⁵⁴, A.X.Y. Kong ¹, T. Kono ¹¹⁹, V. Konstantinides ⁹⁷, N. Konstantinidis ⁹⁷, P. Kontaxakis ⁵⁶, B. Konya ⁹⁹, R. Kopeliansky ⁴¹, S. Koperny ^{86a}, K. Korcyl ⁸⁷, K. Kordas ^{153,e}, A. Korn ⁹⁷, S. Korn ⁵⁵, I. Korolkov ¹³, N. Korotkova ³⁷, B. Kortman ¹¹⁵, O. Kortner ¹¹¹, S. Kortner ¹¹¹, W.H. Kostecka ¹¹⁶, V.V. Kostyukhin ¹⁴², A. Kotsokechagia ¹³⁶, A. Kotwal ⁵¹, A. Koulouris ³⁶, A. Kourkoumeli-Charalampidi ^{73a,73b}, C. Kourkoumelis ⁹, E. Kourlitis ^{111,ac}, O. Kovanda ¹²⁴, R. Kowalewski ¹⁶⁶, W. Kozanecki ¹³⁶, A.S. Kozhin ³⁷, V.A. Kramarenko ³⁷, G. Kramberger ⁹⁴, P. Kramer ¹⁰¹, M.W. Krasny ¹²⁸, A. Krasznahorkay ³⁶, J.W. Kraus ¹⁷², J.A. Kremer ⁴⁸, T. Kresse ⁵⁰, J. Kretschmar ⁹³, K. Kreul ¹⁸, P. Krieger ¹⁵⁶, S. Krishnamurthy ¹⁰⁴, M. Krivos ¹³⁴, K. Krizka ²⁰, K. Kroeninger ⁴⁹, H. Kroha ¹¹¹, J. Kroll ¹³², J. Kroll ¹²⁹, K.S. Krowpman ¹⁰⁸, U. Kruchonak ³⁸, H. Krüger ²⁴, N. Krumnack ⁸¹, M.C. Kruse ⁵¹, O. Kuchinskaia ³⁷, S. Kuday ^{3a}, S. Kuehn ³⁶, R. Kuesters ⁵⁴, T. Kuhl ⁴⁸, V. Kukhtin ³⁸, Y. Kulchitsky ^{37,a}, S. Kuleshov ^{138d,138b}, M. Kumar ^{33g}, N. Kumari ⁴⁸, P. Kumari ^{157b}, A. Kupco ¹³², T. Kupfer ⁴⁹, A. Kupich ³⁷, O. Kuprash ⁵⁴, H. Kurashige ⁸⁵, L.L. Kurchaninov ^{157a}, O. Kurdysh ⁶⁶, Y.A. Kurochkin ³⁷, A. Kurova ³⁷, M. Kuze ¹⁵⁵, A.K. Kvam ¹⁰⁴, J. Kvita ¹²³, T. Kwan ¹⁰⁵, N.G. Kyriacou ¹⁰⁷, L.A.O. Laatu ¹⁰³, C. Lacasta ¹⁶⁴, F. Lacava ^{75a,75b}, H. Lacker ¹⁸, D. Lacour ¹²⁸, N.N. Lad ⁹⁷, E. Ladygin ³⁸, A. Lafarge ⁴⁰, B. Laforge ¹²⁸, T. Lagouri ¹⁷³, F.Z. Lahbabi ^{35a}, S. Lai ⁵⁵, I.K. Lakomic ^{86a}, N. Lalloue ⁶⁰, J.E. Lambert ¹⁶⁶, S. Lammers ⁶⁸, W. Lampl ⁷, C. Lampoudis ^{153,e}, G. Lamprinoudis ¹⁰¹, A.N. Lancaster ¹¹⁶, E. Lançon ²⁹, U. Landgraf ⁵⁴, M.P.J. Landon ⁹⁵, V.S. Lang ⁵⁴, O.K.B. Langrekken ¹²⁶, A.J. Lankford ¹⁶⁰, F. Lanni ³⁶, K. Lantzsch ²⁴, A. Lanza ^{73a}, A. Lapertosa ^{57b,57a}, J.F. Laporte ¹³⁶, T. Lari ^{71a}, F. Lasagni Manghi ^{23b}, M. Lassnig ³⁶, V. Latonova ¹³², A. Laudrain ¹⁰¹, A. Laurier ¹⁵¹, S.D. Lawlor ¹⁴⁰, Z. Lawrence ¹⁰², R. Lazaridou ¹⁶⁸, M. Lazzaroni ^{71a,71b}, B. Le ¹⁰², E.M. Le Boulicaut ⁵¹, L.T. Le Pottier ^{17a}, B. Leban ^{23b,23a}, A. Lebedev ⁸¹, M. LeBlanc ¹⁰², F. Ledroit-Guillon ⁶⁰, A.C.A. Lee ⁹⁷, S.C. Lee ¹⁴⁹, S. Lee ^{47a,47b}, T.F. Lee ⁹³, L.L. Leeuw ^{33c}, H.P. Lefebvre ⁹⁶, M. Lefebvre ¹⁶⁶, C. Leggett ^{17a}, G. Lehmann Miotto ³⁶, M. Leigh ⁵⁶, W.A. Leight ¹⁰⁴, W. Leinonen ¹¹⁴, A. Leisos ^{153,r}, M.A.L. Leite ^{83c}, C.E. Leitgeb ¹⁸, R. Leitner ¹³⁴, K.J.C. Leney ⁴⁴, T. Lenz ²⁴, S. Leone ^{74a}, C. Leonidopoulos ⁵², A. Leopold ¹⁴⁵, C. Leroy ¹⁰⁹, R. Les ¹⁰⁸, C.G. Lester ³², M. Levchenko ³⁷, J. Levêque ⁴, L.J. Levinson ¹⁷⁰, G. Levrini ^{23b,23a}, M.P. Lewicki ⁸⁷, D.J. Lewis ⁴, A. Li ⁵, B. Li ^{62b}, C. Li ^{62a}, C-Q. Li ¹¹¹, H. Li ^{62a}, H. Li ^{62b}, H. Li ^{14c}, H. Li ^{14b}, H. Li ^{62b}, J. Li ^{62c}, K. Li ¹³⁹, L. Li ^{62c}, M. Li ^{14a,14e}, Q.Y. Li ^{62a}, S. Li ^{14a,14e}, S. Li ^{62d,62c,d}, T. Li ⁵, X. Li ¹⁰⁵, Z. Li ¹²⁷, Z. Li ¹⁰⁵, Z. Li ^{14a,14e}, S. Liang ^{14a,14e}, Z. Liang ^{14a}, M. Liberatore ¹³⁶, B. Liberti ^{76a}, K. Lie ^{64c}, J. Lieber Marin ^{83e}, H. Lien ⁶⁸, K. Lin ¹⁰⁸, R.E. Lindley ⁷, J.H. Lindon ², E. Lipeles ¹²⁹, A. Lipniacka ¹⁶, A. Lister ¹⁶⁵, J.D. Little ⁴, B. Liu ^{14a}, B.X. Liu ¹⁴³, D. Liu ^{62d,62c}, E.H.L. Liu ²⁰, J.B. Liu ^{62a}, J.K.K. Liu ³², K. Liu ^{62d}, K. Liu ^{62d,62c}, M. Liu ^{62a}, M.Y. Liu ^{62a}, P. Liu ^{14a}, Q. Liu ^{62d,139,62c}, X. Liu ^{62a}, X. Liu ^{62b}, Y. Liu ^{14d,14e}, Y.L. Liu ^{62b}, Y.W. Liu ^{62a}, J. Llorente Merino ¹⁴³, S.L. Lloyd ⁹⁵, E.M. Lobodzinska ⁴⁸, P. Loch ⁷, T. Lohse ¹⁸, K. Lohwasser ¹⁴⁰, E. Loiacono ⁴⁸,







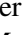




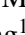



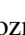
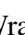
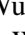


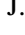
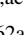
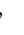

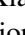
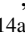
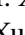






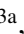
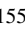


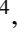
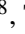


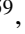


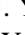
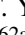


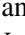


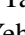

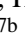







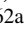




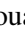












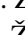

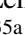

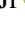


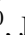
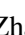


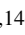



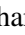

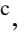



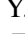


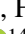
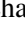


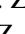



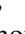


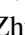
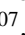
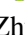






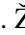




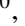

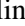





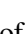
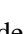











M. Lokajicek ^{132,*}, J.D. Lomas ²⁰, J.D. Long ¹⁶³, I. Longarini ¹⁶⁰, L. Longo ^{70a,70b},
R. Longo ¹⁶³, I. Lopez Paz ⁶⁷, A. Lopez Solis ⁴⁸, N. Lorenzo Martinez ⁴, A.M. Lory ¹¹⁰,
G. Löschcke Centeno ¹⁴⁷, O. Loseva ³⁷, X. Lou ^{47a,47b}, X. Lou ^{14a,14e}, A. Lounis ⁶⁶,
P.A. Love ⁹², G. Lu ^{14a,14e}, M. Lu ⁶⁶, S. Lu ¹²⁹, Y.J. Lu ⁶⁵, H.J. Lubatti ¹³⁹, C. Luci ^{75a,75b},
F.L. Lucio Alves ^{14c}, F. Luehring ⁶⁸, I. Luise ¹⁴⁶, O. Lukianchuk ⁶⁶, O. Lundberg ¹⁴⁵,
B. Lund-Jensen ¹⁴⁵, N.A. Luongo ⁶, M.S. Lutz ³⁶, A.B. Lux ²⁵, D. Lynn ²⁹, R. Lysak ¹³²,
E. Lytken ⁹⁹, V. Lyubushkin ³⁸, T. Lyubushkina ³⁸, M.M. Lyukova ¹⁴⁶, M.Firdaus M. Soberi ⁵²,
H. Ma ²⁹, K. Ma ^{62a}, L.L. Ma ^{62b}, W. Ma ^{62a}, Y. Ma ¹²², D.M. Mac Donell ¹⁶⁶,
G. Maccarrone ⁵³, J.C. MacDonald ¹⁰¹, P.C. Machado De Abreu Farias ^{83e}, R. Madar ⁴⁰,
T. Madula ⁹⁷, J. Maeda ⁸⁵, T. Maeno ²⁹, H. Maguire ¹⁴⁰, V. Maiboroda ¹³⁶,
A. Maio ^{131a,131b,131d}, K. Maj ^{86a}, O. Majersky ⁴⁸, S. Majewski ¹²⁴, N. Makovec ⁶⁶,
V. Maksimovic ¹⁵, B. Malaescu ¹²⁸, Pa. Malecki ⁸⁷, V.P. Maleev ³⁷, F. Malek ^{60,n}, M. Mali ⁹⁴,
D. Malito ⁹⁶, U. Mallik ⁸⁰, S. Maltezos ¹⁰, S. Malyukov ³⁸, J. Mamuzic ¹³, G. Mancini ⁵³,
M.N. Mancini ²⁶, G. Manco ^{73a,73b}, J.P. Mandalia ⁹⁵, I. Mandić ⁹⁴,
L. Manhaes de Andrade Filho ^{83a}, I.M. Maniatis ¹⁷⁰, J. Manjarres Ramos ⁹⁰, D.C. Mankad ¹⁷⁰,
A. Mann ¹¹⁰, S. Manzoni ³⁶, L. Mao ^{62c}, X. Mapekula ^{33c}, A. Marantis ^{153,r}, G. Marchiori ⁵,
M. Marcisovsky ¹³², C. Marcon ^{71a}, M. Marinescu ²⁰, S. Marium ⁴⁸, M. Marjanovic ¹²¹,
M. Markovitch ⁶⁶, E.J. Marshall ⁹², Z. Marshall ^{17a}, S. Marti-Garcia ¹⁶⁴, T.A. Martin ¹⁶⁸,
V.J. Martin ⁵², B. Martin dit Latour ¹⁶, L. Martinelli ^{75a,75b}, M. Martinez ^{13,s},
P. Martinez Agullo ¹⁶⁴, V.I. Martinez Outschoorn ¹⁰⁴, P. Martinez Suarez ¹³, S. Martin-Haugh ¹³⁵,
G. Martinovicova ¹³⁴, V.S. Martoiu ^{27b}, A.C. Martyniuk ⁹⁷, A. Marzin ³⁶, D. Mascione ^{78a,78b},
L. Masetti ¹⁰¹, T. Mashimo ¹⁵⁴, J. Masik ¹⁰², A.L. Maslennikov ³⁷, P. Massarotti ^{72a,72b},
P. Mastrandrea ^{74a,74b}, A. Mastroberardino ^{43b,43a}, T. Masubuchi ¹⁵⁴, T. Mathisen ¹⁶²,
J. Matousek ¹³⁴, N. Matsuzawa ¹⁵⁴, J. Maurer ^{27b}, A.J. Maury ⁶⁶, B. Maček ⁹⁴, D.A. Maximov ³⁷,
A.E. May ¹⁰², R. Mazini ¹⁴⁹, I. Maznas ¹¹⁶, M. Mazza ¹⁰⁸, S.M. Mazza ¹³⁷, E. Mazzeo ^{71a,71b},
C. Mc Ginn ²⁹, J.P. Mc Gowan ¹⁶⁶, S.P. Mc Kee ¹⁰⁷, C.C. McCracken ¹⁶⁵, E.F. McDonald ¹⁰⁶,
A.E. McDougall ¹¹⁵, J.A. Mcfayden ¹⁴⁷, R.P. McGovern ¹²⁹, G. Mchedlidze ^{150b},
R.P. Mckenzie ^{33g}, T.C. Mclachlan ⁴⁸, D.J. Mclaughlin ⁹⁷, S.J. McMahon ¹³⁵,
C.M. Mcpartland ⁹³, R.A. McPherson ^{166,w}, S. Mehlhase ¹¹⁰, A. Mehta ⁹³, D. Melini ¹⁶⁴,
B.R. Mellado Garcia ^{33g}, A.H. Melo ⁵⁵, F. Meloni ⁴⁸, S.B. Menary ¹⁰²,
A.M. Mendes Jacques Da Costa ¹⁰², H.Y. Meng ¹⁵⁶, L. Meng ⁹², S. Menke ¹¹¹, M. Mentink ³⁶,
E. Meoni ^{43b,43a}, G. Mercado ¹¹⁶, C. Merlassino ^{69a,69c}, L. Merola ^{72a,72b}, C. Meroni ^{71a,71b},
J. Metcalfe ⁶, A.S. Mete ⁶, C. Meyer ⁶⁸, J-P. Meyer ¹³⁶, R.P. Middleton ¹³⁵, L. Mijović ⁵²,
G. Mikenberg ¹⁷⁰, M. Mikestikova ¹³², M. Mikuž ⁹⁴, H. Mildner ¹⁰¹, A. Milic ³⁶,
D.W. Miller ³⁹, E.H. Miller ¹⁴⁴, L.S. Miller ³⁴, A. Milov ¹⁷⁰, D.A. Milstead ^{47a,47b}, T. Min ^{14c},
A.A. Minaenko ³⁷, I.A. Minashvili ^{150b}, L. Mince ⁵⁹, A.I. Mincer ¹¹⁸, B. Mindur ^{86a},
M. Mineev ³⁸, Y. Mino ⁸⁸, L.M. Mir ¹³, M. Miralles Lopez ⁵⁹, M. Mironova ^{17a}, A. Mishima ¹⁵⁴,
M.C. Missio ¹¹⁴, A. Mitra ¹⁶⁸, V.A. Mitsou ¹⁶⁴, Y. Mitsumori ¹¹², O. Miu ¹⁵⁶,
P.S. Miyagawa ⁹⁵, T. Mkrtychyan ^{63a}, M. Mlinarevic ⁹⁷, T. Mlinarevic ⁹⁷, M. Mlynarikova ³⁶,
S. Mobius ¹⁹, P. Mogg ¹¹⁰, M.H. Mohamed Farook ¹¹³, A.F. Mohammed ^{14a,14e}, S. Mohapatra ⁴¹,
G. Mokgatitswane ^{33g}, L. Moleri ¹⁷⁰, B. Mondal ¹⁴², S. Mondal ¹³³, K. Mönig ⁴⁸,
E. Monnier ¹⁰³, L. Monsonis Romero ¹⁶⁴, J. Montejo Berlingen ¹³, M. Montella ¹²⁰,
F. Montekali ^{77a,77b}, F. Monticelli ⁹¹, S. Monzani ^{69a,69c}, N. Morange ⁶⁶,
A.L. Moreira De Carvalho ^{131a}, M. Moreno Llácer ¹⁶⁴, C. Moreno Martinez ⁵⁶, P. Morettini ^{57b},
S. Morgenstern ³⁶, M. Morii ⁶¹, M. Morinaga ¹⁵⁴, F. Morodei ^{75a,75b}, L. Morvaj ³⁶,
P. Moschovakos ³⁶, B. Moser ³⁶, M. Mosidze ^{150b}, T. Moskalets ⁵⁴, P. Moskvitina ¹¹⁴,
J. Moss ^{31,k}, A. Moussa ^{35d}, E.J.W. Moyse ¹⁰⁴, O. Mtintsilana ^{33g}, S. Muanza ¹⁰³,

J. Mueller ¹³⁰, D. Muenstermann ⁹², R. Müller ¹⁹, G.A. Mullier ¹⁶², A.J. Mullin³², J.J. Mullin¹²⁹, D.P. Mungo ¹⁵⁶, D. Munoz Perez ¹⁶⁴, F.J. Munoz Sanchez ¹⁰², M. Murin ¹⁰², W.J. Murray ^{168,135}, M. Muškinja ⁹⁴, C. Mwewa ²⁹, A.G. Myagkov ^{37,a}, A.J. Myers ⁸, G. Myers ¹⁰⁷, M. Myska ¹³³, B.P. Nachman ^{17a}, O. Nackenhorst ⁴⁹, K. Nagai ¹²⁷, K. Nagano ⁸⁴, J.L. Nagle ^{29,ag}, E. Nagy ¹⁰³, A.M. Nairz ³⁶, Y. Nakahama ⁸⁴, K. Nakamura ⁸⁴, K. Nakkalil ⁵, H. Nanjo ¹²⁵, R. Narayan ⁴⁴, E.A. Narayanan ¹¹³, I. Naryshkin ³⁷, M. Naseri ³⁴, S. Nasri ^{117b}, C. Nass ²⁴, G. Navarro ^{22a}, J. Navarro-Gonzalez ¹⁶⁴, R. Nayak ¹⁵², A. Nayaz ¹⁸, P.Y. Nechaeva ³⁷, F. Nechansky ⁴⁸, L. Nedic ¹²⁷, T.J. Neep ²⁰, A. Negri ^{73a,73b}, M. Negrini ^{23b}, C. Nellist ¹¹⁵, C. Nelson ¹⁰⁵, K. Nelson ¹⁰⁷, S. Nemecek ¹³², M. Nessi ^{36,h}, M.S. Neubauer ¹⁶³, F. Neuhaus ¹⁰¹, J. Neundorf ⁴⁸, R. Newhouse ¹⁶⁵, P.R. Newman ²⁰, C.W. Ng ¹³⁰, Y.W.Y. Ng ⁴⁸, B. Ngair ^{117a}, H.D.N. Nguyen ¹⁰⁹, R.B. Nickerson ¹²⁷, R. Nicolaidou ¹³⁶, J. Nielsen ¹³⁷, M. Niemeyer ⁵⁵, J. Niermann ⁵⁵, N. Nikiforou ³⁶, V. Nikolaenko ^{37,a}, I. Nikolic-Audit ¹²⁸, K. Nikolopoulos ²⁰, P. Nilsson ²⁹, I. Ninca ⁴⁸, H.R. Nindhito ⁵⁶, G. Ninio ¹⁵², A. Nisati ^{75a}, N. Nishu ², R. Nisius ¹¹¹, J-E. Nitschke ⁵⁰, E.K. Nkadimeng ^{33g}, T. Nobe ¹⁵⁴, D.L. Noel ³², T. Nommensen ¹⁴⁸, M.B. Norfolk ¹⁴⁰, R.R.B. Norisam ⁹⁷, B.J. Norman ³⁴, M. Noury ^{35a}, J. Novak ⁹⁴, T. Novak ⁴⁸, L. Novotny ¹³³, R. Novotny ¹¹³, L. Nozka ¹²³, K. Ntekas ¹⁶⁰, N.M.J. Nunes De Moura Junior ^{83b}, E. Nurse⁹⁷, J. Ocariz ¹²⁸, A. Ochi ⁸⁵, I. Ochoa ^{131a}, S. Oerdek ^{48,t}, J.T. Offermann ³⁹, A. Ogrodnik ¹³⁴, A. Oh ¹⁰², C.C. Ohm ¹⁴⁵, H. Oide ⁸⁴, R. Oishi ¹⁵⁴, M.L. Ojeda ⁴⁸, Y. Okumura ¹⁵⁴, L.F. Oleiro Seabra ^{131a}, S.A. Olivares Pino ^{138d}, G. Oliveira Correa ¹³, D. Oliveira Damazio ²⁹, D. Oliveira Goncalves ^{83a}, J.L. Oliver ¹⁶⁰, Ö.O. Öncel ⁵⁴, A.P. O'Neill ¹⁹, A. Onofre ^{131a,131e}, P.U.E. Onyisi ¹¹, M.J. Oreglia ³⁹, G.E. Orellana ⁹¹, D. Orestano ^{77a,77b}, N. Orlando ¹³, R.S. Orr ¹⁵⁶, V. O'Shea ⁵⁹, L.M. Osojnak ¹²⁹, R. Ospanov ^{62a}, G. Otero y Garzon ³⁰, H. Otono ⁸⁹, P.S. Ott ^{63a}, G.J. Ottino ^{17a}, M. Ouchrif ^{35d}, F. Ould-Saada ¹²⁶, T. Ovsiannikova ¹³⁹, M. Owen ⁵⁹, R.E. Owen ¹³⁵, K.Y. Oyulmaz ^{21a}, V.E. Ozcan ^{21a}, F. Ozturk ⁸⁷, N. Ozturk ⁸, S. Ozturk ⁸², H.A. Pacey ¹²⁷, A. Pacheco Pages ¹³, C. Padilla Aranda ¹³, G. Padovano ^{75a,75b}, S. Pagan Griso ^{17a}, G. Palacino ⁶⁸, A. Palazzo ^{70a,70b}, J. Pampel ²⁴, J. Pan ¹⁷³, T. Pan ^{64a}, D.K. Panchal ¹¹, C.E. Pandini ¹¹⁵, J.G. Panduro Vazquez ⁹⁶, H.D. Pandya ¹, H. Pang ^{14b}, P. Pani ⁴⁸, G. Panizzo ^{69a,69c}, L. Panwar ¹²⁸, L. Paolozzi ⁵⁶, S. Parajuli ¹⁶³, A. Paramonov ⁶, C. Paraskevopoulos ⁵³, D. Paredes Hernandez ^{64b}, A. Pareti ^{73a,73b}, K.R. Park ⁴¹, T.H. Park ¹⁵⁶, M.A. Parker ³², F. Parodi ^{57b,57a}, E.W. Parrish ¹¹⁶, V.A. Parrish ⁵², J.A. Parsons ⁴¹, U. Parzefall ⁵⁴, B. Pascual Dias ¹⁰⁹, L. Pascual Dominguez ¹⁵², E. Pasqualucci ^{75a}, S. Passaggio ^{57b}, F. Pastore ⁹⁶, P. Patel ⁸⁷, U.M. Patel ⁵¹, J.R. Pater ¹⁰², T. Pauly ³⁶, C.I. Pazos ¹⁵⁹, J. Pearkes ¹⁴⁴, M. Pedersen ¹²⁶, R. Pedro ^{131a}, S.V. Peleganchuk ³⁷, O. Penc ³⁶, E.A. Pender ⁵², G.D. Penn ¹⁷³, K.E. Pensi ¹¹⁰, M. Penzin ³⁷, B.S. Peralva ^{83d}, A.P. Pereira Peixoto ¹³⁹, L. Pereira Sanchez ¹⁴⁴, D.V. Perepelitsa ^{29,ag}, E. Perez Codina ^{157a}, M. Perganti ¹⁰, H. Pernegger ³⁶, O. Perrin ⁴⁰, K. Peters ⁴⁸, R.F.Y. Peters ¹⁰², B.A. Petersen ³⁶, T.C. Petersen ⁴², E. Petit ¹⁰³, V. Petousis ¹³³, C. Petridou ^{153,e}, T. Petru ¹³⁴, A. Petrukhin ¹⁴², M. Pettee ^{17a}, N.E. Pettersson ³⁶, A. Petukhov ³⁷, K. Petukhova ¹³⁴, R. Pezoa ^{138f}, L. Pezzotti ³⁶, G. Pezzullo ¹⁷³, T.M. Pham ¹⁷¹, T. Pham ¹⁰⁶, P.W. Phillips ¹³⁵, G. Piacquadio ¹⁴⁶, E. Pianori ^{17a}, F. Piazza ¹²⁴, R. Piegai ³⁰, D. Pietreanu ^{27b}, A.D. Pilkington ¹⁰², M. Pinamonti ^{69a,69c}, J.L. Pinfeld ², B.C. Pinheiro Pereira ^{131a}, A.E. Pinto Pinoargote ^{101,136}, L. Pintucci ^{69a,69c}, K.M. Piper ¹⁴⁷, A. Pirttikoski ⁵⁶, D.A. Pizzi ³⁴, L. Pizzimento ^{64b}, A. Pizzini ¹¹⁵, M.-A. Pleier ²⁹, V. Plesanovs⁵⁴, V. Pleskot ¹³⁴, E. Plotnikova³⁸, G. Poddar ⁹⁵, R. Poettgen ⁹⁹, L. Poggioli ¹²⁸, I. Pokharel ⁵⁵, S. Polacek ¹³⁴, G. Polesello ^{73a}, A. Poley ^{143,157a}, A. Polini ^{23b}, C.S. Pollard ¹⁶⁸, Z.B. Pollock ¹²⁰, E. Pompa Pacchi ^{75a,75b}, D. Ponomarenko ¹¹⁴, L. Pontecorvo ³⁶, S. Popa ^{27a}, G.A. Popeneciu ^{27d}, A. Poreba ³⁶, D.M. Portillo Quintero ^{157a},

S. Pospisil ¹³³, M.A. Postill ¹⁴⁰, P. Postolache ^{27c}, K. Potamianos ¹⁶⁸, P.A. Potepa ^{86a},
 I.N. Potrap ³⁸, C.J. Potter ³², H. Potti ¹, J. Poveda ¹⁶⁴, M.E. Pozo Astigarraga ³⁶,
 A. Prades Ibanez ¹⁶⁴, J. Pretel ⁵⁴, D. Price ¹⁰², M. Primavera ^{70a}, M.A. Principe Martin ¹⁰⁰,
 R. Privara ¹²³, T. Procter ⁵⁹, M.L. Proffitt ¹³⁹, N. Proklova ¹²⁹, K. Prokofiev ^{64c}, G. Proto ¹¹¹,
 J. Proudfoot ⁶, M. Przybycien ^{86a}, W.W. Przygoda ^{86b}, A. Psallidas ⁴⁶, J.E. Puddefoot ¹⁴⁰,
 D. Pudzha ³⁷, D. Pyatiizbyantseva ³⁷, J. Qian ¹⁰⁷, D. Qichen ¹⁰², Y. Qin ¹³, T. Qiu ⁵²,
 A. Quadt ⁵⁵, M. Queitsch-Maitland ¹⁰², G. Quetant ⁵⁶, R.P. Quinn ¹⁶⁵, G. Rabanal Bolanos ⁶¹,
 D. Rafanoharana ⁵⁴, F. Ragusa ^{71a,71b}, J.L. Rainbolt ³⁹, J.A. Raine ⁵⁶, S. Rajagopalan ²⁹,
 E. Ramakoti ³⁷, I.A. Ramirez-Berend ³⁴, K. Ran ^{48,14e}, N.P. Rapheeha ^{33g}, H. Rasheed ^{27b},
 V. Raskina ¹²⁸, D.F. Rassloff ^{63a}, A. Rastogi ^{17a}, S. Rave ¹⁰¹, B. Ravina ⁵⁵, I. Ravinovich ¹⁷⁰,
 M. Raymond ³⁶, A.L. Read ¹²⁶, N.P. Readioff ¹⁴⁰, D.M. Rebutzi ^{73a,73b}, G. Redlinger ²⁹,
 A.S. Reed ¹¹¹, K. Reeves ²⁶, J.A. Reidelsturz ¹⁷², D. Reikher ¹⁵², A. Rej ⁴⁹, C. Rembser ³⁶,
 M. Renda ^{27b}, M.B. Rendel ¹¹¹, F. Renner ⁴⁸, A.G. Rennie ¹⁶⁰, A.L. Rescia ⁴⁸, S. Resconi ^{71a},
 M. Ressegotti ^{57b,57a}, S. Rettie ³⁶, J.G. Reyes Rivera ¹⁰⁸, E. Reynolds ^{17a}, O.L. Rezanova ³⁷,
 P. Reznicek ¹³⁴, H. Riani ^{35d}, N. Ribaric ⁹², E. Ricci ^{78a,78b}, R. Richter ¹¹¹, S. Richter ^{47a,47b},
 E. Richter-Was ^{86b}, M. Ridel ¹²⁸, S. Ridouani ^{35d}, P. Rieck ¹¹⁸, P. Riedler ³⁶, E.M. Riefel ^{47a,47b},
 J.O. Rieger ¹¹⁵, M. Rijssenbeek ¹⁴⁶, M. Rimoldi ³⁶, L. Rinaldi ^{23b,23a}, T.T. Rinn ²⁹,
 M.P. Rinnagel ¹¹⁰, G. Ripellino ¹⁶², I. Riu ¹³, J.C. Rivera Vergara ¹⁶⁶, F. Rizatdinova ¹²²,
 E. Rizvi ⁹⁵, B.R. Roberts ^{17a}, S.H. Robertson ^{105,w}, D. Robinson ³², C.M. Robles Gajardo ^{138f},
 M. Robles Manzano ¹⁰¹, A. Robson ⁵⁹, A. Rocchi ^{76a,76b}, C. Roda ^{74a,74b}, S. Rodriguez Bosca ³⁶,
 Y. Rodriguez Garcia ^{22a}, A. Rodriguez Rodriguez ⁵⁴, A.M. Rodríguez Vera ¹¹⁶, S. Roe ³⁶,
 J.T. Roemer ¹⁶⁰, A.R. Roepe-Gier ¹³⁷, J. Roggel ¹⁷², O. Røhne ¹²⁶, R.A. Rojas ¹⁰⁴,
 C.P.A. Roland ¹²⁸, J. Roloff ²⁹, A. Romaniouk ³⁷, E. Romano ^{73a,73b}, M. Romano ^{23b},
 A.C. Romero Hernandez ¹⁶³, N. Rompotis ⁹³, L. Roos ¹²⁸, S. Rosati ^{75a}, B.J. Rosser ³⁹,
 E. Rossi ¹²⁷, E. Rossi ^{72a,72b}, L.P. Rossi ⁶¹, L. Rossini ⁵⁴, R. Rosten ¹²⁰, M. Rotaru ^{27b},
 B. Rottler ⁵⁴, C. Rougier ⁹⁰, D. Rousseau ⁶⁶, D. Rouso ³², A. Roy ¹⁶³, S. Roy-Garand ¹⁵⁶,
 A. Rozanov ¹⁰³, Z.M.A. Rozario ⁵⁹, Y. Rozen ¹⁵¹, A. Rubio Jimenez ¹⁶⁴, A.J. Ruby ⁹³,
 V.H. Ruelas Rivera ¹⁸, T.A. Ruggeri ¹, A. Ruggiero ¹²⁷, A. Ruiz-Martinez ¹⁶⁴, A. Rummler ³⁶,
 Z. Rurikova ⁵⁴, N.A. Rusakovich ³⁸, H.L. Russell ¹⁶⁶, G. Russo ^{75a,75b}, J.P. Rutherford ⁷,
 S. Rutherford Colmenares ³², K. Rybacki ⁹², M. Rybar ¹³⁴, E.B. Rye ¹²⁶, A. Ryzhov ⁴⁴,
 J.A. Sabater Iglesias ⁵⁶, P. Sabatini ¹⁶⁴, H.F.W. Sadrozinski ¹³⁷, F. Safai Tehrani ^{75a},
 B. Safarzadeh Samani ¹³⁵, S. Saha ¹, M. Sahinsoy ¹¹¹, A. Saibel ¹⁶⁴, M. Saimpert ¹³⁶,
 M. Saito ¹⁵⁴, T. Saito ¹⁵⁴, A. Sala ^{71a,71b}, D. Salamani ³⁶, A. Salnikov ¹⁴⁴, J. Salt ¹⁶⁴,
 A. Salvador Salas ¹⁵², D. Salvatore ^{43b,43a}, F. Salvatore ¹⁴⁷, A. Salzburger ³⁶, D. Sammel ⁵⁴,
 E. Sampson ⁹², D. Sampsonidis ^{153,e}, D. Sampsonidou ¹²⁴, J. Sánchez ¹⁶⁴,
 V. Sanchez Sebastian ¹⁶⁴, H. Sandaker ¹²⁶, C.O. Sander ⁴⁸, J.A. Sandesara ¹⁰⁴, M. Sandhoff ¹⁷²,
 C. Sandoval ^{22b}, D.P.C. Sankey ¹³⁵, T. Sano ⁸⁸, A. Sansoni ⁵³, L. Santi ^{75a,75b}, C. Santoni ⁴⁰,
 H. Santos ^{131a,131b}, A. Santra ¹⁷⁰, K.A. Saoucha ¹⁶¹, J.G. Saraiva ^{131a,131d}, J. Sardain ⁷,
 O. Sasaki ⁸⁴, K. Sato ¹⁵⁸, C. Sauer ^{63b}, F. Sauerburger ⁵⁴, E. Sauvan ⁴, P. Savard ^{156,ae},
 R. Sawada ¹⁵⁴, C. Sawyer ¹³⁵, L. Sawyer ⁹⁸, I. Sayago Galvan ¹⁶⁴, C. Sbarra ^{23b}, A. Sbrizzi ^{23b,23a},
 T. Scanlon ⁹⁷, J. Schaarschmidt ¹³⁹, U. Schäfer ¹⁰¹, A.C. Schaffer ^{66,44}, D. Schaile ¹¹⁰,
 R.D. Schamberger ¹⁴⁶, C. Scharf ¹⁸, M.M. Schefer ¹⁹, V.A. Schegelsky ³⁷, D. Scheirich ¹³⁴,
 F. Schenck ¹⁸, M. Schernau ¹⁶⁰, C. Scheulen ⁵⁵, C. Schiavi ^{57b,57a}, M. Schioppa ^{43b,43a},
 B. Schlag ^{144,m}, K.E. Schleicher ⁵⁴, S. Schlenker ³⁶, J. Schmeing ¹⁷², M.A. Schmidt ¹⁷²,
 K. Schmieden ¹⁰¹, C. Schmitt ¹⁰¹, N. Schmitt ¹⁰¹, S. Schmitt ⁴⁸, L. Schoeffel ¹³⁶,
 A. Schoening ^{63b}, P.G. Scholer ³⁴, E. Schopf ¹²⁷, M. Schott ¹⁰¹, J. Schovancova ³⁶,
 S. Schramm ⁵⁶, T. Schroer ⁵⁶, H-C. Schultz-Coulon ^{63a}, M. Schumacher ⁵⁴, B.A. Schumm ¹³⁷,

Ph. Schune ¹³⁶, A.J. Schuy ¹³⁹, H.R. Schwartz ¹³⁷, A. Schwartzman ¹⁴⁴, T.A. Schwarz ¹⁰⁷,
 Ph. Schwemling ¹³⁶, R. Schwienhorst ¹⁰⁸, A. Sciandra ¹³⁷, G. Sciolla ²⁶, F. Scuri ^{74a},
 C.D. Sebastiani ⁹³, K. Sedlaczek ¹¹⁶, P. Seema ¹⁸, S.C. Seidel ¹¹³, A. Seiden ¹³⁷,
 B.D. Seidlitz ⁴¹, C. Seitz ⁴⁸, J.M. Seixas ^{83b}, G. Sekhniaidze ^{72a}, L. Selem ⁶⁰,
 N. Semprini-Cesari ^{23b,23a}, D. Sengupta ⁵⁶, V. Senthilkumar ¹⁶⁴, L. Serin ⁶⁶, L. Serkin ^{69a,69b},
 M. Sessa ^{76a,76b}, H. Severini ¹²¹, F. Sforza ^{57b,57a}, A. Sfyrla ⁵⁶, Q. Sha ^{14a}, E. Shabalina ⁵⁵,
 A.H. Shah ³², R. Shaheen ¹⁴⁵, J.D. Shahinian ¹²⁹, D. Shaked Renous ¹⁷⁰, L.Y. Shan ^{14a},
 M. Shapiro ^{17a}, A. Sharma ³⁶, A.S. Sharma ¹⁶⁵, P. Sharma ⁸⁰, P.B. Shatalov ³⁷, K. Shaw ¹⁴⁷,
 S.M. Shaw ¹⁰², A. Shcherbakova ³⁷, Q. Shen ^{62c,5}, D.J. Sheppard ¹⁴³, P. Sherwood ⁹⁷, L. Shi ⁹⁷,
 X. Shi ^{14a}, C.O. Shimmin ¹⁷³, J.D. Shinner ⁹⁶, I.P.J. Shipsey ¹²⁷, S. Shirabe ⁸⁹,
 M. Shiyakova ^{38,u}, J. Shlomi ¹⁷⁰, M.J. Shochet ³⁹, J. Shojaii ¹⁰⁶, D.R. Shope ¹²⁶,
 B. Shrestha ¹²¹, S. Shrestha ^{120,ah}, E.M. Shrif ^{33g}, M.J. Shroff ¹⁶⁶, P. Sicho ¹³²,
 A.M. Sickles ¹⁶³, E. Sideras Haddad ^{33g}, A.C. Sidley ¹¹⁵, A. Sidoti ^{23b}, F. Siegert ⁵⁰,
 Dj. Sijacki ¹⁵, F. Sili ⁹¹, J.M. Silva ⁵², M.V. Silva Oliveira ²⁹, S.B. Silverstein ^{47a}, S. Simion ⁶⁶,
 R. Simoniello ³⁶, E.L. Simpson ⁵⁹, H. Simpson ¹⁴⁷, L.R. Simpson ¹⁰⁷, N.D. Simpson ⁹⁹,
 S. Simsek ⁸², S. Sindhu ⁵⁵, P. Sinervo ¹⁵⁶, S. Singh ¹⁵⁶, S. Sinha ⁴⁸, S. Sinha ¹⁰²,
 M. Sioli ^{23b,23a}, I. Siral ³⁶, E. Sitnikova ⁴⁸, J. Sjölin ^{47a,47b}, A. Skaf ⁵⁵, E. Skorda ²⁰,
 P. Skubic ¹²¹, M. Slawinska ⁸⁷, V. Smakhtin ¹⁷⁰, B.H. Smart ¹³⁵, S.Yu. Smirnov ³⁷, Y. Smirnov ³⁷,
 L.N. Smirnova ^{37,a}, O. Smirnova ⁹⁹, A.C. Smith ⁴¹, E.A. Smith ³⁹, H.A. Smith ¹²⁷,
 J.L. Smith ¹⁰², R. Smith ¹⁴⁴, M. Smizanska ⁹², K. Smolek ¹³³, A.A. Snesev ³⁷, S.R. Snider ¹⁵⁶,
 H.L. Snoek ¹¹⁵, S. Snyder ²⁹, R. Sobie ^{166,w}, A. Soffer ¹⁵², C.A. Solans Sanchez ³⁶,
 E.Yu. Soldatov ³⁷, U. Soldevila ¹⁶⁴, A.A. Solodkov ³⁷, S. Solomon ²⁶, A. Soloshenko ³⁸,
 K. Solovieva ⁵⁴, O.V. Solovyanov ⁴⁰, V. Solovyev ³⁷, P. Sommer ³⁶, A. Sonay ¹³,
 W.Y. Song ^{157b}, A. Sopczak ¹³³, A.L. Sopio ⁹⁷, F. Sopkova ^{28b}, J.D. Sorenson ¹¹³,
 I.R. Sotarriva Alvarez ¹⁵⁵, V. Sothilingam ^{63a}, O.J. Soto Sandoval ^{138c,138b}, S. Sottocornola ⁶⁸,
 R. Soualah ¹⁶¹, Z. Soumami ^{35e}, D. South ⁴⁸, N. Soybelman ¹⁷⁰, S. Spagnolo ^{70a,70b},
 M. Spalla ¹¹¹, D. Sperlich ⁵⁴, T.M. Spieker ^{63a}, G. Spigo ³⁶, S. Spinali ⁹², D.P. Spiteri ⁵⁹,
 M. Spousta ¹³⁴, E.J. Staats ³⁴, R. Stamen ^{63a}, A. Stampekis ²⁰, M. Standke ²⁴, E. Stanecka ⁸⁷,
 W. Stanek-Maslouska ⁴⁸, M.V. Stange ⁵⁰, B. Stanislaus ^{17a}, M.M. Stanitzki ⁴⁸, B. Stapf ⁴⁸,
 E.A. Starchenko ³⁷, G.H. Stark ¹³⁷, J. Stark ⁹⁰, P. Staroba ¹³², P. Starovoitov ^{63a}, S. Stärz ¹⁰⁵,
 R. Staszewski ⁸⁷, G. Stavropoulos ⁴⁶, J. Steentoft ¹⁶², P. Steinberg ²⁹, B. Stelzer ^{143,157a},
 H.J. Stelzer ¹³⁰, O. Stelzer-Chilton ^{157a}, H. Stenzel ⁵⁸, T.J. Stevenson ¹⁴⁷, G.A. Stewart ³⁶,
 J.R. Stewart ¹²², M.C. Stockton ³⁶, G. Stoicea ^{27b}, M. Stolarski ^{131a}, S. Stonjek ¹¹¹,
 A. Straessner ⁵⁰, J. Strandberg ¹⁴⁵, S. Strandberg ^{47a,47b}, M. Stratmann ¹⁷², M. Strauss ¹²¹,
 T. Streblner ¹⁰³, P. Strizenec ^{28b}, R. Ströhmer ¹⁶⁷, D.M. Strom ¹²⁴, R. Stroynowski ⁴⁴,
 A. Strubig ^{47a,47b}, S.A. Stucci ²⁹, B. Stugu ¹⁶, J. Stupak ¹²¹, N.A. Styles ⁴⁸, D. Su ¹⁴⁴,
 S. Su ^{62a}, W. Su ^{62d}, X. Su ^{62a}, D. Suchy ^{28a}, K. Sugizaki ¹⁵⁴, V.V. Sulini ³⁷, M.J. Sullivan ⁹³,
 D.M.S. Sultan ¹²⁷, L. Sultanaliyeva ³⁷, S. Sultansoy ^{3b}, T. Sumida ⁸⁸, S. Sun ¹⁰⁷, S. Sun ¹⁷¹,
 O. Sunneborn Gudnadottir ¹⁶², N. Sur ¹⁰³, M.R. Sutton ¹⁴⁷, H. Suzuki ¹⁵⁸, M. Svatos ¹³²,
 M. Swiatlowski ^{157a}, T. Swirski ¹⁶⁷, I. Sykora ^{28a}, M. Sykora ¹³⁴, T. Sykora ¹³⁴, D. Ta ¹⁰¹,
 K. Tackmann ^{48,t}, A. Taffard ¹⁶⁰, R. Tafirout ^{157a}, J.S. Tafoya Vargas ⁶⁶, Y. Takubo ⁸⁴,
 M. Talby ¹⁰³, A.A. Talyshv ³⁷, K.C. Tam ^{64b}, N.M. Tamir ¹⁵², A. Tanaka ¹⁵⁴, J. Tanaka ¹⁵⁴,
 R. Tanaka ⁶⁶, M. Tanasini ^{57b,57a}, Z. Tao ¹⁶⁵, S. Tapia Araya ^{138f}, S. Tapprogge ¹⁰¹,
 A. Tarek Abouelfadl Mohamed ¹⁰⁸, S. Tarem ¹⁵¹, K. Tariq ^{14a}, G. Tarna ^{103,27b}, G.F. Tartarelli ^{71a},
 P. Tas ¹³⁴, M. Tasevsky ¹³², E. Tassi ^{43b,43a}, A.C. Tate ¹⁶³, G. Tateno ¹⁵⁴, Y. Tayalati ^{35e,v},
 G.N. Taylor ¹⁰⁶, W. Taylor ^{157b}, A.S. Tee ¹⁷¹, R. Teixeira De Lima ¹⁴⁴, P. Teixeira-Dias ⁹⁶,
 J.J. Teoh ¹⁵⁶, K. Terashi ¹⁵⁴, J. Terron ¹⁰⁰, S. Terzo ¹³, M. Testa ⁵³, R.J. Teuscher ^{156,w},

A. Thaler ⁷⁹, O. Theiner ⁵⁶, N. Themistokleous ⁵², T. Theveneaux-Pelzer ¹⁰³, O. Thielmann ¹⁷²,
 D.W. Thomas ⁹⁶, J.P. Thomas ²⁰, E.A. Thompson ^{17a}, P.D. Thompson ²⁰, E. Thomson ¹²⁹,
 R.E. Thornberry ⁴⁴, Y. Tian ⁵⁵, V. Tikhomirov ^{37,a}, Yu.A. Tikhonov ³⁷, S. Timoshenko ³⁷,
 D. Timoshyn ¹³⁴, E.X.L. Ting ¹, P. Tipton ¹⁷³, S.H. Tlou ^{33g}, K. Todome ¹⁵⁵,
 S. Todorova-Nova ¹³⁴, S. Todt ⁵⁰, M. Togawa ⁸⁴, J. Tojo ⁸⁹, S. Tokár ^{28a}, K. Tokushuku ⁸⁴,
 O. Toldaiev ⁶⁸, R. Tombs ³², M. Tomoto ^{84,112}, L. Tompkins ^{144,m}, K.W. Topolnicki ^{86b},
 E. Torrence ¹²⁴, H. Torres ⁹⁰, E. Torró Pastor ¹⁶⁴, M. Toscani ³⁰, C. Toscirci ³⁹, M. Tost ¹¹,
 D.R. Tovey ¹⁴⁰, A. Traeet ¹⁶, I.S. Trandafir ^{27b}, T. Trefzger ¹⁶⁷, A. Tricoli ²⁹, I.M. Trigger ^{157a},
 S. Trincaz-Duvoid ¹²⁸, D.A. Trischuk ²⁶, B. Trocmé ⁶⁰, L. Truong ^{33c}, M. Trzebinski ⁸⁷,
 A. Trzupke ⁸⁷, F. Tsai ¹⁴⁶, M. Tsai ¹⁰⁷, A. Tsiamis ^{153,e}, P.V. Tsiareshka ³⁷, S. Tsigaridas ^{157a},
 A. Tsirigotis ^{153,r}, V. Tsiskaridze ¹⁵⁶, E.G. Tskhadadze ^{150a}, M. Tsopoulou ¹⁵³, Y. Tsujikawa ⁸⁸,
 I.I. Tsukerman ³⁷, V. Tsulaia ^{17a}, S. Tsuno ⁸⁴, K. Tsuru ¹¹⁹, D. Tsybychev ¹⁴⁶, Y. Tu ^{64b},
 A. Tudorache ^{27b}, V. Tudorache ^{27b}, A.N. Tuna ⁶¹, S. Turchikhin ^{57b,57a}, I. Turk Cakir ^{3a},
 R. Turra ^{71a}, T. Turtuvshin ^{38,x}, P.M. Tuts ⁴¹, S. Tzamarias ^{153,e}, E. Tzovara ¹⁰¹, F. Ukegawa ¹⁵⁸,
 P.A. Ulloa Poblete ^{138c,138b}, E.N. Umaka ²⁹, G. Unal ³⁶, A. Undrus ²⁹, G. Unel ¹⁶⁰, J. Urban ^{28b},
 P. Urquijo ¹⁰⁶, P. Urrejola ^{138a}, G. Usai ⁸, R. Ushioda ¹⁵⁵, M. Usman ¹⁰⁹, Z. Uysal ⁸²,
 V. Vacek ¹³³, B. Vachon ¹⁰⁵, K.O.H. Vadla ¹²⁶, T. Vafeiadis ³⁶, A. Vaitkus ⁹⁷, C. Valderanis ¹¹⁰,
 E. Valdes Santurio ^{47a,47b}, M. Valente ^{157a}, S. Valentinetti ^{23b,23a}, A. Valero ¹⁶⁴,
 E. Valiente Moreno ¹⁶⁴, A. Vallier ⁹⁰, J.A. Valls Ferrer ¹⁶⁴, D.R. Van Arneman ¹¹⁵,
 T.R. Van Daalen ¹³⁹, A. Van Der Graaf ⁴⁹, P. Van Gemmeren ⁶, M. Van Rijnbach ¹²⁶,
 S. Van Stroud ⁹⁷, I. Van Vulpen ¹¹⁵, P. Vana ¹³⁴, M. Vanadia ^{76a,76b}, W. Vandelli ³⁶,
 E.R. Vandewall ¹²², D. Vannicola ¹⁵², L. Vannoli ⁵³, R. Vari ^{75a}, E.W. Varnes ⁷, C. Varni ^{17b},
 T. Varol ¹⁴⁹, D. Varouchas ⁶⁶, L. Varriale ¹⁶⁴, K.E. Varvell ¹⁴⁸, M.E. Vasile ^{27b}, L. Vaslin ⁸⁴,
 G.A. Vasquez ¹⁶⁶, A. Vasyukov ³⁸, R. Vavricka ¹⁰¹, F. Vazeille ⁴⁰, T. Vazquez Schroeder ³⁶,
 J. Veatch ³¹, V. Vecchio ¹⁰², M.J. Veen ¹⁰⁴, I. Veliscek ²⁹, L.M. Veloce ¹⁵⁶, F. Veloso ^{131a,131c},
 S. Veneziano ^{75a}, A. Ventura ^{70a,70b}, S. Ventura Gonzalez ¹³⁶, A. Verbytskyi ¹¹¹,
 M. Verducci ^{74a,74b}, C. Vergis ⁹⁵, M. Verissimo De Araujo ^{83b}, W. Verkerke ¹¹⁵,
 J.C. Vermeulen ¹¹⁵, C. Vernieri ¹⁴⁴, M. Vessella ¹⁰⁴, M.C. Vetterli ^{143,ae}, A. Vgenopoulos ^{153,e},
 N. Viaux Maira ^{138f}, T. Vickey ¹⁴⁰, O.E. Vickey Boeriu ¹⁴⁰, G.H.A. Viehhauser ¹²⁷, L. Vignani ^{63b},
 M. Villa ^{23b,23a}, M. Villaplana Perez ¹⁶⁴, E.M. Villhauer ⁵², E. Vilucchi ⁵³, M.G. Vincter ³⁴,
 G.S. Virdee ²⁰, A. Vishwakarma ⁵², A. Visibile ¹¹⁵, C. Vittori ³⁶, I. Vivarelli ^{23b,23a},
 E. Voevodina ¹¹¹, F. Vogel ¹¹⁰, J.C. Voigt ⁵⁰, P. Vokac ¹³³, Yu. Volkotrub ^{86b}, J. Von Ahnen ⁴⁸,
 E. Von Toerne ²⁴, B. Vormwald ³⁶, V. Vorobel ¹³⁴, K. Vorobev ³⁷, M. Vos ¹⁶⁴, K. Voss ¹⁴²,
 M. Vozak ¹¹⁵, L. Vozdecky ¹²¹, N. Vranjes ¹⁵, M. Vranjes Milosavljevic ¹⁵, M. Vreeswijk ¹¹⁵,
 N.K. Vu ^{62d,62c}, R. Vuillermet ³⁶, O. Vujanovic ¹⁰¹, I. Vukotic ³⁹, S. Wada ¹⁵⁸, C. Wagner ¹⁰⁴,
 J.M. Wagner ^{17a}, W. Wagner ¹⁷², S. Wahdan ¹⁷², H. Wahlberg ⁹¹, M. Wakida ¹¹², J. Walder ¹³⁵,
 R. Walker ¹¹⁰, W. Walkowiak ¹⁴², A. Wall ¹²⁹, E.J. Wallin ⁹⁹, T. Wamorkar ⁶, A.Z. Wang ¹³⁷,
 C. Wang ¹⁰¹, C. Wang ¹¹, H. Wang ^{17a}, J. Wang ^{64c}, R.-J. Wang ¹⁰¹, R. Wang ⁶¹, R. Wang ⁶,
 S.M. Wang ¹⁴⁹, S. Wang ^{62b}, T. Wang ^{62a}, W.T. Wang ⁸⁰, W. Wang ^{14a}, X. Wang ^{14c},
 X. Wang ¹⁶³, X. Wang ^{62c}, Y. Wang ^{62d}, Y. Wang ^{14c}, Z. Wang ¹⁰⁷, Z. Wang ^{62d,51,62c},
 Z. Wang ¹⁰⁷, A. Warburton ¹⁰⁵, R.J. Ward ²⁰, N. Warrack ⁵⁹, S. Waterhouse ⁹⁶, A.T. Watson ²⁰,
 H. Watson ⁵⁹, M.F. Watson ²⁰, E. Watton ^{59,135}, G. Watts ¹³⁹, B.M. Waugh ⁹⁷, J.M. Webb ⁵⁴,
 C. Weber ²⁹, H.A. Weber ¹⁸, M.S. Weber ¹⁹, S.M. Weber ^{63a}, C. Wei ^{62a}, Y. Wei ¹²⁷,
 A.R. Weidberg ¹²⁷, E.J. Weik ¹¹⁸, J. Weingarten ⁴⁹, M. Weirich ¹⁰¹, C. Weiser ⁵⁴, C.J. Wells ⁴⁸,
 T. Wenaus ²⁹, B. Wendland ⁴⁹, T. Wengler ³⁶, N.S. Wenke ¹¹¹, N. Wermes ²⁴, M. Wessels ^{63a},
 A.M. Wharton ⁹², A.S. White ⁶¹, A. White ⁸, M.J. White ¹, D. Whiteson ¹⁶⁰,
 L. Wickremasinghe ¹²⁵, W. Wiedenmann ¹⁷¹, M. Wielers ¹³⁵, C. Wiglesworth ⁴², D.J. Wilbern ¹²¹,

H.G. Wilkens , J.J.H. Wilkinson , D.M. Williams , H.H. Williams¹²⁹, S. Williams , S. Willocq , B.J. Wilson , P.J. Windischhofer , F.I. Winkel , F. Winklmeier , B.T. Winter , J.K. Winter , M. Wittgen¹⁴⁴, M. Wobisch , Z. Wolffs , J. Wollrath¹⁶⁰, M.W. Wolter , H. Wolters , M.C. Wong¹³⁷, E.L. Woodward , S.D. Worm , B.K. Wosiek , K.W. Woźniak , S. Wozniowski , K. Wraight , C. Wu , M. Wu , M. Wu , S.L. Wu , X. Wu , Y. Wu , Z. Wu , J. Wuerzinger , T.R. Wyatt , B.M. Wynne , S. Xella , L. Xia , M. Xia , J. Xiang , M. Xie , X. Xie , S. Xin , A. Xiong , J. Xiong , D. Xu , H. Xu , L. Xu , R. Xu , T. Xu , Y. Xu , Z. Xu , B. Yabsley , S. Yacoob , Y. Yamaguchi , E. Yamashita , H. Yamauchi , T. Yamazaki , Y. Yamazaki , J. Yan , S. Yan , Z. Yan , H.J. Yang , H.T. Yang , S. Yang , T. Yang , X. Yang , X. Yang , Y. Yang , Y. Yang , Z. Yang , W-M. Yao , H. Ye , H. Ye , J. Ye , S. Ye , X. Ye , Y. Yeh , I. Yeletsikh , B.K. Yeo , M.R. Yexley , P. Yin , K. Yorita , S. Younas , C.J.S. Young , C. Young , C. Yu , Y. Yu , M. Yuan , R. Yuan , L. Yue , M. Zaazoua , B. Zabinski , E. Zaid⁵², Z.K. Zak , T. Zakareishvili , N. Zakharchuk , S. Zambito , J.A. Zamora Saa , J. Zang , D. Zanzi , O. Zaplatilek , C. Zeitnitz , H. Zeng , J.C. Zeng , D.T. Zenger Jr , O. Zenin , T. Ženiš , S. Zenz , S. Zerradi , D. Zerwas , M. Zhai , D.F. Zhang , J. Zhang , J. Zhang , K. Zhang , L. Zhang , P. Zhang , R. Zhang , S. Zhang , T. Zhang , X. Zhang , X. Zhang , Y. Zhang , Y. Zhang , Z. Zhang , H. Zhao , T. Zhao , Y. Zhao , Z. Zhao , A. Zhemchugov , J. Zheng , K. Zheng , X. Zheng , Z. Zheng , D. Zhong , B. Zhou , H. Zhou , N. Zhou , Y. Zhou , Y. Zhou⁷, C.G. Zhu , J. Zhu , Y. Zhu , Y. Zhu , X. Zhuang , K. Zhukov , N.I. Zimine , J. Zinsser , M. Ziolkowski , L. Živković , A. Zoccoli , K. Zoch , T.G. Zorbas , O. Zormpa , W. Zou , L. Zwalinski .

¹Department of Physics, University of Adelaide, Adelaide; Australia.

²Department of Physics, University of Alberta, Edmonton AB; Canada.

³(^a)Department of Physics, Ankara University, Ankara; (^b)Division of Physics, TOBB University of Economics and Technology, Ankara; Türkiye.

⁴LAPP, Université Savoie Mont Blanc, CNRS/IN2P3, Annecy; France.

⁵APC, Université Paris Cité, CNRS/IN2P3, Paris; France.

⁶High Energy Physics Division, Argonne National Laboratory, Argonne IL; United States of America.

⁷Department of Physics, University of Arizona, Tucson AZ; United States of America.

⁸Department of Physics, University of Texas at Arlington, Arlington TX; United States of America.

⁹Physics Department, National and Kapodistrian University of Athens, Athens; Greece.

¹⁰Physics Department, National Technical University of Athens, Zografou; Greece.

¹¹Department of Physics, University of Texas at Austin, Austin TX; United States of America.

¹²Institute of Physics, Azerbaijan Academy of Sciences, Baku; Azerbaijan.

¹³Institut de Física d'Altes Energies (IFAE), Barcelona Institute of Science and Technology, Barcelona; Spain.

¹⁴(^a)Institute of High Energy Physics, Chinese Academy of Sciences, Beijing; (^b)Physics Department, Tsinghua University, Beijing; (^c)Department of Physics, Nanjing University, Nanjing; (^d)School of Science, Shenzhen Campus of Sun Yat-sen University; (^e)University of Chinese Academy of Science (UCAS), Beijing; China.

¹⁵Institute of Physics, University of Belgrade, Belgrade; Serbia.

- ¹⁶Department for Physics and Technology, University of Bergen, Bergen; Norway.
- ¹⁷(^a)Physics Division, Lawrence Berkeley National Laboratory, Berkeley CA; (^b)University of California, Berkeley CA; United States of America.
- ¹⁸Institut für Physik, Humboldt Universität zu Berlin, Berlin; Germany.
- ¹⁹Albert Einstein Center for Fundamental Physics and Laboratory for High Energy Physics, University of Bern, Bern; Switzerland.
- ²⁰School of Physics and Astronomy, University of Birmingham, Birmingham; United Kingdom.
- ²¹(^a)Department of Physics, Bogazici University, Istanbul; (^b)Department of Physics Engineering, Gaziantep University, Gaziantep; (^c)Department of Physics, Istanbul University, Istanbul; Türkiye.
- ²²(^a)Facultad de Ciencias y Centro de Investigaciones, Universidad Antonio Nariño, Bogotá; (^b)Departamento de Física, Universidad Nacional de Colombia, Bogotá; Colombia.
- ²³(^a)Dipartimento di Fisica e Astronomia A. Righi, Università di Bologna, Bologna; (^b)INFN Sezione di Bologna; Italy.
- ²⁴Physikalisches Institut, Universität Bonn, Bonn; Germany.
- ²⁵Department of Physics, Boston University, Boston MA; United States of America.
- ²⁶Department of Physics, Brandeis University, Waltham MA; United States of America.
- ²⁷(^a)Transilvania University of Brasov, Brasov; (^b)Horia Hulubei National Institute of Physics and Nuclear Engineering, Bucharest; (^c)Department of Physics, Alexandru Ioan Cuza University of Iasi, Iasi; (^d)National Institute for Research and Development of Isotopic and Molecular Technologies, Physics Department, Cluj-Napoca; (^e)National University of Science and Technology Politehnica, Bucharest; (^f)West University in Timisoara, Timisoara; (^g)Faculty of Physics, University of Bucharest, Bucharest; Romania.
- ²⁸(^a)Faculty of Mathematics, Physics and Informatics, Comenius University, Bratislava; (^b)Department of Subnuclear Physics, Institute of Experimental Physics of the Slovak Academy of Sciences, Kosice; Slovak Republic.
- ²⁹Physics Department, Brookhaven National Laboratory, Upton NY; United States of America.
- ³⁰Universidad de Buenos Aires, Facultad de Ciencias Exactas y Naturales, Departamento de Física, y CONICET, Instituto de Física de Buenos Aires (IFIBA), Buenos Aires; Argentina.
- ³¹California State University, CA; United States of America.
- ³²Cavendish Laboratory, University of Cambridge, Cambridge; United Kingdom.
- ³³(^a)Department of Physics, University of Cape Town, Cape Town; (^b)iThemba Labs, Western Cape; (^c)Department of Mechanical Engineering Science, University of Johannesburg, Johannesburg; (^d)National Institute of Physics, University of the Philippines Diliman (Philippines); (^e)University of South Africa, Department of Physics, Pretoria; (^f)University of Zululand, KwaDlangezwa; (^g)School of Physics, University of the Witwatersrand, Johannesburg; South Africa.
- ³⁴Department of Physics, Carleton University, Ottawa ON; Canada.
- ³⁵(^a)Faculté des Sciences Ain Chock, Réseau Universitaire de Physique des Hautes Energies - Université Hassan II, Casablanca; (^b)Faculté des Sciences, Université Ibn-Tofail, Kénitra; (^c)Faculté des Sciences Semlalia, Université Cadi Ayyad, LPHEA-Marrakech; (^d)LPMR, Faculté des Sciences, Université Mohamed Premier, Oujda; (^e)Faculté des sciences, Université Mohammed V, Rabat; (^f)Institute of Applied Physics, Mohammed VI Polytechnic University, Ben Guerir; Morocco.
- ³⁶CERN, Geneva; Switzerland.
- ³⁷Affiliated with an institute covered by a cooperation agreement with CERN.
- ³⁸Affiliated with an international laboratory covered by a cooperation agreement with CERN.
- ³⁹Enrico Fermi Institute, University of Chicago, Chicago IL; United States of America.
- ⁴⁰LPC, Université Clermont Auvergne, CNRS/IN2P3, Clermont-Ferrand; France.
- ⁴¹Nevis Laboratory, Columbia University, Irvington NY; United States of America.
- ⁴²Niels Bohr Institute, University of Copenhagen, Copenhagen; Denmark.

- ^{43(a)}Dipartimento di Fisica, Università della Calabria, Rende; ^(b)INFN Gruppo Collegato di Cosenza, Laboratori Nazionali di Frascati; Italy.
- ⁴⁴Physics Department, Southern Methodist University, Dallas TX; United States of America.
- ⁴⁵Physics Department, University of Texas at Dallas, Richardson TX; United States of America.
- ⁴⁶National Centre for Scientific Research "Demokritos", Agia Paraskevi; Greece.
- ^{47(a)}Department of Physics, Stockholm University; ^(b)Oskar Klein Centre, Stockholm; Sweden.
- ⁴⁸Deutsches Elektronen-Synchrotron DESY, Hamburg and Zeuthen; Germany.
- ⁴⁹Fakultät Physik, Technische Universität Dortmund, Dortmund; Germany.
- ⁵⁰Institut für Kern- und Teilchenphysik, Technische Universität Dresden, Dresden; Germany.
- ⁵¹Department of Physics, Duke University, Durham NC; United States of America.
- ⁵²SUPA - School of Physics and Astronomy, University of Edinburgh, Edinburgh; United Kingdom.
- ⁵³INFN e Laboratori Nazionali di Frascati, Frascati; Italy.
- ⁵⁴Physikalisches Institut, Albert-Ludwigs-Universität Freiburg, Freiburg; Germany.
- ⁵⁵II. Physikalisches Institut, Georg-August-Universität Göttingen, Göttingen; Germany.
- ⁵⁶Département de Physique Nucléaire et Corpusculaire, Université de Genève, Genève; Switzerland.
- ^{57(a)}Dipartimento di Fisica, Università di Genova, Genova; ^(b)INFN Sezione di Genova; Italy.
- ⁵⁸II. Physikalisches Institut, Justus-Liebig-Universität Giessen, Giessen; Germany.
- ⁵⁹SUPA - School of Physics and Astronomy, University of Glasgow, Glasgow; United Kingdom.
- ⁶⁰LPSC, Université Grenoble Alpes, CNRS/IN2P3, Grenoble INP, Grenoble; France.
- ⁶¹Laboratory for Particle Physics and Cosmology, Harvard University, Cambridge MA; United States of America.
- ^{62(a)}Department of Modern Physics and State Key Laboratory of Particle Detection and Electronics, University of Science and Technology of China, Hefei; ^(b)Institute of Frontier and Interdisciplinary Science and Key Laboratory of Particle Physics and Particle Irradiation (MOE), Shandong University, Qingdao; ^(c)School of Physics and Astronomy, Shanghai Jiao Tong University, Key Laboratory for Particle Astrophysics and Cosmology (MOE), SKLPPC, Shanghai; ^(d)Tsung-Dao Lee Institute, Shanghai; ^(e)School of Physics and Microelectronics, Zhengzhou University; China.
- ^{63(a)}Kirchhoff-Institut für Physik, Ruprecht-Karls-Universität Heidelberg, Heidelberg; ^(b)Physikalisches Institut, Ruprecht-Karls-Universität Heidelberg, Heidelberg; Germany.
- ^{64(a)}Department of Physics, Chinese University of Hong Kong, Shatin, N.T., Hong Kong; ^(b)Department of Physics, University of Hong Kong, Hong Kong; ^(c)Department of Physics and Institute for Advanced Study, Hong Kong University of Science and Technology, Clear Water Bay, Kowloon, Hong Kong; China.
- ⁶⁵Department of Physics, National Tsing Hua University, Hsinchu; Taiwan.
- ⁶⁶IJCLab, Université Paris-Saclay, CNRS/IN2P3, 91405, Orsay; France.
- ⁶⁷Centro Nacional de Microelectrónica (IMB-CNM-CSIC), Barcelona; Spain.
- ⁶⁸Department of Physics, Indiana University, Bloomington IN; United States of America.
- ^{69(a)}INFN Gruppo Collegato di Udine, Sezione di Trieste, Udine; ^(b)ICTP, Trieste; ^(c)Dipartimento Politecnico di Ingegneria e Architettura, Università di Udine, Udine; Italy.
- ^{70(a)}INFN Sezione di Lecce; ^(b)Dipartimento di Matematica e Fisica, Università del Salento, Lecce; Italy.
- ^{71(a)}INFN Sezione di Milano; ^(b)Dipartimento di Fisica, Università di Milano, Milano; Italy.
- ^{72(a)}INFN Sezione di Napoli; ^(b)Dipartimento di Fisica, Università di Napoli, Napoli; Italy.
- ^{73(a)}INFN Sezione di Pavia; ^(b)Dipartimento di Fisica, Università di Pavia, Pavia; Italy.
- ^{74(a)}INFN Sezione di Pisa; ^(b)Dipartimento di Fisica E. Fermi, Università di Pisa, Pisa; Italy.
- ^{75(a)}INFN Sezione di Roma; ^(b)Dipartimento di Fisica, Sapienza Università di Roma, Roma; Italy.
- ^{76(a)}INFN Sezione di Roma Tor Vergata; ^(b)Dipartimento di Fisica, Università di Roma Tor Vergata, Roma; Italy.
- ^{77(a)}INFN Sezione di Roma Tre; ^(b)Dipartimento di Matematica e Fisica, Università Roma Tre, Roma;

Italy.

^{78(a)}INFN-TIFPA;^(b)Università degli Studi di Trento, Trento; Italy.

⁷⁹Universität Innsbruck, Department of Astro and Particle Physics, Innsbruck; Austria.

⁸⁰University of Iowa, Iowa City IA; United States of America.

⁸¹Department of Physics and Astronomy, Iowa State University, Ames IA; United States of America.

⁸²Istinye University, Sariyer, Istanbul; Türkiye.

^{83(a)}Departamento de Engenharia Elétrica, Universidade Federal de Juiz de Fora (UFJF), Juiz de Fora;^(b)Universidade Federal do Rio De Janeiro COPPE/EE/IF, Rio de Janeiro;^(c)Instituto de Física, Universidade de São Paulo, São Paulo;^(d)Rio de Janeiro State University, Rio de Janeiro;^(e)Federal University of Bahia, Bahia; Brazil.

⁸⁴KEK, High Energy Accelerator Research Organization, Tsukuba; Japan.

⁸⁵Graduate School of Science, Kobe University, Kobe; Japan.

^{86(a)}AGH University of Krakow, Faculty of Physics and Applied Computer Science, Krakow;^(b)Marian Smoluchowski Institute of Physics, Jagiellonian University, Krakow; Poland.

⁸⁷Institute of Nuclear Physics Polish Academy of Sciences, Krakow; Poland.

⁸⁸Faculty of Science, Kyoto University, Kyoto; Japan.

⁸⁹Research Center for Advanced Particle Physics and Department of Physics, Kyushu University, Fukuoka ; Japan.

⁹⁰L2IT, Université de Toulouse, CNRS/IN2P3, UPS, Toulouse; France.

⁹¹Instituto de Física La Plata, Universidad Nacional de La Plata and CONICET, La Plata; Argentina.

⁹²Physics Department, Lancaster University, Lancaster; United Kingdom.

⁹³Oliver Lodge Laboratory, University of Liverpool, Liverpool; United Kingdom.

⁹⁴Department of Experimental Particle Physics, Jožef Stefan Institute and Department of Physics, University of Ljubljana, Ljubljana; Slovenia.

⁹⁵School of Physics and Astronomy, Queen Mary University of London, London; United Kingdom.

⁹⁶Department of Physics, Royal Holloway University of London, Egham; United Kingdom.

⁹⁷Department of Physics and Astronomy, University College London, London; United Kingdom.

⁹⁸Louisiana Tech University, Ruston LA; United States of America.

⁹⁹Fysiska institutionen, Lunds universitet, Lund; Sweden.

¹⁰⁰Departamento de Física Teórica C-15 and CIAFF, Universidad Autónoma de Madrid, Madrid; Spain.

¹⁰¹Institut für Physik, Universität Mainz, Mainz; Germany.

¹⁰²School of Physics and Astronomy, University of Manchester, Manchester; United Kingdom.

¹⁰³CPPM, Aix-Marseille Université, CNRS/IN2P3, Marseille; France.

¹⁰⁴Department of Physics, University of Massachusetts, Amherst MA; United States of America.

¹⁰⁵Department of Physics, McGill University, Montreal QC; Canada.

¹⁰⁶School of Physics, University of Melbourne, Victoria; Australia.

¹⁰⁷Department of Physics, University of Michigan, Ann Arbor MI; United States of America.

¹⁰⁸Department of Physics and Astronomy, Michigan State University, East Lansing MI; United States of America.

¹⁰⁹Group of Particle Physics, University of Montreal, Montreal QC; Canada.

¹¹⁰Fakultät für Physik, Ludwig-Maximilians-Universität München, München; Germany.

¹¹¹Max-Planck-Institut für Physik (Werner-Heisenberg-Institut), München; Germany.

¹¹²Graduate School of Science and Kobayashi-Maskawa Institute, Nagoya University, Nagoya; Japan.

¹¹³Department of Physics and Astronomy, University of New Mexico, Albuquerque NM; United States of America.

¹¹⁴Institute for Mathematics, Astrophysics and Particle Physics, Radboud University/Nikhef, Nijmegen; Netherlands.

- ¹¹⁵Nikhef National Institute for Subatomic Physics and University of Amsterdam, Amsterdam; Netherlands.
- ¹¹⁶Department of Physics, Northern Illinois University, DeKalb IL; United States of America.
- ¹¹⁷(^a)New York University Abu Dhabi, Abu Dhabi;(^b)United Arab Emirates University, Al Ain; United Arab Emirates.
- ¹¹⁸Department of Physics, New York University, New York NY; United States of America.
- ¹¹⁹Ochanomizu University, Otsuka, Bunkyo-ku, Tokyo; Japan.
- ¹²⁰Ohio State University, Columbus OH; United States of America.
- ¹²¹Homer L. Dodge Department of Physics and Astronomy, University of Oklahoma, Norman OK; United States of America.
- ¹²²Department of Physics, Oklahoma State University, Stillwater OK; United States of America.
- ¹²³Palacký University, Joint Laboratory of Optics, Olomouc; Czech Republic.
- ¹²⁴Institute for Fundamental Science, University of Oregon, Eugene, OR; United States of America.
- ¹²⁵Graduate School of Science, Osaka University, Osaka; Japan.
- ¹²⁶Department of Physics, University of Oslo, Oslo; Norway.
- ¹²⁷Department of Physics, Oxford University, Oxford; United Kingdom.
- ¹²⁸LPNHE, Sorbonne Université, Université Paris Cité, CNRS/IN2P3, Paris; France.
- ¹²⁹Department of Physics, University of Pennsylvania, Philadelphia PA; United States of America.
- ¹³⁰Department of Physics and Astronomy, University of Pittsburgh, Pittsburgh PA; United States of America.
- ¹³¹(^a)Laboratório de Instrumentação e Física Experimental de Partículas - LIP, Lisboa;(^b)Departamento de Física, Faculdade de Ciências, Universidade de Lisboa, Lisboa;(^c)Departamento de Física, Universidade de Coimbra, Coimbra;(^d)Centro de Física Nuclear da Universidade de Lisboa, Lisboa;(^e)Departamento de Física, Universidade do Minho, Braga;(^f)Departamento de Física Teórica y del Cosmos, Universidad de Granada, Granada (Spain);(^g)Departamento de Física, Instituto Superior Técnico, Universidade de Lisboa, Lisboa; Portugal.
- ¹³²Institute of Physics of the Czech Academy of Sciences, Prague; Czech Republic.
- ¹³³Czech Technical University in Prague, Prague; Czech Republic.
- ¹³⁴Charles University, Faculty of Mathematics and Physics, Prague; Czech Republic.
- ¹³⁵Particle Physics Department, Rutherford Appleton Laboratory, Didcot; United Kingdom.
- ¹³⁶IRFU, CEA, Université Paris-Saclay, Gif-sur-Yvette; France.
- ¹³⁷Santa Cruz Institute for Particle Physics, University of California Santa Cruz, Santa Cruz CA; United States of America.
- ¹³⁸(^a)Departamento de Física, Pontificia Universidad Católica de Chile, Santiago;(^b)Millennium Institute for Subatomic physics at high energy frontier (SAPHIR), Santiago;(^c)Instituto de Investigación Multidisciplinario en Ciencia y Tecnología, y Departamento de Física, Universidad de La Serena;(^d)Universidad Andres Bello, Department of Physics, Santiago;(^e)Instituto de Alta Investigación, Universidad de Tarapacá, Arica;(^f)Departamento de Física, Universidad Técnica Federico Santa María, Valparaíso; Chile.
- ¹³⁹Department of Physics, University of Washington, Seattle WA; United States of America.
- ¹⁴⁰Department of Physics and Astronomy, University of Sheffield, Sheffield; United Kingdom.
- ¹⁴¹Department of Physics, Shinshu University, Nagano; Japan.
- ¹⁴²Department Physik, Universität Siegen, Siegen; Germany.
- ¹⁴³Department of Physics, Simon Fraser University, Burnaby BC; Canada.
- ¹⁴⁴SLAC National Accelerator Laboratory, Stanford CA; United States of America.
- ¹⁴⁵Department of Physics, Royal Institute of Technology, Stockholm; Sweden.
- ¹⁴⁶Departments of Physics and Astronomy, Stony Brook University, Stony Brook NY; United States of

America.

¹⁴⁷Department of Physics and Astronomy, University of Sussex, Brighton; United Kingdom.

¹⁴⁸School of Physics, University of Sydney, Sydney; Australia.

¹⁴⁹Institute of Physics, Academia Sinica, Taipei; Taiwan.

¹⁵⁰(^a) E. Andronikashvili Institute of Physics, Iv. Javakhishvili Tbilisi State University, Tbilisi; (^b) High Energy Physics Institute, Tbilisi State University, Tbilisi; (^c) University of Georgia, Tbilisi; Georgia.

¹⁵¹Department of Physics, Technion, Israel Institute of Technology, Haifa; Israel.

¹⁵²Raymond and Beverly Sackler School of Physics and Astronomy, Tel Aviv University, Tel Aviv; Israel.

¹⁵³Department of Physics, Aristotle University of Thessaloniki, Thessaloniki; Greece.

¹⁵⁴International Center for Elementary Particle Physics and Department of Physics, University of Tokyo, Tokyo; Japan.

¹⁵⁵Department of Physics, Tokyo Institute of Technology, Tokyo; Japan.

¹⁵⁶Department of Physics, University of Toronto, Toronto ON; Canada.

¹⁵⁷(^a) TRIUMF, Vancouver BC; (^b) Department of Physics and Astronomy, York University, Toronto ON; Canada.

¹⁵⁸Division of Physics and Tomonaga Center for the History of the Universe, Faculty of Pure and Applied Sciences, University of Tsukuba, Tsukuba; Japan.

¹⁵⁹Department of Physics and Astronomy, Tufts University, Medford MA; United States of America.

¹⁶⁰Department of Physics and Astronomy, University of California Irvine, Irvine CA; United States of America.

¹⁶¹University of Sharjah, Sharjah; United Arab Emirates.

¹⁶²Department of Physics and Astronomy, University of Uppsala, Uppsala; Sweden.

¹⁶³Department of Physics, University of Illinois, Urbana IL; United States of America.

¹⁶⁴Instituto de Física Corpuscular (IFIC), Centro Mixto Universidad de Valencia - CSIC, Valencia; Spain.

¹⁶⁵Department of Physics, University of British Columbia, Vancouver BC; Canada.

¹⁶⁶Department of Physics and Astronomy, University of Victoria, Victoria BC; Canada.

¹⁶⁷Fakultät für Physik und Astronomie, Julius-Maximilians-Universität Würzburg, Würzburg; Germany.

¹⁶⁸Department of Physics, University of Warwick, Coventry; United Kingdom.

¹⁶⁹Waseda University, Tokyo; Japan.

¹⁷⁰Department of Particle Physics and Astrophysics, Weizmann Institute of Science, Rehovot; Israel.

¹⁷¹Department of Physics, University of Wisconsin, Madison WI; United States of America.

¹⁷²Fakultät für Mathematik und Naturwissenschaften, Fachgruppe Physik, Bergische Universität Wuppertal, Wuppertal; Germany.

¹⁷³Department of Physics, Yale University, New Haven CT; United States of America.

^a Also Affiliated with an institute covered by a cooperation agreement with CERN.

^b Also at An-Najah National University, Nablus; Palestine.

^c Also at Borough of Manhattan Community College, City University of New York, New York NY; United States of America.

^d Also at Center for High Energy Physics, Peking University; China.

^e Also at Center for Interdisciplinary Research and Innovation (CIRI-AUTH), Thessaloniki; Greece.

^f Also at Centro Studi e Ricerche Enrico Fermi; Italy.

^g Also at CERN, Geneva; Switzerland.

^h Also at Département de Physique Nucléaire et Corpusculaire, Université de Genève, Genève; Switzerland.

ⁱ Also at Departament de Física de la Universitat Autònoma de Barcelona, Barcelona; Spain.

^j Also at Department of Financial and Management Engineering, University of the Aegean, Chios; Greece.

^k Also at Department of Physics, California State University, Sacramento; United States of America.

- ^l Also at Department of Physics, King's College London, London; United Kingdom.
- ^m Also at Department of Physics, Stanford University, Stanford CA; United States of America.
- ⁿ Also at Department of Physics, Stellenbosch University; South Africa.
- ^o Also at Department of Physics, University of Fribourg, Fribourg; Switzerland.
- ^p Also at Department of Physics, University of Thessaly; Greece.
- ^q Also at Department of Physics, Westmont College, Santa Barbara; United States of America.
- ^r Also at Hellenic Open University, Patras; Greece.
- ^s Also at Institutio Catalana de Recerca i Estudis Avancats, ICREA, Barcelona; Spain.
- ^t Also at Institut für Experimentalphysik, Universität Hamburg, Hamburg; Germany.
- ^u Also at Institute for Nuclear Research and Nuclear Energy (INRNE) of the Bulgarian Academy of Sciences, Sofia; Bulgaria.
- ^v Also at Institute of Applied Physics, Mohammed VI Polytechnic University, Ben Guerir; Morocco.
- ^w Also at Institute of Particle Physics (IPP); Canada.
- ^x Also at Institute of Physics and Technology, Mongolian Academy of Sciences, Ulaanbaatar; Mongolia.
- ^y Also at Institute of Physics, Azerbaijan Academy of Sciences, Baku; Azerbaijan.
- ^z Also at Institute of Theoretical Physics, Ilia State University, Tbilisi; Georgia.
- ^{aa} Also at Lawrence Livermore National Laboratory, Livermore; United States of America.
- ^{ab} Also at National Institute of Physics, University of the Philippines Diliman (Philippines); Philippines.
- ^{ac} Also at Technical University of Munich, Munich; Germany.
- ^{ad} Also at The Collaborative Innovation Center of Quantum Matter (CICQM), Beijing; China.
- ^{ae} Also at TRIUMF, Vancouver BC; Canada.
- ^{af} Also at Università di Napoli Parthenope, Napoli; Italy.
- ^{ag} Also at University of Colorado Boulder, Department of Physics, Colorado; United States of America.
- ^{ah} Also at Washington College, Chestertown, MD; United States of America.
- ^{ai} Also at Yeditepe University, Physics Department, Istanbul; Türkiye.
- * Deceased

Real-time portable muography with Hankuk Atmospheric-muon Wide Landscaping : HAWL

J. Seo^a, N. Carlin^b, D. F. F. S. Cavalcante^b, J. S. Chung^a, L. E. França^b, C. Ha^{a,1}, J. Kim^a, J. Y. Kim^a, H. Kimku^a, B. C. Koh^a, Y. J. Lee^a, B. B. Manzato^b, S. W. Oh^a, R. L. C. Pitta^b, S. J. Won^a

^a*Department of Physics, Chung-Ang University, Seoul, 06974, Republic of Korea*

^b*Physics Institute, University of São Paulo, São Paulo, 05508-090, Brazil*

Abstract

Cosmic ray muons prove valuable across various fields, from particle physics experiments to non-invasive tomography, thanks to their high flux and exceptional penetrating capability. Utilizing a scintillator detector, one can effectively study the topography of mountains situated above tunnels and underground spaces. The Hankuk Atmospheric-muon Wide Landscaping (HAWL) project successfully charts the mountainous region of eastern Korea by measuring cosmic ray muons with a detector in motion. The real-time muon flux measurement shows a tunnel length accuracy of 6.5 %, with a detectable overburden range spanning from 8 to 400 meter-water-equivalent depth. This is the first real-time portable muon tomography.

Keywords: Muon tomography, Plastic scintillator, Portable radiation detector

1. Introduction

A cosmic-ray muon is an elementary particle generated when a primary cosmic-ray particle collides with atmospheric nuclei Workman et al. (2022). Cosmic-ray muons, in abundance, can traverse high-density materials non-destructively, and their unique energy loss in a material renders them valuable in various applications, from particle physics experiments to muon tomography. In particle physics experiments, a high spatial and temporal resolution muon counter can measure muon flux, track final state particles in an accelerator beam Hewes et al. (2021), and reveal yearly modulations with zenith angle dependence Tilav et al. (2020). Muon tomography has uncovered unknown spaces within pyramids Procureur et al. (2023b) and is employed to assess the condition of nuclear power plants Procureur et al. (2023a). Furthermore, recent advancements in high-resolution muon imaging tech-

nology and portable detectors have broadened their applications, notably in volcanic activity detection Tioukov et al. (2019) and archaeological site investigations Avgitas et al. (2022).

The primary goal of this research is to map the land forms and features above the underground spaces quickly and non-invasively using a moving muon detector. To reconstruct mountainous topography using measured muon flux, we launched the Hankuk Atmospheric-muon Wide Landscaping (HAWL) project. HAWL precisely gauges changes in muon flux within tunnels situated above the Seoul-Yangyang highway and Yangyang Underground Laboratory (Y2L) Adhikari et al. (2018a) in South Korea while moving in high speed as schematically shown in Fig. 1. With data collected by the HAWL detector, we measured the muon flux as a function of elevation, and the detector sensitivity in terms of depth and length resolutions for the tunnels.

Email address: chha@cau.ac.kr (C. Ha)

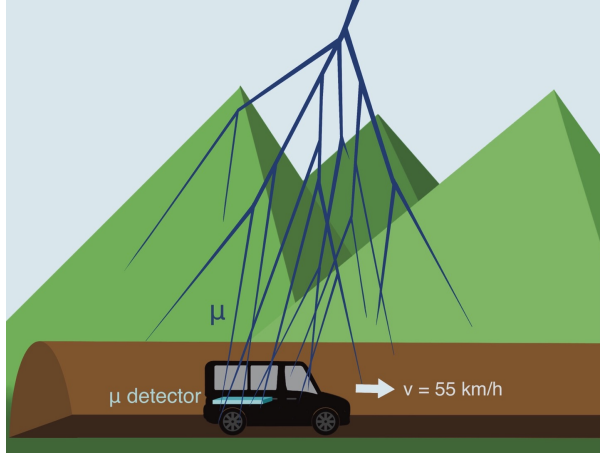


Figure 1: Schematic diagram of the HAWL tomography measurement. The cosmic-ray muon flux is measured in real-time by the HAWL detector loaded in a moving vehicle. The change in the flux relative to the open area can represent the vertical overburden of the rock above the detector.

2. Experimental Method

The main design goal of the HAWL experiment is to be compact to fit in a vehicle and to be simply-integrated to consume low power. We chose the plastic scintillator (PS) as the main detection medium which is durable in rough conditions and relatively easy to handle Knoll (2010). To be efficient in power and space usage, small-sized silicon photomultipliers (SiPMs) coupled with optical fibers are used for the light sensor. A customized data acquisition system is developed to make the overall data processing easily streamlined.

2.1. Detector Construction

The muon counter is constructed from rectangular PS material (Eljen Technology, EJ-200) Eljen (2023) with dimensions of 490 mm \times 600 mm \times 30 mm. A total of 56 optical fibers coupled with 28 SiPMs are laid out as a grid on the top and bottom surfaces of the PS material.

The cylindrical fiber (Kuraray, double-cladding Y-11) Kuraray (2024) is a wavelength-shifting scintillator with 1 mm diameter that has an absorption peak at 430 nm and an emission peak at 476 nm with an attenuation length greater than 3.5 m. The SiPM (Hamamatsu, S13360-1375PE) MPPC (2024) consists of 285 pixels and has a

gain of 4.0×10^6 in a 1.3×1.3 mm² photosensitive area. Six SiPMs are placed on short sides and eight on long sides. The arrangement included 56 optical fibers crossing each other at 19 mm intervals on both the top and bottom of the PS scintillator with 4 ends of optical fibers joined together to couple one SiPM. For optimal performance, the tip of each optical fiber was polished, and a small amount of optical grease was applied at the junction between the SiPM and the optical fiber ends.

To better couple the tip of the optical fibers on a SiPM sensitive area, a fixture as shown in Fig. 2 is installed to the SiPM front-end board. The optical fiber fixture has a hole with a diameter of 4.0 mm and a vertical depth of 8.0 mm stabilizing the fiber bundle and providing better contact to the sensor.

To prevent leakage of scintillation photons and block external photons, the panel with fibers is first wrapped in a Tyvek sheet which has more than 90 % reflectivity in the scintillation spectrum Janecek (2012) and then is covered by a layer of 50 μ m-thick aluminum foil. A layout of the detector is shown in Fig. 2 and its construction procedures are displayed in Fig. 3.

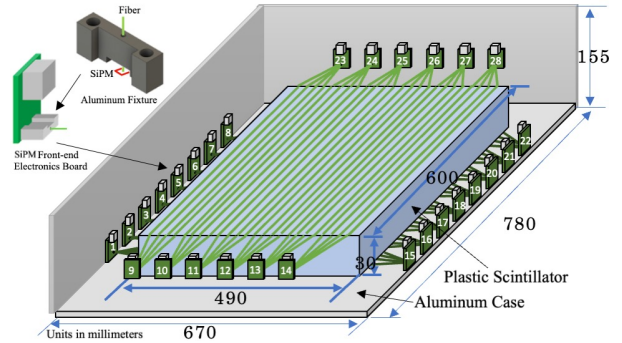


Figure 2: The HAWL detector design. The optical fibers are laid out on top and bottom of a PS panel and their ends are coupled with 28 SiPM light sensors. A SiPM is mounted on a front-end electronics board which sends signals to DAQ via LAN cables. A fixture aids the coupling between the SiPM sensitive area and the tip of the optical fibers. The entire setup is encased in an aluminum housing.

2.2. Data Acquisition

The data acquisition system consists of slow analog to digital converter (SADC), trigger-clock board (TCB) and

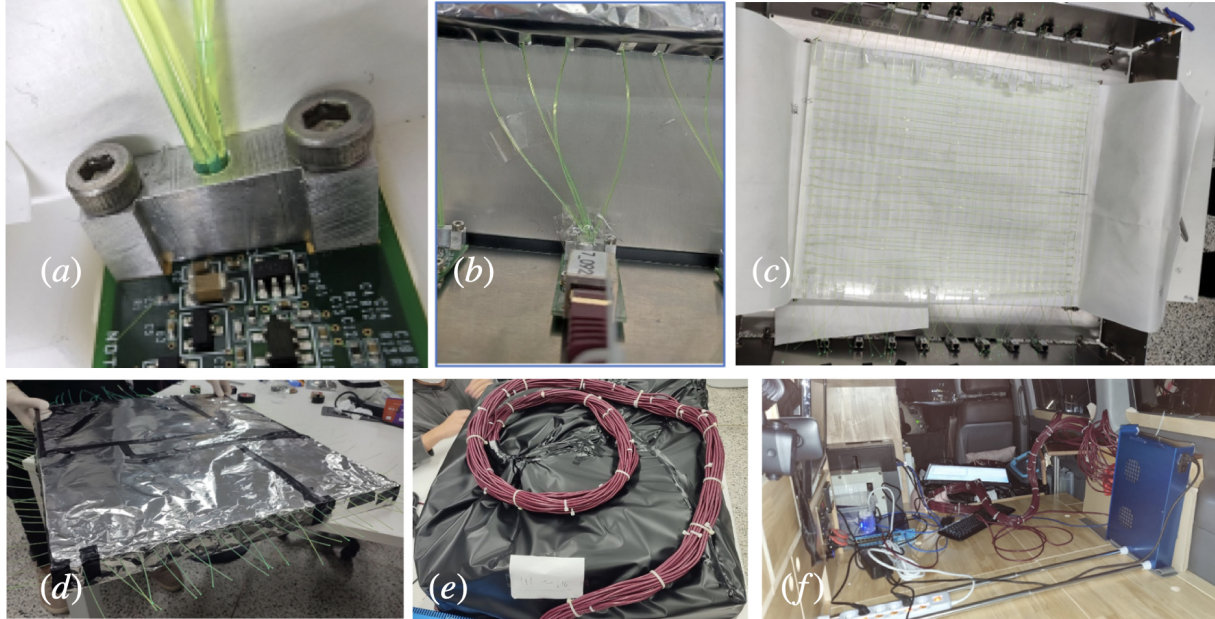


Figure 3: Photos of the HAWL detector assembly. A front-end board connected with four fiber ends are shown in (a) and (b). The layout of the fibers with Tyvek sheets and additional aluminum foil covers are visible in (c) and (d), respectively. The completed HAWL detector is seen in (e) and it is set in place in a van (f) with other DAQ system.

a desktop computer Adhikari et al. (2018b). The 28 SiPM front-end boards are connected to a custom-made SADC module via a LAN connector. The SADC module provides required voltages to each channel and digitizes the analog signals. The SADC uses 16 ns sampling and has two modes; full waveform mode and sum charge mode. In the waveform mode, all 40-channel waveforms per event are stored while in the sum charge mode, reduced information consisting of only integrated ADC values and average time values for each channel are stored. Example waveforms for the same signal event are shown in Fig. 4.

The time synchronization and trigger decision are performed by the TCB which is connected to the SADC module via a USB cable. A channel hit is defined when a SiPM signal exceeds the preset threshold level on that channel. A trigger is formed if 8 or more hits out of 28 active channels are recorded within a 1000 ns time window and an event is constructed by padding the trigger

time around $4 \mu\text{s}$ readout window aligning the trigger hit times near $1.2 \mu\text{s}$.

The collected raw data is a binary format which is immediately converted into a ROOT format Brun and Rademakers (1997). The detector tests are done in a waveform mode where the trigger settings and the individual channel signal analysis are determined in advance. Then, those conditions are applied to the real-time physics runs using a sum charge mode to minimize the power and disc space loads.

The completed detector has been tested in a lab to set a muon selection cut and check the stability before beginning the physics run collections. Figure 5 shows event distributions in terms of their measured charge. Muons are well separated from the environmental gamma background. A Landau function plus a linear function was used to model the data for muon and gamma components, respectively. A muon selection cut was set at 95 % signal

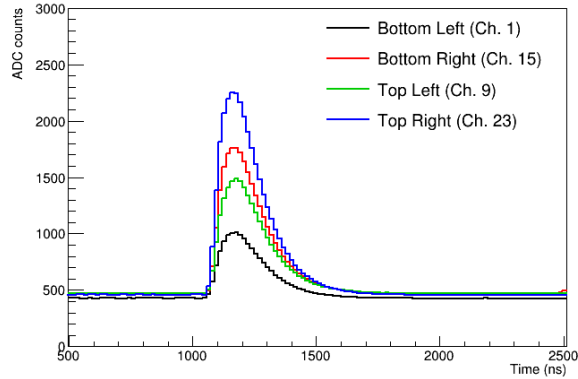


Figure 4: SiPM raw waveform data. Four signal waveforms selected from each side of the detector are displayed. Baselines are typically set around 500 ADC and the amplitude can go up to 4096 ADC. The trigger time starts around 1000 ns and readout window goes to 4096 ns.

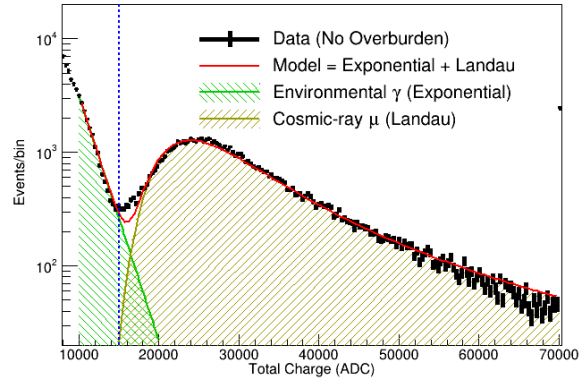


Figure 5: Muon event selection. The rate measurements in a open space are shown as a function of 28-SiPM sum charge. Data are fit to a model defined by an exponential component for environmental radiation (green fills) plus a Landau component for cosmic-ray muons (yellow fills). The vertical dotted line at 15000 ADC is the cut to select muon events.

efficiency, allowing 10% gamma contamination. Subsequently, all equipment was loaded onto the vehicle with a battery. The total power consumption was measured to be 100 Watts. The real-time monitoring was established, allowing results to be broadcasted via wifi. The lab test at 18 m above sea level shows a muon flux of 149.8 events/m²/s.

Muon flux measurements commenced with the portable HAWL detector on November 25, 2022. The trip began from the Gapyeong service area which is located approximately 60 km east of Seoul in the Seoul-Yangyang national highway and traveled to the easterly direction. The muon event rate as a function of time has been displayed in a car. At the same time, the same event rate is broadcasted in real-time by Internet so that it can be simultaneously monitored remotely. To record the speed of the car and the locations of tunnels, we kept camera recording using a smart phone.

The campaign is divided into three sections based on their geographical uniqueness. The section I consists of many tunnels of varying lengths and types while the section II includes the longest tunnel. We enter Yangyang underground laboratory (Y2L) which is the 700 m deep facility that can be accessed by a car in the section III. These sections covered about 100 km out of the total length of the 150 km highway as shown in Fig. 6. We maintained

the speed at 55 km/h (the highway lanes have low speed limit of 50 km/h).

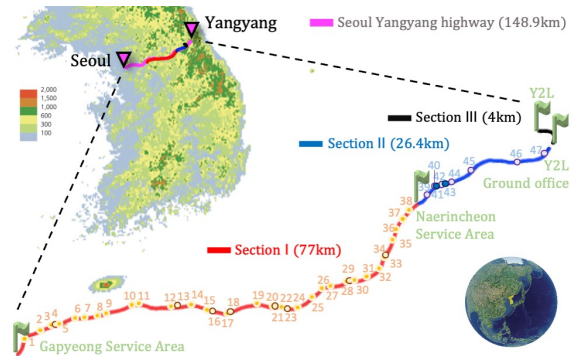


Figure 6: Measurement campaign sections and tunnels. The trip was divided into three sections (I,II, and III). Section I (red line) is from Gapyeong service area to Naerincheon service area and Section II (blue line) is to Y2L ground office. Section III (black line) is on a local road from Y2L ground office to Y2L underground lab. Tunnels are numbered in sequence. The specification of each tunnel can be found in Table .1.

3. Analysis and Results

Physics data of 10822 seconds have been collected and divided in three sections (run-times are 5259 s, 2475 s, and 3088 s, respectively for section I, II, and III). The raw trigger rate was measured at 1901.5 Hz and the rate was reduced to 52 Hz after the cosmic-ray muon selection cut in Fig 5. The moment the van enters a tunnel, the HAWL detector was able to show the muon rate decrease visually as displayed in Fig. 7 and in a video of the Supplementary material.

Figure 7 show the muon event rates as a function of time for the three section measurements. The HAWL detector was able to delineate all tunnels, overpasses, and features above the moving car. The average muon rate was measured at 53.0 ± 0.1 Hz throughout the campaign. it became reduced to a certain amount when passing a tunnel depending on its length and depth. The section-II includes the 11 km-long tunnel (Inje-Yangyang tunnel) where the maximum vertical overburden is 440 m. For the third section, we recorded the muon rate for the Yangyang underground space. Data show a clear suppression in rates inside the tunnels where we were able to measure the tunnel width and a maximum depth of overburden.

We model the muon flux reduction based on the extended Sigmoid function $f(t)$ which is defined by

$$f(t) = \frac{A}{1 + e^{b(t-m)}} + \frac{A}{1 + e^{-b(t-m-w)}} + d, \quad (1)$$

where A describes open area muon rate, b models the slope of the mountain, m and w represent entrance and width of the tunnel, respectively, and d is the depth parameter. The first term of Eq. 1 is for the entrance side of the tunnel while the second term is mirror reflection for the exiting side. The data segments that show rate reductions were fitted with Eq. 1 using the χ^2 minimization to get the best-fit parameters and their uncertainties. An example fit is shown in Fig. 8.

The fitting results show correct identification of all tunnels when we compared our measurements with the original civil engineering data and satellite images. The short overpasses are identified with limited data points which are constrained by the speed of the vehicle and the size of the detector. A model fit based on the Eq. 1 reveals continuous measurements of the muon flux in open spaces in between the tunnels. Because the highway has been built

on an increasing slope (maximum elevation difference is about 400 m) towards the end of the section I and II and a decreasing slope at the end of section II, the muon rate appears to follow the similar characteristics of the elevation. Figure 9 shows the muon flux in an open space as a function of elevation. A constant muon flux model is rejected at more than 5 standard deviation. The correlation coefficient $R = 0.72$ between the muon flux and engineering elevation data has been obtained supporting the flux increase as a function of the altitude.

Assuming the constant speed of the car at 55 km/h, we estimated the tunnel entrance location and the width as shown in Fig. 10. The width accuracy was measured as 6.5 % by the spread of the relative difference between the measured and true length. The three shortest structures detected were animal overpasses that have lengths of 35 m, 40 m, and 60 m each with 3 m, 3 m, and 5.5 m overburden, respectively.

The muon rates inside the tunnels have been measured as a function of their true maximum depths. Assuming the metamorphic rock contents ($\rho = 2.7 \text{ g/cm}^3$) in north-eastern Korean provinces, the depth is converted into the meter-water-equivalent depth. Figure 11 shows the expected exponential reduction behavior Workman et al. (2022). The minimum overburden that data recorded is 3 meters while the maximum overburden is determined at 150 meters which was estimated by the kink in the decay of the data points. The tunnel specifications and measured values are tabulated in Table .1.

4. Discussion and Conclusion

The primary challenge lies in acquiring muon data more efficiently, especially considering the speed limits on highways and therefore, a bigger size panel is preferable. Secondly, the separation power between the environmental gammas and muons determines the depth resolution. A detailed analysis after the return of the trip shows most of those events recorded under deeper tunnels (i.e. depth larger than 150 meters) are dominated by gamma background events. Due to the relatively fast speed of the car and the small area detector, it is not efficient to collect a large amount of muon data in a deeper tunnel. On the other hand, we were able to map the short-to-medium tunnels with better accuracy thanks to high count rates. For example, data show that the entrance or

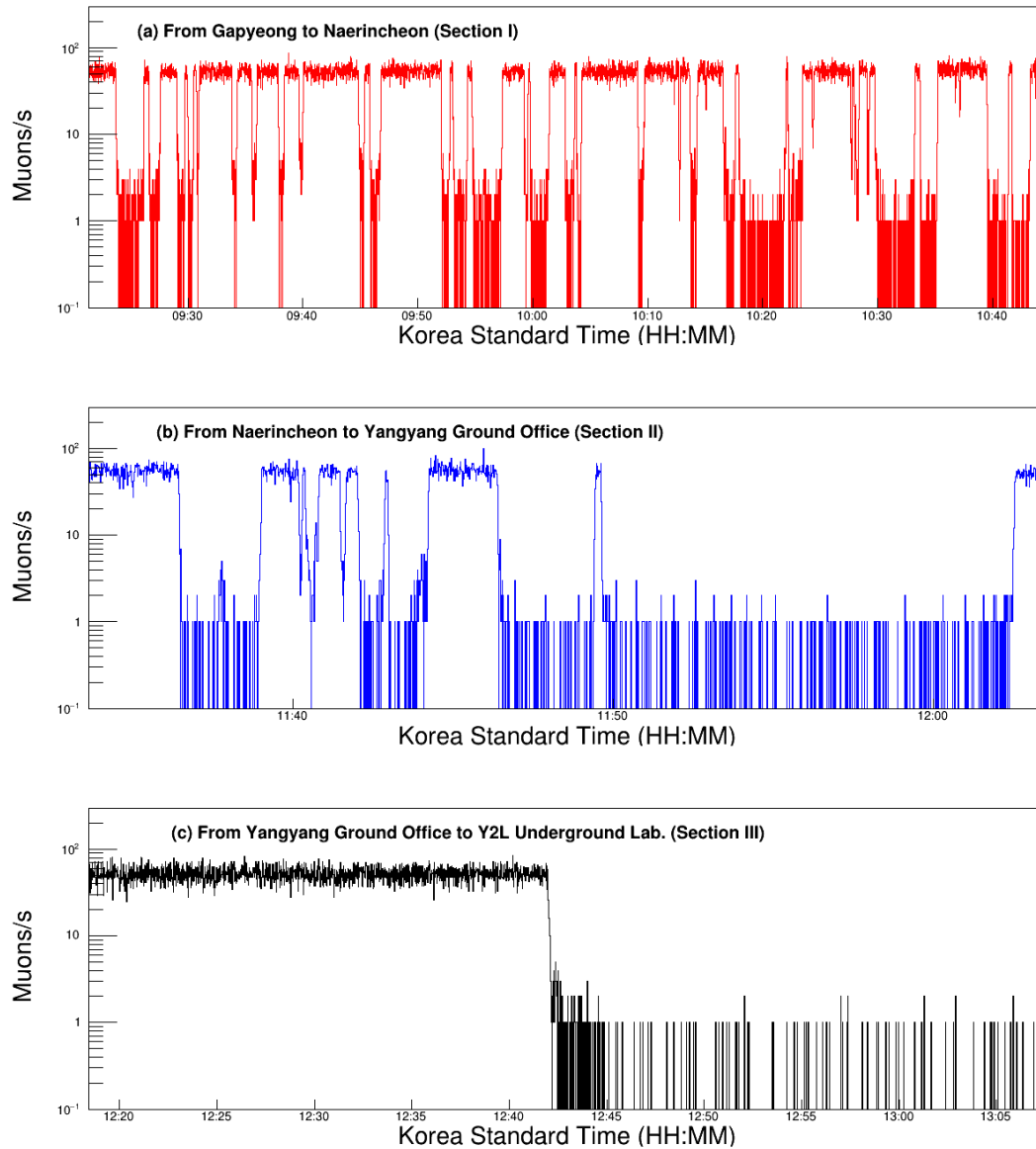


Figure 7: Muon flux measurement campaign. Muon count rates per second is displayed in Section I(a), II(b), and III(c). The rate drops are shown when passing tunnels. Note that the low count rates at deep tunnels in plot (b) and plot (c) appear to be mostly gamma background events.

exit of the tunnels can be measured with a high precision which helps determine the length of the tunnel. The steepness of mountains near the entrance or exit of the tunnels could be estimated utilizing the slope parameter in the fit.

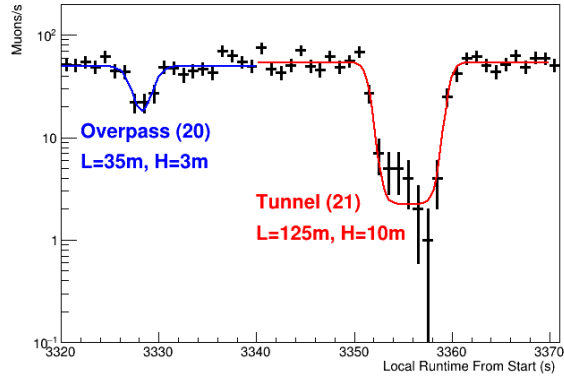


Figure 8: Short tunnel measurements. Two short tunnels are fitted separately. The blue fit line is for the 35 m-long animal overpass with height of 3 m while the red fit line is for the 125 m-long tunnel with maximum height of 10 m.

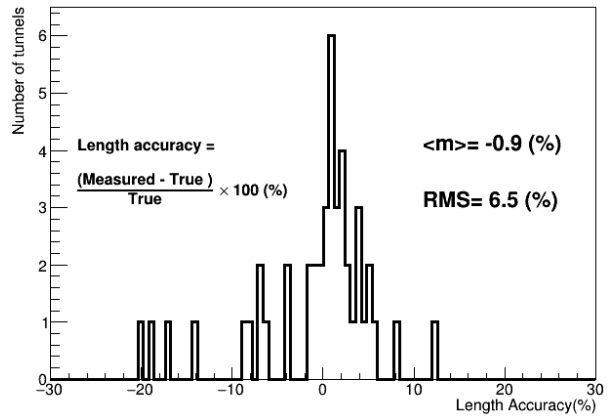


Figure 10: Length accuracy distribution. The relative difference between measured and actual lengths of tunnels is drawn. The accuracy is measured to be 6.5 % while the bias is -0.9 %. The length accuracy is driven by the outliers which are mostly short tunnels.

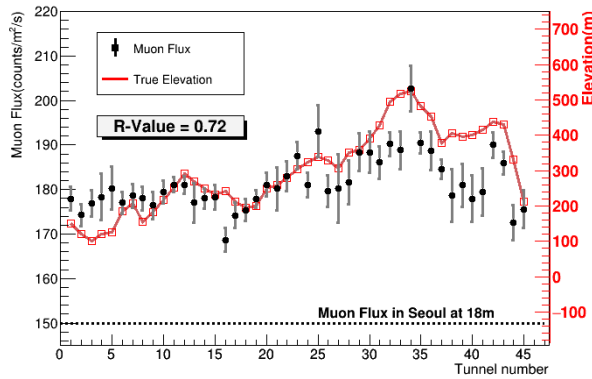


Figure 9: Muon flux as a function of the tunnel location. The muon rate is closely following the elevation changes of the Seoul-Yangyang highway. The correlation coefficient is measured to be $R = 0.72$. Please note that the dotted line is reference muon flux measured at 18 m above sea level with the same detector.

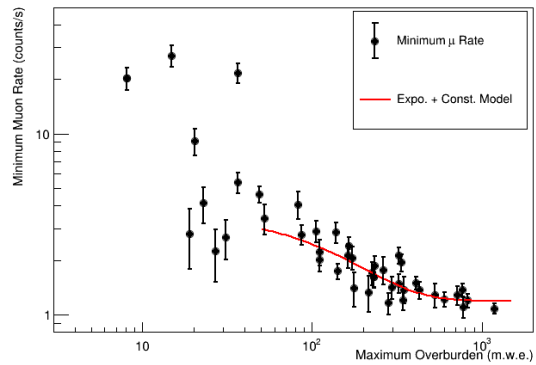


Figure 11: Measured minimum muon rate as a function of true maximum overburden in the meter-water-equivalent (m.w.e.) unit. The muon rate drops exponentially until it is saturated by the gamma contamination. Above 400 m.w.e deep tunnel, the events are dominated by the background gammas.

However, to measure the depths more accurately, a tighter control of environmental gamma ray interactions and a larger detector that can collect enough counts are needed.

The HAWL portable muon detector, utilizing a plastic scintillator, was successfully developed to create a mountainous topography, demonstrating muon flux variations based on rock thickness. The completed test validated

the detector's functionality, particularly evident in the expected decrease in muon flux when passing through a tunnel beneath a mountain in the eastern Korea. Analyzing muon flux data along the Seoul-Yangyang highway revealed a close alignment with anticipated tunnel dimensions and tomography above it, achieving a length ac-

curacy of 6.5 % for tunnels at depths ranging from 8 to 400 m.w.e. The HAWL detector demonstrated its unique capability to measure muon rates, while in motion. An upgraded version of HAWL is in development, featuring two thicker panel detectors with anti-coincidence and directional sensitivity. Given its versatility in shallow-depth applications, the HAWL detector is planned to be used in subway systems and underwater tunnels to enhance safety measures.

5. Acknowledgments

This work was supported by National Research Foundation of Korea (NRF) grant funded by the Korean government (MSIT) (NRF-2021R1A2C1013761) and under the framework of international cooperation program managed by the National Research Foundation of Korea (NRF-2021K2A9A1A0609413312), Republic of Korea; Grant No. 2021/06743-1, 2022/12002-7 and 2022/13293-5 FAPESP, CAPES Finance Code 001, CNPq 304658/2023-5 and 303122/2020-0, Brazil.









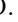


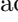





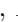
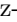
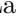
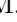
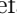
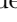

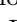
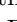



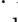










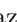

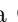







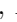
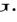



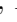
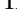
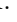




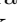













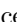








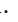

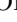

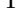

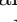
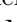
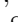




References











- Adhikari, G., et al., 2018a. Initial Performance of the COSINE-100 Experiment. *Eur. Phys. J. C* 78, 107. doi:10.1140/epjc/s10052-018-5590-x, arXiv:1710.05299.
- Adhikari, G., et al. (COSINE-100), 2018b. The COSINE-100 Data Acquisition System. *JINST* 13, P09006. doi:10.1088/1748-0221/13/09/P09006, arXiv:1806.09788.
- Avgitas, T., Elles, S., Goy, C., Karyotakis, Y., Marteau, J., 2022. Muography applied to archaeology, in: 27e édition de la Réunion des Sciences de la Terre. arXiv:2203.00946.
- Brun, R., Rademakers, F., 1997. ROOT - An Object Oriented Data Analysis Framework. *Nuclear Instruments and Methods in Physics Research Section A: Accelerators, Spectrometers, Detectors and Associated Equipment* 389, 81.
- Eljen, 2023. Eljen Technology, GENERAL PURPOSE EJ-200, EJ-204, EJ-208, EJ-212. URL: <https://eljentechnology.com/products/plastic-scintillators/ej-200-ej-204-ej-208-ej-212>.
- Hewes, V., et al. (DUNE), 2021. Deep Underground Neutrino Experiment (DUNE) Near Detector Conceptual Design Report. *Instruments* 5, 31. doi:10.3390/instruments5040031, arXiv:2103.13910.
- Janecek, M., 2012. Reflectivity spectra for commonly used reflectors. *IEEE Transactions on Nuclear Science* 59, 490–497. doi:10.1109/TNS.2012.2183385.
- Knoll, G.F., 2010. Radiation detection and measurement. John Wiley and Sons, New York.
- Kuraray, 2024. Plastic scintillating fibers (PSF). URL: <https://www.kuraray.com/products/psf>.
- MPPC, 2024. MPPC for precision measurement, S13360-1375PE. URL: <https://www.hamamatsu.com/eu/en/product/optical-sensors/mppc>.
- Procureur, S., et al., 2023a. 3D imaging of a nuclear reactor using muography measurements. *Science Advances* 9, eabq8431.
- Procureur, S., et al., 2023b. Precise characterization of a corridor-shaped structure in Khufu’s Pyramid by observation of cosmic-ray muons. *Nature Communications* 14, 1144.
- Tilav, S., Gaisser, T.K., Soldin, D., Desiati, P. (IceCube), 2020. Seasonal variation of atmospheric muons in IceCube. *PoS ICRC2019*, 894. doi:10.22323/1.358.0894, arXiv:1909.01406.
- Tioukov, V., et al., 2019. First muography of Stromboli volcano. *Scientific Reports* 9, 6695.
- Workman, R., et al. (Particle Data Group), 2022. The Review of Particle Physics. *Prog. Theor. Exp. Phys.* 2022, 083C01.

Table .1: Tunnel specifications and HAWL measurements. Lengths (L) and maximum depths (H) are obtained from engineering blueprints. The elevations are an average value Measured L is equal to the fit width parameter w multiplied by the speed 55 km/h.

No.	Name	L (m)	Max. H (m)	Elev. (m)	Meas. L(m)	Depth H(s)	μ Flux(/m ² /s)
1	Misa	2171	284	155	2218.3	1.37	177.9
2	Magok	919	85	124	914.0	1.62	174.3
3	Balsan 1	633	84	106	633.9	1.70	176.9
4	Balsan 2	480	97.5	126	460.6	1.77	178.3
5	Balsan 3	254	30.5	129	211.2	4.07	180.3
6	Balsan 4	433	60.5	189	435.4	2.13	177.0
7	Chugok	433	32	211	428.5	2.78	178.6
8	Haengchon	463	63.5	160	488.4	2.06	178.0
9	Gwangpan	358	18	186	360.9	4.64	176.4
10	Gunja 1	474	51	220	483.8	2.86	179.4
11	Gunja 2	885	120	255	891.4	2.12	181.1
12	Dongsan 1	680	86	295	689.7	1.87	181.0
13	Dongsan 2	1113	120.5	273	1168.8	1.49	177.0
14	Bukbang 1	2307	152	252	2391.6	1.50	178.0
15	Bukbang 2	326	65	235	328.2	1.41	178.3
16	Bukbang 3	1518	159	246	1550.1	1.37	168.7
17	Hwachon 1	721	85	216	724.0	1.62	174.2
18	Hwachon 2	378	80	200	396.6	1.33	175.4
19	Hwachon 3	527	61	204	522.9	2.39	177.9
20	Hwachon 4	35	3	252	36.3	20.4	181.1
21	Hwachon 5	125	10	264	123.4	2.24	180.2
22	Hwachon 6	629	41	283	606.0	2.01	183.0
23	Hwachon 7	40	3	308	37.5	20.3	182.7
24	Hwachon 8	978	124	328	987.2	1.94	181.0
25	Hwachon 9	3705	304	342	3764.1	1.20	193.1
26	Naechon 1	1261	52.5	332	1155.6	1.74	179.7
27	Naechon 2	88	7.5	309	86.8	9.12	180.2
28	Naechon 3	135	8.5	354	151.3	4.14	181.6
29	Naechon 4	355	39	362	365.8	2.90	188.4
30	Naechon 5	205	19.5	393	176.7	3.42	188.4
31	Seoseok	3061	221.5	430	3183.2	1.22	186.1
32	Haengchiryong	1422	104	497	1434.9	1.16	190.2
33	Sangnam 1	60	5.5	520	48.1	27.1	190.0
34	Sangnam 2	115	13.5	527	105.3	21.7	201.7
35	Sangnam 3	1719	126.5	485	1714.6	1.20	190.5
36	Sangnam 4	1434	195	454	1472.3	1.29	188.7
37	Sangnam 7	2278	264	381	2342.6	1.28	184.6
38	Girin 1	114	7	408	92.7	2.81	178.7
39	Girin 2	397	41	398	370.4	2.23	181.0
40	Girin 3	162	11.5	402	163.4	2.68	177.9
41	Girin 4	750	128.5	418	765.1	1.38	179.5
42	Girin 5	1148	109.5	441	1165.3	1.42	190.0
43	Girin 6	2665	288.5	432	2785.4	1.10	186.0
44	Inje-Yangyang	10962	440	335	11821.4	1.08	172.5
45	Seomyeon 2	248	13.5	417	230.5	5.38	175.6

Measurement of CP asymmetries in $B^0 \rightarrow K_S^0 K_S^0 K_S^0$ decays at Belle II

I. Adachi , L. Aggarwal , H. Ahmed , H. Aihara , N. Akopov , A. Aloisio , N. Anh Ky , D. M. Asner ,
H. Atmacan , T. Aushev , V. Aushev , M. Aversano , R. Ayad , V. Babu , H. Bae , S. Bahinipati ,
P. Bambade , Sw. Banerjee , S. Bansal , M. Barrett , J. Baudot , M. Bauer , A. Baur , A. Beaubien ,
F. Becherer , J. Becker , P. K. Behera , J. V. Bennett , F. U. Bernlochner , V. Bertacchi , M. Bertemes ,
E. Bertholet , M. Bessner , S. Bettarini , B. Bhuyan , F. Bianchi , L. Bierwirth , T. Bilka , D. Biswas ,
A. Bobrov , D. Bodrov , A. Bolz , A. Bondar , J. Borah , A. Bozek , M. Bračko , P. Branchini ,
R. A. Briere , T. E. Browder , A. Budano , S. Bussino , M. Campajola , L. Cao , G. Casarosa ,
C. Cecchi , J. Cerasoli , M.-C. Chang , P. Chang , R. Cheaib , P. Cheema , V. Chekelian , C. Chen ,
B. G. Cheon , K. Chilikin , K. Chirapatpimol , H.-E. Cho , K. Cho , S.-J. Cho , S.-K. Choi ,
S. Choudhury , J. Cochran , L. Corona , L. M. Cremaldi , S. Das , F. Dattola , E. De La Cruz-Burelo ,
S. A. De La Motte , G. De Nardo , M. De Nuccio , G. De Pietro , R. de Sangro , M. Destefanis ,
S. Dey , A. De Yta-Hernandez , R. Dhamija , A. Di Canto , F. Di Capua , J. Dingfelder , Z. Doležal ,
I. Domínguez Jiménez , T. V. Dong , M. Dorigo , K. Dort , D. Dossett , S. Dreyer , S. Dubey ,
G. Dujany , P. Ecker , M. Eliachevitch , D. Epifanov , P. Feichtinger , T. Ferber , D. Ferlewicz ,
T. Fillinger , C. Finck , G. Finocchiaro , A. Fodor , F. Forti , A. Frey , B. G. Fulsom , A. Gabrielli ,
E. Ganiev , M. Garcia-Hernandez , R. Garg , A. Garmash , G. Gaudino , V. Gaur , A. Gaz , A. Gellrich ,
G. Ghevondyan , D. Ghosh , H. Ghumaryan , G. Giakoustidis , R. Giordano , A. Giri , A. Glazov ,
B. Gobbo , R. Godang , O. Gogota , P. Goldenzweig , W. Gradl , T. Grammatico , S. Granderath ,
E. Graziani , D. Greenwald , Z. Gruberová , T. Gu , Y. Guan , K. Gudkova , S. Halder , Y. Han ,
K. Hara , T. Hara , K. Hayasaka , H. Hayashii , S. Hazra , C. Hearty , M. T. Hedges , A. Heidelberg ,
I. Heredia de la Cruz , M. Hernández Villanueva , A. Hershenhorn , T. Higuchi , E. C. Hill , M. Hoek ,
M. Hohmann , P. Horak , C.-L. Hsu , T. Humair , T. Iijima , K. Inami , N. Ipsita , A. Ishikawa , S. Ito ,
R. Itoh , M. Iwasaki , P. Jackson , W. W. Jacobs , D. E. Jaffe , E.-J. Jang , Q. P. Ji , S. Jia , Y. Jin ,
A. Johnson , K. K. Joo , H. Junkerkalefeld , H. Kakuno , M. Kaleta , D. Kalita , A. B. Kaliyar ,
J. Kandra , K. H. Kang , S. Kang , G. Karyan , T. Kawasaki , F. Keil , C. Ketter , C. Kiesling ,
C.-H. Kim , D. Y. Kim , K.-H. Kim , Y.-K. Kim , H. Kindo , K. Kinoshita , P. Kodyš , T. Koga ,
S. Kohani , K. Kojima , T. Konno , A. Korobov , S. Korpar , E. Kovalenko , R. Kowalewski ,
T. M. G. Kraetzschmar , P. Križan , P. Krokovny , Y. Kulii , T. Kuhr , J. Kumar , M. Kumar ,
R. Kumar , K. Kumara , T. Kunigo , A. Kuzmin , Y.-J. Kwon , S. Lacaprara , Y.-T. Lai , T. Lam ,
L. Lancieri , J. S. Lange , M. Laurenza , K. Lautenbach , R. Lebourcher , F. R. Le Diberder , P. Leitl ,
D. Levit , C. Li , L. K. Li , Y. Li , J. Libby , Q. Y. Liu , Z. Q. Liu , D. Liventsev , S. Longo , A. Lozar ,
T. Lueck , C. Lyu , Y. Ma , M. Maggiora , S. P. Maharana , R. Maiti , S. Maity , G. Mancinelli ,
R. Manfredi , E. Manoni , M. Mantovano , D. Marcantonio , S. Marcello , C. Marinas , L. Martel ,
C. Martellini , A. Martini , T. Martinov , L. Massaccesi , M. Masuda , T. Matsuda , D. Matvienko ,
S. K. Maurya , J. A. McKenna , R. Mehta , F. Meier , M. Merola , F. Metzner , M. Milesi , C. Miller ,
M. Mirra , K. Miyabayashi , H. Miyake , R. Mizuk , G. B. Mohanty , N. Molina-Gonzalez , S. Mondal ,
S. Moneta , H.-G. Moser , M. Mrvar , R. Mussa , I. Nakamura , K. R. Nakamura , M. Nakao ,
Y. Nakazawa , A. Narimani Charan , M. Naruki , Z. Natkaniec , A. Natochii , L. Nayak , M. Nayak ,
G. Nazaryan , M. Neu , C. Niebuhr , N. K. Nisar , S. Nishida , S. Ogawa , Y. Onishchuk , H. Ono ,
Y. Onuki , P. Oskin , F. Otani , P. Pakhlov , G. Pakhlova , A. Paladino , A. Panta , E. Paoloni ,
S. Pardi , K. Parham , H. Park , S.-H. Park , B. Paschen , A. Passeri , S. Patra , S. Paul , T. K. Pedlar ,
I. Peruzzi , R. Peschke , R. Pestotnik , F. Pham , M. Piccolo , L. E. Piilonen , G. Pinna Angioni ,
P. L. M. Podesta-Lerma , T. Podobnik , S. Pokharel , C. Praz , S. Prell , E. Principe , M. T. Prim ,
H. Purwar , N. Rad , P. Rados , G. Raeuber , S. Raiz , N. Rauls , M. Reif , S. Reiter , M. Remnev ,
I. Ripp-Baudot , G. Rizzo , L. B. Rizzuto , S. H. Robertson , M. Roehrken , J. M. Roney , A. Rostomyan ,
N. Rout , G. Russo , D. Sahoo , D. A. Sanders , S. Sandilya , A. Sangal , L. Santelj , Y. Sato ,
V. Savinov , B. Scavino , C. Schmitt , C. Schwanda , A. J. Schwartz , Y. Seino , A. Selce , K. Senyo ,
J. Serrano , M. E. Sevir , C. Sfienti , W. Shan , C. Sharma

A. Thaller , O. Tittel , R. Tiwary , D. Tonelli , E. Torassa , N. Toutounji , K. Trabelsi , I. Tsaklidis , M. Uchida , I. Ueda , Y. Uematsu , T. Uglov , K. Unger , Y. Unno , K. Uno , S. Uno , P. Urquijo , Y. Ushiroda , S. E. Vahsen , R. van Tonder , G. S. Varner , K. E. Varvell , M. Veronesi , V. S. Vismaya , L. Vitale , V. Vobbiliseti , R. Volpe , B. Wach , M. Wakai , S. Wallner , E. Wang , M.-Z. Wang , X. L. Wang , Z. Wang , A. Warburton , M. Watanabe , S. Watanuki , M. Welsch , C. Wessel , X. P. Xu , B. D. Yabsley , S. Yamada , W. Yan , S. B. Yang , J. Yelton , J. H. Yin , K. Yoshihara , C. Z. Yuan , Y. Yusa , L. Zani , Y. Zhang , V. Zhilich , J. S. Zhou , Q. D. Zhou , X. Y. Zhou , and V. I. Zhukova
(The Belle II Collaboration)

We report a measurement of decay-time dependent charge-parity (CP) asymmetries in $B^0 \rightarrow K_S^0 K_S^0 K_S^0$ decays. We use 387×10^6 $B\bar{B}$ pairs collected at the $\Upsilon(4S)$ resonance with the Belle II detector at the SuperKEKB asymmetric-energy electron-positron collider. We reconstruct 220 signal events and extract the CP -violating parameters S and C from a fit to the distribution of the decay-time difference between the two B mesons. The resulting confidence region is consistent with previous measurements in $B^0 \rightarrow K_S^0 K_S^0 K_S^0$ and $B^0 \rightarrow (c\bar{c})K^0$ decays, and with predictions based on the standard model.

I. INTRODUCTION

In the standard model (SM), the charmless three-body decay $B^0 \rightarrow K_S^0 K_S^0 K_S^0$ is mediated by the $b \rightarrow sq\bar{q}$ quark transition, which is dominated by a one-loop process, the so-called penguin amplitude. Charge-conjugate decays are implied hereafter unless specified otherwise. Penguin amplitudes are suppressed in the SM, e.g. $\mathcal{B}(B^0 \rightarrow K_S^0 K_S^0 K_S^0) = (6.0 \pm 0.5) \times 10^{-6}$ [1], and imply exchanges of virtual particles where SM particles can be replaced by a broad class of non-SM particles. These features make these decays sensitive to possible contributions from non-SM physics [2]. A key probe of such contributions is provided by decay-time dependent CP -violating asymmetries of the B^0 and \bar{B}^0 decay rates. These asymmetries arise from interference between amplitudes for direct decay and decay following flavor oscillations, due to the irreducible phase in the Cabibbo-Kobayashi-Maskawa (CKM) quark-mixing matrix [3]. Precise measurements of these asymmetries using $B^0\bar{B}^0$ pairs are a primary goal of experiments in electron-positron collisions at the $\Upsilon(4S)$ resonance. If one of the neutral B mesons, B_{CP} , decays into a CP eigenstate f_{CP} at proper time t_{CP} and the other, B_{tag} , decays into a flavor-specific final state f_{tag} at proper time t_{tag} , the probability density for observing a B_{tag} with flavor q_f at $\Delta t \equiv t_{CP} - t_{\text{tag}}$ is [4–6]

$$\mathcal{P}(\Delta t, q_f) = \frac{e^{-|\Delta t|/\tau_{B^0}}}{4\tau_{B^0}} \left(1 + q_f [S \sin(\Delta m_d \Delta t) - C \cos(\Delta m_d \Delta t)] \right), \quad (1)$$

where the flavor q_f is $+1(-1)$ for $B_{\text{tag}} = B^0(\bar{B}^0)$, τ_{B^0} is the B^0 lifetime, Δm_d is the mass difference between the two mass eigenstates of the $B^0\bar{B}^0$ system, and the CP asymmetries S and C express mixing-induced and direct CP violation, respectively [7]. The SM predicts that $S = -\sin 2\phi_1 - 0.02$ and $C = -0.007$ for decays into the CP -even final state $K_S^0 K_S^0 K_S^0$ [8]. The mixing phase $\phi_1 \equiv \arg[-V_{cd}V_{cb}^*/V_{td}V_{tb}^*]$ is a combination of

CKM matrix-elements. The uncertainty in the SM prediction for S is smaller than 0.01; hence, a large deviation in $B^0 \rightarrow K_S^0 K_S^0 K_S^0$ decays would indicate non-SM physics. The Belle [9] and BaBar [10] experiments reported these asymmetries with comparable uncertainties dominated by the sample size, yielding world-average values $S = -0.83 \pm 0.17$ and $C = -0.15 \pm 0.12$ [11]. While these agree with the SM predictions, the large uncertainties limit the sensitivity to non-SM sources. Additional measurements are needed.

We report a measurement of S and C in $B^0 \rightarrow K_S^0 K_S^0 K_S^0$ decays using electron-positron collisions at the $\Upsilon(4S)$ collected by the Belle II experiment. We reconstruct signal (B_{CP}) $B^0 \rightarrow K_S^0 K_S^0 K_S^0$ decays followed by $K_S^0 \rightarrow \pi^+\pi^-$ decays and suppress background using two multivariate classifiers. We then measure q_f using the remaining charged particles in the event and Δt from the distance between the decay positions of B_{CP} and B_{tag} . We divide the $B^0 \rightarrow K_S^0 K_S^0 K_S^0$ events into two classes based on the quality of the Δt information: time-differential (TD) events use Δt and determine S and C , while time-integrated (TI) events do not use Δt and contribute to the determination of C only. Fits to signal-discriminating observables and decay time (when appropriate) determine the signal yield and CP asymmetries. We use the decay $B^+ \rightarrow K_S^0 K_S^0 K^+$ as a control channel to constrain the fit model from data.

II. THE BELLE II DETECTOR AND DATA SAMPLE

The Belle II experiment is located at SuperKEKB, which collides electrons and positrons at and near the $\Upsilon(4S)$ resonance [12]. The Belle II detector [13] has a cylindrical geometry and includes a six-layer silicon detector (VXD) and a 56-layer central drift chamber (CDC). These detectors reconstruct trajectories of charged particles (tracks). The VXD consists of two layers of silicon-pixel detectors (PXD) surrounded by four layers of double-sided silicon-strip detectors [14]. Only

the innermost PXD layer, and one sixth of the outermost layer are installed for the data analyzed here. The symmetry axis of these detectors, defined as the z axis, is almost coincident with the direction of the electron beam. Surrounding the CDC, which also provides dE/dx energy-loss measurements, is a time-of-propagation counter [15] in the central region and an aerogel-based ring-imaging Cherenkov counter in the forward region. These detectors provide charged-particle identification. Surrounding them is an electromagnetic calorimeter based on CsI(Tl) crystals that primarily provides energy and timing measurements for photons and electrons. Outside of the calorimeter is a superconducting solenoid magnet. The magnet provides a 1.5 T magnetic field parallel to the z axis. Its flux return is instrumented with resistive-plate chambers and plastic-scintillator modules to detect muons, K_L^0 mesons, and neutrons.

We use data collected at the $\Upsilon(4S)$ resonance in 2019–2022, corresponding to an integrated luminosity of $(362 \pm 2) \text{ fb}^{-1}$ and containing $(387 \pm 6) \times 10^6 B\bar{B}$ pairs. We use simulated samples to train the multivariate classifiers and define fit models. The $e^+e^- \rightarrow \Upsilon(4S) \rightarrow B\bar{B}$ sample is generated using EVTGEN [16] and PYTHIA [17]. In the simulated signal sample, one of the B mesons decays to the $B^0 \rightarrow K_s^0 K_s^0 K_s^0$ signal mode or the $B^+ \rightarrow K_s^0 K_s^0 K^+$ control mode according to phase space. The simulated $e^+e^- \rightarrow q\bar{q}$ sample, where q indicates an u , d , s , or c quark, is generated using the KKMC [18] generator interfaced with PYTHIA. We also use EVTGEN to simulate the decay of short-lived particles. The detector response is simulated by GEANT4 [19]. Experimental and simulated data are analyzed with the Belle II software [20, 21].

III. EVENT RECONSTRUCTION

The $\Upsilon(4S)$ is produced at the e^+e^- collision point with a Lorentz boost ($\beta\gamma$) of 0.288 and subsequently decays to a B and a \bar{B} meson, which are both nearly at rest in the e^+e^- center-of-mass (c.m.) frame. Therefore, the B -meson pairs propagate nearly along the boost direction with known velocity in the laboratory. This allows one to approximate the difference between their decay times as $\Delta t = (z_{CP} - z_{\text{tag}})/\beta\gamma c$, where $z_{CP(\text{tag})}$ is the decay position of $B_{CP(\text{tag})}$ projected onto the boost axis.

Events are selected online based on the number of charged particles and total energy deposited in the calorimeter with nearly 100% efficiency. Pairs of oppositely-charged particles are used to reconstruct $K_s^0 \rightarrow \pi^+\pi^-$ candidates. The four-momentum and decay vertex of the K_s^0 candidate are obtained from a kinematic fit of the π^+ and π^- tracks. To reduce combinatorial background from incorrectly reconstructed K_s^0 candidates, we use a boosted-decision-tree (BDT) classifier $O_{K_s^0}$ with 15 input variables that include the K_s^0 flight length, the impact parameters of the K_s^0 candidate and the π^\pm , and the number of measurement points

(hits) in the VXD associated with the π^\pm . The most discriminating variables are the angle between the K_s^0 momentum and the displacement of the K_s^0 decay vertex from the beam interaction point (IP) and the K_s^0 flight length normalized by its uncertainty. We select K_s^0 candidates with invariant mass $M(\pi^+\pi^-)$ between $462.6 \text{ MeV}/c^2$ and $532.6 \text{ MeV}/c^2$, corresponding to about 35 units of the relevant resolution, and with an $O_{K_s^0}$ requirement that accepts 91% of K_s^0 mesons. The mass window is wide since the BDT efficiently suppresses the background. These criteria are optimized as described later.

We reconstruct B_{CP} candidates by combining three K_s^0 candidates and treat the particles not belonging to B_{CP} as B_{tag} decay products. We select B_{CP} candidates using the invariant mass $M(K_s^0 K_s^0 K_s^0)$ and the beam energy constrained mass $M_{\text{bc}} \equiv \sqrt{E_{\text{beam}}^2 - |\vec{p}_B|^2 c^2}/c^2$, where E_{beam} and \vec{p}_B are the beam energy and the momentum of the B meson in the e^+e^- c.m. frame. We retain B_{CP} candidates satisfying $5.2 < M_{\text{bc}} < 5.29 \text{ GeV}/c^2$ and $5.08 < M(K_s^0 K_s^0 K_s^0) < 5.48 \text{ GeV}/c^2$, but exclude those satisfying $5.265 < M_{\text{bc}} < 5.29 \text{ GeV}/c^2$ and $5.08 < M(K_s^0 K_s^0 K_s^0) < 5.2 \text{ GeV}/c^2$ to avoid contamination by $B^{0(+)} \rightarrow K_s^0 K_s^0 K^{*0(+)}$ decays.

The dominant source of background is the $e^+e^- \rightarrow q\bar{q}$ continuum. We suppress this background by using another BDT classifier, O_{CS} , with the following input variables that exploit event topology: the cosine of the angle between the thrust axes of B_{CP} and B_{tag} in the e^+e^- c.m. frame; the magnitude of the B_{tag} thrust; the sum of the transverse momenta of the particles in the event; the squared four-momentum difference between the beams and the detected particles in the c.m. frame; and the modified Fox-Wolfram moments [22]. The B thrust axis is a unit vector \hat{t} that maximizes the thrust magnitude $T \equiv (\sum_i |\hat{t} \cdot \vec{p}_i|) / (\sum_i |\vec{p}_i|)$, where \vec{p}_i is the momentum of the B meson's i -th decay-product in the c.m. frame. The BDT classifier O_{CS} ranges from zero for background-like events to one for signal-like events. We use simulated events to train the classifier. A requirement of $O_{\text{CS}} > 0.1$ results in 51% background rejection with a signal efficiency of 98%. We then calculate a transformation of the classifier, $O'_{\text{CS}} = \log[(O_{\text{CS}} - 0.1)/(1 - O_{\text{CS}})]$, which yields a classifier distribution more convenient to parametrize. The selection criteria on K_s^0 candidate mass and $O_{K_s^0}$ are determined by maximizing $N_{\text{sig}}/\sqrt{N_{\text{sig}} + N_{\text{bkg}}}$, where N_{sig} and N_{bkg} are the expected yields of B_{CP} signal and background events determined from simulation, respectively, meeting the following signal-enhancement conditions: $5.27 < M_{\text{bc}} < 5.29 \text{ GeV}/c^2$, $5.18 < M(K_s^0 K_s^0 K_s^0) < 5.38 \text{ GeV}/c^2$, and $O_{\text{CS}} > 0.5$.

In addition to the nonresonant decay amplitude, quasi-two-body decays $B^0 \rightarrow X(\rightarrow K_s^0 K_s^0)K_s^0$ via intermediate resonances X due to $b \rightarrow s$ and $b \rightarrow c$ transitions contribute to $B^0 \rightarrow K_s^0 K_s^0 K_s^0$ decays. We consider $b \rightarrow s$ decays to be signal, but we veto $b \rightarrow c$ contributions to measure the CP asymmetries for the

$b \rightarrow s$ transition. We expect a significant $b \rightarrow c$ contribution only from $B^0 \rightarrow \chi_{c0} K_s^0 K_s^0$ decays based on the rates of $B^0 \rightarrow X(\rightarrow K_s^0 K_s^0) K_s^0$ decays where X indicates a $\bar{D}^0, \chi_{c0}, \chi_{c1}, \chi_{c2}, \eta_c, J/\psi$, or $\psi(2S)$ meson [1]. The $B^0 \rightarrow \chi_{c0}(\rightarrow K_s^0 K_s^0) K_s^0$ branching fraction is around 5% of the signal branching fraction. We reject signal B_{CP} candidates if the invariant mass of any combination of two K_s^0 candidates is in the range $3.379 < M(K_s^0 K_s^0) < 3.447 \text{ GeV}/c^2$. This requirement rejects 90% of the background from $B^0 \rightarrow \chi_{c0}(\rightarrow K_s^0 K_s^0) K_s^0$ decays and 7.2% of signal.

The control channel $B^+ \rightarrow K_s^0 K_s^0 K^+$ is reconstructed from two K_s^0 mesons and a track and is similar to the signal decay. We require the particle identification information for the track to be consistent with a K^+ . We use the control channel to constrain the parameters of B -vertex-resolution model for signal, as well as those of the shapes of the B_{CP} mass and O'_{CS} background distributions. We do not veto $\chi_{c0} K^+$ decays for the control channel because their kinematic distributions are the same as those of the $K_s^0 K_s^0 K^+$ final state.

IV. MEASUREMENT OF B -MESON FLAVOR AND DECAY-TIME DIFFERENCE

We use a category-based BDT algorithm to identify the B_{tag} flavor [23]. The algorithm uses 13 BDTs, each geared toward discriminating a specific signature of $b \rightarrow c \rightarrow s$ cascade decays using particle identification and kinematic variables of the B_{tag} charged decay products. The outputs from these BDTs are combined by the top-level BDT to return the flavor value q_f and tagging quality $r \equiv 1 - 2w$, where w is the probability for wrong flavor assignment. The probability density of Eq. (1) is modified to include the parameter w , and its difference between B^0 and \bar{B}^0 , Δw ,

$$\mathcal{P}_{\text{sig}}^{\text{TD}}(\Delta t, q_f) = \frac{e^{-|\Delta t|/\tau_{B^0}}}{4\tau_{B^0}} \left(1 - q_f \Delta w + q_f(1 - 2w)[S \sin(\Delta m_d \Delta t) - C \cos(\Delta m_d \Delta t)] \right). \quad (2)$$

The events are classified into seven independent r intervals (bins). For each bin, w and Δw are determined using flavor-specific B meson decays with large branching fractions [24]. Since the signal purity varies as a function of r , using the distribution of r improves the statistical sensitivity to the CP asymmetries.

To measure Δt , we reconstruct the B_{CP} and B_{tag} decay vertices using information about the IP. The spatial distribution of the IP is described by a three-dimensional Gaussian whose parameters are regularly measured in a calibration based on $e^+e^- \rightarrow \mu^+\mu^-$ events. The IP size is typically $250 \mu\text{m}$ in the boost direction, $10 \mu\text{m}$ in the horizontal direction, and $0.3 \mu\text{m}$ in the vertical direction [25]. The B_{CP} vertex position is reconstructed from the six final-state pions using a decay-chain vertex fit,

which constrains the B_{CP} to originate from the IP (IP constraint) [26]. Due to their long lifetime, a fraction of K_s^0 mesons decay outside of the VXD volume resulting in poorly measured decay positions. This causes the B_{CP} vertex resolution to depend strongly on the number of K_s^0 mesons with associated VXD hits. In simulation, the fractions of signal decays in which zero, one, two, or three K_s^0 mesons have VXD hits are 0.4%, 7.9%, 37.9%, or 53.8%, respectively. When only one K_s^0 meson has VXD hits, the IP constraint significantly improves the B_{CP} vertex resolution, reducing the average vertex-position uncertainty in the boost direction from around $270 \mu\text{m}$ to $120 \mu\text{m}$. The average uncertainty with the IP constraint is $49 \mu\text{m}$ when two K_s^0 mesons have VXD hits and $35 \mu\text{m}$ when all three have such hits.

We use the B_{tag} tracks to reconstruct the B_{tag} vertex, excluding those having no associated PXD hits. We also exclude pairs of oppositely-charged pions consistent with a K_s^0 decay because they are likely to be produced away from the B_{tag} vertex. Similarly to the B_{CP} vertex, we constrain the B_{tag} to originate from the IP to improve the vertex resolution and reconstruction efficiency [27]. In order to reduce the contamination from tracks from secondary and tertiary displaced vertices, which would bias the determination of the B_{CP} vertex position, the fit is repeated by iteratively removing the tracks contributing the largest increase to the vertex-fit χ^2 until a satisfactory fit quality is achieved. A selection on fit quality and vertex-position uncertainty is applied to ensure the quality of the Δt measurement.

We divide the remaining $B^0 \rightarrow K_s^0 K_s^0 K_s^0$ candidates into two classes based on the quality of the Δt information to maximize the sensitivity of the measurement of S and C . For the time-differential (TD) analysis that determines both S and C , we require candidates that satisfy the following criteria: both tracks from one or more signal K_s^0 are associated with at least one VXD hit, the decay-time-difference satisfies $-30 < \Delta t < 30$ ps, satisfactory vertex-fit quality, and small vertex-position uncertainty. The Δt resolution is around 0.9 ps in the TD events. The Δt information of the other events is not used. They are included in the time-integrated (TI) analysis, which contributes only to C . The probability density in Eq. (2) is integrated over Δt for TI events, yielding

$$\mathcal{P}_{\text{sig}}^{\text{TI}}(q_f) = \frac{1}{2} \left(1 - q_f \Delta w - q_f(1 - 2w)C \frac{1}{1 + \Delta m_d^2 \tau_{B^0}^2} \right). \quad (3)$$

For 1.1% of simulated signal events, multiple (typically two) B_{CP} candidates are reconstructed. We choose the candidate with the best vertex-fit quality for such events, which retains the correctly reconstructed B_{CP} candidates in 82% of these events. This requirement has negligible impact on the Δt distribution and the CP asymmetry results. The reconstruction efficiency including the B_{tag} selection is 28.3% in simulation. For the control channel, we reconstruct the $B^+ \rightarrow K_s^0 K_s^0 K^+$ vertex without using

the K^+ track to emulate the $B^0 \rightarrow K_s^0 K_s^0 K_s^0$ vertex fit. We discard $B^+ \rightarrow K_s^0 K_s^0 K^+$ candidates that fail the TD criteria. The reconstruction efficiency for the control channel is 24.7%.

V. DETERMINATION OF SIGNAL YIELD

We extract the yields for TD, TI, and control channel events from a three-dimensional likelihood fit to the unbinned distributions of M_{bc} ; $M(K_s^0 K_s^0 K)$, where K indicates a K_s^0 or K^+ meson; and O'_{CS} . The likelihood function includes two sample components, signal and background. We determine the shape of the signal component from fits to distributions of simulated signal and control samples. The M_{bc} distribution is modeled with a Gaussian function for the signal TD and control samples and with a Crystal Ball shape [28, 29] for the signal TI sample. The signal and control-sample $M(K_s^0 K_s^0 K)$ distribution is modeled with the sum of a Gaussian function and an asymmetric Breit-Wigner function. The signal and control-sample O'_{CS} distribution is modeled with the sum of a symmetric and an asymmetric Gaussian function. For the background, the M_{bc} distribution is modeled with an ARGUS function [30], the $M(K_s^0 K_s^0 K)$ distribution with a linear function, and the O'_{CS} distribution with the sum of a symmetric and an asymmetric Gaussian function. The endpoint of the ARGUS function is set to E_{beam} , which is calibrated using other B decays. The parameter sets for the O'_{CS} shapes are shared between TD and TI events. We use the same parameter set for the M_{bc} and $M(K_s^0 K_s^0 K)$ background shapes across the three samples as the $B^+ \rightarrow K_s^0 K_s^0 K^+$ kinematic properties are similar to those of the signal decay, as confirmed in simulation. The fit simultaneously determines the yield of each sample and 14 background shape parameters [31].

Figures 1, 2, and 3 show the data distributions with fit results overlaid. The low-mass tails of the $M(K_s^0 K_s^0 K)$ distribution of the signal TI component is mainly due to $\pi \rightarrow \mu\nu\mu$ decays, which occur in 3% of the reconstructed signal $B^0 \rightarrow K_s^0 K_s^0 K_s^0$ events. Such events are mostly classified as TI events due to the poor vertex fit quality. We define the signal region as $5.272 < M_{bc} < 5.288 \text{ GeV}/c^2$, $5.2 < M(K_s^0 K_s^0 K) < 5.36 \text{ GeV}/c^2$, and $-4.44 < O'_{CS} < 8.85$. Each range for M_{bc} and O'_{CS} retains 99.73% of signal TD events. The signal yield and the purity in the signal region is 158^{+14}_{-13} and 57% for TD events, 62 ± 9 and 40% for TI events, and 403^{+24}_{-23} and 22% for the control channel events.

VI. DETERMINATION OF CP ASYMMETRIES

We determine the CP asymmetries S and C from a maximum-likelihood fit to the unbinned Δt and binned q_f distributions combining TD, TI, and $B^+ \rightarrow K_s^0 K_s^0 K^+$ events restricted to the signal region. The contribution

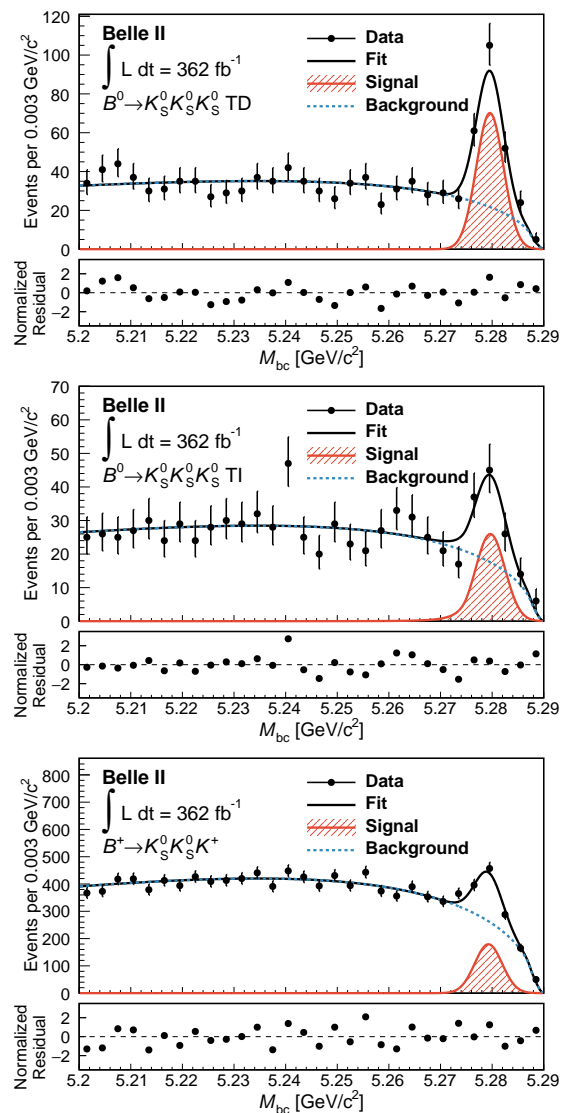


Figure 1. Distributions of M_{bc} for (top) TD, (middle) TI, and (bottom) $B^+ \rightarrow K_s^0 K_s^0 K^+$ candidates with fit projections overlaid. The black dots with error bars represent the data points; the black, solid curve shows the total fit projection; the red hatched area is the signal projection; and the blue, dashed curve is the background projection. The distributions are restricted to events in the $M(K_s^0 K_s^0 K)$ signal region. Lower panels show the differences between data and fit results normalized by the statistical uncertainty of the data.

to the likelihood function from the i -th TD event is

$$\begin{aligned} \mathcal{L}_i^{\text{TD}}(S, C | \Delta t_i, q_f, i) = & \\ & f_i^{\text{sig}} \int d(\Delta t') R(\Delta t_i - \Delta t') \mathcal{P}_{\text{sig}}^{\text{TD}}(\Delta t', q_f, i) \\ & + (1 - f_i^{\text{sig}}) \mathcal{P}_{\text{bkg}}(\Delta t_i), \end{aligned} \quad (4)$$

where $R(\Delta t_i - \Delta t')$ is the response function of the Δt measurement (resolution function), f_i^{sig} is the signal probability of the i -th event, and \mathcal{P}_{bkg} is the Δt distribution of background events. We use a resolution func-

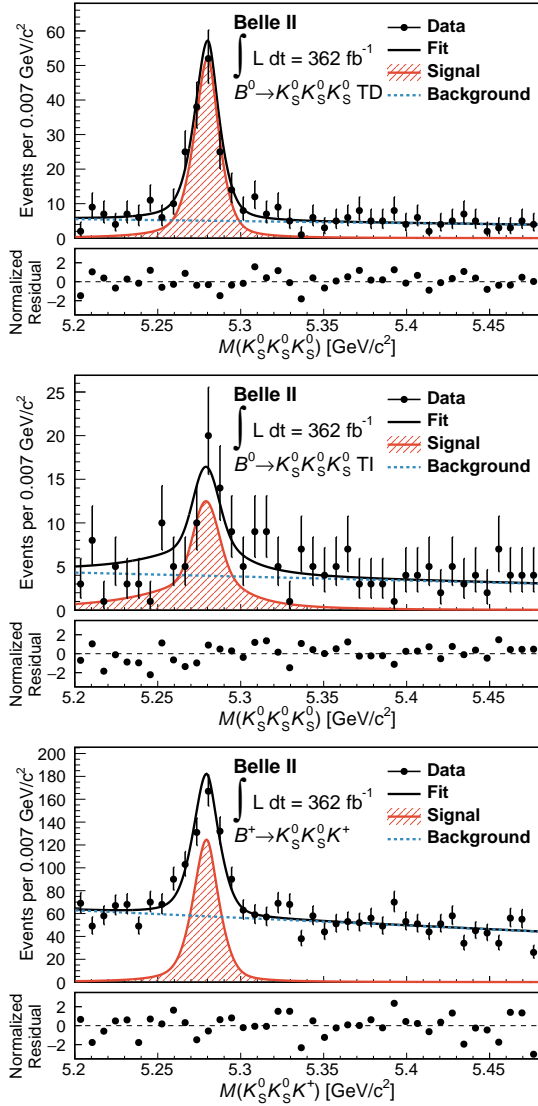


Figure 2. Distributions of $M(K_S^0 K_S^0 K)$ for (top) TD, (middle) TI, and (bottom) $B^+ \rightarrow K_S^0 K_S^0 K^+$ candidates with fit projections overlaid. The black dots with error bars represent the data points; the black, solid curve shows the total fit projection; the red hatched area is the signal projection; and the blue, dashed curve is the background projection. The distributions are restricted to events in the M_{bc} signal region. Lower panels show the differences between data and fit results normalized by the statistical uncertainty of the data.

tion developed by the Belle collaboration [32]. The resolution function is the convolution of four components: detector resolution for the B_{CP} vertex, detector resolution for the B_{tag} vertex, bias due to secondary particles from charmed intermediate states for the B_{tag} vertex, and corrections to the boost factor due to the nonzero c.m. momentum of the B mesons. The correction to the boost factor is calculated analytically using the cosine of the angle between the B_{CP} momentum and the boost direction in the e^+e^- c.m. frame, $\cos\theta_B^*$, on an event-

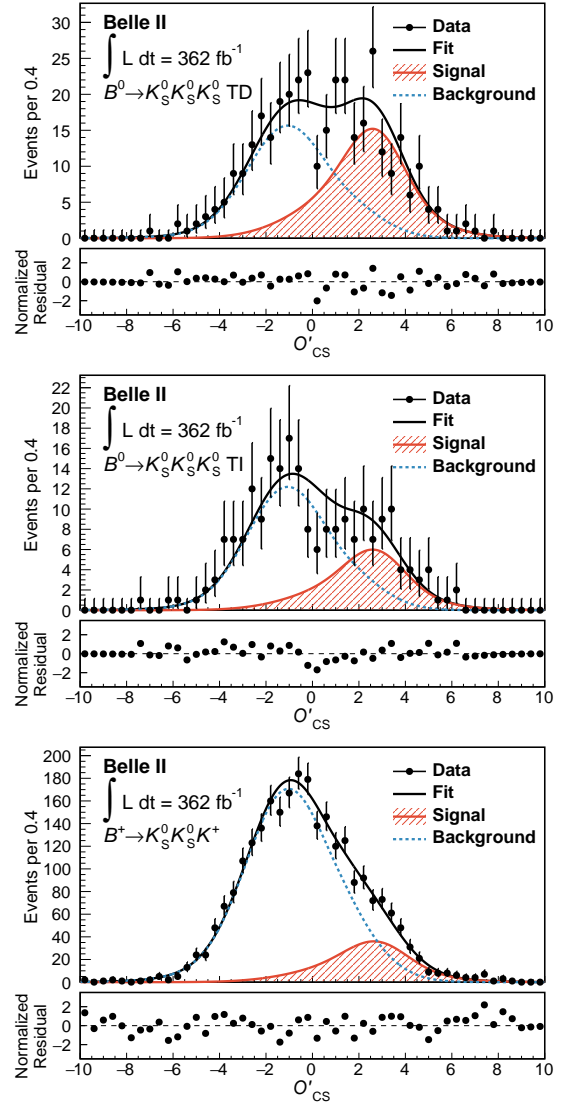


Figure 3. Distributions of O'_{CS} for (top) TD, (middle) TI, and (bottom) $B^+ \rightarrow K_S^0 K_S^0 K^+$ candidates with fit projections overlaid. The black dots with error bars represent the data points; the black, solid curve shows the total fit projection; the red hatched area is the signal projection; and the blue, dashed curve is the background projection. The distributions are restricted to events in the M_{bc} signal region. Lower panels show the differences between data and fit results normalized by the statistical uncertainty of the data.

by-event basis. The resolution-function parameters are fixed to those obtained from a fit to simulated signal events, but the width in simulation is scaled by a parameter s_{det} that accounts for data-simulation differences and that is determined simultaneously with S and C . The distribution \mathcal{P}_{bkg} is the sum of two Gaussian functions that depend on vertex quality and vertex-position uncertainty. The \mathcal{P}_{bkg} parameters are determined by a fit to the M_{bc} sideband data. We calculate the signal probability on an event-by-event basis using the five-dimensional

PDF of M_{bc} , $M(K_S^0 K_S^0 K)$, O'_{CS} , r , and $\cos \theta_B^*$. The PDF contains signal and background components, whose fractions are determined by the signal and background yields. No correlation is assumed between the variables. The last two variables are included to avoid fit biases (0.03 for S and 0.02 for C) due to implicitly assuming equal distributions that differ across sample components [33]. The r distribution for background is obtained from the $M_{bc} < 5.265 \text{ GeV}/c^2$ sideband. For $\cos \theta_B^*$, we assume a uniform distribution for background and $\frac{3}{4}(1 - \cos^2 \theta_B^*)$ for signal. For TI events, we use the likelihood in Eq. (4) integrated over Δt ,

$$\mathcal{L}_i^{\text{TI}}(C|q_{f,i}) = f_i^{\text{sig}} \mathcal{P}_{\text{sig}}^{\text{TI}}(q_{f,i}) + \frac{1 - f_i^{\text{sig}}}{2}. \quad (5)$$

We include the $B^+ \rightarrow K_S^0 K_S^0 K^+$ decays in the fit using the likelihood in Eq. (4) summed over q_f and using the B^+ lifetime instead of the B^0 lifetime. The control channel helps to constrain s_{det} since its signal yield is 2.5 times larger than the TD signal. The resolution-function parameters and s_{det} are the same as those of the $B^0 \rightarrow K_S^0 K_S^0 K_S^0$ events except for the parameters that model the effect of secondary particles. They differ since, compared to B^0 mesons, B^+ mesons yield fewer D^- mesons and more \bar{D}^0 mesons, which have shorter lifetimes. We define the background Δt distribution for $B^+ \rightarrow K_S^0 K_S^0 K^+$ with an independent parameter set from $B^0 \rightarrow K_S^0 K_S^0 K_S^0$ and with an additional Gaussian function.

Figure 4 shows the background-subtracted Δt distributions using the s Plot technique [34] and their asymmetry with fit projections overlaid. We obtain $S = -1.37^{+0.32}_{-0.26}$, $C = -0.07 \pm 0.17$, and $s_{\text{det}} = 1.16 \pm 0.15$. Linear correlation coefficients are -0.02 between S and C , -0.16 between S and s_{det} , and -0.07 between C and s_{det} . However, simulation studies show that the above point estimates are not reliable. While the likelihood has no secondary maxima, the small sample size leads to biases and non-Gaussian uncertainties. For more reliable results, we construct confidence intervals for the CP -violating parameters as described in Sec. VIII.

VII. SYSTEMATIC UNCERTAINTIES

We consider various sources of systematic uncertainties, which are listed in Table I. To evaluate the systematic uncertainties in S and C related to assumptions made on parameters of the fit model, we repeat the fit on data using alternative values of the parameters sampled from Gaussian distributions based on their uncertainties. The widths of the resulting distributions of S and C are taken as contributions to the systematic uncertainty. This approach is used for τ_{B^0} , τ_{B^+} , and Δm_d ; the parameters of the M_{bc} , $M(K_S^0 K_S^0 K)$, and O'_{CS} shapes (referred to as signal modeling in the table); the parameters describing the resolution function; the parameters

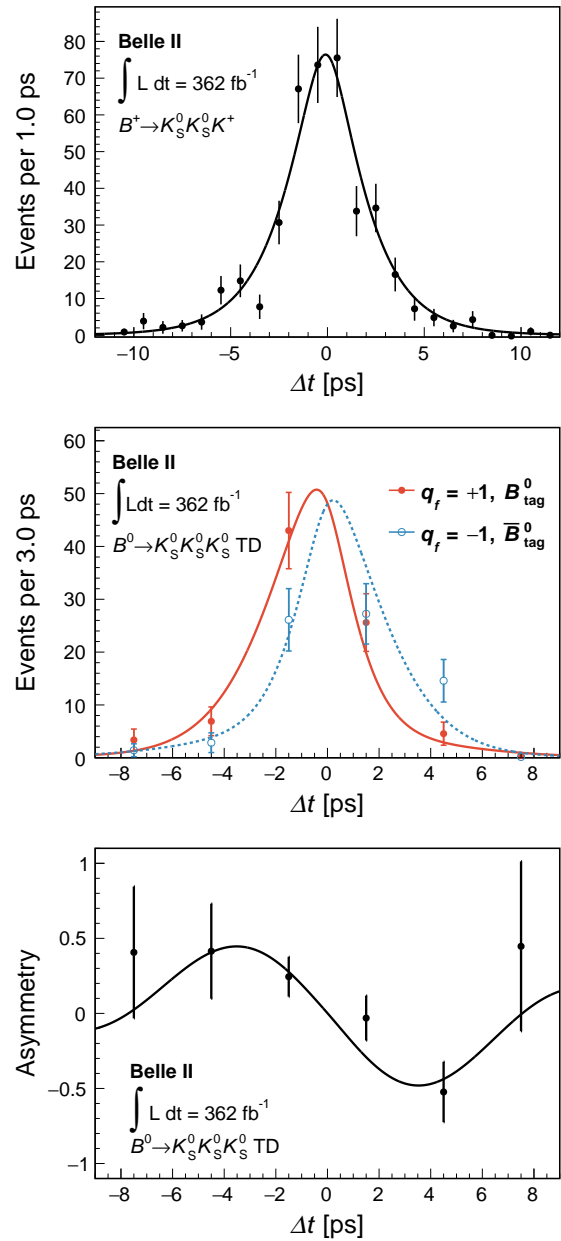


Figure 4. Background-subtracted Δt distributions for (top) $B^+ \rightarrow K_S^0 K_S^0 K^+$ candidates and (middle) $B^0 \rightarrow K_S^0 K_S^0 K_S^0$ TD candidates separated for $q_f = \pm 1$ along with (bottom) the resulting B_{tag}^0 minus \bar{B}_{tag}^0 yield-asymmetry as a function of Δt . Points with error bars represent data and the curves show the fit results. Red, filled circles and solid curves show the data for $q_f = +1$ and fit results, respectively, while blue, open circles and dashed curves are for $q_f = -1$.

for the background Δt shape; and the parameters related to flavor tagging.

We sample the world averages of the B^0 and B^+ lifetimes and Δm_d including their uncertainties [1]. The parameters of signal probability, resolution function, and background Δt shape have uncertainties from the fits

Table I. Systematic uncertainties

Source	S	C
τ_{B^0} , τ_{B^+} , and Δm_d	0.009	0.000
Signal modeling	0.014	0.008
Δt resolution function	0.013	0.008
Background Δt modeling	0.004	0.002
Flavor tagging	0.013	0.012
Fit bias	0.014	0.004
Tag-side interference	0.011	0.006
Vertex reconstruction	0.011	0.004
Tracker misalignment	0.008	0.007
Total	0.032	0.020

used to determine them, which depend on the size of data and simulated samples. The systematic uncertainty in the resolution function includes the uncertainty due to the choice of the model, which is determined by analyzing a simulated sample with alternative resolution models whose dependence on the vertex-fit quality is partly or entirely removed. The simulation assumes $S = -0.7$ and $C = 0$. The systematic uncertainty due to flavor tagging includes the bias due to the flavor asymmetry in the tagging efficiency between B^0 and \bar{B}^0 . Two sets of simplified simulated experiments are generated, with and without the asymmetry, and fits for S and C are performed in both ignoring the asymmetry. The difference between the mean values of S and C obtained in the two sets is the uncertainty. We repeat the simplified simulation assuming various input CP asymmetries and take the maximum difference. We observe correlations between $M(K_s^0 K_s^0 K)$ and vertex-fit quality for B_{CP} (-0.06 for TD events), and between O'_{CS} and r (0.15), which are not included in the default model. To evaluate the bias due to these correlations, and to a mismodeling of the $\cos\theta_B^*$ distribution, we use simplified simulated samples generated with and without these effects in the same way as above. The CP asymmetries are affected by the interference between a CKM-favored transition $\bar{b} \rightarrow \bar{c}u\bar{d}$ and a doubly CKM-suppressed transition $b \rightarrow u\bar{c}d$ on the tag side [35]. We assign as a systematic uncertainty the effect of the tag-side interference assuming the world average values $S = -0.83$ and $C = -0.15$ [11]. The systematic uncertainty due to the vertex reconstruction is determined by varying the parameters describing the IP profile and boost vector, the track requirements used in the B_{tag} vertex reconstruction, and the criteria to select TD events, and repeating the fit on data. To evaluate the effect from possible misalignment of the vertex detector, we use four simulated samples, each assuming a different misalignment configuration and CP asymmetries of $S = -1.0$ and $C = 0$. We compare the resulting CP asymmetries with those in the sample without misalignment and the maximum deviation is taken as the systematic uncertainty.

VIII. RESULTS AND SUMMARY

Since the point estimates from the fit are not reliable, we construct confidence intervals for our results based on likelihood-ratio ordering [36]. For the construction, simplified simulated experiments are generated by sampling the likelihoods of the yield fit and asymmetry fit. The nuisance parameters in the models are fixed to the values fitted to the data and the systematic uncertainty is not taken into account as its size is negligible. Figure 5 shows the resulting two-dimensional confidence intervals where S and C are constrained within their physical boundary, $S^2 + C^2 \leq 1$. The two-dimensional intervals are $-1 < S < -0.72$ and $-0.29 < C < 0.14$ at the 68.3% confidence level, $-1 < S < -0.41$ and $-0.45 < C < 0.32$ at the 95.5% confidence level, and $-1 < S < -0.09$ and $-0.61 < C < 0.49$ at the 99.7% confidence level. The results are consistent with the SM predictions and current best determinations by the Belle and BaBar experiments [9–11].

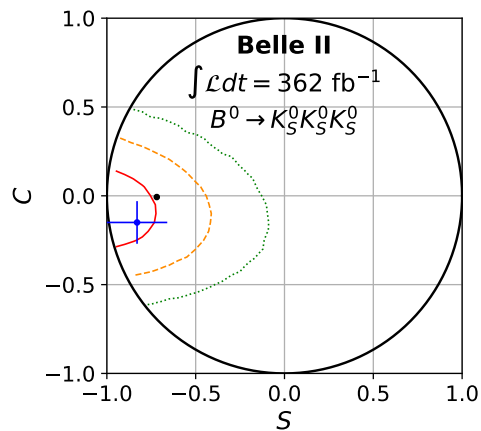


Figure 5. Two-dimensional confidence intervals for S and C based on likelihood-ratio ordering. The red solid, orange dashed, and green dotted contours represent the 68.27%, 95.45%, and 99.73% confidence intervals for S and C given the physical constraint $S^2 + C^2 \leq 1$. The blue dot with the error bar is the average value based on results by Belle and BaBar [9, 10]. The black dot represents the SM prediction $(S, C) = (-\sin 2\phi_1 - 0.02, -0.007)$ based on measurements in $B^0 \rightarrow (c\bar{c})K^0$ decays [11].

In summary, we report a measurement of decay-time dependent CP asymmetries in $B^0 \rightarrow K_s^0 K_s^0 K_s^0$ decays using a data set of $387 \times 10^6 B\bar{B}$ pairs reconstructed from electron-positron collisions at the $\Upsilon(4S)$ and collected with Belle II experiment from 2019 to 2022. We reconstruct 220 signal events and extract the CP -violating parameters from a fit to the distribution of the decay-time difference of the two B mesons. We determine a two-dimensional confidence region for the relevant parameters S and C obtaining results that are consistent with the SM predictions and previous determinations.

This work, based on data collected using the Belle II detector, which was built and commissioned prior to March 2019, was supported by Higher Education and Science Committee of the Republic of Armenia Grant No. 23LCG-1C011; Australian Research Council and Research Grants No. DP200101792, No. DP210101900, No. DP210102831, No. DE220100462, No. LE210100098, and No. LE230100085; Austrian Federal Ministry of Education, Science and Research, Austrian Science Fund No. P 31361-N36 and No. J4625-N, and Horizon 2020 ERC Starting Grant No. 947006 “InterLeptons”; Natural Sciences and Engineering Research Council of Canada, Compute Canada and CANARIE; National Key R&D Program of China under Contract No. 2022YFA1601903, National Natural Science Foundation of China and Research Grants No. 11575017, No. 11761141009, No. 11705209, No. 11975076, No. 12135005, No. 12150004, No. 12161141008, and No. 12175041, and Shandong Provincial Natural Science Foundation Project ZR2022JQ02; the Czech Science Foundation Grant No. 22-18469S; European Research Council, Seventh Framework PIF-GA-2013-622527, Horizon 2020 ERC-Advanced Grants No. 267104 and No. 884719, Horizon 2020 ERC-Consolidator Grant No. 819127, Horizon 2020 Marie Skłodowska-Curie Grant Agreement No. 700525 “NIOBE” and No. 101026516, and Horizon 2020 Marie Skłodowska-Curie RISE project JENNIFER2 Grant Agreement No. 822070 (European grants); L’Institut National de Physique Nucléaire et de Physique des Particules (IN2P3) du CNRS and L’Agence Nationale de la Recherche (ANR) under grant ANR-21-CE31-0009 (France); BMBF, DFG, HGF, MPG, and AvH Foundation (Germany); Department of Atomic Energy under Project Identification No. RTI 4002, Department of Science and Technology, and UPES SEED funding programs No. UPES/R&D-SEED-INFRA/17052023/01 and No. UPES/R&D-SOE/20062022/06 (India); Israel Science Foundation Grant No. 2476/17, U.S.-Israel Binational Science Foundation Grant No. 2016113, and Israel Ministry of Science Grant No. 3-16543; Istituto Nazionale di Fisica Nucleare and the Research Grants BELLE2; Japan Society for the Promotion of Science, Grant-in-Aid for Scientific Research Grants No. 16H03968, No. 16H03993, No. 16H06492, No. 16K05323, No. 17H01133, No. 17H05405, No. 18K03621, No. 18H03710, No. 18H05226, No. 19H00682, No. 20H05850, No. 20H05858, No. 22H00144, No. 22K14056, No. 22K21347, No. 23H05433, No. 26220706, and No. 26400255, the National Institute of Informatics, and Science Information NETwork 5 (SINET5), and the Ministry of Education, Culture, Sports, Science, and Technology (MEXT) of Japan; National Research Foundation

(NRF) of Korea Grants No. 2016R1D1A1B02012900, No. 2018R1A2B3003643, No. 2018R1A6A1A06024970, No. 2019R1I1A3A01058933, No. 2021R1A6A1A-03043957, No. 2021R1F1A1060423, No. 2021R1F1A-1064008, No. 2022R1A2C1003993, and No. RS-2022-00197659, Radiation Science Research Institute, Foreign Large-Size Research Facility Application Supporting project, the Global Science Experimental Data Hub Center of the Korea Institute of Science and Technology Information and KREONET/GLORIAD; Universiti Malaya RU grant, Akademi Sains Malaysia, and Ministry of Education Malaysia; Frontiers of Science Program Contracts No. FOINS-296, No. CB-221329, No. CB-236394, No. CB-254409, and No. CB-180023, and SEP-CINVESTAV Research Grant No. 237 (Mexico); the Polish Ministry of Science and Higher Education and the National Science Center; the Ministry of Science and Higher Education of the Russian Federation and the HSE University Basic Research Program, Moscow; University of Tabuk Research Grants No. S-0256-1438 and No. S-0280-1439 (Saudi Arabia); Slovenian Research Agency and Research Grants No. J1-9124 and No. P1-0135; Agencia Estatal de Investigación, Spain Grant No. RYC2020-029875-I and Generalitat Valenciana, Spain Grant No. CIDEGENT/2018/020; National Science and Technology Council, and Ministry of Education (Taiwan); Thailand Center of Excellence in Physics; TUBITAK ULAKBIM (Turkey); National Research Foundation of Ukraine, Project No. 2020.02/0257, and Ministry of Education and Science of Ukraine; the U.S. National Science Foundation and Research Grants No. PHY-1913789 and No. PHY-2111604, and the U.S. Department of Energy and Research Awards No. DE-AC06-76RLO1830, No. DE-SC0007983, No. DE-SC0009824, No. DE-SC0009973, No. DE-SC0010007, No. DE-SC0010073, No. DE-SC0010118, No. DE-SC0010504, No. DE-SC0011784, No. DE-SC0012704, No. DE-SC0019230, No. DE-SC0021274, No. DE-SC0021616, No. DE-SC0022350, No. DE-SC0023470; and the Vietnam Academy of Science and Technology (VAST) under Grants No. NVCC.05.12/22-23 and No. DL0000.02/24-25.

These acknowledgements are not to be interpreted as an endorsement of any statement made by any of our institutes, funding agencies, governments, or their representatives.

We thank the SuperKEKB team for delivering high-luminosity collisions; the KEK cryogenics group for the efficient operation of the detector solenoid magnet; the KEK computer group and the NII for on-site computing support and SINET6 network support; and the raw-data centers at BNL, DESY, GridKa, IN2P3, INFN, and the University of Victoria for off-site computing support.

[1] R. L. Workman *et al.* (Particle Data Group), PTEP **2022**, 083C01 (2022).

[2] Y. Grossman and M. P. Worah, Phys. Lett. B **395**, 241

- (1997), arXiv:hep-ph/9612269.
- [3] M. Kobayashi and T. Maskawa, *Prog. Theor. Phys.* **49**, 652 (1973).
- [4] A. B. Carter and A. I. Sanda, *Phys. Rev. Lett.* **45**, 952 (1980).
- [5] A. B. Carter and A. I. Sanda, *Phys. Rev. D* **23**, 1567 (1981).
- [6] I. I. Y. Bigi and A. I. Sanda, *Nucl. Phys. B* **193**, 85 (1981).
- [7] The coefficients (S, C) are written ($S, -A$) elsewhere.
- [8] H. Y. Cheng, C. K. Chua, and A. Soni, *Phys. Rev. D* **72**, 094003 (2005), arXiv:hep-ph/0506268.
- [9] K. H. Kang *et al.* (Belle Collaboration), *Phys. Rev. D* **103**, 032003 (2021), arXiv:2011.00793 [hep-ex].
- [10] J. P. Lees *et al.* (BaBar Collaboration), *Phys. Rev. D* **85**, 054023 (2012), arXiv:1111.3636 [hep-ex].
- [11] Y. S. Amhis *et al.* (HFLAV Collaboration), *Phys. Rev. D* **107**, 052008 (2023), arXiv:2206.07501 [hep-ex].
- [12] K. Akai, K. Furukawa, and H. Koiso (SuperKEKB), *Nucl. Instrum. Meth. A* **907**, 188 (2018), arXiv:1809.01958 [physics.acc-ph].
- [13] T. Abe *et al.* (Belle II Collaboration), (2010), arXiv:1011.0352 [physics.ins-det].
- [14] K. Adamczyk *et al.* (Belle II SVD Collaboration), *JINST* **17**, P11042 (2022), arXiv:2201.09824 [physics.ins-det].
- [15] D. Kotchetkov *et al.*, *Nucl. Instrum. Meth. A* **941**, 162342 (2019), arXiv:1804.10782 [physics.ins-det].
- [16] D. J. Lange, *Proceedings, 7th International Conference on B physics at hadron machines (BEAUTY 2000): Maagan, Israel, September 13-18, 2000*, *Nucl. Instrum. Meth. A* **462**, 152 (2001).
- [17] T. Sjöstrand, S. Ask, J. R. Christiansen, R. Corke, N. Desai, P. Ilten, S. Mrenna, S. Prestel, C. O. Rasmussen, and P. Z. Skands, *Comput. Phys. Commun.* **191**, 159 (2015), arXiv:1410.3012 [hep-ph].
- [18] S. Jadach, B. F. L. Ward, and Z. Was, *Comput. Phys. Commun.* **130**, 260 (2000), arXiv:hep-ph/9912214 [hep-ph].
- [19] S. Agostinelli *et al.*, *Nucl. Instrum. Meth. A* **506**, 250 (2003).
- [20] T. Kuhr, C. Pulvermacher, M. Ritter, T. Hauth, and N. Braun (Belle II Framework Software Group), *Comput. Softw. Big Sci.* **3**, 1 (2019), arXiv:1809.04299 [physics.comp-ph].
- [21] Belle II Collaboration, “Belle ii analysis software framework (basf2),” Zenodo.
- [22] S. H. Lee *et al.* (Belle Collaboration), *Phys. Rev. Lett.* **91**, 261801 (2003), arXiv:hep-ex/0308040.
- [23] F. Abudinén *et al.* (Belle II Collaboration), *Eur. Phys. J. C* **82**, 283 (2022), arXiv:2110.00790 [hep-ex].
- [24] I. Adachi *et al.* (Belle II Collaboration), (2023), The calibration described in this note has been updated with the larger dataset used in the present analysis., arXiv:2302.12898 [hep-ex].
- [25] F. J. Abudinen *et al.* (Belle II Collaboration), *Phys. Rev. D* **107**, L031103 (2023), arXiv:2208.08573 [hep-ex].
- [26] J. F. Krohn *et al.* (Belle II Analysis Software Group), *Nucl. Instrum. Meth. A* **976**, 164269 (2020), arXiv:1901.11198 [hep-ex].
- [27] S. Dey and A. Soffer, *Springer Proc. Phys.* **248**, 411 (2020).
- [28] J. Gaiser, *Charmonium Spectroscopy from Radiative Decays of the J/ψ and ψ'* , Ph.D. thesis, Stanford University (1982).
- [29] T. Skwarnicki, *A study of the radiative CASCADE transitions between the Upsilon-Prime and Upsilon resonances*, Ph.D. thesis, Cracow, INP (1986).
- [30] H. Albrecht *et al.* (ARGUS Collaboration), *Phys. Lett. B* **241**, 278 (1990).
- [31] F. James and M. Roos, *Comput. Phys. Commun.* **10**, 343 (1975).
- [32] H. Tajima *et al.*, *Nucl. Instrum. Meth. A* **533**, 370 (2004), arXiv:hep-ex/0301026.
- [33] G. Punzi, eConf **C030908**, WELT002 (2003), arXiv:physics/0401045.
- [34] M. Pivk and F. R. Le Diberder, *Nucl. Instrum. Meth. A* **555**, 356 (2005), arXiv:physics/0402083.
- [35] O. Long, M. Baak, R. N. Cahn, and D. P. Kirkby, *Phys. Rev. D* **68**, 034010 (2003), arXiv:hep-ex/0303030.
- [36] G. J. Feldman and R. D. Cousins, *Phys. Rev. D* **57**, 3873 (1998), arXiv:physics/9711021.

Two-particle angular correlations of identified particles in pp and p–Pb collisions at LHC energies with ALICE

DANIELA RUGGIANO

Warsaw University of Technology – Warsaw, Poland

Summary. — The two-particle angular correlations in the $\Delta y, \Delta\varphi$ space provide valuable insights into the properties of hadronization mechanisms and quark–gluon plasma properties. The correlation functions are influenced by several physical sources, including mini-jet correlations, Bose–Einstein quantum statistics, resonance decays, conservation of energy and momentum, and other factors. Each correlation source has unique properties, and therefore each correlation function has a distinct form depending on transverse momentum and/or multiplicity. Previous results from angular correlation analysis of pp collisions at the LHC energies indicate an anti-correlation for pairs of baryons of the same sign in $\Delta\eta, \Delta\varphi$ space. This contradicts the predictions of Monte Carlo models, such as PYTHIA8 and EPOS.

This study aims to investigate this behavior by exploring the correlation functions of different charge combinations of the detected particles (specifically, π^\pm , K^\pm , and $p\bar{p}$) and multiplicity classes in the $\Delta y, \Delta\varphi$ space for pp and p–Pb collisions at LHC energies. In addition, the study includes a comparison of the results obtained from both collision systems.

1. – Introduction

The lack of a clear understanding of the production processes of one of the most abundant and fundamental particles in the universe, the proton, is one of the open and unresolved questions in the field of nuclear physics. Angular correlations are a powerful tool used to describe the mechanism of particle production in high-energy heavy-ion collisions. They are influenced by multiple effects such as (mini)jets, Bose–Einstein or Fermi–Dirac quantum statistics (in the case of identical bosons or fermions), resonance decays, Coulomb interactions, conservation of energy and momentum, and others, all of which contribute with some structure to the overall shape. Moreover, each correlation shows a unique behavior with its shape, and its individuality, as already observed in studies of proton–proton (pp) collisions at $\sqrt{s} = 7$ TeV by the ALICE Collaboration at LHC [1]. In particular, correlations of baryon–baryon pairs (combined with antibaryon–

antibaryon pairs) in pp collisions exhibit a depletion, i.e., an anticorrelation, around $(\Delta\eta, \Delta\varphi) \sim (0, 0)$. The origin of this phenomenon is still unclear. Several studies have been conducted on it, becoming a puzzle for many researchers [1, 2]. These studies have been extended to different baryons to investigate the shape of the correlation functions, which are related to the intrinsic nature of baryon production. None of the observed baryon–baryon correlations agree even qualitatively with the theoretical Monte Carlo models [1, 3]. In this work, which is an extension of the analysis of the pp collision at $\sqrt{s} = 13$ TeV [3], another piece is proposed to be added to the puzzle. The study concerns the analysis of correlation functions in four different multiplicity classes in $\Delta y, \Delta\varphi$ in the proton–nucleus (p–Pb) collision at $\sqrt{s_{NN}} = 5.02$ TeV. The results will be compared with the corresponding ones from pp collisions.

2. – Definition of two-particle correlation function

In Ref.[1] the results were obtained using the so-called probability-ratio definition of the correlation function [4], which experimentally is constructed as follows

$$(1) \quad C_P(\Delta y \Delta \varphi) = \frac{N_{pairs}^{mixed} S(\Delta y \Delta \varphi)}{N_{pairs}^{signal} B(\Delta y \Delta \varphi)},$$

where $S(\Delta y \Delta \varphi)$ is the signal distribution and $B(\Delta y \Delta \varphi)$ is the background distribution. The signal distribution consists of pairs of particles from the same events, whereas the background distribution consists of pairs of particles from different events. It is normalized by the ratio of the number of pairs from the background and signal distributions. This definition has some limitations for studying correlations over different multiplicity classes due to the normalization factor that produces a trivial scaling of $1/N$, where N is the number of particles per collision [3]. This makes the comparison of different collision systems difficult because they are characterized by a large difference in multiplicity. To avoid this issue, the rescaled two-particle cumulant definition is used for the first time in ALICE [5]. This new correlation function is defined as

$$(2) \quad C_C(\Delta y \Delta \varphi) = \frac{N_{av}}{\Delta y \Delta \varphi} (C_P - 1).$$

where N_{av} is the average number of particles produced in the analyzed multiplicity classes.

3. – Analysis details

The analysis is based on data recorded by the ALICE detector in p–Pb collisions at $\sqrt{s_{NN}} = 5.02$ TeV in 2016. To make the results of the two collision systems comparable, the same event and track selection criteria were used in both analyses [3]. The angular correlation functions of the pairs of pions, kaons, and protons with the same and opposite

sign were analyzed for four multiplicity classes corresponding to 0–20% (highest multiplicities), 20–40%, 40–70%, and 70–100% (lowest multiplicities) of the total interaction cross-section. The data sample consists of $\sim 9.05 \cdot 10^8$ minimum bias events [7]. The angular acceptance for this analysis is $|y| < 0.5$ covering the full azimuthal angle. The analysis is based on reconstructed tracks in the following transverse momentum ranges: $0.2 < p_T < 2.5$ GeV/ c for pions and $0.5 < p_T < 2.5$ GeV/ c for kaons and protons. Particle identification (PID) of pions, kaons, and protons is performed track by track using information from the TPC and TOF detectors [6]. It is based on N_σ method, where N_σ is the number of standard deviations of the Gaussian distribution around the theoretical signal. For $p_T < 0.5$ GeV/ c , only the TPC information is used.

4. – Results

4.1. Correlation functions in p-Pb. – Figures 1 and 2 show the correlation functions for pion, kaon, and proton pairs measured in the p-Pb collisions at $\sqrt{s_{NN}} = 5.02$ TeV using the probability-ratio definition and the rescaled two-particle cumulants in the four multiplicity classes, respectively. Using the definition of probability ratio, the correlation functions are a convolution of physical phenomena plus the trivial scaling over different multiplicity classes. Indeed, there is an increase toward lower multiplicity classes due

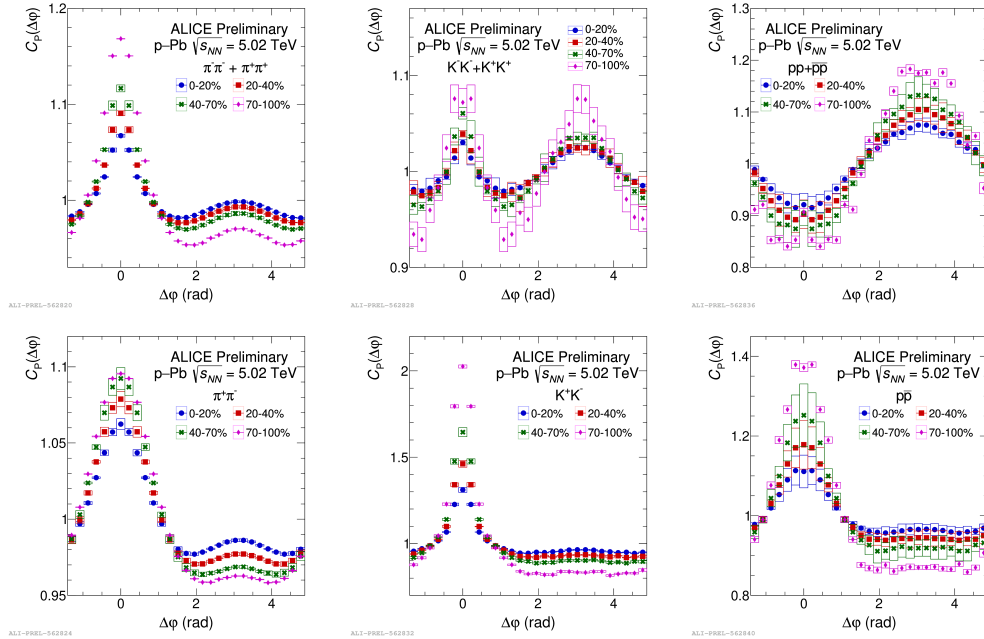


Fig. 1. – The $\Delta\varphi$ projection of correlation functions using the probability ratio definition in p-Pb collisions at $\sqrt{s_{NN}} = 5.02$ TeV for four multiplicity classes. Particles with like signs are depicted on the top panels, while those with unlike signs are shown on the bottom panels.

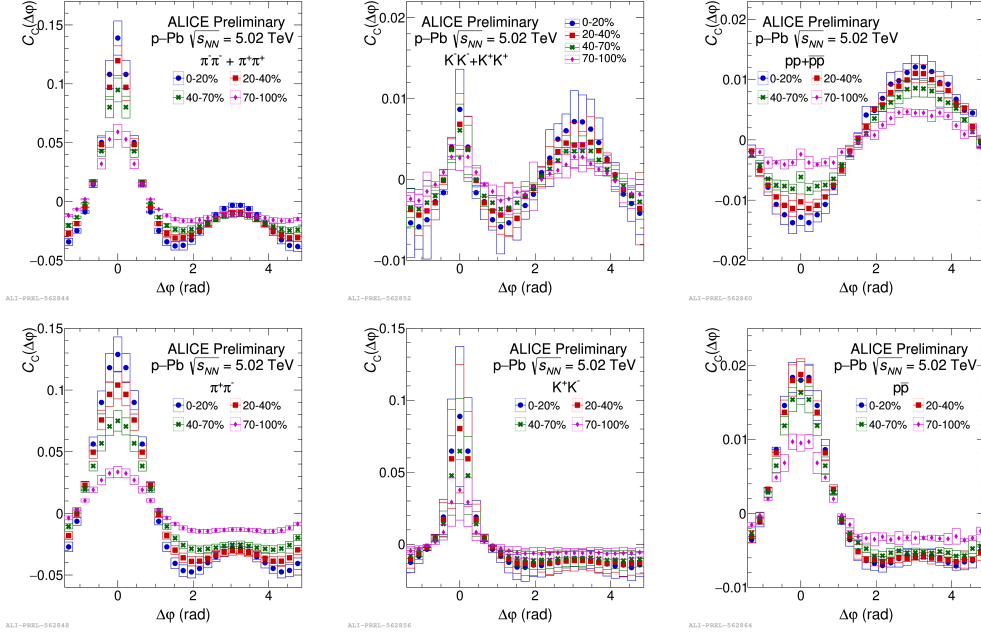


Fig. 2. – The $\Delta\varphi$ projection of correlation functions using the rescaled two-particle cumulant definition in p–Pb collisions at $\sqrt{s_{NN}} = 5.02$ TeV for four multiplicity classes. Particles with like signs are depicted in the top panels, while those with unlike signs are shown on the bottom panels.

to the $1/N$ scaling. In contrast, the rescaled two-particle cumulant shows an opposite trend, that is, an increase in the correlation function with higher multiplicity. Therefore, by removing the $1/N$ factor, it is possible to make a more detailed study of the various physical phenomena that define the correlation functions.

4.2. Comparison of $\Delta y, \Delta\varphi$ correlation functions between pp and p–Pb. – The results obtained in pp collisions [3] are compared with those for p–Pb collisions using the definition of rescaled two-particle cumulant in Fig. 3. In p–Pb collisions, the correlation functions are stronger than in pp collisions due to the higher multiplicities, which is also evident in the baryon–baryon correlations, where an anticorrelation is observed. In the case of proton–antiproton correlation, it is observed that for the highest multiplicity class (0–20%) the correlation function for pp collisions appears to be stronger than that observed in p–Pb collisions. This is due to the annihilation phenomenon visible in the correlation function represented by the dashed black line, which shows an anti-peak at $\Delta\varphi = 0$. This physical effect has been studied previously using the femtoscopy method with Monte Carlo simulations of PYTHIA 8 from pp collisions at $\sqrt{s} = 13$ TeV [9]. The observed depletion due to the strong interaction is qualitatively in agreement with experimental observations of the STAR Collaboration in Au–Au collisions and model comparisons, which confirm that the anticorrelation in $p\bar{p}$ is caused by the annihila-

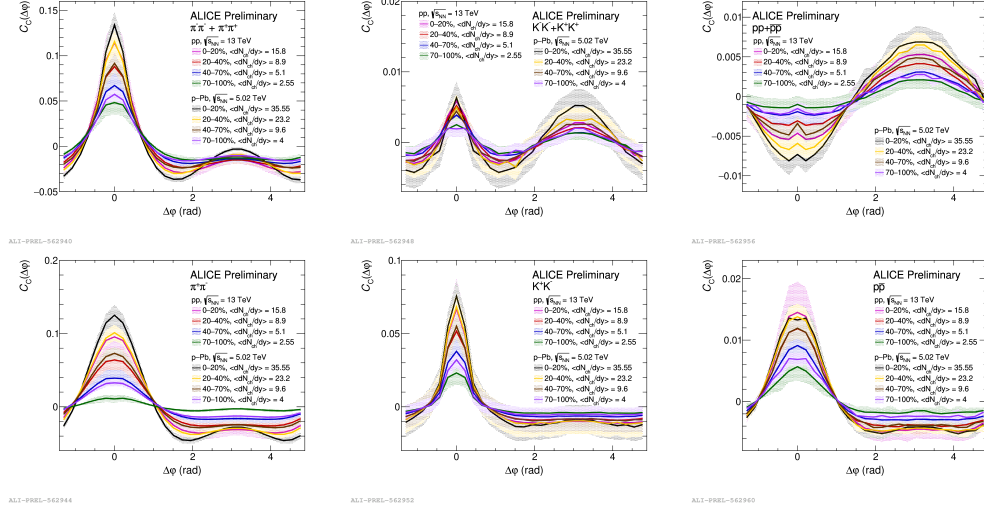


Fig. 3. – Multiplicity dependence of the correlation functions measured using the rescaled two-particle cumulant from pp collisions at $\sqrt{s} = 13$ TeV and p-Pb collisions at $\sqrt{s_{NN}} = 5.02$ TeV.

tion phenomenon [8]. It is therefore difficult to make a comparison with the correlation function in pp collisions in the 0–20% multiplicity class.

4.3. Multiplicity comparison between pp and p-Pb. – The $dN_{ch}/d\eta$ values for all multiplicity classes in pp and p-Pb collisions included in this analysis are taken from Refs. [10, 11] and are listed in Tab. I.

$dN_{ch}/d\eta$	pp	p-Pb
0-20%	15.8	35.55
20-40%	8.9	23.2
40-70%	5.1	9.6
70-100%	2.55	4

TABLE I. – The $dN_{ch}/d\eta$ values for the investigated multiplicity classes in pp and p-Pb collisions.

Based on these values, a rigorous comparison of the correlation functions is made between the closest multiplicities, i.e., 20–40% for pp and 40–70% for p-Pb. A good agreement between the two correlation functions is observed. This reveals the genuine behavior of correlations, as the rescaled two-particle cumulant eliminates the $1/N$ scaling. Although the comparison between the two systems is not a perfect match, since the values of $dN_{ch}/d\eta$ are not perfectly equal, they agree within the experimental uncertainties.

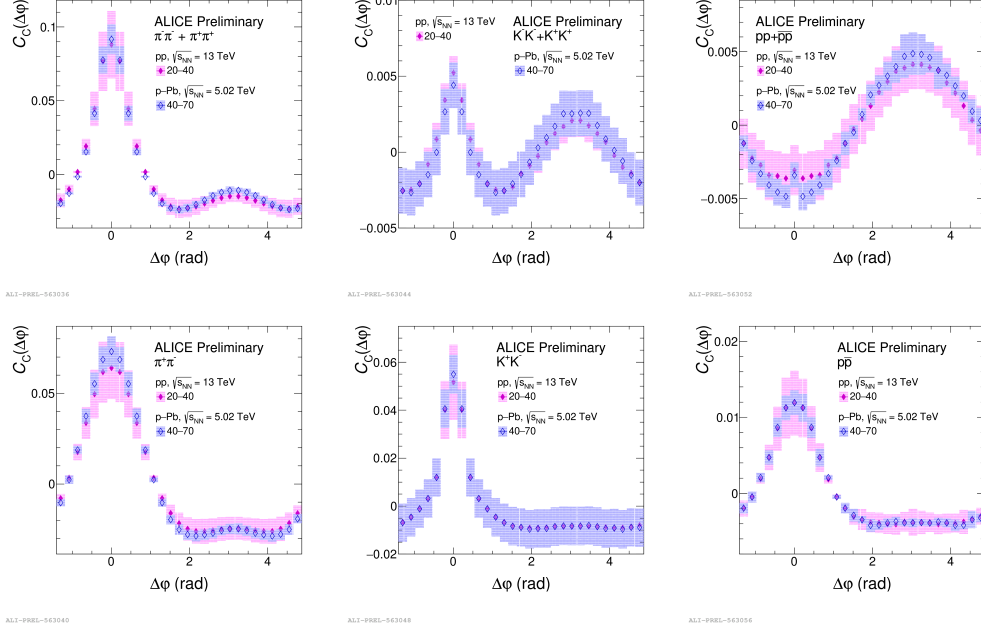


Fig. 4. – The comparison of the correlation functions between pp at $\sqrt{s} = 13$ TeV and p-Pb at $\sqrt{s_{NN}} = 5.02$ TeV for the similar multiplicity classes using the rescaled two-particle cumulant definition.

5. – Conclusion

This analysis concerns the two-particle angular correlation in $\Delta y, \Delta\varphi$ space for pp and p-Pb collisions at the LHC energies using alternative definitions, i.e., the probability ratio and the rescaled two-particle cumulant. The results reveal that the correlation functions obtained using the latter, increase with the multiplicity. Furthermore, the implementation of the following definition allows us to explore in depth the physical phenomena that contribute to the overall shape of the correlation functions by eliminating the trivial scaling of $1/N$. When comparing the results between the two collision systems, a multiplicity dependence is observed where the number of correlated particles grows very fast compared with those of the underlying event. The anticorrelation between proton pairs is still present and becomes stronger at high multiplicities. The comparison of the correlation function with the rescaled two-particle cumulant definition in the pp and p-Pb systems shows good agreement within the experimental uncertainties for the closest multiplicity classes.

6. – Acknowledgments

This work was supported by the Polish National Science Centre under agreements [UMO-2021/43/D/ST2/02214](#) and [UMO-2022/45/B/ST2/02029](#), by the Polish Ministry for Education and Science under agreements no. [2022/WK/01](#) and [5236/CERN/2022/0](#), as well as by the [IDUB-POB-FWEiTE-3](#) project granted by Warsaw University of Technology under the program Excellence Initiative: Research University (ID-UB).

7. – References

- [1] ALICE COLLABORATION, *The European Physical Journal C*, **77** (2017) 569;
- [2] STAR COLLABORATION, *Physical Review C*, **101** (2020) 014916;
- [3] RUGGIANO D., *arXiv*, **2023** (2311.09833) ;
- [4] KISIEL A., *Phys. Rev. C*, **81** (2010) 064906;
- [5] STAR COLLABORATION, *Phys. Rev. C*, **86** (2012) 064902;
- [6] ALICE COLLABORATION, *Journal of Instrumentation*, **3** (2008) S08002;
- [7] KRIVDA M. ET AL., *Journal of Instrumentation*, **7** (2012) C01057;
- [8] STAR COLLABORATION, *Phys. Rev. C*, **101** (2020) 014916;
- [9] GRACZYKOWSKI, Ł. AND JANIK, M., *Phys. Rev. C*, **104** (2021) 054909;
- [10] ALICE COLLABORATION, *The European Physical Journal C*, **80** (2020) 1434-6052;
- [11] ALICE COLLABORATION, *Physics Letters B*, **728** (2015) 0370-2693;



The quest to discover supersymmetry at the ATLAS experiment

The ATLAS Collaboration

The search for supersymmetry with the ATLAS experiment at the CERN Large Hadron Collider intensified after the discovery of the Higgs boson in 2012. The search programme expanded in both breadth and depth, profiting from the increased integrated luminosity and higher centre-of-mass energy of Run 2, and gaining new sensitivity to unexplored areas of supersymmetry parameter space through the use of new experimental signatures and innovative analysis techniques. This report summarises the supersymmetry searches at ATLAS using up to 140 fb^{-1} of pp collisions at $\sqrt{s} = 13 \text{ TeV}$, including the limits set on the production of gluinos, squarks, and electroweakinos for scenarios either with or without R-parity conservation, and including models where some of the supersymmetric particles are long-lived.

Contents

1	Introduction	2
2	Supersymmetric models	4
3	The ATLAS detector	8
4	Analysis strategy	8
5	Strongly produced supersymmetric particles	10
5.1	Gluino pair production	11
5.2	Squark pair production	14
6	Weakly produced supersymmetric particles	18
6.1	Slepton pair production	18
6.2	Electroweakino pair production	20
7	R-parity-violating decays	23
8	Long-lived supersymmetric particles	26
9	Beyond simplified models	29
10	Discussion and conclusions	31

1 Introduction

One of the most significant contributions of the CERN Large Hadron Collider (LHC) [1] to high-energy physics comes through the particles that the ATLAS [2] and CMS [3] collaborations have *not* found. Both collaborations have pursued an unprecedented programme of searches for phenomena not predicted by the Standard Model (SM). The wide variety of signatures explored, and the richness of the models considered, has had a powerful influence on community's paradigms of physics beyond the Standard Model.

Among these paradigms, supersymmetry (SUSY) [4–9] is one of the most closely examined. The approach of imposing symmetries on Lagrangians led to the construction of electroweak theory, the unification of the weak and electromagnetic interaction and, eventually, the development of the Standard Model. The phenomenology of SUSY stems from requiring the Lagrangian to be invariant under an operator that maps fermionic fields into bosonic ones, and vice versa. It was found that only additional space-time symmetry could be added to the Poincaré group [5]. To impose this symmetry, one needs to add many new *superpartners* of the Standard Model particles. The much richer particle content, and some of the free parameters that one needs to add to make SUSY a broken symmetry (for example, it is known that there is no superpartner of the electron with mass $m = 0.511$ MeV), makes SUSY an ideal framework to accommodate many of the shortcomings of the Standard Model. The quantum corrections to the Higgs boson mass coming from the fermions are counterbalanced by those coming from their superpartners, stabilising the mass to a value near the electroweak scale in a natural way. On top of that, the modified particle content changes the evolution of the running gauge couplings of the SM, potentially allowing

them to converge to a common value, a necessary condition for unification of the electroweak and strong interactions. The additional particles come with new mixing parameters, potentially allowing additional sources of CP violation and thus paving the way for an explanation of the cosmological matter–antimatter asymmetry. SUSY even offers the attractive possibility of generating electroweak symmetry breaking dynamically. Finally, there may be room for one or more dark-matter candidates among the particles introduced in the model.

Because of its elegance and flexibility, SUSY has received significant theoretical and experimental attention in the past decades. The generic prediction of the existence of SUSY particles at the TeV scale created widespread expectations for experimental results from the LHC collaborations in the early 2000s. The ATLAS Collaboration rose to these expectations by developing a thorough, robust and extensive experimental effort to search for SUSY in data from Run 1, at $\sqrt{s} = 7$ and 8 TeV, and Run 2, at $\sqrt{s} = 13$ TeV. The aim of this paper is to review and summarise this monumental effort at the end of the Run 2. Section 2 gives a quick overview of the main theoretical and phenomenological aspects of supersymmetry, introducing the approach ATLAS used to explore the vast SUSY parameter space. Section 3 provides a brief description of the ATLAS detector before Section 4 discusses generic aspects related to the design of SUSY searches, the background estimation, and the statistical approach used to interpret the search results and set limits on sparticle masses, couplings, and production cross-sections.

These searches covered a large variety of experimental signatures arising from models featuring a stable weakly interacting particle (the R-parity-conserving, or RPC, models) and from models without such a potential dark-matter candidate (R-parity-violating, or RPV, models). Both types of models are described in Section 2. Sections 5 and 6 review the analyses targeting the production of SUSY particles via strong or electroweak interactions, respectively, when using RPC SUSY models: generically speaking, the common feature of these searches is the presence of missing transverse momentum $\mathbf{p}_T^{\text{miss}}$ (with magnitude E_T^{miss}) in signal events, arising from the presence of a dark-matter candidate, which goes undetected. Section 7 discusses RPV SUSY searches, where an E_T^{miss} signature is typically absent. Experimental signatures involving long-lived particles arise quite naturally in some regions of the parameter space: Section 8 focuses on the effort to target such signatures with unconventional experimental techniques.

Each of the searches discussed in these sections makes use of simplified models (discussed in Section 2) to optimise the analysis and interpret the results. While the simplified-model approach gives a direct connection to the signal topologies, it has the drawback of yielding mass limits that rarely generalise to more complex/complete SUSY models. Section 9 focuses on reinterpreting the analyses designed using simplified models in the more general phenomenological Minimal Supersymmetric Standard Model, with the aim of giving an overall picture of the actual impact of ATLAS on the supersymmetric landscape.

This paper has multiple purposes. The authors hope that it will serve as a useful introduction to the field for those wanting to take an active role in research activities connected to SUSY. At the same time, it may be a handy collection of information and references for the HEP community, either for easy access to ATLAS research on the subject or simply as an overview of the searches performed.

2 Supersymmetric models

To make the SM supersymmetric,¹ one has first to postulate the existence of an extended Higgs field sector: two complex doublets provide the minimum number of fields that can give mass to the up-type and down-type particles without spoiling gauge invariance. The next step is to introduce the supersymmetric partners of each SM field: for each fermion f (characterised by a left-handed and a right-handed component, f_L and f_R , respectively), one introduces two supersymmetric scalar fields \tilde{f}_L and \tilde{f}_R . Although the subscripts L and R have nothing to do with chirality at this point, one often refers to these scalar fields as the *left-* and *right-chiral sfermions*.² These two fields mix to yield the mass eigenstates \tilde{f}_1 and \tilde{f}_2 , with $m(\tilde{f}_1) < m(\tilde{f}_2)$ by convention. For the electroweak boson fields, one starts from 16 spin degrees of freedom before electroweak symmetry breaking (two each for the B and W massless spin-1 fields, eight corresponding to the two complex Higgs doublets). This requires the introduction of eight supersymmetric fermionic partners: one *bino*, three *winos* and four *higgsinos*. The electroweak symmetry breaking results in the usual three massive vector bosons W^\pm and Z , and the massless γ (11 degrees of freedom), plus five spin-0 bosons (h, H, A, H^\pm ; it is often assumed that the 125 GeV scalar particle is the h). The bino, winos and higgsinos mix, yielding eight fermionic mass eigenstates (the neutralinos $\tilde{\chi}_1^0 \dots \tilde{\chi}_4^0$ and the charginos $\tilde{\chi}_1^\pm$ and $\tilde{\chi}_2^\pm$, with the subscript increasing with increasing mass), corresponding to 16 degrees of freedom. Finally, the fermionic *gluino*, \tilde{g} , is introduced as a superpartner of the gluon, and in models where SUSY is broken by supergravity, the gravitino, \tilde{G} , is the fermionic superpartner of the hypothetical graviton.

The particle content of the SM is therefore more than doubled by its supersymmetrisation. Supersymmetry requires that the couplings of the SUSY partners are identical to the corresponding ones in the SM (after accounting for the extended Higgs sector). If supersymmetry were an exact symmetry of nature, then the SUSY particle masses would be equal to those of the corresponding SM partners. The absence, so far, of any observed SUSY particle implies that SUSY must be a broken symmetry. The SUSY breaking mechanism, although unknown, can modify the phenomenology and mass spectrum of the SUSY sector. For example, conventional theories of gravity-mediated SUSY breaking, ‘supergravity’ (SUGRA) theories, include massive gravitinos due to a modified Higgs mechanism. Gauge-mediated SUSY breaking (GMSB) theories usually have a nearly massless gravitino as the lightest supersymmetric particle (LSP), while anomaly-mediated SUSY breaking (AMSB) models usually feature long-lived $\tilde{\chi}_1^\pm$ decays to pure-wino $\tilde{\chi}_1^0$ LSPs. The scale at which SUSY is broken is inherently tied to the breaking mechanism, and also impacts naturalness arguments that favour light top squarks, higgsinos, and moderately light gluinos to avoid excessive tuning of the Higgs boson mass corrections. The complexity of defining the mechanism and scale of SUSY breaking is usually avoided by incorporating effective *soft-SUSY-breaking* terms in the model. They include many parameters: 105, including supersymmetric particle masses and field phases that cannot be absorbed by a redefinition of the fields. The model sketched so far is called the Minimal Supersymmetric Standard Model (MSSM).

Vast regions of the MSSM parameter space are not consistent with the observed particle physics phenomenology. Further assumptions motivated by experimental results are often made. To prevent the proton from decaying too quickly [10], conservation of a multiplicative quantum number called R-parity is often assumed. The R-parity of a particle is a function of its baryon number B , the lepton number L , and

¹ Non-minimal extensions of the SM can be obtained by first extending the SM and then completing it by introducing the supersymmetric partners of the SM fields, or by considering multiple versions of the SUSY operators applied to the SM fields.

² The supersymmetric scalars (partners of SM fermions) take the name of the SM partner with an ‘s’ prepended. For example, the electron has two partner *selectrons*. The supersymmetric fermions (partners of SM bosons) take the name of their SM partner with an ‘ino’ suffix. For example, the supersymmetric partner of the gluon is the *gluino*.

the spin S , and is defined as

$$R = (-1)^{3(B-L)+2S},$$

giving a value of -1 for SUSY particles and $+1$ for SM particles. Its conservation has important phenomenological consequences because an even number of SUSY particles must always appear at a Feynman vertex. This implies that SUSY particles must be produced in pairs, and that the LSP is stable. A necessary condition for the LSP to be a good dark-matter candidate is that it interacts with ordinary matter only through weak interactions, which implies that LSPs produced (either directly or from the decay of a SUSY particle) in pp collisions do not interact with the detector, and missing transverse momentum becomes a characteristic event signature.

While R-parity conservation gives rise to a compelling phenomenology, it is not dictated by any fundamental principle. R-parity-violating (RPV) couplings are allowed, as long as their magnitude is not incompatible with existing observations. Because of this constraint, RPV couplings are typically small enough to be neglected in the production of SUSY particles, but they can have important consequences for SUSY particle decays: in particular, the LSP can decay into SM particles. This eliminates, in general, the possibility of retaining a good dark-matter candidate, and opens many options for the identity of the LSP, which can essentially be any SUSY particle. Since the LSP can decay, there is no expectation of having missing transverse momentum in the final state. RPV SUSY delivers very different event topologies than RPC SUSY.

Other assumptions can be made in order to reduce the volume of parameter space to be explored in the MSSM. Relatively general and well-motivated assumptions [11–13] about the flavour and mass structures of the MSSM allow the number of free parameters to be reduced to 19 or 20 (depending on the nature of the LSP): this so-called phenomenological MSSM (pMSSM) was investigated extensively during Run 1 of the LHC by both ATLAS [14] and CMS [15].

The strategy chosen by ATLAS to map its search programme to such a vast parameter space was to make use of simplified models [16–18]. In a simplified model, one assumes that only a handful of SUSY particles are relevant for the phenomenology of pp collisions. It is often assumed that a single type of SUSY particle is produced, with its decay involving only a few SUSY particles, or only the LSP. Designing an analysis for a specific simplified model means targeting a specific event topology. The limits obtained for simplified models hold whenever the assumed particle mass hierarchy and decays are realised in a fully developed SUSY model (either the MSSM or some more complex model). The main drawback of this approach is that it is often difficult to generalise a mass exclusion limit obtained for a SUSY particle. In a general SUSY model, many production processes and decay chains often compete with each other, and sometimes interference structures need to be taken into account when computing cross-sections. In short, the complexity of the actual model clashes with the clean and simple assumptions of the simplified models, so the simplified-model limits should always be presented along with caveats due to the assumptions made in designing the models, namely the (typically single) production process and decay mode.

The production cross-sections for strongly interacting SUSY particles hardly depend on any SUSY model parameter beside the sparticle masses. This is a consequence of the $SU(3)$ gauge interaction driving the process. The Feynman diagrams involved in strong production are the equivalent of those for production of gluons and quarks in the SM. At the next-to-leading order in the strong coupling constant α_s and beyond, interference between diagrams containing squarks and gluinos makes the production cross-section for each of the relevant processes ($\tilde{g}\tilde{g}$, $\tilde{g}\tilde{q}$, $\tilde{q}\tilde{q}$) dependent on the specific mass spectrum of the model. For example, destructive interference between t -channel exchange of \tilde{g} and \tilde{q} makes the $\tilde{g}\tilde{g}$ production cross-section

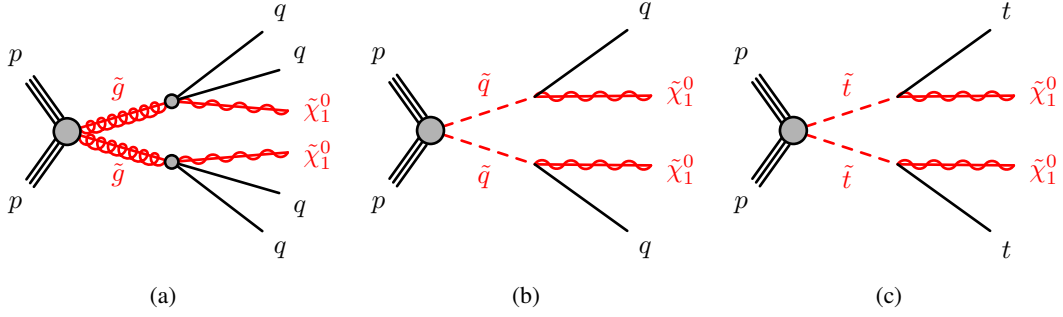


Figure 1: Simplified models of (a) gluino pair production followed by $\tilde{g} \rightarrow q\bar{q}\tilde{\chi}_1^0$; (b) squark pair production followed by $\tilde{q} \rightarrow q\tilde{\chi}_1^0$; and (c) top squark (stop) pair production followed by $\tilde{t} \rightarrow t^{(*)}\tilde{\chi}_1^0$. No distinction between particle and antiparticle is done in these diagrams.

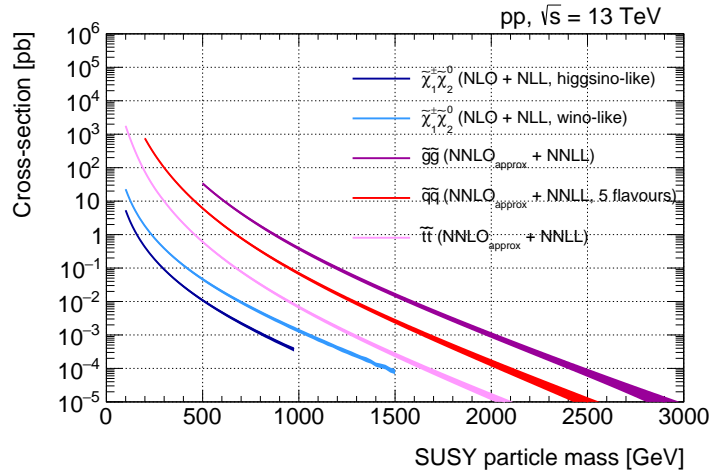


Figure 2: Direct pair-production cross-sections for a few processes mediated by the strong or electroweak processes. The width of the line represents the theoretical uncertainty. The values of the cross-sections and uncertainties are those agreed upon by the LHC SUSY Cross Section Working Group [19].

dependent on the \tilde{q} masses. However, if the other SUSY particles are assumed not to take part (not even virtually) in the production process, then the production cross-sections depend only on the sparticle mass. These are the assumptions typically made in simplified models of gluino or squark pair production, shown in Figures 1(a) and 1(b) respectively, and in Figure 1(c) if the squark is a top squark (or ‘stop’).

The production cross-sections for squarks and gluinos with simplified-model assumptions are shown in Figure 2. The cross-section shown for squark production assumes that the 10 squarks corresponding to the $u, d, c, s,$ and b flavours (and two chirality states) are all degenerate in mass. The cross-section scales linearly with the number of squark types that can be produced.

For example, the production cross-section for a pair of gluinos with $m(\tilde{g}) = 2 \text{ TeV}$ is about 1 fb, assuming that the mass of all other SUSY particles is large enough for them to be irrelevant in the cross-section evaluation. Consequently, between 100 and 200 gluinos with $m_{\tilde{g}} = 2 \text{ TeV}$ would have been produced at the ATLAS interaction point during Run 2. The production of SUSY particles with such a large mass

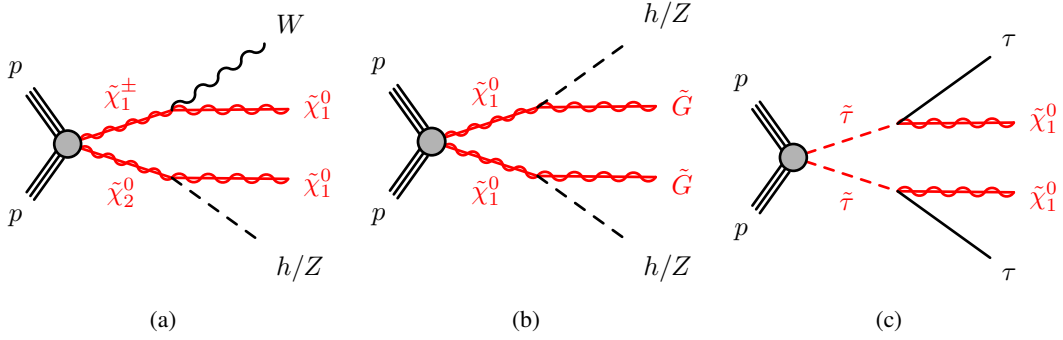


Figure 3: Simplified models of (a) $\tilde{\chi}_1^\pm \tilde{\chi}_2^0$ production followed by $\tilde{\chi}_1^\pm \rightarrow W^\pm \tilde{\chi}_1^0, \tilde{\chi}_2^0 \rightarrow h/Z \tilde{\chi}_1^0$; (b) $\tilde{\chi}_1^0 \tilde{\chi}_1^0$ production followed by $\tilde{\chi}_1^0 \rightarrow h/Z \tilde{G}$; and (c) direct $\tilde{\tau}$ pair production followed by $\tilde{\tau} \rightarrow \tau \tilde{\chi}_1^0$. No distinction between particle and antiparticle is done in these diagrams.

typically results in a quite distinctive event topology, so that the event selection can achieve sufficient background rejection while retaining relatively large signal acceptance and efficiency. It is therefore not surprising that ATLAS is typically sensitive to gluinos in the mass range up to $m_{\tilde{g}} = 2$ TeV or somewhat higher, unless specific mass hierarchies are realised such that event selections with very small acceptance and/or efficiency need to be deployed. Following the same logic, one sees that the sensitivity of ATLAS to tenfold-degenerate squark pair production reaches masses approximately 0.5 TeV lower than those corresponding to gluino pair production.

The electroweak interaction couples SUSY particles to the SM quarks in the protons with a strength that depends specifically on the model parameters affecting the electroweak sector. Therefore, the production cross-section for electroweakinos (Figures 3(a) and 3(b)), for example, depends on the mixing in terms of wino, higgsino and (for neutralinos) bino states. Thus the production cross-section for a $\tilde{\chi}_1^\pm \tilde{\chi}_2^0$ pair is larger if each is a pure wino state, and smaller if each is a pure higgsino state, as shown in Figure 2. Likewise, the production cross-section for a $\tilde{\chi}_1^0 \tilde{\chi}_1^0$ pair vanishes if the $\tilde{\chi}_1^0$ is a pure higgsino. Similarly, the production cross-section for slepton pairs (Figure 3(c)) depends on the weak-isospin structure of the sleptons, i.e. on the mixing of the slepton in terms of right- and left-handed chirality.

Because of the number of mass eigenstates available and the variety of possible electroweak parameter-space configurations, families of simplified models of electroweakino production have been defined. They stem from specific electroweakino mass hierarchies that arise in limit cases of the electroweak-sector mass parameters. In the MSSM, the soft SUSY-breaking mass term for the bino, winos and higgsinos are indicated with M_1 , M_2 and μ , respectively. The structure of the electroweakino mass matrices is such that a well-defined hierarchy of these parameters translates into a clear mass-eigenstate structure. If, for example, $M_1 < M_2 \ll \mu$, one has a bino-like $\tilde{\chi}_1^0$ LSP with $m(\tilde{\chi}_1^0) \sim M_1$, and nearly degenerate $\tilde{\chi}_2^0$ and $\tilde{\chi}_1^\pm$ with masses of the order of M_2 . If $\mu \ll M_1, M_2$, then the first four electroweakinos ($\tilde{\chi}_1^0, \tilde{\chi}_2^0$ and two charginos $\tilde{\chi}_1^\pm, \tilde{\chi}_2^\pm$) will all have almost degenerate masses of the order of μ , leading to a very compressed scenario. Such a higgsino LSP case will yield event topologies with soft decay products emitted in transitions between the electroweakino states. Similarly, $M_2 \ll \mu, M_1$ (wino LSP) yields $m(\tilde{\chi}_1^0) \sim m(\tilde{\chi}_1^\pm) \sim M_2$. Most of the SUSY scenarios that inspire the models described in Sections 6 and 8 refer to one of these paradigms.

3 The ATLAS detector

The ATLAS experiment [2] is a multipurpose particle detector with a forward–backward symmetric cylindrical geometry and nearly 4π coverage in solid angle.³ It is designed to identify a wide variety of particles and measure their momenta and energies. These particles include electrons, muons, τ -leptons and photons, as well as gluons and quarks, which produce collimated jets of particles in the detector. It consists of an inner tracking detector surrounded by a thin superconducting solenoid providing a 2 T axial magnetic field to measure charged-particle trajectories and momenta, followed by electromagnetic (EM) and hadron calorimeters that are used in the identification of particles and in the measurement of their energies, and a muon spectrometer (MS) for measuring the trajectories and momenta of muons. A two-level trigger system is used to select events [20]. The first-level trigger is implemented in hardware and uses a subset of the detector information to accept events at a rate below 100 kHz from the LHC’s 40 MHz proton bunch crossings. This is followed by a software-based trigger that reduces the accepted event rate to 1 kHz on average depending on the data-taking conditions. An extensive software suite [21] is used in data simulation, in the reconstruction and analysis of real and simulated data, in detector operations, and in the trigger and data acquisition systems of the experiment.

4 Analysis strategy

The analyses that produced the SUSY mass exclusion limits discussed in Sections 5 to 8 were designed to be complementary, and target many different event topologies that can arise from the production and decay of SUSY particles. They employ a variety of tools and techniques, which makes each of them largely unique in terms of analysis strategy and, of course, sensitivity to the SUSY parameter space. However, all the analyses discussed apply similar strategies for background estimation, and they all share a common statistical approach in testing, first of all, for compatibility with the SM background prediction (and, therefore, whether the analysis observed a SUSY signal or not), and, in absence of a signal, in setting limits on SUSY production cross-sections, and eventually on sparticle masses.

The design of the analysis starts from the definition of one or more selections determining the signal region(s) (SR). Typically, the SR are designed by maximising the significance of the targeted signal process relative to the SM background as predicted by a Monte Carlo (MC) simulation. Actual collision data is not used in selection regions with a large expected signal contribution, to avoid any bias while defining the selection. This first phase identifies the set of variables to be used for the selection. They are typically employed in a multivariate selection, using either a boosted decision tree (BDT) or a neural network (NN), or varied to identify a set of selection criteria to be applied to each of them, sometimes referred to as a ‘cut-and-count’ approach. In all cases, the final selection criteria (for the BDT or NN discriminant, or for the individual variables) are set after the final background estimation is in place.

The preliminary SR definition allows the identification of the relevant SM background processes for the analysis. *Reducible* background processes pass the signal region selection despite not having the signal characteristics at particle level. Reducible backgrounds are relevant when some events from a

³ ATLAS uses a right-handed coordinate system with its origin at the nominal interaction point (IP) in the center of the detector and the z -axis along the beam pipe. The x -axis points from the IP to the center of the LHC ring, and the y -axis points upwards. Cylindrical coordinates (r, ϕ) are used in the transverse plane, ϕ being the azimuthal angle around the z -axis. The pseudorapidity is defined in terms of the polar angle θ as $\eta = -\ln \tan(\theta/2)$. Angular distance is measured in units of $\Delta R \equiv \sqrt{(\Delta\eta)^2 + (\Delta\phi)^2}$.

high-cross-section SM process (e.g. multijet, W + jets, or Z + jets production) ‘fake’ one or several of the SR criteria. The faking probabilities are typically small, but the high cross-section may make the process relevant. Reducible backgrounds are often estimated by using techniques that strongly rely on the use of data from real collisions, since the faking mechanisms are not always reproduced reliably by the detector simulation. Some of the most common contexts where estimation of reducible background is relevant are as follows:

- In analyses where signal events have many leptons, or lepton pairs of the same charge (‘same-sign’, or SS leptons), backgrounds contributions from jets faking leptons, ‘fake’ leptons from photon conversions, and non-prompt leptons from hadron decays, can become relevant. Contributions from fake and non-prompt (FNP) leptons are typically estimated using a loose-to-tight method [22]: the FNP contribution to the ‘tight’ leptons used in the selection is estimated from ‘loose’ leptons by using scale factors estimated in a dedicated FNP-lepton-dominated selection. Similar techniques are employed to estimate fake- τ -lepton contributions to SR selecting events containing hadronic τ -lepton decays [23].
- Analyses using SS leptons may suffer from contributions from processes involving leptons with opposite charges (‘opposite-sign’, or OS leptons), where one of the two lepton charges is misidentified. The charge-flip probability is estimated by comparing yields in OS and SS regions where a $Z \rightarrow \ell\ell$ peak is clearly visible. Obviously, $Z \rightarrow \ell^\pm\ell^\pm$ arises from $Z \rightarrow \ell^\pm\ell^\mp$ with a charge-flip. Charge-flip probabilities are typically negligible for muons.
- The background affecting analyses looking for signals from long-lived particles is almost always reducible. For example, one of the main backgrounds when looking for displaced secondary vertices due to decays of long-lived particles arises from random crossings of tracks that the detector is not able to resolve. The probability to have a random crossing is assumed to be independent of the tracks forming the vertex and is determined from a control region and then applied to lower track-multiplicity vertices to estimate the background contribution.

Irreducible backgrounds are those that have the same event topology as the signal. They are typically estimated by relying on MC predictions for their kinematic distributions. Sometimes the overall normalisation of the process is determined in a fit with the help of dedicated control regions (CR), i.e. selection regions where event rates are dominated by the process whose normalisation needs to be estimated. In addition, validation regions (VR) can be defined, with a topology as similar as possible to the SR, but with only a small expected signal contamination: they are used to verify that the background prediction agrees with the data before looking at the yields in the SR. Validation regions are not used in the statistical interpretation of the results. A sketch of a possible generic analysis set-up for an analysis using two variables (for example, two output nodes of a multiclass NN classifier) as the final discriminant, highlighting generic expectations for the signal and background yields, relative background (statistical and systematic) uncertainty, and signal significance, is shown in Figure 4.

In the following, the background estimation strategy of some of the analyses considered is sketched as an example of the approaches above, or in case it is particularly relevant to the discussion.

A likelihood function is built as the product of Poisson probability functions $P(n_i^{\text{obs}}, n_i^{\text{exp}})$, describing the probability of observing n_i^{obs} events in region i (where i is any CR or SR) when n_i^{exp} are expected. Here n_i^{exp} depends on free-floating normalisation parameters for the signal μ_s and for the relevant irreducible background processes μ_b . These free-floating parameters are defined so that the yield corresponding to the nominal cross-section is obtained for $\mu = 1$. Systematic uncertainties are treated as nuisance parameters

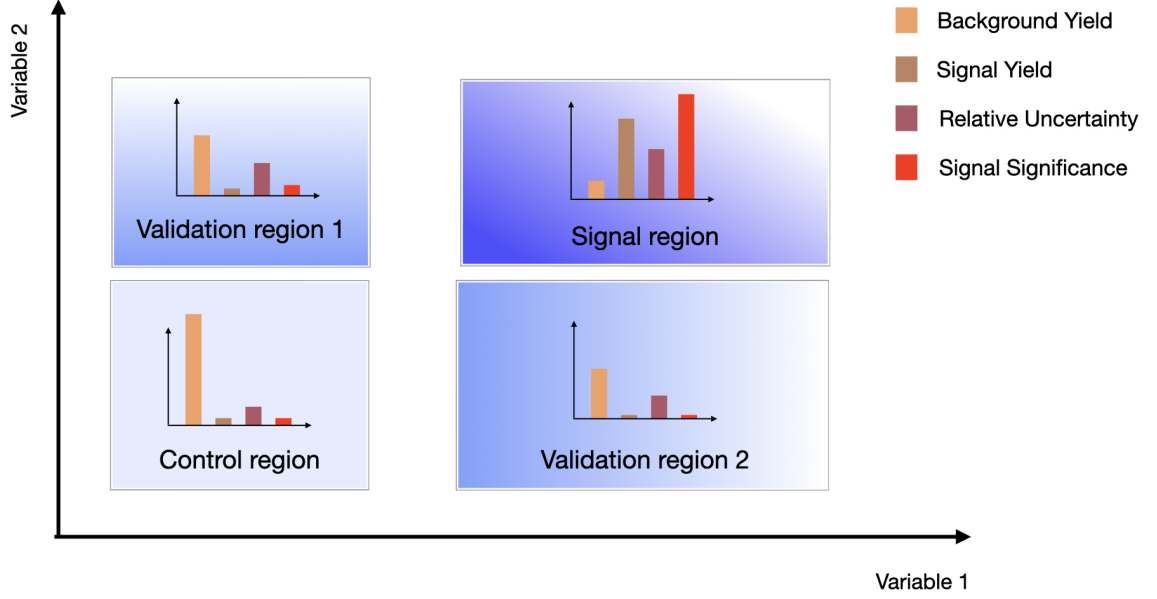


Figure 4: Illustrative set-up for an analysis using two variables as the final discriminant. The definition of mutually exclusive signal, control and validation regions is sketched, and indicative values for the signal and background yields, relative uncertainty and signal significance in each region are shown (on an arbitrary scale).

and are constrained with normal distributions $G(\theta_j^0 - \theta_j)$, where θ_j^0 is the expected value of the nuisance parameter corresponding to the j^{th} systematic uncertainty. The parameters μ_s , μ_b and θ are determined by maximum-likelihood fits. The resulting likelihood is:

$$\mathcal{L}(\mathbf{n}^{\text{obs}}, \theta^0 | \mu_s, \mu_b, \theta) = \prod_{i \in \text{SR, CR}} P(n_i^{\text{obs}}, n_i^{\text{exp}}(\mu_s, \mu_b, \theta^0, \theta)) \times \prod_{j \in \text{syst. unc.}} G(\theta_j^0 - \theta_j).$$

The test statistic used to test whether new physics is observed or to determine exclusion limits is the profile likelihood ratio [24]. No significant excess above the SM expectation has been observed at the LHC, so this paper concentrates on the resulting exclusion limits. A quantity $\hat{\mu}_s$ is defined as the μ_s value corresponding to a CL_s [25] of 0.05 for the profile-likelihood-ratio test statistic obtained under the signal-plus-background hypothesis. Models for which $\hat{\mu}_s \leq 1$ are said to be excluded at 95% confidence level (CL). All limits described in this paper are at 95% CL.

5 Strongly produced supersymmetric particles

Squarks and gluinos are produced with couplings that are proportional to the strong coupling constant α_s . Therefore, their production cross-sections are significantly larger than for sleptons and electroweakinos of the same mass. This also implies that squark and gluino production were the first sparticle production processes to which ATLAS achieved sensitivity: the sensitivity to gluinos, for example, was already well into the TeV range by the end of LHC Run 1.

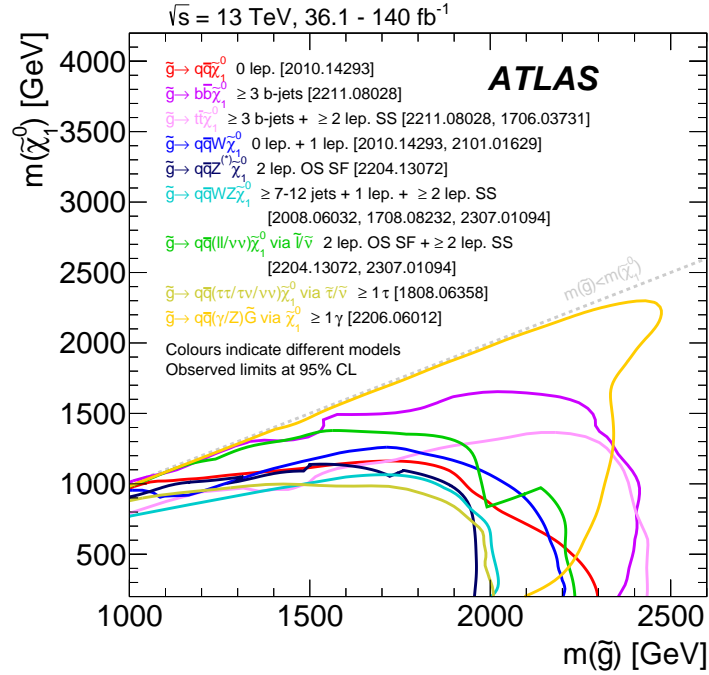


Figure 5: Exclusion limits from 13 TeV data in the $m(\tilde{g})-m(\tilde{\chi}_1^0)$ plane for different simplified models featuring the decay of the gluino to the lightest supersymmetric particle (lightest neutralino or gravitino) either directly or through a cascade chain featuring other SUSY particles with intermediate masses. For each line, the gluino decay mode is reported in the legend and it is assumed to proceed with 100% branching fraction. Some limits depend on additional assumptions about the masses of intermediate states, as described in the references cited in the plot.

5.1 Gluino pair production

The sensitivity of ATLAS to gluino pair production followed by RPC decays of the \tilde{g} is shown in Figure 5. All the limits shown were obtained by assuming a simplified signal model and the cross-sections shown in Figure 2: in particular, the production cross-section is a function of the gluino mass only, and it therefore decreases strongly at increasing values along the $m(\tilde{g})$ -axis. In all cases, the limits are presented as a function of the gluino mass and lightest neutralino mass. Different curves represent either different assumptions about the gluino decay chain, or different analysis results.

Focusing on the limit intercepts with the $m(\tilde{g})$ -axis, i.e. those for $m(\tilde{\chi}_1^0) = 0$ GeV, the first observation is that the 2 TeV range predicted from simple cross-section considerations in Section 2 is indeed realised. The second observation is that the limits on the gluino mass depend significantly on the line considered (i.e. the assumed gluino decay), and on $m(\tilde{\chi}_1^0)$. This is readily understood as a consequence of the total energy available in the decay being determined by the mass difference $m(\tilde{g}) - m(\tilde{\chi}_1^0)$. A small value of this quantity corresponds to smaller values of the momenta of the final-state objects, and, therefore, to signal topologies that are more difficult to separate from the SM background.

The different models in Figure 5 correspond to scenarios that assume different RPC gluino decays. Together, they give a very good overview of the extent of the effort made in the search for this sparticle.

The simplest RPC Feynman vertex that can be considered is one where the gluino couples to a squark

and a quark. The flavour of the squark, and the way it couples to the electroweak sector determines the complexity of the final state. In one of the simplest simplified models, the squarks and all electroweakino states but one ($\tilde{\chi}_1^0$) have a very large mass. The first case considered is one where the squark is not the stop. The gluino decay chain is $\tilde{g} \rightarrow \tilde{q}^* q \rightarrow qq\tilde{\chi}_1^0$. The case where the virtuality of the \tilde{q}^* is such that the \tilde{g} becomes long-lived is phenomenologically compelling and theoretically very interesting (arising from models of split-SUSY [26, 27]), and it is discussed in Section 8. Here the discussion is limited to the case where the \tilde{g} decay is prompt. The analysis that drives the sensitivity [28] targets both direct gluino and direct squark pair production by requiring no leptons in the final state and significant E_T^{miss} , which is also exploited for triggering purposes: the corresponding limit is indicated by the red line in Figure 5. The analysis selection is based on the jet multiplicity in the event (N_{jet}), the significance of the missing transverse momentum E_T^{miss}/H_T , and $m_{\text{eff}} = H_T + E_T^{\text{miss}}$. Here H_T denotes the scalar sum of the transverse momentum (p_T) of the jets in the event. The dominant background process in the considered signal regions is $Z(\rightarrow \nu\bar{\nu}) + \text{jets}$. This is estimated using simulated events corrected with auxiliary measurements of the $\gamma + \text{jets}$ and $Z(\rightarrow \ell^\pm \ell^\mp) + \text{jets}$ processes in a similar phase-space region. Other relevant background processes are $W + \text{jets}$ and $t\bar{t}$ production, with a $W \rightarrow \ell\nu$ decay to satisfy the E_T^{miss} requirement. For the latter class of processes, the lepton either fails the identification requirements or is a hadronically decaying τ -lepton. A small contribution from multijet production is estimated with the jet smearing method, where the background prediction is seeded from simulated events corrected to account for the detector's response to jets as measured in data [29].

Gluino masses up to about 2.2 TeV are excluded for massless $\tilde{\chi}_1^0$. For gluinos decaying to $\tilde{\chi}_1^0$ LSPs, there is no sensitivity to gluinos with masses above about 1.3 TeV if the masses of the gluino and $\tilde{\chi}_1^0$ are similar. It is important to always bear in mind that the obtained limits assume a branching fraction of 100% for the particular decay. Also, the assumption that squarks do not affect the gluino production cross-sections can be quite a strong one, requiring squarks with masses of tens of TeV. Further interpretations in Ref. [28] address some of these points, providing limits in models where the gluino and squark masses are similar.

If the assumptions about the electroweak sector are modified, and a richer spectrum of relatively light electroweakino states is allowed, then the phenomenology becomes more complex, with different squark decays potentially competing with each other. ATLAS has considered various benchmark gluino decays, especially focusing on models involving longer gluino decay chains. In some cases, the gluino decay chain may lead to the production of vector bosons, which opens up possibilities for final states containing leptons, possibly with same-sign charges. Additionally, longer gluino decay chains with hadronic vector-boson decays can result in final states with a higher jet multiplicity or involve hadronic resonances. Figure 5 shows some of the limits obtained in these scenarios in different shades of blue. In one scenario (light blue line in Figure 5, also shown in Figure 6), the squark is assumed to decay as $\tilde{q}^* \rightarrow q\tilde{\chi}_1^\pm \rightarrow qW\tilde{\chi}_1^0$, leading to $\tilde{g} \rightarrow q\tilde{q}'W\tilde{\chi}_1^0$. This scenario is targeted both by Ref. [28], already discussed, and by an analysis requiring the presence of one lepton from the W decay [30]. The latter applies a selection that rejects background processes containing one W boson decaying leptonically by requiring large values of the transverse mass m_T of the lepton and $\mathbf{p}_T^{\text{miss}}$, based on the jet multiplicity. The rest of the selection exploits the topology of the expected final state by using variables such as E_T^{miss} , N_{jet} , and m_{eff} (including the lepton p_T in the scalar sum of transverse momenta). The two analyses selecting events with either no or one lepton in the final state have dedicated selections for models where the \tilde{g} and $\tilde{\chi}_1^0$ masses are similar, resulting in improved exclusion limits for such compressed mass-difference scenarios. The resulting exclusion limits from the two analyses in this simplified model are similar, with each excluding a range up to $m(\tilde{g}) = 2.2$ TeV for $m(\tilde{\chi}_1^0) = 0$. The limit is reduced by about 1 TeV in the compressed scenario.

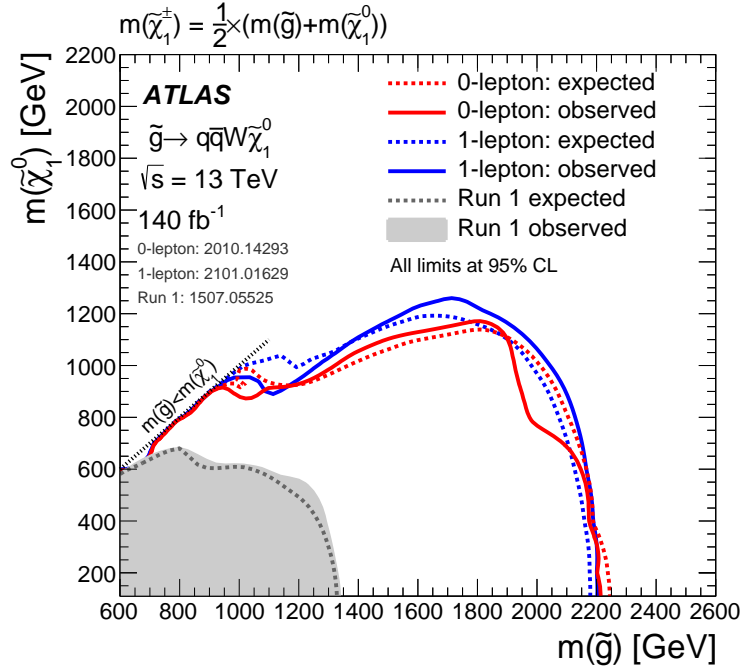


Figure 6: Exclusion limits from 13 TeV data in the $m(\tilde{g})-m(\tilde{\chi}_1^0)$ plane for the simplified model where a pair of gluinos are produced, and each decays promptly via an on-shell chargino into a pair of quarks, a W boson, and the lightest neutralino. The chargino mass is assumed to be midway between the gluino and neutralino masses. Theoretical signal cross-section uncertainties are not included in the limits shown.

Other cases considered explicitly in Figure 5 are those with $\tilde{q}^* \rightarrow q\tilde{\chi}_2^0 \rightarrow qZ\tilde{\chi}_1^0$, targeted by an analysis requiring an opposite-sign same-flavour (OS SF) lepton pair compatible with a Z boson in association with E_T^{miss} and jets [31], and those arising from a longer decay chain such as $\tilde{q}^* \rightarrow q\tilde{\chi}_2^0 \rightarrow q\tilde{\chi}^\pm \rightarrow qW\tilde{\chi}_1^0 \rightarrow qWZ\tilde{\chi}_1^0$, targeted by multiple analyses requiring either large jet multiplicities [32] or SS leptons in addition to jets [33]. Scenarios involving intermediate electroweakino decays via sleptons have also been considered.

The yellow line in Figure 5 displays a behaviour completely different from the others. It applies to scenarios inspired by General Gauge Mediation (GGM) [34], where the LSP is often a light gravitino with a mass around 1 GeV or less. The phenomenology in these scenarios is determined by the nature of the next-to-lightest supersymmetric particle (NLSP). The case shown here is one where the NLSP is a neutralino that decays to the LSP with photon or Z boson emissions, and the resulting topology includes photons in the final state, yielding a distinctive $\gamma + E_T^{\text{miss}} + \text{jets}$ final-state signature. The amount of E_T^{miss} in the event largely determines the analysis acceptance: in this case it is proportional to $m(\tilde{\chi}_1^0) - m(\tilde{G})$, so the maximum acceptance is obtained for large neutralino masses. Overall, the limits on the gluino mass are in line with those of the other analyses.

The cases where the virtual squark produced in the gluino decay is a third-generation squark are singled out in pink and purple in Figure 5. The physics reason to single them out is connected with naturalness considerations and is discussed in Section 5.2. The topological reason to single them out comes from the presence of b -quarks in the final state, yielding a powerful experimental handle with the application

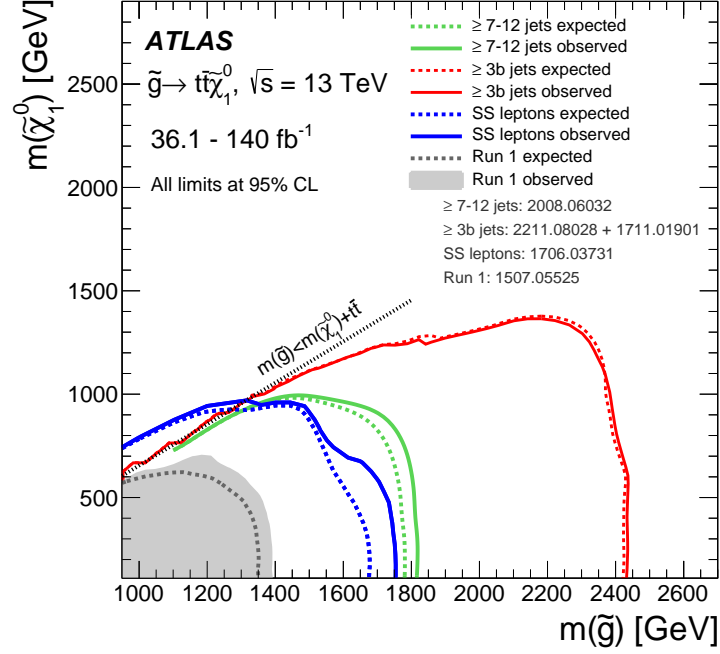


Figure 7: Exclusion limits from 13 TeV data in the $m(\tilde{g})-m(\tilde{\chi}_1^0)$ plane for a simplified model where a pair of gluinos decay promptly via off-shell top squarks into four top quarks and two lightest neutralinos. The SS lepton analysis sensitivity covers $m(\tilde{g}) < m(\tilde{\chi}_1^0) + 2m(t)$ due to the off-shell top quark contribution. Theoretical signal cross-section uncertainties are not included in the limits shown.

of b -tagging techniques [35] to identify b -jets. Neglecting potential flavour-violating decays of the stop or sbottom, the decay of a gluino pair via a third-generation squark with a branching fraction of 100% yields four b -jets in the final state. An analysis selecting events with three or more b -jets [36] dominates the sensitivity to these scenarios. The selection is based on a neural network that uses the kinematic variables of the jets, b -jets, leptons and $\mathbf{p}_T^{\text{miss}}$ as input. The network was trained to separate the $\tilde{g} \rightarrow t\bar{t}\tilde{\chi}_1^0$ and $\tilde{g} \rightarrow b\bar{b}\tilde{\chi}_1^0$ decays from the SM background, dominated by $t\bar{t}$, single top and Z + jets production. A different selection, which did not make use of multivariate techniques, was optimised to target mixed final states such as those arising from scenarios where both the stop and the sbottom take part in gluino decay, leading to final states with variable numbers of b - and t -quarks.

Summary limits on the model of gluino pair production yielding four top quarks and E_T^{miss} are shown in Figure 7. The richness of the topology of the final state makes it a target of many analyses. In particular, SS analyses achieve sensitivity to regions of the parameter space where the top quarks emitted in the decay are virtual.

5.2 Squark pair production

The search for pair production of squarks is closely connected with that of gluinos. A summary of the mass exclusion limits is shown in Figure 8, assuming an eightfold mass degeneracy for the squarks (two chirality states for each of the four lightest SM flavours). Depending on the structure and mass hierarchy

of the electroweak sector, the squarks will have decay chains that resemble those already discussed for gluino pair production. If the only electroweak state that couples to the quark is a neutralino LSP, then the squark decay chain is $\tilde{q} \rightarrow q\tilde{\chi}_1^0$. The final state will contain jets and missing transverse momentum, and the analysis discussed in Ref. [28] has good sensitivity for most values of the mass difference $\Delta m(\tilde{q}, \tilde{\chi}_1^0) = m(\tilde{q}) - m(\tilde{\chi}_1^0)$. For small $\Delta m(\tilde{q}, \tilde{\chi}_1^0)$, the final state contains very small E_T^{miss} , unless one focuses on the production of squarks recoiling against substantial QCD initial-state radiation (ISR). This case is explicitly targeted in Ref. [37]: the analysis searches for an excess of events with large E_T^{miss} recoiling against substantial hadronic activity. After a number of selections aimed at making sure that the events under investigation do not arise from jet energy mismeasurement or beam backgrounds, the dominant background processes are $W(\rightarrow \ell\nu) + \text{jets}$ (where the ℓ is lost or is a τ -lepton) and $Z(\rightarrow \nu\bar{\nu}) + \text{jets}$ production. A sophisticated background estimation procedure exploits the similarity of these processes with $Z(\rightarrow \ell^\pm\ell^\mp) + \text{jets}$ and $\gamma + \text{jets}$. As in the gluino case, a richer electroweak spectrum leads to longer decay chains, producing one-step $\tilde{q} \rightarrow qW\tilde{\chi}_1^0$ [28, 30] or $\tilde{q} \rightarrow qZ^{(*)}\tilde{\chi}_1^0$ [31] decays, or two-step $\tilde{q} \rightarrow qWZ\tilde{\chi}_1^0$ [33] decays. Similarly to the gluino case, scenarios involving sleptons in the electroweak-state decays, or GGM-like scenarios with a gravitino LSP, were also considered and targeted by specific analyses.

Overall, mass exclusion limits for eightfold-degenerate squarks range from 1.3 TeV to 1.8–1.9 TeV for $m(\tilde{\chi}_1^0) = 0$ GeV, and worsen with decreasing values of $\Delta m(\tilde{q}, \tilde{\chi}_1^0)$. For $\Delta m(\tilde{q}, \tilde{\chi}_1^0)$ of the order of a few GeV, the exclusion limit is about 900 GeV. These limits were obtained assuming simplified models.

The production cross-section for squarks scales linearly with the assumed degeneracy. For example, the limit in Ref. [28] for $m(\tilde{\chi}_1^0) = 0$ GeV decreases from about 1.85 TeV to about 1.2 TeV if production of a single \tilde{q} chirality state is assumed.

Third-generation squarks (\tilde{b} and \tilde{t}), and to some extent the \tilde{c} , have been targeted by dedicated analyses. The presence of b -jets (or c -jets) in the final state offers an additional experimental handle for improving the background rejection. The third-generation squarks are also constrained to be at the TeV scale by naturalness considerations: because of the large Yukawa coupling, stop loops are the main contribution to the first-order corrections to the lightest Higgs boson's mass in the MSSM [38]. Naturalness requirements place constraints on the stop masses and mixing between \tilde{t}_L and \tilde{t}_R . They also constrain the \tilde{b}_L because it belongs to the same weak-isospin doublet as the \tilde{t}_L and therefore shares the same SUSY mass parameter.

A summary of the \tilde{b} mass exclusion limits is shown in Figure 9. The limit in blue corresponds to the simplest decay chain, involving only a $\tilde{\chi}_1^0$ LSP. The analysis targeting this final state [39] requires the presence of b -jets and E_T^{miss} , and exploits the presence of kinematical endpoints in contranverse mass [40] for the dominant $t\bar{t}$ production background. Compressed scenarios are targeted by an analysis exploiting ISR hadronic activity and using dedicated techniques for tagging low- p_T b -jets [41]. Longer \tilde{b} decay chains are targeted by analyses explicitly looking for the presence of a Higgs boson in the $\tilde{\chi}_2^0 \rightarrow h\tilde{\chi}_1^0$ decay [42, 43].

Dedicated training of neural networks using input variables sensitive to the displaced decays of b -hadrons can produce relatively efficient c -jet tagging algorithms, which can be used effectively in the search for $\tilde{c} \rightarrow c\tilde{\chi}_1^0$. The analysis [44] was performed with a fraction of the available Run 2 integrated luminosity and follows a logic similar to that in Ref. [39].

Stop pair production was the target of an extensive search campaign as early as Run 1 [45], and Run 2 saw further development of the search strategy, with a variety of new final states being targeted. The popularity of stop searches is due to the stop's connection with the naturalness problem. From an

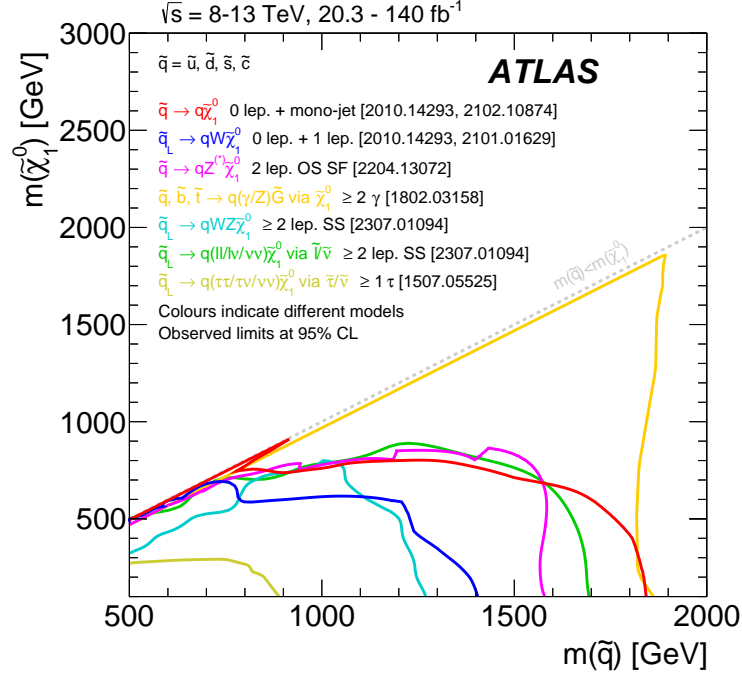


Figure 8: Exclusion limits from 8 TeV and 13 TeV data in the $m(\tilde{q})-m(\tilde{\chi}_1^0)$ plane for different simplified models featuring the decay of squarks to the lightest supersymmetric particle (lightest neutralino or gravitino) either directly or through a cascade chain featuring other SUSY particles with intermediate masses. For each line, the squark decay mode is reported in the legend and it is assumed to proceed with 100% branching fraction. The limits on $\tilde{q}_L \rightarrow qW\tilde{\chi}_1^0$ assume the chargino mass to be midway between the squark and neutralino masses. The other \tilde{q}_L interpretations assume the first intermediate particle to be midway between the squark and neutralino masses, and the second intermediate particle to be midway between the first intermediate particle and neutralino masses. The additional assumptions about the masses of the intermediate states are described in the references cited in the plot.

experimental point of view, the phenomenology of stop decay is very rich because of the large top quark mass: assuming the simplest electroweak-sector configuration (a $\tilde{\chi}_1^0$ LSP), the kinematics of the decay is determined not only by the \tilde{t}_1 and $\tilde{\chi}_1^0$ masses, but also by how their difference $\Delta m(\tilde{t}_1, \tilde{\chi}_1^0)$ compares to the top quark and W boson masses. If $\Delta m(\tilde{t}_1, \tilde{\chi}_1^0) > m(t)$, then the \tilde{t}_1 will experience a two-body decay $\tilde{t}_1 \rightarrow t\tilde{\chi}_1^0$, followed by an on-shell decay of the top quark into an on-shell W boson and a b -quark. If $m(W) + m(b) < \Delta m(\tilde{t}_1, \tilde{\chi}_1^0) < m(t)$, the stop will decay into three bodies, $\tilde{t}_1 \rightarrow bW\tilde{\chi}_1^0$, via an off-shell top. Finally, if $m(b) < \Delta m(\tilde{t}_1, \tilde{\chi}_1^0) < m(W) + m(b)$, the decay will be into four bodies, $\tilde{t}_1 \rightarrow bff'\tilde{\chi}_1^0$, with f representing a generic fermion. These different regions are clearly displayed in Figure 10. The parameter space is targeted with a suite of analyses looking for different lepton (electron and muon) multiplicities. Depending on the decay of the $W^{(*)}$, the final state can contain zero [46], one [47] or two [48] leptons.

The zero-lepton analysis defines a series of different signal regions based on the number of top quark and W boson decays that can be tagged by making use of large-radius jets to collect all the decay products. Depending on the region, the selection is completed by using additional variables such as E_T^{miss} and the transverse mass of the E_T^{miss} and b -jets to reject the dominant background from $t\bar{t}$ and Z + jets production. As in Ref. [39], the compressed region is targeted with dedicated tools to tag low- p_T b -jets.

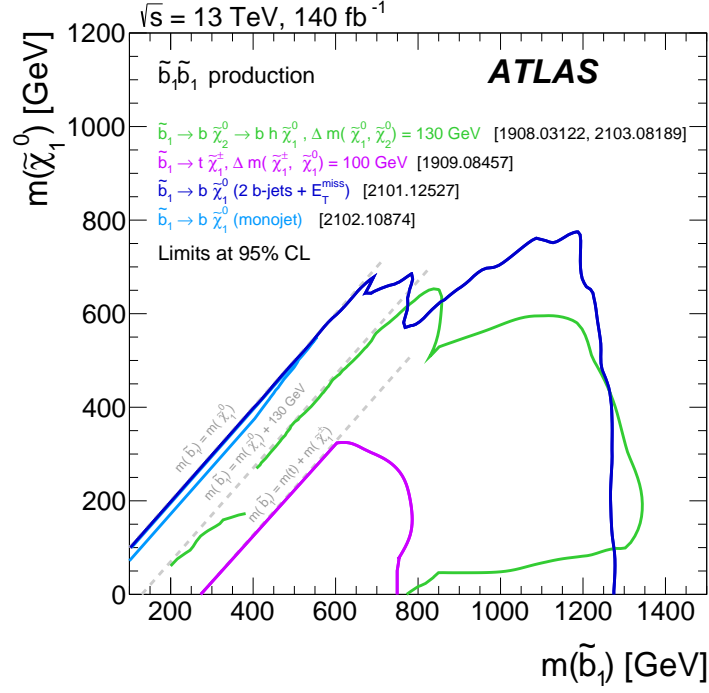


Figure 9: Exclusion limits in the $m(\tilde{b}_1)$ – $m(\tilde{\chi}_1^0)$ plane for direct sbottom production. The lightest neutralino ($\tilde{\chi}_1^0$) is assumed to be the LSP. Several different decay scenarios are shown, along with different parameterisations of the intermediate particles in the models.

The one-lepton analysis also utilises a set of signal regions targeting the two-, three- and four-body decays separately. A challenging background process is $t\bar{t}$ production where both top quarks decay leptonically, and one lepton is lost or is a hadronically decaying τ -lepton. This background process is targeted by making use of a variable called *topness*, which yields an estimate of how much a given event with one lepton in the final state resembles a dileptonic $t\bar{t}$ decay, based on expected detector resolutions and mass constraints present in such events. An updated result (shown in red in Figure 10) is obtained by separating events into mutually exclusive categories based on the number of reconstructed large-radius jets, and the number of those compatible with arising from the decay of a top quark: for each category, dedicated neural networks are trained to disentangle the signal from the background. This improves the sensitivity, especially at intermediate stop masses and large neutralino masses.

A challenging mass hierarchy is the one where $\Delta m(\tilde{t}_1, \tilde{\chi}_1^0) \approx m(t)$: the final state and kinematics of $\tilde{t}_1 \tilde{t}_1 \rightarrow t\bar{t} \tilde{\chi}_1^0 \tilde{\chi}_1^0$ closely resemble those from $t\bar{t}$ production, especially if $m(\tilde{\chi}_1^0) \approx 0$. In this case, precision measurements of SM $t\bar{t}$ production can come to the rescue, as indicated in the inset plot of Figure 10: a precise measurement of spin correlations in $t\bar{t}$ events [49] allows constraints to be placed on the additional production of a pair of scalar particles.

Figure 10 shows that stop pair production is excluded (for the decays considered) up to stop masses of about 1.3 TeV for $m(\tilde{\chi}_1^0) = 0$. The limit drops to about $m(\tilde{t}_1) \sim 600$ GeV in the compressed region.

If a more complex electroweak sector is considered, for example one allowing $\tilde{t}_1 \rightarrow b\tilde{\chi}_1^+$ and $\tilde{t}_1 \rightarrow t\tilde{\chi}_2^0$, then additional kinematic configurations and particles become possible. Typically, the analyses discussed have good sensitivity to these scenarios. Additional analyses explicitly looking for the presence of a Higgs

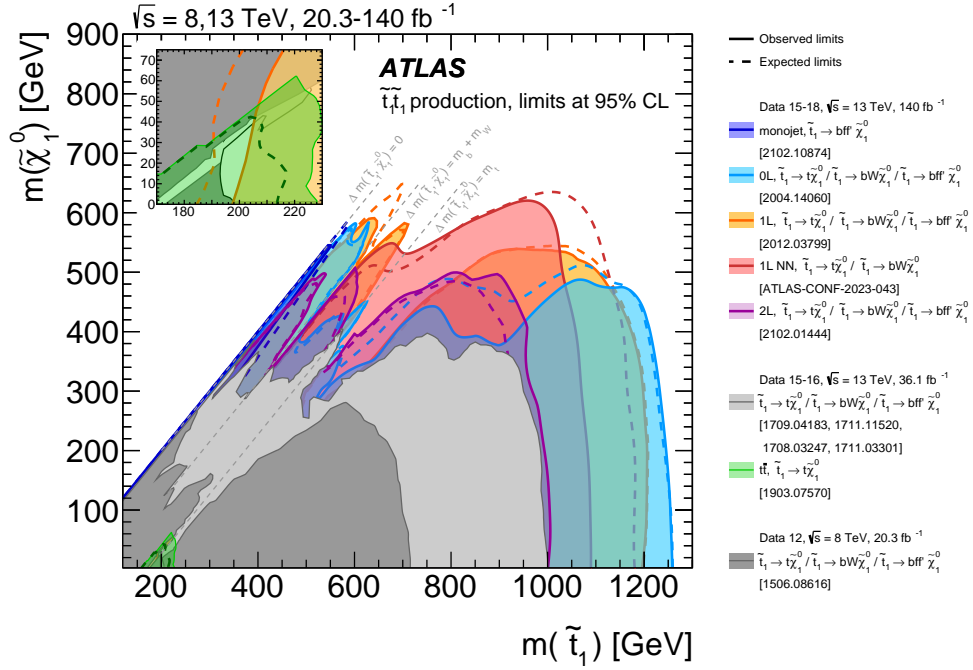


Figure 10: Summary of the dedicated ATLAS searches for top squark (stop) pair production based on pp collision data taken at $\sqrt{s} = 13$ TeV. Exclusion limits are shown in the $m(\tilde{t}_1) - m(\tilde{\chi}_1^0)$ plane. The dashed and solid lines show the expected and observed limits, respectively, including all uncertainties except the theoretical signal cross-section uncertainty (PDF and scale). Three decay modes are considered separately with 100% branching fraction: $\tilde{t}_1 \rightarrow t + \tilde{\chi}_1^0$ (where the \tilde{t}_1 is mostly \tilde{t}_R), $\tilde{t}_1 \rightarrow Wb\tilde{\chi}_1^0$ (three-body decay for $m(\tilde{t}_1) < m(t) + m(\tilde{\chi}_1^0)$), and $\tilde{t}_1 \rightarrow ff'b\tilde{\chi}_1^0$ (four-body decay).

or Z boson in the final state have also been developed [50], achieving interesting sensitivities. The case of a stop decay explicitly involving a $\tilde{\tau}$ has also been explored [51]. Finally, the flavour-changing decay of a stop into a charm quark and a neutralino LSP was targeted in Ref. [52]

6 Weakly produced supersymmetric particles

The electroweak production of SUSY particles includes some of the smallest cross-section processes at the LHC, with final-state signatures that are difficult to separate from SM processes. The ATLAS search programme aims to exploit all channels – from the clean, but rare, leptonic final states to the higher branching-fraction hadronic decays – in the quest to discover SUSY.

6.1 Slepton pair production

First- and second-generation slepton production, with decays into a charged lepton and a $\tilde{\chi}_1^0$ LSP ($\tilde{\ell}\tilde{\ell}$, with $\tilde{\ell} \rightarrow \ell\tilde{\chi}_1^0$) with 100% branching fraction, results in a clean final state of two OS SF leptons (e^+e^- or $\mu^+\mu^-$) and E_T^{miss} . A Run 2 search [53] considering general slepton production scenarios had the simple goal of

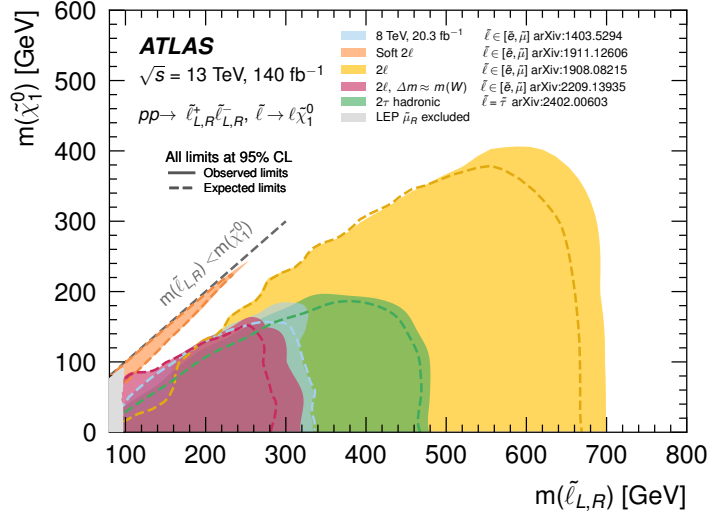


Figure 11: Exclusion limits in the $m(\tilde{\ell})-m(\tilde{\chi}_1^0)$ plane for different analyses probing the direct production of sleptons with decays into a lepton and neutralino. The types of sleptons (flavour and coupling) included in each search is specified in the legend.

achieving better sensitivity to higher slepton and neutralino masses than in the Run 1 search. A more recent search was more targeted and focused on the more compressed slepton production scenarios with $m(\tilde{\ell}) - m(\tilde{\chi}_1^0) < 100$ GeV [54], dividing the search between signatures with or without an ISR jet to exploit the boosted topology of $\tilde{\ell}\tilde{\ell}$ production with ISR. Both approaches use multiple bins in transverse mass, m_{T2} [55], which are optimised for mass exclusion potential in $\tilde{\ell}\tilde{\ell}$ production. SM backgrounds containing Z boson or low-mass resonances are suppressed by discarding OS SF lepton pairs with compatible invariant mass, while $t\bar{t}$ production is suppressed by discarding events containing b -tagged jets. At least moderate E_T^{miss} significance is required in order to suppress backgrounds with misreconstructed E_T^{miss} .

The most compressed slepton scenarios are targeted using a bespoke analysis requiring two low- p_T leptons, an ISR jet, and high E_T^{miss} [56]. Low m_{T2} is used for signal-background discrimination, along with R_{ISR} , the ratio of the E_T^{miss} to the p_T of the ISR system. A novel muon identification working point is used to recover some of the efficiency otherwise lost as $3 \text{ GeV} < p_T < 6 \text{ GeV}$ muons traverse the calorimeters.

The three searches see no significant excesses in the data compared to the SM background expectation, allowing limits to be set in simplified SUSY models, as shown in Figure 11. For mass-degenerate left- and right-handed slepton pair production, $\tilde{\ell}$ masses up to 700 GeV are excluded for massless $\tilde{\chi}_1^0$. For the very compressed scenarios with $m(\tilde{\ell}) - m(\tilde{\chi}_1^0) \sim 10$ GeV, sleptons are excluded up to masses of 251 GeV. The so-called ‘slepton-gap’ between the LEP and LHC limits is now closed with the results from the latest slepton search, excluding sleptons up to 150 GeV for $m(\tilde{\ell}) - m(\tilde{\chi}_1^0) \sim 50$ GeV. This still leaves an interesting parameter-space region to explore between the sensitivities in Ref. [56] and Refs. [53, 54].

Searches for third-generation sleptons, the staus, use final states with two hadronically decaying τ -leptons and high E_T^{miss} . The analysis in Ref. [57] uses a cut-and-count approach with two signal regions. The more recent analysis in Ref. [58] improves upon this by using four overlapping BDTs targeting different $\tilde{\tau}-\tilde{\chi}_1^0$ mass regimes. All four BDT signal regions show a $0.7\sigma-1.3\sigma$ deficit – a common deficit since the signal regions partially overlap. The exclusion limits for mass-degenerate left- and right-handed staus are shown

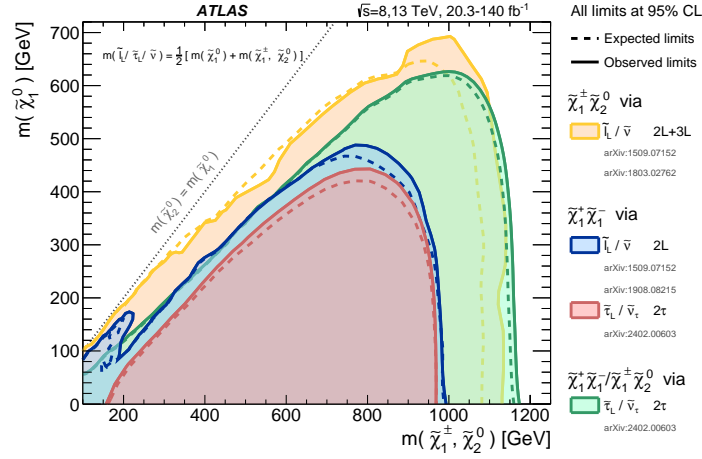


Figure 12: The exclusion limits on $\tilde{\chi}_1^+ \tilde{\chi}_1^-$ and $\tilde{\chi}_1^\pm \tilde{\chi}_2^0$ production with $\tilde{\ell}$ -mediated decays, as a function of the $\tilde{\chi}_1^\pm$, $\tilde{\chi}_2^0$ and $\tilde{\chi}_1^0$ masses. The production cross-section is for pure-wino $\tilde{\chi}_1^+ \tilde{\chi}_1^-$ and $\tilde{\chi}_1^\pm \tilde{\chi}_2^0$. Each individual exclusion contour represents a union of the excluded regions from one or more analyses.

in Figure 11, where stau masses up to 500 GeV are excluded. When considering the production of purely right-handed staus, which has a lower cross-section, staus masses up to 350 GeV are excluded. There is little sensitivity to the more compressed $\tilde{\tau}-\tilde{\chi}_1^0$ mass scenarios, because the searches rely on high- p_T hadronically decaying τ -leptons to trigger the event.

6.2 Electroweakino pair production

Sleptons may also feature as intermediate states in chargino and neutralino decay chains. The production of chargino pairs or chargino–neutralino pairs decaying via slepton results in two-lepton or three-lepton final states, respectively, along with E_T^{miss} . The exclusion limits in these models set by these searches [53, 58, 59] are shown in Figure 12, where chargino production is excluded for chargino masses up to 1 TeV and chargino–neutralino production is excluded for masses up to 1.15 TeV.

Charginos and neutralinos will decay via SM W , Z or h bosons if decays via sleptons are not kinematically allowed. The decays from the SM bosons include a rich array of hadronic and leptonic final states, allowing searches to be made using jets only, or one, two or three leptons in the final state. The same two-lepton search described above for slepton production is also used to search for production of low-mass chargino pairs decaying via W bosons [53], with further searches improving sensitivity to the $\Delta m(\tilde{\chi}_1^\pm, \tilde{\chi}_1^0) \sim m(W)$ scenarios [54]. The all-hadronic final state [60] makes use of the large hadronic branching fraction of SM boson decays to target very high-mass chargino production with large $\Delta m(\tilde{\chi}_1^\pm, \tilde{\chi}_1^0)$. The large mass splittings lead to boosted topologies, motivating the use of large-radius jets and boson-tagging algorithms to identify potential signal from boosted SM boson decays. Finally, a one-lepton, two-jet final state targets the intermediate chargino mass scenarios [61], which are not covered by the all-hadronic and two-lepton searches. No significant excesses were observed in the searches for chargino pair production, and a statistical combination of the three channels is performed in Ref. [62] and shown in Figure 13 for pure-wino charginos. Chargino masses up to 780 GeV are excluded for massless $\tilde{\chi}_1^0$, and $\tilde{\chi}_1^0$ masses up to 170 GeV are excluded for $\tilde{\chi}_1^\pm$ masses of ~ 400 – 600 GeV.

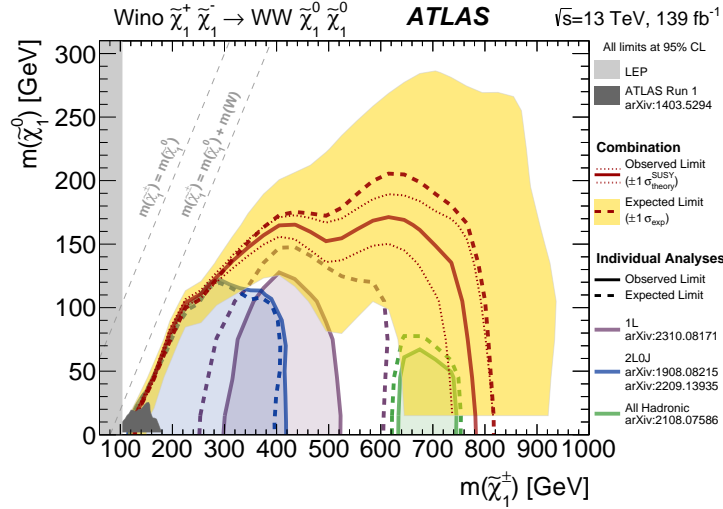


Figure 13: The exclusion limits on $\tilde{\chi}_1^\pm \tilde{\chi}_1^\mp$ production with W -boson-mediated decays, as a function of the $\tilde{\chi}_1^\pm$ and $\tilde{\chi}_1^0$ masses. The production cross-section is for pure-wino $\tilde{\chi}_1^\pm \tilde{\chi}_1^\mp$.

The all-hadronic channel is also powerful in the search for chargino–neutralino production and dominates the sensitivity to high-mass, large- $\Delta m(\tilde{\chi}_1^\pm/\tilde{\chi}_2^0, \tilde{\chi}_1^0)$ scenarios with decays via SM bosons, as seen in Figures 14(a) and 14(b). A two-lepton, two-jet search [31] selecting $Z \rightarrow \ell\ell$ and $W \rightarrow qq$ events with large E_T^{miss} is sensitive to moderately high mass $\tilde{\chi}_1^\pm \tilde{\chi}_2^0$ scenarios with decays via W and Z bosons. A few of the two-lepton, two-jet signal regions with closely spaced jets observed 2σ deficits, resulting in a stronger observed limit than expected. The sensitivity to moderately low mass $\tilde{\chi}_1^\pm \tilde{\chi}_2^0 \rightarrow WZ\tilde{\chi}_1^0 \tilde{\chi}_1^0$ scenarios is dominated by the three-lepton channel [63], which selects for decays of on- and off-shell W/Z bosons, with signal regions binned in OS SF lepton invariant mass, E_T^{miss} , m_T , and hadronic activity. Finally, the two-lepton compressed analysis described above is sensitive to $\tilde{\chi}_1^\pm \tilde{\chi}_2^0$ WZ scenarios with the smallest mass splittings.

When the $\tilde{\chi}_2^0$ decays via a Higgs boson, the one-lepton plus two- b -jet channel [64] is almost as powerful as the all-hadronic channel, and has unique sensitivity to moderate-mass scenarios. Here, pairs of b -tagged jets consistent with a $h \rightarrow b\bar{b}$ decay, as well as high E_T^{miss} , m_T and m_{CT} , are used to suppress SM processes. Leptonic final states are also used to search for these scenarios, but the sensitivity is limited to low masses due to the low branching fraction of the Higgs boson decay to leptons (possibly via SM bosons) [58, 63, 65]. A statistical combination of all the channels targeting chargino–neutralino production is performed in Ref. [62] and shown in Figures 14 and 14(b). Pure-wino chargino–neutralino production is excluded up to $\tilde{\chi}_1^\pm/\tilde{\chi}_2^0$ masses of ~ 1000 GeV for massless $\tilde{\chi}_1^0$, and up to $\tilde{\chi}_1^0$ masses of ~ 400 GeV for $\tilde{\chi}_1^\pm/\tilde{\chi}_2^0$ masses of ~ 800 GeV – whether the $\tilde{\chi}_2^0$ decays via a Z or Higgs boson. For decays solely through W and Z bosons, $\tilde{\chi}_1^\pm/\tilde{\chi}_2^0$ masses up to 300 GeV are excluded for $\Delta m(\tilde{\chi}_1^\pm/\tilde{\chi}_2^0, \tilde{\chi}_1^0) \sim m(Z)$, decreasing to 240 GeV for $\Delta m(\tilde{\chi}_1^\pm/\tilde{\chi}_2^0, \tilde{\chi}_1^0) = 10$ GeV.

The higgsino mass parameter μ enters into the MSSM expression for the light Higgs boson’s mass at tree level [38]. Therefore, a relatively low μ (of the order of a few hundred GeV at most) is one of the firm predictions of naturalness arguments applied to SUSY [66]. The search for pure-higgsino chargino–neutralino production is driven by the two-lepton compressed [56] and three-lepton analyses [63]

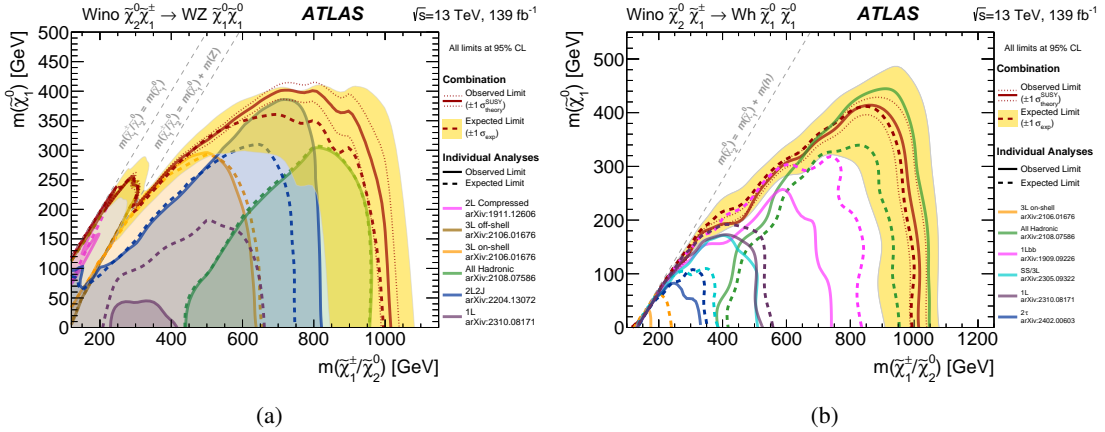


Figure 14: The exclusion limits on $\tilde{\chi}_1^\pm \tilde{\chi}_2^0$ production with $\tilde{\chi}_1^\pm \rightarrow \tilde{\chi}_1^0 W^\pm$ and (a) $\tilde{\chi}_2^0 \rightarrow \tilde{\chi}_1^0 Z$ or (b) $\tilde{\chi}_2^0 \rightarrow \tilde{\chi}_1^0 h$, as a function of the $\tilde{\chi}_1^\pm$, $\tilde{\chi}_2^0$ and $\tilde{\chi}_1^0$ masses. The production cross-section is for pure-wino $\tilde{\chi}_1^\pm$ and $\tilde{\chi}_2^0$.

described above, as well as the disappearing-track analysis [67] (see Section 8). The off-shell regions of the three-lepton analysis provide sensitivity to the larger mass splittings between the produced higgsinos and the LSP, $\Delta m(\tilde{\chi}_1^\pm, \tilde{\chi}_1^0) > 15$ GeV, while the more compressed analysis covers the smaller mass splittings down to about 1 GeV. A statistical combination of the two-lepton compressed analysis and three-lepton analysis is performed in Ref. [63], excluding pure-higgsino production of charginos with masses up to 180 GeV (190 GeV) for $\Delta m(\tilde{\chi}_1^\pm, \tilde{\chi}_1^0) \sim 30$ GeV (5 GeV). This decreases to 135 GeV for the intermediate mass splittings, where the combination has the most impact compared to the individual analyses. For $\Delta m(\tilde{\chi}_1^\pm, \tilde{\chi}_1^0) < 1$ GeV, the pair produced higgsinos start to have a flight path of a fraction of a mm, and their decay products are mildly displaced with respect to the primary vertex. An innovative analysis, exploiting the presence of a low- p_T isolated, good-quality track with only loose requirements on its impact parameter targets the prompt decay of the produced charginos and neutralinos into $\tilde{\chi}_1^0$, achieving sensitivity up to chargino masses of about 170 GeV for mass splittings $0.3 \text{ GeV} < \Delta m(\tilde{\chi}_1^\pm, \tilde{\chi}_1^0) < 0.9$ GeV [68]. For the smallest mass splittings, the chargino is long-lived and is targeted by the disappearing-track analysis, where chargino masses below 210 GeV are excluded for $\Delta m(\tilde{\chi}_1^\pm, \tilde{\chi}_1^0) \lesssim 0.3$ GeV. All these results are summarised in Figure 15.

Higgsino GGM scenarios are targeted by numerous ATLAS SUSY analyses selecting for either the leptonic or hadronic decays of the Z boson, or Higgs boson decays to b -quarks. A statistical combination of the channels targeting higgsino GGM models is performed in Ref. [62] and shown in Figure 16. For high $\tilde{\chi}_1^0 \rightarrow Z\tilde{G}$ branching fractions, the four-lepton search [70] and all-hadronic search [60] both select for two Z candidates and high E_T^{miss} , and dominate the sensitivity to low and high higgsino masses, respectively. The two-lepton two-jet channel [31] spans the intermediate higgsino mass range and extends to the lowest $\tilde{\chi}_1^0 \rightarrow Z\tilde{G}$ branching fraction in the searches involving a Z boson. The multi- b -jet search [71] and two- γ two- b -jet search [72] target GGM scenarios with high $\tilde{\chi}_1^0 \rightarrow h\tilde{G}$ branching fractions. The multi- b -jet channel makes use of the common Higgs boson decay into $b\bar{b}$, with signal regions binned in E_T^{miss} and m_{eff} for low-mass scenarios, or selecting on a BDT parameterized in higgsino mass for high-mass scenarios. The $\tilde{\chi}_1^0$ branching fraction into either $Z\tilde{G}$ or $h\tilde{G}$ is fully covered by the individual searches, with higgsino masses up to 960 GeV excluded for the two extreme branching fraction scenarios. The sensitivity drops

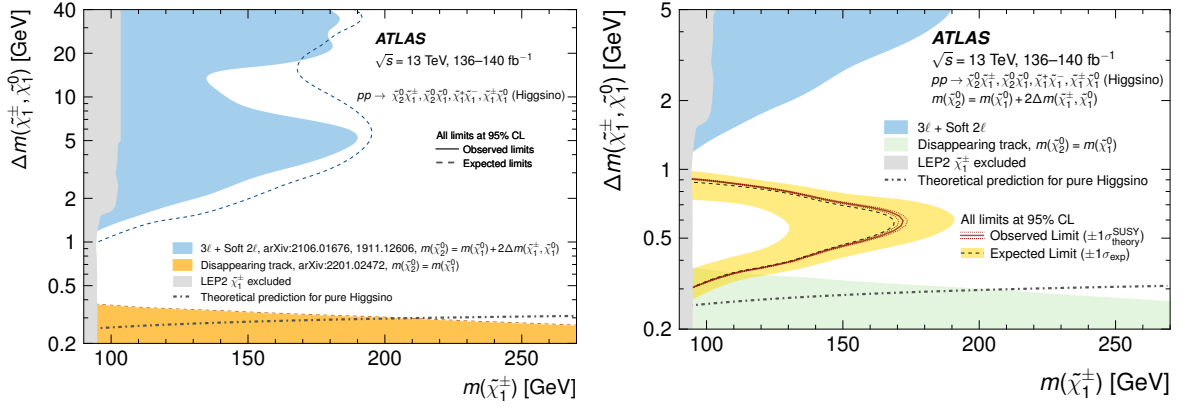


Figure 15: Exclusion limits for higgsino pair production $\tilde{\chi}_1^+ \tilde{\chi}_1^-$, $\tilde{\chi}_1^\pm \tilde{\chi}_1^0$, $\tilde{\chi}_1^\pm \tilde{\chi}_2^0$, and $\tilde{\chi}_1^0 \tilde{\chi}_2^0$ with off-shell SM-boson-mediated decays to the lightest neutralino, $\tilde{\chi}_1^0$, as a function of the $\tilde{\chi}_1^\pm$ and $\tilde{\chi}_1^0$ masses. The production cross-section is for pure higgsinos. The LEP2 $\tilde{\chi}_1^\pm$ exclusion is taken from Ref. [69]

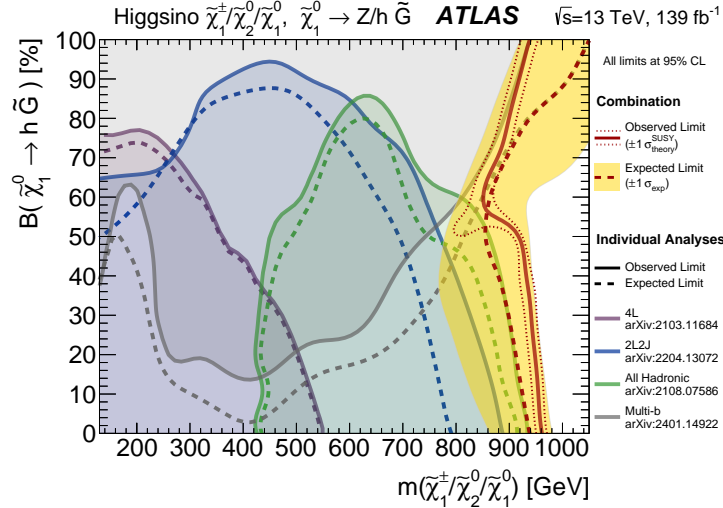


Figure 16: Exclusion limits in a General Gauge Mediation model from 13 TeV data. The model assumes a pure-higgsino NLSP that promptly decays into either a Z boson and gravitino or a Higgs boson and gravitino. The limits are displayed as a function of the mass of the nearly mass-degenerate higgsino multiplet and the branching fraction of the lightest higgsino into a Higgs boson and gravitino.

to masses of 850 GeV for the mixed branching fraction scenarios, where the combination has the most impact.

7 R-parity-violating decays

The MSSM potential includes terms that violate the conservation of baryon number and lepton number,

$$\frac{1}{2} \lambda_{ijk} L_i L_j \bar{E}_k + \lambda'_{ijk} L_i Q_j \bar{D}_k + \frac{1}{2} \lambda''_{ijk} \bar{U}_i \bar{D}_j \bar{D}_k + \kappa_i L_i H_2,$$

where L_i and Q_i are the lepton and quark SU(2)-doublet superfields, respectively, and \bar{E}_i , \bar{U}_i and \bar{D}_i are the corresponding singlet superfields. The fermion generations are denoted by the indices i , j and k , while the Higgs field that couples to up-type quarks is represented by the Higgs SU(2)-doublet superfield H_2 . The λ_{ijk} , λ'_{ijk} and λ''_{ijk} parameters are three sets of new Yukawa couplings, while the κ_i parameters have dimensions of mass. In this section, RPV couplings are assumed to be large enough to allow decays to be prompt. In the case of very small RPV couplings, SUSY particles could be long-lived, leading to rather different experimental signatures which are discussed in Section 8.

The nine λ_{ijk} couplings violate lepton number conservation via interactions between the three generations of leptons and sleptons, allowing a $\tilde{\chi}_1^0$ LSP to decay via virtual sleptons into $\ell_k^\pm \ell_{i/j}^\mp \nu_{j/i}$. Pair production of a promptly decaying NLSP is assumed, potentially producing four or more charged leptons from the two $\tilde{\chi}_1^0$ decays in the event. These scenarios were explored with the four-lepton final state in Ref. [70], selecting electrons, muons and hadronically decaying τ -leptons for sensitivity to the λ_{12k} and λ_{i33} couplings, where $i, k \in 1, 2$. Since the electron and muon reconstruction efficiencies at the ATLAS experiment are similarly high, the sensitivities to λ_{121} and λ_{122} scenarios are nearly identical [73] and can be considered simply as λ_{12k} (and similarly for λ_{i33}). The $\lambda_{12k} \neq 0$ couplings are targeted using electrons and muons only, while sensitivity to the $\lambda_{i33} \neq 0$ couplings is increased by including up to two hadronically decaying τ -leptons among the four leptons. For each coupling scenario, three different NLSP production processes are considered: wino pair production ($\tilde{\chi}_1^\pm / \tilde{\chi}_2^0 / \tilde{\chi}_1^+ \tilde{\chi}_1^-$), slepton pair production ($\tilde{\ell} \tilde{\ell} / \tilde{\nu} \tilde{\nu} / \tilde{\ell} \tilde{\nu}$), or gluino pair production ($\tilde{g} \tilde{g}$). The strongest limits are set on $\tilde{g} \tilde{g}$ production with $\lambda_{12k} \neq 0$ as shown in Figure 17, where gluino masses up to 2.5 TeV are excluded. This mass limit decreases to 1.9 TeV for $\lambda_{i33} \neq 0$ scenarios, due to the lower reconstruction efficiency for hadronic τ -lepton decays. Lower mass exclusion limits of 1.6 TeV and 1.2 TeV (1.1 TeV and 0.9 TeV) are set on $\lambda_{12k} \neq 0$ ($\lambda_{i33} \neq 0$) scenarios of wino pair production and slepton pair production, respectively, due to the lower cross-sections. The sensitivity for other λ_{ijk} scenarios is expected to fall between the two extremes of the λ_{12k} and λ_{i33} scenarios studied.

The 27 λ'_{ijk} couplings violate lepton and baryon number conservation with interactions between leptons, quarks, and squarks, allowing a $\tilde{\chi}_1^0$ LSP to now decay via virtual squarks into $\ell_k^\pm q_i \bar{q}_j / \nu_k q_i q_j$, where q_i and \bar{q}_j may be up-type or down-type quarks as needed to conserve charge. The lepton from one or each $\tilde{\chi}_1^0$ decay, along with several jets, is used to probe models of gluino pair production. The one-lepton analysis [74] divides the search regions according to the number of jets and number of b -tagged jets, as well as the charge of the lepton. Increasing thresholds are set on the p_T of the counted jets to obtain sensitivity to a wide range of scenarios. A second search selects two leptons with same-sign charges [33], multiple jets and high m_{eff} , benefiting from a lower SM background than in the one-lepton search. Figure 17 shows that the two searches set similar mass limits in the gluino production models, excluding gluinos with masses below ~ 2.2 TeV. The two-lepton search has less reliance on reconstructing the jet from the gluino decay ($\tilde{g} \rightarrow q q \tilde{\chi}_1^0$) and has a slight advantage if $m(\tilde{g}) - m(\tilde{\chi}_1^0)$ is small.

Finally, the nine λ''_{ijk} couplings violate baryon number conservation with interactions between quarks and squarks, allowing a $\tilde{\chi}_1^0$ LSP to now decay via virtual squarks into $q_k q_i q_j$, where q_k is an up-type quark and $q_{i/j}$ are down-type quarks. The one-lepton analysis already mentioned [74] also sets (for the first time) limits on higgsino pair production followed by their decay via λ'' couplings into third-generation quarks. The multijet search [75] selects events with a large number of high- p_T jets, allowing the presence of b -tagged jets to increase the sensitivity to b -quarks from the RPV $\tilde{\chi}_1^0$ decay. Again, gluinos with masses below ~ 2.2 TeV are excluded in Figure 17, but the sensitivity drops off rapidly for high and low $\tilde{\chi}_1^0$ masses where the jets are either too low in momentum or too collimated to be reconstructed. The analysis uses an

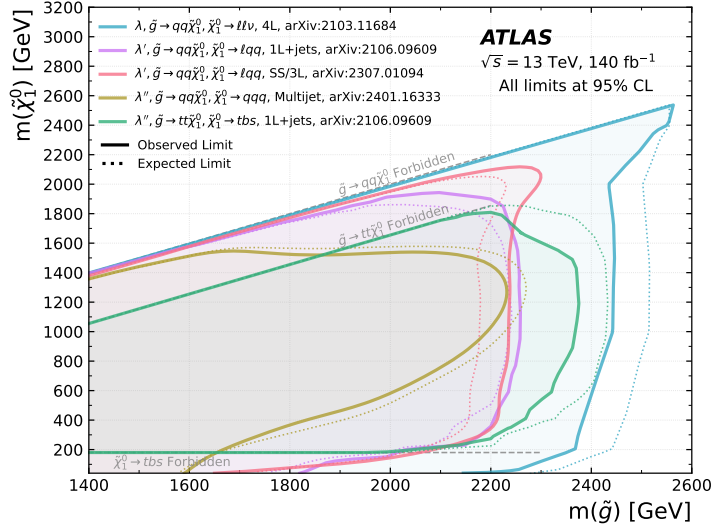


Figure 17: Exclusion limits at 95% CL based on 13 TeV data in the (gluino, lightest neutralino) mass plane for different simplified models featuring the decay of the gluino to the lightest supersymmetric particle (lightest neutralino) which in turn decays via R-parity-violating couplings to Standard Model particles. For each line, the gluino decay mode is reported in the legend and it is assumed to proceed with 100% branching fraction. Some limits depend on additional assumptions, as described in the references cited in the plot.

approach similar to that of the one-lepton search described above [74], which itself is also sensitive to the $\lambda''_{ijk} \neq 0$ scenarios when leptons are produced in top quark decays. The one-lepton signal regions with many b -tagged jets have good sensitivity to the $\tilde{g} \rightarrow tt\tilde{\chi}_1^0, \tilde{\chi}_1^0 \rightarrow tbs$ scenarios, excluding gluinos with masses below ~ 2.35 TeV as shown in Figure 17. A second approach in the multijet analysis uses a neural network with an architecture based on transformers to group jets together in order to help deal with the large combinatorial problem caused by the large number of jets in the final state, and search for a mass resonance from the two gluinos decaying directly via the λ''_{ijk} coupling, $\tilde{g} \rightarrow qq\tilde{g}$. In this case, gluinos with masses below ~ 1.8 TeV are excluded.

Less simple RPV SUSY scenarios have also been explored by the ATLAS Collaboration. For example, an MSSM scenario explored in Ref. [76] adds $B - L$ symmetry breaking with right-handed sneutrinos that is small enough to satisfy proton decay constraints, and also adds L symmetry breaking at tree level. The latter gives rise to charginos and neutralinos that decay into a SM boson and a lepton, e.g. $\tilde{\chi}_1^\pm \rightarrow Z\ell$, where a fully leptonic decay of the Z boson allows the chargino mass resonance to be fully reconstructed. The invariant mass of the three leptons is binned to achieve good sensitivity to a wide range of these $B - L$ SUSY scenarios, and the presence of additional leptons can be used to identify the presence of SM boson decays from the second produced sparticle. With no significant excess seen in the data, chargino masses up to 1.1 TeV are excluded for $\mathcal{B}(\tilde{\chi}_1^\pm \rightarrow Z\mu) = 100\%$, with lower mass exclusion limits obtained with different assumptions.

No direct limits have yet been placed on the size of the RPV couplings. However, if the coupling is not particularly small, it allows prompt sparticle decay and its effect is included in the limits set here. When the RPV coupling becomes very small, the sparticle becomes long-lived and experimental signatures are rather different – these are the topic of Section 8.

8 Long-lived supersymmetric particles

As is the case for SM particles, SUSY particles produced at the LHC may be long-lived and travel a significant distance before decaying. Longer lifetimes may be due to weak couplings to their decay products, decays through heavy mediator particles, or small mass differences between the particle and the decay products. The experimental signatures of long-lived new particles can be unconventional and depend on where and how the SUSY particle decays. A long-lived SUSY particle could travel from the ATLAS interaction point, through the inner-detector tracking system and then the calorimeters, and even through the muon spectrometer (or decay at any point along the way), leaving different signatures along its path depending on its properties. A charged particle decaying in the inner detector to a nearly degenerate stable neutral particle will manifest itself as a disappearing (or kinked) track, while a neutral particle's decay in the inner detector to charged and neutral particles would appear as tracks pointing back to a displaced vertex. The calorimeters may also be used for long-lived particle signatures, with photons that do not point back to the original interaction point ('non-pointing' photons), or strongly interacting long-lived particles that are stopped in the calorimeters by ionisation energy loss and nuclear scattering. Finally, if a SUSY particle is charged and very long-lived, the experimental signature would be similar to that of a muon, albeit with high mass. A neutral, weakly interacting long-lived new particle traversing the ATLAS detector would not be detected and would appear as missing transverse momentum.

A long-lived charged SUSY particle, such as a slepton or chargino, may be produced directly in pp collisions, or from prompt decays of other SUSY particles, such as a gluino. If its lifetime is $\sim 0.1\text{--}10$ ns because it is nearly degenerate with the invisible LSP, the charged SUSY particle would leave a track in the inner detector until the point of decay, where that track then disappears (the emitted charged decay products typically have momenta which are too low for their tracks to be reconstructed efficiently by the standard algorithm, although there is enough activity to reconstruct the additional decay products with a dedicated technique [77]). The backgrounds to such a signature include badly measured tracks, leptons undergoing large bremsstrahlung or scattering, and high-momentum charged hadrons interacting with material in the inner detector, and all are estimated directly from data using smeared tracks in control regions. Additional objects in the events, such as large E_T^{miss} , are usually selected to improve sensitivity to particular SUSY scenarios. The disappearing-track analysis [67] excludes pure-wino charginos with masses up to ~ 850 GeV for lifetimes of about 1 ns, as shown in Figure 18. The mass sensitivity for lower lifetimes is limited by the requirement of a minimum number of hits on the different layers of the inner detector, while the veto on track extensions imposed to satisfy the 'disappearing track' criterion limits the sensitivity at longer lifetimes.

If a charged particle has a longer lifetime, it may propagate beyond the inner detector before decaying. The track it leaves would be rather distinctive, with high ionisation energy loss since the expected high mass of the SUSY particle dictates it must be moving slowly, with $\beta = v/c \ll 1$. An analysis selecting tracks with large ionisation energy loss (dE/dx) in the pixel detector, instead of disappearing tracks, is used to search for longer-lived charged SUSY particles [78]. Careful corrections to the measured dE/dx and reconstructed mass are made to account for the tracker's decreasing charge collection efficiency due to radiation damage as the integrated luminosity increases. The sensitivity offered by the large- dE/dx analysis is complementary to that of the disappearing-track analysis, covering the longer-lifetime scenarios. Wino-like charginos with masses up to ~ 1050 GeV are excluded for lifetimes longer than 10 ns, as shown in Figure 18. The observed limits are weaker than the expected ones because the number of observed events exceeds the background prediction, quantified by a global Z significance of 3.3. This excess was investigated in a more recent

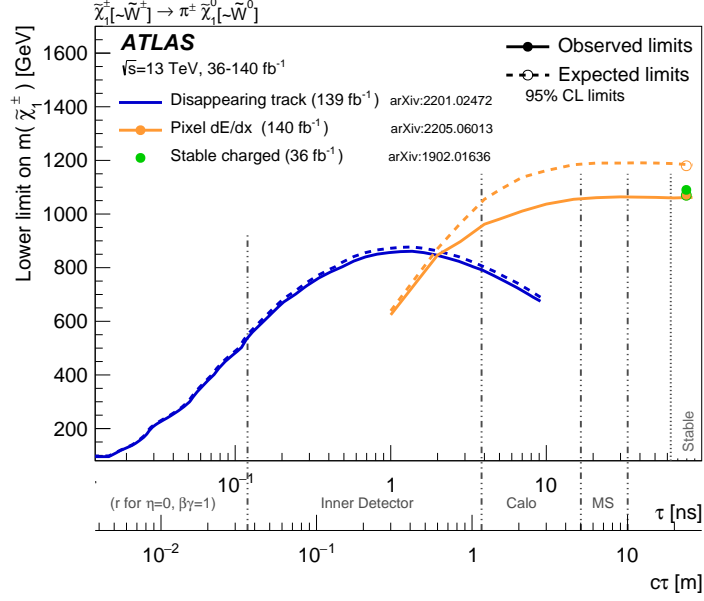


Figure 18: Constraints in the chargino mass-vs-lifetime plane for an AMSB model with $\tan\beta = 5$ and $\mu > 0$. The wino-like chargino is pair-produced and decays into a wino-like neutralino and a very soft charged pion. The solid lines indicate the observed limits, while the dashed lines indicate the expected limits. The area below the curves is excluded. “Calo” and “MS” refer to the ATLAS calorimeter and muon spectrometer systems, respectively. The analyses also have sensitivity at lifetimes other than those shown, but only the limits at tested lifetimes are shown. The three dots at large lifetime represent results for which the particle is assumed to be stable. In this context, stable means escaping the detector. The exclusion contours from the pixel dE/dx search are each extrapolated to the stable regime with a straight line.

analysis [79] which considered measurements of time-of-flight to the calorimeter as well as dE/dx in the pixel detector, and found compatibility with the background prediction.

An alternative approach, sensitive to neutral long-lived SUSY particles leaving no tell-tale track in the inner detector, is to reconstruct the long-lived particle’s decay products. Charged decay products leave tracks that can be traced back to a common displaced vertex, with those from SUSY decays easily distinguishable from SM decays by their large invariant mass. A specialised track reconstruction algorithm optimised for tracks with large impact parameters was used to improve the efficiency of displaced-vertex reconstruction [80]. Random track combinations and merged vertices mimicking a high-mass displaced vertex typically dominate the backgrounds. A smaller component comes from hadronic interactions with detector material that are usually concentrated in regions with high matter density and are vetoed. However, those occurring in less dense regions can also appear as a high-mass displaced vertex. The searches for long-lived SUSY particles using displaced vertices [81] have excluded gluino masses up to 2400 GeV for lifetimes of ~ 0.1 ns, as shown in Figure 19. Prompt-decay SUSY analyses are typically more sensitive to gluino lifetimes below 0.01 ns, while the large- dE/dx and stopped-gluino searches cover the longer lifetimes above ~ 5 ns.

A long-lived gluino may form an R-hadron with a SM vacuum quark, travel part way through the detector, and then stop in the calorimeter due to energy losses via ionisation and nuclear scattering. It may decay at a much later time, from about 100 ns to one year later, so a search for hadronic activity in the absence of collisions, while empty LHC beam bunches pass through ATLAS, is used [82]. The efficiency of R-hadron

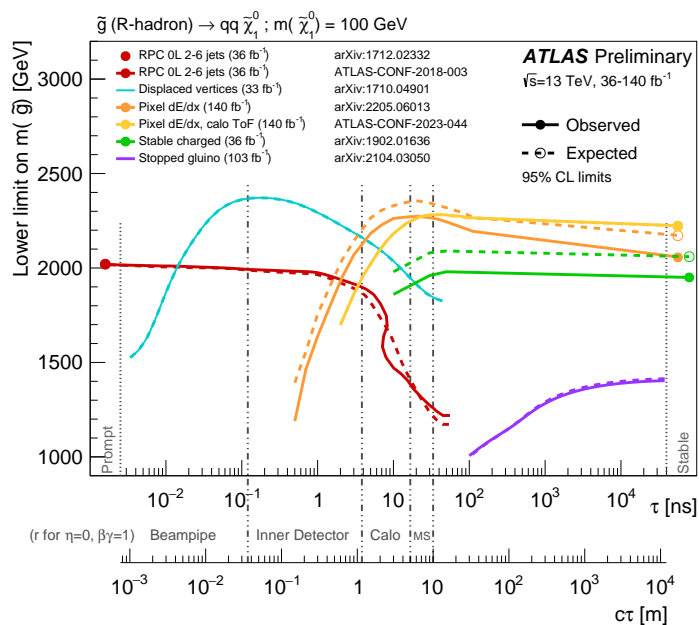


Figure 19: Constraints in the gluino mass-vs-lifetime plane for a split-supersymmetry model with the gluino R-hadron decaying into a gluon or light quarks and a neutralino with a mass of 100 GeV. The solid lines indicate the observed limits, while the dashed lines indicate the expected limits. The regions below the curves are excluded. “Calo” and “MS” refer to the ATLAS calorimeter and muon spectrometer systems, respectively.

detection depends on the fraction that stop in the detector, the probability of R-hadron decay during empty bunches, and the efficiency of hadronic-activity reconstruction [83]. The cosmic-ray muon background is taken from low-luminosity run periods, while the beam-halo background is estimated from unpaired crossings. Long-lived gluinos with masses up to 1400 GeV are excluded for lifetimes of 10^4 – 10^{12} ns, as shown in Figure 19.

Reconstructed objects, such as electrons, muons, and photons, can also be used to search for long-lived SUSY particles. In these cases, the leptons and photons should point back to the decay vertex of the SUSY particle rather than the interaction point, i.e. their tracks should be displaced. The specialised tracking procedure in Ref. [80] reconstructs electrons and muons with large transverse impact parameters, $10 \text{ mm} < |d_0| < 300 \text{ mm}$. The signature is very simple, requiring two large impact parameter ($|d_0| > 3 \text{ mm}$) leptons as expected from the decay of a pair of sleptons [84]. With no significant excess observed in the data, long-lived selectrons and smuons with masses up to about 700 GeV are excluded for lifetimes of about 0.1 ns (or, equivalently, co-NSLP selectron/smuon masses up to 820 GeV), while long-lived staus with masses up to about 340 GeV are excluded for the same lifetime. Another analysis, in Ref. [85], covers shorter-lifetime slepton scenarios, in an attempt to cover any sensitivity gap between long-lived and promptly decaying sleptons: in this case, the analysis uses standard tracking algorithms to select ‘micro-displaced’ leptons with $0.1 \text{ mm} < |d_0| < 3 \text{ mm}$ forming high-mass pairs. With this approach, smuon masses up to 520 GeV are excluded for lifetimes of about 10^{-2} ns.

Despite the lack of tracking information, the flight path of a photon can be traced back to a location other than the collision vertex by using the spatial measurement and timing capabilities of the ATLAS detector’s liquid-argon EM calorimeter. A photon from a long-lived particle decay will have delayed timing compared to promptly produced photons, and the longitudinal shape of the shower will point back to a displaced

vertex instead of the collision vertex. Two such non-pointing photons forming a high-mass displaced vertex are selected (assumed to be from the same decay) in Ref. [86], and these non-pointing photons may also be interpreted as displaced electrons since only EM calorimeter information is used. The background is estimated from data by exploiting the non-correlation in timing and pointing for photons from SM processes. Long-lived neutralinos that decay into a Z boson and gravitino and have lifetimes of 0.2 ns and masses below about 700 GeV are excluded.

In summary, an array of unconventional signatures in the ATLAS detector have been used to search for long-lived SUSY particles. From the implementation of specialised tracking algorithms, to searching for activity in the absence of collisions, the effort extends beyond the boundaries of typical SUSY searches at ATLAS and sets stringent limits on the masses of SUSY particles with lifetimes spanning many orders of magnitude.

9 Beyond simplified models

Having summarised and discussed in Sections 5 to 8 the main exclusion limits obtained from ATLAS Run 2 data when using simplified models, the obvious question is: how do these limits change when more realistic SUSY models are considered?

At the end of Run 1, ATLAS produced two papers trying to answer this question using slightly different methodologies. Reference [14] used a general 19-parameter pMSSM [12, 87] and sampled the parameter space while assuming a flat prior within the chosen parameter range. The models were checked to see if they were excluded by any of the ATLAS analyses available at the time. Results were quoted in terms of the fraction of models excluded at a given sparticle mass. A further study was performed [88] by varying only the pMSSM parameters affecting the electroweak sector ($\tan\beta$, M_1 , M_2 , μ , and M_A) and evaluating a global likelihood for models relevant for an explanation of the dark-matter relic density.

A similar study was repeated at the end of Run 2 [89]. The emphasis was again on the electroweak sector, with the gluino, squarks, and sleptons having very high masses. The five parameters mentioned above were varied (along with other parameters to satisfy constraints connected with the Higgs sector). Two samplings were performed: the ‘EWKino’ sample started from 20 000 models randomly sampled with uniform priors, while the ‘Bino-DM’ sample started with 437 500 models with a bino-like LSP that satisfy a requirement on the observed dark-matter relic density as an upper limit. The ability of several ATLAS Run 2 analyses targeting electroweak production to exclude each of the models considered was assessed. The impact of additional constraints from electroweak precision measurements, flavour observables and dark-matter direct detection experiments was also considered. The technical aspects of processing the large number of models are a testament to the evolution of the reinterpretation and recasting tools that the ATLAS Collaboration produced during Run 2 [90–92], but their discussion is beyond the scope of this paper.

Figure 20 shows, as a function of the electroweakino mass, the fraction of models in the EWKino sample that pass all external constraints but are excluded by ATLAS. In general, the excluded fraction decreases with increasing sparticle mass. About 50% of the models featuring a neutralino LSP with a mass of 500 GeV are excluded by ATLAS. This fraction increases to about 80% for masses of 200 GeV. Heavier electroweakinos with large masses are excluded in a significant fraction of the models: this is often the effect of correlations with the lighter states. For example, in models with a long-lived wino-like lightest chargino, its lifetime is determined by the mass of $\tilde{\chi}_2^0$.

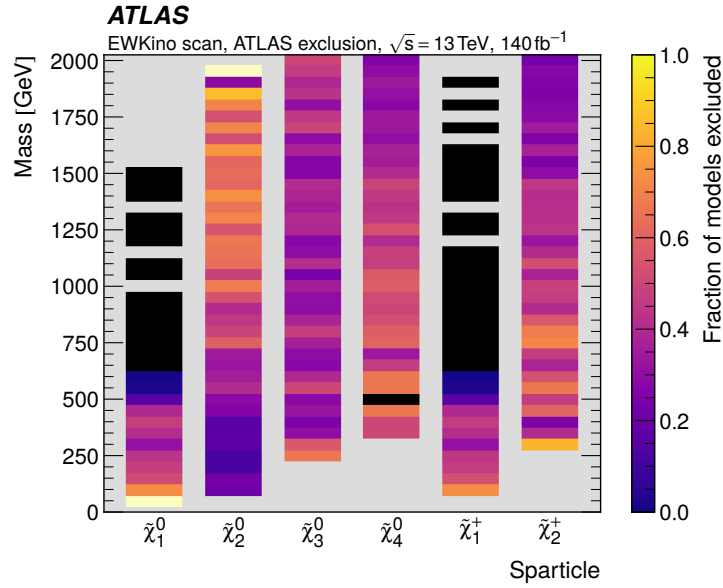


Figure 20: Fraction of models passing external constraints but excluded by ATLAS, depending on the mass of the electroweakinos for the EWKino samples.

A complementary view is given in Figure 21: here the Bino-DM sample is considered, and the fraction of models excluded is given in the format usually used by experiments doing direct searches for dark matter, i.e. in the plane of the WIMP–nucleon spin-independent scattering cross-section versus the mass of the WIMP. ATLAS excludes a very large fraction of the Z/H funnel, where the WIMP mass is close to half the mass of one of the bosons, so that the WIMP self-interaction is regulated by an enhanced cross-section for annihilation via boson exchange. A large fraction of the models are generally excluded for WIMP masses up to about 150 GeV, while the exclusion is progressively more limited above this WIMP mass.

A very useful by-product of studies like the one in Ref. [89] is the identification of classes of models that are not excluded by ATLAS, despite the masses of the involved sparticles being well within the exclusion limits provided by the simplified models. This information was used at the end of Run 1 to design some of the simplified models for Run 2, and will be used again to guide the evolution of the research programme in Run 3 and beyond.

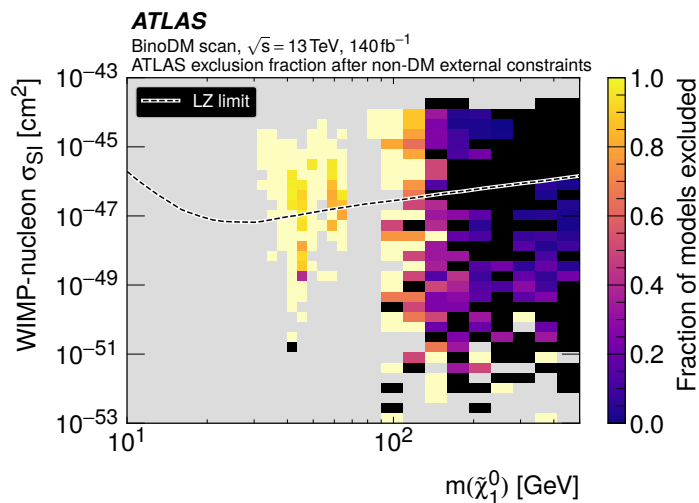


Figure 21: Fraction of models passing all non-DM external constraints but excluded by ATLAS in the WIMP–nucleon spin-independent scattering cross-section vs $m(\tilde{\chi}_1^0)$ plane.

10 Discussion and conclusions

The main results of searches for direct production of supersymmetric particles by the ATLAS Collaboration using the Run 2 dataset are summarised in this paper. The authors hope that the material will provide a useful overview for the casual reader, and a handy collection of references for those actively interested in the subject.

The achievements of the ATLAS Collaboration (and of its counterpart, CMS) are remarkable, and exclude important regions of the parameter space. The question that anyone reading this paper is likely to have in mind at this point is: where does this monumental experimental effort leave the community in terms of the existence of SUSY in nature?

In this form, the question is simply too wide to be answered in a convincing way. Since it is probably impossible to prove that the mass of the photon is exactly zero, it is experimentally impossible to prove that the superpartners of the SM particles do not exist, not even at some very large mass scale. However, the community has concluded that the mass of the photon is small enough to not have any phenomenological consequences for a large variety of phenomena at a cosmological scale. Likewise, one can try to provide answers to specific questions once they are asked in the framework of a supersymmetric theory.

The pre-LHC SUSY landscape was dominated by a relatively small number of frameworks arising from specific top-down approaches to the way SUSY was broken. Models that belong to this family are the constrained MSSM (cMSSM, or mSUGRA), anomaly-mediated SUSY breaking (AMSB), and gauge-mediated SUSY breaking (GMSB). In their minimal forms, the predictions of these models were already under very severe pressure by the end of Run 1. The limits on the masses of the gluinos and squarks (already in the TeV regime at the time) excluded a vast amount of the parameter space for the cMSSM [93]. The limits on pure-wino dark matter imposed by the disappearing-track results severely constrained the existence of long-lived charginos, and the difficulty in accommodating a Higgs boson with a mass of 125 GeV strongly excluded AMSB as a viable framework [94]. Similarly, minimal GMSB needs

top squarks with very high mass to obtain a Higgs boson mass compatible with that observed [95]. Beyond the need to connect searches to specific topologies, the rise of simplified models in Run 2 is also partly due to the heavy pressure of the Run 1 searches and Higgs boson results on mainstream SUSY-breaking models. In short, the Run 1 results changed the theoretical thinking and opened up the parameter space.

The Run 2 research programme was driven by a more agnostic approach – the big questions (such as: Is SUSY the way nature has chosen to stabilise the Higgs boson mass at the electroweak scale? Is SUSY the reason for the existence of dark matter?) were still used as a guideline, but the approach was much closer to ‘turn every stone’ than in the past. The classical paradigm of SUSY as a solution to the hierarchy problem requires higgsinos with masses of at most a few hundred GeV, top squarks at the TeV scale, and gluinos not too far above that. The current limits, well into the few-TeV region for gluinos and a TeV for top squarks, exceed the expectations for classical naturalness definitions, although more modern reanalysis of the arguments relaxes the constraints [96]. For the first time, hadron collider experiments started to surpass the LEP limits on higgsinos – and further investigations into the existence of higgsinos will be a highlight of Run 3 and beyond. As discussed in Section 9, many scenarios that include viable dark-matter candidates have been severely constrained by the LHC results, most notably the Z/h funnels for bino dark matter (those models where the self-annihilation cross-section for binos is enhanced by the proximity of the neutralino mass to half that of the Z or h boson). First sensitivity to the existence of a light stau was achieved during Run 2, although the interesting region for probing the stau funnel as a dark-matter regulation mechanism is still beyond experimental reach.

These results have led to a culture shock in the community: from being the prime candidate as a framework for physics beyond the SM, SUSY at the EW scale seems now to be perceived as a somewhat disfavoured candidate mechanism to extend the SM. Regardless of the community’s perception, the pMSSM scans clearly show that SUSY still has a lot to offer, both as a source of viable models of new physics and as a spectacular tool for generating new signatures, and is thus a source of new ideas for searches. Hopefully, one of the benefits of reviews like this one is to help the average high-energy physicist to put the experimental effort in the right context: despite its main incarnations having been severely impacted by data from the LHC, the framework of EW-scale SUSY still offers viable extensions of the SM.

Together with those from the CMS Collaboration, the results summarised in this paper represent the state of the art (at the time of writing) in the worldwide experimental search for SUSY. No large increase in the centre-of-mass energy of the collisions is foreseen (in the ongoing Run 3, protons are collided at $\sqrt{s} = 13.6$ TeV). While it will take a long time for the size of the available dataset to increase substantially, the authors are confident that the creativity and skill of the experimentalists will improve the sensitivity of ATLAS to SUSY particles at a rate well beyond simple integrated luminosity scaling, as has happened so many times in the past. Therefore, while the results discussed in this paper are based on much of the overall capability of the LHC to probe unexplored territory in the SUSY parameter space, experimental breakthroughs will open new sensitivity windows, and, hopefully, start to shed some light on the questions that still today, more than ever, call for an extension of the Standard Model of particle physics.

Acknowledgements

We thank CERN for the very successful operation of the LHC and its injectors, as well as the support staff at CERN and at our institutions worldwide without whom ATLAS could not be operated efficiently.

The crucial computing support from all WLCG partners is acknowledged gratefully, in particular from CERN, the ATLAS Tier-1 facilities at TRIUMF/SFU (Canada), NDGF (Denmark, Norway, Sweden), CC-IN2P3 (France), KIT/GridKA (Germany), INFN-CNAF (Italy), NL-T1 (Netherlands), PIC (Spain), RAL (UK) and BNL (USA), the Tier-2 facilities worldwide and large non-WLCG resource providers. Major contributors of computing resources are listed in Ref. [97].

We gratefully acknowledge the support of ANPCyT, Argentina; YerPhI, Armenia; ARC, Australia; BMWFW and FWF, Austria; ANAS, Azerbaijan; CNPq and FAPESP, Brazil; NSERC, NRC and CFI, Canada; CERN; ANID, Chile; CAS, MOST and NSFC, China; Minciencias, Colombia; MEYS CR, Czech Republic; DNRF and DNSRC, Denmark; IN2P3-CNRS and CEA-DRF/IRFU, France; SRNSFG, Georgia; BMBF, HGF and MPG, Germany; GSRI, Greece; RGC and Hong Kong SAR, China; ISF and Benoziyo Center, Israel; INFN, Italy; MEXT and JSPS, Japan; CNRST, Morocco; NWO, Netherlands; RCN, Norway; MEiN, Poland; FCT, Portugal; MNE/IFA, Romania; MESTD, Serbia; MSSR, Slovakia; ARRS and MIZŠ, Slovenia; DSI/NRF, South Africa; MICINN, Spain; SRC and Wallenberg Foundation, Sweden; SERI, SNSF and Cantons of Bern and Geneva, Switzerland; MOST, Taipei; TENMAK, Türkiye; STFC, United Kingdom; DOE and NSF, United States of America.

Individual groups and members have received support from BCKDF, CANARIE, CRC and DRAC, Canada; PRIMUS 21/SCI/017 and UNCE SCI/013, Czech Republic; COST, ERC, ERDF, Horizon 2020, ICSC-NextGenerationEU and Marie Skłodowska-Curie Actions, European Union; Investissements d’Avenir Labex, Investissements d’Avenir Idex and ANR, France; DFG and AvH Foundation, Germany; Herakleitos, Thales and Aristeia programmes co-financed by EU-ESF and the Greek NSRF, Greece; BSF-NSF and MINERVA, Israel; Norwegian Financial Mechanism 2014-2021, Norway; NCN and NAWA, Poland; La Caixa Banking Foundation, CERCA Programme Generalitat de Catalunya and PROMETEO and GenT Programmes Generalitat Valenciana, Spain; Göran Gustafssons Stiftelse, Sweden; The Royal Society and Leverhulme Trust, United Kingdom.

In addition, individual members wish to acknowledge support from CERN: European Organization for Nuclear Research (CERN PJAS); Chile: Agencia Nacional de Investigación y Desarrollo (FONDECYT 1190886, FONDECYT 1210400, FONDECYT 1230987); China: National Natural Science Foundation of China (NSFC - 12175119, NSFC 12275265); European Union: European Research Council (ERC - 948254, ERC 101089007), Horizon 2020 Framework Programme (MUCCA - CHIST-ERA-19-XAI-00), Italian Center for High Performance Computing, Big Data and Quantum Computing (ICSC, NextGenerationEU); France: Agence Nationale de la Recherche (ANR-20-CE31-0013, ANR-21-CE31-0022), Investissements d’Avenir Labex (ANR-11-LABX-0012); Germany: Baden-Württemberg Stiftung (BW Stiftung-Postdoc Eliteprogramme), Deutsche Forschungsgemeinschaft (DFG - 469666862, DFG - CR 312/5-2); Italy: Istituto Nazionale di Fisica Nucleare (ICSC, NextGenerationEU); Japan: Japan Society for the Promotion of Science (JSPS KAKENHI 22H01227, JSPS KAKENHI 22KK0227, JSPS KAKENHI JP21H05085, JSPS KAKENHI JP22H04944); Netherlands: Netherlands Organisation for Scientific Research (NWO Veni 2020 - VI.Veni.202.179); Norway: Research Council of Norway (RCN-314472); Poland: Polish National Agency for Academic Exchange (PPN/PPO/2020/1/00002/U/00001), Polish National Science Centre (NCN 2021/42/E/ST2/00350, NCN OPUS nr 2022/47/B/ST2/03059, NCN UMO-2019/34/E/ST2/00393, UMO-2020/37/B/ST2/01043, UMO-2022/47/O/ST2/00148); Slovenia: Slovenian Research Agency (ARIS grant J1-3010); Spain: BBVA Foundation (LEO22-1-603), Generalitat Valenciana (Artemisa, FEDER, IDIFEDER/2018/048), La Caixa Banking Foundation (LCF/BQ/PI20/11760025), Ministry of Science and Innovation (RYC2019-028510-I, RYC2020-030254-I), PROMETEO and GenT Programmes Generalitat Valenciana (CIDEAGENT/2019/023, CIDEAGENT/2019/027); Sweden: Swedish Research Council (VR 2022-03845), Knut and Alice Wallenberg Foundation (KAW 2022.0358); Switzerland: Swiss National

Science Foundation (SNSF - PCEFP2_194658); United Kingdom: Leverhulme Trust (Leverhulme Trust RPG-2020-004); United States of America: Neubauer Family Foundation.

References

- [1] L. Evans and P. Bryant, *LHC Machine*, [JINST 3 \(2008\) S08001](#).
- [2] ATLAS Collaboration, *The ATLAS Experiment at the CERN Large Hadron Collider*, [JINST 3 \(2008\) S08003](#).
- [3] CMS Collaboration, *The CMS Experiment at the CERN LHC*, [JINST 3 \(2008\) S08004](#).
- [4] Y. Golfand and E. Likhtman, *Extension of the Algebra of Poincare Group Generators and Violation of P Invariance*, *JETP Lett.* **13** (1971) 323, [*Pisma Zh. Eksp. Teor. Fiz.* **13** (1971) 452].
- [5] D. Volkov and V. Akulov, *Is the neutrino a goldstone particle?*, [Phys. Lett. B 46 \(1973\) 109](#).
- [6] J. Wess and B. Zumino, *Supergauge transformations in four dimensions*, [Nucl. Phys. B 70 \(1974\) 39](#).
- [7] J. Wess and B. Zumino, *Supergauge invariant extension of quantum electrodynamics*, [Nucl. Phys. B 78 \(1974\) 1](#).
- [8] S. Ferrara and B. Zumino, *Supergauge invariant Yang-Mills theories*, [Nucl. Phys. B 79 \(1974\) 413](#).
- [9] A. Salam and J. Strathdee, *Super-symmetry and non-Abelian gauges*, [Phys. Lett. B 51 \(1974\) 353](#).
- [10] G. R. Farrar and P. Fayet, *Phenomenology of the production, decay, and detection of new hadronic states associated with supersymmetry*, [Phys. Lett. B 76 \(1978\) 575](#).
- [11] A. Djouadi, J.-L. Kneur and G. Moultaka, *SuSpect: A Fortran code for the supersymmetric and Higgs particle spectrum in the MSSM*, [Comput. Phys. Commun. 176 \(2007\) 426](#), arXiv: [hep-ph/0211331](#).
- [12] C. F. Berger, J. S. Gainer, J. L. Hewett and T. G. Rizzo, *Supersymmetry Without Prejudice*, [JHEP 02 \(2009\) 023](#), arXiv: [0812.0980 \[hep-ph\]](#).
- [13] A. Djouadi et al., ‘The Minimal supersymmetric standard model: Group summary report’, *GDR (Groupement De Recherche) - Supersymetrie*, 1999, arXiv: [hep-ph/9901246](#).
- [14] ATLAS Collaboration, *Summary of the ATLAS experiment’s sensitivity to supersymmetry after LHC Run 1 — interpreted in the phenomenological MSSM*, [JHEP 10 \(2015\) 134](#), arXiv: [1508.06608 \[hep-ex\]](#).
- [15] CMS Collaboration, *Phenomenological MSSM interpretation of CMS searches in pp collisions at $\sqrt{s} = 7$ and 8 TeV*, [JHEP 10 \(2016\) 129](#), arXiv: [1606.03577 \[hep-ex\]](#).
- [16] J. Alwall, M.-P. Le, M. Lisanti and J. G. Wacker, *Searching for directly decaying gluinos at the Tevatron*, [Phys. Lett. B 666 \(2008\) 34](#), arXiv: [0803.0019 \[hep-ph\]](#).
- [17] J. Alwall, P. Schuster and N. Toro, *Simplified models for a first characterization of new physics at the LHC*, [Phys. Rev. D 79 \(2009\) 075020](#), arXiv: [0810.3921 \[hep-ph\]](#).

- [18] D. Alves et al., *Simplified models for LHC new physics searches*, *J. Phys. G* **39** (2012) 105005, arXiv: [1105.2838 \[hep-ph\]](#).
- [19] <https://twiki.cern.ch/twiki/bin/view/LHCPhysics/SUSYCrossSections>.
- [20] ATLAS Collaboration, *Performance of the ATLAS trigger system in 2015*, *Eur. Phys. J. C* **77** (2017) 317, arXiv: [1611.09661 \[hep-ex\]](#).
- [21] ATLAS Collaboration, *The ATLAS Collaboration Software and Firmware*, ATL-SOFT-PUB-2021-001, 2021, URL: <https://cds.cern.ch/record/2767187>.
- [22] ATLAS Collaboration, *Tools for estimating fake/non-prompt lepton backgrounds with the ATLAS detector at the LHC*, *JINST* **18** (2023) T11004, arXiv: [2211.16178 \[hep-ex\]](#).
- [23] ATLAS Collaboration, *Improved description of the di-tau final state in events with associated production of a W boson and jets in the ATLAS detector using the tau-promotion method*, ATL-PHYS-PUB-2019-039, 2019, URL: <https://cds.cern.ch/record/2692073>.
- [24] G. Cowan, K. Cranmer, E. Gross and O. Vitells, *Asymptotic formulae for likelihood-based tests of new physics*, *Eur. Phys. J. C* **71** (2011) 1554, arXiv: [1007.1727 \[physics.data-an\]](#), Erratum: *Eur. Phys. J. C* **73** (2013) 2501.
- [25] A. L. Read, *Presentation of search results: the CL_S technique*, *J. Phys. G* **28** (2002) 2693.
- [26] G. Giudice and A. Romanino, *Split supersymmetry*, *Nucl. Phys. B* **699** (2004) 65, arXiv: [hep-ph/0406088](#), Erratum: *Nucl. Phys. B* **706** (2005) 65.
- [27] N. Arkani-Hamed and S. Dimopoulos, *Supersymmetric unification without low energy supersymmetry and signatures for fine-tuning at the LHC*, *JHEP* **06** (2005) 073, arXiv: [hep-th/0405159](#).
- [28] ATLAS Collaboration, *Search for squarks and gluinos in final states with jets and missing transverse momentum using 139 fb^{-1} of $\sqrt{s} = 13\text{ TeV}$ pp collision data with the ATLAS detector*, *JHEP* **02** (2021) 143, arXiv: [2010.14293 \[hep-ex\]](#).
- [29] ATLAS Collaboration, *Search for squarks and gluinos with the ATLAS detector in final states with jets and missing transverse momentum using 4.7 fb^{-1} of $\sqrt{s} = 7\text{ TeV}$ proton–proton collision data*, *Phys. Rev. D* **87** (2013) 012008, arXiv: [1208.0949 \[hep-ex\]](#).
- [30] ATLAS Collaboration, *Search for squarks and gluinos in final states with one isolated lepton, jets, and missing transverse momentum at $\sqrt{s} = 13\text{ TeV}$ with the ATLAS detector*, *Eur. Phys. J. C* **81** (2021) 600, arXiv: [2101.01629 \[hep-ex\]](#), Erratum: *Eur. Phys. J. C* **81** (2021) 956.
- [31] ATLAS Collaboration, *Searches for new phenomena in events with two leptons, jets, and missing transverse momentum in 139 fb^{-1} of $\sqrt{s} = 13\text{ TeV}$ pp collisions with the ATLAS detector*, *Eur. Phys. J. C* **83** (2023) 515, arXiv: [2204.13072 \[hep-ex\]](#).
- [32] ATLAS Collaboration, *Search for new phenomena in final states with large jet multiplicities and missing transverse momentum using $\sqrt{s} = 13\text{ TeV}$ proton–proton collisions recorded by ATLAS in Run 2 of the LHC*, *JHEP* **10** (2020) 062, arXiv: [2008.06032 \[hep-ex\]](#).
- [33] ATLAS Collaboration, *Search for pair production of squarks or gluinos decaying via sleptons or weak bosons in final states with two same-sign or three leptons with the ATLAS detector*, *JHEP* **02** (2024) 107, arXiv: [2307.01094 \[hep-ex\]](#).

- [34] P. Meade, N. Seiberg and D. Shih, *General Gauge Mediation*, *Prog. Theor. Phys. Suppl.* **177** (2009) 143, arXiv: [0801.3278 \[hep-ph\]](#).
- [35] ATLAS Collaboration, *ATLAS flavour-tagging algorithms for the LHC Run 2 pp collision dataset*, *Eur. Phys. J. C* **83** (2023) 681, arXiv: [2211.16345 \[physics.data-an\]](#).
- [36] ATLAS Collaboration, *Search for supersymmetry in final states with missing transverse momentum and three or more b-jets in 139 fb^{-1} of proton–proton collisions at $\sqrt{s} = 13\text{ TeV}$ with the ATLAS detector*, *Eur. Phys. J. C* **83** (2023) 561, arXiv: [2211.08028 \[hep-ex\]](#).
- [37] ATLAS Collaboration, *Search for new phenomena in events with an energetic jet and missing transverse momentum in pp collisions at $\sqrt{s} = 13\text{ TeV}$ with the ATLAS detector*, *Phys. Rev. D* **103** (2021) 112006, arXiv: [2102.10874 \[hep-ex\]](#).
- [38] S. Heinemeyer, *MSSM Higgs physics at higher orders*, *Int. J. Mod. Phys. A* **21** (2006) 2659, arXiv: [hep-ph/0407244](#).
- [39] ATLAS Collaboration, *Search for new phenomena in final states with b-jets and missing transverse momentum in $\sqrt{s} = 13\text{ TeV}$ pp collisions with the ATLAS detector*, *JHEP* **05** (2021) 093, arXiv: [2101.12527 \[hep-ex\]](#).
- [40] D. R. Tovey, *On measuring the masses of pair-produced semi-invisibly decaying particles at hadron colliders*, *JHEP* **04** (2008) 034, arXiv: [0802.2879 \[hep-ph\]](#).
- [41] ATLAS Collaboration, *Soft b-hadron tagging for compressed SUSY scenarios*, ATLAS-CONF-2019-027, 2019, URL: <https://cds.cern.ch/record/2682131>.
- [42] ATLAS Collaboration, *Search for bottom-squark pair production with the ATLAS detector in final states containing Higgs bosons, b-jets and missing transverse momentum*, *JHEP* **12** (2019) 060, arXiv: [1908.03122 \[hep-ex\]](#).
- [43] ATLAS Collaboration, *Search for bottom-squark pair production in pp collision events at $\sqrt{s} = 13\text{ TeV}$ with hadronically decaying τ -leptons, b-jets and missing transverse momentum using the ATLAS detector*, *Phys. Rev. D* **104** (2021) 032014, arXiv: [2103.08189 \[hep-ex\]](#).
- [44] ATLAS Collaboration, *Search for supersymmetry in final states with charm jets and missing transverse momentum in 13 TeV pp collisions with the ATLAS detector*, *JHEP* **09** (2018) 050, arXiv: [1805.01649 \[hep-ex\]](#).
- [45] ATLAS Collaboration, *ATLAS Run 1 searches for direct pair production of third-generation squarks at the Large Hadron Collider*, *Eur. Phys. J. C* **75** (2015) 510, arXiv: [1506.08616 \[hep-ex\]](#).
- [46] ATLAS Collaboration, *Search for a scalar partner of the top quark in the all-hadronic $t\bar{t}$ plus missing transverse momentum final state at $\sqrt{s} = 13\text{ TeV}$ with the ATLAS detector*, *Eur. Phys. J. C* **80** (2020) 737, arXiv: [2004.14060 \[hep-ex\]](#).
- [47] ATLAS Collaboration, *Search for new phenomena with top quark pairs in final states with one lepton, jets, and missing transverse momentum in pp collisions at $\sqrt{s} = 13\text{ TeV}$ with the ATLAS detector*, *JHEP* **04** (2021) 174, arXiv: [2012.03799 \[hep-ex\]](#).

- [48] ATLAS Collaboration, *Search for new phenomena in events with two opposite-charge leptons, jets and missing transverse momentum in pp collisions at $\sqrt{s} = 13$ TeV with the ATLAS detector*, [JHEP **04** \(2021\) 165](#), arXiv: [2102.01444 \[hep-ex\]](#).
- [49] ATLAS Collaboration, *Measurements of top-quark pair spin correlations in the $e\mu$ channel at $\sqrt{s} = 13$ TeV using pp collisions in the ATLAS detector*, [Eur. Phys. J. C **80** \(2020\) 754](#), arXiv: [1903.07570 \[hep-ex\]](#).
- [50] ATLAS Collaboration, *Search for top squarks in events with a Higgs or Z boson using 139fb^{-1} of pp collision data at $\sqrt{s} = 13$ TeV with the ATLAS detector*, [Eur. Phys. J. C **80** \(2020\) 1080](#), arXiv: [2006.05880 \[hep-ex\]](#).
- [51] ATLAS Collaboration, *Search for new phenomena in pp collisions in final states with tau leptons, b-jets, and missing transverse momentum with the ATLAS detector*, [Phys. Rev. D **104** \(2021\) 112005](#), arXiv: [2108.07665 \[hep-ex\]](#).
- [52] ATLAS Collaboration, *A search for top-squark pair production, in final states containing a top quark, a charm quark and missing transverse momentum, using the 139fb^{-1} of pp collision data collected by the ATLAS detector*, (2024), arXiv: [2402.12137 \[hep-ex\]](#).
- [53] ATLAS Collaboration, *Search for electroweak production of charginos and sleptons decaying into final states with two leptons and missing transverse momentum in $\sqrt{s} = 13$ TeV pp collisions using the ATLAS detector*, [Eur. Phys. J. C **80** \(2020\) 123](#), arXiv: [1908.08215 \[hep-ex\]](#).
- [54] ATLAS Collaboration, *Search for direct pair production of sleptons and charginos decaying to two leptons and neutralinos with mass splittings near the W-boson mass in $\sqrt{s} = 13$ TeV pp collisions with the ATLAS detector*, [JHEP **06** \(2023\) 031](#), arXiv: [2209.13935 \[hep-ex\]](#).
- [55] C. G. Lester and D. J. Summers, *Measuring masses of semi-invisibly decaying particle pairs produced at hadron colliders*, [Phys. Lett. B **463** \(1999\) 99](#), arXiv: [hep-ph/9906349](#).
- [56] ATLAS Collaboration, *Searches for electroweak production of supersymmetric particles with compressed mass spectra in $\sqrt{s} = 13$ TeV pp collisions with the ATLAS detector*, [Phys. Rev. D **101** \(2020\) 052005](#), arXiv: [1911.12606 \[hep-ex\]](#).
- [57] ATLAS Collaboration, *Search for direct stau production in events with two hadronic τ -leptons in $\sqrt{s} = 13$ TeV pp collisions with the ATLAS detector*, [Phys. Rev. D **101** \(2020\) 032009](#), arXiv: [1911.06660 \[hep-ex\]](#).
- [58] ATLAS Collaboration, *Search for electroweak production of supersymmetric particles in final states with two τ -leptons in $\sqrt{s} = 13$ TeV pp collisions with the ATLAS detector*, (2024), arXiv: [2402.00603 \[hep-ex\]](#).
- [59] ATLAS Collaboration, *Search for electroweak production of supersymmetric particles in final states with two or three leptons at $\sqrt{s} = 13$ TeV with the ATLAS detector*, [Eur. Phys. J. C **78** \(2018\) 995](#), arXiv: [1803.02762 \[hep-ex\]](#).
- [60] ATLAS Collaboration, *Search for charginos and neutralinos in final states with two boosted hadronically decaying bosons and missing transverse momentum in pp collisions at $\sqrt{s} = 13$ TeV with the ATLAS detector*, [Phys. Rev. D **104** \(2021\) 112010](#), arXiv: [2108.07586 \[hep-ex\]](#).

- [61] ATLAS Collaboration, *Search for direct production of electroweakinos in final states with one lepton, jets and missing transverse momentum in pp collisions at $\sqrt{s} = 13$ TeV with the ATLAS detector*, (2023), arXiv: [2310.08171 \[hep-ex\]](#).
- [62] ATLAS Collaboration, *A statistical combination of ATLAS Run 2 searches for charginos and neutralinos at the LHC*, (2024), arXiv: [2402.08347 \[hep-ex\]](#).
- [63] ATLAS Collaboration, *Search for chargino–neutralino pair production in final states with three leptons and missing transverse momentum in $\sqrt{s} = 13$ TeV pp collisions with the ATLAS detector*, *Eur. Phys. J. C* **81** (2021) 1118, arXiv: [2106.01676 \[hep-ex\]](#).
- [64] ATLAS Collaboration, *Search for direct production of electroweakinos in final states with one lepton, missing transverse momentum and a Higgs boson decaying into two b-jets in pp collisions at $\sqrt{s} = 13$ TeV with the ATLAS detector*, *Eur. Phys. J. C* **80** (2020) 691, arXiv: [1909.09226 \[hep-ex\]](#).
- [65] ATLAS Collaboration, *Search for direct production of winos and higgsinos in events with two same-charge leptons or three leptons in pp collision data at $\sqrt{s} = 13$ TeV with the ATLAS detector*, *JHEP* **11** (2023) 150, arXiv: [2305.09322 \[hep-ex\]](#).
- [66] H. Baer, V. Barger, P. Huang and X. Tata, *Natural Supersymmetry: LHC, dark matter and ILC searches*, *JHEP* **05** (2012) 109, arXiv: [1203.5539 \[hep-ph\]](#).
- [67] ATLAS Collaboration, *Search for long-lived charginos based on a disappearing-track signature using 136fb^{-1} of pp collisions at $\sqrt{s} = 13$ TeV with the ATLAS detector*, *Eur. Phys. J. C* **82** (2022) 606, arXiv: [2201.02472 \[hep-ex\]](#).
- [68] ATLAS Collaboration, *Search for nearly mass-degenerate higgsinos using low-momentum mildly-displaced tracks in pp collisions at $\sqrt{s} = 13$ TeV with the ATLAS detector*, (2024), arXiv: [2401.14046 \[hep-ex\]](#).
- [69] The LEP SUSY Working Group and the ALEPH, DELPHI, L3 and OPAL experiments, note LEPSUSYWG/02-04.1, <http://lepsusy.web.cern.ch/lepsusy/Welcome.html>.
- [70] ATLAS Collaboration, *Search for supersymmetry in events with four or more charged leptons in 139fb^{-1} of $\sqrt{s} = 13$ TeV pp collisions with the ATLAS detector*, *JHEP* **07** (2021) 167, arXiv: [2103.11684 \[hep-ex\]](#).
- [71] ATLAS Collaboration, *Search for pair production of higgsinos in events with two Higgs bosons and missing transverse momentum in $\sqrt{s}=13$ TeV pp collisions at the ATLAS experiment*, (2024), arXiv: [2401.14922 \[hep-ex\]](#).
- [72] ATLAS Collaboration, *Search for pair-produced Higgsinos decaying via Higgs or Z bosons to final states containing a pair of photons and a pair of b-jets with the ATLAS detector*, ATLAS-CONF-2023-009, 2023, URL: <https://cds.cern.ch/record/2854839>.
- [73] ATLAS Collaboration, *Search for supersymmetry in events with four or more leptons in $\sqrt{s} = 8$ TeV pp collisions with the ATLAS detector*, *Phys. Rev. D* **90** (2014) 052001, arXiv: [1405.5086 \[hep-ex\]](#).
- [74] ATLAS Collaboration, *Search for R-parity-violating supersymmetry in a final state containing leptons and many jets with the ATLAS experiment using $\sqrt{s} = 13$ TeV proton–proton collision data*, *Eur. Phys. J. C* **81** (2021) 1023, arXiv: [2106.09609 \[hep-ex\]](#).

- [75] ATLAS Collaboration, *A search for R-parity-violating supersymmetry in final states containing many jets in pp collisions at $\sqrt{s} = 13$ TeV with the ATLAS detector*, 2024, arXiv: [2401.16333 \[hep-ex\]](#).
- [76] ATLAS Collaboration, *Search for trilepton resonances from chargino and neutralino pair production in $\sqrt{s} = 13$ TeV pp collisions with the ATLAS detector*, *Phys. Rev. D* **103** (2021) 112003, arXiv: [2011.10543 \[hep-ex\]](#).
- [77] ATLAS Collaboration, *Performance of tracking and vertexing techniques for a disappearing track plus soft track signature with the ATLAS detector*, ATL-PHYS-PUB-2019-011, 2019, URL: <https://cds.cern.ch/record/2669015>.
- [78] ATLAS Collaboration, *Search for heavy, long-lived, charged particles with large ionisation energy loss in pp collisions at $\sqrt{s} = 13$ TeV using the ATLAS experiment and the full Run 2 dataset*, *JHEP* **06** (2023) 158, arXiv: [2205.06013 \[hep-ex\]](#).
- [79] ATLAS Collaboration, *Search for heavy, long-lived charged particles with large specific ionisation and low-beta in 140fb^{-1} of pp collisions at $\sqrt{s} = 13$ TeV using the ATLAS experiment*, ATLAS-CONF-2023-044, 2023, URL: <https://cds.cern.ch/record/2870112>.
- [80] ATLAS Collaboration, *Performance of the reconstruction of large impact parameter tracks in the inner detector of ATLAS*, ATL-PHYS-PUB-2017-014, 2017, URL: <https://cds.cern.ch/record/2275635>.
- [81] ATLAS Collaboration, *Search for long-lived, massive particles in events with displaced vertices and multiple jets in pp collisions at $\sqrt{s} = 13$ TeV with the ATLAS detector*, *JHEP* **06** (2023) 200, arXiv: [2301.13866 \[hep-ex\]](#).
- [82] ATLAS Collaboration, *A search for the decays of stopped long-lived particles at $\sqrt{s} = 13$ TeV with the ATLAS detector*, *JHEP* **07** (2021) 173, arXiv: [2104.03050 \[hep-ex\]](#).
- [83] ATLAS Collaboration, *Generation and Simulation of R-Hadrons in the ATLAS Experiment*, ATL-PHYS-PUB-2019-019, 2019, URL: <https://cds.cern.ch/record/2676309>.
- [84] ATLAS Collaboration, *Search for displaced leptons in $\sqrt{s} = 13$ TeV pp collisions with the ATLAS detector*, *Phys. Rev. Lett.* **127** (2021) 051802, arXiv: [2011.07812 \[hep-ex\]](#).
- [85] ATLAS Collaboration, *Search for pairs of muons with small displacements in pp collisions at $\sqrt{s} = 13$ TeV with the ATLAS detector*, *Phys. Lett. B* **846** (2023) 138172, arXiv: [2305.02005 \[hep-ex\]](#).
- [86] ATLAS Collaboration, *Search in diphoton and dielectron final states for displaced production of Higgs or Z bosons with the ATLAS detector in $\sqrt{s} = 13$ TeV pp collisions*, *Phys. Rev. D* **108** (2023) 012012, arXiv: [2304.12885 \[hep-ex\]](#).
- [87] M. W. Cahill-Rowley, J. L. Hewett, S. Hoeche, A. Ismail and T. G. Rizzo, *The New Look pMSSM with Neutralino and Gravitino LSPs*, *Eur. Phys. J. C* **72** (2012) 2156, arXiv: [1206.4321 \[hep-ph\]](#).
- [88] ATLAS Collaboration, *Dark matter interpretations of ATLAS searches for the electroweak production of supersymmetric particles in $\sqrt{s} = 8$ TeV proton-proton collisions*, *JHEP* **09** (2016) 175, arXiv: [1608.00872 \[hep-ex\]](#).
- [89] ATLAS Collaboration, *ATLAS Run 2 searches for electroweak production of supersymmetric particles interpreted within the pMSSM*, (2024), arXiv: [2402.01392 \[hep-ex\]](#).

- [90] ATLAS Collaboration, *SimpleAnalysis: Truth-level Analysis Framework*, ATL-PHYS-PUB-2022-017, 2022, URL: <https://cds.cern.ch/record/2805991>.
- [91] ATLAS Collaboration, *Implementation of simplified likelihoods in HistFactory for searches for supersymmetry*, ATL-PHYS-PUB-2021-038, 2021, URL: <https://cds.cern.ch/record/2782654>.
- [92] ATLAS Collaboration, *Reproducing searches for new physics with the ATLAS experiment through publication of full statistical likelihoods*, ATL-PHYS-PUB-2019-029, 2019, URL: <https://cds.cern.ch/record/2684863>.
- [93] O. Buchmueller et al., *The CMSSM and NUHM1 after LHC Run 1*, *Eur. Phys. J. C* **74** (2014) 2922, arXiv: [1312.5250](https://arxiv.org/abs/1312.5250) [hep-ph].
- [94] H. Baer, V. Barger and D. Sengupta, *Anomaly-mediated SUSY breaking model retrofitted for naturalness*, *Phys. Rev. D* **98** (2018) 015039, arXiv: [1801.09730](https://arxiv.org/abs/1801.09730) [hep-ph].
- [95] A. Delgado, M. Garcia-Pepin and M. Quiros, *GMSB with Light Stops*, *JHEP* **08** (2015) 159, arXiv: [1505.07469](https://arxiv.org/abs/1505.07469) [hep-ph].
- [96] H. Baer et al., *What hadron collider is required to discover or falsify natural supersymmetry?*, *Phys. Lett. B* **774** (2017) 451, arXiv: [1702.06588](https://arxiv.org/abs/1702.06588) [hep-ph].
- [97] ATLAS Collaboration, *ATLAS Computing Acknowledgements*, ATL-SOFT-PUB-2023-001, 2023, URL: <https://cds.cern.ch/record/2869272>.

The ATLAS Collaboration

G. Aad ¹⁰³, E. Aakvaag ¹⁶, B. Abbott ¹²¹, K. Abeling ⁵⁵, N.J. Abicht ⁴⁹, S.H. Abidi ²⁹, M. Aboeela ⁴⁴, A. Aboulhorma ^{35e}, H. Abramowicz ¹⁵², H. Abreu ¹⁵¹, Y. Abulaiti ¹¹⁸, B.S. Acharya ^{69a,69b,1}, A. Ackermann ^{63a}, C. Adam Bourdarios ⁴, L. Adamczyk ^{86a}, S.V. Addepalli ²⁶, M.J. Addison ¹⁰², J. Adelman ¹¹⁶, A. Adiguzel ^{21c}, T. Adye ¹³⁵, A.A. Affolder ¹³⁷, Y. Afik ³⁹, M.N. Agaras ¹³, J. Agarwala ^{73a,73b}, A. Aggarwal ¹⁰¹, C. Agheorghiesei ^{27c}, A. Ahmad ³⁶, F. Ahmadov ^{38,y}, W.S. Ahmed ¹⁰⁵, S. Ahuja ⁹⁶, X. Ai ^{62e}, G. Aielli ^{76a,76b}, A. Aikot ¹⁶⁴, M. Ait Tamlihat ^{35e}, B. Aitbenchikh ^{35a}, I. Aizenberg ¹⁷⁰, M. Akbiyik ¹⁰¹, T.P.A. Åkesson ⁹⁹, A.V. Akimov ³⁷, D. Akiyama ¹⁶⁹, N.N. Akolkar ²⁴, S. Aktas ^{21a}, K. Al Houry ⁴¹, G.L. Alberghi ^{23b}, J. Albert ¹⁶⁶, P. Albicocco ⁵³, G.L. Albouy ⁶⁰, S. Alderweireldt ⁵², Z.L. Alegria ¹²², M. Aleksa ³⁶, I.N. Aleksandrov ³⁸, C. Alexa ^{27b}, T. Alexopoulos ¹⁰, F. Alfonsi ^{23b}, M. Algren ⁵⁶, M. Alhroob ¹⁴², B. Ali ¹³³, H.M.J. Ali ⁹², S. Ali ¹⁴⁹, S.W. Alibocus ⁹³, M. Aliev ^{33c}, G. Alimonti ^{71a}, W. Alkakhri ⁵⁵, C. Allaire ⁶⁶, B.M.M. Allbrooke ¹⁴⁷, J.F. Allen ⁵², C.A. Allendes Flores ^{138f}, P.P. Allport ²⁰, A. Aloisio ^{72a,72b}, F. Alonso ⁹¹, C. Alpigiani ¹³⁹, M. Alvarez Estevez ¹⁰⁰, A. Alvarez Fernandez ¹⁰¹, M. Alves Cardoso ⁵⁶, M.G. Alviggi ^{72a,72b}, M. Aly ¹⁰², Y. Amaral Coutinho ^{83b}, A. Ambler ¹⁰⁵, C. Amelung ³⁶, M. Amerl ¹⁰², C.G. Ames ¹¹⁰, D. Amidei ¹⁰⁷, K.J. Amirie ¹⁵⁶, S.P. Amor Dos Santos ^{131a}, K.R. Amos ¹⁶⁴, S. An ⁸⁴, V. Ananiev ¹²⁶, C. Anastopoulos ¹⁴⁰, T. Andeen ¹¹, J.K. Anders ³⁶, S.Y. Andrean ^{47a,47b}, A. Andreazza ^{71a,71b}, S. Angelidakis ⁹, A. Angerami ^{41,aa}, A.V. Anisenkov ³⁷, A. Annovi ^{74a}, C. Antel ⁵⁶, M.T. Anthony ¹⁴⁰, E. Antipov ¹⁴⁶, M. Antonelli ⁵³, F. Anulli ^{75a}, M. Aoki ⁸⁴, T. Aoki ¹⁵⁴, J.A. Aparisi Pozo ¹⁶⁴, M.A. Aparo ¹⁴⁷, L. Aperio Bella ⁴⁸, C. Appelt ¹⁸, A. Apyan ²⁶, S.J. Arbiol Val ⁸⁷, C. Arcangeletti ⁵³, A.T.H. Arce ⁵¹, E. Arena ⁹³, J-F. Arguin ¹⁰⁹, S. Argyropoulos ⁵⁴, J.-H. Arling ⁴⁸, O. Arnaez ⁴, H. Arnold ¹¹⁵, G. Artoni ^{75a,75b}, H. Asada ¹¹², K. Asai ¹¹⁹, S. Asai ¹⁵⁴, N.A. Asbah ³⁶, K. Assamagan ²⁹, R. Astalos ^{28a}, K.S.V. Astrand ⁹⁹, S. Atashi ¹⁶⁰, R.J. Atkin ^{33a}, M. Atkinson ¹⁶³, H. Atmani ^{35f}, P.A. Atlasiddha ¹²⁹, K. Augsten ¹³³, S. Auricchio ^{72a,72b}, A.D. Auriol ²⁰, V.A. Austrup ¹⁰², G. Avolio ³⁶, K. Axiotis ⁵⁶, G. Azuelos ^{109,ae}, D. Babal ^{28b}, H. Bachacou ¹³⁶, K. Bachas ^{153,p}, A. Bachi ³⁴, F. Backman ^{47a,47b}, A. Badea ³⁹, T.M. Baer ¹⁰⁷, P. Bagnaia ^{75a,75b}, M. Bahmani ¹⁸, D. Bahner ⁵⁴, K. Bai ¹²⁴, A.J. Bailey ¹⁶⁴, J.T. Baines ¹³⁵, L. Baines ⁹⁵, O.K. Baker ¹⁷³, E. Bakos ¹⁵, D. Bakshi Gupta ⁸, V. Balakrishnan ¹²¹, R. Balasubramanian ¹¹⁵, E.M. Baldin ³⁷, P. Balek ^{86a}, E. Ballabene ^{23b,23a}, F. Balli ¹³⁶, L.M. Baltes ^{63a}, W.K. Balunas ³², J. Balz ¹⁰¹, E. Banas ⁸⁷, M. Bandieramonte ¹³⁰, A. Bandyopadhyay ²⁴, S. Bansal ²⁴, L. Barak ¹⁵², M. Barakat ⁴⁸, E.L. Barberio ¹⁰⁶, D. Barberis ^{57b,57a}, M. Barbero ¹⁰³, M.Z. Barel ¹¹⁵, K.N. Barends ^{33a}, T. Barillari ¹¹¹, M-S. Barisits ³⁶, T. Barklow ¹⁴⁴, P. Baron ¹²³, D.A. Baron Moreno ¹⁰², A. Baroncelli ^{62a}, G. Barone ²⁹, A.J. Barr ¹²⁷, J.D. Barr ⁹⁷, F. Barreiro ¹⁰⁰, J. Barreiro Guimarães da Costa ^{14a}, U. Barron ¹⁵², M.G. Barros Teixeira ^{131a}, S. Barsov ³⁷, F. Bartels ^{63a}, R. Bartoldus ¹⁴⁴, A.E. Barton ⁹², P. Bartos ^{28a}, A. Basan ¹⁰¹, M. Baselga ⁴⁹, A. Bassalat ^{66,b}, M.J. Basso ^{157a}, R.L. Bates ⁵⁹, S. Batlamous ^{35e}, B. Batool ¹⁴², M. Battaglia ¹³⁷, D. Battulga ¹⁸, M. Baucé ^{75a,75b}, M. Bauer ³⁶, P. Bauer ²⁴, L.T. Bazzano Hurrell ³⁰, J.B. Beacham ⁵¹, T. Beau ¹²⁸, J.Y. Beaucamp ⁹¹, P.H. Beauchemin ¹⁵⁹, P. Bechtel ²⁴, H.P. Beck ^{19,o}, K. Becker ¹⁶⁸, A.J. Beddall ⁸², V.A. Bednyakov ³⁸, C.P. Bee ¹⁴⁶, L.J. Beemster ¹⁵, T.A. Beermann ³⁶, M. Begalli ^{83d}, M. Begel ²⁹, A. Behera ¹⁴⁶, J.K. Behr ⁴⁸, J.F. Beirer ³⁶, F. Beisiegel ²⁴, M. Belfkir ^{117b}, G. Bella ¹⁵², L. Bellagamba ^{23b}, A. Bellerive ³⁴, P. Bellos ²⁰, K. Beloborodov ³⁷, D. Bencheikroun ^{35a}, F. Bendebba ^{35a}, Y. Benhammou ¹⁵²,

K.C. Benkendorfer ⁶¹, L. Beresford ⁴⁸, M. Beretta ⁵³, E. Bergeaas Kuutmann ¹⁶², N. Berger ⁴,
 B. Bergmann ¹³³, J. Beringer ^{17a}, G. Bernardi ⁵, C. Bernius ¹⁴⁴, F.U. Bernlochner ²⁴,
 F. Bernon ^{36,103}, A. Berrocal Guardia ¹³, T. Berry ⁹⁶, P. Berta ¹³⁴, A. Berthold ⁵⁰, S. Bethke ¹¹¹,
 A. Betti ^{75a,75b}, A.J. Bevan ⁹⁵, N.K. Bhalla ⁵⁴, M. Bhamjee ^{33c}, S. Bhatta ¹⁴⁶,
 D.S. Bhattacharya ¹⁶⁷, P. Bhattarai ¹⁴⁴, K.D. Bhide ⁵⁴, V.S. Bhopatkar ¹²², R.M. Bianchi ¹³⁰,
 G. Bianco ^{23b,23a}, O. Biebel ¹¹⁰, R. Bielski ¹²⁴, M. Biglietti ^{77a}, C.S. Billingsley ⁴⁴, M. Bindi ⁵⁵,
 A. Bingul ^{21b}, C. Bini ^{75a,75b}, A. Biondini ⁹³, C.J. Birch-sykes ¹⁰², G.A. Bird ³², M. Birman ¹⁷⁰,
 M. Biros ¹³⁴, S. Biryukov ¹⁴⁷, T. Bisanz ⁴⁹, E. Bisceglie ^{43b,43a}, J.P. Biswal ¹³⁵, D. Biswas ¹⁴²,
 K. Bjørke ¹²⁶, I. Bloch ⁴⁸, A. Blue ⁵⁹, U. Blumenschein ⁹⁵, J. Blumenthal ¹⁰¹,
 V.S. Bobrovnikov ³⁷, M. Boehler ⁵⁴, B. Boehm ¹⁶⁷, D. Bogovac ³⁶, A.G. Bogdanchikov ³⁷,
 C. Bohm ^{47a}, V. Boisvert ⁹⁶, P. Bokan ³⁶, T. Bold ^{86a}, M. Bomben ⁵, M. Bona ⁹⁵,
 M. Boonekamp ¹³⁶, C.D. Booth ⁹⁶, A.G. Borbély ⁵⁹, I.S. Bordulev ³⁷, H.M. Borecka-Bielska ¹⁰⁹,
 G. Borissov ⁹², D. Bortoletto ¹²⁷, D. Boscherini ^{23b}, M. Bosman ¹³, J.D. Bossio Sola ³⁶,
 K. Bouaouda ^{35a}, N. Bouchhar ¹⁶⁴, J. Boudreau ¹³⁰, E.V. Bouhova-Thacker ⁹², D. Boumediene ⁴⁰,
 R. Bouquet ^{57b,57a}, A. Boveia ¹²⁰, J. Boyd ³⁶, D. Boye ²⁹, I.R. Boyko ³⁸, J. Bracinik ²⁰,
 N. Brahimy ⁴, G. Brandt ¹⁷², O. Brandt ³², F. Braren ⁴⁸, B. Brau ¹⁰⁴, J.E. Brau ¹²⁴,
 R. Brenner ¹⁷⁰, L. Brenner ¹¹⁵, R. Brenner ¹⁶², S. Bressler ¹⁷⁰, D. Britton ⁵⁹, D. Britzger ¹¹¹,
 I. Brock ²⁴, G. Brooijmans ⁴¹, E. Brost ²⁹, L.M. Brown ¹⁶⁶, L.E. Bruce ⁶¹, T.L. Bruckler ¹²⁷,
 P.A. Bruckman de Renstrom ⁸⁷, B. Brüers ⁴⁸, A. Bruni ^{23b}, G. Bruni ^{23b}, M. Bruschi ^{23b},
 N. Brusino ^{75a,75b}, T. Buanes ¹⁶, Q. Buat ¹³⁹, D. Buchin ¹¹¹, A.G. Buckley ⁵⁹, O. Bulekov ³⁷,
 B.A. Bullard ¹⁴⁴, S. Burdin ⁹³, C.D. Burgard ⁴⁹, A.M. Burger ³⁶, B. Burghgrave ⁸,
 O. Burlayenko ⁵⁴, J.T.P. Burr ³², C.D. Burton ¹¹, J.C. Burzynski ¹⁴³, E.L. Busch ⁴¹,
 V. Büscher ¹⁰¹, P.J. Bussey ⁵⁹, J.M. Butler ²⁵, C.M. Buttar ⁵⁹, J.M. Butterworth ⁹⁷,
 W. Buttinger ¹³⁵, C.J. Buxo Vazquez ¹⁰⁸, A.R. Buzykaev ³⁷, S. Cabrera Urbán ¹⁶⁴,
 L. Cadamuro ⁶⁶, D. Caforio ⁵⁸, H. Cai ¹³⁰, Y. Cai ^{14a,14e}, Y. Cai ^{14c}, V.M.M. Cairo ³⁶,
 O. Cakir ^{3a}, N. Calace ³⁶, P. Calafiura ^{17a}, G. Calderini ¹²⁸, P. Calfayan ⁶⁸, G. Callea ⁵⁹,
 L.P. Caloba ^{83b}, D. Calvet ⁴⁰, S. Calvet ⁴⁰, M. Calvetti ^{74a,74b}, R. Camacho Toro ¹²⁸,
 S. Camarda ³⁶, D. Camarero Munoz ²⁶, P. Camarri ^{76a,76b}, M.T. Camerlingo ^{72a,72b},
 D. Cameron ³⁶, C. Camincher ¹⁶⁶, M. Campanelli ⁹⁷, A. Camplani ⁴², V. Canale ^{72a,72b},
 A.C. Canbay ^{3a}, E. Canonero ⁹⁶, J. Cantero ¹⁶⁴, Y. Cao ¹⁶³, F. Capocasa ²⁶, M. Capua ^{43b,43a},
 A. Carbone ^{71a,71b}, R. Cardarelli ^{76a}, J.C.J. Cardenas ⁸, F. Cardillo ¹⁶⁴, G. Carducci ^{43b,43a},
 T. Carli ³⁶, G. Carlino ^{72a}, J.I. Carlotto ¹³, B.T. Carlson ^{130,q}, E.M. Carlson ^{166,157a},
 L. Carminati ^{71a,71b}, A. Carnelli ¹³⁶, M. Carnesale ^{75a,75b}, S. Caron ¹¹⁴, E. Carquin ^{138f},
 S. Carrá ^{71a}, G. Carratta ^{23b,23a}, A.M. Carroll ¹²⁴, T.M. Carter ⁵², M.P. Casado ^{13,i},
 M. Caspar ⁴⁸, F.L. Castillo ⁴, L. Castillo Garcia ¹³, V. Castillo Gimenez ¹⁶⁴, N.F. Castro ^{131a,131e},
 A. Catinaccio ³⁶, J.R. Catmore ¹²⁶, T. Cavaliere ⁴, V. Cavaliere ²⁹, N. Cavalli ^{23b,23a},
 Y.C. Cekmecelioglu ⁴⁸, E. Celebi ^{21a}, S. Cella ³⁶, F. Celli ¹²⁷, M.S. Centonze ^{70a,70b},
 V. Cepaitis ⁵⁶, K. Cerny ¹²³, A.S. Cerqueira ^{83a}, A. Cerri ¹⁴⁷, L. Cerrito ^{76a,76b}, F. Cerutti ^{17a},
 B. Cervato ¹⁴², A. Cervelli ^{23b}, G. Cesarini ⁵³, S.A. Cetin ⁸², D. Chakraborty ¹¹⁶, J. Chan ¹⁷¹,
 W.Y. Chan ¹⁵⁴, J.D. Chapman ³², E. Chapon ¹³⁶, B. Chargeishvili ^{150b}, D.G. Charlton ²⁰,
 M. Chatterjee ¹⁹, C. Chauhan ¹³⁴, Y. Che ^{14c}, S. Chekanov ⁶, S.V. Chekulaev ^{157a},
 G.A. Chelkov ^{38,a}, A. Chen ¹⁰⁷, B. Chen ¹⁵², B. Chen ¹⁶⁶, H. Chen ^{14c}, H. Chen ²⁹,
 J. Chen ^{62c}, J. Chen ¹⁴³, M. Chen ¹²⁷, S. Chen ¹⁵⁴, S.J. Chen ^{14c}, X. Chen ^{62c,136},
 X. Chen ^{14b,ad}, Y. Chen ^{62a}, C.L. Cheng ¹⁷¹, H.C. Cheng ^{64a}, S. Cheong ¹⁴⁴, A. Cheplakov ³⁸,
 E. Cheremushkina ⁴⁸, E. Cherepanova ¹¹⁵, R. Cherkaoui El Moursli ^{35e}, E. Cheu ⁷, K. Cheung ⁶⁵,
 L. Chevalier ¹³⁶, V. Chiarella ⁵³, G. Chiarelli ^{74a}, N. Chiedde ¹⁰³, G. Chiodini ^{70a},
 A.S. Chisholm ²⁰, A. Chitan ^{27b}, M. Chitishvili ¹⁶⁴, M.V. Chizhov ³⁸, K. Choi ¹¹, Y. Chou ¹³⁹,

E.Y.S. Chow ¹¹⁴, K.L. Chu ¹⁷⁰, M.C. Chu ^{64a}, X. Chu ^{14a,14e}, J. Chudoba ¹³²,
 J.J. Chwastowski ⁸⁷, D. Cieri ¹¹¹, K.M. Ciesla ^{86a}, V. Cindro ⁹⁴, A. Ciocio ^{17a}, F. Cirotto ^{72a,72b},
 Z.H. Citron ¹⁷⁰, M. Citterio ^{71a}, D.A. Ciubotaru ^{27b}, A. Clark ⁵⁶, P.J. Clark ⁵², C. Clarry ¹⁵⁶,
 J.M. Clavijo Columbie ⁴⁸, S.E. Clawson ⁴⁸, C. Clement ^{47a,47b}, J. Clercx ⁴⁸, Y. Coadou ¹⁰³,
 M. Cobal ^{69a,69c}, A. Coccaro ^{57b}, R.F. Coelho Barrue ^{131a}, R. Coelho Lopes De Sa ¹⁰⁴,
 S. Coelli ^{71a}, B. Cole ⁴¹, J. Collot ⁶⁰, P. Conde Muiño ^{131a,131g}, M.P. Connell ^{33c},
 S.H. Connell ^{33c}, E.I. Conroy ¹²⁷, F. Conventi ^{72a,af}, H.G. Cooke ²⁰, A.M. Cooper-Sarkar ¹²⁷,
 A. Cordeiro Oudot Choi ¹²⁸, L.D. Corpe ⁴⁰, M. Corradi ^{75a,75b}, F. Corriveau ^{105,w},
 A. Cortes-Gonzalez ¹⁸, M.J. Costa ¹⁶⁴, F. Costanza ⁴, D. Costanzo ¹⁴⁰, B.M. Cote ¹²⁰,
 G. Cowan ⁹⁶, K. Cranmer ¹⁷¹, D. Cremonini ^{23b,23a}, S. Crépe-Renaudin ⁶⁰, F. Crescioli ¹²⁸,
 M. Cristinziani ¹⁴², M. Cristoforetti ^{78a,78b}, V. Croft ¹¹⁵, J.E. Crosby ¹²², G. Crosetti ^{43b,43a},
 A. Cueto ¹⁰⁰, H. Cui ^{14a,14e}, Z. Cui ⁷, W.R. Cunningham ⁵⁹, F. Curcio ¹⁶⁴, J.R. Curran ⁵²,
 P. Czodrowski ³⁶, M.M. Czurylo ³⁶, M.J. Da Cunha Sargedas De Sousa ^{57b,57a},
 J.V. Da Fonseca Pinto ^{83b}, C. Da Via ¹⁰², W. Dabrowski ^{86a}, T. Dado ⁴⁹, S. Dahbi ¹⁴⁹,
 T. Dai ¹⁰⁷, D. Dal Santo ¹⁹, C. Dallapiccola ¹⁰⁴, M. Dam ⁴², G. D'amen ²⁹, V. D'Amico ¹¹⁰,
 J. Damp ¹⁰¹, J.R. Dandoy ³⁴, M. Danninger ¹⁴³, V. Dao ³⁶, G. Darbo ^{57b}, S.J. Das ^{29,ag},
 F. Dattola ⁴⁸, S. D'Auria ^{71a,71b}, A. D'avanzo ^{72a,72b}, C. David ^{33a}, T. Davidek ¹³⁴,
 B. Davis-Purcell ³⁴, I. Dawson ⁹⁵, H.A. Day-hall ¹³³, K. De ⁸, R. De Asmundis ^{72a},
 N. De Biase ⁴⁸, S. De Castro ^{23b,23a}, N. De Groot ¹¹⁴, P. de Jong ¹¹⁵, H. De la Torre ¹¹⁶,
 A. De Maria ^{14c}, A. De Salvo ^{75a}, U. De Sanctis ^{76a,76b}, F. De Santis ^{70a,70b}, A. De Santo ¹⁴⁷,
 J.B. De Vivie De Regie ⁶⁰, D.V. Dedovich ³⁸, J. Degens ⁹³, A.M. Deiana ⁴⁴, F. Del Corso ^{23b,23a},
 J. Del Peso ¹⁰⁰, F. Del Rio ^{63a}, L. Delagrangé ¹²⁸, F. Deliot ¹³⁶, C.M. Delitzsch ⁴⁹,
 M. Della Pietra ^{72a,72b}, D. Della Volpe ⁵⁶, A. Dell'Acqua ³⁶, L. Dell'Asta ^{71a,71b}, M. Delmastro ⁴,
 P.A. Delsart ⁶⁰, S. Demers ¹⁷³, M. Demichev ³⁸, S.P. Denisov ³⁷, L. D'Eramo ⁴⁰,
 D. Derendarz ⁸⁷, F. Derue ¹²⁸, P. Dervan ⁹³, K. Desch ²⁴, C. Deutsch ²⁴, F.A. Di Bello ^{57b,57a},
 A. Di Ciaccio ^{76a,76b}, L. Di Ciaccio ⁴, A. Di Domenico ^{75a,75b}, C. Di Donato ^{72a,72b},
 A. Di Girolamo ³⁶, G. Di Gregorio ³⁶, A. Di Luca ^{78a,78b}, B. Di Micco ^{77a,77b}, R. Di Nardo ^{77a,77b},
 M. Diamantopoulou ³⁴, F.A. Dias ¹¹⁵, T. Dias Do Vale ¹⁴³, M.A. Diaz ^{138a,138b},
 F.G. Diaz Capriles ²⁴, M. Didenko ¹⁶⁴, E.B. Diehl ¹⁰⁷, S. Díez Cornell ⁴⁸, C. Diez Pardo ¹⁴²,
 C. Dimitriadi ^{162,24}, A. Dimitrievska ^{17a}, J. Dingfelder ²⁴, I-M. Dinu ^{27b}, S.J. Dittmeier ^{63b},
 F. Dittus ³⁶, M. Divisek ¹³⁴, F. Djama ¹⁰³, T. Djobava ^{150b}, C. Doglioni ^{102,99}, A. Dohnalova ^{28a},
 J. Dolejsi ¹³⁴, Z. Dolezal ¹³⁴, K.M. Dona ³⁹, M. Donadelli ^{83c}, B. Dong ¹⁰⁸, J. Donini ⁴⁰,
 A. D'Onofrio ^{72a,72b}, M. D'Onofrio ⁹³, J. Dopke ¹³⁵, A. Doria ^{72a}, N. Dos Santos Fernandes ^{131a},
 P. Dougan ¹⁰², M.T. Dova ⁹¹, A.T. Doyle ⁵⁹, M.A. Draguet ¹²⁷, E. Dreyer ¹⁷⁰,
 I. Drivas-koulouris ¹⁰, M. Drnevich ¹¹⁸, M. Drozdova ⁵⁶, D. Du ^{62a}, T.A. du Pree ¹¹⁵,
 F. Dubinin ³⁷, M. Dubovsky ^{28a}, E. Duchovni ¹⁷⁰, G. Duckeck ¹¹⁰, O.A. Ducu ^{27b}, D. Duda ⁵²,
 A. Dudarev ³⁶, E.R. Duden ²⁶, M. D'uffizi ¹⁰², L. Duflost ⁶⁶, M. Dührssen ³⁶, I. Duminica ^{27g},
 A.E. Dumitriu ^{27b}, M. Dunford ^{63a}, S. Dungs ⁴⁹, K. Dunne ^{47a,47b}, A. Duperrin ¹⁰³,
 H. Duran Yildiz ^{3a}, M. Düren ⁵⁸, A. Durglishvili ^{150b}, B.L. Dwyer ¹¹⁶, G.I. Dyckes ^{17a},
 M. Dyndal ^{86a}, B.S. Dziedzic ⁸⁷, Z.O. Earnshaw ¹⁴⁷, G.H. Eberwein ¹²⁷, B. Eckerova ^{28a},
 S. Eggebrecht ⁵⁵, E. Egidio Purcino De Souza ¹²⁸, L.F. Ehrke ⁵⁶, G. Eigen ¹⁶, K. Einsweiler ^{17a},
 T. Ekelof ¹⁶², P.A. Ekman ⁹⁹, S. El Farkh ^{35b}, Y. El Ghazali ^{35b}, H. El Jarrari ³⁶,
 A. El Moussaouy ¹⁰⁹, V. Ellajosyula ¹⁶², M. Ellert ¹⁶², F. Ellinghaus ¹⁷², N. Ellis ³⁶,
 J. Elmsheuser ²⁹, M. Elsayy ^{117a}, M. Elsing ³⁶, D. Emelianov ¹³⁵, Y. Enari ¹⁵⁴, I. Ene ^{17a},
 S. Epari ¹³, P.A. Erland ⁸⁷, M. Errenst ¹⁷², M. Escalier ⁶⁶, C. Escobar ¹⁶⁴, E. Etzion ¹⁵²,
 G. Evans ^{131a}, H. Evans ⁶⁸, L.S. Evans ⁹⁶, A. Ezhilov ³⁷, S. Ezzarqtouni ^{35a}, F. Fabbri ^{23b,23a},
 L. Fabbri ^{23b,23a}, G. Facini ⁹⁷, V. Fadeyev ¹³⁷, R.M. Fakhruddinov ³⁷, D. Fakoudis ¹⁰¹,

S. Falciano ^{75a}, L.F. Falda Ulhoa Coelho ³⁶, P.J. Falke ²⁴, J. Faltova ¹³⁴, C. Fan ¹⁶³, Y. Fan ^{14a},
 Y. Fang ^{14a,14e}, M. Fanti ^{71a,71b}, M. Faraj ^{69a,69b}, Z. Farazpay ⁹⁸, A. Farbin ⁸, A. Farilla ^{77a},
 T. Farooque ¹⁰⁸, S.M. Farrington ⁵², F. Fassi ^{35e}, D. Fassouliotis ⁹, M. Faucci Giannelli ^{76a,76b},
 W.J. Fawcett ³², L. Fayard ⁶⁶, P. Federic ¹³⁴, P. Federicova ¹³², O.L. Fedin ^{37,a}, M. Feickert ¹⁷¹,
 L. Feligioni ¹⁰³, D.E. Fellers ¹²⁴, C. Feng ^{62b}, M. Feng ^{14b}, Z. Feng ¹¹⁵, M.J. Fenton ¹⁶⁰,
 L. Ferencz ⁴⁸, R.A.M. Ferguson ⁹², S.I. Fernandez Luengo ^{138f}, P. Fernandez Martinez ¹³,
 M.J.V. Fernoux ¹⁰³, J. Ferrando ⁹², A. Ferrari ¹⁶², P. Ferrari ^{115,114}, R. Ferrari ^{73a}, D. Ferrere ⁵⁶,
 C. Ferretti ¹⁰⁷, F. Fiedler ¹⁰¹, P. Fiedler ¹³³, A. Filipčič ⁹⁴, E.K. Filmer ¹, F. Filthaut ¹¹⁴,
 M.C.N. Fiolhais ^{131a,131c,c}, L. Fiorini ¹⁶⁴, W.C. Fisher ¹⁰⁸, T. Fitschen ¹⁰², P.M. Fitzhugh ¹³⁶,
 I. Fleck ¹⁴², P. Fleischmann ¹⁰⁷, T. Flick ¹⁷², M. Flores ^{33d,ab}, L.R. Flores Castillo ^{64a},
 L. Flores Sanz De Acedo ³⁶, F.M. Follega ^{78a,78b}, N. Fomin ¹⁶, J.H. Foo ¹⁵⁶, A. Formica ¹³⁶,
 A.C. Forti ¹⁰², E. Fortin ³⁶, A.W. Fortman ^{17a}, M.G. Foti ^{17a}, L. Fountas ^{9j}, D. Fournier ⁶⁶,
 H. Fox ⁹², P. Francavilla ^{74a,74b}, S. Francescato ⁶¹, S. Franchellucci ⁵⁶, M. Franchini ^{23b,23a},
 S. Franchino ^{63a}, D. Francis ³⁶, L. Franco ¹¹⁴, V. Franco Lima ³⁶, L. Franconi ⁴⁸, M. Franklin ⁶¹,
 G. Frattari ²⁶, W.S. Freund ^{83b}, Y.Y. Frid ¹⁵², J. Friend ⁵⁹, N. Fritzsche ⁵⁰, A. Froch ⁵⁴,
 D. Froidevaux ³⁶, J.A. Frost ¹²⁷, Y. Fu ^{62a}, S. Fuenzalida Garrido ^{138f}, M. Fujimoto ¹⁰³,
 K.Y. Fung ^{64a}, E. Furtado De Simas Filho ^{83e}, M. Furukawa ¹⁵⁴, J. Fuster ¹⁶⁴, A. Gabrielli ^{23b,23a},
 A. Gabrielli ¹⁵⁶, P. Gadow ³⁶, G. Gagliardi ^{57b,57a}, L.G. Gagnon ^{17a}, S. Galantzan ¹⁵²,
 E.J. Gallas ¹²⁷, B.J. Gallop ¹³⁵, K.K. Gan ¹²⁰, S. Ganguly ¹⁵⁴, Y. Gao ⁵²,
 F.M. Garay Walls ^{138a,138b}, B. Garcia ²⁹, C. García ¹⁶⁴, A. Garcia Alonso ¹¹⁵,
 A.G. Garcia Caffaro ¹⁷³, J.E. García Navarro ¹⁶⁴, M. Garcia-Sciveres ^{17a}, G.L. Gardner ¹²⁹,
 R.W. Gardner ³⁹, N. Garelli ¹⁵⁹, D. Garg ⁸⁰, R.B. Garg ^{144,m}, J.M. Gargan ⁵², C.A. Garner ¹⁵⁶,
 C.M. Garvey ^{33a}, P. Gaspar ^{83b}, V.K. Gassmann ¹⁵⁹, G. Gaudio ^{73a}, V. Gautam ¹³, P. Gauzzi ^{75a,75b},
 I.L. Gavrilenko ³⁷, A. Gavrilyuk ³⁷, C. Gay ¹⁶⁵, G. Gaycken ⁴⁸, E.N. Gazis ¹⁰, A.A. Geanta ^{27b},
 C.M. Gee ¹³⁷, A. Gekow ¹²⁰, C. Gemme ^{57b}, M.H. Genest ⁶⁰, A.D. Gentry ¹¹³, S. George ⁹⁶,
 W.F. George ²⁰, T. Geralis ⁴⁶, P. Gessinger-Befurt ³⁶, M.E. Geyik ¹⁷², M. Ghani ¹⁶⁸,
 K. Ghorbanian ⁹⁵, A. Ghosal ¹⁴², A. Ghosh ¹⁶⁰, A. Ghosh ⁷, B. Giacobbe ^{23b}, S. Giagu ^{75a,75b},
 T. Giani ¹¹⁵, P. Giannetti ^{74a}, A. Giannini ^{62a}, S.M. Gibson ⁹⁶, M. Gignac ¹³⁷, D.T. Gil ^{86b},
 A.K. Gilbert ^{86a}, B.J. Gilbert ⁴¹, D. Gillberg ³⁴, G. Gilles ¹¹⁵, L. Ginabat ¹²⁸,
 D.M. Gingrich ^{2,ae}, M.P. Giordani ^{69a,69c}, P.F. Giraud ¹³⁶, G. Giugliarelli ^{69a,69c}, D. Giugni ^{71a},
 F. Giuli ³⁶, I. Gkialas ^{9j}, L.K. Gladilin ³⁷, C. Glasman ¹⁰⁰, G.R. Gledhill ¹²⁴, G. Glemža ⁴⁸,
 M. Glisic ¹²⁴, I. Gnesi ^{43b,f}, Y. Go ²⁹, M. Goblirsch-Kolb ³⁶, B. Gocke ⁴⁹, D. Godin ¹⁰⁹,
 B. Gokturk ^{21a}, S. Goldfarb ¹⁰⁶, T. Golling ⁵⁶, M.G.D. Gololo ^{33g}, D. Golubkov ³⁷,
 J.P. Gombas ¹⁰⁸, A. Gomes ^{131a,131b}, G. Gomes Da Silva ¹⁴², A.J. Gomez Delegido ¹⁶⁴,
 R. Gonçalves ^{131a,131c}, L. Gonella ²⁰, A. Gongadze ^{150c}, F. Gonnella ²⁰, J.L. Gonski ¹⁴⁴,
 R.Y. González Andana ⁵², S. González de la Hoz ¹⁶⁴, R. Gonzalez Lopez ⁹³,
 C. Gonzalez Renteria ^{17a}, M.V. Gonzalez Rodrigues ⁴⁸, R. Gonzalez Suarez ¹⁶²,
 S. Gonzalez-Sevilla ⁵⁶, L. Goossens ³⁶, B. Gorini ³⁶, E. Gorini ^{70a,70b}, A. Gorišek ⁹⁴,
 T.C. Gosart ¹²⁹, A.T. Goshaw ⁵¹, M.I. Gostkin ³⁸, S. Goswami ¹²², C.A. Gottardo ³⁶,
 S.A. Gotz ¹¹⁰, M. Gouighri ^{35b}, V. Goumarre ⁴⁸, A.G. Goussiou ¹³⁹, N. Govender ^{33c},
 I. Grabowska-Bold ^{86a}, K. Graham ³⁴, E. Gramstad ¹²⁶, S. Grancagnolo ^{70a,70b}, C.M. Grant ^{1,136},
 P.M. Gravila ^{27f}, F.G. Gravili ^{70a,70b}, H.M. Gray ^{17a}, M. Greco ^{70a,70b}, C. Grefe ²⁴,
 I.M. Gregor ⁴⁸, K.T. Greif ¹⁶⁰, P. Grenier ¹⁴⁴, S.G. Grewe ¹¹¹, A.A. Grillo ¹³⁷, K. Grimm ³¹,
 S. Grinstein ^{13,s}, J.-F. Grivaz ⁶⁶, E. Gross ¹⁷⁰, J. Grosse-Knetter ⁵⁵, J.C. Grundy ¹²⁷,
 L. Guan ¹⁰⁷, C. Gubbels ¹⁶⁵, J.G.R. Guerrero Rojas ¹⁶⁴, G. Guerrieri ^{69a,69c}, F. Guescini ¹¹¹,
 R. Gugel ¹⁰¹, J.A.M. Guhit ¹⁰⁷, A. Guida ¹⁸, E. Guilloton ¹⁶⁸, S. Guindon ³⁶, F. Guo ^{14a,14e},
 J. Guo ^{62c}, L. Guo ⁴⁸, Y. Guo ¹⁰⁷, R. Gupta ⁴⁸, R. Gupta ¹³⁰, S. Gurbuz ²⁴, S.S. Gurdasani ⁵⁴,

G. Gustavino ³⁶, M. Guth ⁵⁶, P. Gutierrez ¹²¹, L.F. Gutierrez Zagazeta ¹²⁹, M. Gutsche ⁵⁰, C. Gutschow ⁹⁷, C. Gwenlan ¹²⁷, C.B. Gwilliam ⁹³, E.S. Haaland ¹²⁶, A. Haas ¹¹⁸, M. Habedank ⁴⁸, C. Haber ^{17a}, H.K. Hadavand ⁸, A. Hadeef ⁵⁰, S. Hadzic ¹¹¹, A.I. Hagan ⁹², J.J. Hahn ¹⁴², E.H. Haines ⁹⁷, M. Haleem ¹⁶⁷, J. Haley ¹²², J.J. Hall ¹⁴⁰, G.D. Hallewell ¹⁰³, L. Halser ¹⁹, K. Hamano ¹⁶⁶, M. Hamer ²⁴, G.N. Hamity ⁵², E.J. Hampshire ⁹⁶, J. Han ^{62b}, K. Han ^{62a}, L. Han ^{14c}, L. Han ^{62a}, S. Han ^{17a}, Y.F. Han ¹⁵⁶, K. Hanagaki ⁸⁴, M. Hance ¹³⁷, D.A. Hangal ⁴¹, H. Hanif ¹⁴³, M.D. Hank ¹²⁹, J.B. Hansen ⁴², P.H. Hansen ⁴², K. Hara ¹⁵⁸, D. Harada ⁵⁶, T. Harenberg ¹⁷², S. Harkusha ³⁷, M.L. Harris ¹⁰⁴, Y.T. Harris ¹²⁷, J. Harrison ¹³, N.M. Harrison ¹²⁰, P.F. Harrison ¹⁶⁸, N.M. Hartman ¹¹¹, N.M. Hartmann ¹¹⁰, Y. Hasegawa ¹⁴¹, S. Hassan ¹⁶, R. Hauser ¹⁰⁸, C.M. Hawkes ²⁰, R.J. Hawkins ³⁶, Y. Hayashi ¹⁵⁴, S. Hayashida ¹¹², D. Hayden ¹⁰⁸, C. Hayes ¹⁰⁷, R.L. Hayes ¹¹⁵, C.P. Hays ¹²⁷, J.M. Hays ⁹⁵, H.S. Hayward ⁹³, F. He ^{62a}, M. He ^{14a,14e}, Y. He ¹⁵⁵, Y. He ⁴⁸, Y. He ⁹⁷, N.B. Heatley ⁹⁵, V. Hedberg ⁹⁹, A.L. Heggelund ¹²⁶, N.D. Hehir ^{95,*}, C. Heidegger ⁵⁴, K.K. Heidegger ⁵⁴, W.D. Heidorn ⁸¹, J. Heilman ³⁴, S. Heim ⁴⁸, T. Heim ^{17a}, J.G. Heinlein ¹²⁹, J.J. Heinrich ¹²⁴, L. Heinrich ^{111,ac}, J. Hejbal ¹³², A. Held ¹⁷¹, S. Hellesund ¹⁶, C.M. Helling ¹⁶⁵, S. Hellman ^{47a,47b}, R.C.W. Henderson ⁹², L. Henkelmann ³², A.M. Henriques Correia ³⁶, H. Herde ⁹⁹, Y. Hernández Jiménez ¹⁴⁶, L.M. Herrmann ²⁴, T. Herrmann ⁵⁰, G. Herten ⁵⁴, R. Hertenberger ¹¹⁰, L. Hervas ³⁶, M.E. Hesping ¹⁰¹, N.P. Hessey ^{157a}, E. Hill ¹⁵⁶, S.J. Hillier ²⁰, J.R. Hinds ¹⁰⁸, F. Hinterkeuser ²⁴, M. Hirose ¹²⁵, S. Hirose ¹⁵⁸, D. Hirschbuehl ¹⁷², T.G. Hitchings ¹⁰², B. Hiti ⁹⁴, J. Hobbs ¹⁴⁶, R. Hobincu ^{27e}, N. Hod ¹⁷⁰, M.C. Hodgkinson ¹⁴⁰, B.H. Hodgkinson ¹²⁷, A. Hoecker ³⁶, D.D. Hofer ¹⁰⁷, J. Hofer ⁴⁸, T. Holm ²⁴, M. Holzbock ¹¹¹, L.B.A.H. Hommels ³², B.P. Honan ¹⁰², J. Hong ^{62c}, T.M. Hong ¹³⁰, B.H. Hooberman ¹⁶³, W.H. Hopkins ⁶, Y. Horii ¹¹², S. Hou ¹⁴⁹, A.S. Howard ⁹⁴, J. Howarth ⁵⁹, J. Hoya ⁶, M. Hrabovsky ¹²³, A. Hrynevich ⁴⁸, T. Hryn'ova ⁴, P.J. Hsu ⁶⁵, S.-C. Hsu ¹³⁹, M. Hu ^{17a}, Q. Hu ^{62a}, S. Huang ^{64b}, X. Huang ^{14a,14e}, Y. Huang ¹⁴⁰, Y. Huang ^{14a}, Z. Huang ¹⁰², Z. Hubacek ¹³³, M. Huebner ²⁴, F. Huegging ²⁴, T.B. Huffman ¹²⁷, C.A. Hugli ⁴⁸, M. Huhtinen ³⁶, S.K. Huiberts ¹⁶, R. Hulsken ¹⁰⁵, N. Huseynov ¹², J. Huston ¹⁰⁸, J. Huth ⁶¹, R. Hyneman ¹⁴⁴, G. Iacobucci ⁵⁶, G. Iakovidis ²⁹, I. Ibragimov ¹⁴², L. Iconomidou-Fayard ⁶⁶, J.P. Iddon ³⁶, P. Iengo ^{72a,72b}, R. Iguchi ¹⁵⁴, T. Iizawa ¹²⁷, Y. Ikegami ⁸⁴, N. Ilic ¹⁵⁶, H. Imam ^{35a}, M. Ince Lezki ⁵⁶, T. Ingebretsen Carlson ^{47a,47b}, G. Introzzi ^{73a,73b}, M. Iodice ^{77a}, V. Ippolito ^{75a,75b}, R.K. Irwin ⁹³, M. Ishino ¹⁵⁴, W. Islam ¹⁷¹, C. Issever ^{18,48}, S. Istin ^{21a,ai}, H. Ito ¹⁶⁹, R. Iuppa ^{78a,78b}, A. Ivina ¹⁷⁰, J.M. Izen ⁴⁵, V. Izzo ^{72a}, P. Jacka ^{132,133}, P. Jackson ¹, B.P. Jaeger ¹⁴³, C.S. Jagfeld ¹¹⁰, G. Jain ^{157a}, P. Jain ⁵⁴, K. Jakobs ⁵⁴, T. Jakoubek ¹⁷⁰, J. Jamieson ⁵⁹, K.W. Janas ^{86a}, M. Javurkova ¹⁰⁴, L. Jeanty ¹²⁴, J. Jejelava ^{150a,z}, P. Jenni ^{54,g}, C.E. Jessiman ³⁴, C. Jia ^{62b}, J. Jia ¹⁴⁶, X. Jia ⁶¹, X. Jia ^{14a,14e}, Z. Jia ^{14c}, S. Jiggins ⁴⁸, J. Jimenez Pena ¹³, S. Jin ^{14c}, A. Jinaru ^{27b}, O. Jinnouchi ¹⁵⁵, P. Johansson ¹⁴⁰, K.A. Johns ⁷, J.W. Johnson ¹³⁷, D.M. Jones ¹⁴⁷, E. Jones ⁴⁸, P. Jones ³², R.W.L. Jones ⁹², T.J. Jones ⁹³, H.L. Joos ^{55,36}, R. Joshi ¹²⁰, J. Jovicevic ¹⁵, X. Ju ^{17a}, J.J. Junggeburth ¹⁰⁴, T. Junkermann ^{63a}, A. Juste Rozas ^{13,s}, M.K. Juzek ⁸⁷, S. Kabana ^{138e}, A. Kaczmarska ⁸⁷, M. Kado ¹¹¹, H. Kagan ¹²⁰, M. Kagan ¹⁴⁴, A. Kahn ⁴¹, A. Kahn ¹²⁹, C. Kahra ¹⁰¹, T. Kaji ¹⁵⁴, E. Kajomovitz ¹⁵¹, N. Kakati ¹⁷⁰, I. Kalaitzidou ⁵⁴, C.W. Kalderon ²⁹, N.J. Kang ¹³⁷, D. Kar ^{33g}, K. Karava ¹²⁷, M.J. Kareem ^{157b}, E. Karentzos ⁵⁴, I. Karkanias ¹⁵³, O. Karkout ¹¹⁵, S.N. Karpov ³⁸, Z.M. Karpova ³⁸, V. Kartvelishvili ⁹², A.N. Karyukhin ³⁷, E. Kasimi ¹⁵³, J. Katzy ⁴⁸, S. Kaur ³⁴, K. Kawade ¹⁴¹, M.P. Kawale ¹²¹, C. Kawamoto ⁸⁸, T. Kawamoto ^{62a}, E.F. Kay ³⁶, F.I. Kaya ¹⁵⁹, S. Kazakos ¹⁰⁸, V.F. Kazanin ³⁷, Y. Ke ¹⁴⁶, J.M. Keaveney ^{33a}, R. Keeler ¹⁶⁶, G.V. Kehris ⁶¹, J.S. Keller ³⁴, A.S. Kelly ⁹⁷, J.J. Kempster ¹⁴⁷, P.D. Kennedy ¹⁰¹, O. Kepka ¹³², B.P. Kerridge ¹³⁵, S. Kersten ¹⁷², B.P. Kerševan ⁹⁴, L. Keszeghova ^{28a},

S. Ketabchi Haghighat ¹⁵⁶, R.A. Khan ¹³⁰, A. Khanov ¹²², A.G. Kharlamov ³⁷, T. Kharlamova ³⁷,
 E.E. Khoda ¹³⁹, M. Kholodenko ³⁷, T.J. Khoo ¹⁸, G. Khorauli ¹⁶⁷, J. Khubua ^{150b},
 Y.A.R. Khwaira ⁶⁶, B. Kibirige ^{33g}, A. Kilgallon ¹²⁴, D.W. Kim ^{47a,47b}, Y.K. Kim ³⁹,
 N. Kimura ⁹⁷, M.K. Kingston ⁵⁵, A. Kirchhoff ⁵⁵, C. Kirfel ²⁴, F. Kirfel ²⁴, J. Kirk ¹³⁵,
 A.E. Kiryunin ¹¹¹, C. Kitsaki ¹⁰, O. Kivernyk ²⁴, M. Klassen ^{63a}, C. Klein ³⁴, L. Klein ¹⁶⁷,
 M.H. Klein ⁴⁴, S.B. Klein ⁵⁶, U. Klein ⁹³, P. Klimek ³⁶, A. Klimentov ²⁹, T. Klioutchnikova ³⁶,
 P. Kluit ¹¹⁵, S. Kluth ¹¹¹, E. Kneringer ⁷⁹, T.M. Knight ¹⁵⁶, A. Knue ⁴⁹, R. Kobayashi ⁸⁸,
 D. Kobylanskii ¹⁷⁰, S.F. Koch ¹²⁷, M. Kocian ¹⁴⁴, P. Kodyš ¹³⁴, D.M. Koeck ¹²⁴,
 P.T. Koenig ²⁴, T. Koffas ³⁴, O. Kolay ⁵⁰, I. Koletsou ⁴, T. Komarek ¹²³, K. Köneke ⁵⁴,
 A.X.Y. Kong ¹, T. Kono ¹¹⁹, N. Konstantinidis ⁹⁷, P. Kontaxakis ⁵⁶, B. Konya ⁹⁹,
 R. Kopeliansky ⁴¹, S. Koperny ^{86a}, K. Korcyl ⁸⁷, K. Kordas ^{153,e}, A. Korn ⁹⁷, S. Korn ⁵⁵,
 I. Korolkov ¹³, N. Korotkova ³⁷, B. Kortman ¹¹⁵, O. Kortner ¹¹¹, S. Kortner ¹¹¹,
 W.H. Kostecka ¹¹⁶, V.V. Kostyukhin ¹⁴², A. Kotsokechagia ¹³⁶, A. Kotwal ⁵¹, A. Koulouris ³⁶,
 A. Kourkoumeli-Charalampidi ^{73a,73b}, C. Kourkoumelis ⁹, E. Kourlitis ^{111,ac}, O. Kovanda ¹²⁴,
 R. Kowalewski ¹⁶⁶, W. Kozanecki ¹³⁶, A.S. Kozhin ³⁷, V.A. Kramarenko ³⁷, G. Kramberger ⁹⁴,
 P. Kramer ¹⁰¹, M.W. Krasny ¹²⁸, A. Krasznahorkay ³⁶, J.W. Kraus ¹⁷², J.A. Kremer ⁴⁸,
 T. Kresse ⁵⁰, J. Kretschmar ⁹³, K. Kreul ¹⁸, P. Krieger ¹⁵⁶, S. Krishnamurthy ¹⁰⁴,
 M. Krivos ¹³⁴, K. Krizka ²⁰, K. Kroeninger ⁴⁹, H. Kroha ¹¹¹, J. Kroll ¹³², J. Kroll ¹²⁹,
 K.S. Krowpman ¹⁰⁸, U. Kruchonak ³⁸, H. Krüger ²⁴, N. Krumnack ⁸¹, M.C. Kruse ⁵¹,
 O. Kuchinskaia ³⁷, S. Kuday ^{3a}, S. Kuehn ³⁶, R. Kuesters ⁵⁴, T. Kuhl ⁴⁸, V. Kukhtin ³⁸,
 Y. Kulchitsky ^{37,a}, S. Kuleshov ^{138d,138b}, M. Kumar ^{33g}, N. Kumari ⁴⁸, P. Kumari ^{157b},
 A. Kupco ¹³², T. Kupfer ⁴⁹, A. Kupich ³⁷, O. Kuprash ⁵⁴, H. Kurashige ⁸⁵, L.L. Kurchaninov ^{157a},
 O. Kurdysh ⁶⁶, Y.A. Kurochkin ³⁷, A. Kurova ³⁷, M. Kuze ¹⁵⁵, A.K. Kvam ¹⁰⁴, J. Kvita ¹²³,
 T. Kwan ¹⁰⁵, N.G. Kyriacou ¹⁰⁷, L.A.O. Laatu ¹⁰³, C. Lacasta ¹⁶⁴, F. Lacava ^{75a,75b},
 H. Lacker ¹⁸, D. Lacour ¹²⁸, N.N. Lad ⁹⁷, E. Ladygin ³⁸, A. Lafarge ⁴⁰, B. Laforge ¹²⁸,
 T. Lagouri ¹⁷³, F.Z. Lahbabi ^{35a}, S. Lai ⁵⁵, I.K. Lakomic ^{86a}, N. Lalloue ⁶⁰, J.E. Lambert ¹⁶⁶,
 S. Lammers ⁶⁸, W. Lampl ⁷, C. Lampoudis ^{153,e}, G. Lamprinoudis ¹⁰¹, A.N. Lancaster ¹¹⁶,
 E. Lançon ²⁹, U. Landgraf ⁵⁴, M.P.J. Landon ⁹⁵, V.S. Lang ⁵⁴, O.K.B. Langrekken ¹²⁶,
 A.J. Lankford ¹⁶⁰, F. Lanni ³⁶, K. Lantzsch ²⁴, A. Lanza ^{73a}, A. Lapertosa ^{57b,57a},
 J.F. Laporte ¹³⁶, T. Lari ^{71a}, F. Lasagni Manghi ^{23b}, M. Lassnig ³⁶, V. Latonova ¹³²,
 A. Laudrain ¹⁰¹, A. Laurier ¹⁵¹, S.D. Lawlor ¹⁴⁰, Z. Lawrence ¹⁰², R. Lazaridou ¹⁶⁸,
 M. Lazzaroni ^{71a,71b}, B. Le ¹⁰², E.M. Le Boulicaut ⁵¹, L.T. Le Pottier ^{17a}, B. Leban ^{23b,23a},
 A. Lebedev ⁸¹, M. LeBlanc ¹⁰², F. Ledroit-Guillon ⁶⁰, A.C.A. Lee ⁹⁷, S.C. Lee ¹⁴⁹, S. Lee ^{47a,47b},
 T.F. Lee ⁹³, L.L. Leeuw ^{33c}, H.P. Lefebvre ⁹⁶, M. Lefebvre ¹⁶⁶, C. Leggett ^{17a},
 G. Lehmann Miotto ³⁶, M. Leigh ⁵⁶, W.A. Leight ¹⁰⁴, W. Leinonen ¹¹⁴, A. Leisos ^{153,r},
 M.A.L. Leite ^{83c}, C.E. Leitgeb ¹⁸, R. Leitner ¹³⁴, K.J.C. Leney ⁴⁴, T. Lenz ²⁴, S. Leone ^{74a},
 C. Leonidopoulos ⁵², A. Leopold ¹⁴⁵, C. Leroy ¹⁰⁹, R. Les ¹⁰⁸, C.G. Lester ³²,
 M. Levchenko ³⁷, J. Levêque ⁴, L.J. Levinson ¹⁷⁰, G. Levrini ^{23b,23a}, M.P. Lewicki ⁸⁷,
 D.J. Lewis ⁴, A. Li ⁵, B. Li ^{62b}, C. Li ^{62a}, C-Q. Li ¹¹¹, H. Li ^{62a}, H. Li ^{62b}, H. Li ^{14c},
 H. Li ^{14b}, H. Li ^{62b}, J. Li ^{62c}, K. Li ¹³⁹, L. Li ^{62c}, M. Li ^{14a,14e}, Q.Y. Li ^{62a}, S. Li ^{14a,14e},
 S. Li ^{62d,62c,d}, T. Li ⁵, X. Li ¹⁰⁵, Z. Li ¹²⁷, Z. Li ¹⁰⁵, Z. Li ^{14a,14e}, S. Liang ^{14a,14e}, Z. Liang ^{14a},
 M. Liberatore ¹³⁶, B. Liberti ^{76a}, K. Lie ^{64c}, J. Lieber Marin ^{83b}, H. Lien ⁶⁸, K. Lin ¹⁰⁸,
 R.E. Lindley ⁷, J.H. Lindon ², E. Lipeles ¹²⁹, A. Lipniacka ¹⁶, A. Lister ¹⁶⁵, J.D. Little ⁴,
 B. Liu ^{14a}, B.X. Liu ¹⁴³, D. Liu ^{62d,62c}, E.H.L. Liu ²⁰, J.B. Liu ^{62a}, J.K.K. Liu ³², K. Liu ^{62d},
 K. Liu ^{62d,62c}, M. Liu ^{62a}, M.Y. Liu ^{62a}, P. Liu ^{14a}, Q. Liu ^{62d,139,62c}, X. Liu ^{62a}, X. Liu ^{62b},
 Y. Liu ^{14d,14e}, Y.L. Liu ^{62b}, Y.W. Liu ^{62a}, J. Llorente Merino ¹⁴³, S.L. Lloyd ⁹⁵,
 E.M. Lobodzinska ⁴⁸, P. Loch ⁷, T. Lohse ¹⁸, K. Lohwasser ¹⁴⁰, E. Loiacono ⁴⁸,

M. Lokajicek ^{132,*}, J.D. Lomas ²⁰, J.D. Long ¹⁶³, I. Longarini ¹⁶⁰, L. Longo ^{70a,70b},
R. Longo ¹⁶³, I. Lopez Paz ⁶⁷, A. Lopez Solis ⁴⁸, N. Lorenzo Martinez ⁴, A.M. Lory ¹¹⁰,
G. Löschcke Centeno ¹⁴⁷, O. Loseva ³⁷, X. Lou ^{47a,47b}, X. Lou ^{14a,14e}, A. Lounis ⁶⁶,
P.A. Love ⁹², G. Lu ^{14a,14e}, M. Lu ⁶⁶, S. Lu ¹²⁹, Y.J. Lu ⁶⁵, H.J. Lubatti ¹³⁹, C. Luci ^{75a,75b},
F.L. Lucio Alves ^{14c}, F. Luehring ⁶⁸, I. Luise ¹⁴⁶, O. Lukianchuk ⁶⁶, O. Lundberg ¹⁴⁵,
B. Lund-Jensen ¹⁴⁵, N.A. Luongo ⁶, M.S. Lutz ³⁶, A.B. Lux ²⁵, D. Lynn ²⁹, R. Lysak ¹³²,
E. Lytken ⁹⁹, V. Lyubushkin ³⁸, T. Lyubushkina ³⁸, M.M. Lyukova ¹⁴⁶, H. Ma ²⁹, K. Ma ^{62a},
L.L. Ma ^{62b}, W. Ma ^{62a}, Y. Ma ¹²², D.M. Mac Donell ¹⁶⁶, G. Maccarrone ⁵³,
J.C. MacDonald ¹⁰¹, P.C. Machado De Abreu Farias ^{83e}, R. Madar ⁴⁰, T. Madula ⁹⁷, J. Maeda ⁸⁵,
T. Maeno ²⁹, H. Maguire ¹⁴⁰, V. Maiboroda ¹³⁶, A. Maio ^{131a,131b,131d}, K. Maj ^{86a},
O. Majersky ⁴⁸, S. Majewski ¹²⁴, N. Makovec ⁶⁶, V. Maksimovic ¹⁵, B. Malaescu ¹²⁸,
Pa. Malecki ⁸⁷, V.P. Maleev ³⁷, F. Malek ^{60,n}, M. Mali ⁹⁴, D. Malito ⁹⁶, U. Mallik ⁸⁰,
S. Maltezos ¹⁰, S. Malyukov ³⁸, J. Mamuzic ¹³, G. Mancini ⁵³, M.N. Mancini ²⁶, G. Manco ^{73a,73b},
J.P. Mandalia ⁹⁵, I. Mandić ⁹⁴, L. Manhaes de Andrade Filho ^{83a}, I.M. Maniatis ¹⁷⁰,
J. Manjarres Ramos ⁹⁰, D.C. Mankad ¹⁷⁰, A. Mann ¹¹⁰, S. Manzoni ³⁶, L. Mao ^{62c},
X. Mapekula ^{33c}, A. Marantis ^{153,r}, G. Marchiori ⁵, M. Marcisovsky ¹³², C. Marcon ^{71a},
M. Marinescu ²⁰, S. Marium ⁴⁸, M. Marjanovic ¹²¹, M. Markovitch ⁶⁶, E.J. Marshall ⁹²,
Z. Marshall ^{17a}, S. Marti-Garcia ¹⁶⁴, T.A. Martin ¹⁶⁸, V.J. Martin ⁵², B. Martin dit Latour ¹⁶,
L. Martinelli ^{75a,75b}, M. Martinez ^{13,s}, P. Martinez Agullo ¹⁶⁴, V.I. Martinez Outschoorn ¹⁰⁴,
P. Martinez Suarez ¹³, S. Martin-Haugh ¹³⁵, G. Martinovicova ¹³⁴, V.S. Martoiu ^{27b},
A.C. Martyniuk ⁹⁷, A. Marzin ³⁶, D. Mascione ^{78a,78b}, L. Masetti ¹⁰¹, T. Mashimo ¹⁵⁴,
J. Masik ¹⁰², A.L. Maslennikov ³⁷, P. Massarotti ^{72a,72b}, P. Mastrandrea ^{74a,74b},
A. Mastroberardino ^{43b,43a}, T. Masubuchi ¹⁵⁴, T. Mathisen ¹⁶², J. Matousek ¹³⁴, N. Matsuzawa ¹⁵⁴,
J. Maurer ^{27b}, A.J. Maury ⁶⁶, B. Maček ⁹⁴, D.A. Maximov ³⁷, R. Mazini ¹⁴⁹, I. Maznas ¹¹⁶,
M. Mazza ¹⁰⁸, S.M. Mazza ¹³⁷, E. Mazzeo ^{71a,71b}, C. Mc Ginn ²⁹, J.P. Mc Gowan ¹⁶⁶,
S.P. Mc Kee ¹⁰⁷, C.C. McCracken ¹⁶⁵, E.F. McDonald ¹⁰⁶, A.E. McDougall ¹¹⁵,
J.A. Mcfayden ¹⁴⁷, R.P. McGovern ¹²⁹, G. Mchedlidze ^{150b}, R.P. Mckenzie ^{33g},
T.C. McLachlan ⁴⁸, D.J. McLaughlin ⁹⁷, S.J. McMahon ¹³⁵, C.M. Mcpartland ⁹³,
R.A. McPherson ^{166,w}, S. Mehlhase ¹¹⁰, A. Mehta ⁹³, D. Melini ¹⁶⁴, B.R. Mellado Garcia ^{33g},
A.H. Melo ⁵⁵, F. Meloni ⁴⁸, A.M. Mendes Jacques Da Costa ¹⁰², H.Y. Meng ¹⁵⁶, L. Meng ⁹²,
S. Menke ¹¹¹, M. Mentink ³⁶, E. Meoni ^{43b,43a}, G. Mercado ¹¹⁶, C. Merlassino ^{69a,69c},
L. Merola ^{72a,72b}, C. Meroni ^{71a,71b}, J. Metcalfe ⁶, A.S. Mete ⁶, C. Meyer ⁶⁸, J-P. Meyer ¹³⁶,
R.P. Middleton ¹³⁵, L. Mijović ⁵², G. Mikenberg ¹⁷⁰, M. Mikestikova ¹³², M. Mikuž ⁹⁴,
H. Mildner ¹⁰¹, A. Milic ³⁶, D.W. Miller ³⁹, E.H. Miller ¹⁴⁴, L.S. Miller ³⁴, A. Milov ¹⁷⁰,
D.A. Milstead ^{47a,47b}, T. Min ^{14c}, A.A. Minaenko ³⁷, I.A. Minashvili ^{150b}, L. Mince ⁵⁹,
A.I. Mincer ¹¹⁸, B. Mindur ^{86a}, M. Mineev ³⁸, Y. Mino ⁸⁸, L.M. Mir ¹³, M. Miralles Lopez ⁵⁹,
M. Mironova ^{17a}, A. Mishima ¹⁵⁴, M.C. Missio ¹¹⁴, A. Mitra ¹⁶⁸, V.A. Mitsou ¹⁶⁴,
Y. Mitsumori ¹¹², O. Miu ¹⁵⁶, P.S. Miyagawa ⁹⁵, T. Mkrtychyan ^{63a}, M. Mlinarevic ⁹⁷,
T. Mlinarevic ⁹⁷, M. Mlynarikova ³⁶, S. Mobius ¹⁹, P. Mogg ¹¹⁰, M.H. Mohamed Farook ¹¹³,
A.F. Mohammed ^{14a,14e}, S. Mohapatra ⁴¹, G. Mokgatitwane ^{33g}, L. Moleri ¹⁷⁰, B. Mondal ¹⁴²,
S. Mondal ¹³³, K. Mönig ⁴⁸, E. Monnier ¹⁰³, L. Monsonis Romero ¹⁶⁴, J. Montejo Berlingen ¹³,
M. Montella ¹²⁰, F. Montereali ^{77a,77b}, F. Monticelli ⁹¹, S. Monzani ^{69a,69c}, N. Morange ⁶⁶,
A.L. Moreira De Carvalho ^{131a}, M. Moreno Llácer ¹⁶⁴, C. Moreno Martinez ⁵⁶, P. Morettini ^{57b},
S. Morgenstern ³⁶, M. Morii ⁶¹, M. Morinaga ¹⁵⁴, F. Morodei ^{75a,75b}, L. Morvaj ³⁶,
P. Moschovakos ³⁶, B. Moser ³⁶, M. Mosidze ^{150b}, T. Moskalets ⁵⁴, P. Moskvitina ¹¹⁴,
J. Moss ^{31,k}, A. Moussa ^{35d}, E.J.W. Moyse ¹⁰⁴, O. Mtintsilana ^{33g}, S. Muanza ¹⁰³,
J. Mueller ¹³⁰, D. Muenstermann ⁹², R. Müller ¹⁹, G.A. Mullier ¹⁶², A.J. Mullin ³², J.J. Mullin ¹²⁹,

D.P. Mungo ¹⁵⁶, D. Munoz Perez ¹⁶⁴, F.J. Munoz Sanchez ¹⁰², M. Murin ¹⁰², W.J. Murray ^{168,135},
 M. Muškinja ⁹⁴, C. Mwewa ²⁹, A.G. Myagkov ^{37,a}, A.J. Myers ⁸, G. Myers ¹⁰⁷, M. Myska ¹³³,
 B.P. Nachman ^{17a}, O. Nackenhorst ⁴⁹, K. Nagai ¹²⁷, K. Nagano ⁸⁴, J.L. Nagle ^{29,ag}, E. Nagy ¹⁰³,
 A.M. Nairz ³⁶, Y. Nakahama ⁸⁴, K. Nakamura ⁸⁴, K. Nakkalil ⁵, H. Nanjo ¹²⁵, R. Narayan ⁴⁴,
 E.A. Narayanan ¹¹³, I. Naryshkin ³⁷, M. Naseri ³⁴, S. Nasri ^{117b}, C. Nass ²⁴, G. Navarro ^{22a},
 J. Navarro-Gonzalez ¹⁶⁴, R. Nayak ¹⁵², A. Nayaz ¹⁸, P.Y. Nechaeva ³⁷, F. Nechansky ⁴⁸,
 L. Nedic ¹²⁷, T.J. Neep ²⁰, A. Negri ^{73a,73b}, M. Negrini ^{23b}, C. Nellist ¹¹⁵, C. Nelson ¹⁰⁵,
 K. Nelson ¹⁰⁷, S. Nemecek ¹³², M. Nessi ^{36,h}, M.S. Neubauer ¹⁶³, F. Neuhaus ¹⁰¹,
 J. Neundorff ⁴⁸, R. Newhouse ¹⁶⁵, P.R. Newman ²⁰, C.W. Ng ¹³⁰, Y.W.Y. Ng ⁴⁸, B. Ngair ^{117a},
 H.D.N. Nguyen ¹⁰⁹, R.B. Nickerson ¹²⁷, R. Nicolaidou ¹³⁶, J. Nielsen ¹³⁷, M. Niemeyer ⁵⁵,
 J. Niermann ⁵⁵, N. Nikiforou ³⁶, V. Nikolaenko ^{37,a}, I. Nikolic-Audit ¹²⁸, K. Nikolopoulos ²⁰,
 P. Nilsson ²⁹, I. Ninca ⁴⁸, H.R. Nindhito ⁵⁶, G. Ninio ¹⁵², A. Nisati ^{75a}, N. Nishu ²,
 R. Nisius ¹¹¹, J-E. Nitschke ⁵⁰, E.K. Nkadimeng ^{33g}, T. Nobe ¹⁵⁴, D.L. Noel ³²,
 T. Nommensen ¹⁴⁸, M.B. Norfolk ¹⁴⁰, R.R.B. Norisam ⁹⁷, B.J. Norman ³⁴, M. Noury ^{35a},
 J. Novak ⁹⁴, T. Novak ⁴⁸, L. Novotny ¹³³, R. Novotny ¹¹³, L. Nozka ¹²³, K. Ntekas ¹⁶⁰,
 N.M.J. Nunes De Moura Junior ^{83b}, J. Ocariz ¹²⁸, A. Ochi ⁸⁵, I. Ochoa ^{131a}, S. Oerdek ^{48,t},
 J.T. Offermann ³⁹, A. Ogrodnik ¹³⁴, A. Oh ¹⁰², C.C. Ohm ¹⁴⁵, H. Oide ⁸⁴, R. Oishi ¹⁵⁴,
 M.L. Ojeda ⁴⁸, Y. Okumura ¹⁵⁴, L.F. Oleiro Seabra ^{131a}, S.A. Olivares Pino ^{138d},
 G. Oliveira Correa ¹³, D. Oliveira Damazio ²⁹, D. Oliveira Goncalves ^{83a}, J.L. Oliver ¹⁶⁰,
 Ö.O. Öncel ⁵⁴, A.P. O'Neill ¹⁹, A. Onofre ^{131a,131e}, P.U.E. Onyisi ¹¹, M.J. Oreglia ³⁹,
 G.E. Orellana ⁹¹, D. Orestano ^{77a,77b}, N. Orlando ¹³, R.S. Orr ¹⁵⁶, V. O'Shea ⁵⁹,
 L.M. Osojnak ¹²⁹, R. Ospanov ^{62a}, G. Otero y Garzon ³⁰, H. Otono ⁸⁹, P.S. Ott ^{63a},
 G.J. Ottino ^{17a}, M. Ouchrif ^{35d}, F. Ould-Saada ¹²⁶, T. Ovsianikova ¹³⁹, M. Owen ⁵⁹,
 R.E. Owen ¹³⁵, K.Y. Oyulmaz ^{21a}, V.E. Ozcan ^{21a}, F. Ozturk ⁸⁷, N. Ozturk ⁸, S. Ozturk ⁸²,
 H.A. Pacey ¹²⁷, A. Pacheco Pages ¹³, C. Padilla Aranda ¹³, G. Padovano ^{75a,75b},
 S. Pagan Griso ^{17a}, G. Palacino ⁶⁸, A. Palazzo ^{70a,70b}, J. Pampel ²⁴, J. Pan ¹⁷³, T. Pan ^{64a},
 D.K. Panchal ¹¹, C.E. Pandini ¹¹⁵, J.G. Panduro Vazquez ⁹⁶, H.D. Pandya ¹, H. Pang ^{14b},
 P. Pani ⁴⁸, G. Panizzo ^{69a,69c}, L. Panwar ¹²⁸, L. Paolozzi ⁵⁶, S. Parajuli ¹⁶³, A. Paramonov ⁶,
 C. Paraskevopoulos ⁵³, D. Paredes Hernandez ^{64b}, A. Pareti ^{73a,73b}, K.R. Park ⁴¹, T.H. Park ¹⁵⁶,
 M.A. Parker ³², F. Parodi ^{57b,57a}, E.W. Parrish ¹¹⁶, V.A. Parrish ⁵², J.A. Parsons ⁴¹,
 U. Parzefall ⁵⁴, B. Pascual Dias ¹⁰⁹, L. Pascual Dominguez ¹⁵², E. Pasqualucci ^{75a},
 S. Passaggio ^{57b}, F. Pastore ⁹⁶, P. Patel ⁸⁷, U.M. Patel ⁵¹, J.R. Pater ¹⁰², T. Pauly ³⁶,
 C.I. Pazos ¹⁵⁹, J. Pearkes ¹⁴⁴, M. Pedersen ¹²⁶, R. Pedro ^{131a}, S.V. Peleganchuk ³⁷, O. Penc ³⁶,
 E.A. Pender ⁵², G.D. Penn ¹⁷³, K.E. Penski ¹¹⁰, M. Penzin ³⁷, B.S. Peralva ^{83d},
 A.P. Pereira Peixoto ¹³⁹, L. Pereira Sanchez ¹⁴⁴, D.V. Perepelitsa ^{29,ag}, E. Perez Codina ^{157a},
 M. Perganti ¹⁰, H. Pernegger ³⁶, O. Perrin ⁴⁰, K. Peters ⁴⁸, R.F.Y. Peters ¹⁰², B.A. Petersen ³⁶,
 T.C. Petersen ⁴², E. Petit ¹⁰³, V. Petousis ¹³³, C. Petridou ^{153,e}, T. Petru ¹³⁴, A. Petrukhin ¹⁴²,
 M. Pettee ^{17a}, N.E. Pettersson ³⁶, A. Petukhov ³⁷, K. Petukhova ¹³⁴, R. Pezoa ^{138f},
 L. Pezzotti ³⁶, G. Pezzullo ¹⁷³, T.M. Pham ¹⁷¹, T. Pham ¹⁰⁶, P.W. Phillips ¹³⁵, G. Piacquadio ¹⁴⁶,
 E. Pianori ^{17a}, F. Piazza ¹²⁴, R. Piegai ³⁰, D. Pietreanu ^{27b}, A.D. Pilkington ¹⁰²,
 M. Pinamonti ^{69a,69c}, J.L. Pinfeld ², B.C. Pinheiro Pereira ^{131a}, A.E. Pinto Pinoargote ^{101,136},
 L. Pintucci ^{69a,69c}, K.M. Piper ¹⁴⁷, A. Pirttikoski ⁵⁶, D.A. Pizzi ³⁴, L. Pizzimento ^{64b},
 A. Pizzini ¹¹⁵, M.-A. Pleier ²⁹, V. Plesanovs ⁵⁴, V. Pleskot ¹³⁴, E. Plotnikova ³⁸, G. Poddar ⁹⁵,
 R. Poettgen ⁹⁹, L. Poggioli ¹²⁸, I. Pokharel ⁵⁵, S. Polacek ¹³⁴, G. Polesello ^{73a}, A. Poley ^{143,157a},
 A. Polini ^{23b}, C.S. Pollard ¹⁶⁸, Z.B. Pollock ¹²⁰, E. Pompa Pacchi ^{75a,75b}, D. Ponomarenko ¹¹⁴,
 L. Pontecorvo ³⁶, S. Popa ^{27a}, G.A. Popeneciu ^{27d}, A. Poreba ³⁶, D.M. Portillo Quintero ^{157a},
 S. Pospisil ¹³³, M.A. Postill ¹⁴⁰, P. Postolache ^{27c}, K. Potamianos ¹⁶⁸, P.A. Potepa ^{86a},

I.N. Potrap ³⁸, C.J. Potter ³², H. Potti ¹, J. Poveda ¹⁶⁴, M.E. Pozo Astigarraga ³⁶,
 A. Prades Ibanez ¹⁶⁴, J. Pretel ⁵⁴, D. Price ¹⁰², M. Primavera ^{70a}, M.A. Principe Martin ¹⁰⁰,
 R. Privara ¹²³, T. Procter ⁵⁹, M.L. Proffitt ¹³⁹, N. Proklova ¹²⁹, K. Prokofiev ^{64c}, G. Proto ¹¹¹,
 J. Proudfoot ⁶, M. Przybycien ^{86a}, W.W. Przygoda ^{86b}, A. Psallidas ⁴⁶, J.E. Puddefoot ¹⁴⁰,
 D. Pudzha ³⁷, D. Pyatiizbyantseva ³⁷, J. Qian ¹⁰⁷, D. Qichen ¹⁰², Y. Qin ¹³, T. Qiu ⁵²,
 A. Quadt ⁵⁵, M. Queitsch-Maitland ¹⁰², G. Quetant ⁵⁶, R.P. Quinn ¹⁶⁵, G. Rabanal Bolanos ⁶¹,
 D. Rafanoharana ⁵⁴, F. Ragusa ^{71a,71b}, J.L. Rainbolt ³⁹, J.A. Raine ⁵⁶, S. Rajagopalan ²⁹,
 E. Ramakoti ³⁷, I.A. Ramirez-Berend ³⁴, K. Ran ^{48,14e}, N.P. Rapheeha ^{33g}, H. Rasheed ^{27b},
 V. Raskina ¹²⁸, D.F. Rassloff ^{63a}, A. Rastogi ^{17a}, S. Rave ¹⁰¹, B. Ravina ⁵⁵, I. Ravinovich ¹⁷⁰,
 M. Raymond ³⁶, A.L. Read ¹²⁶, N.P. Readioff ¹⁴⁰, D.M. Rebutzi ^{73a,73b}, G. Redlinger ²⁹,
 A.S. Reed ¹¹¹, K. Reeves ²⁶, J.A. Reidelsturz ¹⁷², D. Reikher ¹⁵², A. Rej ⁴⁹, C. Rembser ³⁶,
 M. Renda ^{27b}, M.B. Rendel ¹¹¹, F. Renner ⁴⁸, A.G. Rennie ¹⁶⁰, A.L. Rescia ⁴⁸, S. Resconi ^{71a},
 M. Ressegotti ^{57b,57a}, S. Rettie ³⁶, J.G. Reyes Rivera ¹⁰⁸, E. Reynolds ^{17a}, O.L. Rezanova ³⁷,
 P. Reznicek ¹³⁴, H. Riani ^{35d}, N. Ribaric ⁹², E. Ricci ^{78a,78b}, R. Richter ¹¹¹, S. Richter ^{47a,47b},
 E. Richter-Was ^{86b}, M. Ridel ¹²⁸, S. Ridouani ^{35d}, P. Rieck ¹¹⁸, P. Riedler ³⁶, E.M. Riefel ^{47a,47b},
 J.O. Rieger ¹¹⁵, M. Rijssenbeek ¹⁴⁶, M. Rimoldi ³⁶, L. Rinaldi ^{23b,23a}, T.T. Rinn ²⁹,
 M.P. Rinnagel ¹¹⁰, G. Ripellino ¹⁶², I. Riu ¹³, J.C. Rivera Vergara ¹⁶⁶, F. Rizatdinova ¹²²,
 E. Rizvi ⁹⁵, B.R. Roberts ^{17a}, S.H. Robertson ^{105,w}, D. Robinson ³², C.M. Robles Gajardo ^{138f},
 M. Robles Manzano ¹⁰¹, A. Robson ⁵⁹, A. Rocchi ^{76a,76b}, C. Roda ^{74a,74b}, S. Rodriguez Bosca ³⁶,
 Y. Rodriguez Garcia ^{22a}, A. Rodriguez Rodriguez ⁵⁴, A.M. Rodriguez Vera ¹¹⁶, S. Roe ³⁶,
 J.T. Roemer ¹⁶⁰, A.R. Roepe-Gier ¹³⁷, J. Roggel ¹⁷², O. Røhne ¹²⁶, R.A. Rojas ¹⁰⁴,
 C.P.A. Roland ¹²⁸, J. Roloff ²⁹, A. Romaniouk ³⁷, E. Romano ^{73a,73b}, M. Romano ^{23b},
 A.C. Romero Hernandez ¹⁶³, N. Rompotis ⁹³, L. Roos ¹²⁸, S. Rosati ^{75a}, B.J. Rosser ³⁹,
 E. Rossi ¹²⁷, E. Rossi ^{72a,72b}, L.P. Rossi ⁶¹, L. Rossini ⁵⁴, R. Rosten ¹²⁰, M. Rotaru ^{27b},
 B. Rottler ⁵⁴, C. Rougier ⁹⁰, D. Rousseau ⁶⁶, D. Rouso ³², A. Roy ¹⁶³, S. Roy-Garand ¹⁵⁶,
 A. Rozanov ¹⁰³, Z.M.A. Rozario ⁵⁹, Y. Rozen ¹⁵¹, A. Rubio Jimenez ¹⁶⁴, A.J. Ruby ⁹³,
 V.H. Ruelas Rivera ¹⁸, T.A. Ruggeri ¹, A. Ruggiero ¹²⁷, A. Ruiz-Martinez ¹⁶⁴, A. Rummler ³⁶,
 Z. Rurikova ⁵⁴, N.A. Rusakovich ³⁸, H.L. Russell ¹⁶⁶, G. Russo ^{75a,75b}, J.P. Rutherford ⁷,
 S. Rutherford Colmenares ³², K. Rybacki ⁹², M. Rybar ¹³⁴, E.B. Rye ¹²⁶, A. Ryzhov ⁴⁴,
 J.A. Sabater Iglesias ⁵⁶, P. Sabatini ¹⁶⁴, H.F.W. Sadrozinski ¹³⁷, F. Safai Tehrani ^{75a},
 B. Safarzadeh Samani ¹³⁵, S. Saha ¹, M. Sahinsoy ¹¹¹, A. Saibel ¹⁶⁴, M. Saimpert ¹³⁶,
 M. Saito ¹⁵⁴, T. Saito ¹⁵⁴, A. Sala ^{71a,71b}, D. Salamani ³⁶, A. Salnikov ¹⁴⁴, J. Salt ¹⁶⁴,
 A. Salvador Salas ¹⁵², D. Salvatore ^{43b,43a}, F. Salvatore ¹⁴⁷, A. Salzburger ³⁶, D. Sammel ⁵⁴,
 E. Sampson ⁹², D. Sampsonidis ^{153,e}, D. Sampsonidou ¹²⁴, J. Sánchez ¹⁶⁴,
 V. Sanchez Sebastian ¹⁶⁴, H. Sandaker ¹²⁶, C.O. Sander ⁴⁸, J.A. Sandesara ¹⁰⁴, M. Sandhoff ¹⁷²,
 C. Sandoval ^{22b}, D.P.C. Sankey ¹³⁵, T. Sano ⁸⁸, A. Sansoni ⁵³, L. Santi ^{75a,75b}, C. Santoni ⁴⁰,
 H. Santos ^{131a,131b}, A. Santra ¹⁷⁰, K.A. Saoucha ¹⁶¹, J.G. Saraiva ^{131a,131d}, J. Sardain ⁷,
 O. Sasaki ⁸⁴, K. Sato ¹⁵⁸, C. Sauer ^{63b}, F. Sauerburger ⁵⁴, E. Sauvan ⁴, P. Savard ^{156,ae},
 R. Sawada ¹⁵⁴, C. Sawyer ¹³⁵, L. Sawyer ⁹⁸, I. Sayago Galvan ¹⁶⁴, C. Sbarra ^{23b}, A. Sbrizzi ^{23b,23a},
 T. Scanlon ⁹⁷, J. Schaarschmidt ¹³⁹, U. Schäfer ¹⁰¹, A.C. Schaffer ^{66,44}, D. Schaile ¹¹⁰,
 R.D. Schamberger ¹⁴⁶, C. Scharf ¹⁸, M.M. Schefer ¹⁹, V.A. Schegelsky ³⁷, D. Scheirich ¹³⁴,
 F. Schenck ¹⁸, M. Schernau ¹⁶⁰, C. Scheulen ⁵⁵, C. Schiavi ^{57b,57a}, M. Schioppa ^{43b,43a},
 B. Schlag ^{144,m}, K.E. Schleicher ⁵⁴, S. Schlenker ³⁶, J. Schmeing ¹⁷², M.A. Schmidt ¹⁷²,
 K. Schmieden ¹⁰¹, C. Schmitt ¹⁰¹, N. Schmitt ¹⁰¹, S. Schmitt ⁴⁸, L. Schoeffel ¹³⁶,
 A. Schoening ^{63b}, P.G. Scholer ³⁴, E. Schopf ¹²⁷, M. Schott ¹⁰¹, J. Schovancova ³⁶,
 S. Schramm ⁵⁶, T. Schroer ⁵⁶, H-C. Schultz-Coulon ^{63a}, M. Schumacher ⁵⁴, B.A. Schumm ¹³⁷,
 Ph. Schune ¹³⁶, A.J. Schuy ¹³⁹, H.R. Schwartz ¹³⁷, A. Schwartzman ¹⁴⁴, T.A. Schwarz ¹⁰⁷,

Ph. Schwemling ¹³⁶, R. Schwienhorst ¹⁰⁸, A. Sciandra ¹³⁷, G. Sciolla ²⁶, F. Scuri ^{74a},
 C.D. Sebastiani ⁹³, K. Sedlaczek ¹¹⁶, P. Seema ¹⁸, S.C. Seidel ¹¹³, A. Seiden ¹³⁷,
 B.D. Seidlitz ⁴¹, C. Seitz ⁴⁸, J.M. Seixas ^{83b}, G. Sekhniaidze ^{72a}, L. Selem ⁶⁰,
 N. Semprini-Cesari ^{23b,23a}, D. Sengupta ⁵⁶, V. Senthilkumar ¹⁶⁴, L. Serin ⁶⁶, L. Serkin ^{69a,69b},
 M. Sessa ^{76a,76b}, H. Severini ¹²¹, F. Sforza ^{57b,57a}, A. Sfyrla ⁵⁶, Q. Sha ^{14a}, E. Shabalina ⁵⁵,
 A.H. Shah ³², R. Shaheen ¹⁴⁵, J.D. Shahinian ¹²⁹, D. Shaked Renous ¹⁷⁰, L.Y. Shan ^{14a},
 M. Shapiro ^{17a}, A. Sharma ³⁶, A.S. Sharma ¹⁶⁵, P. Sharma ⁸⁰, P.B. Shatalov ³⁷, K. Shaw ¹⁴⁷,
 S.M. Shaw ¹⁰², A. Shcherbakova ³⁷, Q. Shen ^{62c,5}, D.J. Sheppard ¹⁴³, P. Sherwood ⁹⁷, L. Shi ⁹⁷,
 X. Shi ^{14a}, C.O. Shimmin ¹⁷³, J.D. Shinner ⁹⁶, I.P.J. Shipsey ¹²⁷, S. Shirabe ⁸⁹,
 M. Shiyakova ^{38,u}, J. Shlomi ¹⁷⁰, M.J. Shochet ³⁹, J. Shojaii ¹⁰⁶, D.R. Shope ¹²⁶,
 B. Shrestha ¹²¹, S. Shrestha ^{120,ah}, E.M. Shrif ^{33g}, M.J. Shroff ¹⁶⁶, P. Sicho ¹³², A.M. Sickles ¹⁶³,
 E. Sideras Haddad ^{33g}, A. Sidoti ^{23b}, F. Siegert ⁵⁰, Dj. Sijacki ¹⁵, F. Sili ⁹¹, J.M. Silva ⁵²,
 M.V. Silva Oliveira ²⁹, S.B. Silverstein ^{47a}, S. Simion ⁶⁶, R. Simoniello ³⁶, E.L. Simpson ⁵⁹,
 H. Simpson ¹⁴⁷, L.R. Simpson ¹⁰⁷, N.D. Simpson ⁹⁹, S. Simsek ⁸², S. Sindhu ⁵⁵, P. Sinervo ¹⁵⁶,
 S. Singh ¹⁵⁶, S. Sinha ⁴⁸, S. Sinha ¹⁰², M. Sioli ^{23b,23a}, I. Siral ³⁶, E. Sitnikova ⁴⁸,
 J. Sjölin ^{47a,47b}, A. Skaf ⁵⁵, E. Skorda ²⁰, P. Skubic ¹²¹, M. Slawinska ⁸⁷, V. Smakhtin ¹⁷⁰,
 B.H. Smart ¹³⁵, S.Yu. Smirnov ³⁷, Y. Smirnov ³⁷, L.N. Smirnova ^{37,a}, O. Smirnova ⁹⁹,
 A.C. Smith ⁴¹, E.A. Smith ³⁹, H.A. Smith ¹²⁷, J.L. Smith ¹⁰², R. Smith ¹⁴⁴, M. Smizanska ⁹²,
 K. Smolek ¹³³, A.A. Snesarev ³⁷, S.R. Snider ¹⁵⁶, H.L. Snoek ¹¹⁵, S. Snyder ²⁹, R. Sobie ^{166,w},
 A. Soffer ¹⁵², C.A. Solans Sanchez ³⁶, E. Yu. Soldatov ³⁷, U. Soldevila ¹⁶⁴, A.A. Solodkov ³⁷,
 S. Solomon ²⁶, A. Soloshenko ³⁸, K. Solovieva ⁵⁴, O.V. Solovyanov ⁴⁰, V. Solovyev ³⁷,
 P. Sommer ³⁶, A. Sonay ¹³, W.Y. Song ^{157b}, A. Sopczak ¹³³, A.L. Sopio ⁹⁷, F. Sopkova ^{28b},
 J.D. Sorenson ¹¹³, I.R. Sotarriva Alvarez ¹⁵⁵, V. Sothilingam ^{63a}, O.J. Soto Sandoval ^{138c,138b},
 S. Sottocornola ⁶⁸, R. Soualah ¹⁶¹, Z. Soumami ^{35e}, D. South ⁴⁸, N. Soybelman ¹⁷⁰,
 S. Spagnolo ^{70a,70b}, M. Spalla ¹¹¹, D. Sperlich ⁵⁴, G. Spigo ³⁶, S. Spinali ⁹², D.P. Spiteri ⁵⁹,
 M. Spousta ¹³⁴, E.J. Staats ³⁴, R. Stamen ^{63a}, A. Stampekis ²⁰, M. Standke ²⁴, E. Stanecka ⁸⁷,
 W. Stanek-Maslouska ⁴⁸, M.V. Stange ⁵⁰, B. Stanislaus ^{17a}, M.M. Stanitzki ⁴⁸, B. Stapf ⁴⁸,
 E.A. Starchenko ³⁷, G.H. Stark ¹³⁷, J. Stark ⁹⁰, P. Staroba ¹³², P. Starovoitov ^{63a}, S. Stärz ¹⁰⁵,
 R. Staszewski ⁸⁷, G. Stavropoulos ⁴⁶, J. Steentoft ¹⁶², P. Steinberg ²⁹, B. Stelzer ^{143,157a},
 H.J. Stelzer ¹³⁰, O. Stelzer-Chilton ^{157a}, H. Stenzel ⁵⁸, T.J. Stevenson ¹⁴⁷, G.A. Stewart ³⁶,
 J.R. Stewart ¹²², M.C. Stockton ³⁶, G. Stoicea ^{27b}, M. Stolarski ^{131a}, S. Stonjek ¹¹¹,
 A. Straessner ⁵⁰, J. Strandberg ¹⁴⁵, S. Strandberg ^{47a,47b}, M. Stratmann ¹⁷², M. Strauss ¹²¹,
 T. Streblner ¹⁰³, P. Strizenec ^{28b}, R. Ströhmer ¹⁶⁷, D.M. Strom ¹²⁴, R. Stroynowski ⁴⁴,
 A. Strubig ^{47a,47b}, S.A. Stucci ²⁹, B. Stugu ¹⁶, J. Stupak ¹²¹, N.A. Styles ⁴⁸, D. Su ¹⁴⁴,
 S. Su ^{62a}, W. Su ^{62d}, X. Su ^{62a}, D. Suchy ^{28a}, K. Sugizaki ¹⁵⁴, V.V. Sulin ³⁷, M.J. Sullivan ⁹³,
 D.M.S. Sultan ¹²⁷, L. Sultanaliyeva ³⁷, S. Sultansoy ^{3b}, T. Sumida ⁸⁸, S. Sun ¹⁰⁷, S. Sun ¹⁷¹,
 O. Sunneborn Gudnadottir ¹⁶², N. Sur ¹⁰³, M.R. Sutton ¹⁴⁷, H. Suzuki ¹⁵⁸, M. Svatos ¹³²,
 M. Swiatlowski ^{157a}, T. Swirski ¹⁶⁷, I. Sykora ^{28a}, M. Sykora ¹³⁴, T. Sykora ¹³⁴, D. Ta ¹⁰¹,
 K. Tackmann ^{48,t}, A. Taffard ¹⁶⁰, R. Tafirout ^{157a}, J.S. Tafoya Vargas ⁶⁶, Y. Takubo ⁸⁴,
 M. Talby ¹⁰³, A.A. Talyshv ³⁷, K.C. Tam ^{64b}, N.M. Tamir ¹⁵², A. Tanaka ¹⁵⁴, J. Tanaka ¹⁵⁴,
 R. Tanaka ⁶⁶, M. Tanasini ^{57b,57a}, Z. Tao ¹⁶⁵, S. Tapia Araya ^{138f}, S. Tapprogge ¹⁰¹,
 A. Tarek Abouelfadl Mohamed ¹⁰⁸, S. Tarem ¹⁵¹, K. Tariq ^{14a}, G. Tarna ^{103,27b}, G.F. Tartarelli ^{71a},
 P. Tas ¹³⁴, M. Tasevsky ¹³², E. Tassi ^{43b,43a}, A.C. Tate ¹⁶³, G. Tateno ¹⁵⁴, Y. Tayalati ^{35e,v},
 G.N. Taylor ¹⁰⁶, W. Taylor ^{157b}, A.S. Tee ¹⁷¹, R. Teixeira De Lima ¹⁴⁴, P. Teixeira-Dias ⁹⁶,
 J.J. Teoh ¹⁵⁶, K. Terashi ¹⁵⁴, J. Terron ¹⁰⁰, S. Terzo ¹³, M. Testa ⁵³, R.J. Teuscher ^{156,w},
 A. Thaler ⁷⁹, O. Theiner ⁵⁶, N. Themistokleous ⁵², T. Thevenaux-Pelzer ¹⁰³, O. Thielmann ¹⁷²,
 D.W. Thomas ⁹⁶, J.P. Thomas ²⁰, E.A. Thompson ^{17a}, P.D. Thompson ²⁰, E. Thomson ¹²⁹,

R.E. Thornberry⁴⁴, Y. Tian⁵⁵, V. Tikhomirov^{37,a}, Yu.A. Tikhonov³⁷, S. Timoshenko³⁷,
 D. Timoshyn¹³⁴, E.X.L. Ting¹, P. Tipton¹⁷³, S.H. Tlou^{33g}, K. Todome¹⁵⁵,
 S. Todorova-Nova¹³⁴, S. Todt⁵⁰, M. Togawa⁸⁴, J. Tojo⁸⁹, S. Tokár^{28a}, K. Tokushuku⁸⁴,
 O. Toldaiev⁶⁸, R. Tombs³², M. Tomoto^{84,112}, L. Tompkins^{144,m}, K.W. Topolnicki^{86b},
 E. Torrence¹²⁴, H. Torres⁹⁰, E. Torró Pastor¹⁶⁴, M. Toscani³⁰, C. Tosciri³⁹, M. Tost¹¹,
 D.R. Tovey¹⁴⁰, A. Traeet¹⁶, I.S. Trandaafir^{27b}, T. Trefzger¹⁶⁷, A. Tricoli²⁹, I.M. Trigger^{157a},
 S. Trincaz-Duvoid¹²⁸, D.A. Trischuk²⁶, B. Trocmé⁶⁰, L. Truong^{33c}, M. Trzebinski⁸⁷,
 A. Trzupke⁸⁷, F. Tsai¹⁴⁶, M. Tsai¹⁰⁷, A. Tsiamis^{153,e}, P.V. Tsiareshka³⁷, S. Tsigaridas^{157a},
 A. Tsirigotis^{153,r}, V. Tsiskaridze¹⁵⁶, E.G. Tskhadadze^{150a}, M. Tsopoulou¹⁵³, Y. Tsujikawa⁸⁸,
 I.I. Tsukerman³⁷, V. Tsulaia^{17a}, S. Tsuno⁸⁴, K. Tsuru¹¹⁹, D. Tsybychev¹⁴⁶, Y. Tu^{64b},
 A. Tudorache^{27b}, V. Tudorache^{27b}, A.N. Tuna⁶¹, S. Turchikhin^{57b,57a}, I. Turk Cakir^{3a},
 R. Turra^{71a}, T. Turtuvshin^{38,x}, P.M. Tuts⁴¹, S. Tzamarias^{153,e}, E. Tzovara¹⁰¹, F. Ukegawa¹⁵⁸,
 P.A. Ulloa Poblete^{138c,138b}, E.N. Umaka²⁹, G. Unal³⁶, A. Undrus²⁹, G. Unel¹⁶⁰, J. Urban^{28b},
 P. Urquijo¹⁰⁶, P. Urrejola^{138a}, G. Usai⁸, R. Ushioda¹⁵⁵, M. Usman¹⁰⁹, Z. Uysal⁸²,
 V. Vacek¹³³, B. Vachon¹⁰⁵, K.O.H. Vadla¹²⁶, T. Vafeiadis³⁶, A. Vaitkus⁹⁷, C. Valderanis¹¹⁰,
 E. Valdes Santurio^{47a,47b}, M. Valente^{157a}, S. Valentinetti^{23b,23a}, A. Valero¹⁶⁴,
 E. Valiente Moreno¹⁶⁴, A. Vallier⁹⁰, J.A. Valls Ferrer¹⁶⁴, D.R. Van Arneman¹¹⁵,
 T.R. Van Daalen¹³⁹, A. Van Der Graaf⁴⁹, P. Van Gemmeren⁶, M. Van Rijnbach¹²⁶,
 S. Van Stroud⁹⁷, I. Van Vulpen¹¹⁵, P. Vana¹³⁴, M. Vanadia^{76a,76b}, W. Vandelli³⁶,
 E.R. Vandewall¹²², D. Vannicola¹⁵², L. Vannoli⁵³, R. Vari^{75a}, E.W. Varnes⁷, C. Varni^{17b},
 T. Varol¹⁴⁹, D. Varouchas⁶⁶, L. Varriale¹⁶⁴, K.E. Varvell¹⁴⁸, M.E. Vasile^{27b}, L. Vaslin⁸⁴,
 G.A. Vasquez¹⁶⁶, A. Vasyukov³⁸, R. Vavricka¹⁰¹, F. Vazeille⁴⁰, T. Vazquez Schroeder³⁶,
 J. Veatch³¹, V. Vecchio¹⁰², M.J. Veen¹⁰⁴, I. Veliscek²⁹, L.M. Veloce¹⁵⁶, F. Veloso^{131a,131c},
 S. Veneziano^{75a}, A. Ventura^{70a,70b}, S. Ventura Gonzalez¹³⁶, A. Verbytskyi¹¹¹,
 M. Verducci^{74a,74b}, C. Vergis²⁴, M. Verissimo De Araujo^{83b}, W. Verkerke¹¹⁵,
 J.C. Vermeulen¹¹⁵, C. Vernieri¹⁴⁴, M. Vessella¹⁰⁴, M.C. Vetterli^{143,ae}, A. Vgenopoulos^{153,e},
 N. Viaux Maira^{138f}, T. Vickey¹⁴⁰, O.E. Vickey Boeriu¹⁴⁰, G.H.A. Viehhauser¹²⁷, L. Vigani^{63b},
 M. Villa^{23b,23a}, M. Villaplana Perez¹⁶⁴, E.M. Villhauer⁵², E. Vilucchi⁵³, M.G. Vincter³⁴,
 G.S. Virdee²⁰, A. Vishwakarma⁵², A. Visibile¹¹⁵, C. Vittori³⁶, I. Vivarelli^{23b,23a},
 E. Voevodina¹¹¹, F. Vogel¹¹⁰, J.C. Voigt⁵⁰, P. Vokac¹³³, Yu. Volkotrub^{86b}, J. Von Ahnen⁴⁸,
 E. Von Toerne²⁴, B. Vormwald³⁶, V. Vorobel¹³⁴, K. Vorobev³⁷, M. Vos¹⁶⁴, K. Voss¹⁴²,
 M. Vozak¹¹⁵, L. Vozdecky¹²¹, N. Vranjes¹⁵, M. Vranjes Milosavljevic¹⁵, M. Vreeswijk¹¹⁵,
 N.K. Vu^{62d,62c}, R. Vuillermet³⁶, O. Vujanovic¹⁰¹, I. Vukotic³⁹, S. Wada¹⁵⁸, C. Wagner¹⁰⁴,
 J.M. Wagner^{17a}, W. Wagner¹⁷², S. Wahdan¹⁷², H. Wahlberg⁹¹, M. Wakida¹¹², J. Walder¹³⁵,
 R. Walker¹¹⁰, W. Walkowiak¹⁴², A. Wall¹²⁹, E.J. Wallin⁹⁹, T. Wamorkar⁶, A.Z. Wang¹³⁷,
 C. Wang¹⁰¹, C. Wang¹¹, H. Wang^{17a}, J. Wang^{64c}, R.-J. Wang¹⁰¹, R. Wang⁶¹, R. Wang⁶,
 S.M. Wang¹⁴⁹, S. Wang^{62b}, T. Wang^{62a}, W.T. Wang⁸⁰, W. Wang^{14a}, X. Wang^{14c},
 X. Wang¹⁶³, X. Wang^{62c}, Y. Wang^{62d}, Y. Wang^{14c}, Z. Wang¹⁰⁷, Z. Wang^{62d,51,62c},
 Z. Wang¹⁰⁷, A. Warburton¹⁰⁵, R.J. Ward²⁰, N. Warrack⁵⁹, S. Waterhouse⁹⁶, A.T. Watson²⁰,
 H. Watson⁵⁹, M.F. Watson²⁰, E. Watton^{59,135}, G. Watts¹³⁹, B.M. Waugh⁹⁷, C. Weber²⁹,
 H.A. Weber¹⁸, M.S. Weber¹⁹, S.M. Weber^{63a}, C. Wei^{62a}, Y. Wei¹²⁷, A.R. Weidberg¹²⁷,
 E.J. Weik¹¹⁸, J. Weingarten⁴⁹, M. Weirich¹⁰¹, C. Weiser⁵⁴, C.J. Wells⁴⁸, T. Wenaus²⁹,
 B. Wendland⁴⁹, T. Wengler³⁶, N.S. Wenke¹¹¹, N. Wermes²⁴, M. Wessels^{63a}, A.M. Wharton⁹²,
 A.S. White⁶¹, A. White⁸, M.J. White¹, D. Whiteson¹⁶⁰, L. Wickremasinghe¹²⁵,
 W. Wiedenmann¹⁷¹, M. Wielers¹³⁵, C. Wiglesworth⁴², D.J. Wilbern¹²¹, H.G. Wilkens³⁶,
 J.J.H. Wilkinson³², D.M. Williams⁴¹, H.H. Williams¹²⁹, S. Williams³², S. Willocq¹⁰⁴,
 B.J. Wilson¹⁰², P.J. Windischhofer³⁹, F.I. Winkel³⁰, F. Winklmeier¹²⁴, B.T. Winter⁵⁴,

J.K. Winter ¹⁰², M. Wittgen ¹⁴⁴, M. Wobisch ⁹⁸, Z. Wolffs ¹¹⁵, J. Wollrath ¹⁶⁰, M.W. Wolter ⁸⁷, H. Wolters ^{131a,131c}, M.C. Wong ¹³⁷, E.L. Woodward ⁴¹, S.D. Worm ⁴⁸, B.K. Wosiek ⁸⁷, K.W. Woźniak ⁸⁷, S. Wozniowski ⁵⁵, K. Wraight ⁵⁹, C. Wu ²⁰, M. Wu ^{14d}, M. Wu ¹¹⁴, S.L. Wu ¹⁷¹, X. Wu ⁵⁶, Y. Wu ^{62a}, Z. Wu ⁴, J. Wuerzinger ^{111,ac}, T.R. Wyatt ¹⁰², B.M. Wynne ⁵², S. Xella ⁴², L. Xia ^{14c}, M. Xia ^{14b}, J. Xiang ^{64c}, M. Xie ^{62a}, X. Xie ^{62a}, S. Xin ^{14a,14e}, A. Xiong ¹²⁴, J. Xiong ^{17a}, D. Xu ^{14a}, H. Xu ^{62a}, L. Xu ^{62a}, R. Xu ¹²⁹, T. Xu ¹⁰⁷, Y. Xu ^{14b}, Z. Xu ⁵², Z. Xu ^{14c}, B. Yabsley ¹⁴⁸, S. Yacoob ^{33a}, Y. Yamaguchi ¹⁵⁵, E. Yamashita ¹⁵⁴, H. Yamauchi ¹⁵⁸, T. Yamazaki ^{17a}, Y. Yamazaki ⁸⁵, J. Yan ^{62c}, S. Yan ⁵⁹, Z. Yan ¹⁰⁴, H.J. Yang ^{62c,62d}, H.T. Yang ^{62a}, S. Yang ^{62a}, T. Yang ^{64c}, X. Yang ³⁶, X. Yang ^{14a}, Y. Yang ⁴⁴, Y. Yang ^{62a}, Z. Yang ^{62a}, W-M. Yao ^{17a}, H. Ye ^{14c}, H. Ye ⁵⁵, J. Ye ^{14a}, S. Ye ²⁹, X. Ye ^{62a}, Y. Yeh ⁹⁷, I. Yeletsikh ³⁸, B.K. Yeo ^{17b}, M.R. Yexley ⁹⁷, P. Yin ⁴¹, K. Yorita ¹⁶⁹, S. Younas ^{27b}, C.J.S. Young ³⁶, C. Young ¹⁴⁴, C. Yu ^{14a,14e}, Y. Yu ^{62a}, M. Yuan ¹⁰⁷, R. Yuan ^{62b}, L. Yue ⁹⁷, M. Zaazoua ^{62a}, B. Zabinski ⁸⁷, E. Zaid ⁵², Z.K. Zak ⁸⁷, T. Zakareishvili ¹⁶⁴, N. Zakharchuk ³⁴, S. Zambito ⁵⁶, J.A. Zamora Saa ^{138d,138b}, J. Zang ¹⁵⁴, D. Zanzi ⁵⁴, O. Zaplatilek ¹³³, C. Zeitnitz ¹⁷², H. Zeng ^{14a}, J.C. Zeng ¹⁶³, D.T. Zenger Jr ²⁶, O. Zenin ³⁷, T. Ženiš ^{28a}, S. Zenz ⁹⁵, S. Zerradi ^{35a}, D. Zerwas ⁶⁶, M. Zhai ^{14a,14e}, D.F. Zhang ¹⁴⁰, J. Zhang ^{62b}, J. Zhang ⁶, K. Zhang ^{14a,14e}, L. Zhang ^{14c}, P. Zhang ^{14a,14e}, R. Zhang ¹⁷¹, S. Zhang ¹⁰⁷, S. Zhang ⁴⁴, T. Zhang ¹⁵⁴, X. Zhang ^{62c}, X. Zhang ^{62b}, Y. Zhang ^{62c,5}, Y. Zhang ⁹⁷, Y. Zhang ^{14c}, Z. Zhang ^{17a}, Z. Zhang ⁶⁶, H. Zhao ¹³⁹, T. Zhao ^{62b}, Y. Zhao ¹³⁷, Z. Zhao ^{62a}, Z. Zhao ^{62a}, A. Zhemchugov ³⁸, J. Zheng ^{14c}, K. Zheng ¹⁶³, X. Zheng ^{62a}, Z. Zheng ¹⁴⁴, D. Zhong ¹⁶³, B. Zhou ¹⁰⁷, H. Zhou ⁷, N. Zhou ^{62c}, Y. Zhou ^{14c}, Y. Zhou ⁷, C.G. Zhu ^{62b}, J. Zhu ¹⁰⁷, Y. Zhu ^{62c}, Y. Zhu ^{62a}, X. Zhuang ^{14a}, K. Zhukov ³⁷, N.I. Zimine ³⁸, J. Zinsser ^{63b}, M. Ziolkowski ¹⁴², L. Živković ¹⁵, A. Zoccoli ^{23b,23a}, K. Zoch ⁶¹, T.G. Zorbas ¹⁴⁰, O. Zormpa ⁴⁶, W. Zou ⁴¹, L. Zwalinski ³⁶.

¹Department of Physics, University of Adelaide, Adelaide; Australia.

²Department of Physics, University of Alberta, Edmonton AB; Canada.

³(^a)Department of Physics, Ankara University, Ankara; (^b)Division of Physics, TOBB University of Economics and Technology, Ankara; Türkiye.

⁴LAPP, Université Savoie Mont Blanc, CNRS/IN2P3, Annecy; France.

⁵APC, Université Paris Cité, CNRS/IN2P3, Paris; France.

⁶High Energy Physics Division, Argonne National Laboratory, Argonne IL; United States of America.

⁷Department of Physics, University of Arizona, Tucson AZ; United States of America.

⁸Department of Physics, University of Texas at Arlington, Arlington TX; United States of America.

⁹Physics Department, National and Kapodistrian University of Athens, Athens; Greece.

¹⁰Physics Department, National Technical University of Athens, Zografou; Greece.

¹¹Department of Physics, University of Texas at Austin, Austin TX; United States of America.

¹²Institute of Physics, Azerbaijan Academy of Sciences, Baku; Azerbaijan.

¹³Institut de Física d'Altes Energies (IFAE), Barcelona Institute of Science and Technology, Barcelona; Spain.

¹⁴(^a)Institute of High Energy Physics, Chinese Academy of Sciences, Beijing; (^b)Physics Department, Tsinghua University, Beijing; (^c)Department of Physics, Nanjing University, Nanjing; (^d)School of Science, Shenzhen Campus of Sun Yat-sen University; (^e)University of Chinese Academy of Science (UCAS), Beijing; China.

¹⁵Institute of Physics, University of Belgrade, Belgrade; Serbia.

¹⁶Department for Physics and Technology, University of Bergen, Bergen; Norway.

¹⁷(^a)Physics Division, Lawrence Berkeley National Laboratory, Berkeley CA; (^b)University of California,

Berkeley CA; United States of America.

¹⁸Institut für Physik, Humboldt Universität zu Berlin, Berlin; Germany.

¹⁹Albert Einstein Center for Fundamental Physics and Laboratory for High Energy Physics, University of Bern, Bern; Switzerland.

²⁰School of Physics and Astronomy, University of Birmingham, Birmingham; United Kingdom.

²¹(^a) Department of Physics, Bogazici University, Istanbul; (^b) Department of Physics Engineering, Gaziantep University, Gaziantep; (^c) Department of Physics, Istanbul University, Istanbul; Türkiye.

²²(^a) Facultad de Ciencias y Centro de Investigaciones, Universidad Antonio Nariño,

Bogotá; (^b) Departamento de Física, Universidad Nacional de Colombia, Bogotá; Colombia.

²³(^a) Dipartimento di Fisica e Astronomia A. Righi, Università di Bologna, Bologna; (^b) INFN Sezione di Bologna; Italy.

²⁴Physikalisches Institut, Universität Bonn, Bonn; Germany.

²⁵Department of Physics, Boston University, Boston MA; United States of America.

²⁶Department of Physics, Brandeis University, Waltham MA; United States of America.

²⁷(^a) Transilvania University of Brasov, Brasov; (^b) Horia Hulubei National Institute of Physics and Nuclear Engineering, Bucharest; (^c) Department of Physics, Alexandru Ioan Cuza University of Iasi, Iasi; (^d) National Institute for Research and Development of Isotopic and Molecular Technologies, Physics Department, Cluj-Napoca; (^e) National University of Science and Technology Politehnica, Bucharest; (^f) West University in Timisoara, Timisoara; (^g) Faculty of Physics, University of Bucharest, Bucharest; Romania.

²⁸(^a) Faculty of Mathematics, Physics and Informatics, Comenius University, Bratislava; (^b) Department of Subnuclear Physics, Institute of Experimental Physics of the Slovak Academy of Sciences, Kosice; Slovak Republic.

²⁹Physics Department, Brookhaven National Laboratory, Upton NY; United States of America.

³⁰Universidad de Buenos Aires, Facultad de Ciencias Exactas y Naturales, Departamento de Física, y CONICET, Instituto de Física de Buenos Aires (IFIBA), Buenos Aires; Argentina.

³¹California State University, CA; United States of America.

³²Cavendish Laboratory, University of Cambridge, Cambridge; United Kingdom.

³³(^a) Department of Physics, University of Cape Town, Cape Town; (^b) iThemba Labs, Western Cape; (^c) Department of Mechanical Engineering Science, University of Johannesburg,

Johannesburg; (^d) National Institute of Physics, University of the Philippines Diliman

(Philippines); (^e) University of South Africa, Department of Physics, Pretoria; (^f) University of Zululand, KwaDlangezwa; (^g) School of Physics, University of the Witwatersrand, Johannesburg; South Africa.

³⁴Department of Physics, Carleton University, Ottawa ON; Canada.

³⁵(^a) Faculté des Sciences Ain Chock, Réseau Universitaire de Physique des Hautes Energies - Université Hassan II, Casablanca; (^b) Faculté des Sciences, Université Ibn-Tofail, Kénitra; (^c) Faculté des Sciences Semlalia, Université Cadi Ayyad, LPHEA-Marrakech; (^d) LPMR, Faculté des Sciences, Université Mohamed Premier, Oujda; (^e) Faculté des sciences, Université Mohammed V, Rabat; (^f) Institute of Applied Physics, Mohammed VI Polytechnic University, Ben Guerir; Morocco.

³⁶CERN, Geneva; Switzerland.

³⁷Affiliated with an institute covered by a cooperation agreement with CERN.

³⁸Affiliated with an international laboratory covered by a cooperation agreement with CERN.

³⁹Enrico Fermi Institute, University of Chicago, Chicago IL; United States of America.

⁴⁰LPC, Université Clermont Auvergne, CNRS/IN2P3, Clermont-Ferrand; France.

⁴¹Nevis Laboratory, Columbia University, Irvington NY; United States of America.

⁴²Niels Bohr Institute, University of Copenhagen, Copenhagen; Denmark.

⁴³(^a) Dipartimento di Fisica, Università della Calabria, Rende; (^b) INFN Gruppo Collegato di Cosenza, Laboratori Nazionali di Frascati; Italy.

- ⁴⁴Physics Department, Southern Methodist University, Dallas TX; United States of America.
- ⁴⁵Physics Department, University of Texas at Dallas, Richardson TX; United States of America.
- ⁴⁶National Centre for Scientific Research "Demokritos", Agia Paraskevi; Greece.
- ⁴⁷(^a) Department of Physics, Stockholm University; (^b) Oskar Klein Centre, Stockholm; Sweden.
- ⁴⁸Deutsches Elektronen-Synchrotron DESY, Hamburg and Zeuthen; Germany.
- ⁴⁹Fakultät Physik, Technische Universität Dortmund, Dortmund; Germany.
- ⁵⁰Institut für Kern- und Teilchenphysik, Technische Universität Dresden, Dresden; Germany.
- ⁵¹Department of Physics, Duke University, Durham NC; United States of America.
- ⁵²SUPA - School of Physics and Astronomy, University of Edinburgh, Edinburgh; United Kingdom.
- ⁵³INFN e Laboratori Nazionali di Frascati, Frascati; Italy.
- ⁵⁴Physikalisches Institut, Albert-Ludwigs-Universität Freiburg, Freiburg; Germany.
- ⁵⁵II. Physikalisches Institut, Georg-August-Universität Göttingen, Göttingen; Germany.
- ⁵⁶Département de Physique Nucléaire et Corpusculaire, Université de Genève, Genève; Switzerland.
- ⁵⁷(^a) Dipartimento di Fisica, Università di Genova, Genova; (^b) INFN Sezione di Genova; Italy.
- ⁵⁸II. Physikalisches Institut, Justus-Liebig-Universität Giessen, Giessen; Germany.
- ⁵⁹SUPA - School of Physics and Astronomy, University of Glasgow, Glasgow; United Kingdom.
- ⁶⁰LPSC, Université Grenoble Alpes, CNRS/IN2P3, Grenoble INP, Grenoble; France.
- ⁶¹Laboratory for Particle Physics and Cosmology, Harvard University, Cambridge MA; United States of America.
- ⁶²(^a) Department of Modern Physics and State Key Laboratory of Particle Detection and Electronics, University of Science and Technology of China, Hefei; (^b) Institute of Frontier and Interdisciplinary Science and Key Laboratory of Particle Physics and Particle Irradiation (MOE), Shandong University, Qingdao; (^c) School of Physics and Astronomy, Shanghai Jiao Tong University, Key Laboratory for Particle Astrophysics and Cosmology (MOE), SKLPPC, Shanghai; (^d) Tsung-Dao Lee Institute, Shanghai; (^e) School of Physics and Microelectronics, Zhengzhou University; China.
- ⁶³(^a) Kirchhoff-Institut für Physik, Ruprecht-Karls-Universität Heidelberg, Heidelberg; (^b) Physikalisches Institut, Ruprecht-Karls-Universität Heidelberg, Heidelberg; Germany.
- ⁶⁴(^a) Department of Physics, Chinese University of Hong Kong, Shatin, N.T., Hong Kong; (^b) Department of Physics, University of Hong Kong, Hong Kong; (^c) Department of Physics and Institute for Advanced Study, Hong Kong University of Science and Technology, Clear Water Bay, Kowloon, Hong Kong; China.
- ⁶⁵Department of Physics, National Tsing Hua University, Hsinchu; Taiwan.
- ⁶⁶IJCLab, Université Paris-Saclay, CNRS/IN2P3, 91405, Orsay; France.
- ⁶⁷Centro Nacional de Microelectrónica (IMB-CNM-CSIC), Barcelona; Spain.
- ⁶⁸Department of Physics, Indiana University, Bloomington IN; United States of America.
- ⁶⁹(^a) INFN Gruppo Collegato di Udine, Sezione di Trieste, Udine; (^b) ICTP, Trieste; (^c) Dipartimento Politecnico di Ingegneria e Architettura, Università di Udine, Udine; Italy.
- ⁷⁰(^a) INFN Sezione di Lecce; (^b) Dipartimento di Matematica e Fisica, Università del Salento, Lecce; Italy.
- ⁷¹(^a) INFN Sezione di Milano; (^b) Dipartimento di Fisica, Università di Milano, Milano; Italy.
- ⁷²(^a) INFN Sezione di Napoli; (^b) Dipartimento di Fisica, Università di Napoli, Napoli; Italy.
- ⁷³(^a) INFN Sezione di Pavia; (^b) Dipartimento di Fisica, Università di Pavia, Pavia; Italy.
- ⁷⁴(^a) INFN Sezione di Pisa; (^b) Dipartimento di Fisica E. Fermi, Università di Pisa, Pisa; Italy.
- ⁷⁵(^a) INFN Sezione di Roma; (^b) Dipartimento di Fisica, Sapienza Università di Roma, Roma; Italy.
- ⁷⁶(^a) INFN Sezione di Roma Tor Vergata; (^b) Dipartimento di Fisica, Università di Roma Tor Vergata, Roma; Italy.
- ⁷⁷(^a) INFN Sezione di Roma Tre; (^b) Dipartimento di Matematica e Fisica, Università Roma Tre, Roma; Italy.
- ⁷⁸(^a) INFN-TIFPA; (^b) Università degli Studi di Trento, Trento; Italy.

- ⁷⁹Universität Innsbruck, Department of Astro and Particle Physics, Innsbruck; Austria.
- ⁸⁰University of Iowa, Iowa City IA; United States of America.
- ⁸¹Department of Physics and Astronomy, Iowa State University, Ames IA; United States of America.
- ⁸²Istinye University, Sariyer, Istanbul; Türkiye.
- ⁸³(^a) Departamento de Engenharia Elétrica, Universidade Federal de Juiz de Fora (UFJF), Juiz de Fora; (^b) Universidade Federal do Rio De Janeiro COPPE/EE/IF, Rio de Janeiro; (^c) Instituto de Física, Universidade de São Paulo, São Paulo; (^d) Rio de Janeiro State University, Rio de Janeiro; (^e) Federal University of Bahia, Bahia; Brazil.
- ⁸⁴KEK, High Energy Accelerator Research Organization, Tsukuba; Japan.
- ⁸⁵Graduate School of Science, Kobe University, Kobe; Japan.
- ⁸⁶(^a) AGH University of Krakow, Faculty of Physics and Applied Computer Science, Krakow; (^b) Marian Smoluchowski Institute of Physics, Jagiellonian University, Krakow; Poland.
- ⁸⁷Institute of Nuclear Physics Polish Academy of Sciences, Krakow; Poland.
- ⁸⁸Faculty of Science, Kyoto University, Kyoto; Japan.
- ⁸⁹Research Center for Advanced Particle Physics and Department of Physics, Kyushu University, Fukuoka ; Japan.
- ⁹⁰L2IT, Université de Toulouse, CNRS/IN2P3, UPS, Toulouse; France.
- ⁹¹Instituto de Física La Plata, Universidad Nacional de La Plata and CONICET, La Plata; Argentina.
- ⁹²Physics Department, Lancaster University, Lancaster; United Kingdom.
- ⁹³Oliver Lodge Laboratory, University of Liverpool, Liverpool; United Kingdom.
- ⁹⁴Department of Experimental Particle Physics, Jožef Stefan Institute and Department of Physics, University of Ljubljana, Ljubljana; Slovenia.
- ⁹⁵School of Physics and Astronomy, Queen Mary University of London, London; United Kingdom.
- ⁹⁶Department of Physics, Royal Holloway University of London, Egham; United Kingdom.
- ⁹⁷Department of Physics and Astronomy, University College London, London; United Kingdom.
- ⁹⁸Louisiana Tech University, Ruston LA; United States of America.
- ⁹⁹Fysiska institutionen, Lunds universitet, Lund; Sweden.
- ¹⁰⁰Departamento de Física Teórica C-15 and CIAFF, Universidad Autónoma de Madrid, Madrid; Spain.
- ¹⁰¹Institut für Physik, Universität Mainz, Mainz; Germany.
- ¹⁰²School of Physics and Astronomy, University of Manchester, Manchester; United Kingdom.
- ¹⁰³CPPM, Aix-Marseille Université, CNRS/IN2P3, Marseille; France.
- ¹⁰⁴Department of Physics, University of Massachusetts, Amherst MA; United States of America.
- ¹⁰⁵Department of Physics, McGill University, Montreal QC; Canada.
- ¹⁰⁶School of Physics, University of Melbourne, Victoria; Australia.
- ¹⁰⁷Department of Physics, University of Michigan, Ann Arbor MI; United States of America.
- ¹⁰⁸Department of Physics and Astronomy, Michigan State University, East Lansing MI; United States of America.
- ¹⁰⁹Group of Particle Physics, University of Montreal, Montreal QC; Canada.
- ¹¹⁰Fakultät für Physik, Ludwig-Maximilians-Universität München, München; Germany.
- ¹¹¹Max-Planck-Institut für Physik (Werner-Heisenberg-Institut), München; Germany.
- ¹¹²Graduate School of Science and Kobayashi-Maskawa Institute, Nagoya University, Nagoya; Japan.
- ¹¹³Department of Physics and Astronomy, University of New Mexico, Albuquerque NM; United States of America.
- ¹¹⁴Institute for Mathematics, Astrophysics and Particle Physics, Radboud University/Nikhef, Nijmegen; Netherlands.
- ¹¹⁵Nikhef National Institute for Subatomic Physics and University of Amsterdam, Amsterdam; Netherlands.

- ¹¹⁶Department of Physics, Northern Illinois University, DeKalb IL; United States of America.
- ¹¹⁷^(a)New York University Abu Dhabi, Abu Dhabi;^(b)United Arab Emirates University, Al Ain; United Arab Emirates.
- ¹¹⁸Department of Physics, New York University, New York NY; United States of America.
- ¹¹⁹Ochanomizu University, Otsuka, Bunkyo-ku, Tokyo; Japan.
- ¹²⁰Ohio State University, Columbus OH; United States of America.
- ¹²¹Homer L. Dodge Department of Physics and Astronomy, University of Oklahoma, Norman OK; United States of America.
- ¹²²Department of Physics, Oklahoma State University, Stillwater OK; United States of America.
- ¹²³Palacký University, Joint Laboratory of Optics, Olomouc; Czech Republic.
- ¹²⁴Institute for Fundamental Science, University of Oregon, Eugene, OR; United States of America.
- ¹²⁵Graduate School of Science, Osaka University, Osaka; Japan.
- ¹²⁶Department of Physics, University of Oslo, Oslo; Norway.
- ¹²⁷Department of Physics, Oxford University, Oxford; United Kingdom.
- ¹²⁸LPNHE, Sorbonne Université, Université Paris Cité, CNRS/IN2P3, Paris; France.
- ¹²⁹Department of Physics, University of Pennsylvania, Philadelphia PA; United States of America.
- ¹³⁰Department of Physics and Astronomy, University of Pittsburgh, Pittsburgh PA; United States of America.
- ¹³¹^(a)Laboratório de Instrumentação e Física Experimental de Partículas - LIP, Lisboa;^(b)Departamento de Física, Faculdade de Ciências, Universidade de Lisboa, Lisboa;^(c)Departamento de Física, Universidade de Coimbra, Coimbra;^(d)Centro de Física Nuclear da Universidade de Lisboa, Lisboa;^(e)Departamento de Física, Universidade do Minho, Braga;^(f)Departamento de Física Teórica y del Cosmos, Universidad de Granada, Granada (Spain);^(g)Departamento de Física, Instituto Superior Técnico, Universidade de Lisboa, Lisboa; Portugal.
- ¹³²Institute of Physics of the Czech Academy of Sciences, Prague; Czech Republic.
- ¹³³Czech Technical University in Prague, Prague; Czech Republic.
- ¹³⁴Charles University, Faculty of Mathematics and Physics, Prague; Czech Republic.
- ¹³⁵Particle Physics Department, Rutherford Appleton Laboratory, Didcot; United Kingdom.
- ¹³⁶IRFU, CEA, Université Paris-Saclay, Gif-sur-Yvette; France.
- ¹³⁷Santa Cruz Institute for Particle Physics, University of California Santa Cruz, Santa Cruz CA; United States of America.
- ¹³⁸^(a)Departamento de Física, Pontificia Universidad Católica de Chile, Santiago;^(b)Millennium Institute for Subatomic physics at high energy frontier (SAPHIR), Santiago;^(c)Instituto de Investigación Multidisciplinario en Ciencia y Tecnología, y Departamento de Física, Universidad de La Serena;^(d)Universidad Andres Bello, Department of Physics, Santiago;^(e)Instituto de Alta Investigación, Universidad de Tarapacá, Arica;^(f)Departamento de Física, Universidad Técnica Federico Santa María, Valparaíso; Chile.
- ¹³⁹Department of Physics, University of Washington, Seattle WA; United States of America.
- ¹⁴⁰Department of Physics and Astronomy, University of Sheffield, Sheffield; United Kingdom.
- ¹⁴¹Department of Physics, Shinshu University, Nagano; Japan.
- ¹⁴²Department Physik, Universität Siegen, Siegen; Germany.
- ¹⁴³Department of Physics, Simon Fraser University, Burnaby BC; Canada.
- ¹⁴⁴SLAC National Accelerator Laboratory, Stanford CA; United States of America.
- ¹⁴⁵Department of Physics, Royal Institute of Technology, Stockholm; Sweden.
- ¹⁴⁶Departments of Physics and Astronomy, Stony Brook University, Stony Brook NY; United States of America.
- ¹⁴⁷Department of Physics and Astronomy, University of Sussex, Brighton; United Kingdom.

- ¹⁴⁸School of Physics, University of Sydney, Sydney; Australia.
- ¹⁴⁹Institute of Physics, Academia Sinica, Taipei; Taiwan.
- ¹⁵⁰(^a) E. Andronikashvili Institute of Physics, Iv. Javakhishvili Tbilisi State University, Tbilisi; (^b) High Energy Physics Institute, Tbilisi State University, Tbilisi; (^c) University of Georgia, Tbilisi; Georgia.
- ¹⁵¹Department of Physics, Technion, Israel Institute of Technology, Haifa; Israel.
- ¹⁵²Raymond and Beverly Sackler School of Physics and Astronomy, Tel Aviv University, Tel Aviv; Israel.
- ¹⁵³Department of Physics, Aristotle University of Thessaloniki, Thessaloniki; Greece.
- ¹⁵⁴International Center for Elementary Particle Physics and Department of Physics, University of Tokyo, Tokyo; Japan.
- ¹⁵⁵Department of Physics, Tokyo Institute of Technology, Tokyo; Japan.
- ¹⁵⁶Department of Physics, University of Toronto, Toronto ON; Canada.
- ¹⁵⁷(^a) TRIUMF, Vancouver BC; (^b) Department of Physics and Astronomy, York University, Toronto ON; Canada.
- ¹⁵⁸Division of Physics and Tomonaga Center for the History of the Universe, Faculty of Pure and Applied Sciences, University of Tsukuba, Tsukuba; Japan.
- ¹⁵⁹Department of Physics and Astronomy, Tufts University, Medford MA; United States of America.
- ¹⁶⁰Department of Physics and Astronomy, University of California Irvine, Irvine CA; United States of America.
- ¹⁶¹University of Sharjah, Sharjah; United Arab Emirates.
- ¹⁶²Department of Physics and Astronomy, University of Uppsala, Uppsala; Sweden.
- ¹⁶³Department of Physics, University of Illinois, Urbana IL; United States of America.
- ¹⁶⁴Instituto de Física Corpuscular (IFIC), Centro Mixto Universidad de Valencia - CSIC, Valencia; Spain.
- ¹⁶⁵Department of Physics, University of British Columbia, Vancouver BC; Canada.
- ¹⁶⁶Department of Physics and Astronomy, University of Victoria, Victoria BC; Canada.
- ¹⁶⁷Fakultät für Physik und Astronomie, Julius-Maximilians-Universität Würzburg, Würzburg; Germany.
- ¹⁶⁸Department of Physics, University of Warwick, Coventry; United Kingdom.
- ¹⁶⁹Waseda University, Tokyo; Japan.
- ¹⁷⁰Department of Particle Physics and Astrophysics, Weizmann Institute of Science, Rehovot; Israel.
- ¹⁷¹Department of Physics, University of Wisconsin, Madison WI; United States of America.
- ¹⁷²Fakultät für Mathematik und Naturwissenschaften, Fachgruppe Physik, Bergische Universität Wuppertal, Wuppertal; Germany.
- ¹⁷³Department of Physics, Yale University, New Haven CT; United States of America.
- ^a Also Affiliated with an institute covered by a cooperation agreement with CERN.
- ^b Also at An-Najah National University, Nablus; Palestine.
- ^c Also at Borough of Manhattan Community College, City University of New York, New York NY; United States of America.
- ^d Also at Center for High Energy Physics, Peking University; China.
- ^e Also at Center for Interdisciplinary Research and Innovation (CIRI-AUTH), Thessaloniki; Greece.
- ^f Also at Centro Studi e Ricerche Enrico Fermi; Italy.
- ^g Also at CERN, Geneva; Switzerland.
- ^h Also at Département de Physique Nucléaire et Corpusculaire, Université de Genève, Genève; Switzerland.
- ⁱ Also at Departament de Física de la Universitat Autònoma de Barcelona, Barcelona; Spain.
- ^j Also at Department of Financial and Management Engineering, University of the Aegean, Chios; Greece.
- ^k Also at Department of Physics, California State University, Sacramento; United States of America.
- ^l Also at Department of Physics, King's College London, London; United Kingdom.
- ^m Also at Department of Physics, Stanford University, Stanford CA; United States of America.

- ⁿ Also at Department of Physics, Stellenbosch University; South Africa.
- ^o Also at Department of Physics, University of Fribourg, Fribourg; Switzerland.
- ^p Also at Department of Physics, University of Thessaly; Greece.
- ^q Also at Department of Physics, Westmont College, Santa Barbara; United States of America.
- ^r Also at Hellenic Open University, Patras; Greece.
- ^s Also at Institutio Catalana de Recerca i Estudis Avancats, ICREA, Barcelona; Spain.
- ^t Also at Institut für Experimentalphysik, Universität Hamburg, Hamburg; Germany.
- ^u Also at Institute for Nuclear Research and Nuclear Energy (INRNE) of the Bulgarian Academy of Sciences, Sofia; Bulgaria.
- ^v Also at Institute of Applied Physics, Mohammed VI Polytechnic University, Ben Guerir; Morocco.
- ^w Also at Institute of Particle Physics (IPP); Canada.
- ^x Also at Institute of Physics and Technology, Mongolian Academy of Sciences, Ulaanbaatar; Mongolia.
- ^y Also at Institute of Physics, Azerbaijan Academy of Sciences, Baku; Azerbaijan.
- ^z Also at Institute of Theoretical Physics, Ilia State University, Tbilisi; Georgia.
- ^{aa} Also at Lawrence Livermore National Laboratory, Livermore; United States of America.
- ^{ab} Also at National Institute of Physics, University of the Philippines Diliman (Philippines); Philippines.
- ^{ac} Also at Technical University of Munich, Munich; Germany.
- ^{ad} Also at The Collaborative Innovation Center of Quantum Matter (CICQM), Beijing; China.
- ^{ae} Also at TRIUMF, Vancouver BC; Canada.
- ^{af} Also at Università di Napoli Parthenope, Napoli; Italy.
- ^{ag} Also at University of Colorado Boulder, Department of Physics, Colorado; United States of America.
- ^{ah} Also at Washington College, Chestertown, MD; United States of America.
- ^{ai} Also at Yeditepe University, Physics Department, Istanbul; Türkiye.
- * Deceased

ACE Science Workshop Report

Stefania Gori (ed.)¹, Nhan Tran (ed.)², Karri DiPetrillo³, Bertrand Echenard⁴, Jeffrey Eldred², Roni Harnik², Pedro Machado², Matthew Touns², I. P. Fernando⁵, Robert Bernstein², Innes Bigaran^{2,6}, Cari Cesarotti⁹, Bhaskar Dutta⁷, Christian Herwig², Sergo Jindariani², Ryan Plestid⁴, Vladimir Shiltsev¹⁰, Matthew Solt⁵, Alexandre Sousa⁸, Diktys Stratakis², Zahra Tabrizi⁶, Anil Thapa⁵, Jacob Zettlemoyer², and Jure Zupan⁸

¹University of California Santa Cruz, Santa Cruz, CA 95064, USA

²Fermi National Accelerator Laboratory, Batavia, IL 60510, USA

³University of Chicago, Chicago, IL 60637, USA

⁴California Institute of Technology, Pasadena, CA 91125, USA

⁵University of Virginia, Charlottesville, VA 22904, USA

⁶Northwestern University, Evanston, IL 60208, USA

⁷Mitchell Institute and Texas A&M University, College Station, TX 77843, USA

⁸University of Cincinnati, Cincinnati, OH 45221, USA

⁹Massachusetts Institute of Technology, Cambridge, MA 02139, USA

¹⁰Northern Illinois University, DeKalb, IL 60115, USA

ABSTRACT

We summarize the Fermilab Accelerator Complex Evolution (ACE) Science Workshop, held on June 14-15, 2023. The workshop presented the strategy for the ACE program in two phases: ACE Main Injector Ramp and Target (MIRT) upgrade and ACE Booster Replacement (BR) upgrade. Four plenary sessions covered the primary experimental physics thrusts: Muon Collider, Neutrinos, Charged Lepton Flavor Violation, and Dark Sectors. Additional physics and technology ideas were presented from the community that could expand or augment the ACE science program. Given the physics framing, a parallel session at the workshop was dedicated to discussing priorities for accelerator R&D. Finally, physics discussion sessions concluded the workshop where experts from the different experimental physics thrusts were brought together to begin understanding the synergies between the different physics drivers and technologies. In December of 2023, the P5 report was released setting the physics priorities for the field in the next decade and beyond, and identified ACE as an important component of the future US accelerator-based program. Given the presentations and discussions at the ACE Science Workshop and the findings of the P5 report, we lay out the topics for study to determine the physics priorities and design goals of the Fermilab ACE project in the near-term.

Contents

1	Executive Summary	3
2	Fermilab Accelerator Complex Evolution (ACE) and physics thrusts	5
2.1	Fermilab Accelerator Complex Evolution	5
2.2	Physics drivers and experimental thrusts	5
2.2.1	Muon Collider	6
2.2.2	Neutrino physics	7
2.2.3	Charged Lepton Flavor Violation	7
2.2.4	Accelerator-based dark sectors	7
2.3	Additional technology and physics directions	8
2.3.1	Physics experiments	8
2.3.2	Technology development	9
3	Physics, detector, and accelerator complementarity	10
3.1	CLFV - Dark Sectors	10
3.2	CLFV - Muon Collider	10
3.3	CLFV - Neutrinos	11
3.4	Dark Sectors - Muon Colliders	12
3.5	Dark Sectors - Neutrinos	12
3.6	Muon Collider - Neutrinos	13
3.7	Accelerator technology and R&D	14

1 Executive Summary

The Fermilab Accelerator Complex Evolution (ACE) Science Workshop [1], held on June 14-15, 2023, brought together an international cohort of physicists with expertise in theory, experiment, and accelerator technologies to begin a coordinated discussion defining the Fermilab ACE physics program. The aim of this intensive workshop was to review the motivations and current state of the primary physics thrusts and their accelerator needs and to outline a strategic road map to understand the complementarity of their emerging scientific demands. A detailed description of the preliminary ACE approach is outlined in the Proton Intensity Upgrade - Central Design Group (PIU-CDG) report [2].

ACE consists of two primary phases:

1. **ACE-MIRT (Main Injector Ramp and Target) upgrade:** this aims to upgrade the Main Injector to reduce the ramp time and deliver more beam power to DUNE (max ~ 2.1 MW) as soon as possible. This also requires target R&D to ensure that DUNE can handle up to 2.4 MW of beam power, the ultimate design goal.
2. **ACE-BR (Booster Replacement) upgrade:** the Booster replacement aims to replace the Booster synchrotron which accelerates protons from 800 MeV to 8 GeV to **deliver** the full >2.4 MW of beam power to DUNE, and to **enable** the development of the next generation of US accelerator-based particle physics experiments while modernizing the complex to provide **reliable** beam to all its users.

The scientific potential of the Fermilab ACE science program is very broad and includes a wide variety of physics topics discussed during the Snowmass 2021 process [3] across the energy, neutrino, rare processes and precision, theory, and cosmic frontiers. The primary experimental physics thrusts and related experiments presented at the workshop were:

- **Charged Lepton Flavor Violation (CLFV) experiments:** using high intensity beams of muons aim to significantly improve indirect searches for new physics up to scales of $\mathcal{O}(10^5 \text{ TeV})$.
- **Dark sector experiments:** using high intensity beams of protons and muons aim to explore uncovered parameter space of thermal dark matter models, as well as models that address the strong CP problem (axion-like-particles), the origin of neutrino masses (sterile neutrinos), and the hierarchy problem (dark scalars).
- **Muon Collider (MC):** enables direct searches for new physics at the $\mathcal{O}(10 \text{ TeV})$ scale with intense proton beams that can serve as technology demonstrators and a front-end proton driver facility. It also enables unique precision measurements of Standard Model (SM) particles, like the Higgs boson.
- **Neutrino experiments beyond DUNE:** enable exploration of the neutrino sector beyond DUNE via direct searches connected to anomalies and high precision Standard Model measurements.

While these focus areas comprise the primary experimental physics thrusts considered, other experimental proposals or ideas outside of these thrusts were presented in open sessions for remarks from the community, as well as in parallel discussion sessions. For example, rare meson decays, mono-energetic neutrino beams, or muon beams could be used to test dark sector physics. ACE can also be used for spin physics studies and energy research. The breadth of these ideas can be synergistic with the primary experimental physics thrusts or expand the overall physics potential of ACE.

The synergy between the several physics thrusts was also discussed during the workshop. Neutrino detectors and neutrino beam measurements can be used to test the physics of the dark sector. A muon collider could be used to test non-standard neutrino interactions and dark matter freeze-out models across a broad range of energies: high mass ($>1 \text{ TeV}$) WIMPs could be produced at the main interaction point, and light muon-philic dark sectors could be produced in the muon dumps. Neutrinos are a probe of lepton flavor symmetries, and, therefore, CLFV and neutrino experiments provide complementary probes of new physics. Finally, CLFV experiments can explore the parameter space of new sub-GeV dark particles with flavor violating couplings.

Outcomes

The preliminary points for study and outcomes of the workshop are discussed below. We discuss the ACE project design constraints, technology R&D, and physics synergies:

ACE design parameters

- **ACE-MIRT (Main Injector Ramp and Targetry) era:**
 - The 8 GeV proton intensity and accelerator timeline economics during the ACE-MIRT era needs to be understood in more detail because the Main Injector (MI) cycle time reduction provides less beam power for the muon program, short baseline neutrino program, and MC R&D.

- The ACE program should continue to provide a fraction of MI cycles to the 120 GeV beam slow extraction program to support test beam, dark sector physics, and spin physics.
- An accumulator ring at 0.8 GeV for pulsed proton beam would greatly enhance the physics capabilities of the proton beam dump dark sector program and the CLFV program.
- **ACE-BR (Booster Replacement) – 2 GeV Linac:** A 2 GeV Linac is a part of all the current ACE-BR designs. The benefits and trade-offs of an earlier construction start need to be understood:
 - Due to increased muon production vs. proton energy, a 2 GeV beam would improve the physics reach of next generation CLFV experiments.
 - A 2 GeV CW beam could serve as good MC cooling demonstrator front-end. Its benefits versus the 8 GeV booster beam during the ACE-MIRT era require more study.
 - Design of an accumulator ring optimized for 2 GeV but that can operate at 0.8 GeV should be explored to enable flexible operations across the ACE-MIRT and ACE-BR eras.
 - Resource benefits by beginning the 2 GeV Linac construction soon after PIP-II completion needs to be understood.
- **ACE-BR (Booster Replacement) – 2→8 GeV:**
 - To deliver 2.4 MW to DUNE, each of the 6 ACE-BR configurations are sufficient.
 - To enable ACE to serve as a Muon Collider proton driver front-end, the ACE-BR configurations need to be re-optimized.
 - An H^- Linac option for ACE-BR is a more natural fit for MC than an RCS due to the requirement synergies with DUNE.
 - Further study is needed to understand if an 8 GeV accumulator ring used in a ACE-BR Linac scenario for DUNE would also be sufficient to serve as the MC proton driver accumulator ring and provide beam for other physics scenarios.

Technology R&D and Physics complementarity

- **Accelerator R&D:**
 - High Power Targetry is the highest priority accelerator R&D area because it is required during the ACE-MIRT era to achieve the DUNE physics goals. It is also identified as a key area of synergistic R&D for the MC and a future CLFV program.
 - Other high priority accelerator R&D topic areas include high power H^- stripping (including laser stripping), MC cooling demonstrator, and high current accumulator ring designs that can operate at 0.8-2 GeV.
- **Physics synergies to be studied:**
 - The physics case for a neutrino factory needs to be re-visited in a post-DUNE scenario. A number of important points were discussed, especially tau neutrino physics and precision neutrino measurements, but the physics cases need to be collated.
 - Better understanding of how neutrino mass benchmark models map onto CLFV physics reach would provide sharp targets for the CLFV program.

Outlook and next steps

Following the release of the P5 report [4], the particle physics community has been provided with a roadmap outlining the physics priorities for the upcoming decade and beyond. The P5 report specifically highlights ACE as an important component of this plan (Recommendation 4(g), Recommendation 6, Area Recommendation 12), due to the potential presented by the Muon Collider. A primary aim of ACE is to facilitate the development of a proton driver essential for the Muon Collider while being able to deliver a world-class experimental physics program that can address several of the P5 physics drivers: Elucidate the Mysteries of Neutrinos; Reveal the Secrets of the Higgs Boson; Search for Direct Evidence of New Particles; Pursue Quantum Imprints of New Phenomena; Determine the Nature of Dark Matter. Defining the exciting potential of the ACE experimental program and the design of the facility are important recommendations of the P5 report.

The immediate future involves holding a series of workshops to gather input from the community and build consensus with the initial focus on refining the accelerator design to align with new P5 priorities. It is also necessary to understand how the various proposed physics concepts can fit together within the ACE design, including research and development paths. After the workshop focused on accelerator design, another physics workshop will be convened. With a concrete ACE layout and design, it will set out to establish physics priorities and explore the possibilities that will lead to a conceptual design (CD-0) in the following years to be presented to a targeted panel that determines the path forward for the US accelerator-based physics program [4].

2 Fermilab Accelerator Complex Evolution (ACE) and physics thrusts

2.1 Fermilab Accelerator Complex Evolution

The Fermilab Accelerator Complex Evolution (ACE) consists of two primary phases, the Main Injector Ramp and Target (MIRT) upgrade and the Booster Replacement (BR) upgrade. ACE-MIRT aims to upgrade the Main Injector to reduce the ramp time and deliver more beam power to DUNE (max ~ 2.1 MW) as soon as possible; this also requires target R&D to ensure that DUNE can handle up to 2.4 MW of beam power. ACE-BR aims to replace the Booster synchrotron which accelerates protons from 800 MeV to 8 GeV to enable full delivery of >2.4 MW of beam power to DUNE and **enable** the development of the next generation of US accelerator-based particle physics experiments, including multi-TeV collider research, while modernizing the complex to provide **reliable** beam to all its users.

The ACE-MIRT upgrade aims to significantly enhance the proton output directed towards the DUNE Phase I detector. By reducing the Main Injector (MI) cycle time from 1.2–1.4 seconds to 0.65 seconds, the initiative seeks to increase beam power and upgrade target systems to accommodate up to 2.1 MW. Achieving this shortened cycle requires a substantial increase in voltage and electrical power, necessitating enhancements to power supplies, transformers, feeders, the size of service buildings, the introduction of additional cooling, and more tunnel penetrations. Additionally, the RF accelerating system will undergo modifications, either by replacing existing cavities with a new design that offers more volts per cavity or by adding more cavities of the current design, alongside updates to regulation, control, and instrumentation systems.

Addressing challenges of beam dynamics, losses, and shielding is crucial for ACE-MIRT. Upgrades to the MI collimators and the abort line are essential to accommodate the changes. During the shortened 0.65-second cycle, before the implementation of a Booster Replacement, the Recycler Ring will not be available for Mu2e, and only one Booster batch will be available for the 8 GeV proton beam experiments. The target research and development (R&D) segment focuses on identifying suitable candidate materials, conducting high-energy proton irradiation and pulsed-beam experiments to simulate expected radiation damage and beam interaction conditions, followed by Post-Irradiation Examination (PIE) to assess material properties, microscopic structural changes, and high-cycle fatigue testing.

Following ACE-MIRT, **the ACE-BR upgrade** aims to construct a new Booster to serve as a reliable platform for the future of the Accelerator Complex. This upgrade will continue to ensure the delivery of high-intensity beams for DUNE while enhancing the Fermilab's capability to support next generation accelerator experiments from precision measurements to searches for new physics with beams ranging from 1-120 GeV. The project also intends to supply the high-intensity proton source necessary for future multi-TeV accelerator research, marking a significant leap forward in the complex's capabilities.

Exploring Booster replacement options, the project considers extending the Superconducting RF (SRF) Linac to higher energies or constructing a new Rapid-Cycling Synchrotron (RCS). Through the evaluation of three representative options for each approach, all requiring an extension of the SRF Linac to 2 GeV, the RCS option emerges as advantageous due to reduced space charge at the increased energy. Conversely, the high-energy linac option necessitates a beam with approximately 2 GeV to leverage high-frequency, $\beta = 1$, high-gradient cavities, which can be efficiently grouped and powered by a single, high-power klystron. The final selection and optimization of ACE-BR design will be based on outcomes of upcoming workshops and community design studies and physics prioritization.

Within this phased upgrade approach for the Fermilab accelerator complex, we can conceive **physics spigots** where additional experiments beyond DUNE would be feasible. We divide them into the ACE-MIRT and ACE-BR eras.

- ACE-MIRT era:
 - **S0A**: 800 MeV, PIP-II continuous wave
 - **S0B**: 800 MeV, PIP-II pulsed linac
 - **S0C**: 800 MeV, PIP-II pulsed with accumulator ring
 - **S0D**: 8 GeV, Booster pulsed
 - **S0E**: 8 GeV, Recycler Ring (RR) & Delivery Ring (RR) (muon campus)
 - **S0F**: 120 GeV, MI continuous wave via slow extraction
- ACE-BR era:
 - **S1A**: 2 GeV, continuous wave or pulsed linac
 - **S1B**: 2 GeV, pulsed with accumulator ring
 - **S1D**: 8 GeV, pulsed, muon campus (RR/DR)
 - **S1E**: 8 GeV, Recycler Ring (RR) & Delivery Ring (RR) (muon campus) [same as ACE-MIRT]
 - **S1F**: 120 GeV, MI continuous wave via slow extraction [same as ACE-MIRT]

2.2 Physics drivers and experimental thrusts

ACE physics aligns well with all three science themes presented in the P5 report: (1) Decipher the Quantum Realm; (2) Explore New Paradigms in Physics; (3) Illuminate the Hidden Universe. Within each theme P5 identified two physics drivers,

that represent the most promising avenues of investigation for the next 10 to 20 years. ACE will address five out of these six physics drivers: **(1.1)** Elucidate the Mysteries of Neutrinos; **(1.2)** Reveal the Secrets of the Higgs Boson; **(2.1)** Search for Direct Evidence of New Particles; **(2.2)** Pursue Quantum Imprints of New Phenomena; **(3.1)** Determine the Nature of Dark Matter. In the following, we briefly highlight the main role of ACE in pursuing these goals.

(1.1) Parameters of the PMNS matrix are much less known than the corresponding parameters of the CKM matrix. Several models predict relations between the two. Therefore, an important goal will be to reach a similar level of precision. Future post-DUNE neutrino experiments with neutrinos produced from muon and anti-muon decays will allow the measurement of new oscillation observables through $\nu_e \rightarrow \nu_\mu$ and $\nu_e \rightarrow \nu_\tau$ transitions. **(1.2)** A future high-energy muon collider will be able to achieve the most precise measurements of several Higgs properties including the $WWHH$ and HHH couplings. **(2.1)** Several open questions in particle physics could be addressed by heavy NP particles with a mass beyond the LHC reach or by light NP particles that are only very weakly coupled to the SM (the “dark sector”). A high-energy muon collider will be able to probe new particles with a mass above 10 TeV. Future neutrino experiments, low energy muon experiments, and proton fixed target experiments will be able to produce and detect a broad range of dark sector particles with a mass at or below the GeV scale. **(2.2)** Lepton flavor universality (LFU) and lepton flavor number are two approximate symmetries of the SM. Searches for charged lepton flavor universality breaking and for charged lepton flavor violation (CLFV) are therefore paramount. A well balanced program should include tests of $\mu \rightarrow e$, $\tau \rightarrow e$ and $\tau \rightarrow \mu$ transitions. Exciting prospects to test CLFV at Fermilab are expected. In particular, the Advanced Muon Facility will push the bound on the New Physics scale responsible for $\mu \rightarrow e$ transitions to $\sim 10^5$ TeV, a factor of several larger than what is obtainable at the Mu2e experiment, and help elucidate the nature of new physics in case of an observation. This is complementary to what can be done at (present and future) high-energy colliders searching for the Higgs decay $H \rightarrow \mu e$. **(3.1)** The progress in DM direct and indirect detection experiments, together with LHC searches, have put under tension vanilla models for Weakly-Interacting-Massive-particle (WIMP) DM. However, several WIMP scenarios, including the famous Higgsino DM scenario, remain unprobed. A high-energy muon collider will be able to probe these scenarios for heavy DM up to masses above 10 TeV. DM could belong to a light dark sector of particles only feebly interacting with the SM. To achieve the observed relic abundance for a DM particle with a mass below the few GeV scale, additional dark sector particles are generically necessary. Fermilab high-intensity beams offer a broad set of opportunities to test the dark sector paradigm, from DM searches in missing momentum signatures at muon fixed target experiments to visible dark sector particle (dark photons, axions, ...) searches at proton beam dump experiments to the production of dark sector particles from meson decays at neutrino experiments.

Inspired by the above P5 physics drivers, we map them onto four primary experimental physics thrusts which are well-suited to the Fermilab ACE and around which we organize a future experimental program. Four sessions at the ACE Science Workshop focused on these experimental thrusts and are summarized below.

2.2.1 Muon Collider

The Muon Collider physics case is broad and exciting, including studying properties of the Higgs boson (including detailed characterization of the Higgs potential); rigorously testing predictions of the Standard Model (SM); investigating WIMP (Weakly Interacting Massive Particles) dark matter; exploring previously uncharted territories of quantum field theories; and enhancing research in the neutrino sector. Furthermore, the Muon Collider offers the potential for auxiliary fixed target and beam dump experiments to maximize its physics potential.

The path to eventual realization of a Muon Collider lies through a vigorous R&D program aimed at demonstrating key accelerator and detector technologies. In the workshop, R&D challenges for both the Muon Collider detectors and accelerator development were presented and discussed. On the accelerator side, the R&D plan includes development of a proton source compatible with the ACE plan, simulation of the proton accumulation and compression stages, and conducting experiments at existing facilities to demonstrate that the required proton bunch structure is attainable. The R&D plan also involves studies of high-power target materials and designing a comprehensive target station that includes proton beam delivery, a production solenoid, cooling systems, a beam dump, and a particle selection chicane. Experimental R&D studies of the target system would strongly benefit from the ACE beam. Beyond the proton driver and the target, ACE can offer a basis for a Muon Cooling Demonstrator facility that will allow the testing of key technologies related to ionization cooling. Such facility will consist of a muon source, a sequence of cooling cells, the upstream and downstream beam diagnostics instrumentation, and the associated infrastructure. The scheme will benchmark a realistic cooling lattice to give us the input, knowledge, and experience to design a real, buildable cooling channel for a Muon Collider. Such a demonstrator will require operation with proton beam, which ACE can potentially provide.

On the detector side, efforts to mitigate Beam-Induced Background (BIB) have demonstrated promising results through the application of innovative detector designs, advanced technologies (e.g. 5D detectors), and modern reconstruction software. The path forward involves substantial R&D on the promising detector technologies (e.g. LGADs, MAPs, Dual Readout Calorimeters) and potential synergies within the high energy physics community in development of the next generation of advanced reconstruction algorithms.

A key outcome of the workshop was that an 8 GeV linac provides more flexible design over an RCS for the Muon Collider proton driver. Another important outcome is that of the 6 configurations considered for ACE currently, all would need to be re-optimized to satisfy the needs of the Muon Collider proton driver.

2.2.2 Neutrino physics

At neutrino factories, the precise knowledge of muon energy and charge allows for highly accurate neutrino energy spectra and exceptionally clean neutrino beams. Charge-identifying detectors can effectively eliminate beam-related background, enabling high-energy neutrino beams to facilitate measurements of electron neutrino to muon neutrino and electron neutrino to tau neutrino oscillations, thereby opening up new oscillation channels and the potential for additional observables. Precision neutrino oscillation measurements are crucial for probing new phenomena, and with current projects like DUNE and Hyper-K underway, muon storage rings emerge as a promising next step. As the Muon Collider garners renewed interest, the neutrino factory concept could serve as an interim step or a complementary program, contingent on a solid physics case and community support.

Fermilab is currently hosting a leading accelerator-based short-baseline neutrino program, focusing on neutrino-argon interaction measurements, neutrino flavor conversion, and dark sector physics. This effort is supported by the Booster Neutrino Beam facility, which has exceeded performance expectations and benefited from decades of data collection by various experiments (MiniBooNE, SciBooNE, ANNIE, MicroBooNE, and the SBN program), resulting in a well-characterized beam. Future upgrades to the Booster and extended running post-2027 could significantly enhance the scientific contributions of this program. The discovery of a new physics signal within the SBN program would be transformative, prompting further investigation either through additional neutrino or antineutrino running. Exploring the feasibility of such additional runs, especially in light of potential Booster upgrades and in conjunction with the forthcoming SBN results, along with possible detector enhancements, is highly valuable for the field.

2.2.3 Charged Lepton Flavor Violation

Charged Lepton Flavor Violating (CLFV) processes are critical in the search for new physics, offering both a high scale reach and the ability to diagnose models by identifying the source(s) of flavor breaking. The study of these processes is highly complementary to searches performed at colliders. If new physics is discovered at the LHC or other experiments, CLFV can provide exclusive insights into its symmetry structure. Conversely, if new physics remains elusive, CLFV stands as one of the best methods to investigate the mass scale of such undiscovered phenomena. Thanks to the availability of intense sources and their relatively long lifetime, muons offer a promising avenue to search for these reactions. A global experimental program is underway in the US, Europe, and Asia, with anticipated improvement in sensitivity of several orders of magnitude during this decade. In particular, the Mu2e experiment [5] at Fermilab is expected to probe muon-to-electron conversion with discovery potential at $\sim 10^{-16}$, a factor 10^4 better than current limits.

Beamline upgrades and a new facility at Fermilab could further extend the discovery potential by orders of magnitude, a tremendous opportunity for the muon program. The Mu2e-II project [6] is a near-term evolution of Mu2e, planning to increase its reach by an order of magnitude. The Advanced Muon Facility (AMF) [7] is a more ambitious proposal for a new high-intensity muon science complex to enable broad muon science - including CLFV searches in at least four muon modes - with unprecedented sensitivity. The AMF complex is based on a fixed-field alternating gradient synchrotron (FFA) to create a cold, intense muon beam with low momentum dispersion. The FFA requires intense proton pulses with a bunch length of the order of 10 ns. A compressor is needed to rebunch the PIP-II beam to obtain the desired structure; several options have been laid out in the context of the ACE upgrade. This facility would provide a unique opportunity to fully exploit the capabilities of PIP-II to produce a world-class physics program. Its development also has strong synergies with current R&D efforts on a muon collider or a future dark matter program at FNAL, two key science priorities.

2.2.4 Accelerator-based dark sectors

Accelerators are key tools for probing dark sectors in the laboratory, particularly within the thermal dark matter regime, and they represent a strategic direction for new physics research at intensity frontier experiments. There is a robust theoretical and experimental push to explore the most plausible models of dark sectors.

The Fermilab Accelerator Complex is slated for upgrades to transition into the PIP-II era by the end of the decade, offering opportunities for additional enhancements as part of the ACE plan, such as incorporating an accumulator ring with short-pulse structures. These upgrades will open up significant physics opportunities, especially at a PIP-II beam dump facility that can accommodate various detector types with different thresholds in a dedicated experimental hall (see also Ref. [8]). Furthermore, existing and planned neutrino facilities are capable of searching for various dark sectors, often in tandem with their primary neutrino research objectives, across different energy ranges (800 MeV, 8 GeV, 120 GeV) that complement each other. Finally, the 120 GeV proton fixed target experiments provide an additional opportunity to searches for dark sectors that are sensitive to a broad spectrum of models. The proposed DarkQuest upgrade [9] to the existing SpinQuest experiment is envisioned

as a catalyst for a sustained dark sector research program, leveraging existing infrastructure for new explorations in a short timeframe and with potential for further enhancements in detector and beam technology to increase sensitivity.

2.3 Additional technology and physics directions

The workshop included contributions from the community that spanned additional physics ideas, accelerator R&D, and detector concepts that should be considered in the design of ACE. These could be provide synergy with the initially identified physics thrusts or may provide additional important motivations or directions for the future facility.

2.3.1 Physics experiments

KPIPE [8 GeV] The KPIPE project aims to employ an extensive liquid scintillator detector to investigate the disappearance of ν_μ neutrinos over a considerable distance, focusing on 236 MeV kaon decay-at-rest (KDAR) ν_μ CC events. It relies on a pure and mono-energetic flux of muon neutrinos for its observations. The extended length of the detector is crucial for accurately measuring the oscillation wave. Notably, KPIPE demonstrates strong sensitivity, particularly effective in scenarios with high- δm^2 values. It serves as a valuable addition to the SBN program, offering complementary insights. Additionally, KPIPE is distinguished by its cost-effectiveness. The 8 GeV proton beam requirements for KPIPE are high power and low duty factor, typically around 10^{-5} .

FerMINI [120 GeV] The FerMINI at MINOS experiment focuses on the exploration of millicharged particles (mCP) through a fixed-target setup employing stacks of scintillators. It investigates triple or double coincident signatures as indicators of the presence of mCPs. There are several motivations behind the study of mCPs including the concept of charge quantization within the framework of Grand Unified Theories (GUTs) and string compactifications; a direct connection to models involving dark photons; and a connection to the 21 cm absorption spectrum, offering insights into fundamental aspects of cosmology and astrophysics.

LongQuest [120 GeV] LongQuest, operating within the current NM4 SpinQuest facility, is dedicated to the pursuit of long-lived particle searches. This initiative has several advantages and distinctive features. Firstly, it offers superior shielding, ensuring minimal interference with ongoing SpinQuest operations. Additionally, the facility could also serve as an alternative site for the FerMINI project. One of the key components of LongQuest is its dark photon decay fiducial volume. Positioned at a baseline distance ranging from 33 to 37 m, this volume is specifically designed for the measurement of di-electrons or di-photons. Equipped with additional EMCal (Electromagnetic Calorimeter) and pre-Shower Detectors, this setup is sensitive to a range of dark sector physics scenarios with an expected 10^{18} - 10^{20} Protons on Target (POT).

REDTOP [≤ 2 GeV] The REDTOP (Rare Eta Decays To Probe New Physics) experiment is being proposed, with the intent of collecting a data sample of order 10^{14} η (10^{12} η') mesons for studying very rare decays. Such statistics are sufficient for investigating several symmetry violations, and for searching for particles and fields beyond the Standard Model. Utilizing a high intensity proton beam of ≤ 2 GeV, REDTOP will have sensitivity to processes that couple the Standard Model to New Physics through all four of the so-called *portals*: the Vector, the Scalar, the Axion and the Heavy Lepton portal. The sensitivity of the experiment is also adequate for probing several conservation laws, in particular CP, T and Lepton Universality, and for the determination of the η form factors, which is crucial for the interpretation of the recent measurement of muon $g-2$.

Muon Beam Dumps [≤ 2 GeV or 8 GeV] Muon-beam dump experiments serve as excellent platforms for the exploration of dark scalars and other light dark sector particles, primarily due to their focus on muon couplings and their sensitivity to displaced decays. These experiments also offer the advantage of seamless integration with other muon-related research endeavors. Notably, the investigation of muonic dark sectors presents a promising avenue for addressing anomalies associated with muons, such as the muon $g-2$ anomaly. FNAL μ , a prominent example, can be feasibly implemented within the existing infrastructure of Fermilab with minor modifications or additions, further enhancing its appeal and potential for significant scientific discovery.

DAMSA [≤ 2 GeV] DAMSA (Dump produced Aboriginal Matter Search at an Accelerator) [10] is a very short baseline beam-dump experiment aimed at uncovering Dark Sector Particles (DSPs) using high-intensity, low-energy proton beams. Developed for 600 MeV proton beams initially, DAMSA is now adaptable to the 800 MeV PIP-II and ACE beams, offering compatibility with Fermilab's infrastructure. With collaborative efforts from ten US institutions and eight South Korean institutions, DAMSA presents an exciting opportunity to transform Fermilab's accelerator facilities into world-leading DSP research hub.

Muonium and future muon physics [≤ 2 GeV] Both the muonium-antimuonium ($M-\bar{M}$ (M is a bound μe atom) and Mu2e experiments are critical and complementary in rare and precision physics searches. While muonium-antimuonium spectroscopy's previous results are over 20 years old, indicating a ripe opportunity for new efforts, the exploration of muonium gravity (testing antigravity on the μ^+) has never been feasible until now, with the development of new techniques like SFHe

production. The Muon Test Area (MTA) presents a unique opportunity to kickstart a leading Fermilab muonium program, facilitating initial investigations into muonium–antimuonium oscillations, spectroscopy, and gravity, each offering unique insights into new physics phenomena. These experiments hold promise for shedding light on CLFV physics and providing a novel avenue for testing gravitational couplings in the second generation.

Muon fixed target missing momentum [120 GeV] The M^3 experiment utilizes the muon missing momentum technique to search for dark matter. Unlike LDMX, which employs electron beams, M^3 employs a muon fixed target experiment, necessitating adjustments to the detector, including a thicker target. The experiment requires a low current muon beam with individual muons having energies greater than or equal to 10 GeV. Additionally, the muons must be individually identifiable, with an expected range of 10^{10} to 10^{13} Muons on Target (MOT). Phase 1 (10^{10} MOT) focuses on achieving complete coverage of the $g-2$ region, enabling the detection of any invisibly-decaying particle lighter than the muon. Phase 2 (10^{13} MOT) allows for the exploration of large portions of the well-motivated dark matter parameter space with an increased MOT count.

Accelerator driven nuclear reactors [≤ 2 GeV] Mu*STAR, short for Muons' Subcritical Technology Advanced Reactor, is an accelerator-driven subcritical reactor (ADSR) designed to burn spent nuclear fuel from other reactors to produce carbon-free nuclear energy. It offers a viable solution to nuclear waste disposal while meeting public and legal demands for responsible nuclear technology.

Exploration of TMDs at a SpinQuest upgrade together with the Dark sector Physics [120 GeV] The extension of the upcoming SpinQuest (E1039) experiment aims to extract gluon transversity distributions from the Deuteron target (ND3). The prospective advancements of the Fermilab's Accelerator Complex Evolution (ACE) plan, enable not only the extraction of gluon transversity distributions with greater statistical accuracy with a deuteron target but also with a range of tensor-polarized nuclear targets with spin ≥ 1 to explore the nuclear dependences. The high-intensity beam and optimized timing between proton spills facilitate the uniqueness of Fermilab's capability for precise polarized target asymmetry measurements in Drell-Yan scattering. Also, this approach opens up the opportunity to measure ten additional leading twist quark transverse-momentum-dependent distributions (TMDs) for tensor-polarized targets, which have not been previously investigated well. The investigation will primarily focus on studying these TMDs through the Drell-Yan process, providing valuable insights into the nuclear EMC effect, as well as the 3-dimensional structure of the nucleon, supported by lattice QCD insights into nucleon spin components, marks a significant advance in understanding strong force, color confinement, and partonic interactions, setting a new standard for spin physics research. Additionally, the investigations into the Dark sector physics [9] will also be conducted at the NM4 facility, concurrently on the 120 GeV Main Injector, representing the proposed SpinQuest-upgrade.

Dedicated Muon EDMs [≤ 2 GeV] A potential EDM experiment could be conducted in the $g-2$ storage ring by modifying the quadrupole system to generate a radial electric dipole field pointing inward, with minimal changes to the current setup, except for altered orbit curvature and a higher potential difference across the inner/outer plates to create the electric field. The adaptation would allow for a significant reduction in the requirements for the existing magnetic dipole field, inflector, and kicker systems. This setup presents an excellent chance to explore the systematics for a future dedicated run, marking the first application of the frozen spin technique and potentially enabling physics EDM measurements within a limited timeframe. Such an experiment could serve as a valuable proof of concept for a future dedicated EDM physics experiment.

2.3.2 Technology development

Test Beams: FTBF [120 GeV] and ITA [800 MeV] The Fermilab Test Beam Facility (FTBF) plays a critical role in supporting a broad spectrum of research and detector development with its two main beamlines, MTest and MCenter, offering particles ranging from 120 GeV protons to secondaries of approximately 200 MeV. Additionally, the facility includes an Irradiation Test Area (ITA) that provides low energy, high rate protons (400 MeV at 2.2×10^{15} protons/hr), with the beam available for about eight months a year, from November through June. MTest facilitates short-term projects with a proton beam of 120 GeV and secondary beams between 1-66 GeV, whereas MCenter caters to longer-term experiments with its secondary and tertiary beams down to 200 MeV.

Despite the extensive capabilities and heavy demand from significant projects like CMS, ATLAS upgrades, and various neutrino-related experiments, the FTBF faces challenges such as over-subscription by 10-20%, aging infrastructure in the switchyard line, and substantial downtime that impacts experiment schedules. The increasing need for clean, low energy secondary beams and the potential discontinuation of the ITA in the absence of LINAC operations in the PIP-II era underscore the pressing requirements for facility updates and expansions to accommodate evolving research needs, including a high-intensity 800 MeV irradiation area for comprehensive particle exposure studies.

High Powered Targetry This is discussed more as a part of Section 3.7.

Time Slicing of Neutrino Fluxes in Oscillation Experiments By utilizing a higher-frequency RF bunch structure for the primary proton beam on target and employing precision timing to select different energy and flavor spectra from a wide-band neutrino beam, based on the neutrinos' relative arrival times with respect to the RF bunch structure, we propose a 'stroboscopic' method. This approach is complementary to techniques that differentiate neutrino energy spectra based on their angle relative to the beam axis, allowing for the selection of varying energy spectra from the same on-axis detector and applying equally to both near and far detectors in an oscillation experiment. Discriminating energy and flavor of neutrinos produced by in-flight hadrons necessitates proton bunch lengths on the order of 100 ps and comparable time resolution in the detector. The correlation of neutrino events with the parent proton interaction is currently hampered by the nanosecond-scale width of the proton bunches targeting the beam. By employing a superconducting RF cavity to rebunch the existing 53.1 MHz RF bunch structure at a tenfold higher RF frequency, the requisite shorter bunch length can be achieved.

Fast tracking for triggering High-rate experiments at PIP-II / ACE could potentially enhance their physics capability significantly through the use of track triggers for signal identification, background rejection, and overcoming the challenges posed by sub-optimal beam timing structures. The success of this approach hinges on the deployment of sufficiently fast and granular tracking detectors. It's crucial to evaluate which experimental signatures, such as those from REDTOP and other experiments, would benefit the most from the incorporation of track triggers, thereby boosting the overall performance and outcome of these high-rate scientific endeavors.

3 Physics, detector, and accelerator complementarity

3.1 CLFV - Dark Sectors

Editors: Matt Solt, Jure Zupan

The advantage of accelerator-based dark sector experiments over direct detection experiments is their relative insensitivity to specific dark matter models due to semi-relativistic versus non-relativistic scattering. Moreover, accelerator-based experiments can perform many type of searches and probe a variety of dark sector models at pp collider, e^+e^- colliders, proton and electron fixed target experiments, and beam dump experiments. One can search for visible final states, either by searching for promptly decaying resonances or displaced vertices, or for invisible final states through various kinematic handles: missing mass, missing momentum, and missing energy. The CLFV decays into light new physics states, should such states be found, would have a parametrically enhanced reach to high effective mass scales. For example, classic CLFV observables (such as $\mu \rightarrow e$, $\mu \rightarrow e\gamma$ and $\mu \rightarrow 3e$) probe scales at the level of $\sim 10^6$ GeV, the decay $\mu \rightarrow ea$, where a is an axion, would probe a scale of 10^9 GeV.

A clear outcome of the session was that the physics cases for performing CLFV measurements and dark sector searches is very strong, with much of the discussion devoted to outline R&D direction to achieve the optimal physics program:

- **How do we maximize probing CLFV and dark sector searches with PIP-II and ACE capabilities?** Through discussions with accelerator experts, a strong case was made to build a compressor ring in stages, build it as soon as possible, and make sure that both the AMF and the beam dump programs are possible. The preferred option would be to build a 2 GeV ring, but operate it first at 0.8 GeV. Accelerator physics considerations showed this should be possible, but the optimal scenario to operate the ring should be refined.
- **What type of beam?** Different experiments prefer different beam operation parameters, and the beam structure depends on how the dark sector is being sourced. Short bunches are probably preferred if it is produced in primary collisions, while the duration of the pulses are less important if it is from muon decays (e.g. from stopped muons).
- **Exotic signatures.** The exotic signatures such as $\mu \rightarrow 5e$, $\mu \rightarrow ea$, ..., are interesting, but they are most motivated if they can be done already as part of an experiment aimed at some of the golden signatures (e.g., $\mu \rightarrow e\gamma$, $\mu \rightarrow e$ conversion, $\mu \rightarrow 3e$).
- **Muonium program.** There are other probes such as muonium-antimuonium oscillations, which are complementary to the rest of the program, since they probe different type of physics, though perhaps more exotic.

3.2 CLFV - Muon Collider

Editors: Bob Bernstein, Sergio Jindariani, Diktys Stratakis

Future Lepton Flavor Violation experiments (e.g. AMF and Mu2e-II) and the Muon Collider (MC) present a number of potential research and development (R&D) opportunities, particularly in accelerator, target, and magnet technologies, that could complement each other and that was the main subject of the discussion. The following components were discussed: the Production Solenoid, the Target, the Compressor Ring, and the Fixed Field Alternating (FFA) Gradient synchrotron. For each component, design parameters for Mu2e-II, AMF, and MC were laid out for commonalities and overlaps.

After the discussion, it became evident that the Production Solenoid has some clear areas of overlap between Mu2e-II, AMF, and the MC. The study of megawatt-class targets is important for all experiments in the 800 MeV to 8 GeV range as AMF and the MC have similar requirements for target beam power, while Mu2e-II has lower requirements. The protection of the superconducting solenoid will be important in all cases as well as the materials under consideration. As the designs of the production solenoids for each experiment evolve, it will be important to understand the synergies and potentially build a common team and test infrastructure for this R&D.

The proton Compressor Ring is another area of synergy although the requirements in energy and bunch length are about an order of magnitude different. Technologically, there are some synergies in the R&D but significant differences in requirements make it unlikely that the same ring can be used for both facilities. For the muon storage/accelerator FFA, because of the large difference in the required energies, the designs do not have a lot of overlap and this is the least likely area of complementarity.

In general, the exploration between the MC and AMF/Mu2e-II offered some interesting directions for a collaborative R&D program that could benefit both experimental thrusts. Shared tools and techniques such as simulation efforts can accelerate progress and cultivate joint expertise.

3.3 CLFV - Neutrinos

Editors: Innes Bigaran, Ryan Plestid, Anil Thapa

Neutrinos are a unique probe of lepton flavor symmetries. Within the standard model, lepton flavor symmetries L_e , L_μ and L_τ are accidentally conserved: their conservation is not built into the theory but is emergent. There is no reason why some more complete theory should continue to preserve these symmetries. Indeed, the measurement of neutrino flavor oscillations (which provides evidence of nonzero neutrino masses) indicates that some physics beyond the renormalisable standard model must break these flavor symmetries. Neutrino masses in some extended theory could be either Dirac or Majorana in nature, where the latter could imply a violation of total lepton number $L = L_e + L_\mu + L_\tau$. Moreover, charged leptons and neutrinos are linked by $SU(2)$ symmetry: as left-handed leptons, they are part of the same electroweak doublet, which leads to many neutrino mass models naturally giving rise to CLFV that can be searched for at experiments.

Our discussion focused on highlighting how CLFV and neutrino experiments could mutually enrich the understanding of fundamental physics, particularly in light of the ACE upgrade. We separated the discussion into three stages: a discussion of CLFV experiments, of neutrino experiments, and complementarity between the two. What emerged as a key take-away message from our discussion was the need for closer interactions (a) between experimentalists in both CLFV and neutrinos, and (b) coordination between theory and experiment, on how best to move forward with united efforts to further explore this interplay. Some topics which were discussed in detail are listed below.

- *Could we have neutrino-mass motivated targets for CLFV experiments?*
CLFV processes involving the muon, i.e. $\mu \rightarrow e\gamma$, $\mu \rightarrow e$ conversion on nuclei, and muonium oscillation can be enhanced in various extensions to the SM that incorporate neutrino masses. Upgrades of experiments probing these processes are part of the ACE upgrade proposal, e.g. Mu2e-II, other CLFV muon decay probes. Models extended by right-handed neutrinos (e.g. type-I seesaw) can lead to large effects in CLFV if one explores the flavor structure of Dirac masses. Furthermore, extensions of the SM with exotic scalars (e.g. type-II seesaw) have a Yukawa coupling structure which correlates neutrino oscillation with CLFV decays.
- *Could the ACE upgrade make it viable for Fermilab to become a world-leader in the study of muon decays and muon conversion?*
Developments of the advanced muon facility (AMF) mean that Fermilab will be a site where the sheer flux of muons produced will be beyond what has been seen elsewhere in the world. Given that this will be the case, then could we harness these muons to do all manners of study of their rare properties? There was broad consensus that provided the muon facility is designed to allow for efficient storage of both μ^+ and μ^- then Fermilab is well positioned to offer the best experiments in all three golden channels of CLFV.
- *Is there a strong physics case for a tau optimized flux?*
Neutrino oscillation experts broadly agreed that such a case is complementary rather than foundational. Statistics will be limited in tau samples, and atmospheric offer an existing probe of the ν_τ sector with better statistical capabilities (and without the difficulties inherent to reconstructing τ^\pm leptons).
- *Could there be room for a neutrino factory-like concept at an AMF or a future muon collider?*
An advantage of having neutrinos produced from muon decay rather than from meson decays is that they have a well-known energy and flavor spectrum. AMF with a muon storage ring could be extended to allow muons to decay and produce a focused beam of neutrinos, which would be essential for precision measurements of neutrino properties. Neutrino factories have historically been considered with a ~ 1 GeV muon storage ring; roughly commensurate with

the needs for a muon collider. CLFV experiments prefer a much lower energy, the AMF plan is for a $\sim 20 - 30$ MeV storage ring with an alternate technology (a fixed field alternating gradient synchrotron). From the perspective of neutrino oscillation physics, the absolute energy scale is not crucial but rather sets the necessary baseline. The tight momentum resolution of the AMF storage ring would allow for a nearly mono-energetic neutrino source. Drawbacks include a smaller boost factor and therefore wider opening angle for the neutrino beam. The broad consensus was that this was worth further investigations.

Although slightly beyond the scope of our discussion group, there was also interest expressed in a controlled neutrino source for hadronic physics studies,

- *Could there be scope for neutrino and/or muon deep-inelastic scattering (DIS) experiments in the ACE upgrade?*
 Muon DIS on polarized targets (an extension of Spin-Quest) could provide a fundamental understanding of the structure of nucleons. Polarized neutrino DIS experiments would open-up new opportunities to understand neutrino scattering cross sections, which are paramount for interpreting future results from experiments like DUNE. In general, these experiments can provide further information about the spin-structure of nucleons and allow for more precise measurements of neutrino properties. Moreover, deviations from SM predictions for neutrino-nucleon interactions could indicate the presence of new-physics effects.

3.4 Dark Sectors - Muon Colliders

Editors: Cari Cesarotti, Yonatan Kahn

The discussion on the complementarity between dark sector experiments and muon colliders proceeded in two stages:

How to leverage *current* muon beams for dark sector searches. We concluded that the requirements for muon beam cooling demonstrators are in some sense maximally orthogonal to the needs for dark sector experiments, which typically require high-intensity beams, a large integrated luminosity, and a regular bunch structure. However, we identified a promising possibility for a future experiment: using the discarded forward muons from Mu2e for a new beam dump experiment. The 8 GeV proton beam results in $\sim 10^{19}$ POT/year, integrating to about 10^{21} POT after PIP II in 2028–2029. Roughly 1% of these protons will result in muons with energy of ~ 3 GeV or above, of which Mu2e only uses a negligible fraction. The time structure of the beam is not amenable to a missing momentum search, but a search for long-lived muophilic particles with mass below $2m_\mu$ which decay to electrons or photons seems possible if a detector could be placed $\mathcal{O}(10$ m) away. Investigating the feasibility of this setup would be an excellent synergistic use of the Fermilab accelerator facilities. While we are particularly interested in a muon beam for the ultimate muon collider, it is worth noting that the proton beam necessary for producing the muons could also be leveraged for auxiliary experiments as well.

How to leverage *future* muon colliders for dark sector searches. To date, muon collider physics studies have mostly focused on Higgs and electroweak precision phenomenology, as well as new particle with electroweak couplings. To our knowledge, a comprehensive study of weakly-coupled dark sectors (for example, the minimal dark photon, or a muon-specific dark force) at the collider itself has not yet been undertaken (though there have been studies of using the muon beam in a beam dump experiment). In addition, as was emphasized in Ian Low’s talk, muon colliders may have access to yet another dark sector portal, the neutrino portal, due to the fact that neutrinos may be visible through their electroweak radiation in calorimeters. Investigating this unique feature of muon colliders may lead to new ideas for dark sector searches, for example those involving right-handed neutrinos, through a long-lived particle experiment analogous to FASER at the LHC.

3.5 Dark Sectors - Neutrinos

Editors: Bhaskar Dutta, Alex Sousa, Jacob Zetlemoyer

In the dark sector and neutrino discussion session, we considered a number of questions around the ACE plans and how the Fermilab neutrino and dark sector program may benefit from the ACE options. We note that complementarity exists within ACE to optimize the location and detection threshold of our detectors to probe a wide range of physics in the neutrino and dark sectors. There is obvious synergy between the detector technologies used for neutrino and dark sector physics. A constant theme of our discussion was the use of beam timing to increase the physics scope or neutrino and dark sector searches, either through coupling PIP-II to a proton accumulator ring, or using the nanosecond pulse structure of PIP-II operating in continuous wave (CW) mode.

We also explored potential options to extend the reach of dark sector search experiments to unexplored regions of parameter space. A PIP-II beam dump facility equipped with a high-Z target, and/or a higher beam energy, with judicious choices of detector location would offer excellent opportunities to probe new ranges of dark sector particle masses. Enhanced kaon production and detection would enable particularly sensitive searches.

We discussed the broad ideas for producing and detecting dark sector particles and possible gaps in what we were considering. Some examples include light dark matter, axion-like particles, heavy neutral leptons, and millicharged particles.

Gathering notable interest during the discussion, was the possibility of using resonant π^0 production at neutrino experiments for complementarity with the dark sector parameter search space using precision measurements of Dalitz decays or pion production.

We discussed how the options under ACE would benefit the DUNE experiment, the current flagship neutrino experiment located in the US. The discussion around the physics scope expansion focused on the ν_τ sector where an expansion of the beam power or energy beyond the baseline under ACE could enable significant inroads into improving our knowledge of this very difficult to measure sector. We noted that it may be possible under ACE to go beyond 2.4 MW, with the likely primary constraints being the target and absorber capabilities. Those constraints notwithstanding, reaching a beam power as high as 4 MW might be possible, with the limitation on the accelerator at that point becoming space charge effects. Additional discussion touched on the capability of the Main Injector to support such enhancements.

We discussed possible detector technologies that we could deploy at PIP-II under ACE for neutrino and dark sector searches. Some of these options are being explored in more detail and were discussed at a recent PIP-II Beam Dump Facility Workshop held at Fermilab in May 2023, with a white paper (Ref. [8]) summarizing the discussions in more detail. Interesting possibilities include water-based liquid scintillator (WbLS), granular detectors such as the LiquidO technology, fast tracking or fully pixelated detectors expanding upon the capabilities of liquid argon TPCs, optical liquid argon detectors with high photocathode coverage, enabling searches for keV-scale physics and expanding the range of dark sector models for which the detector is sensitive. Another possibility are CCD detectors performing powerful searches for millicharged particles. We considered possible synergies with the large tracking detectors used in collider experiments along with direct dark matter detection experiments in exploring how to improve detector development dedicated to searching for dark sector particles.

Further discussion centered on probes of new physics enabled by running the neutrino beam facilities in a beam dump mode, similar to how MiniBooNE operated previously, to pioneer proton beam dump based searches. The main advantage of running in this mode is the drastic reduction of the neutrino decay-in-flight and possible neutron backgrounds affecting new physics measurements by short-baseline detectors. We noted this is a possibility for the SBND detector once PIP-II comes online, making use of the BNB beamline in the PIP-II era, especially before the LBNF beam becomes operational. We note that a beam dump could be installed at the BNB to allow both on- and off-target running concurrently. This could provide a powerful tool for searching for light dark matter due to the detector distance from the target and the lower energy such that it covers complementary parameter space to other planned experiments.

We also discussed other beam dump possibilities that are enabled by the ACE plan. Some experiments such as PIP2-BD can take advantage of the powerful timing capabilities of an $\mathcal{O}(1)$ -GeV accumulator ring coupled to the PIP-II Linac. The Switchyard beamline could offer another potential location for a new beam dump facility, though significant investment would likely be required.

There was an additional comment during the summary session about the increasing synergies of the neutrino and nuclear physics communities. Understanding neutrino-nucleus interactions is becoming essential to make precision measurements and predictions in the neutrino sector, while at the same time there is significant interest in studying nucleon and nuclear structure. One possible question in this direction is whether Fermilab under the ACE plan could provide something unique beyond the HEP community, with one example being nuclear physics measurements using neutrinos produced from a very intense GeV-scale muon beam. Such a beam, with high-precision knowledge of the muon flux, could enable detailed studies of neutrino-nucleus interactions.

3.6 Muon Collider - Neutrinos

Editors: Christian Herwig, Zahra Tabrizi

Projects such as the Deep Underground Neutrino Experiment (DUNE) and Hyper-Kamiokande (Hyper-K), now under construction, aim to achieve the statistical precision necessary to explore leptonic CP-invariance violation. These experiments, along with JUNO, are poised to conduct precision studies on various oscillation parameters, contributing to our understanding of neutrino physics and potentially shedding light on phenomena such as the MSW effect.

Neutrino factories, proposed around the time neutrino oscillations were discovered, offer a distinct approach to generating neutrino beams using muon decay and storage rings. Despite challenges in muon production and acceleration, these facilities present high luminosity and well-defined beam properties, making them ideal for studying neutrino oscillations. The synergy between neutrino factories and muon colliders is evident, as both face similar technological hurdles and stand to benefit from shared advancements.

Given the rich physics opportunities afforded by neutrino factories and the need to prepare for future neutrino physics programs beyond DUNE, detailed studies on their complex and detectors are timely. These efforts are crucial for advancing our understanding of fundamental physics and unlocking new discoveries in the realm of neutrino science.

The ACE upgrade presents various aspects potentially aligned with the needs of a muon collider, such as shared accumulator rings, though the extent of alignment depends on specific considerations. Discussions from other sessions, including S.

Nagaitsev’s talk, provide further insights on these commonalities and may serve as a natural starting point to updated ACE-BR design proposals. However, any of the high-power proton-driven systems put forth as a part of the ACE-BR study can offer numerous opportunities for neutrino sources beyond decay-in-flight pions, including processes such as pion DAR, kaon decay, and muon decay.

Considering the post-DUNE/Hyper-K era, questions arise regarding the ideal experiment in light of anomalies persisting or dissipating. Should anomalies persist, a neutrino factory could offer valuable exploration avenues, while alternative scenarios prompt the consideration of other experimental avenues. In addition to this, a neutrino factory presents the compelling possibility to indirectly search for New Physics in a manner synergistic with high-energy probes through the effective field theory approach, by matching WEFT and SMEFT parameters across energy scales.

In addition to the neutrino factory concept, high-energy neutrinos produced in MC collisions allow the possibility to conduct new measurements and searches through novel processes such as $\nu\bar{\nu}$ fusion processes. Auxiliary MC detectors, akin to FASERnu, may facilitate investigations into additional new physics domains in addition to probing neutrino interactions at some of the highest energy scales. Furthermore, there is potential for novel measurements using high-energy neutrinos, with the physics case for such endeavors well-established since the inception of the neutrino factory concept. Exploration of topics such as Higgs-neutrino couplings and mapping the neutrino floor for dark matter detection are among the intriguing possibilities in this context.

3.7 Accelerator technology and R&D

Editors: Jeff Eldred, Vladimir Shiltsev

There were two talks at the Accelerator Parallel Session of the ACE Science Workshop providing technical overviews of the ACE Booster Replacement (ACE-BR) accelerator upgrade configurations. The first three ACE configurations involve a 2 GeV upgrade of the PIP-II Linac and a new 8 GeV RCS. The second three ACE configurations involve an 8-GeV upgrade of the PIP-II Linac and a new 8-GeV accumulator ring (AR). Overall the configurations concepts feature detailed technical design for many subsystems and have well-precedented projections of accelerator performance [11, 12].

Since the time of the workshop, P5 has called for the development of a new strategic 20-year plan for Fermilab accelerator (Area Recommendation 12) oriented towards a future collider program (Recommendation 6). The ACE-BR scenarios were a detailed look at the proton accelerator complex upgrades with a core mission focus on the DUNE neutrino program. Consequently the exercise was able to identify R&D items for accelerator development that are highly relevant to the P5 vision, but more work is needed to redevelop the specific upgrade scenarios towards incorporating future collider programs. More broadly, the critical need for advancements in accelerator R&D is called out in P5 Recommendations 8-10.

The speakers were asked to identify technical risks and corresponding R&D areas and raised a few topics. For both types of ACE-BR configurations, H^- foil-stripping injection was identified the greatest technical challenge and most constraining performance limit. H^- foil-injection requires managing particle loss scattering off the injection foil as well as mechanical degradation of the foil itself due to beam heating effects. Careful optimization of the H^- foil injection section should proceed in parallel with development of H^- laser-stripping technology (e.g. at Oak Ridge SNS [13]). Aside from injection, the ACE-BR configurations benefit from continuing innovations and improvements in SRF cavity and RF power technology, from Q-factors to accelerator gradients to achievable pulse length [12, 14]. Lastly, two “RCS” ACE-BR configurations require use of metallized ceramic beampipes which would benefit from early prototyping (following J-PARC’s precedent [15] but with new parameters and vendors).

One talk at the Accelerator Parallel Session addressed targetry development for the next-generation Intensity Frontier programs. The ACE Main Injector Ramp and Targetry (ACE-MIRT) plan has DUNE/LBNF beam powers increasing to multi-MW much faster than originally projected (ideally 2 MW around the 2033 possible end of Mu2e run), and in parallel envisions staging a series of neutrino (i.e. low-Z) targets rated for increasingly greater beam powers. Although the instantaneous thermal shock on the LBNF targets are not impacted by the increased repetition rate, the target lifetime will be impacted by the more rapidly accumulating radiation dose on the target materials. P5 called out the ACE-MIRT program in broad terms as part of Recommendation 2a.

In fact, high-power operations requires all targetry materials to perform at a higher accumulated dose; consequently the study of the performance of a variety of irradiated materials is a critical R&D area. The Radiation Damage In Accelerator Target Environments (RaDIATE) collaboration has studied the performance of irradiated materials using the Brookhaven Linac Isotope Producer (BLIP) but there may be the opportunity to enhance Fermilab’s proton irradiation capabilities using the PIP-II linac beam or the 8-GeV extracted beam [16, 17].

The ACE upgrade plan for the Fermilab proton complex envisions a diverse and growing science program at 2 GeV, 8 GeV, 120 GeV. Several of these programs may need targetry R&D program programs of their own. In particular a significant synergy has been identified in the needs of the the Muon CLFV and Muon Collider programs (see Section 3.2 on the complementarity session). The programs require narrow high-Z targets for pion production in a large acceptance solenoid and it should be noted

that Mu2e, Mu2e-II, AMF, and MuC proposals form a natural sequence of ever more ambitious targetry needs. To this end, the muon programs need not only the study of irradiated materials, but also the development and testing of target concepts.

One staging strategy for the AMF or MuC front-end could be to begin a target demonstrator facility at a lesser proton power as soon as possible, with a path to upgrade proton power, targetry, and physics capabilities as the facility matures. For AMF, this could involve the construction of a compact accumulator ring (also called proton compressor) to deliver 200-400 kW 20 ns proton pulses at 0.8 GeV. The program would serve a beam dump physics program [18] and a muon production target demonstrator initially, but compatible with 1+ MW beam power for AMF with a subsequent energy upgrade of the PIP-II linac. For the MuC front-end, this could involve a 8 GeV H^- linac operating at 5mA for 2ms every 10 Hz into an 8 GeV AR (i.e. an ACE-BR configuration) for a 800 kW target demonstrator. Subsequently, the 8 GeV linac current would be upgraded to 10-20mA (1.6-3.2 MW), and a 8 GeV compressor ring and combiner beamline would be constructed to shorten the pulses from the 8-GeV AR for the MuC proton driver front-end.

One talk at the Accelerator Parallel Session specifically addressed immediate Muon Collider R&D needs. P5 called for collider R&D in Recommendation 4. In addition to the targetry development program, R&D for high gradient RF in strong magnetic fields is needed for the cooling cell design. Within the next five years, the talk calls for a (1) conceptual design for a muon cooling demonstrator facility, (2) site identification and cost estimates for a muon cooling demonstrator facility, and (3) to begin fabrication of a prototype cooling cell for the facility. At Fermilab, the 8 GeV beamline and (ACE era) 2 GeV linac beamline are being investigated as locations to host the muon cooling demonstrator.

The final talk at the Accelerator Parallel Session discussed the PIP-II Accumulator Ring (PAR) proposal, a 0.8 GeV AR sited in between the PIP-II linac and the Fermilab Booster. The PAR ring would facilitate injection into the Fermilab Booster and provide a new PIP-II era experimental program. If the PAR ring could be constructed on a sufficiently aggressive timetable, it would provide excellent value in shortening the timetable for beam commissioning to LBNF. Regardless of timing, the PAR ring would concurrently be capable of a 100 kW low-duty factor proton program for beam dump physics [18]. However, the requirement of facilitating injection into the Booster (thereby benefiting the LBNF timeline) comes with tradeoffs for providing powerful beam to GeV-scale experiments. If the AR design had a more compact circumference (instead of matching Booster) it would deliver shorter pulses to experiments (improving the physics reach). Secondly, if the ring were not sited near the Booster, it could be compatible with a later energy upgrade when the PIP-II linac is extended (see staging discussion for AMF above). A conceptual design for an AR with this approach is under development.

Not directly discussed in the Accelerator Parallel Session were the requirements of optimizing the reliability of the Fermilab Booster. Later, P5 highlighted the need for the assessment of Booster reliability and the identification of pro-active measures to guarantee the longevity of Booster operations. On March 5th, 2024 a mini-workshop “AD Prep for DUNE PIP-II Era Workshop” will be held as a preliminary measure towards addressing this important topic. Whether any new upgrades for Booster reliability should be incorporated into ACE-MIRT or considered as standalone items is also a matter to be determined on a case-by-case basis.

Acknowledgments

We would like to thank all the speakers of the workshop for their time and expertise in preparing and giving their presentations. In particular, we thank Sergey Belomestnykh, David Sperka, Ishara Fernando, Evan Niner, Jaehoon Yu for their feedback on this report. We would also like to acknowledge all of the attendees of the workshop for their comments and contributions which provided valuable input and lively discussion.

References

1. ACE Science Workshop. <https://indico.fnal.gov/e/aces2023> (2023).
2. Ainsworth, Robert et al. Report from the Fermilab Proton Intensity Upgrade Central Design Group. <https://indico.fnal.gov/e/aces2023> (2023).
3. Butler, J. N. *et al.* Report of the 2021 U.S. Community Study on the Future of Particle Physics (Snowmass 2021) Summary Chapter. In *Snowmass 2021* (2023). 2301.06581.
4. Muryamama, H. *et al.* Exploring the Quantum Universe: Pathways to Innovation and Discovery in Particle Physics. <https://www.usparticlephysics.org/2023-p5-report/> (2023).
5. Bartoszek, L. *et al.* Mu2e Technical Design Report (2015). 1501.05241.
6. Byrum, K. *et al.* Mu2e-II: Muon to electron conversion with PIP-II. In *2022 Snowmass Summer Study* (2022). 2203.07569.

7. Aoki, M. *et al.* A New Charged Lepton Flavor Violation Program at Fermilab. In *2022 Snowmass Summer Study* (2022). [2203.08278](#).
8. Aguilar-Arevalo, A. A. *et al.* Physics Opportunities at a Beam Dump Facility at PIP-II at Fermilab and Beyond (2023). [2311.09915](#).
9. Apyan, A. *et al.* DarkQuest: A dark sector upgrade to SpinQuest at the 120 GeV Fermilab Main Injector. In *2022 Snowmass Summer Study* (2022). [2203.08322](#).
10. Jang, W. *et al.* Search prospects for axionlike particles at rare nuclear isotope accelerator facilities. *Phys. Rev. D* **107**, L031901, DOI: [10.1103/PhysRevD.107.L031901](#) (2023).
11. Nagaitsev, S. & Lebedev, V. A cost-effective upgrade path for the fermilab accelerator complex (2022). [2111.06932](#).
12. Belomestnykh, S. *et al.* An 8 GeV linac as the booster replacement in the Fermilab power upgrade: a Snowmass 2021 white paper (2023). [2203.05052](#).
13. Cousineau, S. *et al.* High efficiency laser-assisted h^- charge exchange for microsecond duration beams. *Phys. Rev. Accel. Beams* **20**, 120402, DOI: [10.1103/PhysRevAccelBeams.20.120402](#) (2017).
14. Belomestnykh, S. *et al.* RF accelerator technology R&D: Report of AF7-rf topical group to Snowmass 2021 (2022). [2208.12368](#).
15. Kinsho, M., Ogiwara, N., Saito, Y. & Kabeya, Z. Alumina ceramics vacuum duct for the 3gev-racs of the j-parc. vol. 2005, 2604 – 2606, DOI: [10.1109/PAC.2005.1591197](#) (2005).
16. Pellemoine, F. *et al.* Irradiation facilities and irradiation methods for high power target (2022). [2203.08239](#).
17. Ammigan, K. *et al.* Novel materials and concepts for next-generation high power target applications (2022). [2203.08357](#).
18. Toups, M. *et al.* PIP2-BD: GeV Proton Beam Dump at Fermilab's PIP-II Linac. In *2022 Snowmass Summer Study* (2022). [2203.08079](#).

Translationally invariant shell model calculation of the quasielastic $(p, 2p)$ process at intermediate relativistic energies

A.B. Larionov^{1a}, Yu.N. Uzikov^{2,3,4b}

¹ *Bogoliubov Laboratory of Theoretical Physics,
Joint Institute for Nuclear Research, 141980 Dubna, Russia*

² *Laboratory of Nuclear Problems, Joint Institute
for Nuclear Research, 141980 Dubna, Russia*

³ *Department of Physics, Moscow State University, 119991 Moscow, Russia*

⁴ *Dubna State University, 141980 Dubna, Russia*

Abstract

Relativistic beams of heavy ions interacting with various nuclear targets allow to study a broad range of problems starting from nuclear equation of state to the traditional nuclear structure. Some questions which were impossible to answer heretofore – can be addressed nowadays by using inverse kinematics. These includes the structure of short-lived nuclei and the precision study of exclusive channels with production of residual nuclei in certain quantum states. Theoretical understanding such processes is so far based on factorization models which combine the single-step amplitude of the reaction on a bound nucleon or nuclear cluster with a certain wave function of its relative motion with respect to the residual nucleus. The nuclear structure information is encoded in the spectroscopic amplitude, calculable within nuclear many-body theories. In this work, we use for this purpose the translationally-invariant shell model with configuration mixing and demonstrate that it successfully reproduces the single-differential and integrated cross sections of the quasielastic proton knockout, $^{12}\text{C}(p, 2p)^{11}\text{B}$, with outgoing ^{11}B in the ground state and low-lying excited states measured at GSI at 400 MeV/nucleon.

^a e-mail: larionov@theor.jinr.ru

^b e-mail: uzikov@jinr.ru

1. INTRODUCTION

Quasielastic (QE) knock-out reactions are the most direct way to access the momentum distribution of the valence nucleons given by the square of their wave function (WF) in momentum space. In the low-momentum region, the WFs are determined by nuclear mean field potential. Distortions of the incoming and outgoing proton waves including absorption effects are governed by nuclear optical potential that is mostly imaginary at high momenta and proportional to the local nuclear density. The nuclear mean field and optical potentials are rather well known for ordinary stable nuclei but represent a major uncertainty for exotic ones close to the neutron drip line. The studies of the structure of exotic nuclei using inverse kinematics with proton target at rest are in a focus of experiments at RIKEN [1] and GSI [2]. One of the most important questions is the quenching of single-particle strength and the dependence of this effect on the isospin asymmetry, see Ref. [3] for a recent review. As a first step, before being extended towards exotic nuclear region, any theoretical model of (p, pN) reactions should be tested for β -stable nuclear beams where a number of uncertainties in the model parameters is minimal.

In this work, we address the proton knock-out reaction $^{12}\text{C}(p, 2p)^{11}\text{B}$ measured in Ref. [4] with 400 MeV/nucleon ^{12}C beam colliding with proton target. We apply the translationally-invariant shell model (TISM) [5] which allows to calculate the spectroscopic amplitudes of the virtual decay $^{12}\text{C} \rightarrow p^{11}\text{B}$ for the given relative WF of the proton and residual nucleus and internal state of the residual nucleus. The present study is complementary to our previous work [6] where the TISM has been used to analyse the proton knock-out from a short-range correlated pN pair in the ^{12}C nucleus by a proton that yielded a good agreement with the BM@N data [7].

In sec. 2, the basic elements of our model are described starting from the amplitude in the impulse approximation (IA) and then adding the initial- and final state interactions (ISI/FSI) in the eikonal approximation. Explicit expression for the spectroscopic factor is derived from the TISM in the harmonic oscillator (HO) basis. Configuration mixing is accounted for within the intermediate coupling model [8, 9]. Sec. 3 contains results of our calculations of $^{12}\text{C}(p, 2p)^{11}\text{B}$ process at 400 MeV/nucleon in comparison with experimental data [4]. In sec. 4, we discuss various calculations of the spectroscopic factor and other sources of theoretical uncertainties. Sec. 5 summarizes the main results of the present work.

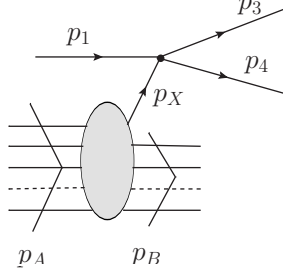


FIG. 1. The amplitude of the process $A(p, 2p)B$. The lines are marked with four-momenta of the particles: the initial (p_A) and final (p_B) nuclei, incident proton (p_1), struck proton (p_X), outgoing protons (p_3 and p_4).

2. THE MODEL

In the Feynman diagram representation, the amplitude of the studied process is shown in Fig. 1 which gives the following invariant matrix element:

$$M = M_{\text{el}}(p_3, p_4, p_1) \frac{i\Gamma_{A \rightarrow XB}(p_A, p_B)}{p_X^2 - m^2 + i\epsilon}, \quad (1)$$

where $M_{\text{el}}(p_3, p_4, p_1)$ is the invariant matrix element of elastic pp scattering amplitude, $\Gamma_{A \rightarrow XB}(p_A, p_B)$ is the nuclear virtual decay vertex, and m is the nucleon mass. The sum over all intermediate state quantum numbers is implicitly assumed in Eq.(1). For the residual nucleus B on the mass shell, in the rest frame (r.f) of the initial nucleus A , the decay vertex can be expressed as follows:

$$\frac{i\Gamma_{A \rightarrow XB}(p_A, p_B)}{p_X^2 - m^2 + i\epsilon} = S_A^X \left(\frac{2E_B m_A}{p_X^0} \right)^{1/2} (2\pi)^{3/2} \psi_{nl}^{m_l}(-\mathbf{p}_X), \quad (2)$$

where $\psi_{nl}^{m_l}(-\mathbf{p}_X)$ is the WF of the relative motion of the struck proton X and the nucleus B in momentum space with n being the HO main quantum number, l – the relative orbital momentum, and m_l – the magnetic quantum number. The WF is normalized as follows:

$$\int d^3 p_X |\psi_{nl}^{m_l}(-\mathbf{p}_X)|^2 = 1. \quad (3)$$

S_A^X is the spectroscopic amplitude, i.e. the virtual decay amplitude $A \rightarrow XB$ expressed via the overlap integral of the WF of the nucleus A and the antisymmetrized product of the

WF of the nucleus B and the relative WF of the proton X and nucleus B [10, 11]:

$$\begin{aligned}
S_A^X([f]LSTJMM_T; [f_B]L_B S_B T_B J_B M_B M_{T_B}; m_l, \sigma) &= A^{1/2} \langle \Psi_A | \Psi_B, nl \rangle \\
&= A^{1/2} \sum_{J_0 M_0} \left\{ \begin{array}{ccc} L_B & S_B & J_B \\ l & 1/2 & J_0 \\ L & S & J \end{array} \right\} \sqrt{(2L+1)(2S+1)(2J_B+1)(2J_0+1)} \\
&\quad \times \langle AN[f]LST | (A-1)N_B [f_B]L_B S_B T_B; nl \rangle \\
&\quad \times (J_B M_B J_0 M_0 | JM) (lm_l \frac{1}{2} \sigma | J_0 M_0) (T_B M_{T_B} \frac{1}{2} \tau | T M_T) , \tag{4}
\end{aligned}$$

where the internal WF of the initial nucleus $|\Psi_A\rangle \equiv |AN[f]LSTJMM_T\rangle$ is determined by N – the number of the oscillator quanta, $[f]$ – the Young scheme, L, S, J – the orbital, spin, and total angular momenta, respectively, T – isospin, M and M_T – z -components of J and T , respectively. The internal WF of the final nucleus is determined by similar quantum numbers $|\Psi_B\rangle \equiv |(A-1)N_B [f_B]L_B S_B T_B J_B M_B M_{T_B}\rangle$. The state of the struck nucleon X is determined by the spin, σ , and isospin, τ , projections. The numbers of oscillator quanta satisfy the sum rule $N = N_B + n$. For the WF of relative $X - B$ motion with quantum numbers $n = l = 1$, the one-particle fractional parentage coefficient (FPC) of the TISM (the term in the angular brackets in Eq.(4)) can be expressed via the FPC of the conventional shell model as follows [10]:

$$\begin{aligned}
&\langle AN[f]LST | (A-1)N_B [f_B]L_B S_B T_B; 11 \rangle \\
&= - \left(\frac{A-4}{A-1} \right)^{1/2} \langle p^{A-4} [f]LST | p^{A-5} [f_B]L_B S_B T_B \rangle . \tag{5}
\end{aligned}$$

The FPC of the conventional shell model can be calculated in a standard way from the tables of Ref. [12] taking into account the correction of phases of some orbital WFs as mentioned in the footnote of Ref. [13].

Equation (2) assumes transition from a TISM state of the nucleus A to a TISM state of the nucleus B . Eigenstates of a realistic nuclear Hamiltonian should be the superposition of TISM states. This means that actual spectroscopic amplitude for the transition between the physical states of the nuclei A and B is obtained by the weighted sum

$$\sum_{i,j} \alpha_i \beta_j^* S_A^X([f_i]L_i S_i T_i J_i M_i M_{T_i}; [f_j]L_j S_j T_j J_B M_B M_{T_B}; m_l, \sigma) \equiv S_A^X(J_i M_i M_{T_i}; J_B M_B M_{T_B}; m_l, \sigma) , \tag{6}$$

where the indices i and j enumerate the TISM states which enter the decomposition of the physical states of the nuclei A and B , respectively. The corresponding partial amplitudes α_i and β_j are model dependent. We will apply the intermediate coupling model of Ref. [9] which produces the real-valued partial amplitudes listed for ^{12}C ground state in Table I, and for ^{11}B ground state and two excited states in Table II.

TABLE I. Contributing $(1p)^8$ TISM states denoted as $[f]^{(2T+1)(2S+1)L}$ with their partial amplitudes for the ^{12}C ground state ($J = T = 0$). Taken from Ref. [9].

$[44]^{11}S$	$[431]^{13}P$	$[422]^{11}S$	$[422]^{15}D$	$[332]^{13}P$
0.840	0.492	0.064	-0.200	0.086

So far we discussed the case of IA neglecting ISI/FSI. We will now include the ISI/FSI in the eikonal approximation, similar to Ref. [6]. This is reached by replacing in Eq. (2)

$$(2\pi)^{3/2}\psi_{nl}^{m_l}(-\mathbf{p}_X) \rightarrow \int d^3r e^{-i\mathbf{p}_X\mathbf{r}} \psi_{nl}^{m_l}(-\mathbf{r}) F_1(\mathbf{r}) F_3(\mathbf{r}) F_4(\mathbf{r}) \equiv (2\pi)^{3/2} \tilde{\psi}_{nl}^{m_l}(-\mathbf{p}_X), \quad (7)$$

where $\mathbf{r} = \mathbf{R}_X - \mathbf{R}_B$ is the relative position vector of the struck proton and the center-of-mass (c.m.) of the residual nucleus B . Thus, Eq.(7) takes into account nuclear absorption introduced via factors

$$F_j(\mathbf{r}) = \exp\left(-\frac{i}{v_j} \int_{-\infty}^0 d\eta U_j(\mathbf{r} \pm \hat{\mathbf{p}}_j \eta)\right), \quad (8)$$

where $v_j = p_j/E_j$ is the j -th particle velocity in the rest frame (r.f.) of the nucleus B , $\hat{\mathbf{p}}_j \equiv \mathbf{p}_j/p_j$, and $U_j(\mathbf{r})$ is the optical potential. In Eq.(8), the integral is taken along the trajectory of the j -th particle that corresponds to the “+” sign for $j = 1$ (incoming proton) and “-” sign for $j = 3, 4$ (outgoing protons). At relativistic energies, in good approximation, the latter can be expressed as follows:

$$U_j(\mathbf{r}) = -\frac{i}{2} v_j \sigma_{NN}(p_j) \rho(\mathbf{r}), \quad (9)$$

where $\sigma_{NN}(p_j)$ is the total NN cross section, and $\rho(\mathbf{r})$ is the nucleon number density of the nucleus B in the point \mathbf{r} . The resulting absorption factors are then essentially similar to those in the Glauber approximation [14].

TABLE II. Same as in Table I but for $(1p)^7$ TISM states in ^{11}B . The ground state and two excited states are included. The values of excitation energy are experimental ones. Taken from Ref. [9].

$E^* = 0 \text{ MeV}, T = 1/2, J = 3/2$							
$[43]^{22}P$	$[43]^{22}D$	$[421]^{22}P$	$[421]^{24}P$	$[421]^{22}D$	$[421]^{24}D$	$[421]^{24}F$	
0.636	0.566	-0.223	-0.168	-0.087	-0.309	0.198	
$[331]^{24}S$	$[331]^{22}D$	$[331]^{24}D$	$[322]^{22}P$	$[322]^{24}P$	$[322]^{26}P$		
0.158	0.123	0.043	-0.016	0.080	0.080		

$E^* = 2.13 \text{ MeV}, T = 1/2, J = 1/2$							
$[43]^{22}P$	$[421]^{22}P$	$[421]^{24}P$	$[421]^{24}D$	$[331]^{22}S$	$[331]^{24}D$	$[322]^{22}P$	$[322]^{24}P$
0.913	0.161	-0.132	-0.314	0.126	-0.088	0.000	0.001

$E^* = 5.02 \text{ MeV}, T = 1/2, J = 3/2$						
$[43]^{22}P$	$[43]^{22}D$	$[421]^{22}P$	$[421]^{24}P$	$[421]^{22}D$	$[421]^{24}D$	$[421]^{24}F$
-0.532	0.721	-0.061	0.207	0.272	0.036	0.079
$[331]^{24}S$	$[331]^{22}D$	$[331]^{24}D$	$[322]^{22}P$	$[322]^{24}P$	$[322]^{26}P$	
-0.166	0.021	0.155	0.048	-0.039	-0.111	

We will consider the case of unpolarized particles and, thus, the matrix element modulus squared should be averaged over spin magnetic quantum numbers of the initial particles and summed over those of final particles:

$$\begin{aligned}
\overline{|M|^2} &\equiv \frac{1}{2(2J+1)} \sum_{\sigma_1, \sigma_3, \sigma_4, M, M_B} |M|^2 \\
&= \frac{1}{2(2J+1)} \sum_{\sigma_1, \sigma_3, \sigma_4, M, M_B} \sum_{\sigma, \sigma'} \sum_{m_l, m'_l} M_{\text{el}}(p_3, p_4, p_1; \sigma_3, \sigma_4, \sigma_1, \sigma) M_{\text{el}}^*(p_3, p_4, p_1; \sigma_3, \sigma_4, \sigma_1, \sigma') \\
&\quad \times \frac{2E_B m_A}{p_X^0} (2\pi)^3 \tilde{\psi}_{11}^{m_l}(-\mathbf{p}_X) \tilde{\psi}_{11}^{m'_l*}(-\mathbf{p}_X) \\
&\quad \times S_A^X(JMM_T; J_B M_B M_{T_B}; m_l, \sigma) S_A^{X*}(JMM_T; J_B M_B M_{T_B}; m'_l, \sigma'), \tag{10}
\end{aligned}$$

where we explicitly included summations over intermediate state quantum numbers $\sigma, \sigma', m_l, m'_l$.

To simplify Eq.(10), we, first, neglect the interference terms with $\sigma' \neq \sigma$ and replace

$$\begin{aligned} & \frac{1}{2} \sum_{\sigma_1, \sigma_3, \sigma_4} |M_{\text{el}}(p_3, p_4, p_1; \sigma_3, \sigma_4, \sigma_1, \sigma)|^2 \\ & \rightarrow \overline{|M_{\text{el}}(p_3, p_4, p_1)|^2} \equiv \frac{1}{4} \sum_{\sigma_1, \sigma_3, \sigma_4, \sigma} |M_{\text{el}}(p_3, p_4, p_1; \sigma_3, \sigma_4, \sigma_1, \sigma)|^2 . \end{aligned} \quad (11)$$

Then, after somewhat lengthy but straightforward derivation we come to the following expression:

$$\overline{|M|^2} = \overline{|M_{\text{el}}(p_3, p_4, p_1)|^2} \frac{2E_B m_A}{p_X^0} (2\pi)^3 \overline{|\tilde{\psi}_{11}(-\mathbf{p}_X)|^2} S , \quad (12)$$

where

$$\overline{|\tilde{\psi}_{11}(-\mathbf{p}_X)|^2} \equiv \frac{1}{3} \sum_{m_l=-1}^1 |\tilde{\psi}_{11}^{m_l}(-\mathbf{p}_X)|^2 . \quad (13)$$

The spectroscopic factor in Eq.(12) is expressed as follows:

$$\begin{aligned} S = & A (T_B M_{T_B} \frac{1}{2} \tau |T M_T|^2 (2J_B + 1) \sum_{J_0} (2J_0 + 1) \left| \sum_{i,j} \alpha_i \beta_j^* \begin{Bmatrix} L_j & S_j & J_B \\ 1 & 1/2 & J_0 \\ L_i & S_i & J \end{Bmatrix} \right| \\ & \times \sqrt{(2L_i + 1)(2S_i + 1)} \langle AN[f_i] L_i S_i T | (A - 1) N_B[f_j] L_j S_j T_B; 11 \rangle|^2 . \end{aligned} \quad (14)$$

Equation (13) for the modulus squared of the ISI/FSI-corrected WF is quite involved but can be simplified. Substituting Eq.(7) in Eq.(13) we have:

$$\begin{aligned} \overline{|\tilde{\psi}_{11}(-\mathbf{p}_X)|^2} &= \frac{1}{3(2\pi)^3} \sum_{m_l} \int d^3 r \int d^3 r' e^{-i\mathbf{p}_X(\mathbf{r}-\mathbf{r}')} \psi_{11}^{m_l}(-\mathbf{r}) \psi_{11}^{m_l*}(-\mathbf{r}') F_{\text{abs}}(\mathbf{r}) F_{\text{abs}}(\mathbf{r}') \\ &\simeq \frac{1}{(2\pi)^3} \int d^3 R f_{11}(-\mathbf{R}, -\mathbf{p}_X) F_{\text{abs}}^2(\mathbf{R}) , \end{aligned} \quad (15)$$

where $F_{\text{abs}}(\mathbf{r}) \equiv F_1(\mathbf{r}) F_3(\mathbf{r}) F_4(\mathbf{r})$ is the absorption factor, and

$$f_{11}(-\mathbf{R}, -\mathbf{p}_X) \equiv \frac{1}{3} \sum_{m_l} \int d^3 \xi e^{-i\mathbf{p}_X \xi} \psi_{11}^{m_l}(-\mathbf{R} - \xi/2) \psi_{11}^{m_l*}(-\mathbf{R} + \xi/2) \quad (16)$$

is a Wigner function. In Eq.(15), in the last step, we introduced variables $\mathbf{R} \equiv (\mathbf{r} + \mathbf{r}')/2$, $\xi \equiv \mathbf{r} - \mathbf{r}'$ and approximately set $\xi = 0$ in the product of absorption factors $F_{\text{abs}}(\mathbf{R} + \xi/2) F_{\text{abs}}(\mathbf{R} - \xi/2)$ (see Ref. [6] for discussion of validity of this approximation).

The TISM WF of the relative $X - B$ motion is

$$\psi_{11}^{m_l}(-\mathbf{R}) = \left(\frac{8}{3\pi^{1/2} R_0^5} \right)^{1/2} R e^{-R^2/2R_0^2} Y_{1m_l}(-\hat{\mathbf{R}}) , \quad (17)$$

where $R_0 = r_0[A/(A-1)]^{1/2}$, and $r_0 = 1.581$ fm is the parameter of the conventional HO shell model [15]. The Wigner function (16) can be then easily calculated:

$$f_{11}(-\mathbf{R}, -\mathbf{p}_X) = 8 e^{-(R^2 + p_X^2 R_0^4)/R_0^2} \left[\frac{2}{3R_0^2} (R^2 + p_X^2 R_0^4) - 1 \right] . \quad (18)$$

This expression can be used in Eq.(15) for numerical calculations of $|\overline{\psi_{11}(-\mathbf{p}_X)}|^2$ taking into account ISI/FSI. In the case of IA, one recovers an analytical formula:

$$|\overline{\psi_{11}(-\mathbf{p}_X)}|^2 = \frac{2R_0^5}{3\pi^{3/2}} p_X^2 e^{-p_X^2 R_0^2} . \quad (19)$$

The invariant matrix element of elastic pp scattering is related to the differential cross section by a standard formula:

$$\frac{d\sigma_{\text{el}}}{dt} = \frac{|M_{\text{el}}(t, s)|^2}{64\pi I_{pp}^2} , \quad (20)$$

where $I_{pp} = \sqrt{(s/4 - m^2)s}$ is the flux factor, $s = (p_3 + p_4)^2$, $t = \max\{(p_1 - p_3)^2, (p_1 - p_4)^2\}$. By using the high-energy parameterization $d\sigma_{\text{el}}/dt \propto e^{bt}$ one obtains the following relation:

$$|\overline{M_{\text{el}}(t, s)}|^2 = 64\pi I_{pp}^2 \frac{b\sigma_{\text{el}}}{1 - e^{bt_0}} e^{bt} , \quad (21)$$

where $t_0 = -2(s/4 - m^2)$. The experimental integrated elastic pp cross section, σ_{el} , and the slope parameter, b , are conveniently parameterized in Ref. [16] as functions of the beam momentum, $p_{\text{lab}} = I_{pp}/m$, for $p_{\text{lab}} \lesssim 5 - 6$ GeV/c.

For the calculation of the optical potential, Eq.(9), one has to specify the total pN cross section and the nucleon density distribution. We apply the proton/neutron-number-weighted formula

$$\sigma_{pN} = [\sigma_{pp}Z_B + \sigma_{pn}(A_B - Z_B)]/A_B , \quad (22)$$

where σ_{pp} and σ_{pn} are, respectively, the total pp and pn cross sections in the parameterizations of Ref. [16] that provide good fits of available experimental data at $p_{\text{lab}} \lesssim 3 - 5$ GeV/c. $A_B = A - 1$ and $Z_B = Z - 1$ are, respectively, the mass and charge numbers of the residual nucleus B . The nucleon density distribution in the nucleus with A_B nucleons in the $s^4 p^{A_B-4}$ configuration is described by the conventional HO shell model formula

$$\rho(r) = \frac{4}{r_0^3 \pi^{3/2}} \left[1 + \frac{A_B - 4}{6} \left(\frac{r}{r_0} \right)^2 \right]^2 e^{-r^2/r_0^2} . \quad (23)$$

The fully differential cross section of the process $A(p, 2p)B$ (see Fig. 1 for notation) is expressed as follows:

$$d\sigma_{1A \rightarrow 34B} = \frac{(2\pi)^4 |\overline{M}|^2}{4I_{pA}} \delta^{(4)}(p_1 + p_A - p_3 - p_4 - p_B) \frac{d^3p_3}{(2\pi)^3 2E_3} \frac{d^3p_4}{(2\pi)^3 2E_4} \frac{d^3p_B}{(2\pi)^3 2E_B}, \quad (24)$$

where $I_{pA} = p_{\text{beam}}m$ is the flux factor, p_{beam} is the momentum of the nucleus A in the r.f. of the proton 1 which will be called ‘‘laboratory frame’’ below.. The experiment of Ref. [4] has been performed at $p_{\text{beam}}/A = 0.951$ GeV/c where the pp elastic cross section is almost isotropic in the effective region of integration over transferred rescattering momentum in the c.m. frame as follows from the used here parameterization [16].

Thus, it is convenient to perform the integration over invariants d^3p_3/E_3 and d^3p_4/E_4 in the c.m. frame of the protons 3 and 4. On the other hand, the matrix element is proportional to the WF of the relative $X - B$ motion which suppresses large absolute values of the momentum \mathbf{p}_B of the residual nucleus in the r.f. of the nucleus A . Thus, the integration over invariant d^3p_B/E_B is reasonable to perform in the r.f. of the nucleus A . As a result, we come to the following expression for the integrated cross section:

$$\sigma_{1A \rightarrow 34B} = \frac{1}{32(2\pi)^5 p_{\text{beam}}m} \int \frac{d^3p_B}{\sqrt{p_B^2 + m_B^2}} \int \frac{p_3 d\Omega_3}{2\sqrt{p_3^2 + m^2}} |\overline{M}|^2, \quad (25)$$

where the momentum \mathbf{p}_B is defined in the r.f. of the nucleus A while the momentum \mathbf{p}_3 and the corresponding solid angle element $d\Omega_3$ – in the c.m. frame of the protons 3 and 4. Due to identity of the differential cross section with respect to the interchange of momenta of the 3-d and 4-th protons, the integration over $d\Omega_3$ should be performed over the solid angle hemisphere of 2π (the orientation of the hemisphere does not play a role). Due to rotational symmetry about the beam axis, it is also possible to reduce the integration order by writing in the spherical coordinates with z -axis along the 1-st proton momentum in the r.f. of A $d^3p_B = p_B^2 dp_B 2\pi d\Theta_B$ and perform all integrations in Eq.(25) with arbitrarily fixed value of the azimuthal angle ϕ_B . Finally, the differential cross sections, $d\sigma_{1A \rightarrow 34B}/dx$, where x is any kinematic variable determined by the momenta \mathbf{p}_3 and \mathbf{p}_B , are evaluated by multiplying the integrand of Eq.(25) by the factor $\delta[x - x(\mathbf{p}_B, \mathbf{p}_3)]$.

3. RESULTS

The integrated cross sections are listed in Table III. One can see from this Table that absorption reduces all partial cross section by a factor of 5.1 but does not change the ra-

tios between the partial cross sections for different states of ^{11}B . The experimental total cross section is reproduced by full calculation surprisingly well, with accuracy of about 3%. The strong dominance of ^{11}B production in the ground state is also correctly reproduced. Discrepancies for excited states are quite large. However, this is still satisfactory given the fact that we did not introduce any additional model parameters (like phenomenological spectroscopic factors, see discussion section) to tune our calculations.

TABLE III. Integrated cross sections of the process $^{12}\text{C}(p, 2p)^{11}\text{B}$ with 400 MeV/nucleon ^{12}C beam for the ground state and two excited states of the residual nucleus ^{11}B . Listed are the results of full calculations (including absorption), calculations in the IA, and the spectroscopic factors calculated using Eq.(14). Experimental data are from Ref. [4]. Total errors are given in parentheses.

E^* (MeV)	J^π	σ_{exp} (mb)	σ_{full} (mb)	σ_{IA} (mb)	S
0.0 (G.S.)	$3/2^-$	15.8(18)	12.3	62.6	2.82
2.13	$1/2^-$	1.9(2)	2.9	14.9	0.67
5.02	$3/2^-$	1.5(2)	3.4	17.5	0.79
Total:		19.2(3)	18.6	95.0	4.28

Fig. 2 shows the distribution of opening angle, $\Theta_{\text{opening}} = \arccos(\mathbf{p}_3\mathbf{p}_4/p_3p_4)$, between outgoing protons in the laboratory frame. The full calculation correctly describes the peak position at 80° and the distribution at smaller angles, although gives a sharper peak and steeper fall-off at larger angles. The full calculation is slightly shifted to larger opening angles as compared to the calculation in the IA.

Fig. 3 shows the distribution of relative azimuthal angle, $\Delta\phi = \arccos(\mathbf{p}_{3t}\mathbf{p}_{4t}/p_{3t}p_{4t})$, between the transverse momenta \mathbf{p}_{3t} and \mathbf{p}_{4t} of outgoing protons. The absorptive ISI/FSI suppress the yield at large deviations of $\Delta\phi$ from 180° leading to a sharper peak at $\Delta\phi = 180^\circ$ and better agreement with experiment.

Figs. 4,5 and 6 show, respectively, the transverse, longitudinal, and total momentum distributions of the residual nucleus. Absorption leads to the depletion of the yield at large transverse and total momenta shifting the maxima of the P_{tr} - and P_{tot} distributions to smaller momenta. This can be understood as follows. In the presence of absorption, the main contribution to the integral in Eq.(15) comes from nuclear periphery (surface ring), since

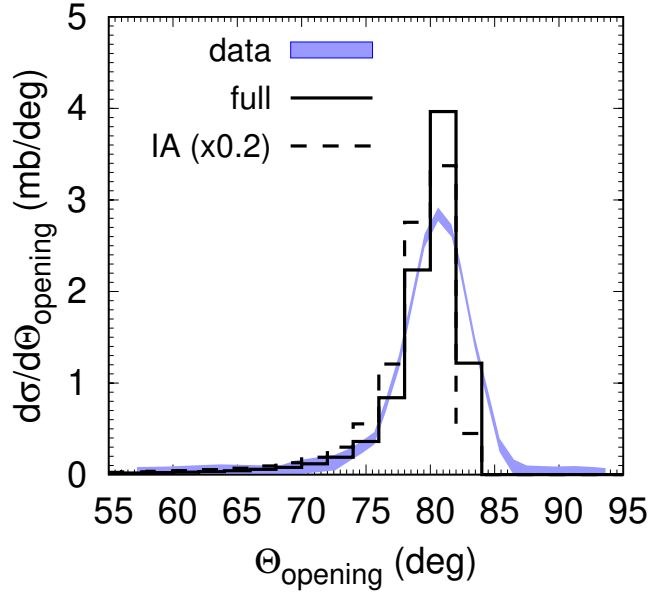


FIG. 2. The distribution of opening angle between outgoing protons in the laboratory frame for the process $^{12}\text{C}(p, 2p)^{11}\text{B}$ at 400 MeV/nucleon. Solid and dashed histograms show, respectively, the full calculation and the calculation without absorption scaled by a factor of 0.2. The band represents experimental data from Ref. [4].

the absorption factor suppresses the integrand deeply inside the nucleus. If the transverse momentum of the residual nucleus is small, then the absorption is in average smaller because both outgoing protons may have small transverse momenta balancing each other and their trajectories avoid the bulk of the nuclear medium. If the transverse momentum of the residual nucleus is large, then at least one of the outgoing protons will have large transverse momentum and, thus, its trajectory will pass through the bulk of the nuclear medium with a larger probability which makes absorption stronger. This is also in-line with stronger absorption at larger deviations of $\Delta\phi$ from 180° (Fig. 3).

A particular form of the Wigner density for the $n = l = 1$ valence nucleon, Eq.(18), acts in the same direction. At small values of R and $p_X (= P_{\text{tot}})$, the Wigner density becomes negative. It means that absorption should then lead to the enhancement of production which is visible at small values of P_{tot} in Fig. 6.

In the IA calculation, the longitudinal momentum distribution (Fig. 5) is shifted to positive P_{\parallel} . This corresponds to the struck proton X moving opposite to the incoming

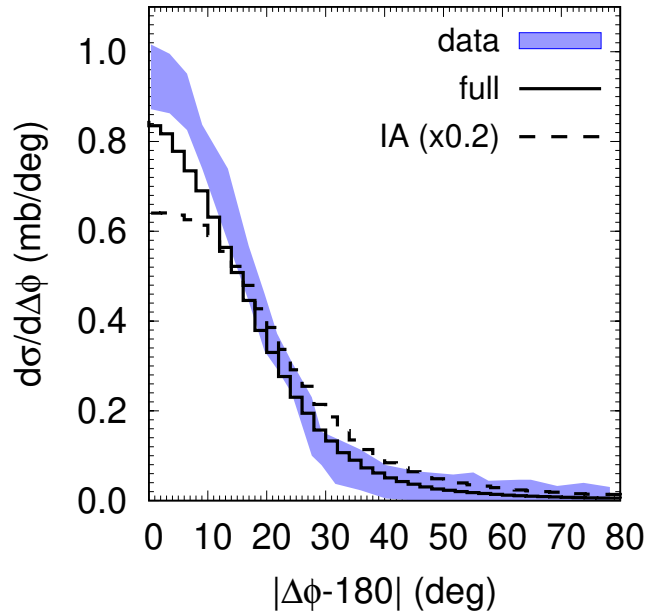


FIG. 3. The distribution of the relative azimuthal angle between transverse momenta of outgoing protons for $^{12}\text{C}(p, 2p)^{11}\text{B}$ at 400 MeV/nucleon. Line notations are the same as in Fig. 2. The band represents experimental data from Ref. [4].

proton 1 in the r.f. of ^{12}C giving a larger two-body phase space volume of the protons 3 and 4 (the term $\propto p_3/\sqrt{p_3^2 + m^2}$ in Eq.(25)). However, with absorption, the P_{\parallel} distribution becomes almost symmetric with respect to the change $P_{\parallel} \rightarrow -P_{\parallel}$. This is a consequence of larger average transverse momenta of the 3-d and 4-th protons at $P_{\parallel} > 0$ leading to their stronger absorption. This observation also explains the stronger absorption at smaller opening angles (Fig. 2).

4. DISCUSSION

Table IV contains results of several other calculations of the spectroscopic factors for the separation of a nucleon from ^{12}C in comparison with our results. The approach of Ref. [17] is based on the FPCs of the conventional shell model but in other aspects is quite close to the intermediate coupling model of Refs. [8, 9] applied in our work. In Ref. [18], the WFs of deformed HO shell model were used without residual interaction taking $K = 0$ for ^{12}C and $K = 1/2, 3/2$ for ^{11}B . (In the spherical HO model this corresponds to considering

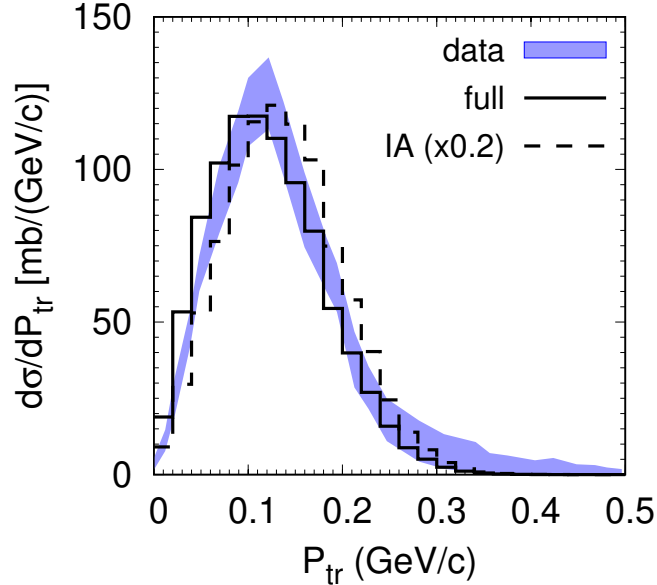


FIG. 4. The distribution of the transverse momentum of the residual nucleus for $^{12}\text{C}(p, 2p)^{11}\text{B}$ at 400 MeV/nucleon. Line notations are the same as in Fig. 2. The band represents experimental data from Ref. [4].

TABLE IV. Spectroscopic factors for the $^{12}\text{C} \rightarrow p^{11}\text{B}(n^{11}\text{C})$ process calculated in different theoretical models.

E^* (MeV)	J^π	[17]	[18]	[19]	this work
0.0 (G.S.)	$3/2^-$	2.85	3.27	2.50	2.82
2.13	$1/2^-$	0.75	0.60	0.48	0.67
5.02	$3/2^-$	0.38	0.12		0.79
Total:		3.98	3.99	2.98	4.28

only the Young scheme [44] for ^{12}C and [43] for ^{11}B .) In Ref. [19], the no-core shell model was employed in the HO basis with c.m. correction, although the authors state that the dependence of their results on the chosen basis is small. According to Ref. [20], however, the “old” definition of the spectroscopic amplitude (c.f. our Eq.(4)) relies on the non-normalized

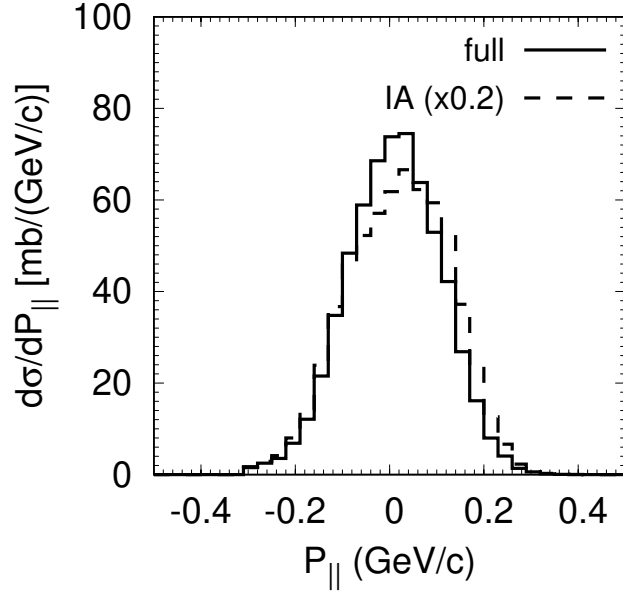


FIG. 5. The distribution of the longitudinal momentum of the residual nucleus in the r.f. of ^{12}C for $^{12}\text{C}(p, 2p)^{11}\text{B}$ at 400 MeV/nucleon. Positive values of $P_{||}$ correspond to the direction of the momentum of the incoming proton. Line notations are the same as in Fig. 2.

WF of the final state and, thus, should be corrected.¹

Comparison with experimental data for the QE (p, pN) processes depends not only on the spectroscopic factors but also on the ISI/FSI used. In phenomenological DWIA approaches [21, 22], the spectroscopic factor is used as a free parameter to fit experimental cross sections for some fixed ISI/FSI. The latter includes in-medium effects due to Pauli blocking of NN scattering [23] (i.e. the antisymmetrization of the full WF of the scattered nucleon and residual nucleus) which can be effectively described by in-medium reduced NN cross sections. It was shown [23], that in heavy-ion induced stripping reactions on nuclear targets at $E_{\text{lab}} = 5 - 300$ MeV/nucleon, the in-medium effects lead to about 10% change in the nucleon knockout cross sections and momentum distributions. In (p, pN) processes, the in-medium effects are expected to be of the same order or smaller. The in-medium effects should decrease with increasing beam energy rendering Glauber model more natural at $E_{\text{lab}} > 1$ GeV/nucleon [14]. Thus, our description of ISI/FSI within Glauber model should

¹ It was pointed out in Ref. [20] that “the numerical differences in the results of calculations employing the “old” and “new” definitions are usually not large for single-nucleon channels, in contrast to cluster channels”. Thus, we do not expect much influence of this correction on our results.

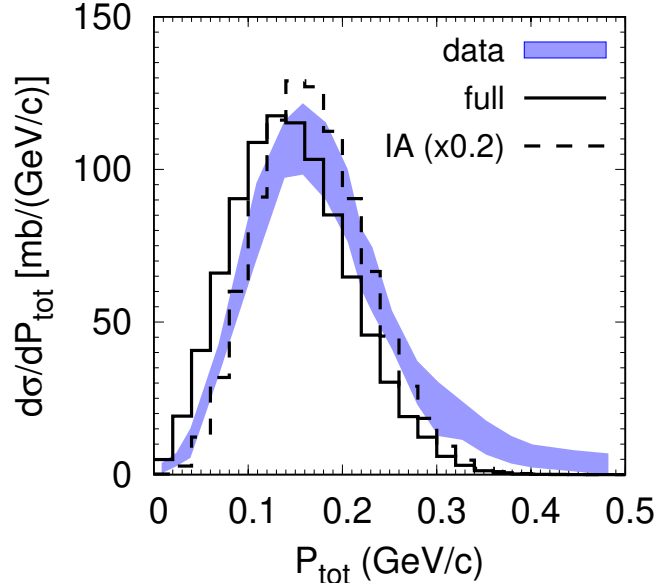


FIG. 6. The distribution of the total momentum of the residual nucleus in the r.f. of ^{12}C for $^{12}\text{C}(p, 2p)^{11}\text{B}$ at 400 MeV/nucleon. Line notations are the same as in Fig. 2. The band represents experimental data from Ref. [4].

be taken with some reservations for possible in-medium corrections.

5. SUMMARY

Based on the TISM, we developed the model for description of fully exclusive $A(p, pp)(A-1)$ reactions at intermediate relativistic energies. The model allows to calculate spectroscopic factors directly from the overlap integral of the WFs. Having in mind future model applications at NICA and FAIR energies, we restricted ourselves to the Glauber model description of the ISI/FSI. As a test case, the model was applied to the reaction $^{12}\text{C}(p, 2p)^{11}\text{B}$ at 400 MeV/nucleon measured at GSI [4] in the inverse kinematics.

The model slightly underestimates the measured integrated cross section for ^{11}B $3/2^-$ ground state, but overpredicts the integrated cross sections for the two excited $1/2^-$ and $3/2^-$ states. The total integrated cross section for the production of all three ^{11}B states is well reproduced, however.

The distributions of the outgoing proton pair in the opening angle and relative azimuthal

angle, as well as the momentum distributions of the residual nucleus, are reproduced reasonably well. Some deficiency in the production of high-momentum residual nuclei can be attributed to the longitudinal momenta mostly and is probably due to the limited HO WF basis.

Last but not least, the present calculation also puts on a firm ground our previous study of the $^{12}\text{C}(p, 2pN_s)^{10}\text{A}$ exclusive reactions at 48 GeV/c [6], where a similar approach has been used.

ACKNOWLEDGMENTS

The authors are grateful to Prof. Eliezer Piassetzky who proposed to apply for the $^{12}\text{C}(p, 2p)^{11}\text{B}$ reaction the same TISM setup as for the $^{12}\text{C}(p, 2pn_s)^{10}\text{B}$ reaction studied in Ref. [6].

-
- [1] Y. Kondo *et al.*, Phys. Rev. C **79**, 014602 (2009).
 - [2] M. Holl *et al.* (R3B), Phys. Lett. B **795**, 682 (2019).
 - [3] T. Aumann *et al.*, Prog. Part. Nucl. Phys. **118**, 103847 (2021), arXiv:2012.12553 [nucl-th].
 - [4] V. Panin *et al.*, Phys. Lett. B **753**, 204 (2016).
 - [5] V. G. Neudatchin and Y. F. Smirnov, *Nuklonnye assotsiatsii v legkikh yadrakh (Nucleon Associations in Light Nuclei)* (Nauka, Moscow, 1969) [in Russian].
 - [6] A. B. Larionov and Y. N. Uzikov, (2023), arXiv:2311.06042 [nucl-th].
 - [7] M. Patsyuk *et al.*, Nature Phys. **17**, 693 (2021), arXiv:2102.02626 [nucl-ex].
 - [8] V. Balashov, A. Boyarkina, and I. Rotter, Nucl. Phys. **59**, 417 (1964).
 - [9] A. N. Boyarkina, *Struktura yader 1p-obolochki (Structure of 1p-shell Nuclei)* (Moskovskij Gosudarstvennij Universitet (Moscow State University), Moscow, 1973) [in Russian].
 - [10] Y. F. Smirnov and Y. M. Tchuvil'sky, Phys. Rev. **C15**, 84 (1977).
 - [11] Y. Uzikov and A. Uvarov, Phys. Part. Nucl. **53**, 426 (2022).
 - [12] H. A. Jahn and H. van Wieringen, Proc. Roy. Soc. A **209**, 502 (1951).
 - [13] J. Elliott, J. Hope, and H. A. Jahn, Phil. Trans. Roy. Soc. **A246**, 241 (1953).
 - [14] B. Van Overmeire, W. Cosyn, P. Lava, and J. Ryckebusch, Phys. Rev. C **73**, 064603 (2006),

arXiv:nucl-th/0603013.

- [15] G. D. Alkhazov, G. M. Amalsky, S. L. Belostotsky, A. A. Vorobyov, O. A. Domchenkov, Y. V. Dotsenko, and V. E. Starodubsky, *Phys. Lett. B* **42**, 121 (1972).
- [16] J. Cugnon, J. Vandermeulen, and D. L'Hote, *Nucl. Instrum. Meth. B* **111**, 215 (1996).
- [17] S. Cohen and D. Kurath, *Nucl. Phys. A* **101**, 1 (1967).
- [18] R. N. Singh, N. De Takacsy, S. I. Hayakawa, R. L. Hutson, and J. J. Kraushaar, *Nucl. Phys. A* **205**, 97 (1973).
- [19] J. Li, C. A. Bertulani, and F. Xu, *Phys. Rev. C* **105**, 024613 (2022), arXiv:2202.04354 [nucl-th].
- [20] D. M. Rodkin and Y. M. Tchuvil'sky, *Phys. Rev. C* **104**, 044323 (2021), arXiv:2104.10499 [nucl-th].
- [21] D. W. Devins, D. L. Friesel, W. P. Jones, A. C. Attard, I. D. Svalbe, V. C. Officer, R. S. Henderson, B. M. Spicer, and G. G. Shute, *Aust. J. Phys.* **32**, 323 (1979).
- [22] T. Aumann, C. A. Bertulani, and J. Ryckebusch, *Phys. Rev. C* **88**, 064610 (2013), arXiv:1311.6734 [nucl-th].
- [23] C. A. Bertulani and C. De Conti, *Phys. Rev. C* **81**, 064603 (2010), arXiv:1004.2096 [nucl-th].

What Can We Learn from Directed Flow at STAR-FTX Energies?

Yu. B. Ivanov^{1,2,*} and M. Kozhevnikova^{3,†}

¹*Bogoliubov Laboratory of Theoretical Physics, JINR Dubna, 141980 Dubna, Russia*

²*National Research Center "Kurchatov Institute", 123182 Moscow, Russia*

³*Veksler and Baldin Laboratory of High Energy Physics, JINR Dubna, 141980 Dubna, Russia*

We present results of simulations of directed flow of various hadrons in Au+Au collisions at collision energies of $\sqrt{s_{NN}} = 3$ and 4.5 GeV. Simulations are performed within the model three-fluid dynamics (3FD) and the event simulator based on it (THESEUS). The results are compared with recent STAR data. The directed flows of various particles provide information on dynamics in various parts and at various stages of the colliding system depending on the particle. However, the information on the equation of state is not always directly accessible because of strong influence of the afterburner stage or insufficient equilibration of the matter. It is found that the crossover scenario gives the best overall description of the data. This crossover EoS is soft in the hadronic phase. The transition into QGP in Au+Au collisions occurs at collision energies between 3 and 4.5 GeV, at baryon densities $n_B \gtrsim 4n_0$ and temperatures ≈ 150 MeV. In-medium effects in the directed flow of (anti)kaons are discussed.

I. INTRODUCTION

The directed flow is one of the most sensitive quantities to the dynamics of nucleus-nucleus collisions and properties of the matter produced in these collisions. It provides information about the stopping power of the nuclear matter, its equation of state (EoS), transition to quark-gluon phase (QGP) and more. All these issues were addressed in the analysis of the STAR data [1] obtained within Beam Energy Scan (BES) program at the Relativistic Heavy-Ion Collider (RHIC). The analysis was performed within various approaches [2–14], which include both hydrodynamic and kinetic models. An important conclusion of these studies is that the transition to the quark-gluon phase is most probably of the crossover or weak-first-order type and it starts at collision energies of $\sqrt{s_{NN}} < 8$ GeV in Au+Au collisions. A promising recent development is prediction of correlation between the directed flow and the angular momentum accumulated in the participant region of colliding nuclei [8, 15–19], which allows a deeper insight into collision dynamics.

The STAR-FXT (fixed-target) data on the directed flow of identified particles at energies $\sqrt{s_{NN}} = 3$ and 4.5 GeV were recently published in Refs. [20, 21]. These data were also analyzed within various, mostly kinetic models [11, 14, 22–33] in relation to various problems: the hyperon production [14, 26, 33], the production of light (hyper)nuclei [30, 31], etc. The EoS of the matter produced in the nucleus-nucleus collisions was the prime topic of the above theoretical considerations. It was discussed mostly in terms of softness and stiffness of the EoS [11, 22–24, 26, 29]. These studies were performed within different transport models: The relativistic version of the quantum molecular dynamics implemented into the transport code JAM [11], the hadronic trans-

port code SMASH [22, 29], the Ultrarelativistic Quantum Molecular Dynamics (UrQMD) [23, 24], and a multi-phase transport model [26].

All the aforementioned papers [11, 22–24, 26, 29] reported that stiff (to a different extent) EoS's are preferable for the reproduction of the directed flow (v_1) at $\sqrt{s_{NN}} = 3$ GeV, while the v_1 data at 4.5 GeV require a softer EoS. The latter was interpreted as indication of onset of the phase transition into QGP. This conclusion about preference of the stiff EoS at the energy of 3 GeV appears to contradict the earlier findings. The analysis of KaoS [34] and FOPI [35] data at collision energies $E_{lab} \leq 2A$ GeV ($\sqrt{s_{NN}} \leq 2.7$ GeV) within the Isospin Quantum Molecular Dynamics model led to the conclusion that the soft EoS with the incompressibility $K = 210$ MeV is strongly preferable [35–38]. Although, this energy range is somewhat below of the STAR-FXT one.

The energy range of the BNL Alternating Gradient Synchrotron (AGS), $E_{lab} = 2 - 10.7$ A·GeV ($\sqrt{s_{NN}} = 2.7$ –4.9 GeV), practically coincide with the currently explored STAR-FXT range. The results of the analysis of the AGS data [39, 40] are more controversial. Strong preference of the soft EoS was reported in Refs. [3, 4, 41–43]. In Refs. [3, 4], the EoS additionally softens at $\sqrt{s_{NN}} > 4$ GeV because of onset of the deconfinement transition. However, in Ref. [44] it was found that the best description of the data on the transverse flow is provided by a rather stiff EoS at 2A·GeV (NL3) while at higher bombarding energies (4–8 A·GeV) a medium EoS ($K = 300$ MeV) leads to better agreement with the data, while the differences in the soft-EoS and stiff-EoS transverse flows become of minor significance at 4–8 A·GeV. In Ref. [45], the proton flow was found to be also independent of stiffness of the EoS, however provided the momentum dependence in the nuclear mean fields is taken into account.

As recent studies [11, 22–26, 29, 32] of the STAR-FXT v_1 data deduced comparatively stiff EoS's at $\sqrt{s_{NN}} = 3$ GeV, some of them predicted comparatively low baryon densities (n_B) for onset of the denfiment transition.

*e-mail: yivanov@theor.jinr.ru

†e-mail: kozhevnikova@jinr.ru

This transition was associated with the softening of the EoS required for v_1 reproduction at the energy of 4.5 GeV. In terms of the normal nuclear density n_0 , the deduced transition densities are $3-4n_0$ [22], $4n_0$ [24], $2.5n_0$ [25], $3-5n_0$ [26], $n_B > 2-3n_0$ [29], and $5n_0$ [32]. The model of three-fluid dynamics (3FD) [46, 47] predicts that the denfiment transition starts at approximately $n_B > 4-5n_0$ at temperatures 100–150 MeV for the crossover EoS. However, the STAR-FXT data on the directed flow of identified particles at energies $\sqrt{s_{NN}} = 3$ and 4.5 GeV have not yet been fully considered within the 3FD model, with the exception of the proton and Λ -hyperon data at 3 GeV, which were analyzed with respect to the light (hyper)nuclei production [30, 31].

In view of the above reviewed developments, the debate about the EoS stiffness and onset of the QGP transition is far from being completed. A more extended discussion of the EoS constraints deduced from the directed-flow analysis can be found in recent review [48].

In the present paper, we present results of calculations of the directed flow of various hadrons at energies $\sqrt{s_{NN}} = 3$ and 4.5 GeV and compare them with recent STAR-FXT data [20, 21]. The calculations are performed within the 3FD model [46, 47] and also within the Three-fluid Hydrodynamics-based Event Simulator Extended by UrQMD final State interactions (THESEUS) [49–51]. The THESEUS simulations are intended to study the effect of the UrQMD afterburner stage on the directed flow. We present some conclusions that can be drawn from agreement or disagreement of the calculated results with the data.

II. 3FD MODEL AND THESEUS GENERATOR

The 3FD model [46, 47] simulates nonequilibrium at the early stage of nuclear collisions by means of two counterstreaming baryon-rich fluids. The third (fireball) fluid accumulates newly produced particles, dominantly populating the midrapidity region. These fluids are governed by conventional hydrodynamic equations coupled by friction terms in the right-hand sides of the Euler equations. The friction terms describe the energy–momentum exchange between the fluids. The hydrodynamic evolution ends with the freeze-out procedure described in Refs. [52, 53]. The 3FD model does not include any kinetic afterburner stage.

The THESEUS event generator [49–51] does include the afterburner stage that is described by the UrQMD model. The THESEUS generator transforms the 3FD output, which is recorded in terms of local flow velocities and thermodynamic quantities on the freeze-out hypersurface, into a set of observed particles, i.e. performs a particlization. The particlization is followed by the afterburner stage.

The afterburner stage is of prime importance for collisions at lower energies, where there is no clear rapidity separation between participant and spectator nucleons at

the freeze-out. When the time for the nuclei to pass each other becomes long relative to the characteristic time scale for the participant evolution, the interaction between participants and spectators (so-called shadowing) becomes important [54–56]. In particular, the squeeze-out effect [57–59], is the consequence of this shadowing, i.e. results from blocking of the expanding central blob by the spectator matter. This shadowing only partially is taken into account within the 3FD evolution because the central fireball remains to be shadowed even after the freeze-out while particles escape from this fireball without interacting with spectators in the 3FD model.

The afterburner stage should, in principle, correct this deficiency. However, it does not do it completely. The reason is that the THESEUS assigns *the same time instant* to all produced particles during the particlization procedure, while different parts of the system are frozen-out at *different time instants* in 3FD. A time-extended transition from hydrodynamic evolution to afterburner dynamics would need treatment of the interaction of the kinetic afterburner phase with still hydrodynamically evolved matter. This is a difficult task both technically and conceptually. The lack of this interaction is the prime reason of shortcoming of the THESEUS particlization. At lower collision energies, participants are frozen out earlier than spectators. The spectators evolve slower because of the lower excitation energy and hence require longer time before the freeze-out. If the particlization is isochronous like in THESEUS, the evolution of the frozen-out participants stops until the spectators also become frozen-out. Therefore, we skip the stage of shadowing the afterburner expansion of the central fireball by spectators still being in the hydrodynamic phase. The afterburner evolution is switched on only when the spectators also become frozen out, when they have already partially passed the expanding central fireball. Thus, the shadowing by spectators turns out to be reduced compared to what it would be if the entire collision process were kinetically treated, like in UrQMD or JAM.

The 3FD model has been extensively used to simulations of Au+Au collisions at AGS energies, which almost coincide with the STAR-FXT ones. Quantities, which are low sensitive to the afterburner stage, were well reproduced by the 3FD simulations. These are various bulk observables [47, 60, 61], proton directed [3, 4] and elliptic (at higher AGS energies) [59] flow, bulk properties and directed flow of light (hyper)nuclei at $\sqrt{s_{NN}} = 3$ GeV [30, 31]. Problems with reproduction of the elliptic flow of protons and light nuclei at $\sqrt{s_{NN}} = 3$ GeV in Ref. [30] are related to the aforementioned deficiency of the isochronous particlization in THESEUS. Precisely the same parameters of the 3FD model as those in Refs. [3, 4, 30, 31, 47, 60, 61] are used in the present simulations.

III. EQUATIONS OF STATE

The 3FD model is designed to work with different EoS's. Three different EoS's are traditionally used in the 3FD simulations: a purely hadronic EoS [62] and two EoS's with deconfinement transitions [63], i.e. an EoS with a first-order phase transition (1PT EoS) and one with a smooth crossover transition. While the hadronic EoS is quite flexible, i.e., it allows for changes of incompressibility, the EoS's with deconfinement transitions are strictly tabulated. These EoS's are illustrated in Fig. 1. As seen, all three EoS's are similar in the hadronic

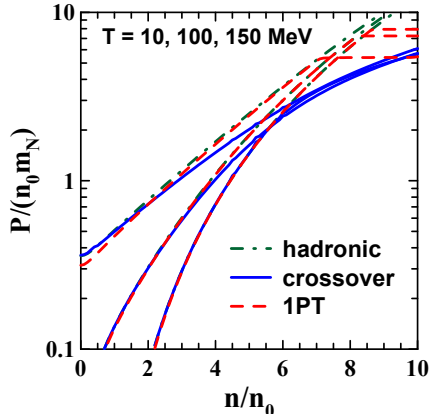


FIG. 1: Pressure (scaled by product of the normal nuclear density, $n_0 = 0.15 \text{ 1/fm}^3$, and the nucleon mass, m_N) at three temperatures, $T = 10, 100$ and 150 MeV (from bottom upwards for corresponding curves), as function of the net baryon density (scaled by n_0) for the hadronic, crossover and 1PT EoS's.

phase. Note that the displayed version of the hadronic EoS is characterized by incompressibility $K = 190 \text{ MeV}$. The simulations below are performed with this version of the hadronic EoS. The crossover pressure starts to deviate from the hadronic one at $n_B > 4\text{--}5n_0$ at temperatures 100–150 MeV that are typical for the collisions at STAR-FXT energies, see Fig. 2.

Dynamical trajectories of the matter in the central cell of the colliding Au+Au nuclei in semicentral collisions ($b = 6 \text{ fm}$) at energies $\sqrt{s_{NN}} = 3$ and 4.5 GeV are presented in Fig. 2 in terms of the baryon density and temperature. Evolution starts from the normal nuclear density and zero temperature and then follows an almost universal trajectory for some time. Shortly before reaching the turning point, at which density and temperature are maximal, the matter in this central cell becomes equilibrated, as it was demonstrated in Ref. [64], and therefore the temperature takes its conventional meaning. The turning points at the energy of 3 GeV only touches the QGP region according to the crossover EoS, see Fig. 1. The the same time the 4.5-GeV trajectories fall well into the crossover QGP region and even enter the the 1PT mixed phase. The trajectories for different EoS's move away from each other at higher densities and

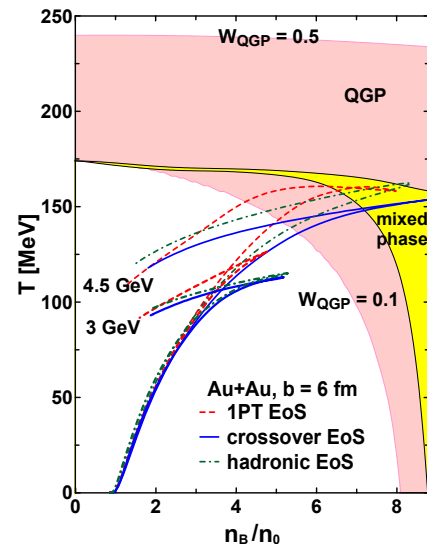


FIG. 2: Dynamical trajectories of the matter in the central cell of the colliding Au+Au nuclei in semicentral collisions (impact parameter is $b = 6 \text{ fm}$) at energies $\sqrt{s_{NN}} = 3$ and 4.5 GeV . The trajectories are plotted in terms of the baryon density (n_B , scaled by the normal nuclear density n_0) and temperature T . The trajectories are presented for the three EoS's. The mixed phase of the 1PT EoS is displayed by the shadowed region marked as “mixed phase”. The wide shadowed area displays the region of the crossover EoS between the QGP fractions $W_{QGP} = 0.1$ and 0.5 .

temperatures. In particular, it demonstrates that the hadronic EoS and the 1PT one are not identical in the whole hadronic phase.

The crossover and 1PT phase diagrams require some comments. The QCD lattice calculations demonstrated that the transition into QGP at zero baryon chemical potential is a smooth crossover [65]. Due to that, the transition temperature is ambiguous because different definitions can lead to different values for it. Observables related to chiral symmetry result in the transition temperature around 155–160 MeV [66]. As seen from Fig. 2, the transition regions at zero baryon density (i.e. chemical potential) in EoS's of Ref. [63] are located at noticeably higher temperatures than 155–160 MeV. This happens because the EoS's of Ref. [63] were fitted to the old, still imperfect lattice data [67–69]. Moreover, the crossover transition constructed in Ref. [63] is very smooth. The hadronic fraction survives up to very high temperatures. In particular, this is seen from Fig. 2: the fraction of the quark-gluon phase (W_{QGP}) reaches value of 0.5 only at very high temperatures. Such a smooth crossover is also used in the PHSD model (Parton-Hadron-String Dynamics) [70]. However, this version of the crossover [63] certainly contradicts results of the lattice QCD calculations at zero chemical potential, where a fast crossover was found [65]. However, the aforementioned shortcomings are not severe for the present simulations at relatively low collision energies, because the system evolution

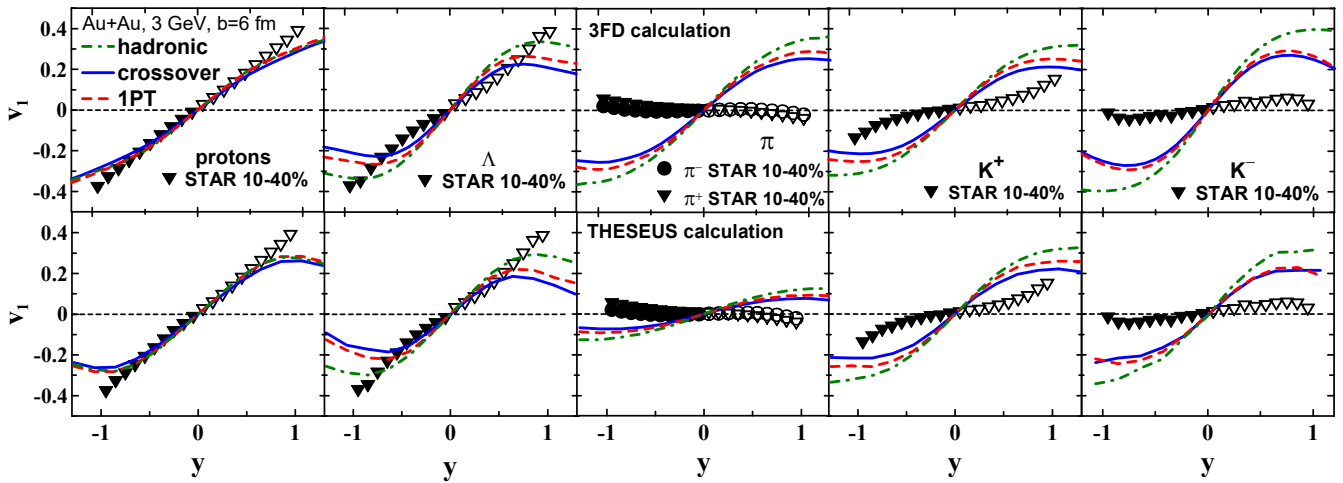


FIG. 3: Directed flow of protons, pions, Λ hyperons, and kaons as function of rapidity in semicentral ($b = 6$ fm) Au+Au collisions at collision energy of $\sqrt{s_{NN}} = 3$ GeV. Results are calculated within the 3FD model (upper row of panels) and the THESEUS (lower row of panels) with hadronic, 1PT, and crossover EoS's. STAR data are from Ref. [21].

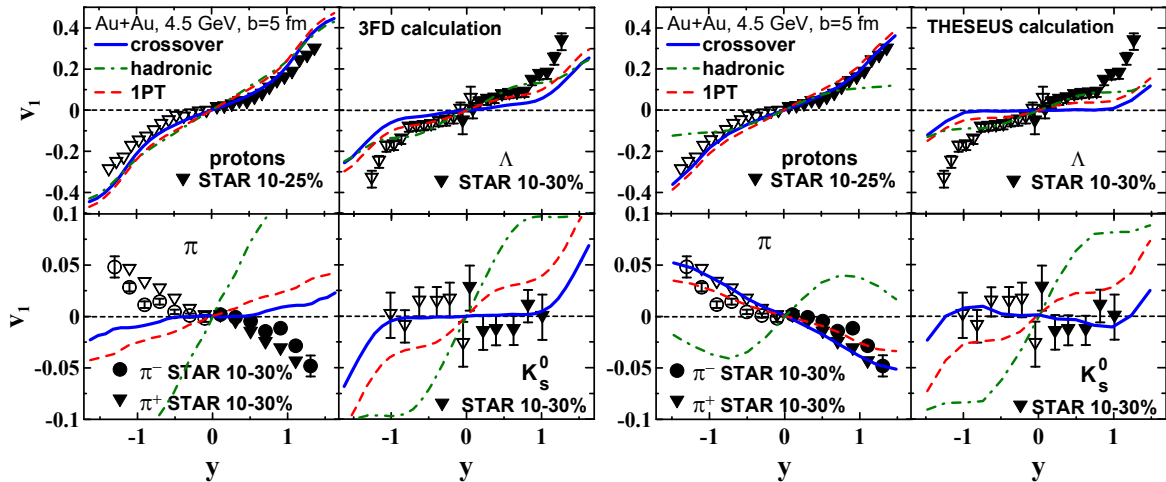


FIG. 4: Directed flow of protons, pions, Λ hyperons, and kaons (K^0 short) as function of rapidity in semicentral ($b = 5$ fm) Au+Au collisions at collision energy of $\sqrt{s_{NN}} = 4.5$ GeV. Results are calculated within the 3FD model (left block of panels) and the THESEUS (right block of panels) with hadronic, 1PT, and crossover EoS's. STAR data are from Ref. [20].

takes place in the region of high baryon densities, where the EoS is not known from the first principles.

IV. DIRECTED FLOW

The calculated directed flow of protons, pions, Λ hyperons, and (anti)kaons as function of rapidity in semicentral Au+Au collisions at collision energies of $\sqrt{s_{NN}} = 3$ and 4.5 GeV are presented in Figs. 3 and 4, respectively. These calculations were performed in the 3FD model without any afterburner and within THESEUS (i.e. with the UrQMD afterburner). The results are compared with STAR data [20, 21].

As seen, the proton v_1 flow is well reproduced with

and without afterburner. The afterburner slightly improves the description at 4.5 GeV, while worsens it at forward/backward rapidities at 3 GeV without changing the midrapidity slope. The midrapidity proton flow turns out to be almost independent of the used EoS even at 4.5 GeV, where the QGP transition already takes place, see Fig. 2. This is because the proton flow is formed at the early stage of the collision [71–73]. At considered collision energies, this stage is developed in the hadronic phase for all considered EoS's, see Fig. 2, where all considered EoS's are very similar, see Fig. 1. Moreover, the stopping power of the matter, i.e. friction forces of the 3FD model [47], are identical in the hadronic phase for all considered scenarios. Consequently, the flow appears to be quite independent of the used EoS even at

4.5 GeV. Note that the proton directed flow does depend on the EoS at the BES RHIC energies [2–4], where the transition to QGP occurs already the early stage of the collision.

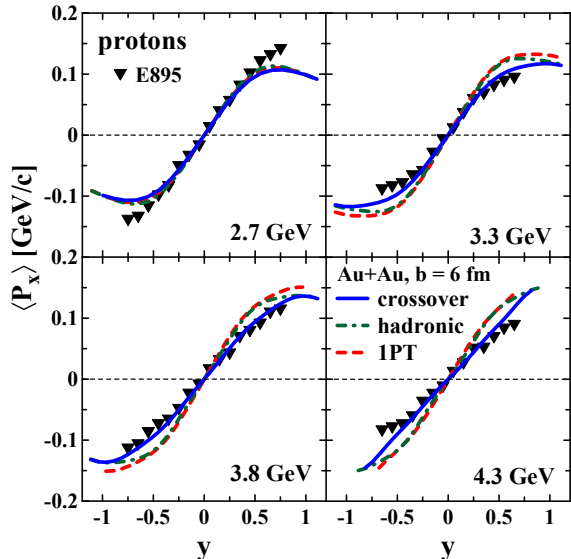


FIG. 5: Transverse flow of protons as function of rapidity in semicentral ($b = 6$ fm) Au+Au collisions at collision energies of $\sqrt{s_{NN}} = 2.7$ –4.3 GeV ($E_{lab} = 2A, 4A, 6A,$ and $8A$ GeV). Results are calculated within the 3FD model with hadronic, 1PT, and crossover EoS’s. E895 data are from Ref. [39].

Figure 5 illustrates the description of the old E895 data [39] in the same collision energy range. These data are presented in terms of transverse flow defined as [74]

$$\langle P_x \rangle(y) = \frac{\int d^2 p_T p_x E dN/d^3 p}{\int d^2 p_T E dN/d^3 p}, \quad (1)$$

where p_x is the transverse momentum of the proton in the reaction plane, $E dN/d^3 p$ is the invariant momentum distribution of protons with E being the proton energy, and integration runs over the transverse momentum p_T . This is done because the E895 data in terms of $v_1(y)$ raised many questions, as it was discussed in Ref. [3] in detail. In addition, they contradict the new STAR-FTX data. As seen from Fig. 5, the crossover EoS gives almost perfect description of the proton transverse flow in the midrapidity regions. This gives hope that the future STAR-FTX proton data at the energies between 3 and 4.5 GeV will be also well reproduced with the crossover scenario. The dependence on the EoS is quite moderate, similar to that at 3 and 4.5 GeV in Figs. 3 and 4.

The Λ flow turns out to be more sensitive to the EoS, see Figs. 3 and 4, because Λ ’s are produced in highly excited but still baryon-rich regions of the colliding system. These regions are formed later, when the temperature reaches high values, see Fig. 2. The afterburner

stronger affects evolution in these regions. It reduces the midrapidity slope of the Λ flow, making the crossover EoS definitely preferable at 3 GeV, while the hadronic EoS turns out to be preferable at 4.5 GeV. In view of this sensitivity to the afterburner, definite conclusions on the EoS relevance can hardly be made based on the Λ flow.

The meson flow probes dynamics in highly excited baryon-rich and baryon-depleted regions of the system. The highly excited baryon-depleted regions are formed even later than the excited baryon-rich regions, when the transverse expansion already dominates. Nevertheless, the mesonic flow is very similar to the baryon one after the 3FD stage at 3 GeV, see Fig. 3, while substantially differ from the baryon flow at 4.5 GeV, see Fig. 4. Note that this difference at 4.5 GeV concerns only the EoS’s involving the transition to the QGP, whereas the hadronic EoS results in the mesonic flow being similar to the baryon one. The reason is that the EoS becomes softer in the QGP and hence the pressure causing the directed flow is reduced. Therefore, the mesonic flow may indicate the transition to the QGP. However, there are other circumstances that may prevent us from drawing definite conclusions from the mesonic flow. One of them is the afterburner.

The pion flow is strongly affected by the afterburner. If the 3FD-calculated pion flow hardly resembles the corresponding data, after the afterburner stage, it almost perfectly describes these data at 4.5 GeV within the crossover and 1PT scenarios. The hadronic scenario evidently fails to reproduce the pion flow at 4.5 GeV. The afterburner even changes the sign of the midrapidity slope of the crossover and 1PT flows at 4.5 GeV. Note that the 3FD model and hence THESEUS do not distinguish positive, neutral, and negative pions. Therefore, the calculated pion flow refers to the flow of all pions. This strong dependence on the afterburner is a consequence of the shadowing discussed in Sec. II. At 3 GeV, the afterburner shifts the 3FD-calculated flow closer to the data but still not enough to reproduce them. This insufficient effect of the afterburner is a result of the shortcoming of the THESEUS particlization discussed in Sec. II: The afterburner skips the stage of shadowing the afterburner expansion of the central fireball by spectators still being in the hydrodynamic phase. At 4.5 GeV, this skipped stage is already of minor importance because the time for the nuclei to pass each other becomes shorter relative to the time scale of the participant evolution.

The K^+ directed flow is not changed by the afterburner stage because of small cross sections of their interactions with other hadrons. Indeed, the kaon-nucleon cross section is about 10 mb, while the nucleon-nucleon one is about 40 mb [38, 75, 76]. Indeed, at somewhat lower energies (2A GeV) it was concluded that after their production the K-mesons suffer not more than one rescattering before escaping [77, 78]. At the energy of 3 GeV ($\approx 3A$ GeV), higher densities are achieved in the collisions and therefore rescatterings become more frequent, however

not frequent enough to thermalize the kaon. This explains why the calculated flow (on the assumption of the kaon thermalization) is so different from the data, see Fig. 3.

At slightly higher collision energy of 3.85 GeV (6A GeV), the rescatterings of the kaons with the nucleons in the dense matter already cause them to flow in the direction of the nucleons, as it was reported in Ref. [41]. Thus, the transition from rare-collisional to collisional regime occurs in the considered energy range. At the energy of 4.5 GeV, the kaons can be considered well thermalized at the late stage of nuclear collision, however the afterburner still does not affect the flow, as seen from Fig. 4.

At the same time, the K^- directed flow at 3 GeV is reduced by the afterburner because the NK^- cross section is of the order of 40 mb or even higher at low relative NK^- energies [38, 75, 76]. However, the calculated K^- flow is still essentially stronger than the experimental one. Apparently, this is a result of the aforementioned shortcoming of the THESEUS particlization, i.e. a lack of shadowing of the central fireball by still hydrodynamically evolving spectators.

Within the 3FD model, we calculate $v_1(y)$ for K_s^0 mesons in terms of those for K^0 and \bar{K}^0 as follows

$$v_1^{K_s^0}(y) = \frac{\left(v_1^{K^0}(y) \frac{dN^{K^0}}{dy} + v_1^{\bar{K}^0}(y) \frac{dN^{\bar{K}^0}}{dy} \right)}{\left(\frac{dN^{K^0}}{dy} + \frac{dN^{\bar{K}^0}}{dy} \right)}, \quad (2)$$

where dN^{K^0}/dy and $dN^{\bar{K}^0}/dy$ are rapidity distributions of the K^0 and \bar{K}^0 mesons. Eq. (2) does not imply that K_s^0 consists of K^0 and \bar{K}^0 in this proportion. It only means that K_s^0 mesons originate from K^0 and \bar{K}^0 mesons that are emitted from the interaction region. These K^0 and \bar{K}^0 mesons keep their momenta and thus their flow pattern after escaping from the interaction region. Therefore, the corresponding fractions of produced K_s^0 mesons carry these K^0 and \bar{K}^0 flow patterns. The \bar{K}^0 number is about 20% of that of K^0 at 4.5 GeV.

The directed flow of K_s^0 mesons at 4.5 GeV strongly depends on the EoS and moderately depends on the afterburner. This moderate dependence on the afterburner is a consequence of the large fraction of K^0 mesons in produced K_s^0 . The K^0 mesons are practically unaffected by the afterburner. Therefore, the K_s^0 directed flow is a good probe of the hot and dense stage of the collision. As seen from Fig. 4, the crossover EoS is certainly preferable for reproduction of the data.

Thus, the directed flows of various particles provide information on dynamics in various parts and at various stages of the colliding system depending on the particle. However, the information on the EoS is not always directly accessible because of strong influence of the afterburner stage or insufficient thermalization of kaons. The crossover scenario gives the best overall description

of the data, of course, with all reservations regarding the above-mentioned difficulties in applying the model.

V. DIRECTED FLOW OF KAONS

The kaons deserve a separate discussion. As has been mentioned above, the afterburner does not affect the flow of kaons because of small cross sections of their interactions with other hadrons but noticeably changes the antikaon flow at 3 GeV, see Fig. 3. It is instructive to consider the kaon and antikaon flows at 4.5 GeV, in spite of absence of the corresponding data.

The directed flow of kaons, antikaons and K_s^0 mesons as function of rapidity in semicentral ($b = 5$ fm) Au+Au collisions at collision energy of $\sqrt{s_{NN}} = 4.5$ GeV is presented in Fig. 6. The flows of kaons and antikaons are marked as (K^0, K^+) and (\bar{K}^0, K^-) , respectively, because the 3FD model does not distinguish the corresponding mesons. The kaon flow again turns out to be insensitive to the afterburner.

The flow of antikaons is enhanced by the afterburner, contrary to the reduction of the antikaon flow at 3 GeV. Notably, midrapidity slopes of the kaon and antikaon flow are of the opposite sign for the crossover and 1PT EoS's while they are both non-negative within the hadronic scenario. Apparently, the antiflow of the antikaons is again related to the aforementioned shadowing of the decay of central blob by the spectator matter. This shadowing is present already in the 3FD stage of the evolution, as seen from the upper row of panels in Fig. 6. The afterburner additionally enhances this shadowing and hence the antiflow, see the middle row of panels in Fig. 6. These opposite signs of the midrapidity slopes of the kaon and antikaon flows can be considered as a prediction for the flow at 4.5 GeV.

In-medium modifications of kaons are discussed in connection with chiral symmetry restoration and neutron star properties, see review [79]. In Refs. [38, 41, 76, 80], it was found that in-medium modifications of kaons are very important for description of the kaon observables, in particular, the kaon directed flow. It was reported that these in-medium effects can even change the midrapidity slope of the kaon flow at the energy of 3.85 GeV (6A GeV) [41], i.e. in the energy range we consider here.

In the relativistic mean-field approximation for the baryon degrees of freedom [81, 82], the in-medium (anti)kaon energy reads

$$E(\mathbf{p}) = \left[m_K^2 + \mathbf{p}^2 - \frac{\Sigma_{KN}}{f_K^2} \rho + \left(\frac{3}{8} \frac{n}{f_K^2} \right)^2 \right]^{1/2} \pm \frac{3}{8} \frac{n}{f_K^2}, \quad (3)$$

where \mathbf{p} is the three-momentum of the (anti)kaon, the upper(lower) sign refers to $K(\bar{K})$.

$$n = \sum_B \langle \bar{B} \gamma^0 B \rangle,$$

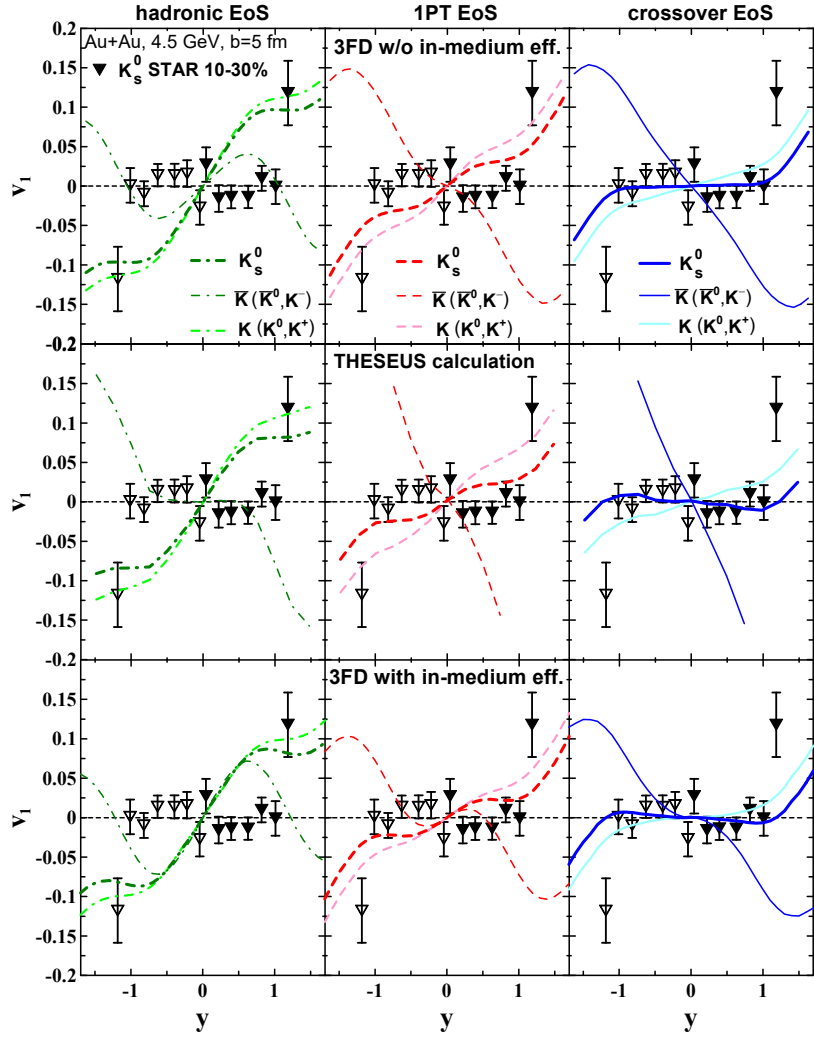


FIG. 6: Directed flow of kaons, antikaons and K_s^0 mesons as function of rapidity in semicentral ($b = 5$ fm) Au+Au collisions at collision energy of $\sqrt{s_{NN}} = 4.5$ GeV. Results are calculated within THESEUS (the middle row of panels) and also within the 3FD model with (the lower row of panels) and without (the upper row of panels) in-medium modifications of (anti)kaons. STAR data are from Ref. [20].

$$\rho = \sum_B \langle \bar{B}B \rangle$$

are the proper baryon density and scalar baryon density, respectively, which are sums over various baryons B . Numerical values of the kaon decay constant, $f_K = 106$ MeV, and the kaon-nucleon sigma term, $\Sigma_{KN} = 350$ MeV, are taken from Ref. [38]. The term proportional to Σ_{KN} results from the attractive scalar interaction due to explicit chiral symmetry breaking.

The above expression was derived for the so-called s -wave interaction. Importance of p -wave kaon-baryon interactions was indicated in Refs. [83, 84]. The treatment of the kaon-baryon interaction beyond the mean-field approximation, i.e. with the G-matrix approach [76, 79], also turned out to be important. Therefore, Eq. (3) can only serve as a basis for the estimation of the in-medium effects in (anti)kaon production. Below we use Eq. (3)

for this purpose. The same form of the in-medium kaon energy was used in Ref. [41].

The version of the UrQMD that is implemented in THESEUS is not suitable for treatment of the medium modified kaons. Therefore, we study the in-medium effects within the 3FD model. Results of the 3FD calculation of the directed flow taking into account the in-medium kaon modification at collision energy of $\sqrt{s_{NN}} = 4.5$ GeV is shown in the lower row of panels of Fig. 6. As seen, the effect of this in-medium modification is quite moderate. However, it slightly improves the agreement with the K_s^0 data within the 1PT EoS and especially the crossover scenario. This improvement is practically the same as that resulted from the afterburner. It is remarkable that the change of the antikaon flow due to the in-medium effects is opposite to that caused by the afterburner.

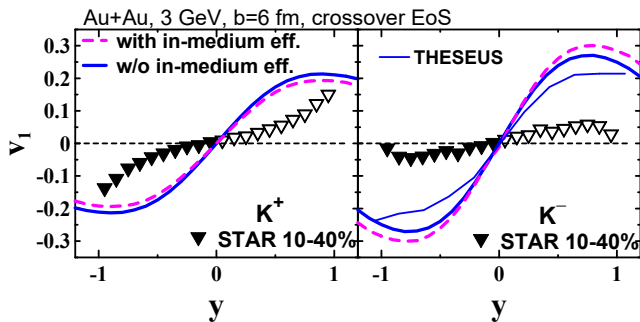


FIG. 7: Directed flow of kaons (left panel) and antikaons (right panel) as function of rapidity in semicentral ($b = 6$ fm) Au+Au collisions at collision energy of $\sqrt{s_{NN}} = 3$ GeV. Results are calculated with and without in-medium modifications of (anti)kaons for the crossover EoS's. STAR data are from Ref. [20].

As seen from Fig. 7, the effect of the in-medium modifications of (anti)kaons is also small contrary to that found in Refs. [38, 41, 76, 80]. Apparently, this is because the kaons were incompletely equilibrated in the matter in kinetic simulations of Refs. [38, 41, 76, 80] and hence the in-medium effect was accumulated throughout the evolution of the system. In the 3FD simulations they are completely equilibrated and the in-medium modifications appear only at the freeze-out, leaving them insufficient time to manifest themselves. Again the in-medium modifications and the afterburner result in opposite changes in the antikaon directed flow. Only the afterburner decreases and the in-medium modification increases the flow, contrary to that at 4.5 GeV. This is because there is the normal flow at 3 GeV instead of antiferflow at 4.5 GeV.

We can conclude that the directed flow of kaons or K_s^0 is a promising probe of the EoS at hot and dense stage of the collision at 4.5 GeV because it is not affected by the afterburner stage. At 3 GeV, the kaons do not appear to be fully equilibrated in matter and therefore do not reflect the EoS of the matter. The antikaon flow is also a good EoS probe, which is however strongly modified during the afterburner evolution.

VI. SUMMARY

The directed flow of various hadrons at energies $\sqrt{s_{NN}} = 3$ and 4.5 GeV were calculated and compared with recent STAR-FXT data [20, 21]. The calculations were performed within the 3FD model [46, 47] and also within the THESEUS generator [49–51] in order to study the effect of the UrQMD afterburner stage on the directed flow. Three different EoS's are used in the simulations: a purely hadronic EoS [62] and two EoS's with deconfinement transitions [63], i.e. an EoS with a strong first-order phase transition and one with a smooth crossover transition.

At these collision energies, the time for the nuclei to

pass each other is long relative to the time scale of the participant evolution and therefore the interaction between participants and spectators (shadowing) is important. In particular, the squeeze-out effect is a consequence of this shadowing. This shadowing only partially is taken into account within the 3FD evolution because the central fireball remains to be shadowed even after the freeze-out. Therefore, the afterburner stage becomes of prime importance.

The afterburner shifts the 3FD-calculated flow closer to the data but still not enough to reproduce the pion and antikaon flow at 3 GeV. This insufficient effect of the afterburner results from shortcoming of the THESEUS isochronous particlization: The afterburner skips the stage of shadowing of the post-freeze-out expansion of the central fireball by spectators still hydrodynamically evolving.

The directed flows of various particles provide information on dynamics in various parts and at various stages of the colliding system depending on the particle. However, the information on the EoS is not always directly accessible because of strong influence of the afterburner stage or insufficient equilibration, as it happens with kaons at 3 GeV. Based on these simulations, the following conclusions were drawn:

- The proton flow is formed at the early stage of the collision, where the matter is not yet equilibrated. Therefore, it probes the properties of this nonequilibrium matter rather than its EoS that implies the equilibrated matter. The proton flow is well reproduced within all three considered scenarios and is practically independent of the afterburner.
- The Λ flow turns out to be more sensitive to the EoS because Λ 's are produced in highly excited but still baryon-rich regions of the colliding system. These regions are formed later, when the temperature reaches high values. The afterburner stronger affects evolution in these regions.
- The meson flow probes dynamics of highly excited baryon-rich and baryon-depleted regions of the system. The highly excited baryon-depleted regions are formed even later than the excited baryon-rich regions, when the transverse expansion already dominates.
- The pion flow is strongly affected by the afterburner. This strong dependence on the afterburner is a consequence of the shadowing.
- The directed flow of kaons or K_s^0 is a promising probe of the EoS at hot and dense stage of the collision at 4.5 GeV because it is not affected by the afterburner stage. At 3 GeV, the kaons do not appear to be fully equilibrated in matter and therefore do not reflect the EoS of the matter. The antikaon flow is also a good EoS probe, which is however strongly modified during the afterburner evolution.

In conclusion, the crossover scenario gives the best overall description of the data, of course, with all reservations regarding the above-mentioned difficulties in applying the model. This crossover EoS is soft in the hadronic phase. This result agrees with that in Refs. [3, 4, 41, 42] but is in contrast to Refs. [11, 22–24, 26, 29], where stiff EoS’s were found being preferable for the reproduction of the directed flow at 3 GeV. The conclusion about the preference of the stiff EoS [11, 22–24, 26, 29], was mostly based on the proton flow, which is formed at the early nonequilibrium stage of the collision. Therefore, the proton flow is a combined result of the EoS and the stopping power of the matter. Different combinations of the EoS and the stopping power can properly describe the proton flow. Directed flows of different hadrons, as well as other bulk observables should be considered together to decouple effects of the EoS and the stopping power.

Within the preferred crossover scenario, the transition

into QGP in Au+Au collisions occurs at collision energies between 3 and 4.5 GeV, at baryon densities $n_B \gtrsim 4n_0$ and temperatures ≈ 150 MeV. This implies that the EoS additionally softens at 4.5 GeV. This softening and hence transition into QGP at 4.5 GeV well agrees with conclusions made in Refs. [11, 22–24, 26, 29].

Acknowledgments

Fruitful discussions with D.N. Voskresensky are gratefully acknowledged. This work was carried out using computing resources of the federal collective usage center “Complex for simulation and data processing for mega-science facilities” at NRC “Kurchatov Institute” [85]. and computing resources of the supercomputer “Govorun” at JINR [86].

-
- [1] L. Adamczyk *et al.* [STAR], Beam-Energy Dependence of the Directed Flow of Protons, Antiprotons, and Pions in Au+Au Collisions, *Phys. Rev. Lett.* **112**, no.16, 162301 (2014) [arXiv:1401.3043 [nucl-ex]].
- [2] V. P. Konchakovski, W. Cassing, Y. B. Ivanov and V. D. Toneev, Examination of the directed flow puzzle in heavy-ion collisions, *Phys. Rev. C* **90**, no.1, 014903 (2014) [arXiv:1404.2765 [nucl-th]].
- [3] Y. B. Ivanov and A. A. Soldatov, Directed flow indicates a cross-over deconfinement transition in relativistic nuclear collisions, *Phys. Rev. C* **91**, no.2, 024915 (2015) [arXiv:1412.1669 [nucl-th]].
- [4] Y. B. Ivanov and A. A. Soldatov, What can we learn from the directed flow in heavy-ion collisions at BES RHIC energies?, *Eur. Phys. J. A* **52**, no.1, 10 (2016) [arXiv:1601.03902 [nucl-th]].
- [5] J. Steinheimer, J. Auvinen, H. Petersen, M. Bleicher and H. Stöcker, Examination of directed flow as a signal for a phase transition in relativistic nuclear collisions, *Phys. Rev. C* **89**, no.5, 054913 (2014) [arXiv:1402.7236 [nucl-th]].
- [6] Y. Nara, H. Niemi, A. Ohnishi and H. Stöcker, Examination of directed flow as a signature of the softest point of the equation of state in QCD matter, *Phys. Rev. C* **94**, no.3, 034906 (2016) [arXiv:1601.07692 [hep-ph]].
- [7] C. Shen and S. Alzhrani, Collision-geometry-based 3D initial condition for relativistic heavy-ion collisions, *Phys. Rev. C* **102**, no.1, 014909 (2020) [arXiv:2003.05852 [nucl-th]].
- [8] S. Ryu, V. Jovic and C. Shen, Probing early-time longitudinal dynamics with the Λ hyperon’s spin polarization in relativistic heavy-ion collisions, *Phys. Rev. C* **104**, no.5, 054908 (2021) [arXiv:2106.08125 [nucl-th]].
- [9] L. Du, C. Shen, S. Jeon and C. Gale, Probing initial baryon stopping and equation of state with rapidity-dependent directed flow of identified particles, *Phys. Rev. C* **108**, no.4, 4 (2023) [arXiv:2211.16408 [nucl-th]].
- [10] Y. Nara, H. Niemi, J. Steinheimer and H. Stöcker, Equation of state dependence of directed flow in a microscopic transport model, *Phys. Lett. B* **769**, 543-548 (2017) [arXiv:1611.08023 [nucl-th]].
- [11] Y. Nara, T. Maruyama and H. Stoecker, Momentum-dependent potential and collective flows within the relativistic quantum molecular dynamics approach based on relativistic mean-field theory, *Phys. Rev. C* **102**, no.2, 024913 (2020) [arXiv:2004.05550 [nucl-th]].
- [12] Y. Nara and H. Stoecker, Sensitivity of the excitation functions of collective flow to relativistic scalar and vector meson interactions in the relativistic quantum molecular dynamics model RQMD.RMF, *Phys. Rev. C* **100**, no.5, 054902 (2019) [arXiv:1906.03537 [nucl-th]].
- [13] Y. Nara and A. Ohnishi, Mean-field update in the JAM microscopic transport model: Mean-field effects on collective flow in high-energy heavy-ion collisions at sNN=2–20 GeV energies, *Phys. Rev. C* **105**, no.1, 014911 (2022) [arXiv:2109.07594 [nucl-th]].
- [14] Y. Nara, A. Jinno, K. Murase and A. Ohnishi, Directed flow of Λ in high-energy heavy-ion collisions and Λ potential in dense nuclear matter, *Phys. Rev. C* **106**, no.4, 044902 (2022) [arXiv:2208.01297 [nucl-th]].
- [15] Y. B. Ivanov and A. A. Soldatov, Correlation between global polarization, angular momentum, and flow in heavy-ion collisions, *Phys. Rev. C* **102**, no.2, 024916 (2020) [arXiv:2004.05166 [nucl-th]].
- [16] N. S. Tsegelnik, E. E. Kolomeitsev and V. Voronyuk, Helicity and vorticity in heavy-ion collisions at energies available at the JINR Nuclotron-based Ion Collider facility, *Phys. Rev. C* **107**, no.3, 034906 (2023) [arXiv:2211.09219 [nucl-th]].
- [17] Z. F. Jiang, X. Y. Wu, S. Cao and B. W. Zhang, Directed flow and global polarization in Au+Au collisions across energies covered by the beam energy scan at RHIC, *Phys. Rev. C* **107**, no.3, 034904 (2023) [arXiv:2301.02960 [nucl-th]].
- [18] Z. F. Jiang, X. Y. Wu, S. Cao and B. W. Zhang, Hyperon polarization and its relation with directed flow in high-energy nuclear collisions, *Phys. Rev. C* **108**, no.6, 6 (2023) [arXiv:2307.04257 [nucl-th]].
- [19] I. Karpenko and J. Cimerman, Directed flow and hyperon polarization at RHIC BES from multi-fluid dynamics,

- [arXiv:2312.11325 [nucl-th]].
- [20] J. Adam *et al.* [STAR], Flow and interferometry results from Au+Au collisions at $\sqrt{s_{NN}} = 4.5$ GeV, Phys. Rev. C **103**, no.3, 034908 (2021) [arXiv:2007.14005 [nucl-ex]].
- [21] M. S. Abdallah *et al.* [STAR], Disappearance of partonic collectivity in $s_{NN}=3$ GeV Au+Au collisions at RHIC, Phys. Lett. B **827**, 137003 (2022) [arXiv:2108.00908 [nucl-ex]].
- [22] D. Oliinychenko, A. Sorensen, V. Koch and L. McLerran, Sensitivity of Au+Au collisions to the symmetric nuclear matter equation of state at 2–5 nuclear saturation densities, Phys. Rev. C **108**, no.3, 034908 (2023) [arXiv:2208.11996 [nucl-th]].
- [23] J. Steinheimer, A. Motornenko, A. Sorensen, Y. Nara, V. Koch and M. Bleicher, The high-density equation of state in heavy-ion collisions: constraints from proton flow, Eur. Phys. J. C **82**, no.10, 911 (2022) [arXiv:2208.12091 [nucl-th]].
- [24] M. Omana Kuttan, J. Steinheimer, K. Zhou and H. Stoecker, QCD Equation of State of Dense Nuclear Matter from a Bayesian Analysis of Heavy-Ion Collision Data, Phys. Rev. Lett. **131**, no.20, 202303 (2023) [arXiv:2211.11670 [hep-ph]].
- [25] A. Li, G. C. Yong and Y. X. Zhang, Testing the phase transition parameters inside neutron stars with the production of protons and lambdas in relativistic heavy-ion collisions, Phys. Rev. D **107**, no.4, 043005 (2023) [arXiv:2211.04978 [nucl-th]].
- [26] Z. M. Wu and G. C. Yong, Probing the incompressibility of dense hadronic matter near the QCD phase transition in relativistic heavy-ion collisions, Phys. Rev. C **107**, no.3, 034902 (2023) [arXiv:2302.11065 [nucl-th]].
- [27] P. Parfenov, Model Study of the Energy Dependence of Anisotropic Flow in Heavy-Ion Collisions at $\sqrt{s_{NN}} = 2-4.5$ GeV, Particles **5**, no.4, 561-579 (2022)
- [28] M. Mamaev and A. Taranenko, Toward the System Size Dependence of Anisotropic Flow in Heavy-Ion Collisions at $\sqrt{s_{NN}}=2-5$ GeV, Particles **6**, no.2, 622-637 (2023)
- [29] N. Yao, A. Sorensen, V. Dexheimer and J. Noronha-Hostler, Structure in the speed of sound: from neutron stars to heavy-ion collisions, [arXiv:2311.18819 [nucl-th]].
- [30] M. Kozhevnikova and Y. B. Ivanov, Light-nuclei production in Au+Au collisions at $s_{NN}=3$ GeV within a thermodynamical approach: Bulk properties and collective flow, Phys. Rev. C **109**, no.1, 014913 (2024) [arXiv:2311.08092 [nucl-th]].
- [31] M. Kozhevnikova and Y. B. Ivanov, Light Hypernuclei Production in Au+Au Collisions at $\sqrt{s_{NN}} = 3$ GeV within Thermodynamic Approach, Phys. Rev. C **109**, no.3, 034901 (2024) [arXiv:2401.04991 [nucl-th]].
- [32] G. C. Yong, Phase diagram determination at fivefold nuclear compression, Phys. Lett. B **848**, 138327 (2024) [arXiv:2306.16005 [nucl-th]].
- [33] S. N. Wei, W. Z. Jiang and Z. Q. Feng, The influence of hyperon potential on neutron star matter and heavy-ion collisions, [arXiv:2401.07653 [nucl-th]].
- [34] C. T. Sturm *et al.* [KAOS], Evidence for a soft nuclear equation of state from kaon production in heavy ion collisions, Phys. Rev. Lett. **86**, 39-42 (2001) [arXiv:nucl-ex/0011001 [nucl-ex]].
- [35] W. Reisdorf *et al.* [FOPI], Systematics of azimuthal asymmetries in heavy ion collisions in the 1 A GeV regime, Nucl. Phys. A **876**, 1-60 (2012) [arXiv:1112.3180 [nucl-ex]].
- [36] C. Fuchs, A. Faessler, E. Zabrodin and Y. M. Zheng, Probing the nuclear equation of state by K+ production in heavy ion collisions, Phys. Rev. Lett. **86**, 1974-1977 (2001) [arXiv:nucl-th/0011102 [nucl-th]].
- [37] C. Hartnack, H. Oeschler and J. Aichelin, Hadronic matter is soft, Phys. Rev. Lett. **96**, 012302 (2006) [arXiv:nucl-th/0506087 [nucl-th]].
- [38] C. Hartnack, H. Oeschler, Y. Leifels, E. L. Bratkovskaya and J. Aichelin, Strangeness Production close to Threshold in Proton-Nucleus and Heavy-Ion Collisions, Phys. Rept. **510**, 119-200 (2012) [arXiv:1106.2083 [nucl-th]].
- [39] H. Liu *et al.* [E895], Sideward flow in Au + Au collisions between 2-A-GeV and 8-A-GeV, Phys. Rev. Lett. **84**, 5488-5492 (2000) [arXiv:nucl-ex/0005005 [nucl-ex]].
- [40] P. Chung *et al.* [E895], Antiflow of K0(s) mesons in 6-A-GeV Au + Au collisions, Phys. Rev. Lett. **85**, 940-943 (2000) [arXiv:nucl-ex/0101003 [nucl-ex]].
- [41] S. Pal, C. M. Ko, Z. w. Lin and B. Zhang, Antiflow of kaons in relativistic heavy ion collisions, Phys. Rev. C **62**, 061903 (2000) [arXiv:nucl-th/0009018 [nucl-th]].
- [42] P. Danielewicz, R. Lacey and W. G. Lynch, Determination of the equation of state of dense matter, Science **298**, 1592-1596 (2002) [arXiv:nucl-th/0208016 [nucl-th]].
- [43] V. N. Russkikh and Y. B. Ivanov, Collective flow in heavy-ion collisions from AGS to SPS, Phys. Rev. C **74**, 034904 (2006) [arXiv:nucl-th/0606007 [nucl-th]].
- [44] P. K. Sahu and W. Cassing, Differential flow of protons in Au+Au collisions at AGS energies, Nucl. Phys. A **712**, 357-369 (2002) [arXiv:nucl-th/0208002 [nucl-th]].
- [45] M. Isse, A. Ohnishi, N. Otuka, P. K. Sahu and Y. Nara, Mean-field effects on collective flows in high-energy heavy-ion collisions from AGS to SPS energies, Phys. Rev. C **72**, 064908 (2005) [arXiv:nucl-th/0502058 [nucl-th]].
- [46] Y. B. Ivanov, V. N. Russkikh and V. D. Toneev, Relativistic heavy-ion collisions within 3-fluid hydrodynamics: Hadronic scenario, Phys. Rev. C **73**, 044904 (2006) [nucl-th/0503088].
- [47] Y. B. Ivanov, Alternative Scenarios of Relativistic Heavy-Ion Collisions: I. Baryon Stopping, Phys. Rev. C **87**, no.6, 064904 (2013) [arXiv:1302.5766 [nucl-th]].
- [48] A. Sorensen, K. Agarwal, K. W. Brown, Z. Chajewski, P. Danielewicz, C. Drischler, S. Gandolfi, J. W. Holt, M. Kaminski and C. M. Ko, *et al.* Dense nuclear matter equation of state from heavy-ion collisions, Prog. Part. Nucl. Phys. **134**, 104080 (2024) [arXiv:2301.13253 [nucl-th]].
- [49] P. Batyuk *et al.*, Event simulation based on three-fluid hydrodynamics for collisions at energies available at the Dubna Nuclotron-based Ion Collider Facility and at the Facility for Antiproton and Ion Research in Darmstadt, Phys. Rev. C **94**, 044917 (2016) [arXiv:1608.00965 [nucl-th]].
- [50] P. Batyuk, D. Blaschke, M. Bleicher, Y. B. Ivanov, I. Karpenko, L. Malinina, S. Merts, M. Nahrgang, H. Petersen and O. Rogachevsky, Three-fluid Hydrodynamics-based Event Simulator Extended by UrQMD final State interactions (THESEUS) for FAIR-NICA-SPSBES/RHIC energies, EPJ Web Conf. **182**, 02056 (2018) [arXiv:1711.07959 [nucl-th]].
- [51] M. Kozhevnikova, Y. B. Ivanov, I. Karpenko, D. Blaschke and O. Rogachevsky, Update of the Three-fluid Hydrodynamics-based Event Simulator: light-nuclei production in heavy-ion collisions, Phys. Rev. C **103**, no.4,

- 044905 (2021) [arXiv:2012.11438 [nucl-th]].
- [52] V. N. Russkikh and Yu. B. Ivanov, Dynamical freeze-out in 3-fluid hydrodynamics, *Phys. Rev. C* **76**, 054907 (2007) [nucl-th/0611094].
- [53] Yu. B. Ivanov and V. N. Russkikh, On freeze-out problem in relativistic hydrodynamics, *Phys. Atom. Nucl.* **72**, 1238 (2009) [arXiv:0810.2262 [nucl-th]].
- [54] S. A. Bass, C. Hartnack, H. Stoecker and W. Greiner, Out-of-plane pion emission in relativistic heavy ion collisions: Spectroscopy of Delta resonance matter, *Phys. Rev. Lett.* **71**, 1144-1147 (1993)
- [55] H. Heiselberg and A. M. Levy, Elliptic flow and HBT in noncentral nuclear collisions, *Phys. Rev. C* **59**, 2716-2727 (1999) [arXiv:nucl-th/9812034 [nucl-th]].
- [56] H. Liu, S. Panitkin and N. Xu, Event anisotropy in high-energy nucleus-nucleus collisions, *Phys. Rev. C* **59**, 348-353 (1999) [arXiv:nucl-th/9807021 [nucl-th]].
- [57] H. Sorge, Elliptical flow: A Signature for early pressure in ultrarelativistic nucleus-nucleus collisions, *Phys. Rev. Lett.* **78**, 2309-2312 (1997) [arXiv:nucl-th/9610026 [nucl-th]].
- [58] P. Danielewicz, R. A. Lacey, P. B. Gossiaux, C. Pinkenburg, P. Chung, J. M. Alexander and R. L. McGrath, Disappearance of elliptic flow: a new probe for the nuclear equation of state, *Phys. Rev. Lett.* **81**, 2438-2441 (1998) [arXiv:nucl-th/9803047 [nucl-th]].
- [59] Y. B. Ivanov and A. A. Soldatov, Elliptic Flow in Heavy-Ion Collisions at Energies $\sqrt{s_{NN}} = 2.7-39$ GeV, *Phys. Rev. C* **91**, no.2, 024914 (2015) [arXiv:1401.2265 [nucl-th]].
- [60] Y. B. Ivanov, Alternative Scenarios of Relativistic Heavy-Ion Collisions: II. Particle Production, *Phys. Rev. C* **87**, no.6, 064905 (2013) [arXiv:1304.1638 [nucl-th]].
- [61] Y. B. Ivanov, Alternative Scenarios of Relativistic Heavy-Ion Collisions: III. Transverse Momentum Spectra, *Phys. Rev. C* **89**, no.2, 024903 (2014) [arXiv:1311.0109 [nucl-th]].
- [62] I. N. Mishustin, V. N. Russkikh and L. M. Satarov, Fluid dynamical model of relativistic heavy ion collision, *Sov. J. Nucl. Phys.* **54**, 260-314 (1991).
- [63] A. S. Khvorostukin, V. V. Skokov, V. D. Toneev and K. Redlich, Lattice QCD constraints on the nuclear equation of state, *Eur. Phys. J. C* **48**, 531 (2006) [nucl-th/0605069].
- [64] Y. B. Ivanov and A. A. Soldatov, Equilibration and baryon densities attainable in relativistic heavy-ion collisions, *Phys. Rev. C* **101**, no.2, 024915 (2020) [arXiv:1911.10872 [nucl-th]].
- [65] Y. Aoki, G. Endrodi, Z. Fodor, S. D. Katz and K. K. Szabo, The Order of the quantum chromodynamics transition predicted by the standard model of particle physics, *Nature* **443**, 675-678 (2006) [arXiv:hep-lat/0611014 [hep-lat]].
- [66] S. Borsanyi, Z. Fodor, J. N. Guenther, R. Kara, S. D. Katz, P. Parotto, A. Pasztor, C. Ratti and K. K. Szabo, QCD Crossover at Finite Chemical Potential from Lattice Simulations, *Phys. Rev. Lett.* **125**, no.5, 052001 (2020) [arXiv:2002.02821 [hep-lat]].
- [67] Z. Fodor, Lattice QCD results at finite temperature and density, *Nucl. Phys. A* **715**, 319-328 (2003) [arXiv:hep-lat/0209101 [hep-lat]].
- [68] F. Csikor, G. I. Egri, Z. Fodor, S. D. Katz, K. K. Szabo and A. I. Toth, Equation of state at finite temperature and chemical potential, lattice QCD results, *JHEP* **05**, 046 (2004) [arXiv:hep-lat/0401016 [hep-lat]].
- [69] F. Karsch, E. Laermann and A. Peikert, Quark mass and flavor dependence of the QCD phase transition, *Nucl. Phys. B* **605**, 579-599 (2001) [arXiv:hep-lat/0012023 [hep-lat]].
- [70] W. Cassing and E. L. Bratkovskaya, Parton-Hadron-String Dynamics: an off-shell transport approach for relativistic energies, *Nucl. Phys. A* **831**, 215-242 (2009) [arXiv:0907.5331 [nucl-th]].
- [71] H. G. Baumgardt, J. U. Schott, Y. Sakamoto, E. Schopper, H. Stoecker, J. Hofmann, W. Scheid and W. Greiner, Shock Waves and MACH Cones in Fast Nucleus-Nucleus Collisions, *Z. Phys. A* **273**, 359-371 (1975)
- [72] H. Stoecker, Collective flow signals the quark gluon plasma, *Nucl. Phys. A* **750**, 121-147 (2005) [arXiv:nucl-th/0406018 [nucl-th]].
- [73] A. M. Poskanzer and S. A. Voloshin, Methods for analyzing anisotropic flow in relativistic nuclear collisions, *Phys. Rev. C* **58**, 1671-1678 (1998) [arXiv:nucl-ex/9805001 [nucl-ex]].
- [74] P. Danielewicz and G. Odyniec, Transverse Momentum Analysis of Collective Motion in Relativistic Nuclear Collisions, *Phys. Lett. B* **157**, 146-150 (1985) [arXiv:2109.05308 [nucl-th]].
- [75] M. Bleicher, E. Zabrodin, C. Spieles, S. A. Bass, C. Ernst, S. Soff, L. Bravina, M. Belkacem, H. Weber and H. Stoecker, *et al.* Relativistic hadron hadron collisions in the ultrarelativistic quantum molecular dynamics model, *J. Phys. G* **25**, 1859-1896 (1999) [arXiv:hep-ph/9909407 [hep-ph]].
- [76] T. Song, L. Tolos, J. Wirth, J. Aichelin and E. Bratkovskaya, In-medium effects in strangeness production in heavy-ion collisions at (sub)threshold energies, *Phys. Rev. C* **103**, no.4, 044901 (2021) [arXiv:2012.05589 [nucl-th]].
- [77] W. Zwermann and B. Schurmann, THE INCLUSIVE PRODUCTION OF KAONS IN RELATIVISTIC NUCLEUS NUCLEUS COLLISIONS BASED ON TRANSPORT THEORY, *Nucl. Phys. A* **423**, 525-553 (1984)
- [78] V. N. Russkikh and Y. B. Ivanov, Kaon production in intermediate-energy nuclear collisions, *Nucl. Phys. A* **543**, 751-766 (1992)
- [79] L. Tolos and L. Fabbietti, Strangeness in Nuclei and Neutron Stars, *Prog. Part. Nucl. Phys.* **112**, 103770 (2020) [arXiv:2002.09223 [nucl-ex]].
- [80] W. Cassing, V. P. Konchakovski, A. Palmese, V. D. Toneev and E. L. Bratkovskaya, Parton/hadron dynamics in heavy-ion collisions at FAIR energies, *EPJ Web Conf.* **95**, 01004 (2015) [arXiv:1408.4313 [nucl-th]].
- [81] G. Q. Li, C. M. Ko and X. S. Fang, Subthreshold anti-kaon production in nucleus-nucleus collisions, *Phys. Lett. B* **329**, 149-156 (1994)
- [82] J. Schaffner, A. Gal, I. N. Mishustin, H. Stoecker and W. Greiner, Kaon effective mass and energy in dense nuclear matter, *Phys. Lett. B* **334**, 268-274 (1994)
- [83] E. E. Kolomeitsev, B. Kampfer and D. N. Voskresensky, Kaon polarization in nuclear matter, *Nucl. Phys. A* **588**, 889-917 (1995)
- [84] E. E. Kolomeitsev and D. N. Voskresensky, Negative kaons in dense baryonic matter, *Phys. Rev. C* **68**, 015803 (2003) [arXiv:nucl-th/0211052 [nucl-th]].
- [85] <http://ckp.nrcki.ru/>
- [86] http://hlit.jinr.ru/supercomputer_govorun/

Double Deeply Virtual Compton Scattering at Jefferson Lab Hall A

Marie Boër^{a,*} and Debaditya Biswas^a

^aVirginia Tech,
Blacksburg, VA, USA.

E-mail: mboer@jlab.org

This paper presents our project and perspectives to measure for the first time beam spin asymmetries from Double Deeply Virtual Compton Scattering in the $eP \rightarrow e'P'\mu^+\mu^-$ reaction at Jefferson Lab. Our goal is to constrain the so-called Generalized Parton Distribution (GPDs) in a kinematic region that isn't accessible from other reactions, such as Deeply Virtual Compton Scattering, to allow for their extrapolation to "zero skewness", i.e. at a specific kinematic point enabling for tomographic interpretations of the nucleon's partonic structure. We are discussing DDVCS phenomenology and our approach, as well as our experimental project aimed at complementing the SoLID experiment at JLab Hall A with a new muon detector.

25th International Spin Physics Symposium (SPIN 2023)
24-29 September 2023
Durham, NC, USA

*Speaker

1. Introduction

The so-called Generalized Parton Distribution (GPDs) [1, 2] are matrix elements parametrizing the soft structure of the nucleon in “Hard Exclusive” reactions [3, 4]. GPDs contain information on the longitudinal momentum versus transverse position of the partons (quarks and gluons) [5, 6]. We have been studying GPDs for the last ~30 years as we are looking to move towards multidimensional images of the nucleon structure. One of the interesting interpretations of GPDs is the possibility to access tomographic views of the nucleon, where we can relate the transverse position of the partons to the quark and gluon densities [7]. This kind of interpretation relies on extrapolations of GPDs to certain kinematics that can’t be accessed experimentally, and on models, referred to as “zero skewness” [8], i.e. reactions where all the momentum transferred to the nucleon is purely transverse. Our goal is to study Double Deeply Virtual Compton Scattering to constrain the GPDs at this limit.

“Hard Exclusive” reactions refers to: a “hard scale” of at least 1 GeV^2 , allowing for factorization between a soft part parametrized by the GPDs, and a hard part, calculable [9]; “exclusivity” refers to all products of the reaction being known, enabling measurement of the total momentum transfer to the nucleon (we use Mandelstam variable “ t ”, the squared momentum transfer). Fig.1 is the general Compton-like process, where a photon is scattered off a quark in the nucleon. We display the factorization lane, the bottom part representing the GPDs. The incoming and scattered photons have to be of different virtuality to allow for a non-zero momentum exchange to the nucleon. We can distinguish between 3 particular cases of “Compton Scattering”: Deeply Virtual Compton Scattering (DVCS), where the incoming photon is virtual (spacelike) and the outgoing one is real; Timelike Compton Scattering (TCS), where the incoming photon is real and the outgoing one is virtual, subsequently decaying into a lepton pair; and Double Deeply Virtual Compton Scattering (DDVCS), where both photons are virtual. DVCS has been measured at multiple facilities [10–25], TCS has recently been measured for the first time at JLab [26], DDVCS has never been measured.

There are several GPDs, for quarks and gluons, and to account for relative helicity states of the quark-nucleon system. At leading order and leading twist (lowest order in photon’s virtuality related to extra-gluon exchanges), for a spin 1/2 nucleon, we have 4 (x2 for quarks and gluons) chiral-even GPDs, and 4 (x2) chiral-odd GPDs (with quark helicity flip), i.e. 16 total (see for instance [5, 27]). These GPDs depend on 3 variables: t , x (nucleon’s longitudinal momentum fraction carried by the parton), ξ (“skewness”, related to the longitudinal momentum transfer to the quark in light cone frame). We will neglect here their evolution with the photons’ virtuality (namely $Q^2=-q^2$ and/or $Q'^2=q'^2$ for incoming and outgoing photons, respectively, defined from their squared 4-momenta). GPDs can’t be measured directly: we measure Compton Form Factors (CFFs), functions of the GPDs, accessible from fits of cross sections and asymmetries of the various reactions. Most models are currently constrained by measurements of DVCS only, where GPDs can only be accessed at specific kinematic points, for $x=\pm\xi$. TCS being the “time-reversal” equivalent of DVCS at leading order and leading twist [28], it accesses GPDs at the same kinematics. On the other hand, we can vary the relative virtualities of the two photons in DDVCS to access different kinematics, such as $|x| < \xi$ [5, 29, 30]. It is essential to deconvolute these 2 variables and extrapolate the GPDs to $\xi=0$ [8], which is needed for tomographic interpretations.

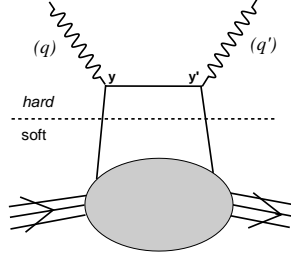


Figure 1: General Compton-like reaction diagram at leading twist, leading order. Dash lane indicates the factorization between a soft part, parameterized by the GPDs and a hard calculable part.

Indeed, one can't directly access the GPDs with DVCS, TCS or DDVCS: we are measuring functions of them, the Compton Form Factors (CFFs), which can be extracted from fitting experimental observables (cross sections, spin or charge asymmetries...). For instance, the CFF \mathcal{H} associated with the GPD H and accessible in DVCS or TCS experiments writes

$$\mathcal{H}(\xi, t) = \sum_q e_q^2 \left\{ \mathcal{P} \int_{-1}^1 dx H^q(x, \xi, t) \left[\frac{1}{\xi - x} - \frac{1}{\xi + x} \right] + i\pi [H^q(\xi, \xi, t) - H^q(-\xi, \xi, t)] \right\} \quad (1)$$

where the sum runs over all parton flavors with elementary electrical charge e_q , and \mathcal{P} indicates the Cauchy principal value of the integral. The imaginary part of the CFF accesses the GPD values at $x = \pm\xi$ and the real part comes in an integral over x . It involves the convolution of parton propagators and the GPD values out-of-the diagonals $x = \pm\xi$ (Fig. 2). Thanks to the virtuality of the final state photon (see section 2), DDVCS provides a way to circumvent this limitation [29, 30], allowing to vary independently x and ξ . Considering the same GPD H , the corresponding CFF for the DDVCS process writes

$$\mathcal{H}(\xi', \xi, t) = \sum_q e_q^2 \left\{ \mathcal{P} \int_{-1}^1 dx H^q(x, \xi, t) \left[\frac{1}{\xi' - x} - \frac{1}{\xi' + x} \right] + i\pi [H^q(\xi', \xi, t) - H^q(-\xi', \xi, t)] \right\} \quad (2)$$

involving an additional scaling variable ξ representing here the GPD skewness. We can therefore explore the GPDs out of the "diagonal" $x = \pm\xi$ (Fig. 2).

2. Phenomenology of DDVCS

DDVCS is measured in the reaction $eN \rightarrow e'N'L^+L^-$, where N is a nucleon, e is a lepton (beam), L^+L^- is a lepton pair coming from the decay of an outgoing virtual photon. At the quark level, the process which occur for DDVCS is: $\gamma_1 N \rightarrow \gamma_2 N'$ (as in Fig. 1). In fact, DDVCS interferes with two Bethe-Heitler like processes ("BH" = BH1 and BH2), where the lepton pair comes from (1) a radiative virtual photon emission from the lepton beam ("BH1") and (2) a lepton pair produced by the exchanged photons ("BH2"). We are representing the different subprocesses Fig. 3: the DDVCS process is displayed at the top, we took the case of an electron beam and a final muon pair; we are displaying the two cases of Bethe-Heitler at the bottom ("BH1" on the left, "BH2" on the right).

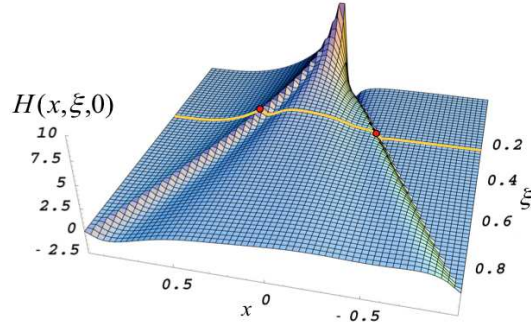


Figure 2: Graphical representation of the DVCS Compton form factor (CFF) showing a typical model for the GPD H at $t=0$; the red points indicates the GPD values involved in the CFF imaginary part, and the yellow line underlines the integral path of the CFF real part.

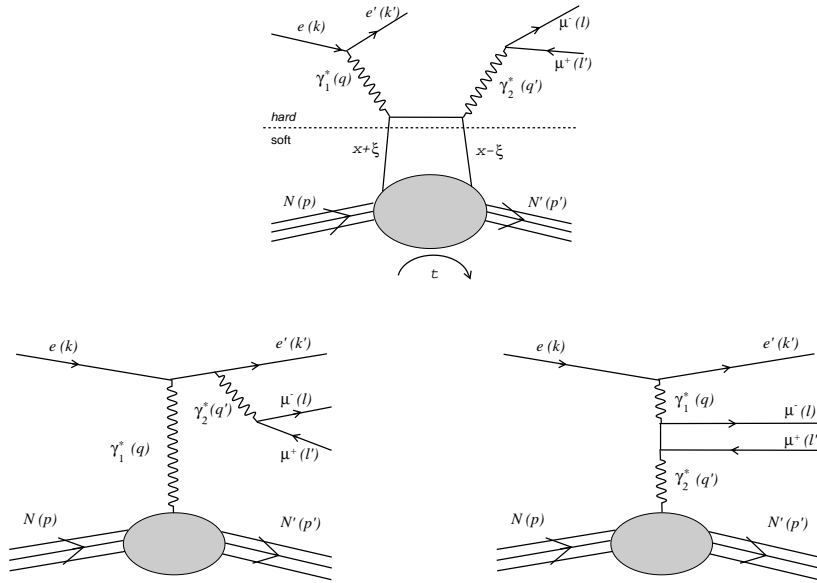


Figure 3: Electroproduction of a muon pair off a quark in a nucleon, at leading order and leading twist (CC not represented). Top: DDVCS process. Bottom left: Bethe-Heitler like process from a radiative virtual photon emission (referred to in this paper as "BH1"). Bottom right: Bethe-Heitler process from exchanged virtual photon conversion (referred to here as "BH2"). We indicated some kinematic variables and 4-momenta as indicated in the text.

Note that crossed diagrams aren't represented. At leading twist and leading order, 6 diagrams interfere in the reaction of electroproduction of a muon pair off a nucleon. We are choosing to study DDCCS+BH in the di-muon channel to avoid concerns in having two electron in the final state (antisymmetrization for the interpretation, particle identification and kinematic reconstruction at the experimental level...), since our available beam at Jefferson Lab (JLab) is an electron beam.

As indicated in Fig.3, we are using here the following notation for the 4-vectors of the different particles involved:

$$e(k) - e'(k') + p(p_1) \equiv \gamma^*(q_1) + p(p_1) \rightarrow p'(p_2) + \gamma^*(q_2) \rightarrow p'(p_2) + \mu^+(l^+) + \mu^-(l^-). \quad (3)$$

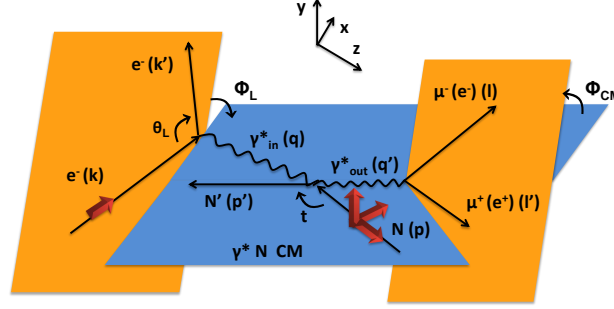


Figure 4: Reference frame, kinematics, angles, for the DDVCS reaction, using notations defined in [29] and our angle's notation.

For our kinematics, we are using the notations defined in [29], expressed in the reference frame represented Fig. 4. The photon virtualities (incoming and outgoing, respectively) are defined as

$$Q^2 = -q^2; \quad Q'^2 = q'^2. \quad (4)$$

We define the symmetrical momentum variables p and q as

$$q = \frac{1}{2}(q + q'); \quad p = p + p', \quad (5)$$

and the four-momentum transfer to the nucleon $\Delta = p - p' = q - q'$ with $t = \Delta^2$. The DDVCS scaling variables write

$$x_B = -\frac{1}{2} \frac{q_1 \cdot q_1}{p_1 \cdot q_1}; \quad \xi' = -\frac{q \cdot q}{p \cdot q}; \quad \xi = \frac{\Delta \cdot q}{p \cdot q}. \quad (6)$$

The symmetrical momentum q can be decomposed as

$$q^2 = -\frac{1}{2} \left(Q^2 - Q'^2 + \frac{\Delta^2}{2} \right). \quad (7)$$

We can decompose the skewness variables in terms of virtualities and Δ :

$$\xi = \frac{Q^2 - Q'^2 + (\Delta^2/2)}{2(Q^2/x_B) - Q^2 - Q'^2 + \Delta^2}, \quad \xi' = -\frac{Q^2 + Q'^2}{2(Q^2/x_B) - Q^2 - Q'^2 + \Delta^2}, \quad (8)$$

which expresses GPDs variables of interest (ξ , ξ' , t) in terms of experimentally measured quantities. Note that the different Q'^2 -dependence in the numerators of ξ and ξ' expresses the ability to access out-of diagonals phase space ($x \neq \xi$) from the "lever arm" in Q^2 versus Q'^2 ; and that for DVCS or TCS, $\xi = \xi'$ (at the asymptotic limit).

We made projections for realistic kinematics accessible at Jefferson Lab, using an 11 GeV electron beam, cuts at $Q^2=1 \text{ GeV}^2$, $Q'^2=4 \text{ GeV}^2$, $Q^2 - Q'^2=1 \text{ GeV}^2$, $W^2 > 2\text{GeV}^2$, $-t < 0.55\text{GeV}^2$, among other kinematic considerations. Neglecting the acceptance effects, we obtained Fig.5, showing how much "off-diagonal" phase space we would be able to cover in an experiment. Red boxes on this figure indicate one proposed binning in t , ξ and ξ' . We decided to exclude the central region ($Q^2 \sim Q'^2$) as it can't be interpreted with our current knowledge (factorization may not hold).

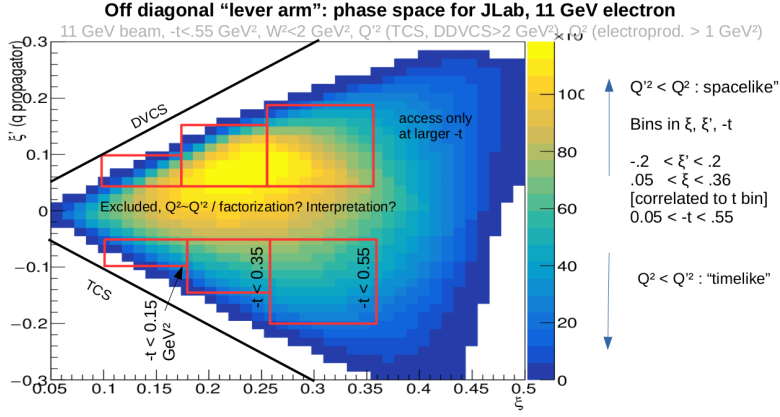


Figure 5: Accessible "off-diagonal" phase-space for DDVCS+BH for experiments at Jefferson Lab. Cuts are indicated on the figure and the main text. Note that the figure (blue/yellow area) integrates our statistics over t : red boxes represent bins in t , where the maximal limits are indicated in the boxes.

3. DDVCS+BH observables and projections

We define as "experimental observables" unpolarized, beam and/or target polarized cross sections and spin asymmetries (normalized difference of 2 relative spin states). At JLab, we would like to measure unpolarized and beam polarized cross sections. CFFs can be extracted from fitting these cross sections. The differential cross section for the electroproduction of muon pair off the nucleon can be written [31]

$$\frac{d^7\sigma}{dx_B dy dt d\phi dQ^2 d\Omega_\mu} = \frac{1}{(2\pi)^3} \frac{\alpha^4}{16} \frac{x_B y}{Q^2 \sqrt{1+\varepsilon^2}} \sqrt{1 - \frac{4m_\mu^2}{Q^2}} |\mathcal{T}|^2, \quad (9)$$

where the reaction amplitude can generically be expressed as

$$|\mathcal{T}|^2 = |\mathcal{T}_{VCS}|^2 + \mathcal{I}_1 + \mathcal{I}_2 + |\mathcal{T}_{BH_1}|^2 + |\mathcal{T}_{BH_2}|^2 + \mathcal{T}_{BH_{12}}, \quad (10)$$

with the pure DDVCS amplitude $|\mathcal{T}_{VCS}|^2$, the interference amplitudes \mathcal{I}_1 and \mathcal{I}_2 between the DDVCS and two Bethe-Heitler sub-processes, and the pure BH amplitude built itself from the two elementary BH subprocesses. We refer to [31] for more details on the harmonic structure of these amplitudes.

The interference amplitude between the BH and DDVCS processes is an observable of interest since it involves linear combinations of Compton form factors. The imaginary part of the amplitudes can be accessed directly via beam spin asymmetries. Not only beam spin asymmetries are easier to measure than cross sections, but "pure" Bethe-Heitler terms in the amplitude cancel in beam spin asymmetries (at the numerator), leading to a better sensitivity to the CFFs and GPDs. Considering the harmonic dependence of the cross section, it was shown [31] that the same basic information about GPDs can be obtained from the appropriate moments in ϕ or φ_μ , a feature of particular interest for experimental consistency. Taking advantage of the symmetry properties of the BH propagators to minimize the BH contribution, the first ϕ -moment and φ_μ -moment of the beam spin asymmetry

can be written [31]

$$\begin{aligned} \begin{pmatrix} A_{LU}^{\sin \phi} \\ A_{LU}^{\sin \varphi_\mu} \end{pmatrix} &= \frac{1}{\mathcal{N}} \int_{\pi/4}^{3\pi/4} d\theta_\mu \int_0^{2\pi} d\varphi_\mu \int_0^{2\pi} d\phi \begin{pmatrix} 2 \sin \phi \\ 2 \sin \varphi_\mu \end{pmatrix} \frac{d^7\vec{\sigma} - d^7\overleftarrow{\sigma}}{dx_B dy dt d\phi dQ'^2 d\Omega_\mu} \\ &\propto \Im \left\{ F_1 \mathcal{H} - \frac{t}{4M_N^2} F_2 \mathcal{E} + \xi' (F_1 + F_2) \tilde{\mathcal{H}} \right\}, \end{aligned} \quad (11)$$

where F_1 and F_2 are the proton's form factors, \mathcal{H} , $\tilde{\mathcal{H}}$, \mathcal{E} are the CFFs depending on GPDs H , \tilde{H} , E , respectively, and with the normalization factor given by

$$\mathcal{N} = \int_{\pi/4}^{3\pi/4} d\theta_\mu \int_0^{2\pi} d\varphi_\mu \int_0^{2\pi} d\phi \frac{d^7\vec{\sigma} + d^7\overleftarrow{\sigma}}{dx_B dy dt d\phi dQ'^2 d\Omega_\mu}, \quad (12)$$

and where we omit for clarity the (ξ', ξ, t) -dependence of the CFFs. In the case of a proton target the measurement gives access to the "out-of diagonal" kinematic dependencies of GPD H (dominant term).

We display in this section some of our projections made for JLab kinematics. Calculations are made from VGG model for GPDs [32], based on the DDVCS calculations from [29], with modifications. Our kinematic studies are performed with our event generator. Fig. 6 displays the differential cross section and the beam spin asymmetry A_{LU} for two relevant kinematics for the determination of GPDs that we aim at measuring at JLab, in Hall A. These experimental observables have been obtained using the prescription of Eq. 11 for the integration over the angular phase space of the di-muon pair. Sizeable asymmetries are predicted together with, as expected, a strong sensitivity of the cross section to kinematic conditions. Since the azimuthal and polar angle of the final muon pair are strongly correlated to each other and to the rate of BH (especially "BH2") in the full DDVCS+BH reaction, we calculated the unpolarized cross section (Fig. 7, left) and beam spin asymmetry (right) at different θ_μ . The "actual" observables that will be used for the extraction of the CFFs are unpolarized cross sections and beam spin asymmetries, differential in the initial and final azimuthal angles, integrated over the final polar angle. Extremes values in θ are cut out from this integral ($40 \leq \theta_\mu \leq 140^\circ$), due to the large BH dominance in these regions coming from the peaks induced by the "BH2" diagrams.

4. Measuring DDVCS with the SoLID spectrometer at JLab Hall A

Different projects exist at JLab to measure DDVCS in Halls A, B, C. The project presented in this paper is based on our letter of intent [33], submitted in 2023, and aiming at measuring the DDVCS+BH beam spin asymmetries with a slightly modified version of the SoLID (future) spectrometer. The projections presented in this section are based on this LOI. Our idea is to supplement the SoLID spectrometer [34], as in its setup approved for the J/Ψ experiment [35], with a dedicated muon detector, also serving as trigger. We are displaying our full setup, from GEANT4 simulations, Fig. 8 (left). The additional muon detector is shown Fig. 8 (right), and made of an alternance of 3 layers of iron (for shielding), 3 layers of straw tubes (for tracking), then 2 layers of plastic scintillators at the back-end to trigger on the muon pair. The iron plates will be coming from CLEO-II.

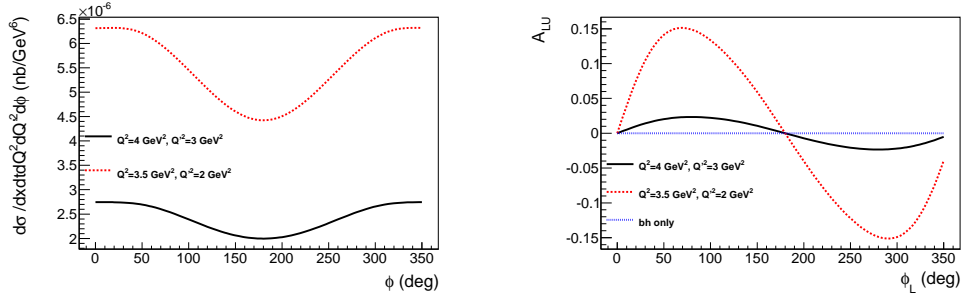


Figure 6: Out-of-plane angular dependence of the differential cross section (left) and the beam spin asymmetry (right) for the $eP \rightarrow e'p\mu^+\mu^-$ process at $E=11 \text{ GeV}$, $x_B=0.25$, $t=-0.4 \text{ GeV}^2$, and different virtual photon masses.

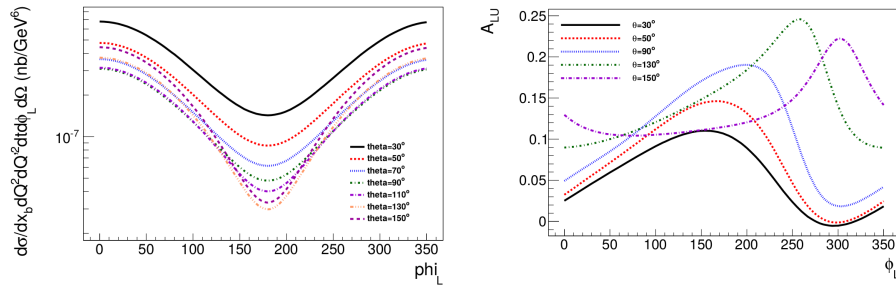


Figure 7: Out-of-plane angular dependence of the differential cross section for various polar angles of the muon (left) and for the differential beam spin asymmetry (right)

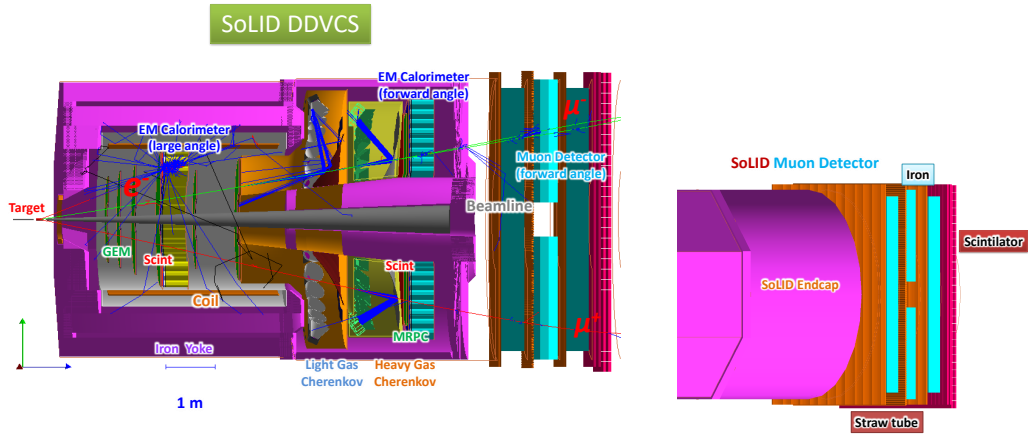


Figure 8: Left: SoLID DDVCS with the forward angle muon detector added to the $J\psi$ setup [35]. Right: Preliminary design of SoLID muon detector at forward angle in Geant4 simulation.

SoLID is designed to use a solenoid field and allows to carry out experiments with high energy ~ 11 GeV electron beams on unpolarized and polarized targets at luminosities of up to $L = 10^{37}$ cm $^{-2}$ sec $^{-1}$ in an open geometry. The solenoid field, reaching about 1.4T is provided by re-using the CLEO-II magnet. Part of the CLEO-II iron flux return will be modified and reused, and two new iron endcaps will be added at the front and back of the solenoid. Forward angle detectors cover polar angles from 8.5° to 16° , and consist of planes of Gas Electron Multipliers (GEM) for tracking, a light-gas Cherenkov (LGCC) for e/π separation, a heavy gas Cherenkov (HGCC) for π/K separation, a Multi-gap Resistive Plate Chamber (MRPC) for time-of-flight, and an Electromagnetic Calorimeter (FAEC). Large-angle detectors cover polar angle from 17° to 24.5° and consist of several planes of GEM for tracking, and an Electromagnetic Calorimeter (LAEC).

5. Summary

We presented the motivations and our proposed setup for an experiment aiming at measuring DDVCS+BH with the SoLID spectrometer at JLab Hall A, supplemented by new muon detectors. The DDVCS+BH azimuthal dependencies of the beam spin asymmetries are sensitive to the imaginary part of the amplitudes and to the interference between DDVCS and BH. DDVCS has never been measured, and accessing CFFs from its observables will enable, for the first time, to deconvolute the proton's and quark's momenta, which is essential for tomographic interpretations of the GPDs.

Acknowledgements: The authors would like to thank, in alphabetic order, for their inputs or contributions, S. Alavarado, A. Camsonne, R. Gilman, M. Guidal, E. Voutier, S. Zhao, Z. Zhao. We also would like to thank all the members of the SoLID collaboration. This work is supported by the Virginia Tech Physics Department.

References

- [1] D. Müller, D. Robaschick, B. Geyer, F.M. Dittes, J. Hořejši, Fortschr. Phys. **42**, 101 (1994).
- [2] X. -D. Ji, Phys. Rev. D **55**, 7114 (1997)
- [3] X. Ji, Phys. Rev. Lett. **78**, 610 (1997).
- [4] A.V. Radyushkin, Phys. Rev. **D 56**, 5524 (1997).
- [5] M. Diehl, Phys. Rep. **388**, 41 (2003).
- [6] A. V. Belitsky, A. V. Radyushkin, Phys. Rept. **418**, 1 (2005).
- [7] M. Burkardt, Phys.Rev.D 66 (2002) 114005
- [8] Y. Guo, X. Ji, G. Santiago, G. Shiells, J. Yangl, JHEP 05 (2023) 150
- [9] J. C. Collins and A. Freund, Phys. Rev. D 59 (1999) 074009.
- [10] (H1 Collaboration) C. Adloff *et al.*, Phys. Lett. B **517**, 47 (2001).

- [11] (HERMES Collaboration) A. Airapetian *et al.*, Phys. Rev. Lett. **87**, 182001 (2001).
- [12] (CLAS Collaboration) S. Stepanyan *et al.*, Phys. Rev. Lett. **87**, 182002 (2001).
- [13] (ZEUS Collaboration) S. Chekanov *et al.*, Phys. Lett. B **573**, 46 (2003).
- [14] (CLAS Collaboration) S. Chen *et al.*, Phys. Rev. Lett. **97**, 072002 (2006).
- [15] (Hall A DVCS Collaboration) C. Muñoz Camacho *et al.*, Phys. Rev. Lett. **97**, 262002 (2006).
- [16] (HERMES Collaboration) A. Airapetian *et al.*, Phys. Rev. D **75**, 011103 (2007).
- [17] (HERMES Collaboration) A. Airapetian *et al.*, JHEP **06**, 066 (2008).
- [18] (CLAS Collaboration) F.X. Girod *et al.*, Phys. Rev. Lett. **100**, 162002 (2008).
- [19] (HERMES Collaboration) A. Airapetian *et al.*, JHEP **06**, 019 (2010).
- [20] (HERMES Collaboration) A. Airapetian *et al.*, Phys. Lett. B **704**, 15 (2011).
- [21] (CLAS Collaboration) H.S. Jo *et al.*, Phys. Rev. Lett. **115**, 212003 (2015).
- [22] (Hall A DVCS) M. Defurne *et al.*, (Jefferson Lab Hall A), Phys. Rev. C **92** (2015) no.5
- [23] N. Hirlinger Saylor *et al.* (CLAS Collaboration), Phys. Rev. C **98**, 045203 (2018).
- [24] R. Akhunzyanov *et al.*, (COMPASS coll), Phys. Lett. B **793** (2019) 188. (Erratum: Phys.Lett.B **800**, 135129 (2020)).
- [25] F. Georges *et al.* (Jefferson Lab Hall A Collaboration) Phys. Rev. Lett. **128**, 252002
- [26] P. Chatagnon *et al.* (CLAS Collaboration) Phys. Rev. Lett. **127**, 262501 (2022)
- [27] M. Guidal, H. Moutarde and M. Vanderhaeghen, Rept. Prog. Phys. **76**, 066202 (2013)
- [28] E. R. Berger, M. Diehl and B. Pire, EPJC **23** (2002) 675-689
- [29] M. Guidal, M. Vanderhaeghen, Phys. Rev. Lett. **90**, 012001 (2003).
- [30] A. V. Belitsky, D. Müller, Phys. Rev. Lett. **90**, 022001 (2003).
- [31] A. V. Belitsky, D. Müller, Phys. Rev. D **68**, 116005 (2003).
- [32] M. Vanderhaeghen, P.A.M. Guichon, M. Guidal, Phys. Rev. D **60**, 094017 (1999).
- [33] A. Camsonne (contact), M. Boër, E. Voutier, Z. Zhao, LOI PAC 51, DDVCS in SoLID (2023)
- [34] SoLID Pre-Conceptual Design Report (2019)
- [35] Z. Meziani *et al.*, J/Ψ SoLID experiment E12-12-006.

Future measurements of TCS at JLab Hall C

Debaditya Biswas^{a,*} and Marie Boër^a

^aVirginia Tech,
Blacksburg, USA

E-mail: debadityab22@vt.edu, mboer@vt.edu

Generalized parton Distributions (GPDs) are important functions to understand the three dimensional structure of the nucleon. Deeply Virtual Compton Scattering is one of the reaction accessing GPDs, and has been measured for the past ~ 20 years. However, to move forward, we need to look for other reactions, such as Timelike Compton Scattering (TCS), its "time-reversal" equivalent. Indeed, accessing GPDs from both DVCS and TCS independently will allow us, for instance, to study their universality. Any assesment on GPD's universality would be a milestone in our field. In this article we discuss our preliminary studies on the feasibility of measuring unpolarized and beam polarized cross sections and beam spin asymmetry for TCS in the dilepton photoproduction reaction. For that purpose, we use a polarized photon beam and an unpolarized target at JLab Hall C. We will discuss our Geant4 simulations, with a dedicated detector setup along with the use of the SBS magnet for separating outgoing e^+ , e^- pairs.

*25th International Symposium on Spin Physics,
24-29 September 2023
Durham, NC, USA*

*Speaker

1. Introduction

This article discuss our preliminary studies for measuring Timelike Compton Scattering (TCS, displayed Fig 1) at Jefferson Lab Hall C, off an unpolarized Liquid Hydrogen target and a circularly polarized high intensity photon beam. Measuring TCS cross sections and beam spin asymmetries with an unpolarized target, is very important to constrain the Generalized Parton Distribution (GPDs) [1, 2]. GPDs are sensitive to the longitudinal momentum versus transverse position structure of partons (quarks and gluons) in the nucleon [3]. They can't be accessed directly from experiments: we are actually measuring functions of GPDs, called Compton Form Factors (CFFs). There are several GPDs corresponding to different possible relative orientations of the helicity of particles involved in the reaction [4]. In our case, the observables we aim to measure are most sensitive to the GPD "H", the one which is insensitive to the quark and to the nucleon's helicities. GPD H is currently well constrained from DVCS measurements, and this is why we would like to obtain similar measurements from TCS, for a comparison, and for universality studies. Furthermore, GPDs are real functions, but CFFs that we are measuring are complex functions: from DVCS measurements, we better constrain the imaginary part of the CFFs. Our equivalent measurement with TCS is sensitive to both real and imaginary parts, and thus will bring more constraints on the real part of the amplitudes in a multi-channel CFF extraction approach. We refer to articles [5, 6] for the phenomenology of TCS off the proton and projections of observables.

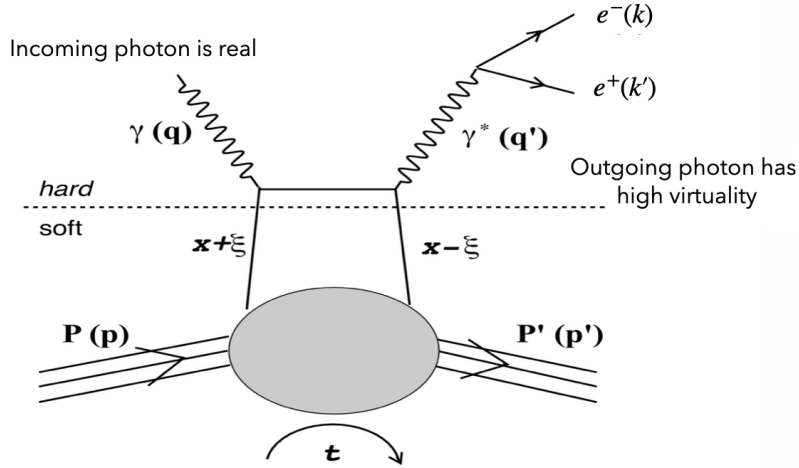


Figure 1: Time Like Compton Scattering (leading order and leading twist, CC not represented).

TCS is measured in the reaction $\gamma P \rightarrow e^+ e^- P'$, where P is a nucleon (a proton here) and e is a lepton (an electron here). It interferes with another process, called Bethe-Heitler (BH) where the lepton pair is produced by a splitting of the incoming photon in the nucleon's field. BH is insensitive to the GPDs. It is parametrized by Form Factors. What we want to measure ("observables") is cross sections (σ) and beam spin asymmetries ($A_{\odot U}$ is mostly sensitive to the interference term in

the TCS+BH amplitude). The beam spin asymmetry is defined as:

$$A_{\odot U} = \frac{\sigma^+ - \sigma^-}{\sigma^+ + \sigma^-}, \quad (1)$$

where \odot represents the beam polarization and U represents the unpolarized target. $+$, $-$ represents the right and left circularly polarized beam respectively. σ is defined as the five differential polarized cross section, which reads

$$\sigma^\pm \equiv \frac{d^5\sigma}{dQ'^2 dt d(\cos\theta) d\phi dE_\gamma}, \quad (2)$$

where Q'^2 is the virtuality of the outgoing photon, t is the squared momentum transfer (Mandelstam variable), θ and ϕ are the polar and azimuthal angles for the scattered electron in the virtual photon's rest frame, relative to the proton-incoming photon's frame. E_γ is the incoming beam energy.

In this paper, we will focus on our experimental setup for the measurement of unpolarized and beam polarized TCS+BH cross sections at JLab Hall C. Our setup is strongly inspired by a similar one, proposed to measure TCS+BH transverse target spin asymmetries off an ammonia target [7].

2. Experimental Setup

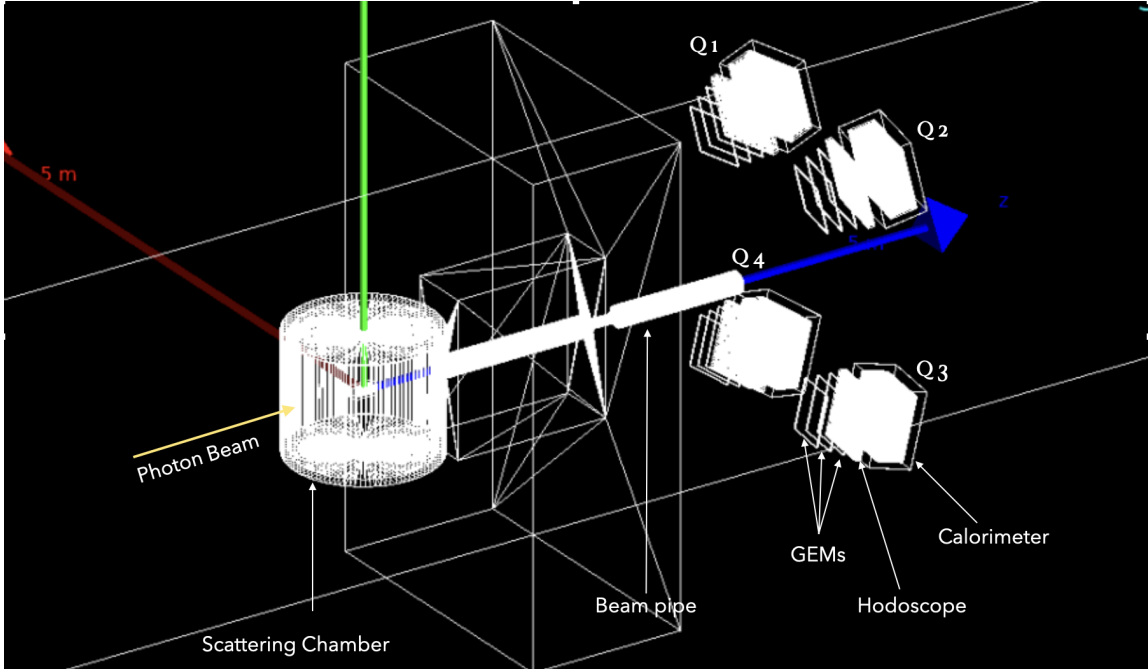


Figure 2: The GEANT4 simulations for the experimental setup for an unpolarized TCS experiment. Q1, Q2, Q3 and Q4 designate four quadrants consisting of the same set of detectors. Each of the four quadrants consists of three layers of GEMs, 3 layers of hodoscopes and an electromagnetic calorimeter. The unpolarized liquid hydrogen target is inside the scattering chamber (on the left). The SBS magnet is shown in between the "quadrants" and the scattering chamber.

To measure unpolarized TCS cross sections at JLab Hall C, we need a dedicated experimental setup. A lot of studies were done for the equivalent polarized TCS case [7], therefore we are replicating part of that setup. Fig 2 shows our Geant4 simulations. The Compact Photon Source (CPS) [8] will be used to generate a high intensity ($\sim 10^{12} \gamma/sec$) circularly polarized photon beam. We are using a 15 cm long liquid hydrogen target, kept inside a scattering chamber. The outgoing particles are an electron, a positron and a recoil proton. To separate the outgoing e^- and e^+ , we placed a magnet in front of the scattering chamber. Q1, Q2, Q3 and Q4 (in Fig. 2) designate four identical "quadrants": each of the four quadrants consists of three layers of GEMs, hodoscopes and electromagnetic calorimeter. For further details about the base setup, see [7]. The electromagnetic calorimeters in each quadrant correspond to $\sim 1/2$ of the surface currently available from the Neutral Particle Spectrometer (NPS) [9], currently used in a DVCS experiment at JLab.

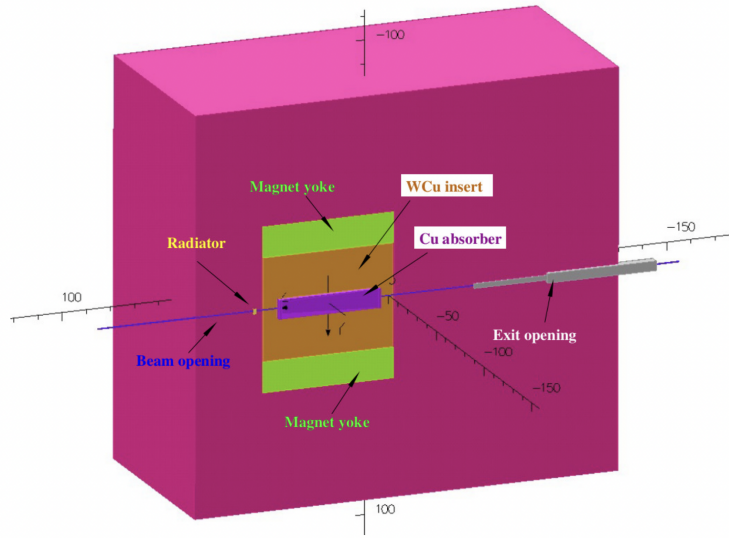


Figure 3: The CPS cut-out side view. Deflected electrons strike a copper absorber, surrounded by a W-Cu insert inside the magnet yoke. The outer rectangular region in this view is the tungsten-powder shield.

2.1 Compact Photon Source (CPS)

The experiment will take advantage of the already approved Compact Photon Source (CPS) for the experiment E12-17-008 [8, 10], to get a pure circularly polarized photon beam. The conceptual design of the CPS is shown in Fig 3. The CPS can generate photons with a flux of $1.5 \times 10^{12} s^{-1}$ with a $2.5 \mu A$ electron beam, for photon energies >5 GeV. The expected spot size of the photon off the target is ~ 1 mm, at 2 m distance of the CPS radiator. For more design details and working principle of CPS, we refer to [12].

2.2 Target

For this experiment, an unpolarized liquid hydrogen target is needed. A 15cm long liquid hydrogen target of Hall C is used in this study. The liquid hydrogen is kept in a 15 cm long aluminum can, and can be seen in the middle of the scattering chamber, in Fig 4. More details

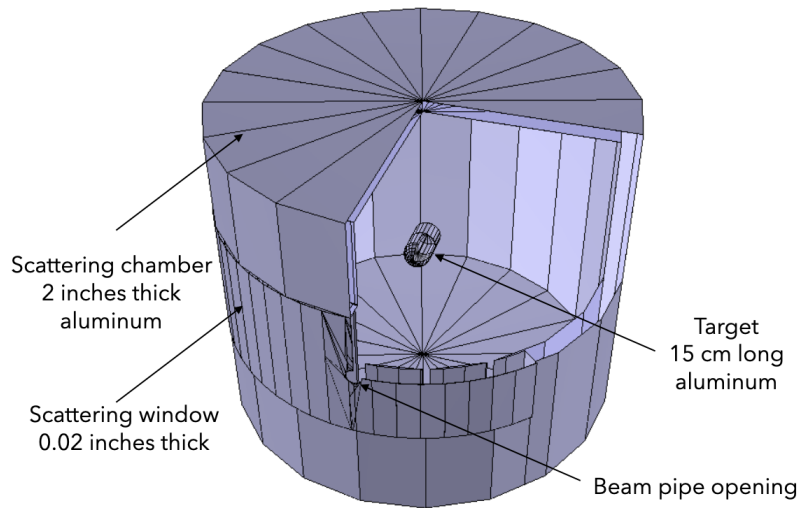


Figure 4: The Geant4 design of the 15 cm long liquid hydrogen, target placed inside the scattering chamber.

about the target geometry can be found in [11]. The target is placed inside the scattering chamber, made of 2 inches thick aluminum wall. The horizontal angular range of the scattering window is from 3.2 deg to 77.0 deg on the High Momentum Spectrometer (HMS, one of the "standard" Hall C detector equipment) side, and from 3.2 deg to 47.0 deg on the Super High Momentum Spectrometer (SHMS, one of the "standard" Hall C detector equipment) side. The thickness of the aluminum for the scattering window is 0.02 inches.

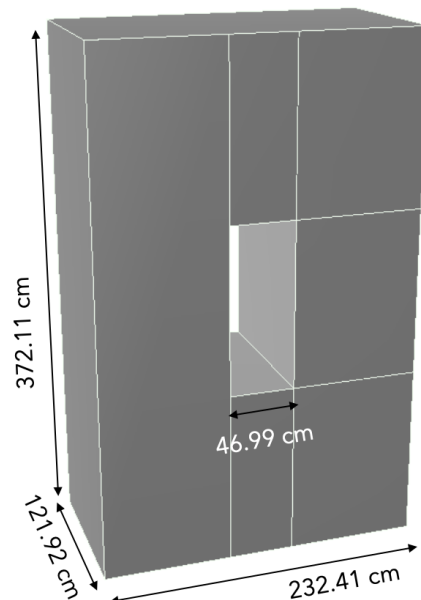


Figure 5: GEANT4 simulation for SBS magnet geometry.

2.3 Magnet

A simple magnet geometry is simulated in Geant4 and placed between the scattering chamber and the detector stack 5. The field strength is $2.4 T\cdot m$ along the x axis (red arrow in Fig 2), with $1.2 m$ long pole as shown in Fig 5. What we eventually want will be to move the Super Big Bite Spectrometer (SBS) magnet from Jlab Hall A into the Hall C, after their experiments. Therefore, we is designed our magnet according to the SBS magnet geometry. We are looking into the possibility of reusing magnets from other experiments as well, to help in cutting the cost of our experiment.

2.4 GEMs

For the reconstruction of the vertex parameters from the track coordinates at the detectors, tracker is needed for the experiment. For this purpose, we put 3 layers of GEMs in our simulations. The GEMs are very useful for the reconstruction of transverse tracks with certainty up to $100 \mu m$. The general knowledge about GEMs assures (compared to other methods of tracking) reliable track reconstruction in the background rates, which we expect to be relatively high (up to $10^6 Hz/mm$ in this experiment). We found that only 2 layers of the GEMs could be enough for the determination of the positions and directions of the tracks, but we decided to put three layers to ensure it's performance in the high background rates and a better particle identification (see studies in [7]).

2.5 Hodoscopes

The detection of recoil protons requires is essential in this experiment, because we are using an untagged photon beam from CPS, therefore are missing it's energy. Indeed, the scattered electron from the primary CEBAF beam is dumped into the CPS magnet. Our secondary photon beam ranges from ~ 5.5 to ~ 11 GeV. We know it's direction (very low scattering angle), but not it's exact energy. This is why, for an exclusive measurement such as TCS, we need to detect absolutely all the outgoing particles. The detection of the protons requires fly's-eye array of scintillators in each of the detector quadrants. The scintillators will be placed just before the NPS calorimeters, and the light sensors need to be coupled at the rear side of the scintillators. Our preliminary results show an optimal size for the scintillators at $2 \times 2 \times 5 cm^3$ for the transverse polarized case. We need to modify this size for our unpolarized TCS experiment, since the magnetic field is different. The proton identifications will require the dE/dX signal from the hodoscopes. The hodoscopes will also be used for the trigger system (from either the lepton pair solely, or all 3 scattered particles). For this experiment, the general idea of the trigger will follow the already proposed polarized TCS experiments. Details on the polarized case we are refering to are in [7].

2.6 Electromagnetic calorimeters

To determine the kinematic variables Q' , ξ , and t , we need to measure the coordinates and the energy of the di-lepton (e^+ , e^-) pair. We are using a highly segmented lead-tungstate calorimeter. As shown in the Fig 2, each of the four detector quadrants has a calorimeter at the end. We plan to use the existing Neutral Particle Spectrometer (NPS) calorimeter (having enough crystals to prepare 2 of our "quadrants"). Our TCS experiment relies on doubling the surface of the NPS, i.e. the total number of crystals. In the polarized TCS [7] experimental setup, for each quadrant we have 23×23 matrix of PbWO4 crystal blocks. Each block has $2.05 \times 2.05 cm^2$ geometrical cross-sections.

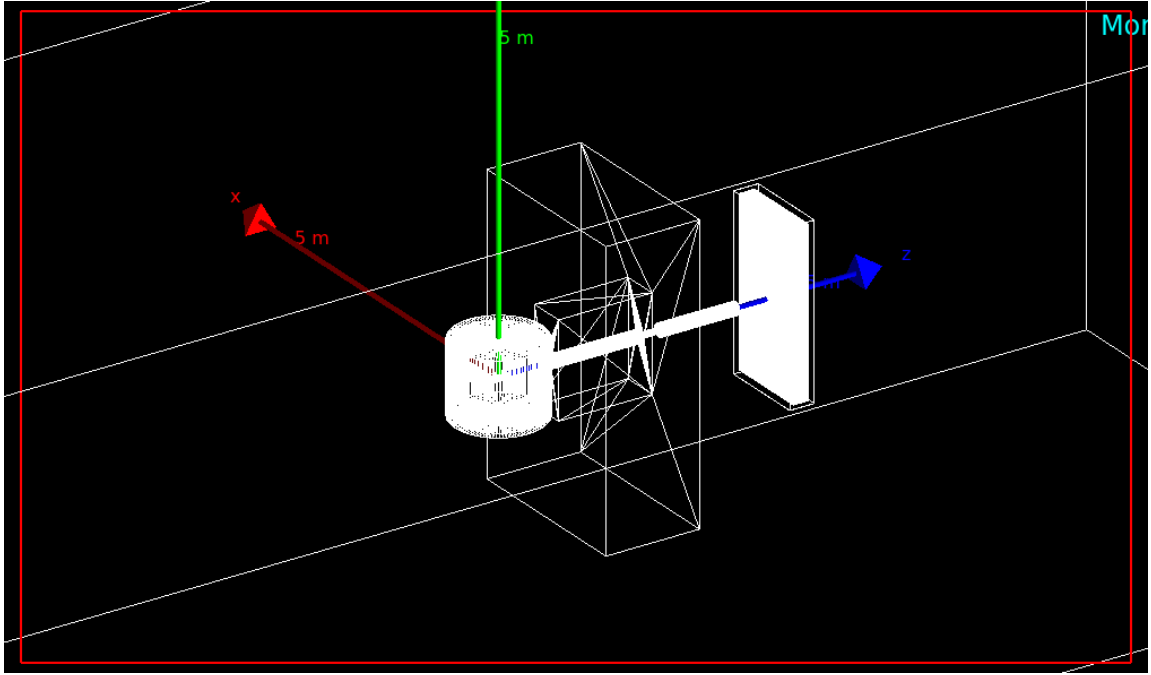


Figure 6: Simple one calorimeter plane unpolarized TCS setup for the preliminary studies.

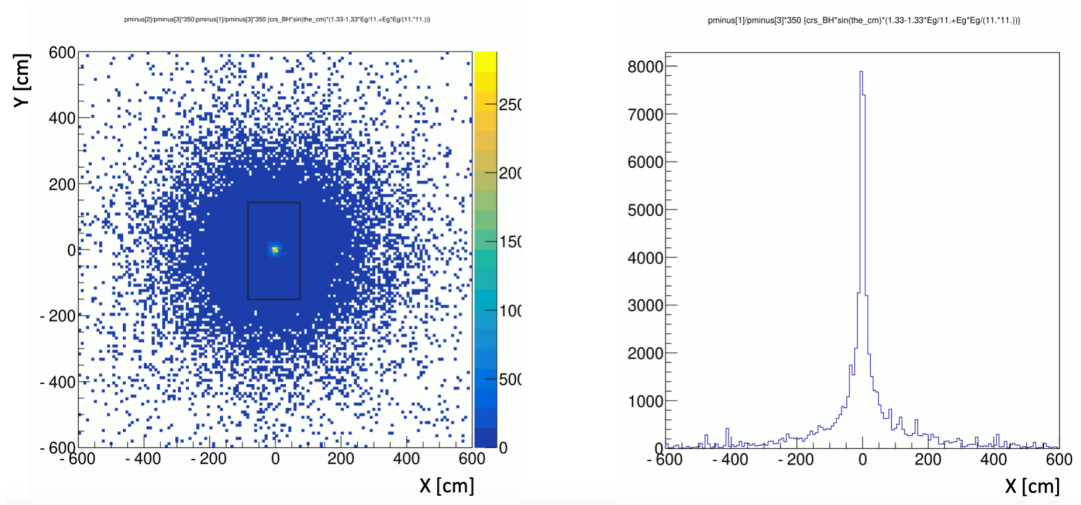
3. Results

At this stage of our studies, we decided to study a simple one plane "calorimetric setup", and check the SBS magnet performances, as shown Fig 6. Here we removed all the detectors that were displayed Fig 2, except for one single plane of calorimeter. The calorimeter plane is placed at the 90 deg with Z axis (parallel to x-y plane), and facing the beam direction. The distance between the center of the target to the face of the calorimeter is ~ 350 cm.

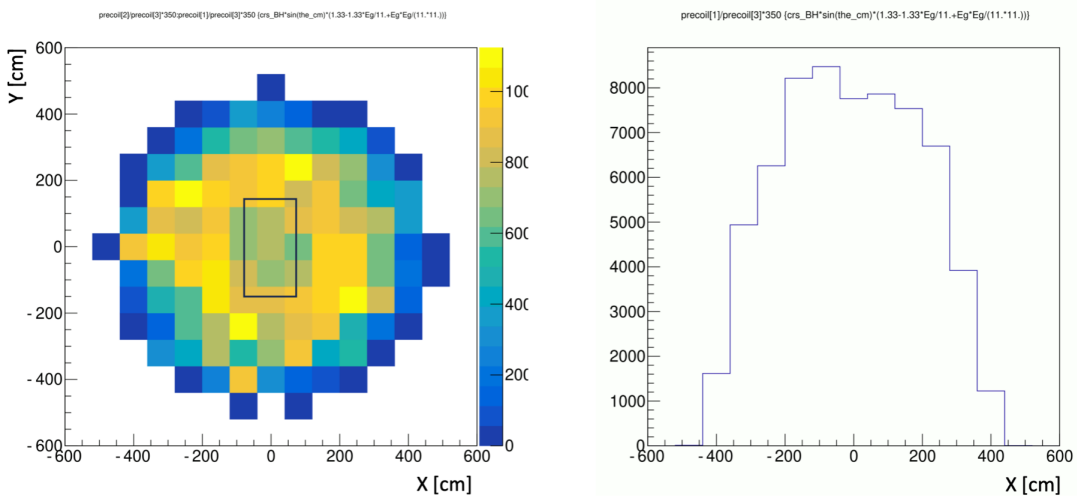
Without any magnetic field, the TCS weighted electron and proton events are projected at the face of the calorimeter. It is evident from Fig 7a that most of the electrons are well within the magnetic bore (black box), i.e. within ± 50 cm in x direction around the center of the calorimeter. So, the chance of SBS iron core blocking the electrons is quite low. As positrons are produced in pair production along with the electrons, we can expect the same positional distributions for them at the face of the calorimeter.

After applying the magnetic field in the magnet, the electrons and positrons are separated and illuminated the different y positions on the calorimeter as shown in the Fig 8a and Fig 8b. As expected there is no separation between the two particles in x direction. Electrons populated the region between column 60 and column 80 of the scintillator segmentation, and the positrons populated the region between column 10 and 35. This clearly shows that our magnetic field simulation is acceptable, and with this setup the electrons and the positrons can be separated in space for particle identification.

As shown in the Fig 7b, even without the magnetic field the protons are not as concentrated in space as the electrons. In the x direction the spread of the proton (without the magnetic field) is as big as -400 cm to $+400$ cm around the center of the calorimeter plane. Here we didn't show the



(a) TCS weighted events for the for electrons, projected at the face of the calorimeter in Fig:6. **No magnetic field** is used in the SBS magnet bore. The black box in the middle shows projected opening of the magnetic bore at the calorimeter face. Same is expected for the positrons. Figures are produced by Vardan Tadevosyan.



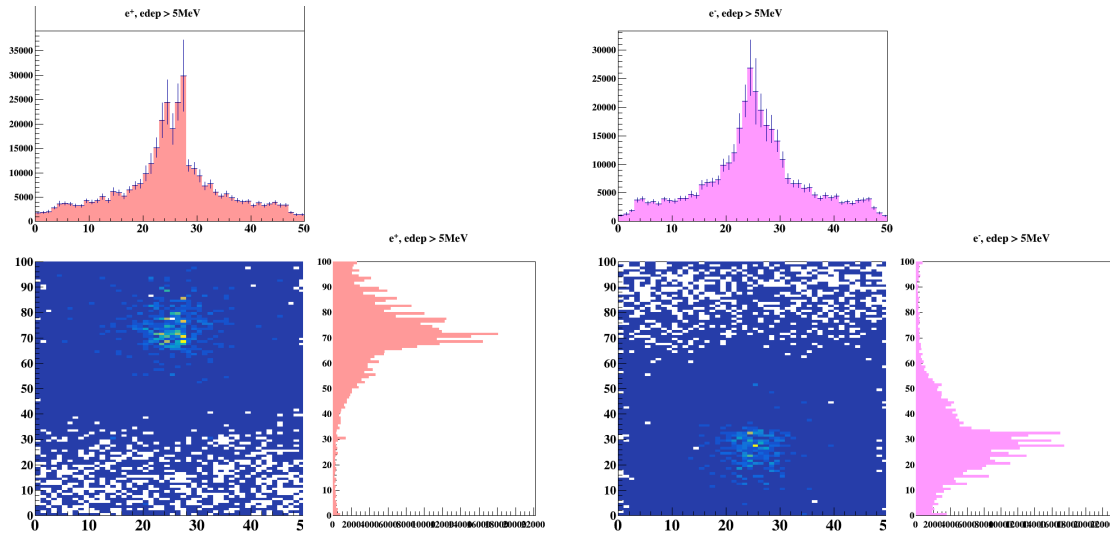
(b) TCS weighted events for the for protons, projected at the face of the calorimeter in Fig:6. **No magnetic field** is used in the SBS magnet bore. The black box in the middle shows projected opening of the magnetic bore at the calorimeter face. Figures are produced by Vardan Tadevosyan.

Figure 7: Projected electron and the proton events at the face of the calorimeter (no magnetic field) in Fig 6.

spread of the protons with the magnetic field in the magnetic bore.

4. Future Work

The work discussed in this paper is still progressing. In the next stage, we aim at getting realistic signal and background rates. We will check if the current opening of the magnetic bore is big enough to detect a sufficient number of protons to conduct our experiment in reasonable amount



(a) TCS weighted events for the for electrons, projected at the face of the calorimeter in Fig:6. $2.4 T$ - m magnetic field is used in the SBS magnet bore. The black box in the middle shows projected opening of the magnetic bore at the calorimeter face.

(b) TCS weighted events for the for protons, projected at the face of the calorimeter in Fig:6. $2.4 T$ - m magnetic field is used in the SBS magnet bore. The black box in the middle shows projected opening of the magnetic bore at the calorimeter face.

Figure 8: Projected electron and the proton events at the face of the calorimeter (with magnetic field) in Fig: 6.

of time. Furthermore, as we are following the basic detector detector geometry of the polarized TCS experiment, we are working together with the proponents of the "polarized case" to the detector design and calculate the full background (physics + experimental) contributions.

5. Summary

We presented our setup to measure unpolarized and beam polarized (circularly) cross sections for the TCS+BH reactions at Hall C in Jefferson Lab. Our work is still ongoing, but our simulators already show that the SBS magnet can be used as a part of the PID process in the di-lepton spectrometer we are proposing. The basic design concept of the experimental setup is very similar to the polarized TCS experiment (already proposed), except the unpolarized target, circularly polarized beam and the SBS magnet added to the setup. We are currently working on optimizing the detectors and the full background simulations. Our goal is to submit a new proposal to the JLab Program Advisor Committee in 2024.

References

- [1] D. Müller, D. Robaschick, B. Geyer, F.M. Dittes, J. Hořejši, Fortschr. Phys. **42**, 101 (1994).
- [2] X. -D. Ji, Phys. Rev. D **55**, 7114 (1997)
- [3] M. Diehl, Phys. Rep. **388**, 41 (2003).
- [4] M. Guidal, H. Moutarde and M. Vanderhaeghen, Rept. Prog. Phys. **76**, 066202 (2013)
- [5] E. R. Berger, M. Diehl and B. Pire, EPJC 23 (2002) 675-689
- [6] M. Boër, M. Guidal and M. Vanderhaeghen, Eur. Phys. J. A 51 (2015) no.8, 103
- [7] Boer, M., Tadevosyan, V., et.al., "Proposal for the PAC 50: Timelike Compton Scattering Off a Transversely Polarized Proton," https://www.jlab.org/exp_prog/proposals/22/C12-18-005.pdf, 2022.
- [8] D. Day et al., Nucl.Instrum.Meth.A 957 (2020) 163429
- [9] Tanja Horn et al. 2015 J. Phys.: Conf. Ser. 587 012048
- [10] Hamilton,G.D., Day,D., Keller, D., Niculescu, G., Wojtsekhowski, B., Zhang, J., "Polarization Observables in Wide-Angle Compton Scattering at large s , t , and u ," https://www.jlab.org/exp_prog/proposals/17/PR12-17-008.pdf, May 2017.
- [11] Woods, S., and Hall C users and staffs, "2019 Version: Jefferson Lab Hall C Standard Equipment Manual," <https://hallcweb.jlab.org/safety-docs/current/Standard-Equipment-Manual.pdf>, 2019.
- [12] Chudakov, E., Day, D., Degtiarenko, P., Ent, R., Hamilton, D.J., Horn, T., Keller, D., Keppel, C., Niculescu, G., Reid, P., Strakovsky, I., Wojtsekhowski, B., Zhang, J., "Documentation of the Conceptual Design of a Compact Photon Source (CPS)," https://wiki.jlab.org/cuawiki/images/1/1c/CPS_document-rev4.1.pdf.